

8.8 NIST Pool Fires

Figure 8.22 displays centerline profiles of mean vertical velocity for 30 cm acetone, ethanol, and methanol pool fires; and 37 cm methane and propane gas burners [363].

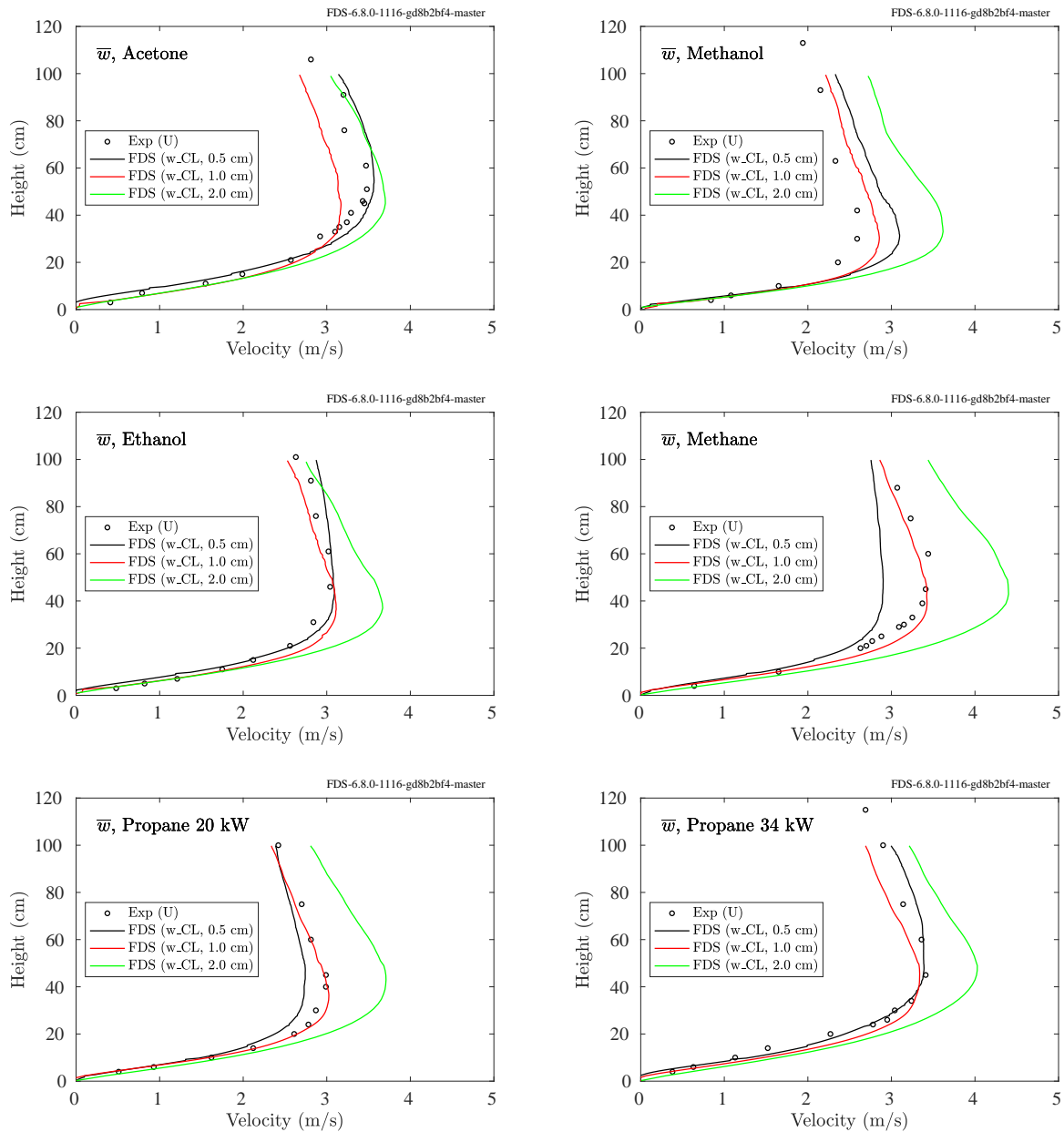


Figure 8.22: NIST Pool Fires, centerline profiles of mean vertical velocity for 30 cm acetone, methanol, and ethanol liquid pool fires, a 37 cm methane fire, and propane fires of 20 kW and 34 kW.

8.9 PRISME DOOR Experiments

Bi-directional probes were placed in the doorway separating the two compartments of the PRISME DOOR experiments. Shown on the plots below are the uppermost and lowest measurement points.

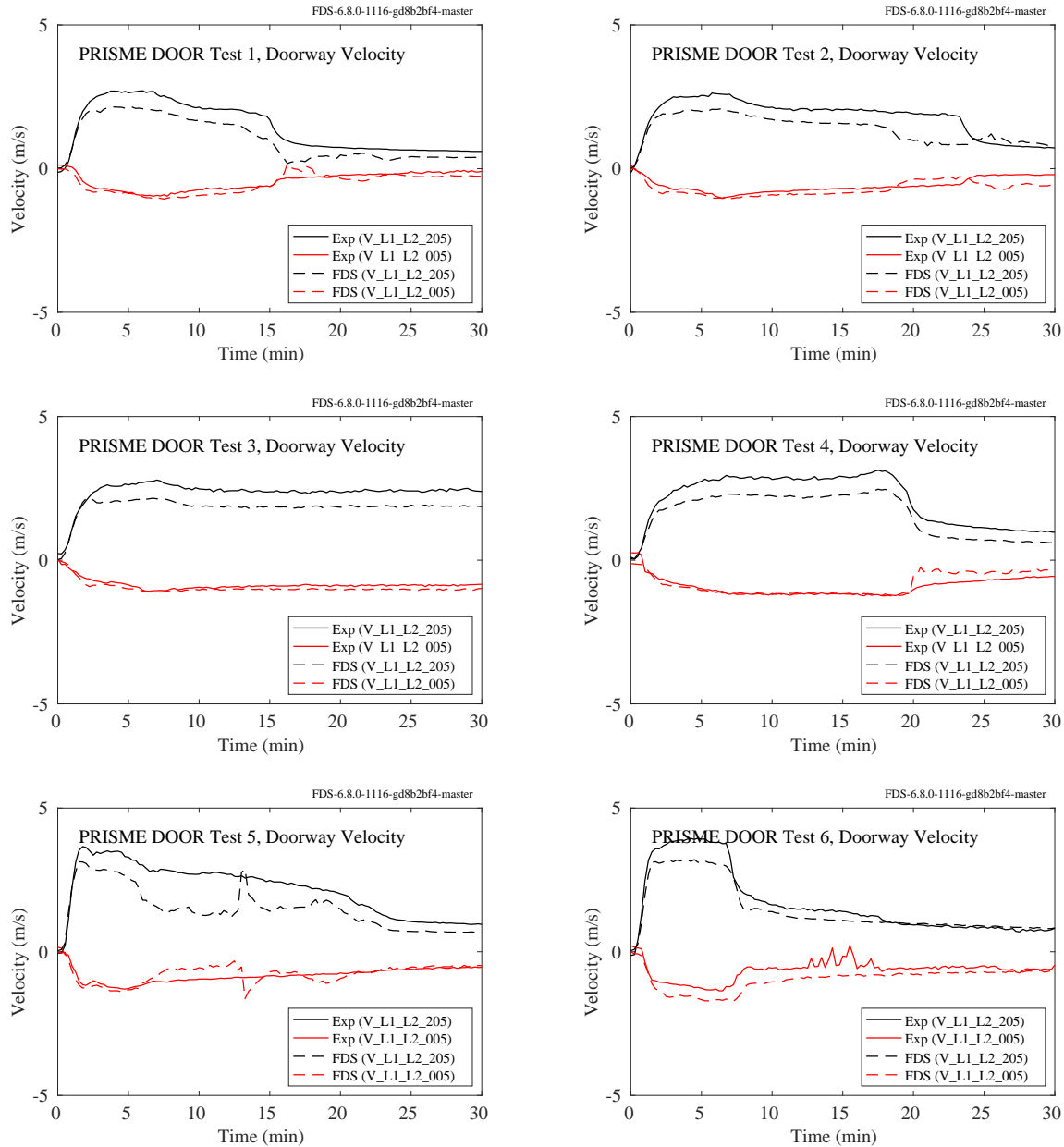


Figure 8.23: PRISME DOOR experiments, gas velocity.

8.10 Restivo Experiment

The results of a simulation of Restivo's room ventilation experiment are presented below. To capture the forced inlet flow, the volume near the supply slot needs a fairly fine grid to capture the mixing of air at the shear layer. For the results shown here, the height of the inlet was spanned with 6 grid cells, roughly 3 cm in the vertical dimension, 6 cm in the other two. Finer grids were used in the Musser study [38], but with no appreciable change in results. The component of velocity in the lengthwise direction was measured in four arrays: two vertical arrays located 3 m and 6 m from the inlet along the centerline of the room, and two horizontal arrays located 8.4 cm above the floor and below the ceiling, respectively. These measurements were taken using hot-wire anemometers. While data on the specific instrumentation used are not readily available, hot-wire systems tend to have limitations at low velocities, with typical thresholds of approximately 0.1 m/s.

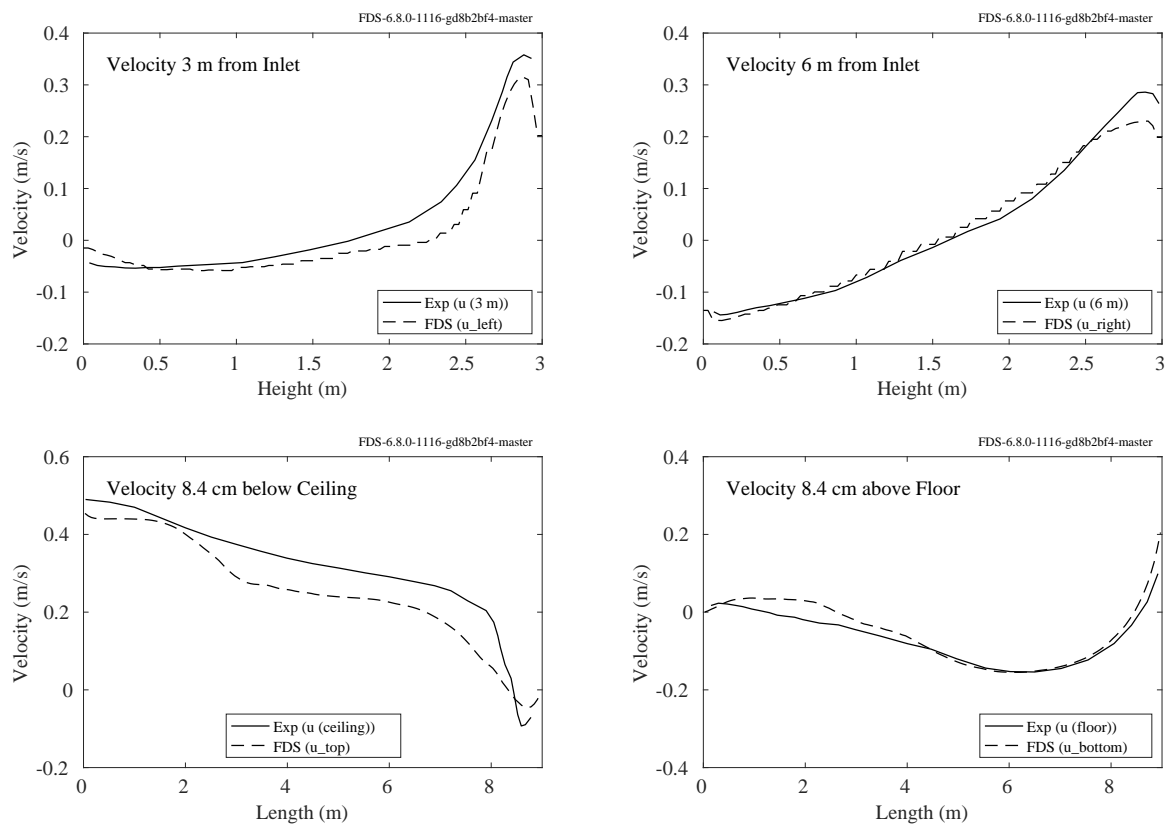


Figure 8.24: Restivo experiment, gas velocity.

8.11 Steckler Compartment Experiments

Steckler et al. [319] mapped the doorway/window flows in 55 compartment fire experiments. The test matrix is presented in Table 3.38. Shown on the following pages are the centerline velocity profiles, compared with model predictions. Off-center profiles are not considered. The vertical spacing of the measurements was approximately 11 cm, with the uppermost velocity probe centered 5.7 cm below the 10 cm thick soffit. The FDS simulations were uniformly gridded with cells of 5 cm on each side. To quantify the difference between prediction and measurement, the maximum outward velocities, which always occurred at the uppermost measurement location, were compared. It has been found that relatively minor changes in the velocity boundary conditions at the edges and bottom of the door soffit can have a noticeable impact on these results.

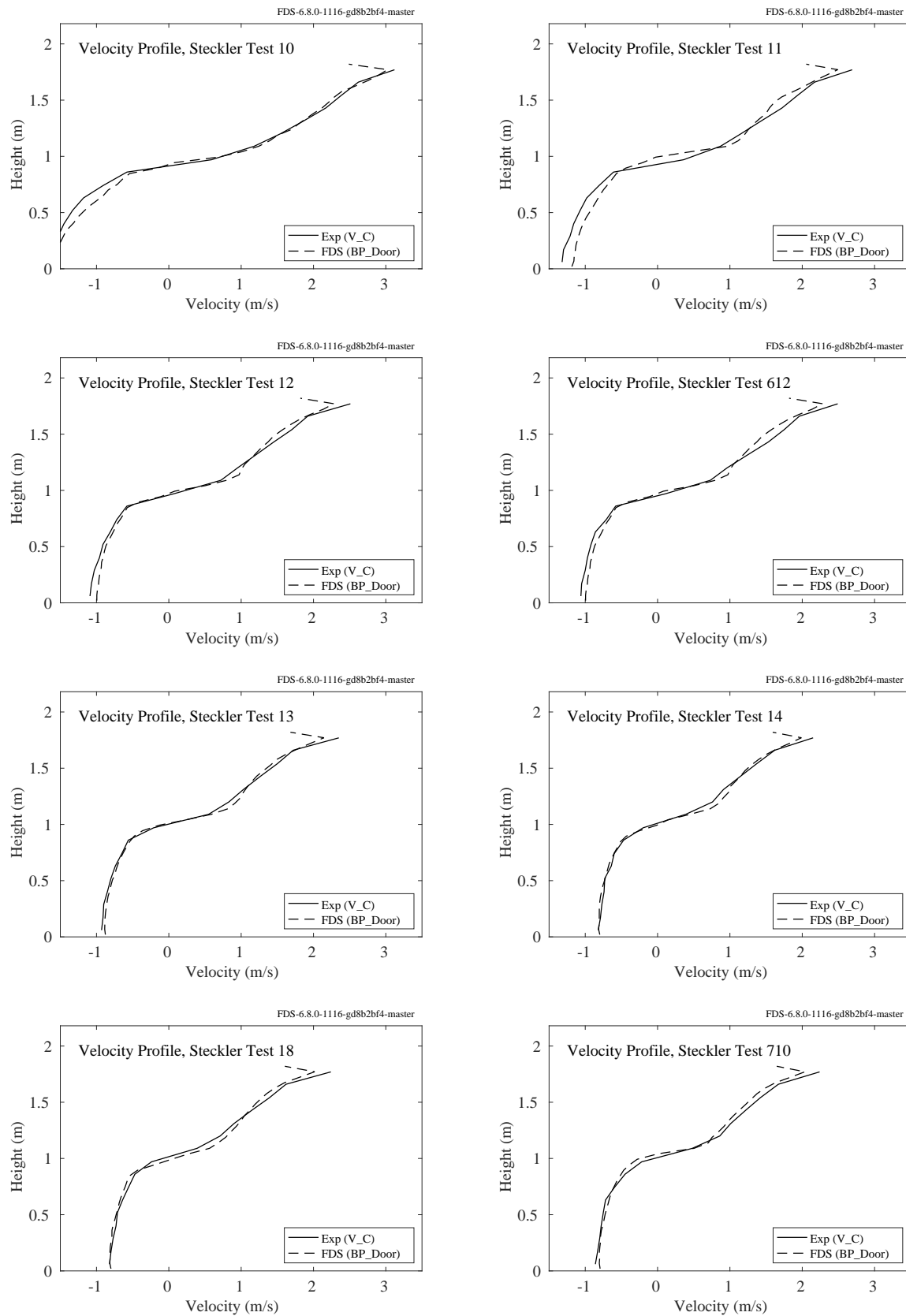


Figure 8.25: Steckler experiments, velocity profiles, Tests 10, 11, 12, 13, 14, 18, 612, 710.

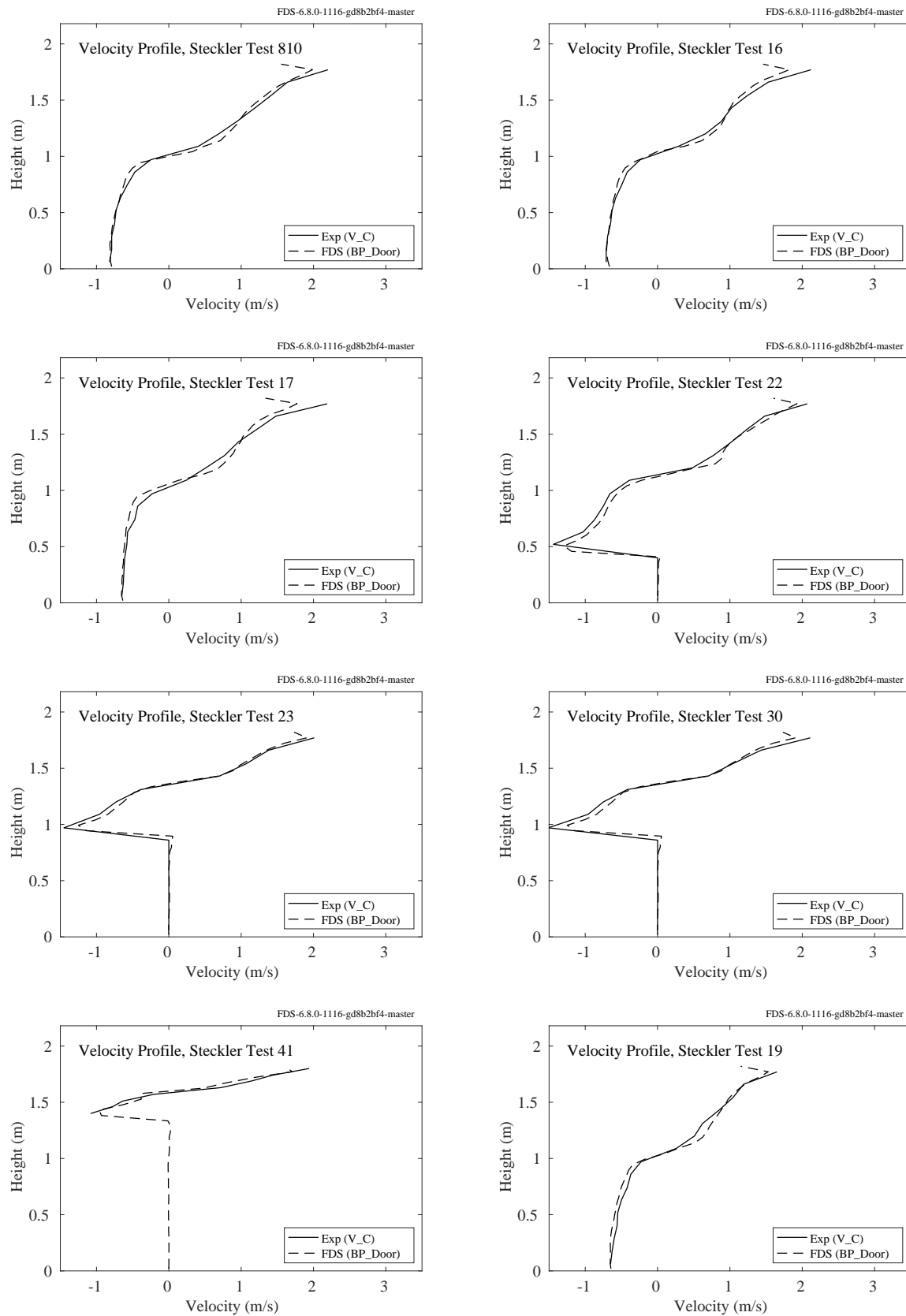


Figure 8.26: Steckler experiments, velocity profiles, Tests 16, 17, 19, 22, 23, 30, 41, 810.

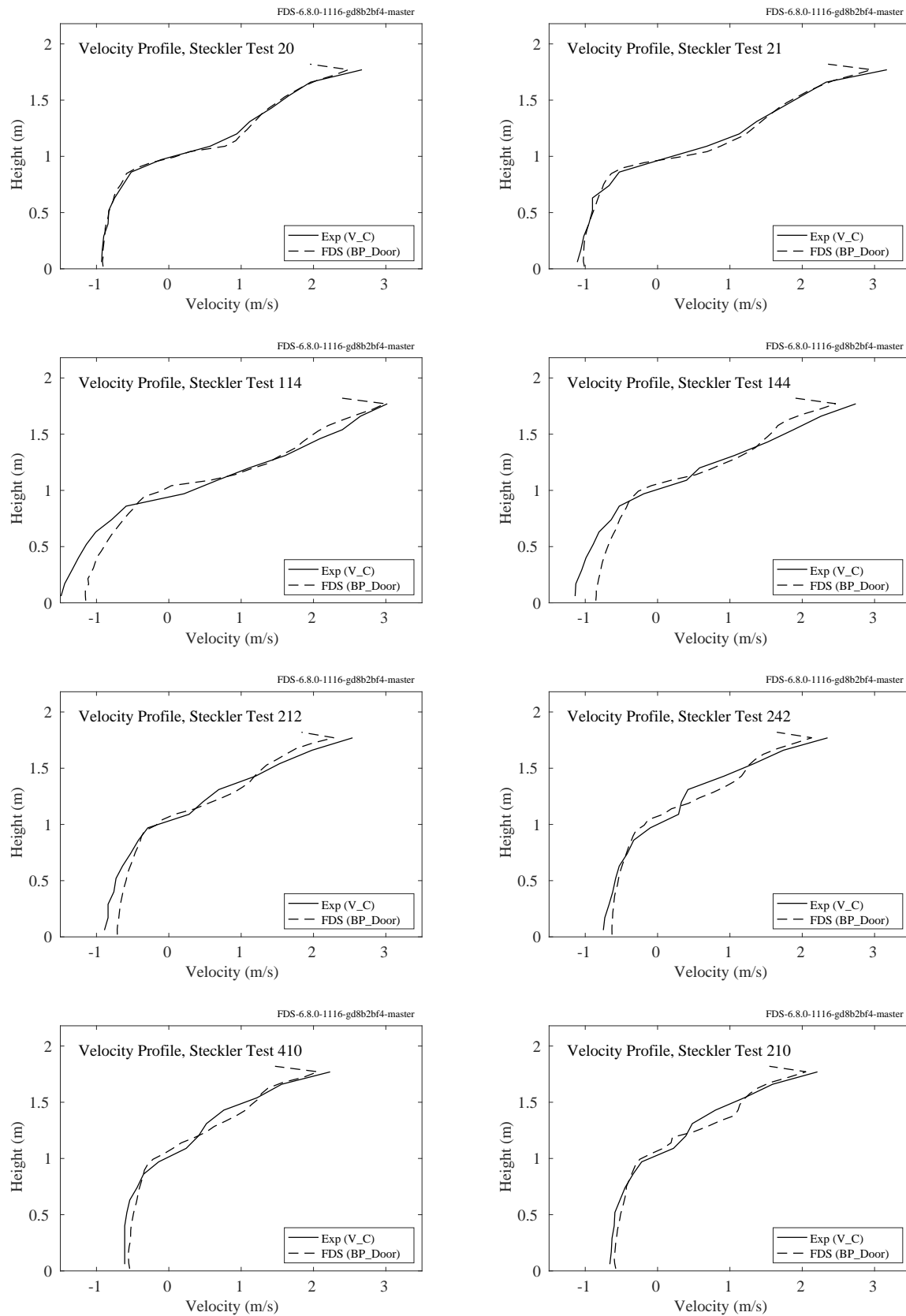


Figure 8.27: Steckler experiments, velocity profiles, Tests 20, 21, 114, 144, 210, 212, 242, 410.

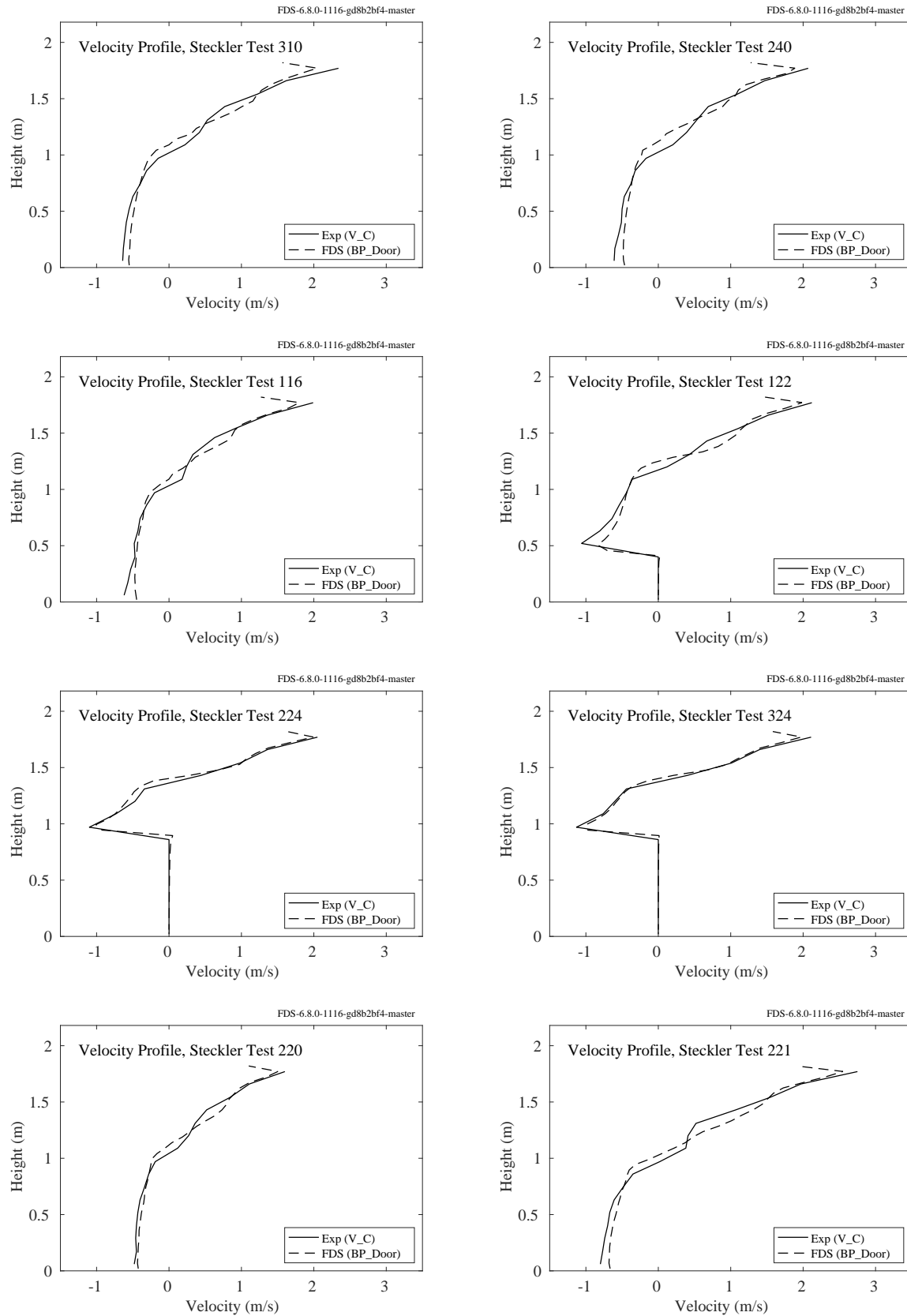


Figure 8.28: Steckler experiments, velocity profiles, Tests 116, 122, 220, 221, 224, 240, 310, 324.

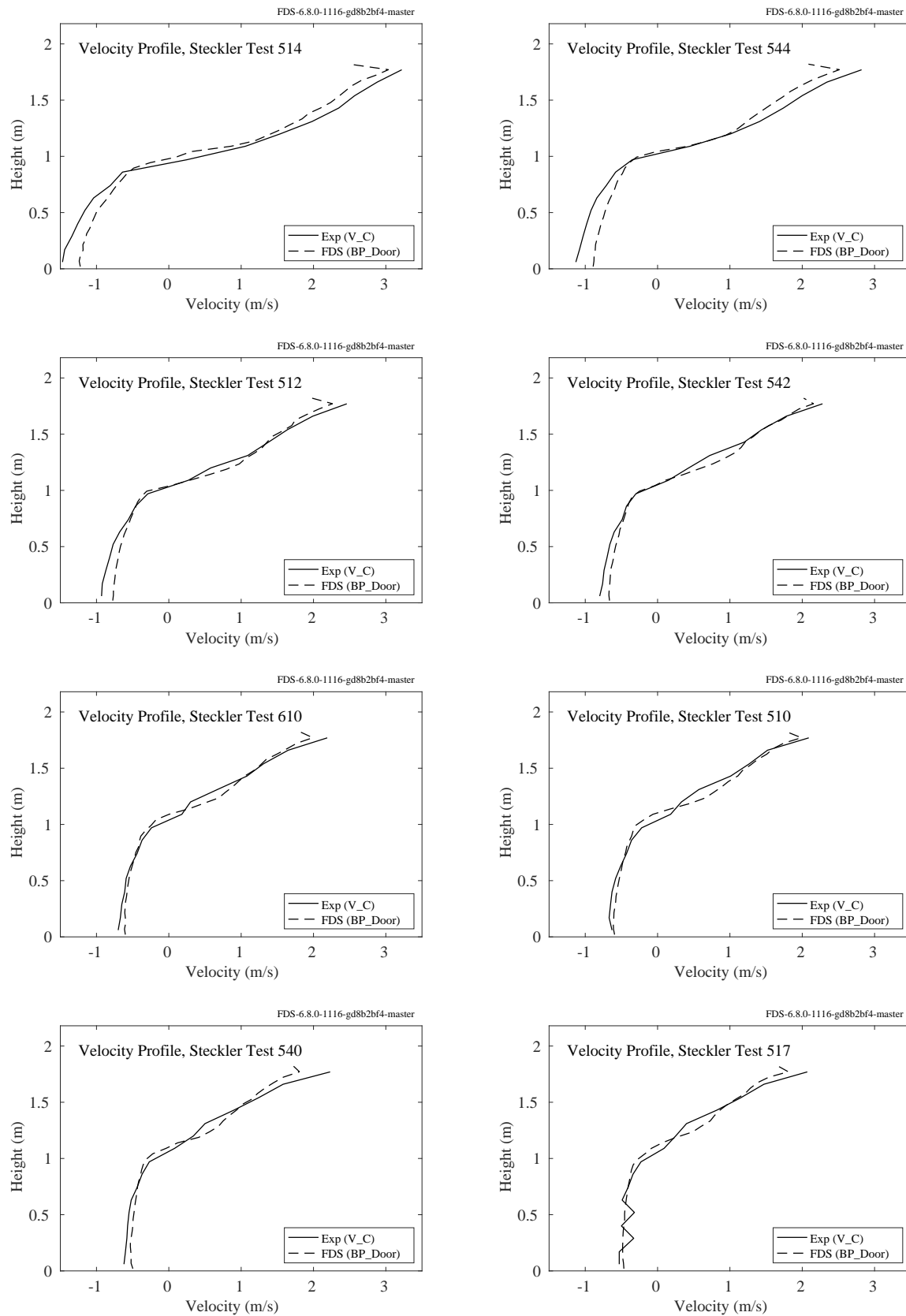


Figure 8.29: Steckler experiments, velocity profiles, Tests 510, 512, 514, 517, 540, 542, 544, 610.

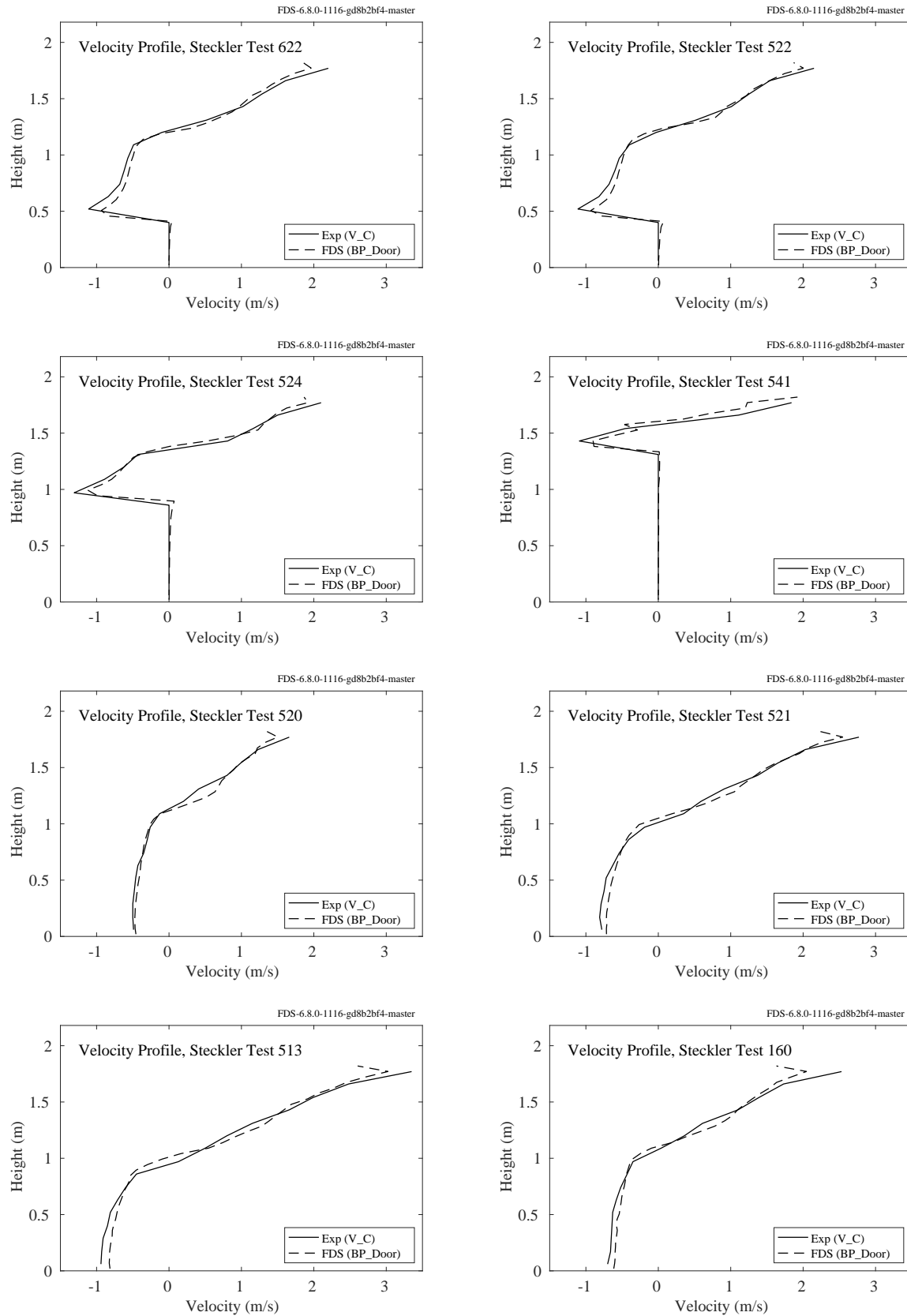


Figure 8.30: Steckler experiments, velocity profiles, Tests 160, 513, 520, 521, 522, 524, 541, 622.

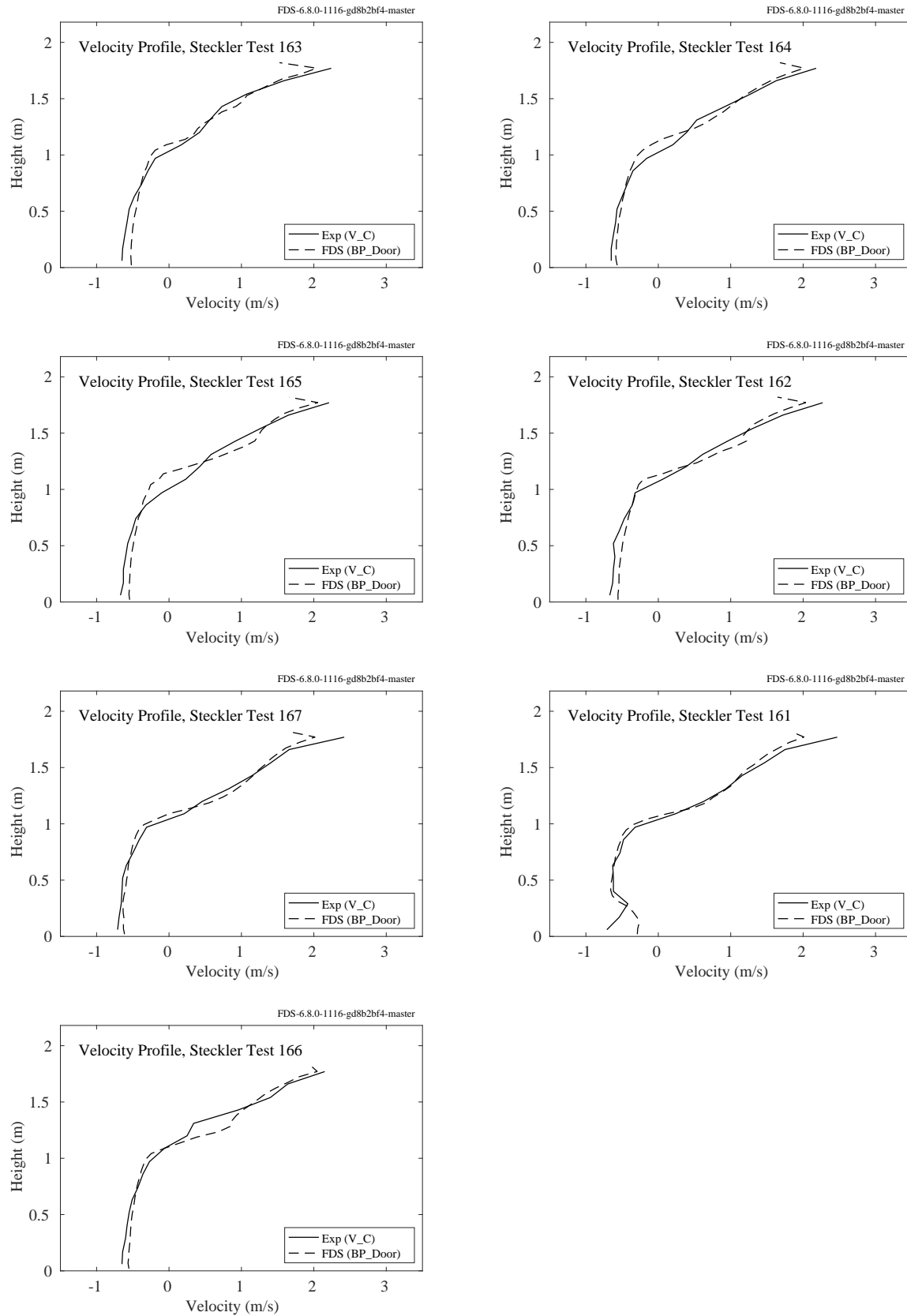


Figure 8.31: Steckler experiments, velocity profiles, Tests 161, 162, 163, 164, 165, 166, 167.

8.12 UL/NIJ House Experiments

Details of the UL/NIJ Experiments are presented in Sec. 3.90.

Velocity was measured at (typically) five vertical locations in the open windows and doorways of the two houses. The bi-directional probes were evenly spaced through the height of each opening.

In the single story house, the velocity profiles in the front doorway and Window E or F are used for comparison. In the two story house, the profiles in the front doorway and Windows K, L or A are used.

Note that this data has not been included in the summary scatter plot, Fig. 8.49 because it is too noisy to make precise comparisons. It is included here mainly for qualitative comparison.

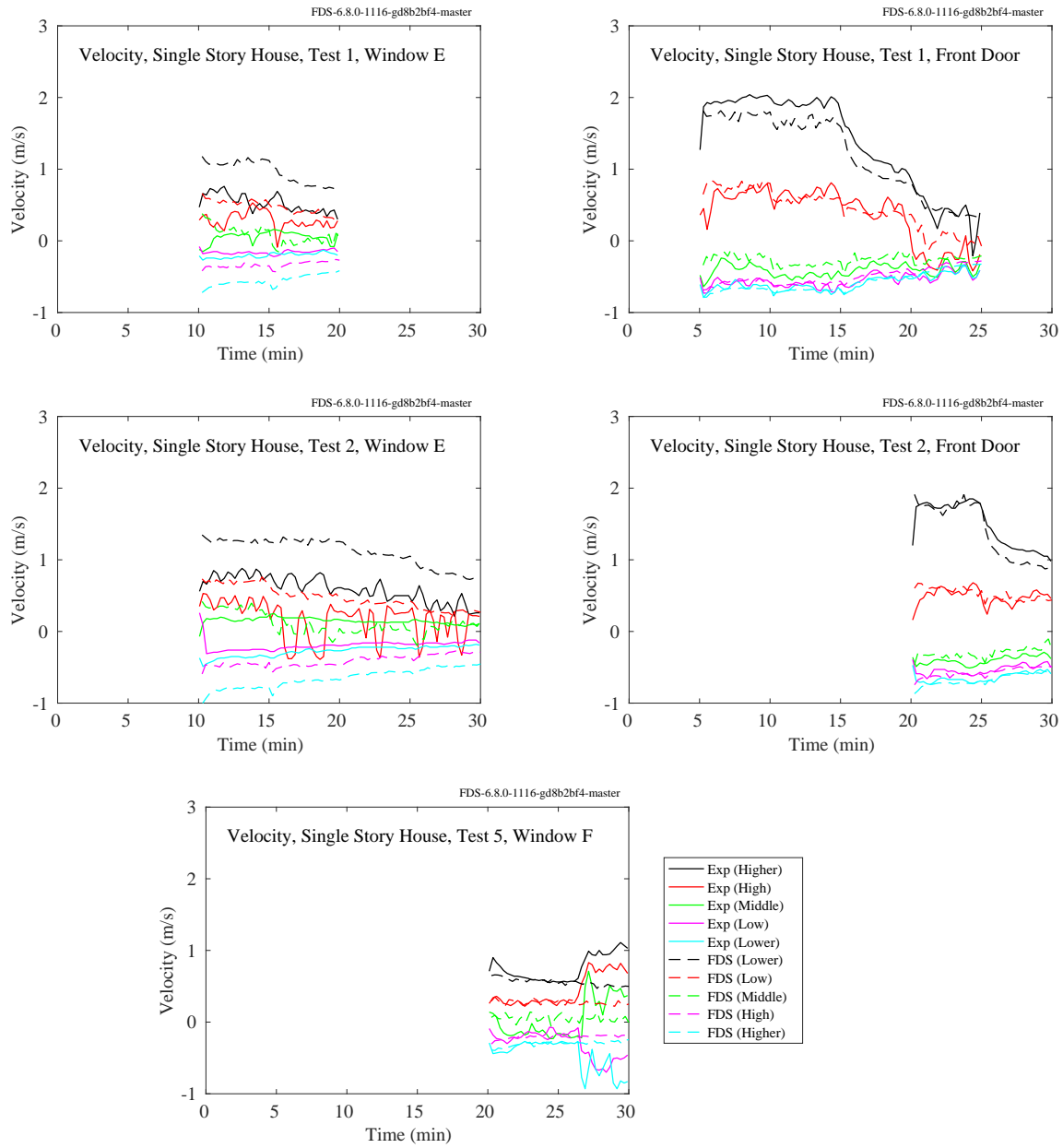


Figure 8.32: UL/NIJ Experiments, Velocity, single story house, Tests 1, 2, and 5.

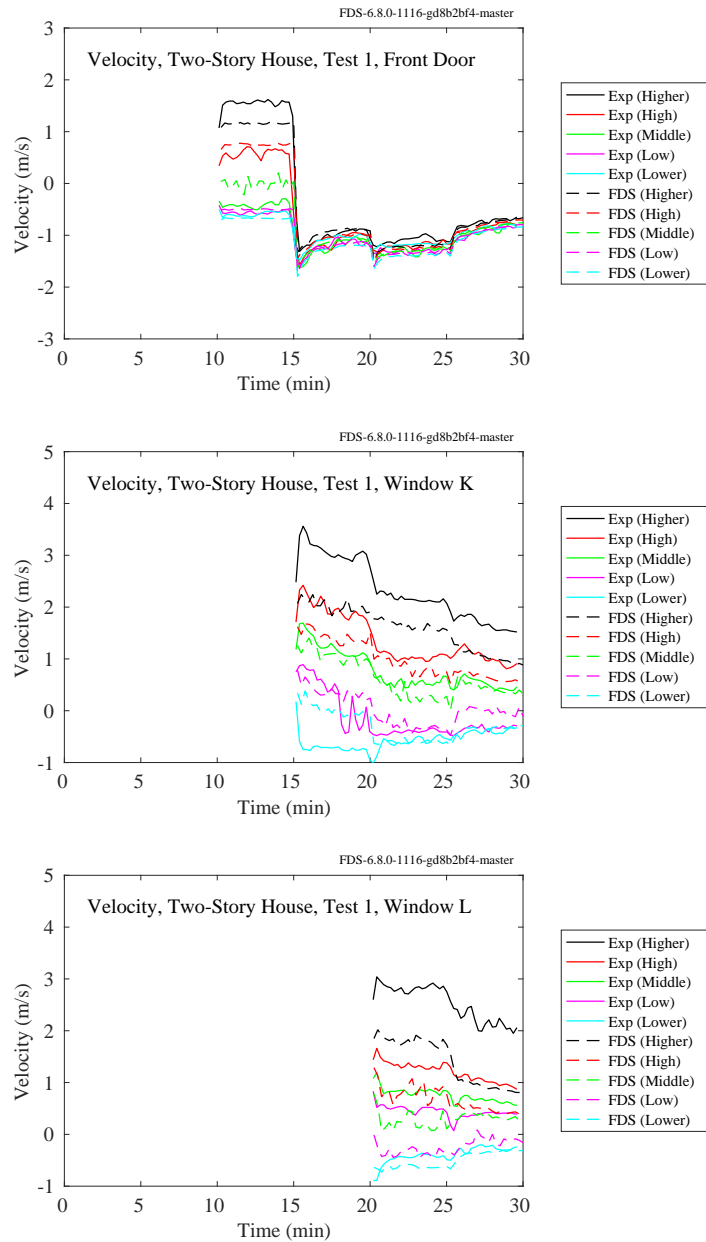


Figure 8.33: UL/NIJ Experiments, Velocity, two-story house, Test 1.

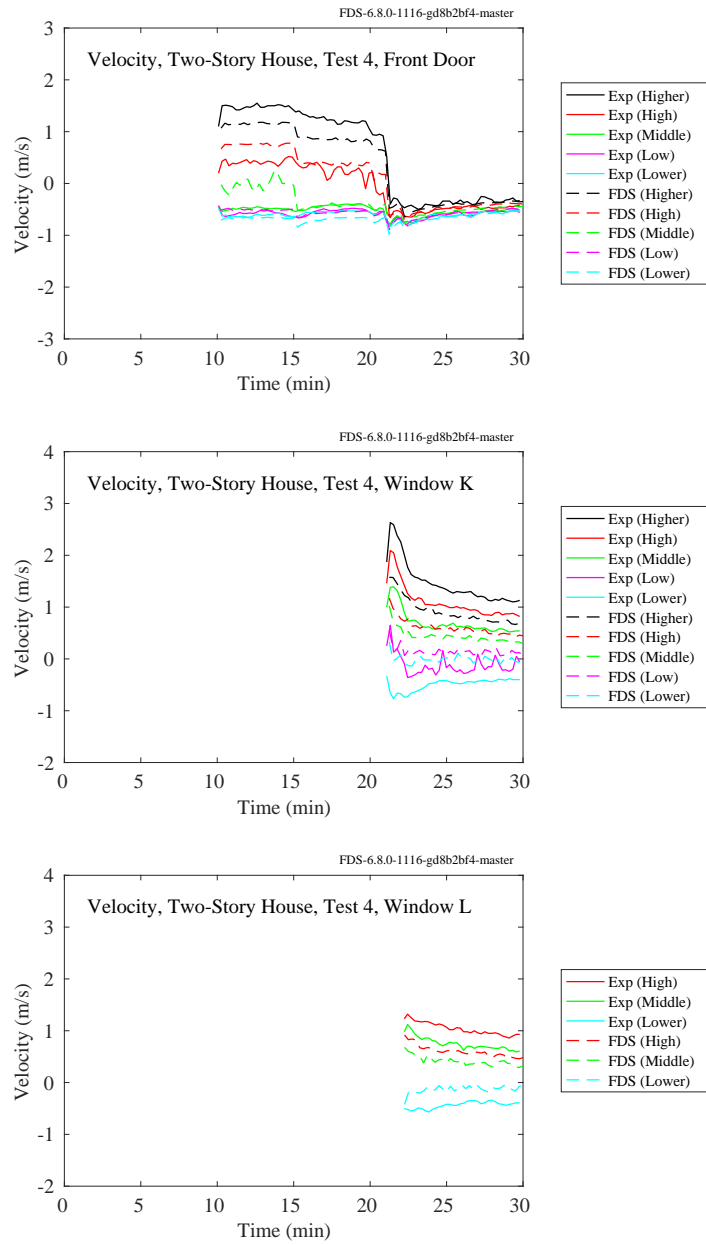


Figure 8.34: UL/NIJ Experiments, Velocity, two-story house, Test 4.

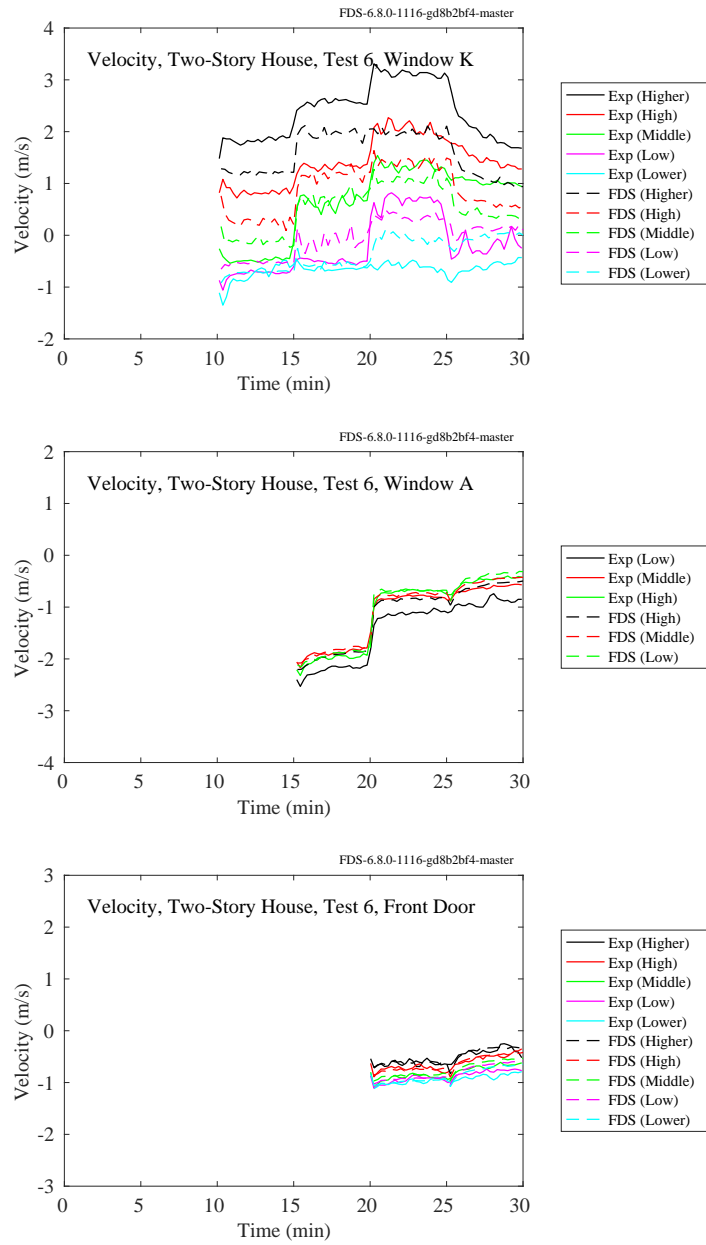


Figure 8.35: UL/NIJ Experiments, Velocity, two-story house, Test 6.

8.13 Waterloo Methanol Pool Fire Experiment

Figures 8.36 through 8.38 display radial profiles of measured and predicted mean (left hand plots) and root mean square (right hand plots) values of the vertical velocity above a 30 cm diameter methanol pool fire. The root mean square of the vertical velocity is given by:

$$(\overline{w'w'})^{1/2} = \sqrt{\frac{\sum_{i=1}^n (w_i - \bar{w})^2}{n-1}} \quad (8.1)$$

where w_i is the instantaneous value of the vertical velocity and \bar{w} is the average value over 50 s. The profile heights range from 2 cm to 30 cm above the pool surface. Time resolved velocity measurements were performed using a two component laser doppler anemometer.

Figures 8.39 through 8.41 display radial profiles of measured and predicted mean (left hand plots) and root mean square (right hand plots) values of the horizontal velocity.

Figures 8.42 through 8.43 display radial profiles of measured and predicted estimates of the horizontal and vertical velocity covariance:

$$\overline{u'w'} = \frac{\sum_{i=1}^n (u_i - \bar{u})(w_i - \bar{w})}{n-1} \quad (8.2)$$

where u_i and w_i are instantaneous values of the horizontal and vertical components of velocity and \bar{u} and \bar{w} are 50 s time averages.

The FDS results are shown at three grid resolutions, 0.5 cm, 1 cm, and 2 cm.

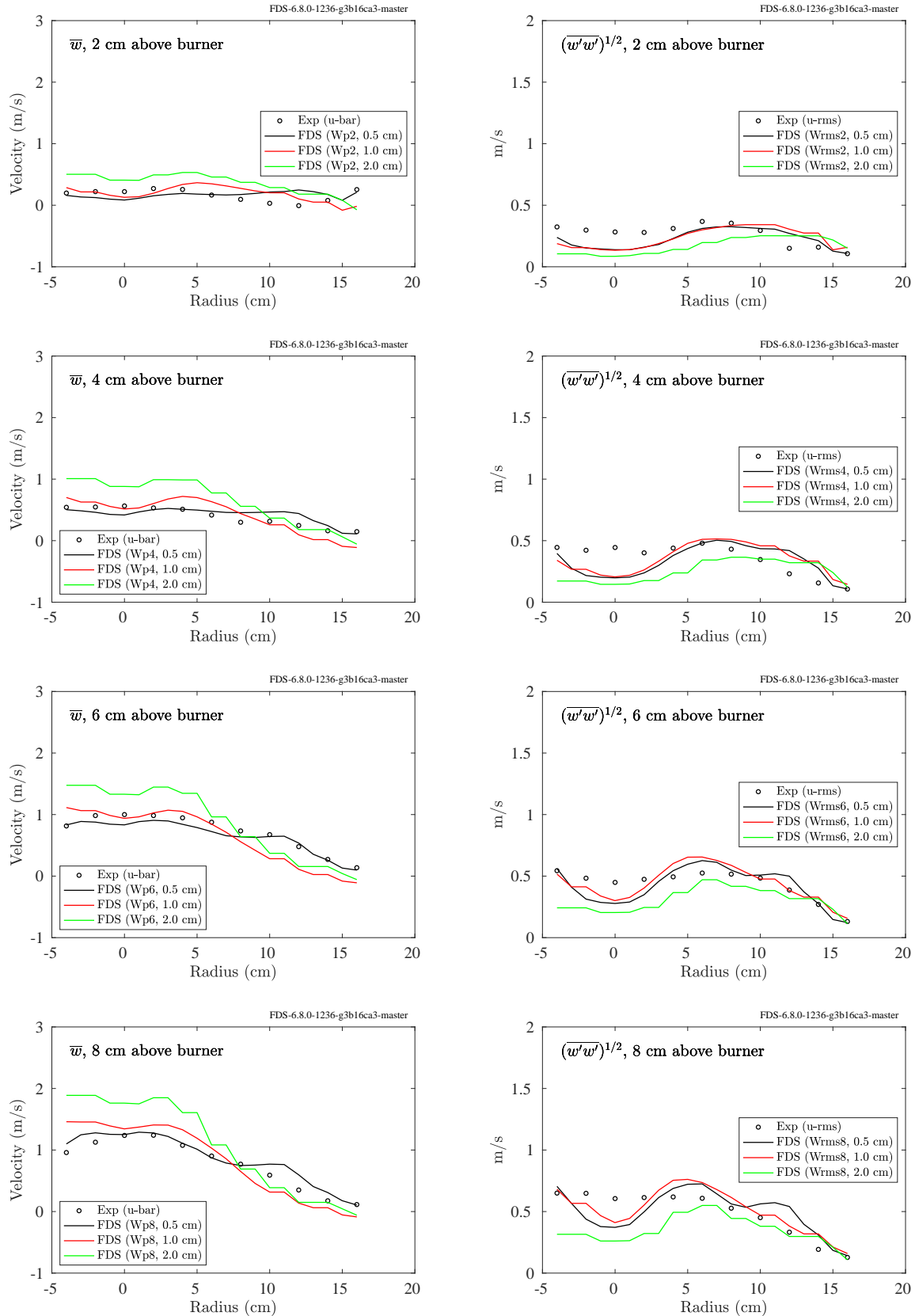


Figure 8.36: Waterloo Methanol, radial profiles of mean and rms vertical velocity, 2 cm to 8 cm above the burner.

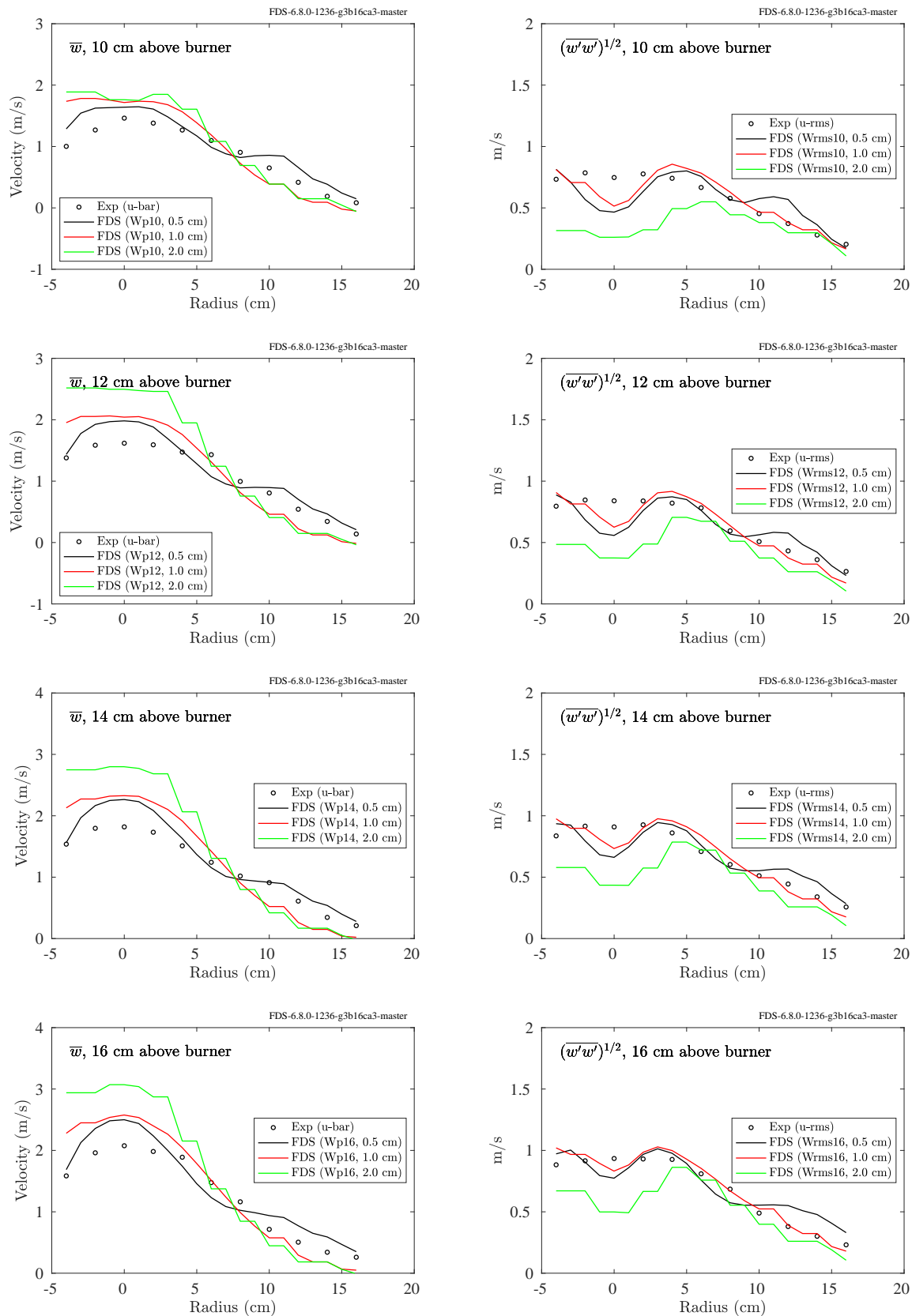


Figure 8.37: Waterloo Methanol, radial profiles of mean and rms vertical velocity, 10 cm to 16 cm above the burner.

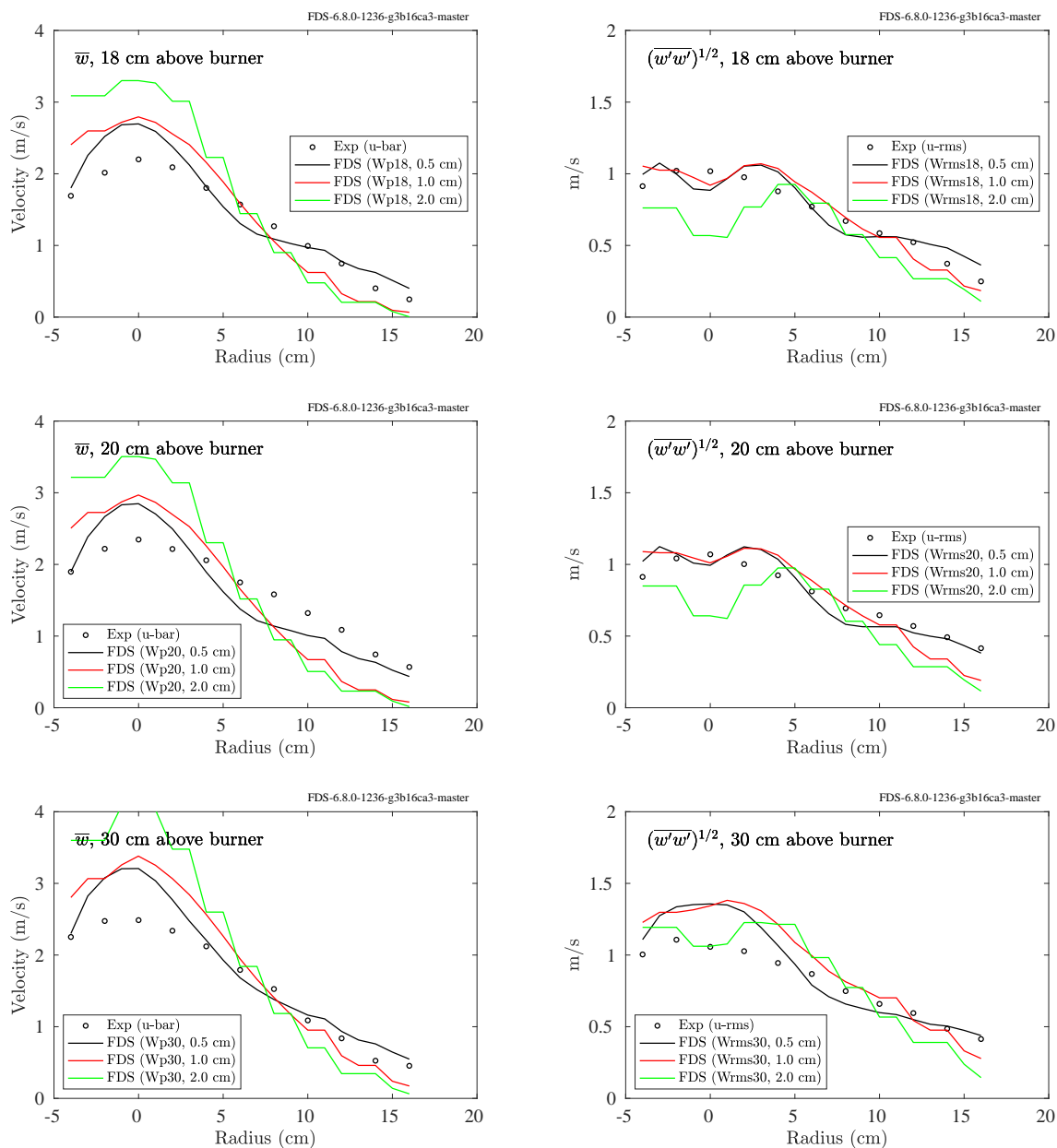


Figure 8.38: Waterloo Methanol, radial profiles of mean and rms vertical velocity, 18 cm to 30 cm above the burner.

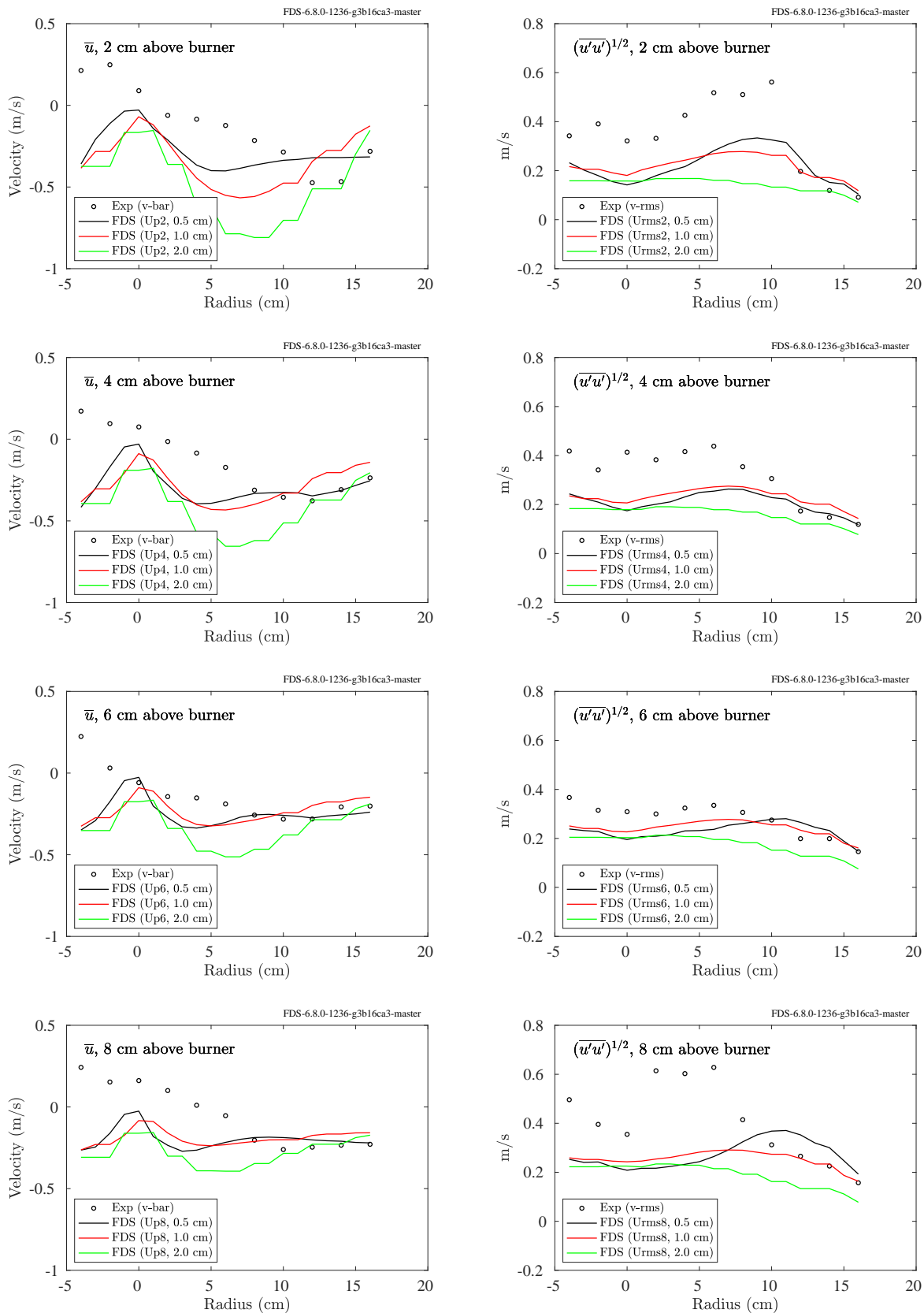


Figure 8.39: Waterloo Methanol, radial profiles of mean and rms horizontal velocity, 2 cm to 8 cm above the burner.

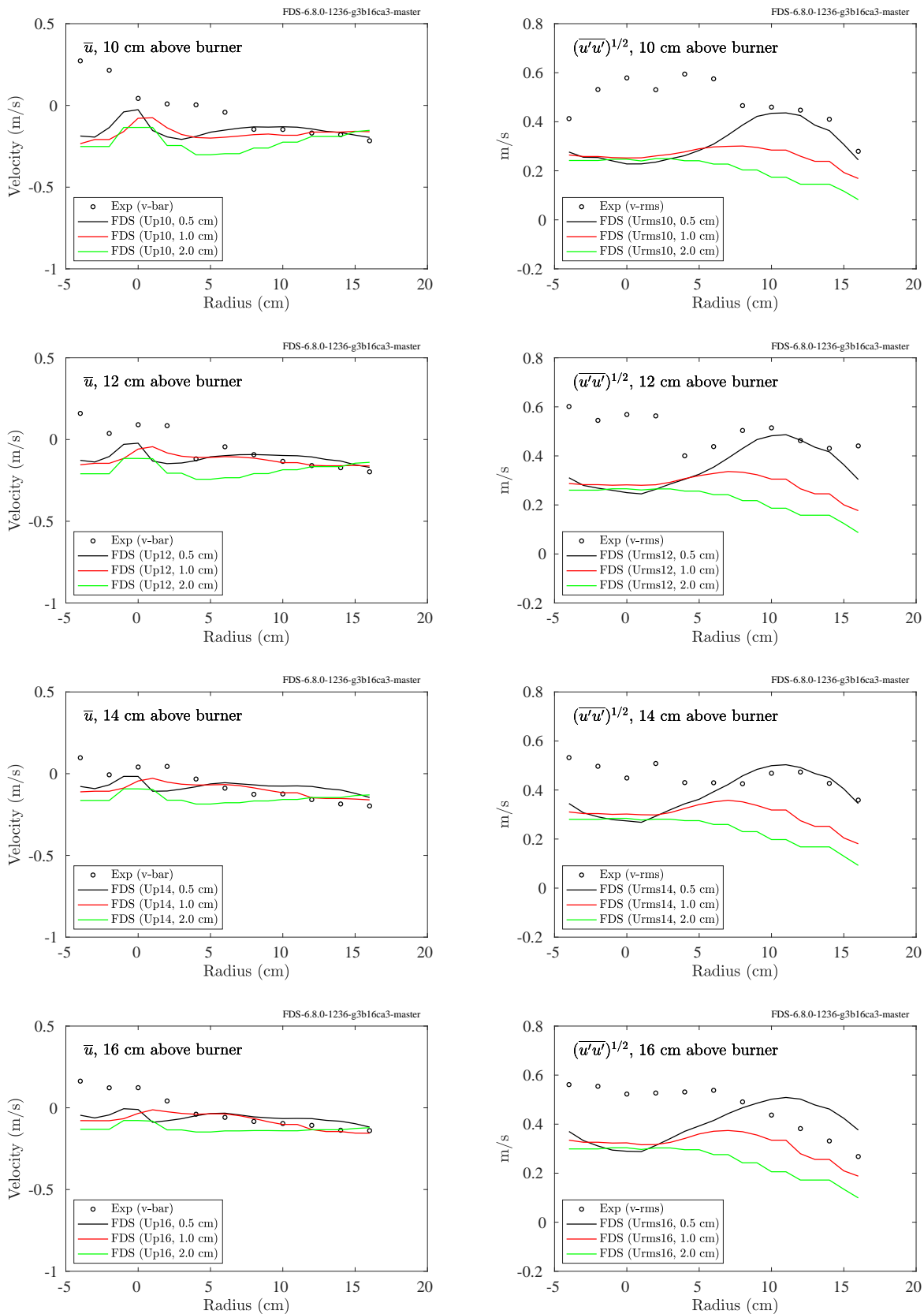


Figure 8.40: Waterloo Methanol, radial profiles of mean and rms horizontal velocity, 10 cm to 16 cm above the burner.

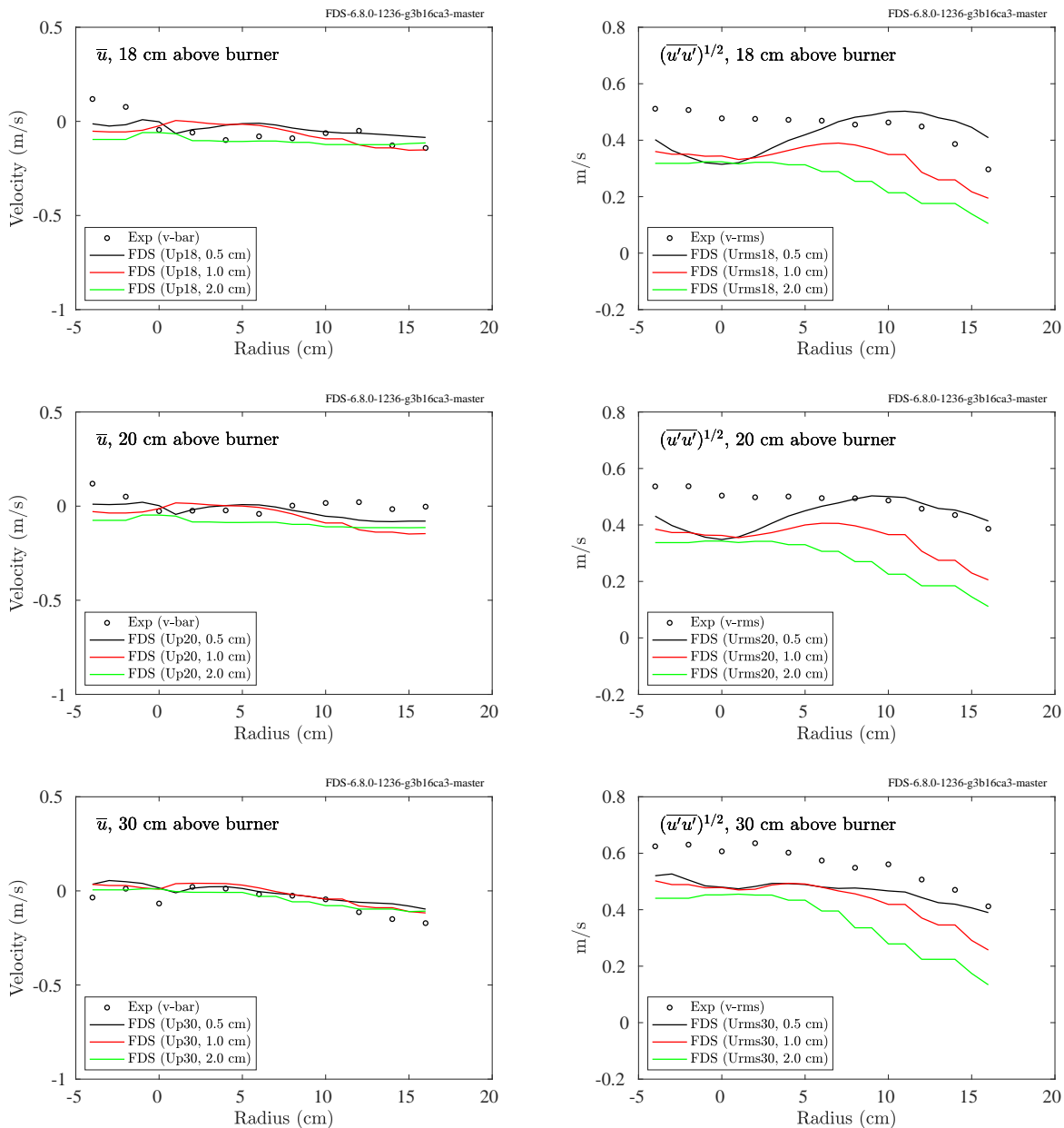


Figure 8.41: Waterloo Methanol, radial profiles of mean and rms horizontal velocity, 18 cm to 30 cm above the burner.

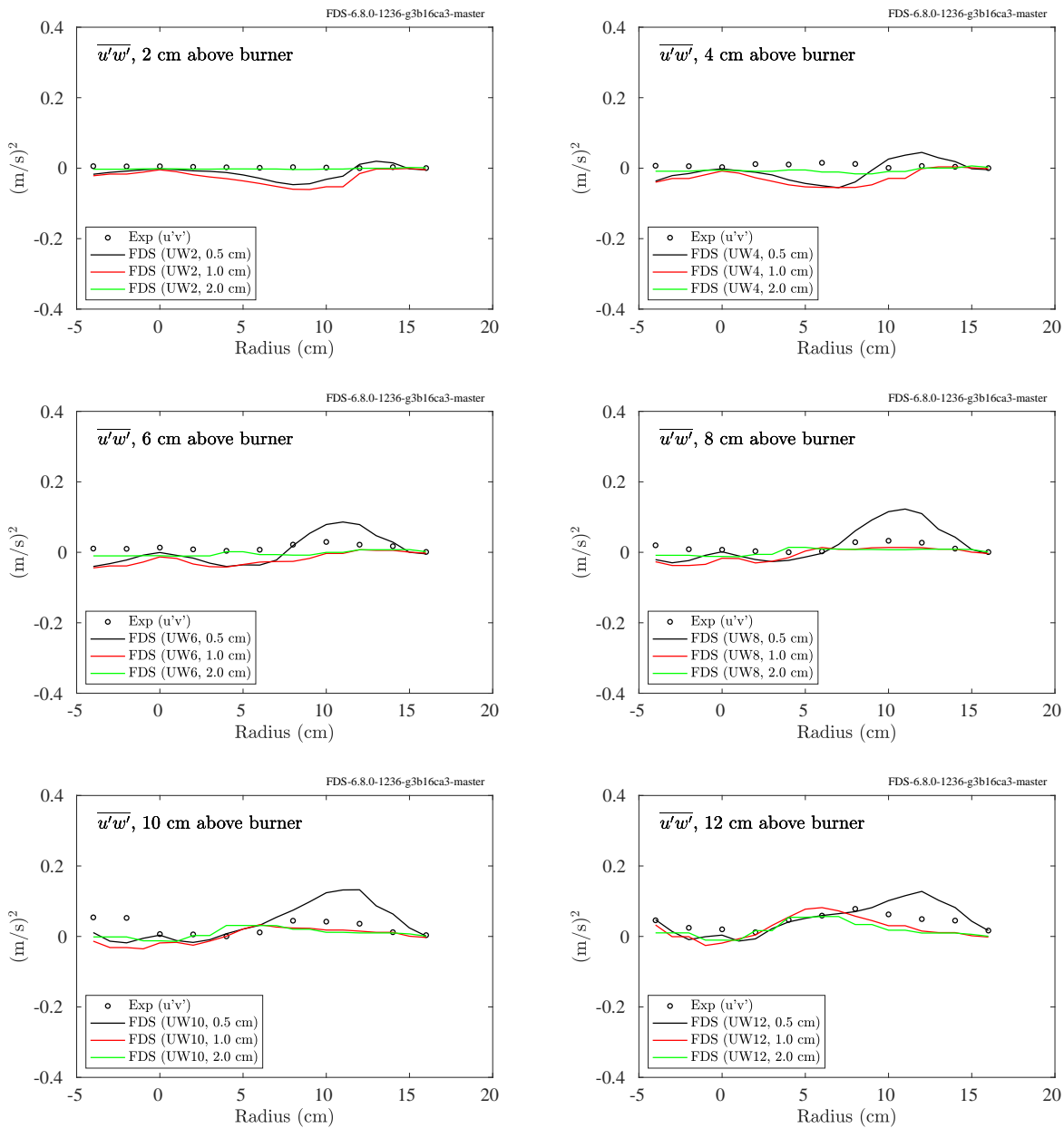


Figure 8.42: Waterloo Methanol, radial profiles of $\overline{u'w'}$, 2 cm to 12 cm above the burner.

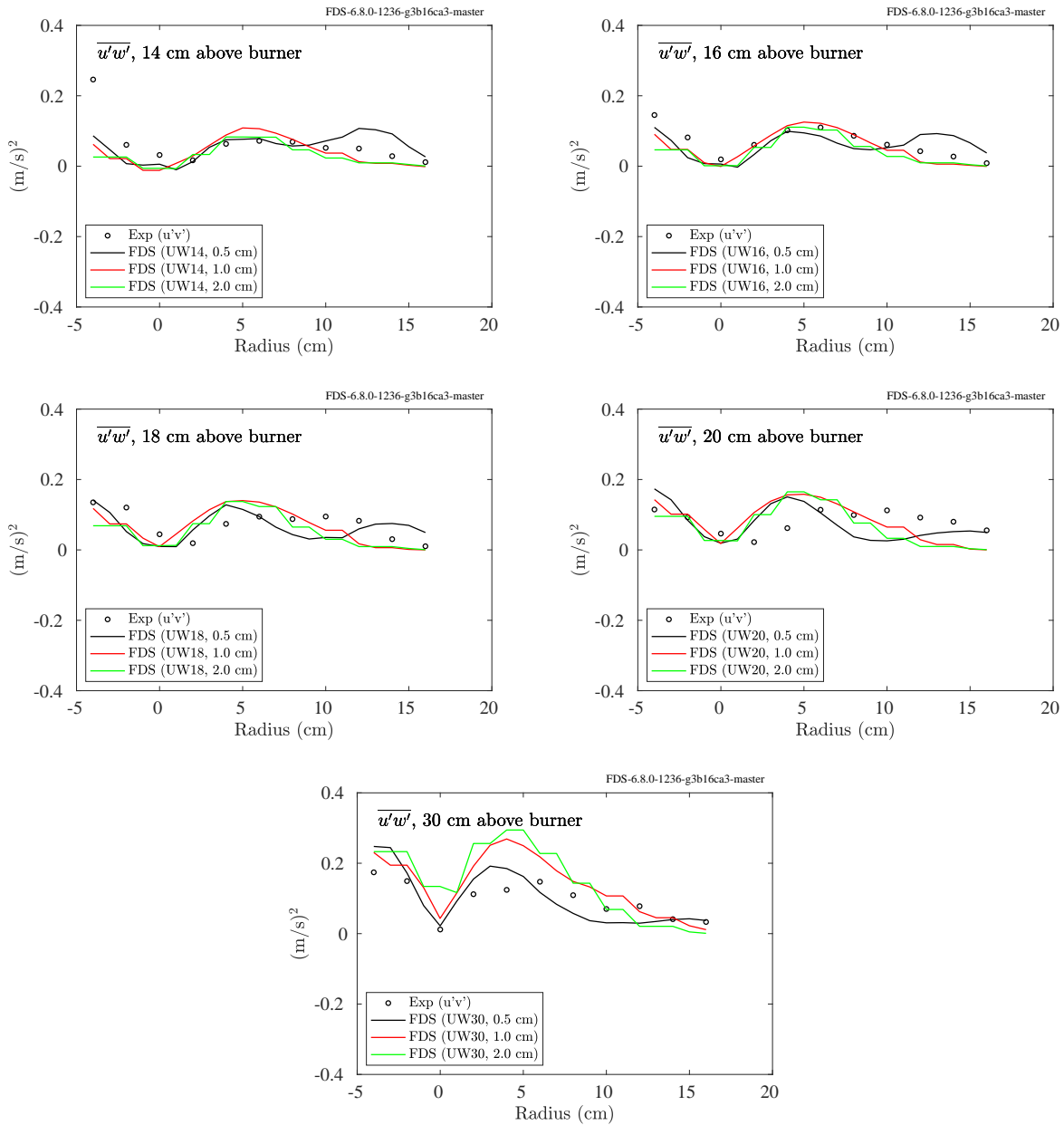


Figure 8.43: Waterloo Methanol, radial profiles of $\overline{u'w'}$, 14 cm to 30 cm above the burner.

8.14 WTC Experiments

Bi-directional probes were positioned inside two of the four inlet openings and three of the four outlet openings. The locations are shown in Fig. 8.44. Exact dimensions are given in Ref. [70].

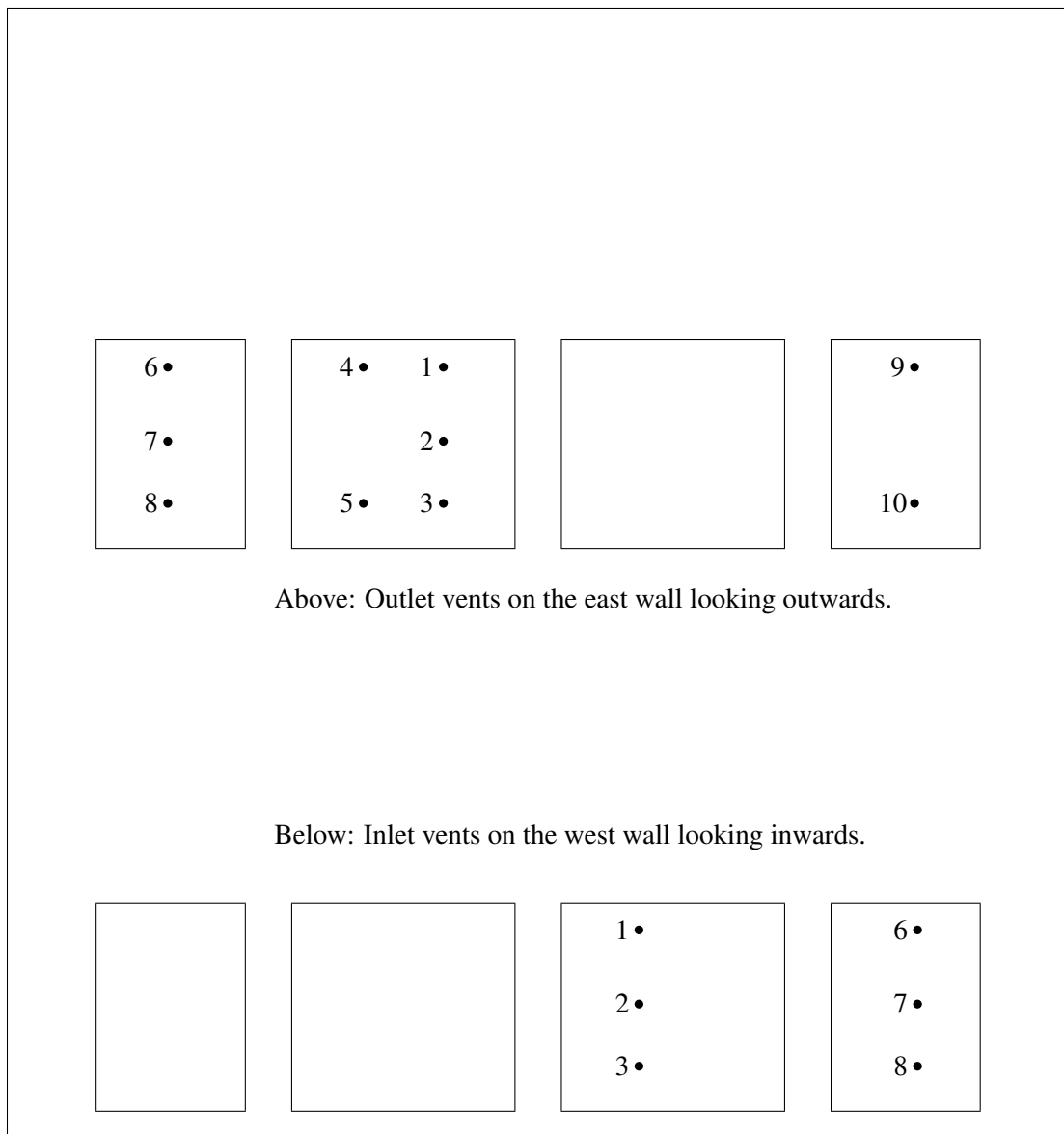


Figure 8.44: Layout of the bi-directional probes in the inlet (west wall) and outlet (east wall) vents, WTC Experiments.

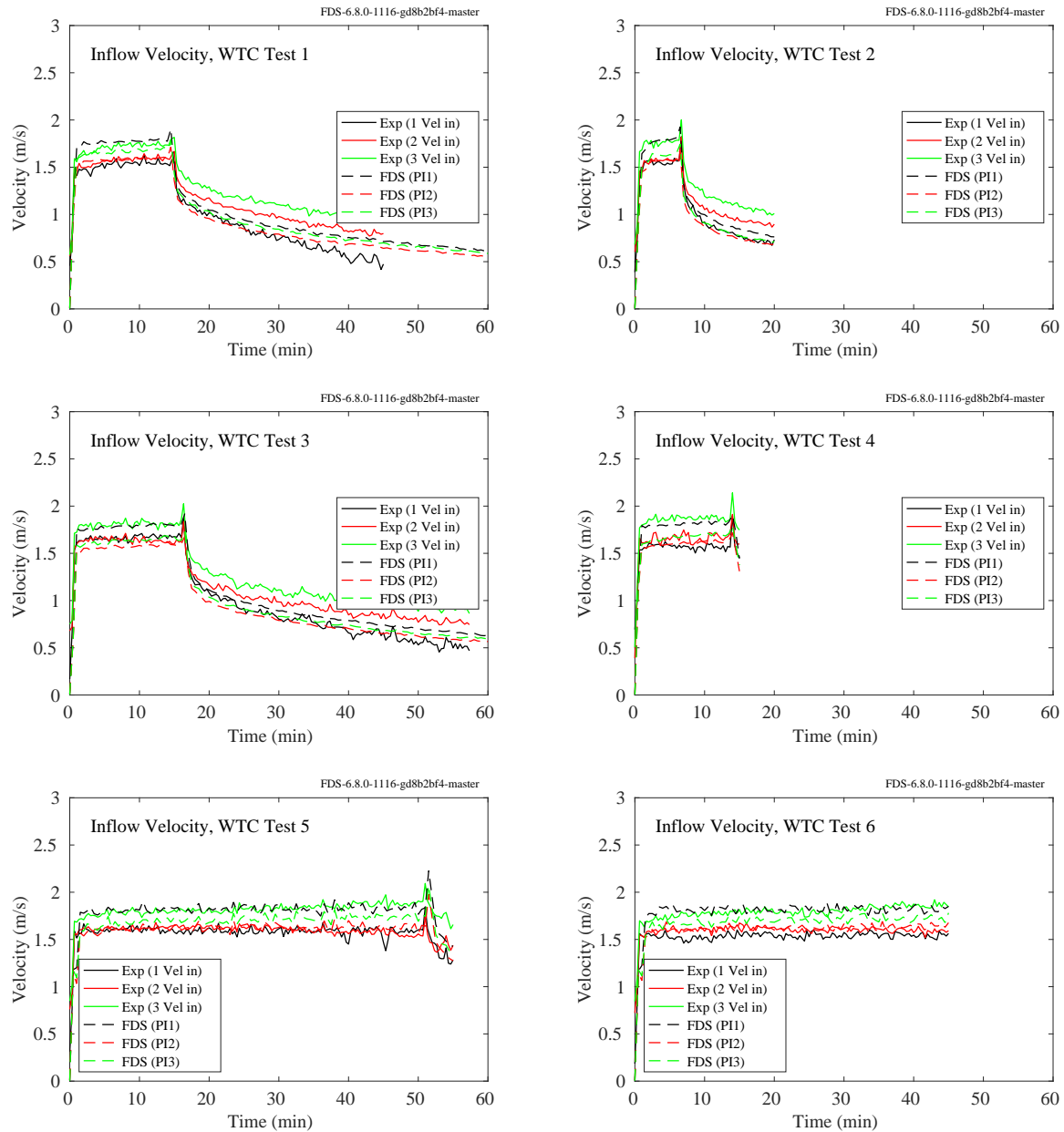


Figure 8.45: WTC experiments, inlet velocity, Points 1-3.

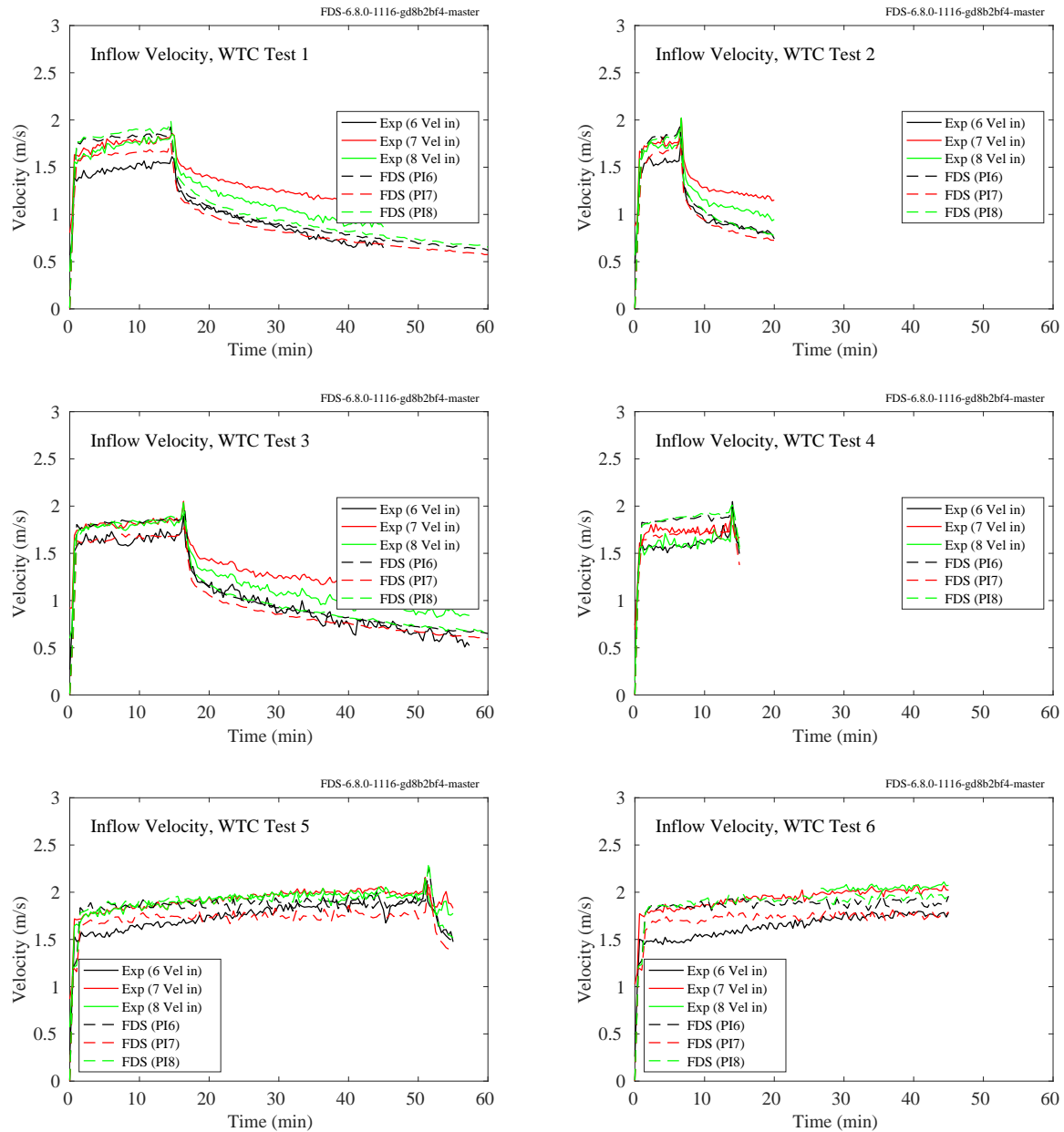


Figure 8.46: WTC experiments, inlet velocity, Points 6-8.

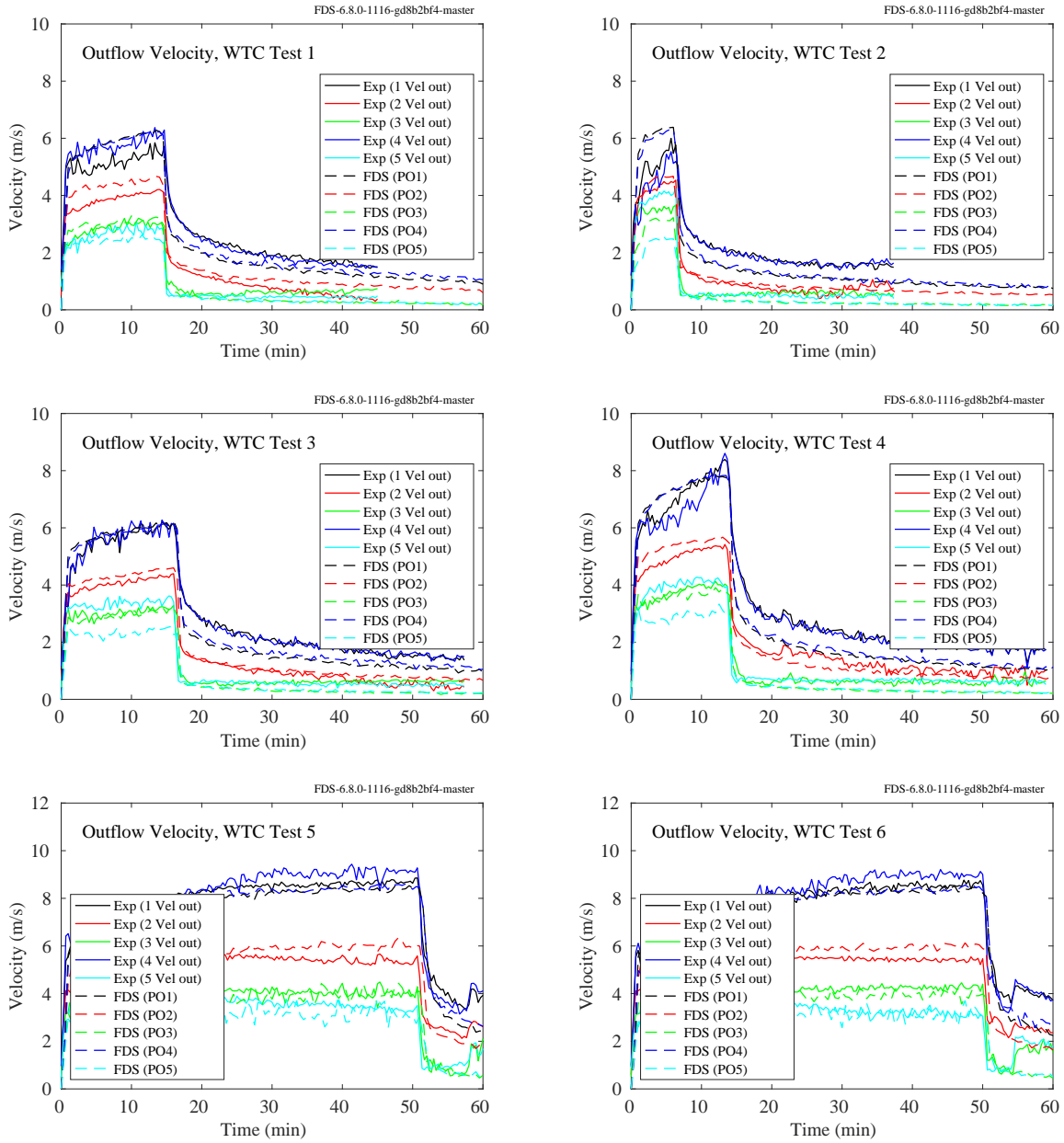


Figure 8.47: WTC experiments, outlet velocity, Points 1-5.

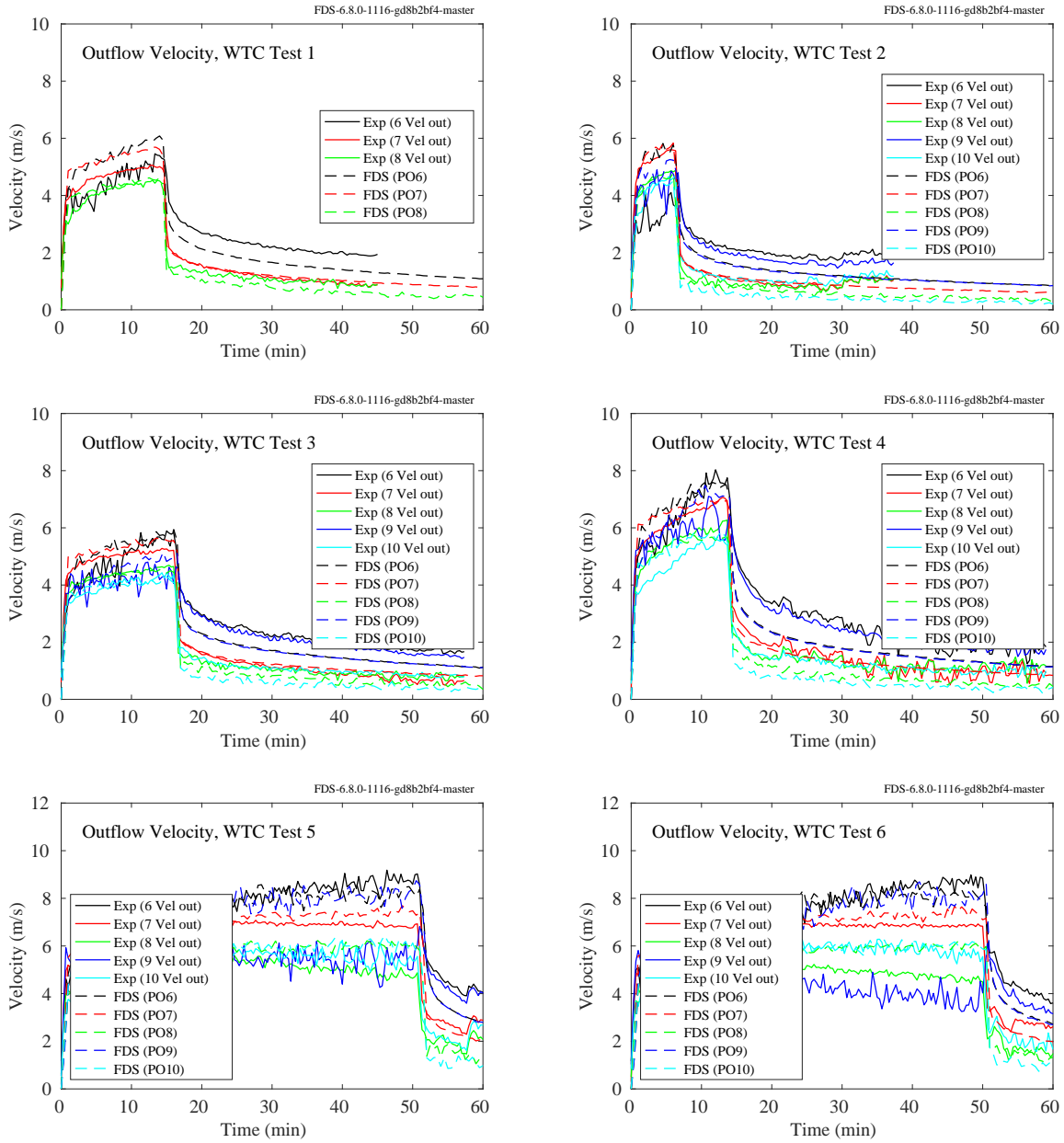


Figure 8.48: WTC experiments, outlet velocity, Points 6-10.

8.15 Summary of Velocity Predictions

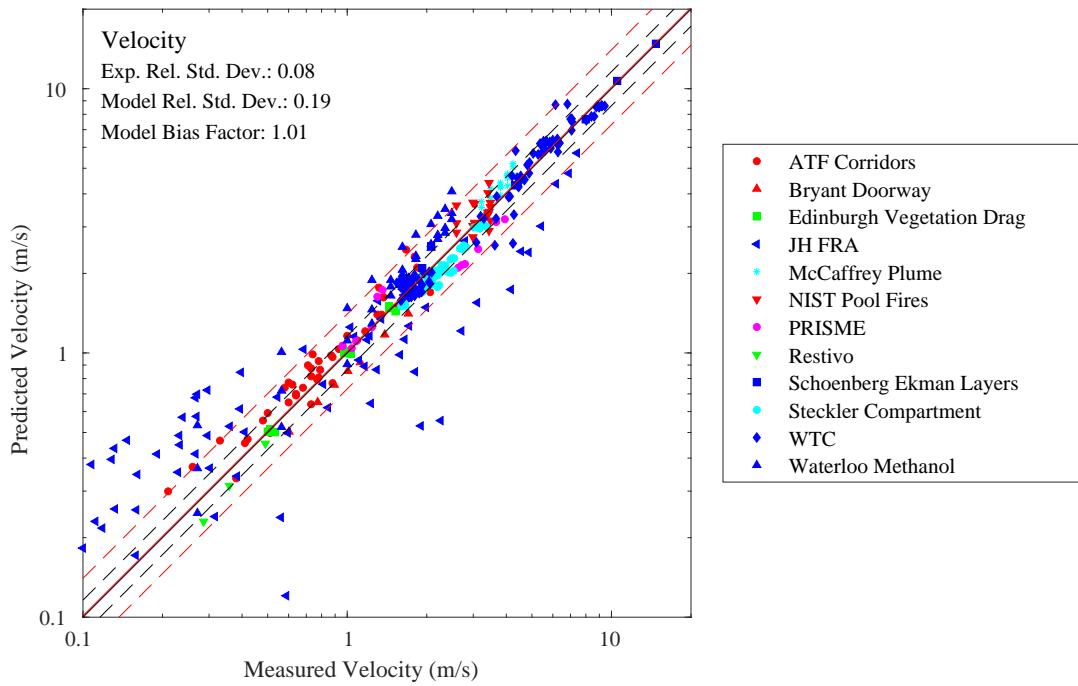


Figure 8.49: Summary of comparisons of predicted and measured maximum velocities.

Chapter 9

Gas Species and Smoke

For most applications, FDS uses a single step, mixing-controlled combustion model. The products of combustion are “lumped” together and tracked as a single gas mixture. These products include CO_2 , H_2O , CO , and soot. However, in some cases, the combustion is incomplete due to a lack of oxygen. In others, a multiple-step reaction scheme is used to predict the production of CO .

9.1 Major Combustion Products, O_2 and CO_2

For any hydrocarbon fuel, the major combustion products are oxygen and carbon dioxide. Accurate predictions of these gases requires knowledge of the chemical composition of the fuel and an accurate transport algorithm for the combustion products.

9.1.1 DelCo Trainers

Oxygen and carbon dioxide measurements were made at several locations in the one and two level DelCo training structures. See Sec. 3.18 for their exact locations.

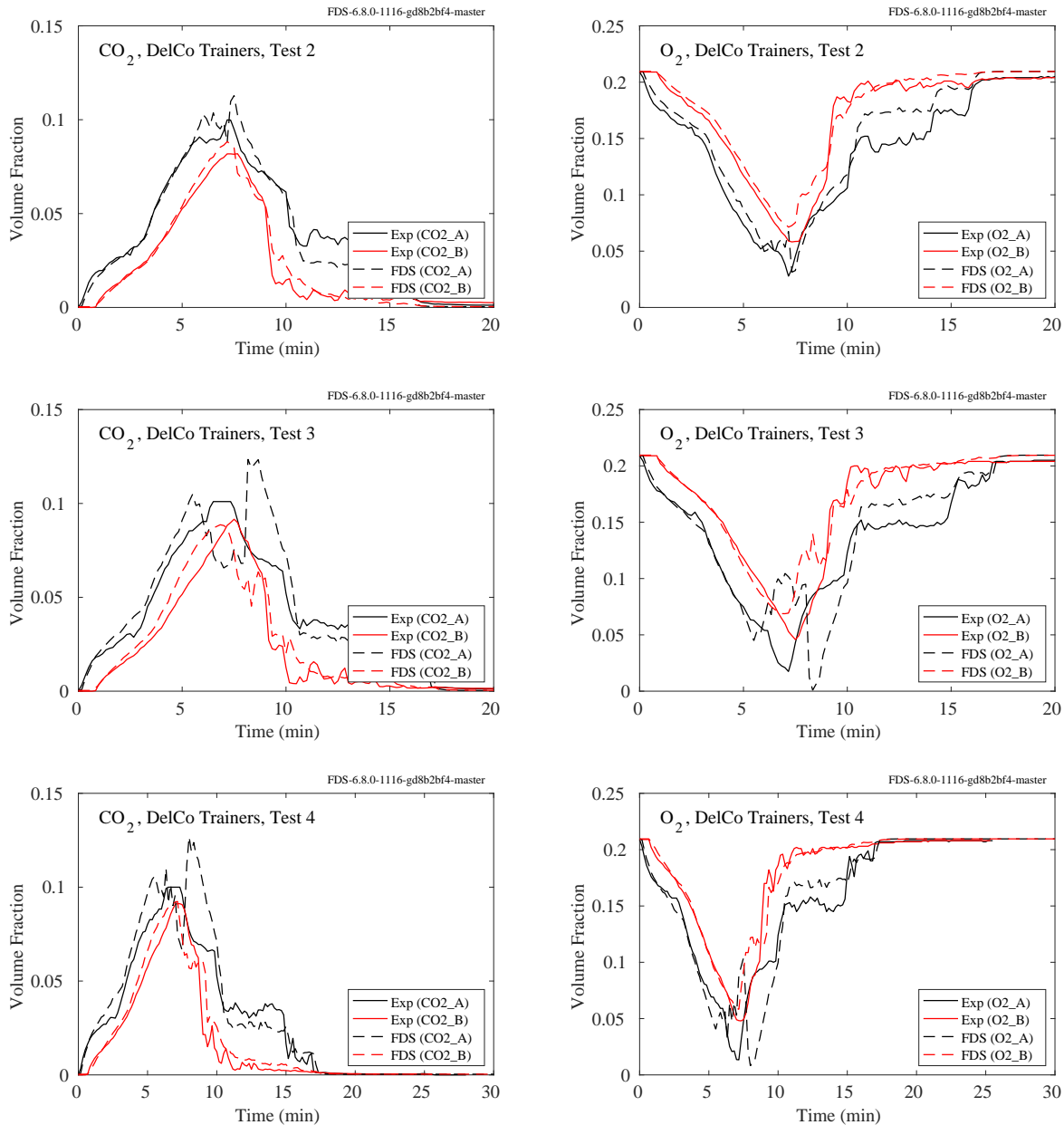
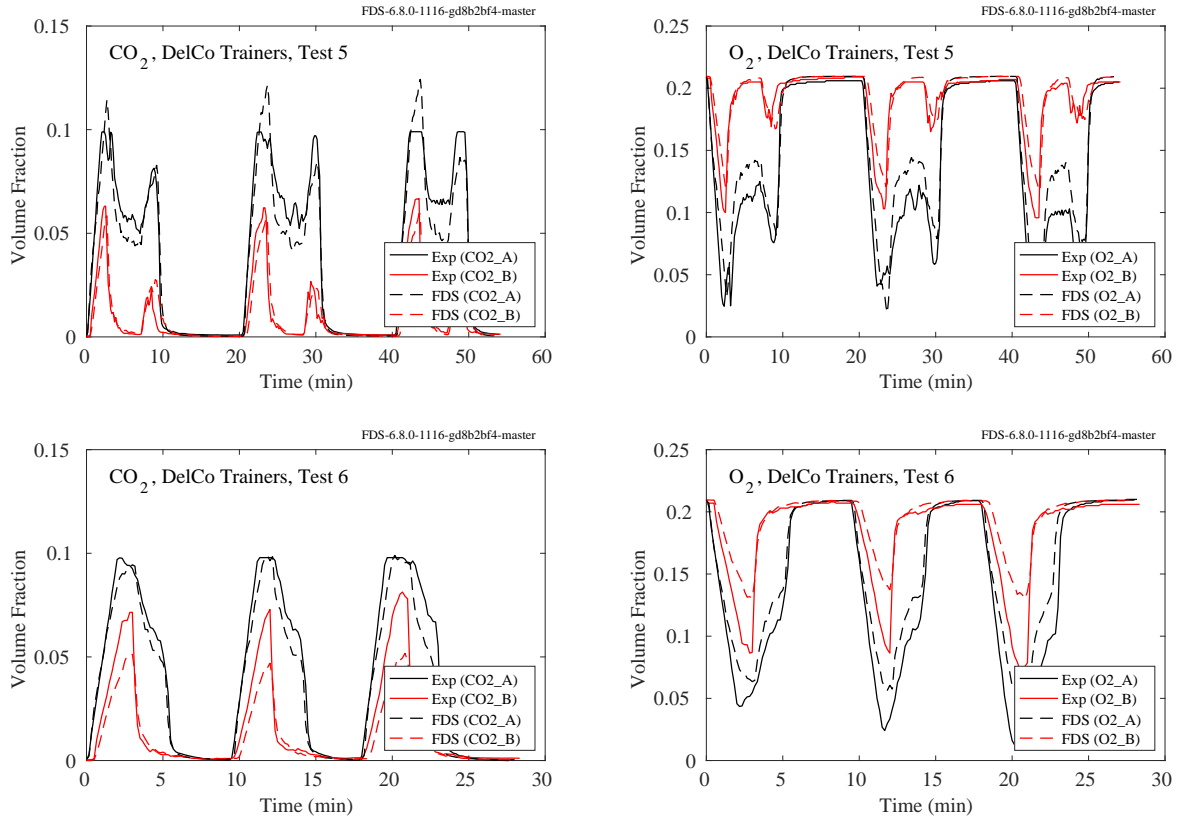
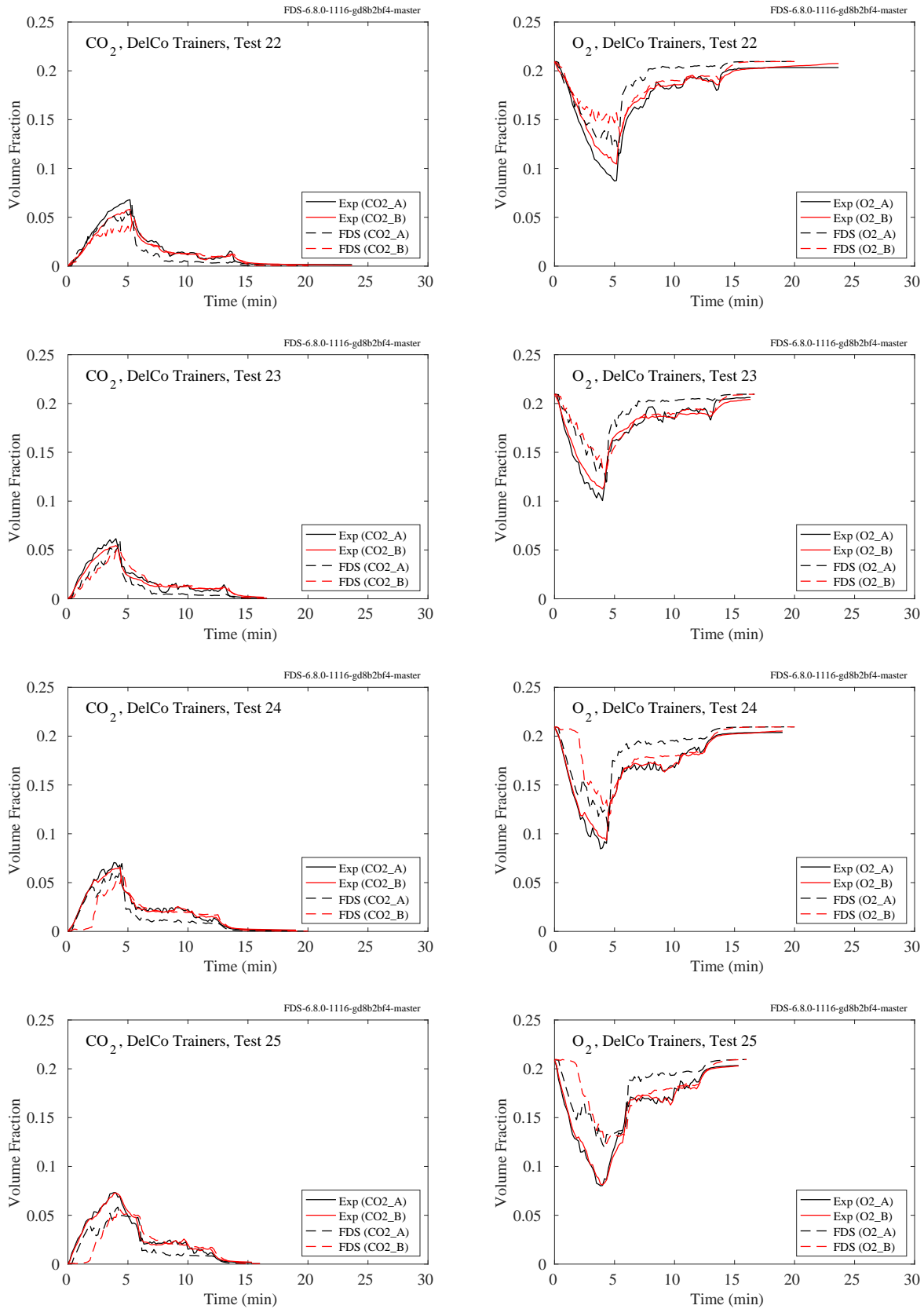


Figure 9.1: DelCo Trainers, CO₂ and O₂ concentration, Tests 2-4.

Figure 9.2: DelCo Trainers, CO₂ and O₂ concentration, Tests 5-6.

Figure 9.3: DelCo Trainers, CO₂ and O₂ concentration, Tests 22-25.

9.1.2 FAA Cargo Compartments

Carbon dioxide and carbon monoxide were measured near the ceiling in the forward, middle, and aft sections of the compartment. Note that all but the middle compartment concentrations were measured in Tests 2 and 3.

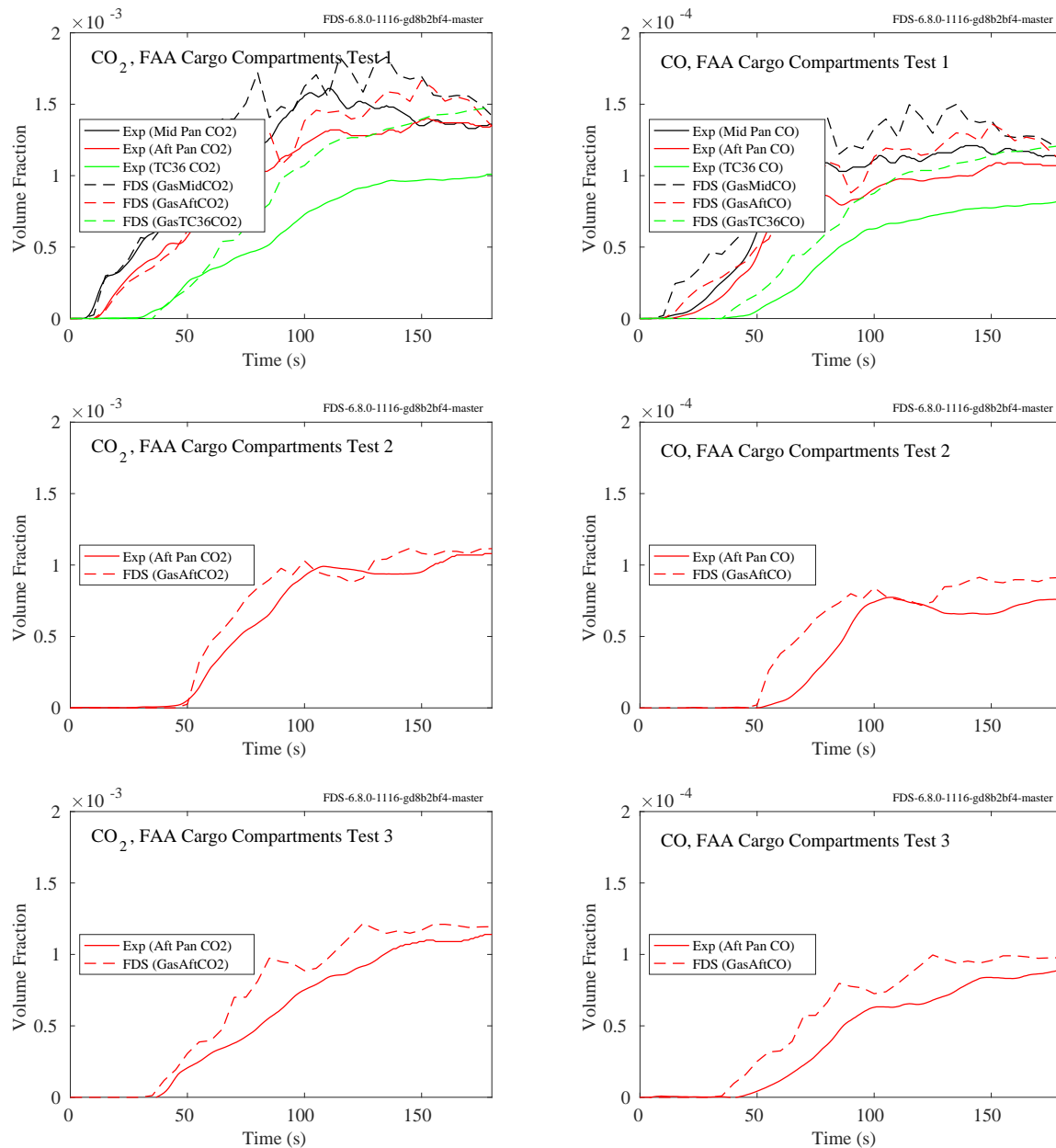


Figure 9.4: FAA Cargo Compartment experiments, CO₂ and O₂ concentration.

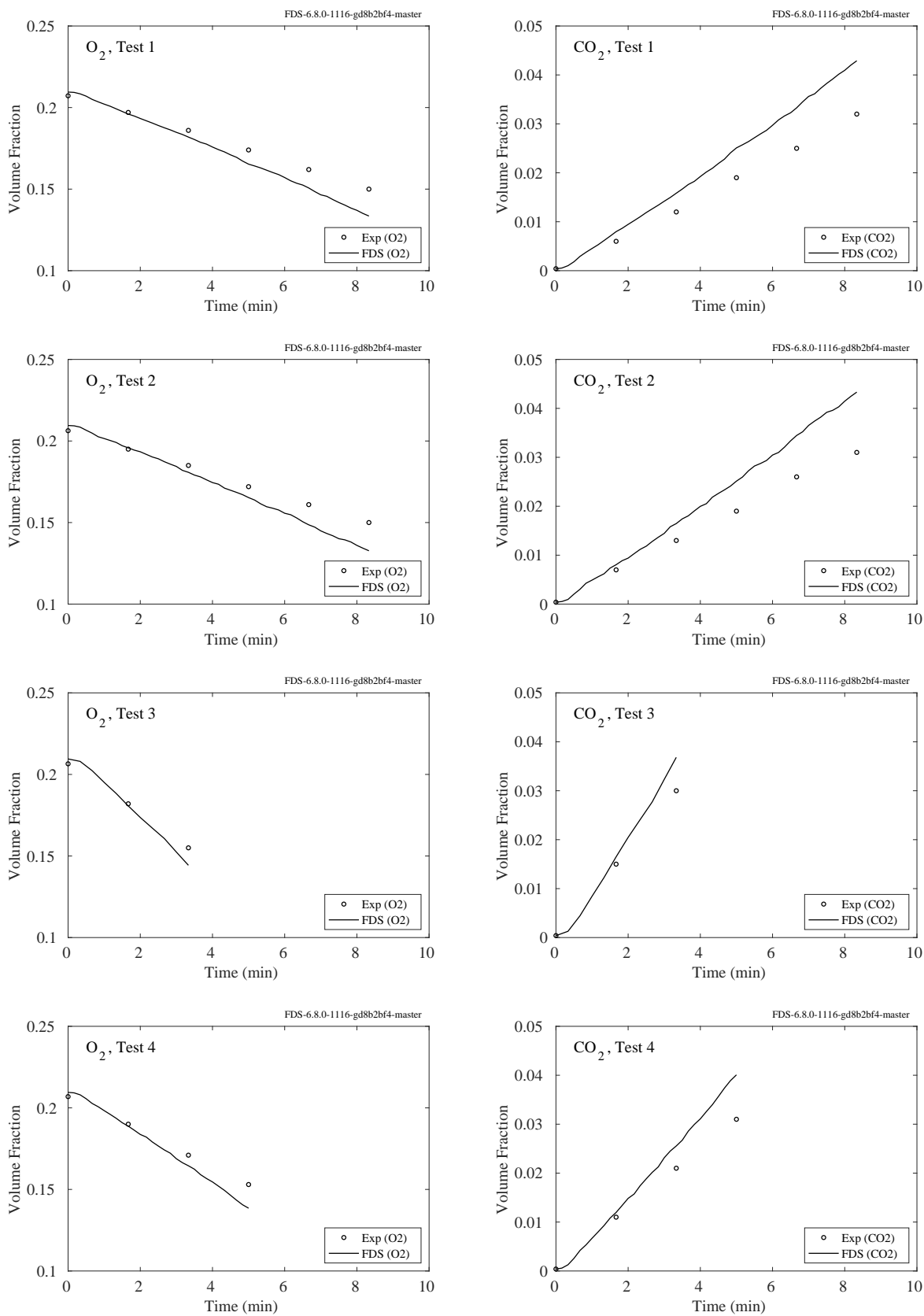
9.1.3 LLNL Enclosure

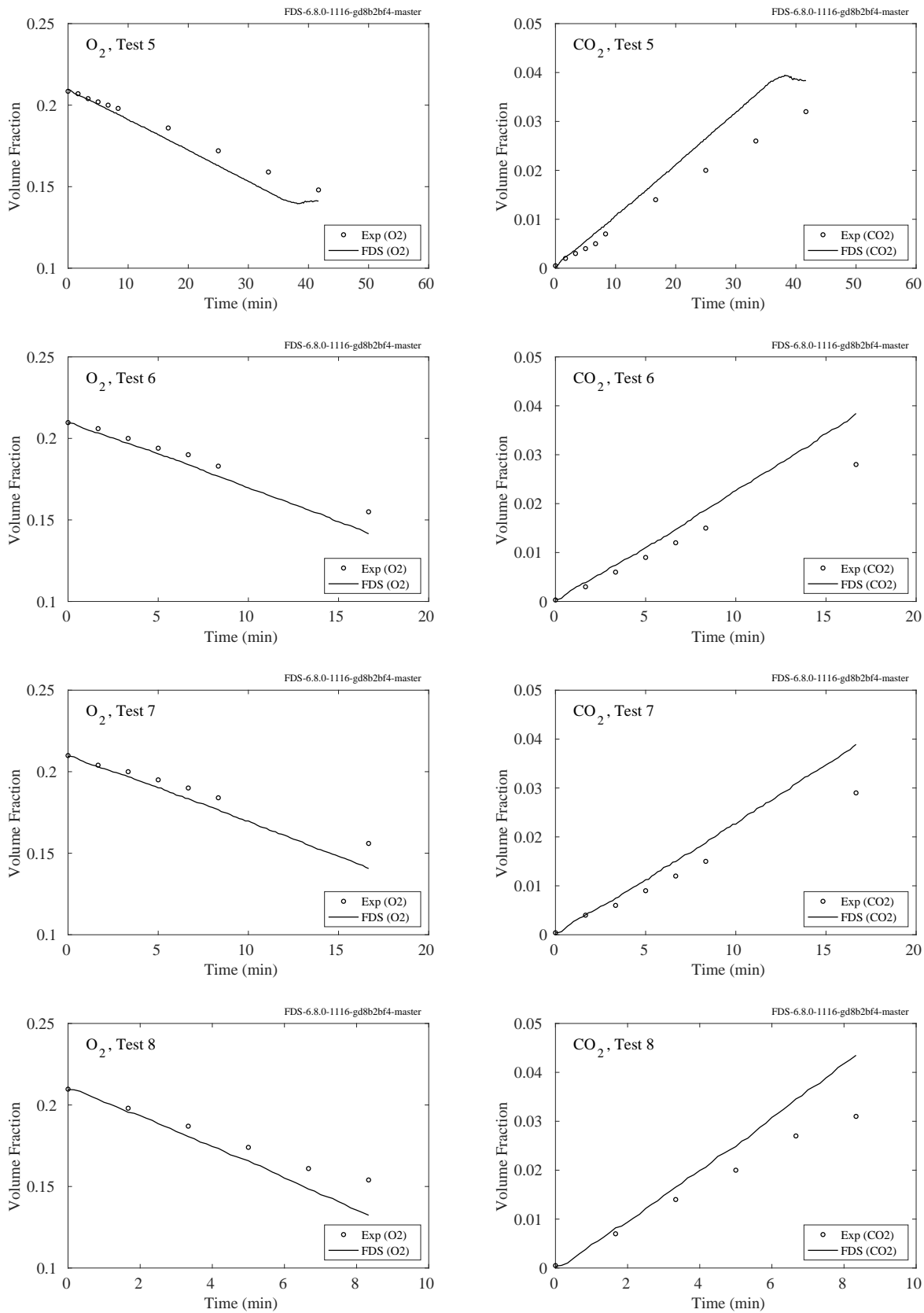
Oxygen and carbon dioxide concentrations were reported for a single location within the LLNL Enclosure. The test report [238] specifies the lateral location of the sensors (1.5 m from the wall opposite the exhaust duct, along the room centerline), but the reported height is only “top of room.” In the model, the sensors were located 4.3 m off the floor, 0.2 m below the ceiling of the compartment.

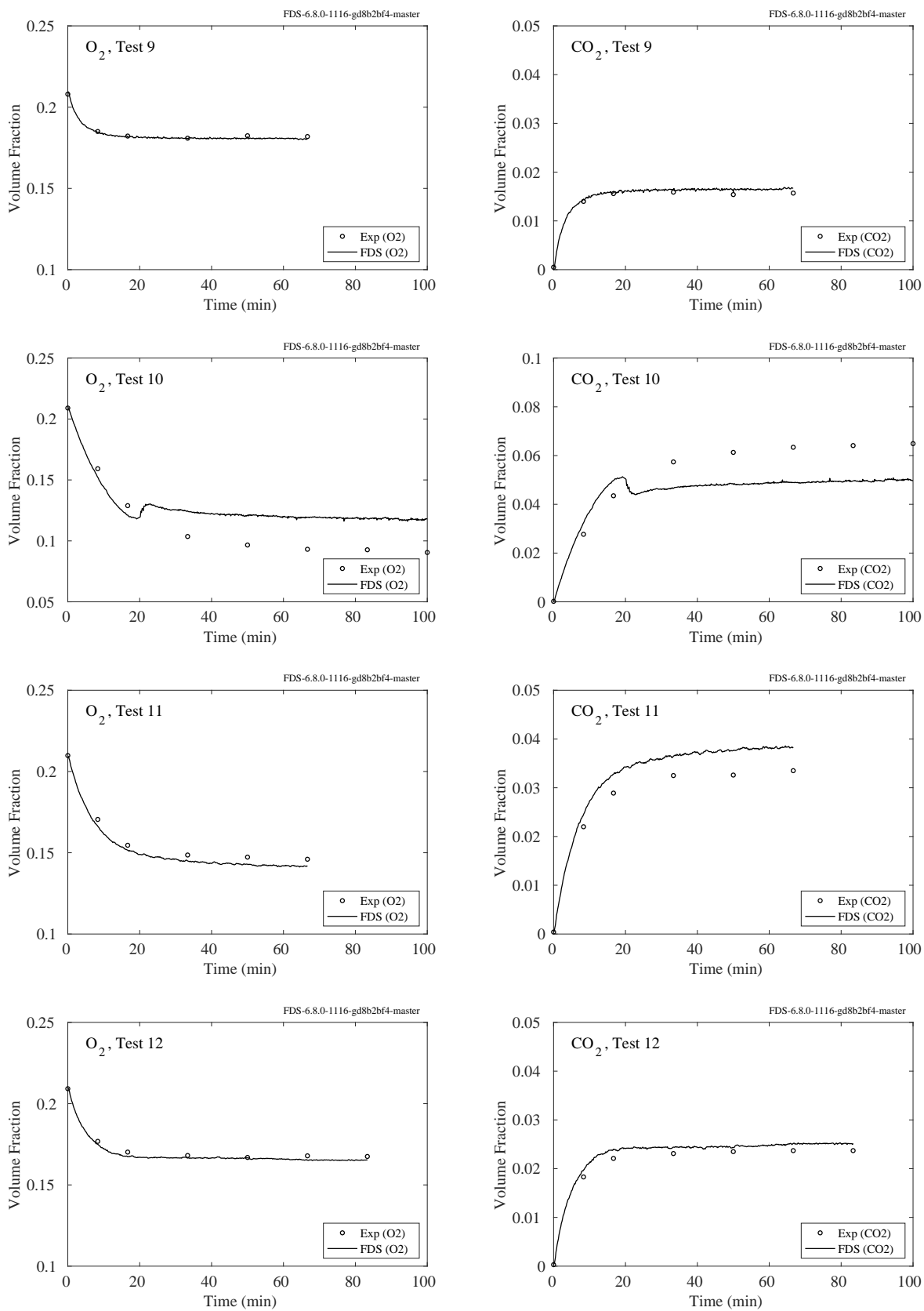
For some experiments, only two concentrations are reported, one being the ambient value. The results of these experiments are shown for completeness, but the values are not included in the calculation of the accuracy statistics.

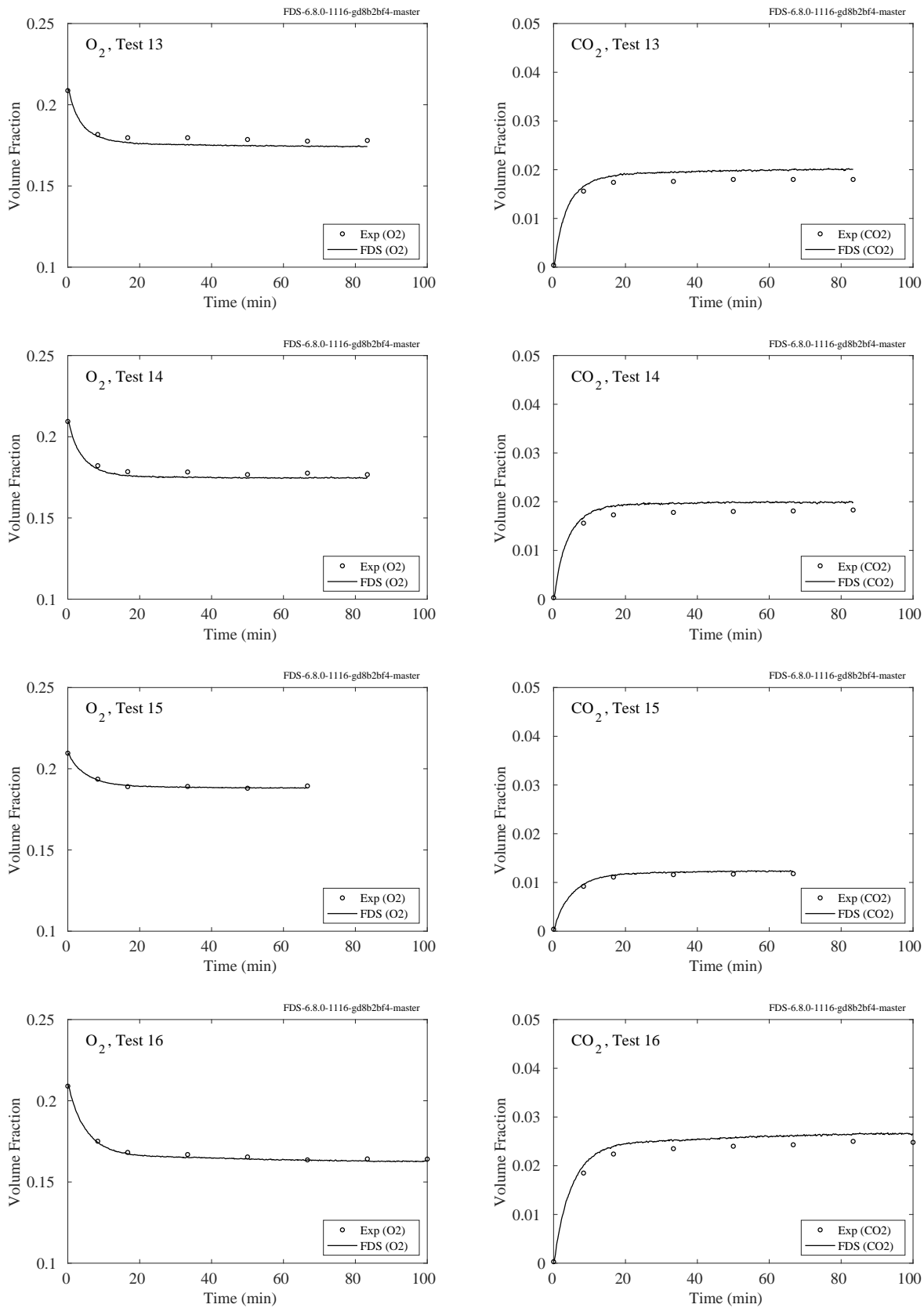
Also, the test report does not indicate whether the reported volume fractions were taken to be “wet” or “dry”; that is, whether the water vapor was condensed out of the sample. For the sake of comparison, the FDS results are assumed to be “dry”.

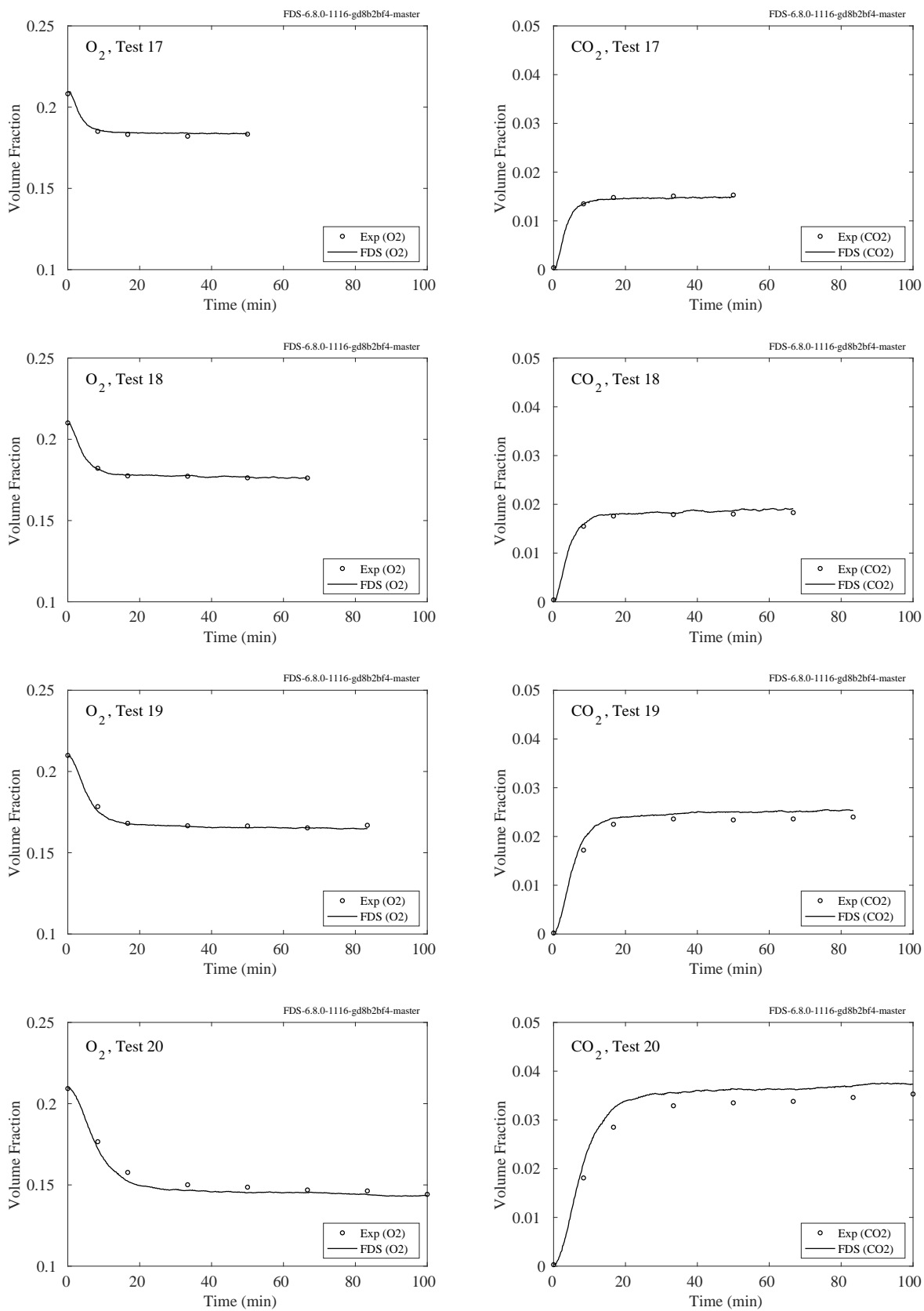
Further details of the modeling can be found in Sec. 3.43.

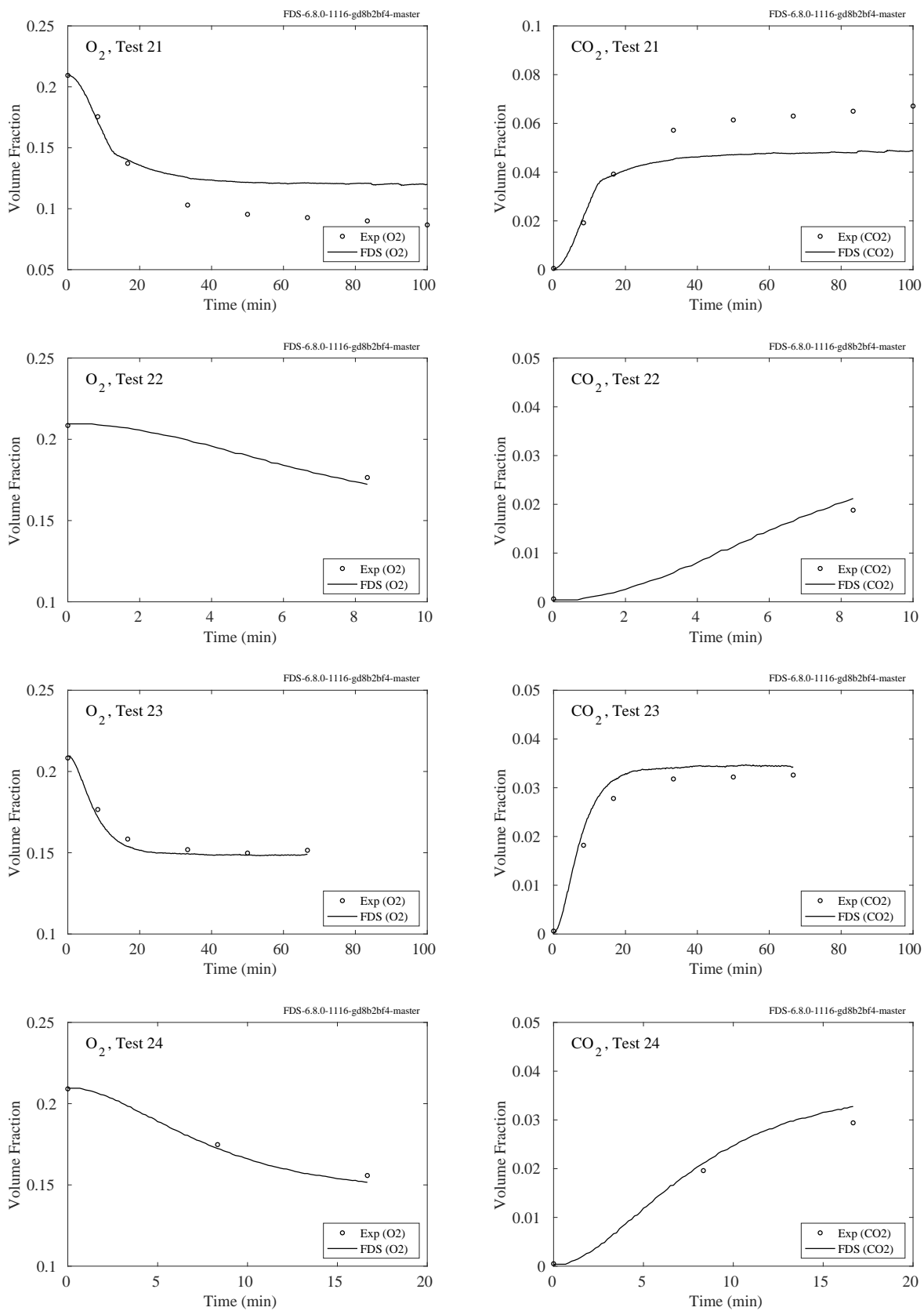
Figure 9.5: LLNL Enclosure, O_2 and CO_2 concentration, Tests 1-4.

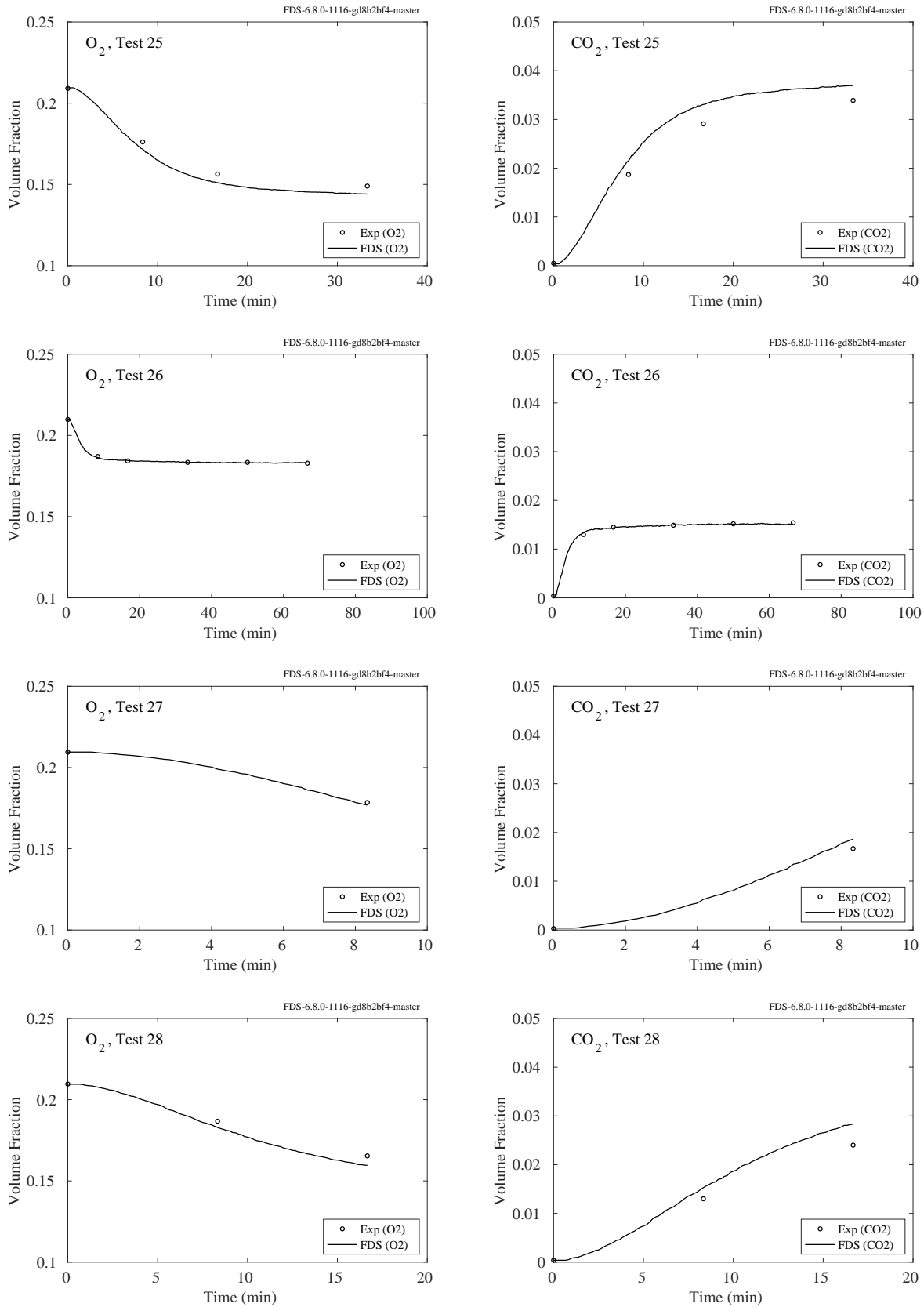
Figure 9.6: LLNL Enclosure, O_2 and CO_2 concentration, Tests 5-8.

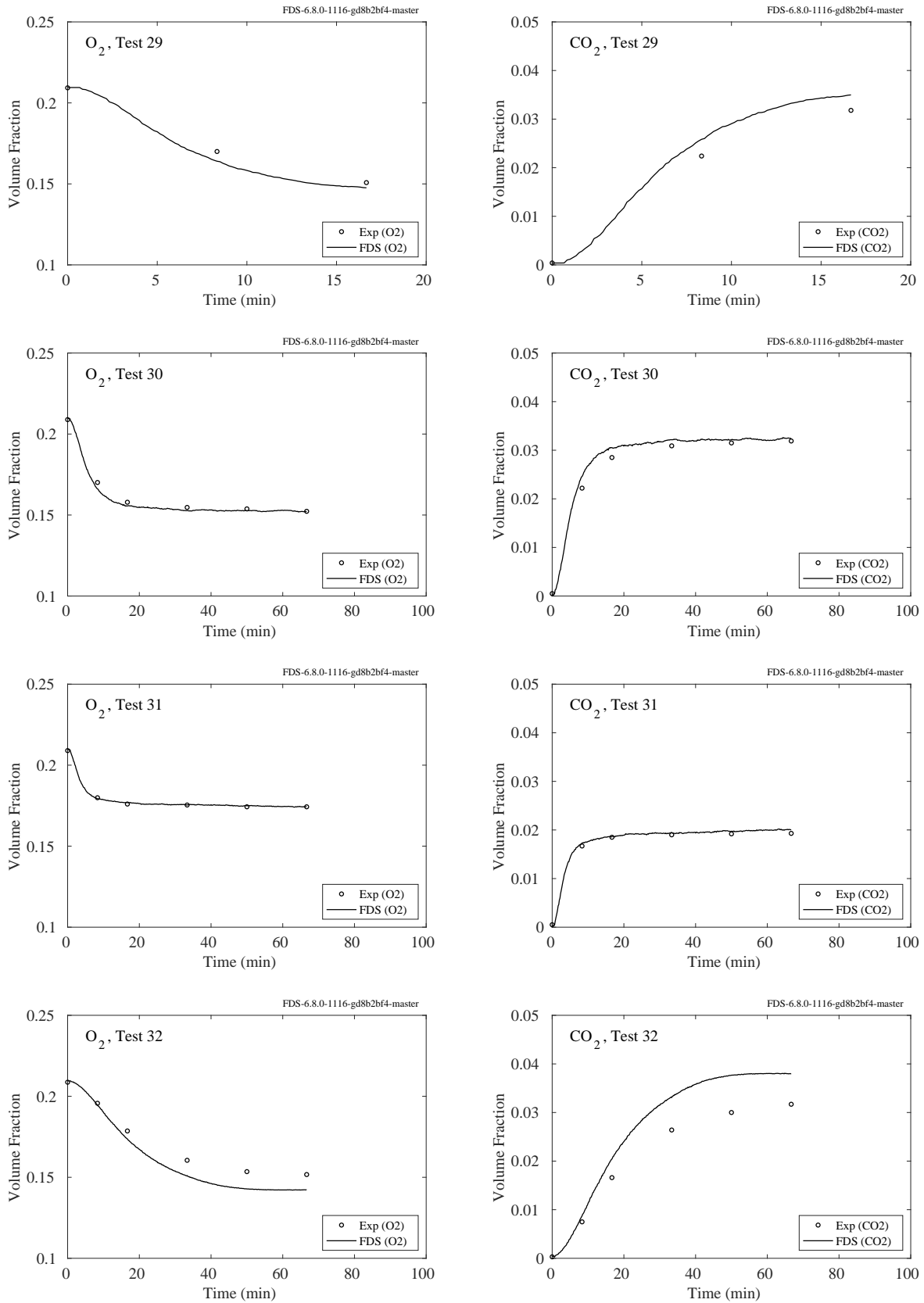
Figure 9.7: LLNL Enclosure, O_2 and CO_2 concentration, Tests 9-12.

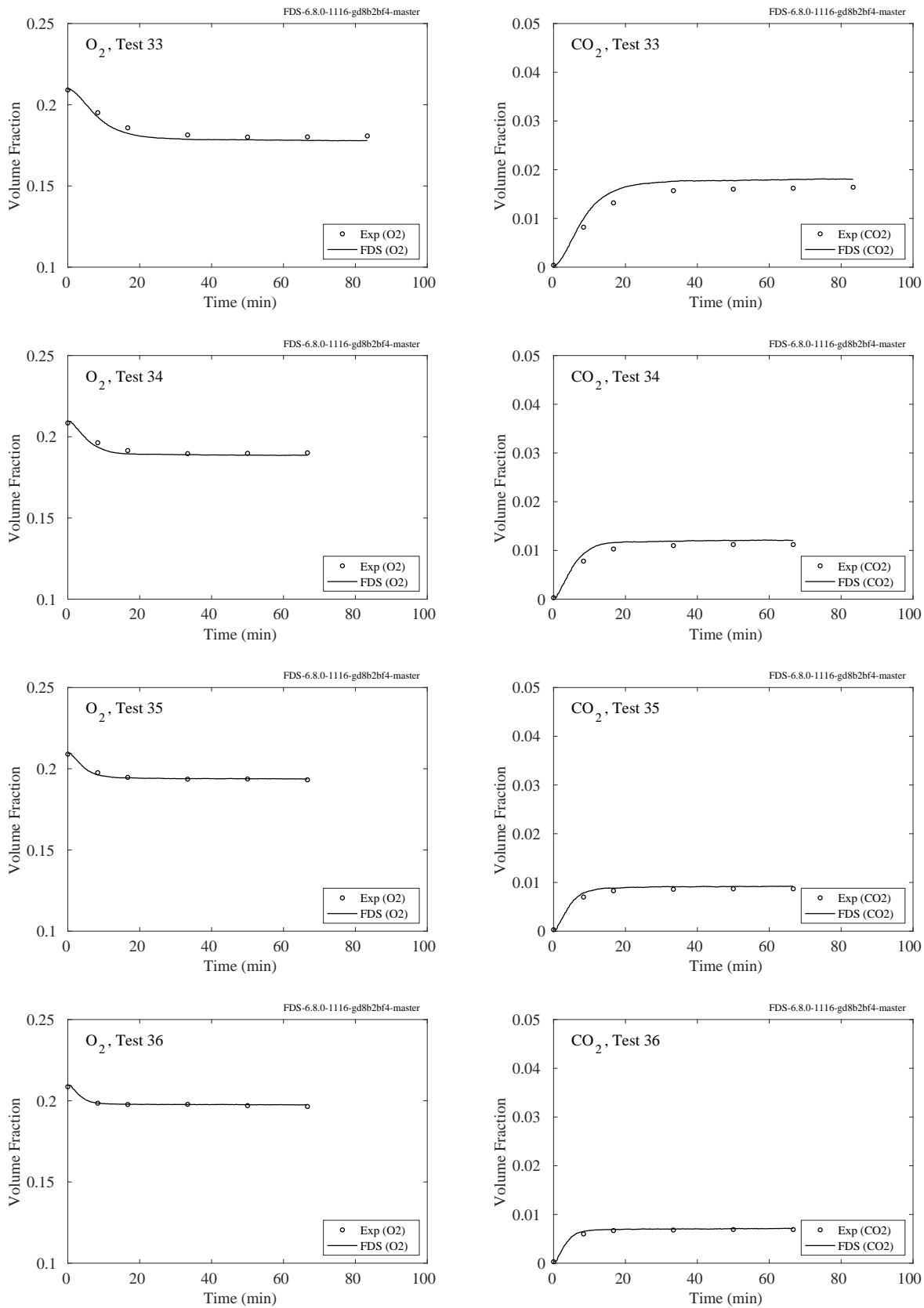
Figure 9.8: LLNL Enclosure, O_2 and CO_2 concentration, Tests 13-16.

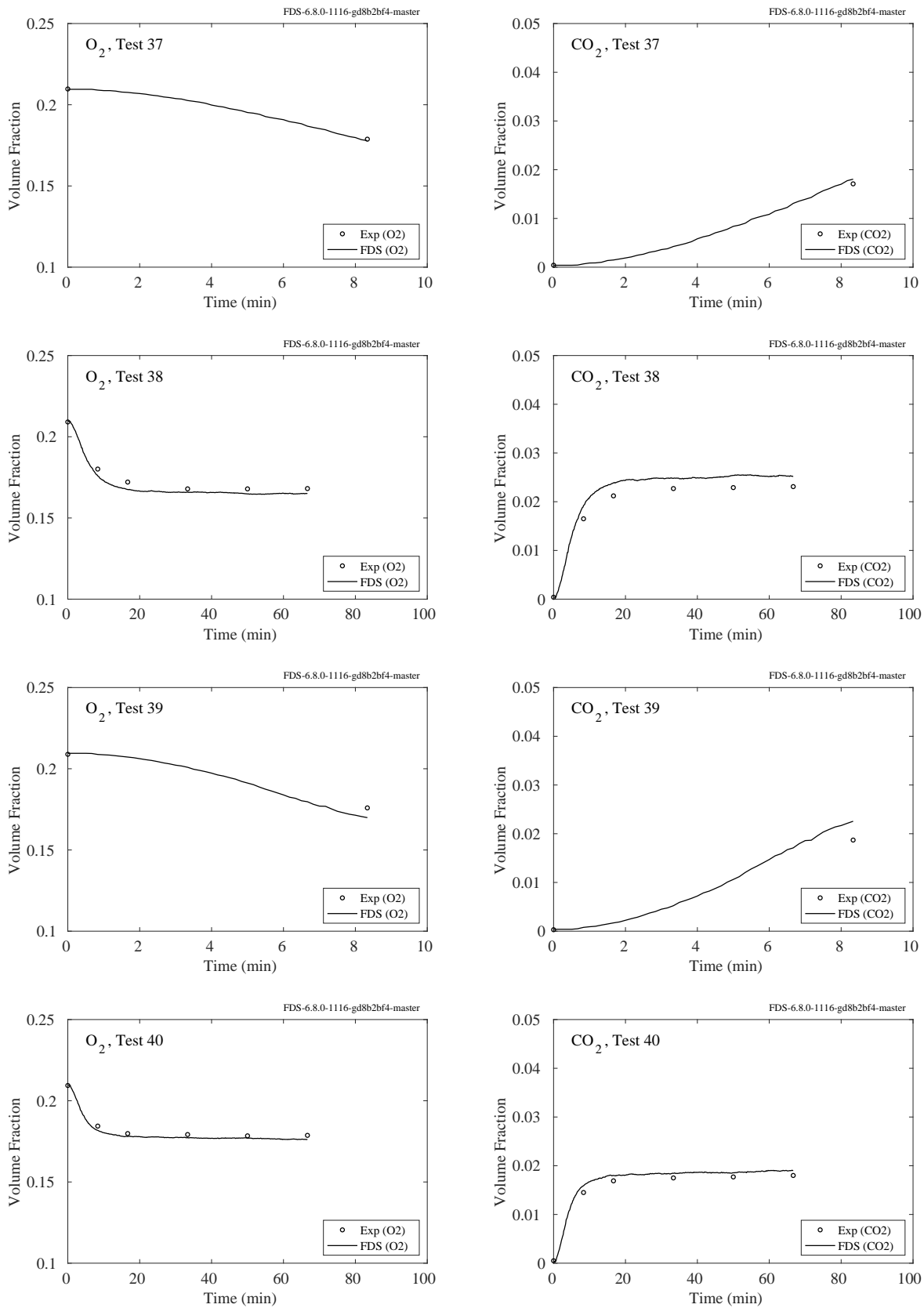
Figure 9.9: LLNL Enclosure, O_2 and CO_2 concentration, Tests 17-20.

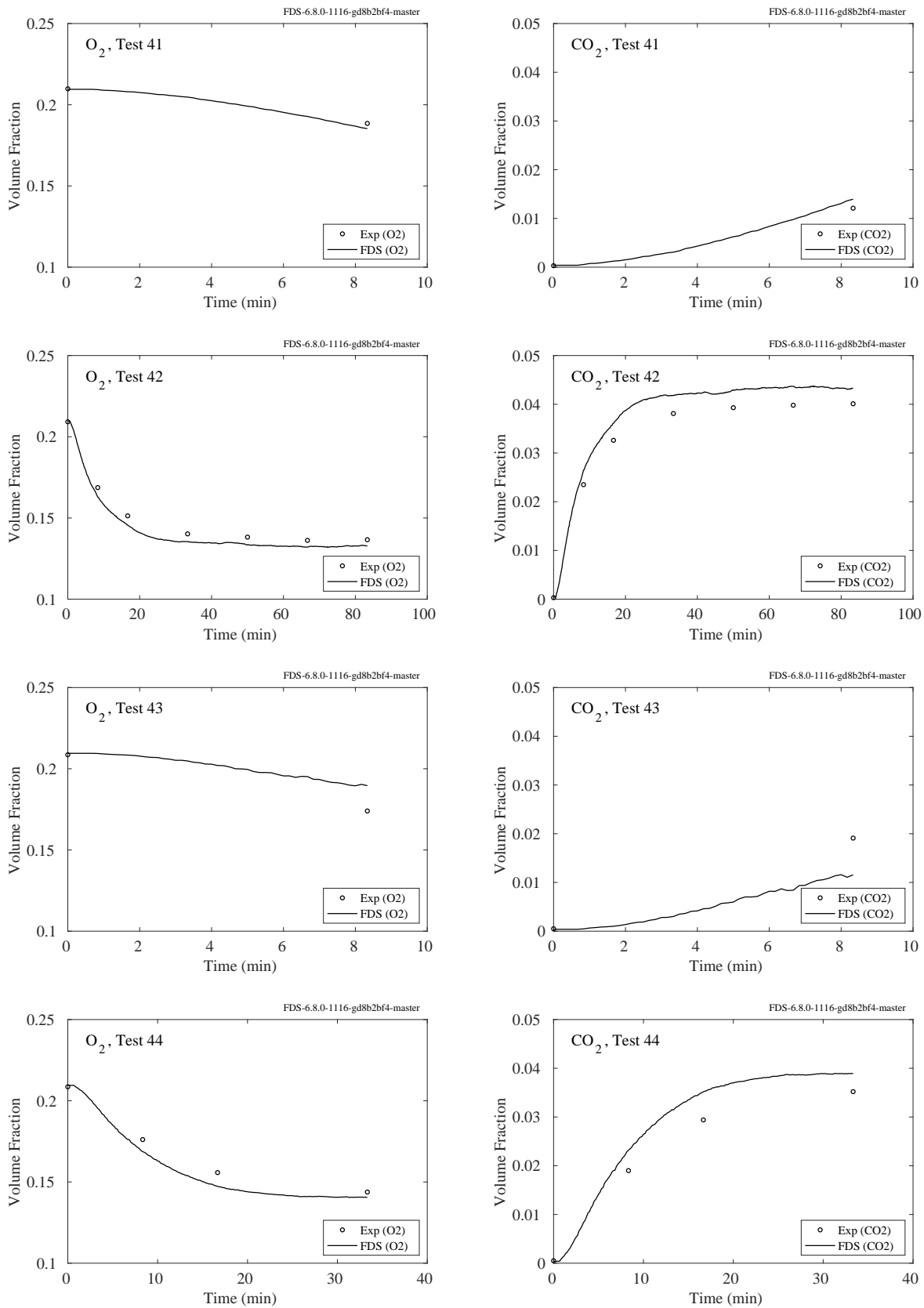
Figure 9.10: LLNL Enclosure, O_2 and CO_2 concentration, Tests 21-24.

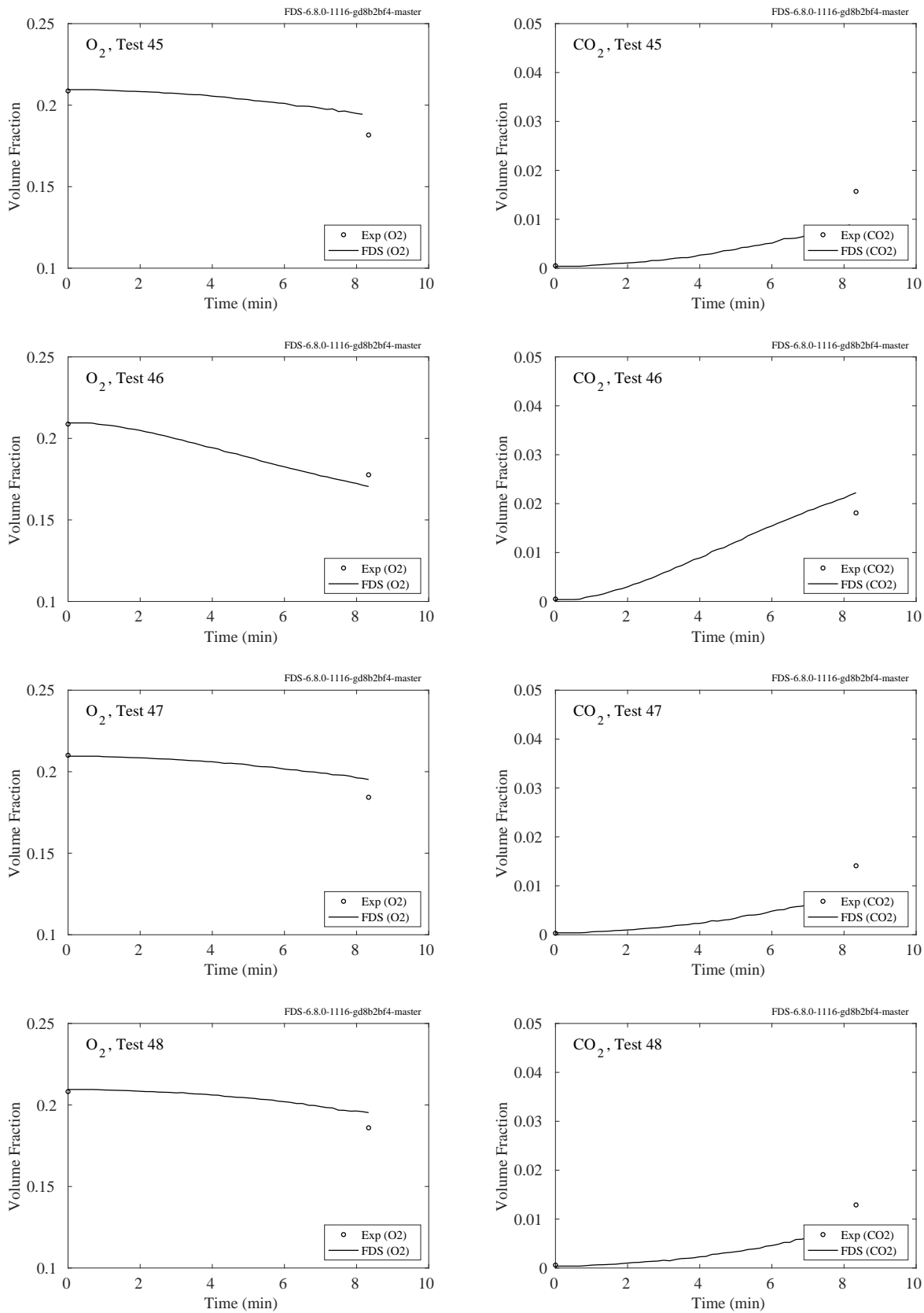
Figure 9.11: LLNL Enclosure, O_2 and CO_2 concentration, Tests 25-28.

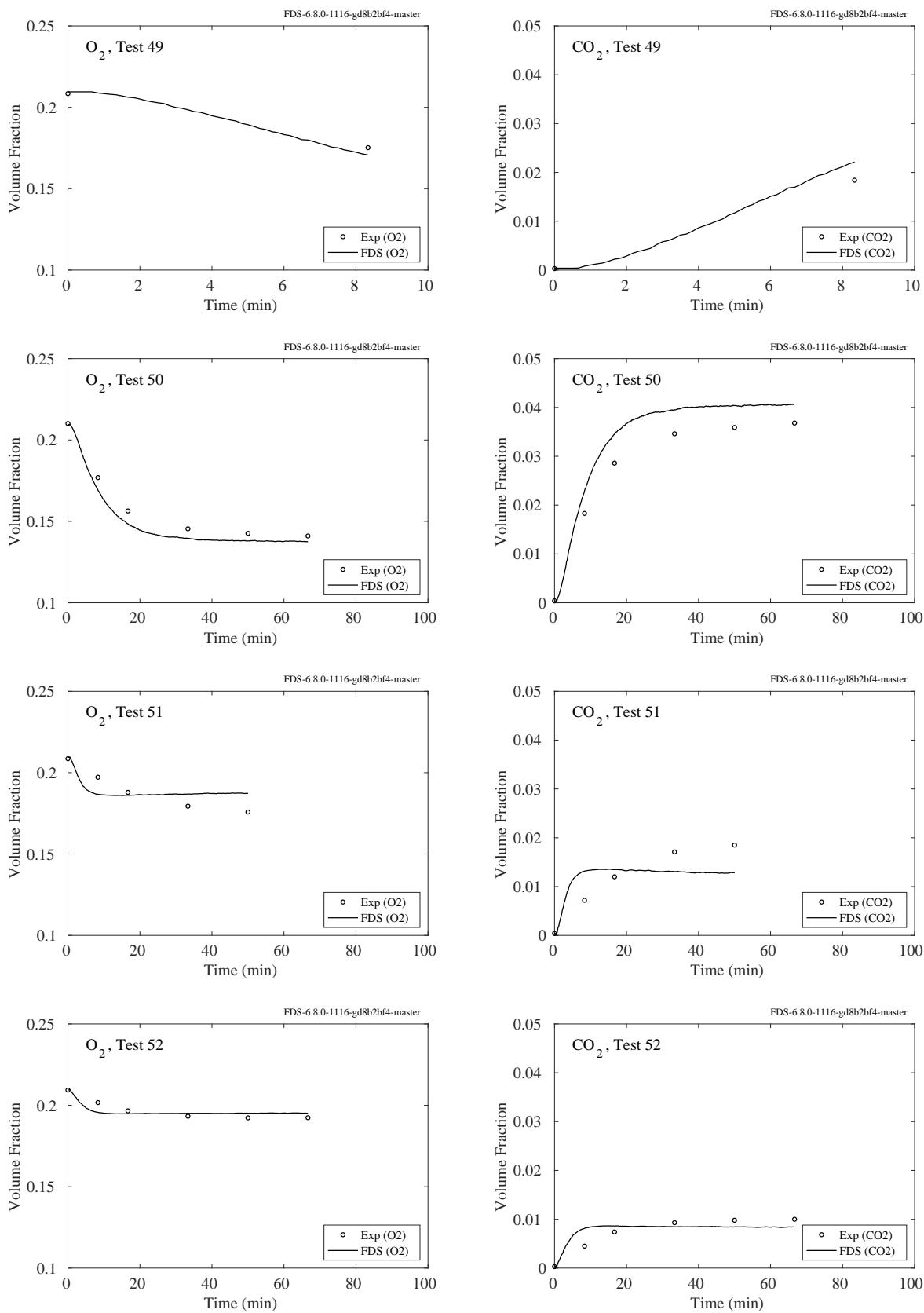
Figure 9.12: LLNL Enclosure, O_2 and CO_2 concentration, Tests 29-32.

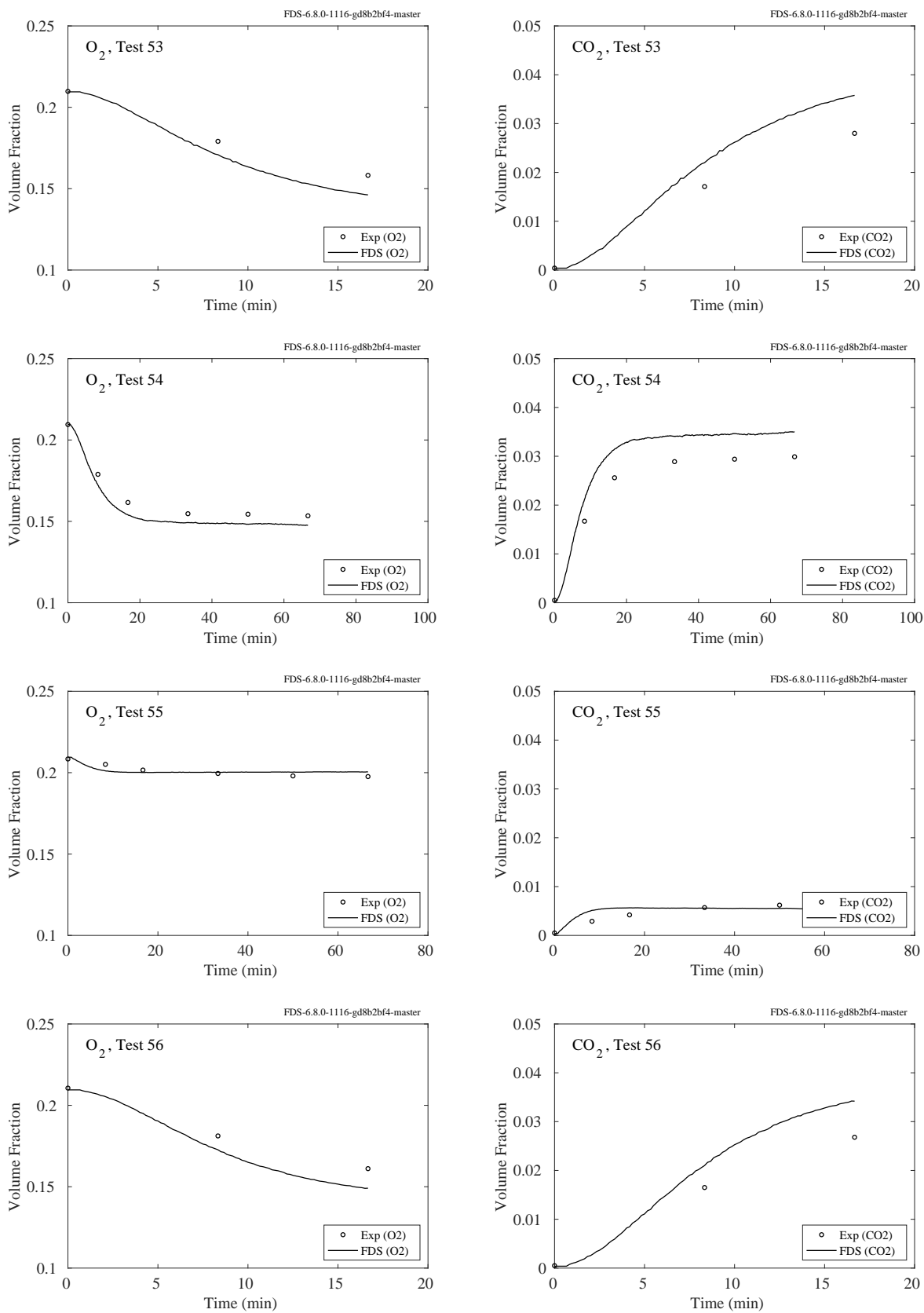
Figure 9.13: LLNL Enclosure, O_2 and CO_2 concentration, Tests 33-36.

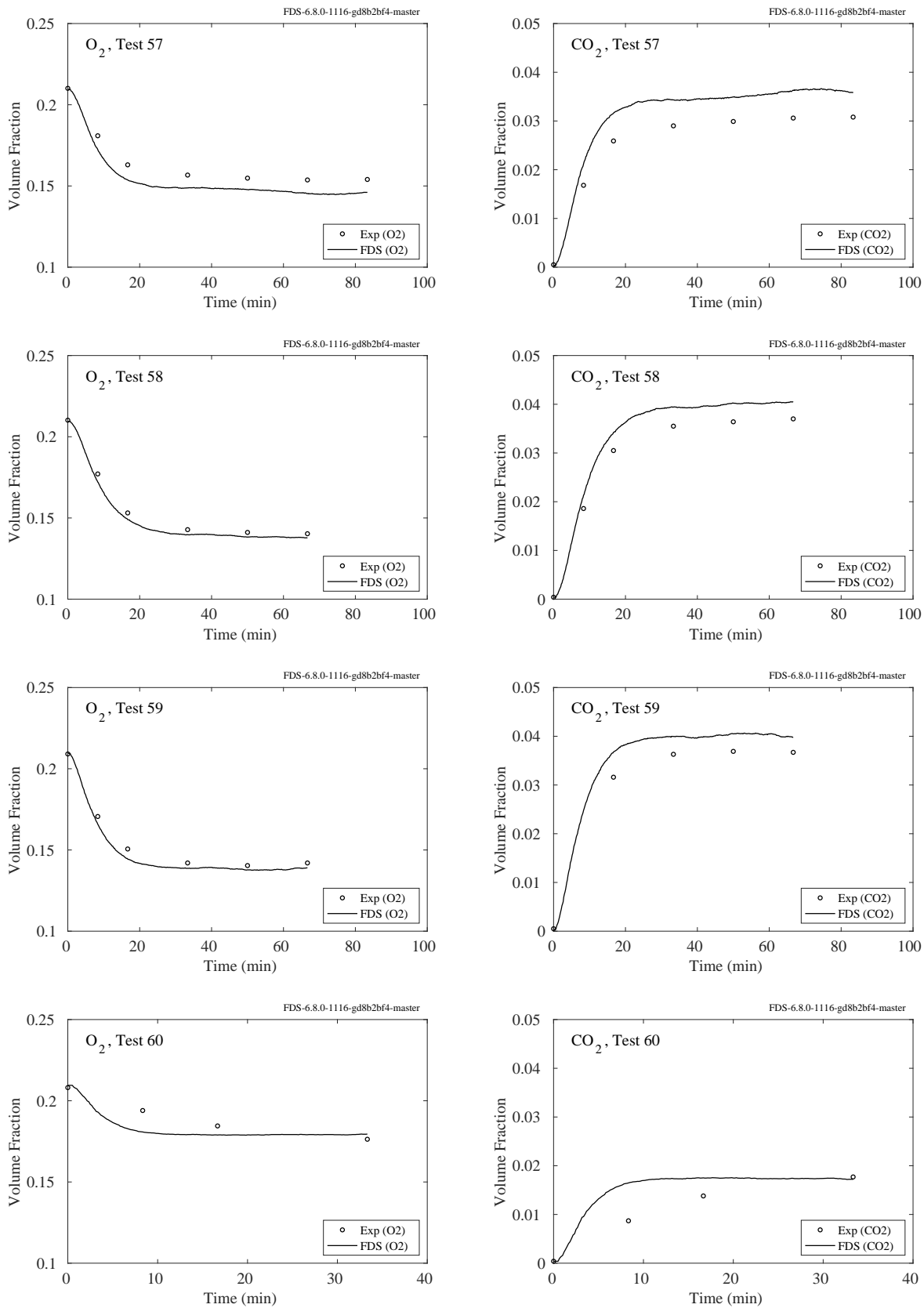
Figure 9.14: LLNL Enclosure, O_2 and CO_2 concentration, Tests 37-40.

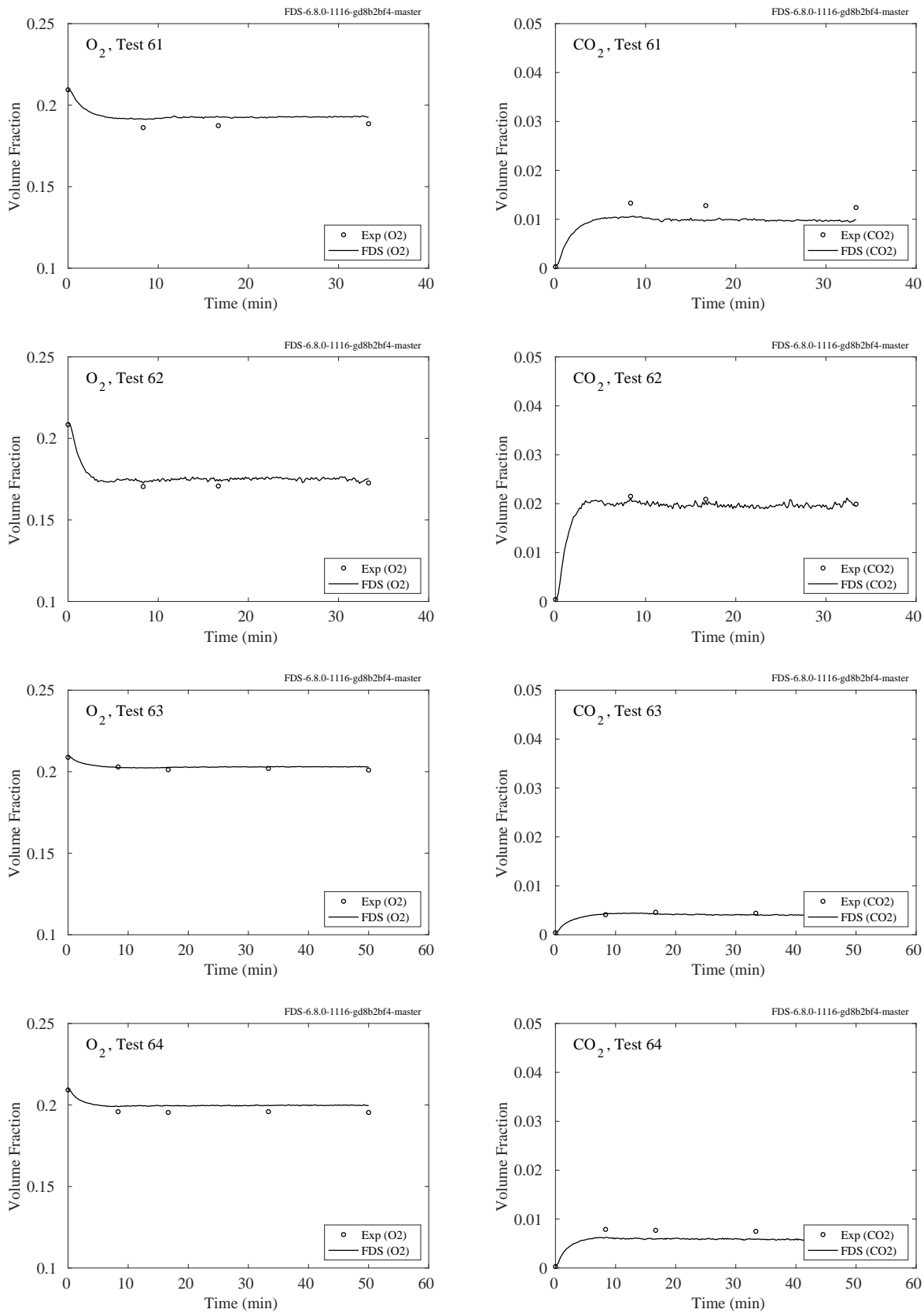
Figure 9.15: LLNL Enclosure, O_2 and CO_2 concentration, Tests 41-44.

Figure 9.16: LLNL Enclosure, O_2 and CO_2 concentration, Tests 45-48.

Figure 9.17: LLNL Enclosure, O_2 and CO_2 concentration, Tests 49-52.

Figure 9.18: LLNL Enclosure, O_2 and CO_2 concentration, Tests 53-56.

Figure 9.19: LLNL Enclosure, O_2 and CO_2 concentration, Tests 57-60.

Figure 9.20: LLNL Enclosure, O_2 and CO_2 concentration, Tests 61-64.

9.1.4 NIST/NRC Experiments

The following pages present comparisons of oxygen and carbon dioxide concentration predictions and measurements for the NIST/NRC series. There were two oxygen measurements, one in the upper layer, one in the lower. There was only one carbon dioxide measurement in the upper layer.

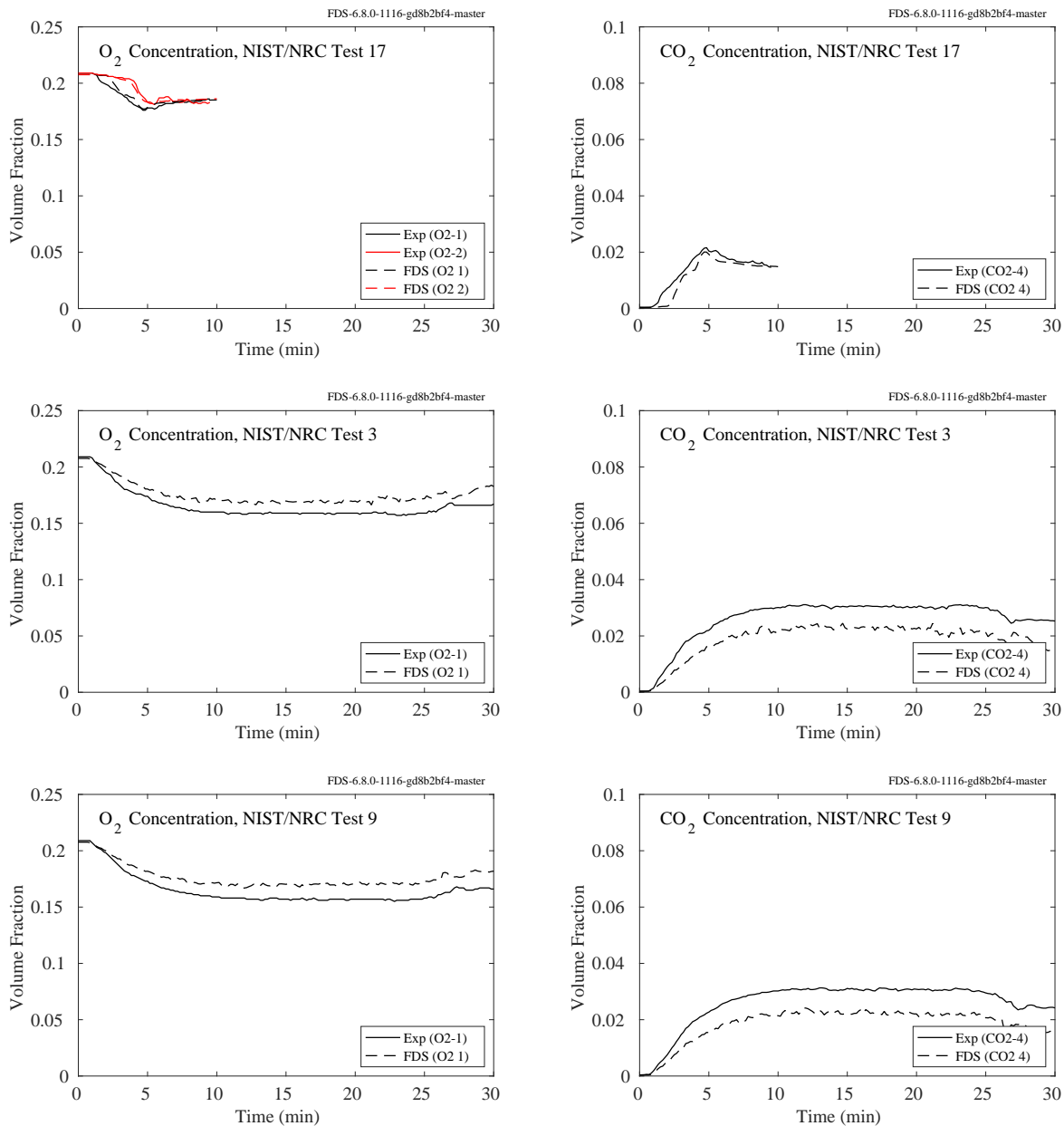
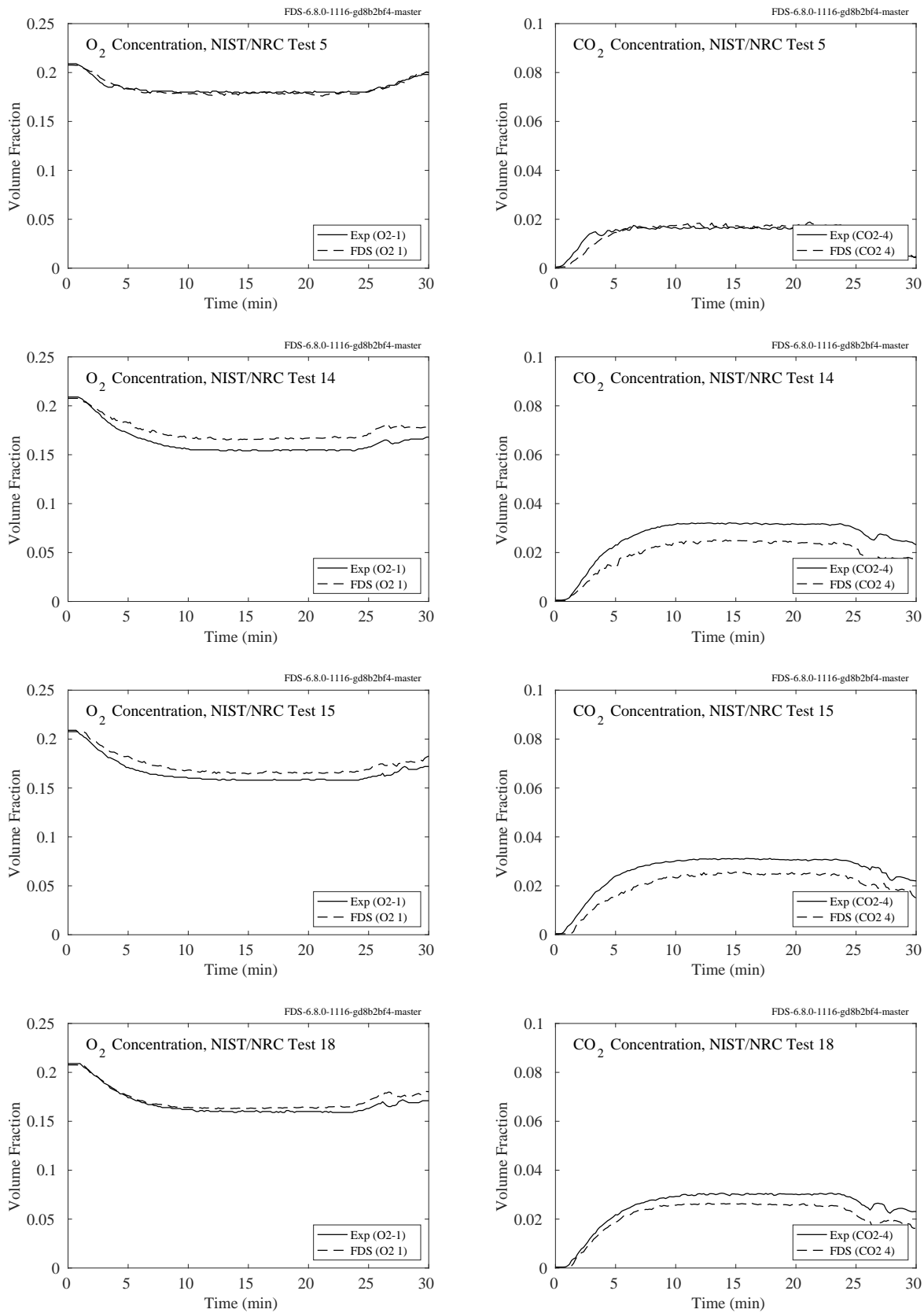
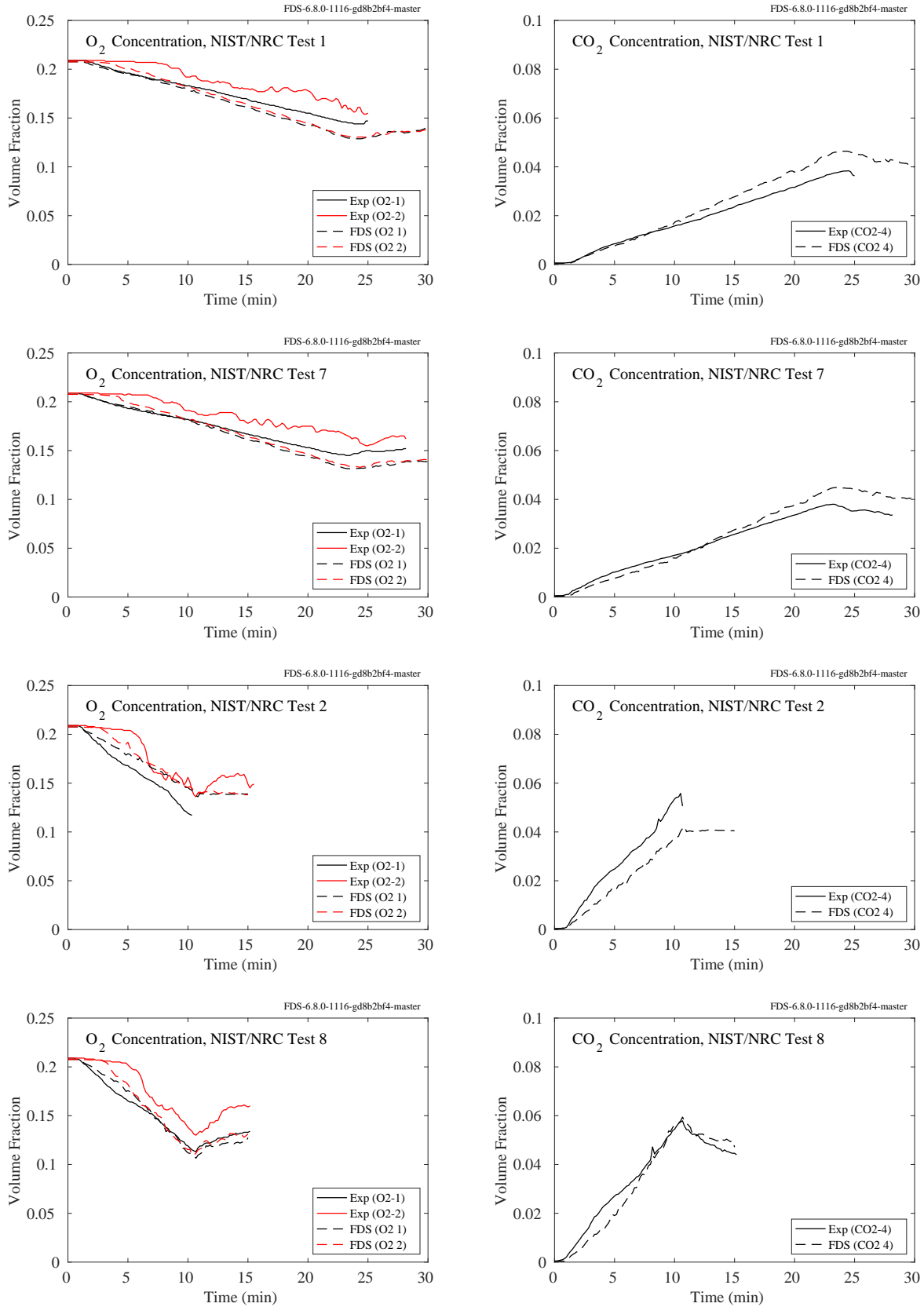
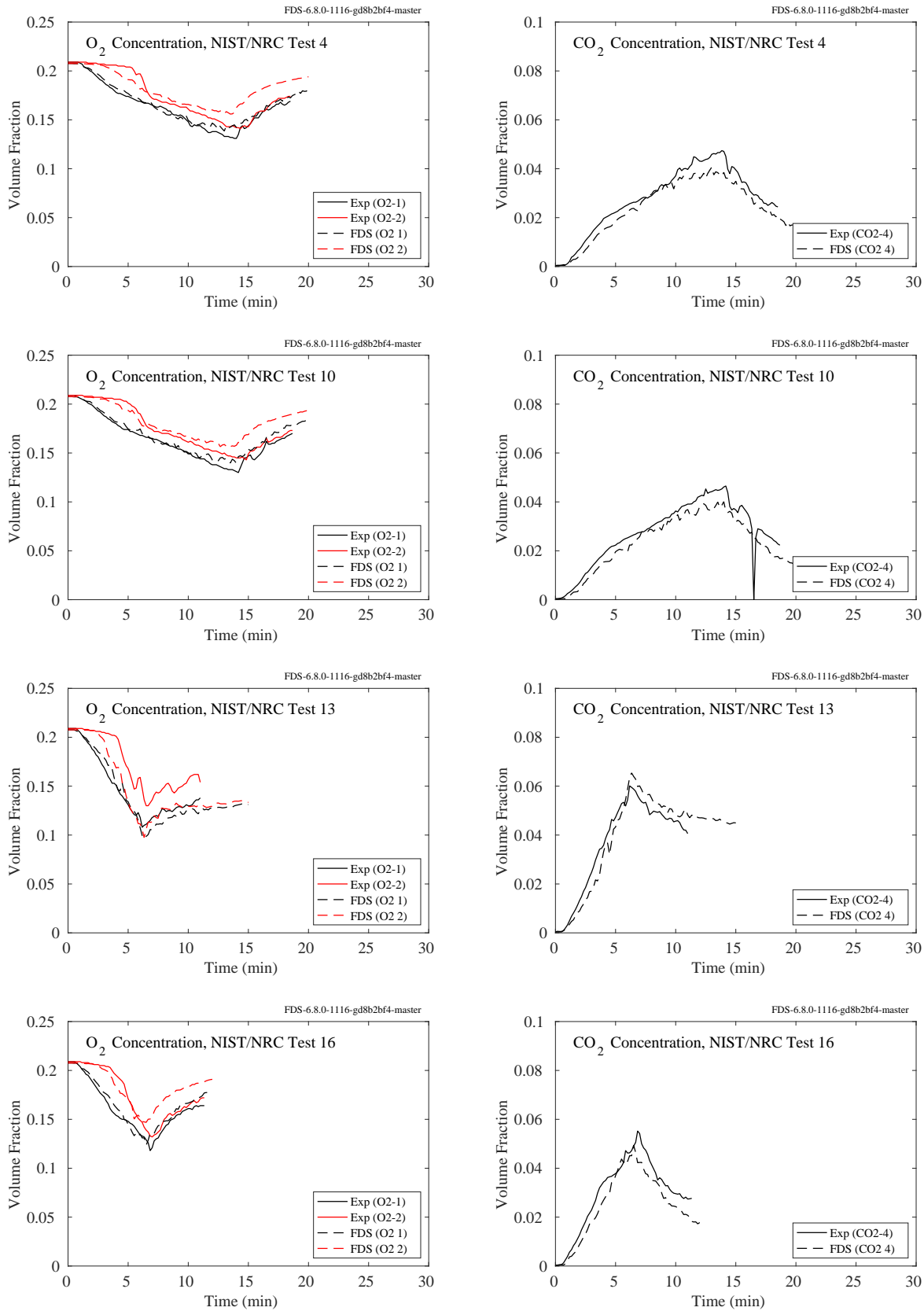


Figure 9.21: NIST/NRC experiments, CO₂ and O₂ concentration, Tests 3, 9, 17.

Figure 9.22: NIST/NRC experiments, CO_2 and O_2 concentration, Tests 5, 14, 15, 18.

Figure 9.23: NIST/NRC experiments, CO_2 and O_2 concentration, Tests 1, 2, 7, 8.

Figure 9.24: NIST/NRC experiments, CO_2 and O_2 concentration, Tests 4, 10, 13, 16.

9.1.5 NRCC Smoke Tower

In the NRCC Smoke Tower experiments, there were oxygen and carbon dioxide analyzers in the stair shaft on the second floor just outside the door of the fire compartment.

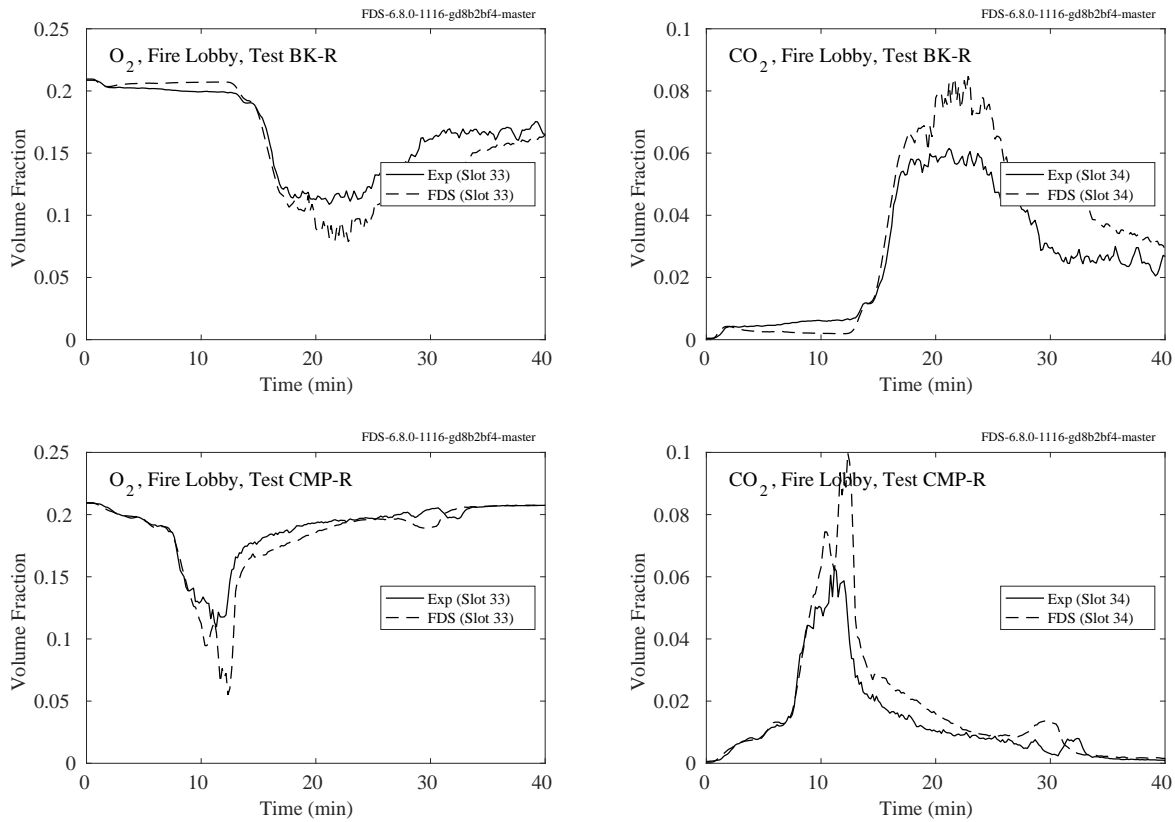


Figure 9.25: NRCC Smoke Tower, CO₂ and O₂ concentration, Tests BK-R and COMP-R.

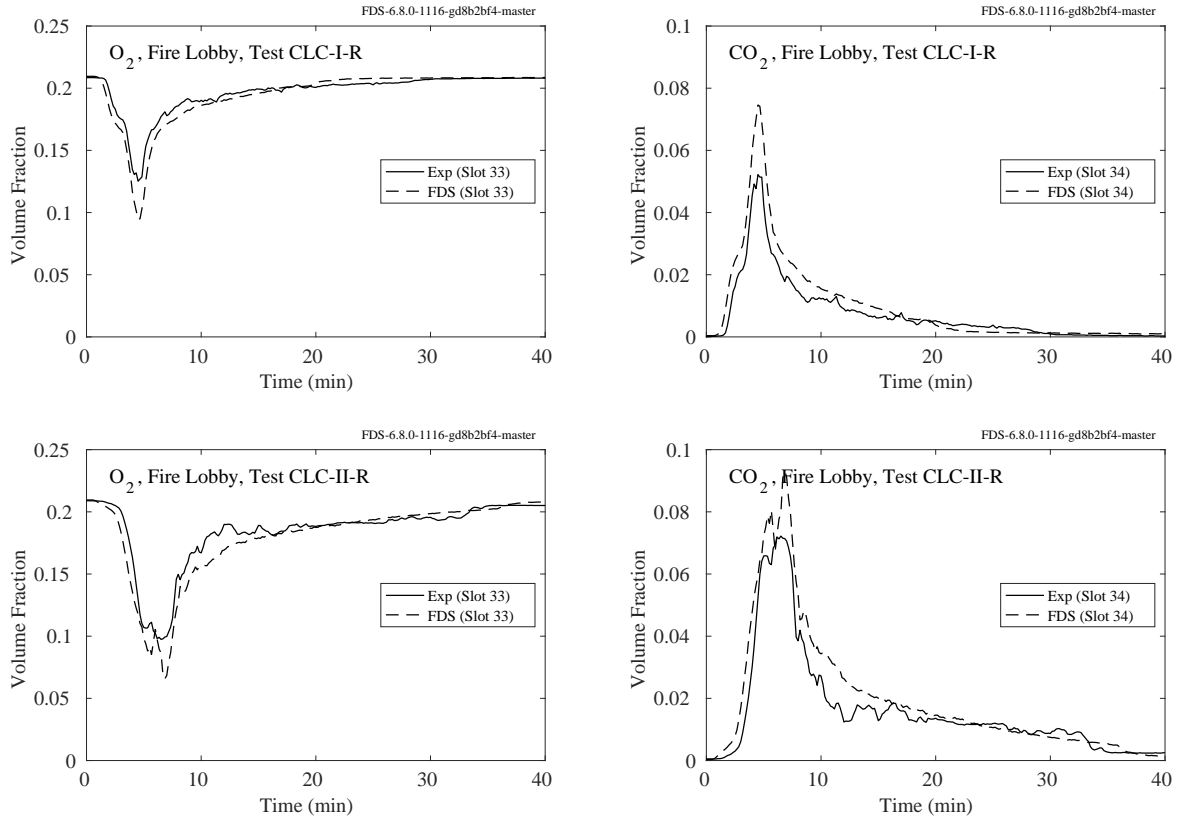


Figure 9.26: NRCC Smoke Tower, CO₂ and O₂ concentration, Tests CLC-I-R and CLC-II-R.

9.1.6 PRISME DOOR Experiments

Each compartment in the PRISME DOOR experiments contained an oxygen and carbon dioxide measurement in the upper (haut) and lower (bas) layers.

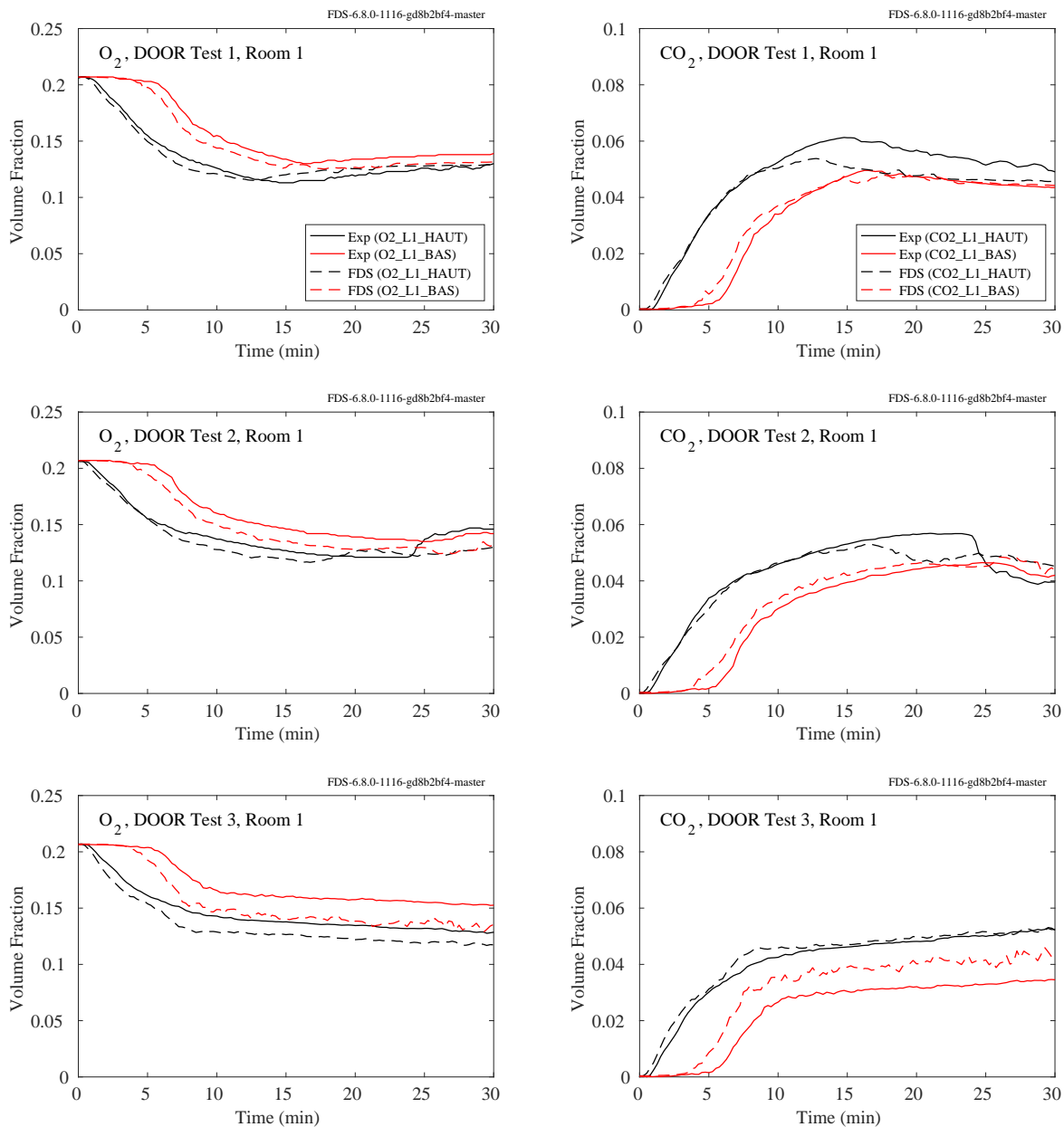


Figure 9.27: PRISME DOOR experiments, CO_2 and O_2 concentration, Room 1, Tests 1-3.

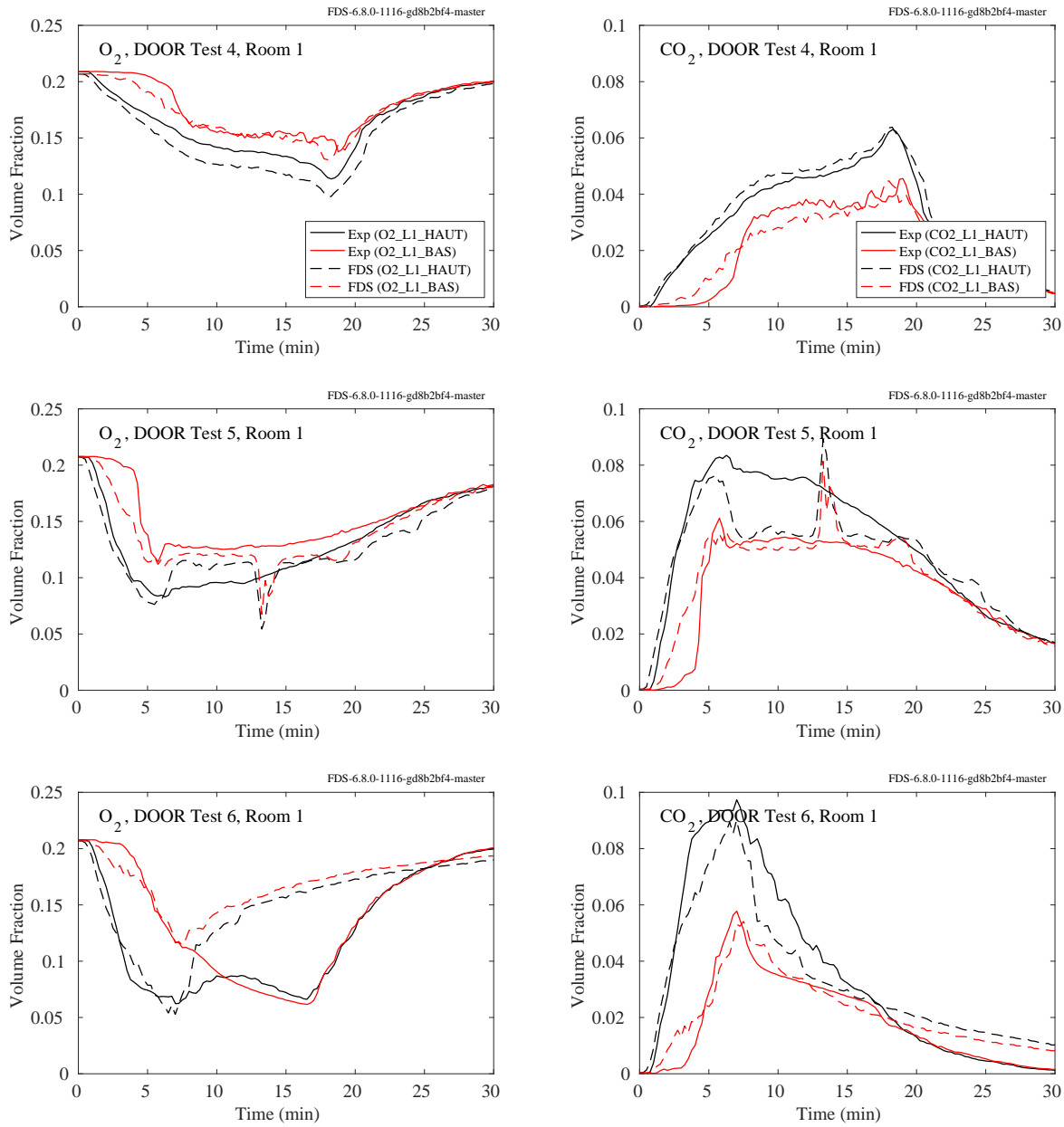


Figure 9.28: PRISME DOOR experiments, CO_2 and O_2 concentration, Room 1, Tests 4-6.

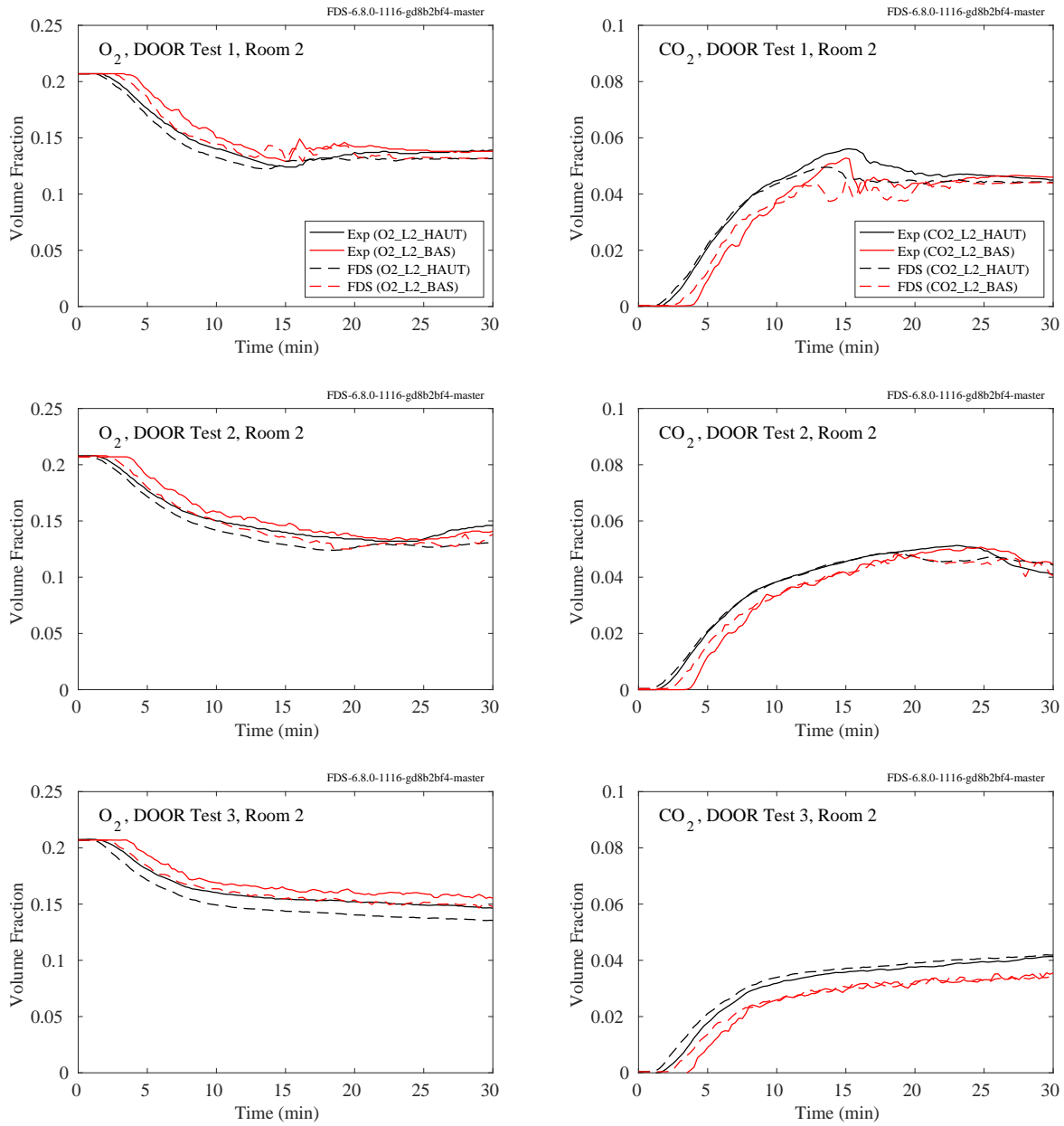


Figure 9.29: PRISME DOOR experiments, CO_2 and O_2 concentration, Room 2, Tests 1-3.

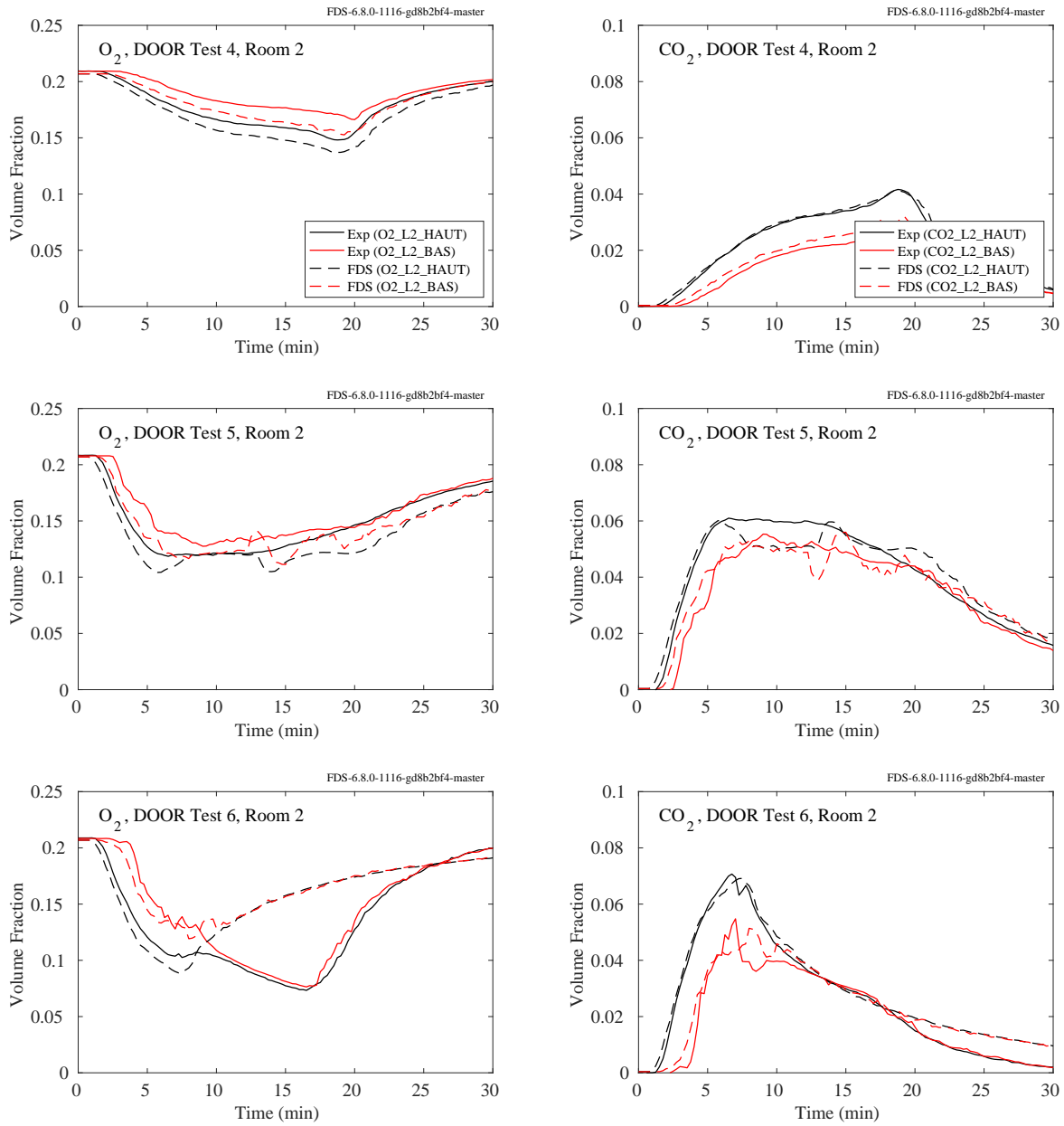
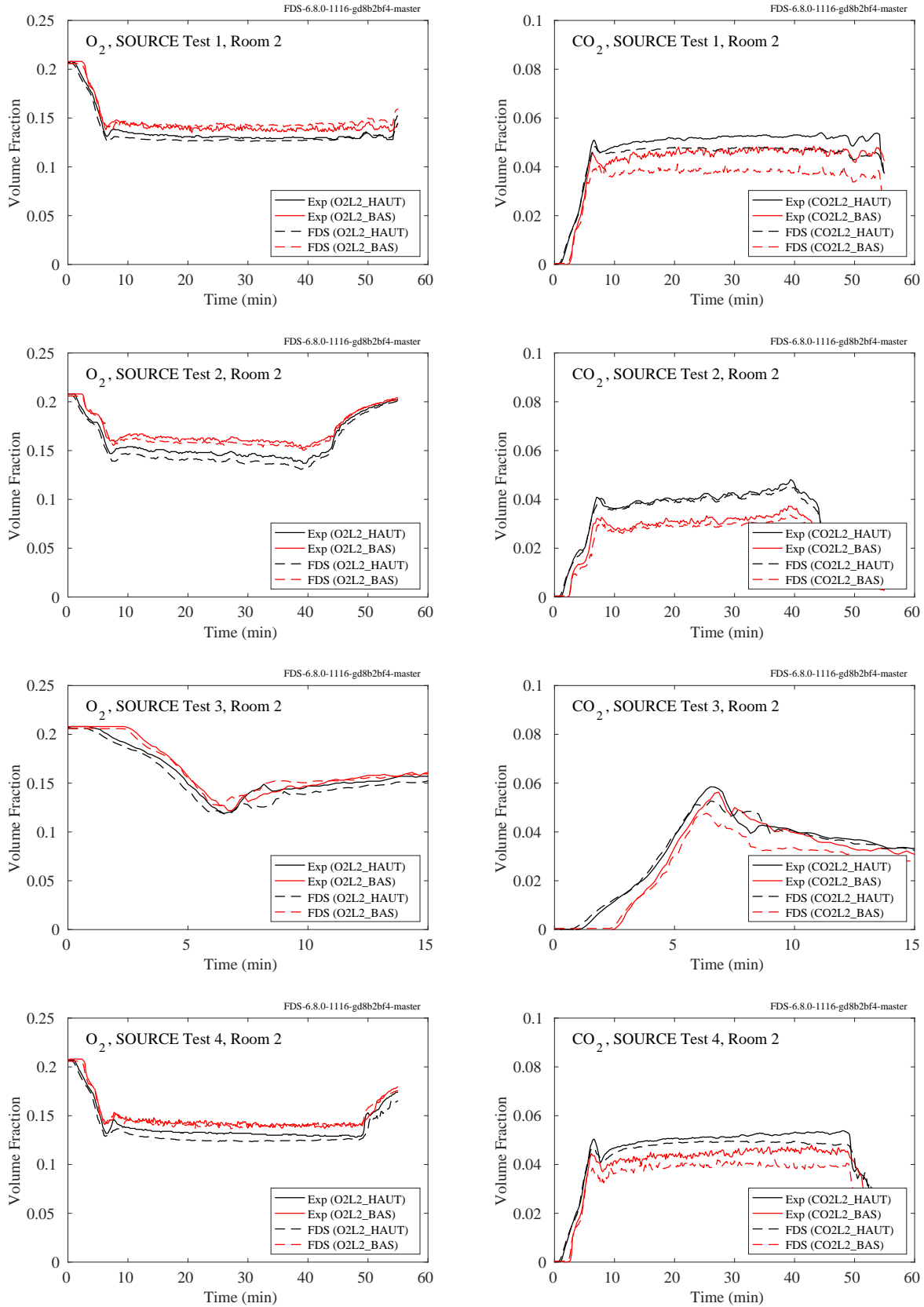
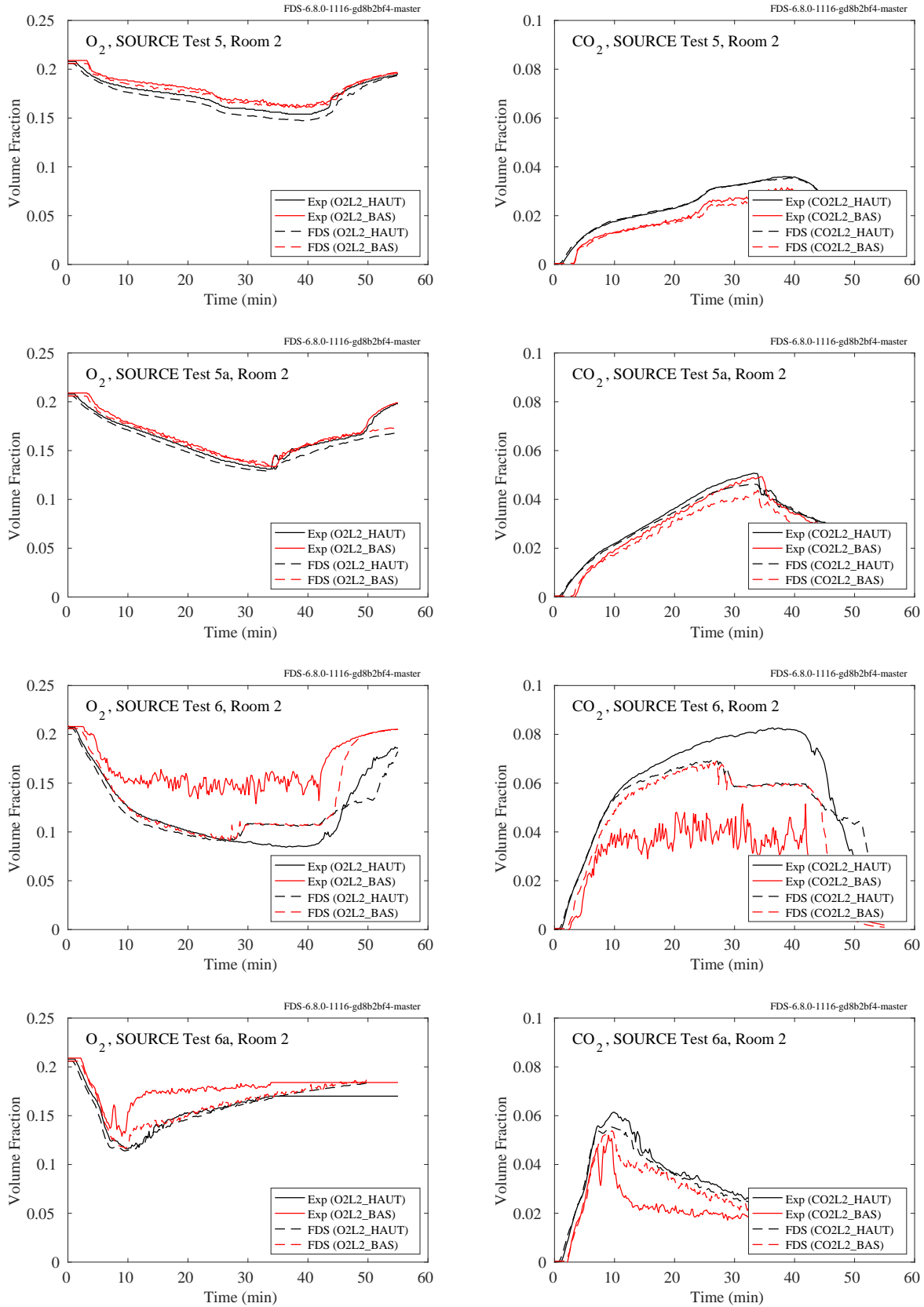


Figure 9.30: PRISME DOOR experiments, CO_2 and O_2 concentration, Room 2, Tests 4-6.

9.1.7 PRISME SOURCE Experiments

The compartment in the PRISME SOURCE experiments contained an oxygen and carbon dioxide measurement in the upper (haut) and lower (bas) layers.

Figure 9.31: PRISME SOURCE experiments, CO_2 and O_2 concentration, Room 2, Tests 1-4.

Figure 9.32: PRISME SOURCE experiments, CO_2 and O_2 concentration, Room 2, Tests 5-6.

9.1.8 WTC Experiments

The following pages present comparisons of oxygen and carbon dioxide concentration predictions and measurements for the WTC experiments. There was only one measurement of each made near the ceiling of the compartment roughly 2 m from the fire.

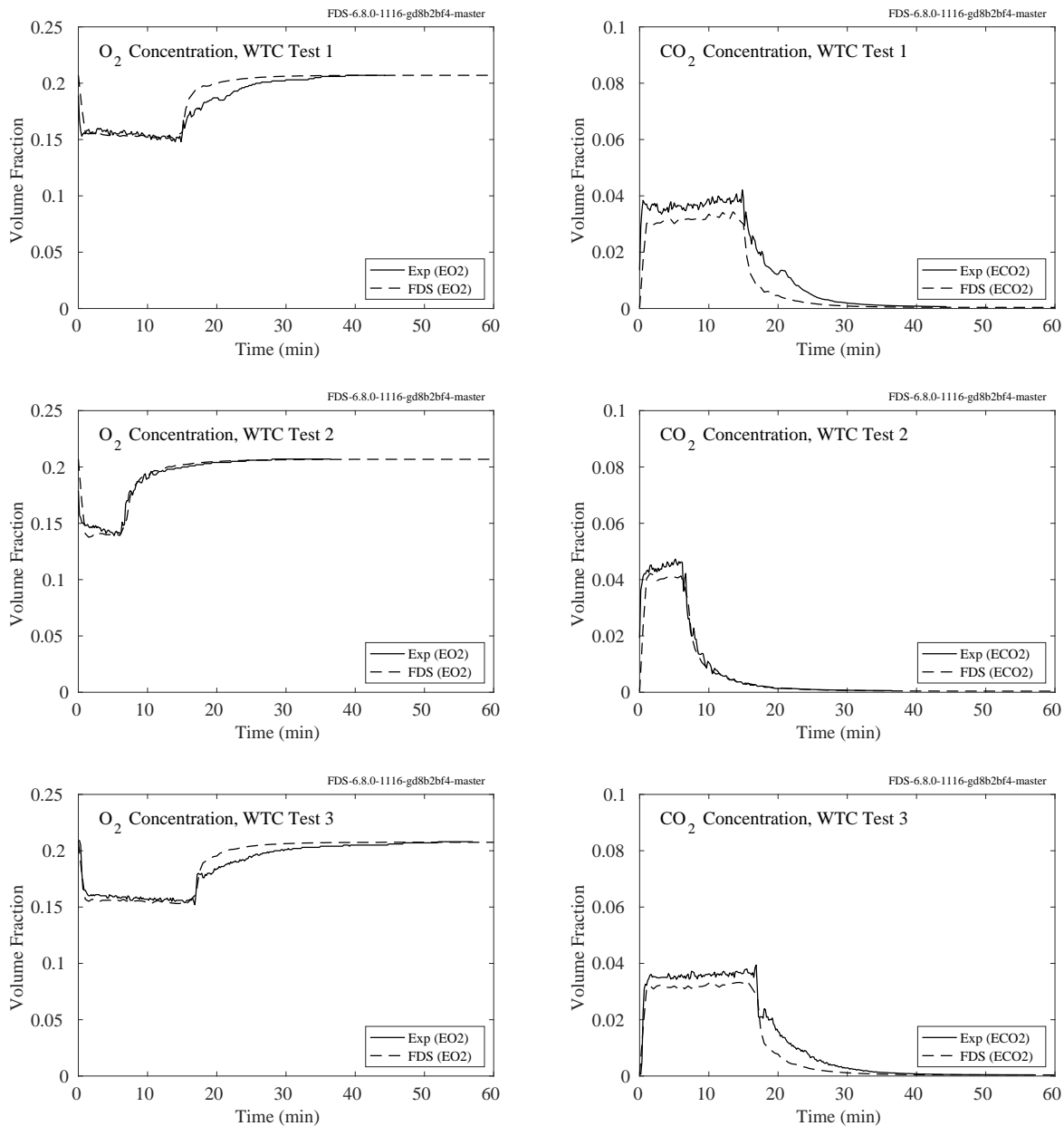
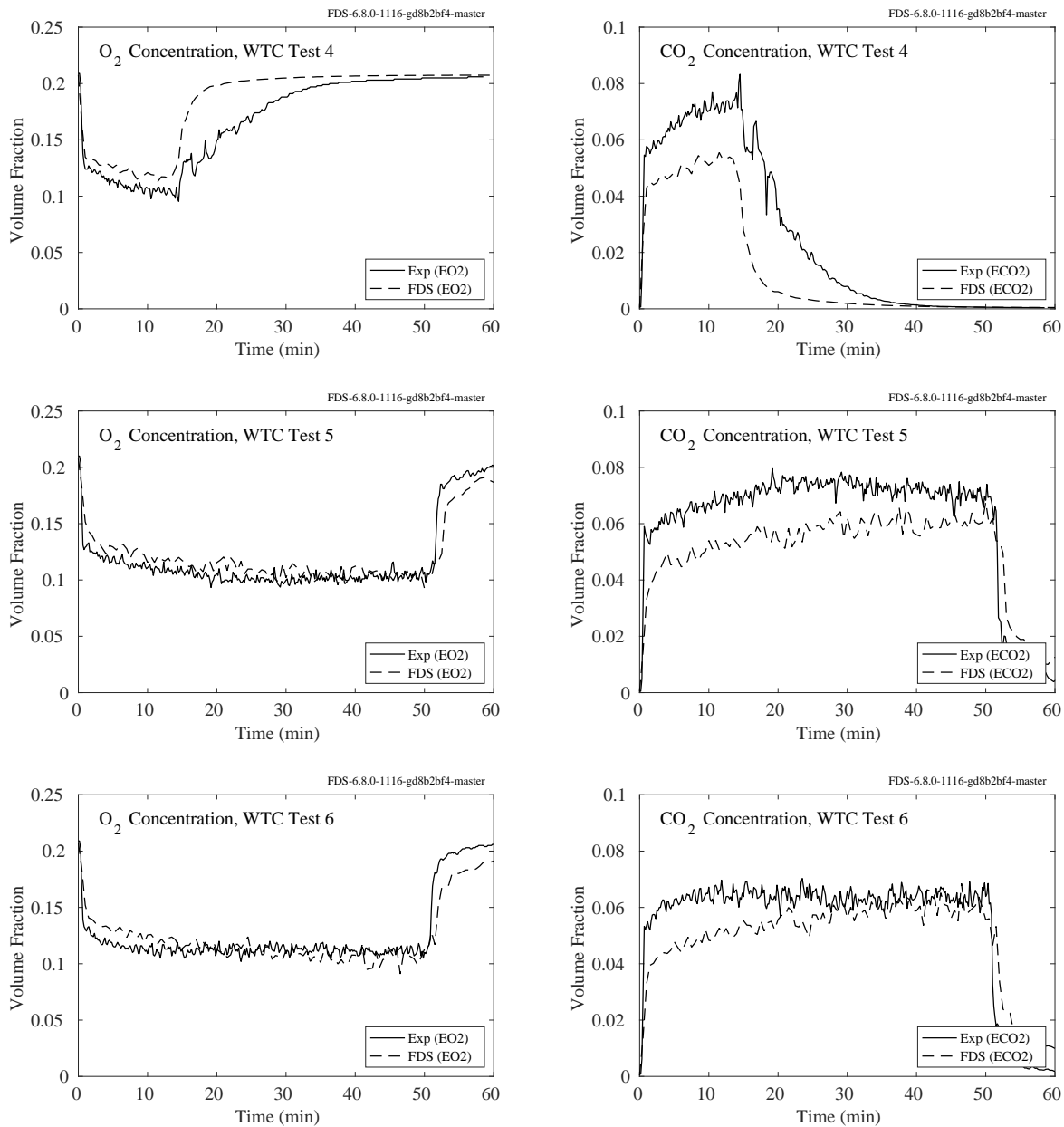


Figure 9.33: WTC experiments, CO₂ and O₂ concentration, Tests 1-3.

Figure 9.34: WTC experiments, CO_2 and O_2 concentration, Tests 4-6.

9.1.9 UMD Line Burner

Oxygen concentration measurements were made across the coflow section of the burner. Fig. 9.35 shows mean volume fraction O_2 profiles for two heights, z , above the burner surface for the experiment with nitrogen dilution of the coflowing air to 18 vol. % O_2 with methane as fuel. Notice that the O_2 level at the outer edge of the burner is the ambient value of 21 vol. %. Further experimental details may be found in White et al. [332]. FDS simulations are performed at three grid resolutions corresponding to $W/\delta x = 4, 8, 16$, where $W = 5$ cm is the width of the line burner (see Fig. 3.57).

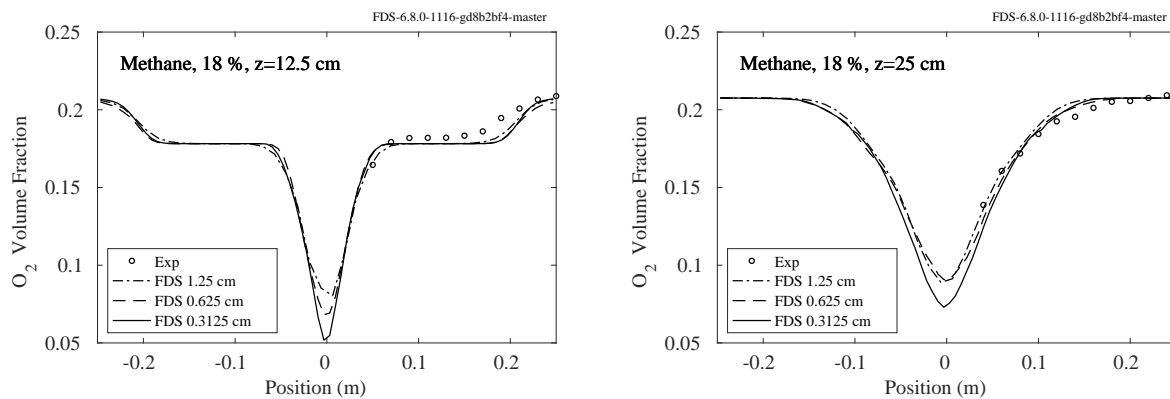


Figure 9.35: Measured and predicted mean oxygen concentration profiles at 18 vol % O_2 .

9.1.10 Summary of Major Combustion Products Predictions

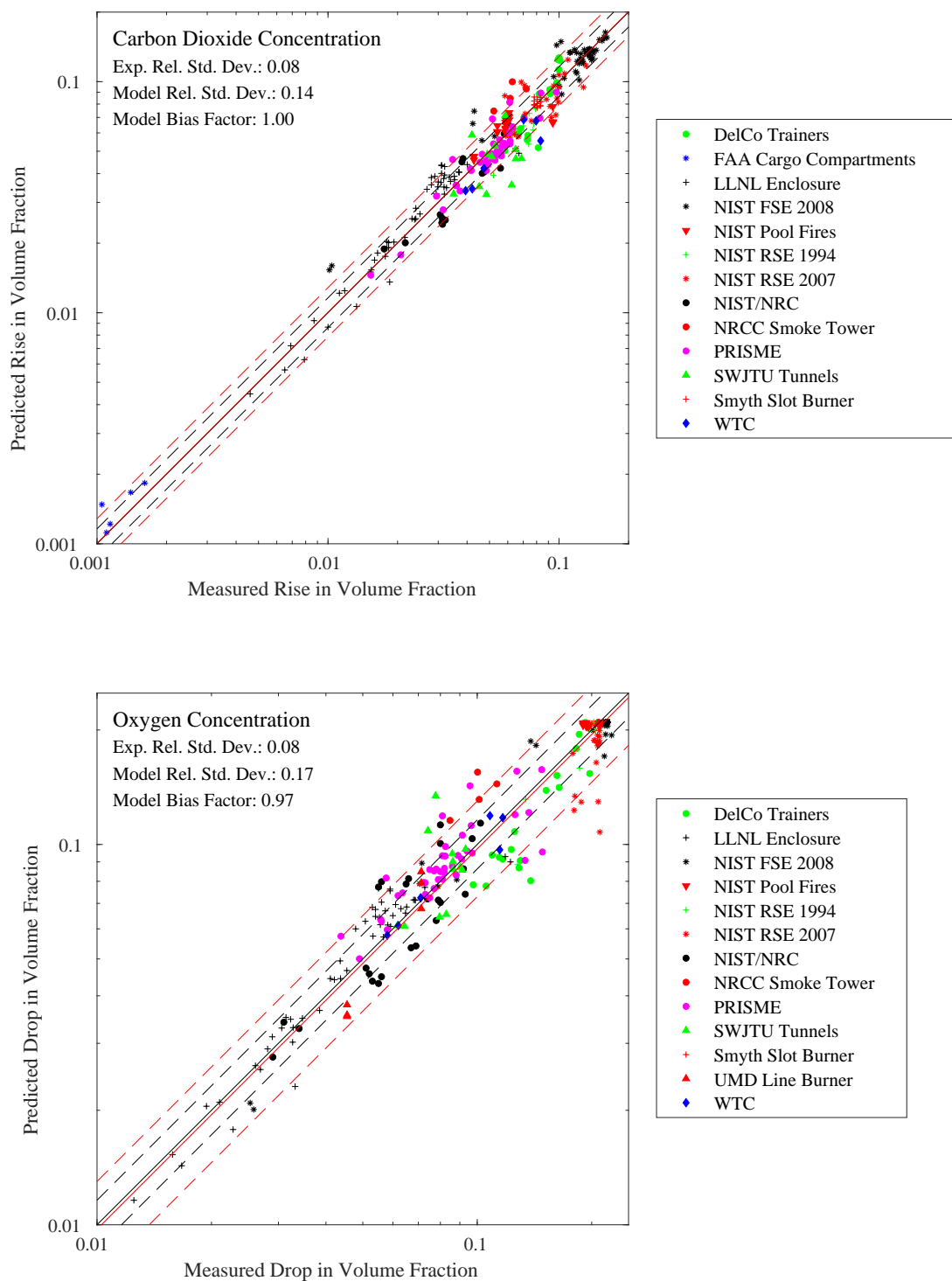


Figure 9.36: Summary of major gas species predictions.

9.2 Smoke

9.2.1 FM Burner Experiments

Mean and rms soot volume fraction measurements were made above a 13.7 cm (inner) diameter, 15 kW ethylene burner. Figures 9.37 through 9.42 display the radial profiles located at heights of 0.5, 1.0, 1.5, 2.5, and 3.5 burner diameters, D . Figures 9.43 through 9.45 display the probability distributions (PDFs) at the five heights and radii of 0 cm, 2 cm, 4 cm, 6 cm, and 8 cm.

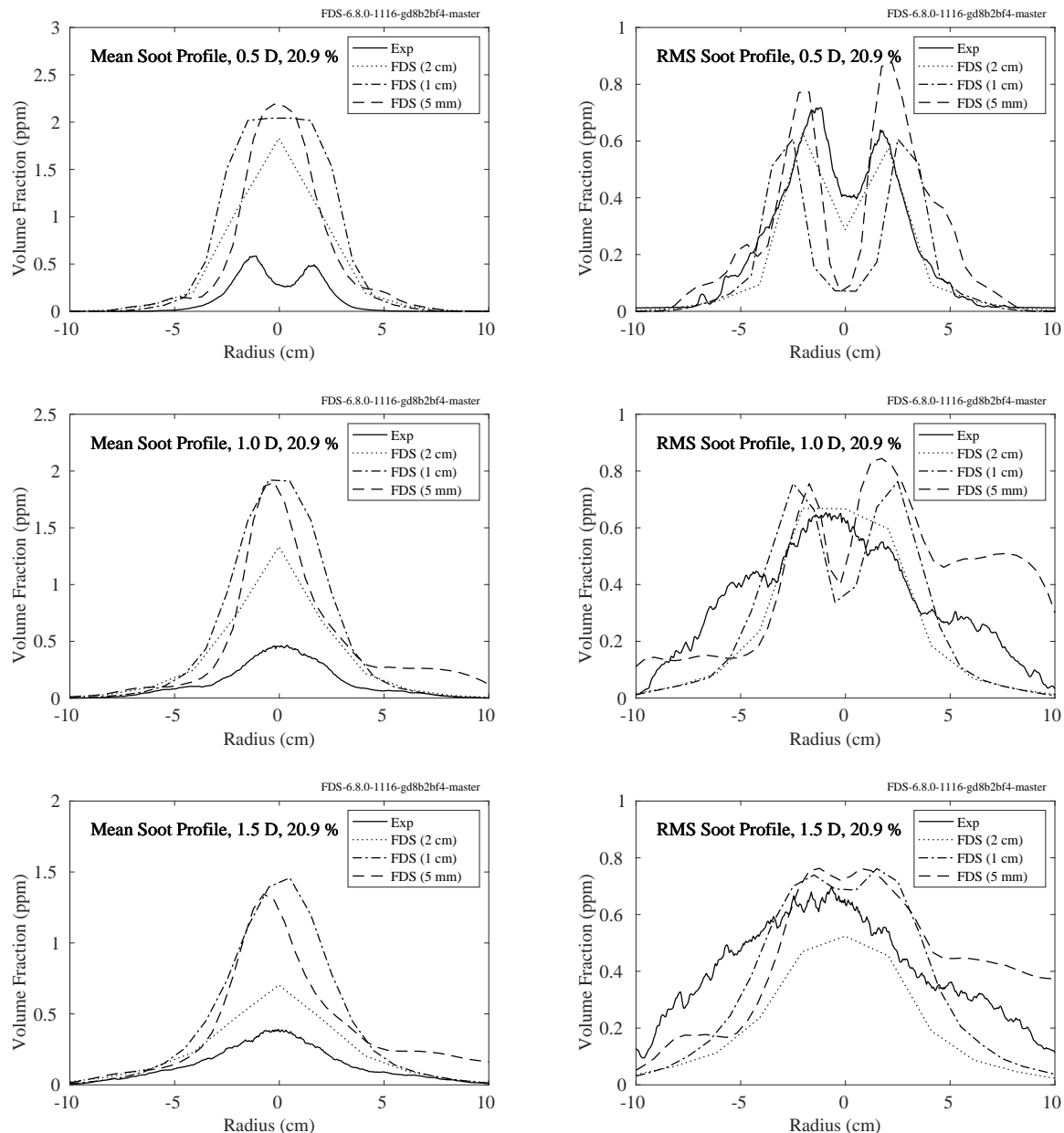


Figure 9.37: FM Burner experiments, plume mean and rms soot volume fraction at heights of 0.5, 1.0, and 1.5 burner diameters, D , 20.9 % O_2 .

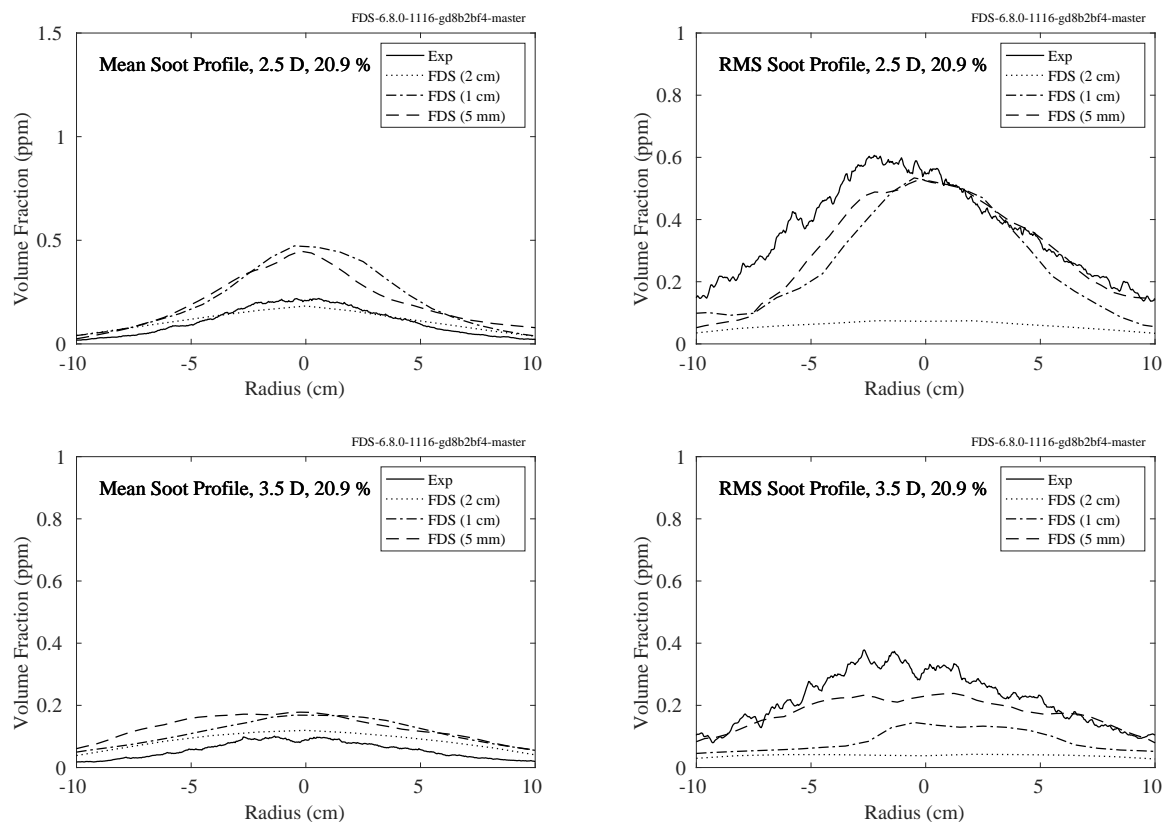


Figure 9.38: FM Burner experiments, plume mean and rms soot volume fraction at heights of 2.5 and 3.5 burner diameters, D, 20.9 % O₂.

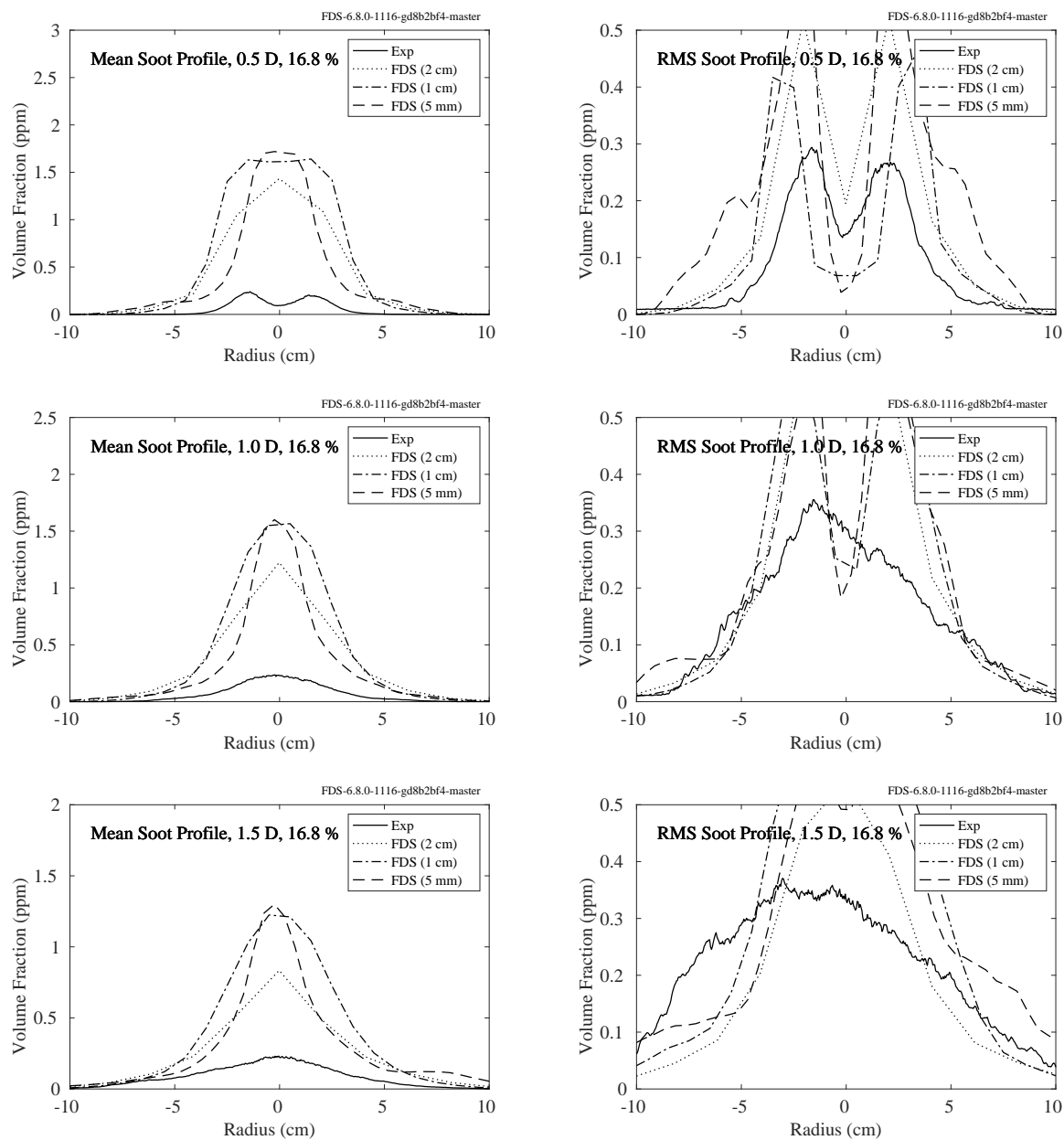


Figure 9.39: FM Burner experiments, plume mean and rms soot volume fraction at heights of 0.5, 1.0, and 1.5 burner diameters, D, 16.8 % O₂.

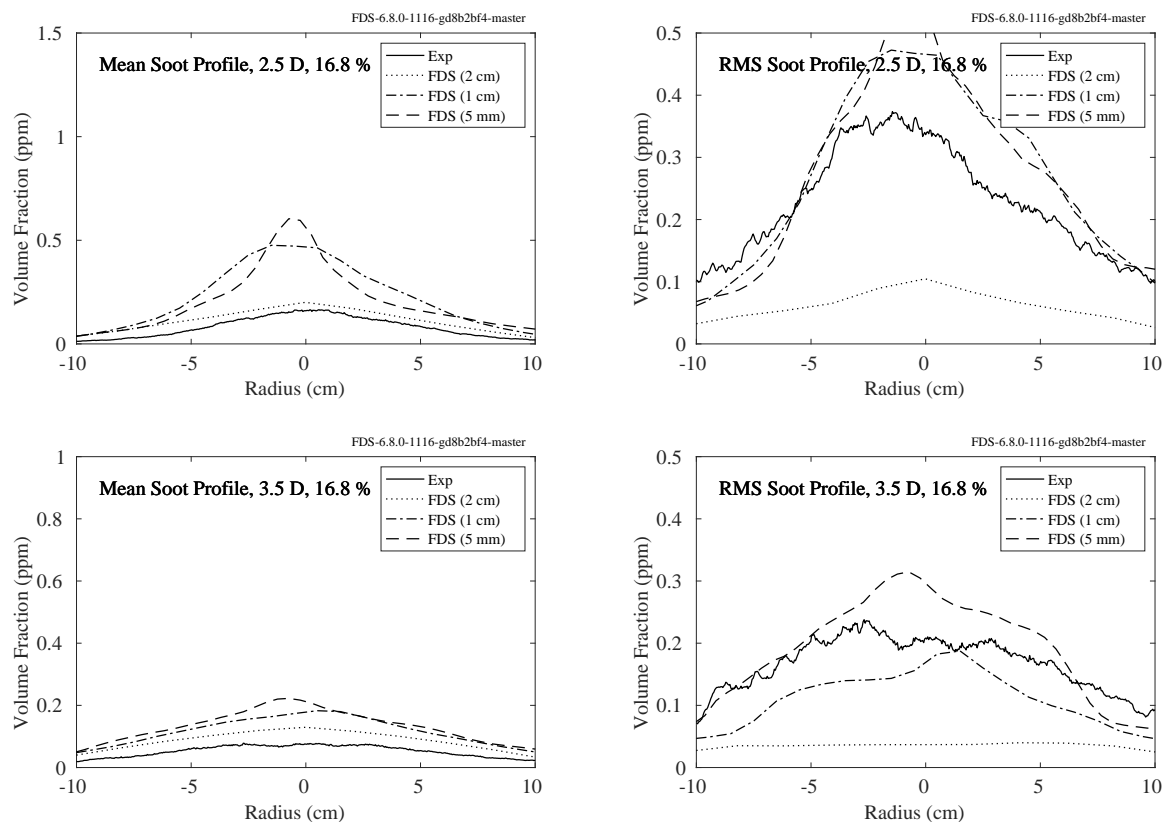


Figure 9.40: FM Burner experiments, plume mean and rms soot volume fraction at heights of 2.5 and 3.5 burner diameters, D, 16.8 % O₂.

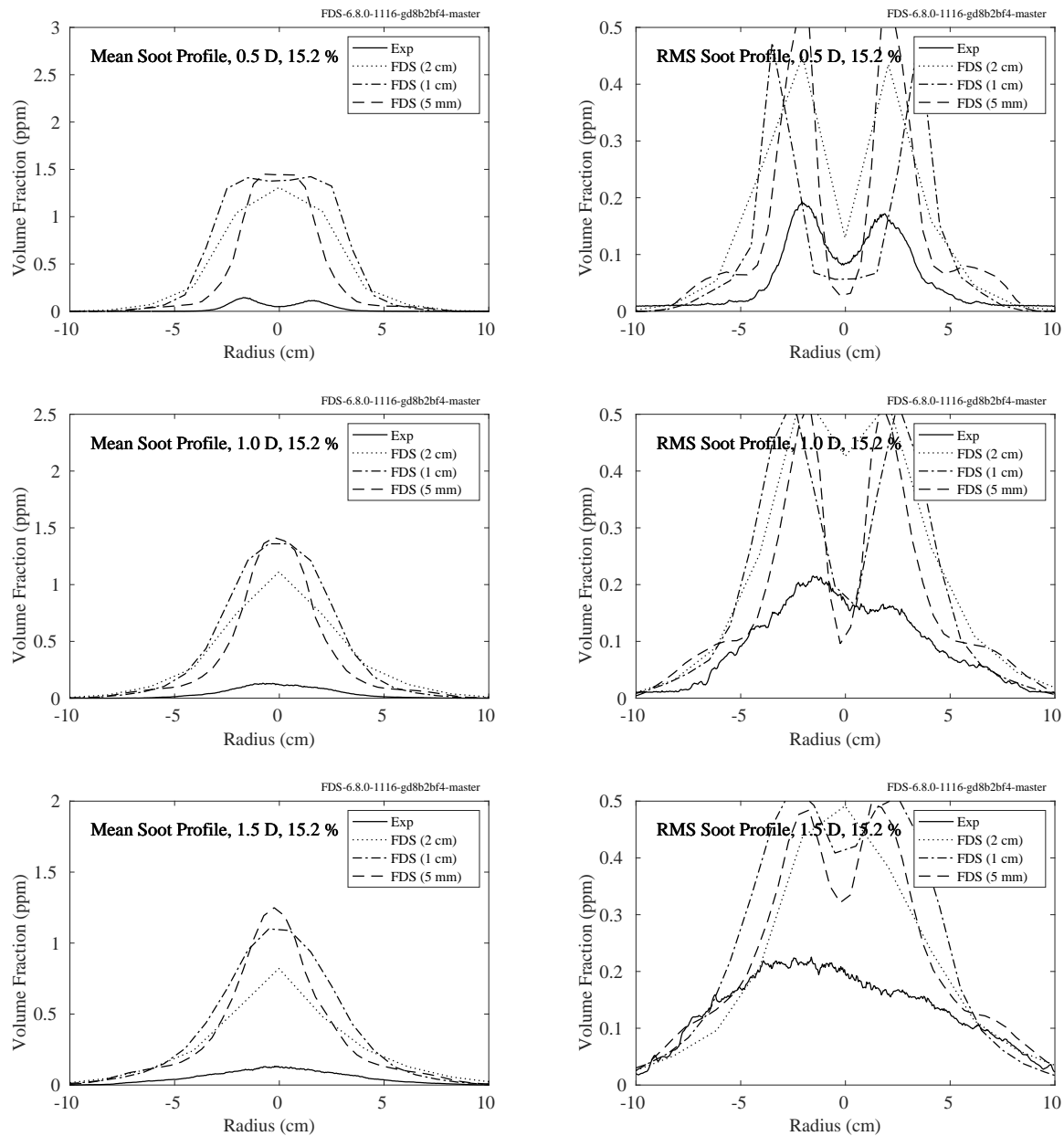


Figure 9.41: FM Burner experiments, plume mean and rms soot volume fraction at heights of 0.5, 1.0, and 1.5 burner diameters, D, 15.2 % O₂.

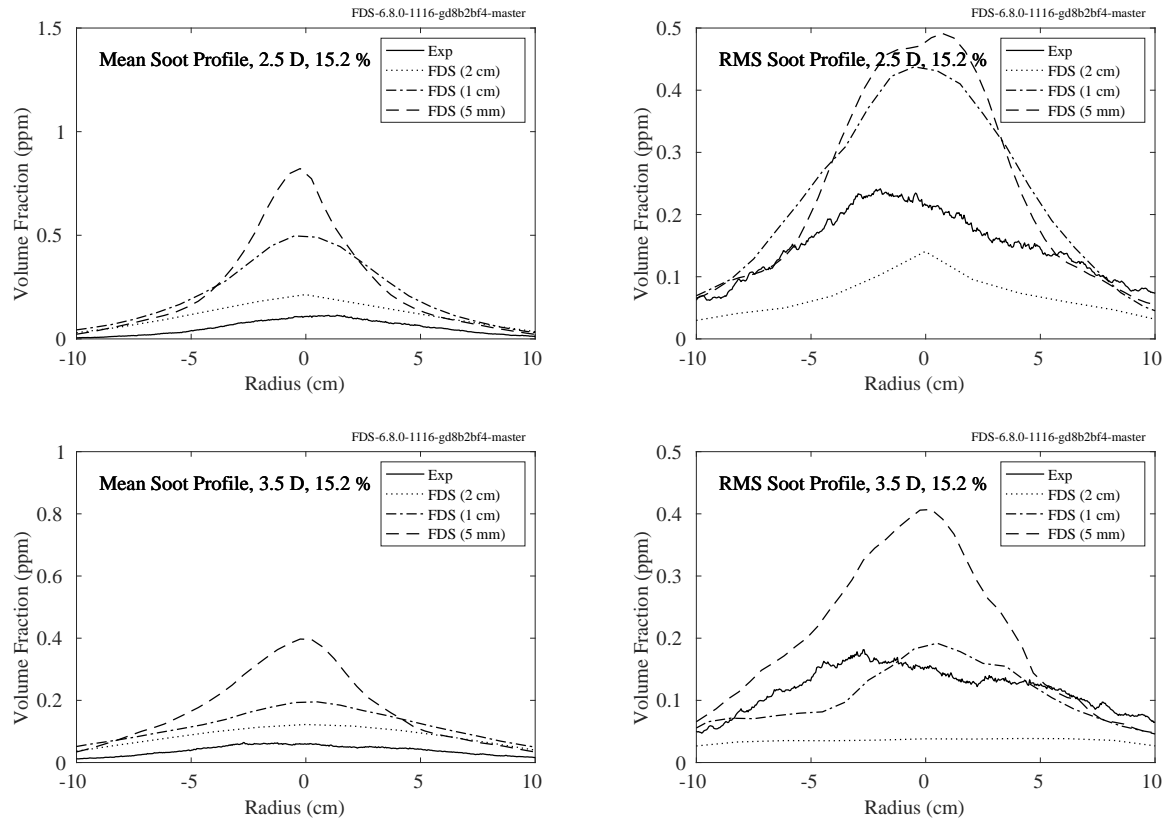


Figure 9.42: FM Burner experiments, plume mean and rms soot volume fraction at heights of 2.5 and 3.5 burner diameters, D, 15.2 % O_2 .

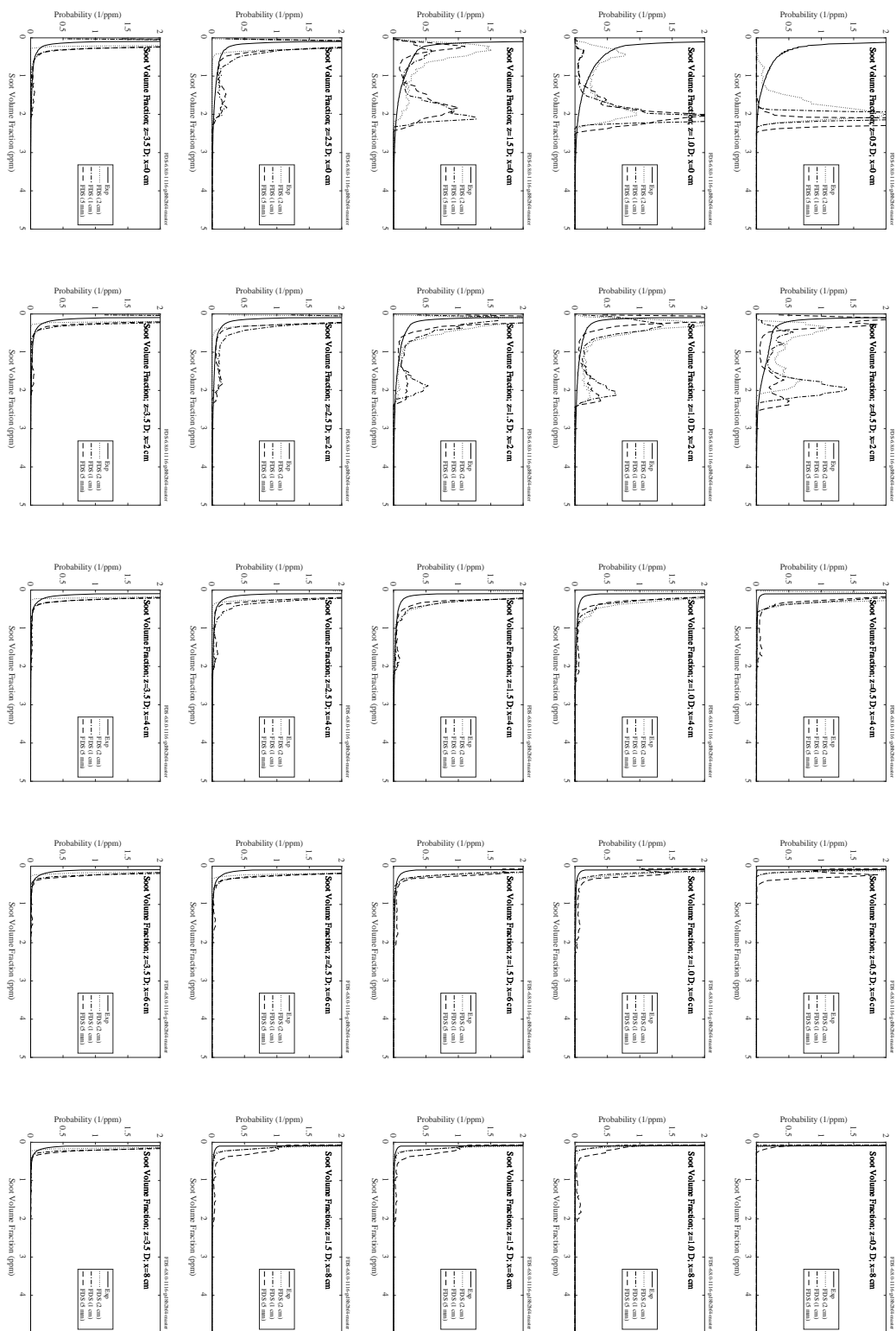
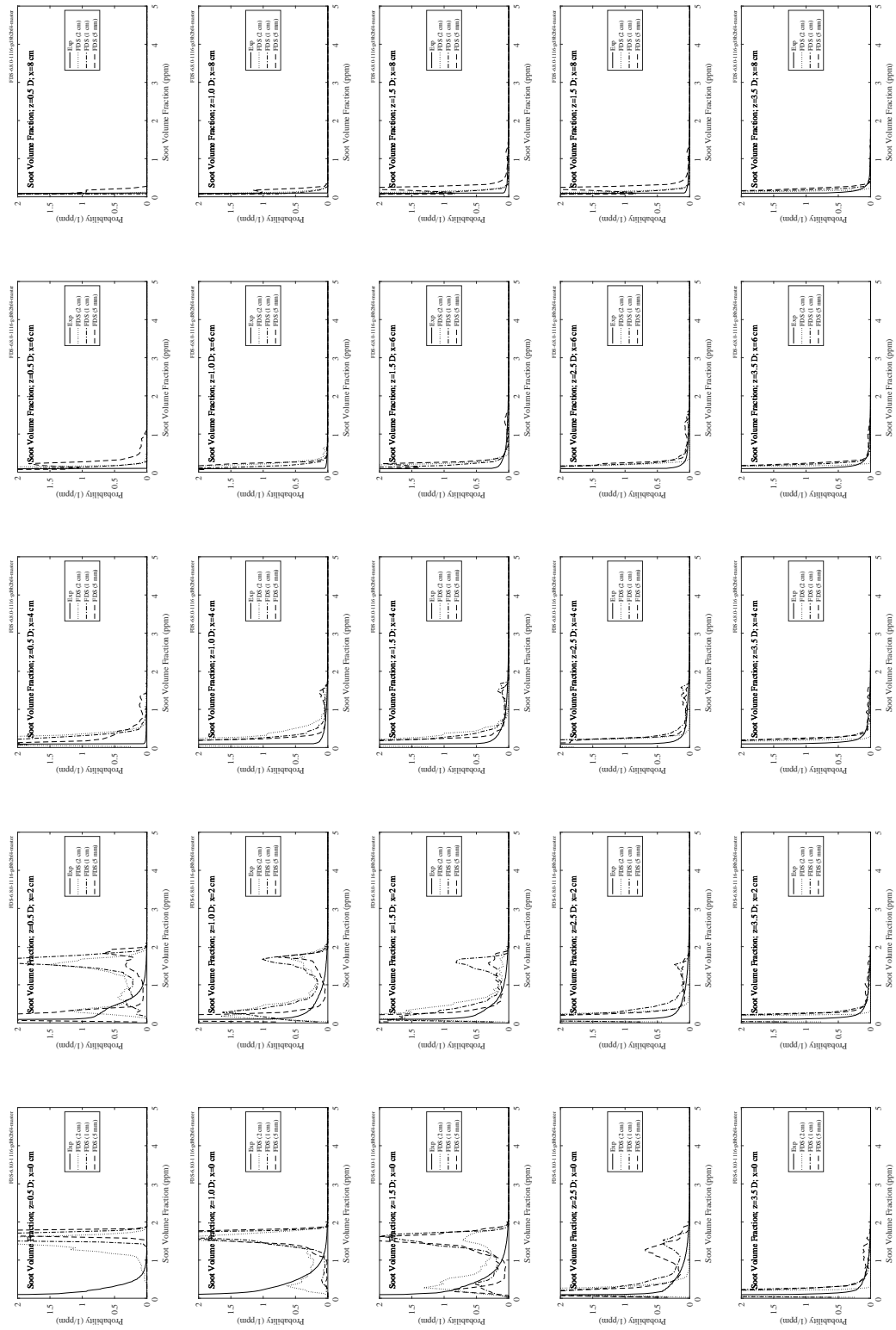


Figure 9.43: FM Burner experiments, soot volume fraction PDFs, 20.9 % O₂.

Figure 9.44: FM Burner experiments, soot volume fraction PDFs, 16.8 % O₂.

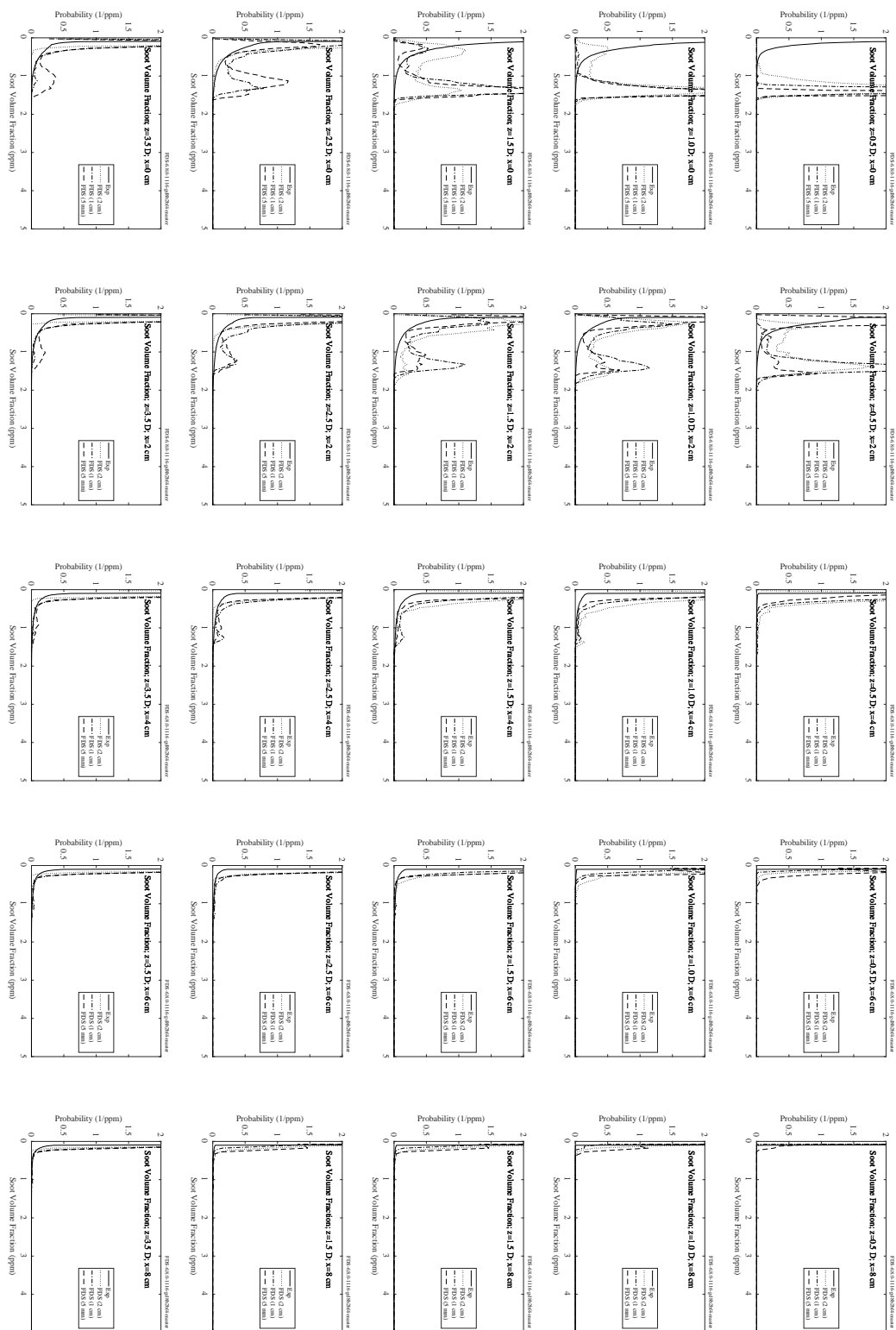


Figure 9.45: FM Burner experiments, soot volume fraction PDFs, 15.2 % O₂.

9.2.2 FM/FPRF Data Center Experiments

Results of the low exhaust rate (78 ACH) and high exhaust rate (265 ACH) tests for propylene and cables is shown in the figure below. Each test had three measurement locations (subfloor, ceiling, and ceiling plenum); however, not all locations for all tests had a measurement above background noise in the laser signal.

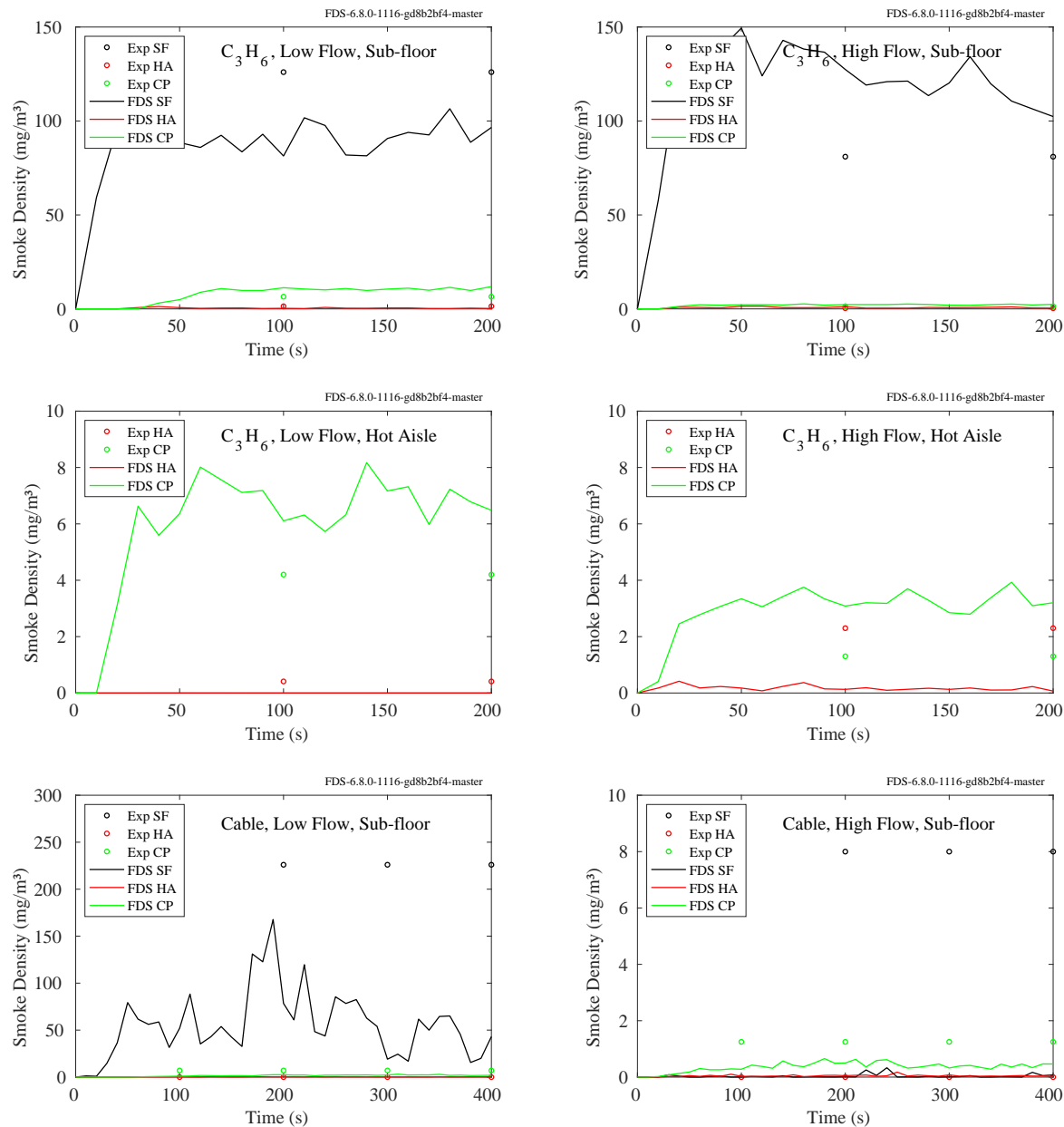


Figure 9.46: FM/FPRF Data Center, smoke concentration, low and high exhaust rate, propylene and cable sources.

9.2.3 NIST/NRC Experiments

The figures on the following pages contain comparisons of measured and predicted smoke concentration at one measuring station in the upper layer. The experiments are divided into two. Figure 9.47 displays the results of the experiments in which the compartment door was closed. Figure 9.48 displays the results of the experiments in which the compartment door was open. The results are significantly different—the simulations of the closed door experiments predict smoke concentrations that are more than twice that of the experiments. The reason for this is that FDS has not accounted for the agglomeration and deposition of the smoke on the walls, something that is far more important when the compartment is not well-ventilated.

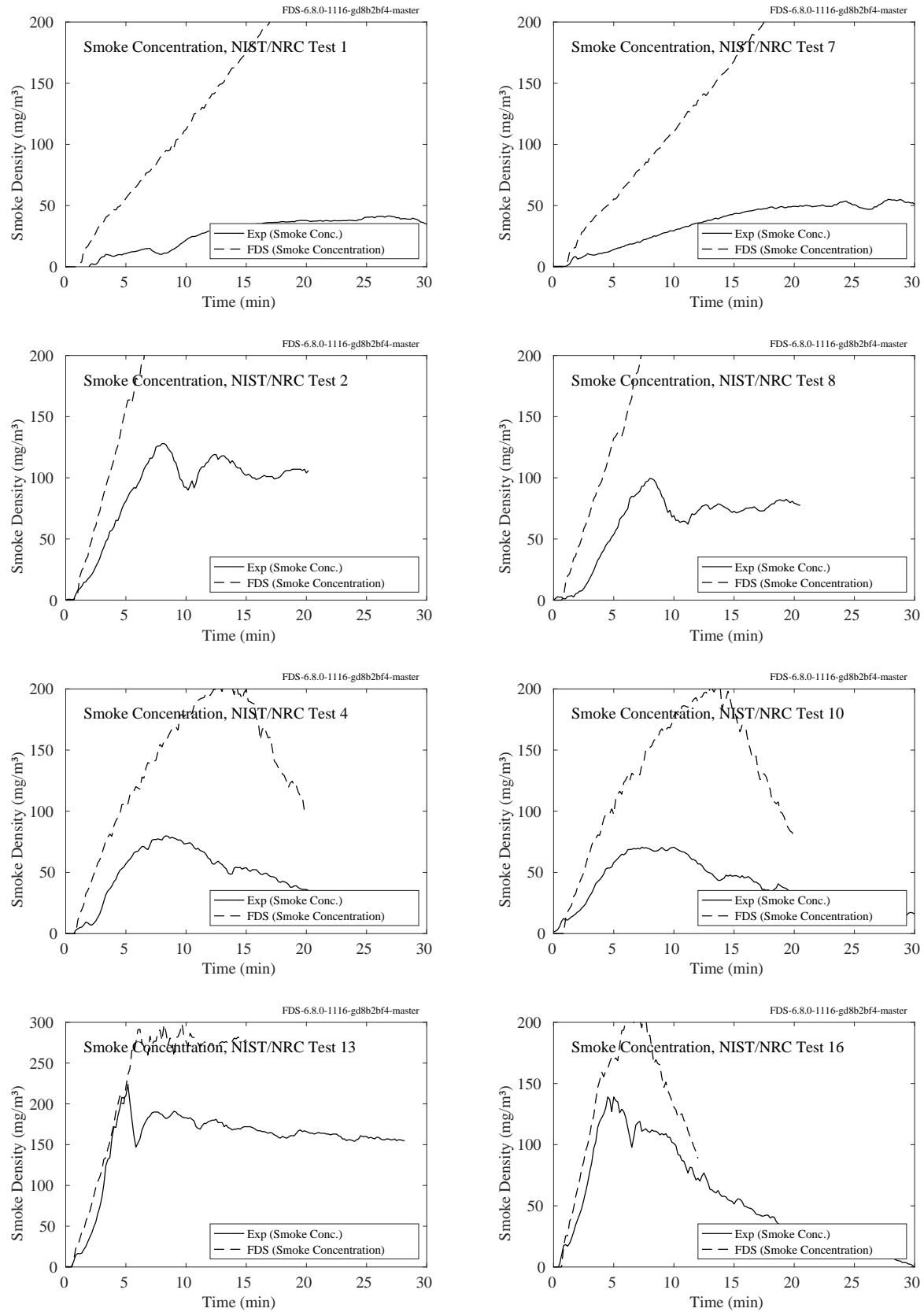


Figure 9.47: NIST/NRC experiments, smoke concentration, closed door experiments.

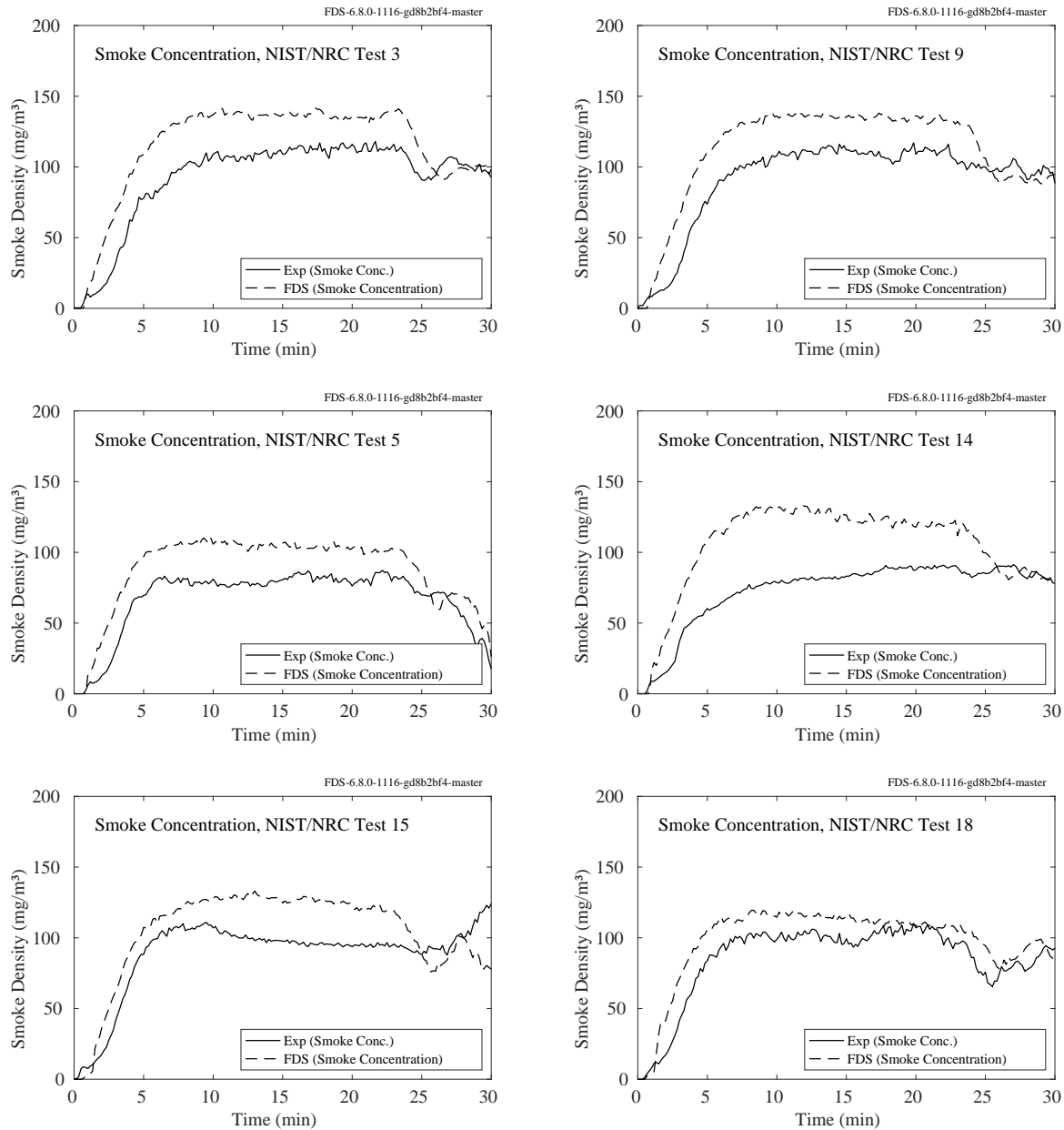


Figure 9.48: NIST/NRC experiments, smoke concentration, open door experiments.

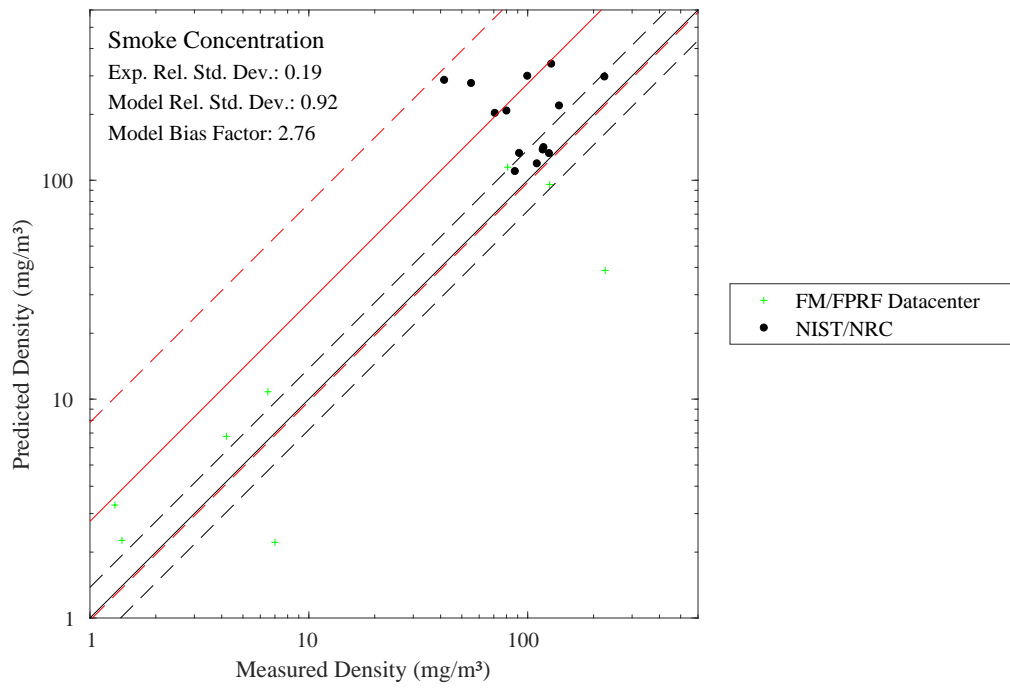


Figure 9.49: Summary of smoke concentration predictions.

9.2.4 FAA Cargo Compartments

Beam obscuration measurements were made at different locations within the compartment (see Fig. 7.10). The data is presented below in terms of percent transmission per meter, $100(I/I_0)^{1/L}$, where I is the light intensity and L is the beam pathlength in units of meters.

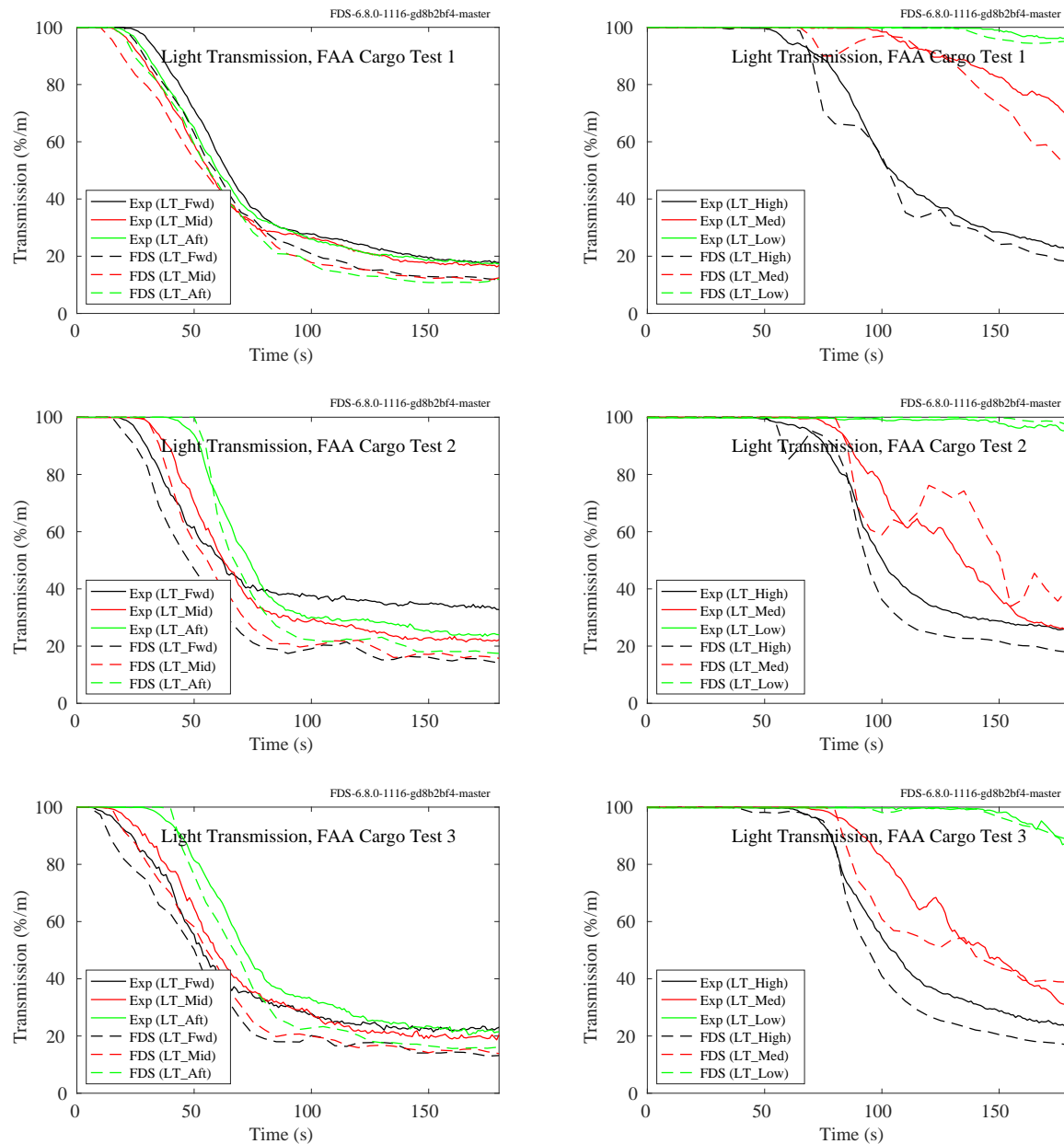


Figure 9.50: FAA Cargo Compartments experiments, smoke obscuration.

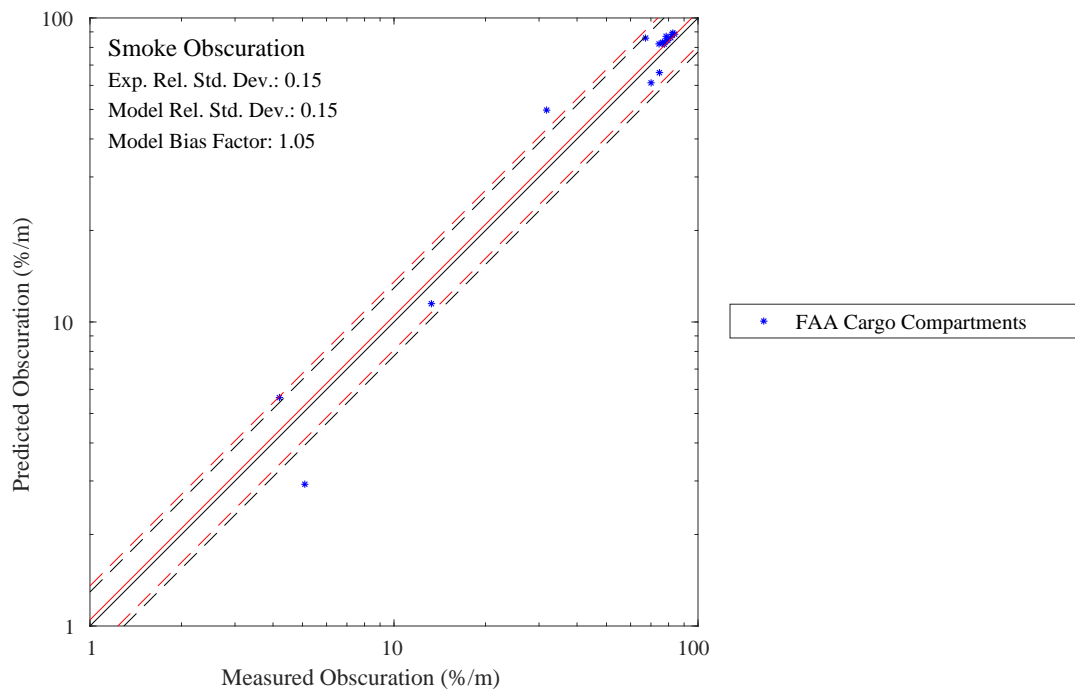


Figure 9.51: Summary of smoke obscuration predictions.

9.3 Aerosols

9.3.1 Sippola Aerosol Deposition Experiments

Figure 9.52 compares the measured and predicted aerosol deposition velocities in the Sippola experiments, and Figure 9.53 shows a summary of the results. Details of the experiment and simulation are found in Sec. 3.80

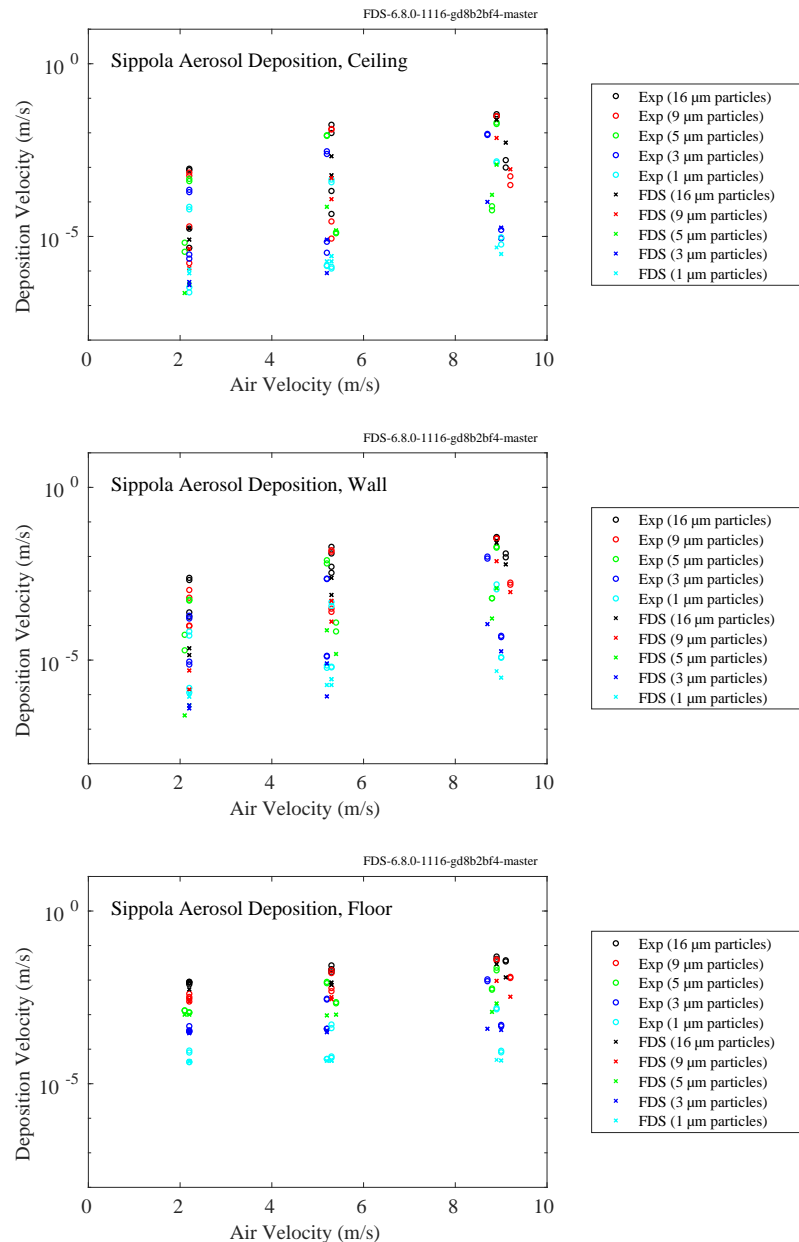


Figure 9.52: Predicted and measured aerosol deposition velocities, Sippola experiments.

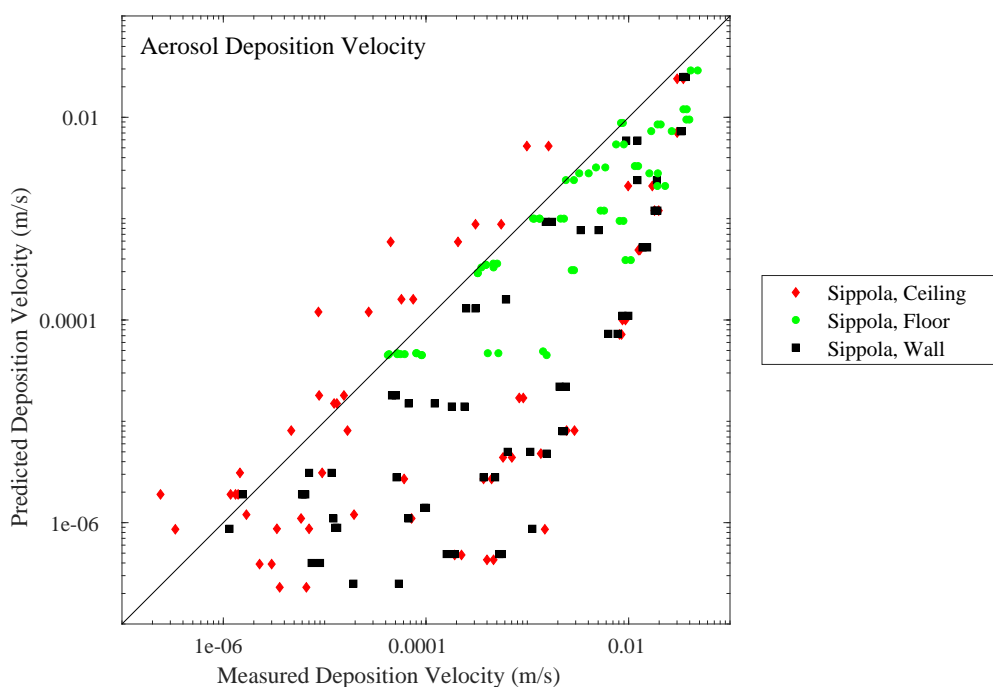


Figure 9.53: Summary of aerosol deposition velocity predictions.

9.3.2 NIST Soot Deposition Gauge Experiments

Figure 9.54 compares the measured and predicted aerosol mass deposition velocities in the NIST Soot Deposition Gauge experiments, and Figure 9.55 shows a summary of the results. Details of the experiment and simulation are found in Sec. 3.63

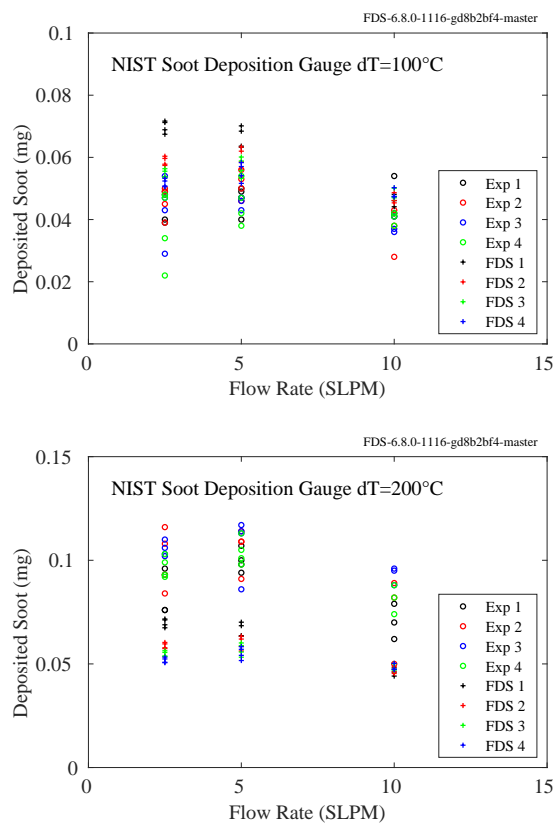


Figure 9.54: Predicted and measured aerosol deposited mass, NIST Soot Deposition Gauge experiments.

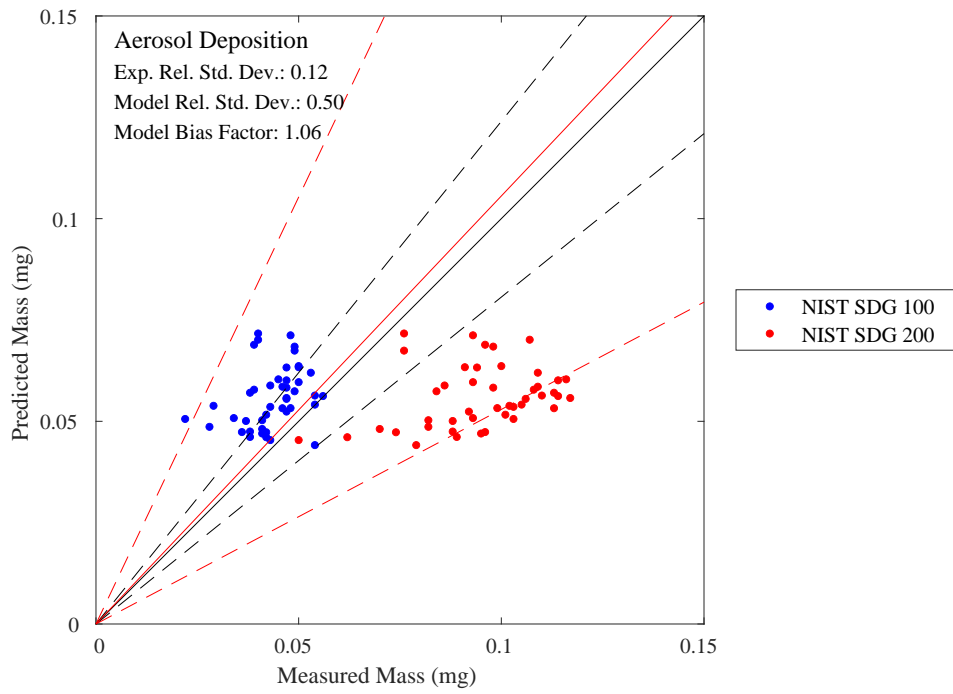


Figure 9.55: Summary of aerosol deposited mass predictions.

9.4 Droplet Evaporation

This section presents the results of simulations of liquid droplet evaporation experiments. The titles of the sections below are named for the experimentalists.

9.4.1 Ranz and Marshall

A description of the experiments is included in Sec. 3.73. Figure 9.56 shows the results of predicting the drop diameter of a single droplet evaporating in dry air.

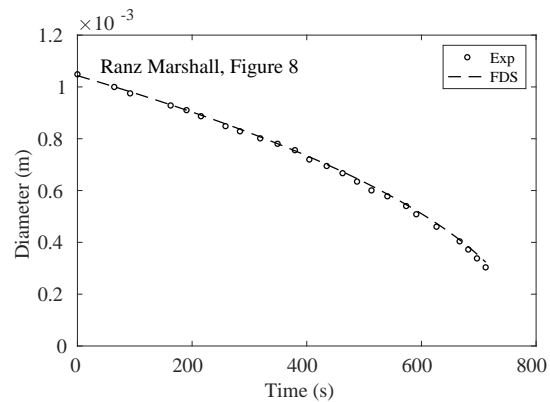


Figure 9.56: Measured and predicted droplet diameter for the Ranz and Marshall experiment shown in Fig. 8 of [296].

Figure 9.57 compares the measured and predicted evaporation rates for Table 1 through Table 4 in [296]. The Table 1 experiments were water droplets in ambient air, the Table 2 experiments were water droplets at in warm air (less than boiling), the Table 3 experiments were water droplets in hot air (greater than boiling), and the Table 4 experiments were benzene droplets in ambient air. A summary of the results is shown in Fig. 9.58.

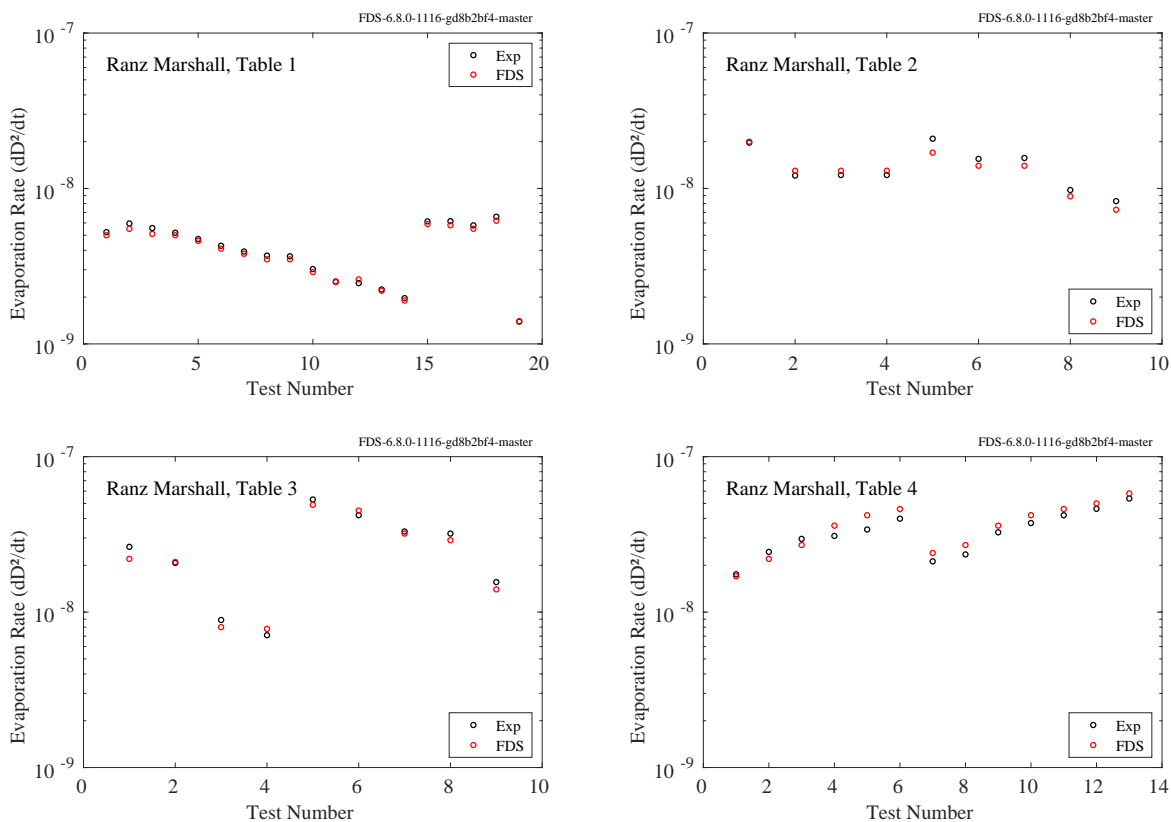


Figure 9.57: Evaporation rates for the Ranz and Marshall experiments [296].

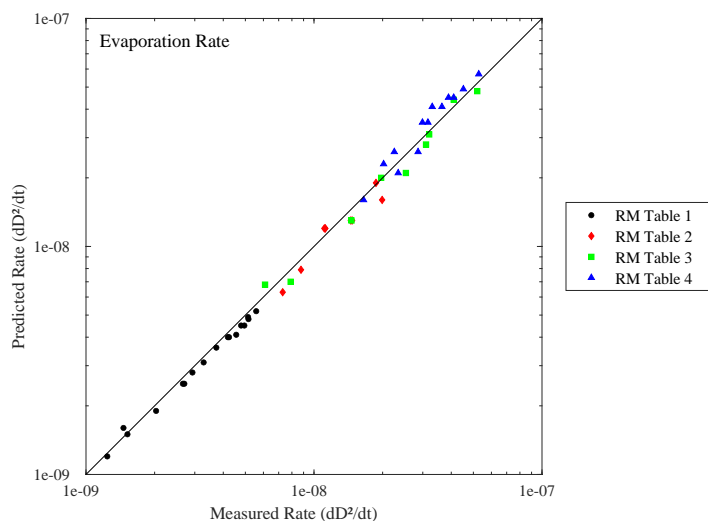


Figure 9.58: Summary of evaporation rates for the Ranz and Marshall experiments [296].

9.4.2 Fujita et al.

A description of the experiments is included in Sec. 3.20. Figure 9.59 shows the droplet area normalized by its initial area, and Fig. 9.60 shows the droplet temperature change.

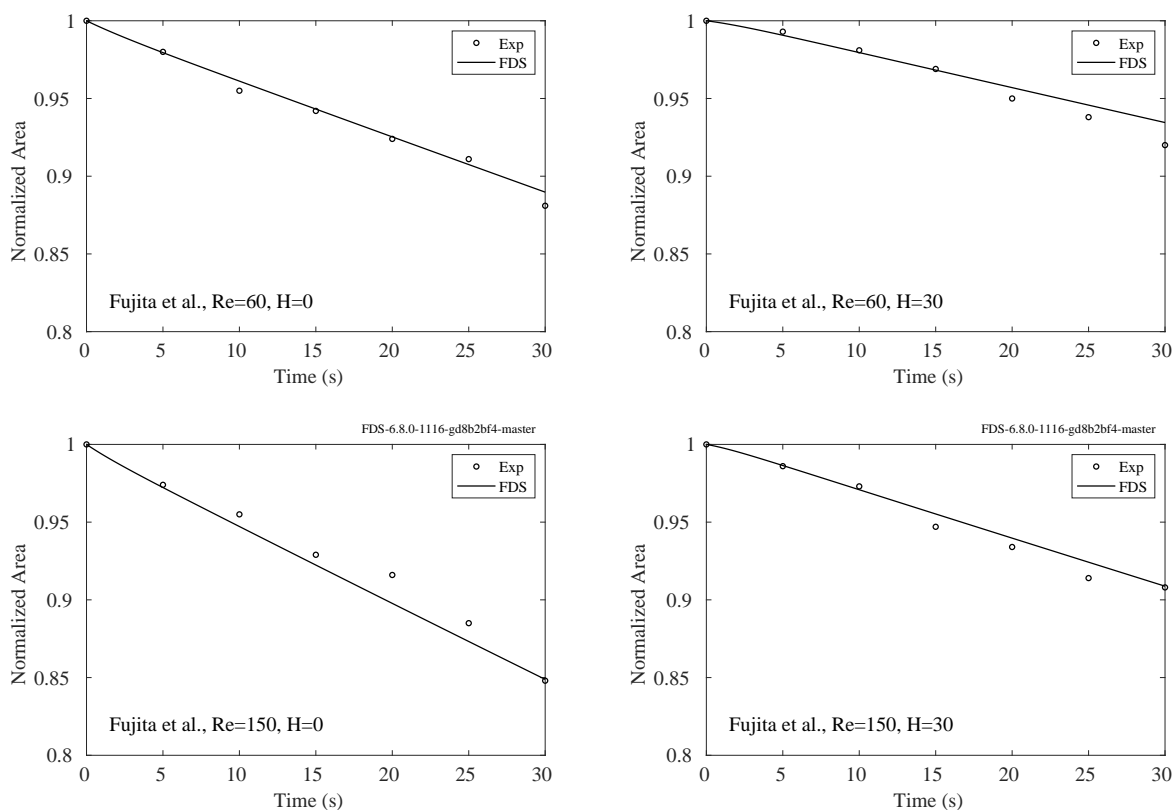


Figure 9.59: Normalized droplet area for the Fujita experiments for varying Reynolds number (Re) and Humidity (H)

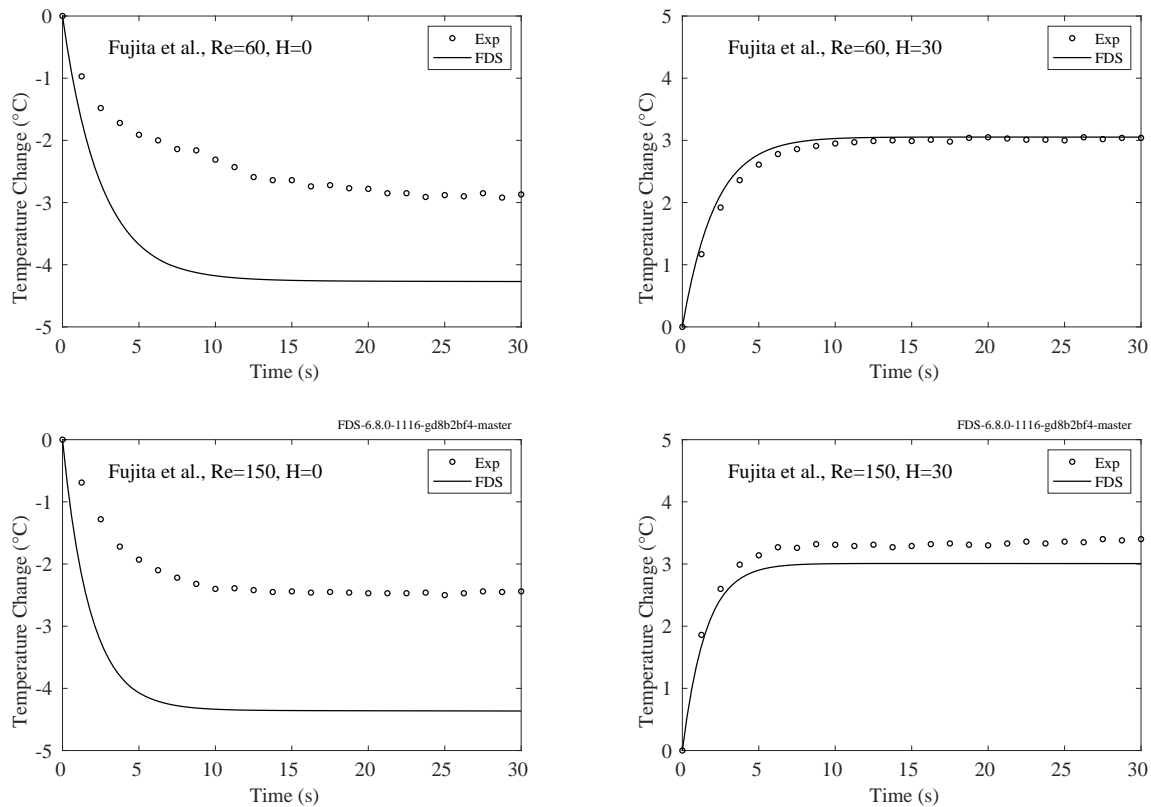


Figure 9.60: Droplet temperature change for the Fujita experiments for varying Reynolds number (Re) and Humidity (H).

9.4.3 Gavin

A description of the experiments is included in Sec. 3.20. Figure 9.61 shows the simulation results for the droplet terminal velocity.

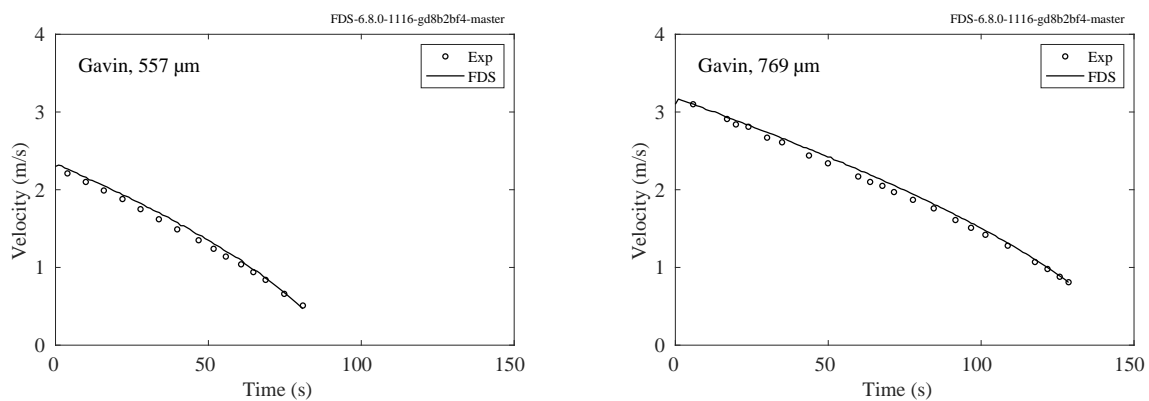


Figure 9.61: Droplet terminal velocity for the Gavin experiments.

9.4.4 Kolaitis and Founti

A description of the experiments is included in Sec. 3.20. Figure 9.62 shows the simulation results for the squared droplet diameter. Figure 9.63 shows the simulation results for the droplet surface temperature.

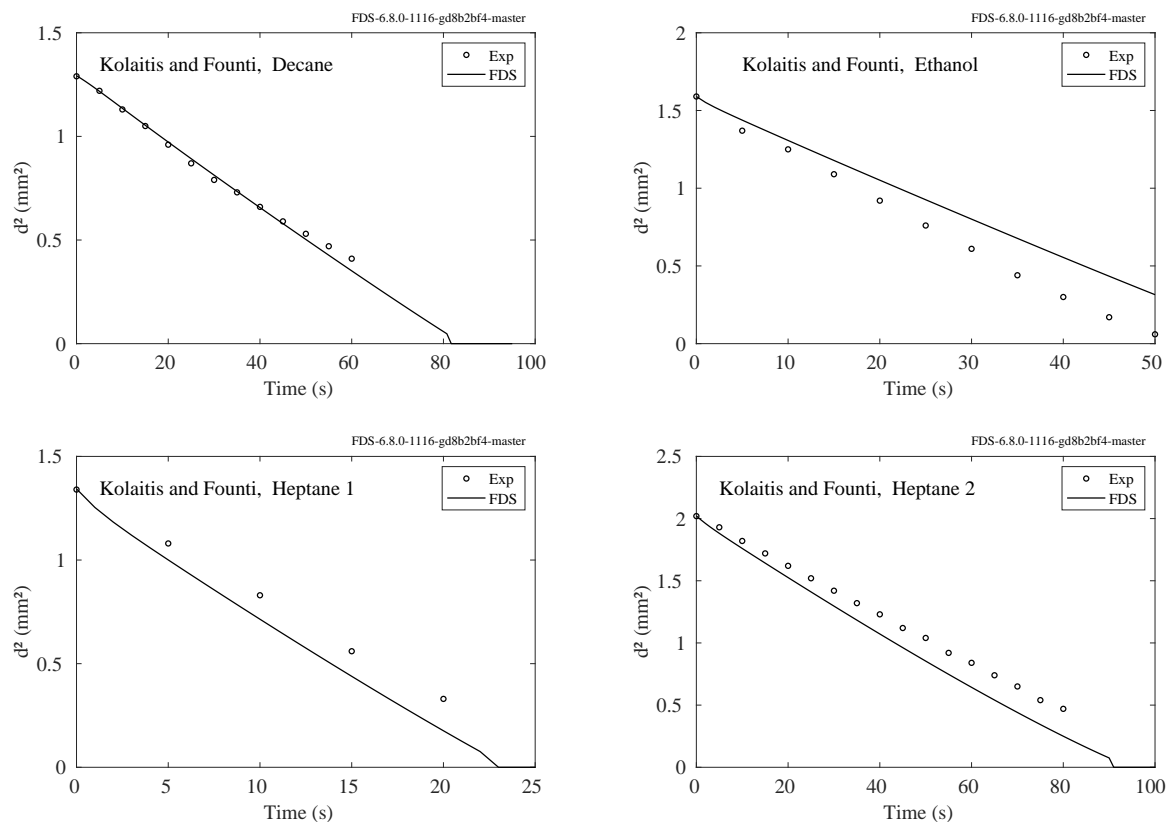


Figure 9.62: Square of the droplet diameter, Kolaitis and Founti.

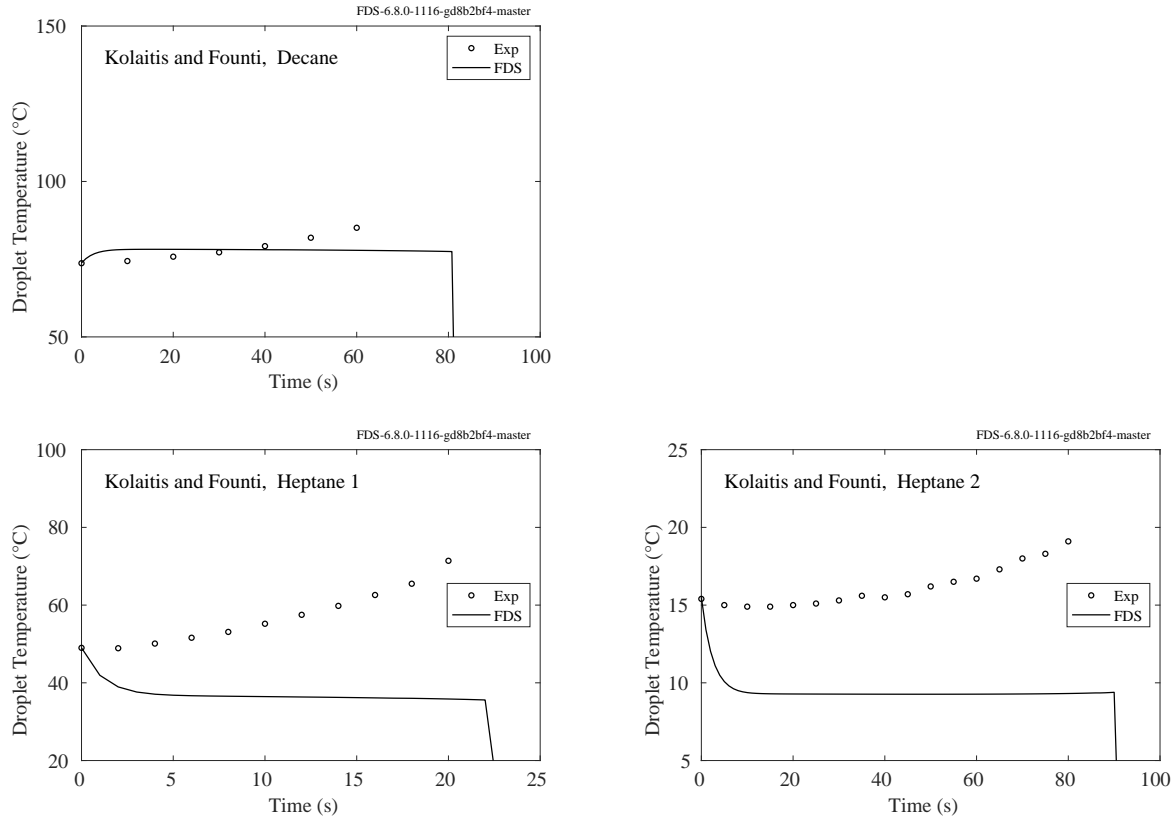


Figure 9.63: Droplet surface temperature, Kolaitis and Founti.

9.4.5 Maqua et al.

A description of the experiments is included in Sec. 3.20. Figure 9.64 shows the droplet surface temperature for the two experiments.

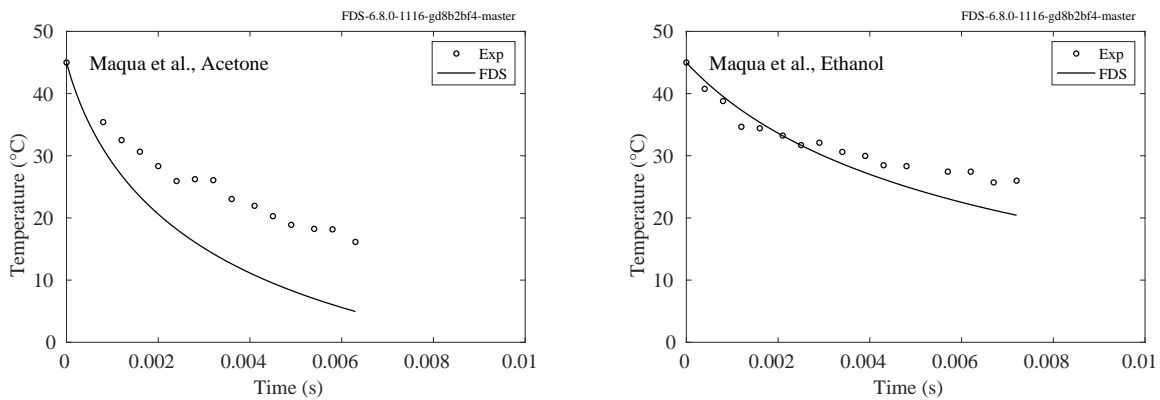


Figure 9.64: Droplet surface temperature for the Maqua et al. experiments.

9.4.6 Taflin Experiments

A description of the experiments is included in Sec. 3.20. Figure 9.65 shows the droplet diameter for the two Taflin experiments.

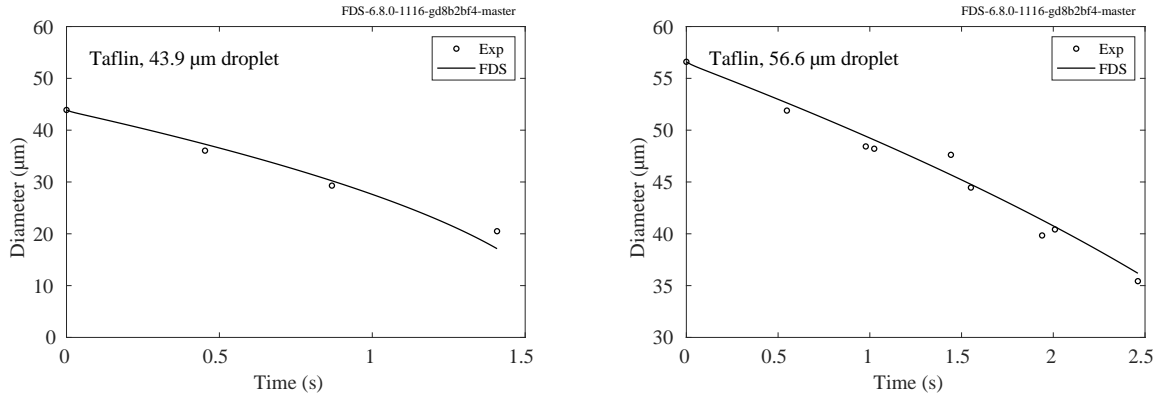


Figure 9.65: Droplet diameter for the Taflin experiments.

9.5 Products of Incomplete Combustion

Predicting the concentration of products of incomplete combustion is challenging because it requires information about the chemical composition of the fuel and the multiple reactions that convert fuel to products. FDS contains a fairly general framework by which users can specify the reaction mechanism, and the examples in the following subsections highlight some of the more commonly used schemes.

9.5.1 Smyth Slot Burner Experiment

Figure 9.66 shows predicted and measured temperatures at three elevations above the Smyth slot burner (see Sec. 3.81 for details). Figures 9.67 through 9.69 show predicted and measured concentrations of CH_4 , O_2 , CO , CO_2 , H_2O and H_2 at the same three elevations. The reported uncertainty in the species concentration measurements ranges from 10 % to 20 %. The abbreviation “FR” in the labels means that the conversion of CO to CO_2 is modeled using a finite-rate, reversible reaction. The word “Fast” implies that this reaction is infinitely fast, but occurs following the first reaction, also infinitely fast.

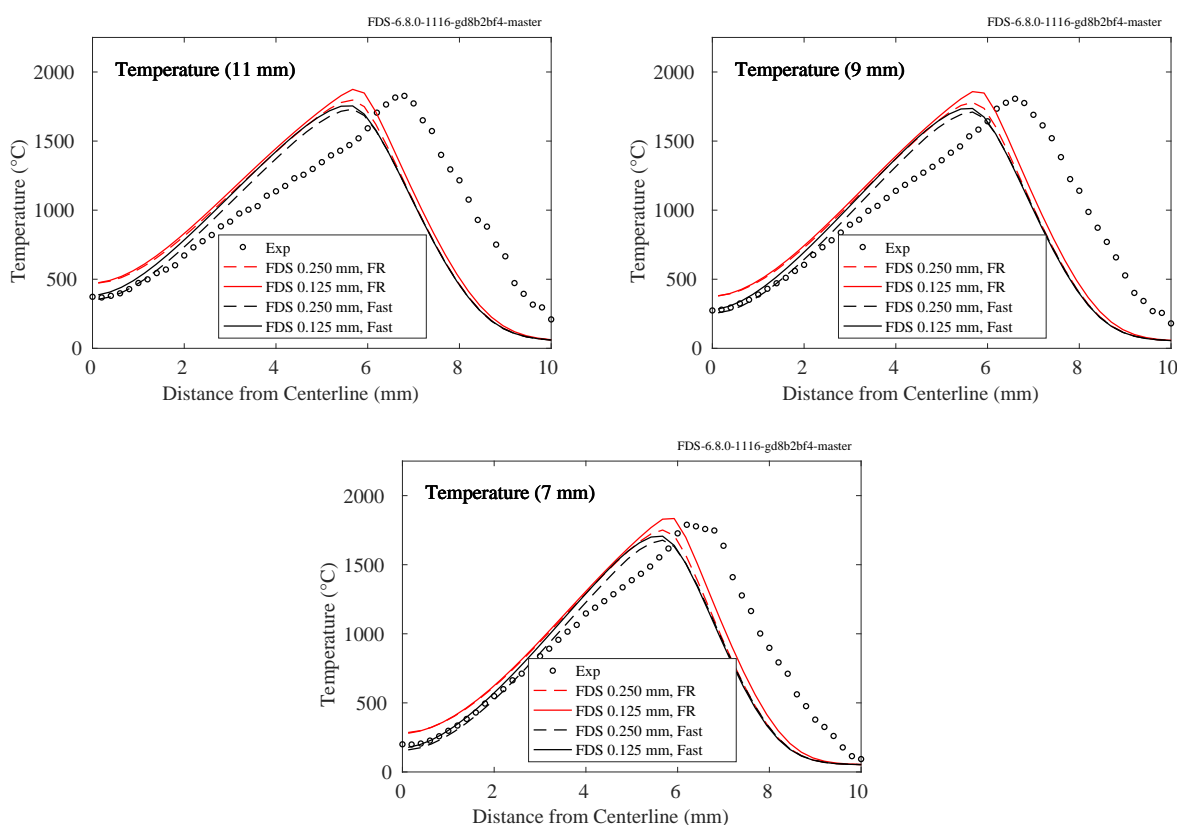


Figure 9.66: Predicted and measured temperature at 7 mm, 9 mm, and 11 mm above a methane-air slot burner.

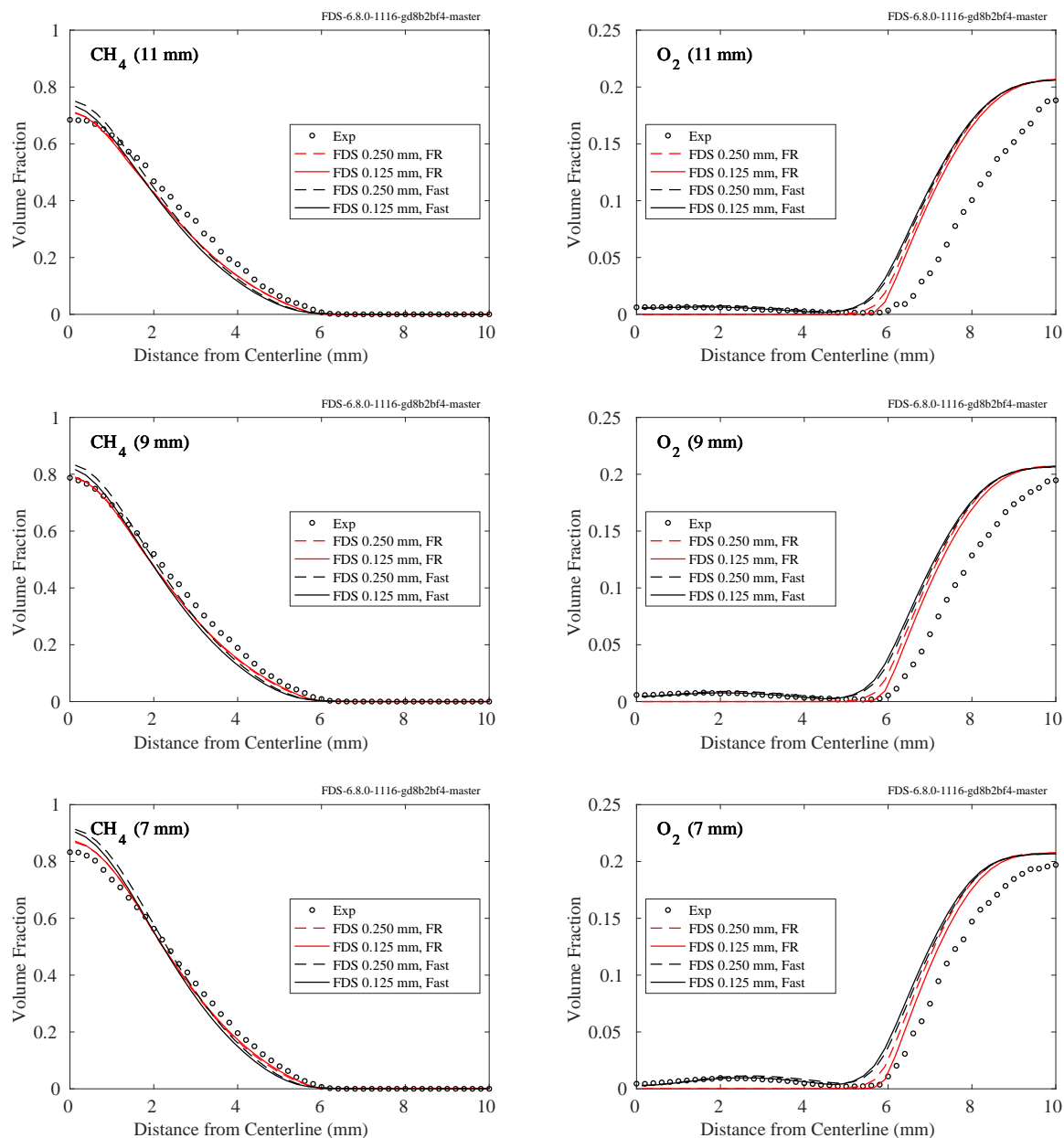


Figure 9.67: Predicted and measured CH_4 and O_2 volume fractions at 11 mm, 9 mm, and 7 mm above a methane-air slot burner.

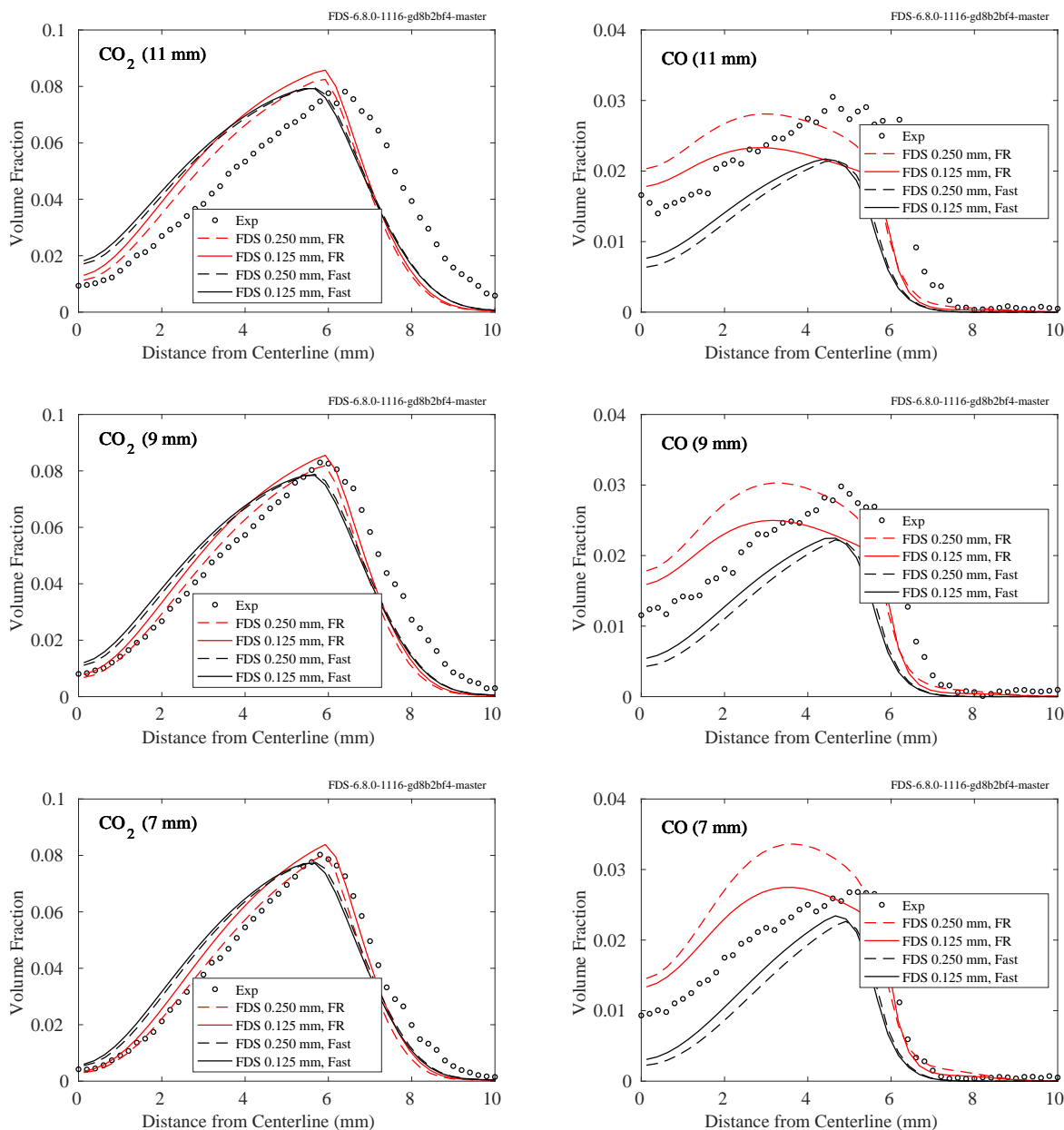


Figure 9.68: Predicted and measured CO_2 and CO volume fractions at 11 mm, 9 mm, and 7 mm above a methane-air slot burner.

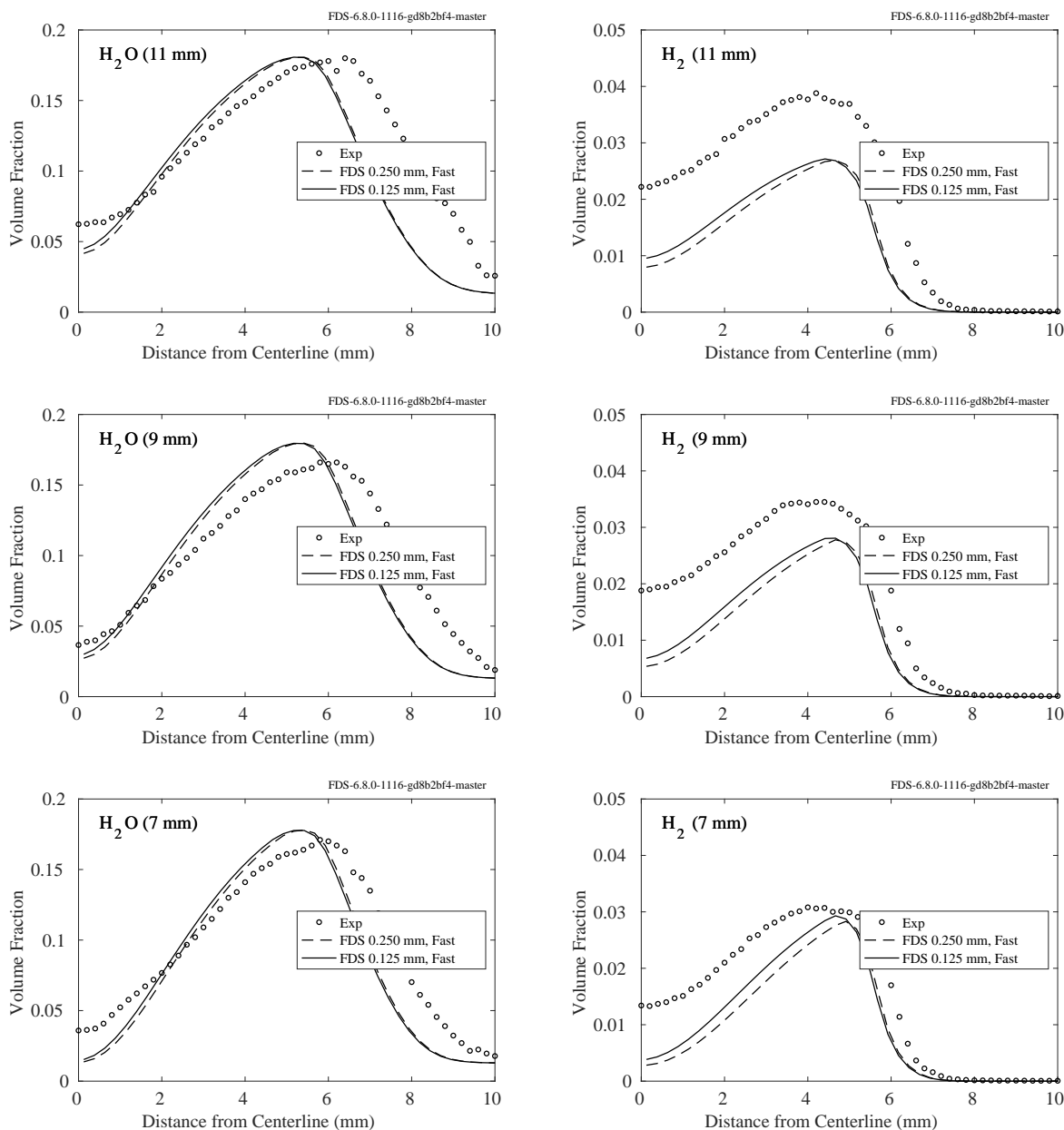


Figure 9.69: Predicted and measured H_2O and H_2 volume fractions at 11 mm, 9 mm, and 7 mm above a methane-air slot burner.

9.5.2 Beyler Hood Experiments

Fig. 9.70 compares measured and predicted species mass fractions in the Beyler Hood experiments. Both measured and predicted values are time-averaged. The FDS results are taken at the extraction vent, whereas the measurements were made downstream of the vent. Details of the experiments can be found in Sec. 3.6.

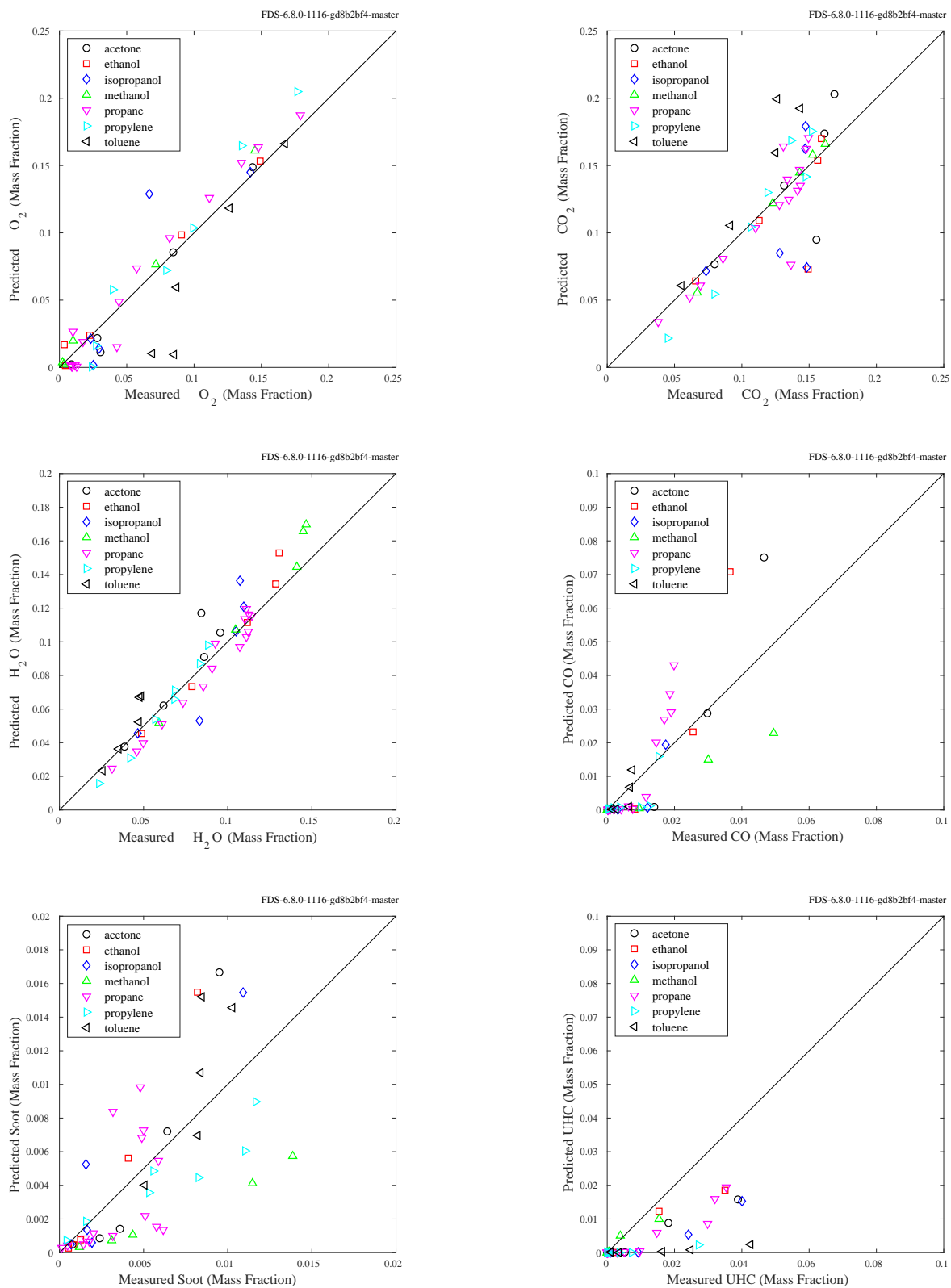


Figure 9.70: Comparison of measured and predicted species concentrations in the Beyler hood experiments

9.5.3 NIST Reduced Scale Enclosure (RSE) Experiments, 1994

Figures 9.71 through 9.74 show the measured and predicted CO, CO₂ and O₂, and H₂O concentrations. Figure 9.75 shows the measured and predicted thermocouple temperatures in the front and rear of the compartment. The measurements were made 10 cm below the ceiling and 30 cm from the left side wall. The front position was 10 cm from the wall with the door; the back position was 30 cm from the rear wall. Details of the experiments are found in Sec. 3.53.1.

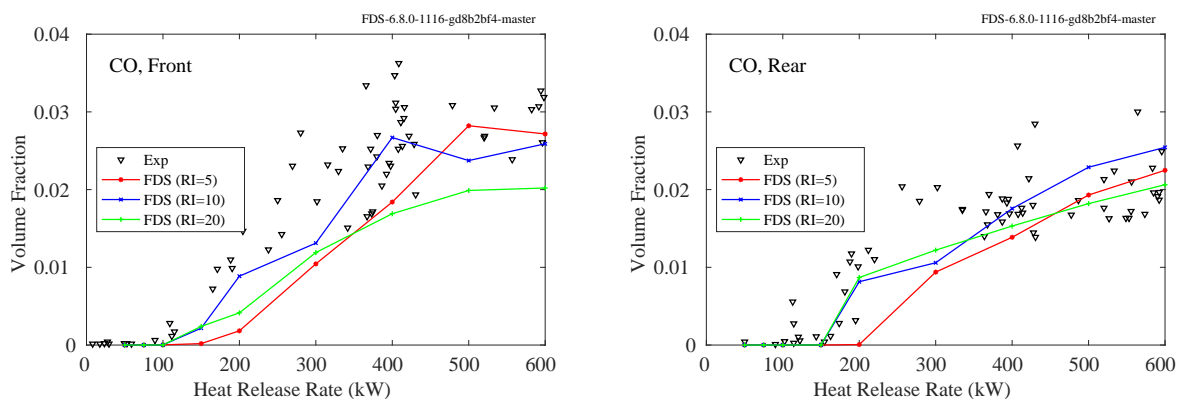


Figure 9.71: Comparison of measured and predicted CO concentration, NIST RSE experiments.

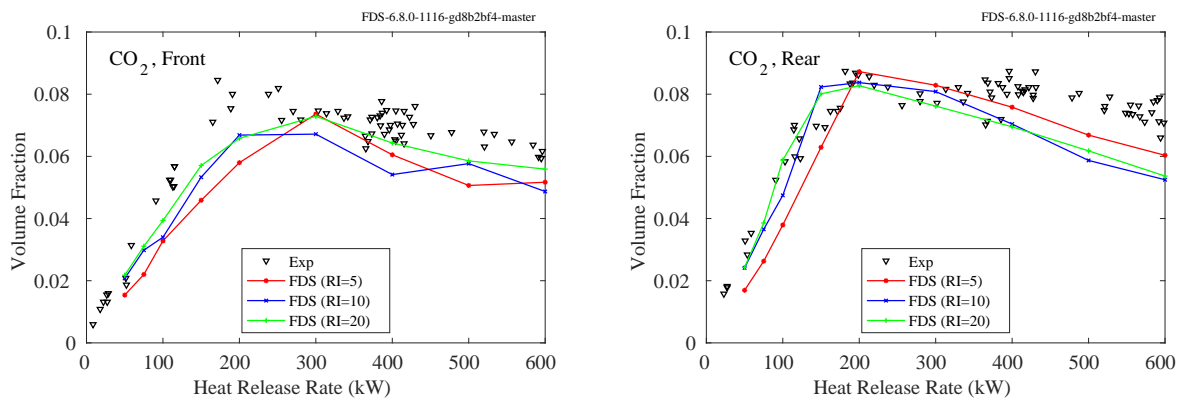


Figure 9.72: Comparison of measured and predicted CO₂ concentration, NIST RSE experiments.

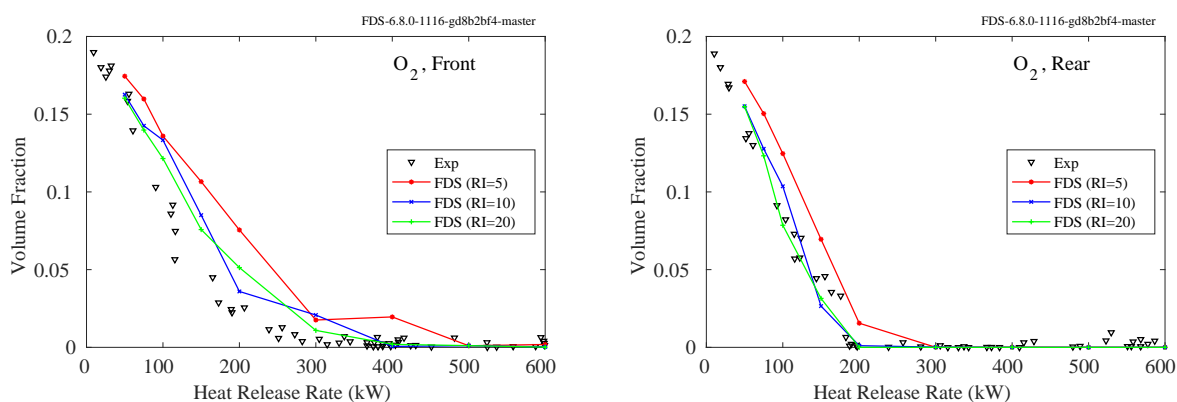
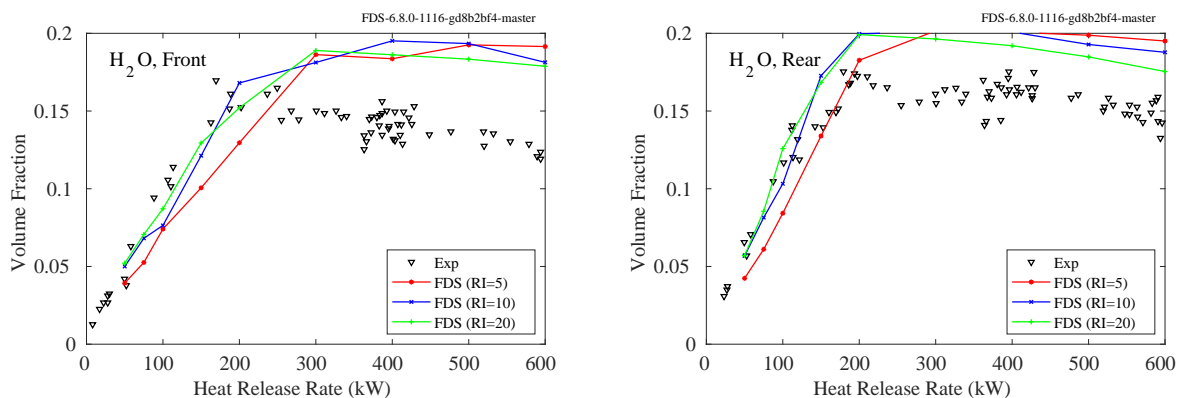
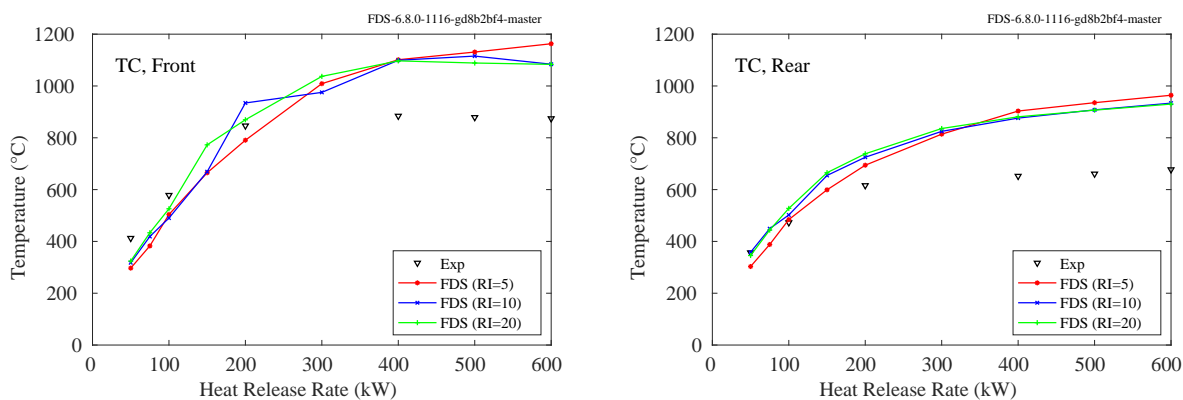
Figure 9.73: Comparison of measured and predicted O_2 concentration, NIST RSE experiments.Figure 9.74: Comparison of measured and predicted H_2O concentration, NIST RSE experiments.

Figure 9.75: Comparison of measured and predicted temperature, NIST RSE experiments.

9.5.4 NIST Reduced-Scale Enclosure (RSE) Experiments, 2007

Species and temperature measurements were made in the front and rear of the compartment, 10 cm below the ceiling, 29 cm from the right wall (looking into the compartment), and 10 cm from the front wall or 29 cm from the rear wall. The compartment was 0.95 m wide by 1.42 m deep by 0.98 m tall with a door 0.48 m wide by 0.81 m tall centered on one of the short walls. Measurements of temperature, O₂, CO₂, CO, and unburned hydrocarbon concentration were made near the ceiling in the front and back of the compartment. Details of the experiments are found in Sec. 3.53.2.

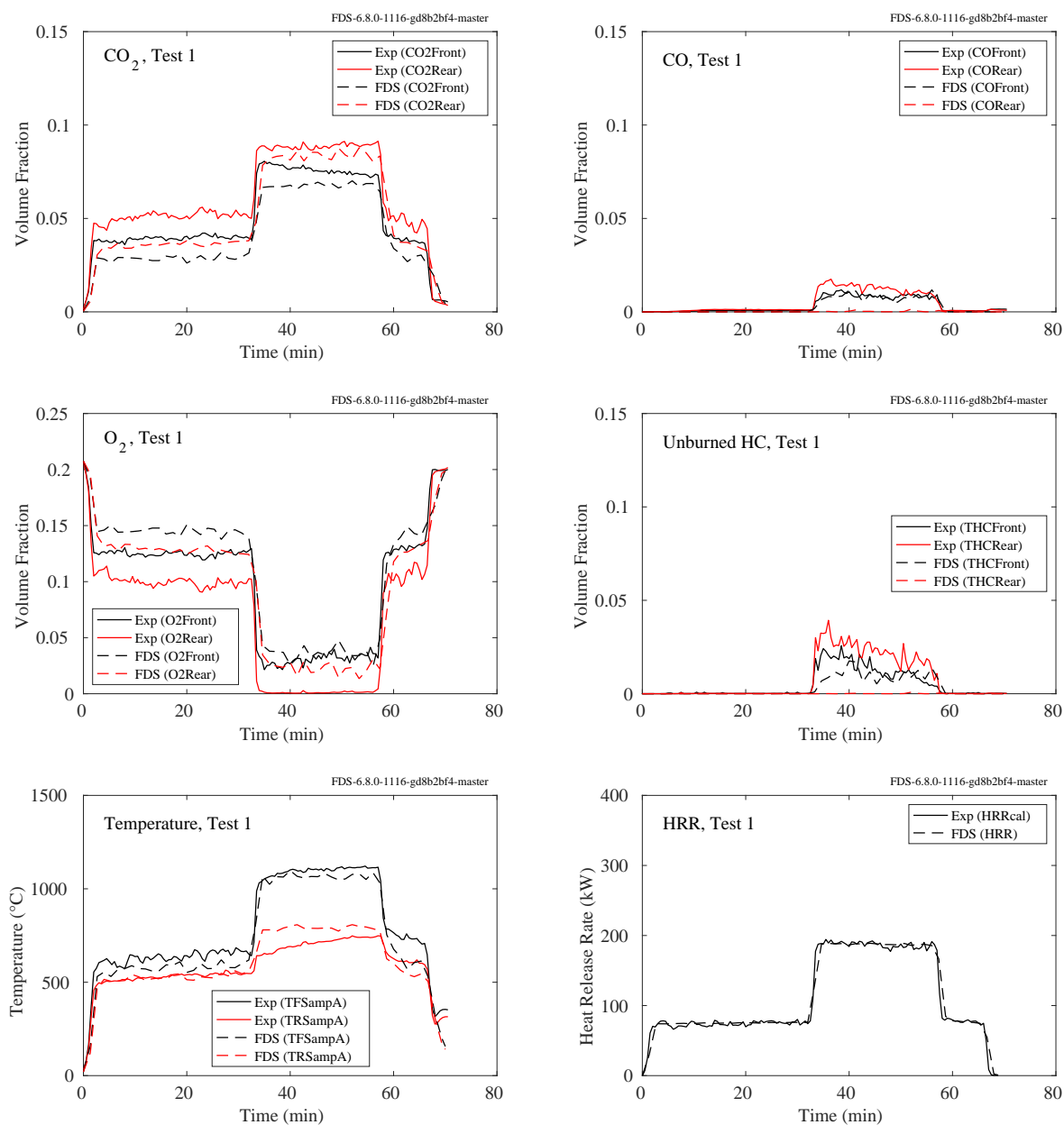


Figure 9.76: Summary of Test 1, NIST RSE 2007.

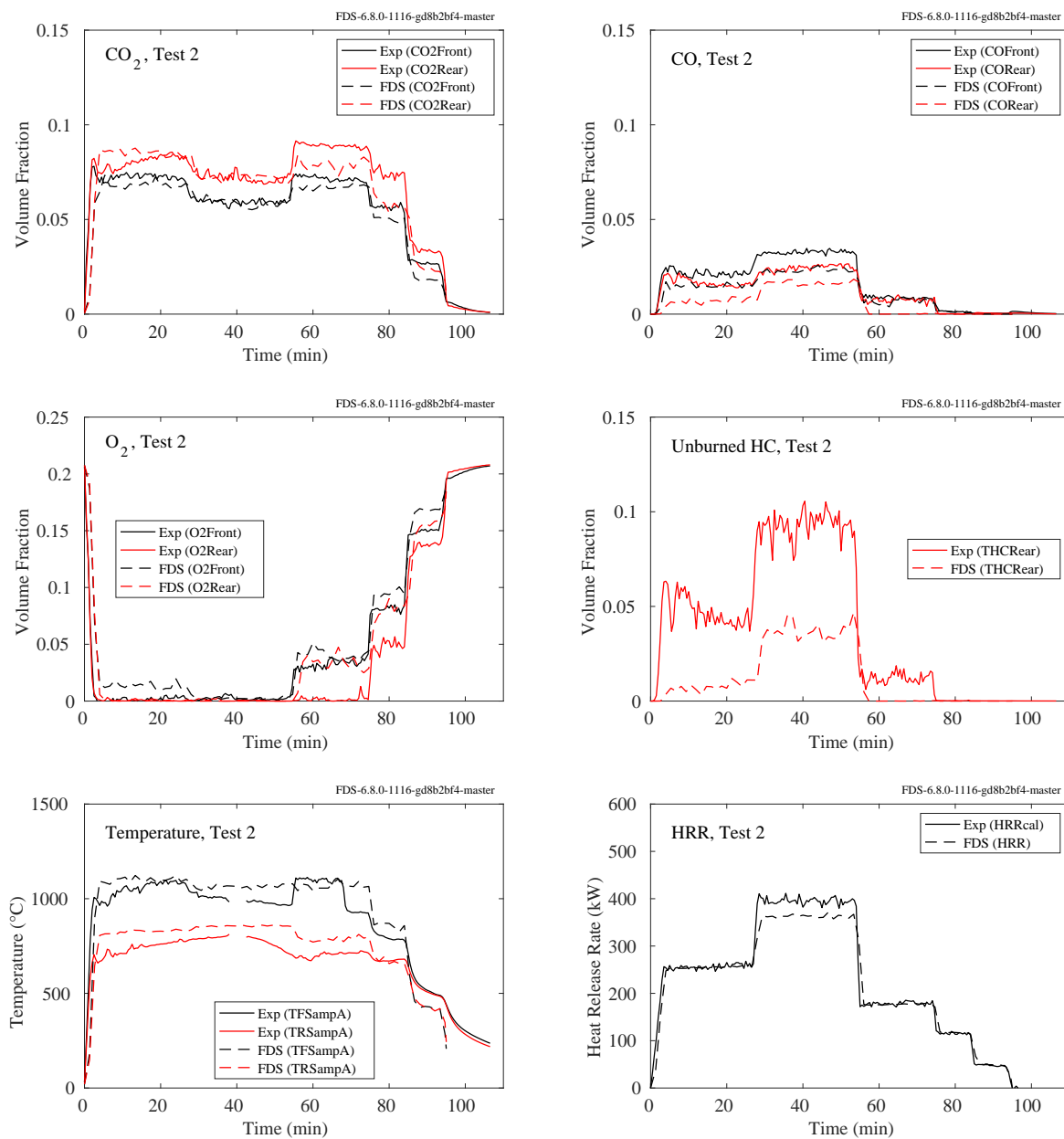


Figure 9.77: Summary of Test 2, NIST RSE 2007.

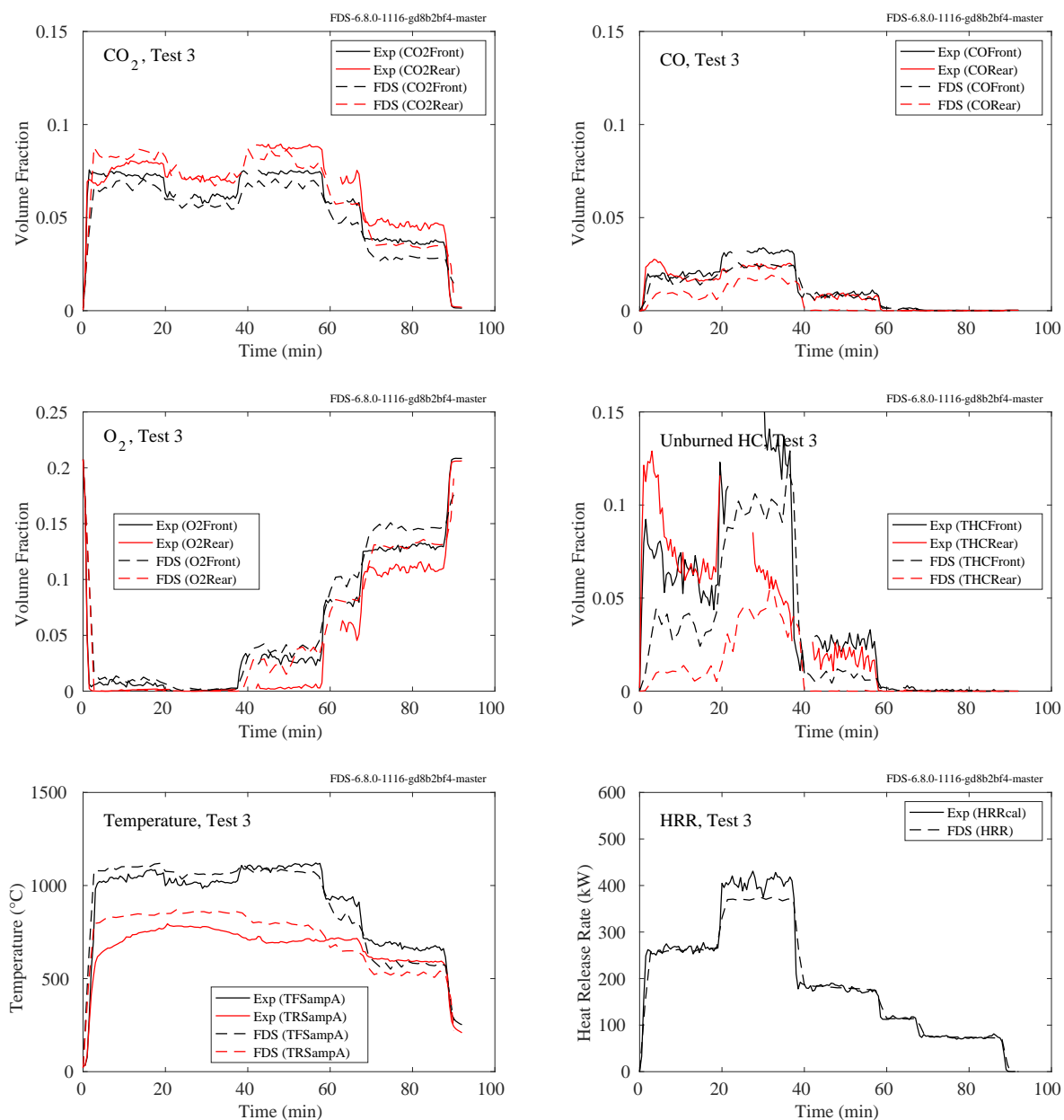


Figure 9.78: Summary of Test 3, NIST RSE 2007.

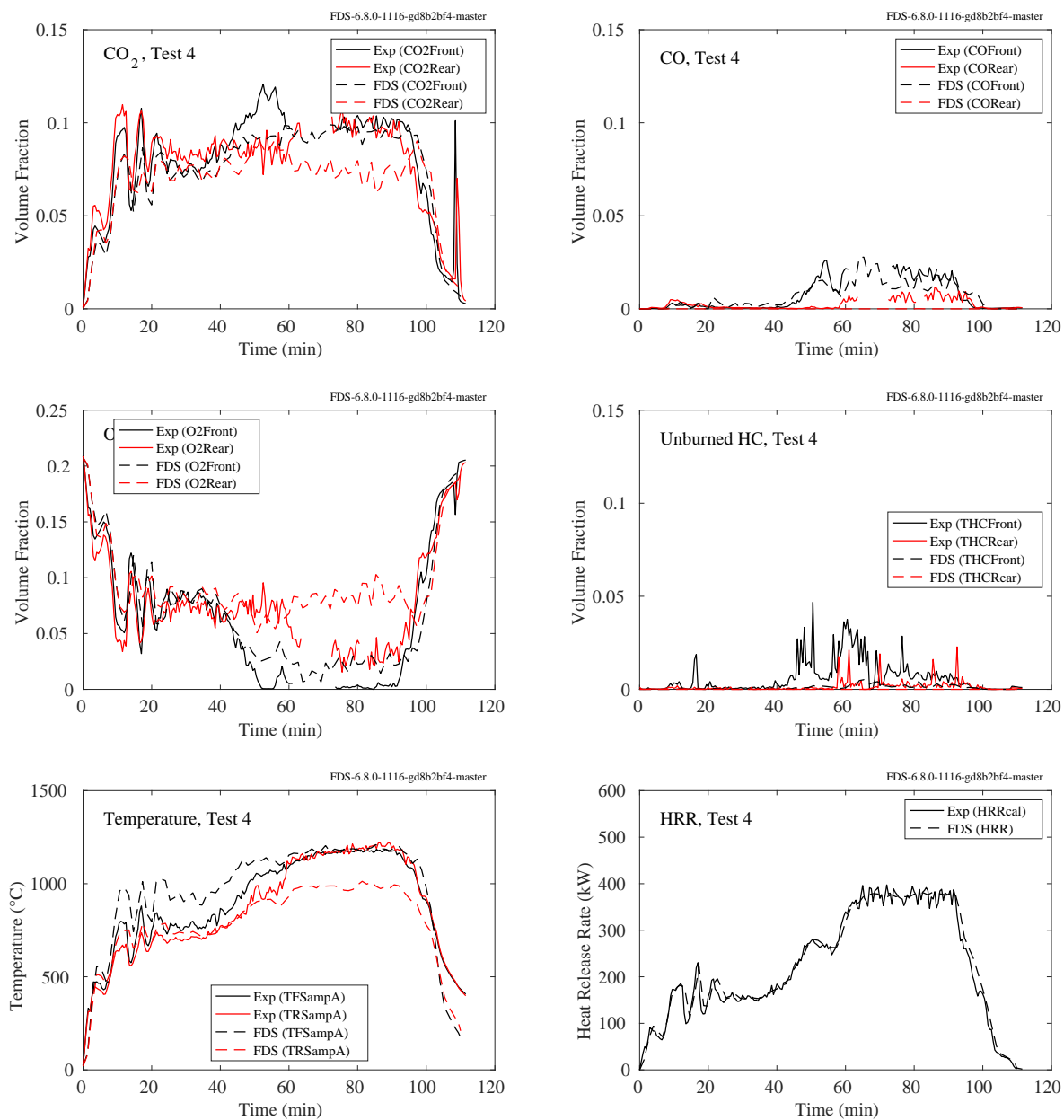


Figure 9.79: Summary of Test 4, NIST RSE 2007.

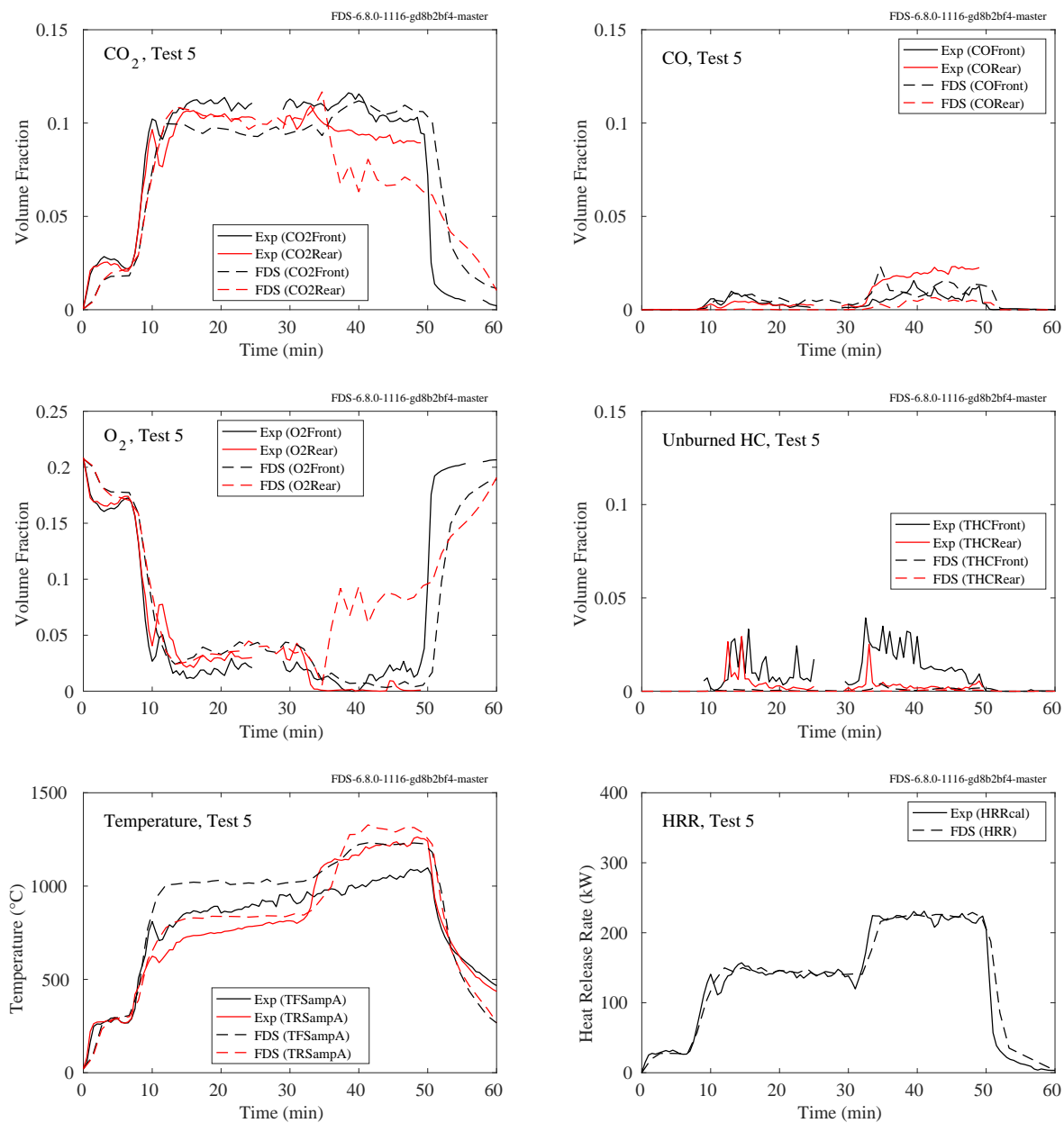


Figure 9.80: Summary of Test 5, NIST RSE 2007.

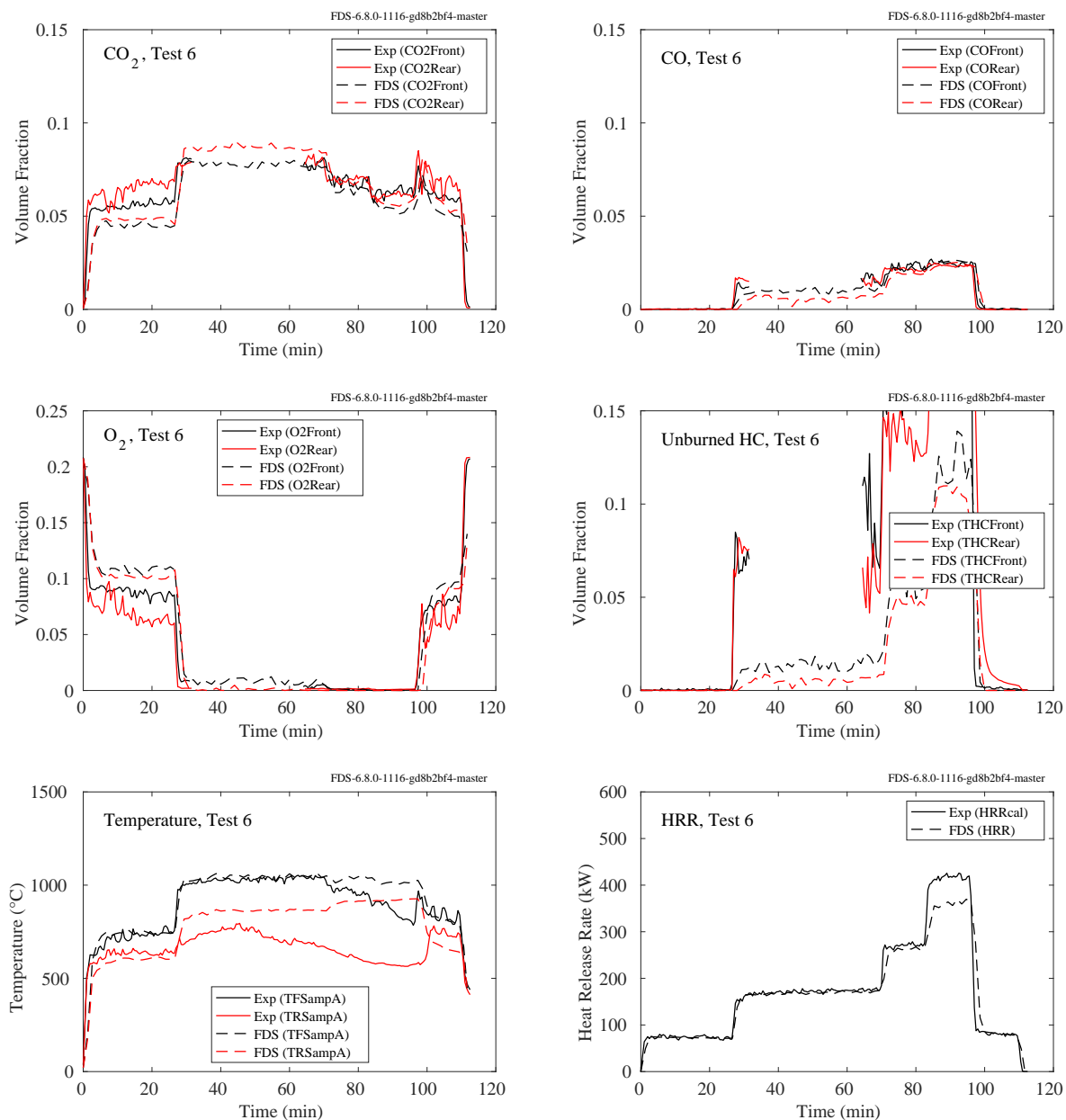


Figure 9.81: Summary of Test 6, NIST RSE 2007.

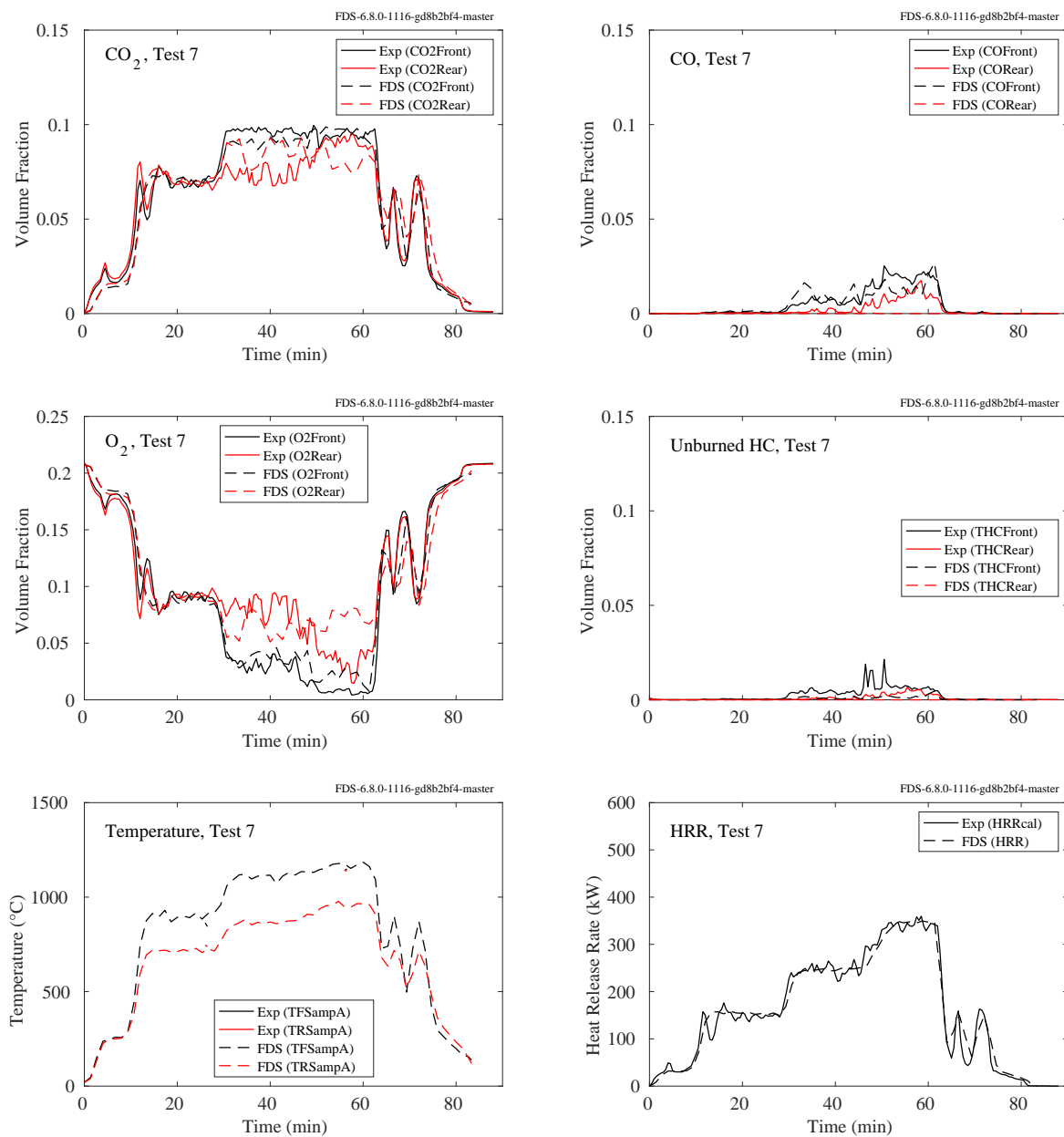


Figure 9.82: Summary of Test 7, NIST RSE 2007.

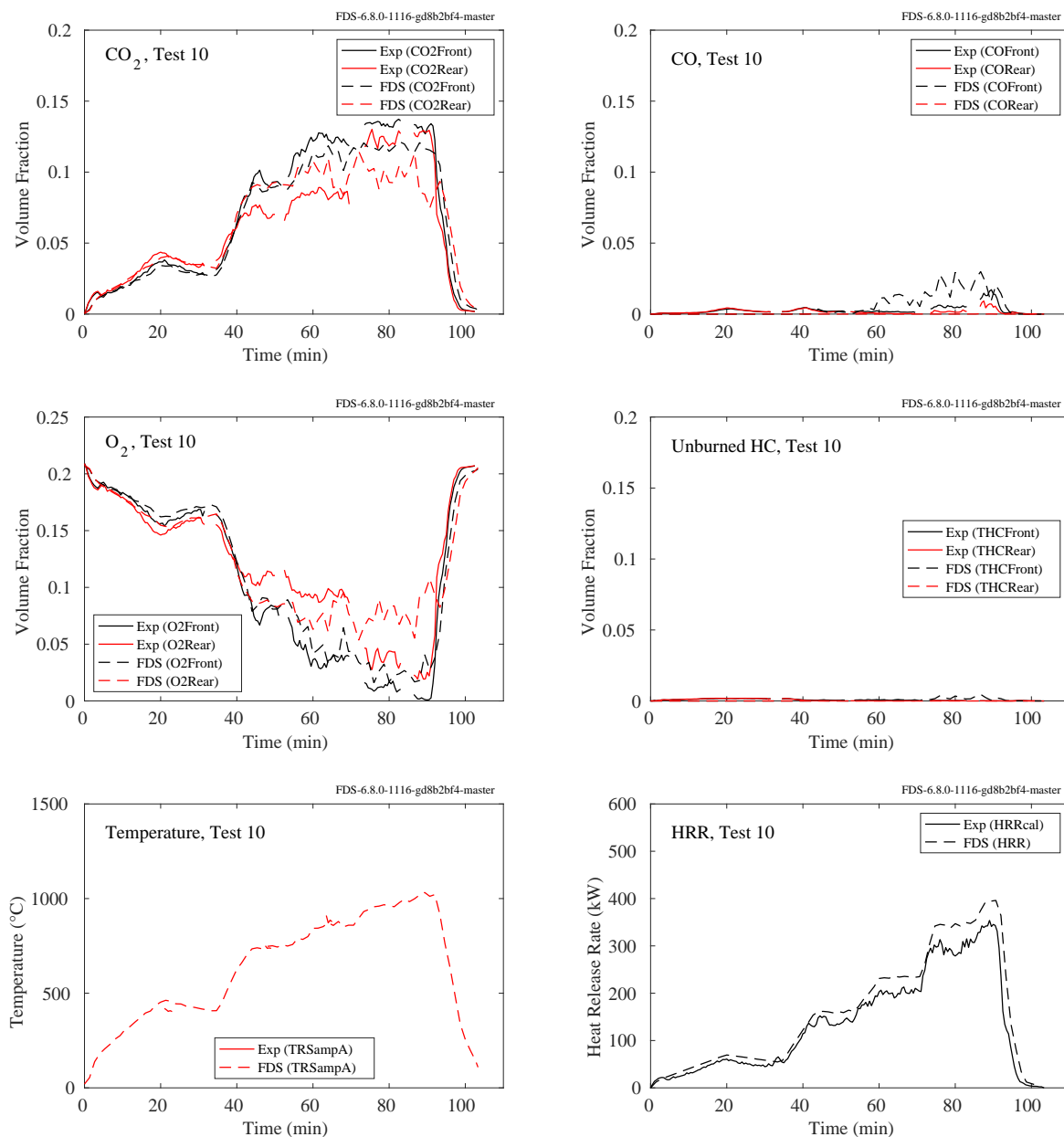


Figure 9.83: Summary of Test 10, NIST RSE 2007.

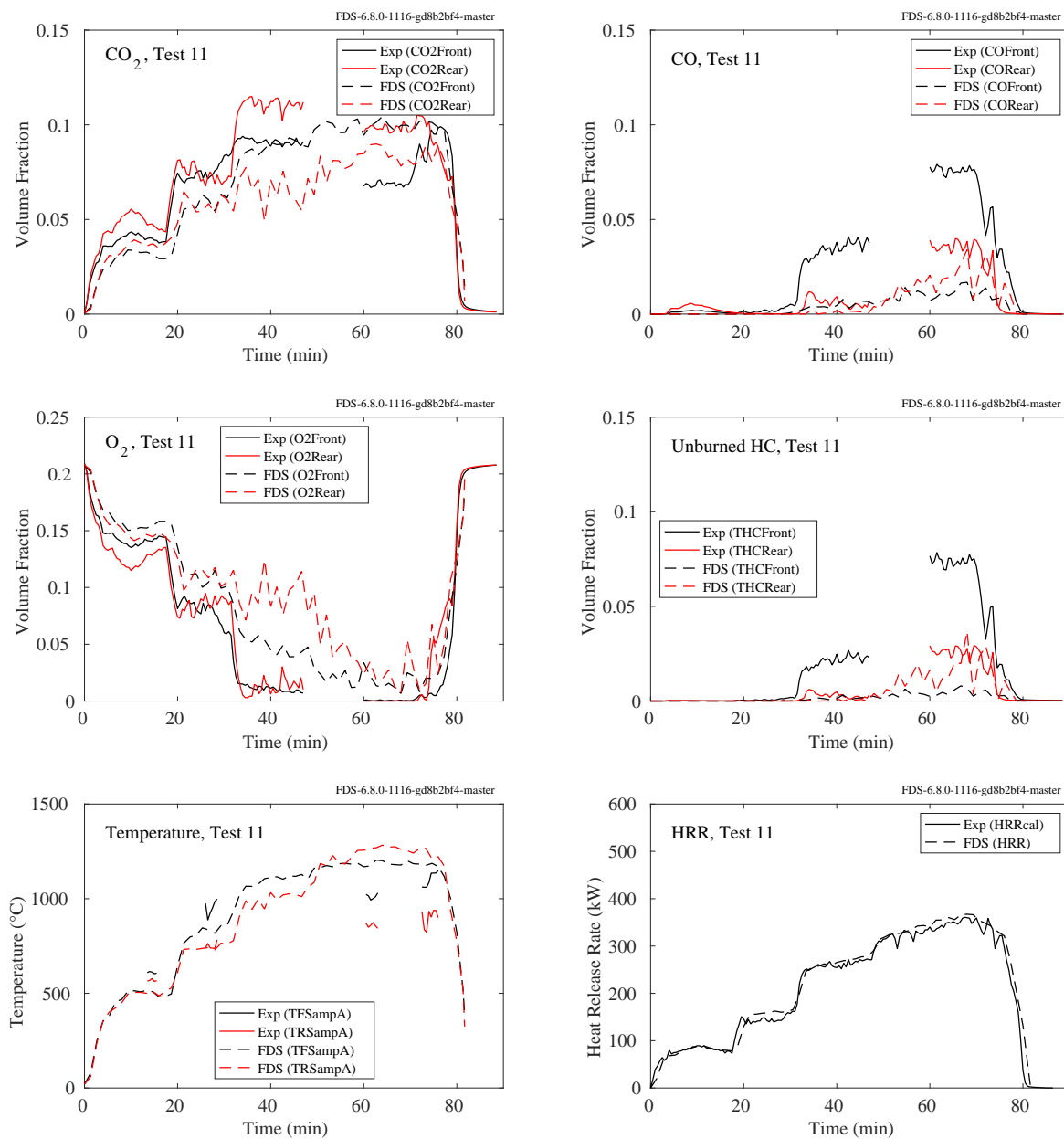


Figure 9.84: Summary of Test 11, NIST RSE 2007.

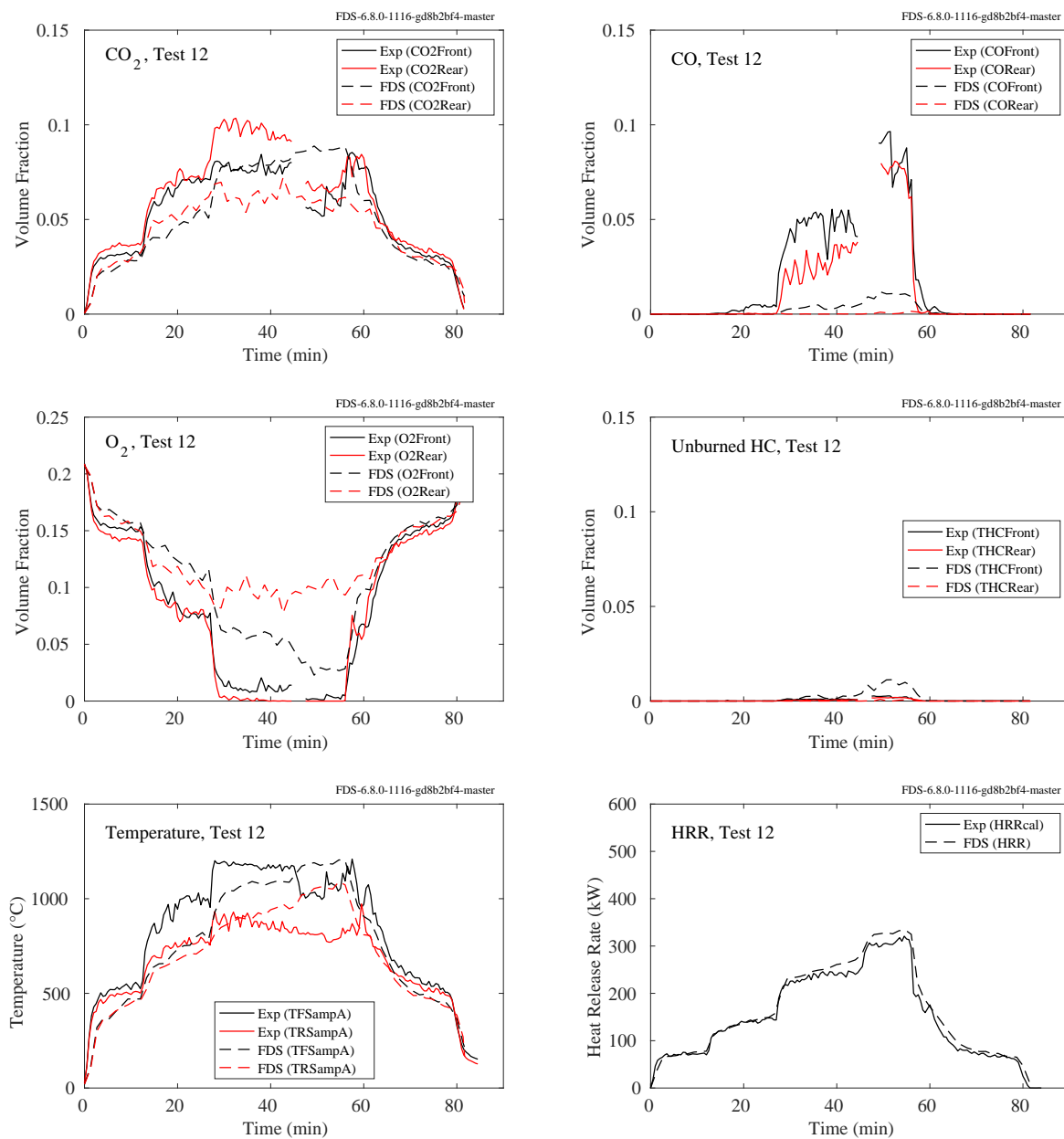


Figure 9.85: Summary of Test 12, NIST RSE 2007.

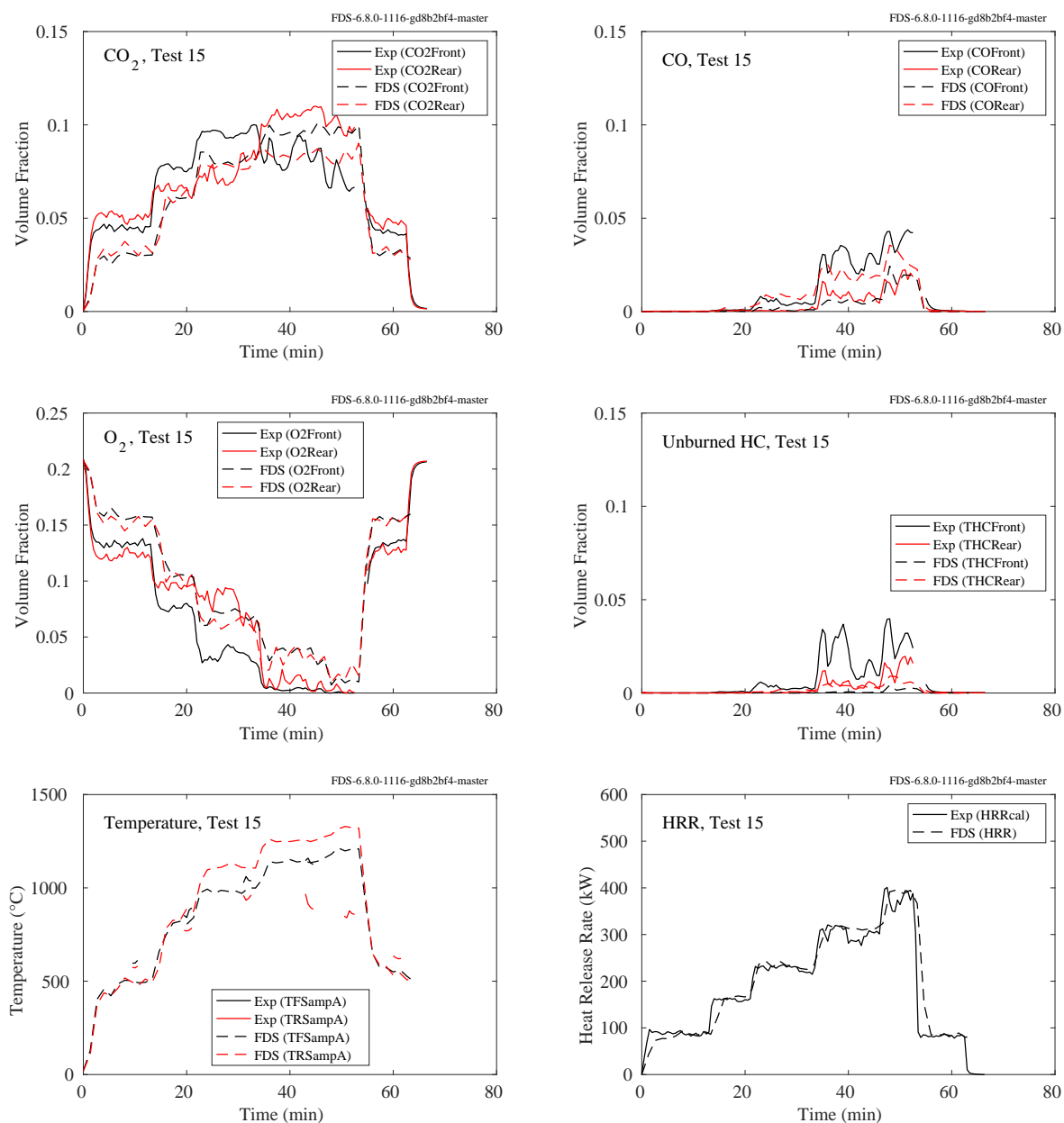


Figure 9.86: Summary of Test 15, NIST RSE 2007.

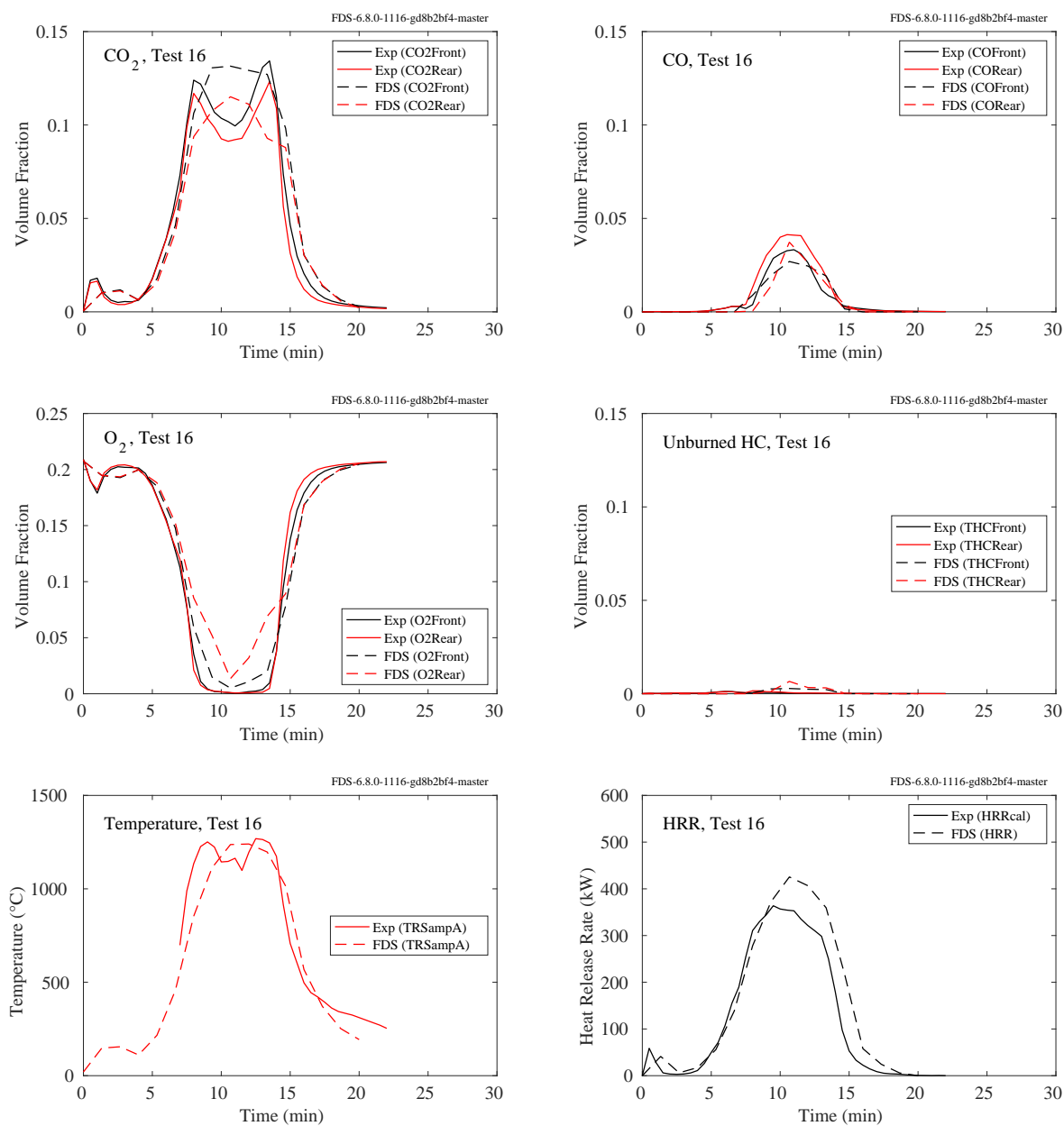


Figure 9.87: Summary of Test 16, NIST RSE 2007.

9.5.5 NIST Full-Scale Enclosure (FSE) Experiments, 2008

Species concentrations and temperature measurements were made at the front and rear of the compartment. Details of the experiments are found in Sec. 3.53.3.

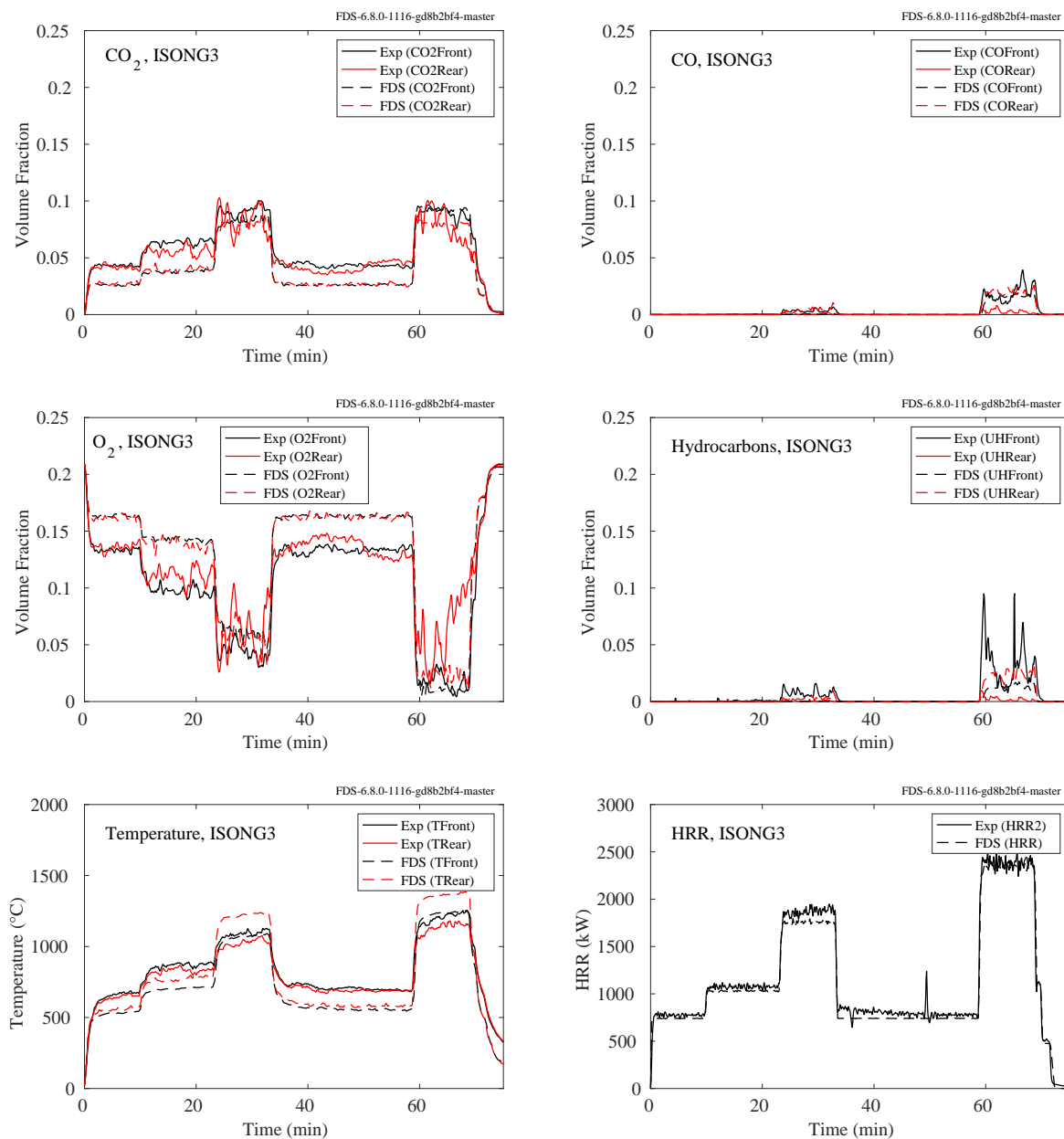


Figure 9.88: Summary of ISONG3, NIST FSE 2008.

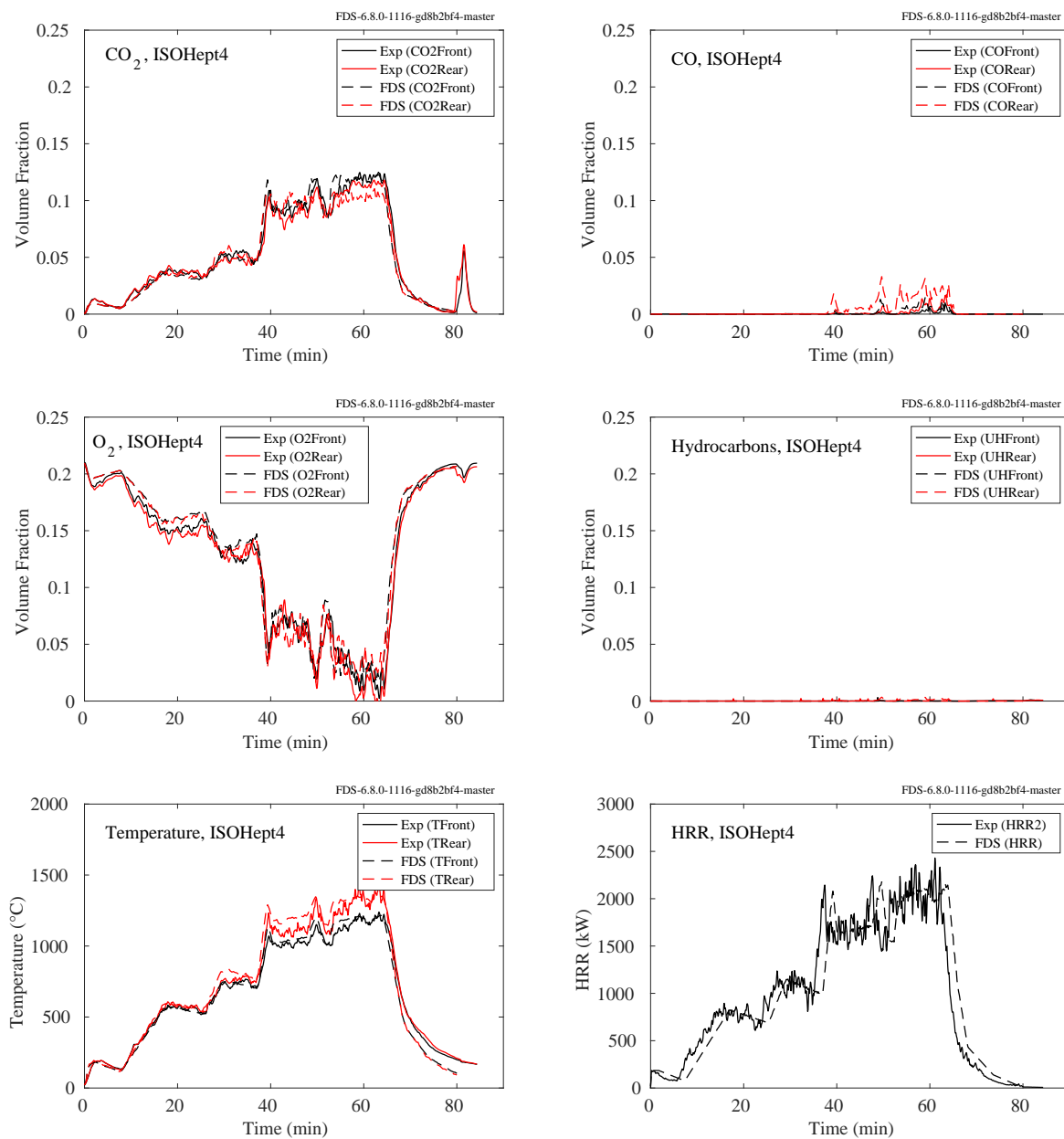


Figure 9.89: Summary of ISOHept4, NIST FSE 2008.

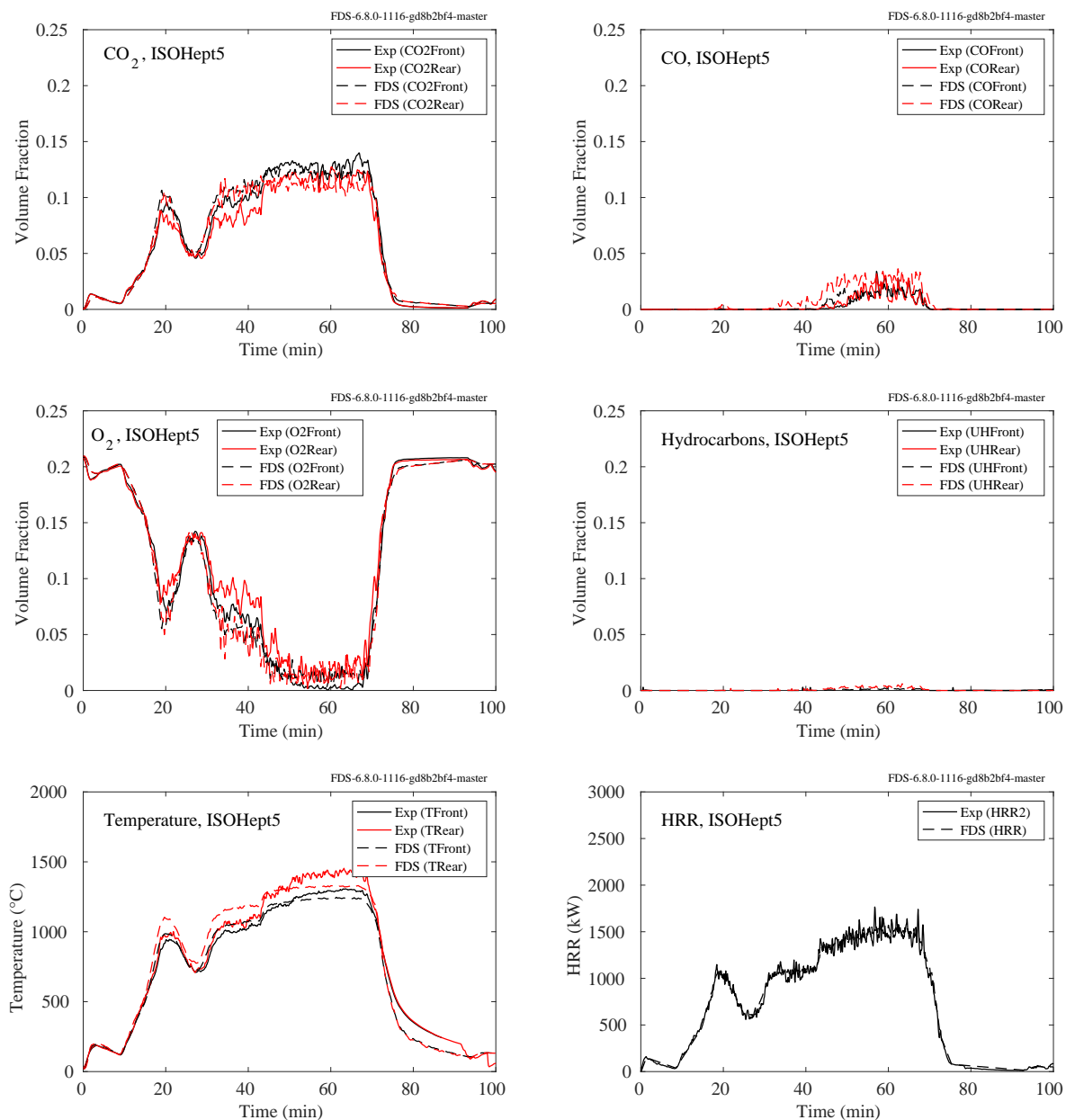


Figure 9.90: Summary of ISOHept5, NIST FSE 2008.

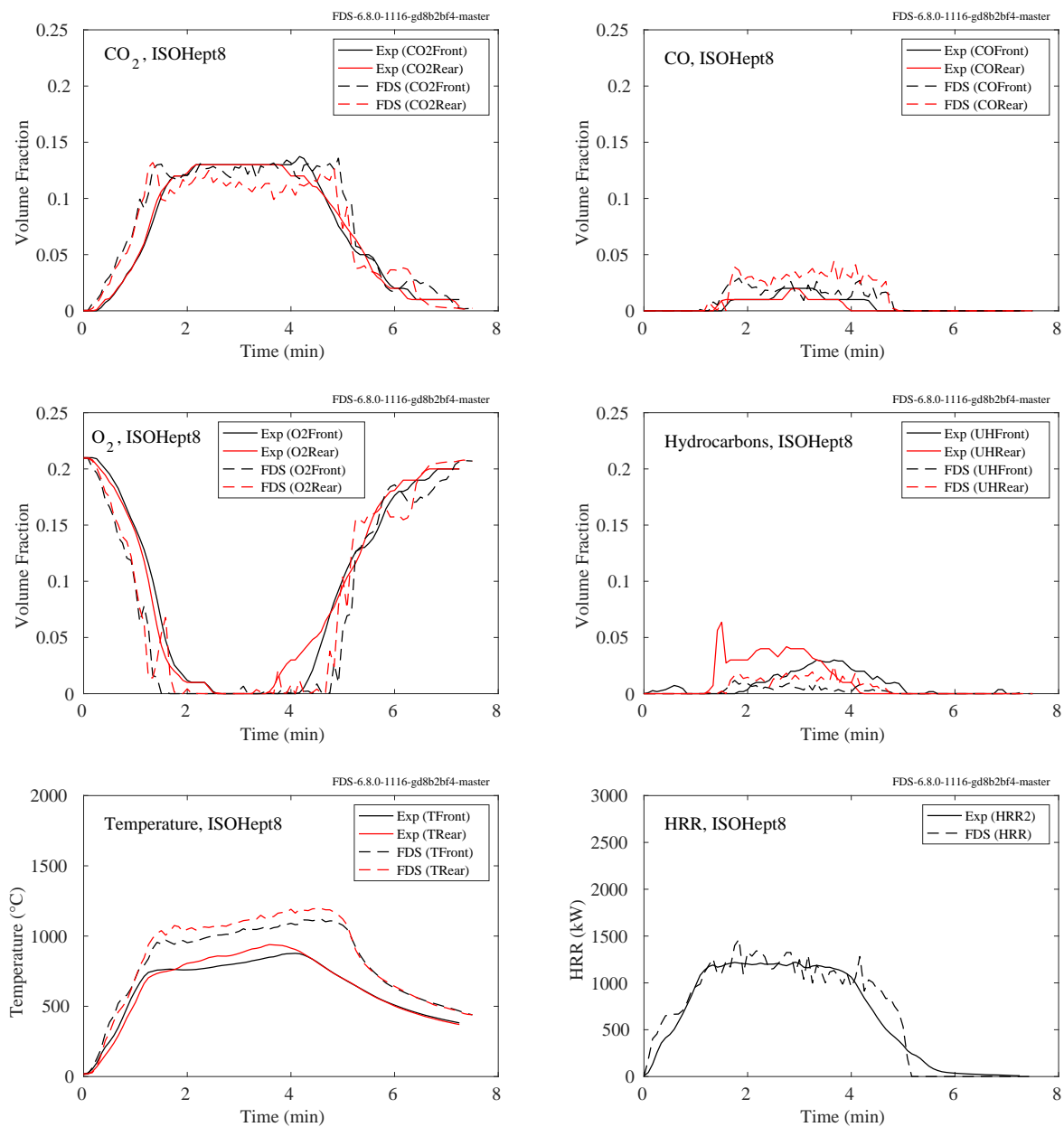


Figure 9.91: Summary of ISOHept8, NIST FSE 2008.

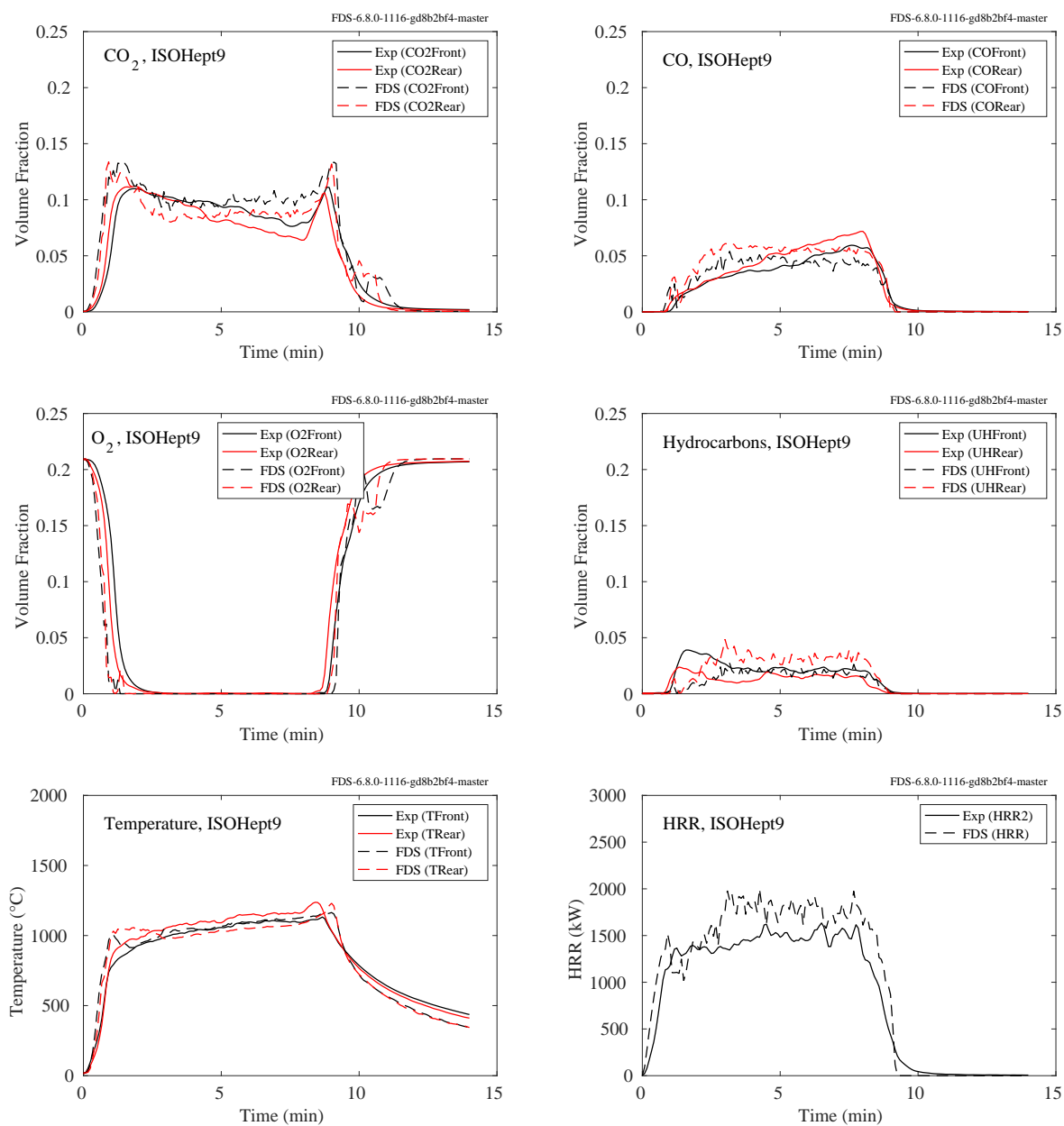


Figure 9.92: Summary of ISOHept9, NIST FSE 2008.

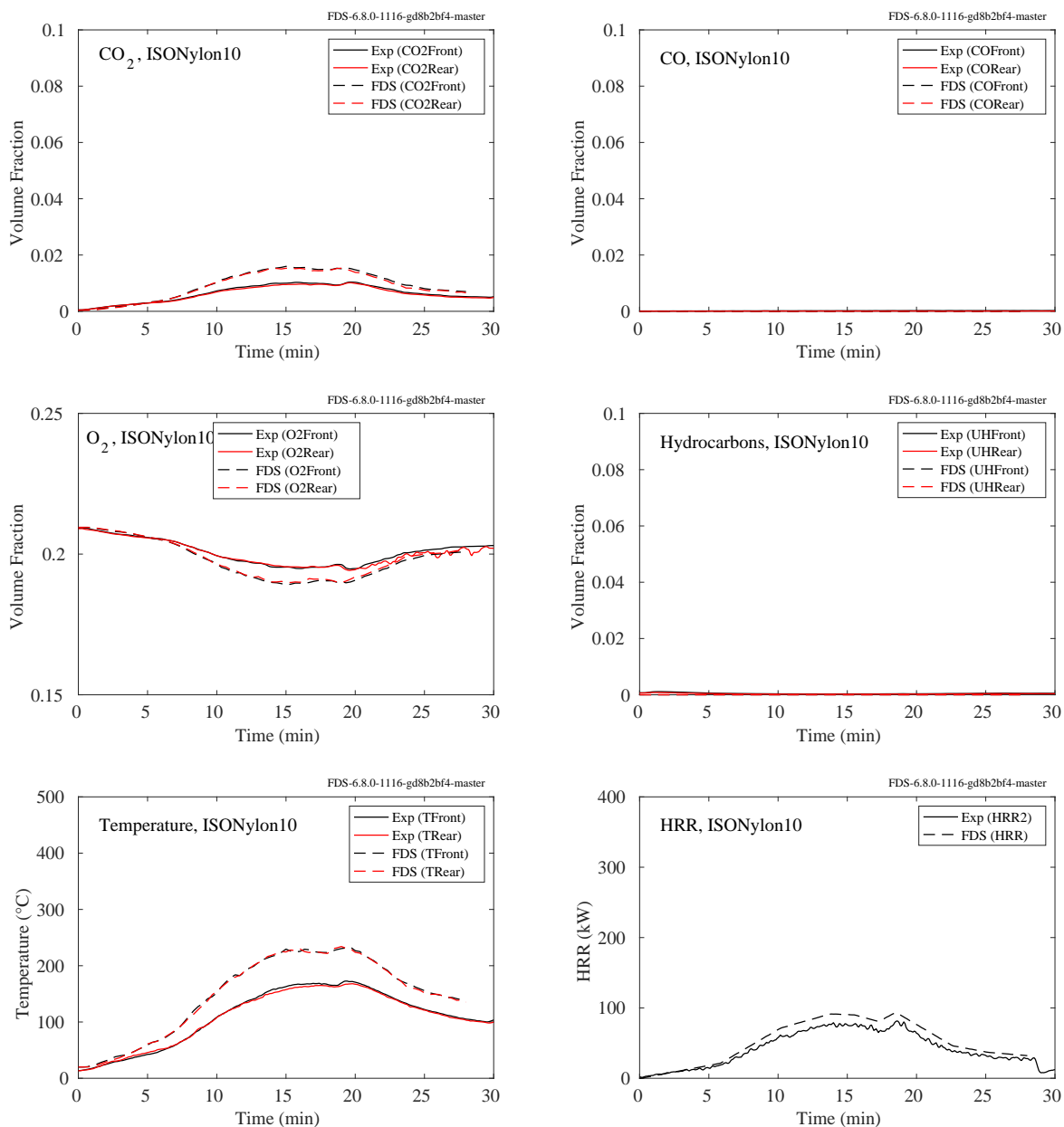


Figure 9.93: Summary of ISONylon10, NIST FSE 2008.

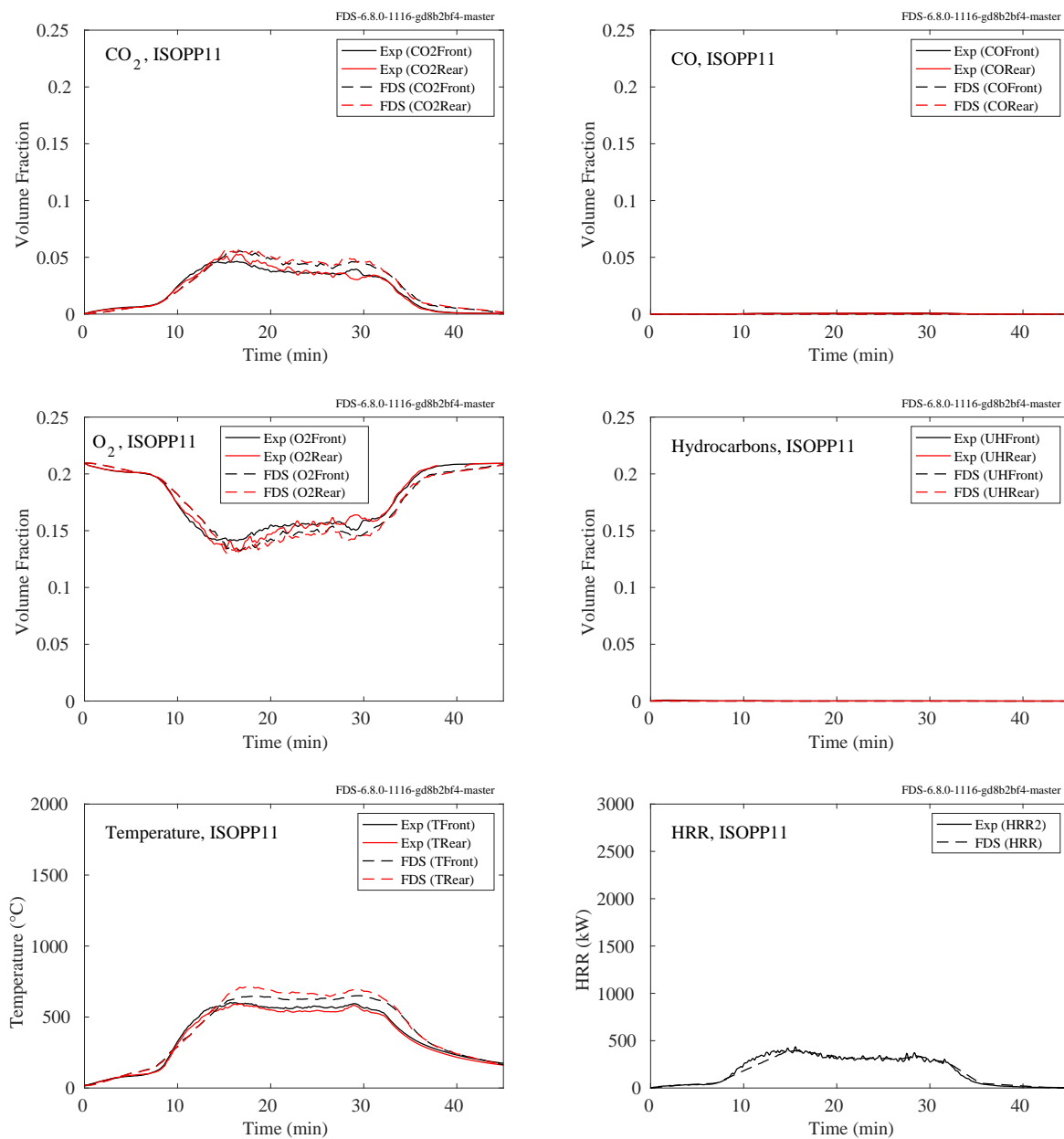


Figure 9.94: Summary of ISOPP11, NIST FSE 2008.

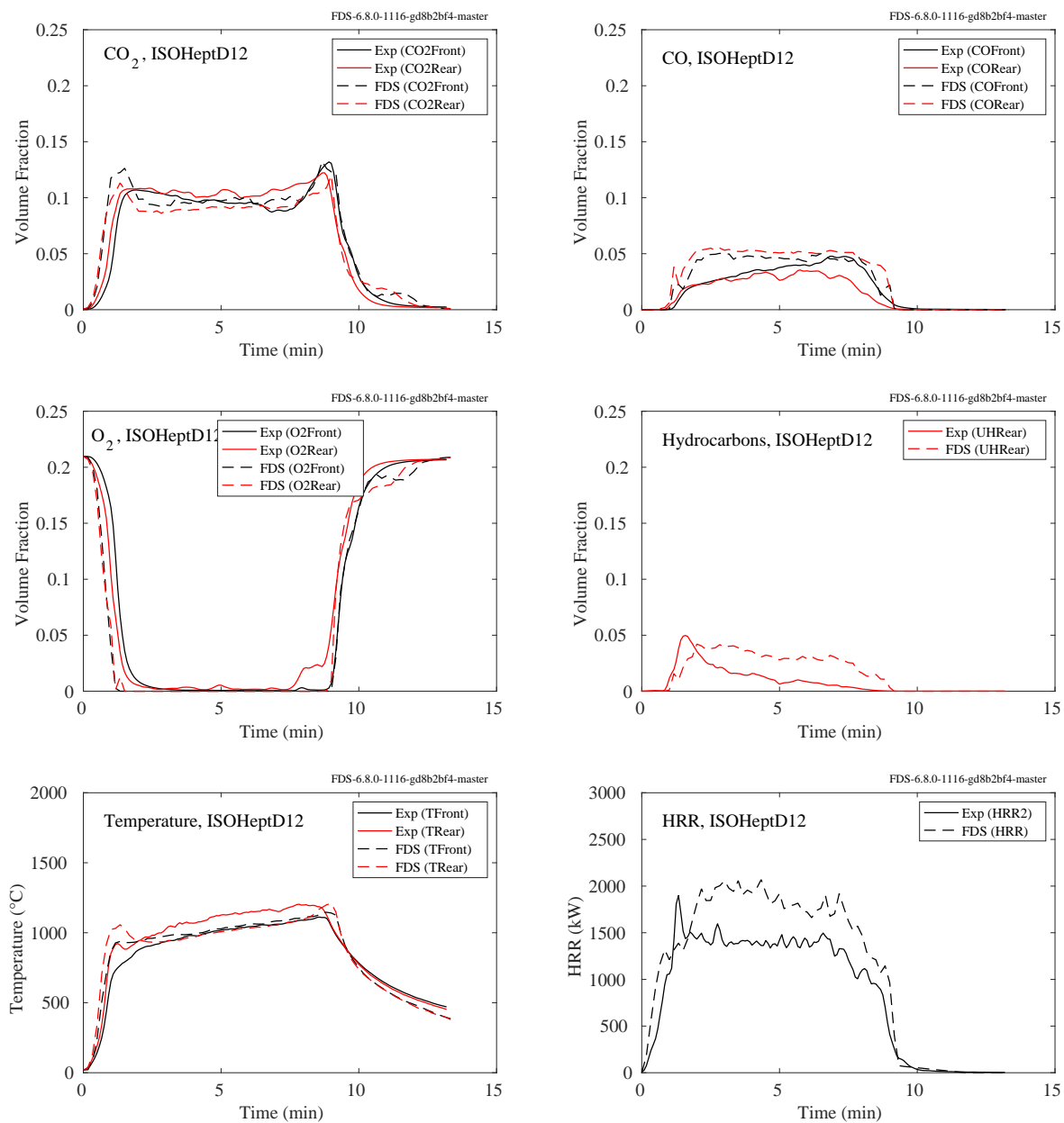


Figure 9.95: Summary of ISOHeptD12, NIST FSE 2008.

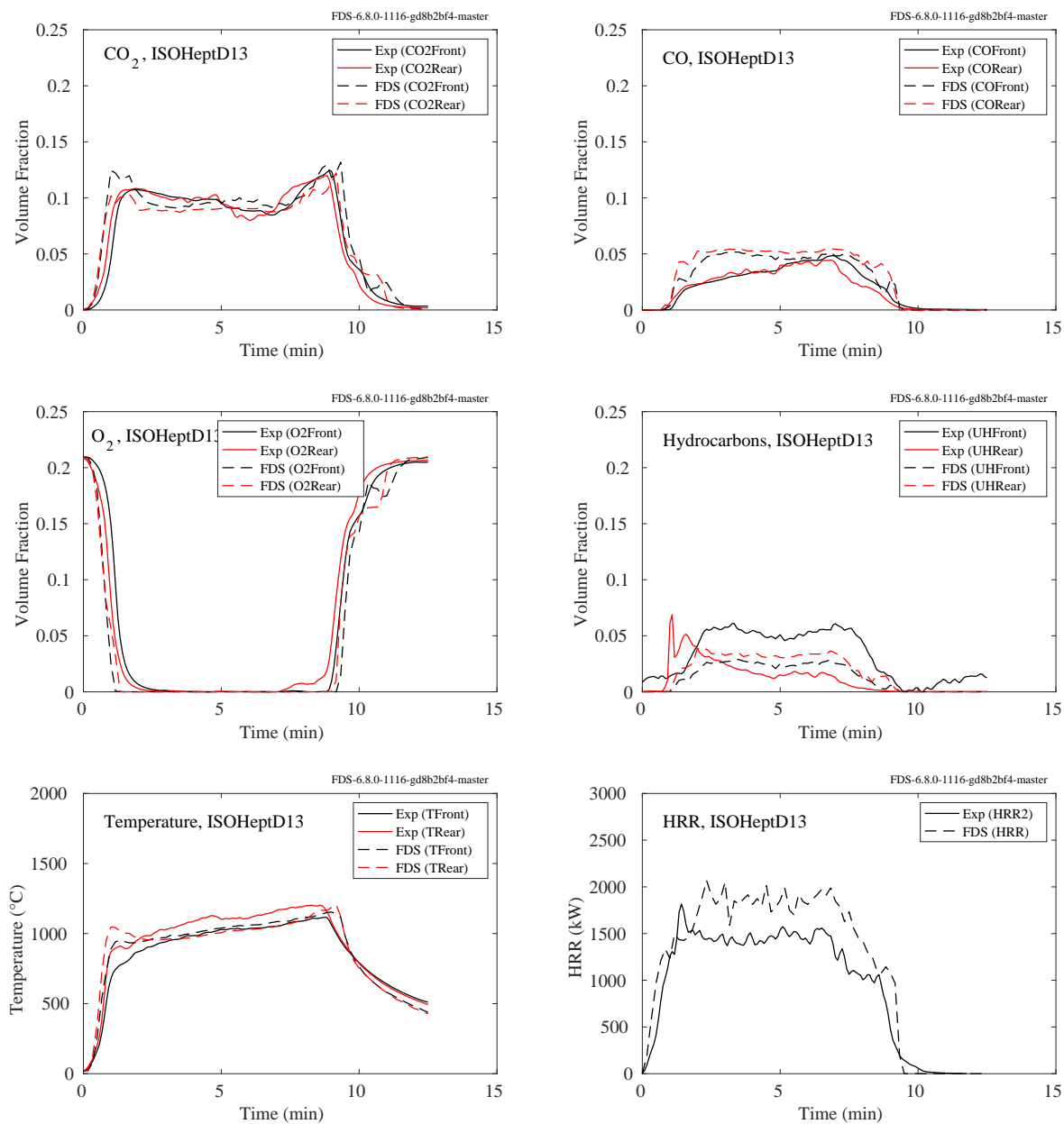


Figure 9.96: Summary of ISOHeptD13, NIST FSE 2008.

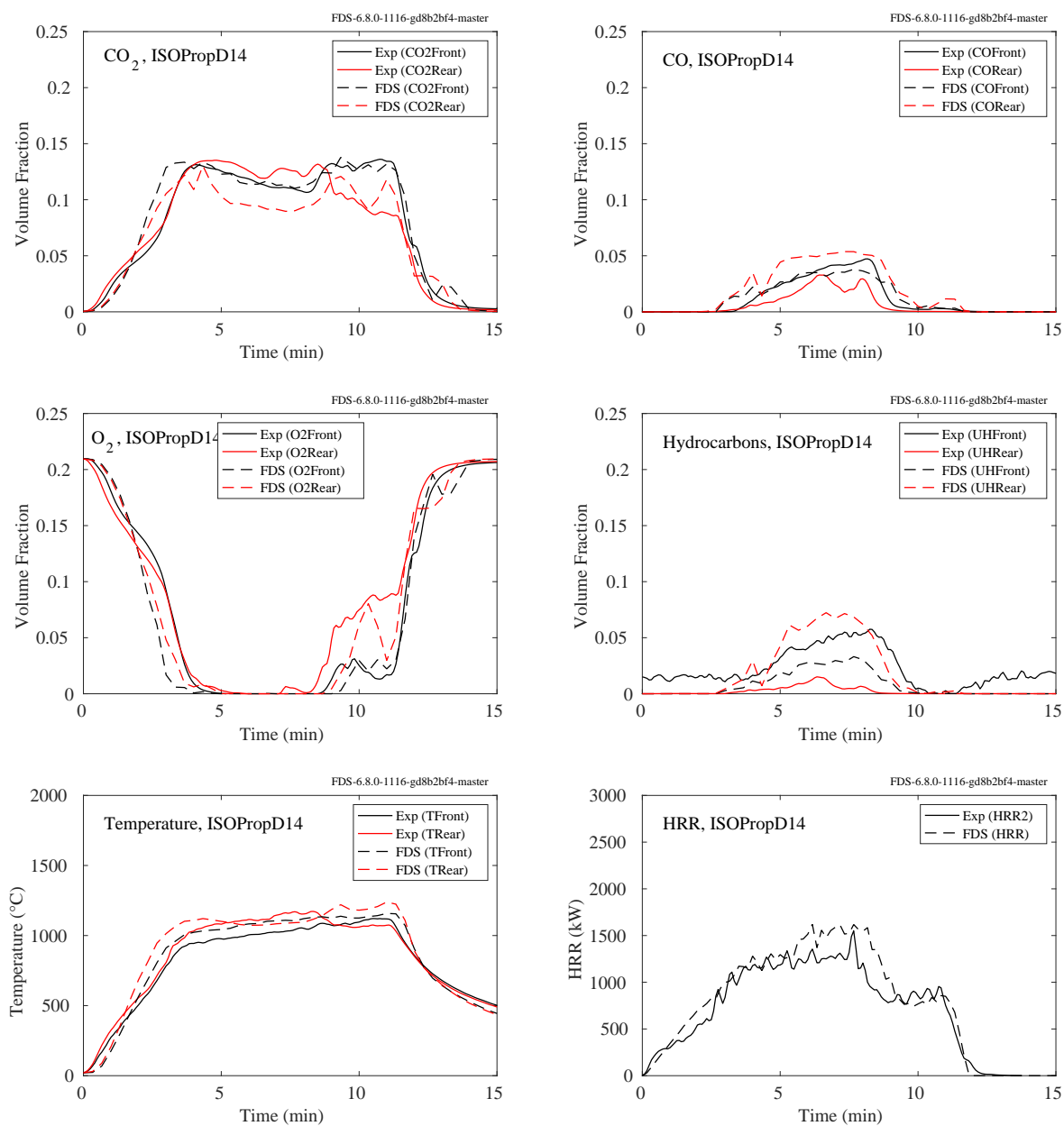


Figure 9.97: Summary of ISOPropD14, NIST FSE 2008.

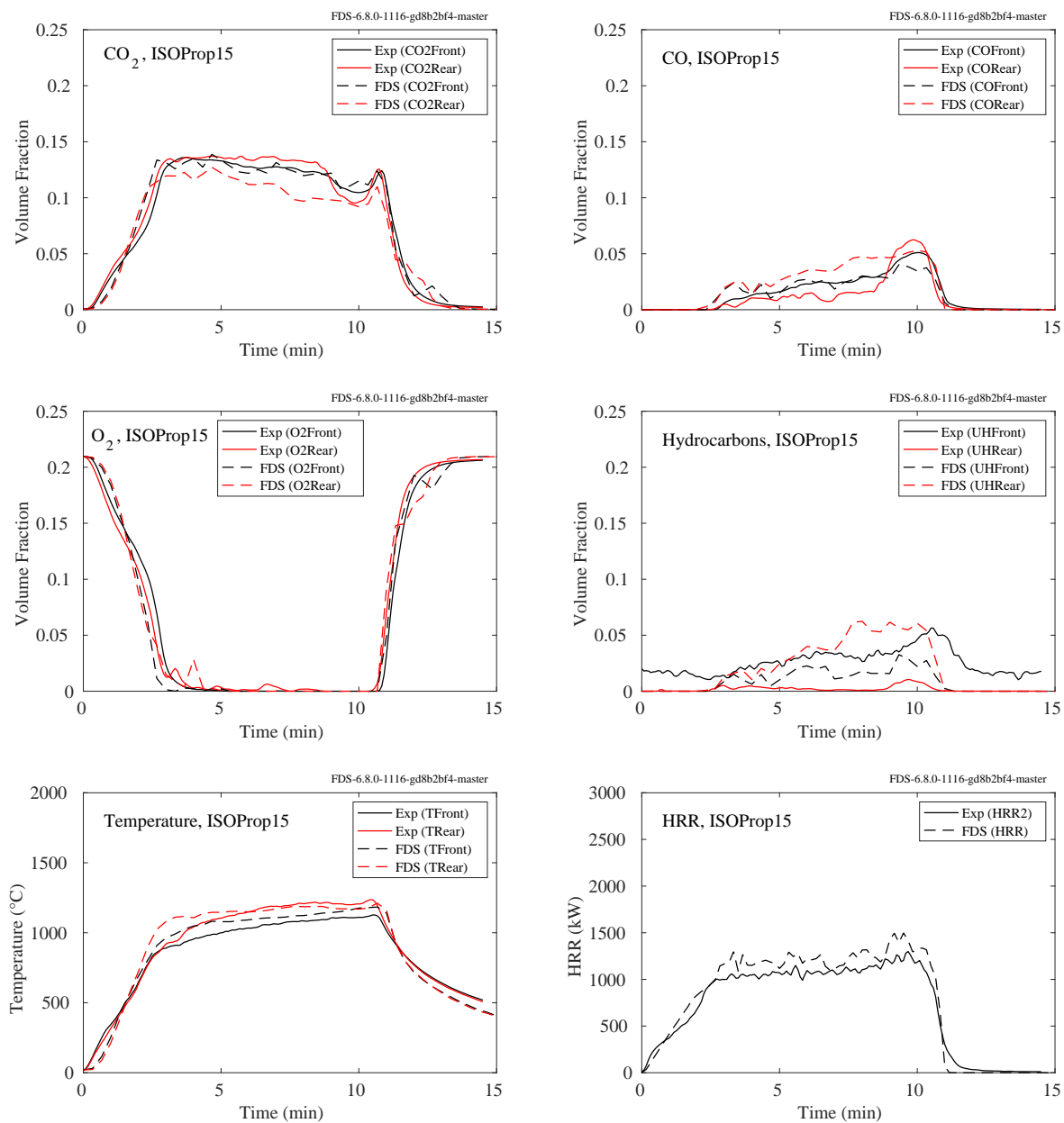


Figure 9.98: Summary of ISOProp15, NIST FSE 2008.

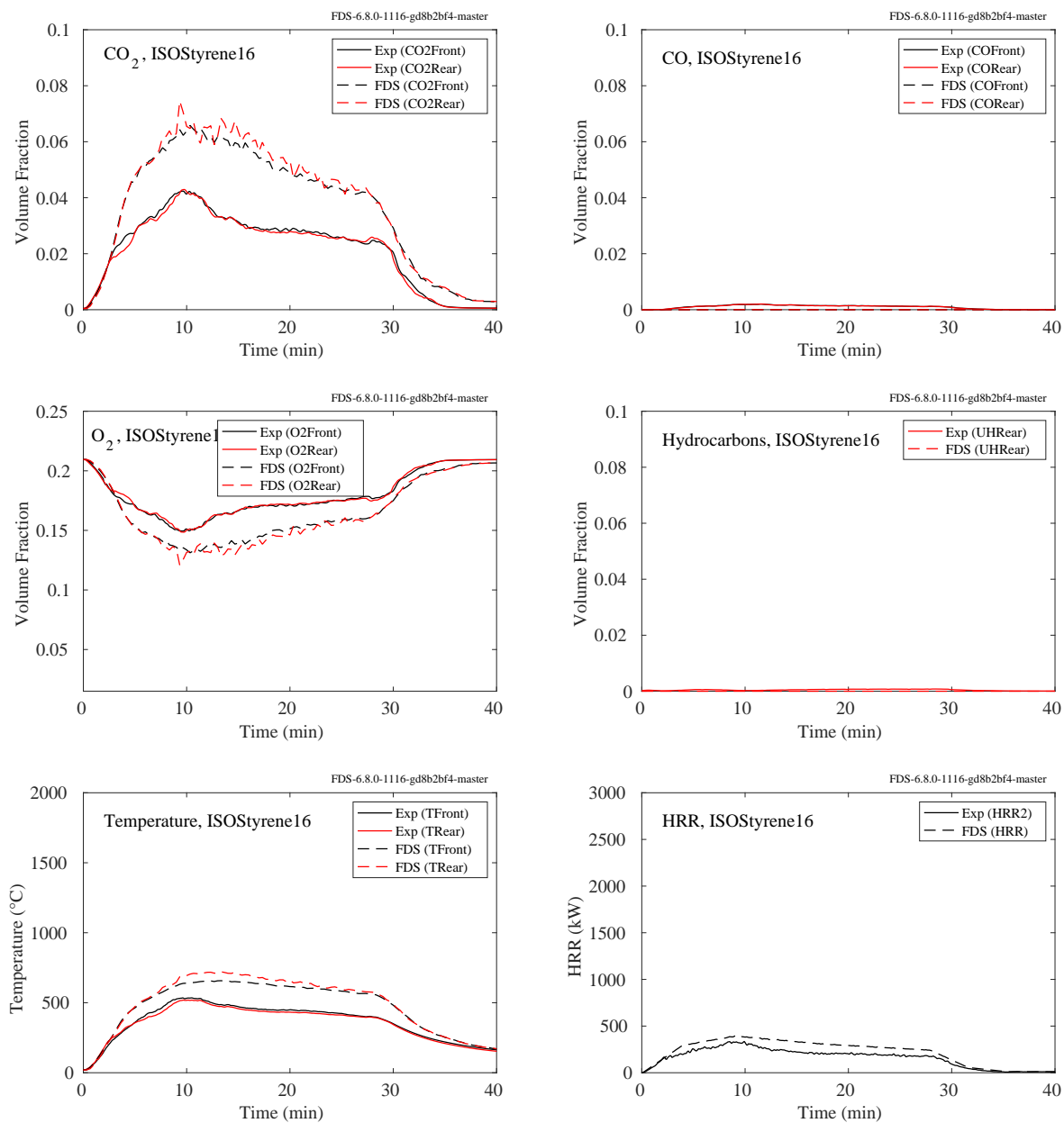


Figure 9.99: Summary of ISOSTyrene16, NIST FSE 2008.

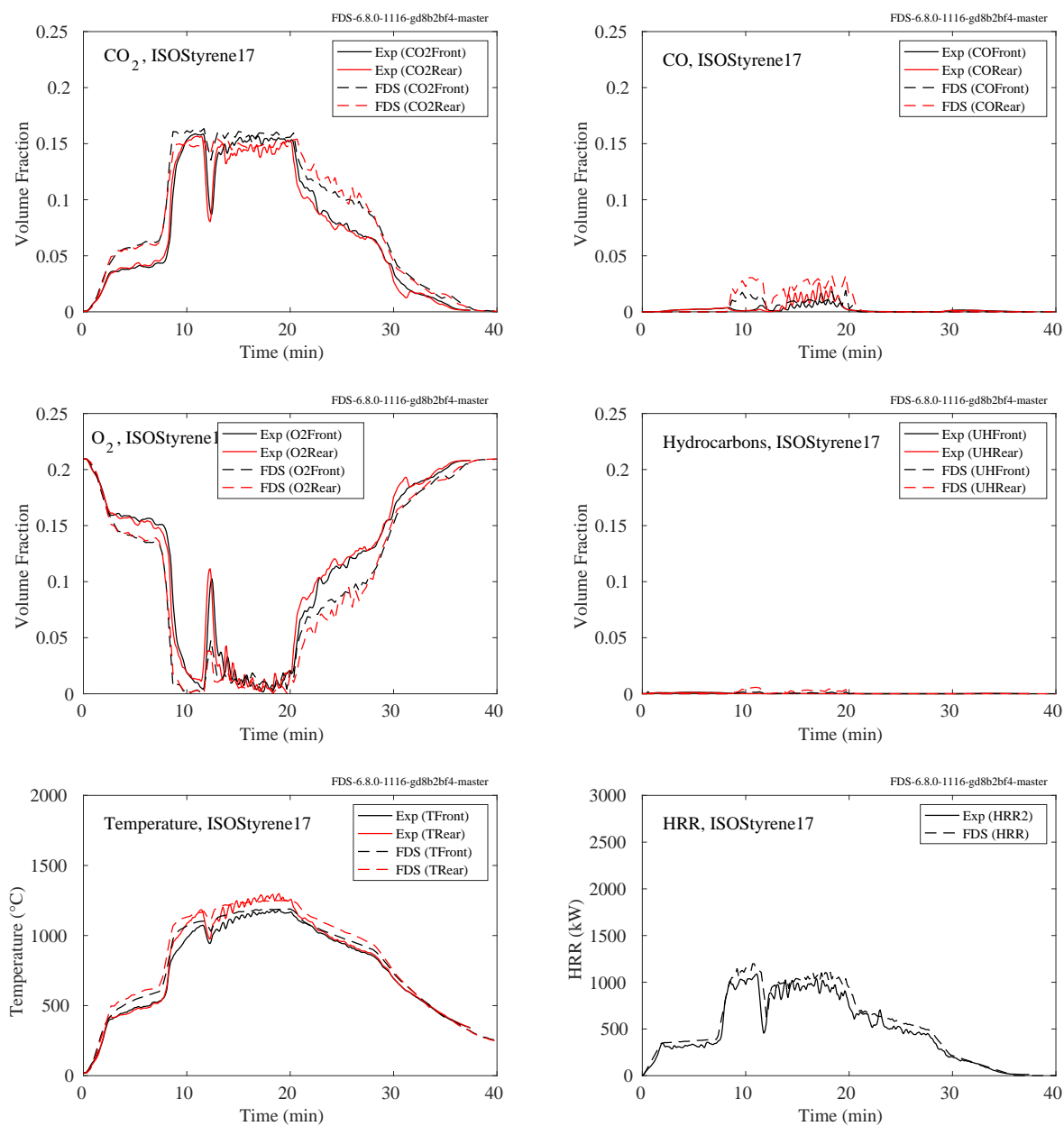


Figure 9.100: Summary of ISOSTyrene17, NIST FSE 2008.

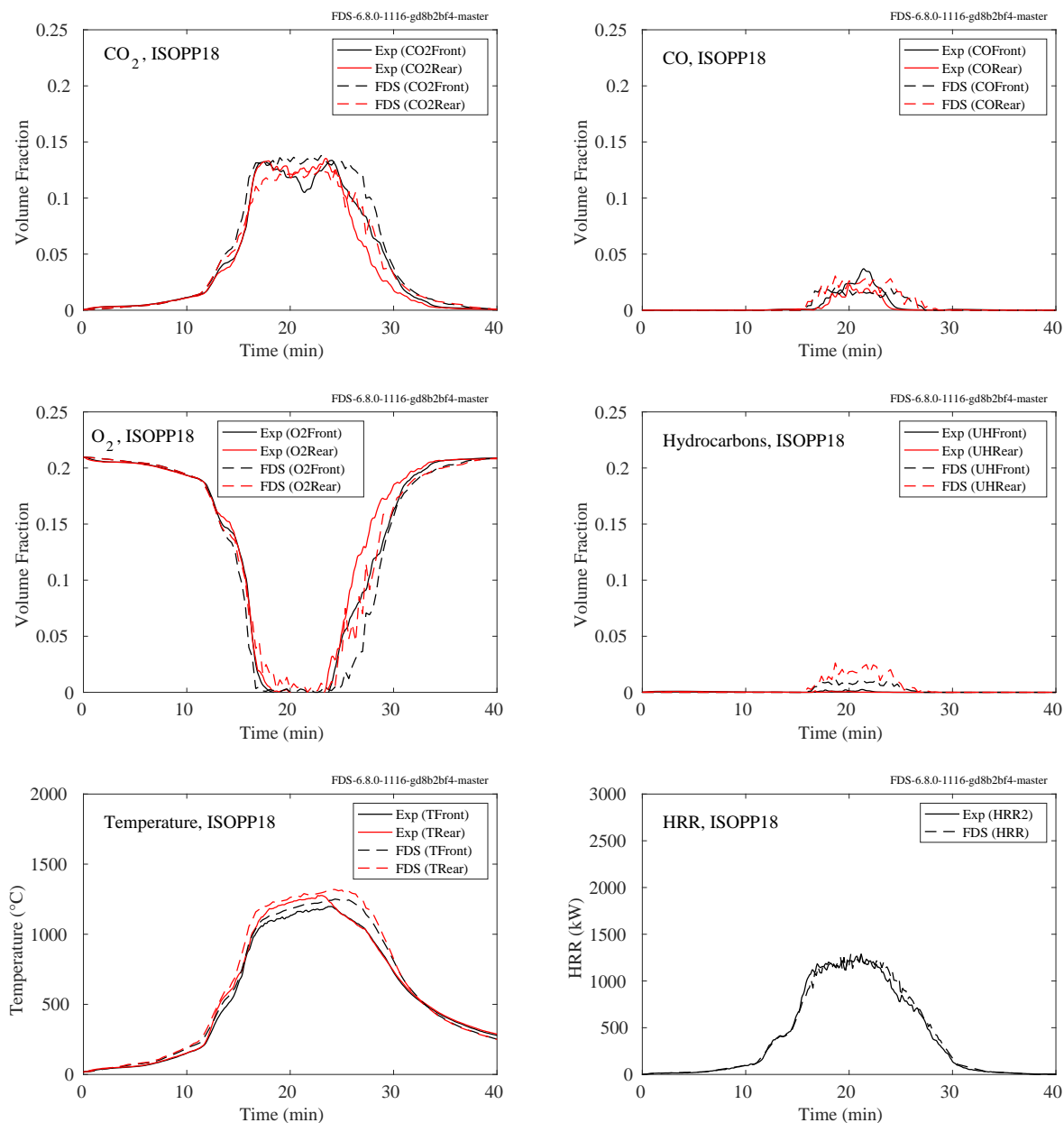


Figure 9.101: Summary of ISOPP18, NIST FSE 2008.

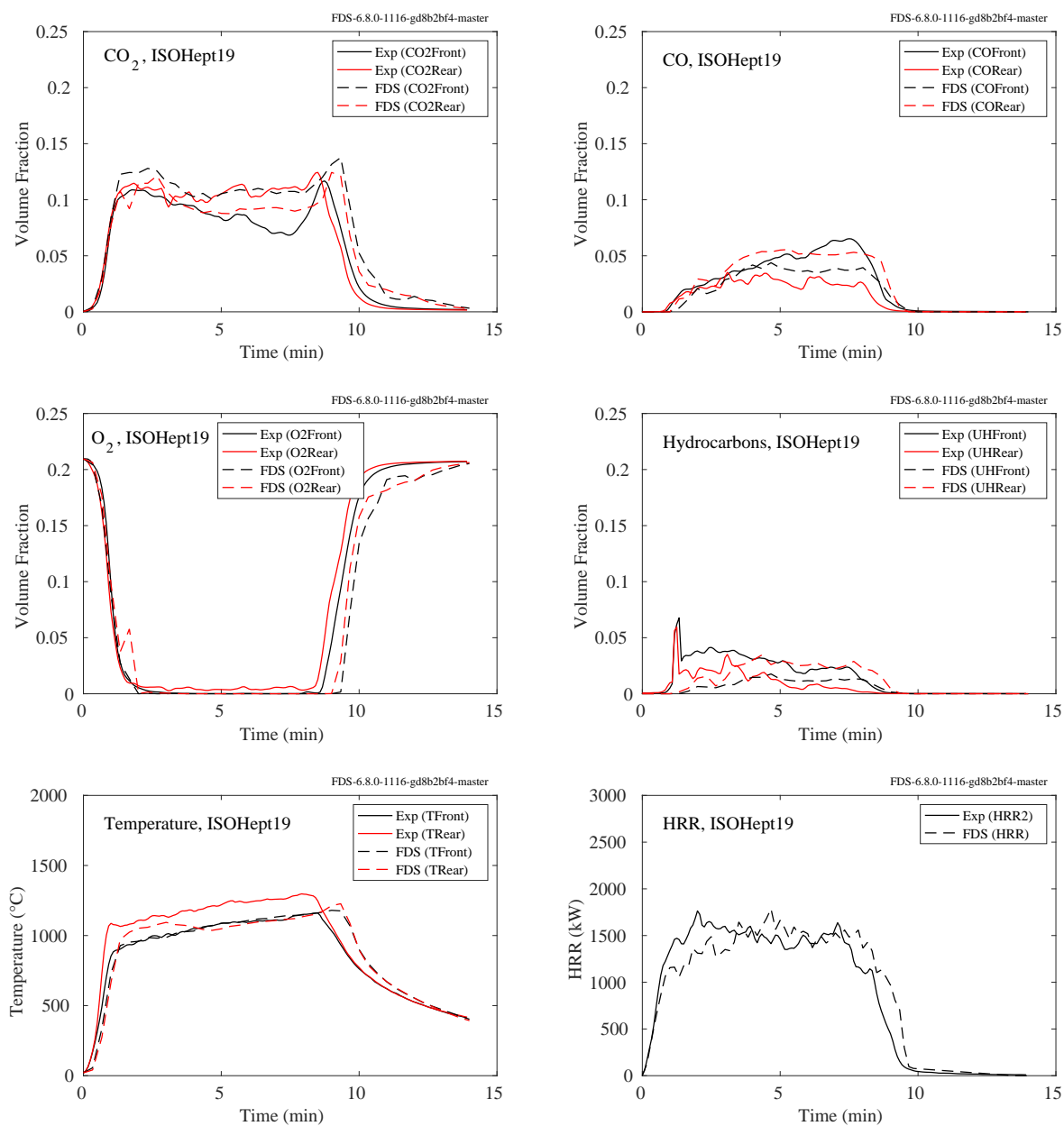


Figure 9.102: Summary of ISOHept19, NIST FSE 2008.

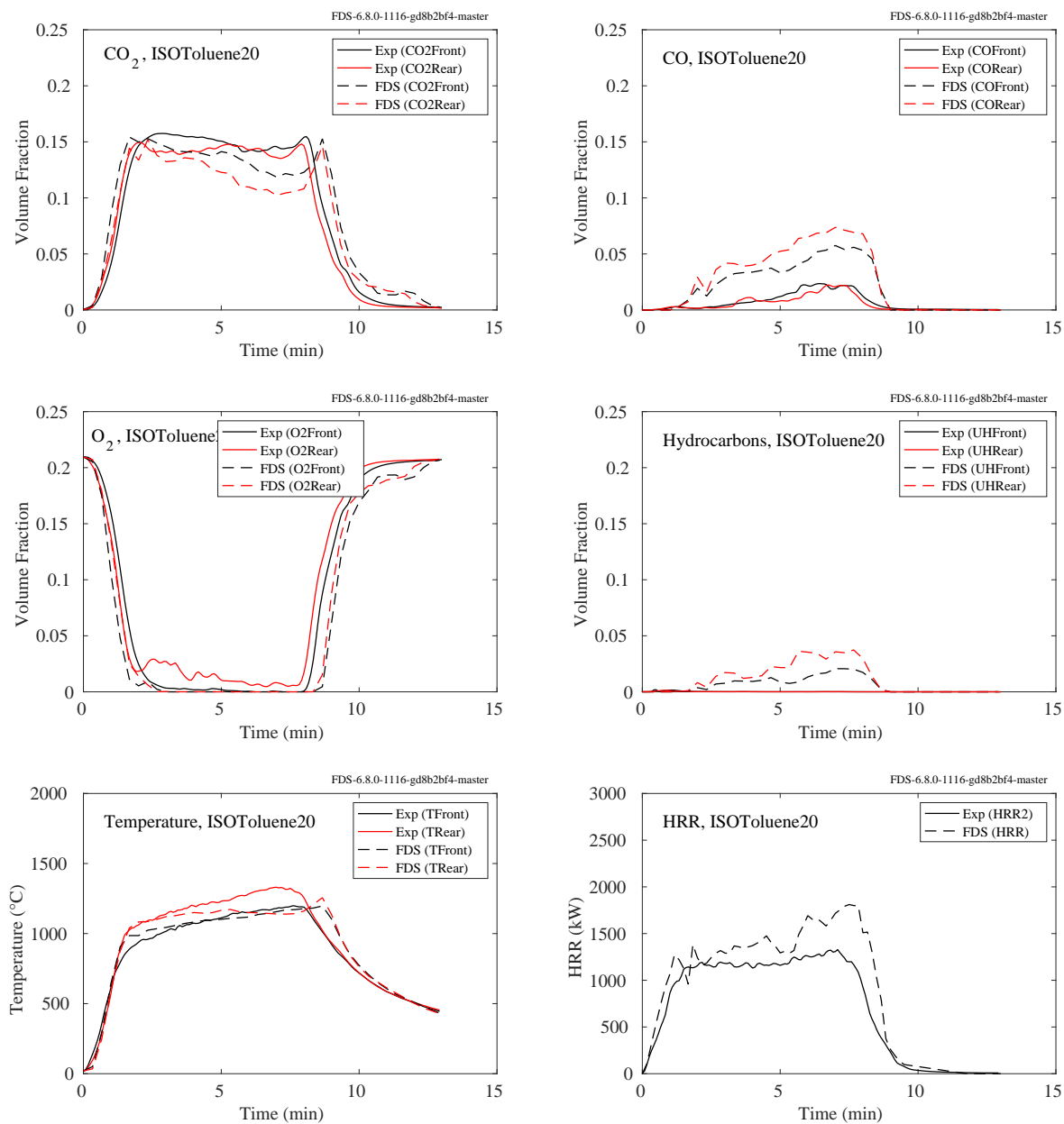


Figure 9.103: Summary of ISOToluene20, NIST FSE 2008.

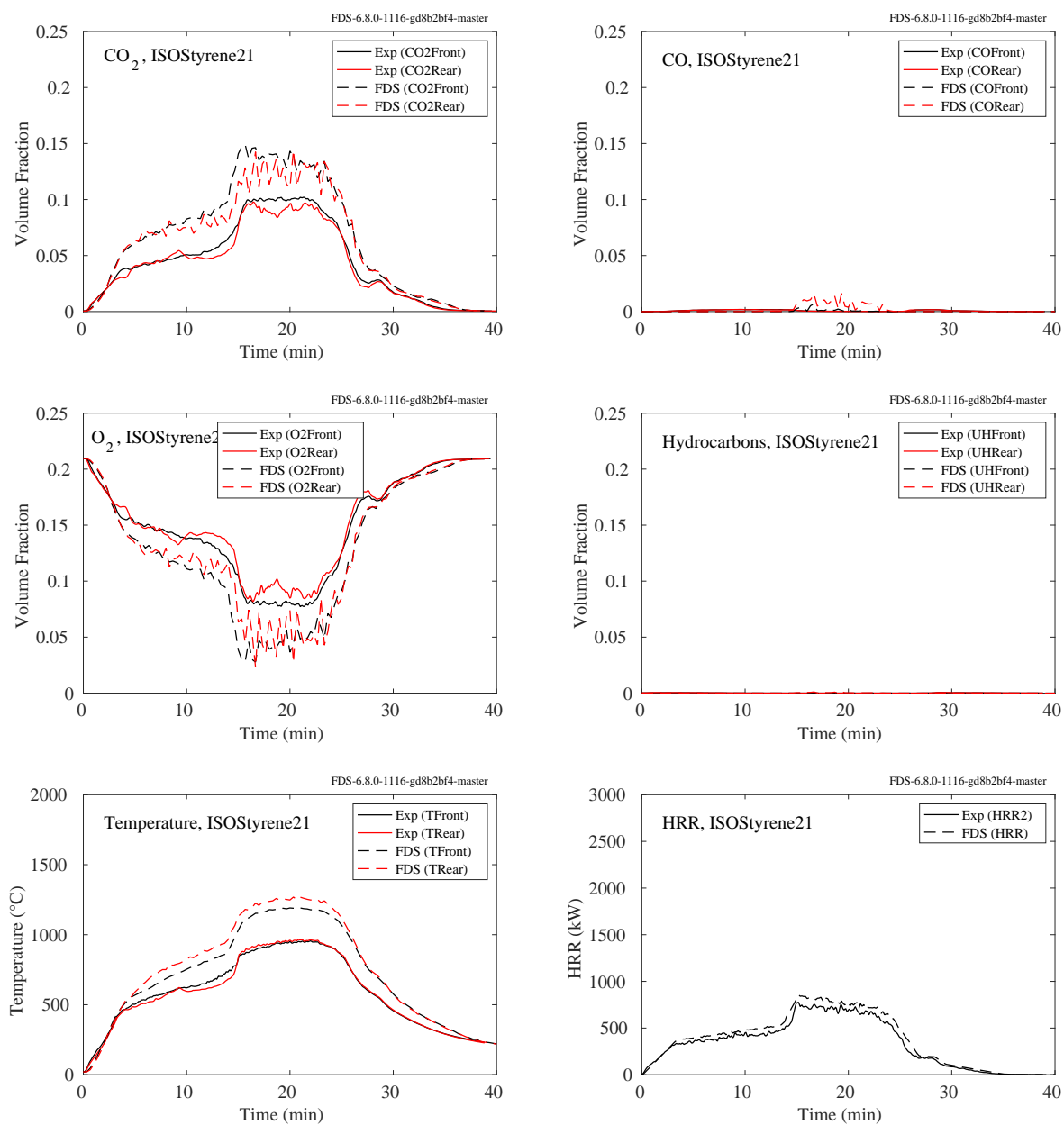


Figure 9.104: Summary of ISOSTyrene21, NIST FSE 2008.

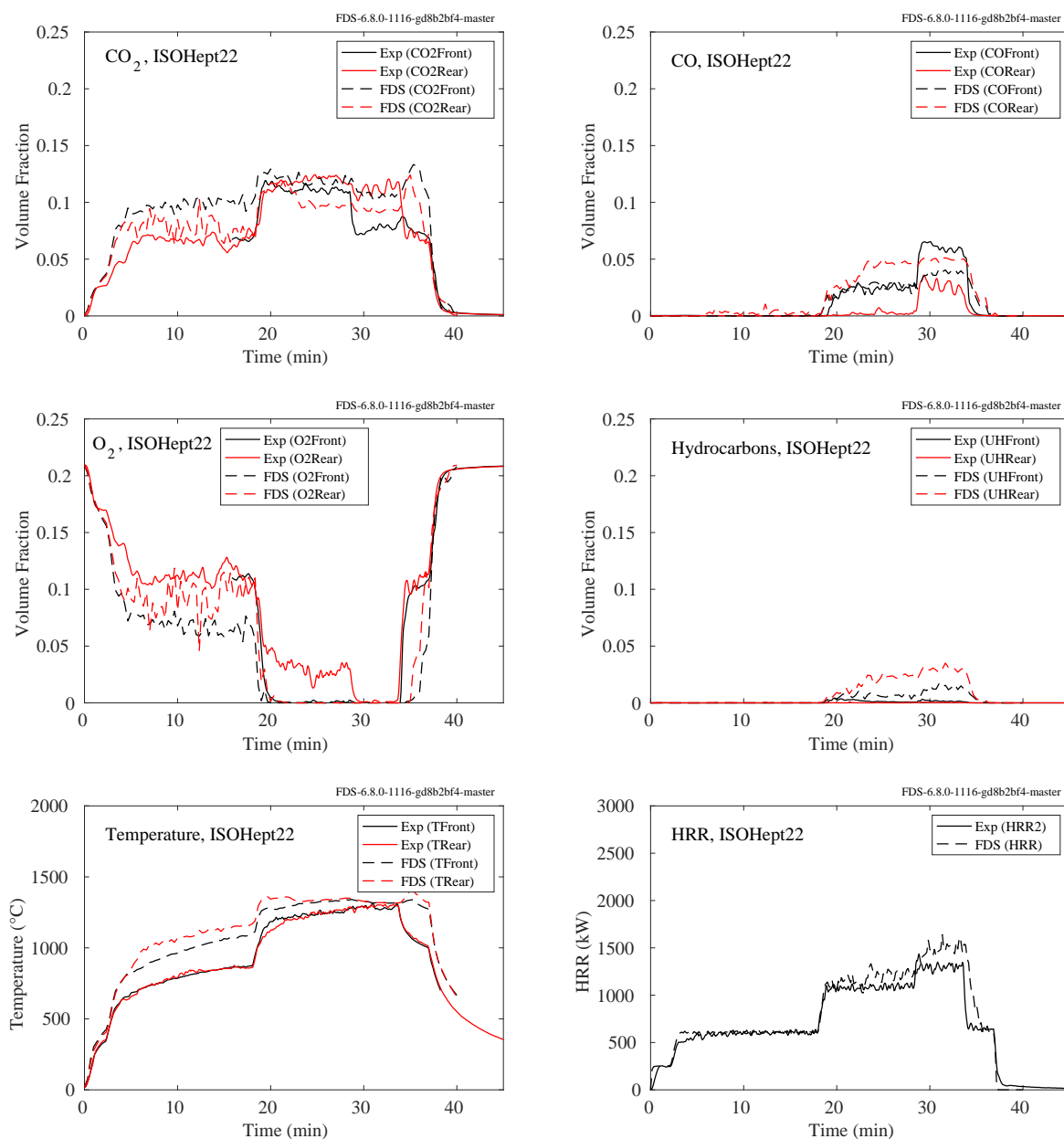


Figure 9.105: Summary of ISOHept22, NIST FSE 2008.

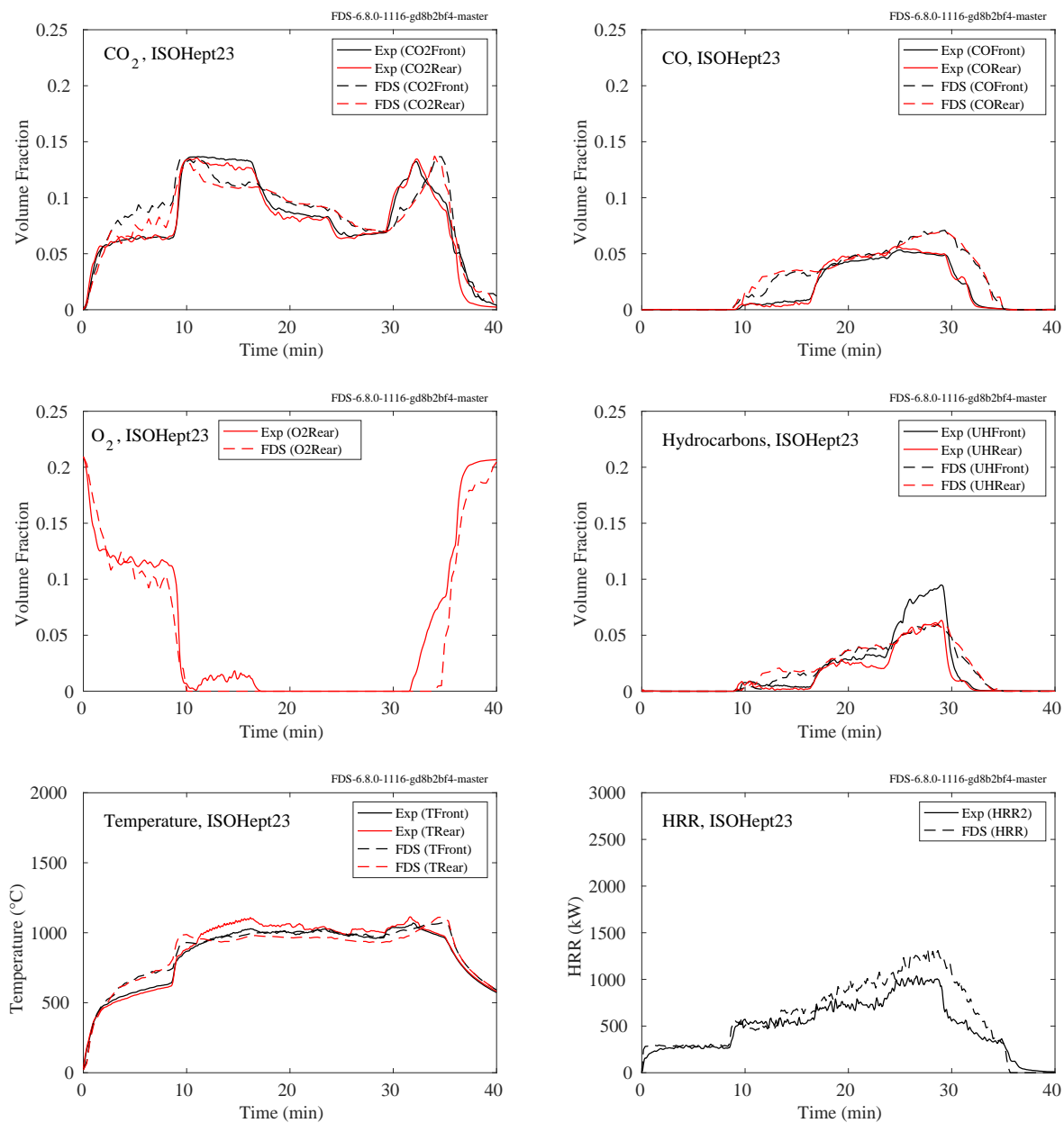


Figure 9.106: Summary of ISOHept23, NIST FSE 2008.

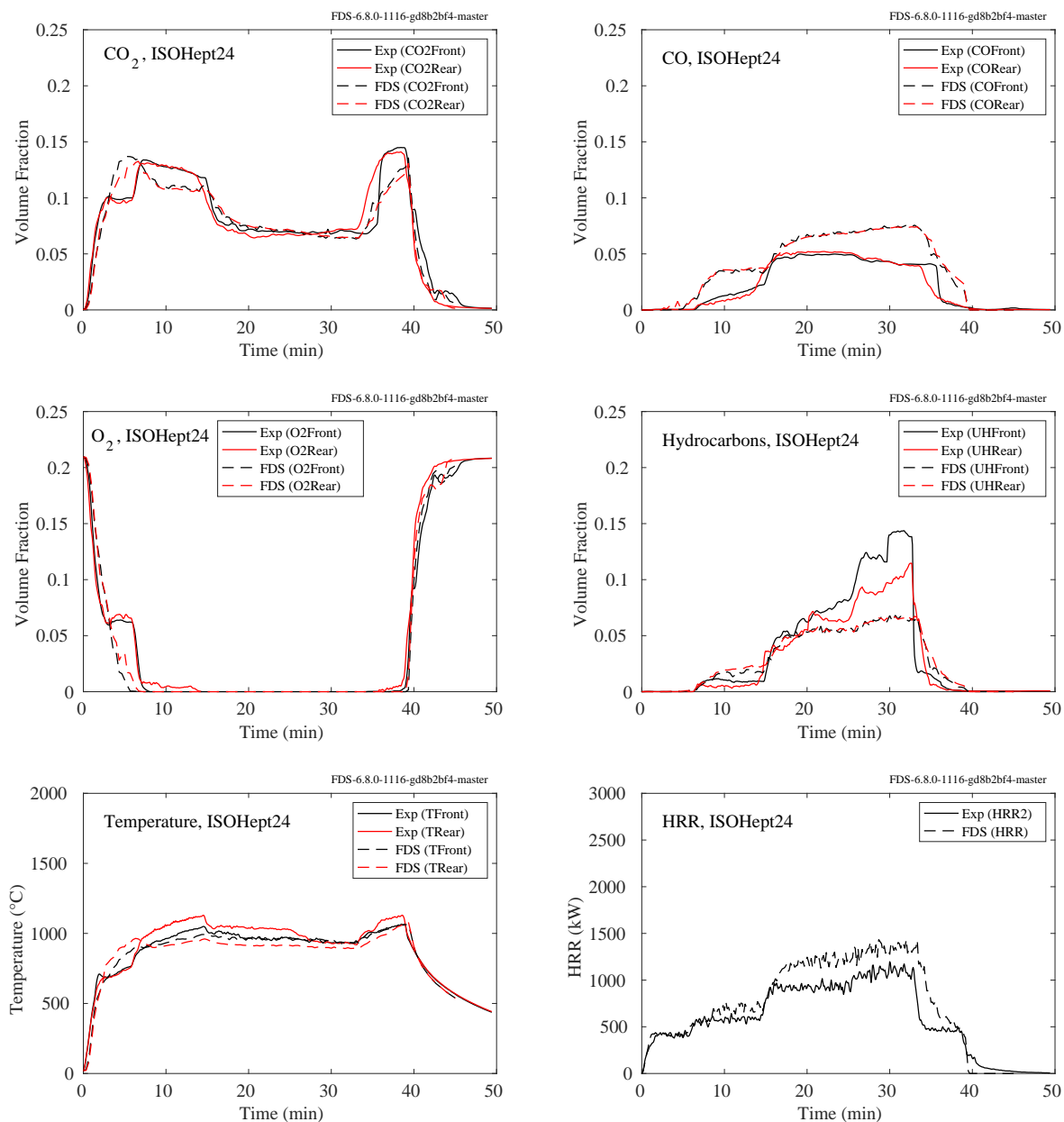


Figure 9.107: Summary of ISOHept24, NIST FSE 2008.

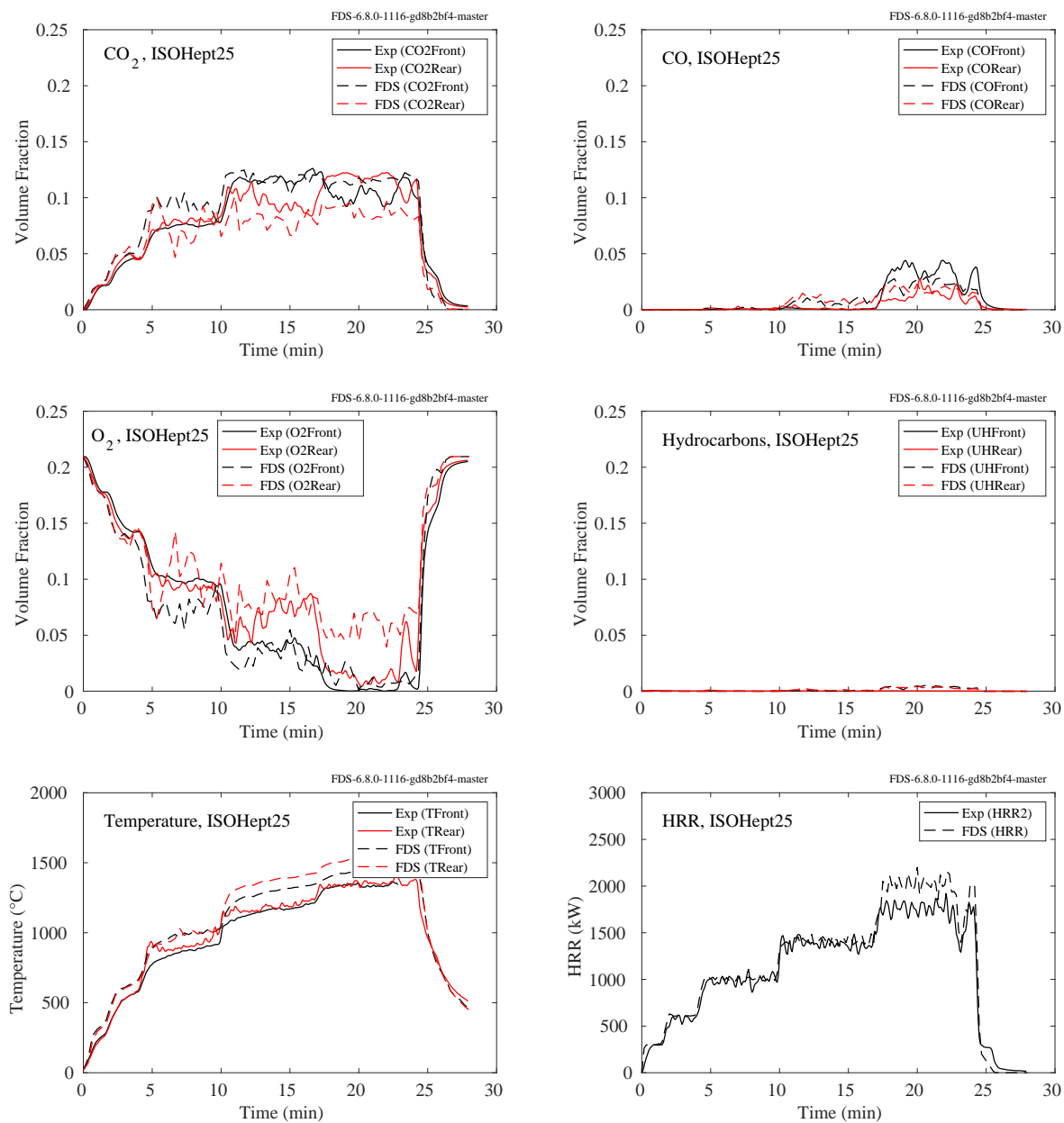


Figure 9.108: Summary of ISOHept25, NIST FSE 2008.

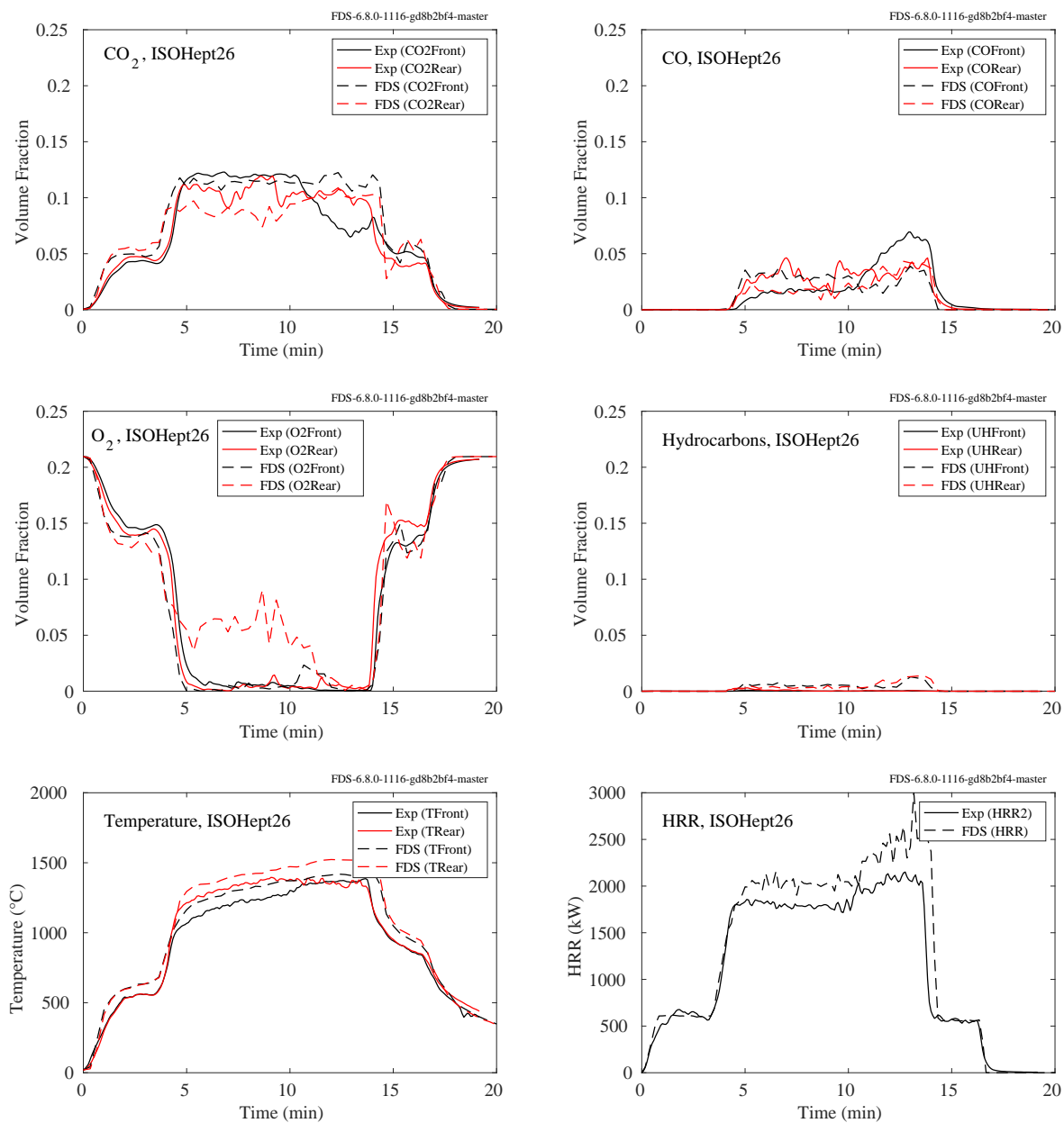


Figure 9.109: Summary of ISOHept26, NIST FSE 2008.

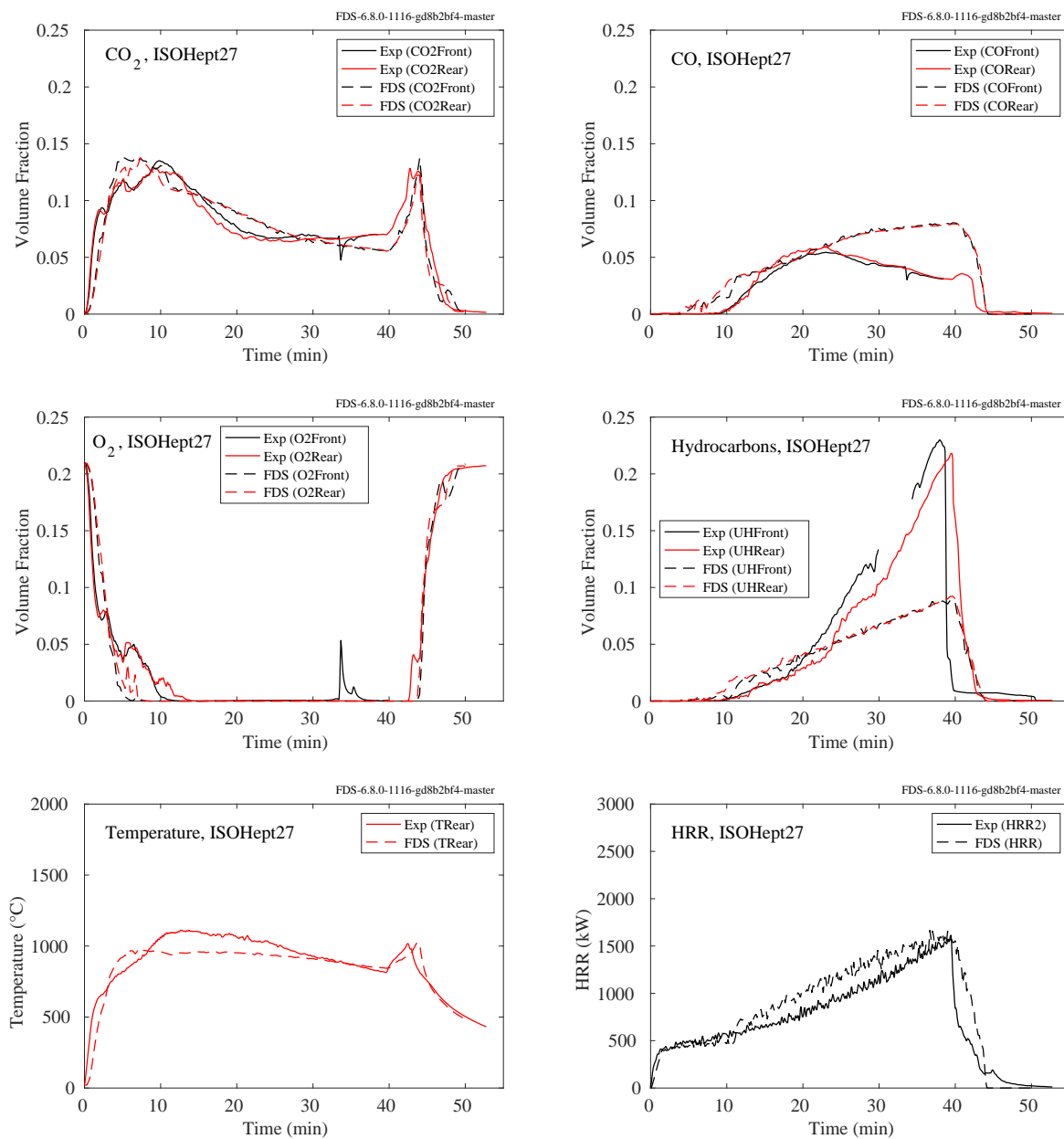


Figure 9.110: Summary of ISOHept27, NIST FSE 2008.

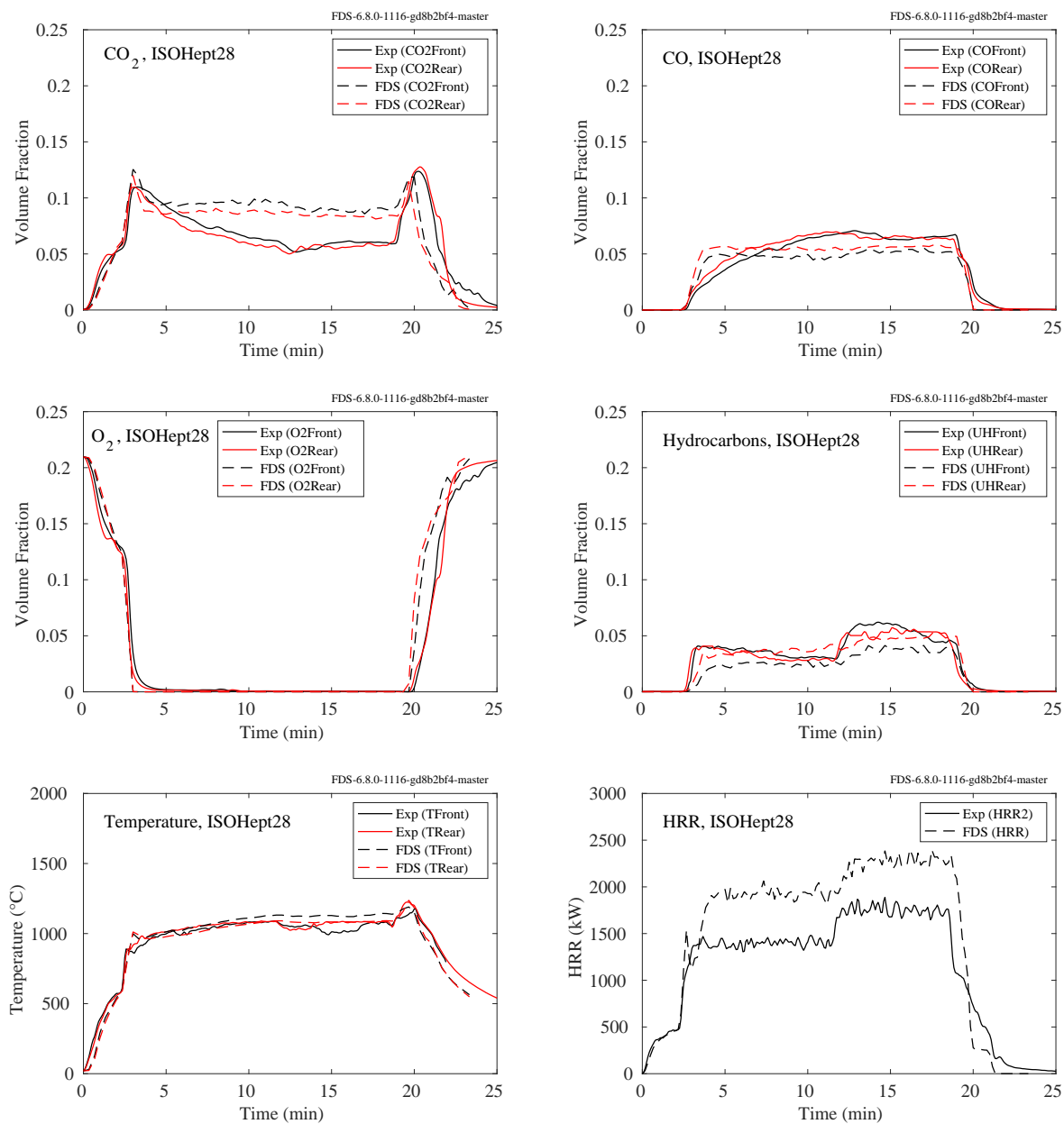


Figure 9.111: Summary of ISOHept28, NIST FSE 2008.

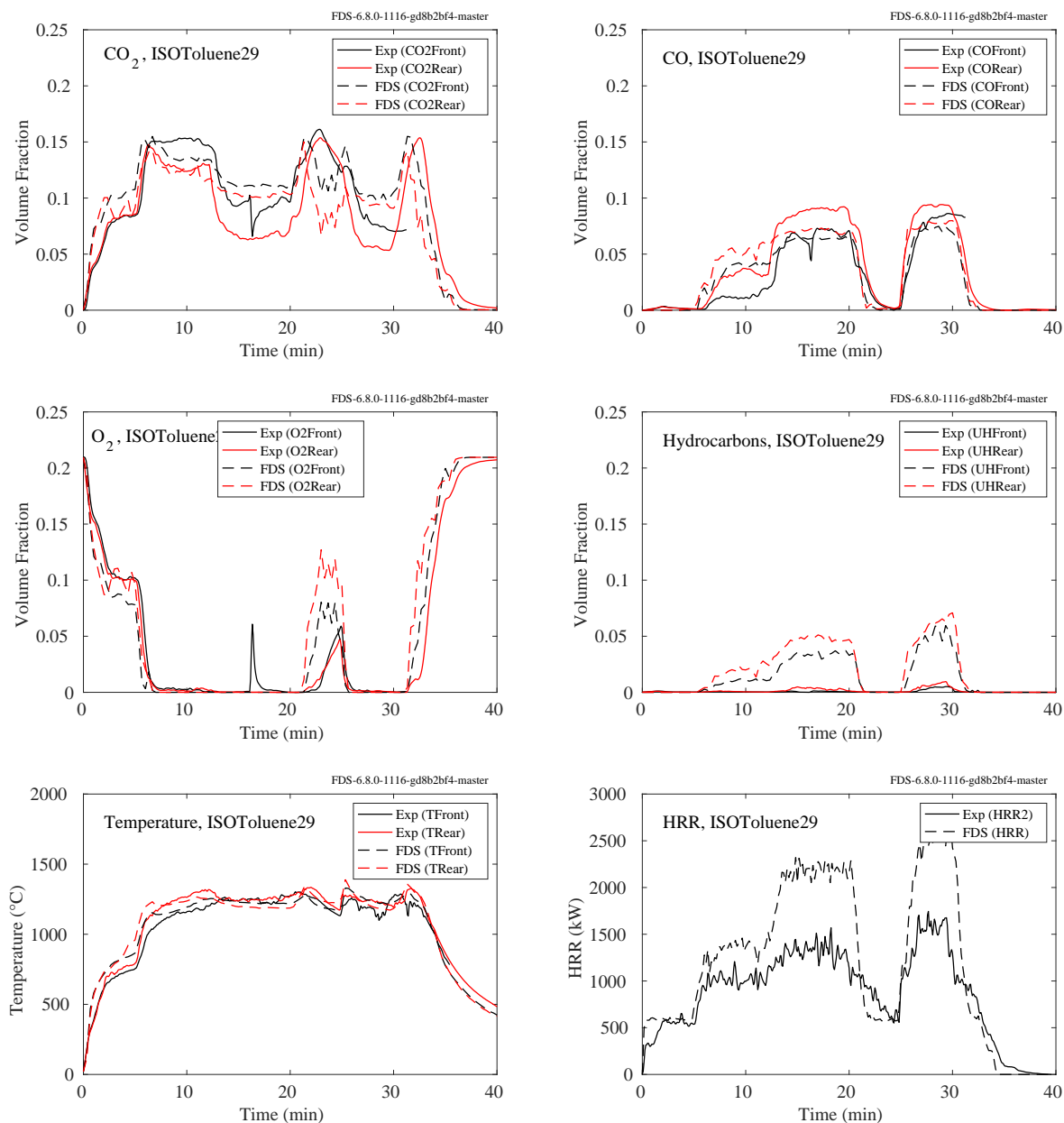


Figure 9.112: Summary of ISOToluene29, NIST FSE 2008.

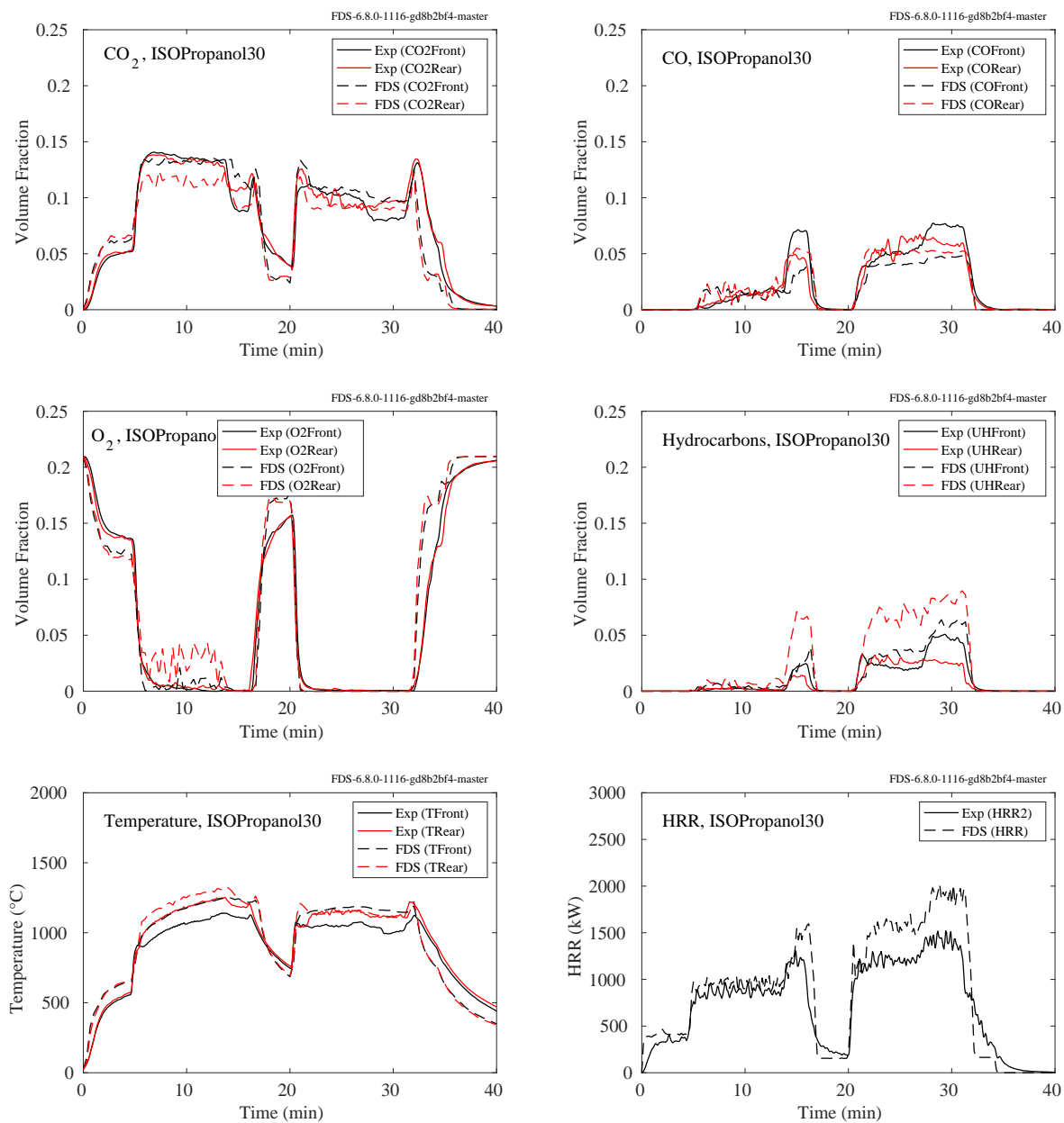


Figure 9.113: Summary of ISOPropanol30, NIST FSE 2008.

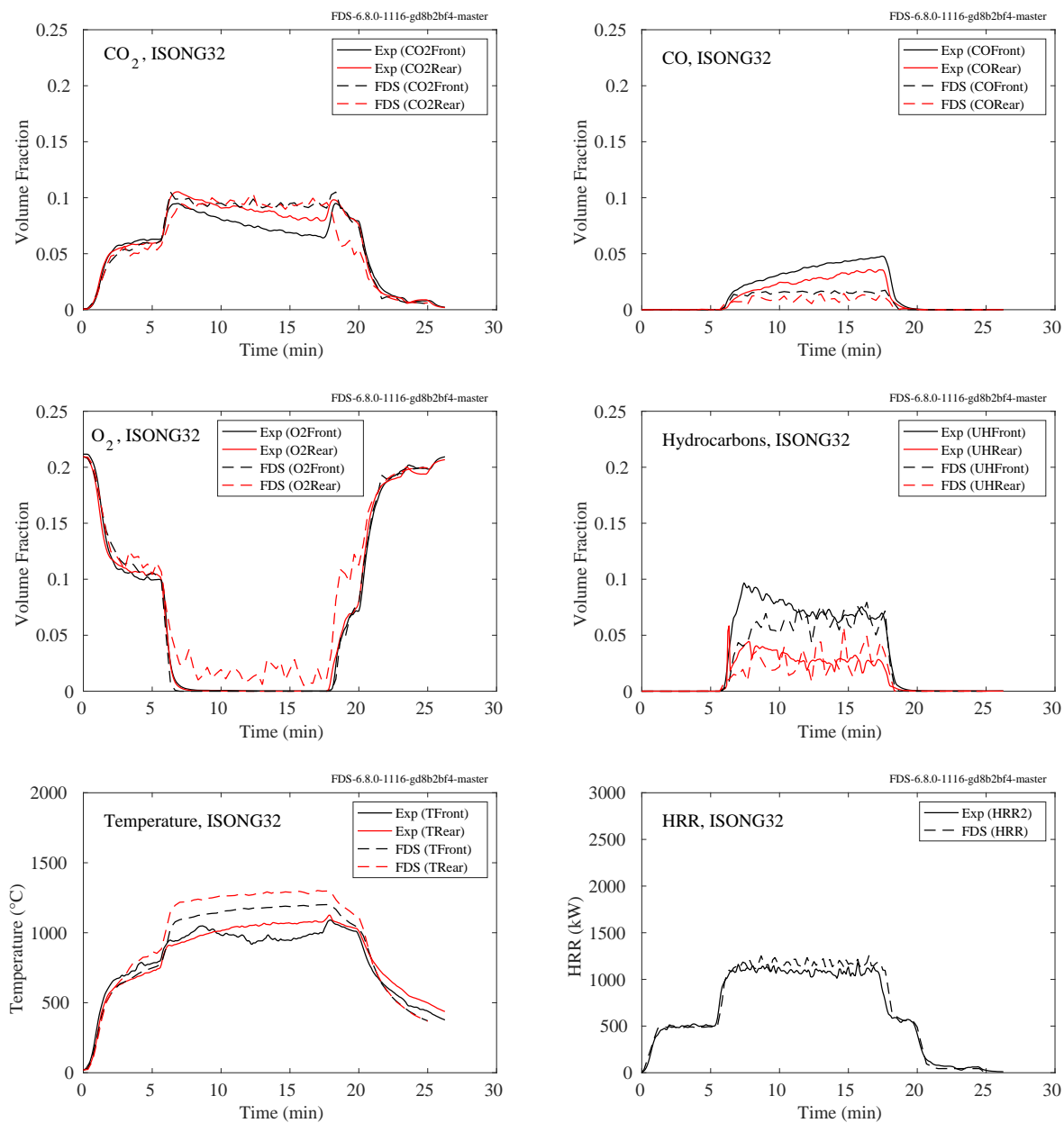


Figure 9.114: Summary of ISONG32, NIST FSE 2008.

9.5.6 NIST Pool Fires

Falkenstein-Smith et al. [362] made mean temperature and product species concentration measurements along the centerline above 30.5 cm diameter liquid pool fires of acetone, ethanol, and methanol; and a 37.0 cm diameter burner of methane and propane. The measurements were made using a gas chromatograph/mass spectrometer system (GC/MSD). The volume fraction of each species was calculated via the number of moles identified by the GC/MSD at each centerline point. Soot mass fractions were measured during the gas sampling process. Note that the species measurements include the vapor form of the primary fuel molecule, in addition to intermediate fuel species. FDS does not model the decomposition of the fuel molecule into intermediate hydrocarbon species except for CO and H₂.

The mean centerline temperature profiles are found in Sec. 6.1.5. The species concentrations are found in Figs. 9.115 through 9.120 on the following pages.

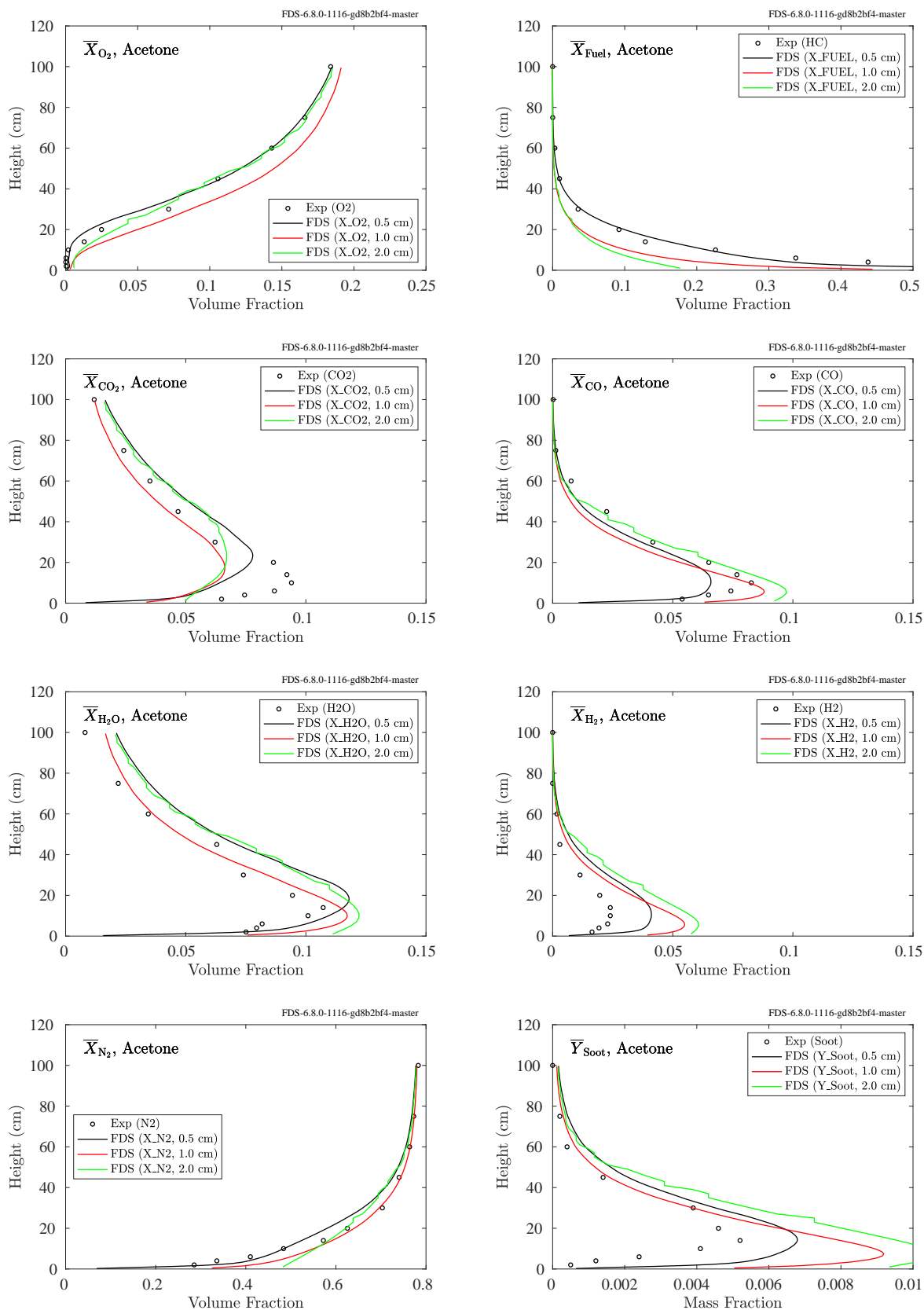


Figure 9.115: NIST Pool Fires, centerline product species, acetone.

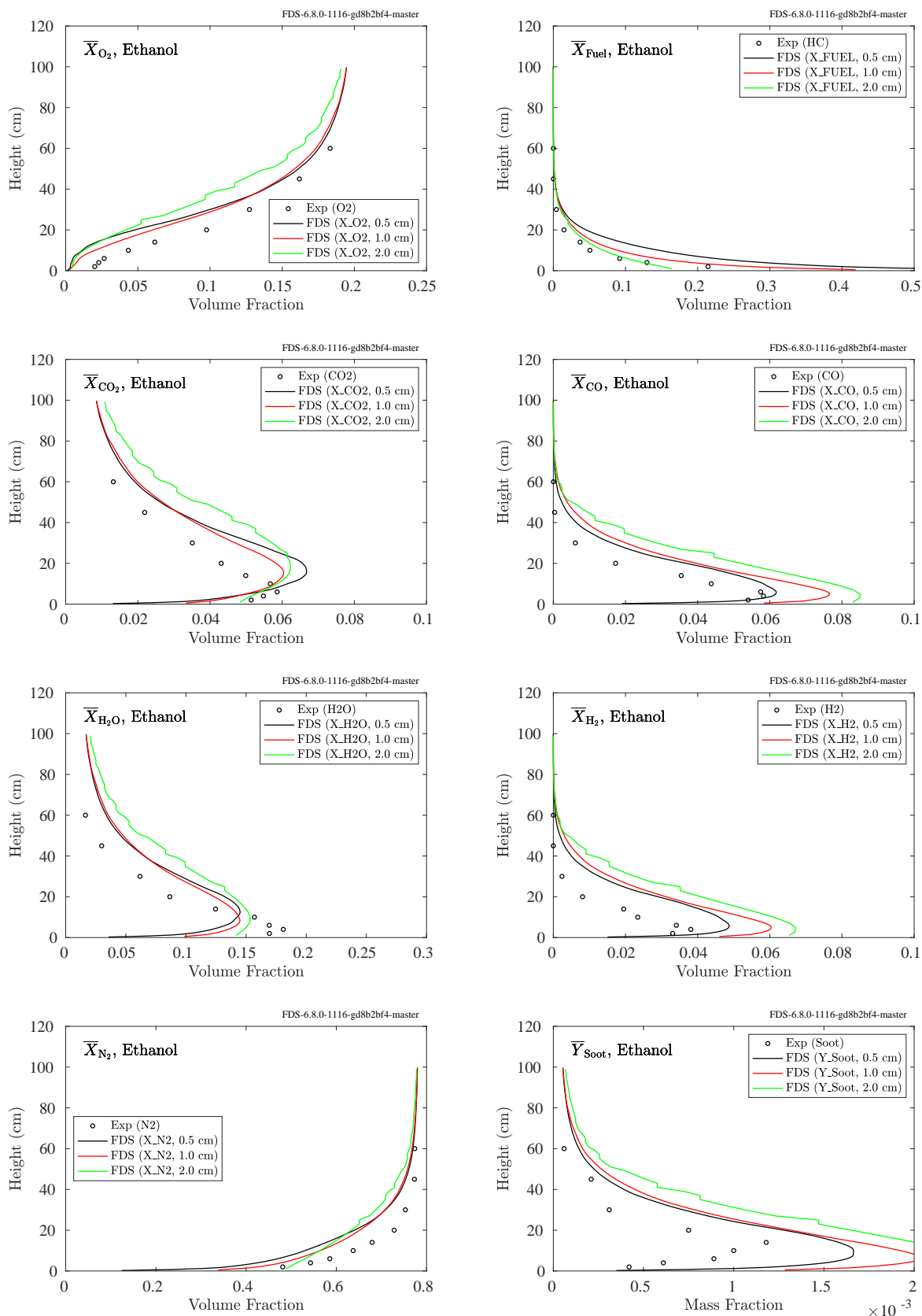


Figure 9.116: NIST Pool Fires, centerline product species, ethanol.

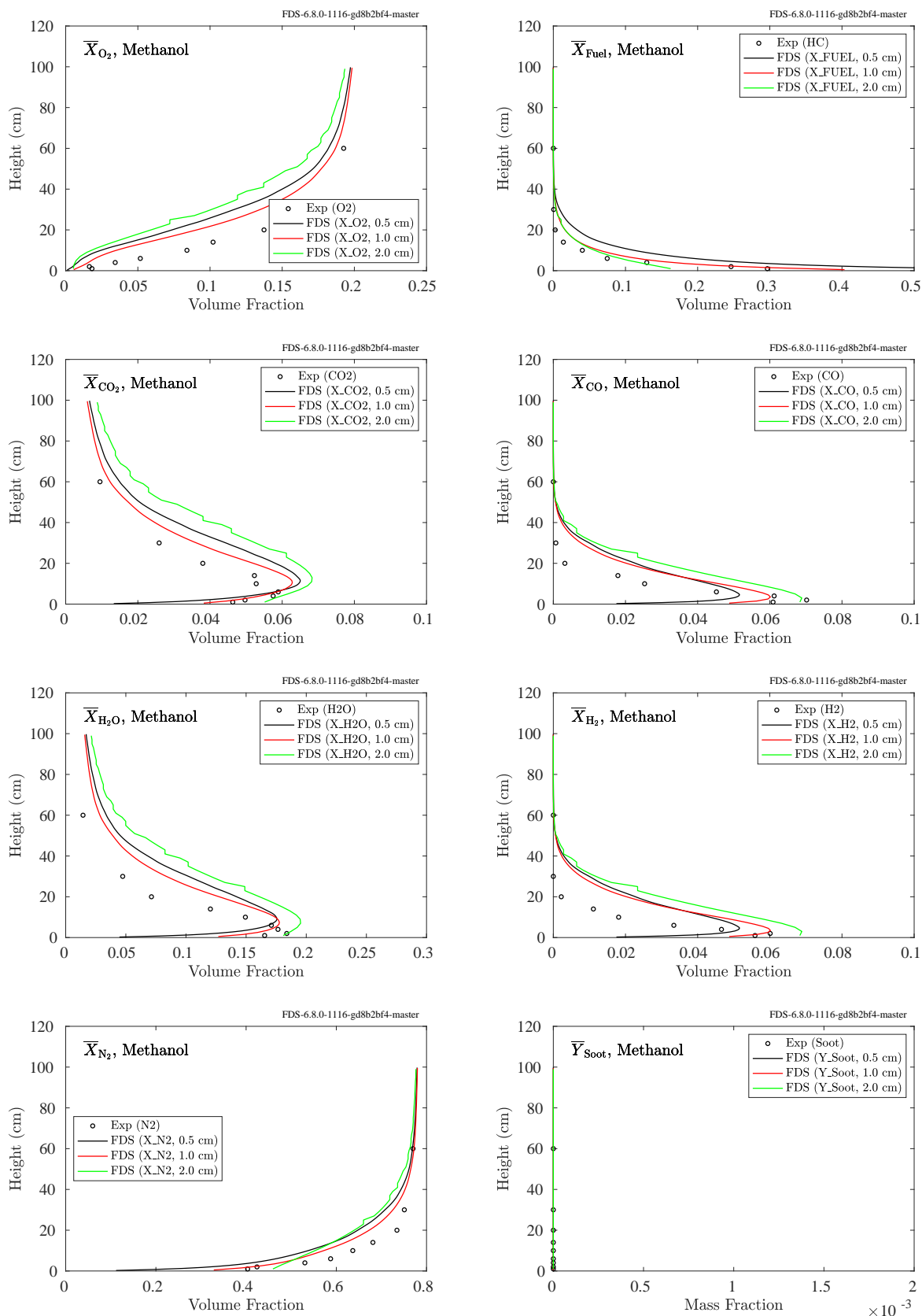


Figure 9.117: NIST Pool Fires, centerline product species, methanol.

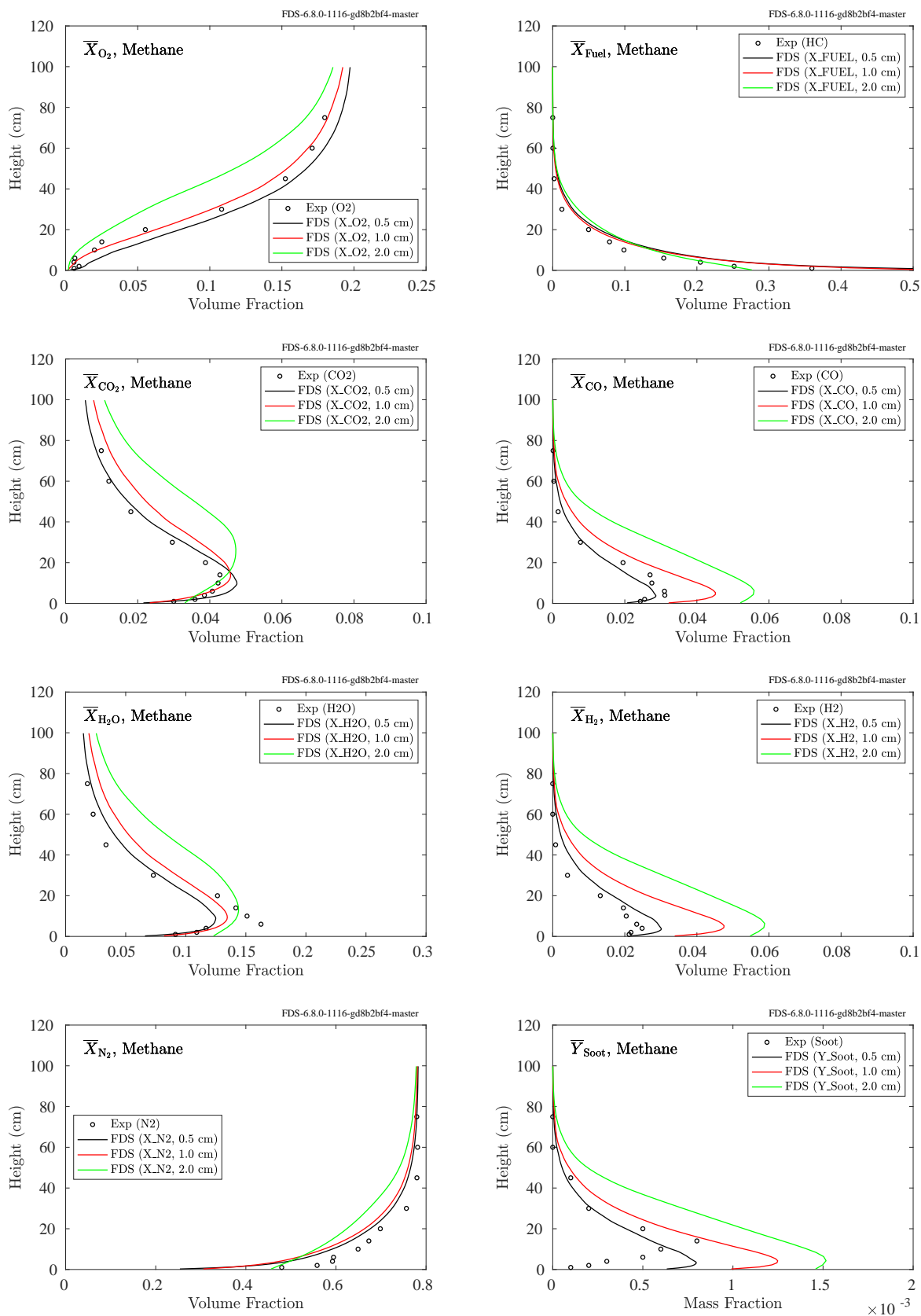


Figure 9.118: NIST Pool Fires, centerline product species, methane.

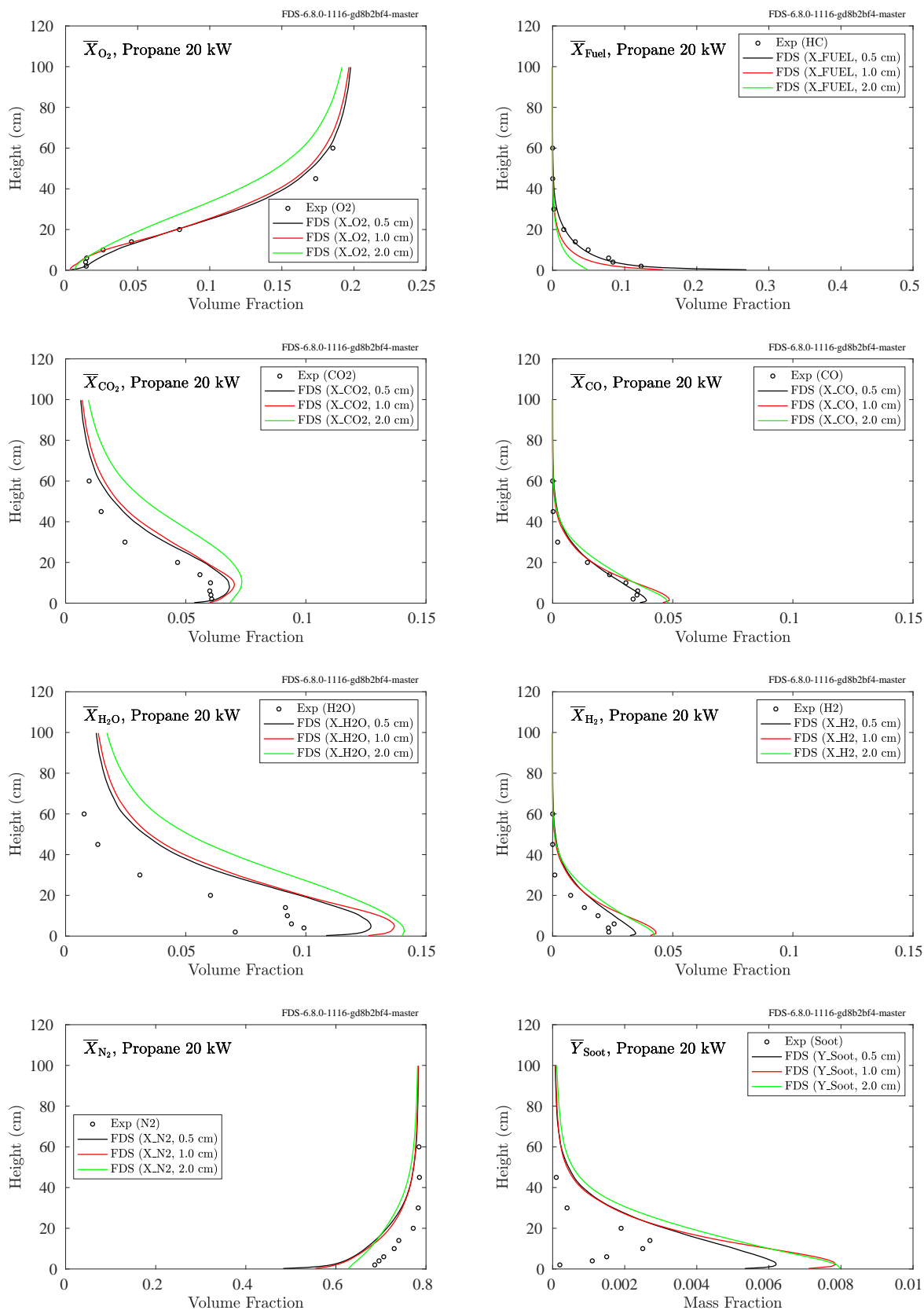


Figure 9.119: NIST Pool Fires, centerline product species, propane, 20 kW.

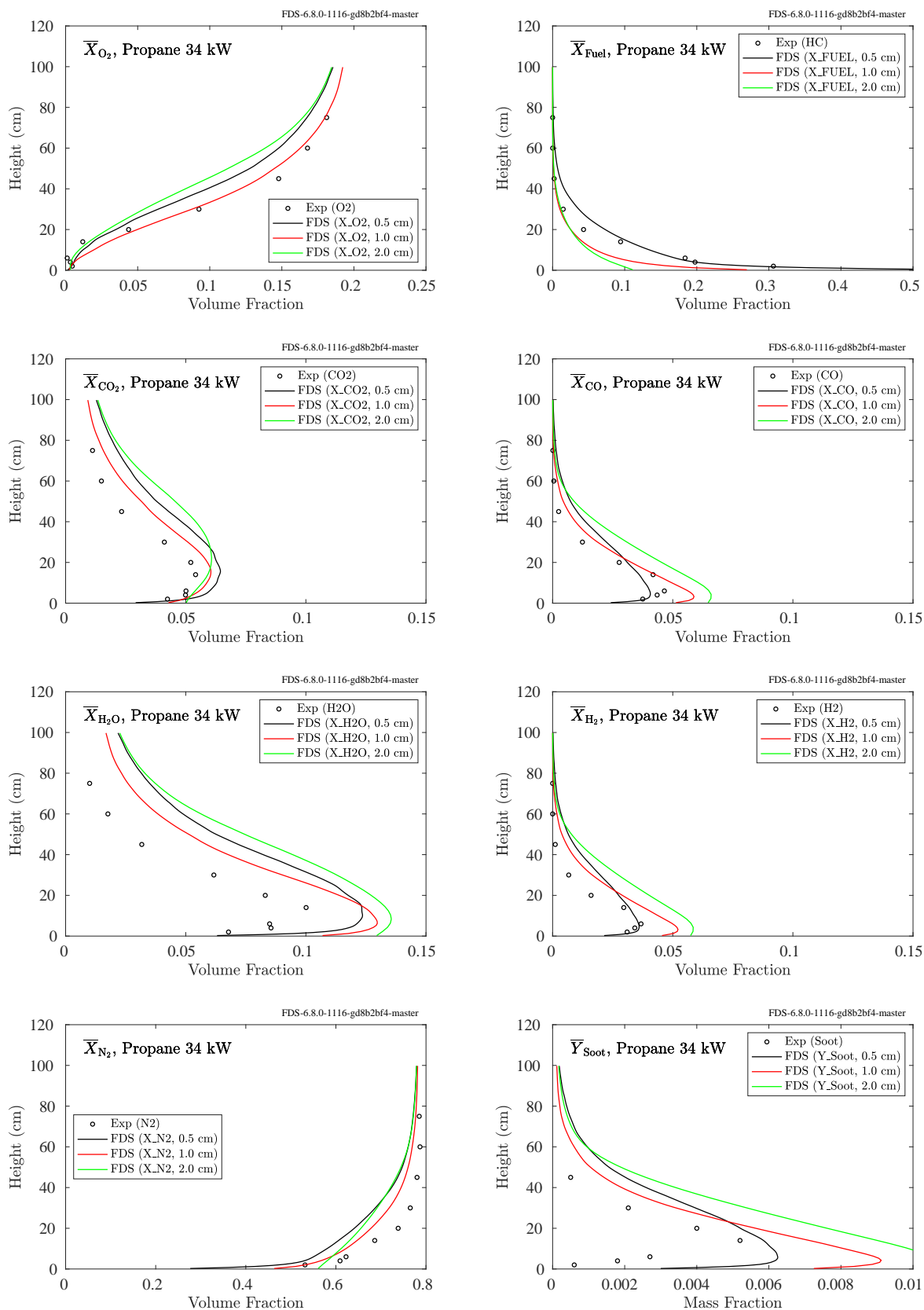


Figure 9.120: NIST Pool Fires, centerline product species, propane, 34 kW.

9.5.7 Summary, Products of Incomplete Combustion

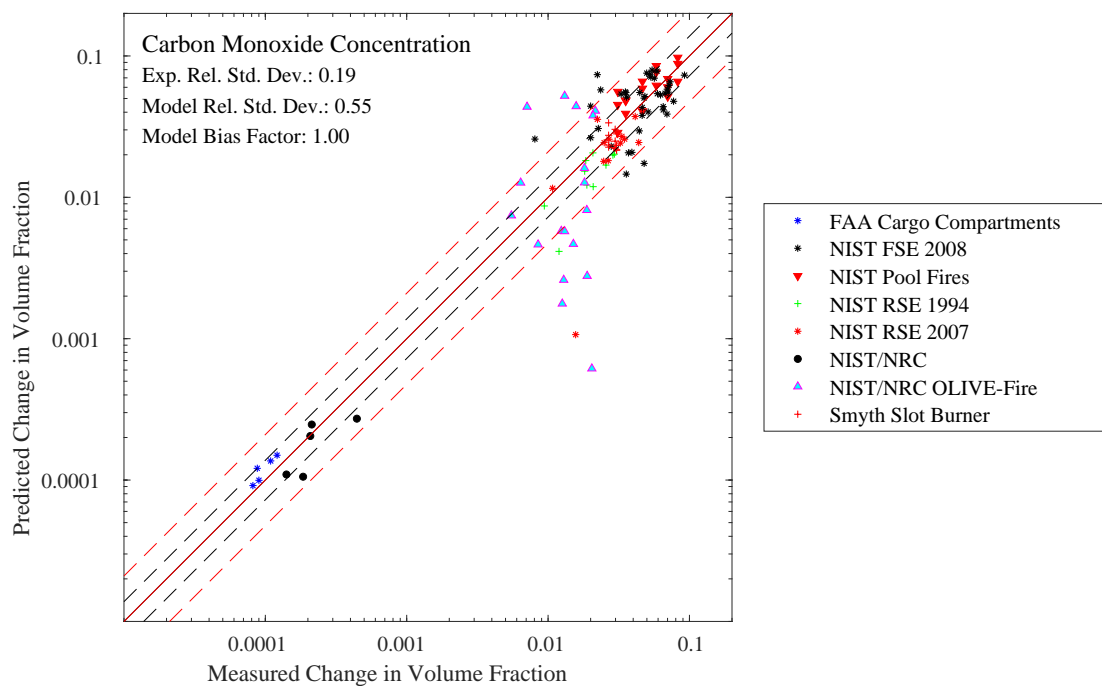


Figure 9.121: Summary of carbon monoxide predictions.

9.6 Helium Release in a Reduced Scale Garage Geometry

FDS simulations were performed to predict the helium release and dispersion in a reduced scale garage geometry. The figures on the following pages show the comparison between the FDS predictions and the measured values for the eighteen experiments. Table 9.1 lists the experimental parameters, including the release duration, release location (21 cm off the floor at the center of the compartment, 21 cm off the floor and 5 cm from the center of the rear wall, and 2.5 cm below the ceiling at the center of the compartment), and the leak area (single small vent, 2.4 cm by 2.4 cm, at the center of the front wall, single large vent, 3.05 cm by 3.05 cm, at the center of the front wall, and a pair of vents, 2.15 cm by 2.15 cm, centered on the front wall, 2.5 cm from the floor and ceiling, respectively). The seven sensors were located 37.5 cm from the front and side walls, at heights of 9 cm, 19 cm, 28 cm, 37 cm, 47 cm, 56 cm, and 65 cm off the floor. In the figures on the following pages, the highest concentrations correspond to the highest measurement locations.

Table 9.1: Test parameters of the NIST_He_2009 experiments.

Test Label	Release Duration (h)	Release Location	Leak Configuration
3600-LC-SSV	1	Lower Center	Single Small Vent
3600-LC-SLV	1	Lower Center	Single Large Vent
3600-LC-ULV	1	Lower Center	Dual Vents
3600-LR-SSV	1	Lower Rear	Single Small Vent
3600-LR-SLV	1	Lower Rear	Single Large Vent
3600-LR-ULV	1	Lower Rear	Dual Vents
3600-UC-SSV	1	Upper Center	Single Small Vent
3600-UC-SLV	1	Upper Center	Single Large Vent
3600-UC-ULV	1	Upper Center	Dual Vents
14400-LC-SSV	4	Lower Center	Single Small Vent
14400-LC-SLV	4	Lower Center	Single Large Vent
14400-LC-ULV	4	Lower Center	Dual Vents
14400-LR-SSV	4	Lower Rear	Single Small Vent
14400-LR-SLV	4	Lower Rear	Single Large Vent
14400-LR-ULV	4	Lower Rear	Dual Vents
14400-UC-SSV	4	Upper Center	Single Small Vent
14400-UC-SLV	4	Upper Center	Single Large Vent
14400-UC-ULV	4	Upper Center	Dual Vents

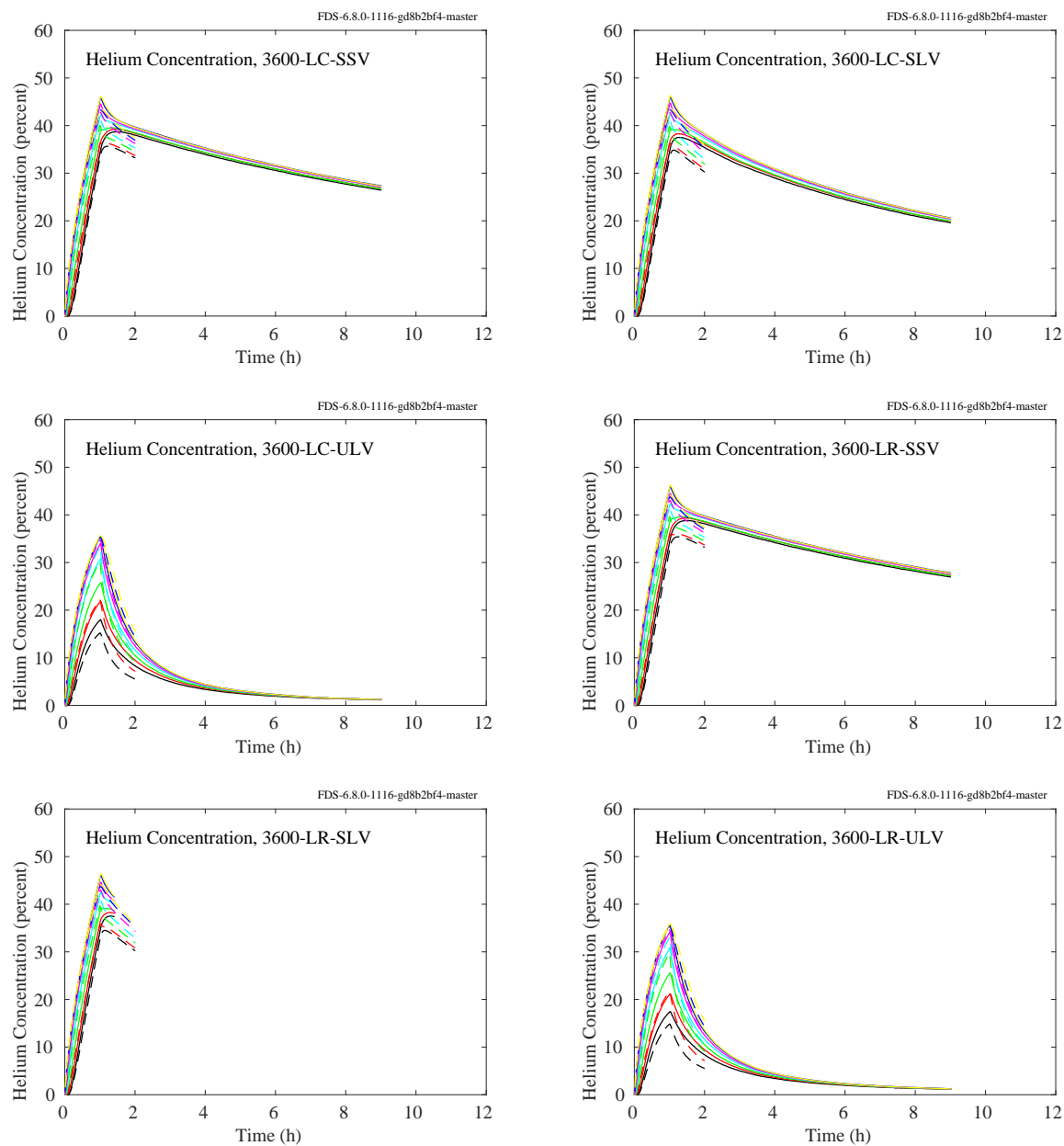


Figure 9.122: Comparison of measured (solid lines) and predicted (dashed lines) helium concentrations in the NIST_He_2009 experiments.

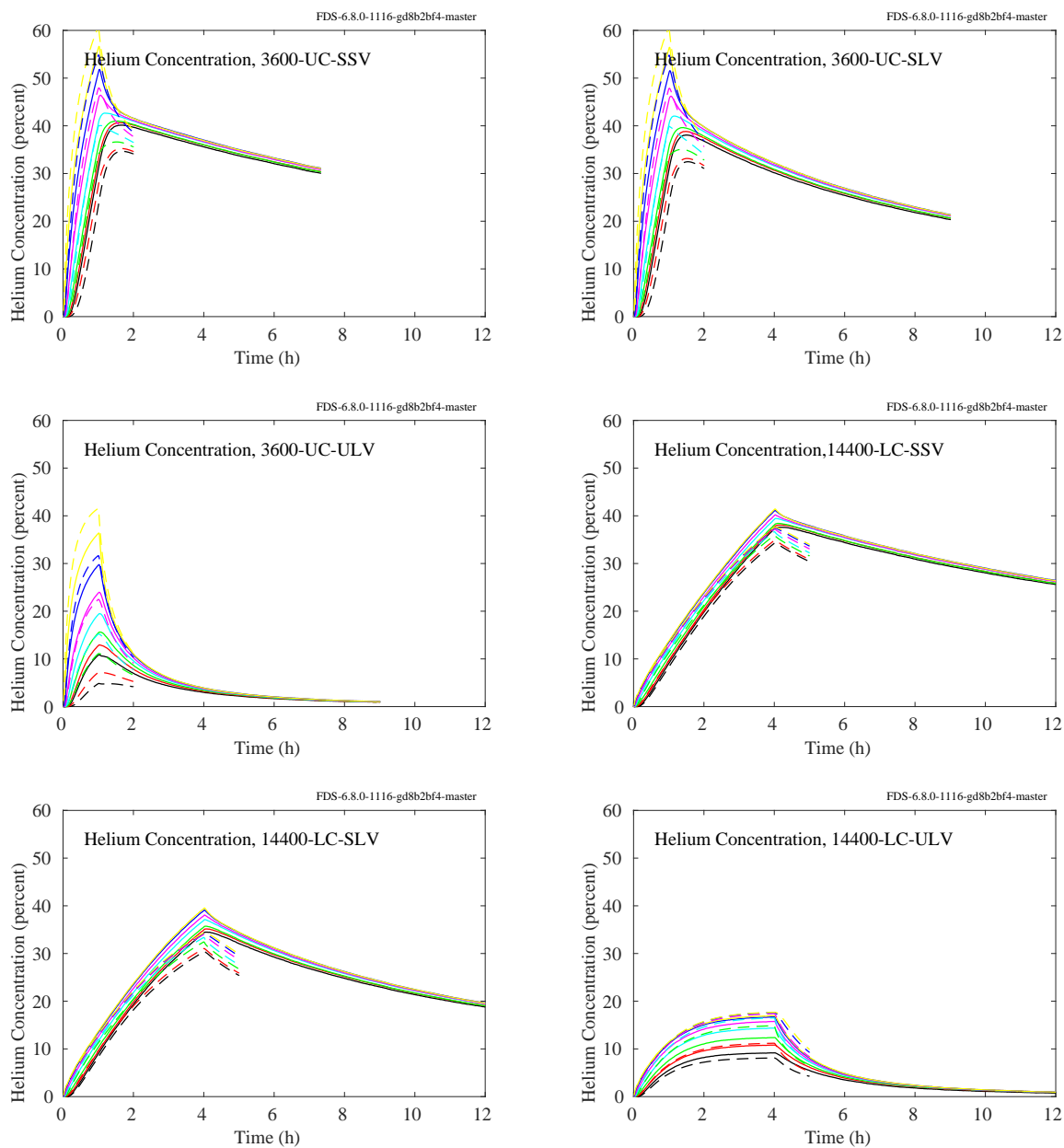


Figure 9.123: Comparison of measured (solid lines) and predicted (dashed lines) helium concentrations in the NIST_He_2009 experiments.

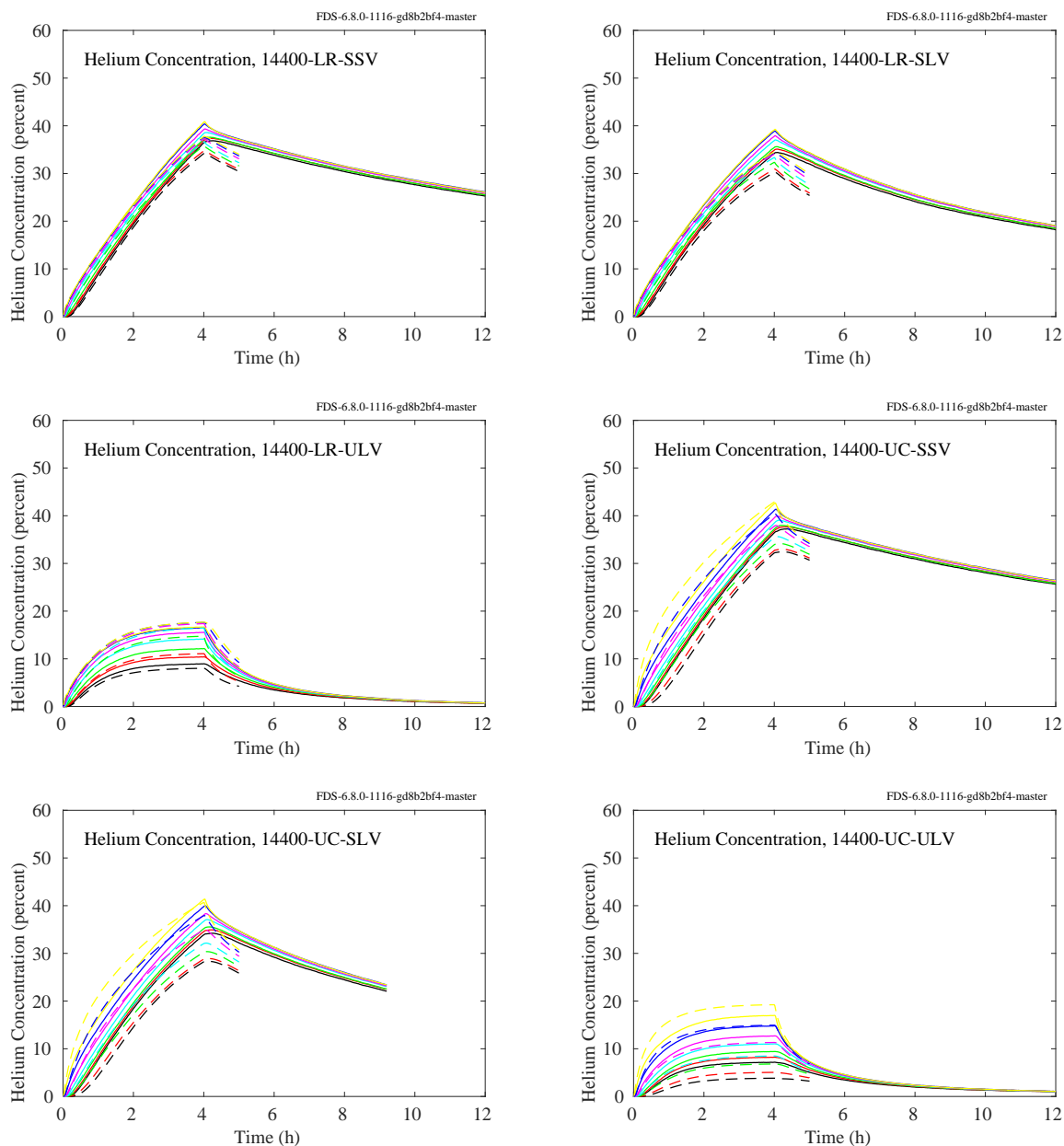


Figure 9.124: Comparison of measured (solid lines) and predicted (dashed lines) helium concentrations in the NIST_He_2009 experiments.

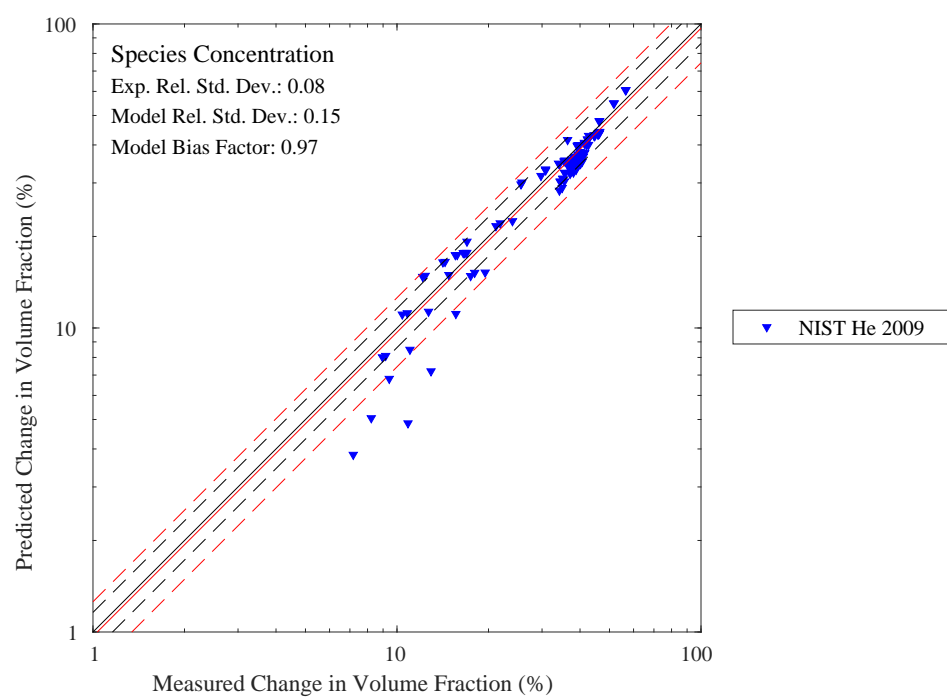


Figure 9.125: Summary of species concentration predictions.

Chapter 10

Pressure

In FDS, the pressure is decomposed into a temporally-varying background pressure plus a temporally and spatially-varying perturbation that drives the flow. The former can be thought of as the “over-pressure” which increases if heat is introduced into a closed compartment. In real buildings, leakage and ventilation affect the compartment “over-pressure” along with the fire.

10.1 FM/FPRF Datacenter Experiments

Measurements made during flow mapping in the FM datacenter mockup included two pairs of differential pressure transmitters. One pair measured the pressure difference between the subfloor (SF) and the cold aisle (CA). The other pair measured the pressure difference between the hot aisle (HA) and the ceiling plenum (CP). A comparison of measured and predicted pressures for the exhaust rate (78 ACH) and high exhaust rate (265 ACH) tests is shown in the figure below.

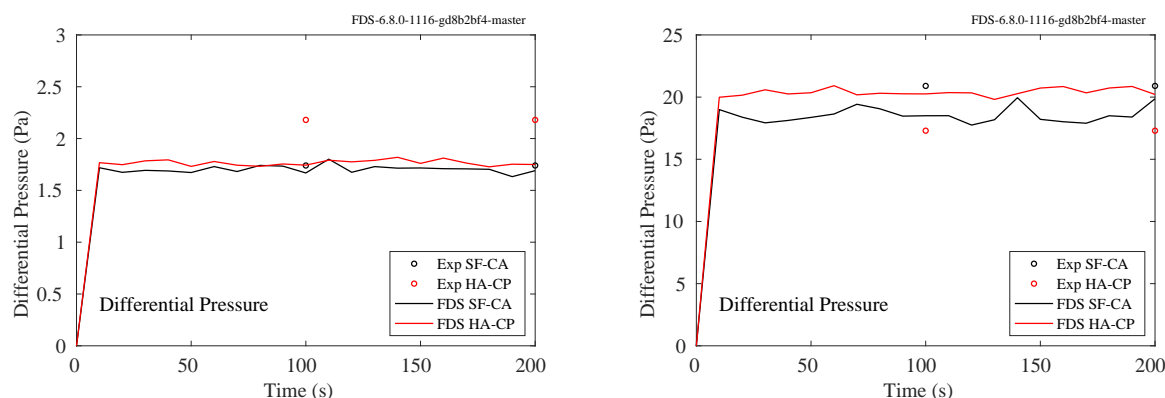


Figure 10.1: FM/FPRF Data Center, differential pressure (Left - low exhaust rate, Right - high exhaust rate)

10.2 NIST/NRC Experiments

Comparisons between measured and predicted pressures for the NIST/NRC series are shown on the following pages. For those tests in which the door to the compartment was open, the over-pressures were only a few Pascals, whereas when the door was closed, the over-pressures were several hundred Pascals. The

pressure within the compartment was measured at a single point, near the floor. For the simulations of the closed door tests, the compartment is assumed to leak via a small uniform flow distributed over the walls and ceiling. The flow rate is calculated based on the assumption that the leakage rate is proportional to the measured leakage area times the square root of compartment over-pressure.

Note that for the closed door tests, there is often a dramatic drop in the predicted compartment pressure. This is the result of the assumption in FDS that the heat release rate is decreased to zero in one second at the time in the experiment when the fuel flow was stopped for safety reasons. In reality, the fire did not extinguish immediately because there was an excess of fuel in the pan following the flow stoppage. For the purpose of model comparison, the peak over-pressures are compared in the closed door tests, and the peak (albeit small) under-pressures are compared in the open door tests.

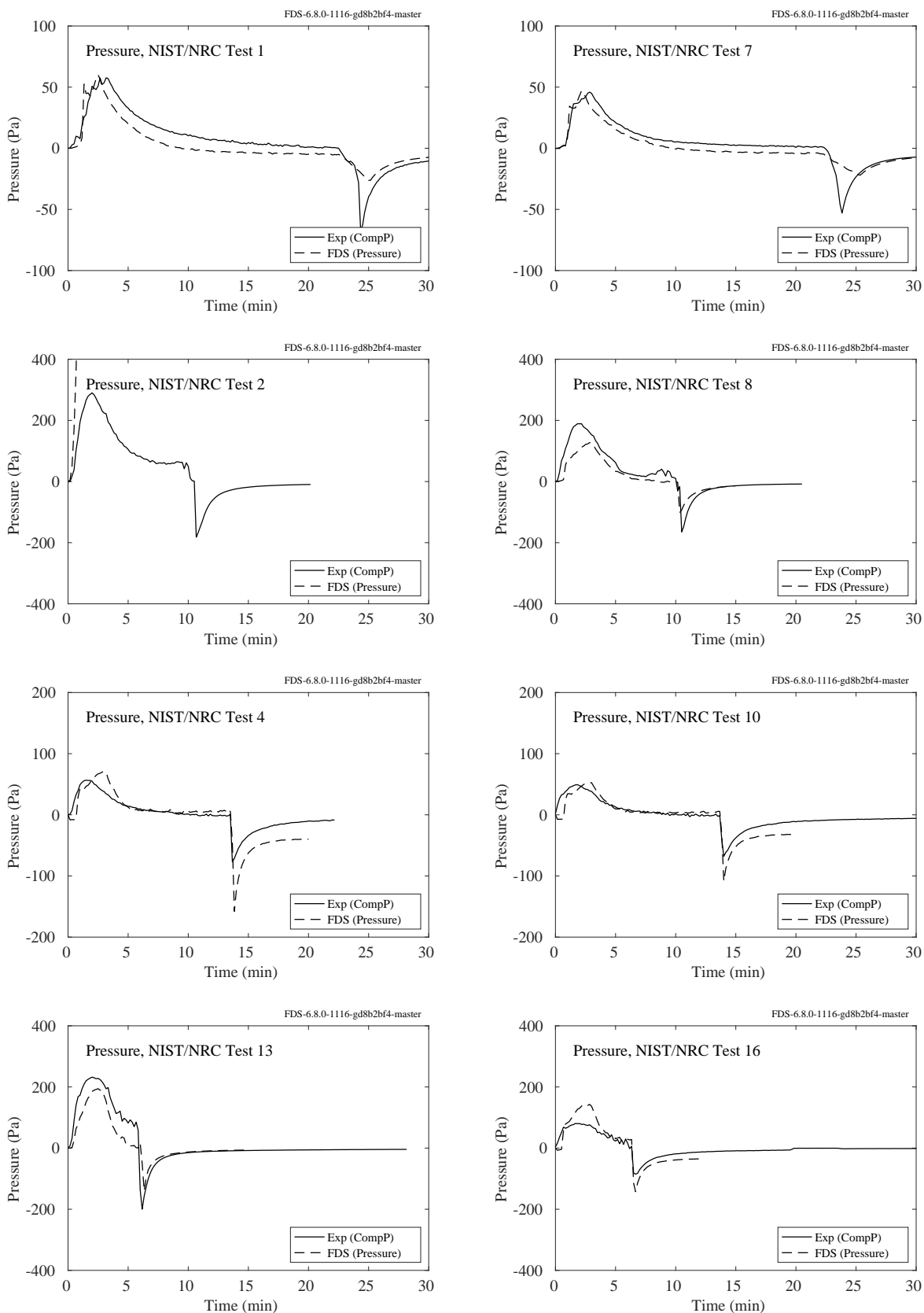


Figure 10.2: NIST/NRC experiments, compartment pressure, Tests 1, 2, 4, 7, 8, 10, 13, 16.

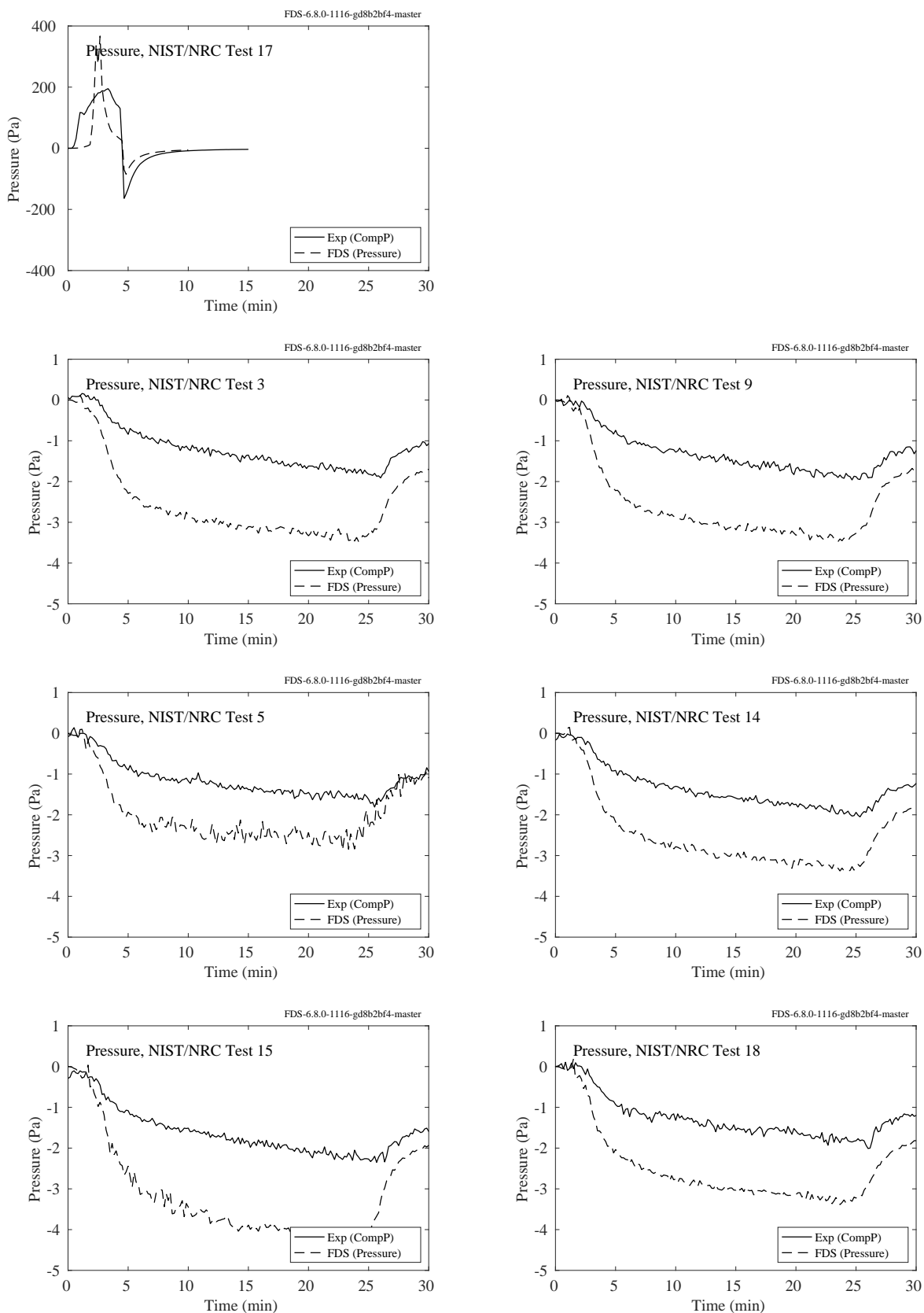


Figure 10.3: NIST/NRC experiments, compartment pressure, Tests 3, 5, 9, 14, 15, 17, 18.

10.3 LLNL Enclosure Experiments

The reported compartment pressure in the LLNL Enclosure experiments was taken near the ceiling of the compartment, 0.6 m from the wall including the exhaust duct, and 0.6 m from the wall opposite the wall with the door. Further details of the experiments can be found in Sec. 3.43.

In the figures on the following pages, the open circles represent the measured pressure; the solid line represents the predicted pressure. The predicted pressures are time-averaged over a time interval of 30 s, whereas the measurements appear to be instantaneous values separated by hundreds or thousands of seconds. Because of this, the short-duration pressure spike that is typical of fires within relatively tight compartments is seen in the model prediction but not necessarily the measured data. The comparison of measurement and prediction is based on the final few pressure points, not the initial spike.

The results of all 64 experiments are plotted for completeness, but a few of the results were excluded from the computation of the summary statistics because the fire self-extinguished near the time of the last pressure measurement, sometimes leading to a reported final pressure being less than the initial pressure, typical when there is a sudden decrease in the heat release rate. In other cases, the difference between initial and final measured pressure was too small to make a meaningful comparison.

For cases where the door to the compartment was open, the measured gauge pressures at the start of the experiment ranged from 0 Pa to 10 Pa. There is not enough information in the test report to explain why the starting pressures were not 0 Pa; thus, the measured pressures were adjusted so that the starting pressure is 0 Pa.

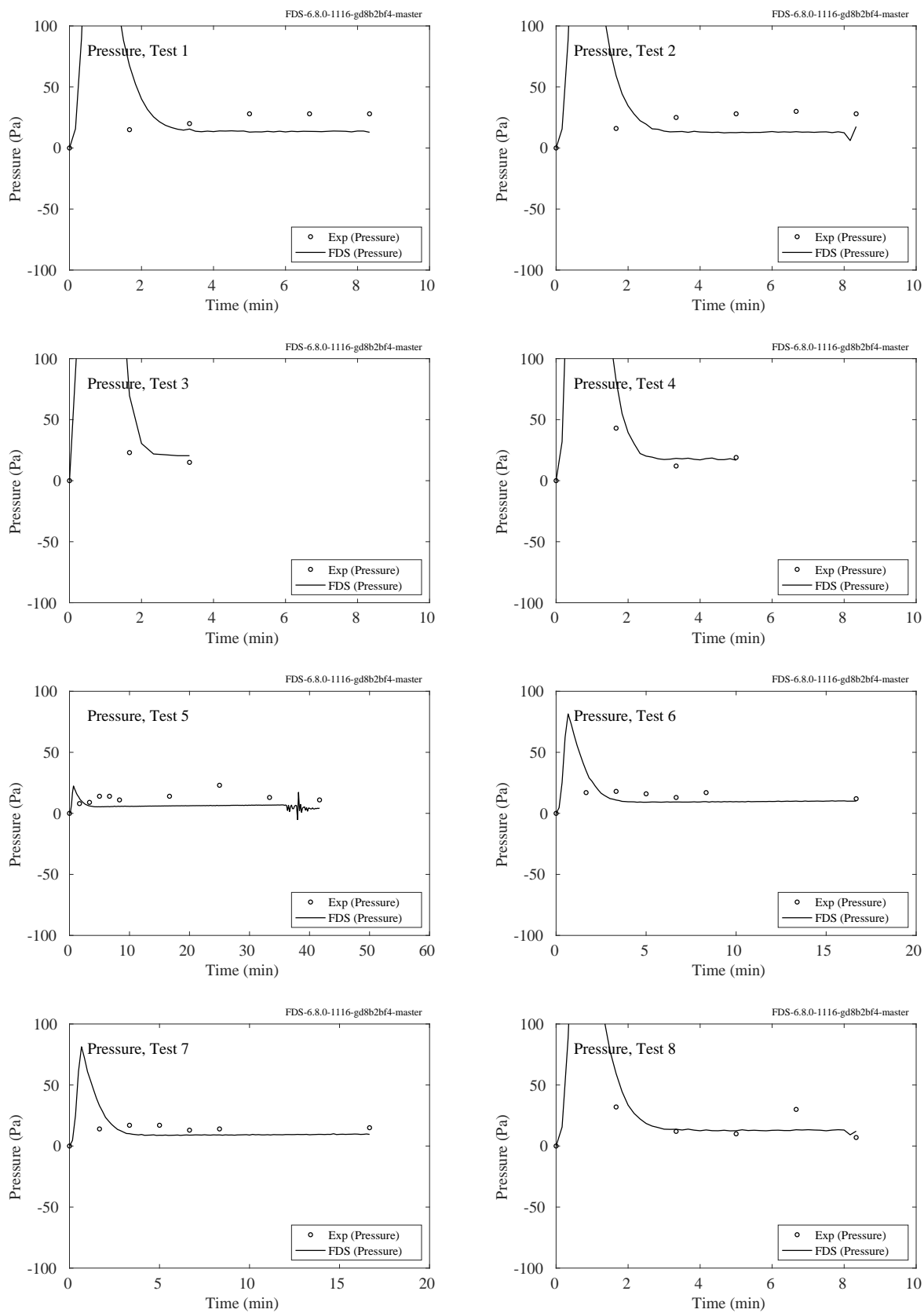


Figure 10.4: LLNL Enclosure experiments, compartment pressure, Tests 1-8.

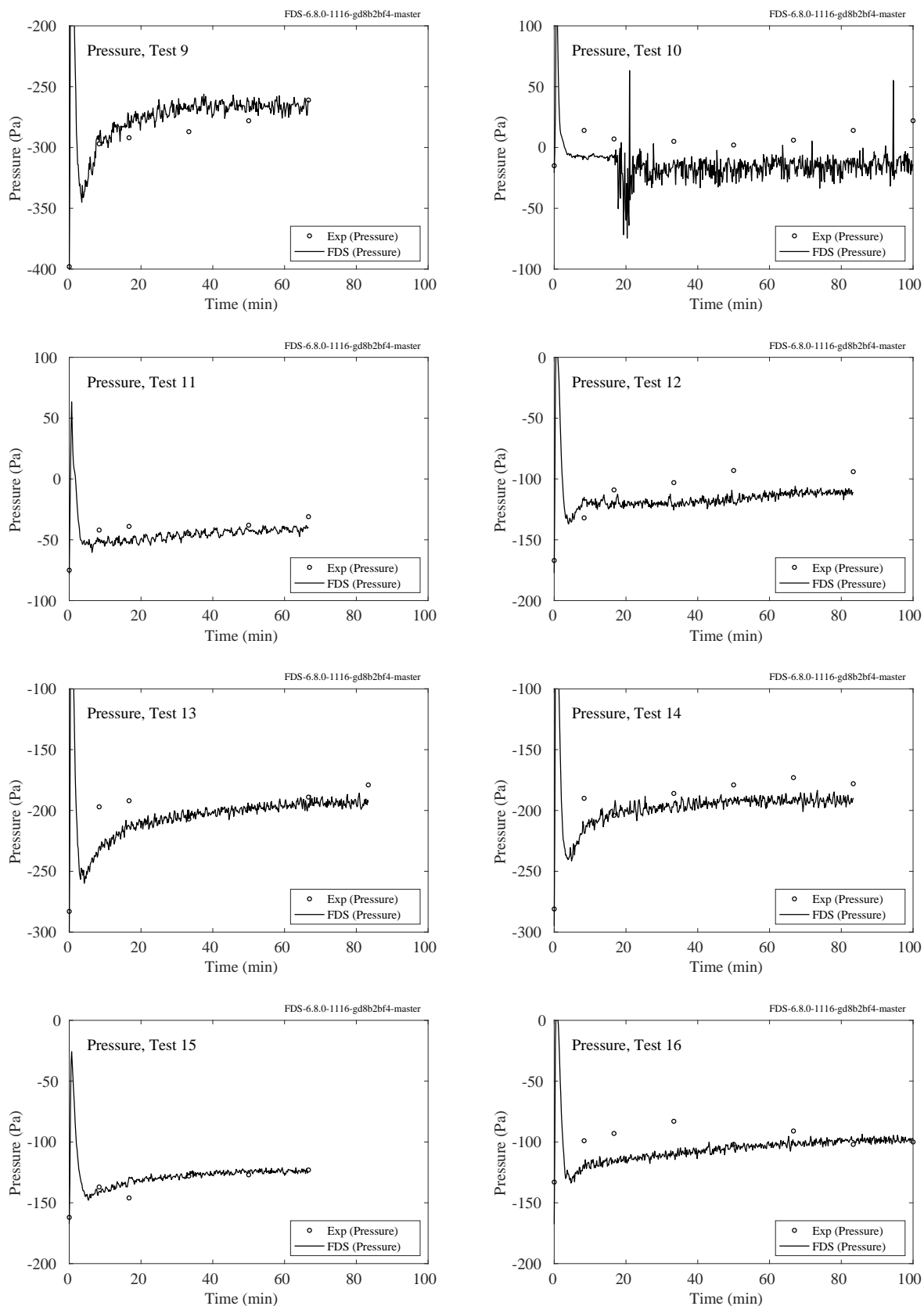


Figure 10.5: LLNL Enclosure experiments, compartment pressure, Tests 9-16.

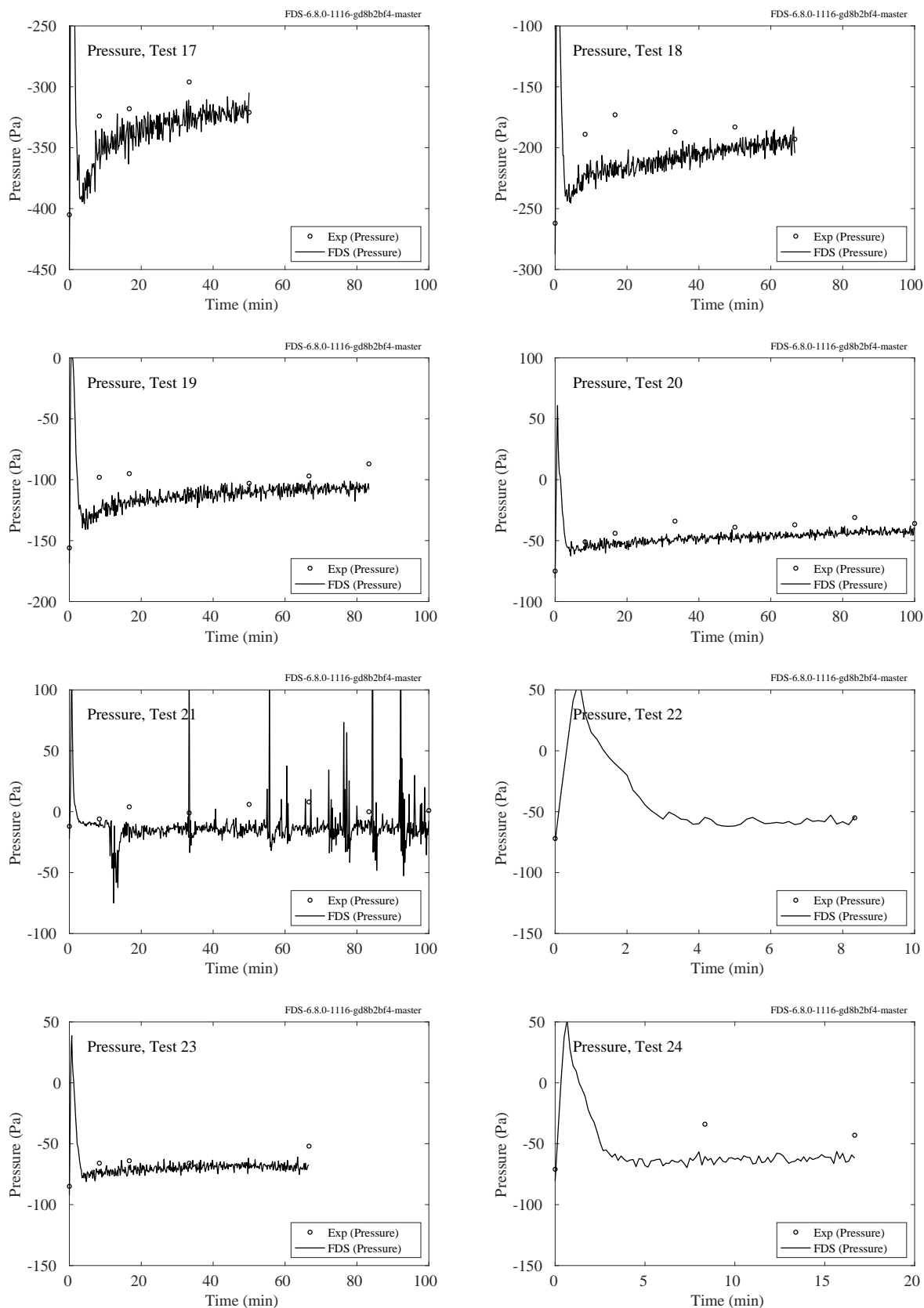


Figure 10.6: LLNL Enclosure experiments, compartment pressure, Tests 17-24.

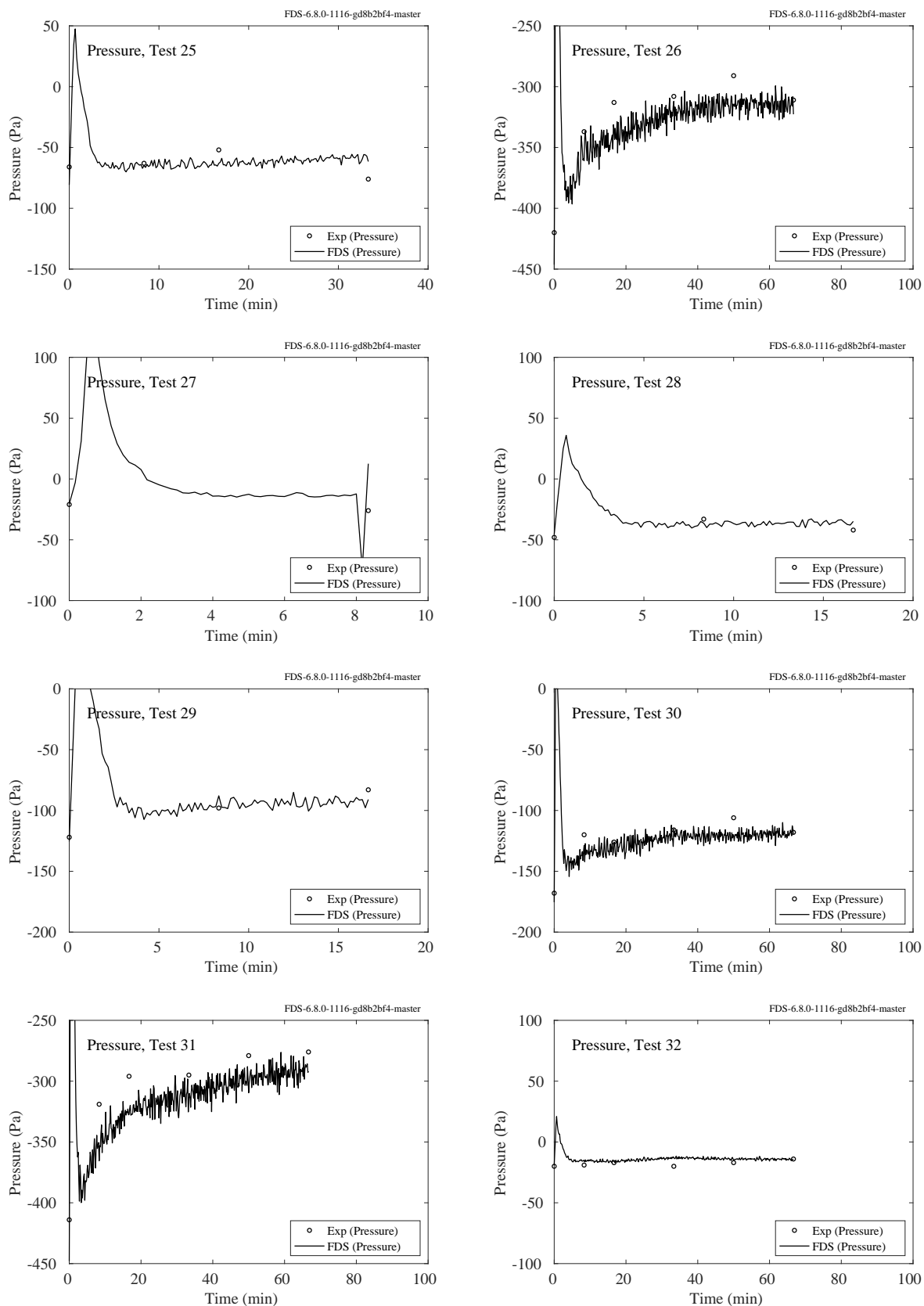


Figure 10.7: LLNL Enclosure experiments, compartment pressure, Tests 25-32.

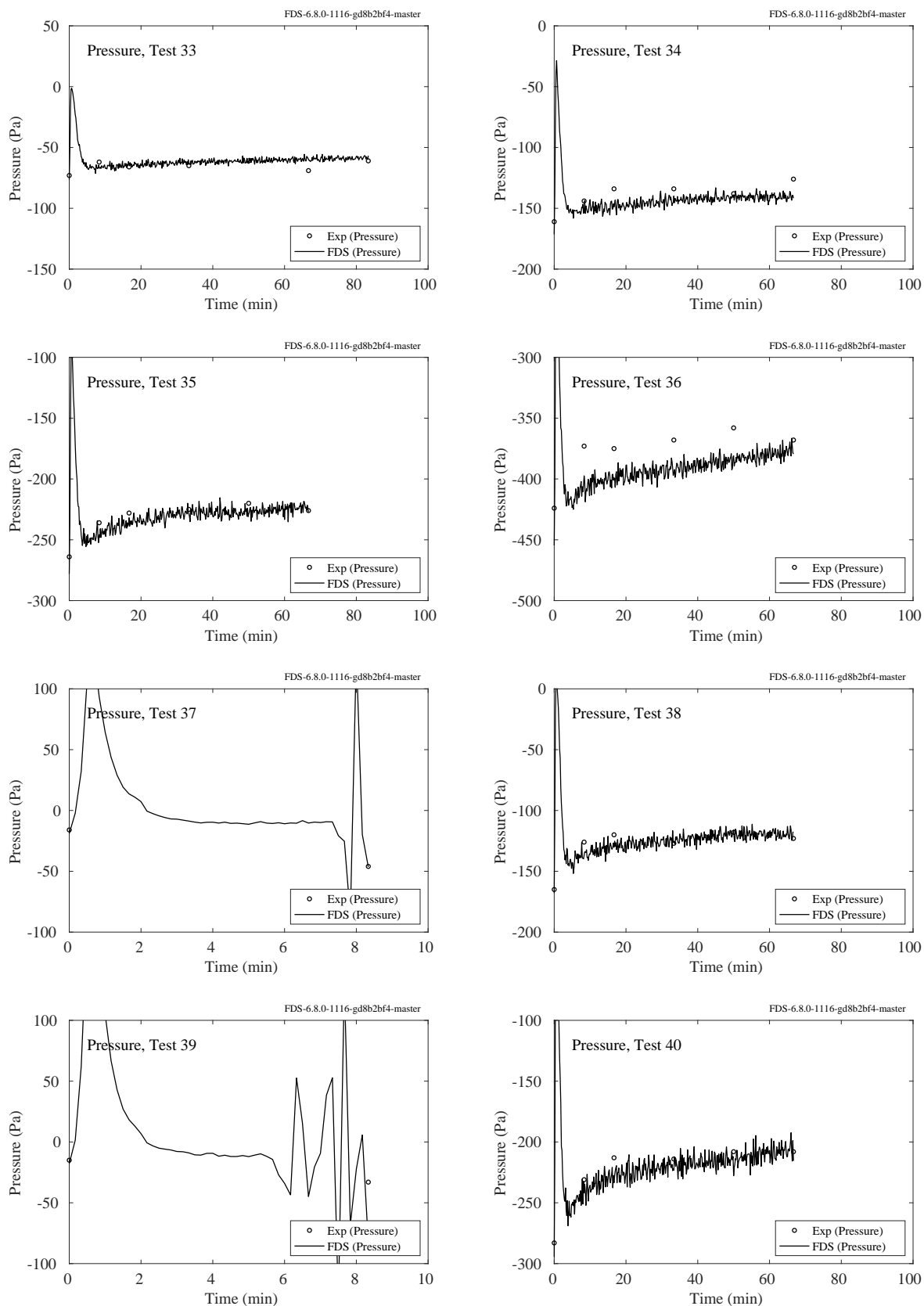


Figure 10.8: LLNL Enclosure experiments, compartment pressure, Tests 33-40.

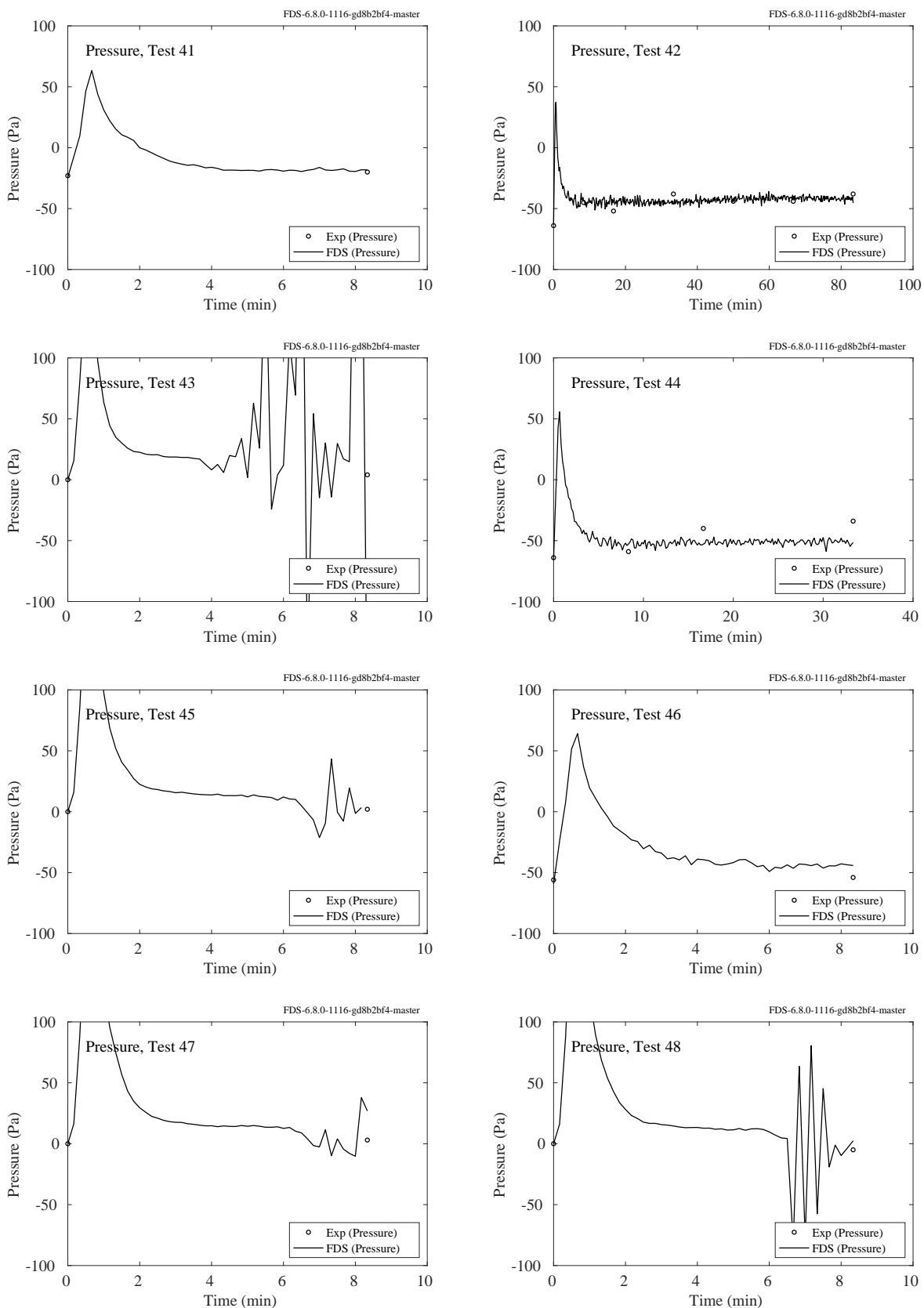


Figure 10.9: LLNL Enclosure experiments, compartment pressure, Tests 41-48.

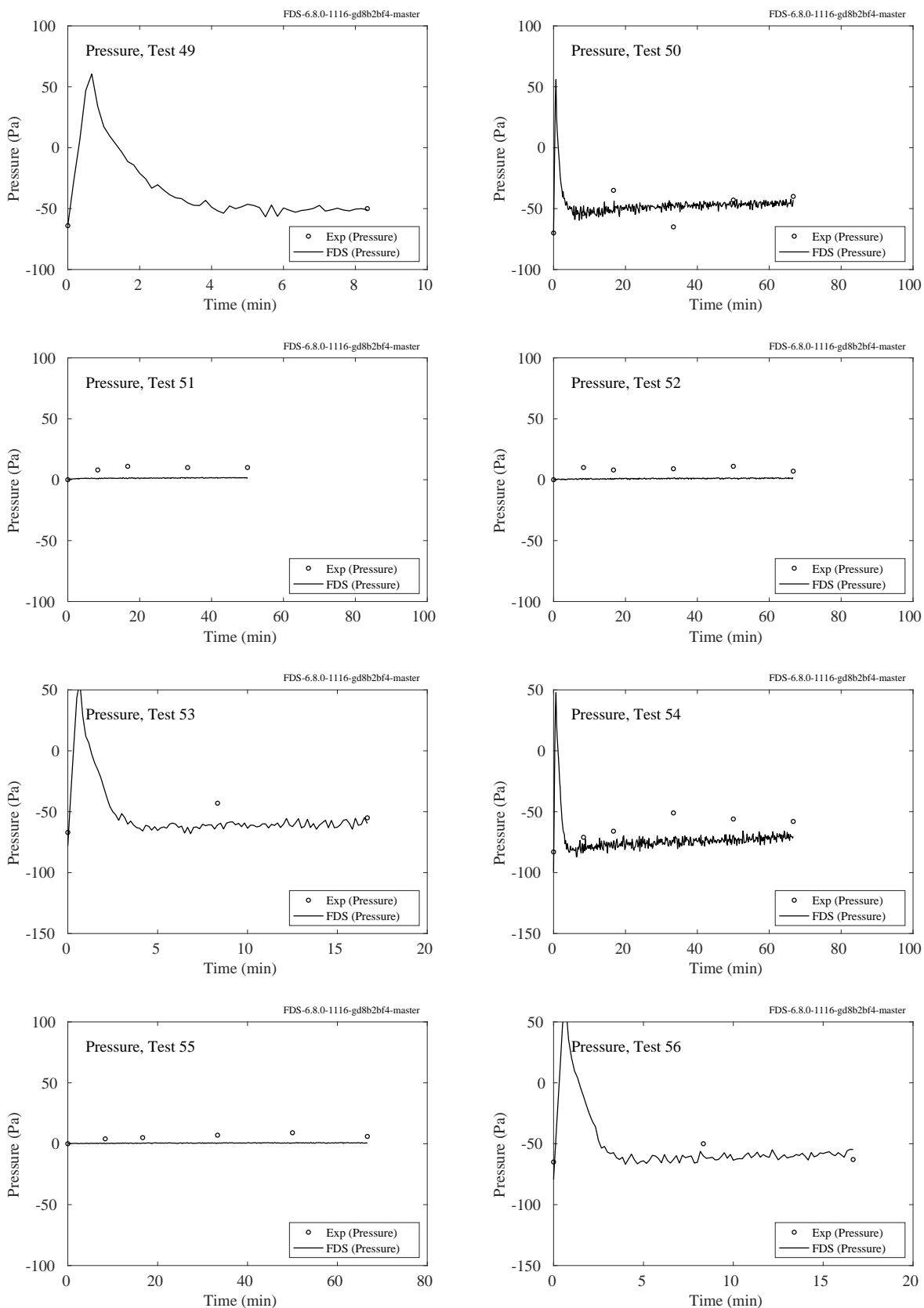


Figure 10.10: LLNL Enclosure experiments, compartment pressure, Tests 49-56.

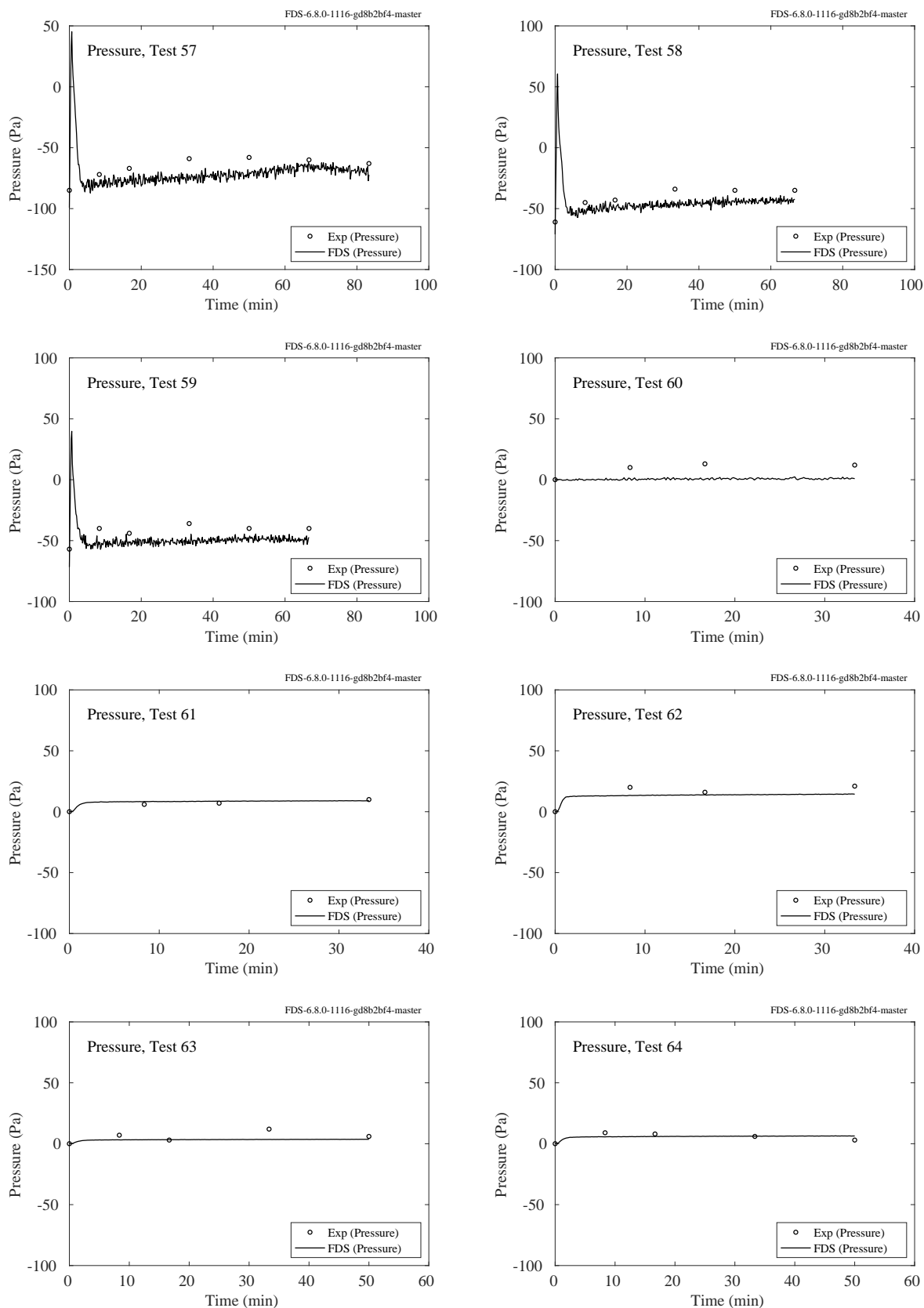


Figure 10.11: LLNL Enclosure experiments, compartment pressure, Tests 57-64.

10.4 PRISME DOOR Experiments

The PRISME experiments were conducted in a relatively well-sealed set of compartments with a well-controlled ventilation system. Supply air was forced into and exhaust products extracted from the test compartments via two fans and a fairly extensive ventilation network. The air flow rates and nodal pressures were measured throughout the system. The FDS simulations included the ventilation system, and for each segment of the network a loss coefficient was calculated so as to match the initial conditions of the experiments. The plots to follow show the predicted and measured compartment pressures and supply and exhaust flows. These air flows were predicted by the model, based on the initial specification of the ventilation system.

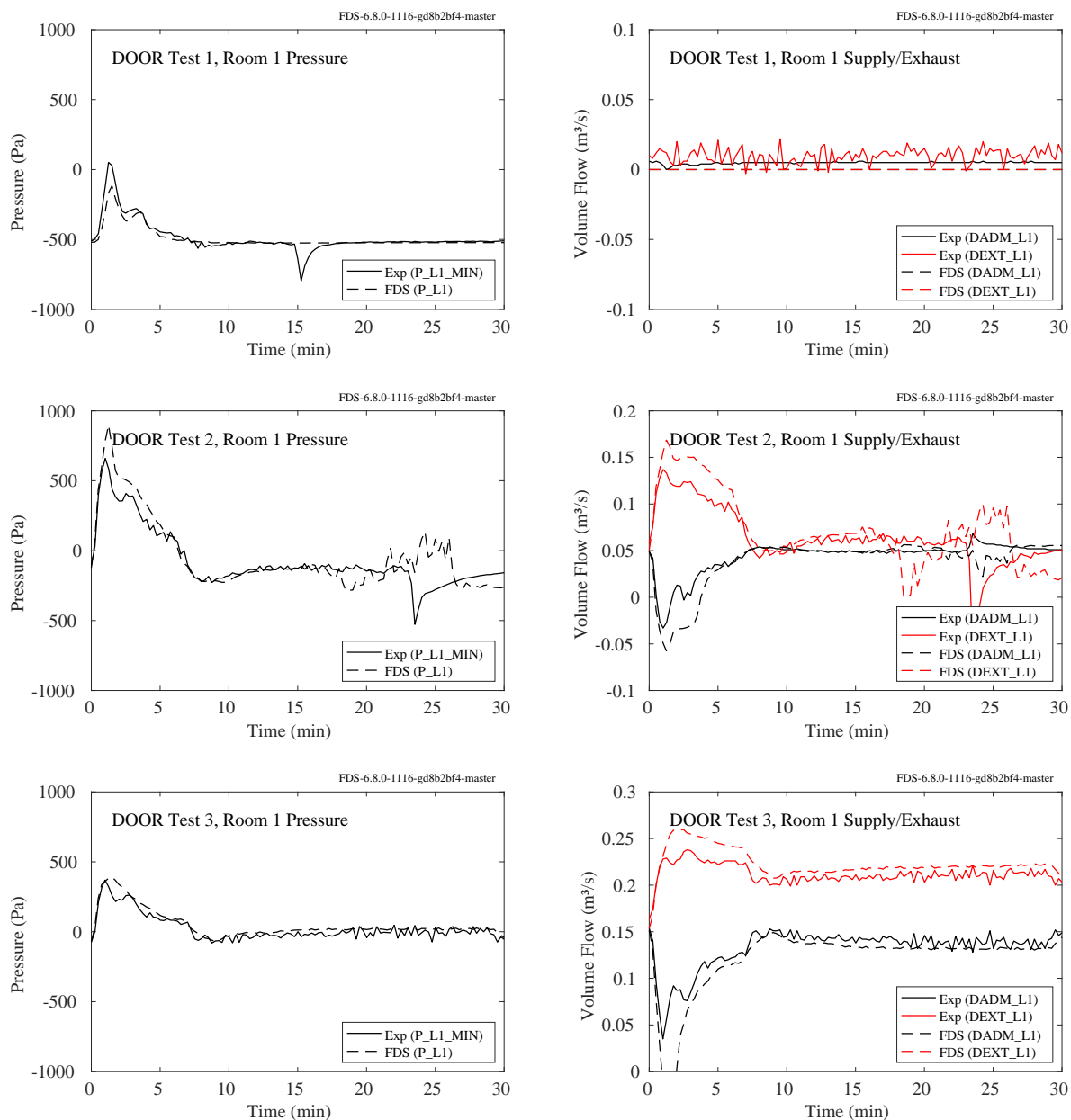


Figure 10.12: PRISME DOOR, compartment pressure and supply/exhaust, Room 1, Tests 1-3.

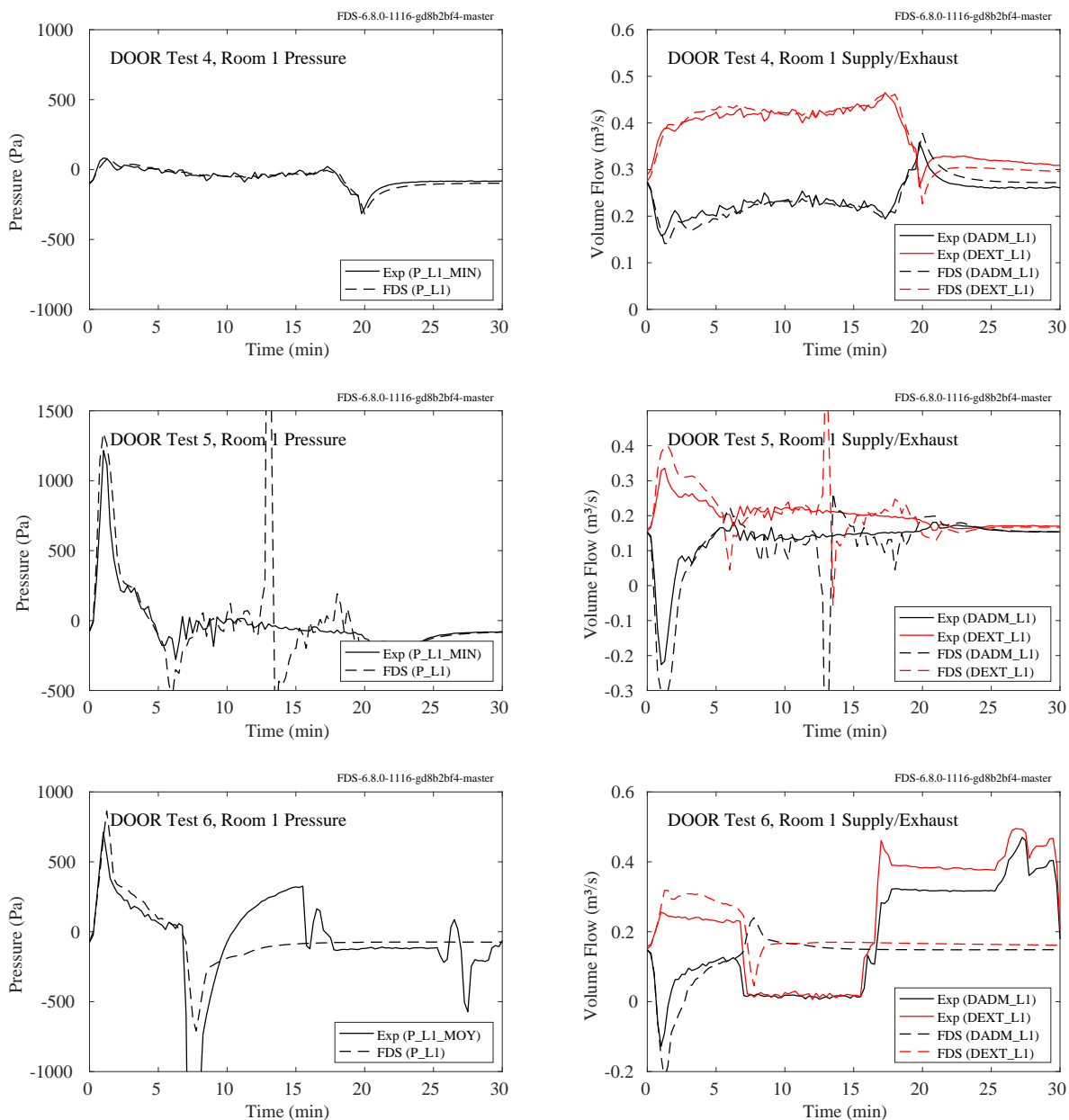


Figure 10.13: PRISME DOOR, compartment pressure and supply/exhaust, Room 1, Tests 4-6.

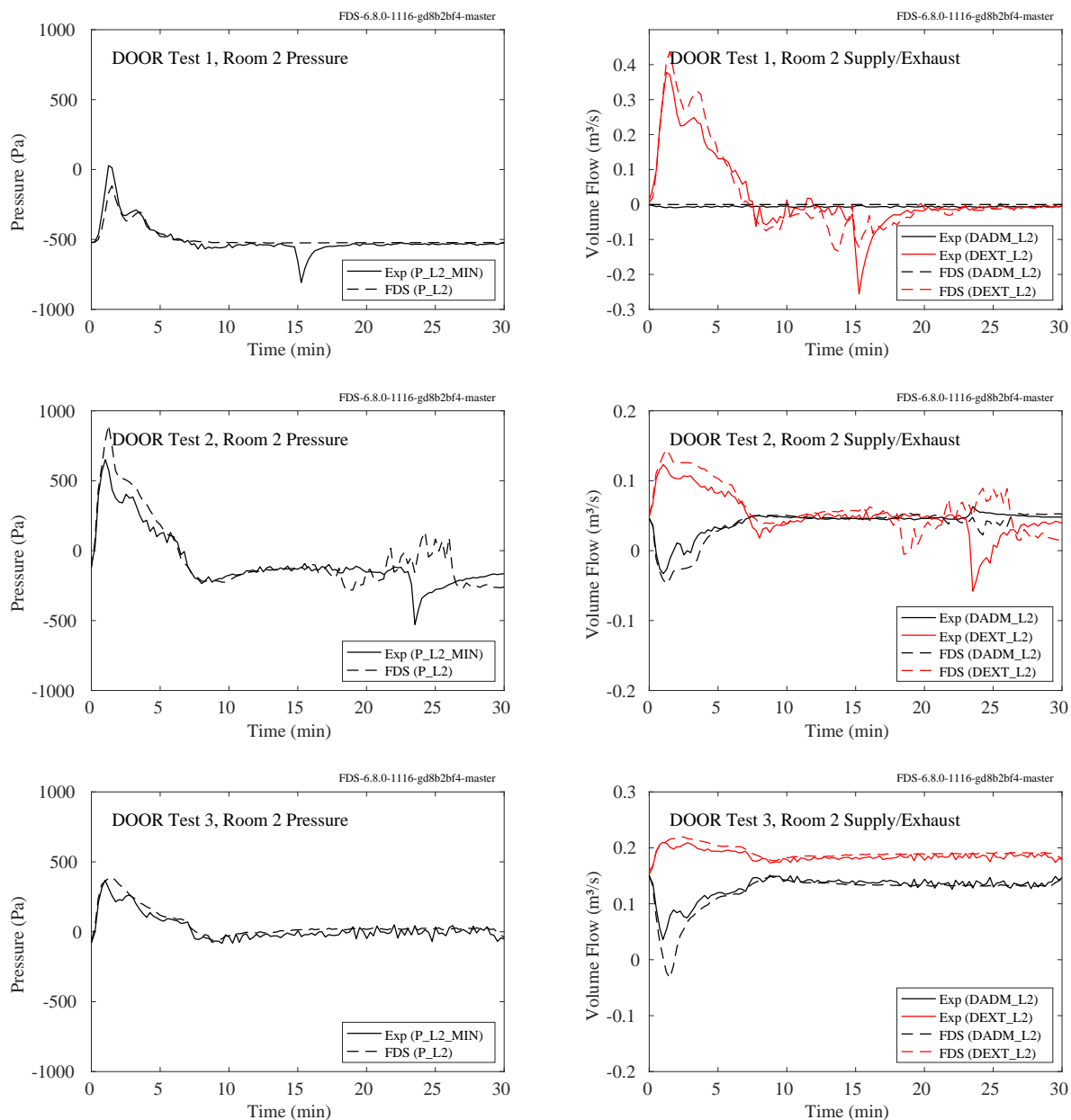


Figure 10.14: PRISME DOOR, compartment pressure and supply/exhaust, Room 2, Tests 1-3.

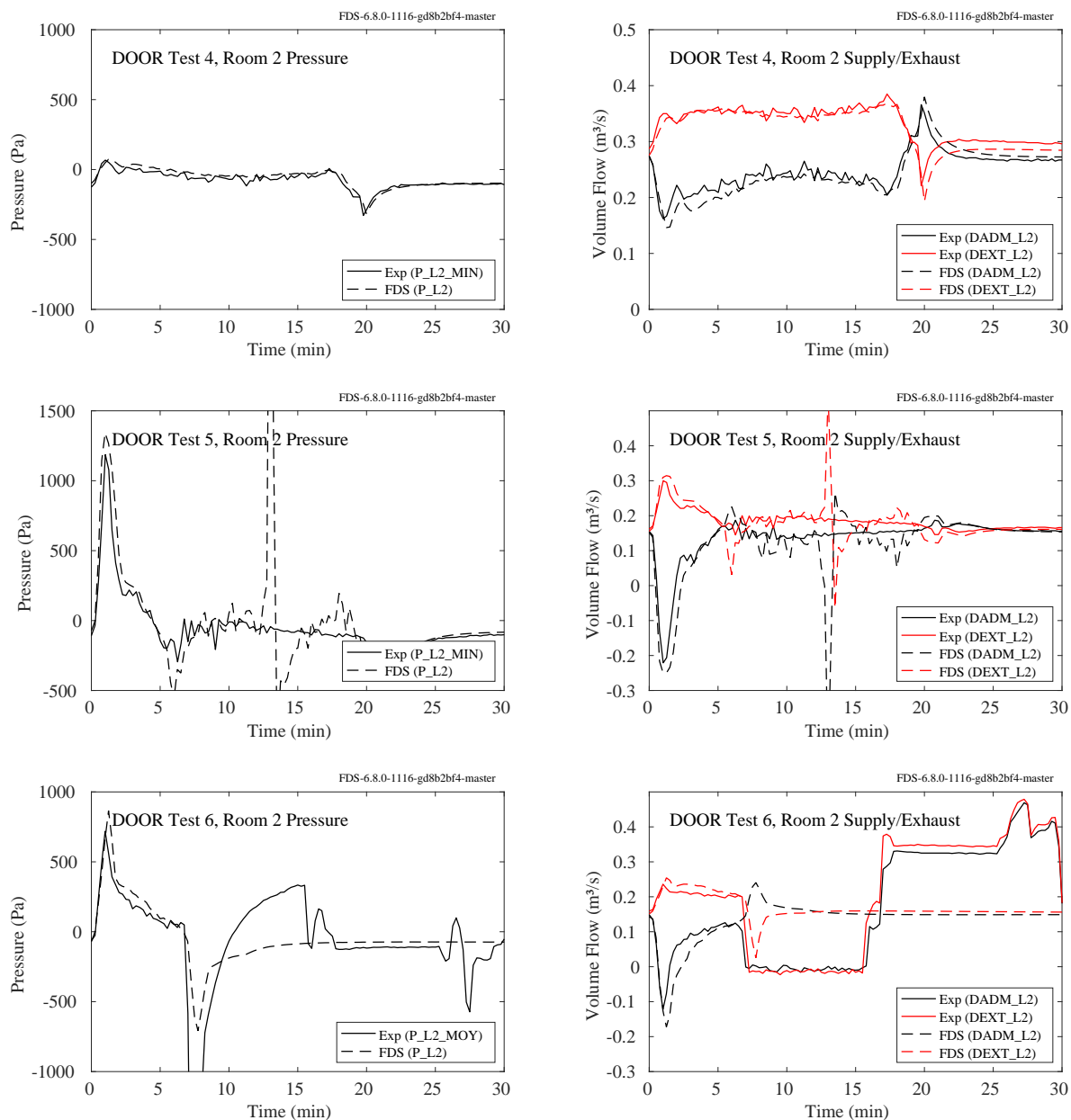


Figure 10.15: PRISME DOOR, compartment pressure and supply/exhaust, Room 2, Tests 4-6.

10.5 PRISME SOURCE Experiments

The PRISME SOURCE experiments were conducted in a single compartment with a well-controlled ventilation system. Supply air was forced into and exhaust products extracted from the test compartment via two fans and a fairly extensive ventilation network. The air flow rates and nodal pressures were measured throughout the system. The FDS simulations included the ventilation system, and for each segment of the network a loss coefficient was calculated so as to match the initial conditions of the experiments. The plots to follow show the predicted and measured compartment pressures and supply and exhaust flows. These air flows were predicted by the model, based on the initial specification of the ventilation system.

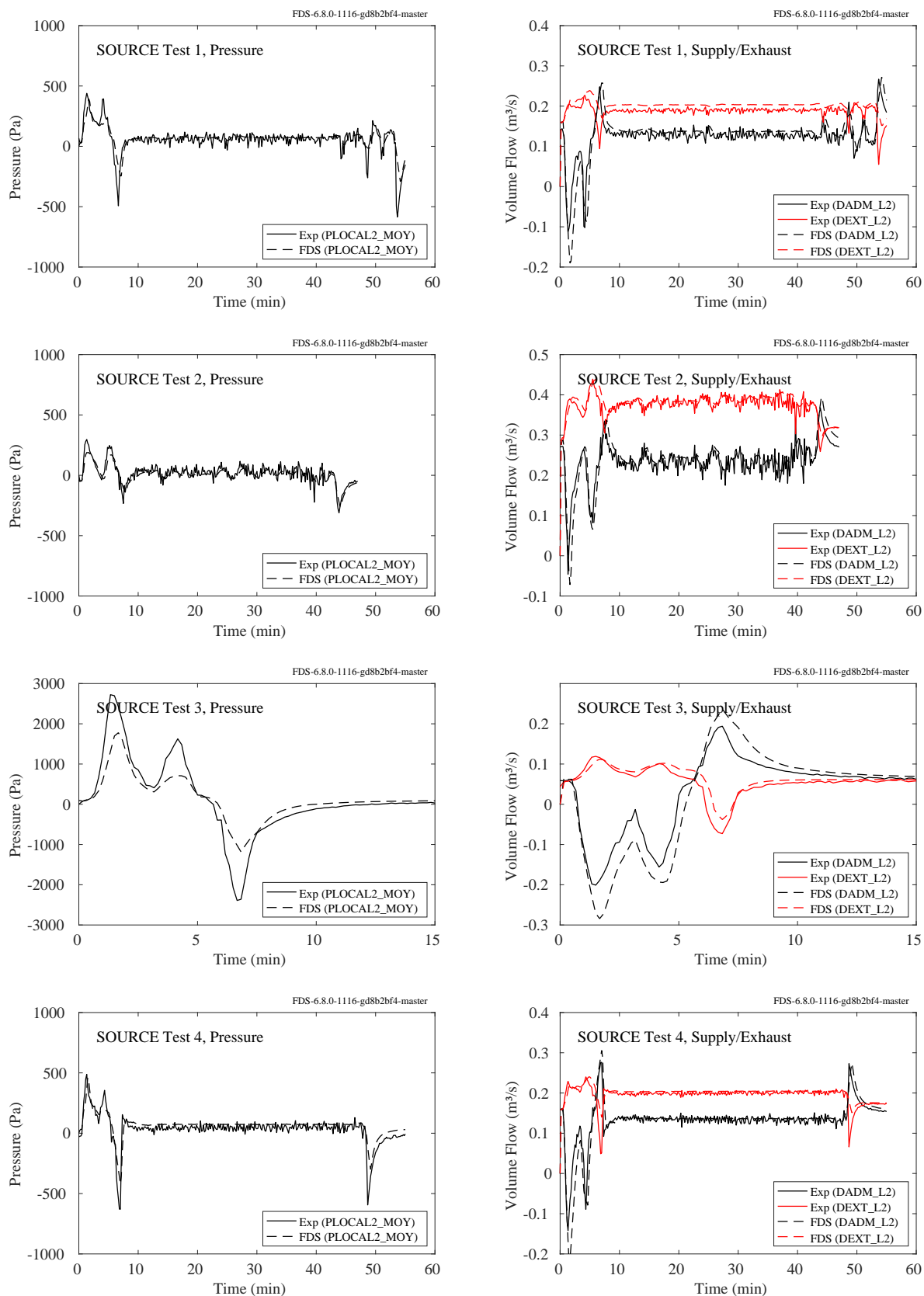


Figure 10.16: PRISME SOURCE, pressure and supply/exhaust flow rates, Tests 1, 2, 3 and 4.

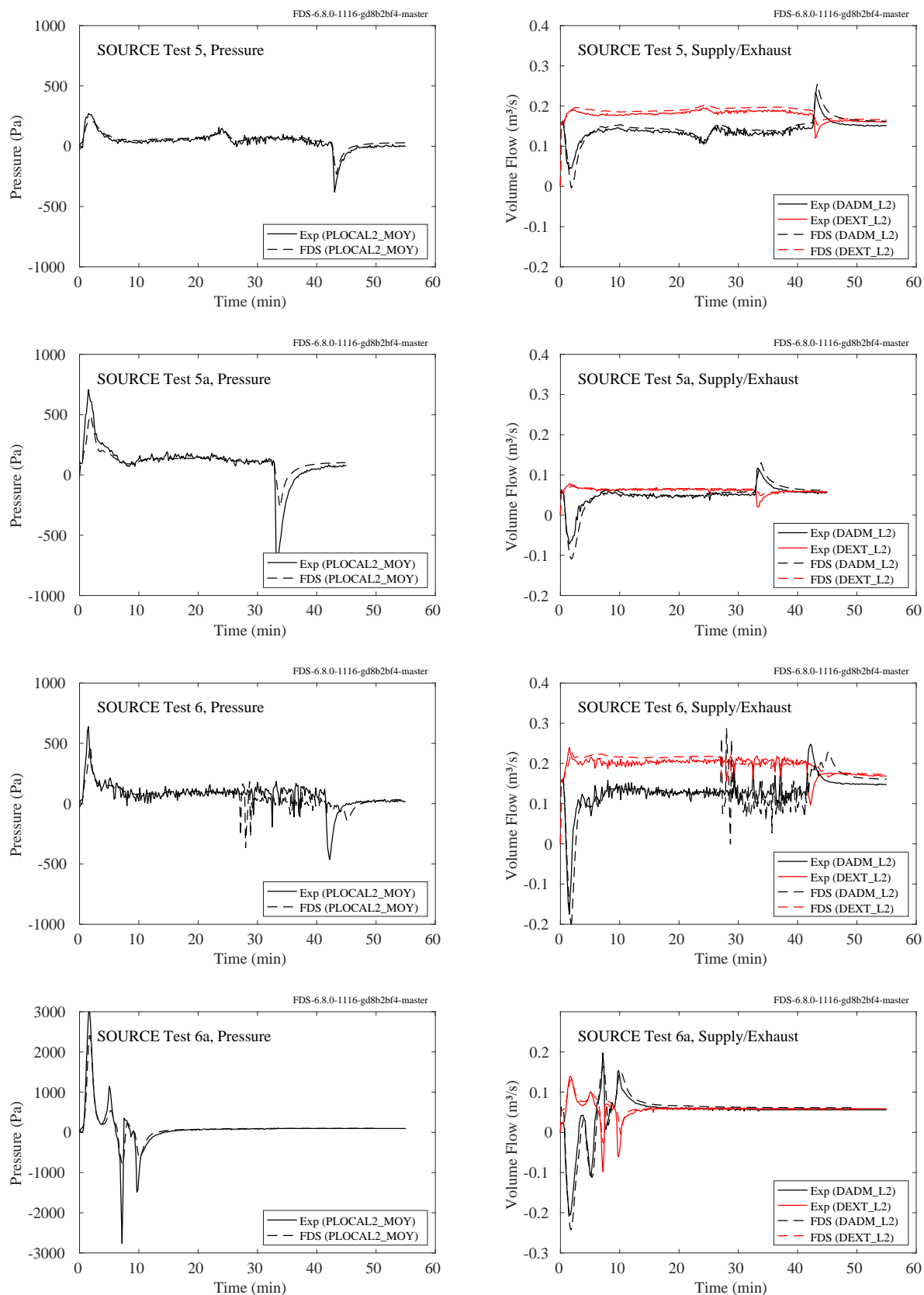


Figure 10.17: PRISME SOURCE, pressure and supply/exhaust flow rates, Tests 5, 5a, 6 and 6a.

10.6 Prétrel/IRSN Water Spray Experiments

A description of the experiment is found in Sec. 3.71 and Refs. [293, 292]. Briefly, a propane burner is placed in the corner of an 8.67 m long, 4.88 m wide, 3.9 m tall closed compartment equipped with two water spray nozzles that are activated after a hot gas layer has developed. Air is supplied at a rate of approximately $0.7 \text{ m}^3/\text{s}$. A sketch of the compartment is shown in Fig. 10.18. The propane burner has a steady heat release rate of approximately 292 kW. The water spray nozzles are positioned 297 cm above the floor and are activated at 6 min, 54 s and deactivated at 11 min, 30 s. The combined flow rate is 109 L/min with a spray angle of approximately 90° and median volumetric droplet diameter of $470 \text{ }\mu\text{m}$.

Shown in Fig. 10.19 are plots of the compartment pressure, exhaust and supply rates, CO_2 and O_2 volume fractions, and near ceiling temperature. The temperature is measured at a height of 390 cm at the southeast (SE) thermocouple array. The gas concentration measurements are made at this same location at heights of 89 cm (bas/low) and 314 cm (haut/high). The last plot in Fig. 10.19 displays the energy budget; that is, the amount of the fire's energy lost to the walls, the exhaust vent, and the water droplets. The method for measuring these quantities is given in Ref. [292].

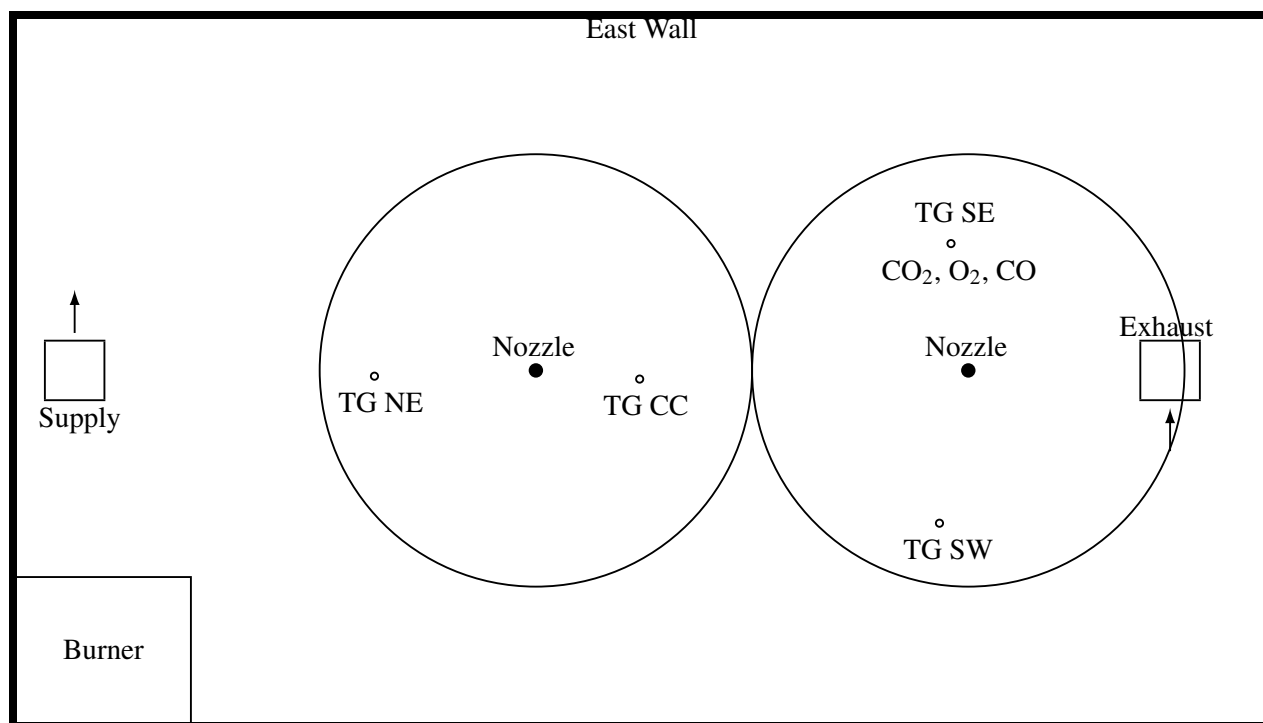


Figure 10.18: Plan view of the Prétrel water spray experiments. The points labelled “TG” are the locations of thermocouple arrays.

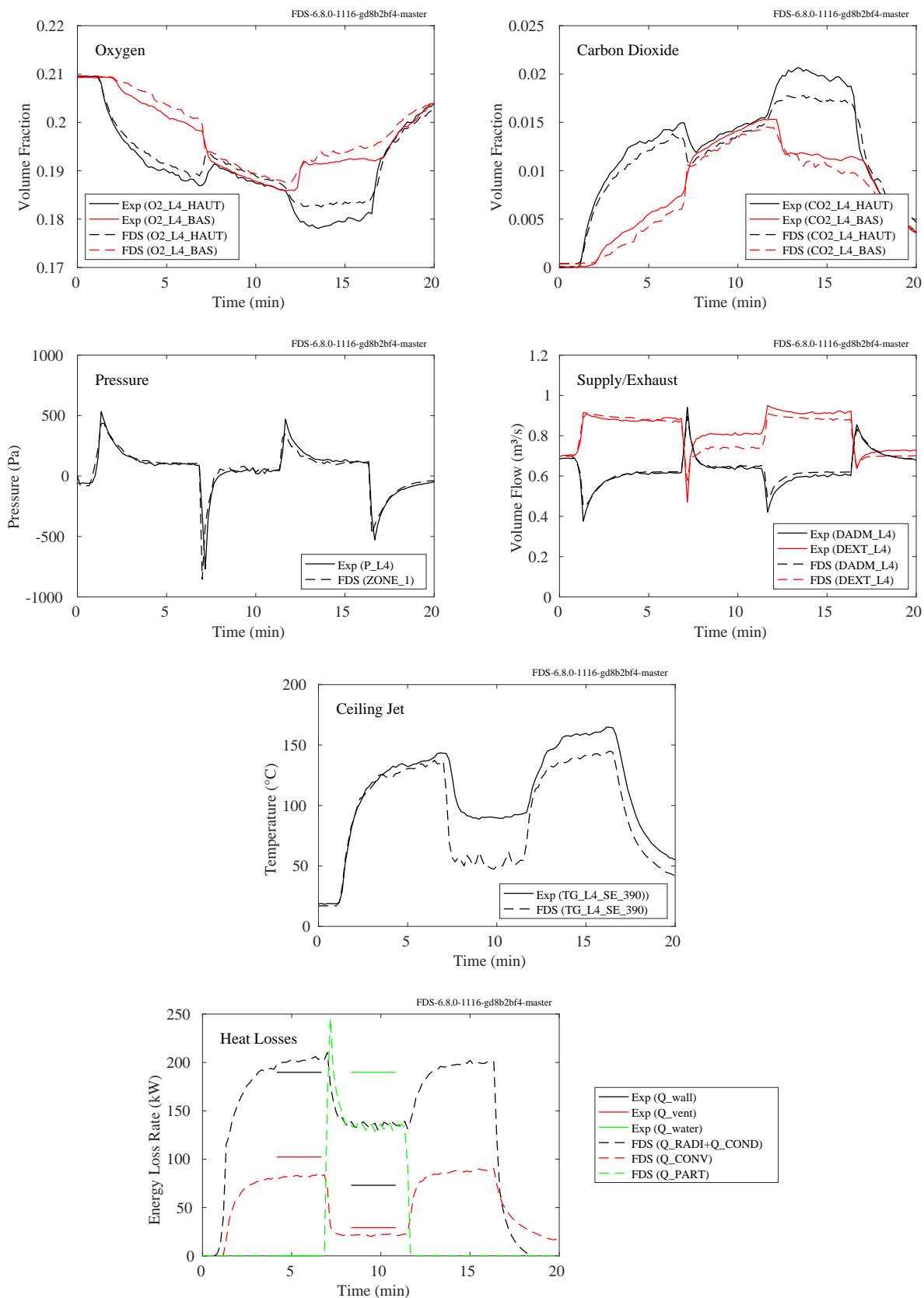


Figure 10.19: Various measurements from the Pr  tre water spray experiment.

10.7 UL/NIJ House Experiments

A description and drawings from these experiments are included in Sec. 3.90

For both the one and two-story house experiments, pressures were measured at three elevations in various locations. All pressure taps were installed within 0.3 m of a wall. In the single-story house, the taps were located 0.3 m (1 ft), 1.2 m (4 ft), and 2.1 m (7 ft) below the ceiling. In the two-story house, the taps were located 0.3 m (1 ft), 2.4 m (8 ft), and 4.6 m (15 ft) below the ceiling in the family room atrium (9PT), and 0.3 m (1 ft), 1.2 m (4 ft), and 2.1 m (7 ft) below the ceiling in all other rooms. Note that for the two-story house, Test 6, the den was closed and no pressure measurements are reported for this room.

The plots on the following pages compare the measured pressures with corresponding model predictions. Note that the pressures are reported relative to the ambient pressure at the given elevation. That is, all reported pressures are zero at the time of ignition.

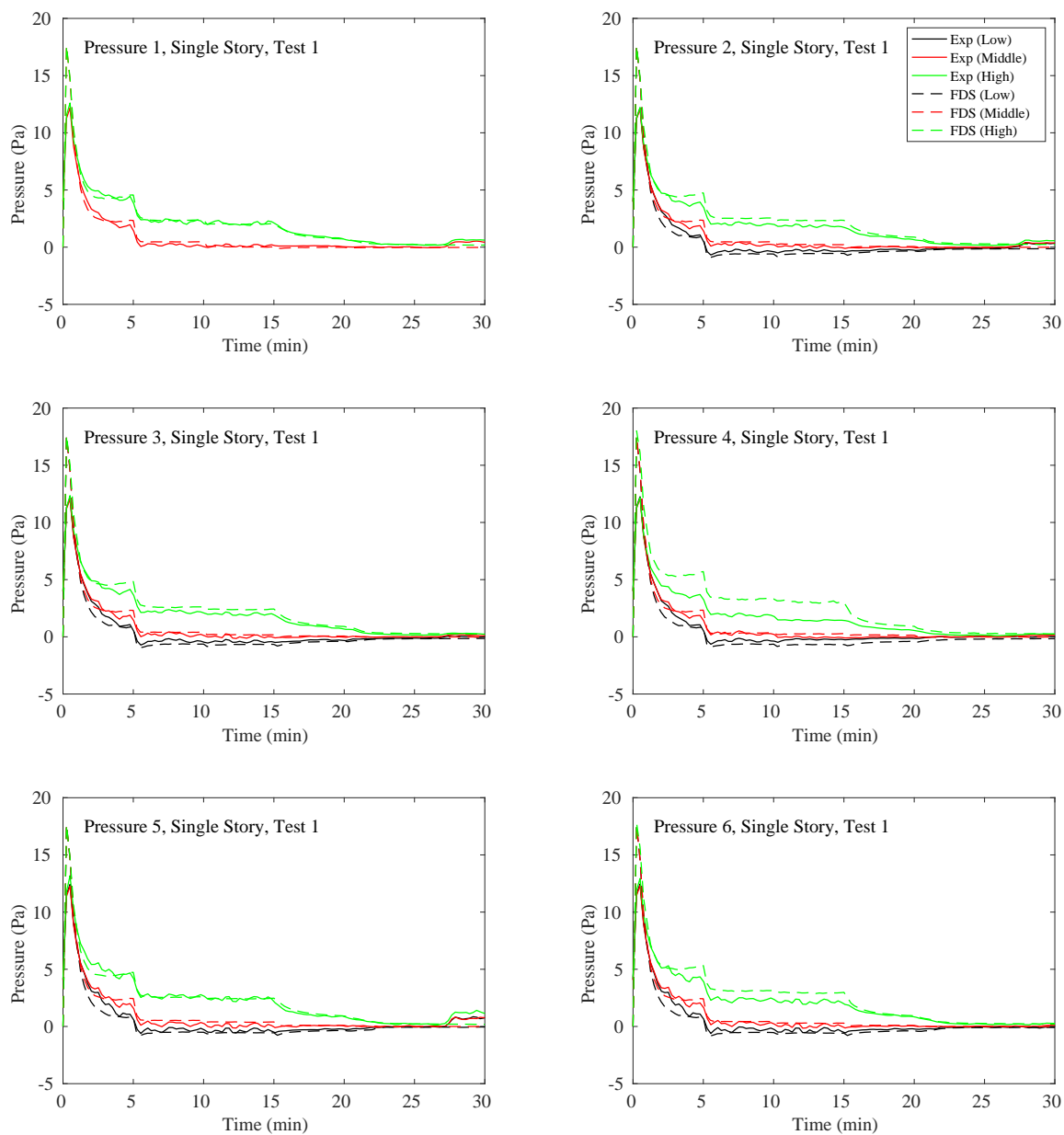


Figure 10.20: UL/NIJ Experiments, Pressure, Single-Story (Ranch) House, Test 1.

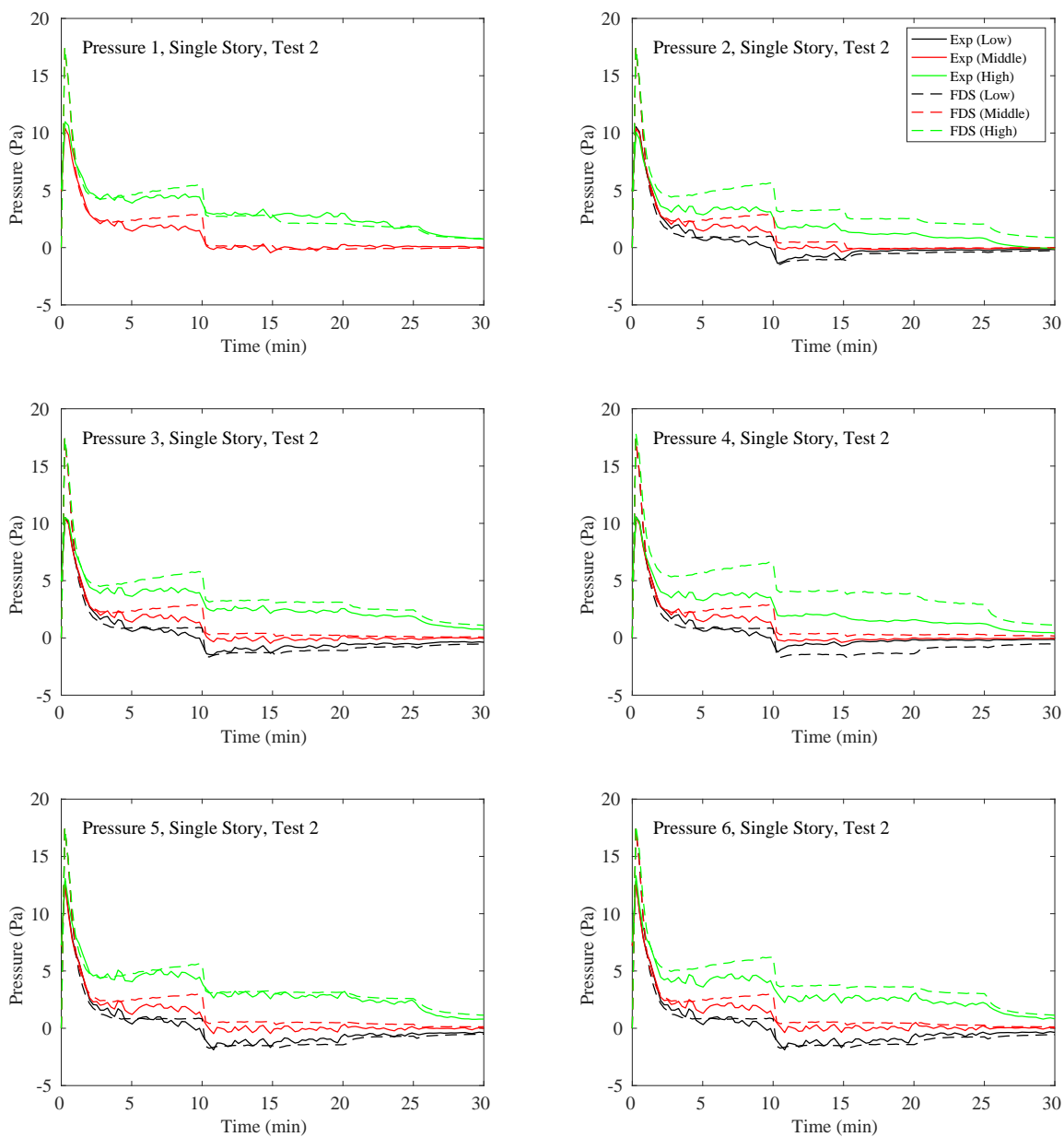


Figure 10.21: UL/NIJ Experiments, Pressure, Single-Story (Ranch) House, Test 2.

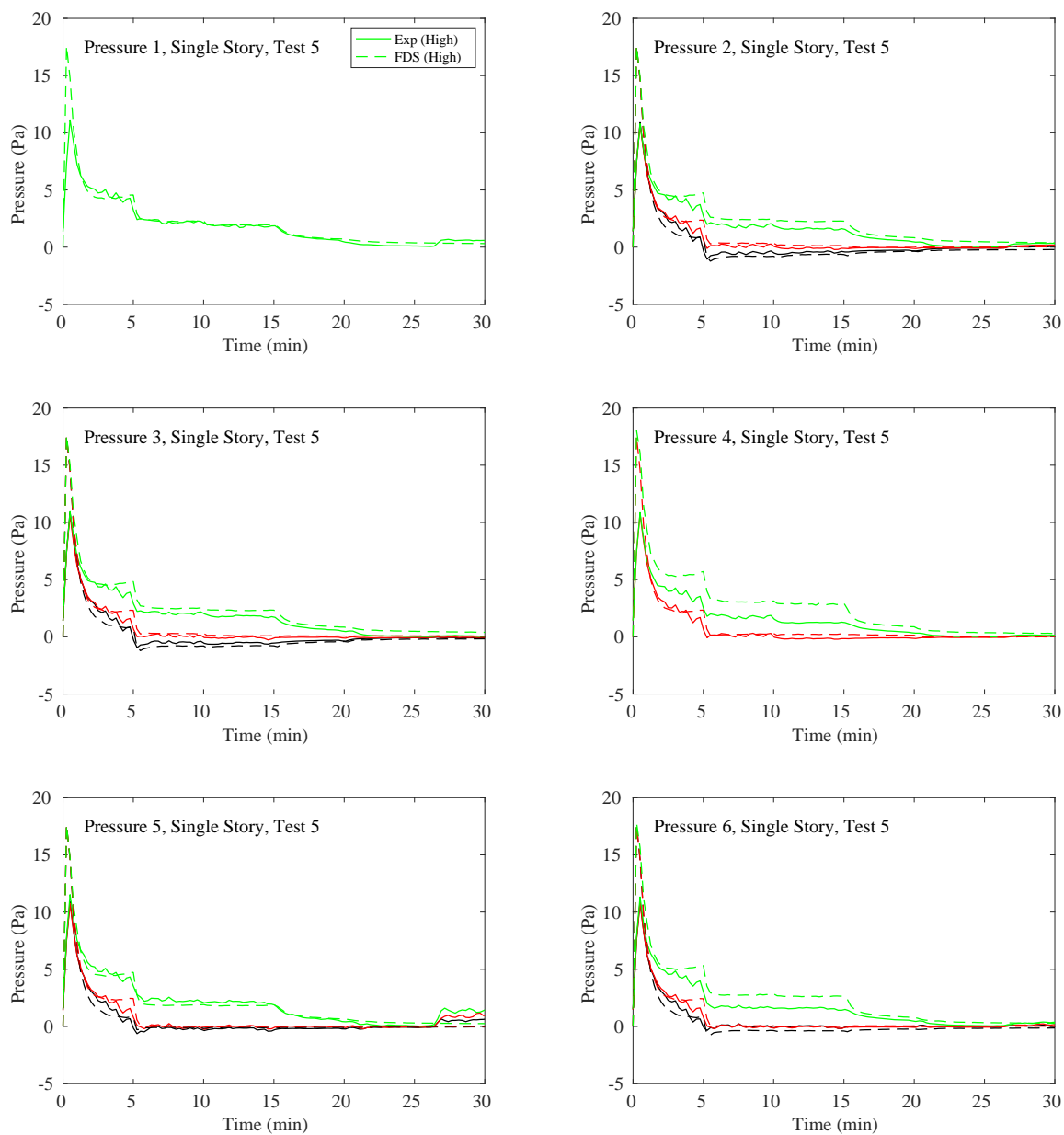


Figure 10.22: UL/NIJ Experiments, Pressure, Single-Story (Ranch) House, Test 5.

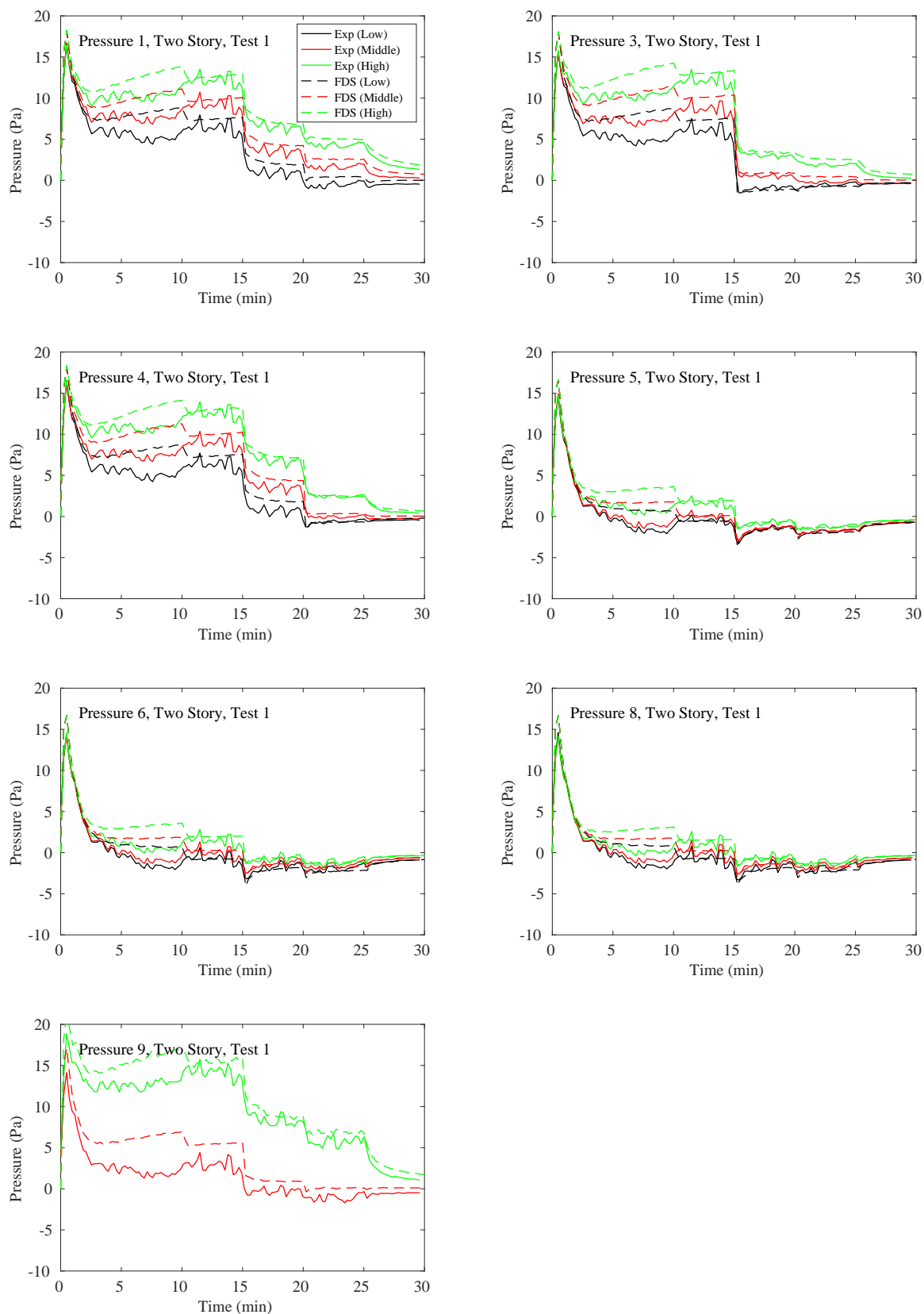


Figure 10.23: UL/NIJ Experiments, Pressure, Two-Story (Colonial) House, Test 1.

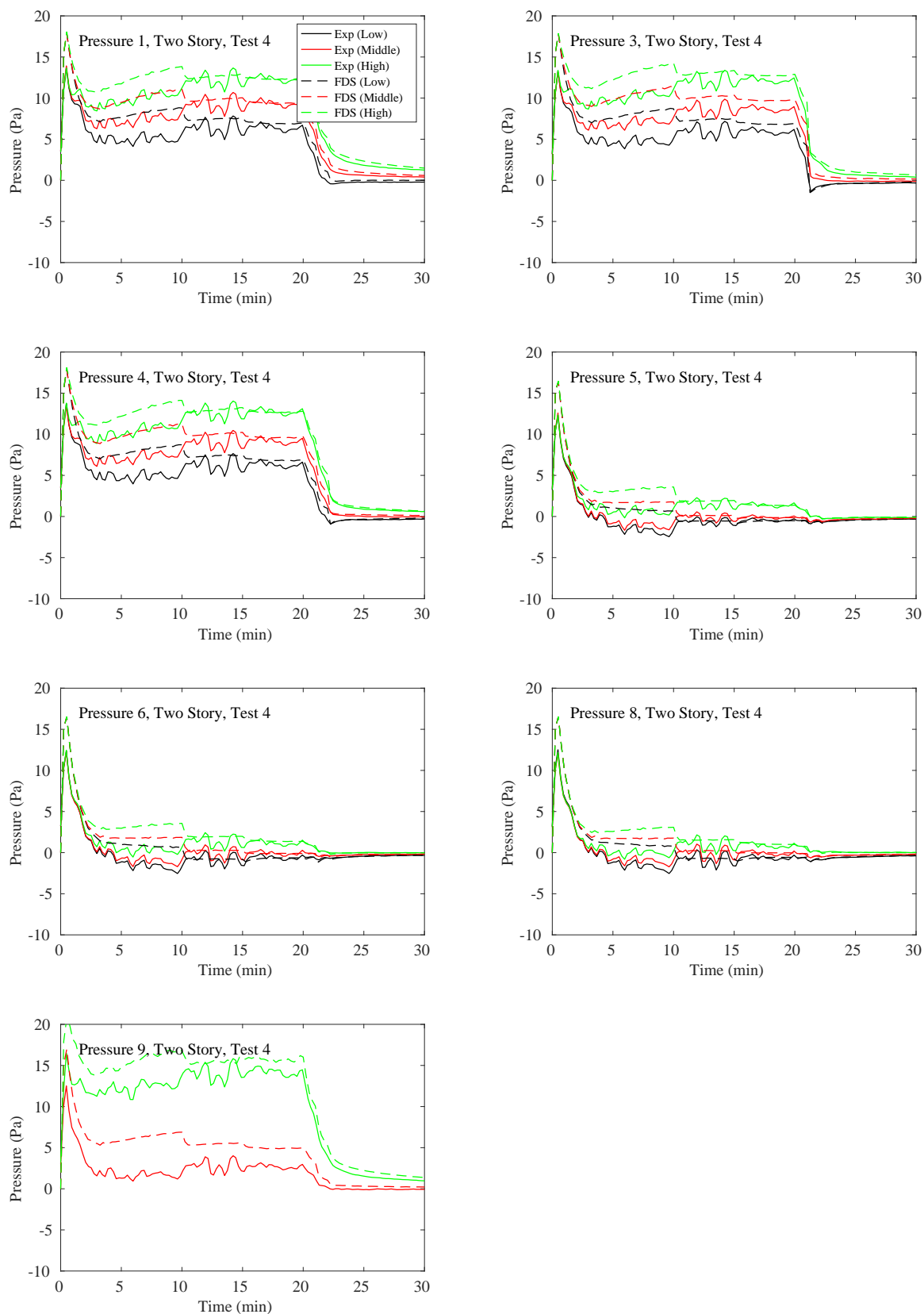


Figure 10.24: UL/NIJ Experiments, Pressure, Two-Story (Colonial) House, Test 4.

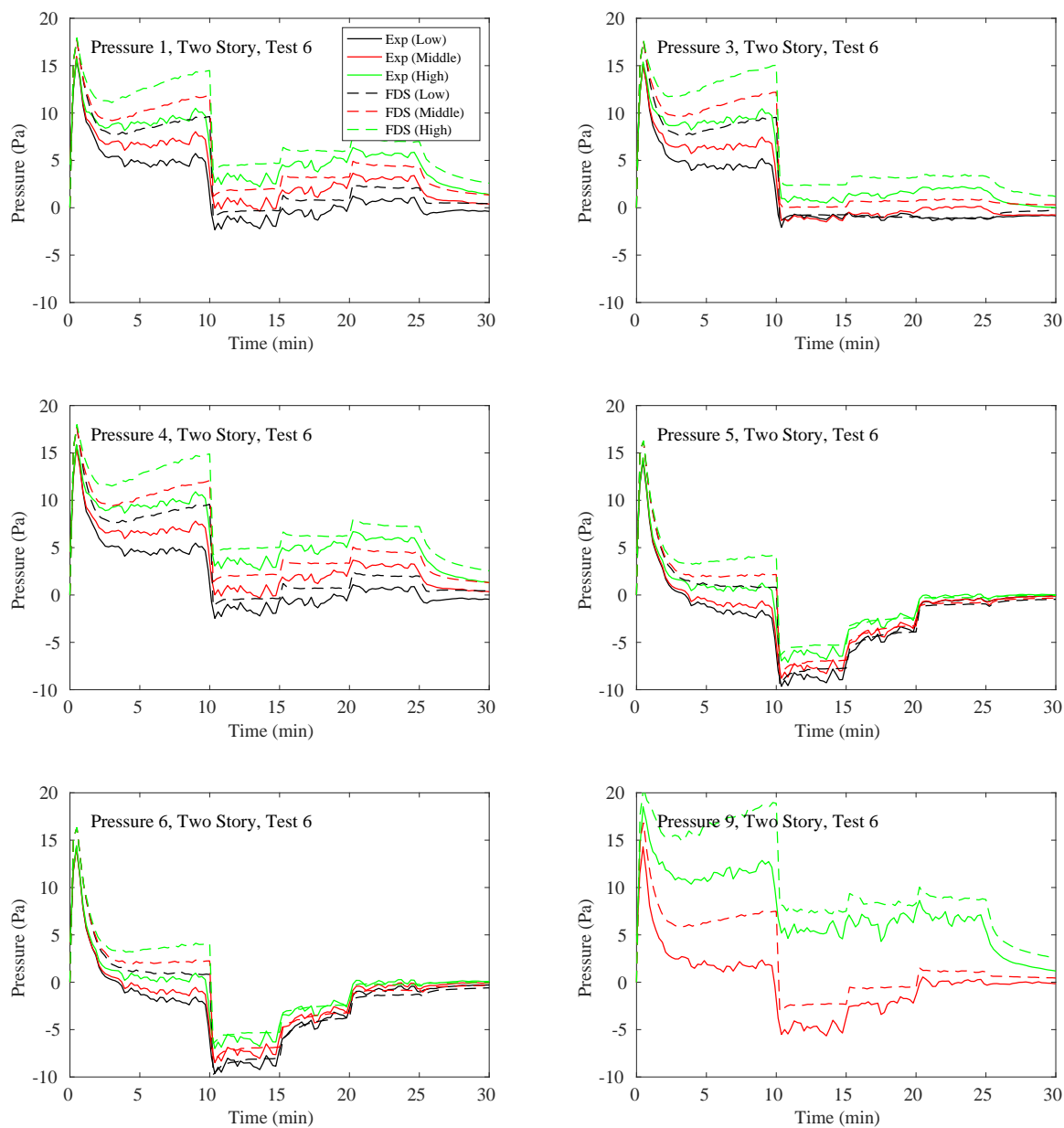


Figure 10.25: UL/NIJ Experiments, Pressure, Two-Story (Colonial) House, Test 6.

10.8 Summary of Pressure Predictions

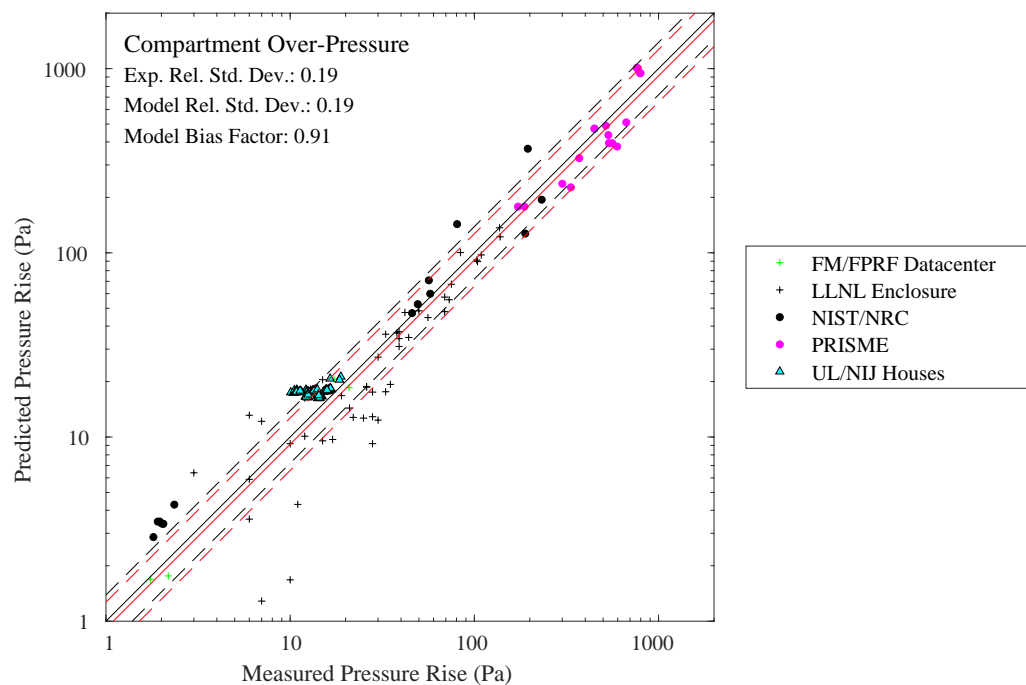


Figure 10.26: Summary of pressure predictions for open and closed compartments.

Chapter 11

Surface Temperature

All solid surfaces in an FDS model are assigned thermal boundary conditions. Heat and mass transfer to and from surfaces is usually handled with empirical correlations, although it is possible to compute directly the heat and mass transfer when performing a Direct Numerical Simulation (DNS). Heat conduction into a solid surface is calculated via a one-dimensional solution of the heat equation in cartesian, cylindrical, or spherical coordinates. The latter two are useful for predicting the thermal response of so-called “targets,” which include structural steel, electrical cables, sensitive equipment, or any type of intervening combustible.

This chapter divides solid surfaces into two major categories – compartment linings (i.e., walls, ceiling, floor) and targets (i.e., anything that is not a wall, ceiling, or floor). The reason for this distinction is that some models treat the two categories differently. In general, FDS does not.

11.1 Wall, Ceiling and Floor Temperatures

11.1.1 FAA Cargo Compartments

Measurements of surface temperature were made at two ceiling locations (denoted A and B in Fig. 7.10). The surface temperature measurements are shown below.

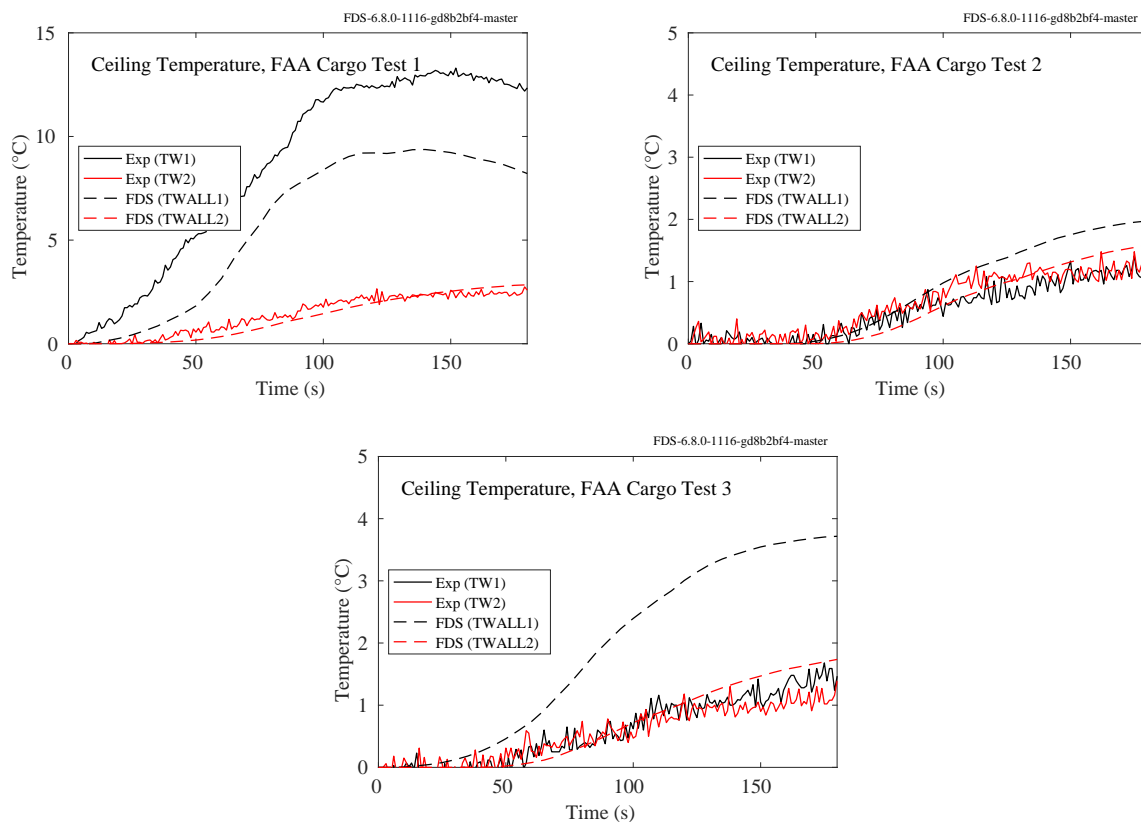


Figure 11.1: FAA Cargo Compartment experiments, ceiling surface temperatures.

11.1.2 NIST Composite Beam

A brief description of the experiments is given in Sec. 3.50. The compartment interior dimensions are 12.4 m long, running east-west, 1.9 m wide, and 3.77 m high. Four experiments with fires were performed, labeled as Tests 2-5. Test 1 did not include a fire.

Figures 11.2 through 11.3 display the under-surface temperature of the steel deck at Sections 3-6. Figures 11.4 through 11.7 display the temperatures of the concrete slab between the concrete and steel deck at Sections 1-8.

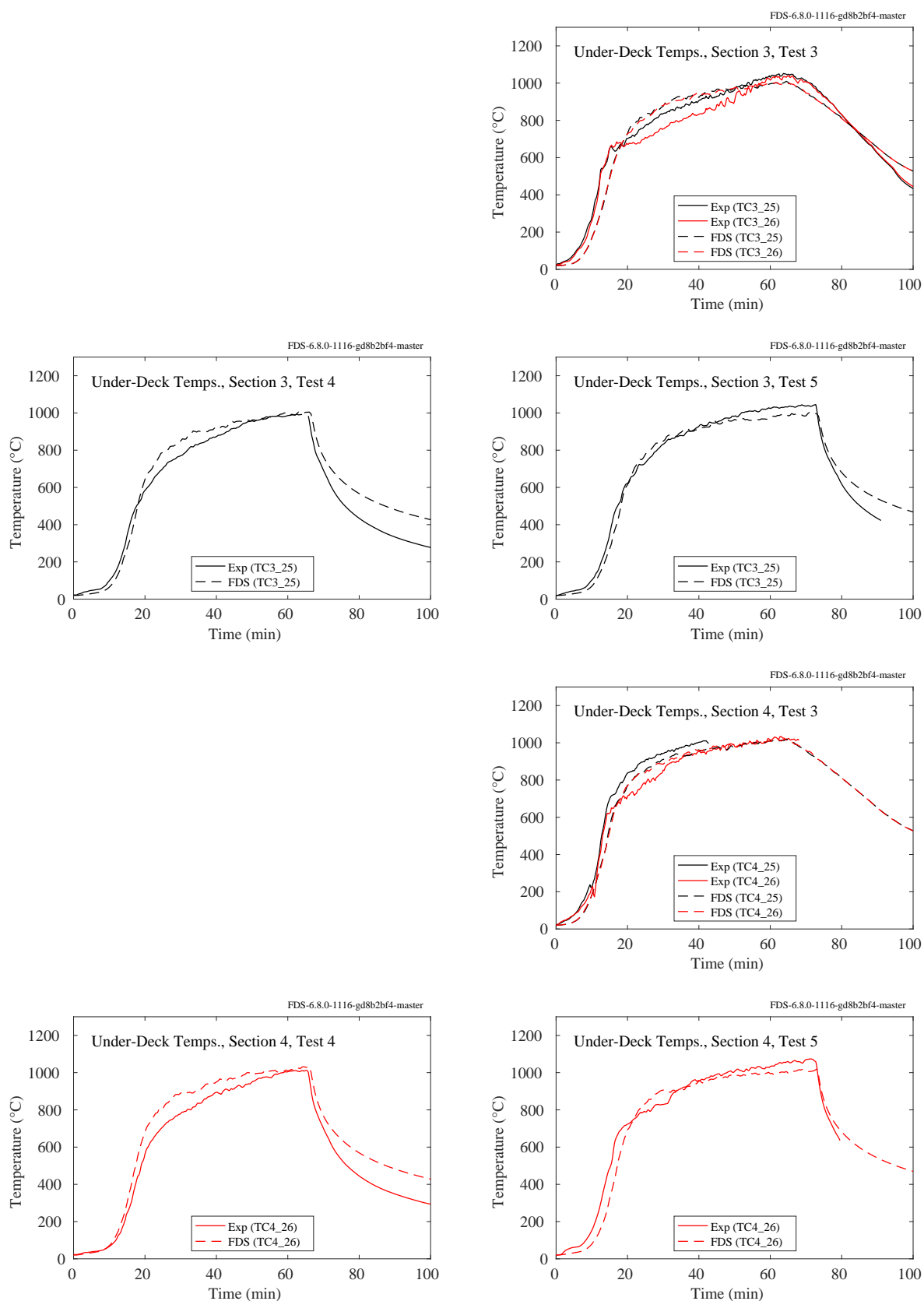


Figure 11.2: NIST Composite Beam, under-deck temperatures, Sections 3 and 4.

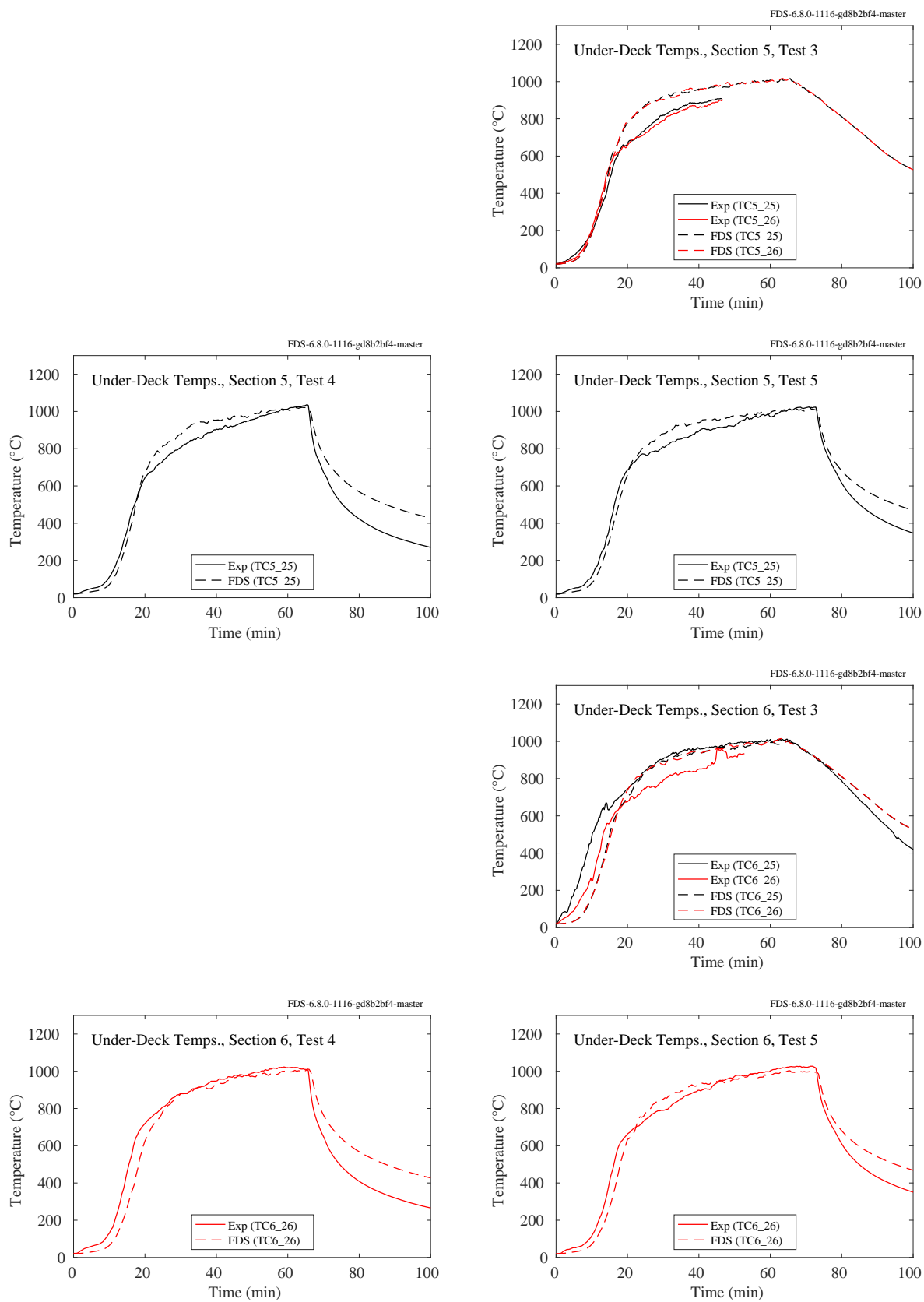


Figure 11.3: NIST Composite Beam, under-deck temperatures, Sections 5 and 6.

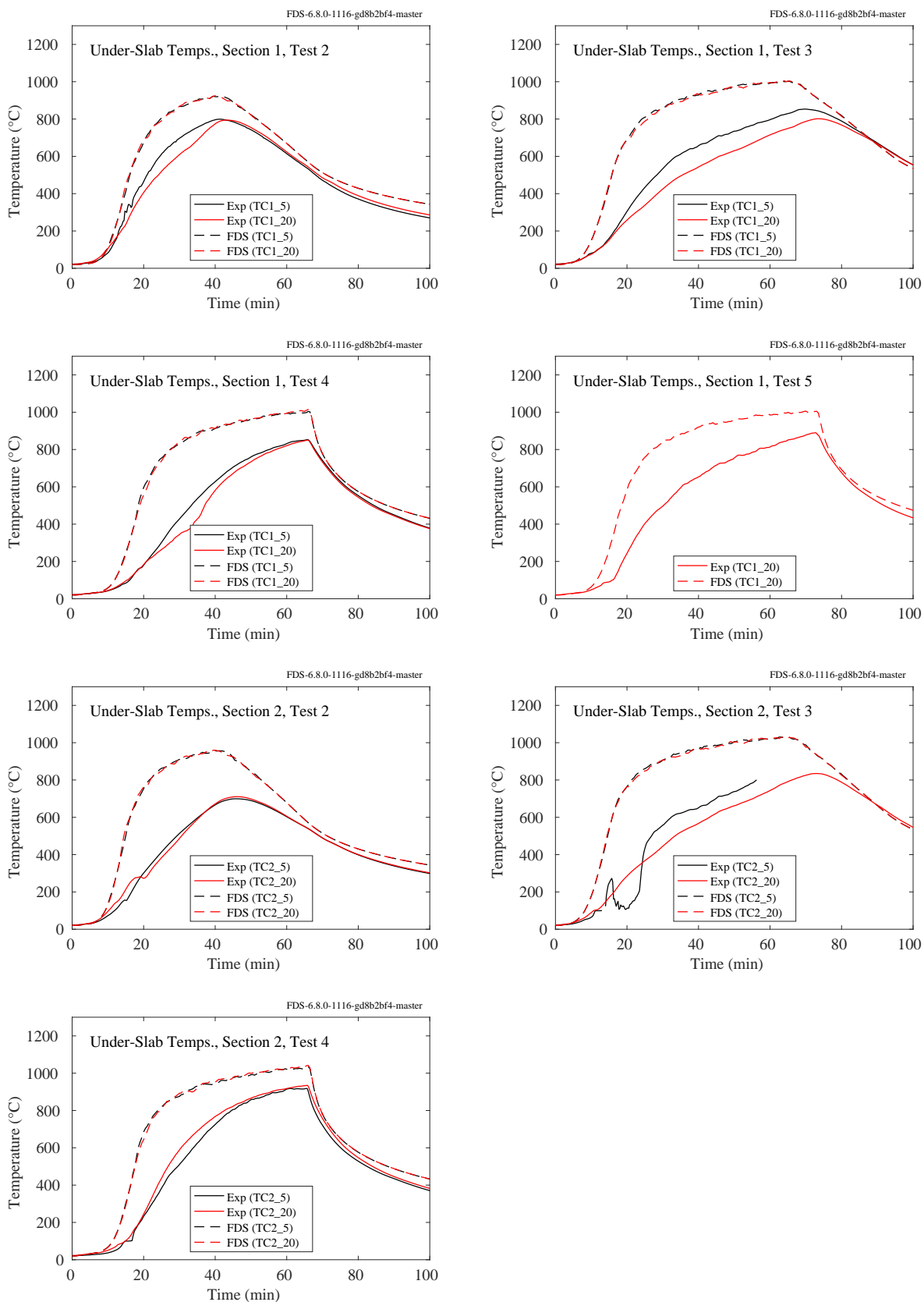


Figure 11.4: NIST Composite Beam, inside-deck temperatures, Sections 1 and 2.

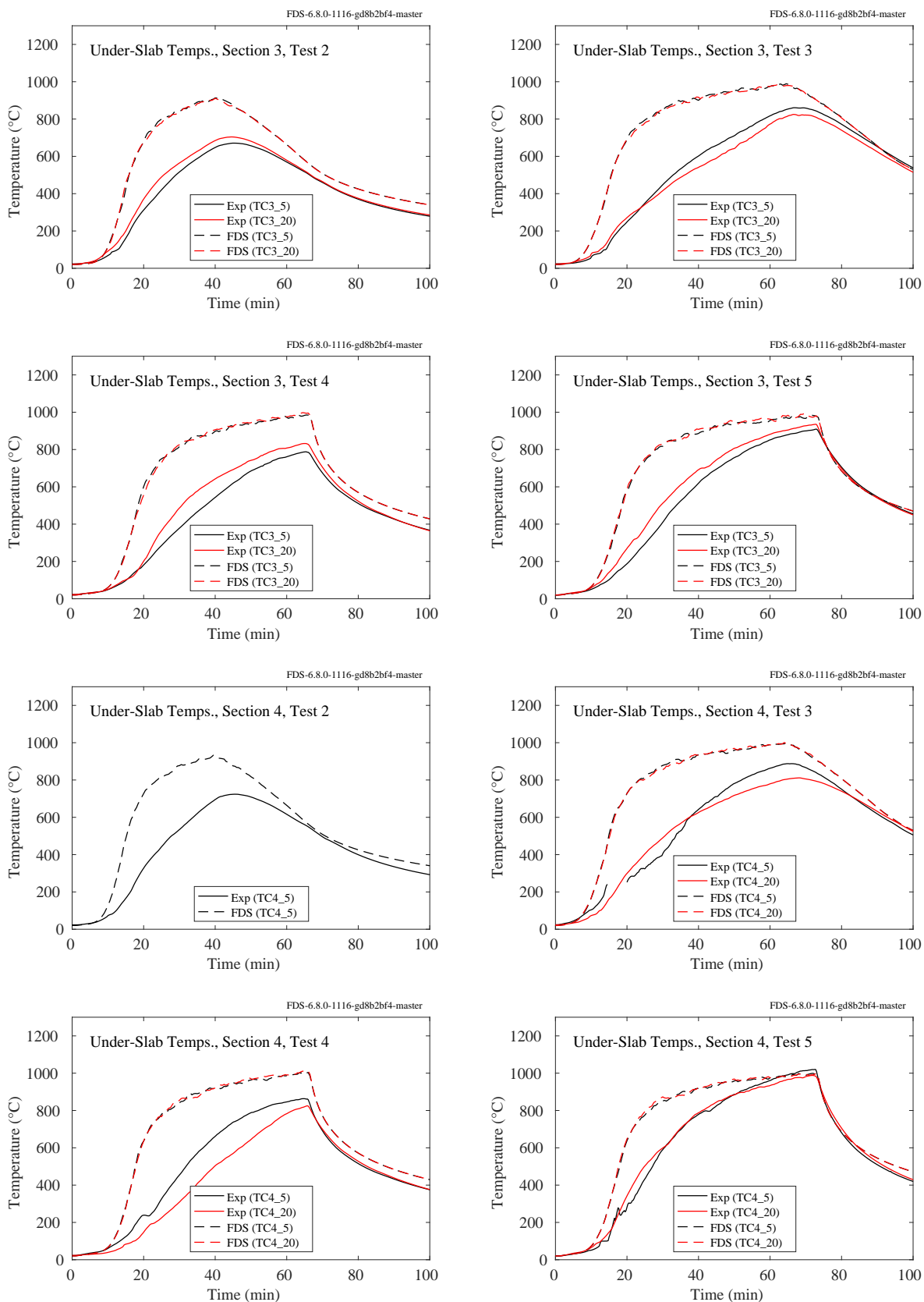


Figure 11.5: NIST Composite Beam, inside-deck temperatures, Sections 3 and 4.

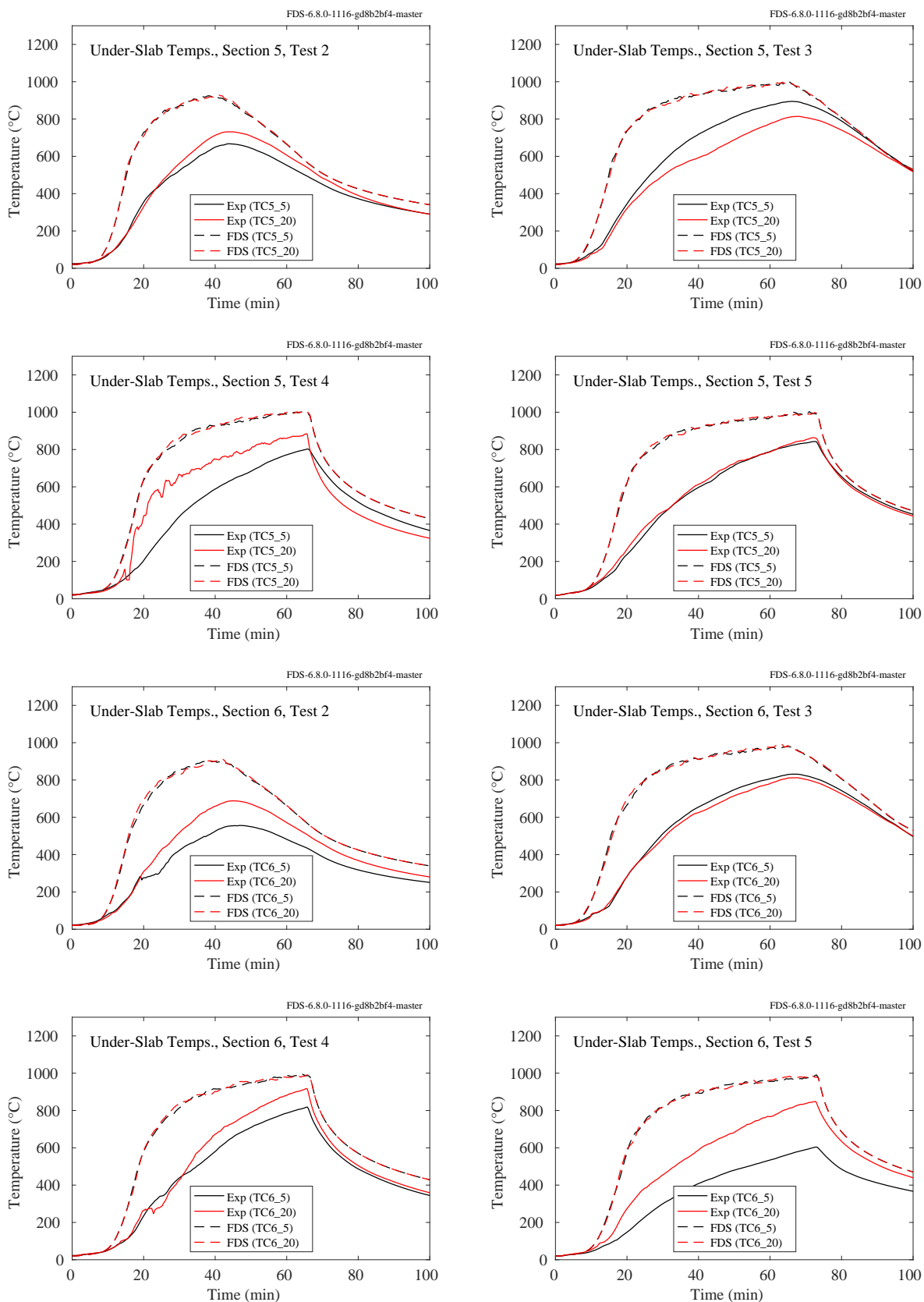


Figure 11.6: NIST Composite Beam, inside-deck temperatures, Sections 5 and 6.

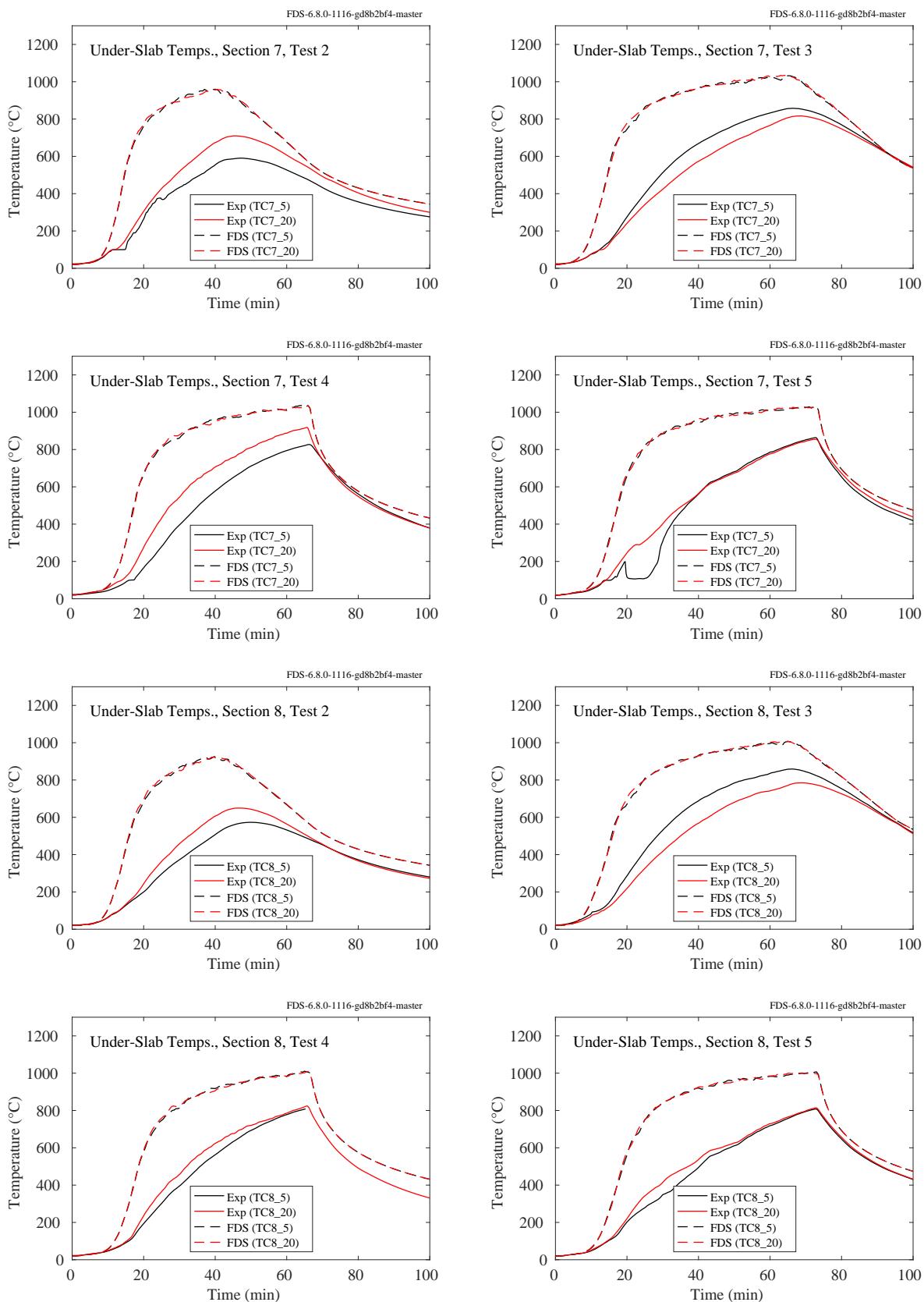


Figure 11.7: NIST Composite Beam, inside-deck temperatures, Sections 7 and 8.

11.1.3 NIST Full-Scale Enclosure (FSE), 2008

Measurements of surface temperature were made at three ceiling and three floor locations in a standard ISO 9705 compartment. In the plots on the following the pages, the ceiling measurements at the rear, center and front of the compartment are denoted by TSHFRCE, TSHFCCE, and TSHFFCE, respectively (Temperature Surface Heat Flux Rear CEiling, etc.). The floor measurements at the rear and front are denoted TSHFRFL and TSHFFFL. The surface temperatures measurements that were made just outside the door were faulty and are not used. All of the floor measurements for the experiment labeled ISOHept8 were faulty.

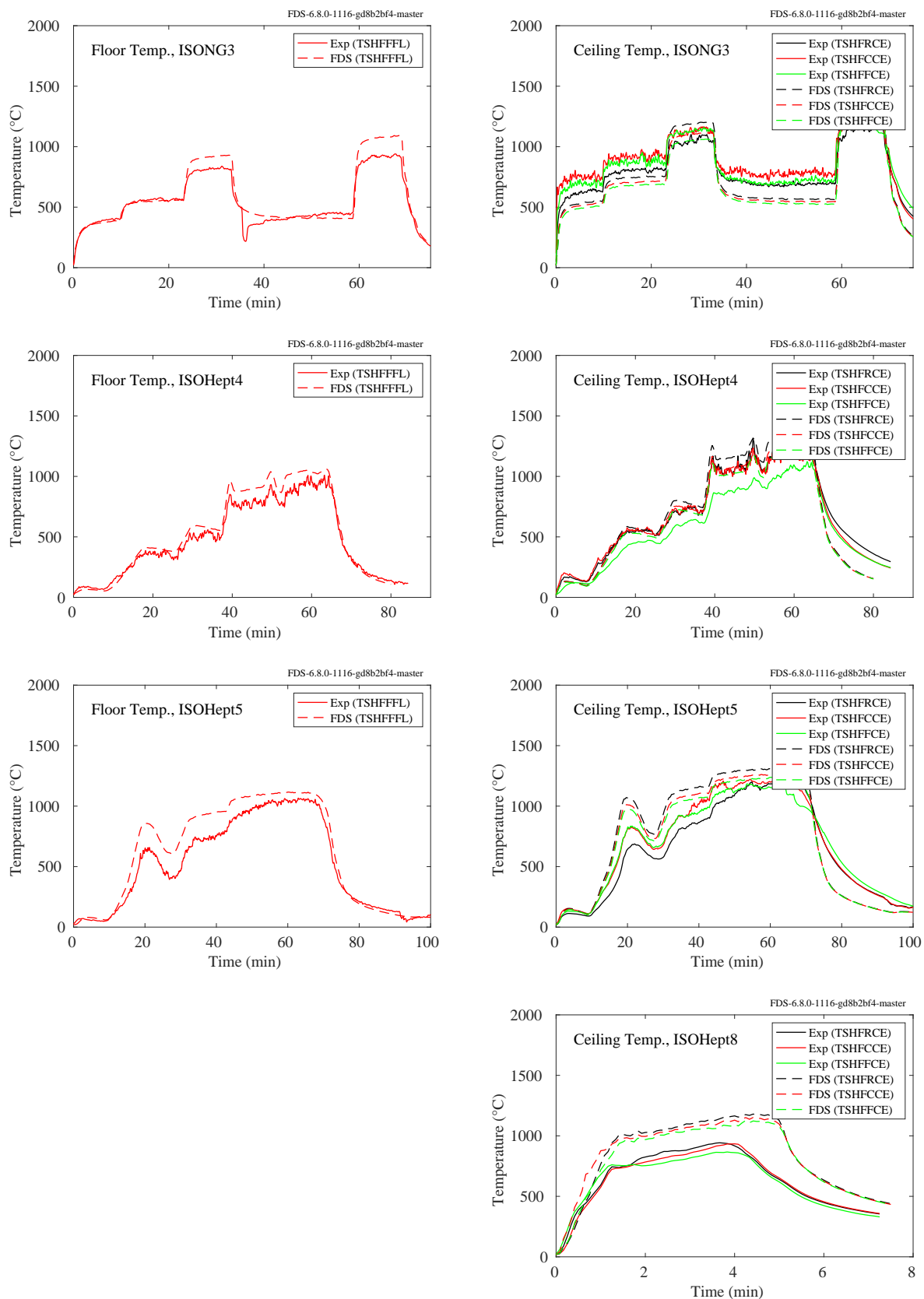


Figure 11.8: NIST FSE experiments, floor and ceiling temperatures, Tests 3-4, 8.

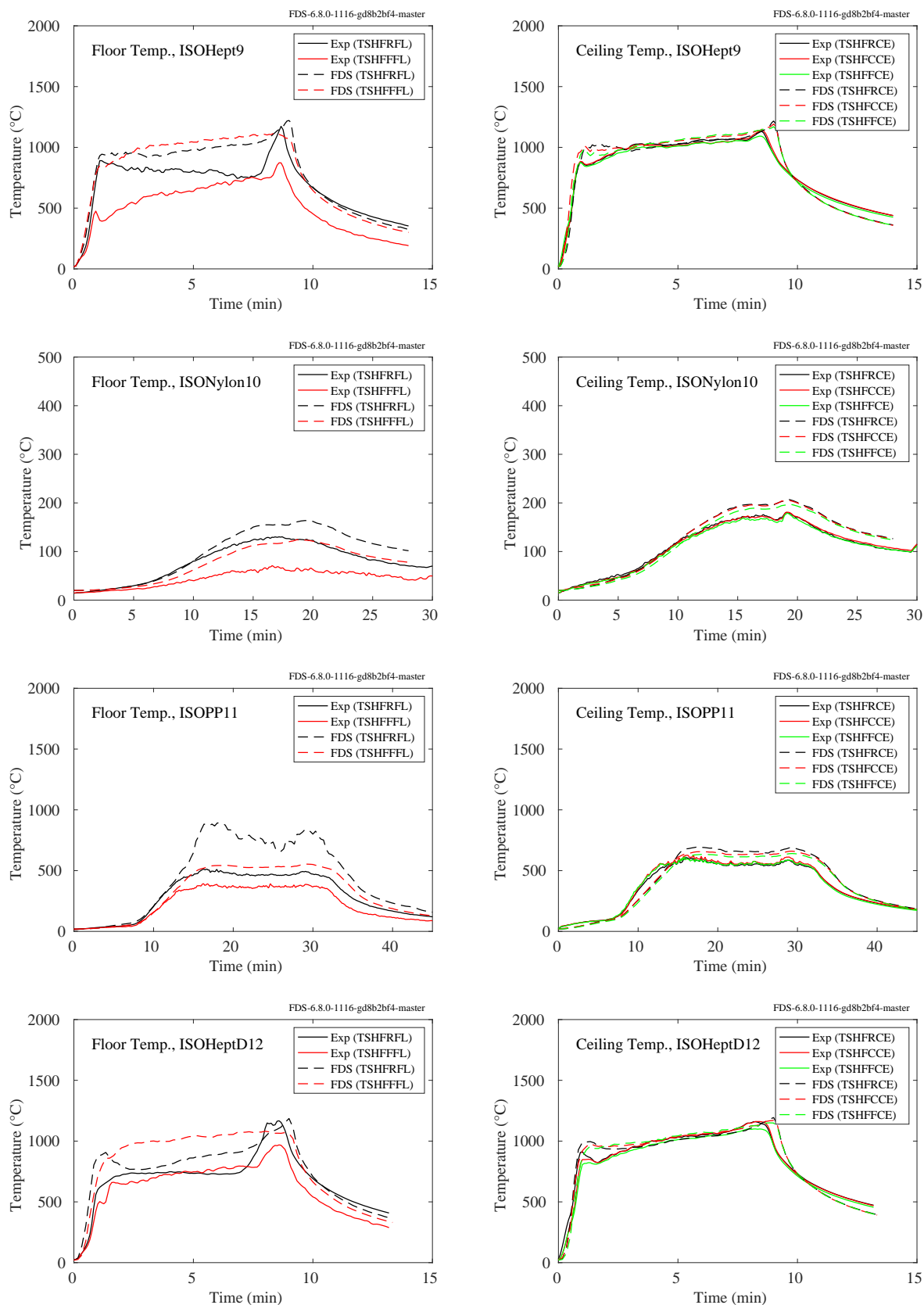


Figure 11.9: NIST FSE experiments, floor and ceiling temperatures, Tests 9-12.

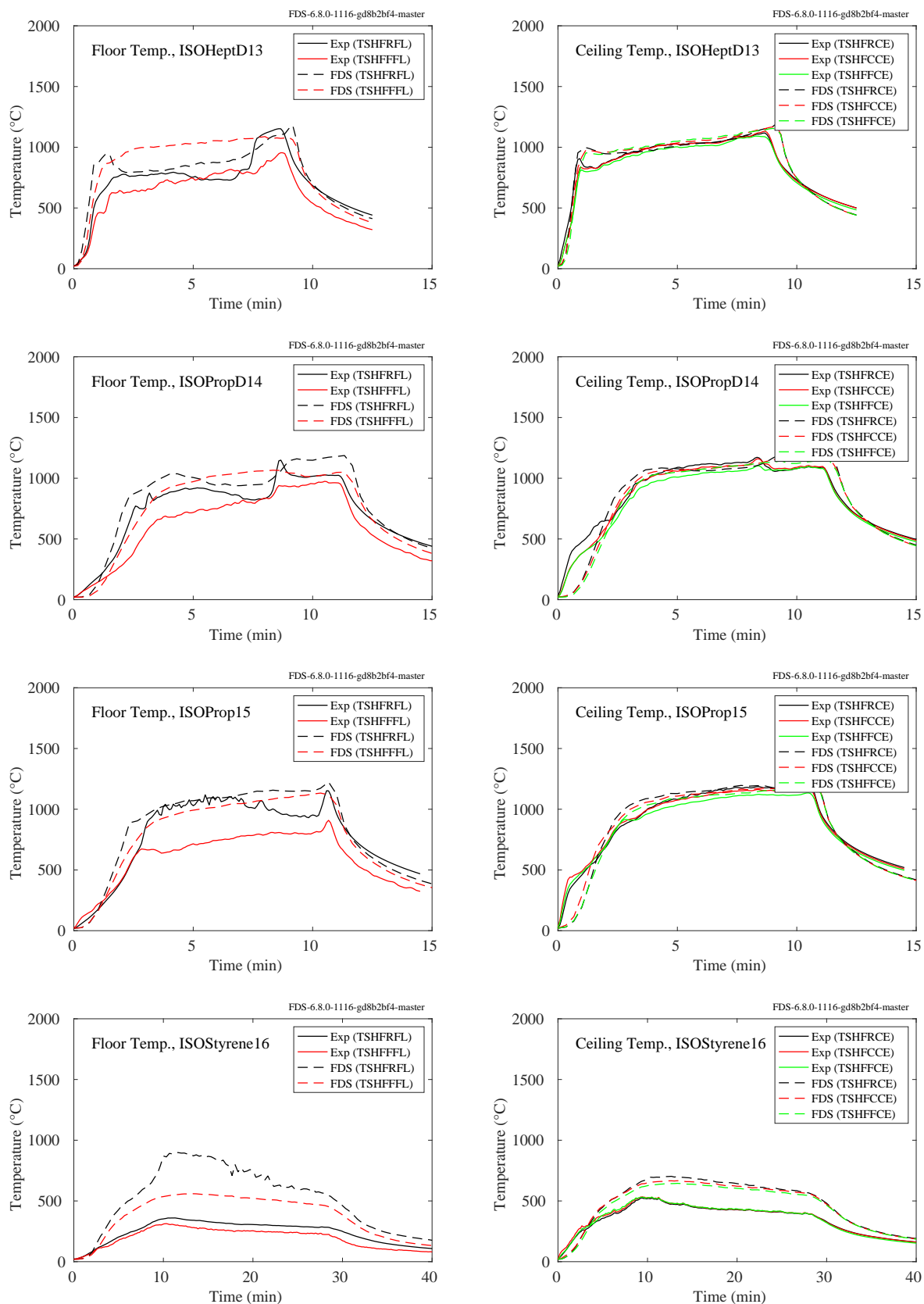


Figure 11.10: NIST FSE experiments, floor and ceiling temperatures, Tests 13-16.

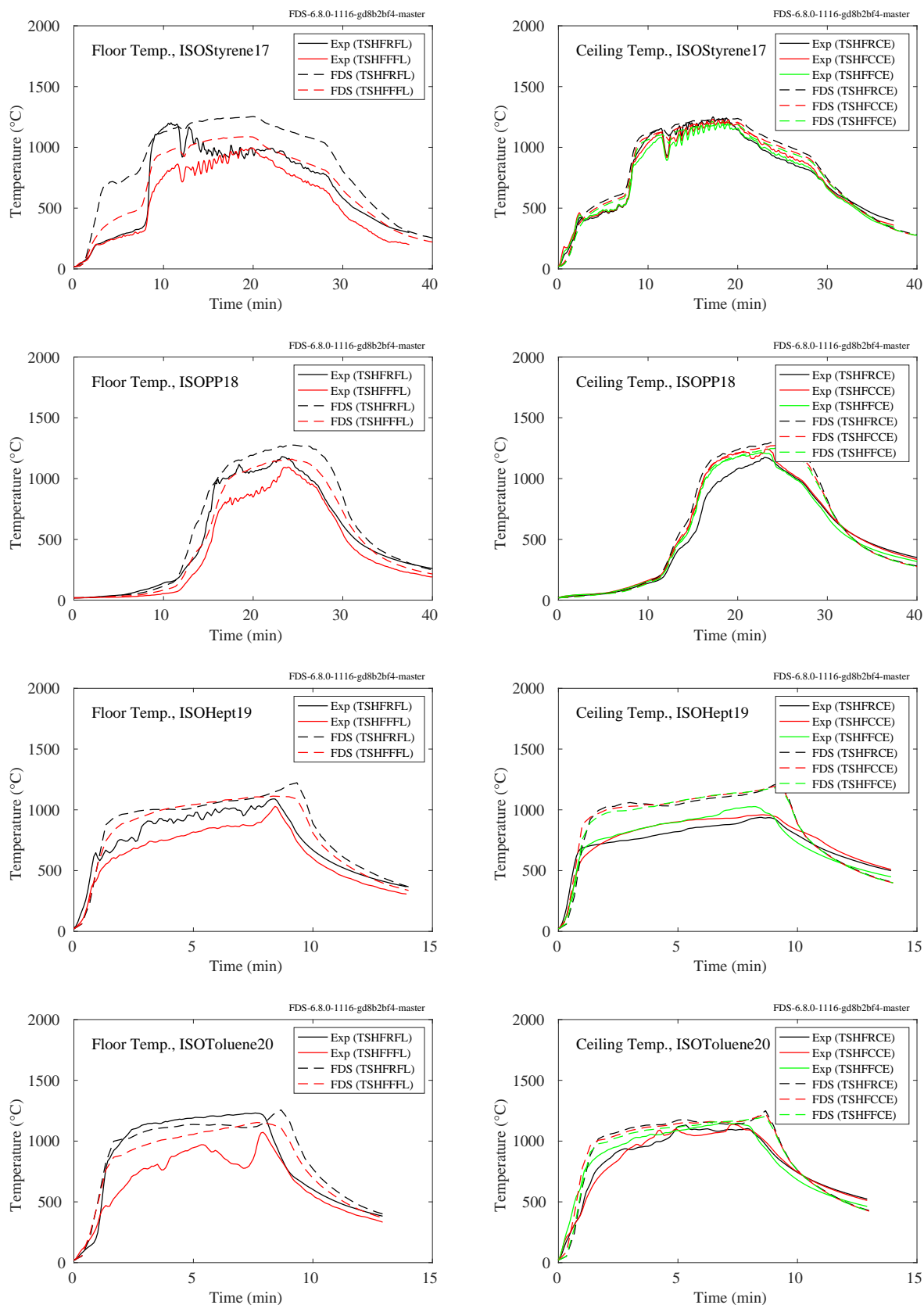


Figure 11.11: NIST FSE experiments, floor and ceiling temperatures, Tests 17-20.

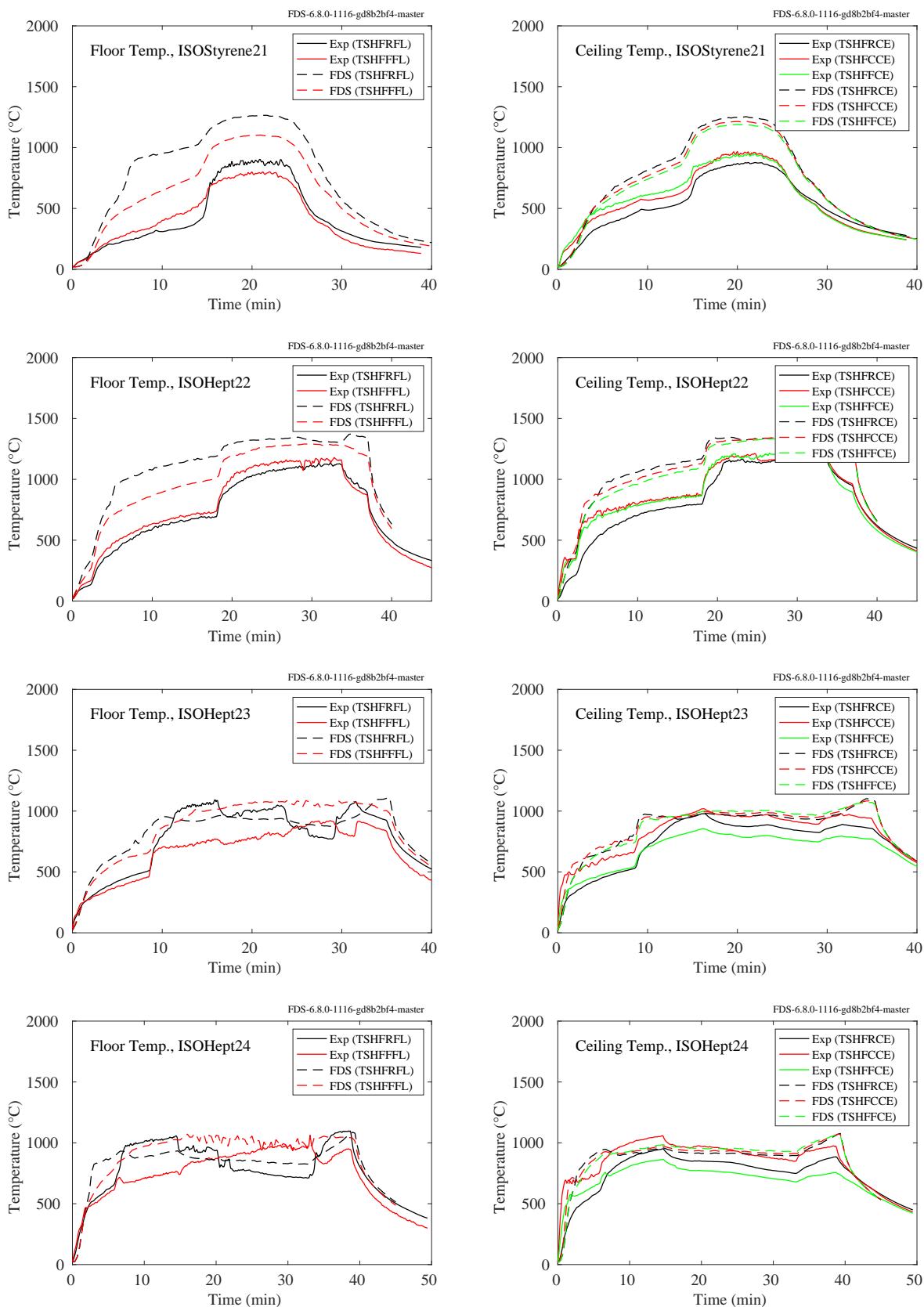


Figure 11.12: NIST FSE experiments, floor and ceiling temperatures, Tests 21-24.

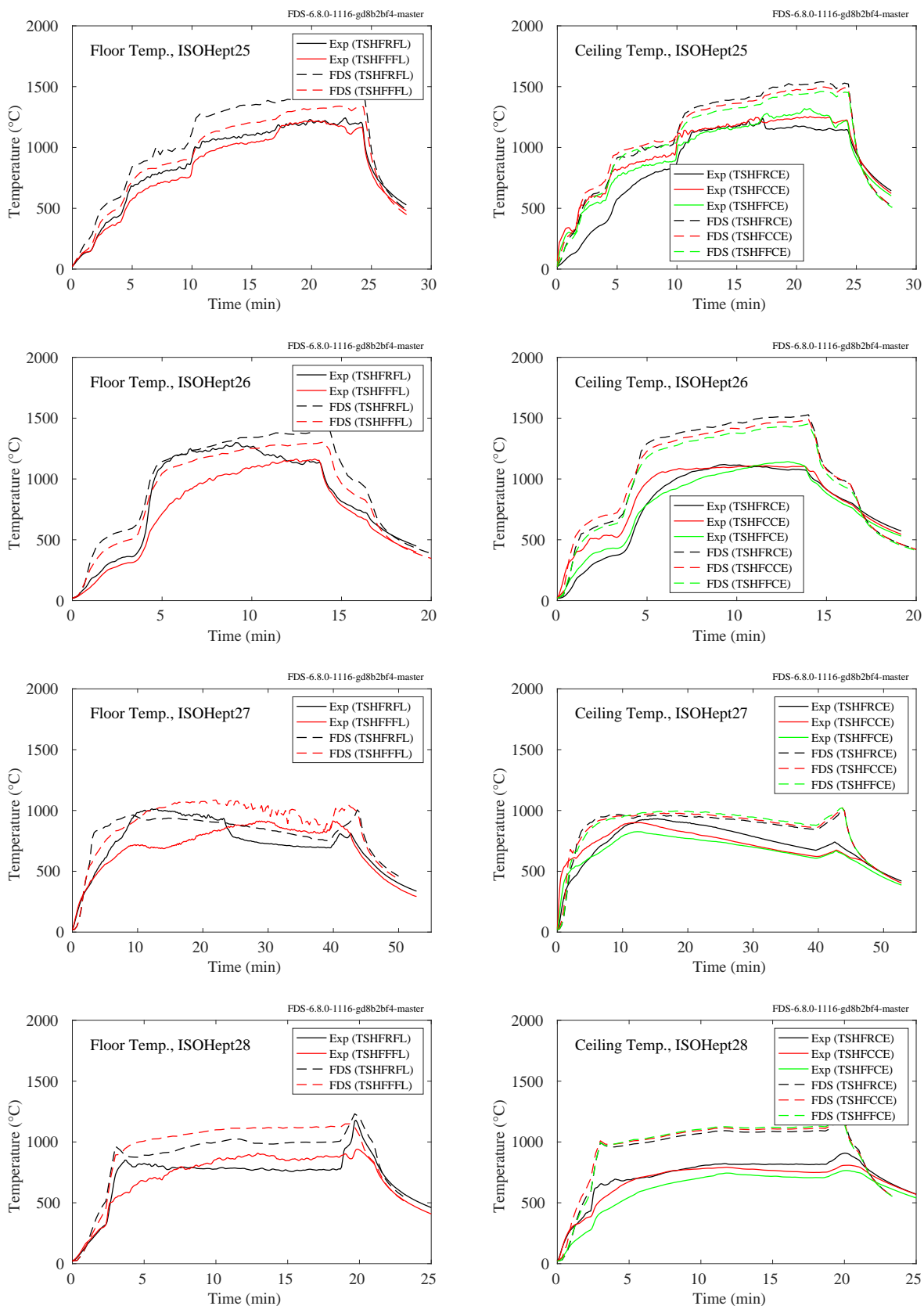


Figure 11.13: NIST FSE experiments, floor and ceiling temperatures, Tests 25-28.

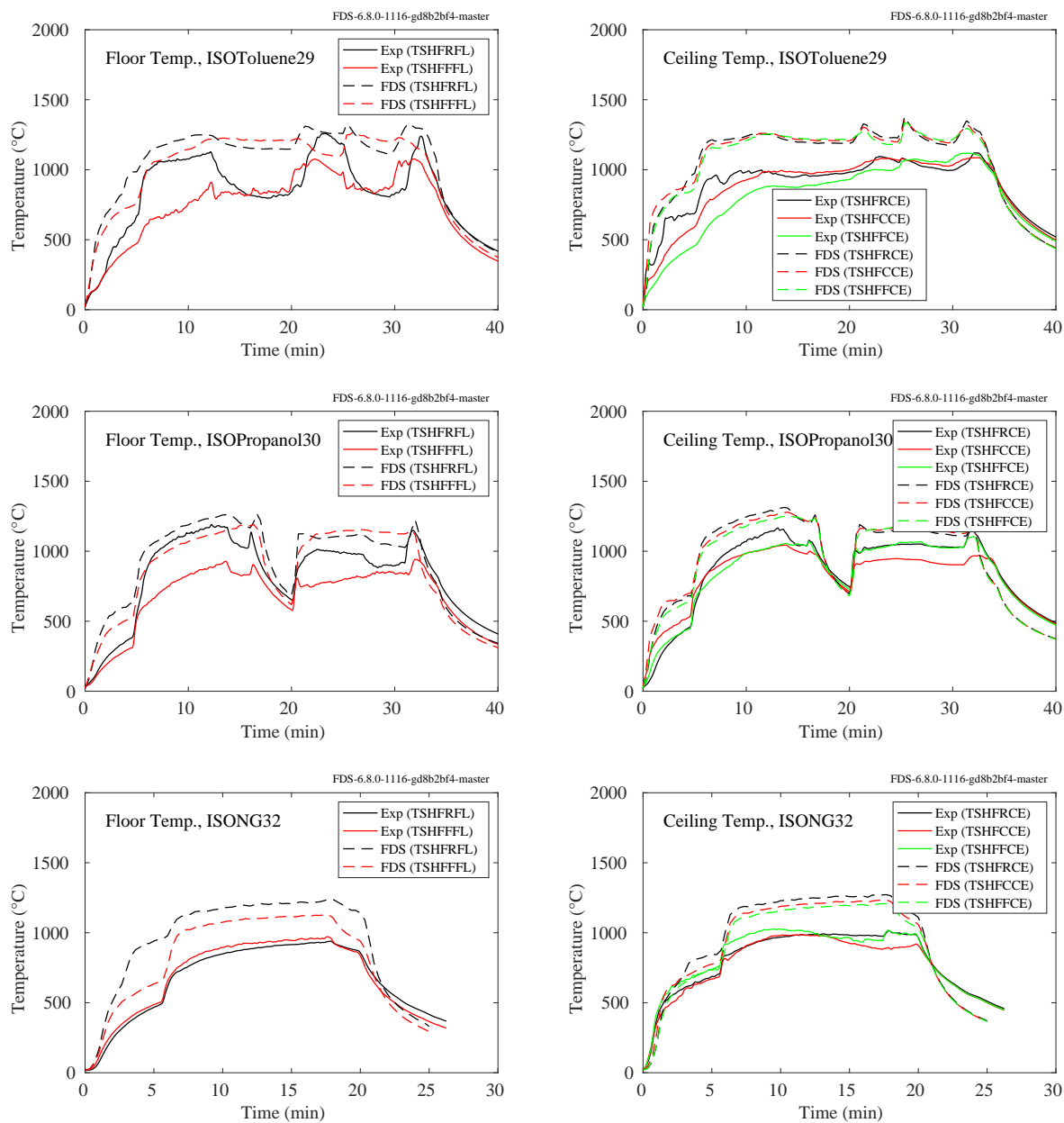


Figure 11.14: NIST FSE experiments, floor and ceiling temperatures, Tests 29, 30, 32.

11.1.4 NIST/NRC Experiments

Thermocouples and heat flux gauges were positioned at various locations on all four walls of the test compartment, plus the ceiling and floor. Comparisons between measured and predicted surface temperatures are shown on the following pages. Over the course of 15 experiments, a number of the thermocouples and gauges failed, but because over half of the measurement points were in roughly the same relative location to the fire, the faulty data was discarded based on examining replicate experiments or locations on the opposite wall. Note that Position 8 for the floor and ceiling is not used, simply because the plotting routine is limited to 7 distinct colors and Position 8 is on the opposite side of the compartment to Position 1. Table 11.1 lists the locations for each test.

Table 11.1: Wall thermocouple and heat flux gauge positions for the NIST/NRC series. The origin of the coordinate system lies on the floor in the southwest corner of the compartment. The designation “U” and “C” is irrelevant, and the last digit “2” indicates that the thermocouple is measuring the wall temperature rather than the heat flux gauge temperature.

Name	x	y	z	Name	x	y	z
TC North U-1-2	3.85	7.04	1.49	TC South U-1-2	3.86	0	1.49
TC North U-2-2	3.86	7.04	3.71	TC South U-2-2	3.86	0	3.82
TC North U-3-2	9.48	7.04	1.86	TC South U-3-2	9.54	0	1.86
TC North U-4-2	12.07	7.04	1.88	TC South U-4-2	12.08	0	1.86
TC North U-5-2	17.69	7.04	1.49	TC South U-5-2	17.69	0	1.50
TC North U-6-2	17.69	7.04	3.69	TC South U-6-2	17.74	0	3.70
TC East U-1-2	21.66	1.52	1.12	TC West U-1-2	0	1.59	1.12
TC East U-2-2	21.66	1.52	2.40	TC West U-2-2	0	1.59	2.42
TC East U-3-2	21.66	5.68	1.13	TC West U-3-2	0	5.70	1.12
TC East U-4-2	21.66	5.70	2.42	TC West U-4-2	0	5.70	2.42
TC Floor U-1-2	3.08	3.51	0	TC Ceiling U-1-2	3.04	3.60	3.82
TC Floor U-2-2	9.08	1.94	0	TC Ceiling C-2-2	8.99	2.00	3.82
TC Floor U-3-2	9.06	5.97	0	TC Ceiling C-3-2	9.03	5.97	3.82
TC Floor U-4-2	10.86	2.38	0	TC Ceiling C-4-2	10.79	2.38	3.82
TC Floor C-5-2	10.93	5.20	0	TC Ceiling C-5-2	10.79	5.20	3.82
TC Floor U-6-2	13.13	1.99	0	TC Ceiling C-6-2	13.00	2.07	3.82
TC Floor U-7-2	13.00	5.92	0	TC Ceiling C-7-2	12.84	5.98	3.82
TC Floor U-8-2	18.63	3.54	0	TC Ceiling U-8-2	18.71	3.54	3.82

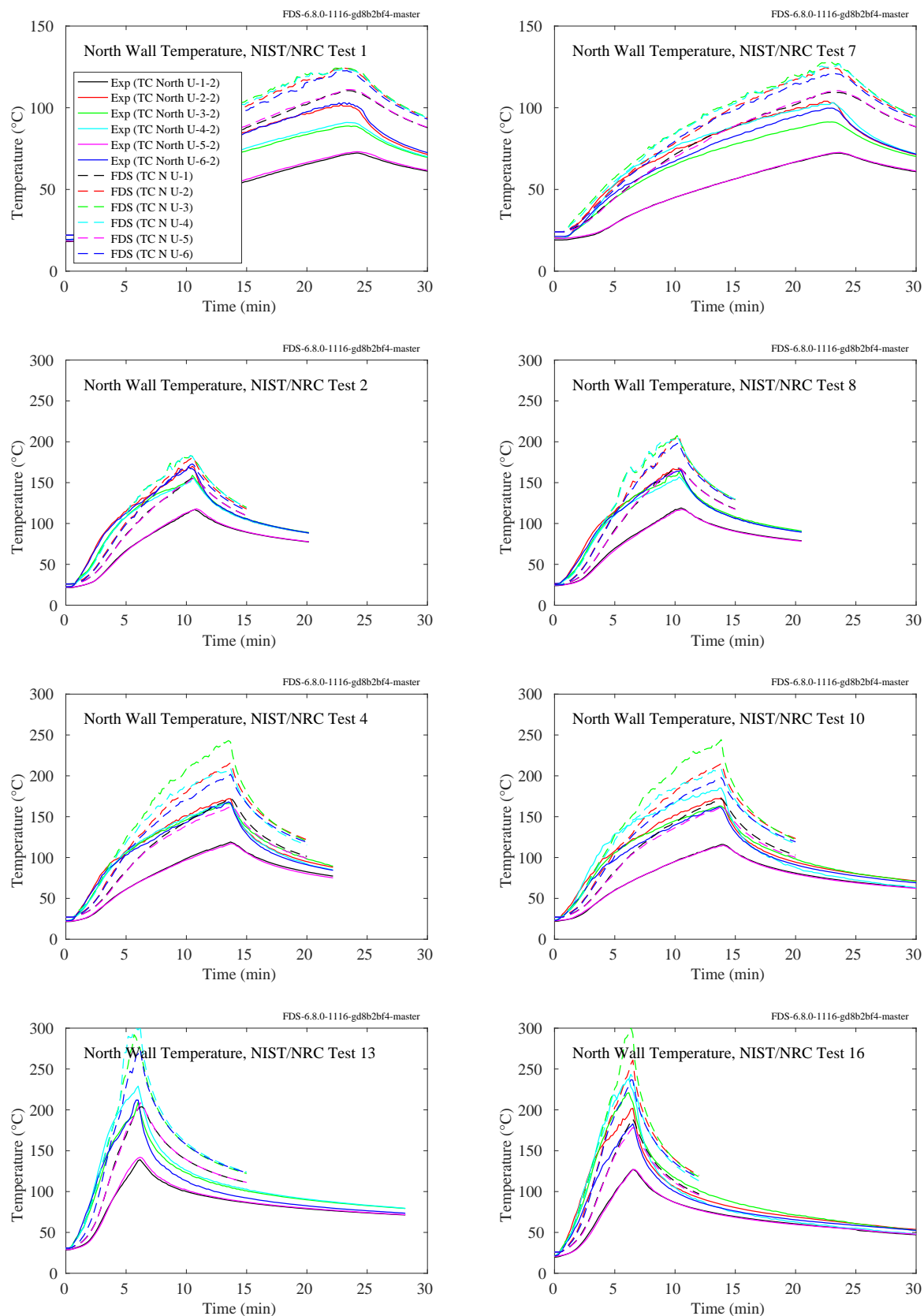


Figure 11.15: NIST/NRC experiments, north wall temperatures, Tests 1, 2, 4, 7, 8, 10, 13, 16.

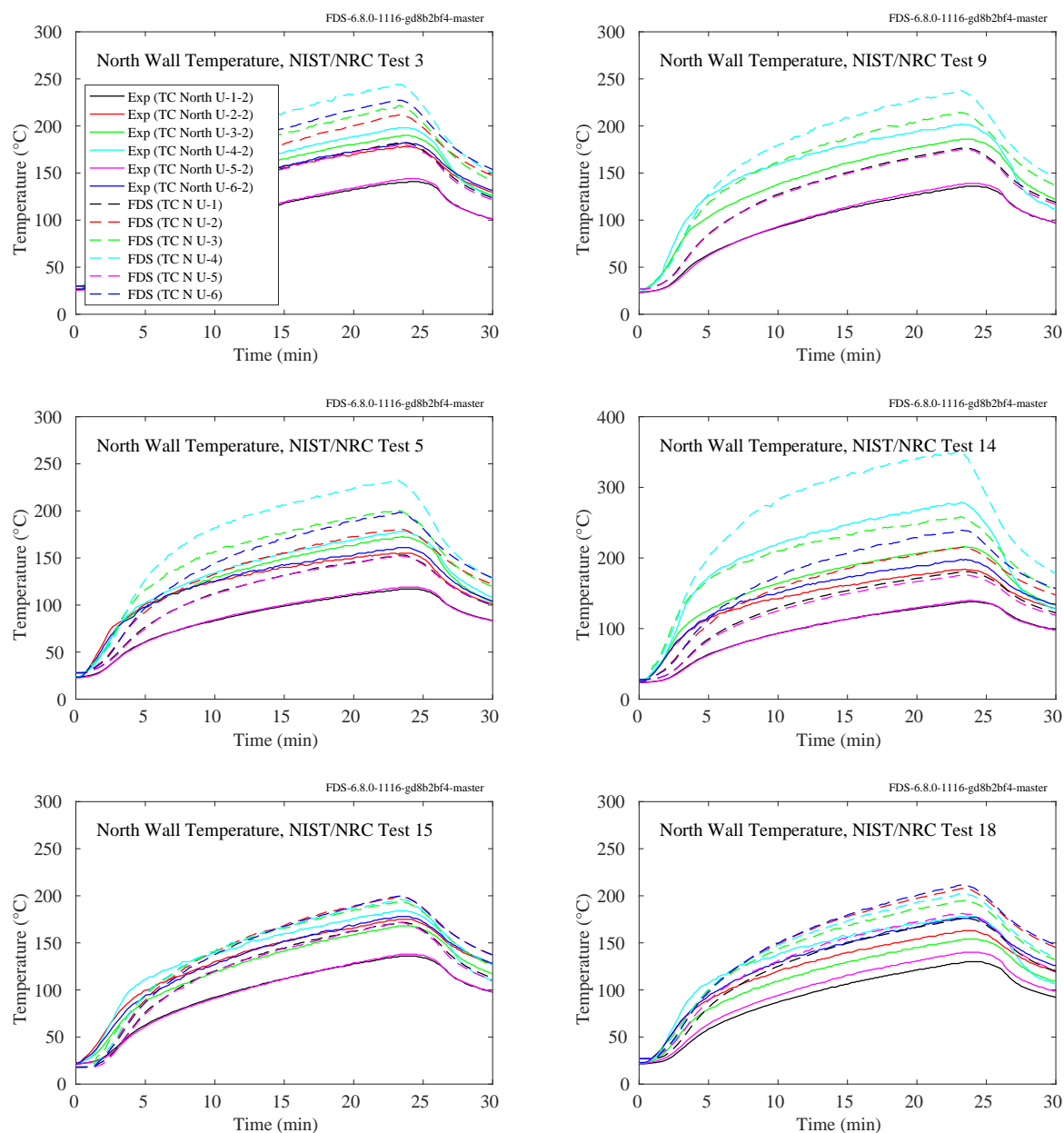


Figure 11.16: NIST/NRC experiments, north wall temperatures, Tests 3, 5, 9, 14, 15, 18.

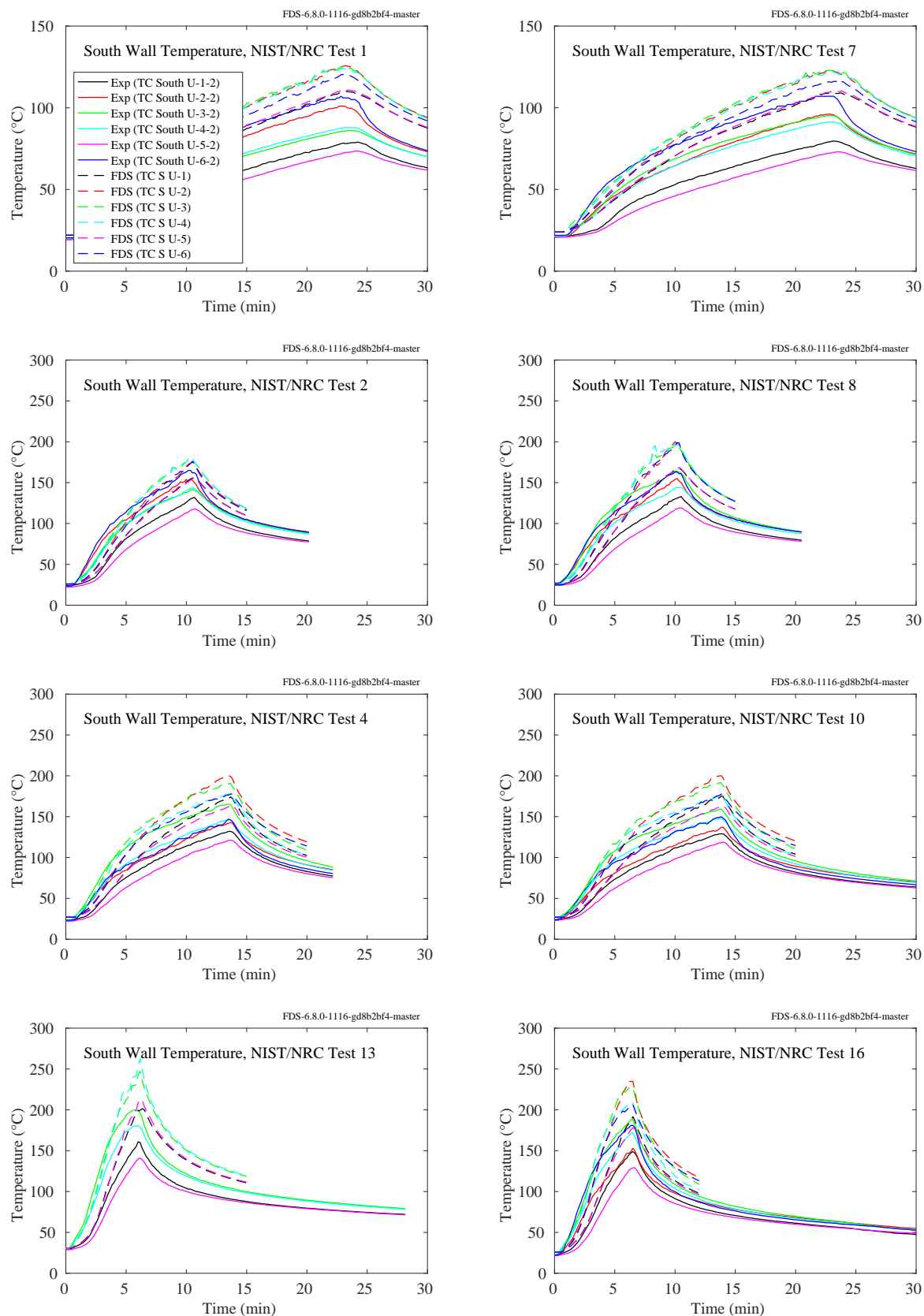


Figure 11.17: NIST/NRC experiments, south wall temperatures, Tests 1, 2, 4, 7, 8, 10, 13, 16.

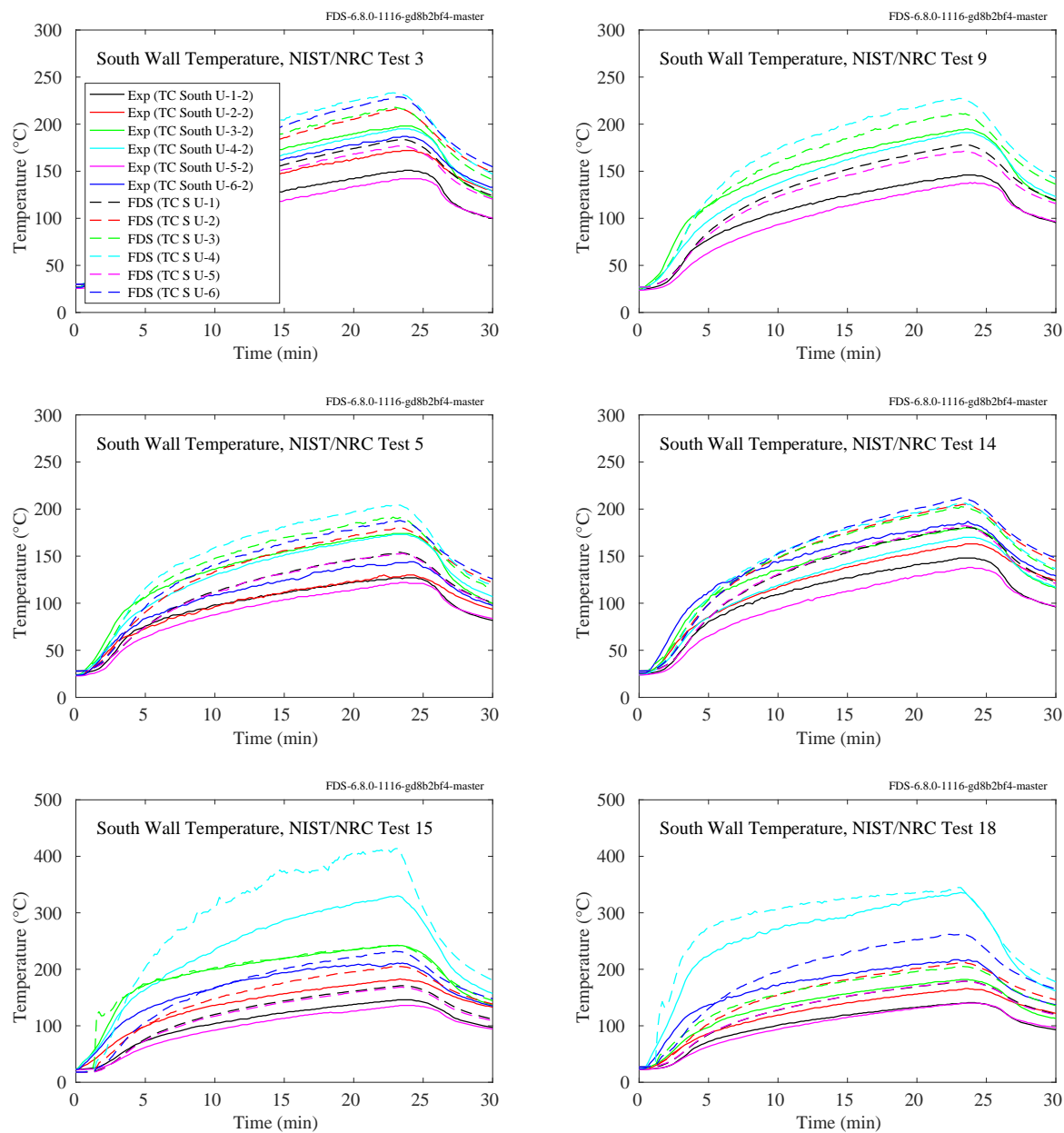


Figure 11.18: NIST/NRC experiments, south wall temperatures, Tests 3, 5, 9, 14, 15, 18.

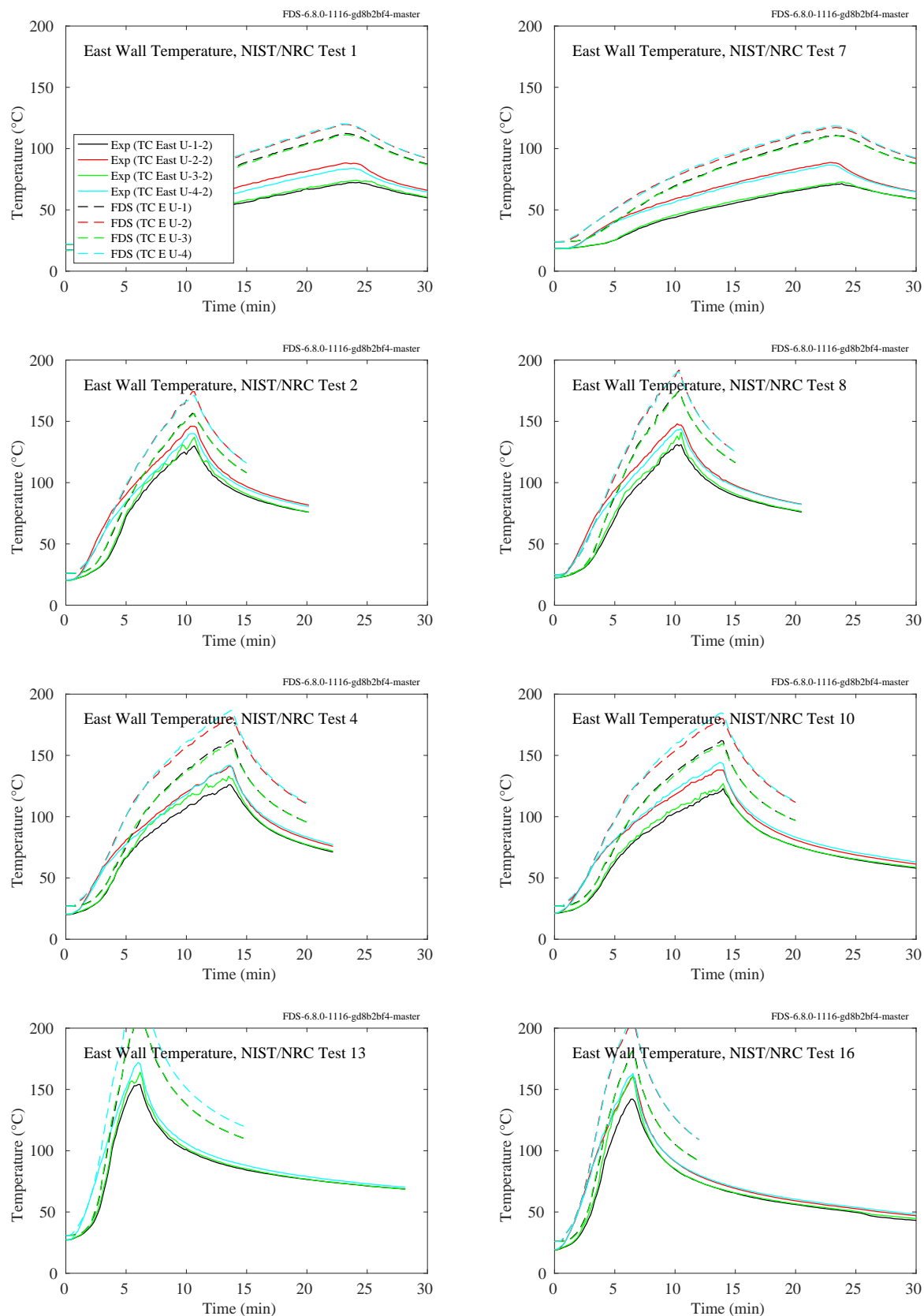


Figure 11.19: NIST/NRC experiments, east wall temperatures, Tests 1, 2, 4, 7, 8, 10, 13, 16.

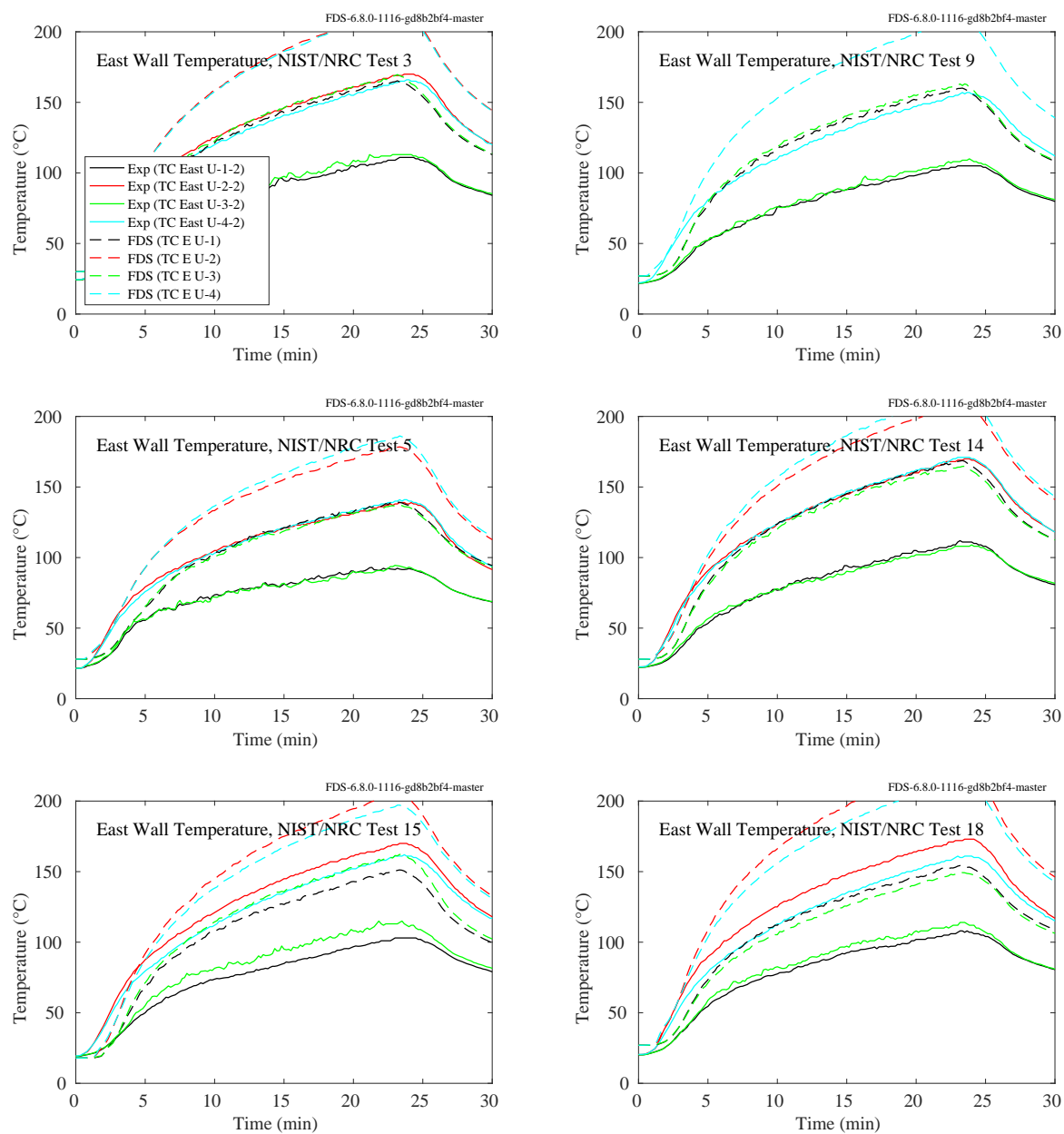


Figure 11.20: NIST/NRC experiments, east wall temperatures, Tests 3, 5, 9, 14, 15, 18.

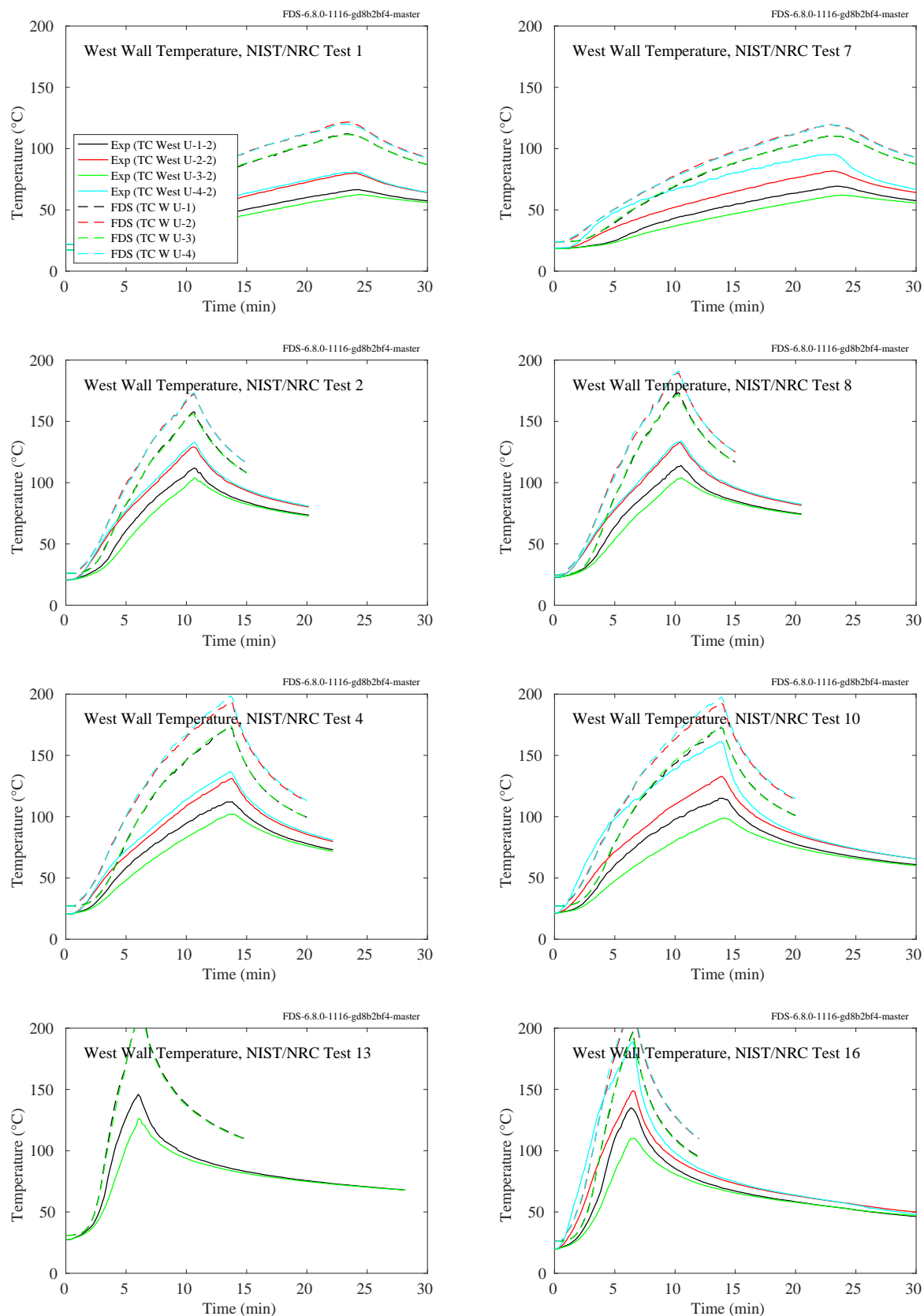


Figure 11.21: NIST/NRC experiments, west wall temperatures, Tests 1, 2, 4, 7, 8, 10, 13, 16.

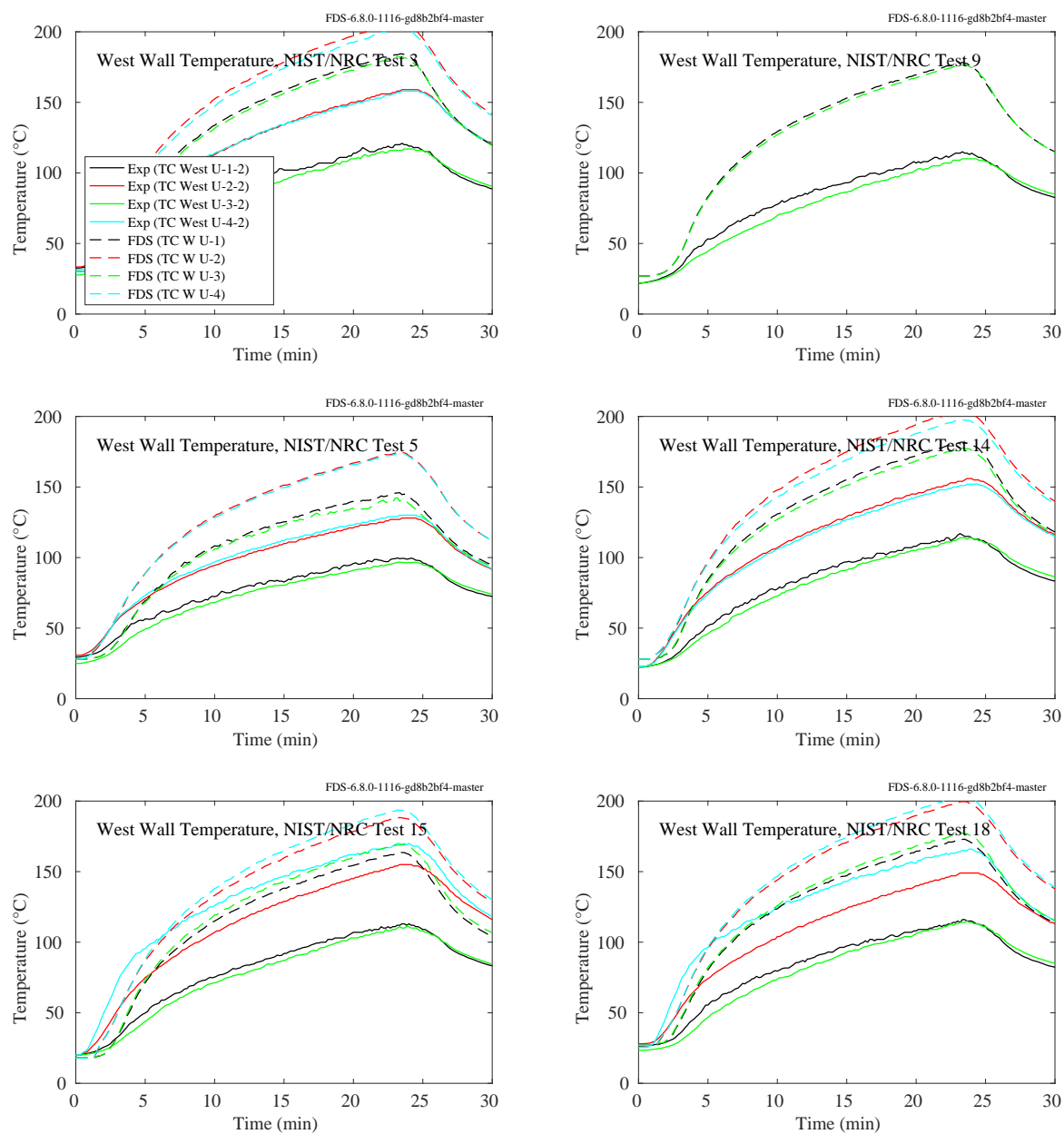


Figure 11.22: NIST/NRC experiments, west wall temperatures, Tests 3, 5, 9, 14, 15, 18.

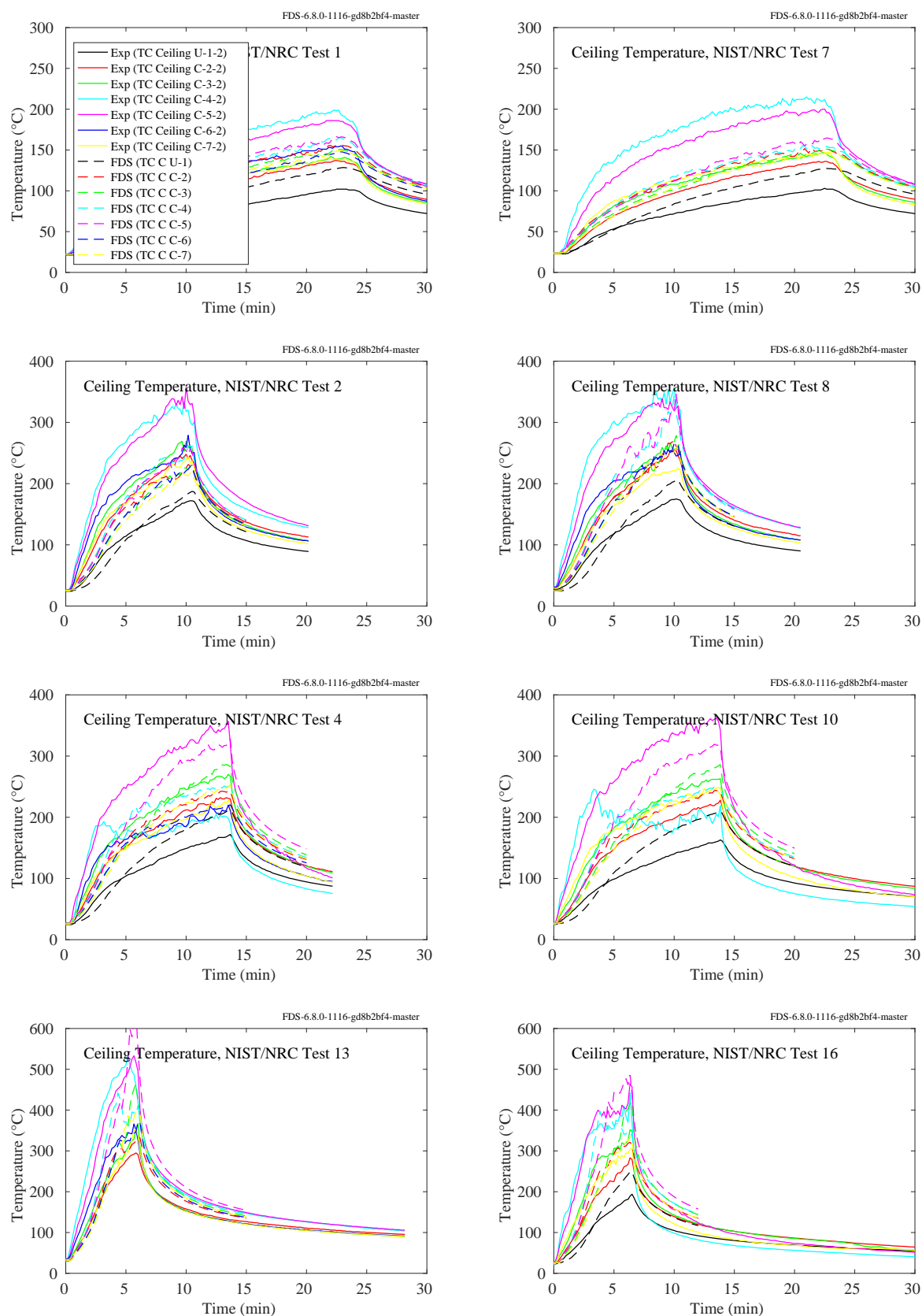


Figure 11.23: NIST/NRC experiments, ceiling temperatures, Tests 1, 2, 4, 7, 8, 10, 13, 16.

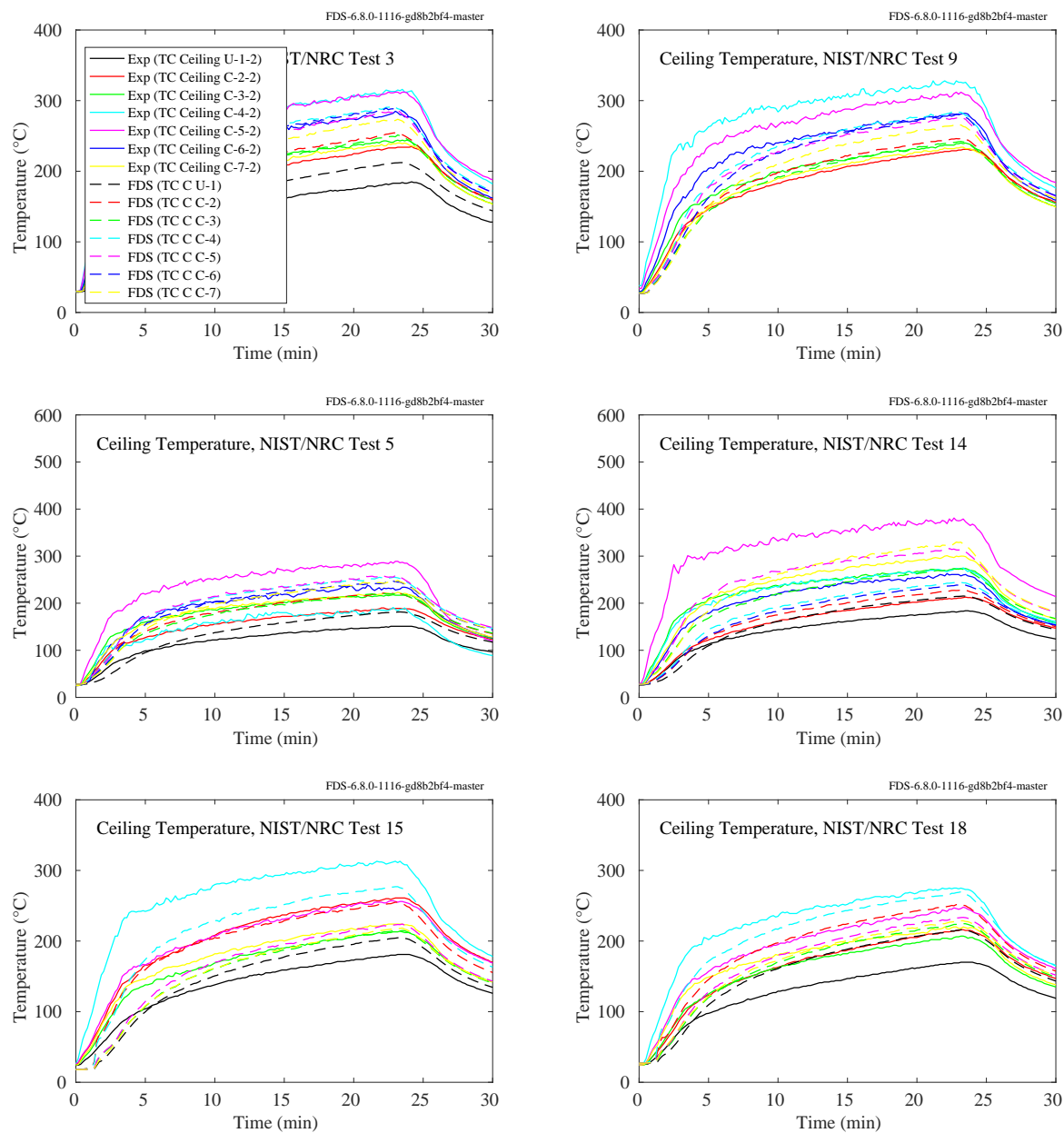


Figure 11.24: NIST/NRC experiments, ceiling temperatures, Tests 3, 5, 9, 14, 15, 18.

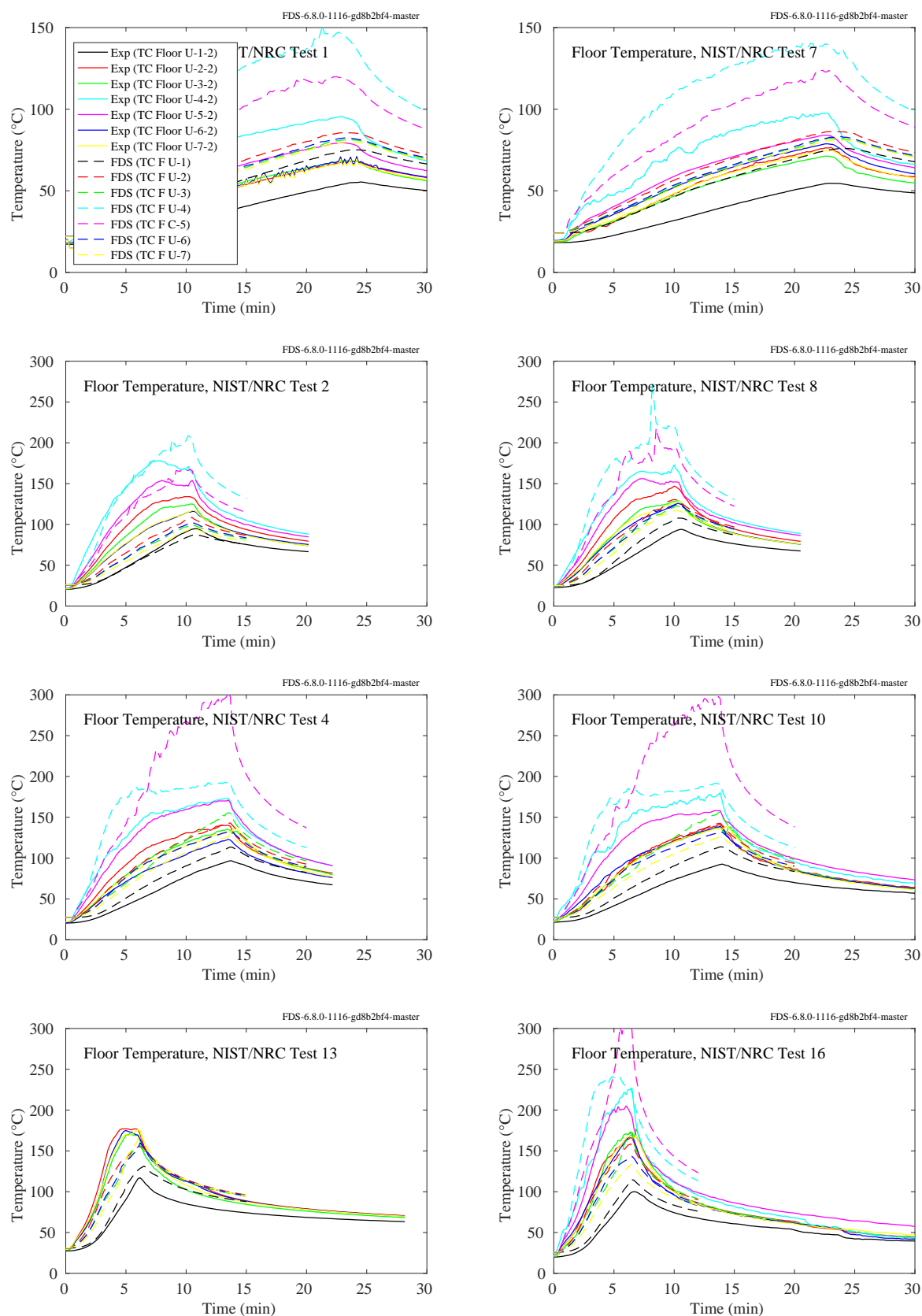


Figure 11.25: NIST/NRC experiments, floor wall temperatures, Tests 1, 2, 4, 7, 8, 10, 13, 16.

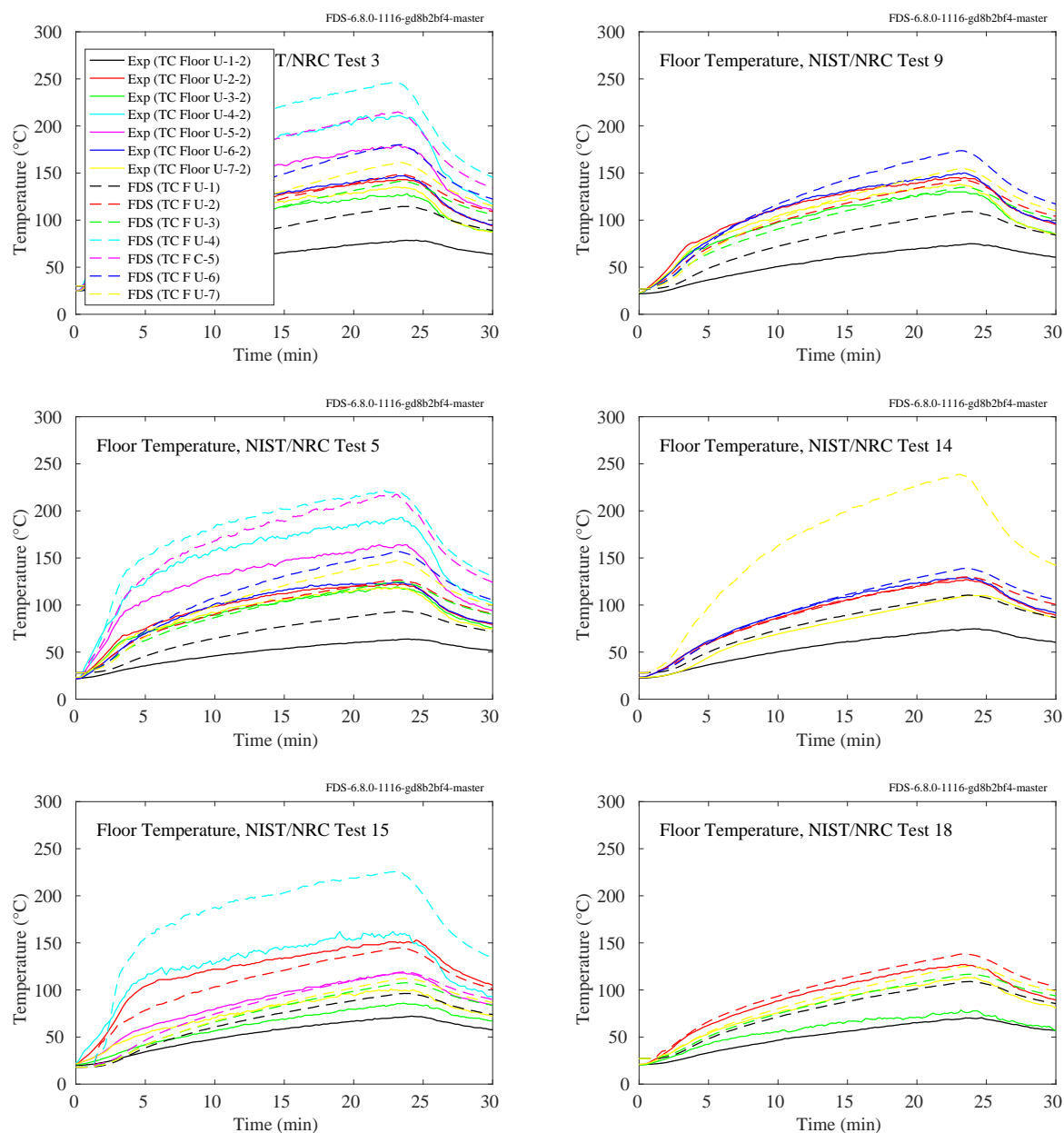


Figure 11.26: NIST/NRC experiments, floor temperatures, Tests 3, 5, 9, 14, 15, 18.

11.1.5 PRISME DOOR Experiments

Thermocouples were positioned at various points on the walls. Each room contained a vertical array labeled, for example, TP_L1_NE265. The TP indicates a surface temperature measurement, L1 indicates compartment 1, which is where the fire was located, NE indicates northeast corner of the room, and 265 indicates the number of centimeters above the floor. In addition, each room contained four measurement points centered on each wall at a height of approximately 260 cm. These points are labeled, for example, TP_L2_SC265, compartment 2, center of south wall, 265 cm high.

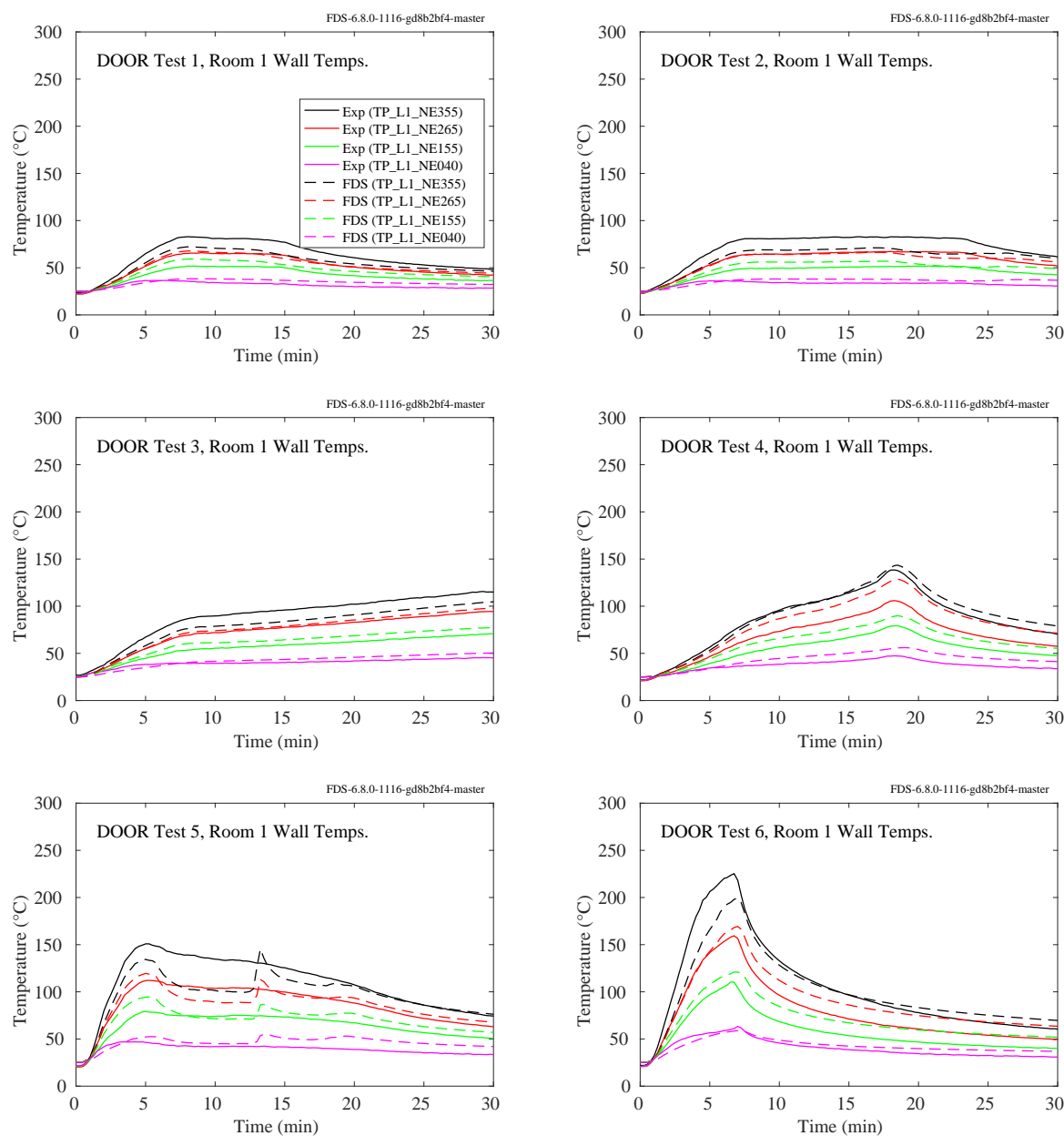


Figure 11.27: PRISME DOOR experiments, wall temperatures, vertical array, Room 1.

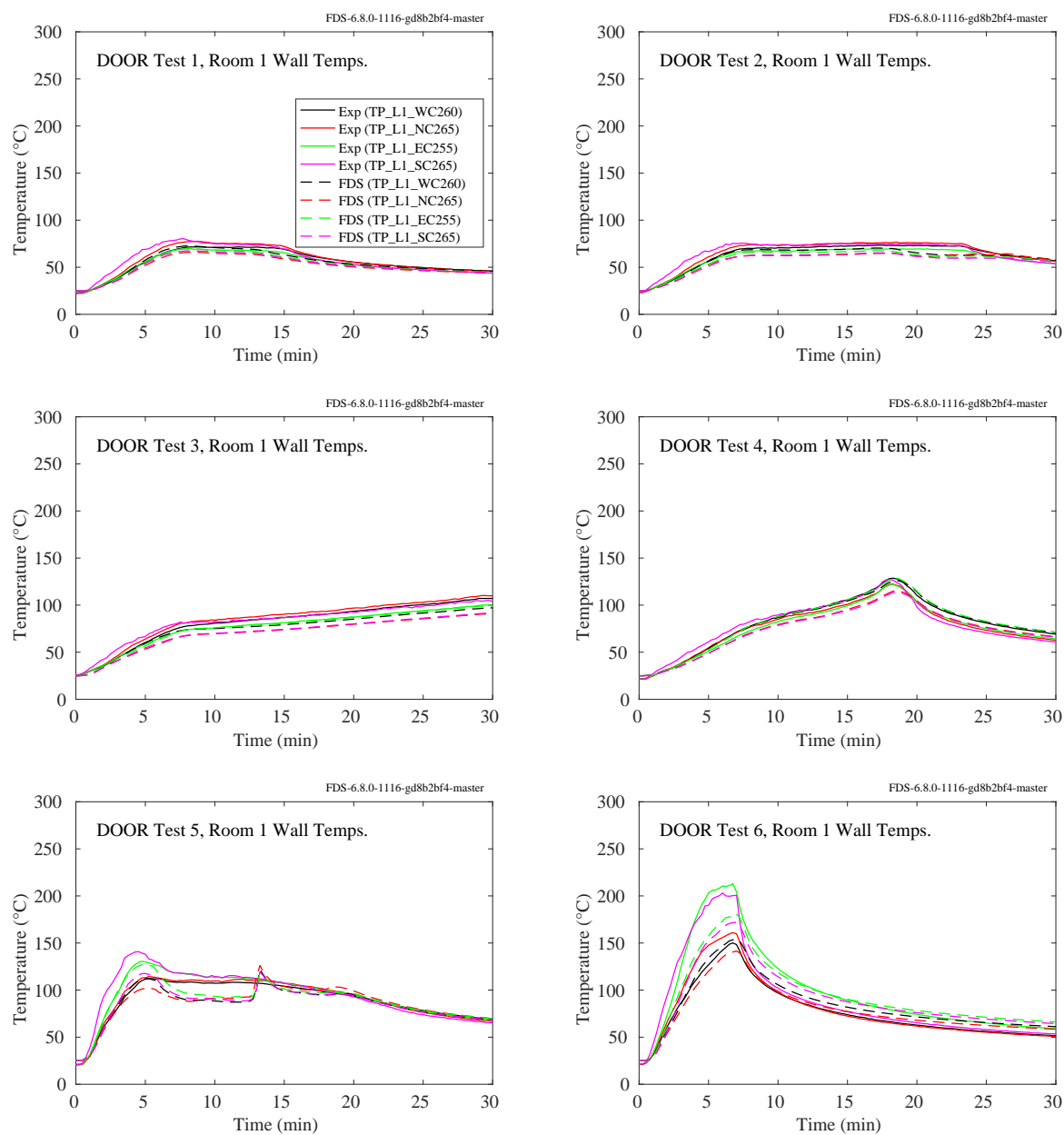


Figure 11.28: PRISME DOOR experiments, wall temperatures, four sides, Room 1.

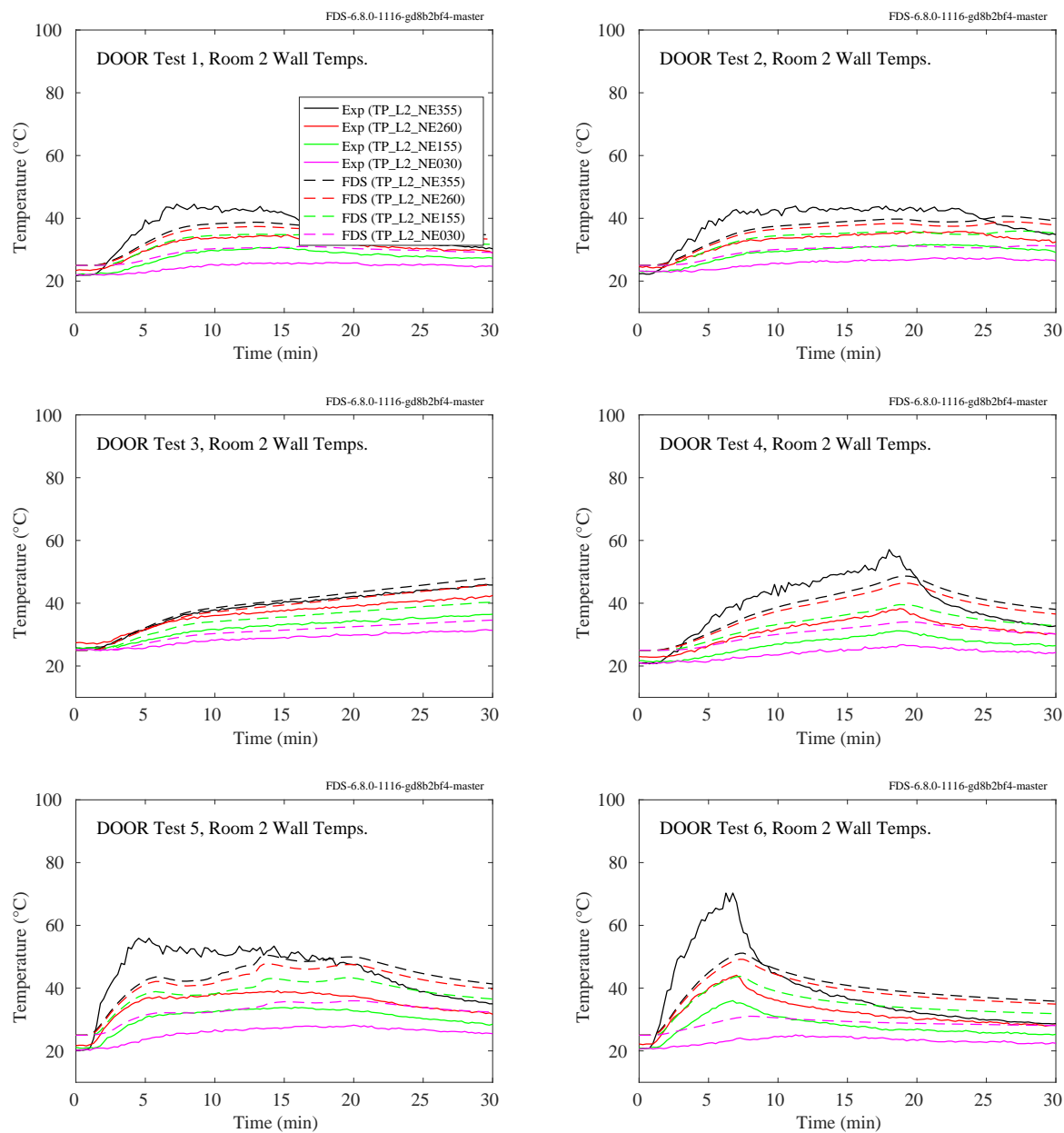


Figure 11.29: PRISME DOOR experiments, wall temperatures, vertical array, Room 2.

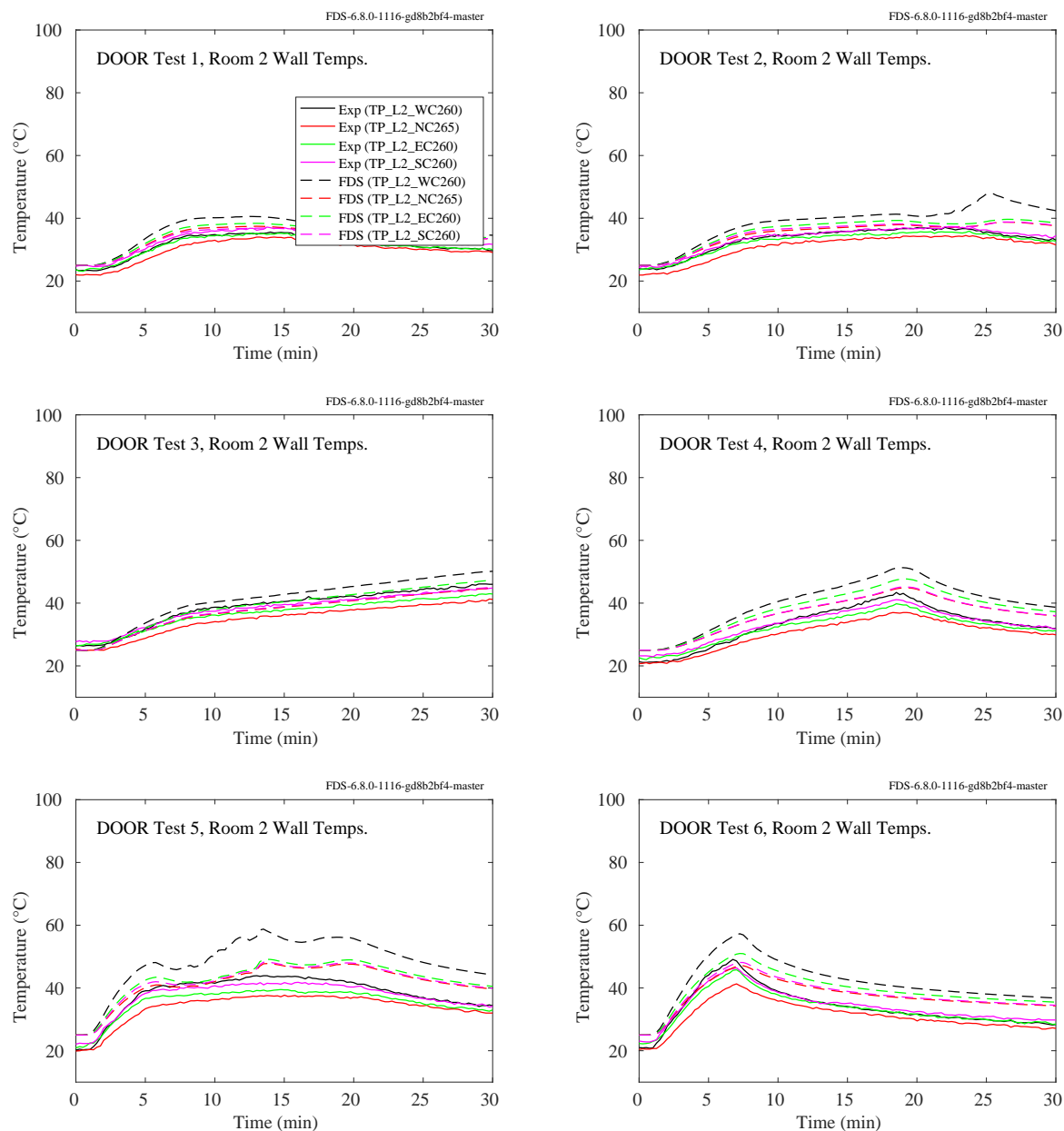


Figure 11.30: PRISME DOOR experiments, wall temperatures, four sides, Room 2.

11.1.6 PRISME SOURCE Experiments

Thermocouples were positioned at various points on the walls. The room contained a vertical array labeled, for example, TP_L2_NE265. The TP indicates a surface temperature measurement, L2 indicates compartment 2, which is where the fire was located, NE indicates northeast corner of the room, and 265 indicates the number of centimeters above the floor. In addition, each room contained four measurement points centered on each wall at a height of approximately 260 cm.

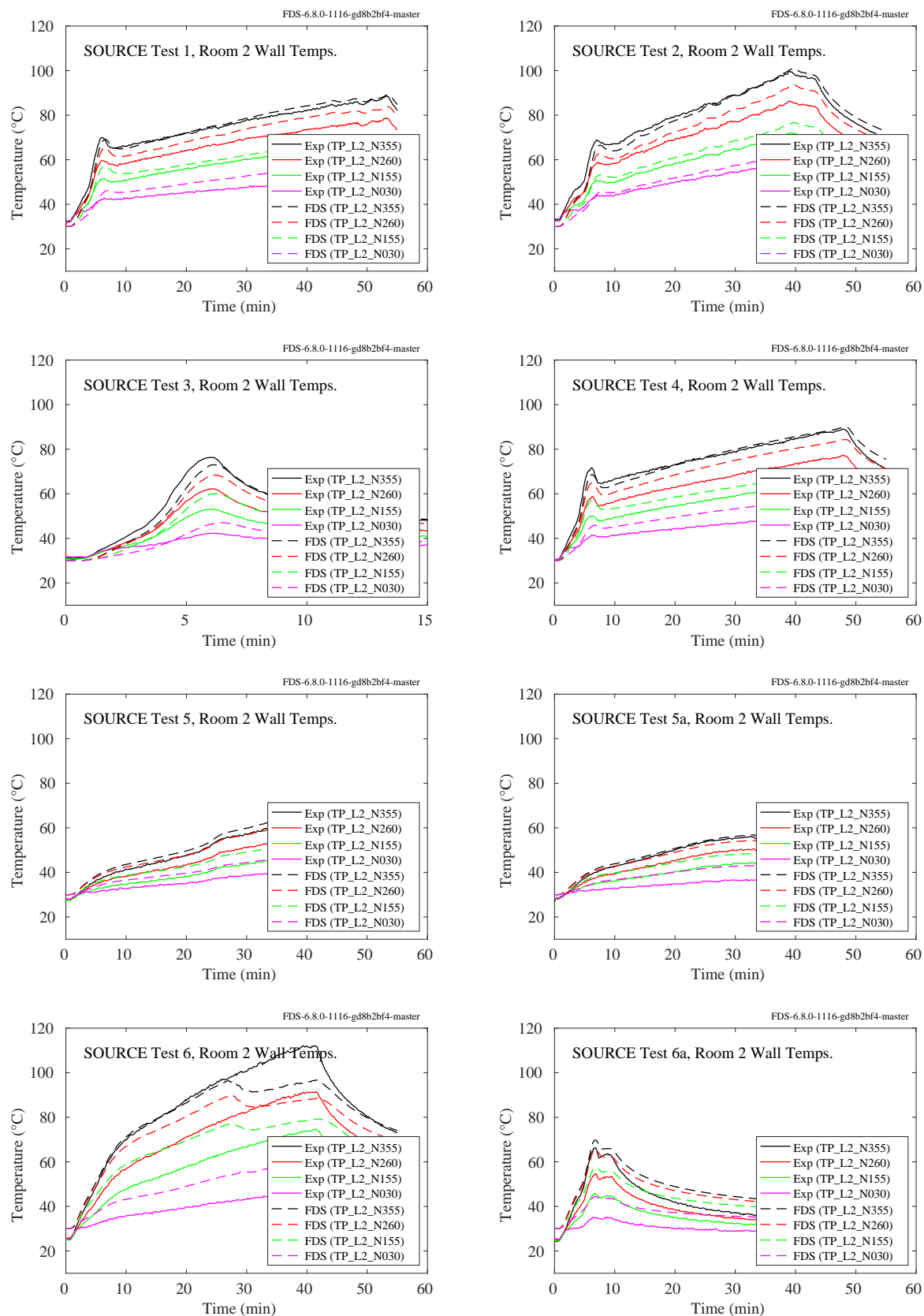


Figure 11.31: PRISME SOURCE experiments, wall temperatures, vertical array, Room 2.

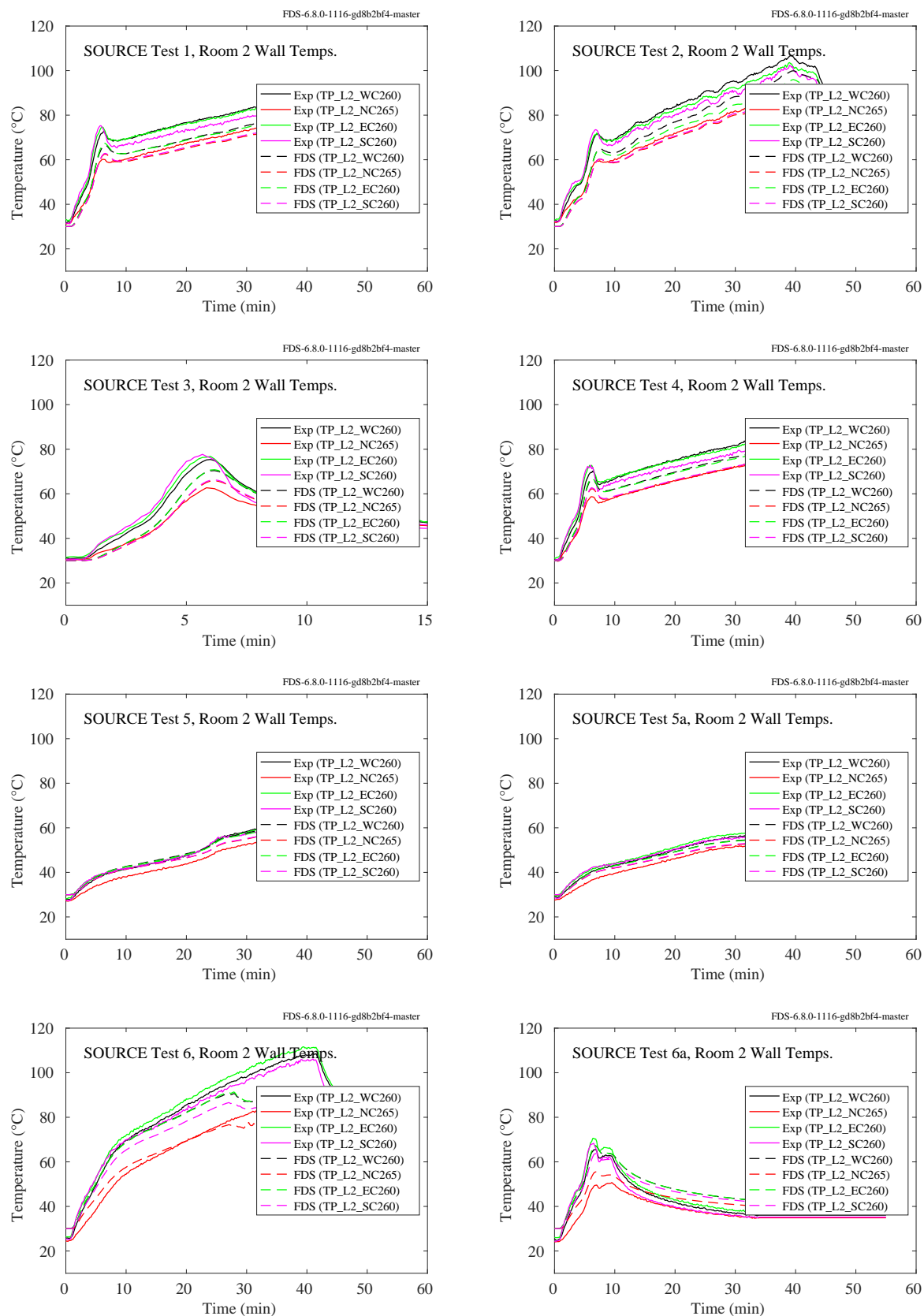


Figure 11.32: PRISME SOURCE experiments, wall temperatures, four sides, Room 2.

11.1.7 WTC Experiments

The following pages contain comparisons of predicted and measured ceiling temperatures, both at the surface and beneath a layer of marinite board. Table 11.2 below lists the coordinates of the measurement locations relative to the center of the fire pan. Names with “IN” appended are measurements made under the marinite board.

Table 11.2: Locations of ceiling surface temperature measurements relative to the fire pan in the WTC series.

Name	x (m)	y (m)	z (m)
TCC	0.62	0.07	3.82
TCN3	0.62	0.67	3.82
TCS3	0.62	-0.53	3.82
TCE7	2.18	0.07	3.82
TCW7	-1.15	0.07	3.82
TCCIN	0.62	0.07	3.83
TCN3IN	0.62	0.67	3.83
TCS3IN	0.62	-0.53	3.83
TCE4IN	1.28	0.07	3.83
TCW4IN	0.05	0.07	3.83

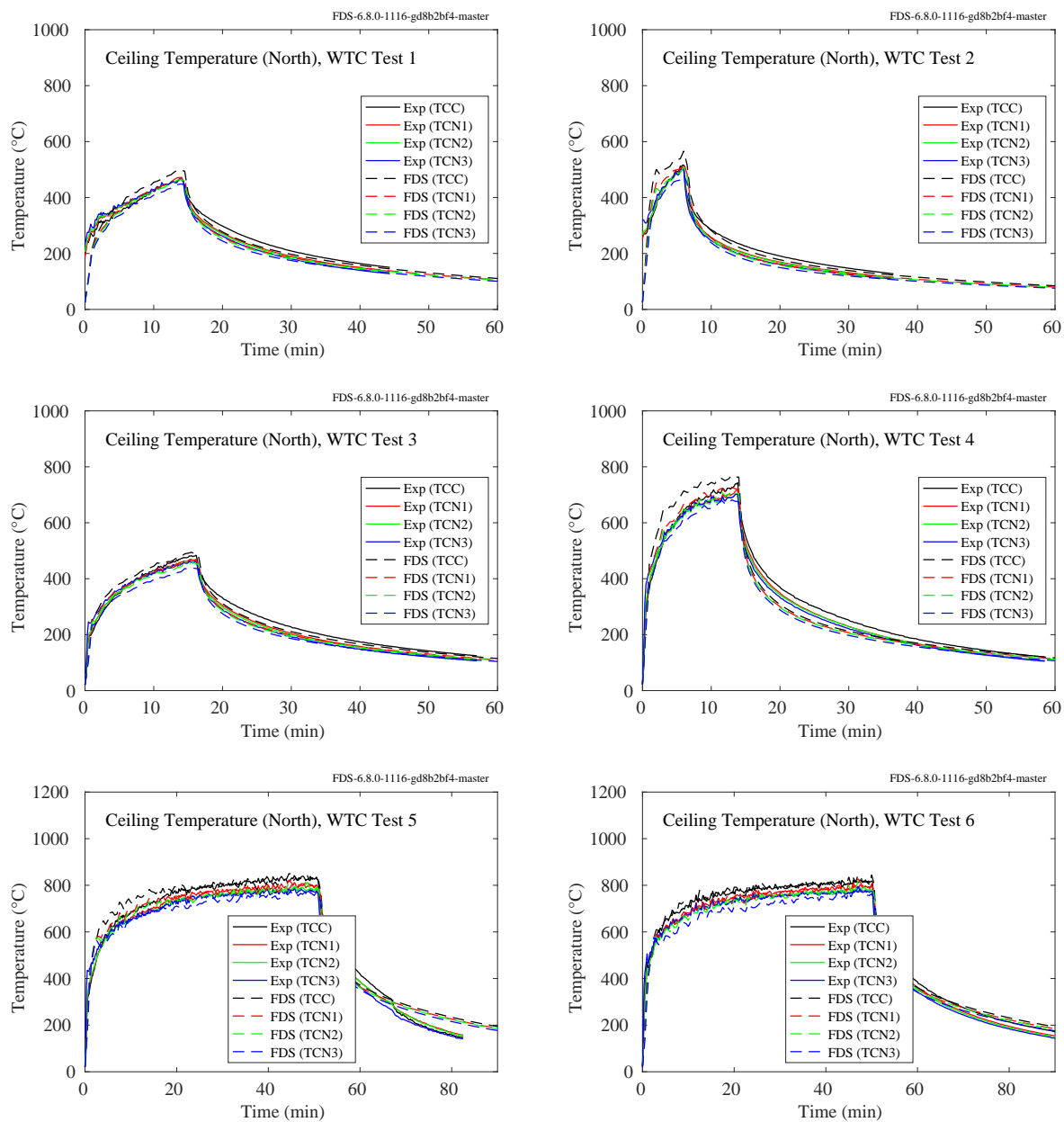


Figure 11.33: WTC experiments, ceiling temperatures, north array.

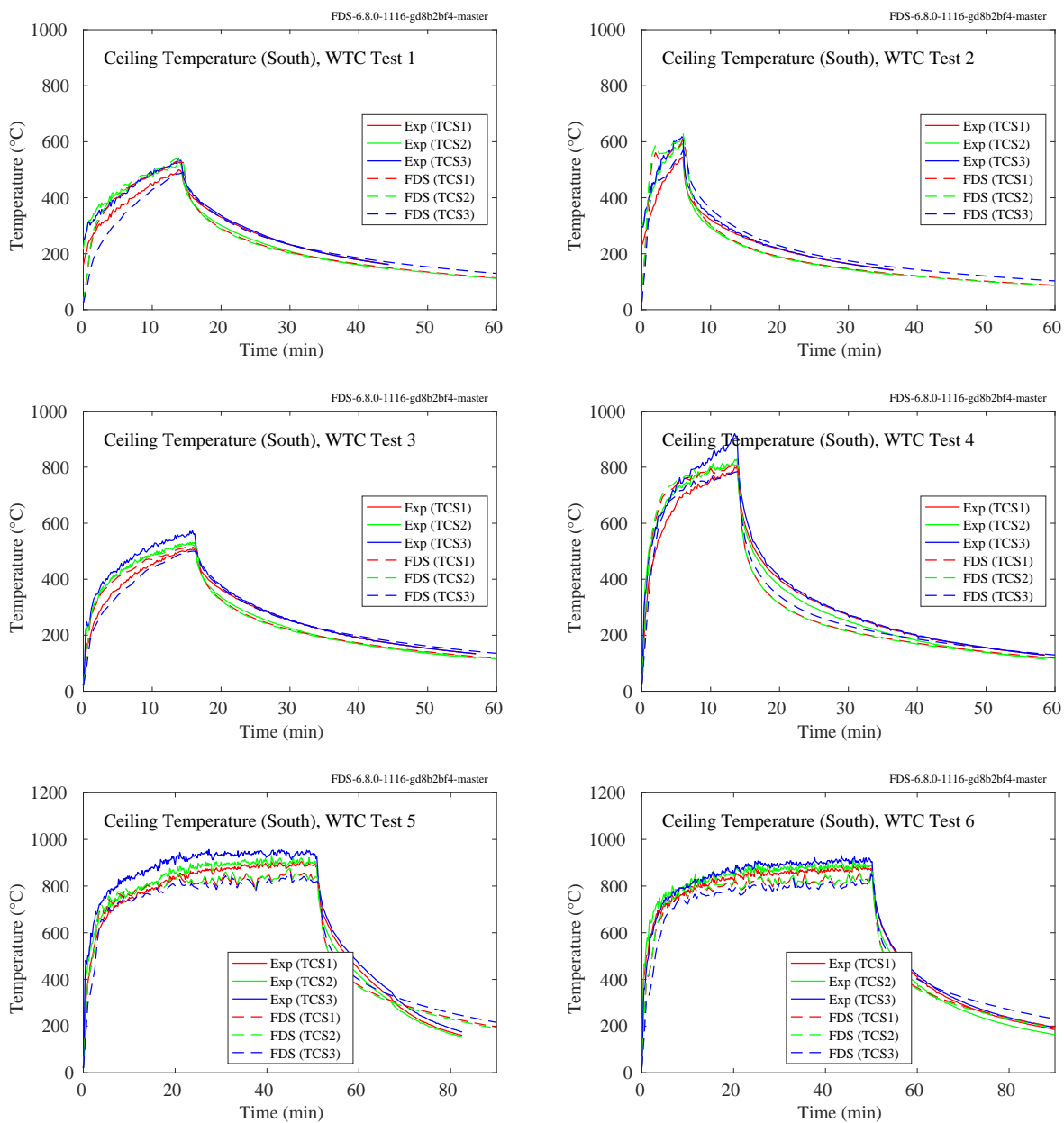


Figure 11.34: WTC experiments, ceiling temperatures, south array.

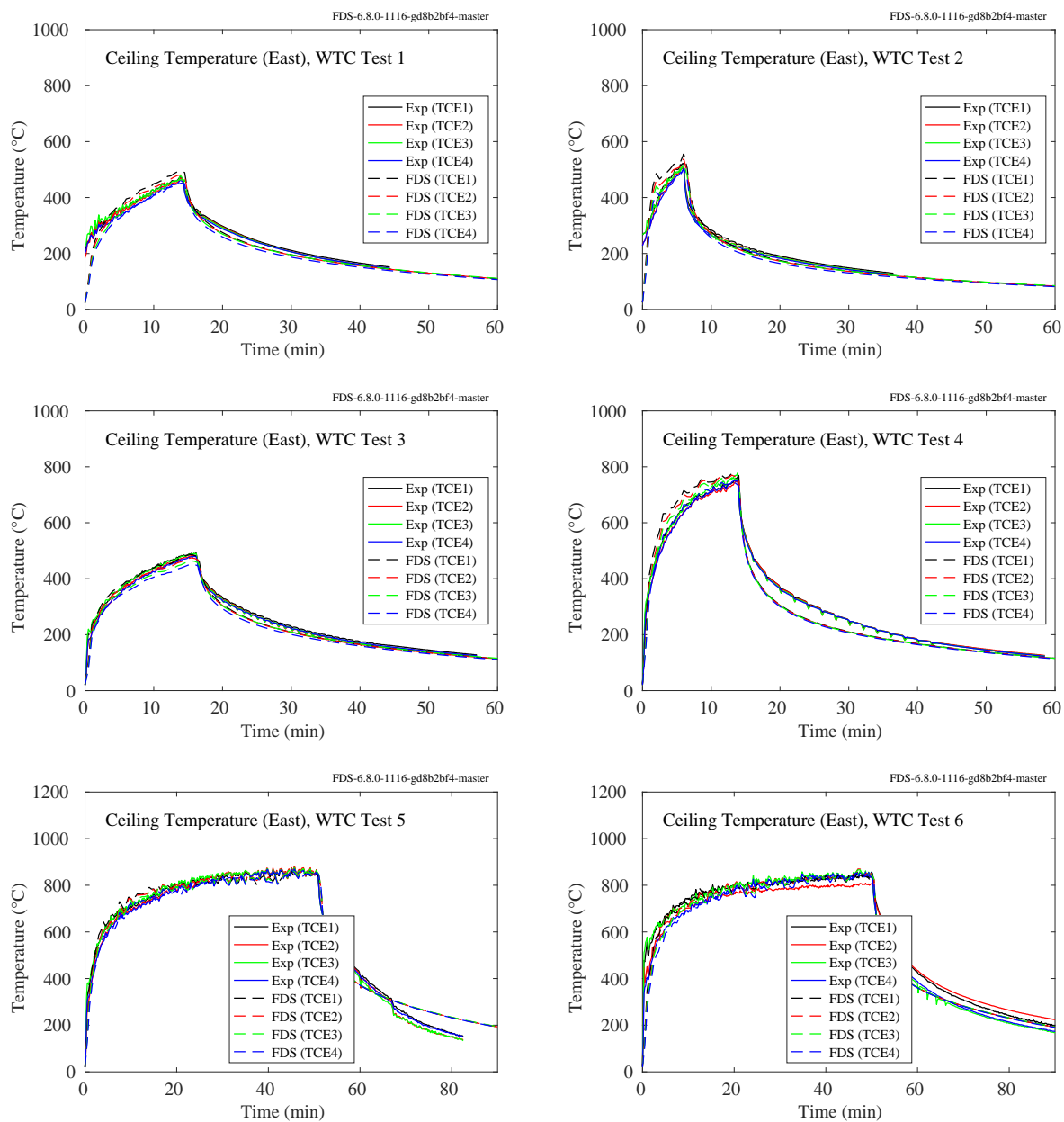


Figure 11.35: WTC experiments, ceiling temperatures, east array, Points 1-4.

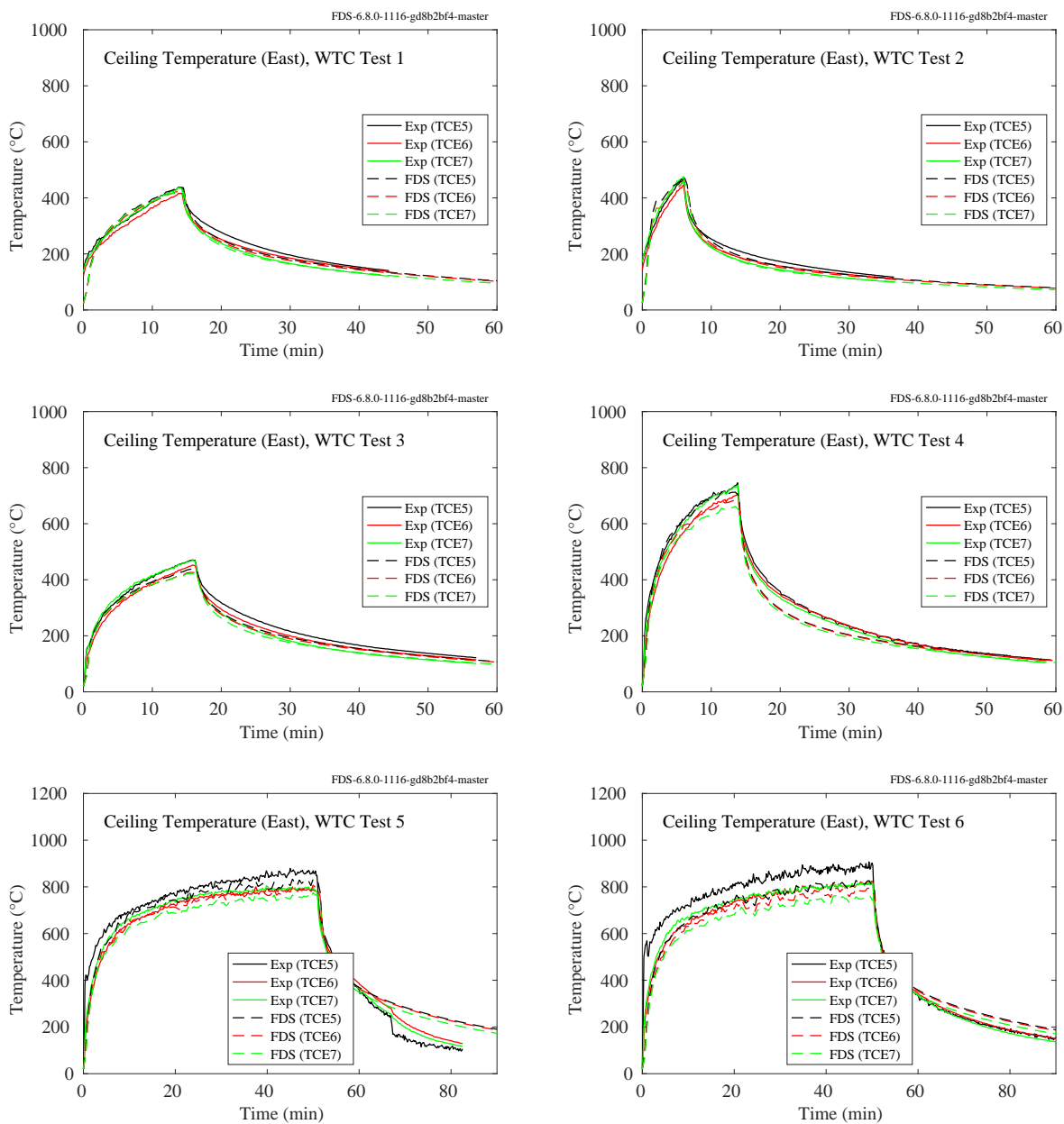


Figure 11.36: WTC experiments, ceiling temperatures, east array, Points 5-7.

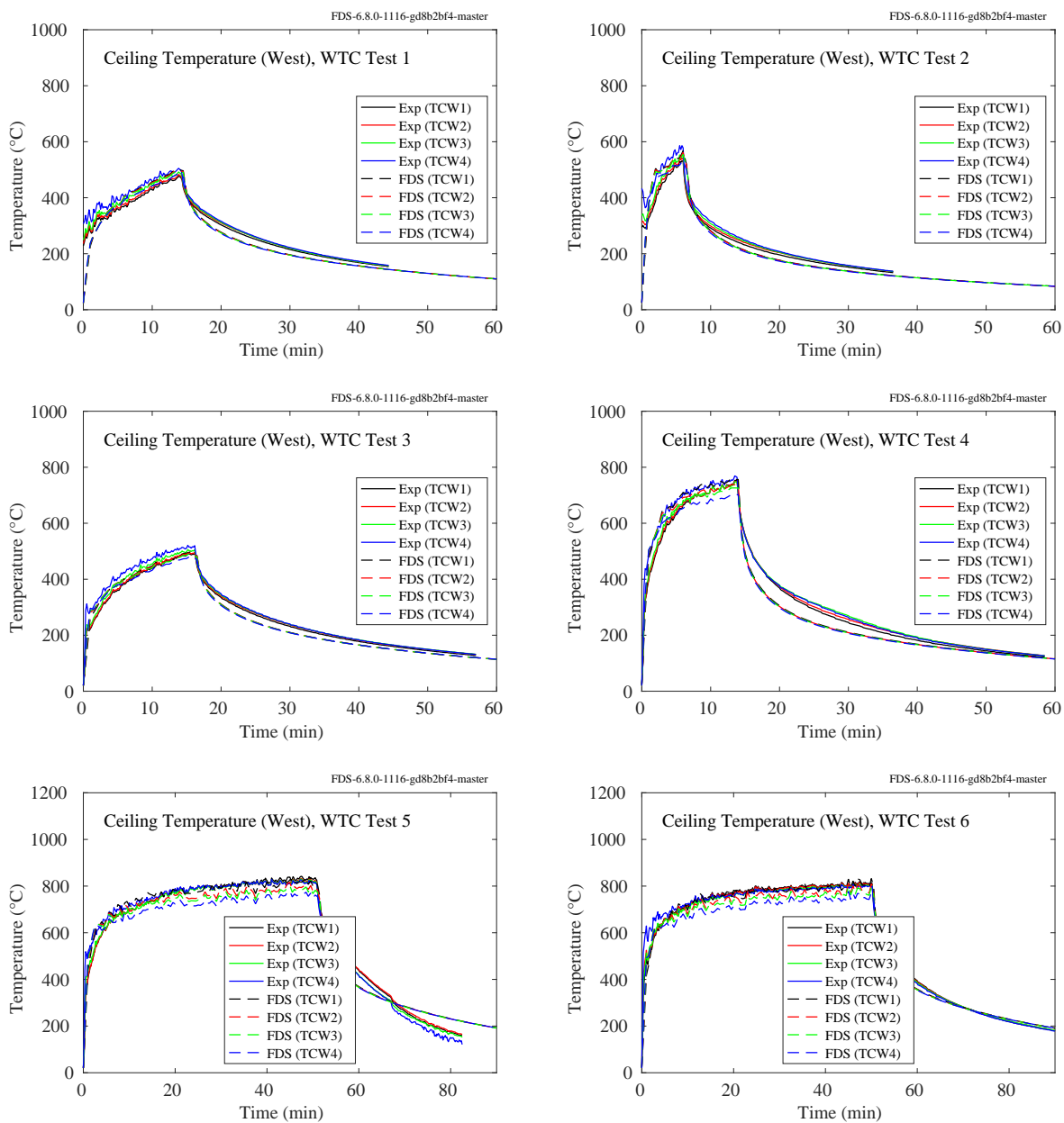


Figure 11.37: WTC experiments, ceiling temperatures, west array, Points 1-4.

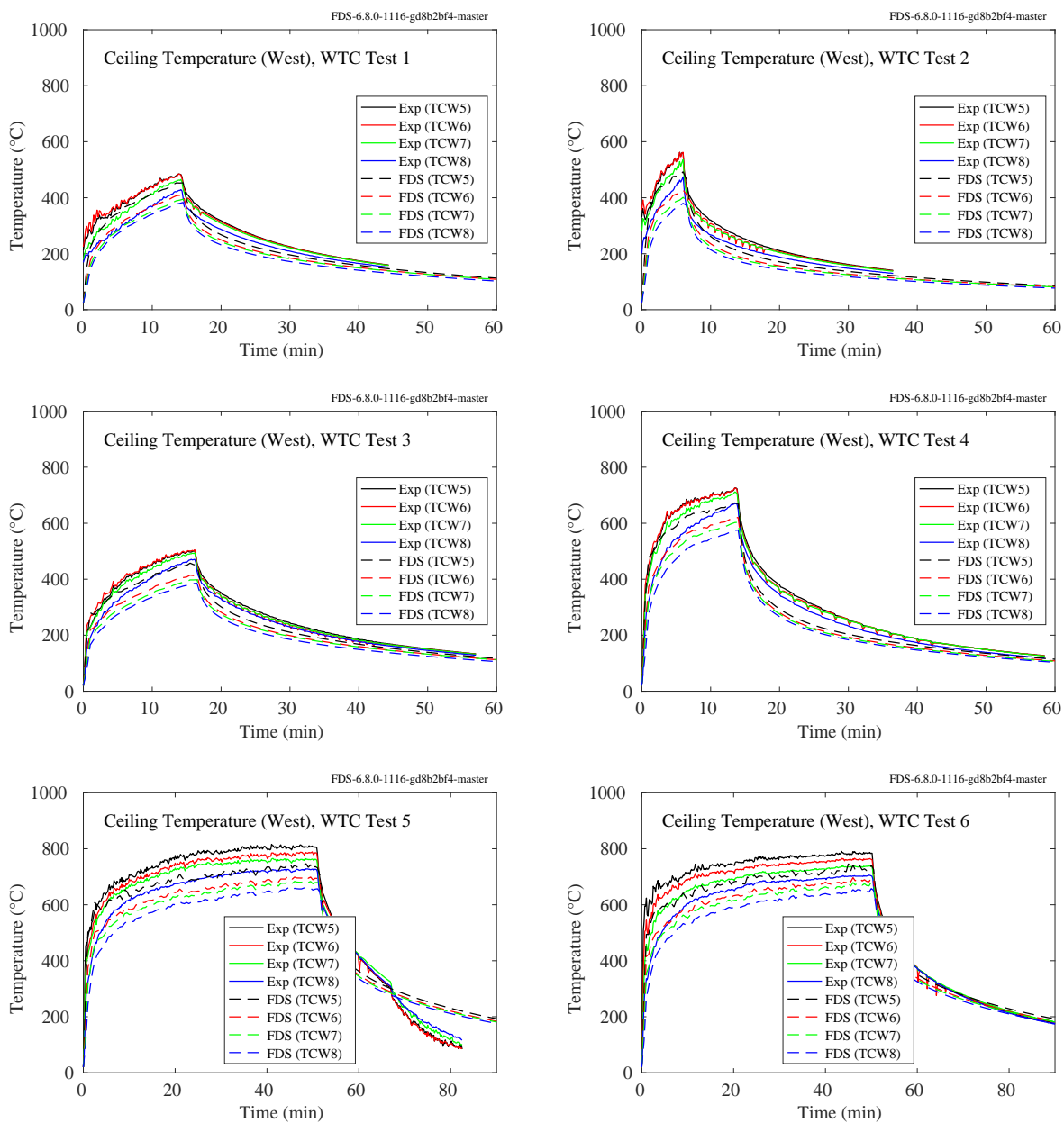


Figure 11.38: WTC experiments, ceiling temperatures, west array, Points 5-8.

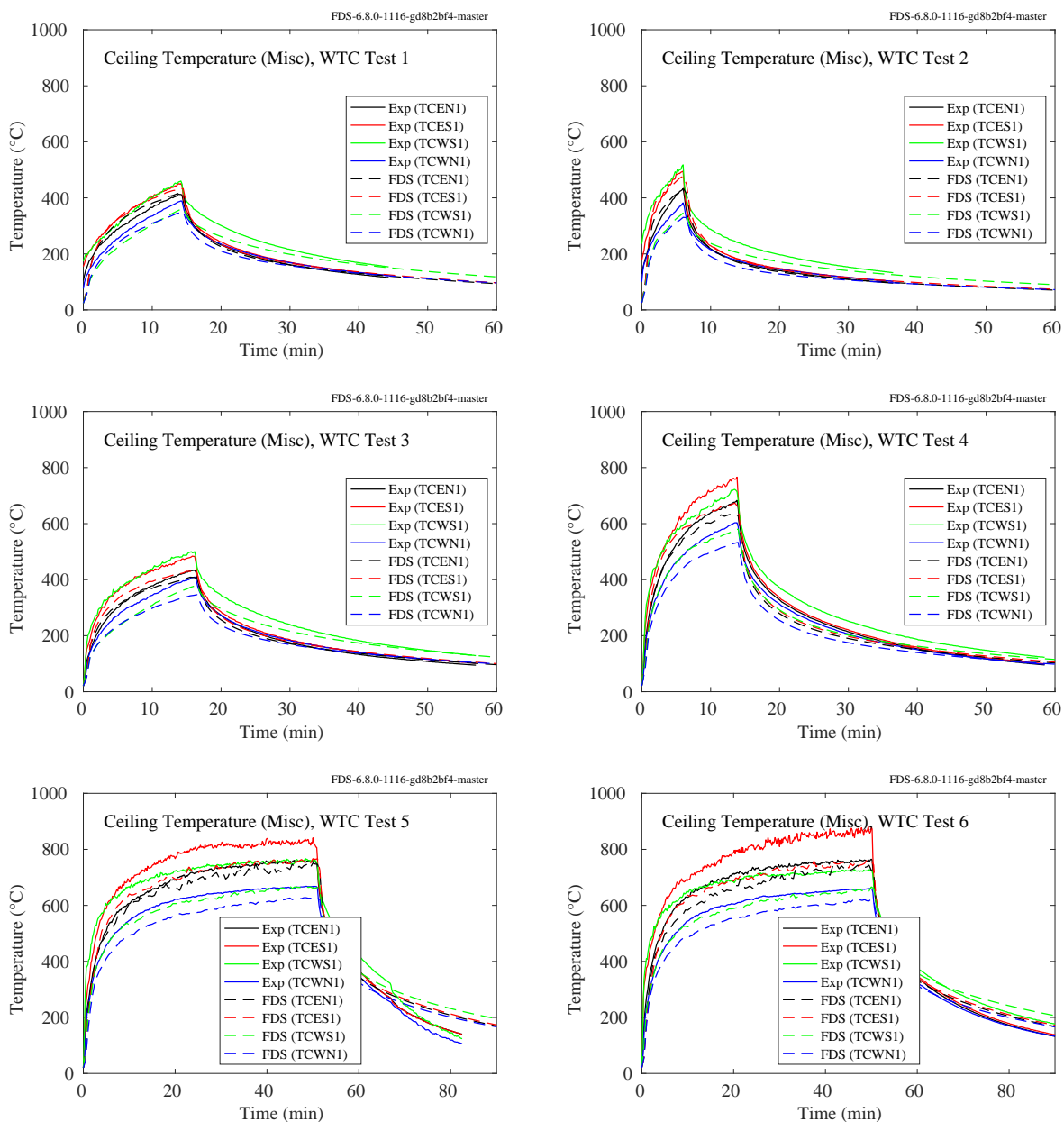


Figure 11.39: WTC experiments, ceiling temperatures, diagonal array.

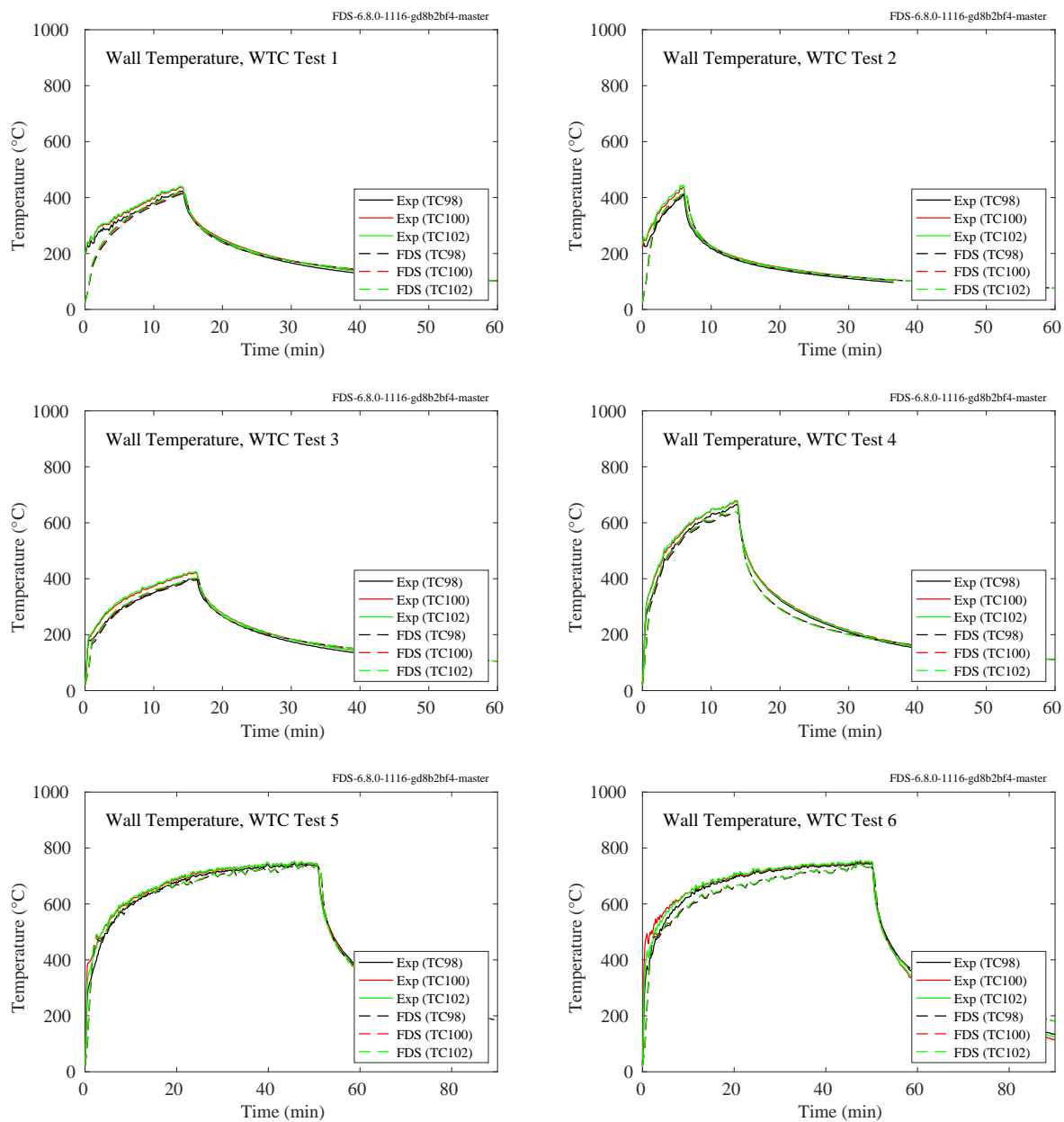


Figure 11.40: WTC experiments, wall temperatures, Points 98, 100, 102.

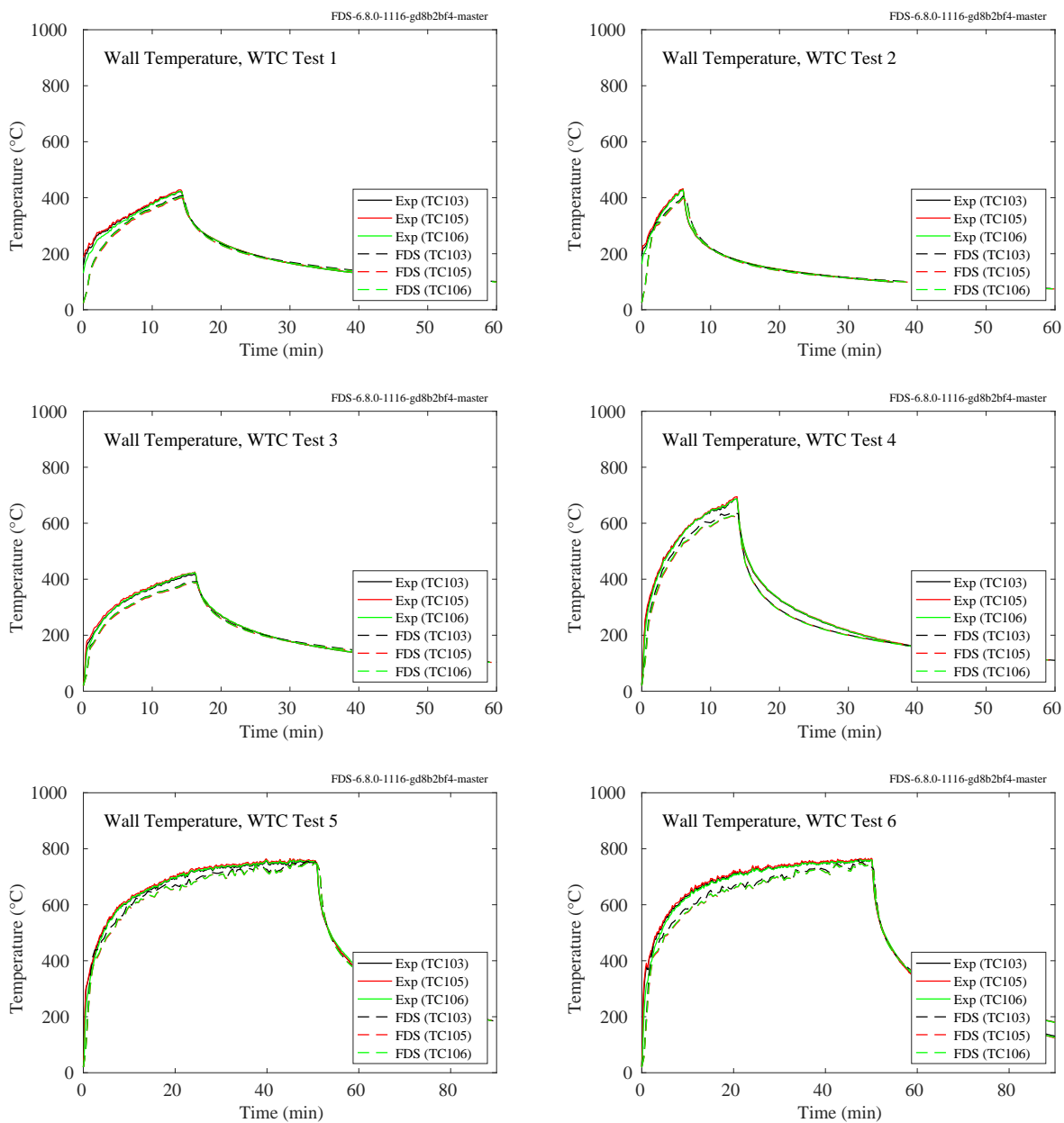


Figure 11.41: WTC experiments, wall temperatures, Points 103, 105, 106.

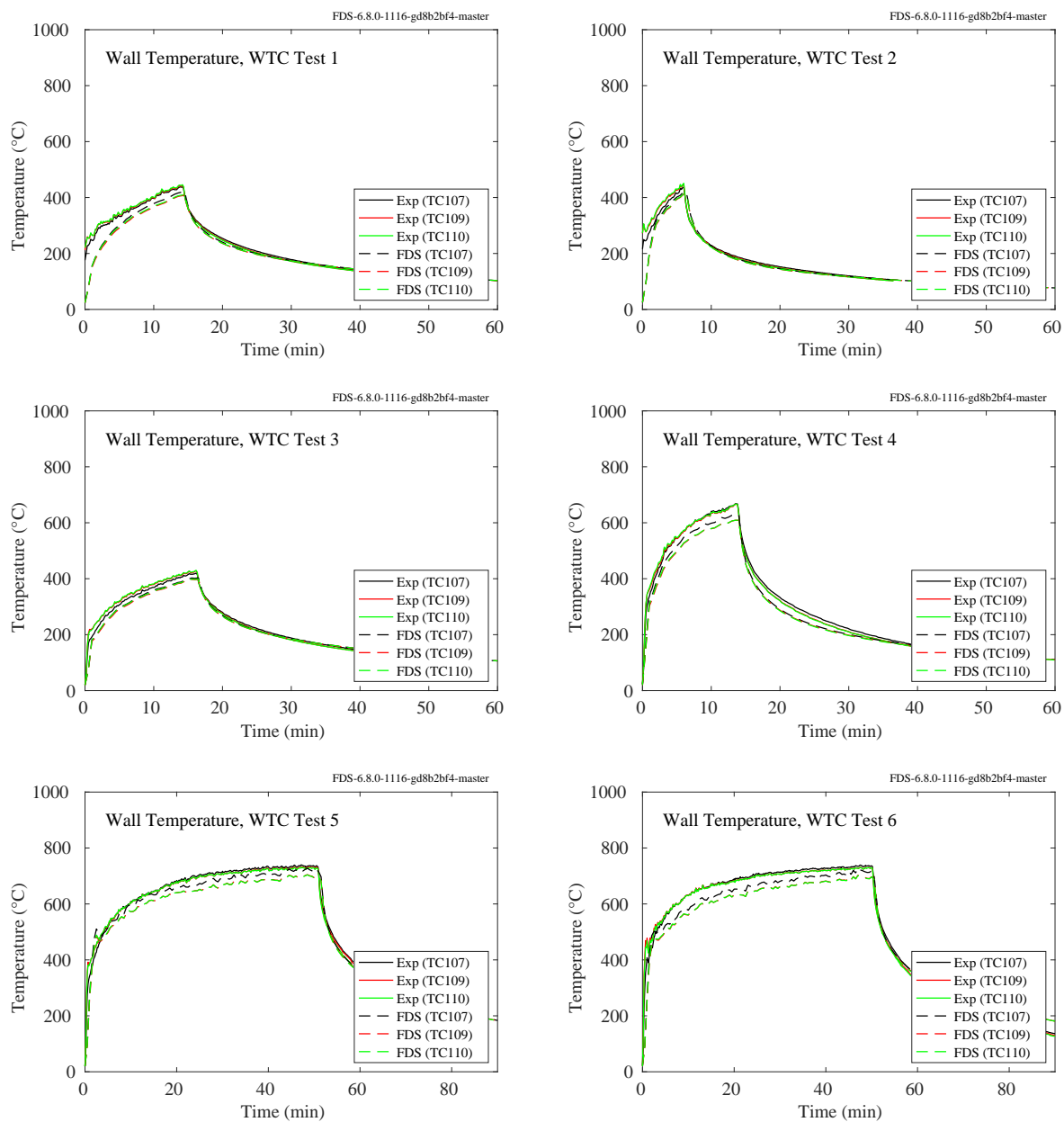


Figure 11.42: WTC experiments, wall temperatures, Points 107, 109, 110.

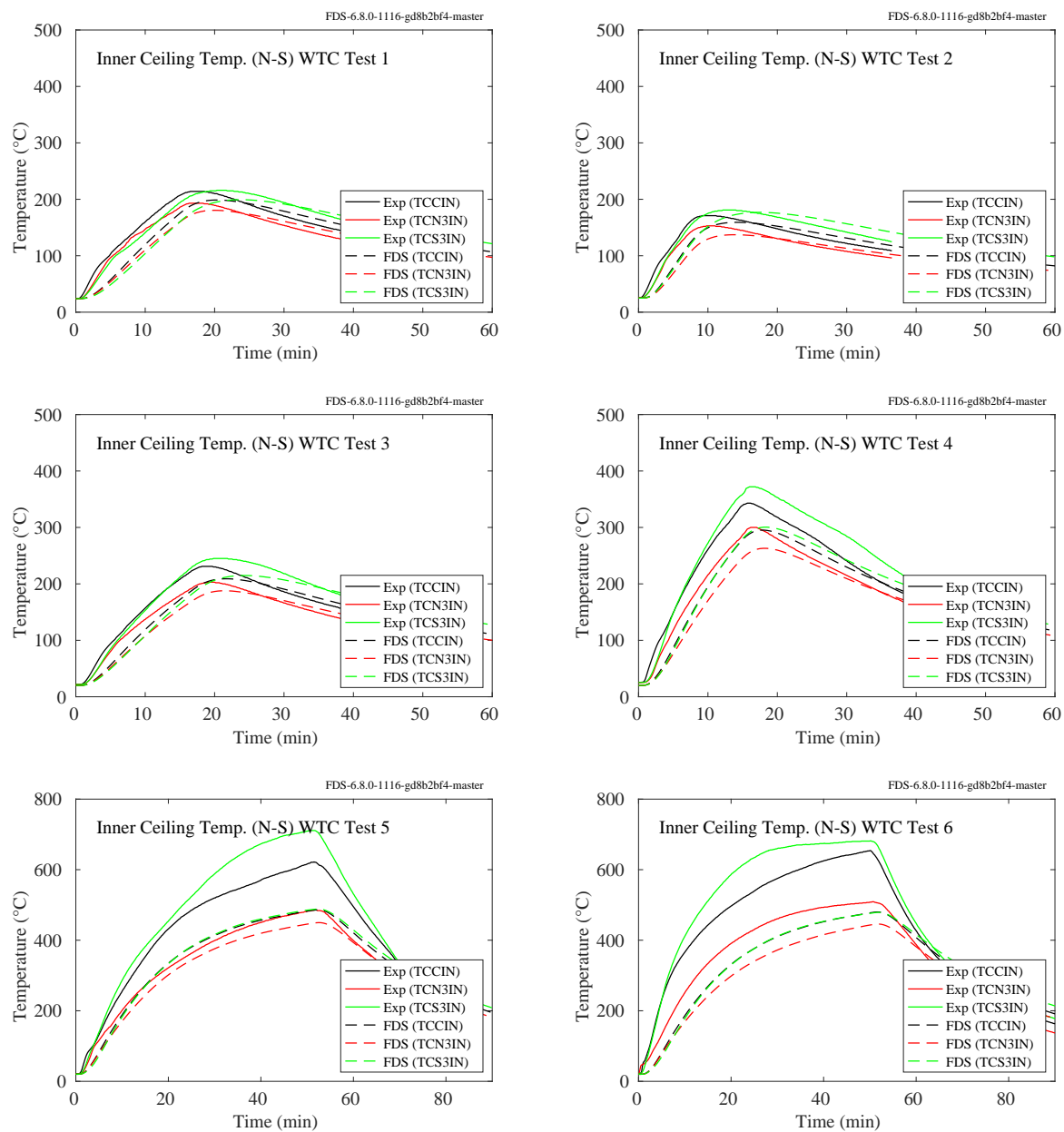


Figure 11.43: WTC experiments, inner ceiling temperatures, north-south axis.

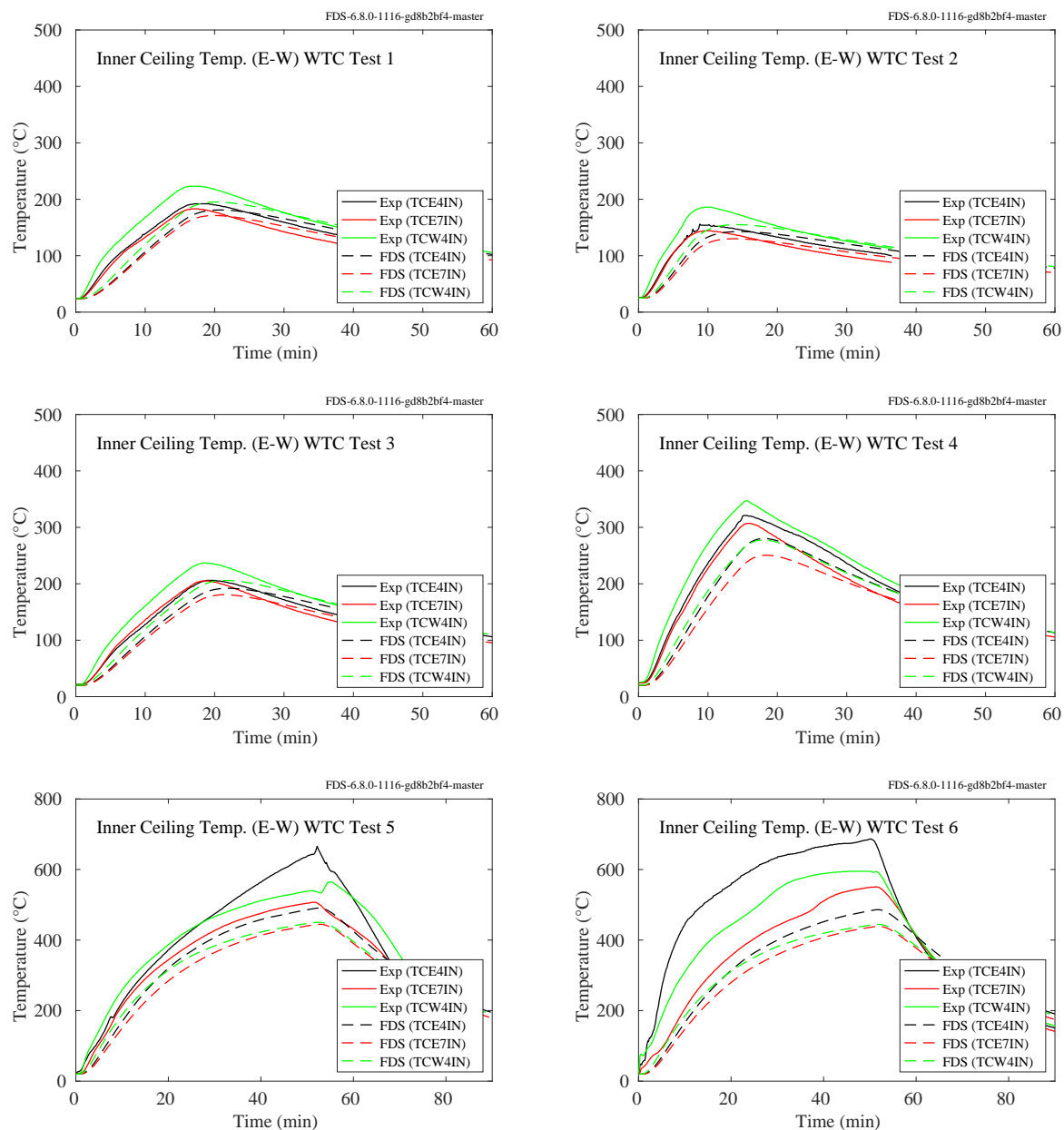


Figure 11.44: WTC experiments, inner ceiling temperatures, east-west axis.

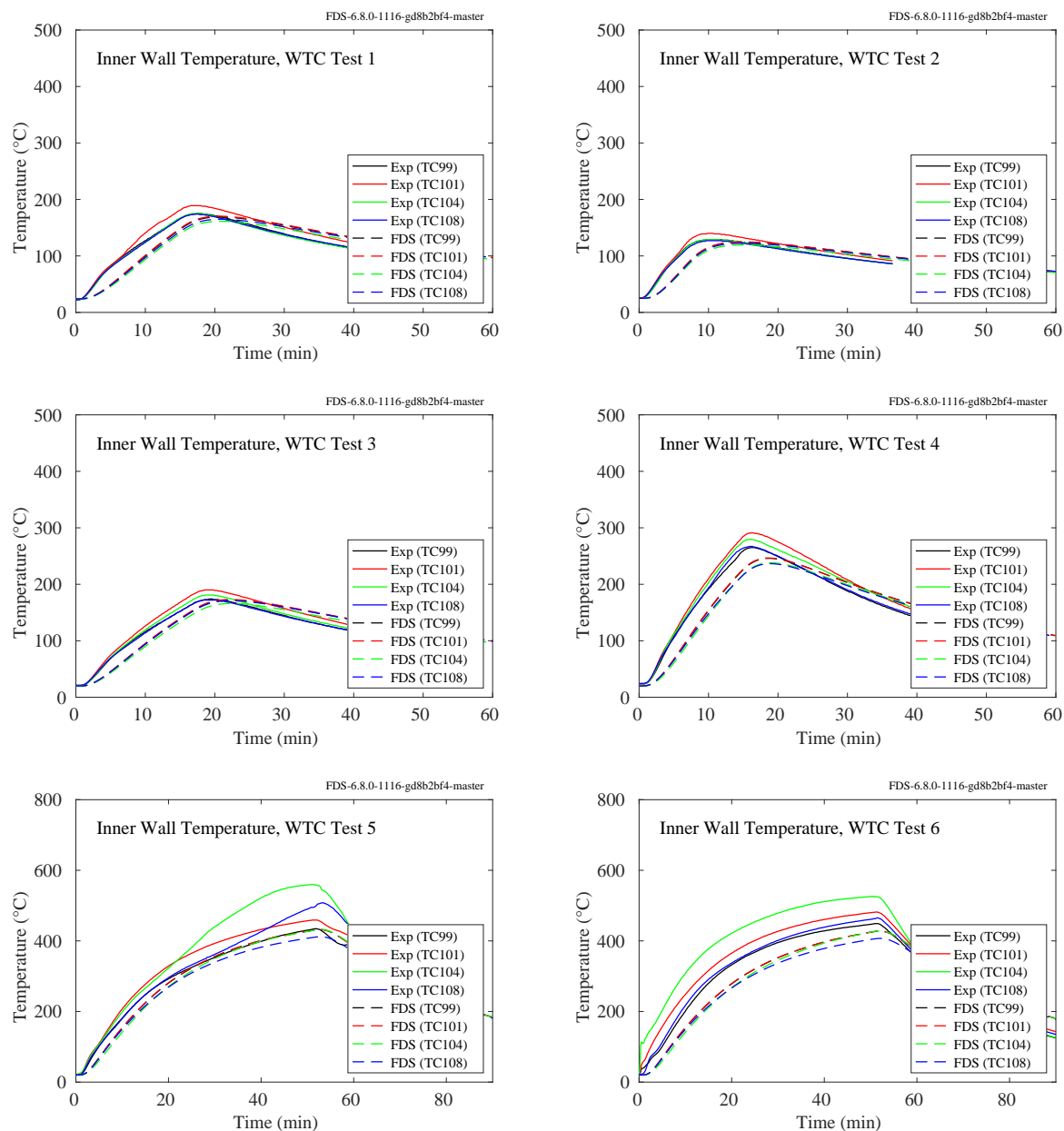


Figure 11.45: WTC experiments, inner wall temperatures.

11.1.8 Insulation Materials Fire Resistance Tests

Figures 11.46 through 11.49 contain comparisons of predicted and measured cold side temperatures of stone wool insulation samples in small-scale fire resistance tests. The measured temperatures are the average of 8 thermocouples. The physical properties of the materials are given in Table 11.3. Further details on the experiments and modeling can be found in Sec. 3.36.

Table 11.3: Physical properties of stone wool insulation materials [229].

Test No.	Thickness (mm)	Density (kg/m ³)	Loss (%)
1	61.9	101.4	1.5
2	62.4	100.5	1.3
3	60.0	97.2	1.4
4	63.2	95.3	1.2
5	61.7	100.7	1.2
6	60.5	100.2	1.1
7	60.0	99.6	1.1
8	61.8	90.2	1.3
9	61.1	69.8	1.3
10	61.7	79.3	1.5
11	60.1	90.3	1.3
12	60.1	90.3	1.4
13	61.4	100.0	1.4
14	60.3	100.9	1.5
15	61.0	138.8	2.1
16	41.2	107.2	1.3
17	72.7	78.9	1.6
18	61.3	141.2	1.9
19	61.9	147.7	1.5
20	52.0	38.3	0.7
21	60.5	147.3	1.3
22	75.7	66.3	6.9
23	75.2	71.1	9.0
24	76.2	51.4	9.8
25	71.5	63.9	1.1
26	72.8	75.1	1.2
27	60.4	85.0	1.3
28	75.0	68.5	4.7
29	75.7	48.7	6.7
30	75.3	48.2	4.8

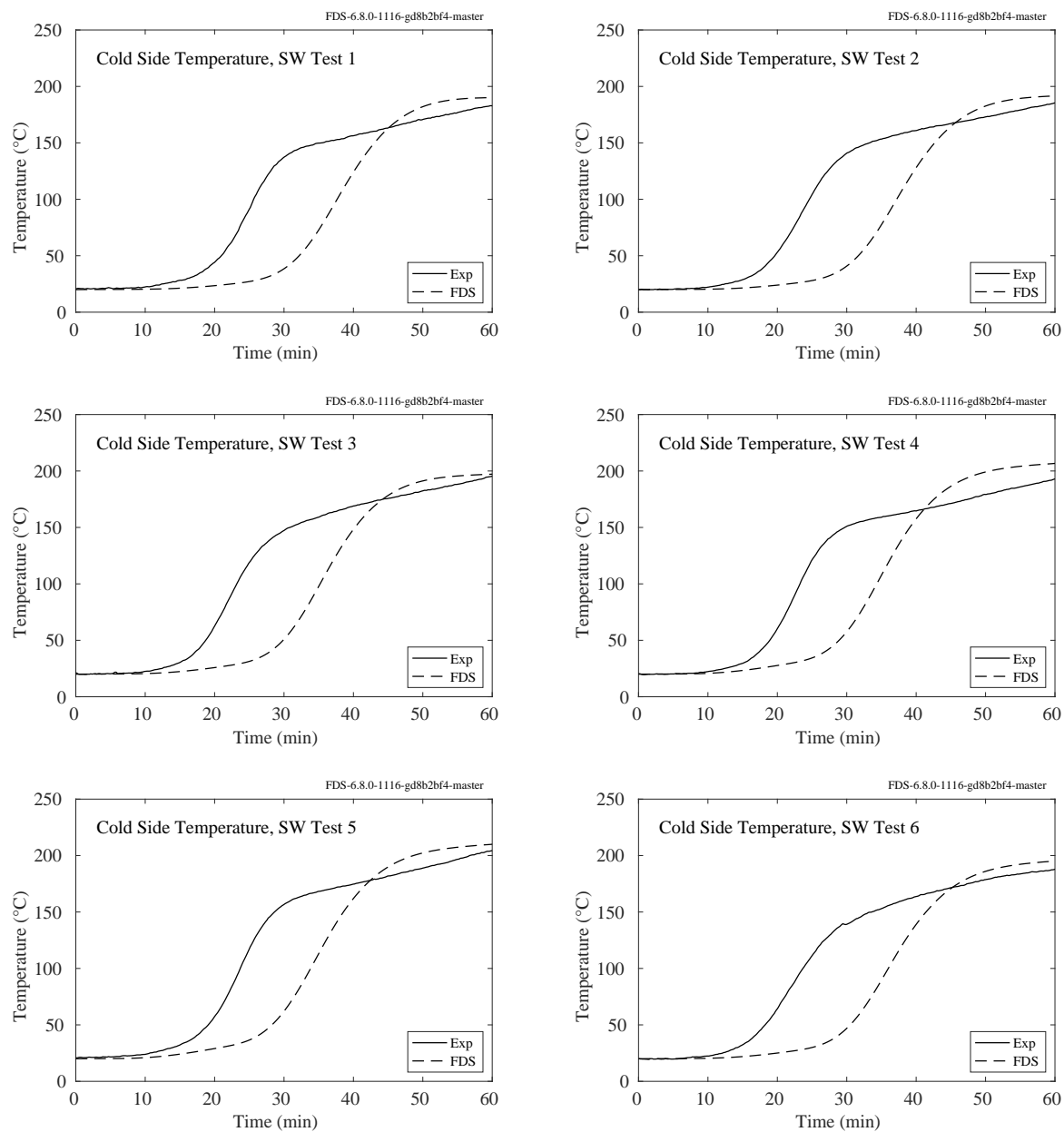


Figure 11.46: Insulation material cold side temperatures, Tests 1-6.

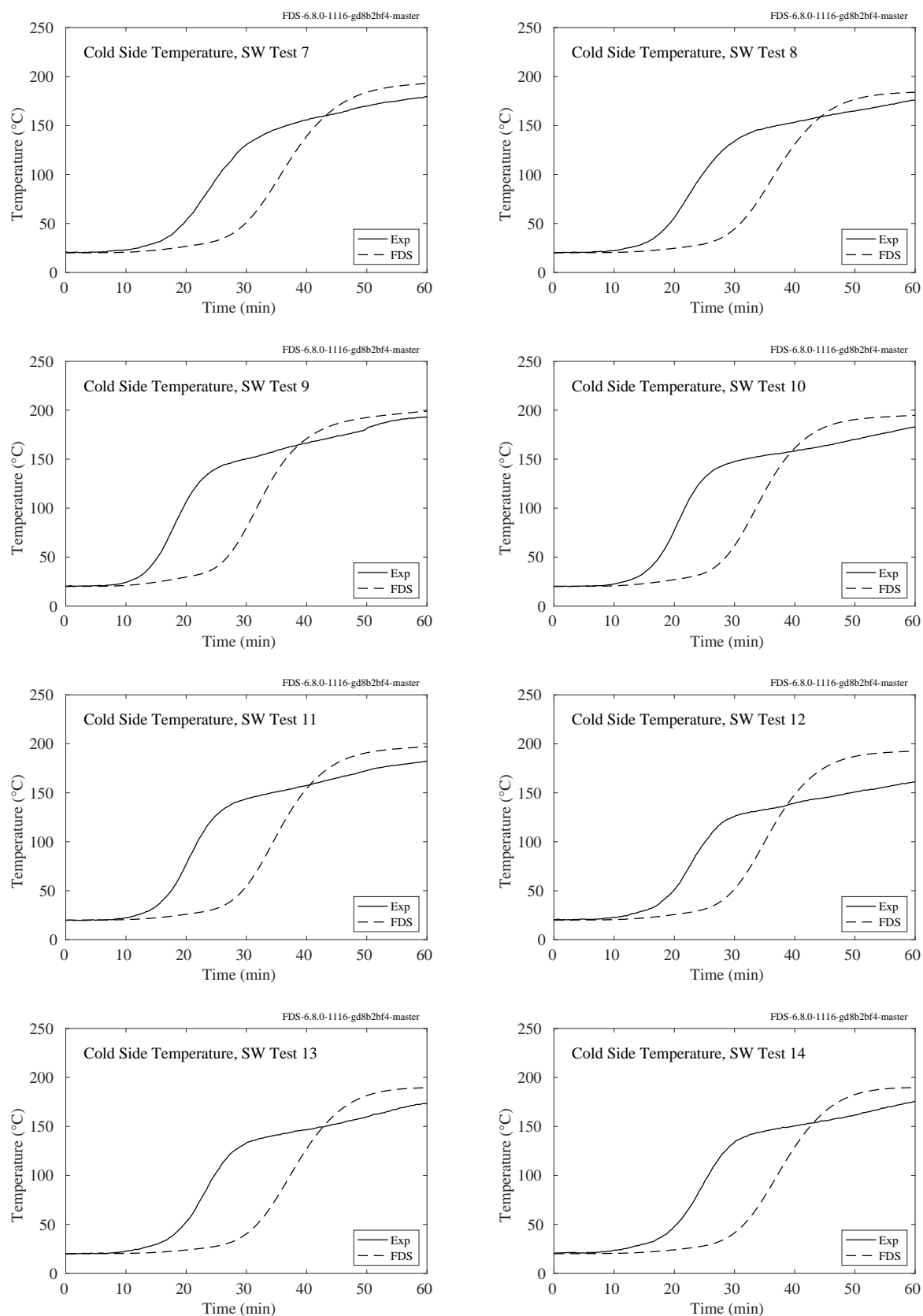


Figure 11.47: Insulation material cold side temperatures, Tests 7-14.

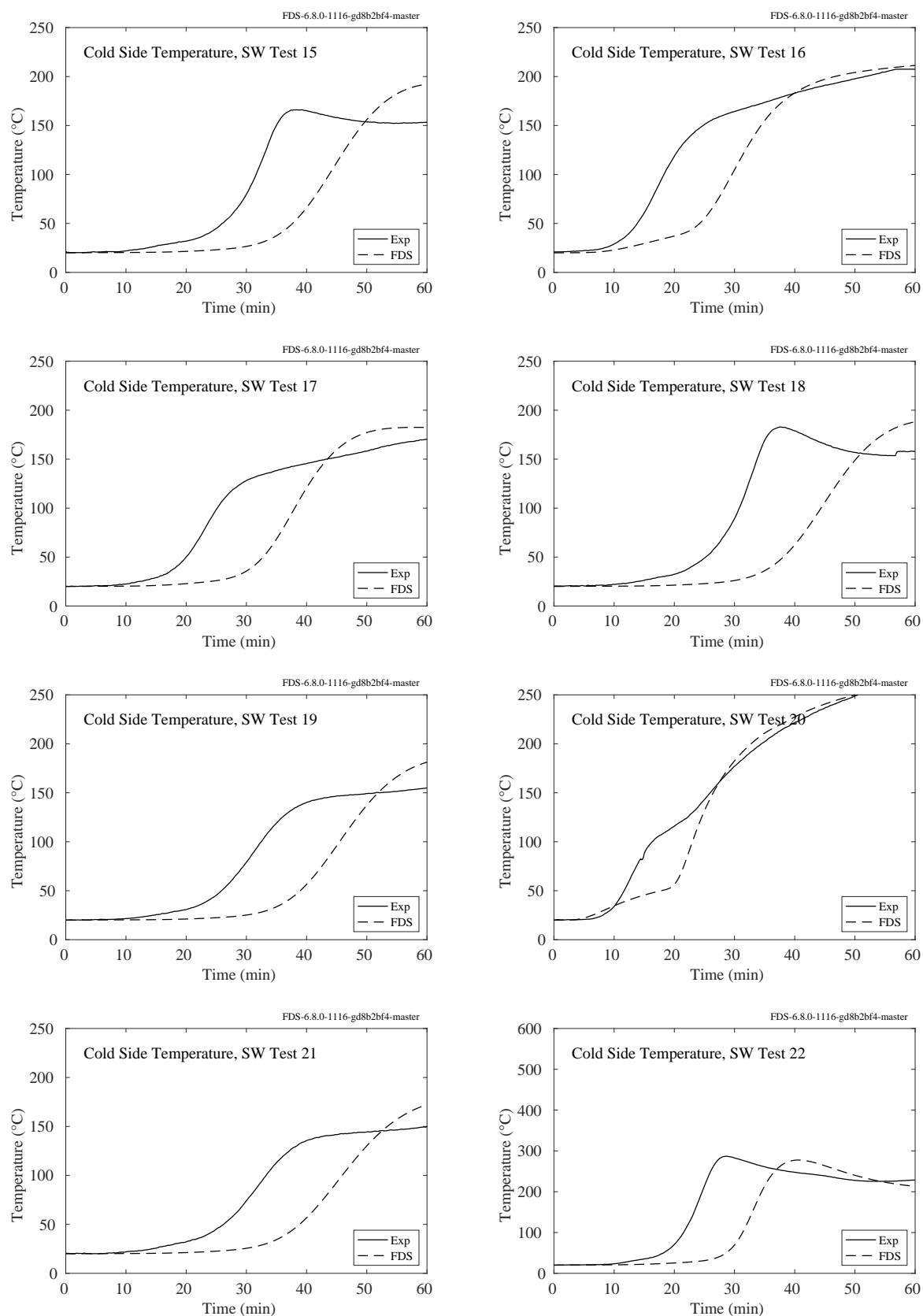


Figure 11.48: Insulation material cold side temperatures, Tests 15-22.

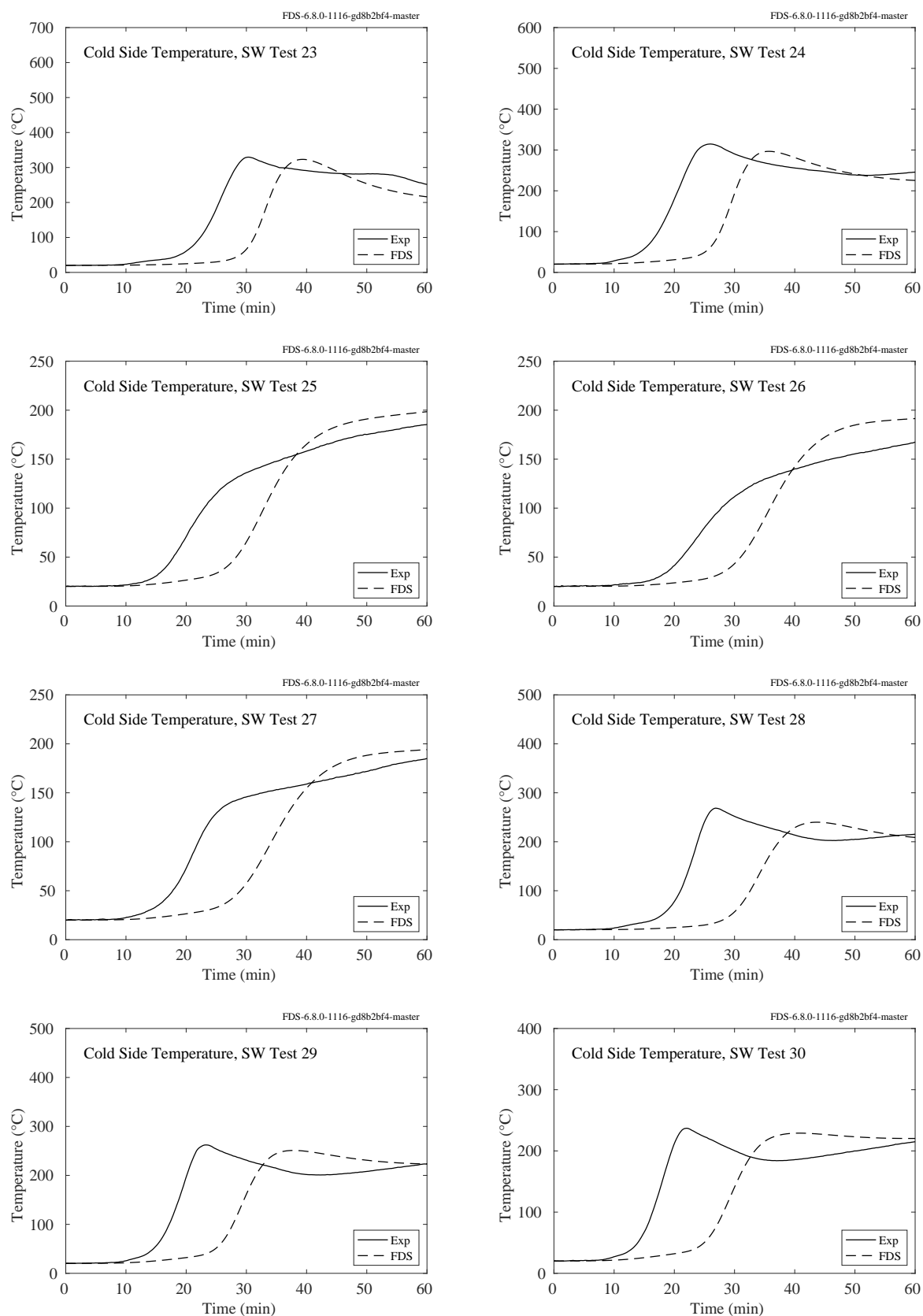


Figure 11.49: Insulation material cold side temperatures, Tests 23-30.

11.1.9 Summary of Wall, Ceiling, and Floor Temperature Predictions

Figure 11.50 summarizes the temperature predictions for walls, ceilings, and floors.

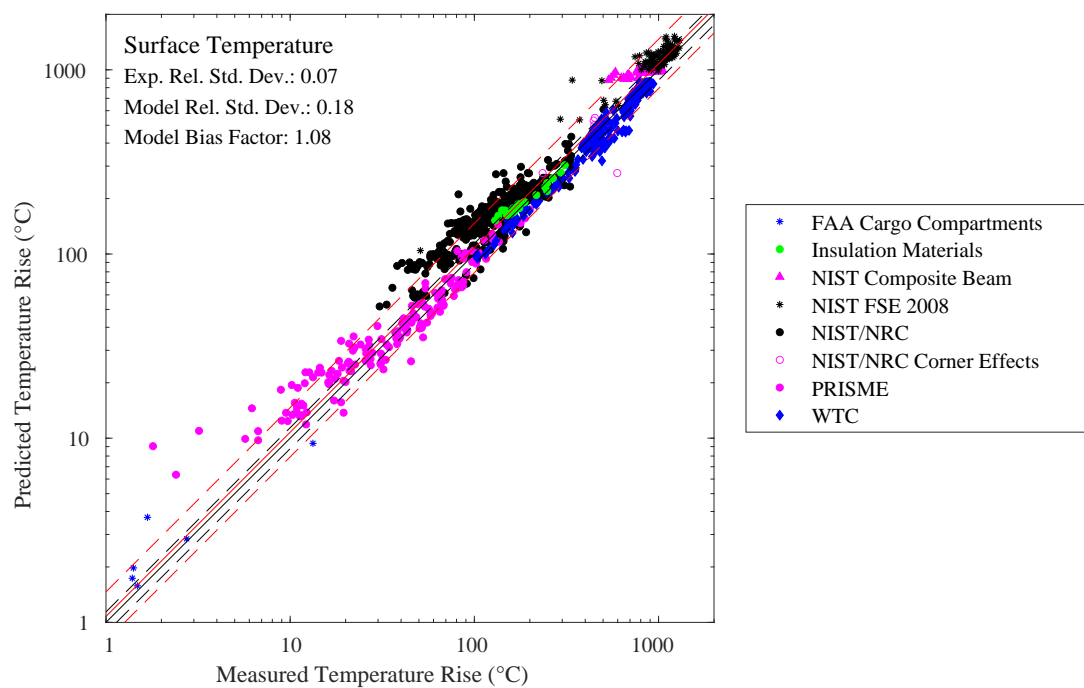


Figure 11.50: Summary of compartment surface temperature predictions.

11.2 Target Temperature

A “target” refers to any object that is not a wall, ceiling, or floor. In the sections to follow, the targets consist of structural steel members, electrical cables, and various other objects.

11.2.1 NIST Composite Beam

A brief description of the experiments is given in Sec. 3.50. The compartment interior dimensions are 12.4 m long, running east-west, 1.9 m wide, and 3.77 m high. Four experiments with fires were performed, labeled as Tests 2-5. Test 1 did not include a fire.

Figure 11.51 displays the plate thermometer temperatures at three locations. PT1 is mounted on the east wall facing west. PT2 is mounted just north of the beam at mid-span, pointing north. PT3 is also mounted at mid-span, just below the beam and facing downward.

Figure 11.52 displays the steel temperature at Sections 1, 3-8 for Test 5 only. TCC11 is the upper flange temperature. TCC12, TCC13, and TCC14 are the web temperatures, and TCC15 is the lower flange temperature.

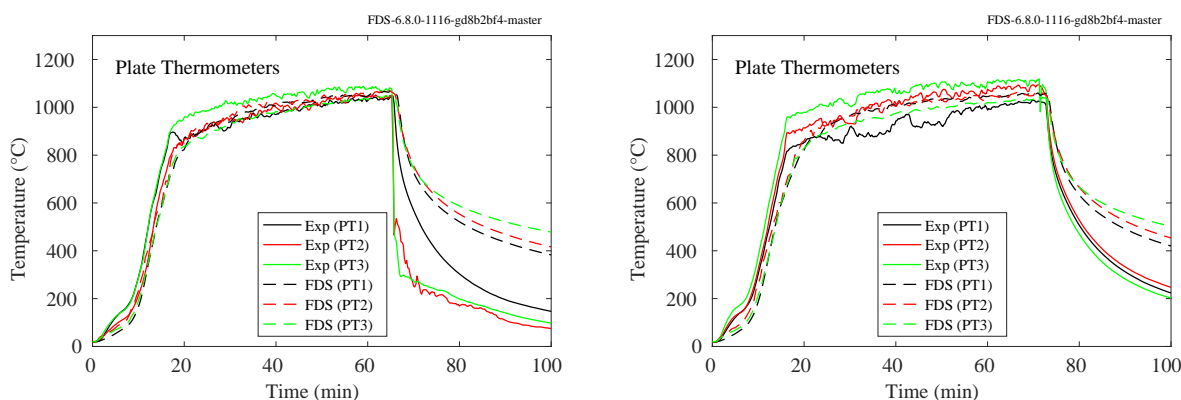


Figure 11.51: NIST Composite Beam, beam temperatures.

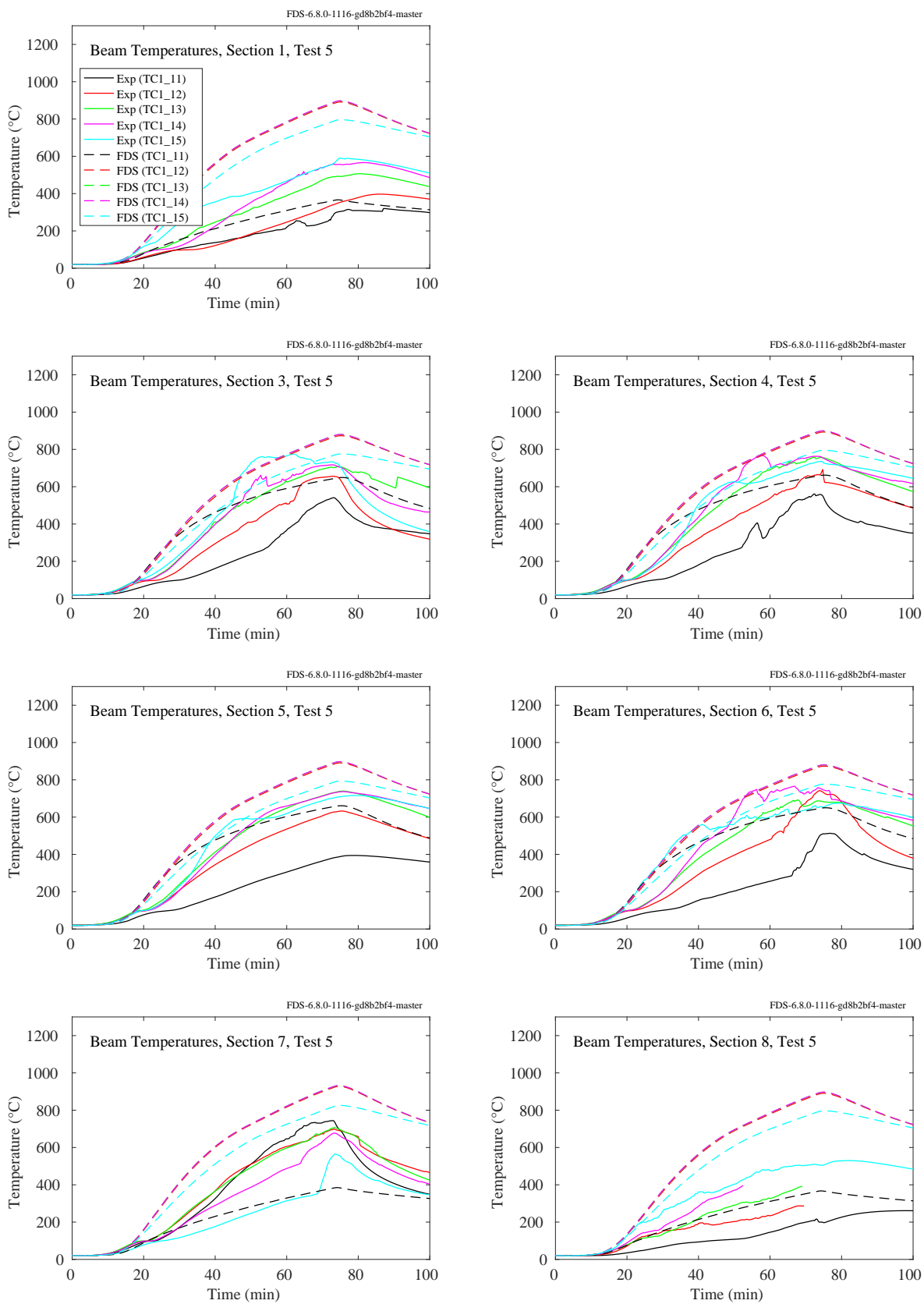


Figure 11.52: NIST Composite Beam, beam temperatures.

11.2.2 NIST E119 Compartment

A brief description of the experiments is given in Sec. 3.51. The compartment interior dimensions are 10.8 m long, running east-west, 7.0 m wide, and 3.8 m high. Three fire experiments were performed, labeled as Tests 1-3.

Figure 11.53 displays the plate thermometer temperatures at three locations. Locations of PT1 through PT3 were shown in Fig. 3.27.

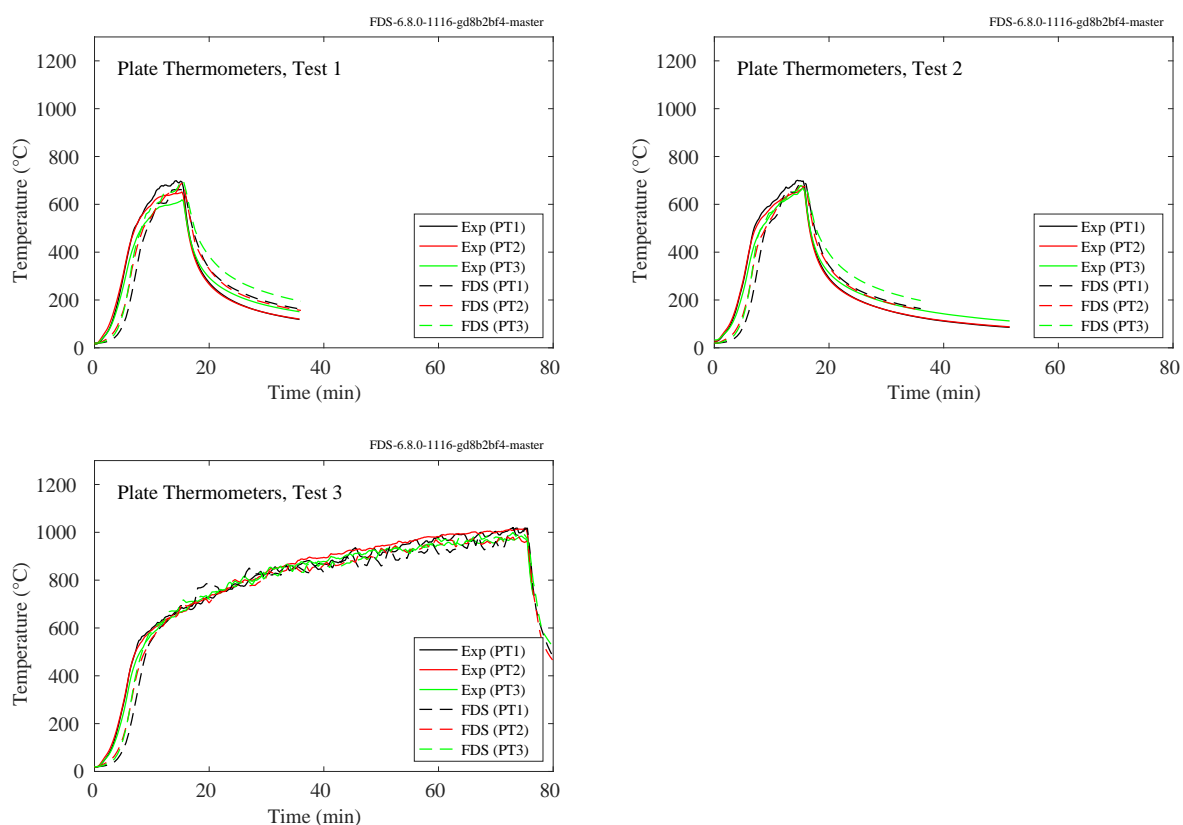


Figure 11.53: NIST E119 Compartment, Plate temperatures.

11.2.3 NIST/NRC Experiments

Electrical cables of various types (power and control), and configurations (horizontal or vertical; in tray or free-hanging), were installed in the test compartment. For each of the four cable targets considered, measurements of the local gas temperature, surface temperature, radiative heat flux, and total heat flux are available. The following pages display comparisons of surface temperature for Control Cable B, Horizontal Cable Tray D, Power Cable F, and Vertical Cable Tray G. For the bundled cables within horizontal and vertical trays (Targets D and G), FDS assumes them to be rectangular slabs of thickness comparable to the diameter of the individual cables. For the free-hanging cables B and F, FDS assumes them to be cylinders of uniform composition.

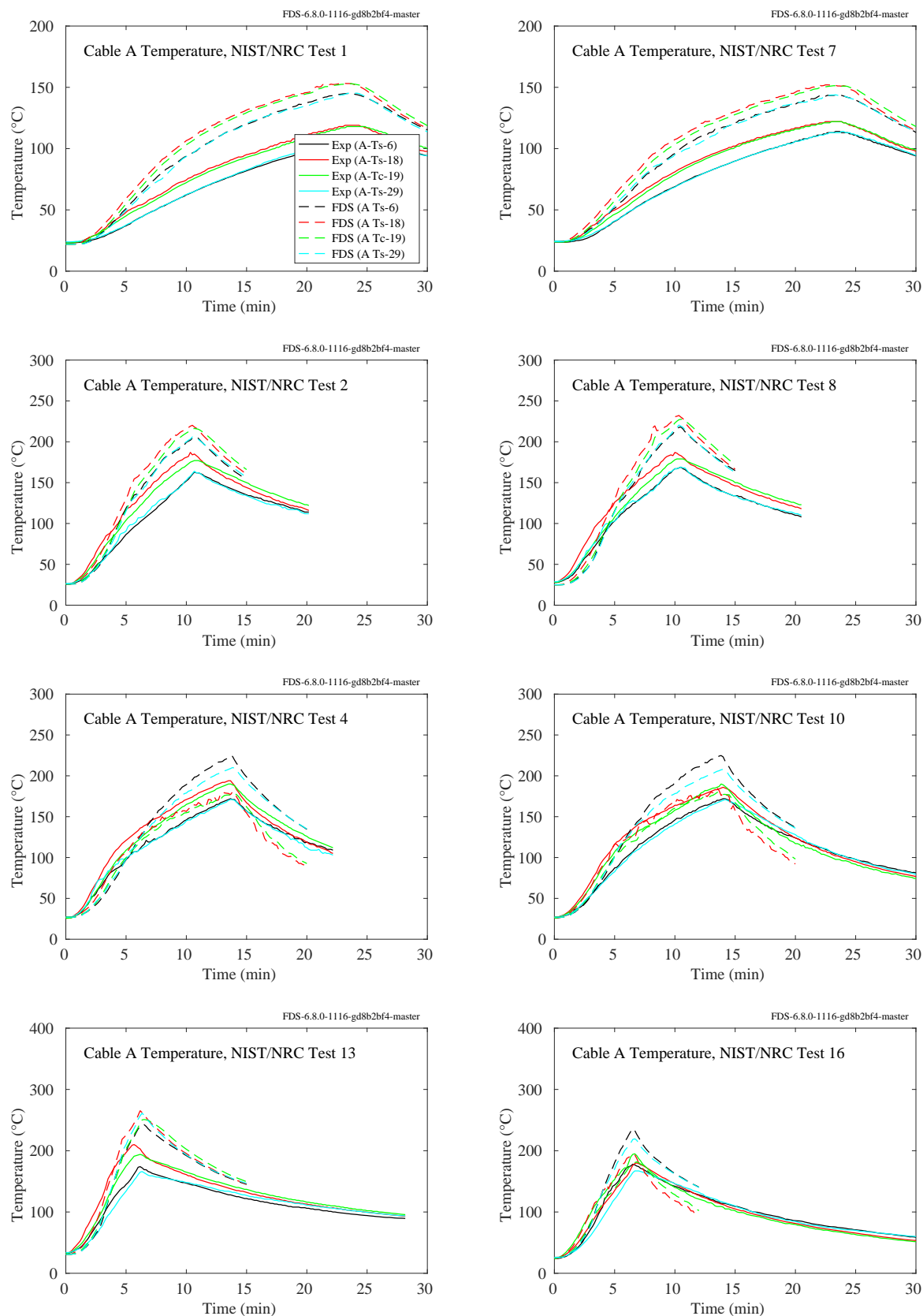


Figure 11.54: NIST/NRC experiments, Cable A temperatures, Tests 1, 2, 4, 7, 8, 10, 13, 16.

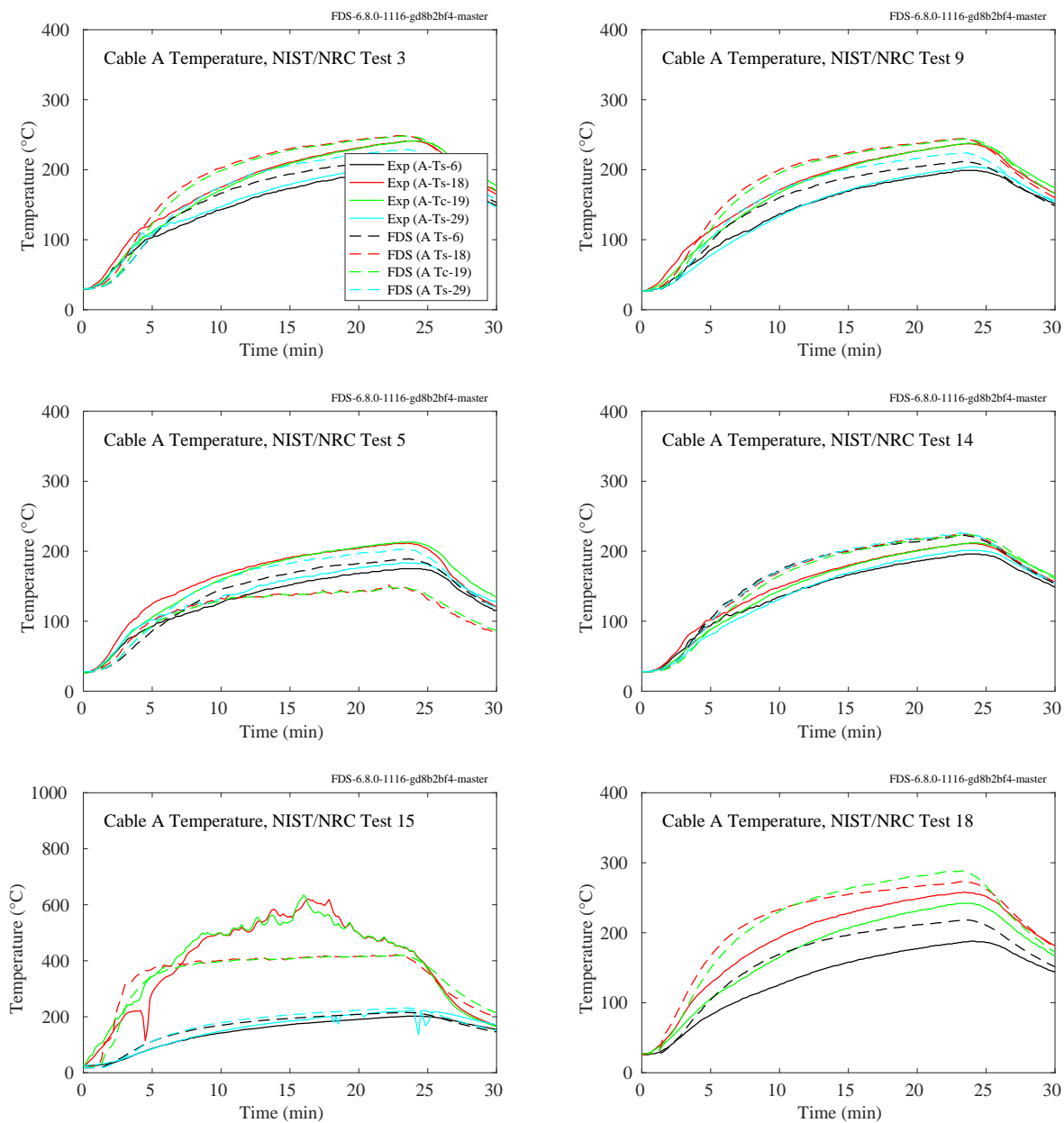


Figure 11.55: NIST/NRC experiments, Cable A temperatures, Tests 3, 5, 9, 14, 15, 18.

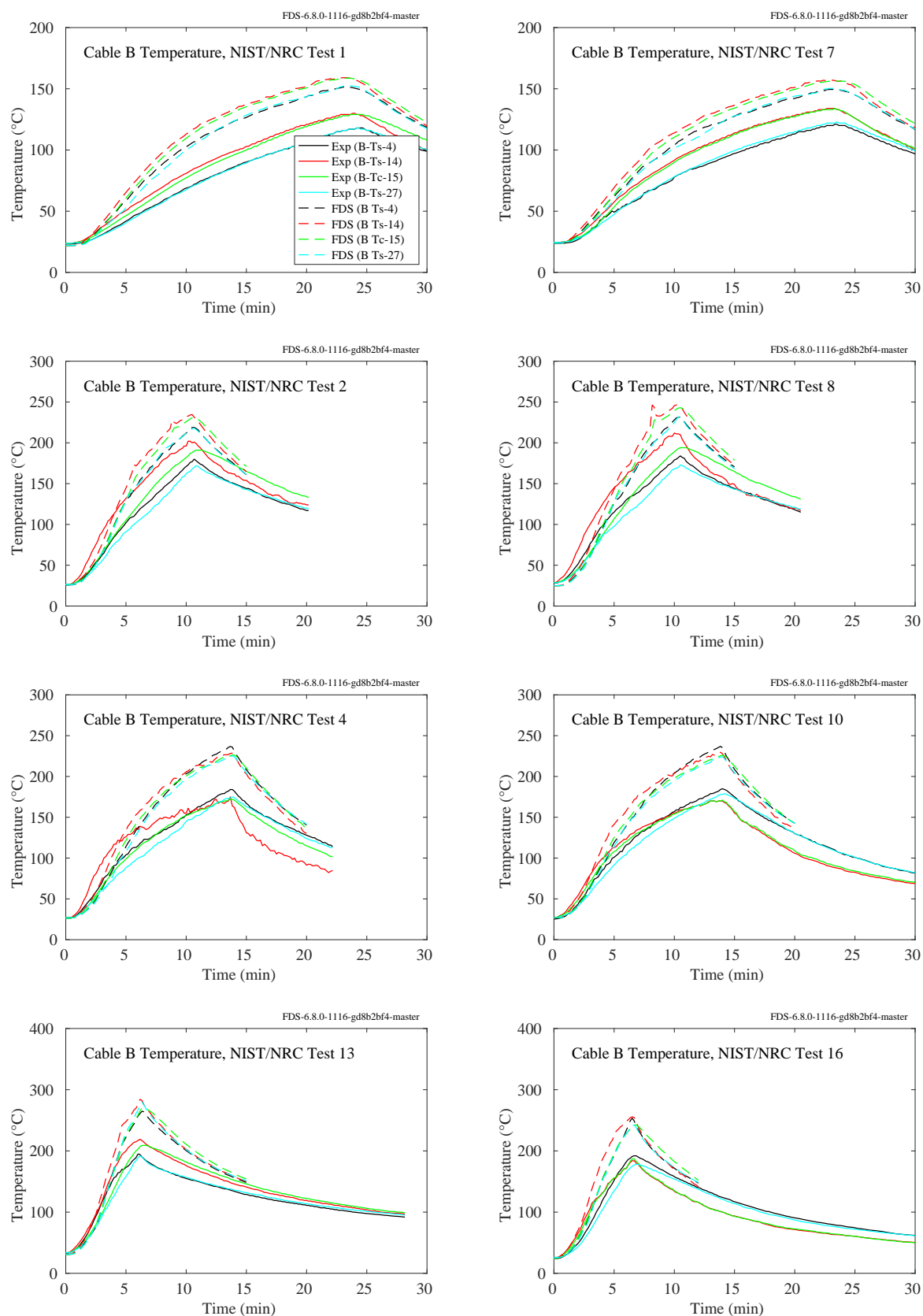


Figure 11.56: NIST/NRC experiments, Cable B temperatures, Tests 1, 2, 4, 7, 8, 10, 13, 16.

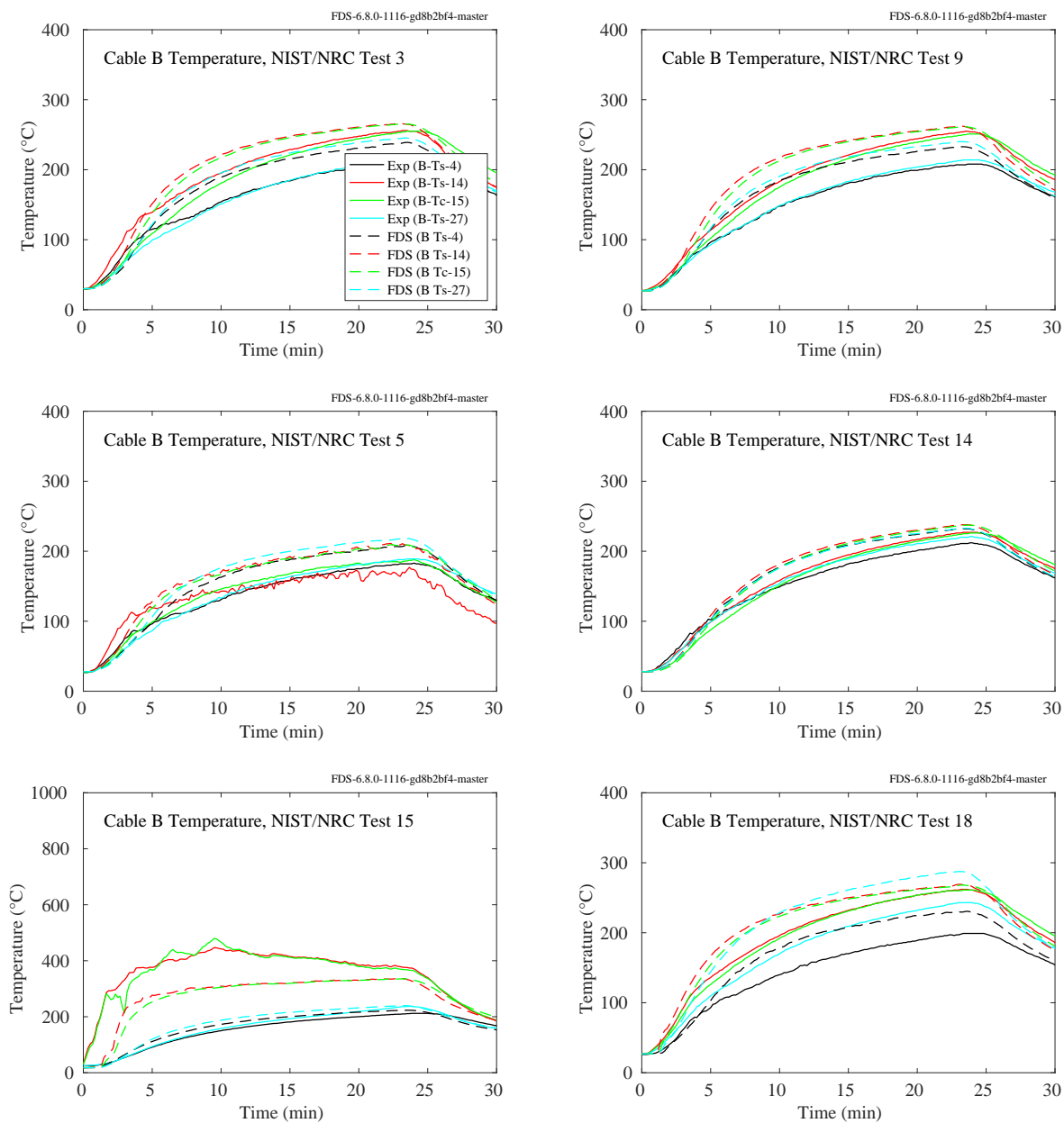


Figure 11.57: NIST/NRC experiments, Cable B temperatures, Tests 3, 5, 9, 14, 15, 18.

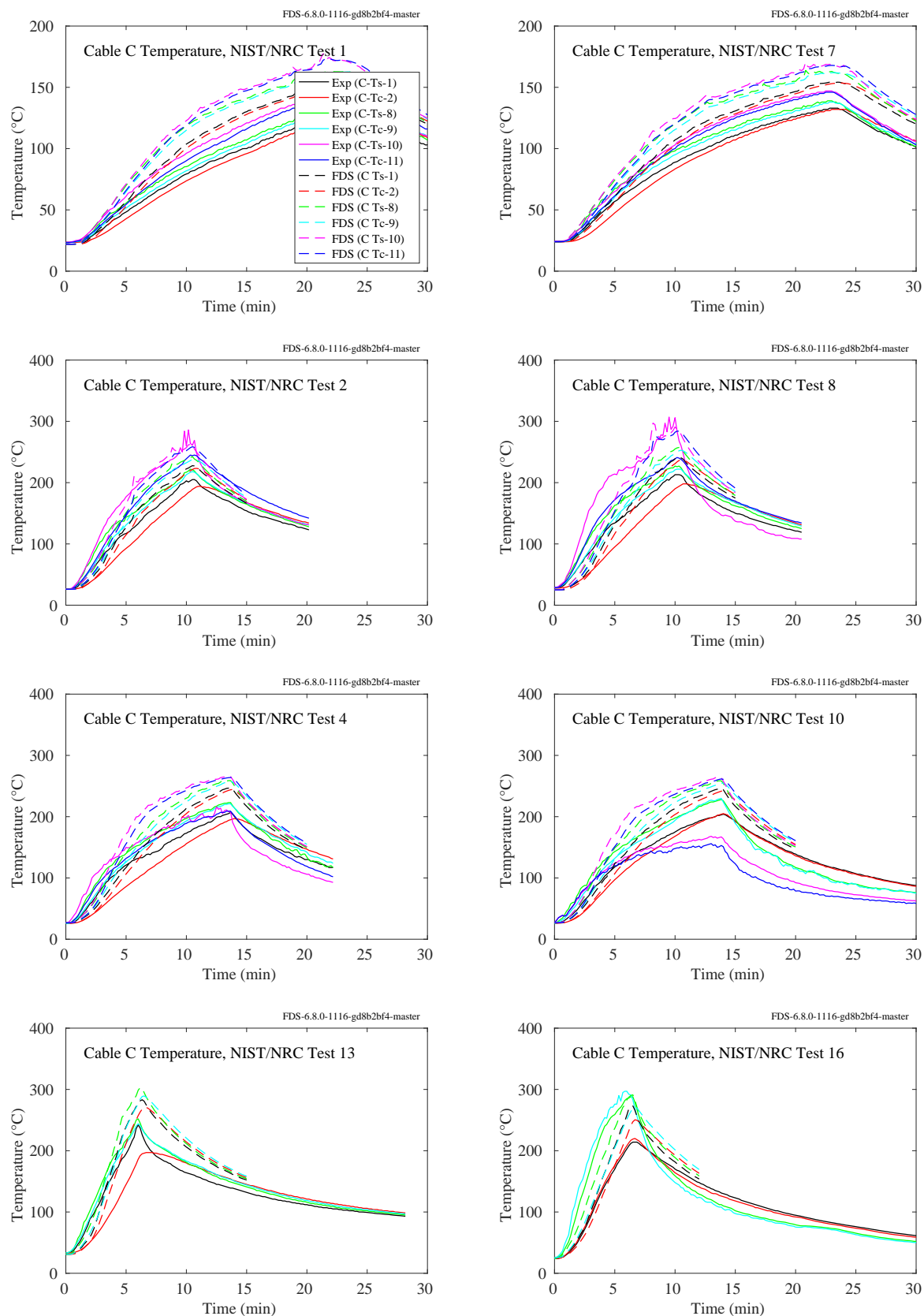


Figure 11.58: NIST/NRC experiments, Cable Ca temperatures, Tests 1, 2, 4, 7, 8, 10, 13, 16.

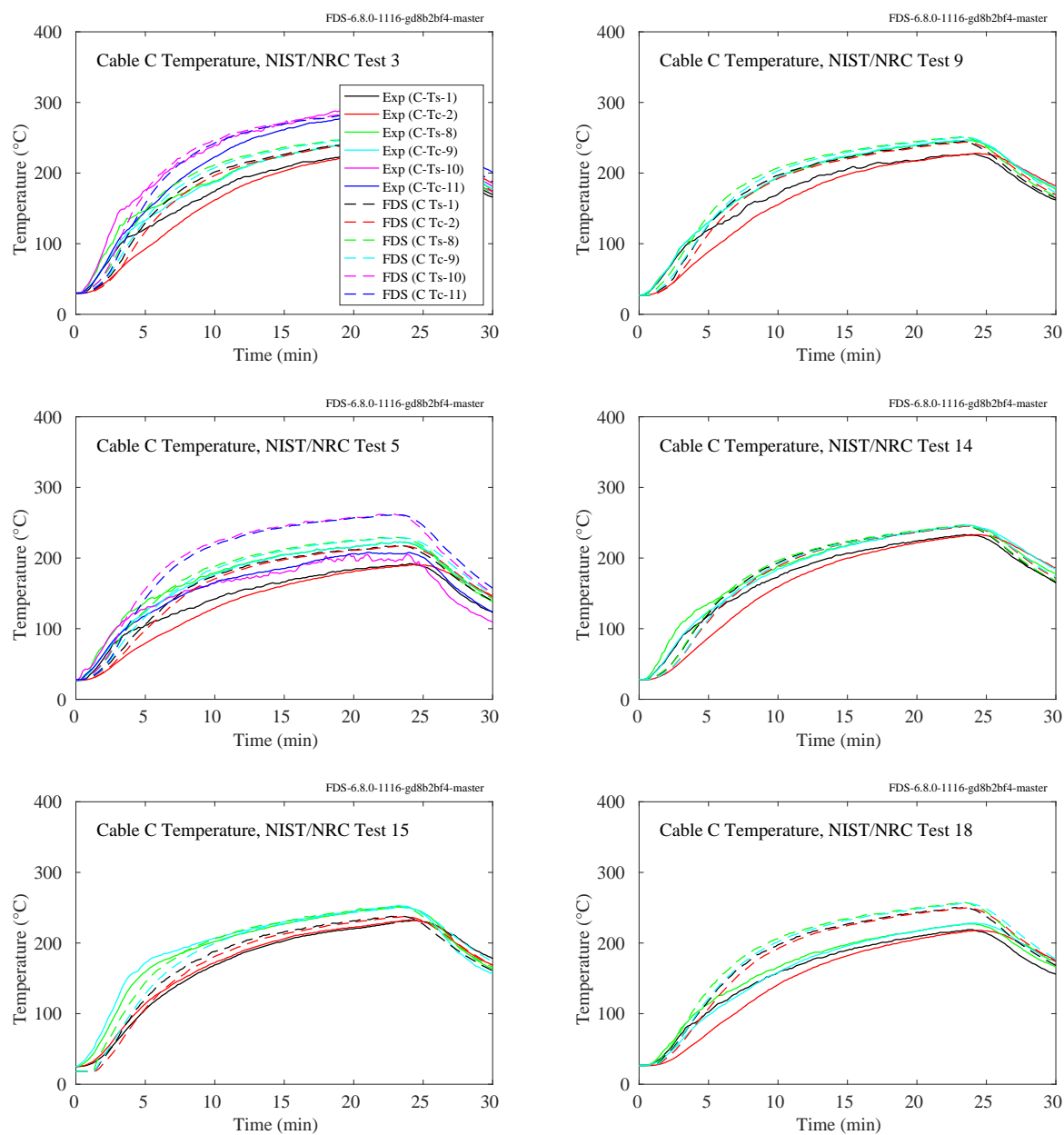


Figure 11.59: NIST/NRC experiments, Cable Ca temperatures, Tests 3, 5, 9, 14, 15, 18.

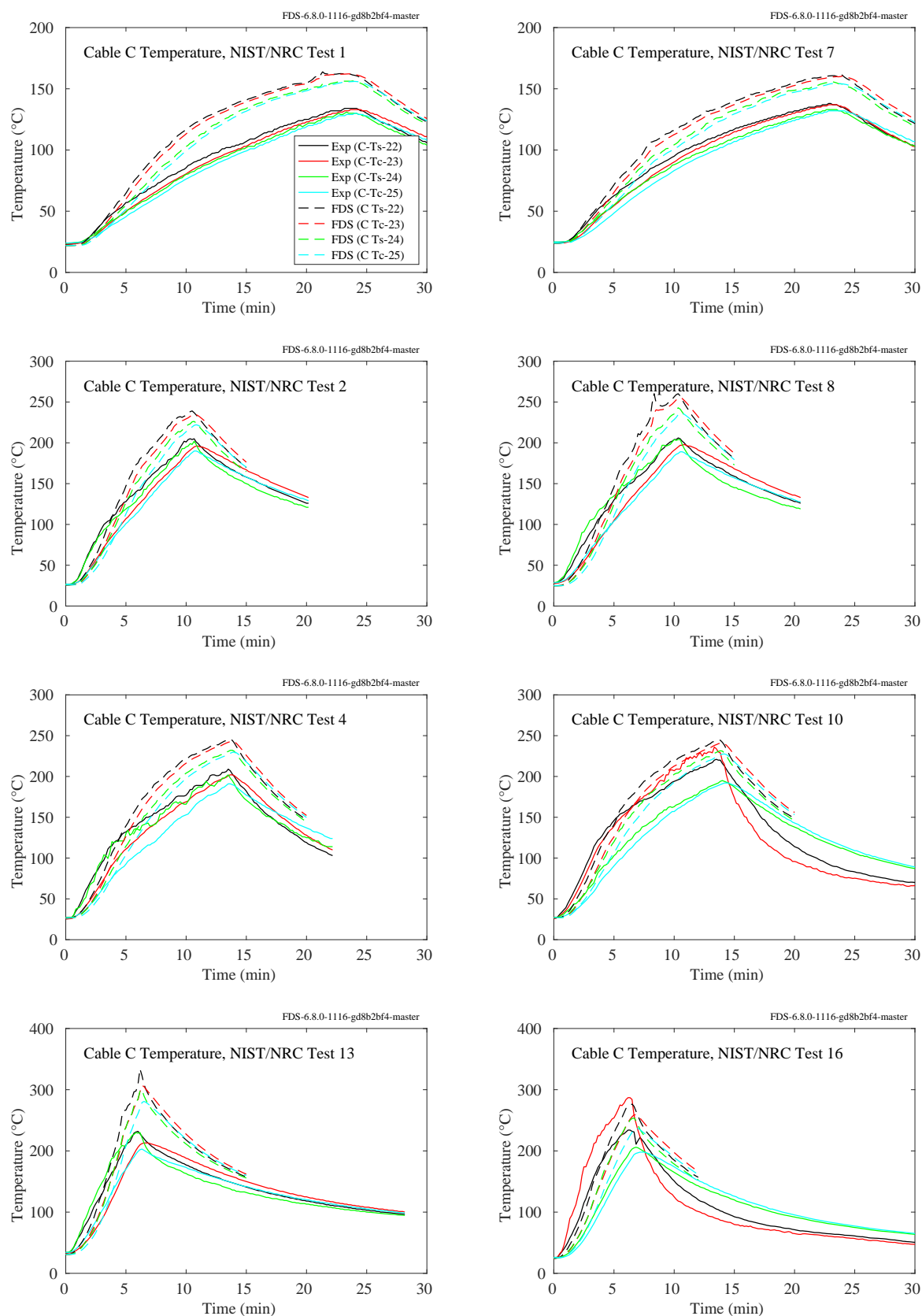


Figure 11.60: NIST/NRC experiments, Cable Cb temperatures, Tests 1, 2, 4, 7, 8, 10, 13, 16.

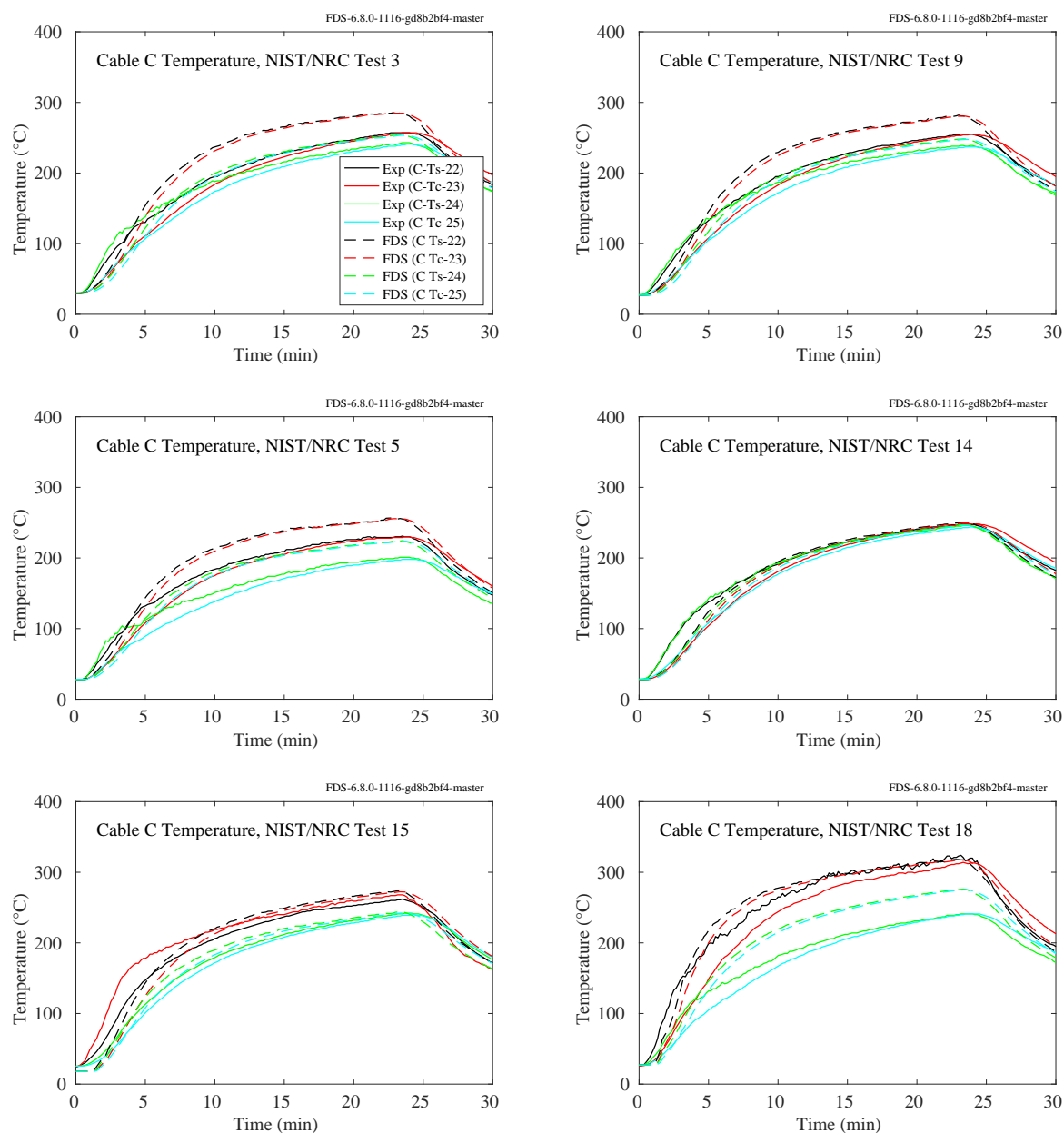


Figure 11.61: NIST/NRC experiments, Cable Cb temperatures, Tests 3, 5, 9, 14, 15, 18.

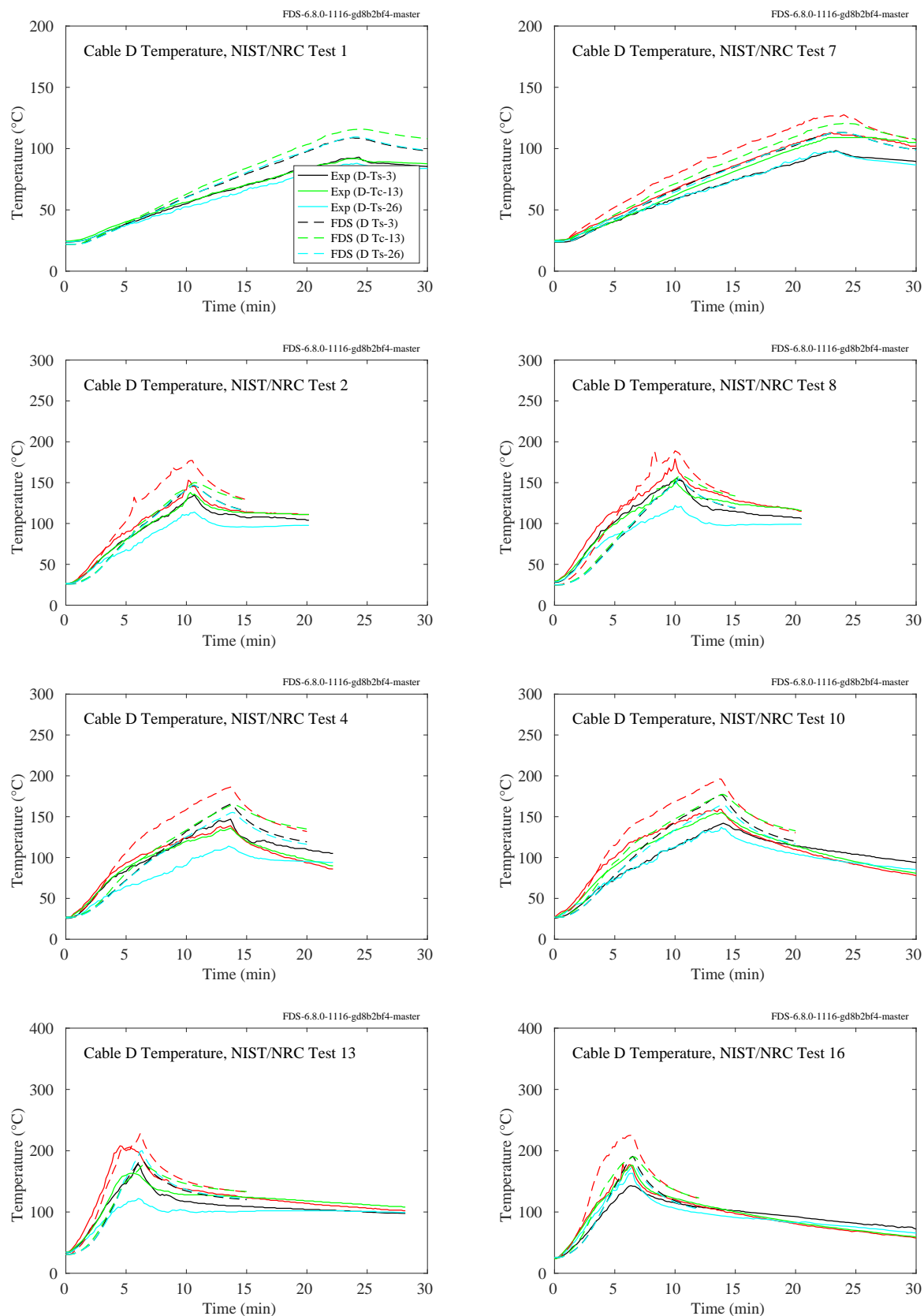


Figure 11.62: NIST/NRC experiments, Cable D temperatures, Tests 1, 2, 4, 7, 8, 10, 13, 16.

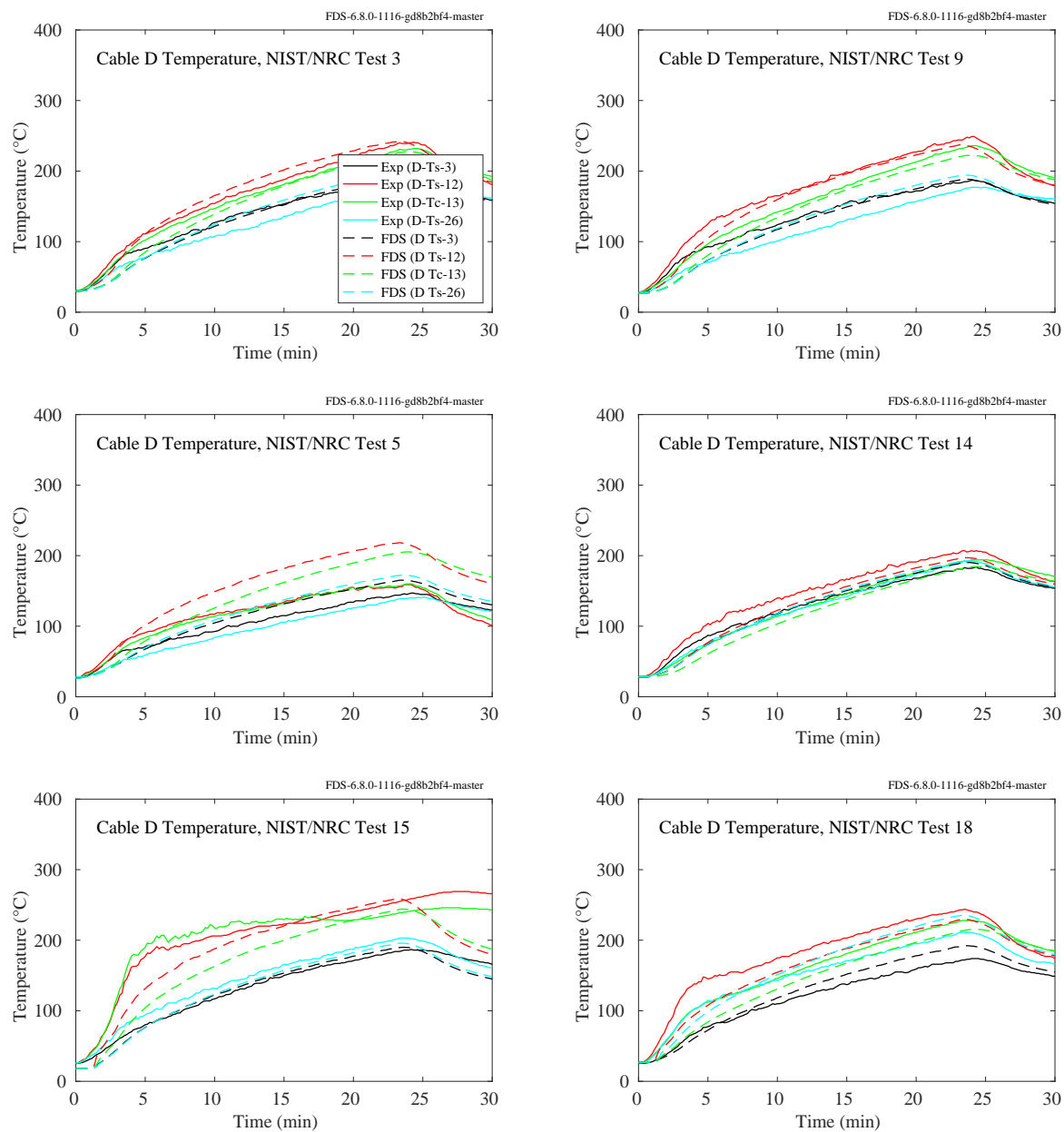


Figure 11.63: NIST/NRC experiments, Cable D temperatures, Tests 3, 5, 9, 14, 15, 18.

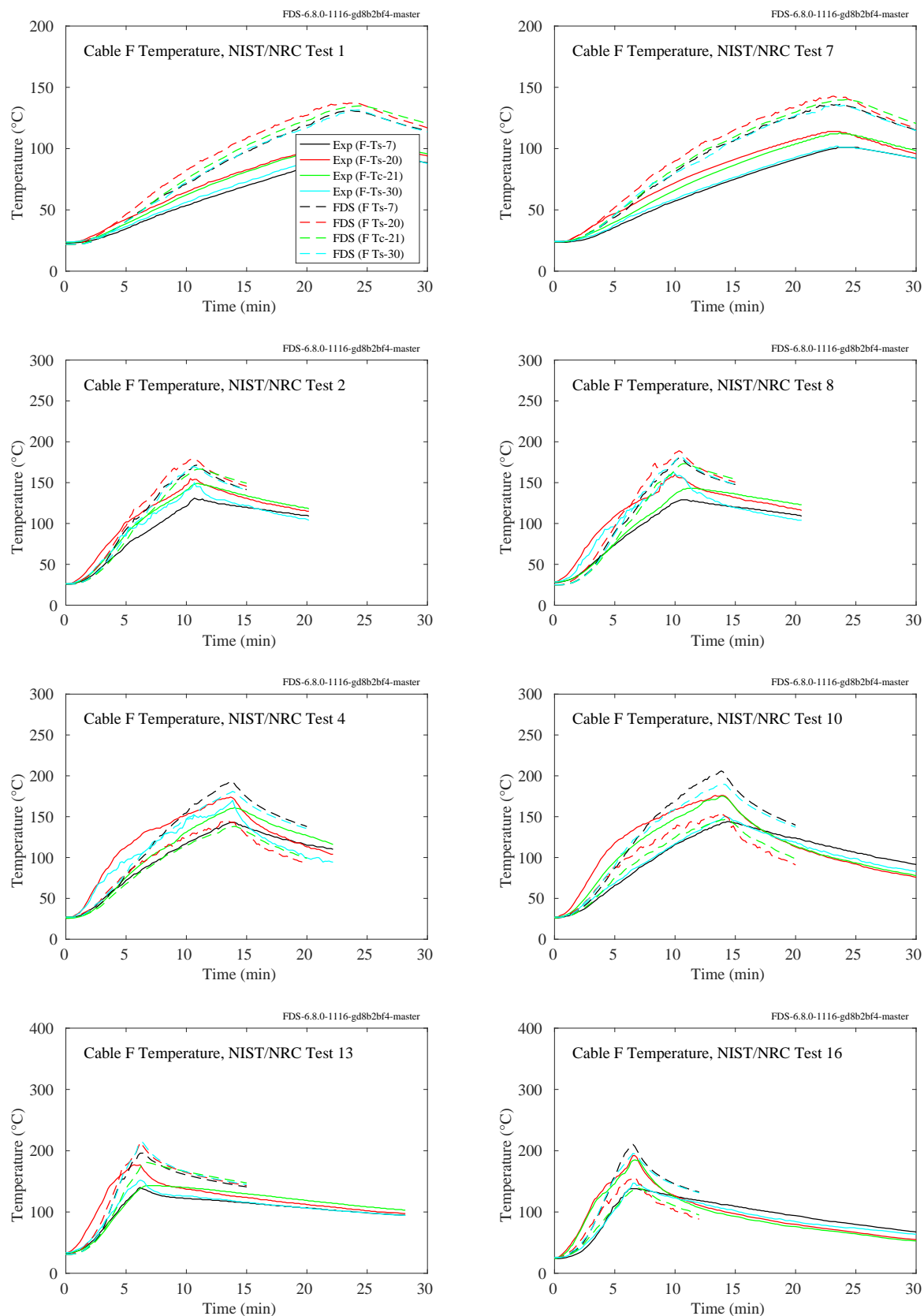


Figure 11.64: NIST/NRC experiments, Cable F temperatures, Tests 1, 2, 4, 7, 8, 10, 13, 16.

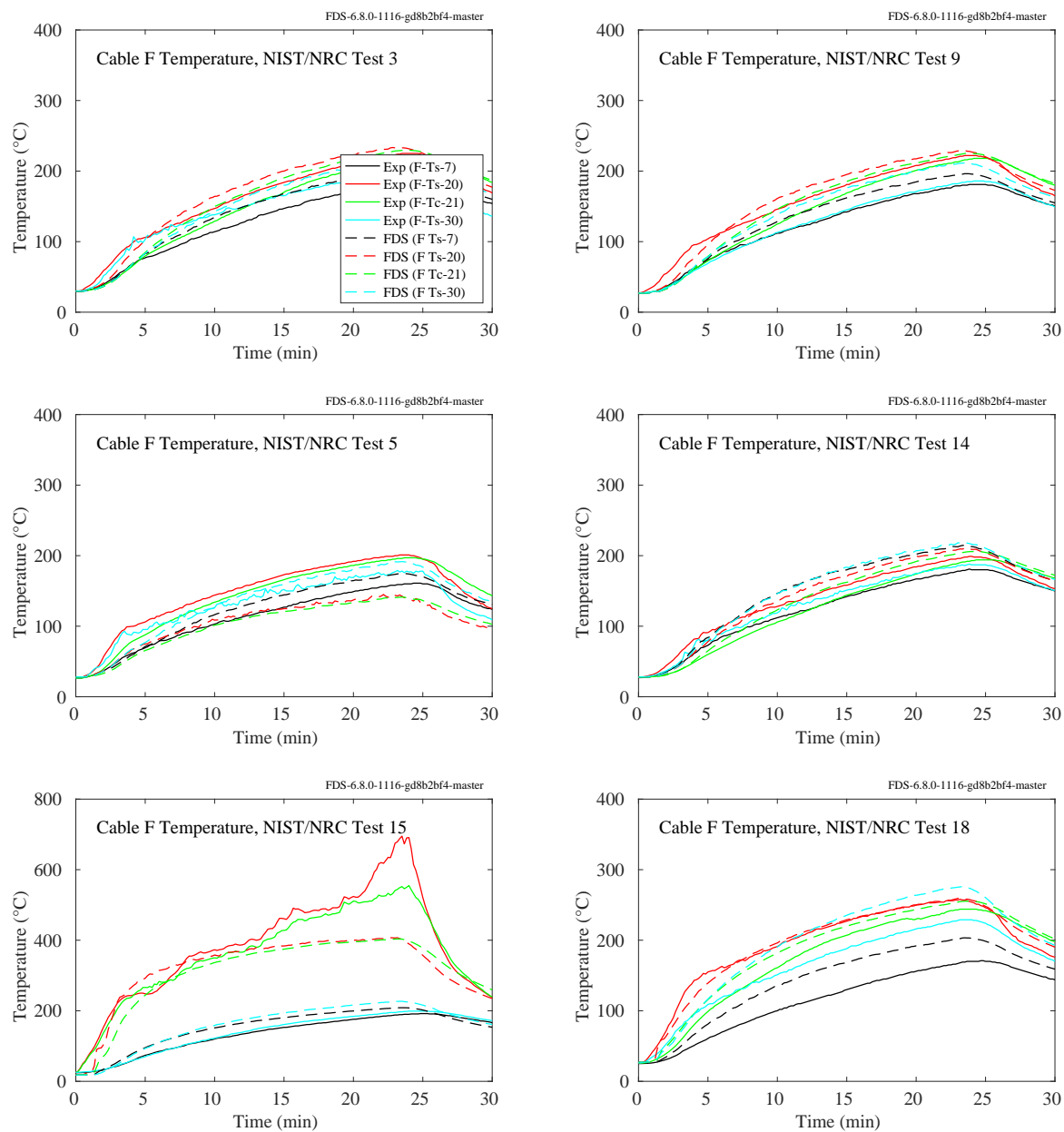


Figure 11.65: NIST/NRC experiments, Cable F temperatures, Tests 3, 5, 9, 14, 15, 18.

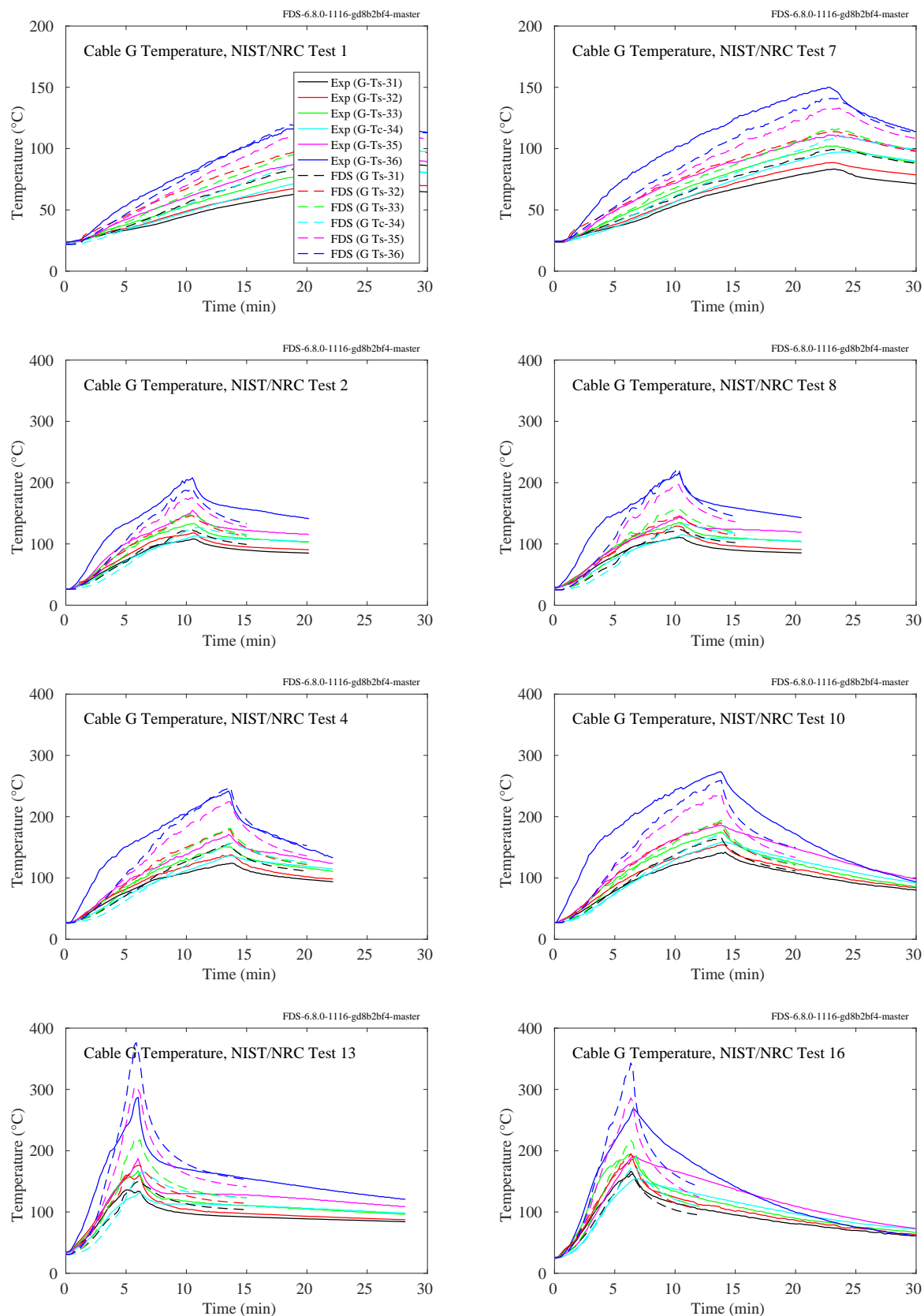


Figure 11.66: NIST/NRC experiments, Cable G temperatures, Tests 1, 2, 4, 7, 8, 10, 13, 16.

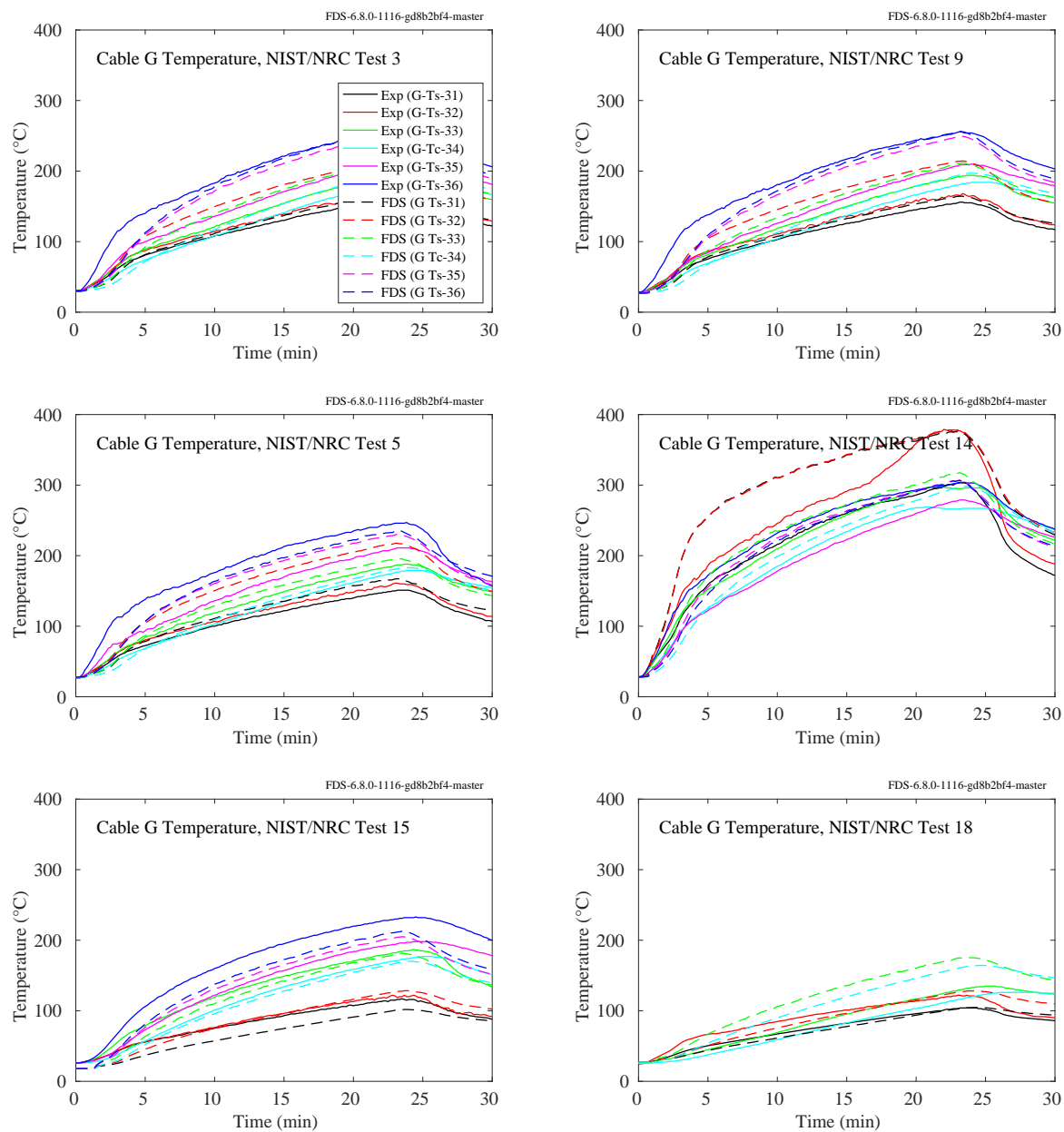


Figure 11.67: NIST/NRC experiments, Cable G temperatures, Tests 3, 5, 9, 14, 15, 18.

11.2.4 NIST/NRC Corner Effects Experiments

The plots on the following pages display comparisons of plate thermometer (PT) temperatures for the cabinet experiments. Two PTs were positioned facing each side of the cabinets, at a distance of 60 cm and heights of 76 cm and 137 cm, on center. In addition, a Type K thermocouple (TC) was welded to the back of the cabinet, centered both horizontally and vertically.

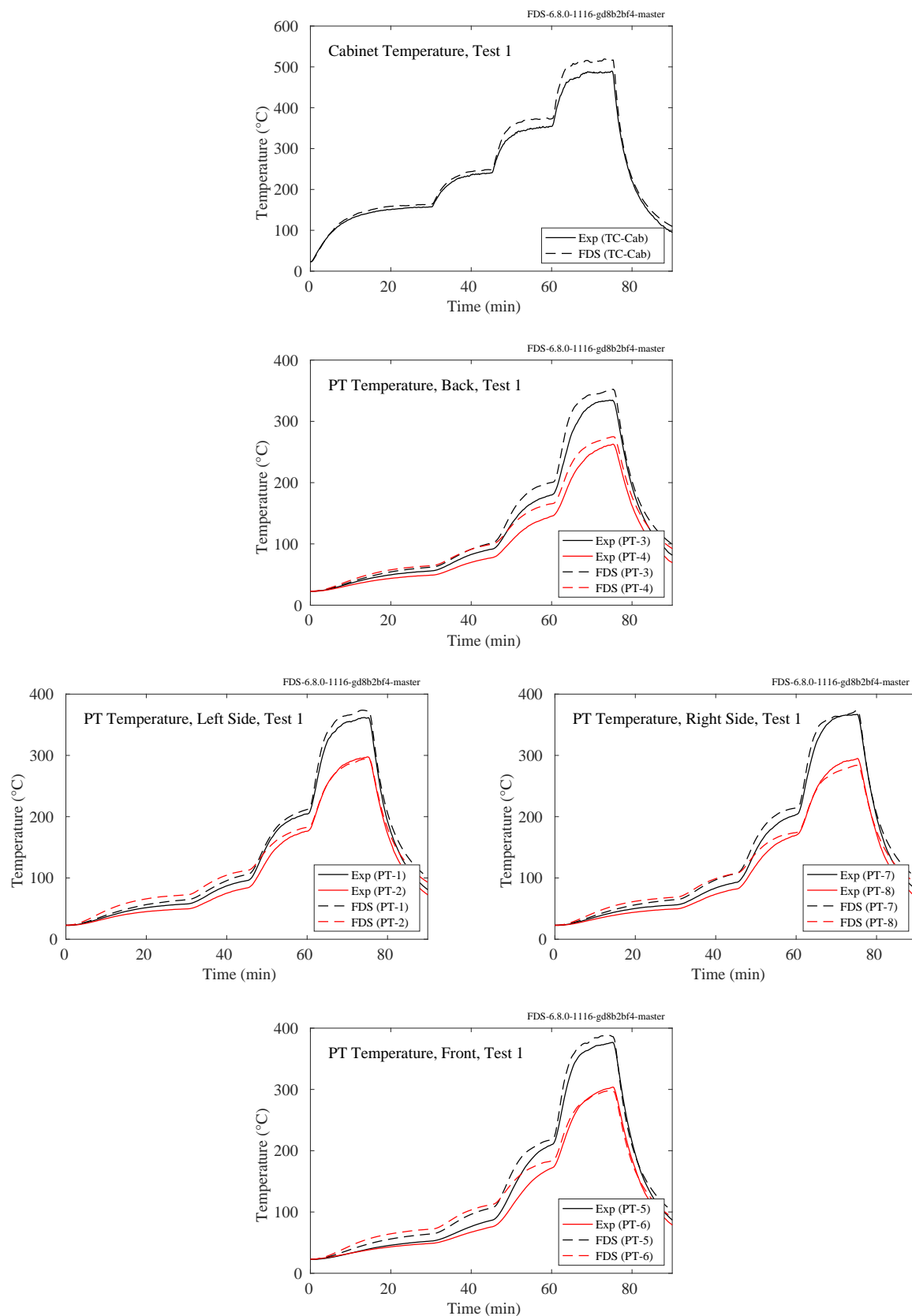


Figure 11.68: NIST/NRC Corner Effects, plate and cabinet temperatures, Test 1.

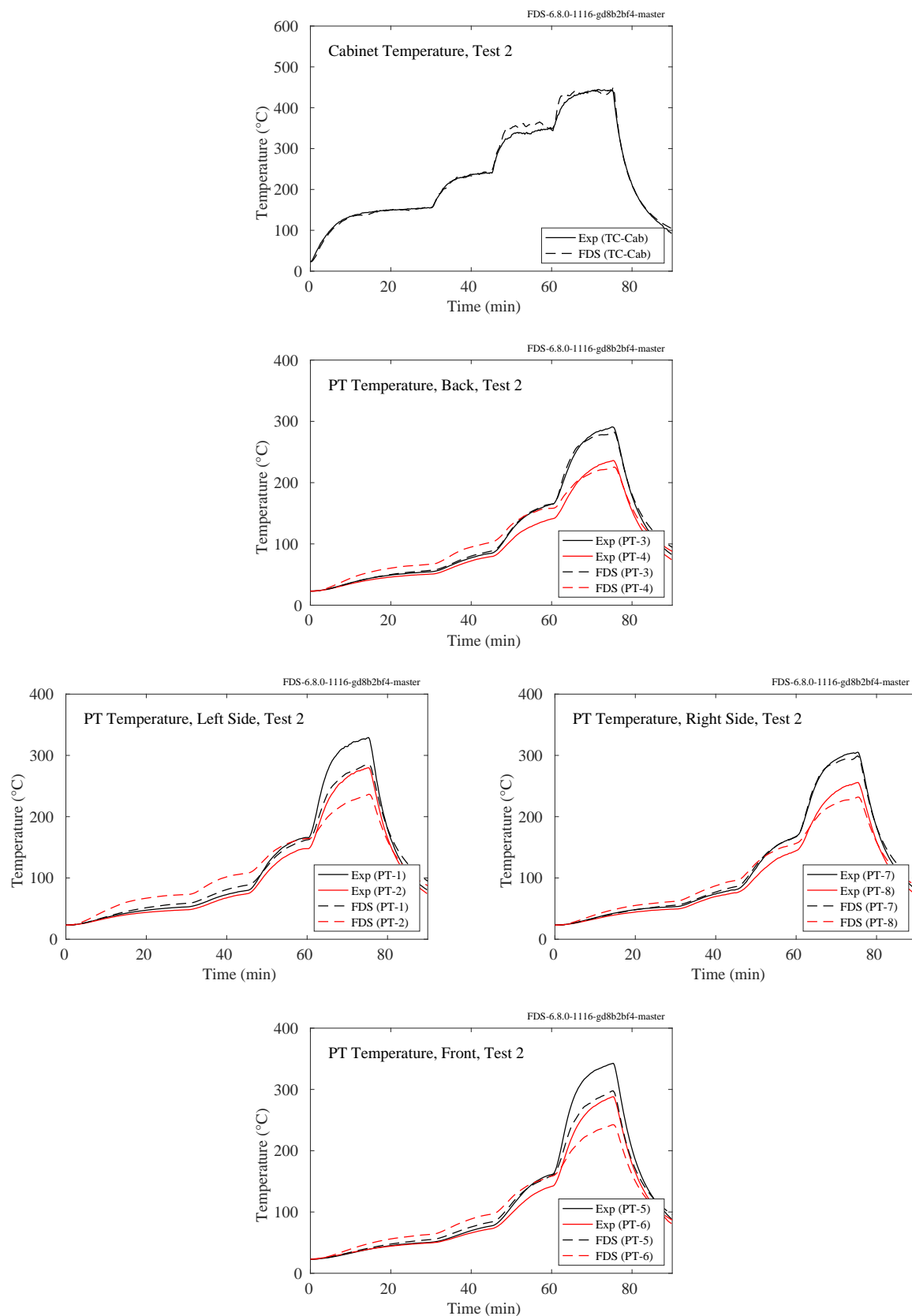


Figure 11.69: NIST/NRC Corner Effects, plate and cabinet temperatures, Test 2.

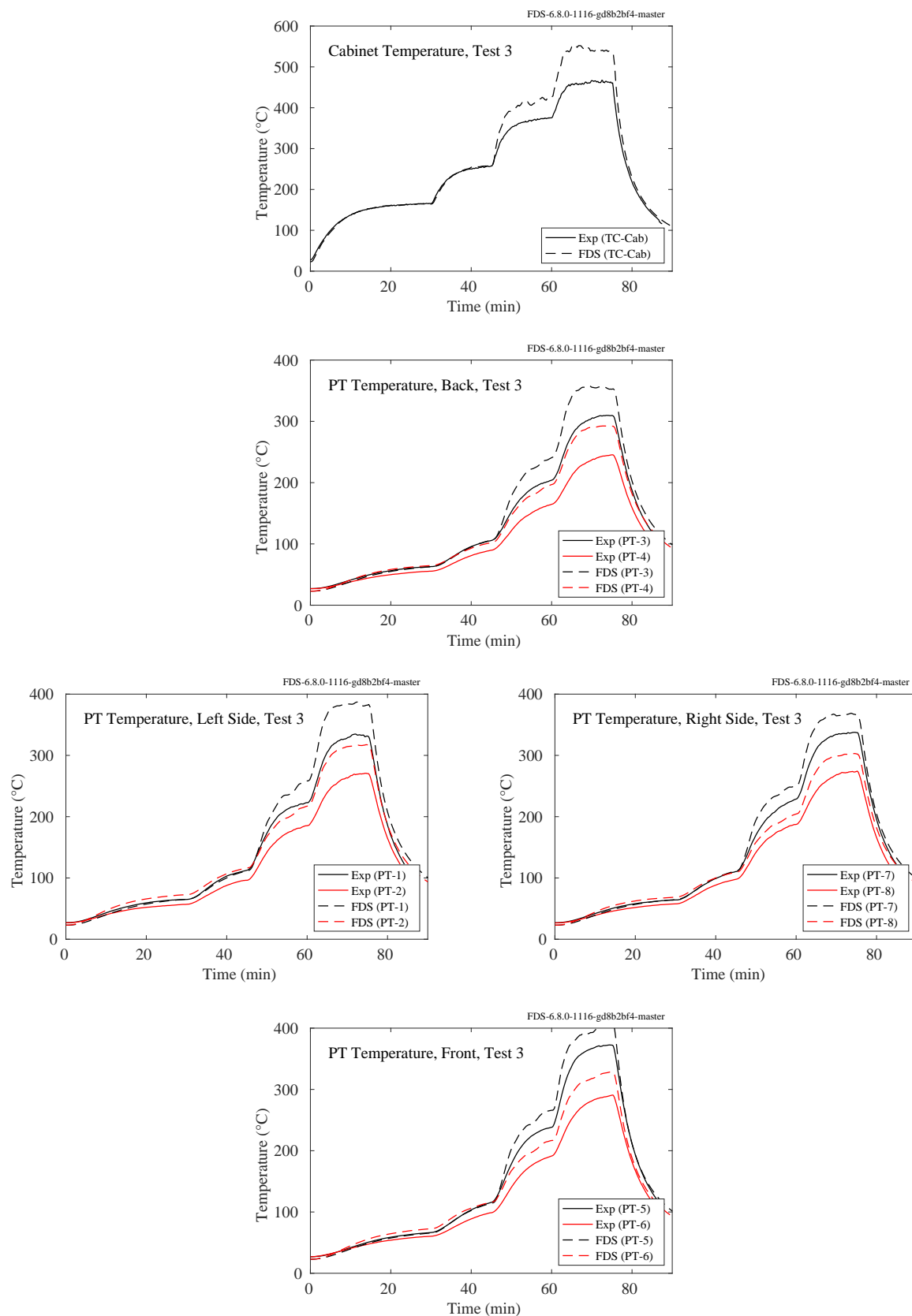


Figure 11.70: NIST/NRC Corner Effects, plate and cabinet temperatures, Test 3.

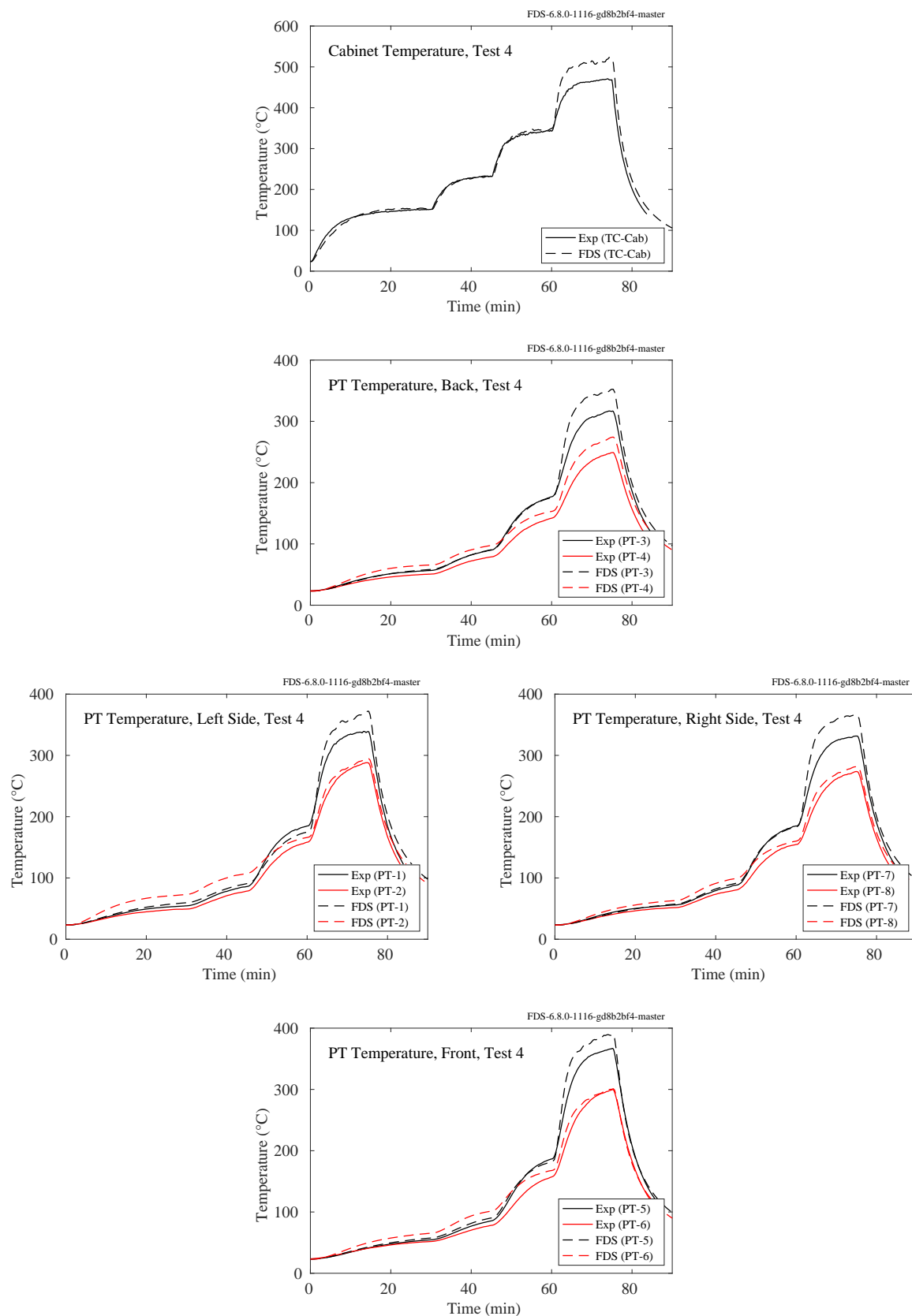


Figure 11.71: NIST/NRC Corner Effects, plate and cabinet temperatures, Test 4.

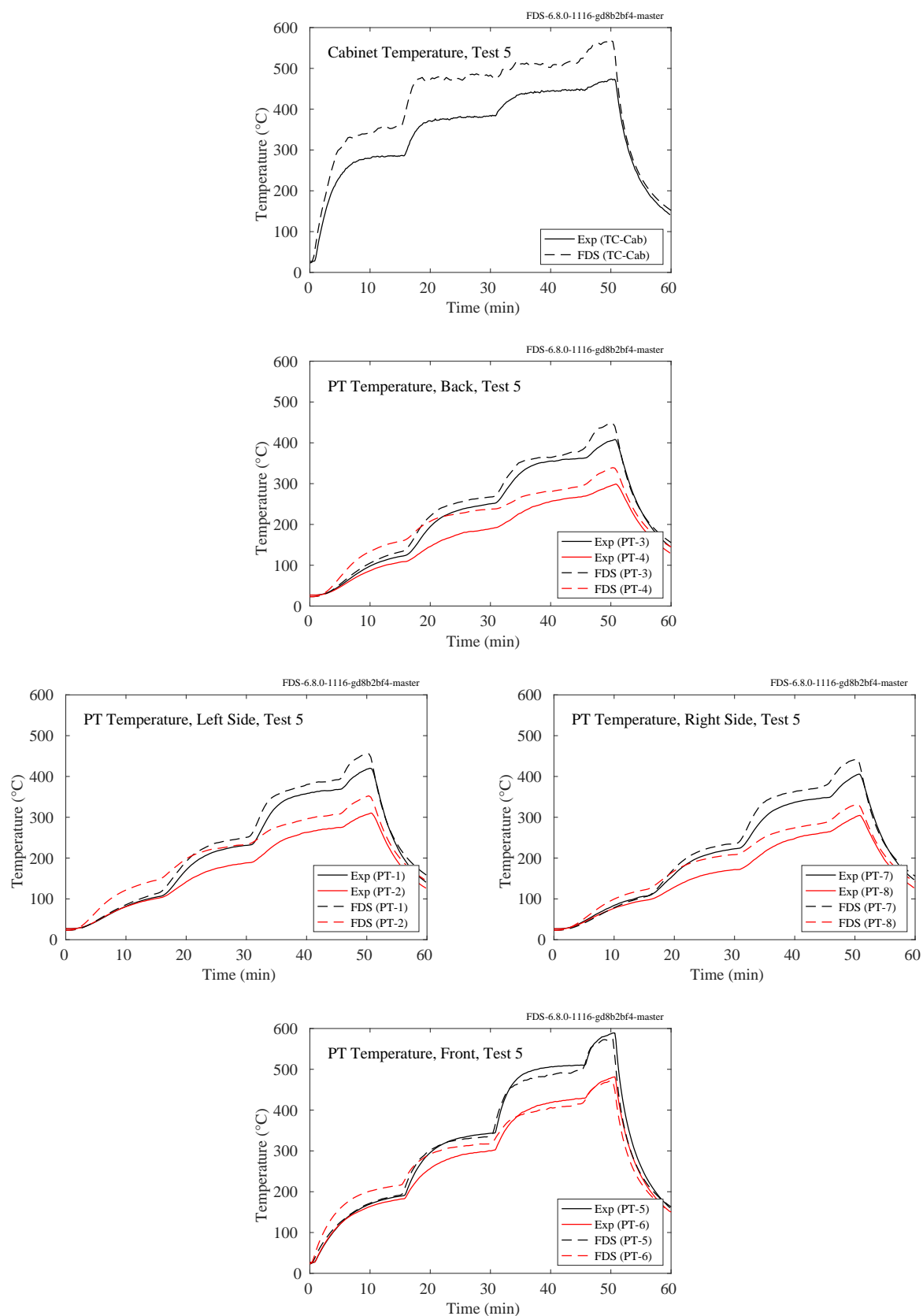


Figure 11.72: NIST/NRC Corner Effects, plate and cabinet temperatures, Test 5.

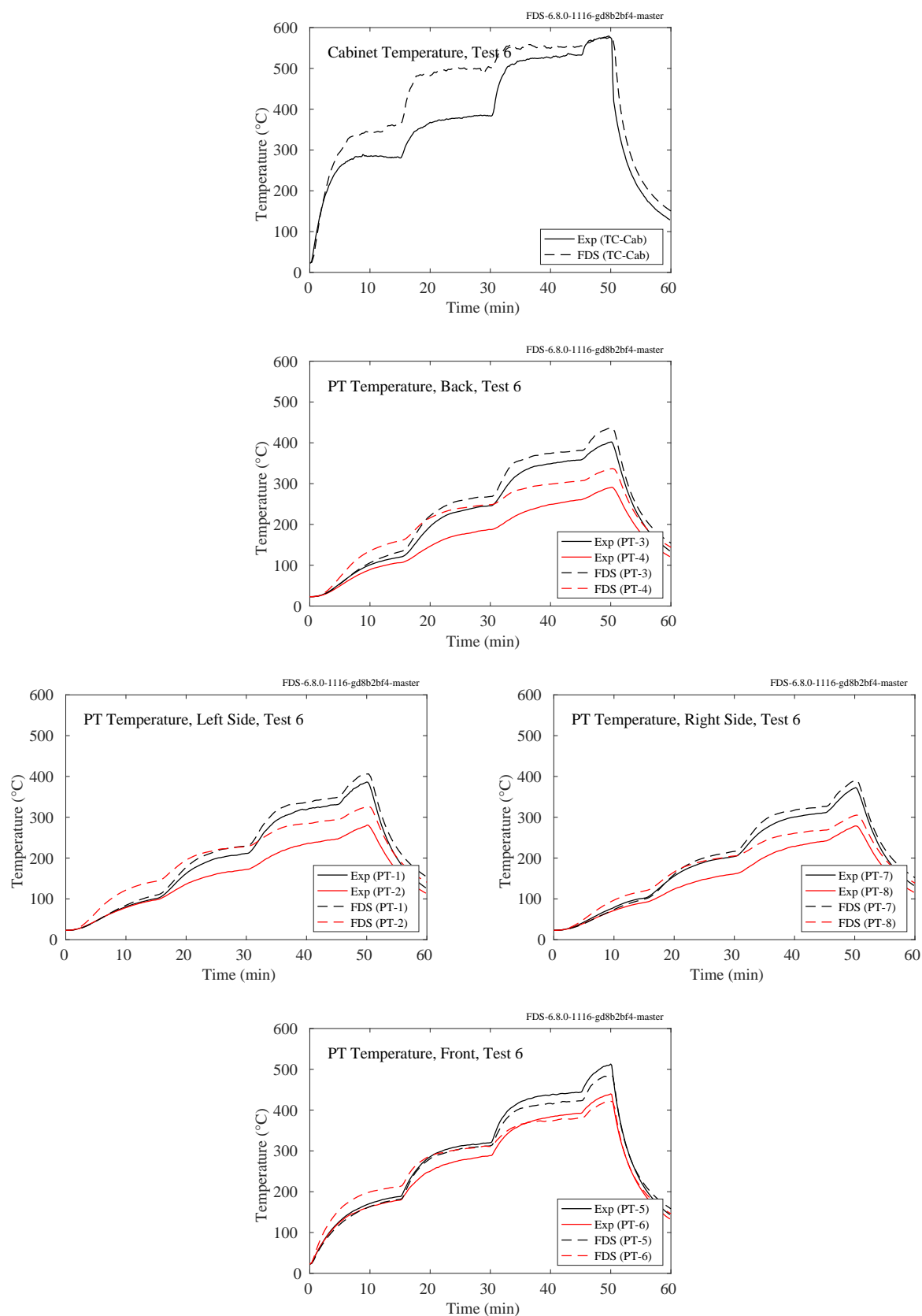


Figure 11.73: NIST/NRC Corner Effects, plate and cabinet temperatures, Test 6.

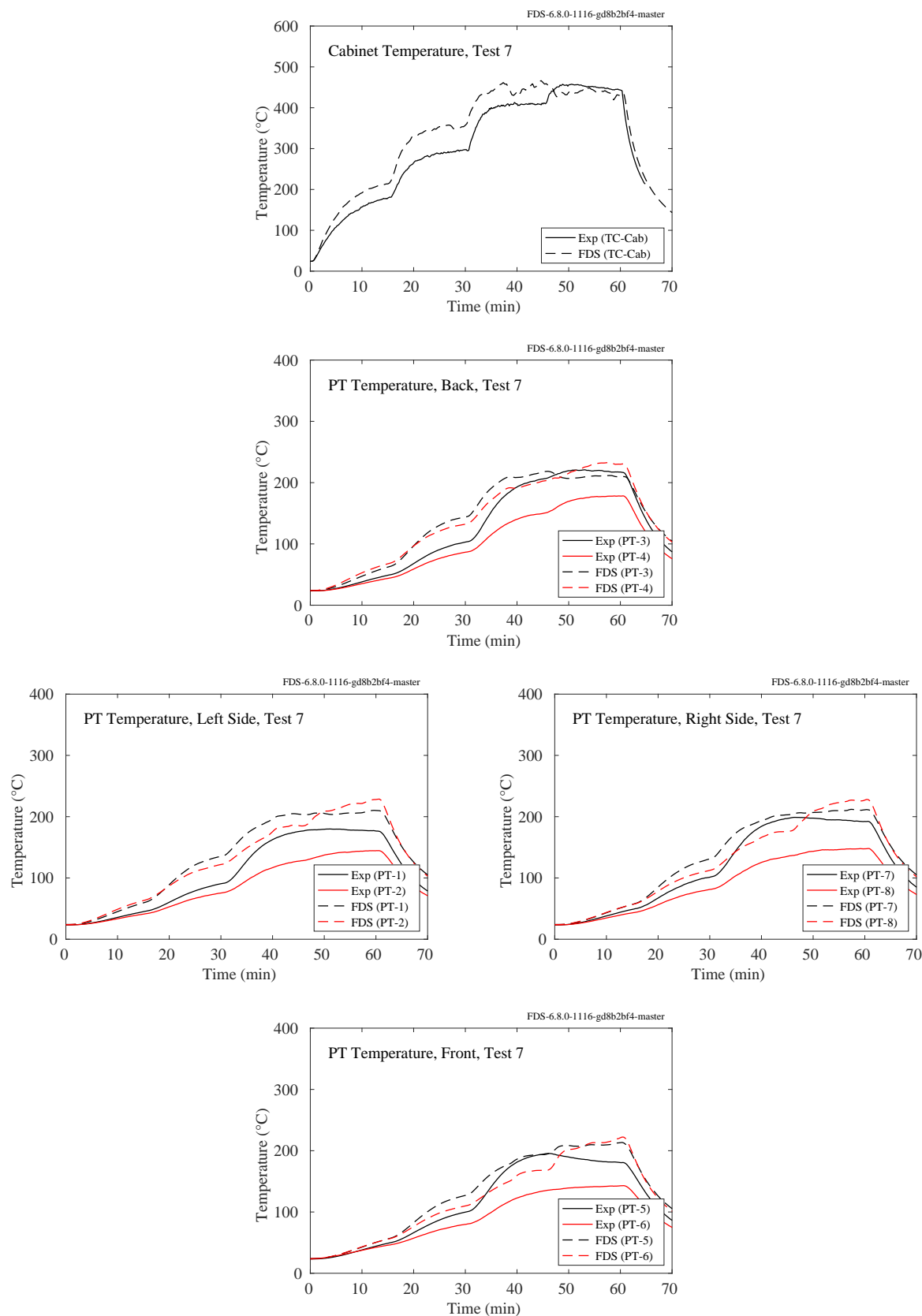


Figure 11.74: NIST/NRC Corner Effects, plate and cabinet temperatures, Test 7.

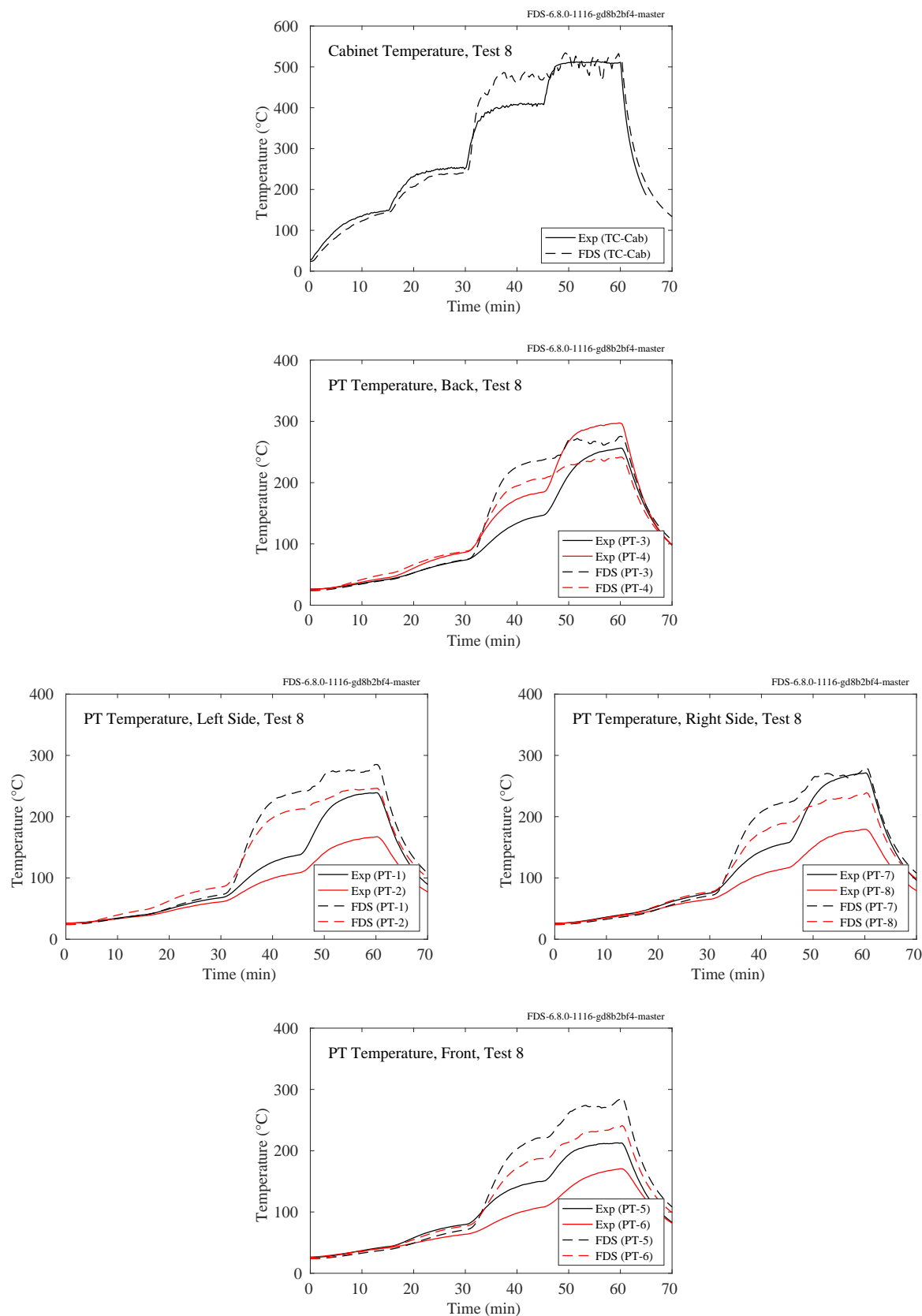


Figure 11.75: NIST/NRC Corner Effects, plate and cabinet temperatures, Test 8.

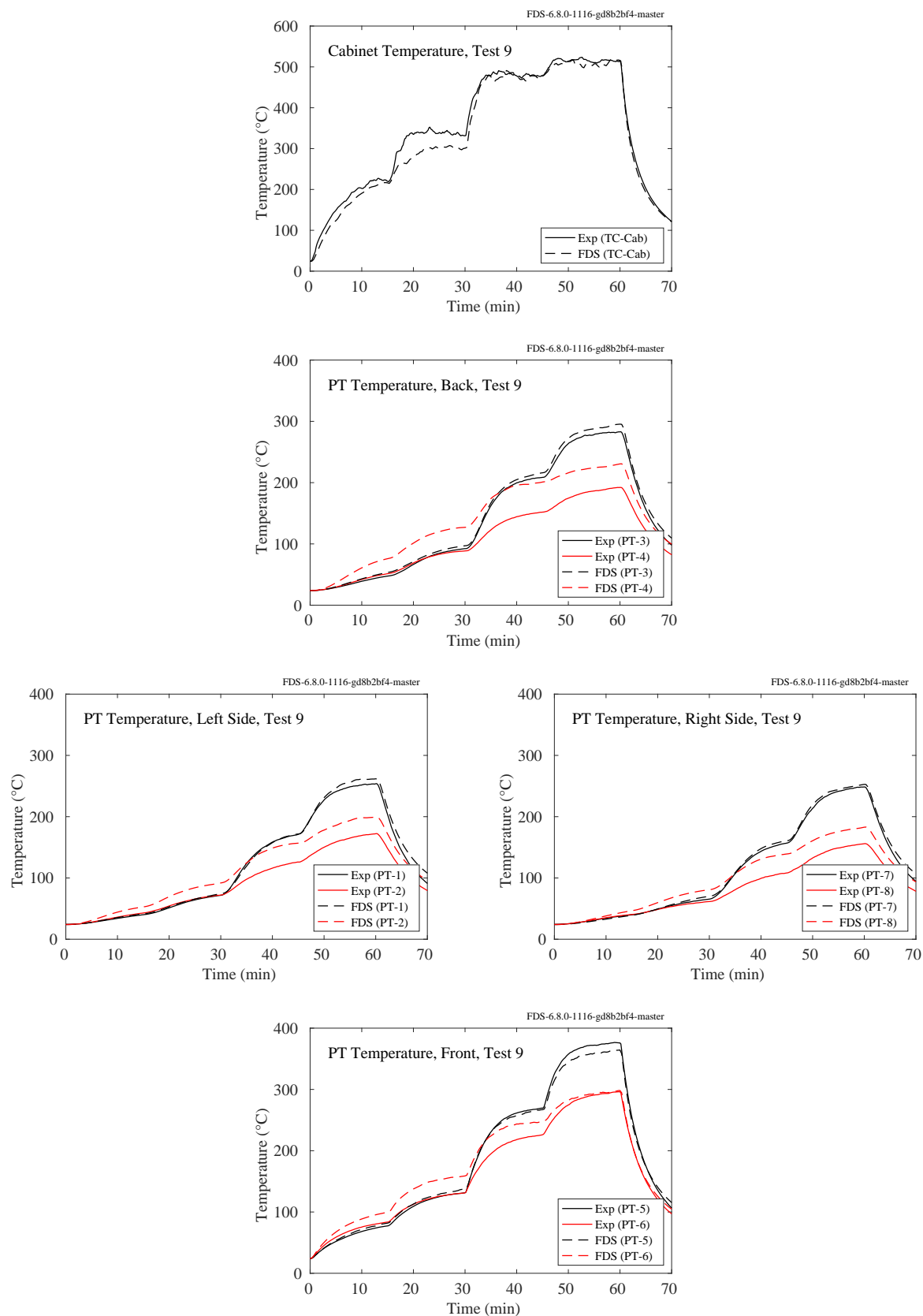


Figure 11.76: NIST/NRC Corner Effects, plate and cabinet temperatures, Test 9.

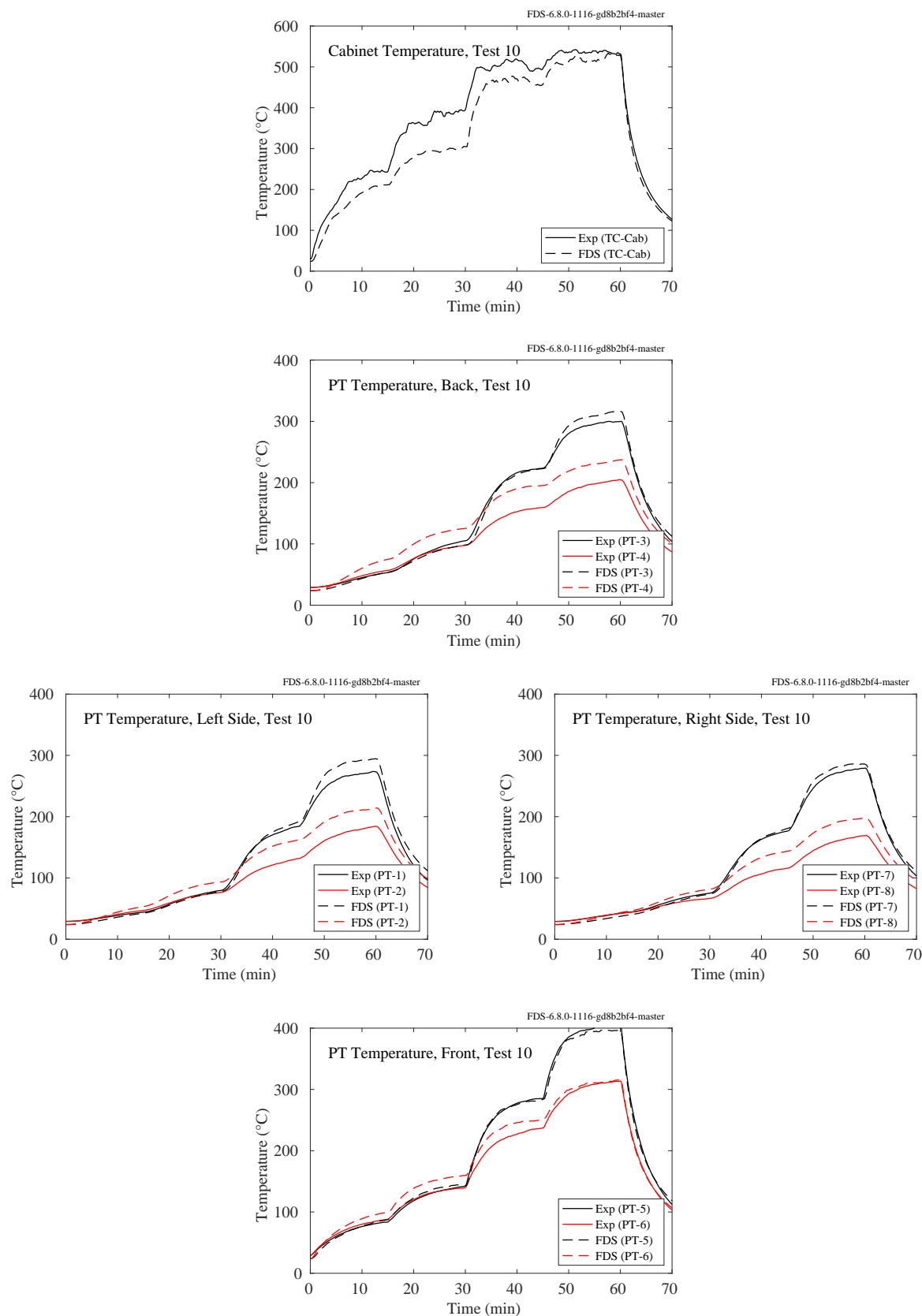


Figure 11.77: NIST/NRC Corner Effects, plate and cabinet temperatures, Test 10.

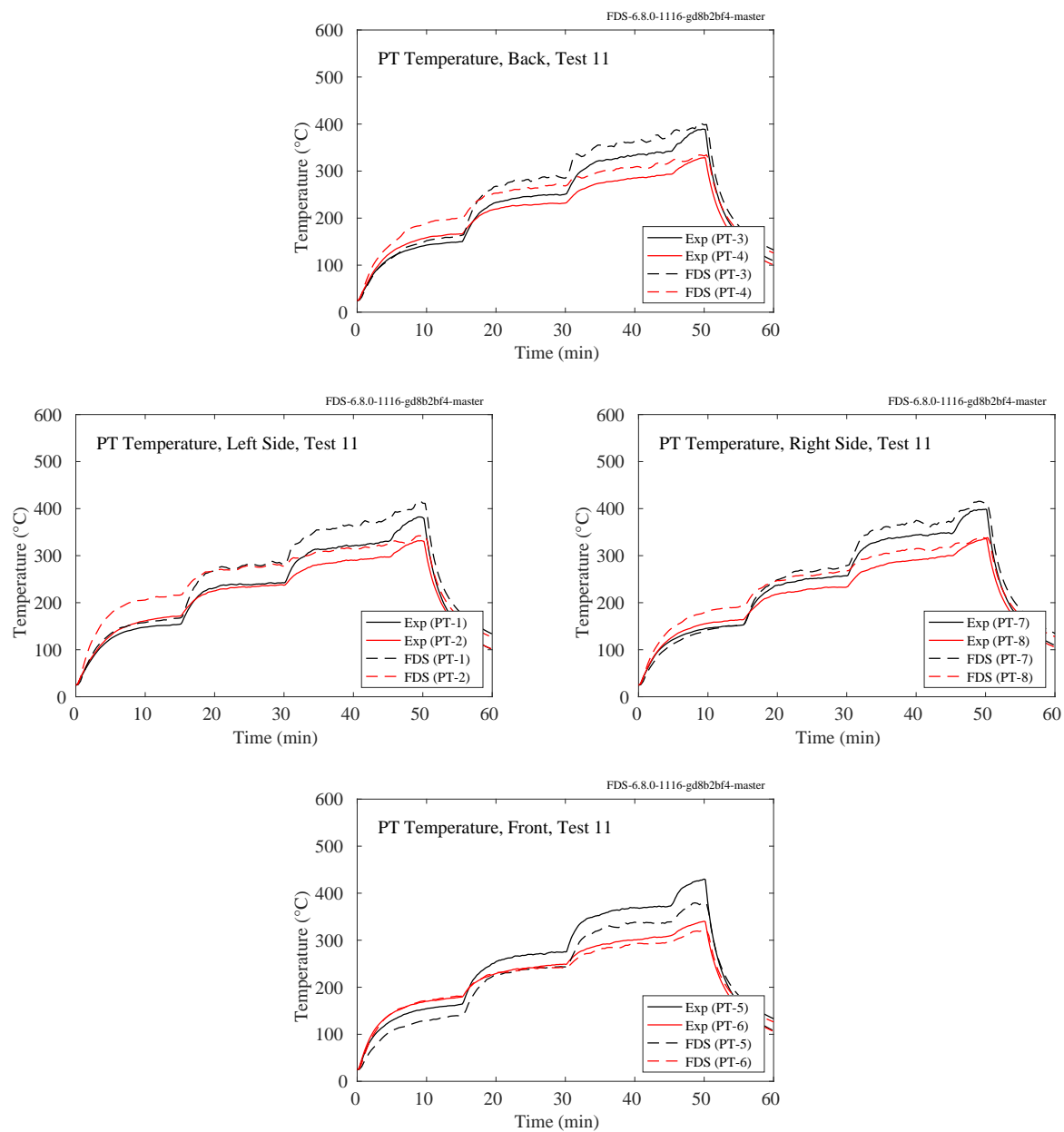


Figure 11.78: NIST/NRC Corner Effects, plate and cabinet temperatures, Test 11.

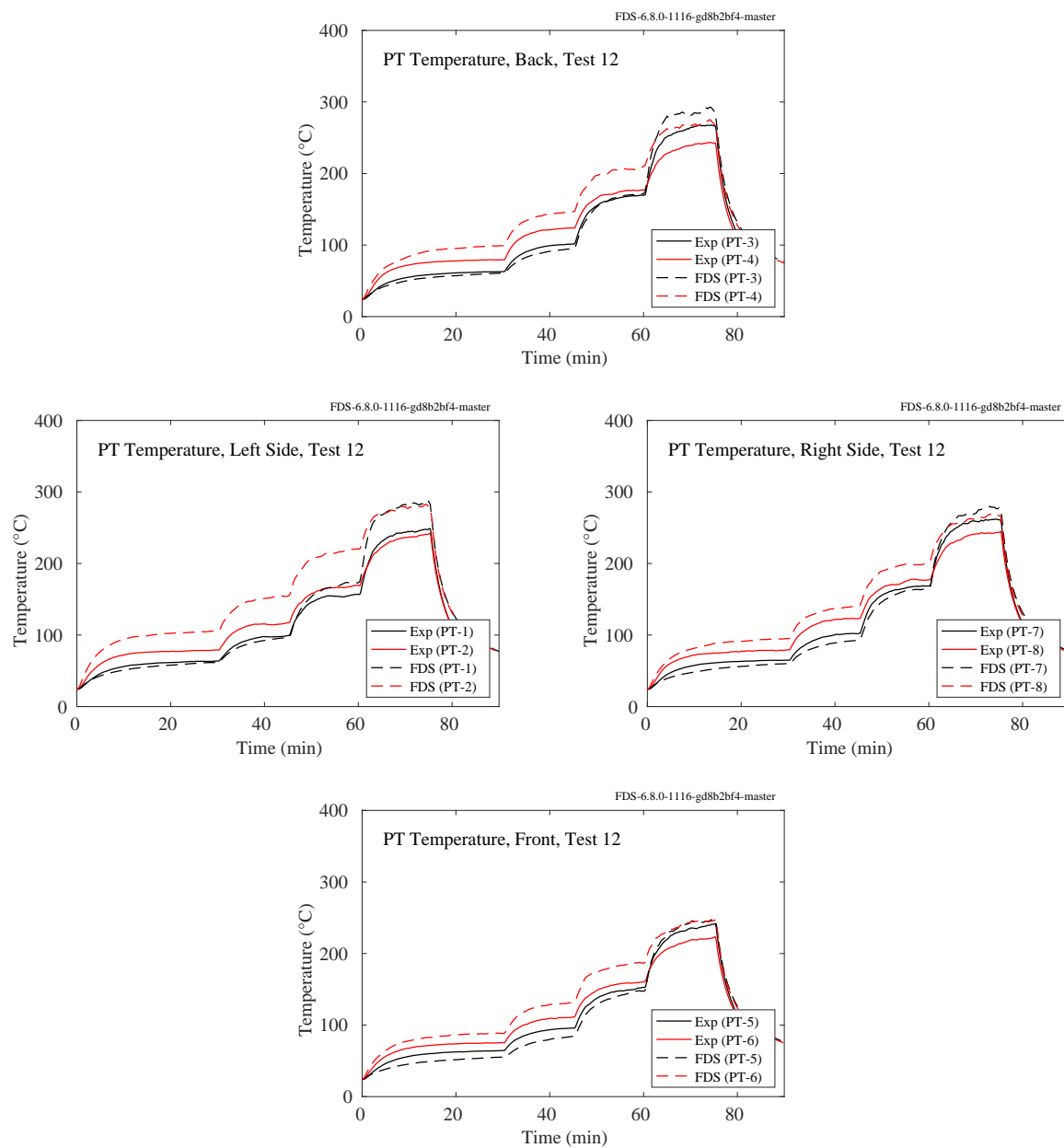


Figure 11.79: NIST/NRC Corner Effects, plate and cabinet temperatures, Test 12.

11.2.5 SP Adiabatic Surface Temperature Experiments

Comparisons of FDS predictions of gas, plate thermometer, and steel temperatures for compartment and pool fire experiments conducted at SP, Sweden, are presented on the following pages.

Compartment Fire Experiments

Three experiments were conducted in a standard compartment, 3.6 m long by 2.4 m wide by 2.4 m high, with a 0.8 m wide by 2.0 m high door centered on the narrow wall. Each experiment used a constant 450 kW propane burner and a single beam suspended 20 cm below the ceiling along the centerline of the compartment. There were three measurement stations along the beam at lengths of 0.9 m (Position A), 1.8 m (Position B), and 2.7 m (Position C) from the far wall where the fire was either positioned in the corner (Tests 1 and 2), or the center (Test 3). The beam in Test 1 was a rectangular steel tube filled with an insulation material. The beam in Tests 2 and 3 was an I-beam. Details can be found in the test report [313].

Each page to follow contains the results for a single experiment and measuring station. There are nine in all. In addition to predictions plate thermometer and steel temperatures, there are predictions of the adiabatic surface temperature (AST) for the locations and orientations of the plate thermometers. The AST is a useful quantity that serves as a boundary condition for thermal resistance calculations of structures. The basic idea is as follows. The *net* heat flux to the solid surface is given as the sum of radiative and convective components:

$$\dot{q}_r'' + \dot{q}_c'' = \varepsilon (\dot{q}_{r,inc}'' - \sigma T_s^4) + h(T_g - T_s) \quad (11.1)$$

where $\dot{q}_{r,inc}''$ is the incident radiative flux, T_s the surface temperature, T_g the gas temperature near the surface, and h the convective heat transfer coefficient. Following the idea proposed by Wickström [374], the AST is defined as the surface temperature of a perfectly insulated solid. This is equivalent to saying that the net heat flux to this (hypothetical) surface is zero:

$$0 = \varepsilon (\dot{q}_{r,inc}'' - \sigma T_{AST}^4) + h(T_g - T_{AST}) \quad (11.2)$$

This definition of the AST forms the theory behind the plate thermometer, a 10 cm by 10 cm thin metal plate with an insulated backing that is designed to measure the AST, albeit with a slight time lag due to the fact that it is not a perfect insulator.

FDS calculates the AST by solving the following equation implicitly for T_{AST} :

$$\dot{q}_r'' + \dot{q}_c'' = \varepsilon (\sigma T_{AST}^4 - \sigma T_s^4) + h(T_{AST} - T_s) \quad (11.3)$$

Equation (11.3) is simply Eq. (11.1) minus Eq. (11.2). As such, it shows that the AST can be regarded as an *effective* gas temperature for the purpose of providing boundary conditions for a detailed heat conduction calculation within the solid.

FDS calculates the AST using Eq. (11.3) and the plate thermometer temperature via its standard one-dimensional heat conduction calculation for a two layer solid of metal and insulating material. In the experiments, the plate thermometer temperature was obtained from a thermocouple attached to the back side of the thin metal plate, and the AST was derived from the measured plate thermometer temperature by a back calculation involving only the thermal lag due to the plate, not the insulation material.

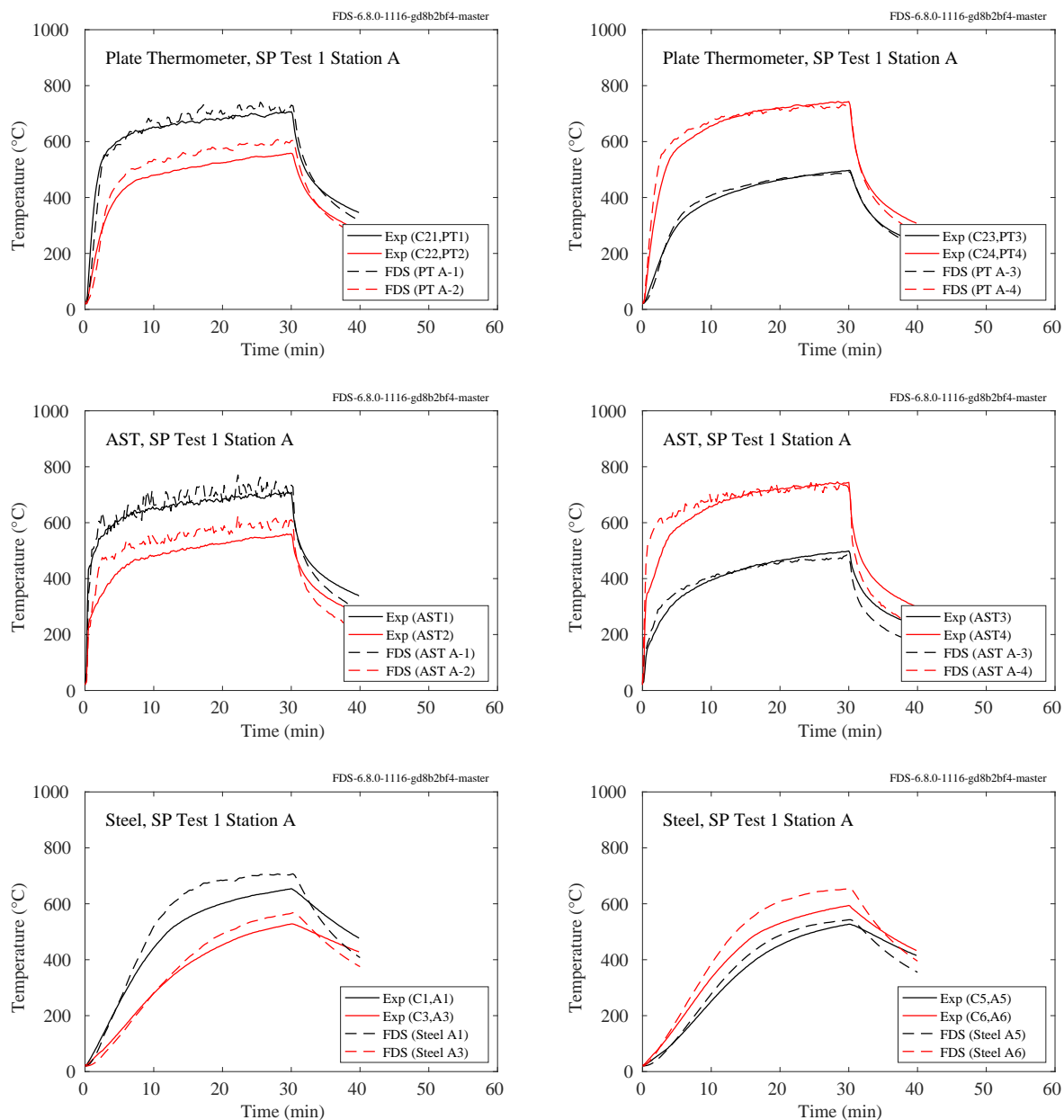


Figure 11.80: SP AST experiments, Station A plate, adiabatic surface, and steel temperatures, Test 1.

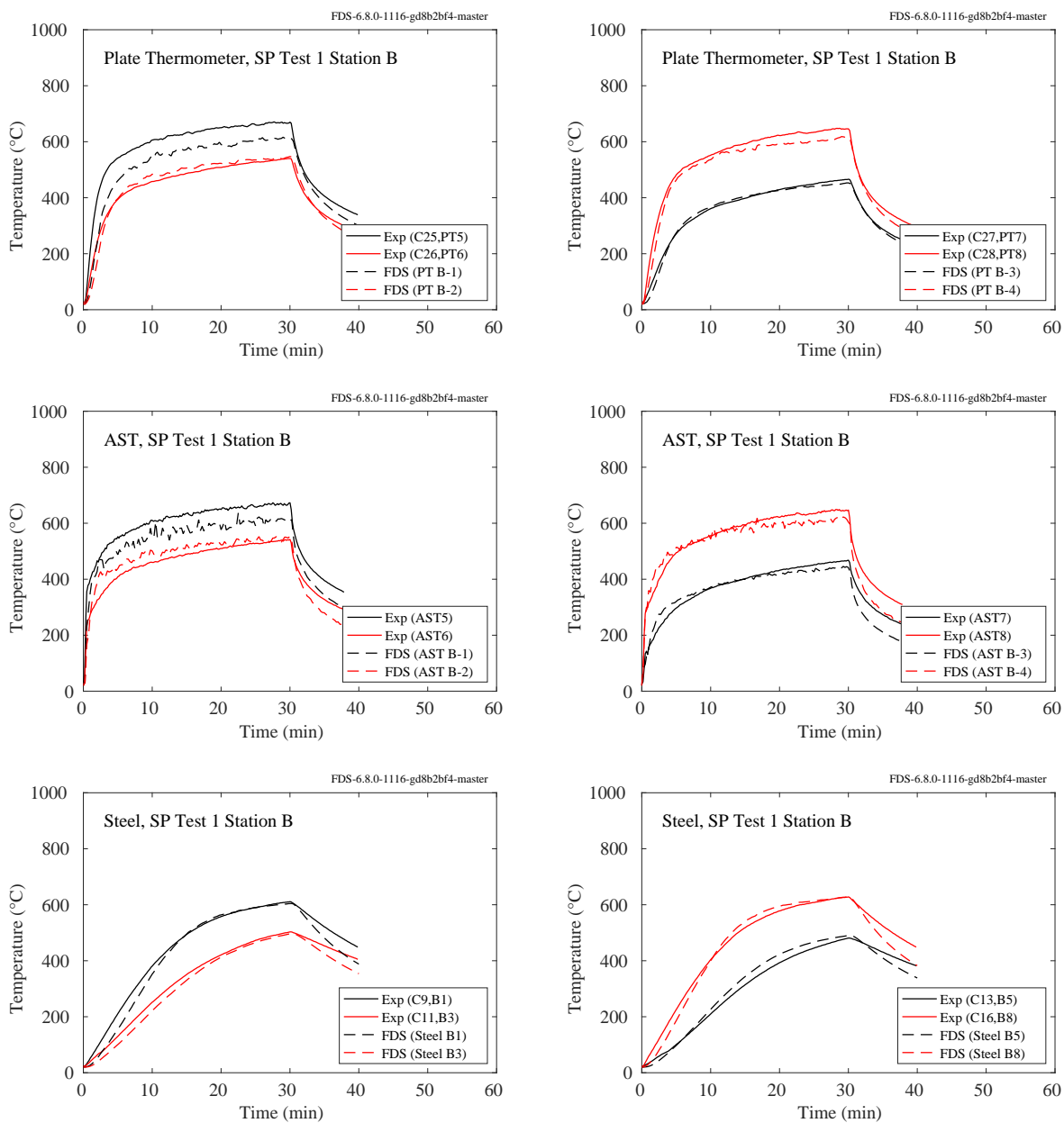


Figure 11.81: SP AST experiments, Station B plate, adiabatic surface, and steel temperatures, Test 1.

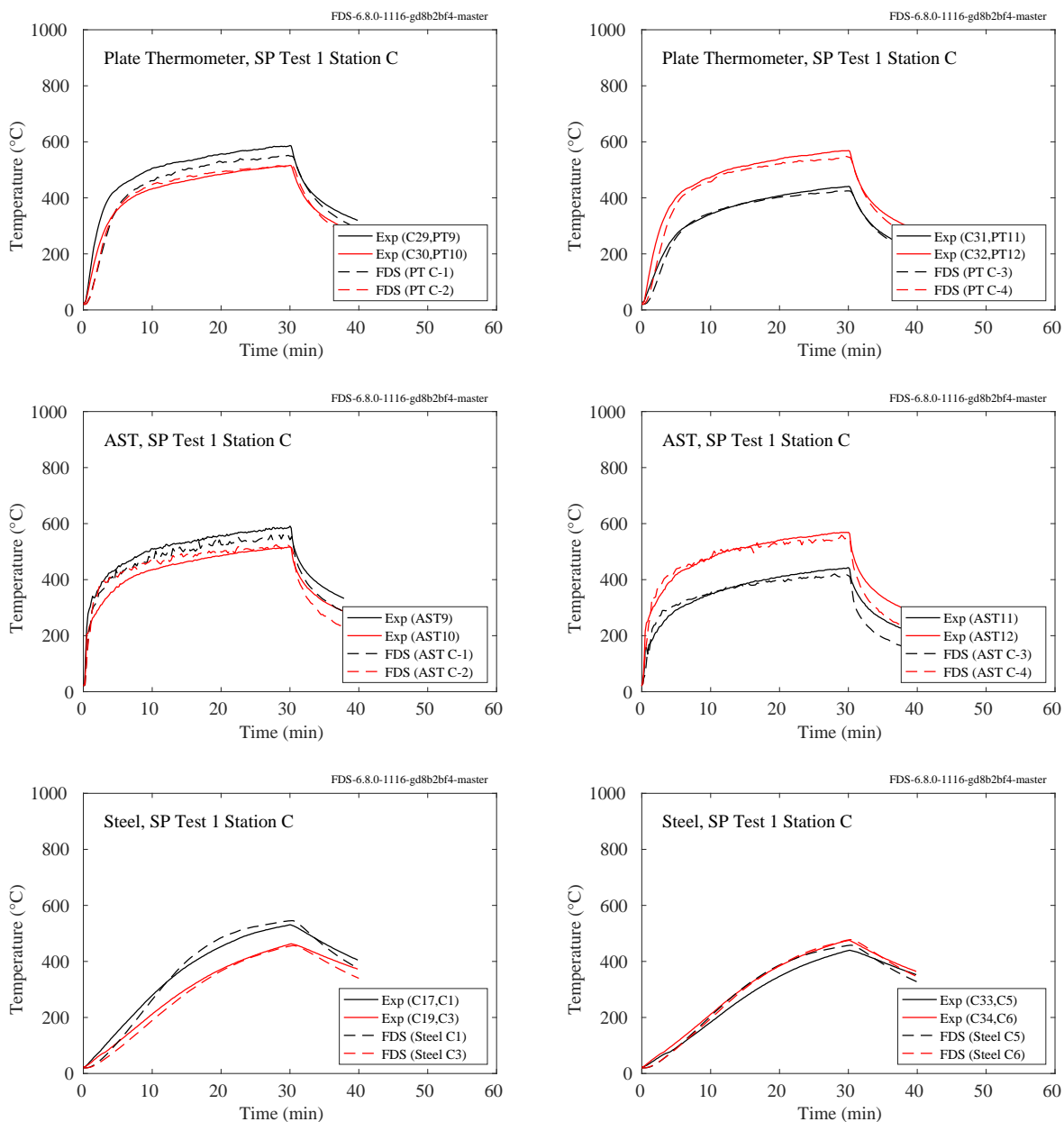


Figure 11.82: SP AST experiments, Station C plate, adiabatic surface, and steel temperatures, Test 1.

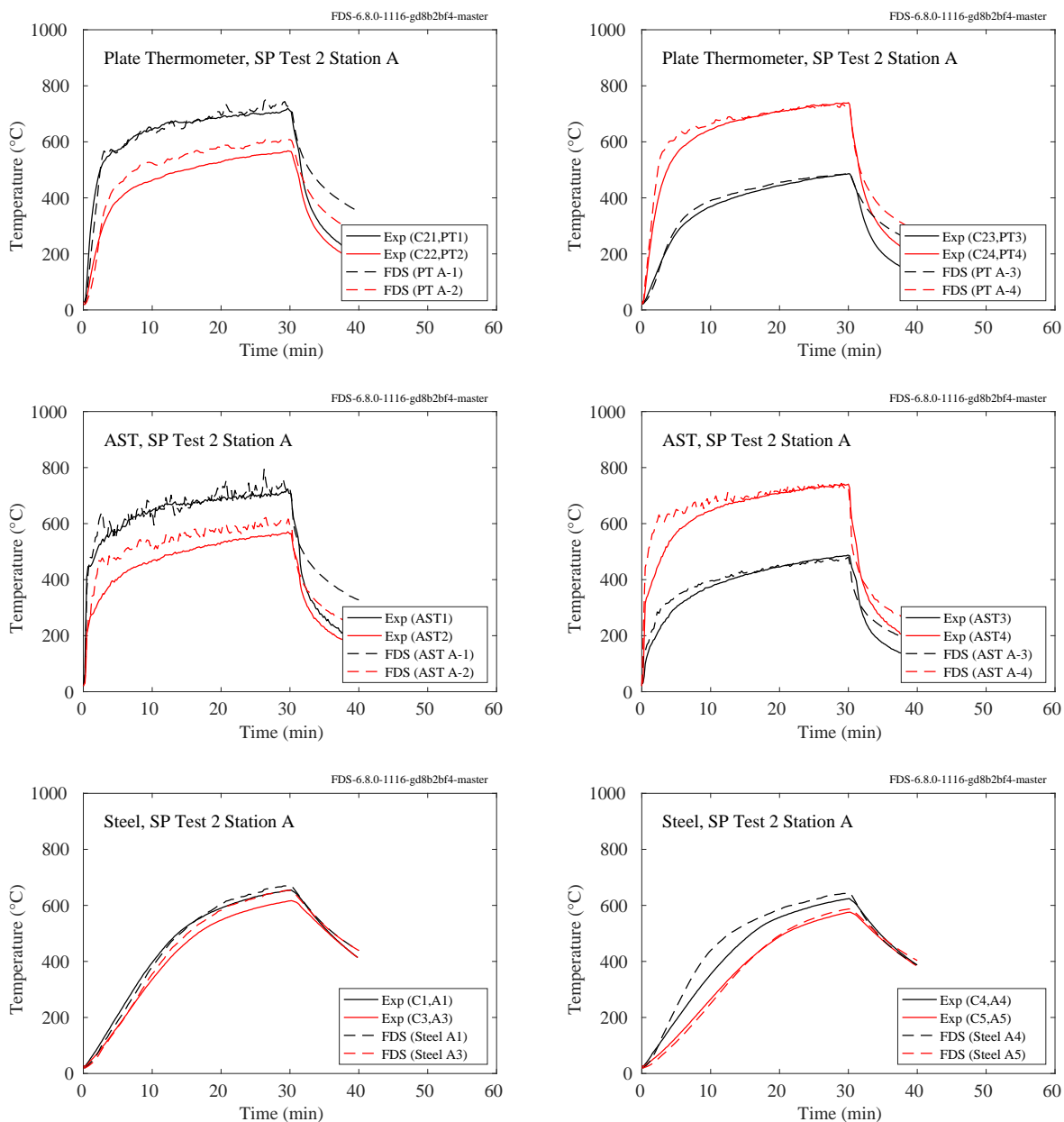


Figure 11.83: SP AST experiments, Station A plate, adiabatic surface, and steel temperatures, Test 2.

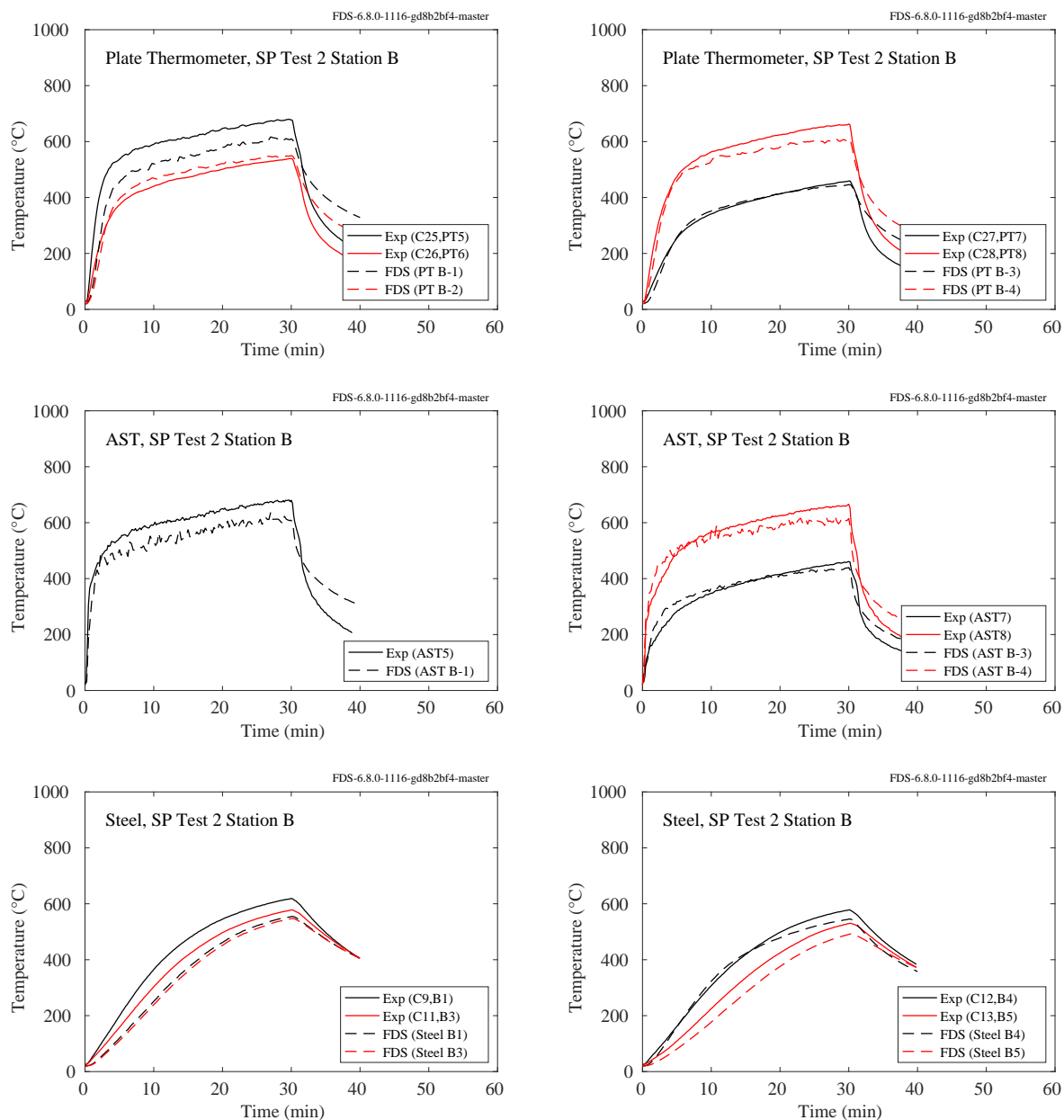


Figure 11.84: SP AST experiments, Station B plate, adiabatic surface, and steel temperatures, Test 2.

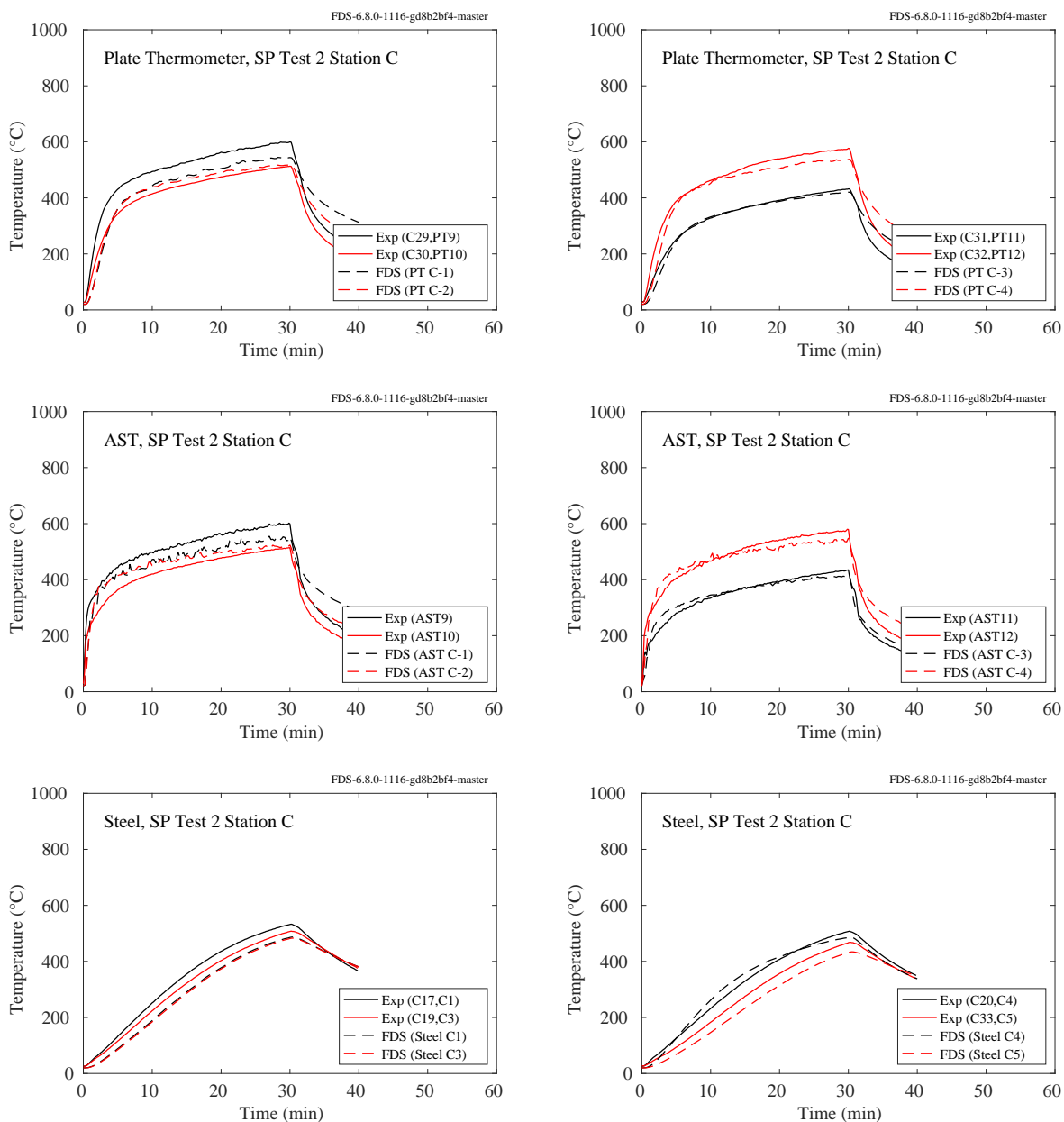


Figure 11.85: SP AST experiments, Station C plate, adiabatic surface, and steel temperatures, Test 2.

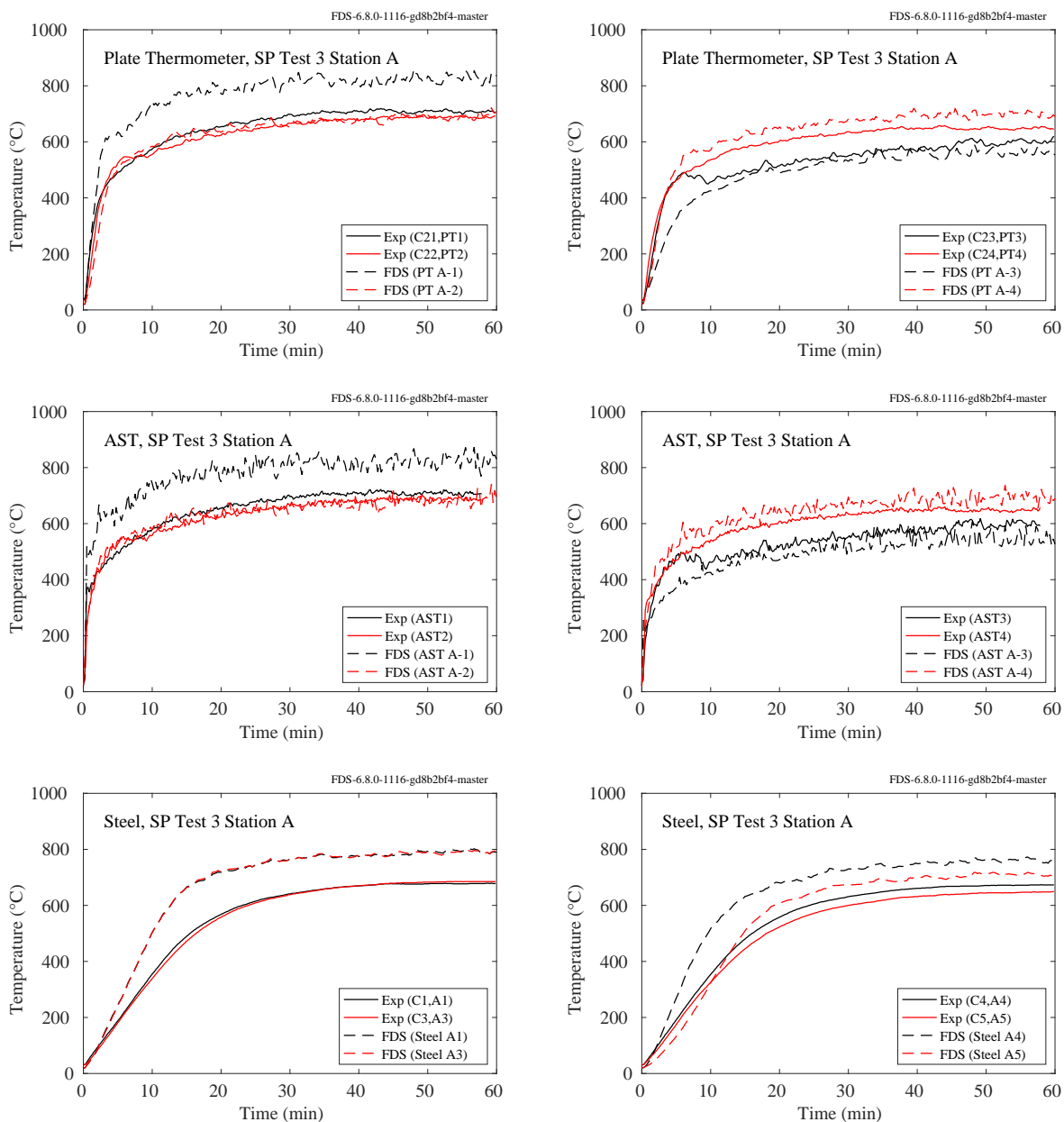


Figure 11.86: SP AST experiments, Station A plate, adiabatic surface, and steel temperatures, Test 3.

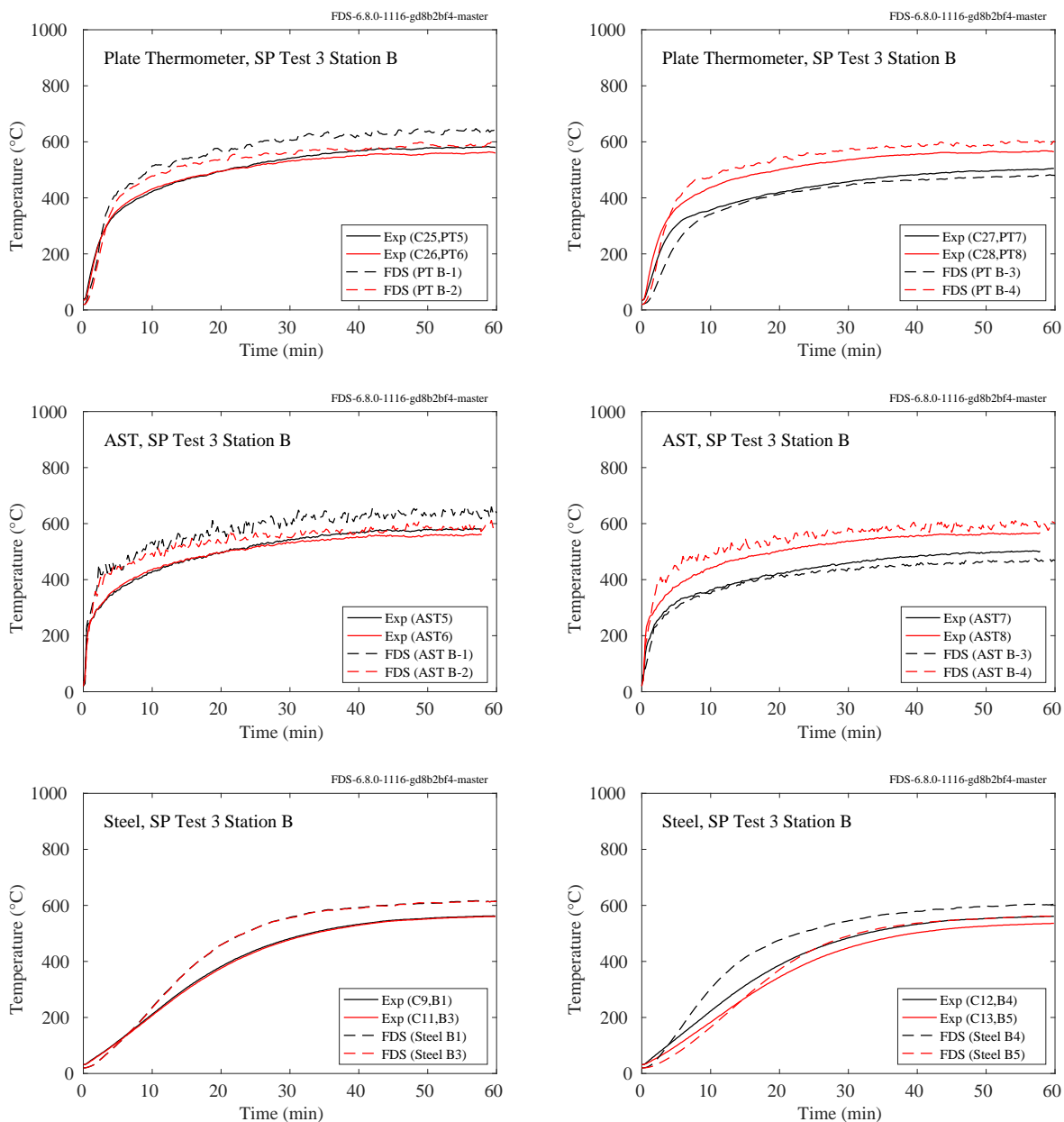


Figure 11.87: SP AST experiments, Station B plate, adiabatic surface, and steel temperatures, Test 3.

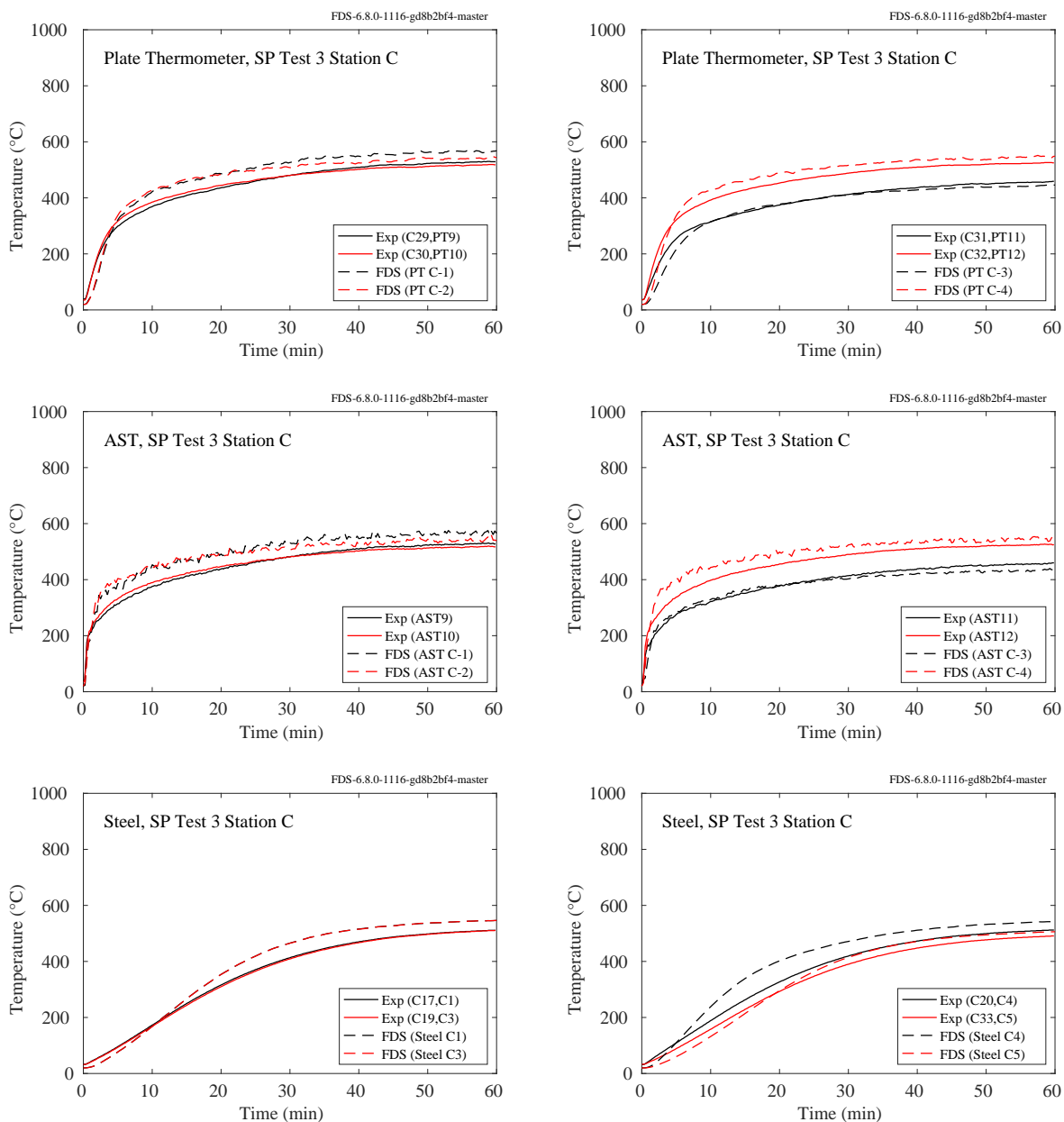


Figure 11.88: SP AST experiments, Station C plate, adiabatic surface, and steel temperatures, Test 3.

Pool Fire Experiments

Three experiments were conducted at SP, Sweden, in 2011, in which a 6 m long, 20 cm diameter vertical column was positioned in the middle of 1.1 m and 1.9 m diesel and 1.1 m heptane pool fires [314]. Gas, plate, and steel surface temperature measurements were made at heights of 1 m, 2 m, 3 m, 4 m, and 5 m above the pool surface. At heights of 1 m, 3 m, and 5 m, these measurements were made at only one angular position. However, at 2 m and 4 m, the measurements were made at four positions. At these heights, two conventional plates thermometers were positioned approximately 10 cm from the column surface, along with two special plate thermometers (SPT) that were installed flush with the column surface. At each height, comparable predictions were made with FDS, but at only one angular position because there is no predominant direction of leaning in the simulation. In the experiments, the fire was reported to lean in the direction of Position 1. The lean was significant for the 1.9 m diesel fuel fires, in which case only data from 1 m and 2 m above the pool are used. Also, FDS assumes the column to be square in cross section (20 cm by 20 cm), rather than circular. The grid spacing is 10 cm.

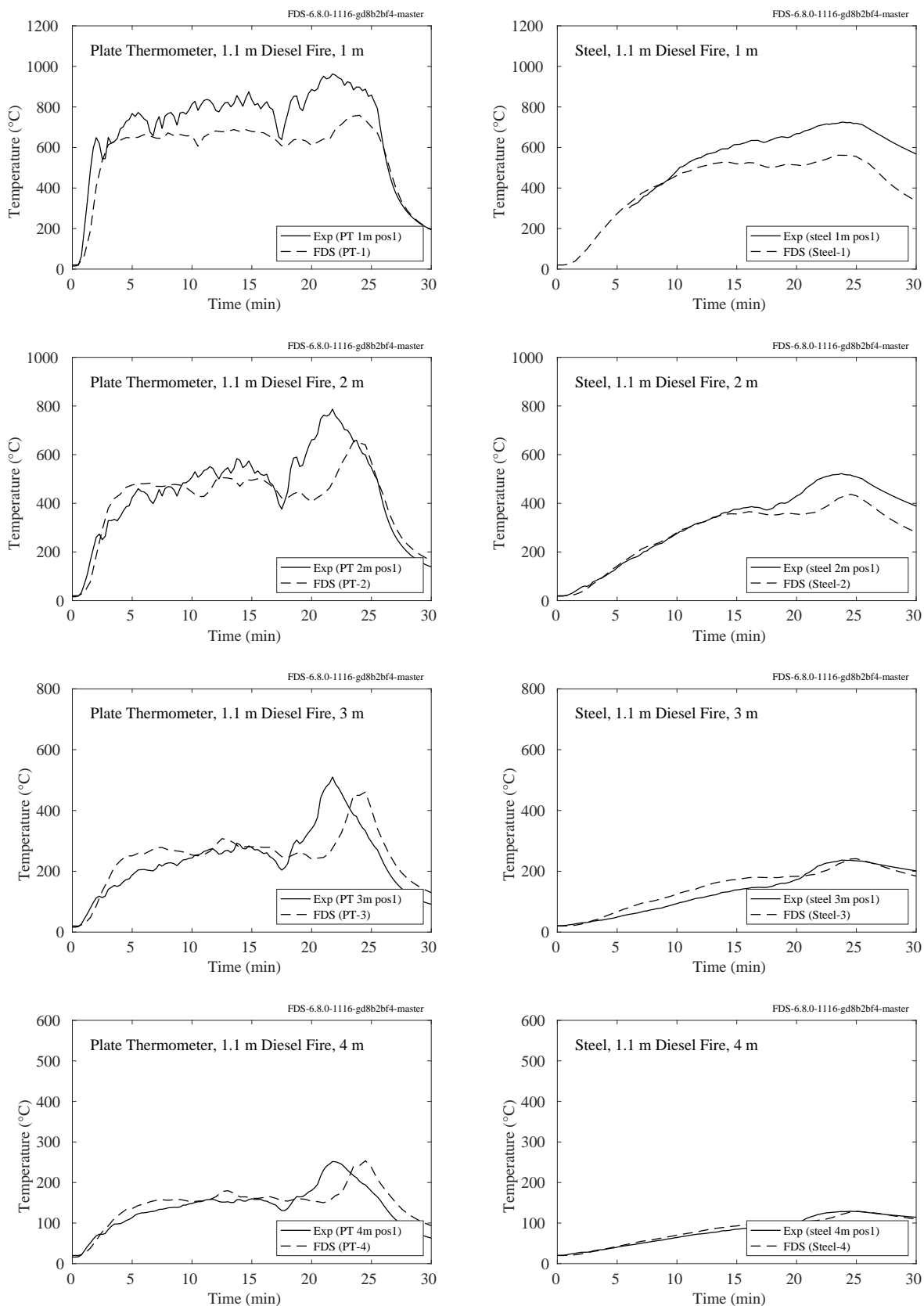


Figure 11.89: SP AST experiments, steel temperatures, 1.1 m diesel fire.

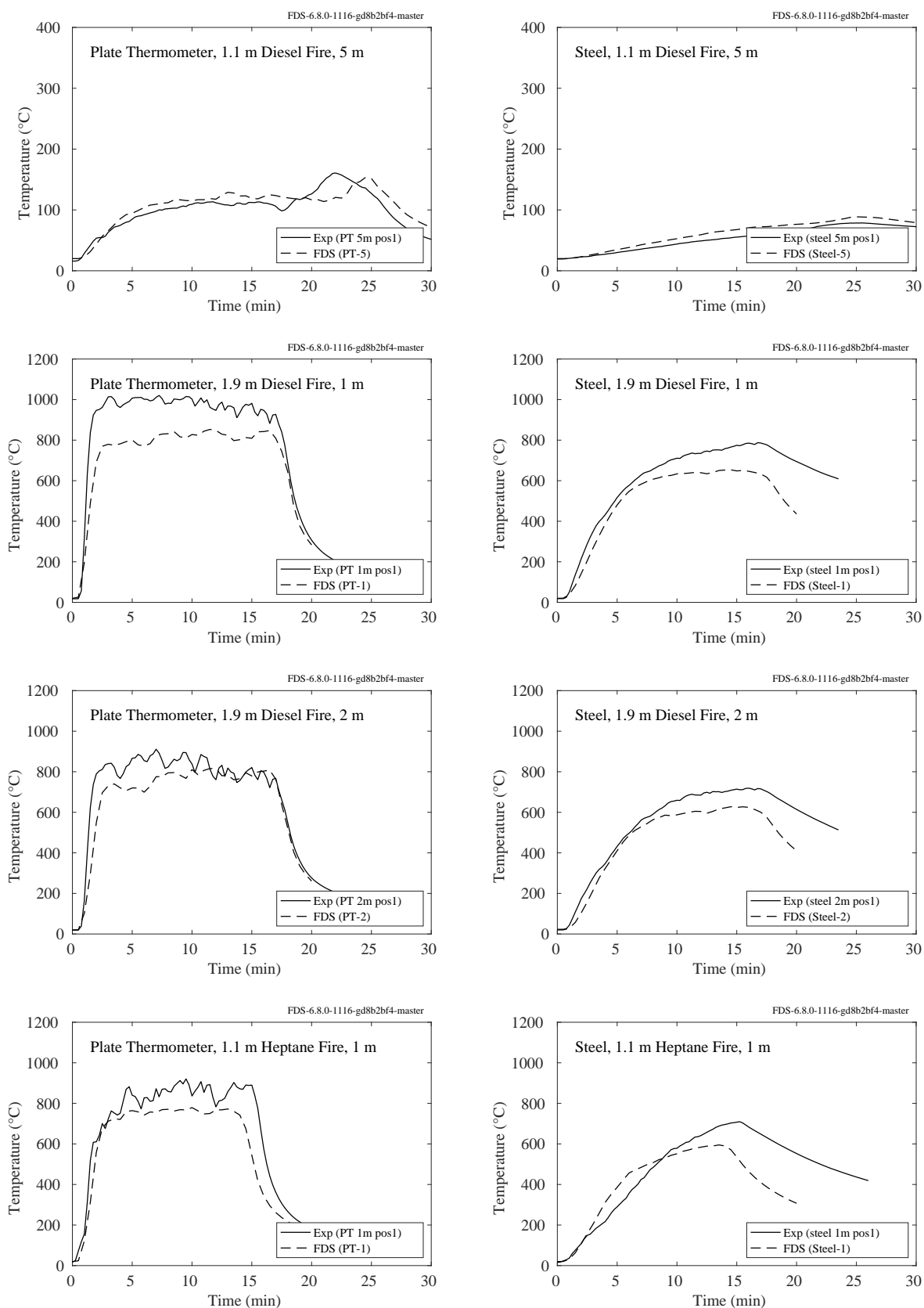


Figure 11.90: SP AST experiments, steel temperatures, 1.1 m and 1.9 m diesel, 1.1 m heptane fires.

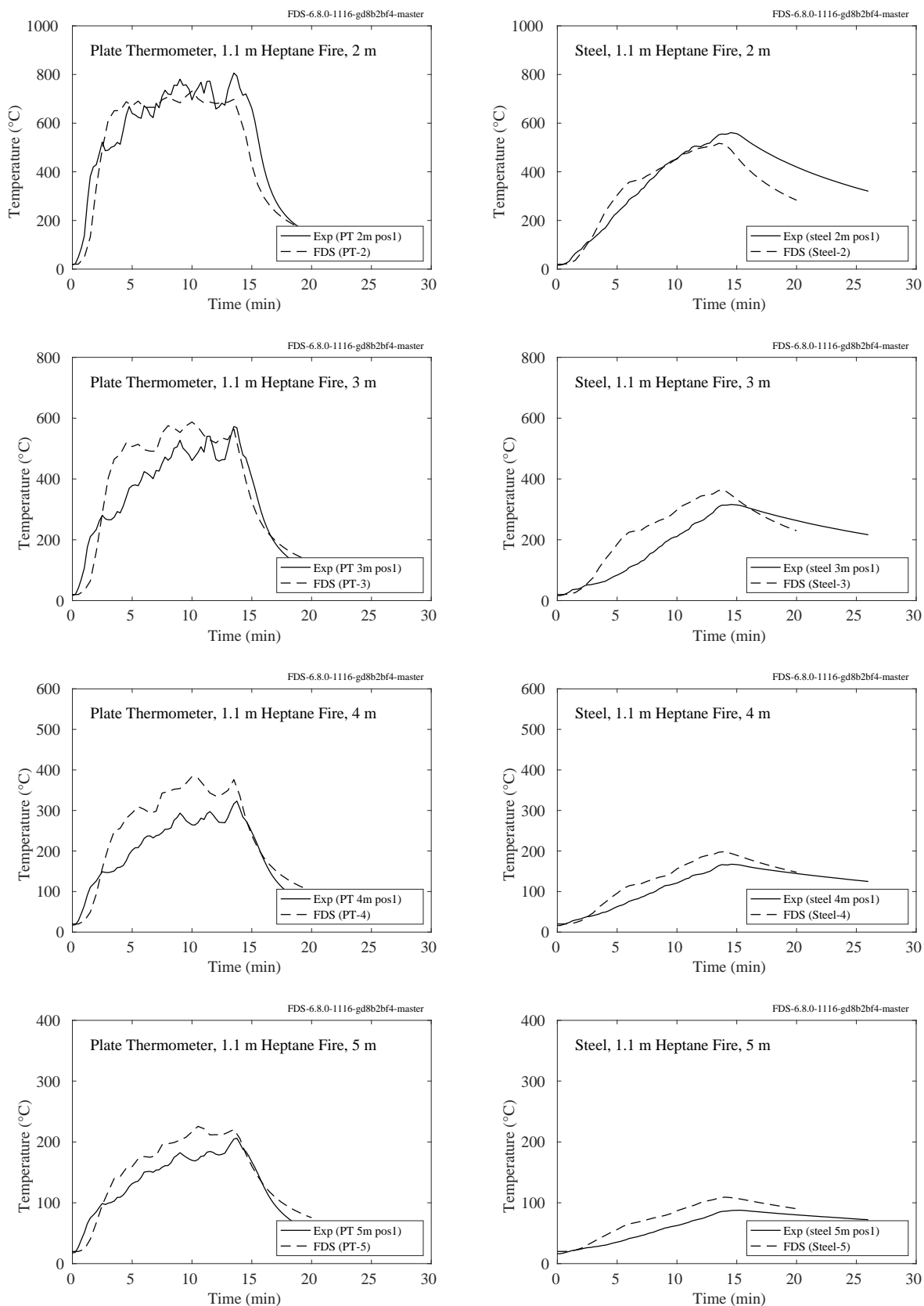


Figure 11.91: SP AST experiments, steel temperatures, 1.1 m heptane fire.

Insulated Room Experiments

The plots on the following pages display measured and predicted plate thermometer (PT) temperatures for a series of single compartment experiments conducted by SP, Sweden [315]. The compartment was 2.7 m long, 1.8 m wide, and 1.8 m tall, with a 0.6 m by 1.5 m door centered on one of the short walls. The PTs were affixed to the walls. The designations of right and left wall are from the perspective of a person looking into the room. The back wall is the short wall without the door; the front wall is opposite. When referring to a given PT, the terms left/right, upper/lower, front/back refer to the quadrant where the PT is located. The PTs are centered within each quadrant, and are thus located at one-fourth or three-fourths of the wall's length, width or height. The term "center" refers to the center point of the entire wall. The designation "back wall upper" refers to the upper left quadrant of the back wall, and "back wall lower" refers to the lower right quadrant of the back wall.

The 12 experiments were conducted with four different wall linings. In Series A, the compartment was lined with a 10 cm thick light concrete block. In Series B, the compartment was lined with a 5 cm thick layer of insulation backed by a 3 mm thick plate of steel. In Series C, the compartment was lined with an uninsulated 3 mm thick steel plate. In Series D, the compartment was lined with a 3 mm thick steel plate backed by a 5 cm thick layer of insulation (the opposite of Series B).

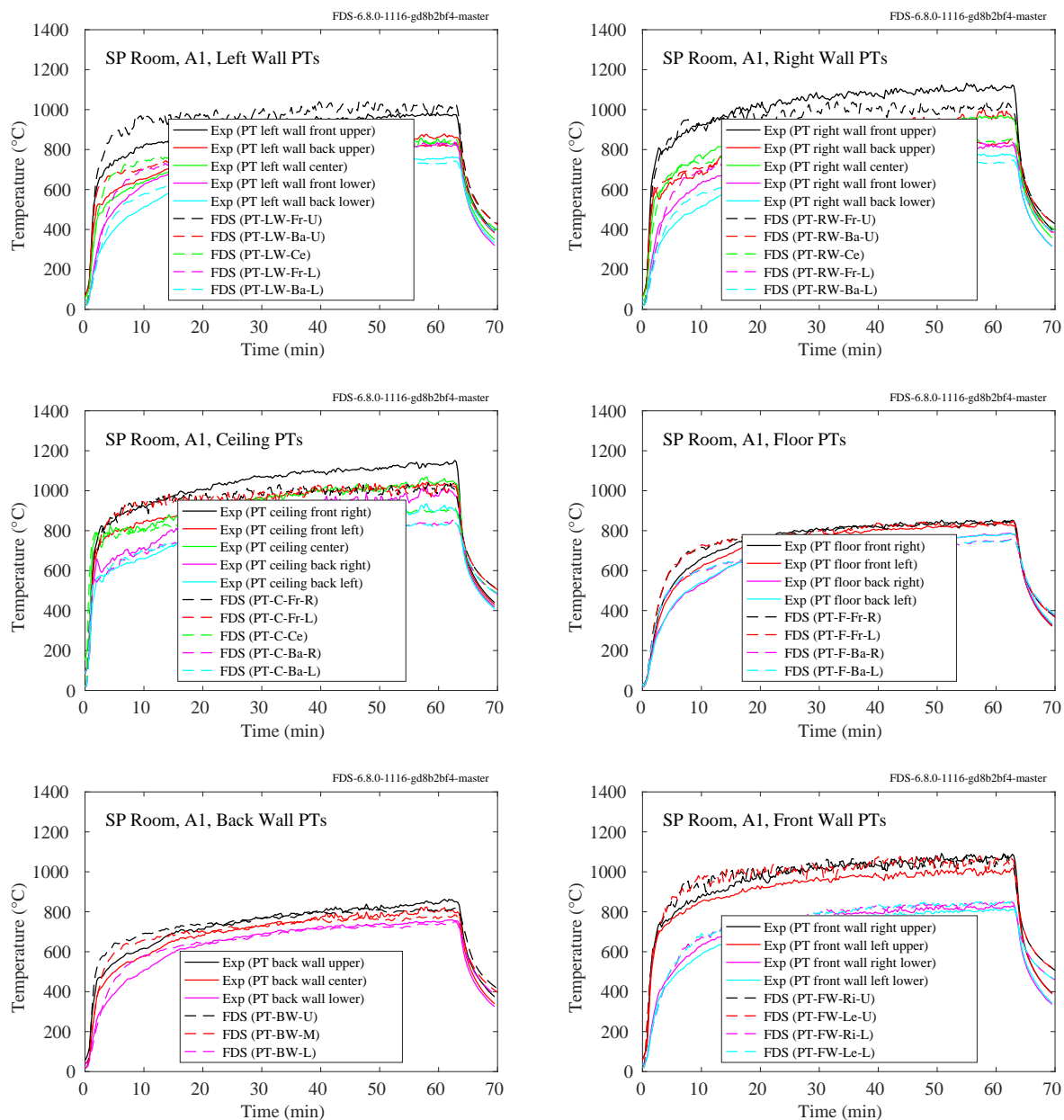


Figure 11.92: SP AST experiments, Insulated Room, Test A1.

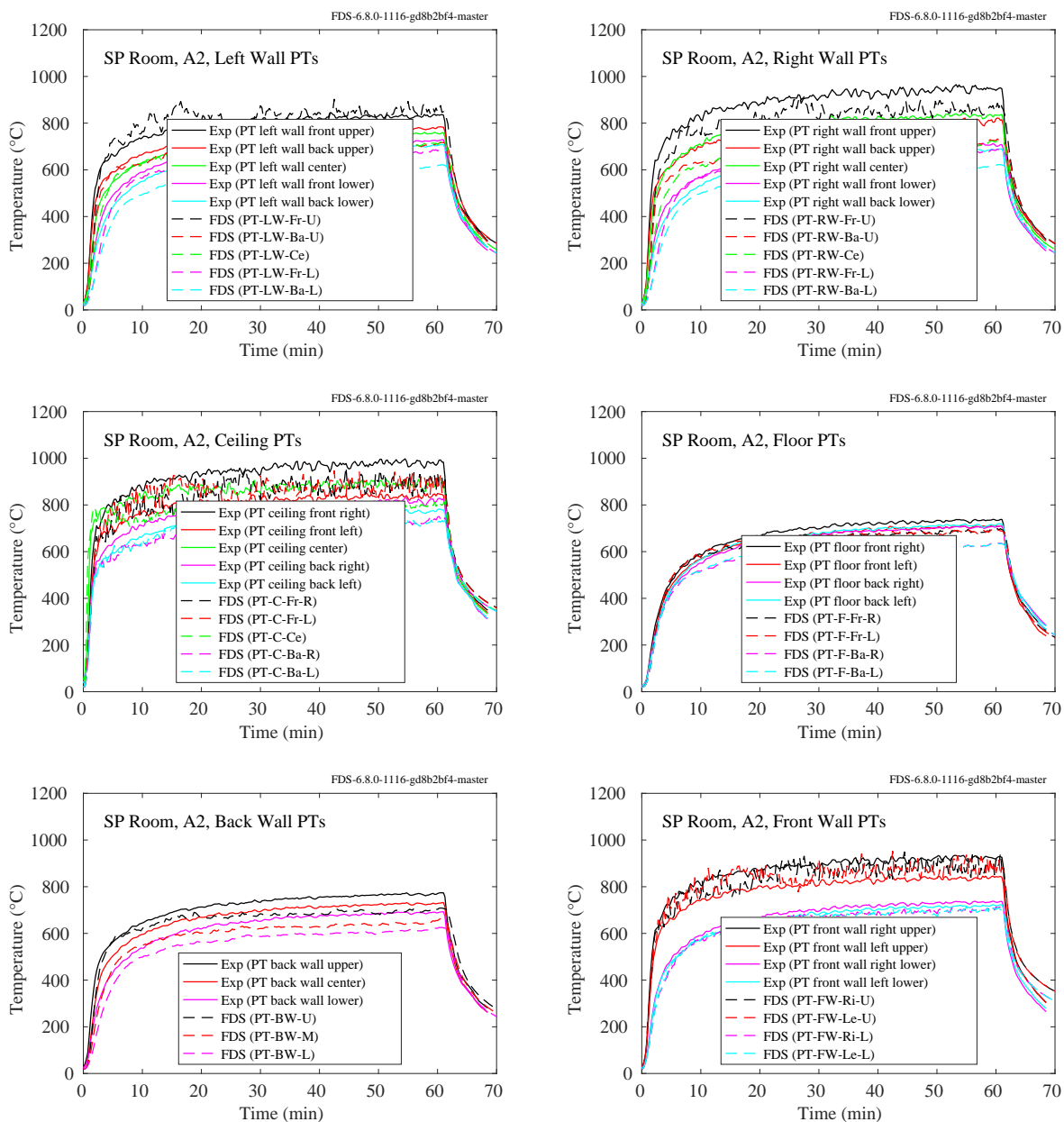


Figure 11.93: SP AST experiments, Insulated Room, Test A2.

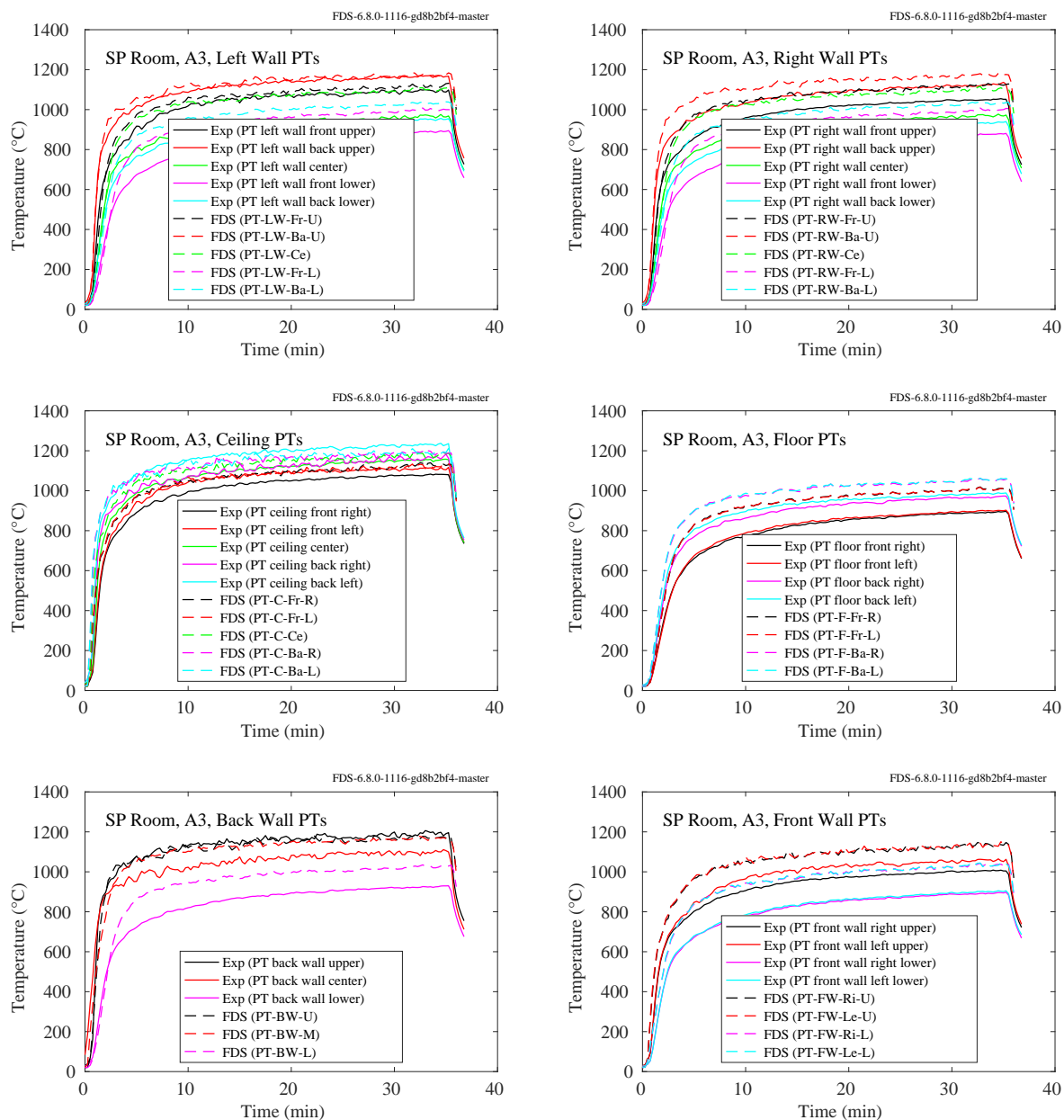


Figure 11.94: SP AST experiments, Insulated Room, Test A3.

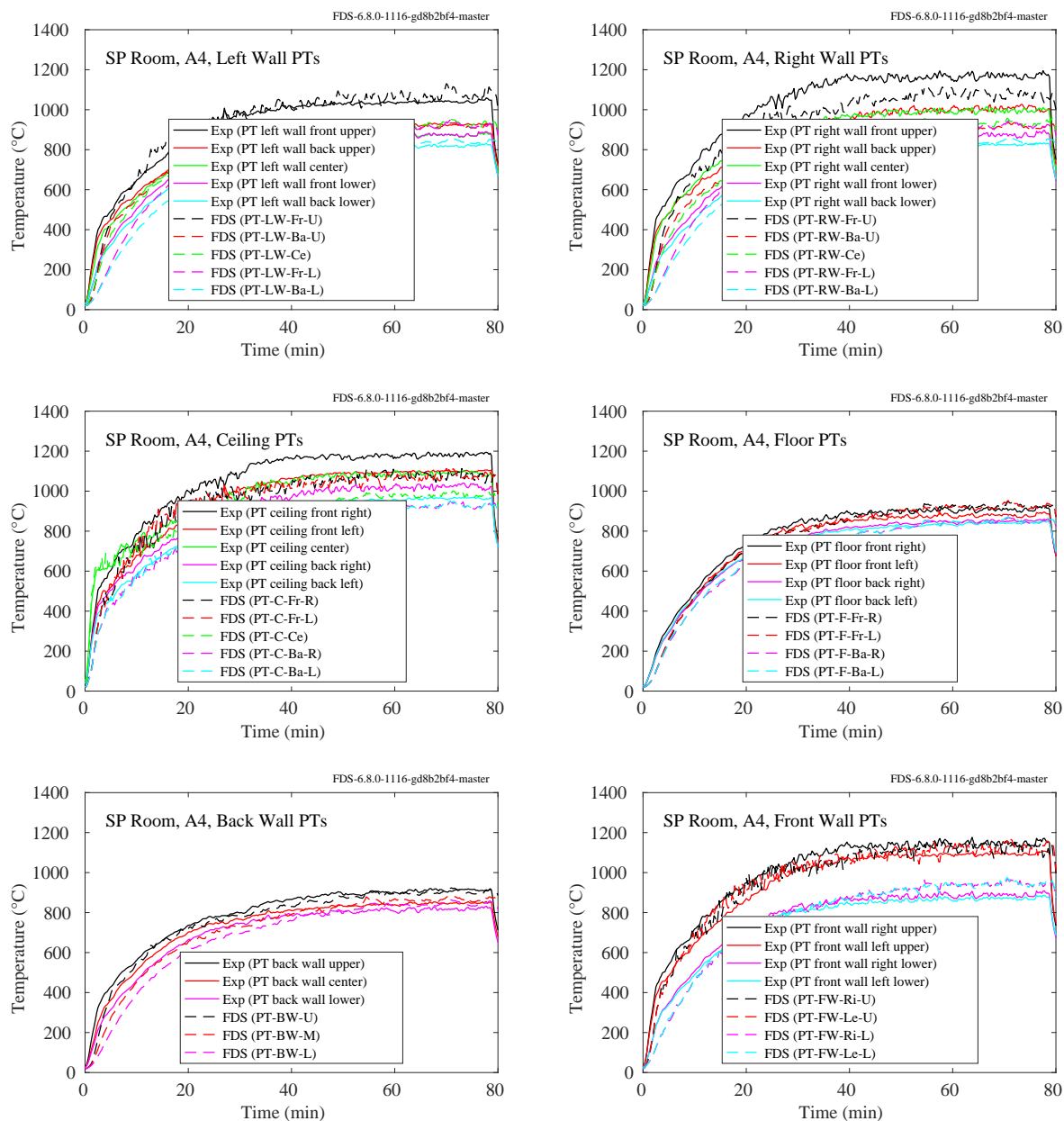


Figure 11.95: SP AST experiments, Insulated Room, Test A4.

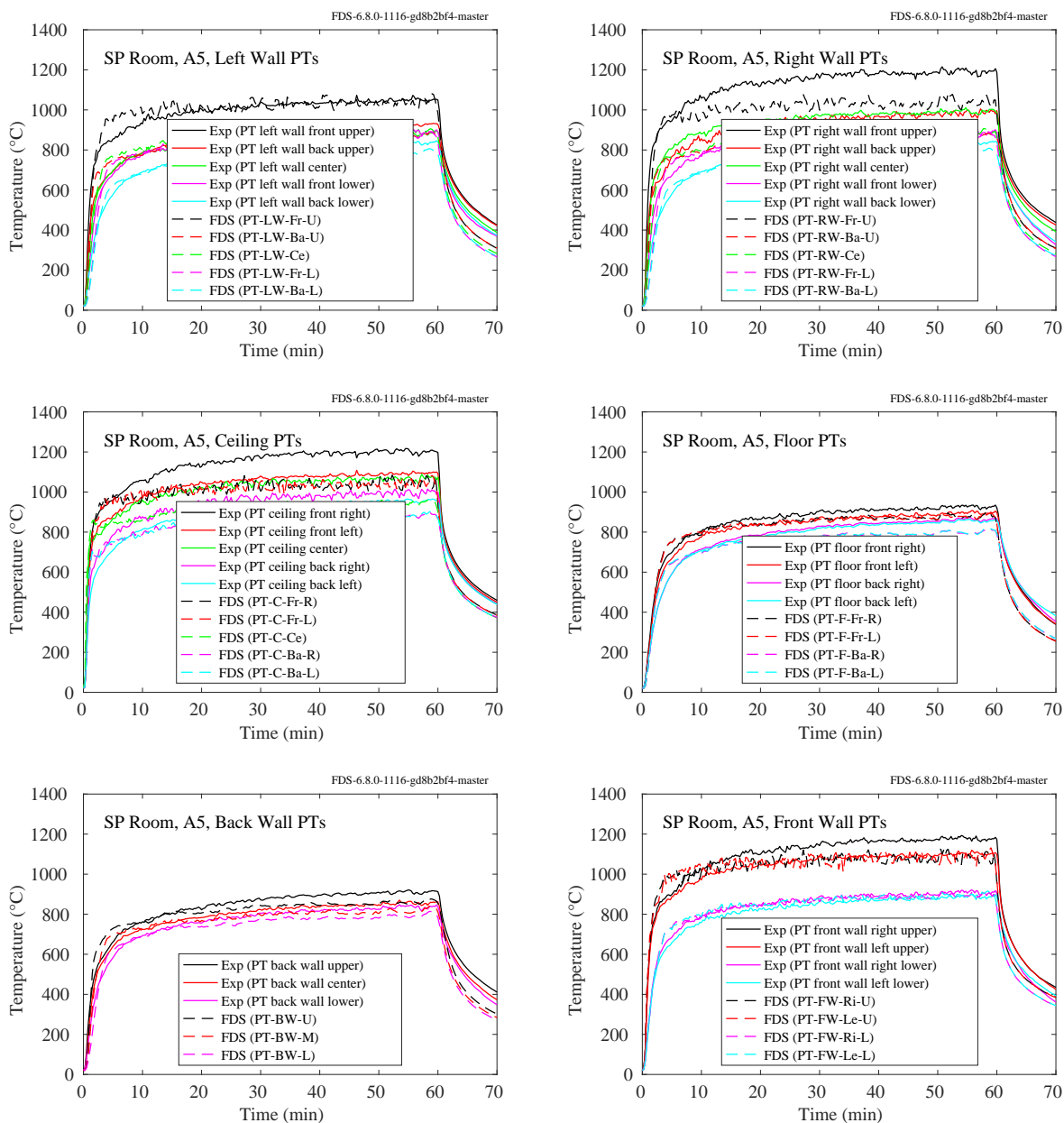


Figure 11.96: SP AST experiments, Insulated Room, Test A5.

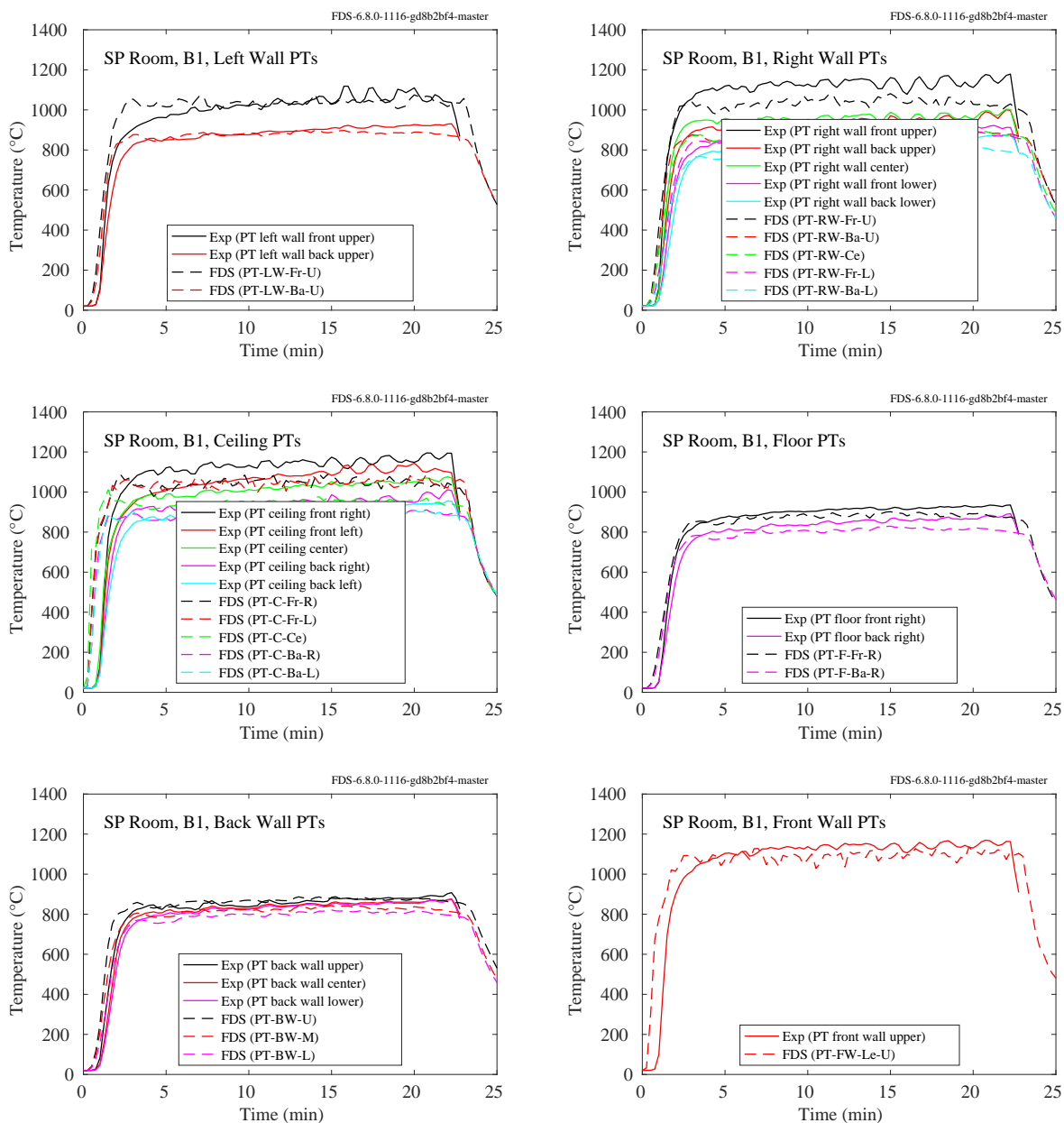


Figure 11.97: SP AST experiments, Insulated Room, Test B1.

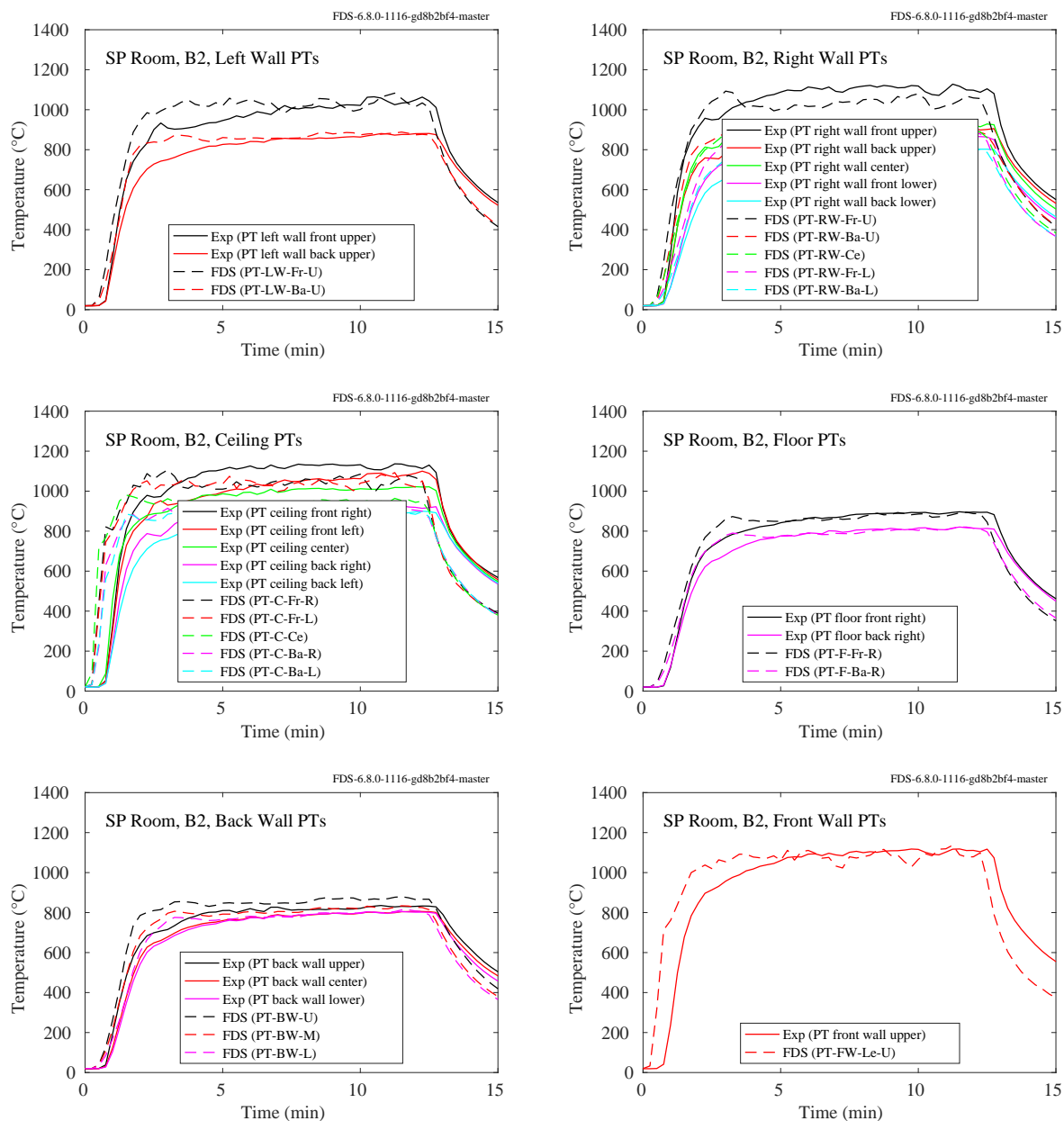


Figure 11.98: SP AST experiments, Insulated Room, Test B2.

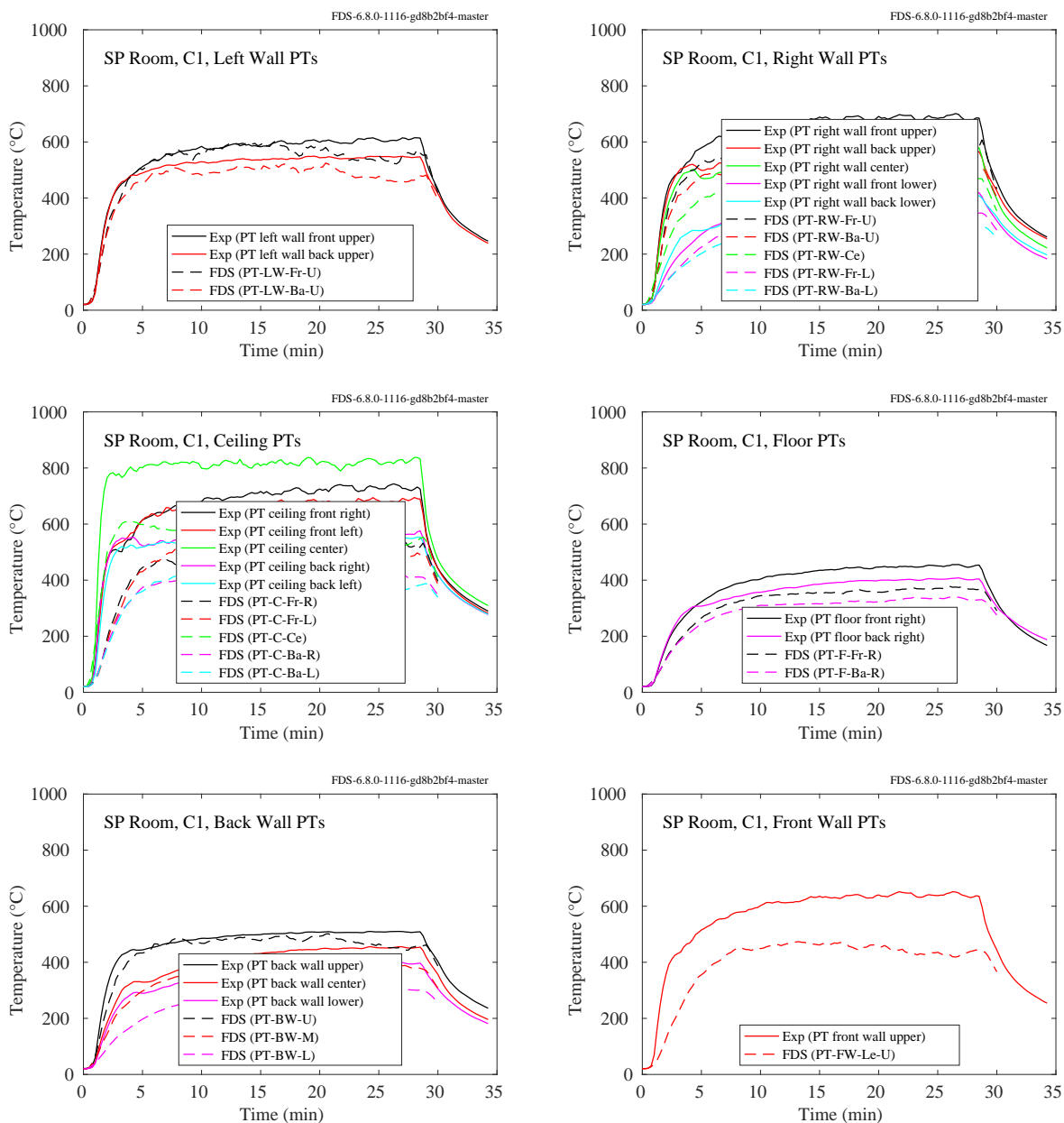


Figure 11.99: SP AST experiments, Insulated Room, Test C1.

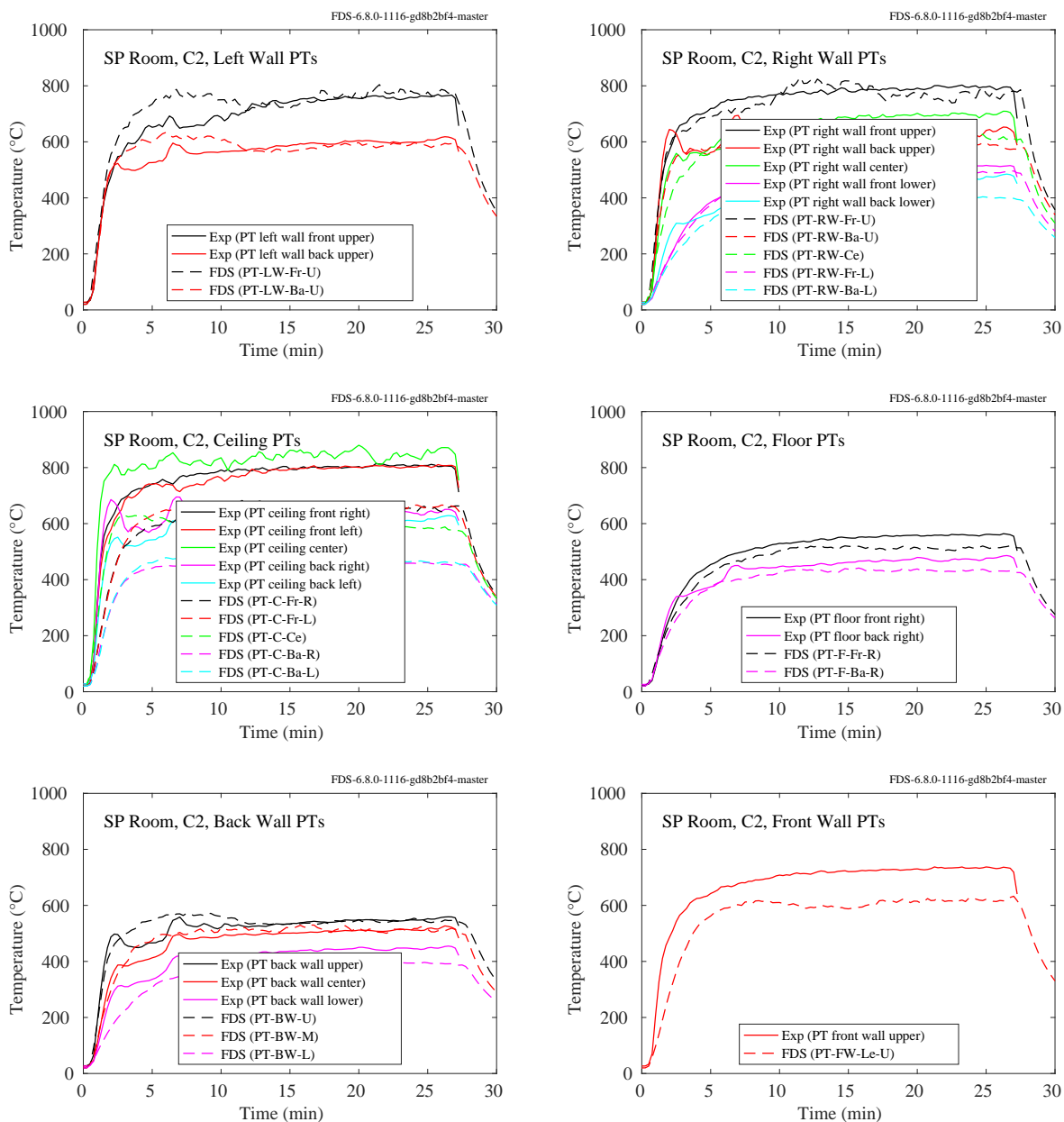


Figure 11.100: SP AST experiments, Insulated Room, Test C2.

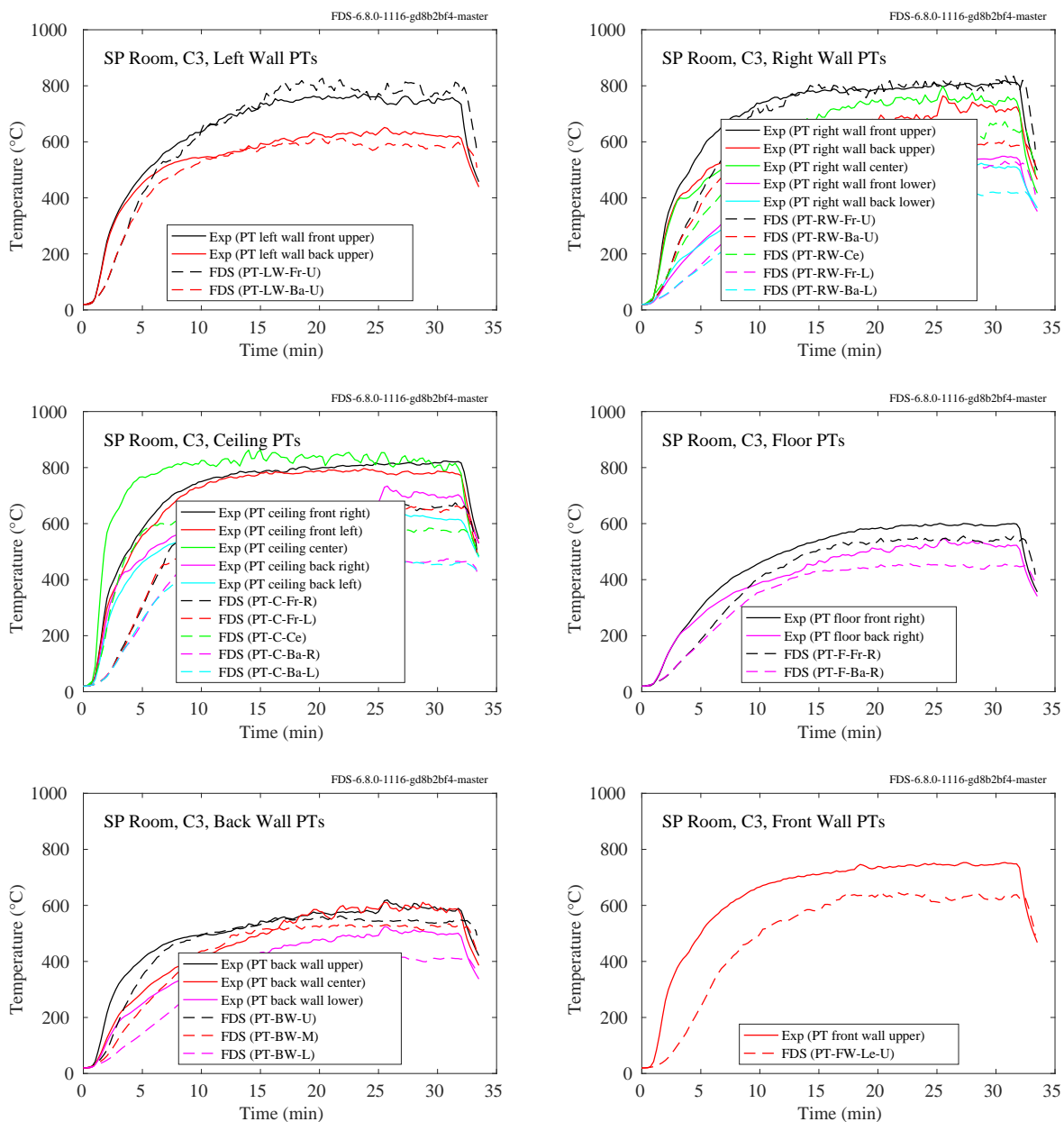


Figure 11.101: SP AST experiments, Insulated Room, Test C3.

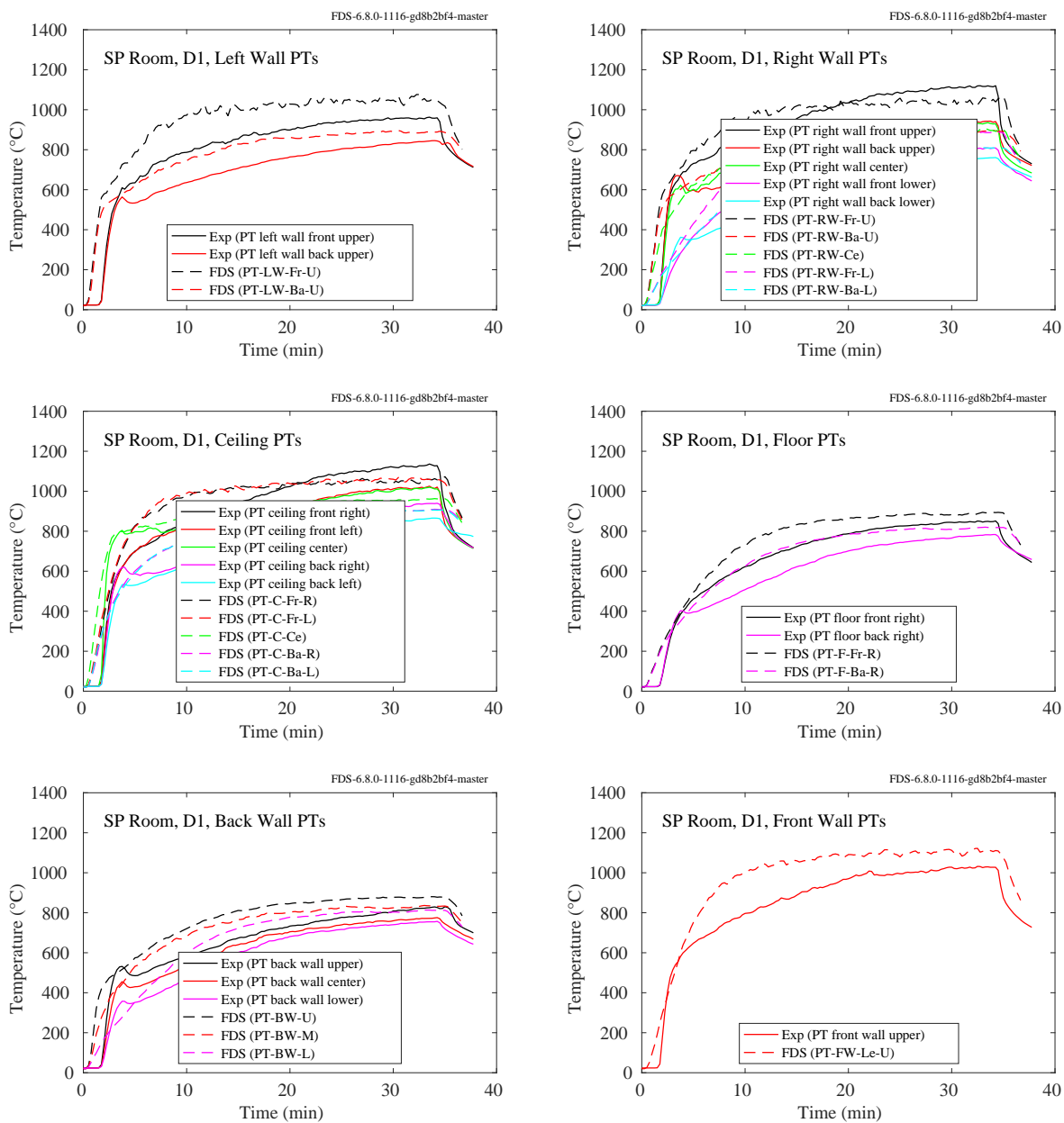


Figure 11.102: SP AST experiments, Insulated Room, Test D1.

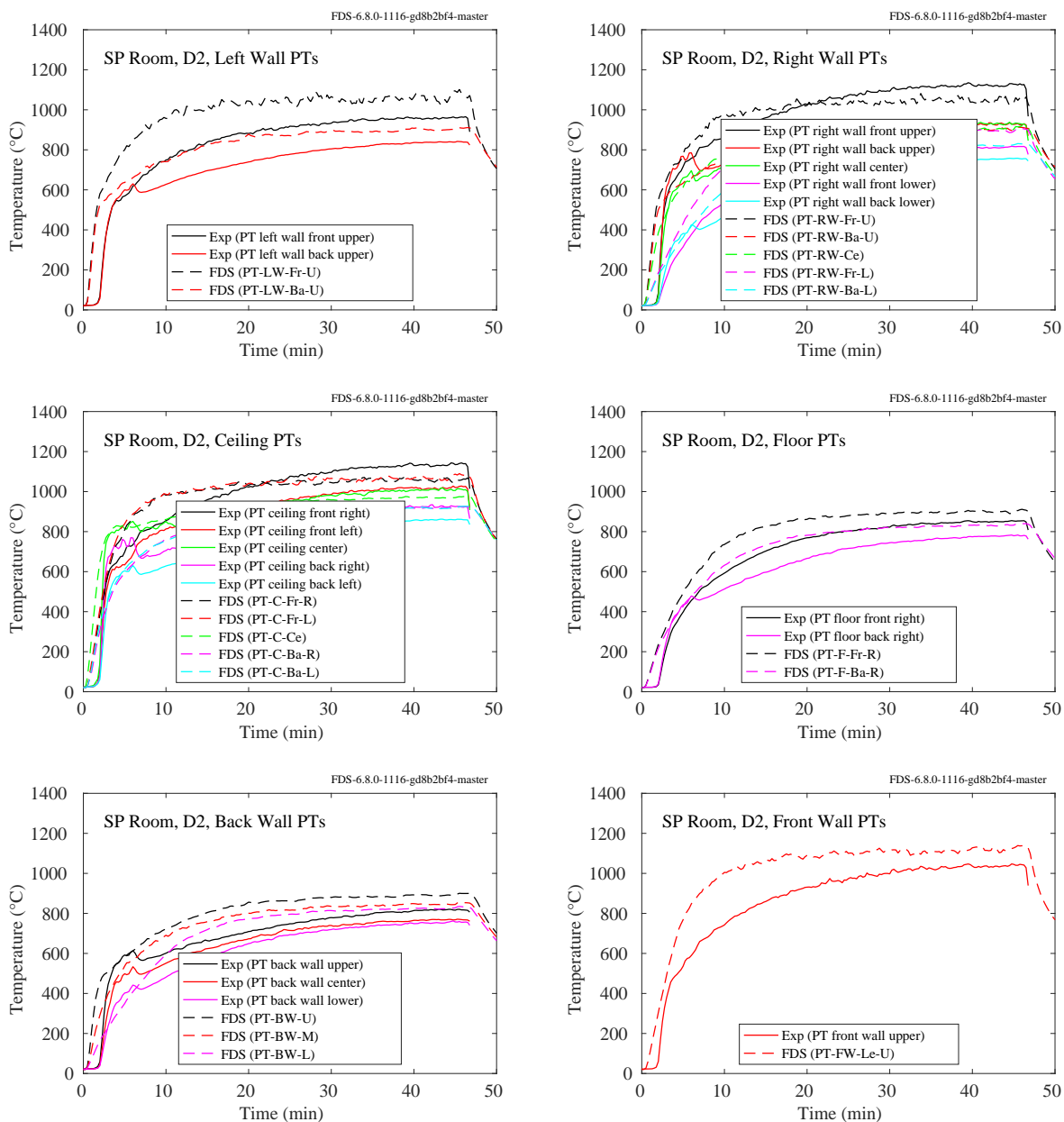


Figure 11.103: SP AST experiments, Insulated Room, Test D2.

Plate Thermometer Validation

The simulations of the SP Adiabatic Surface Temperature experiments include a 1-D model of a plate thermometer (PT), a temperature measurement device constructed of a thin, 10 cm square sheet of Inconel with a single thermocouple attached and backed by a layer of insulation material. To test the FDS PT model, a PT designed by Anthony Putorti at NIST, shown in Fig. 11.104 and described in detail in Ref. [375], was placed in a cone calorimeter and exposed to nominal heat fluxes of 25 kW/m^2 and 75 kW/m^2 . The measured and predicted temperatures are shown in Fig. 11.105.

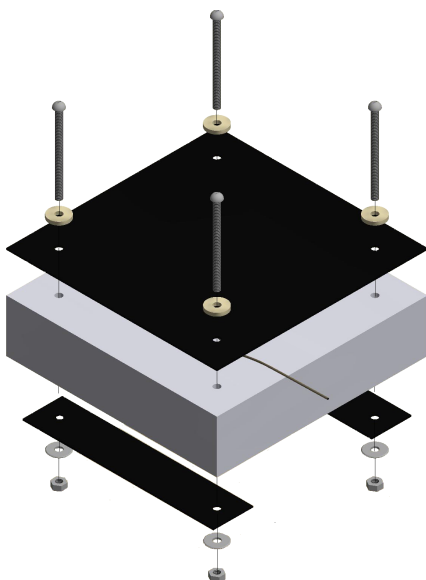


Figure 11.104: Exploded view of a plate thermometer.

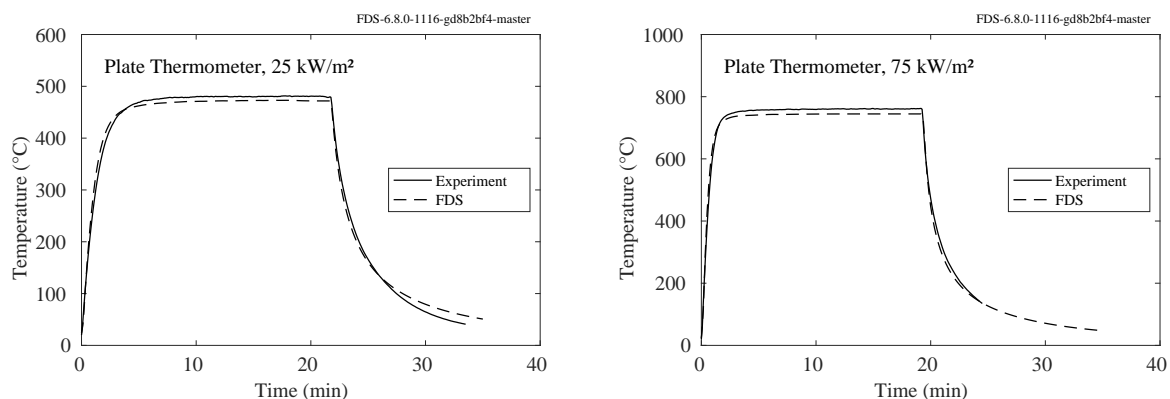


Figure 11.105: Predictions of plate thermometer temperatures in a cone calorimeter.

11.2.6 WTC Experiments

The compartment for the WTC experiments contained a hollow box column roughly 0.5 m from the fire pan, two trusses over the top of the pan, and one or two steel bars resting on the lower truss flanges. In Tests 1, 2 and 3, the steel was bare, and in Tests 4, 5 and 6, the steel was coated with various thicknesses of sprayed fire-resistive materials. The column was instrumented near its base (about 0.5 m from the floor, middle (1.5 m), and upper (2.5 m)). Four measurements of steel (and insulation) temperatures were made at each location, for each of its four sides. These elements were modeled using thin sheet obstructions with a resolution of 10 cm.

In addition to the steel structural elements, five cylinders (“slugs”) of nickel 200 ($\geq 99\%$ nickel), 25.4 cm long and 10.2 cm in diameter, were positioned 50 cm north of the centerline in the WTC experiments. Slugs 1 through 5 were 2.92 m, 1.82 m, 0.57 m, 0.05 m, and 1.56 m, respectively, from the longitudinal axis of the fire pan. All the slugs were 50 cm north of the lateral axis. The fire pan measured 2 m by 1 m. Four thermocouples were inserted into each slug at various locations. All four temperatures for each slug were virtually indistinguishable. Rectangular obstructions were used to model the slugs, but the one-dimensional heat conduction calculation was performed using cylindrical coordinates.

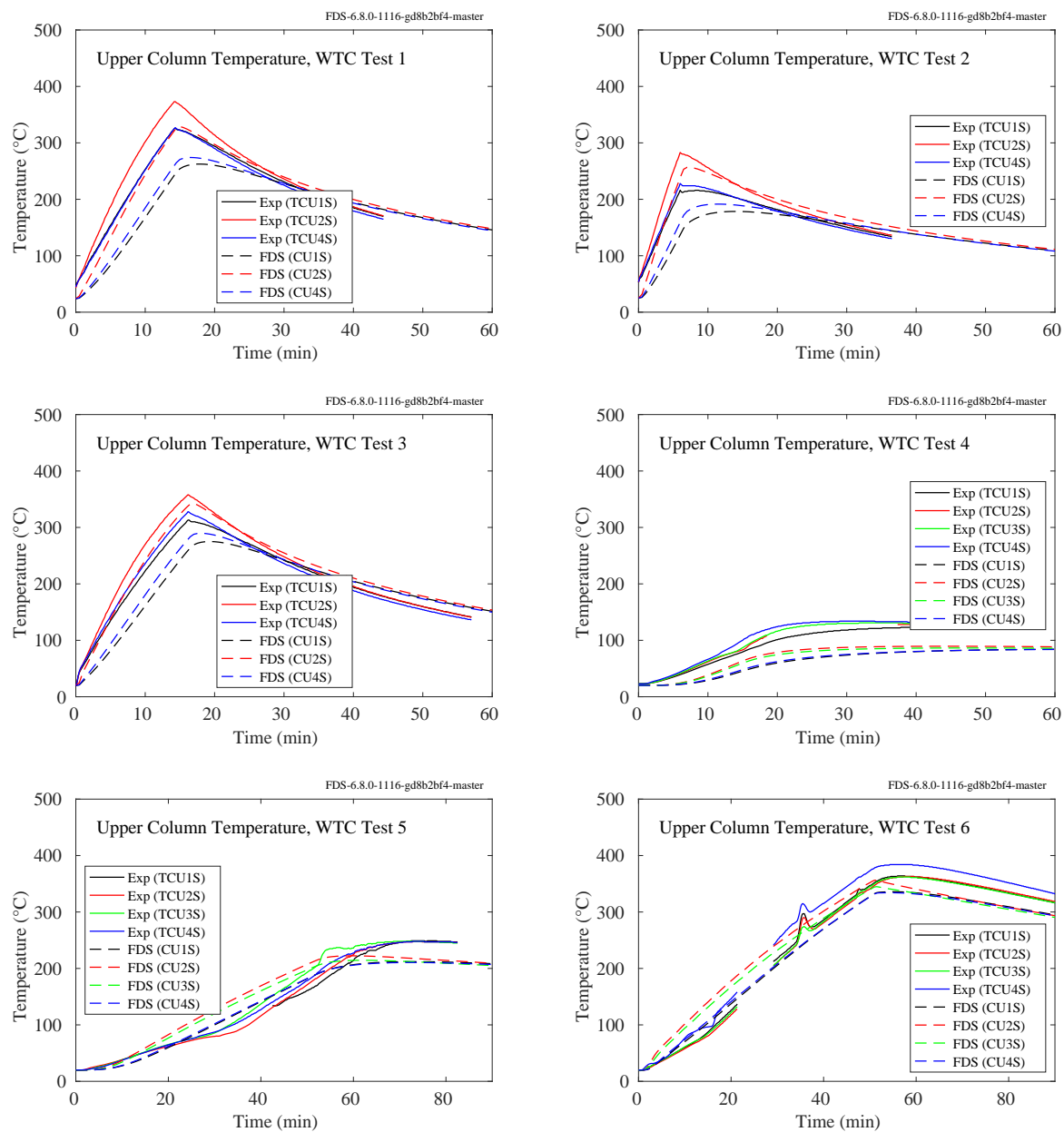


Figure 11.106: WTC experiments, steel temperatures, upper column.

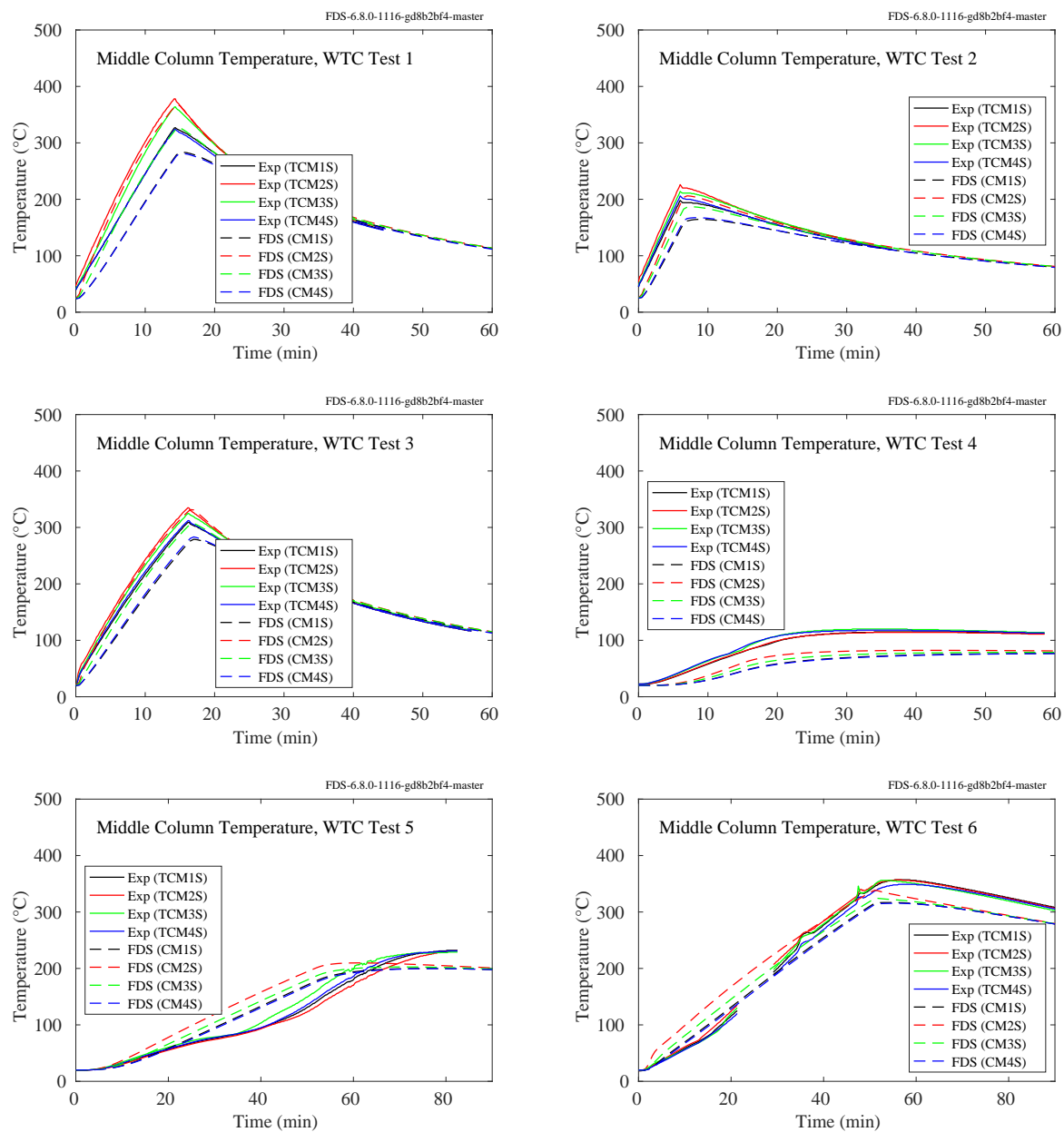


Figure 11.107: WTC experiments, steel temperatures, middle column.

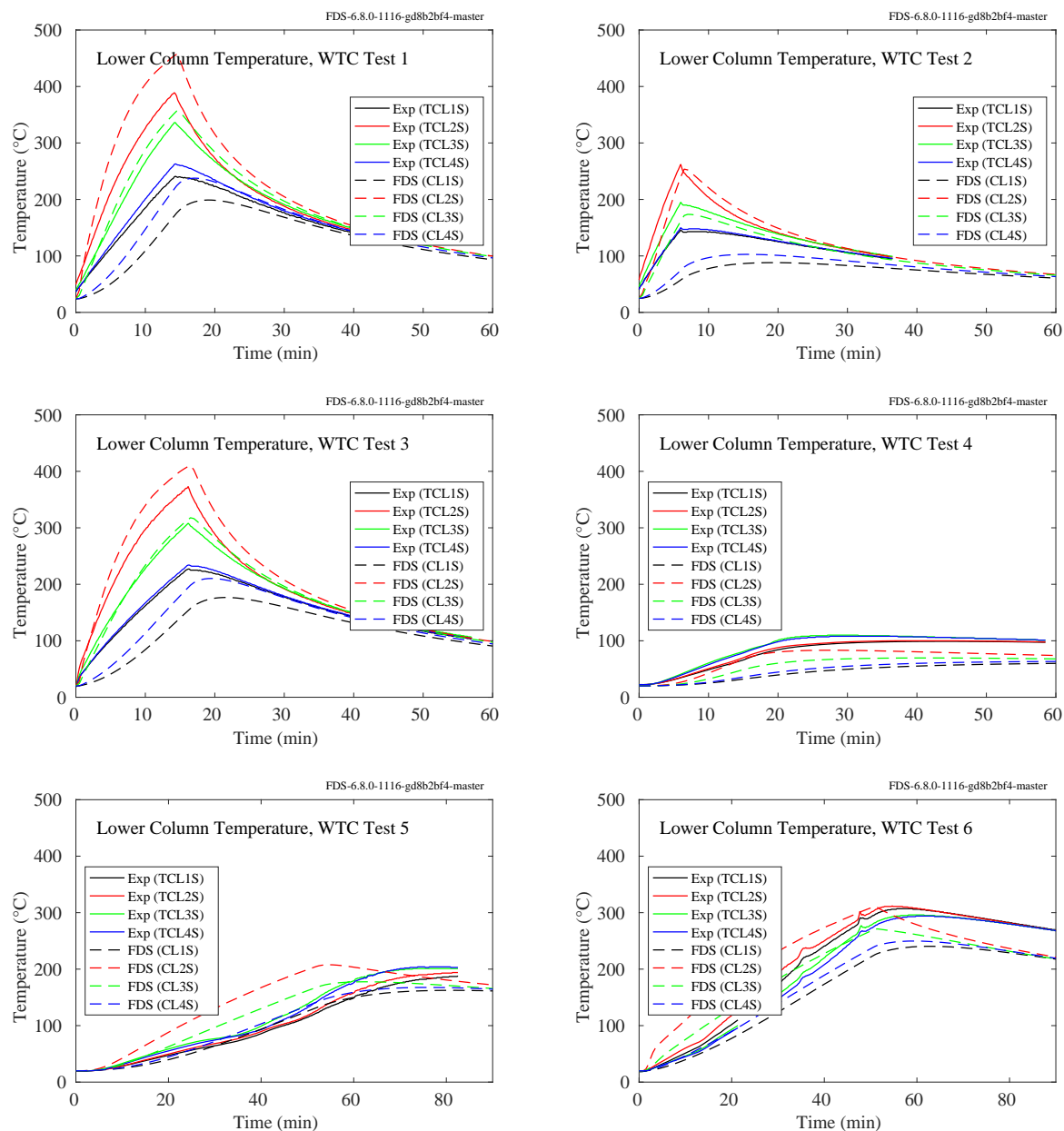


Figure 11.108: WTC experiments, steel temperatures, lower column.

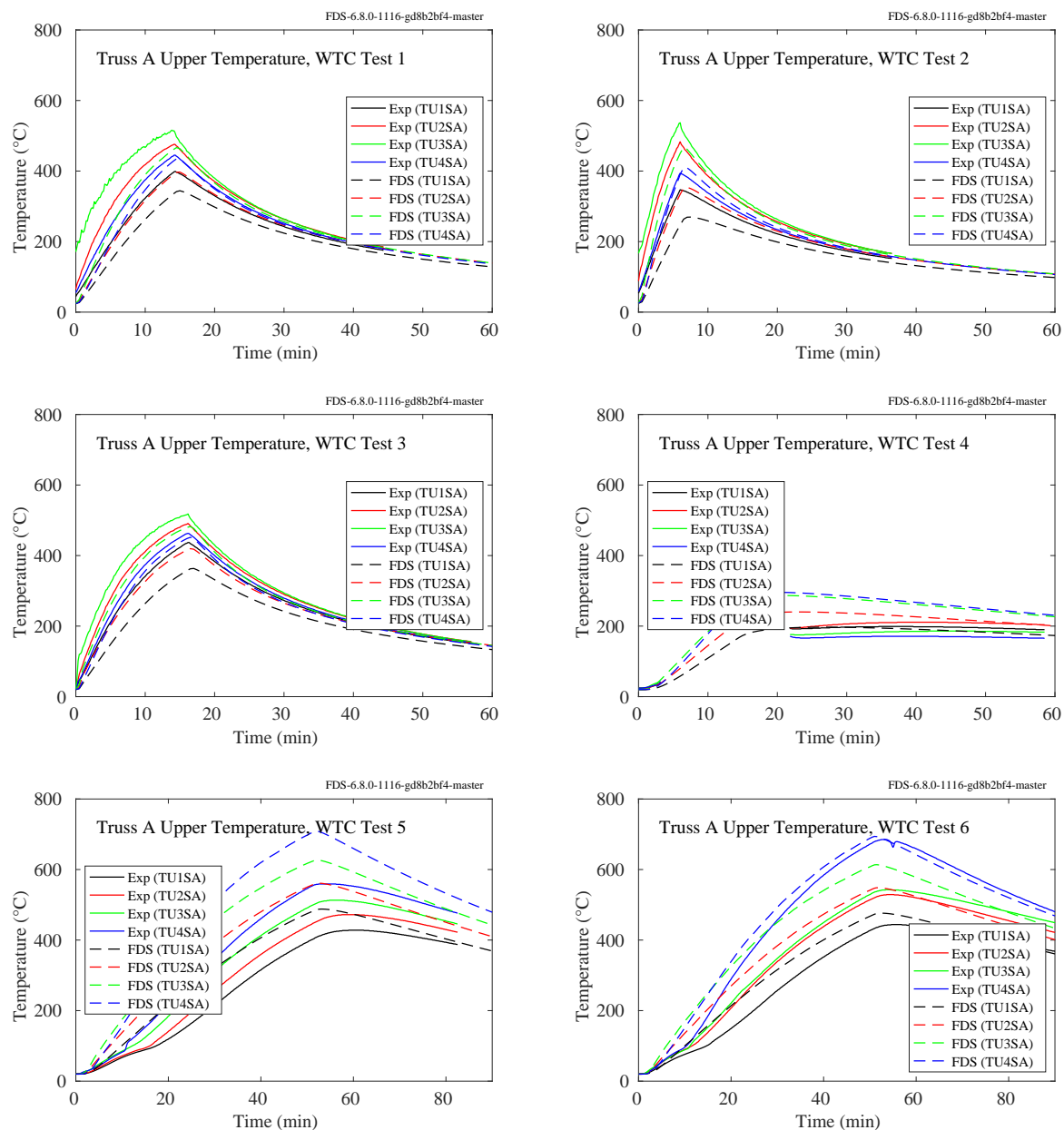


Figure 11.109: WTC experiments, steel temperatures, upper Truss A.

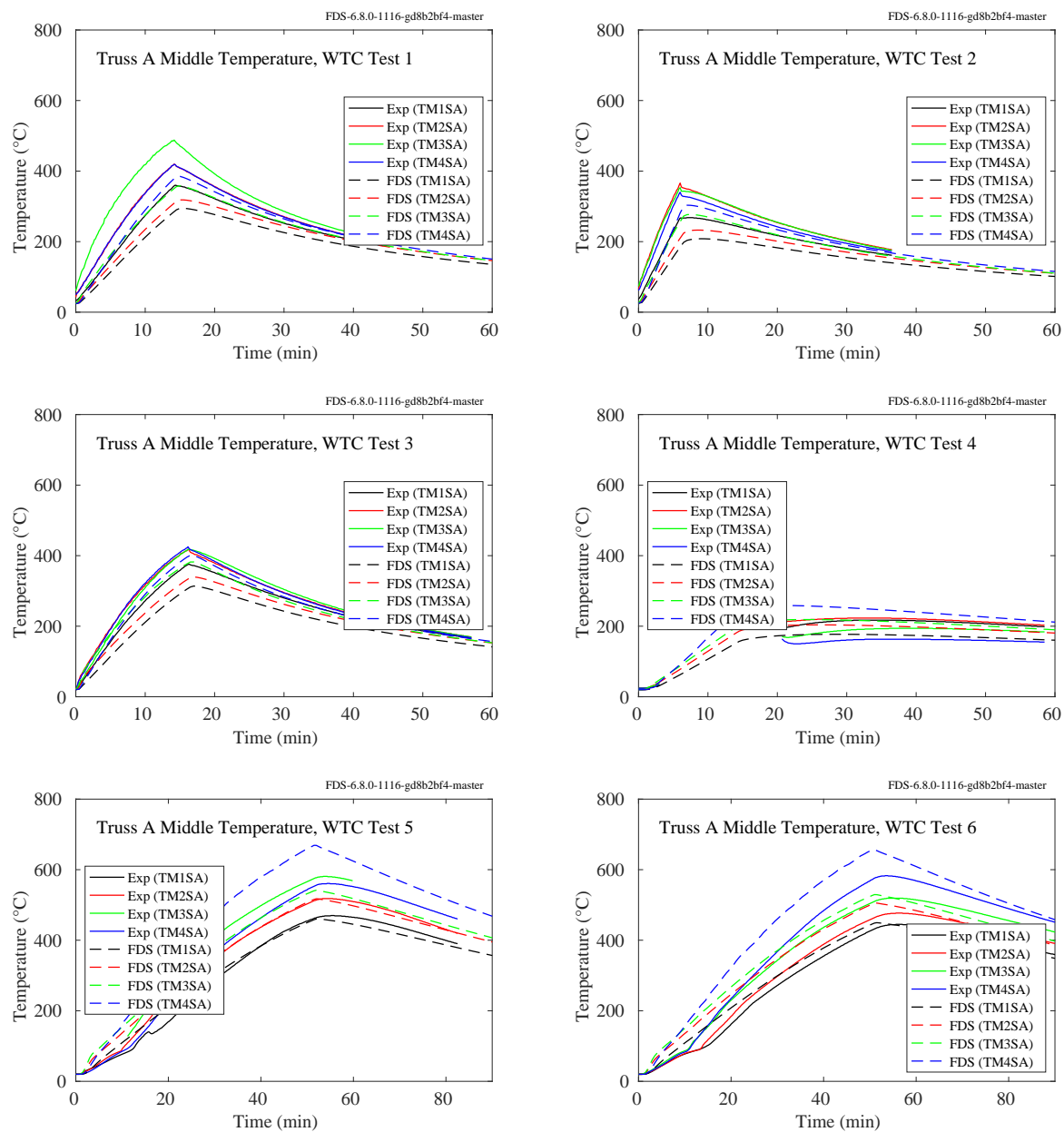


Figure 11.110: WTC experiments, steel temperatures, middle Truss A.

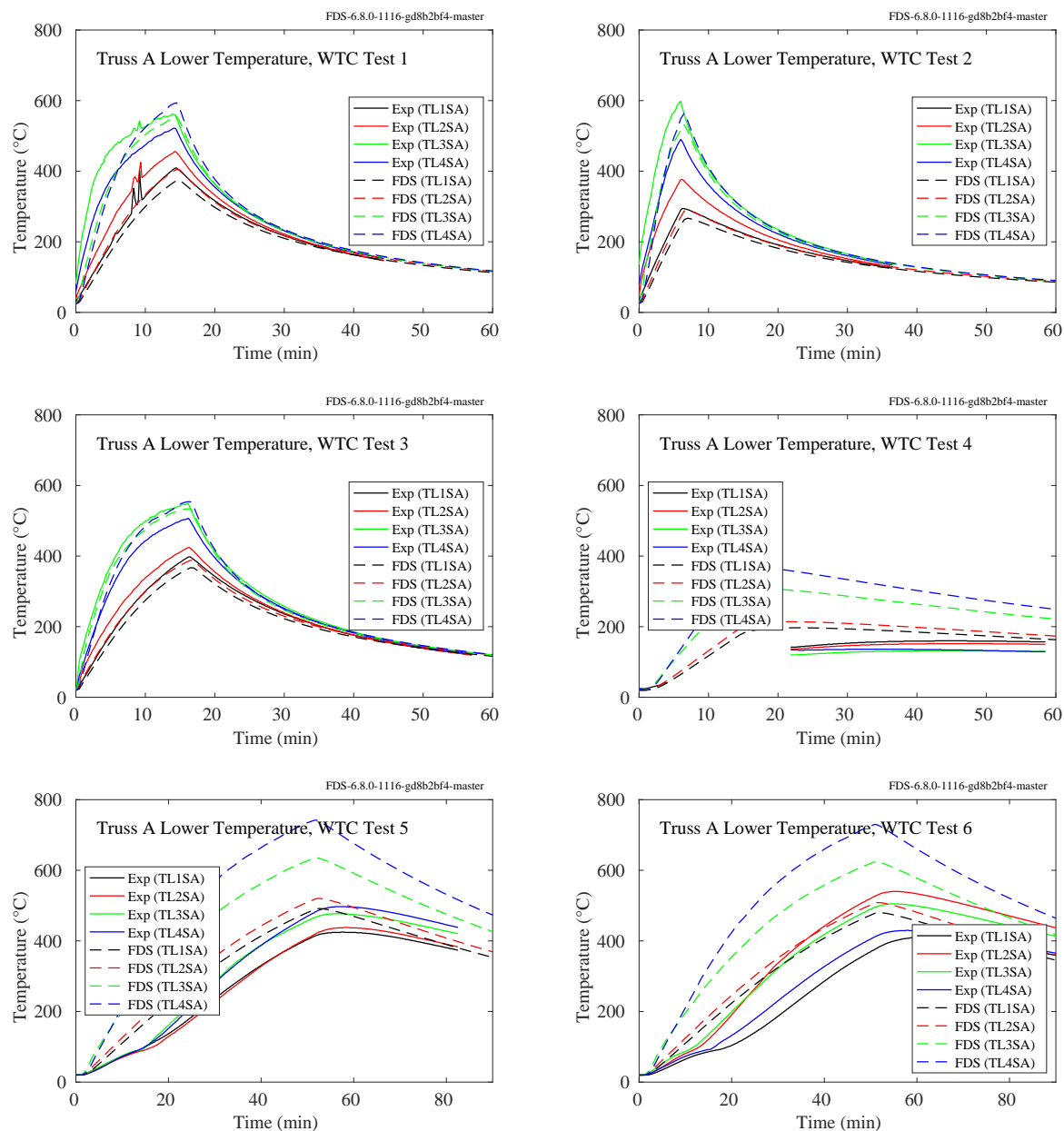


Figure 11.111: WTC experiments, steel temperatures, lower Truss A.

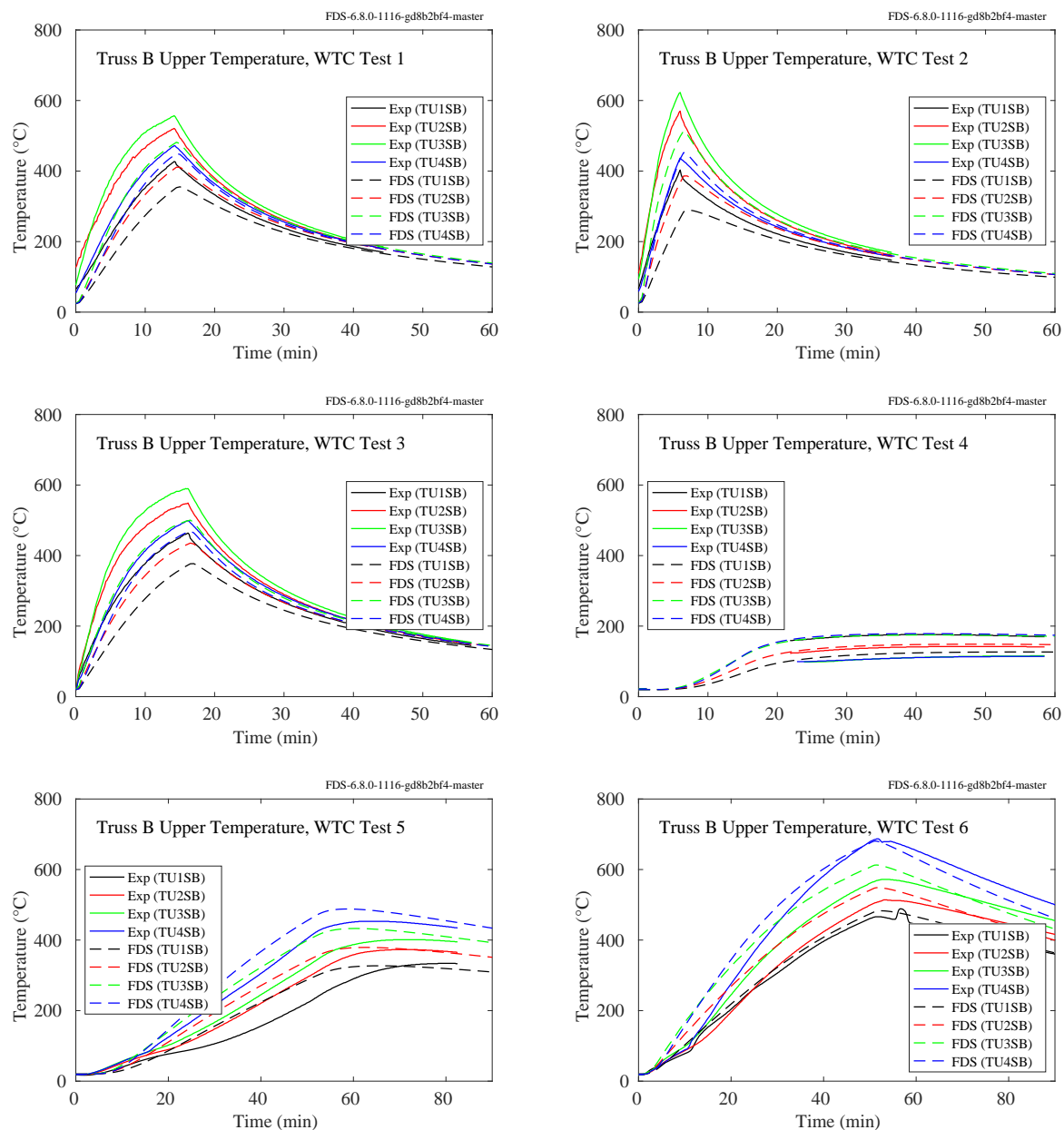


Figure 11.112: WTC experiments, steel temperatures, upper Truss B.

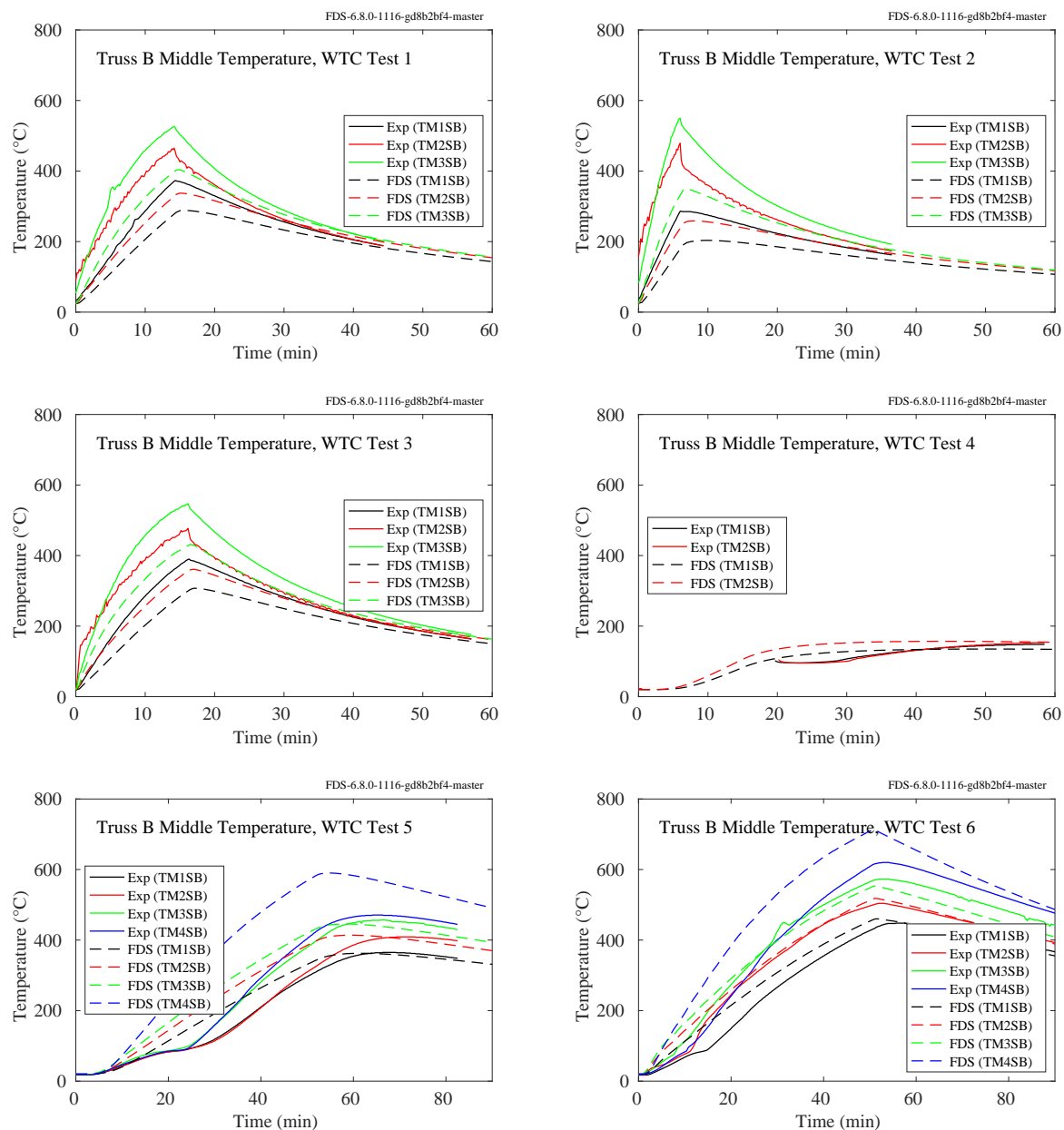


Figure 11.113: WTC experiments, steel temperatures, middle Truss B.

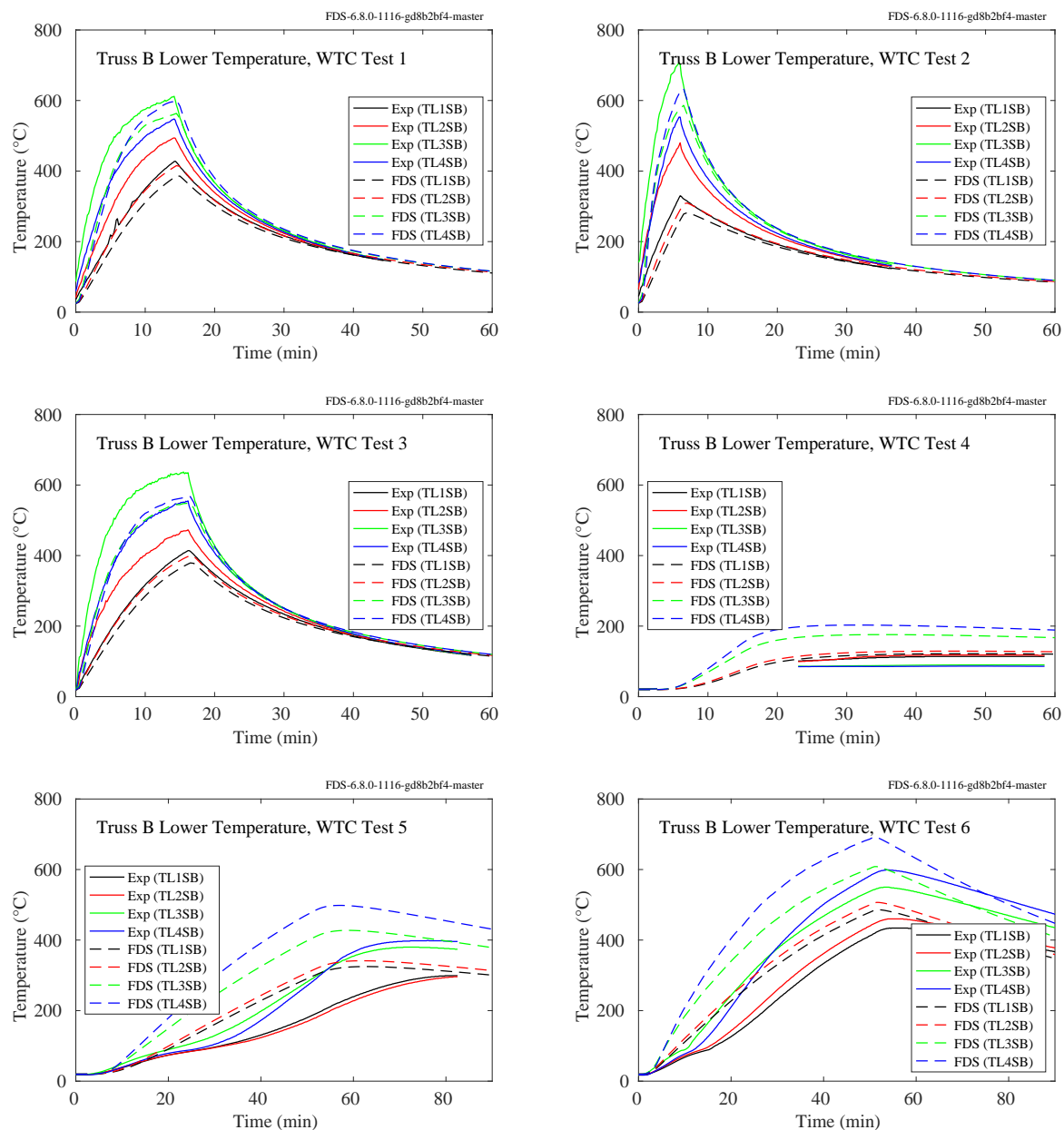


Figure 11.114: WTC experiments, steel temperatures, lower Truss B.

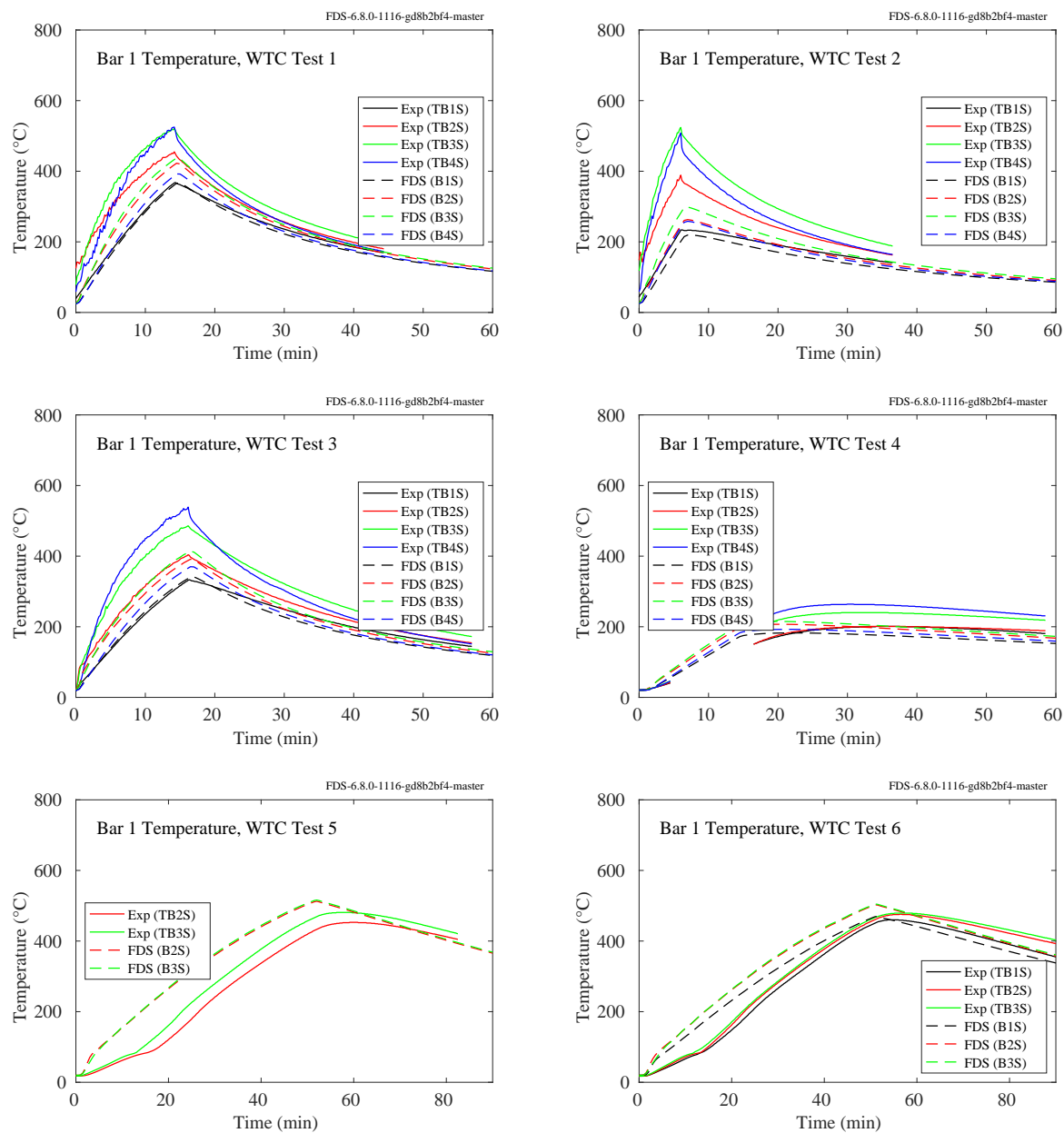


Figure 11.115: WTC experiments, steel temperatures, Bar 1.

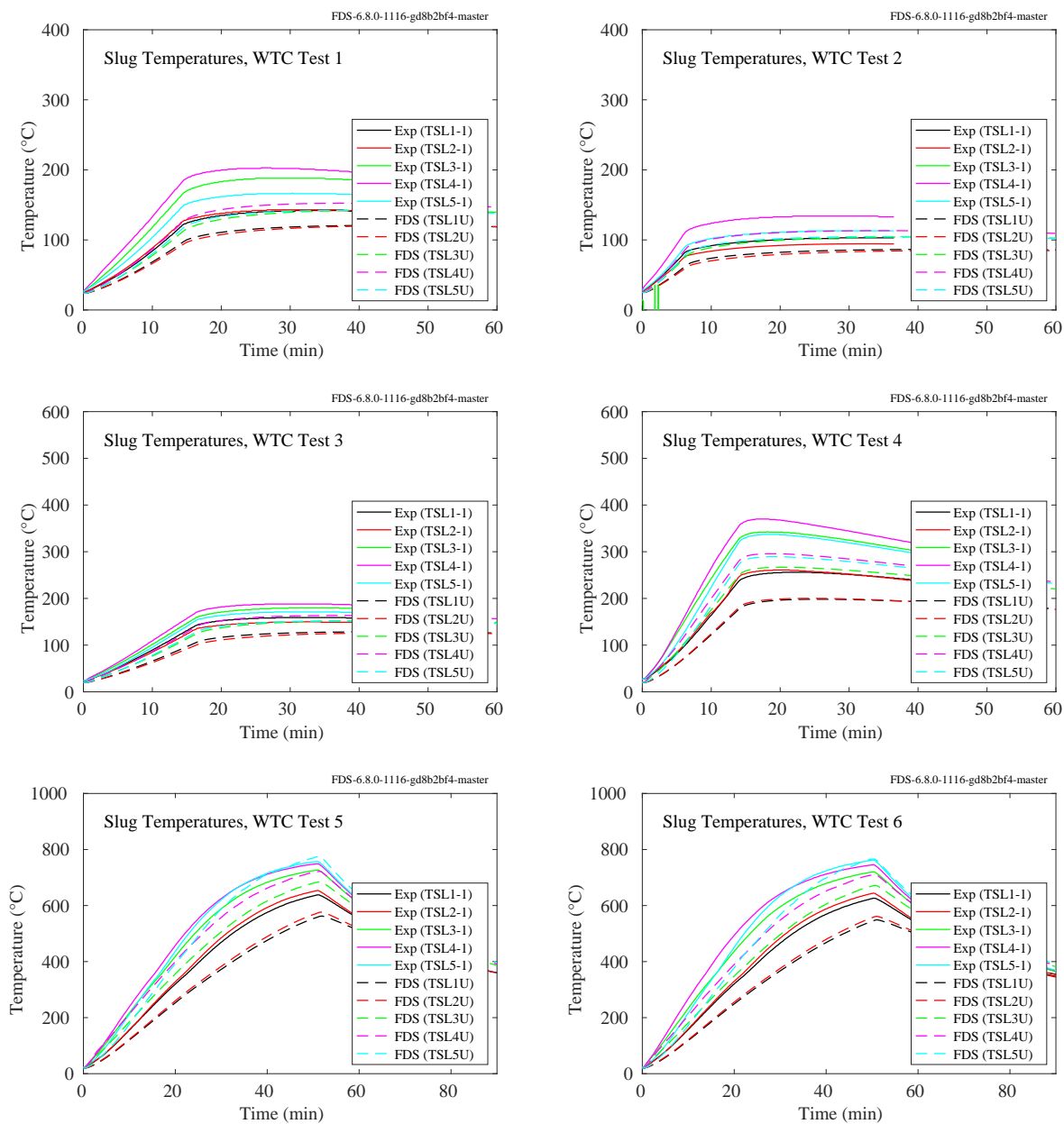


Figure 11.116: WTC experiments, slug temperatures.

11.2.7 CAROLFIRE Experiments

On the following pages are predictions of the THIEF (thermally-induced electrical failure) model compared to 35 experiments conducted at Sandia National Laboratory [164]. In these experiments, an instrumented electrical cable was run through a heated cylindrical “shroud.” The shroud temperature is an input for the model, and the cable temperature (and in some cases that of the steel conduit enclosing the cable) is predicted. Note that the cables generally fall into two categories – thermoset and thermoplastic. Thermoset cables form a char layer when burned and typically fail electrically at temperatures near 400 °C. Thermoplastic cables typically melt and then burn, leaving little residue behind except the conductors. These cables typically fail between 200 °C and 250 °C. Some cables, as in Tests 18 and 31, do not fall into either category. The thermoset cables were exposed to temperatures in the neighborhood of 480 °C, and the thermoplastics were exposed to temperatures near 300 °C.

Note in the plots to follow that the objective of the calculation is to predict the cable temperature just inside of the jacket until the cable fails electrically. In some experiments, the short-circuiting of the cable led to ignition of the pyrolyzates. This behavior is not captured in the model, which is why some of the experimental data shows a rapid rise in temperature at a certain point in the test. In many cases, electrical failure occurred very shortly, or at about the same time, as ignition.

Figure 11.131 compares the measured versus predicted time to a “threshold” temperature. The threshold temperature is 400 °C for thermoset cables and 200 °C for thermoplastics.

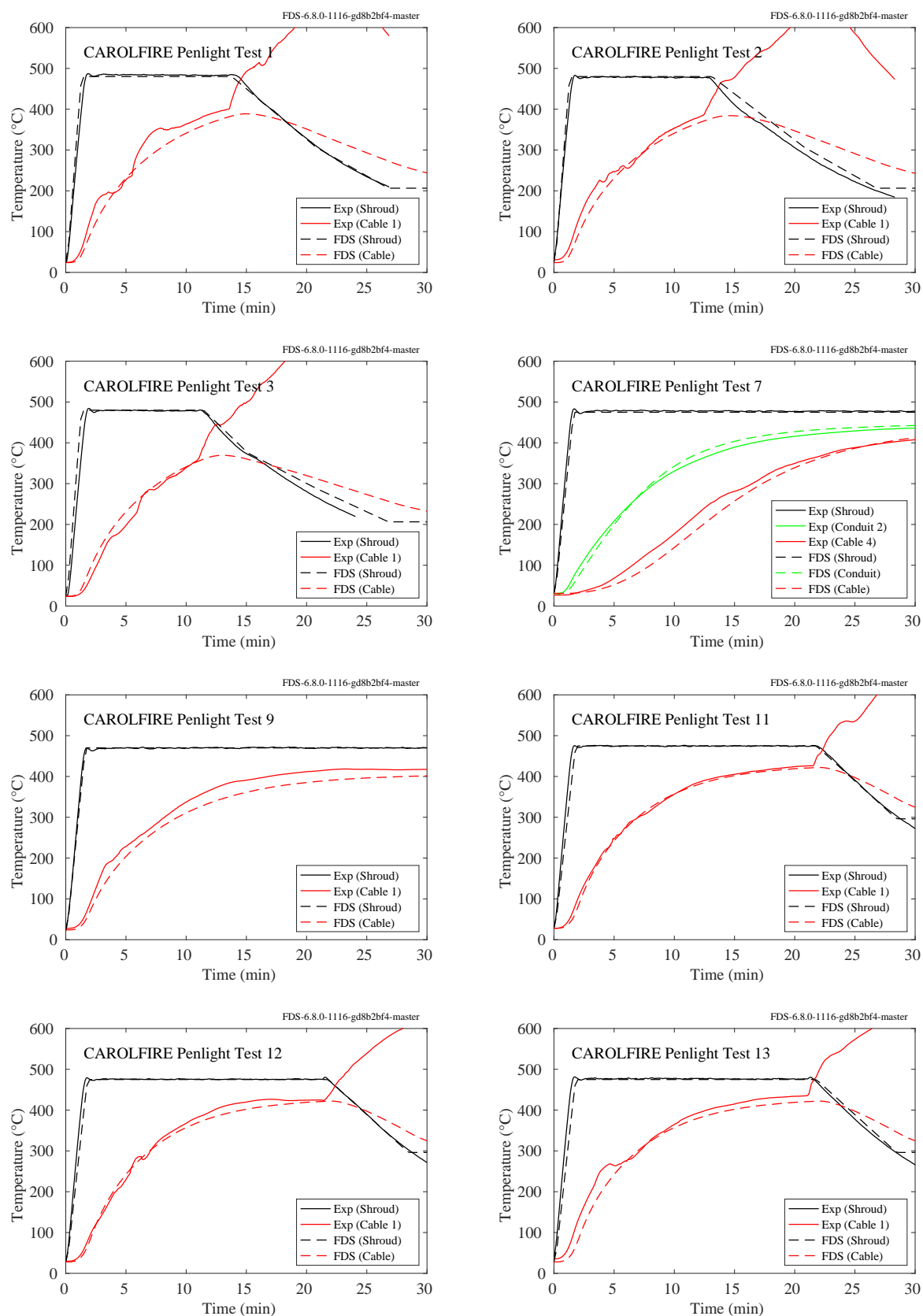


Figure 11.117: CAROLFIRE, electrical cable temperatures, Penlight Tests 1, 2, 3, 7, 9, 11-13.

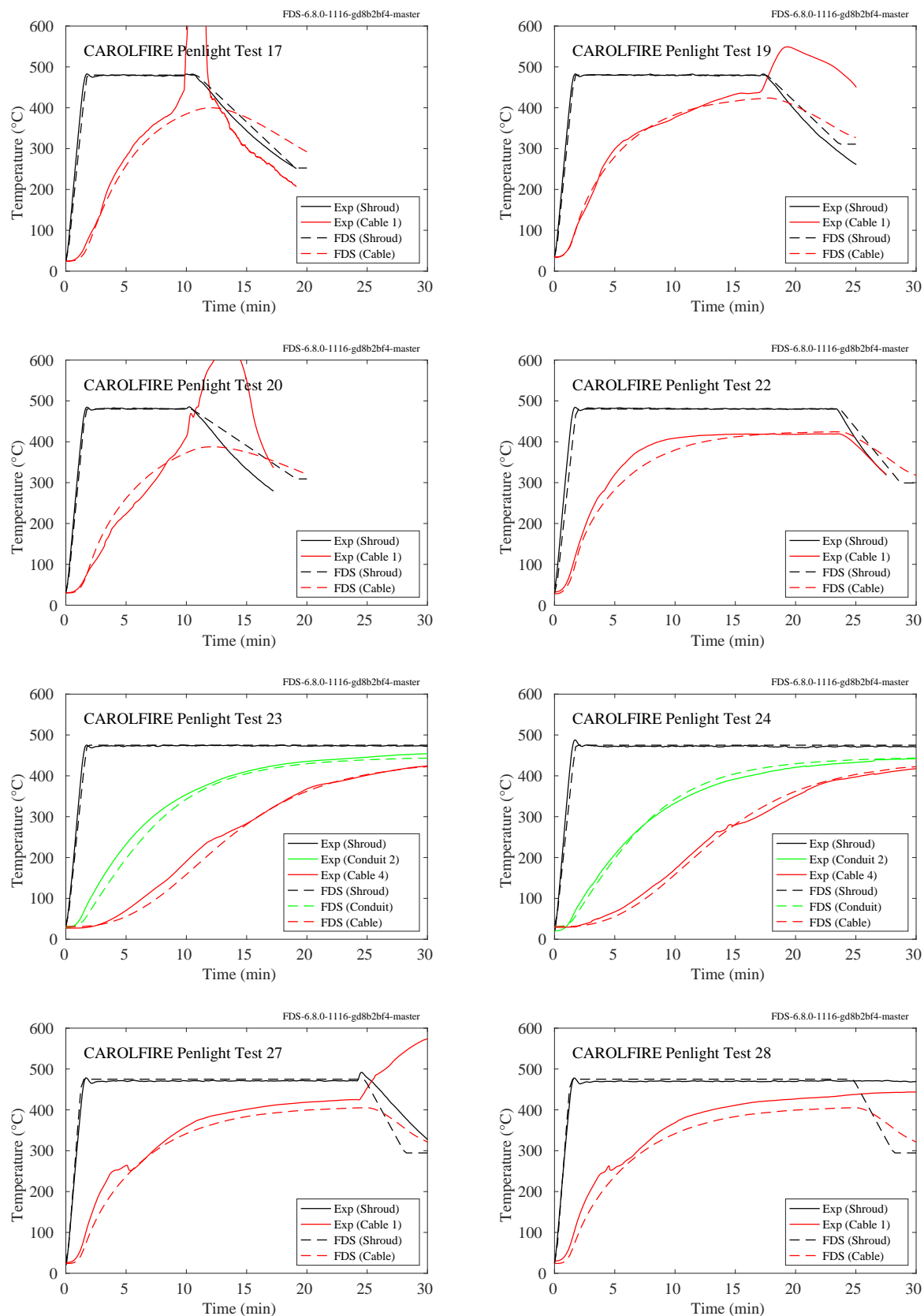


Figure 11.118: CAROLFIRE, electrical cable temperatures, Penlight Tests 17, 19-20, 22-24, 27-28.

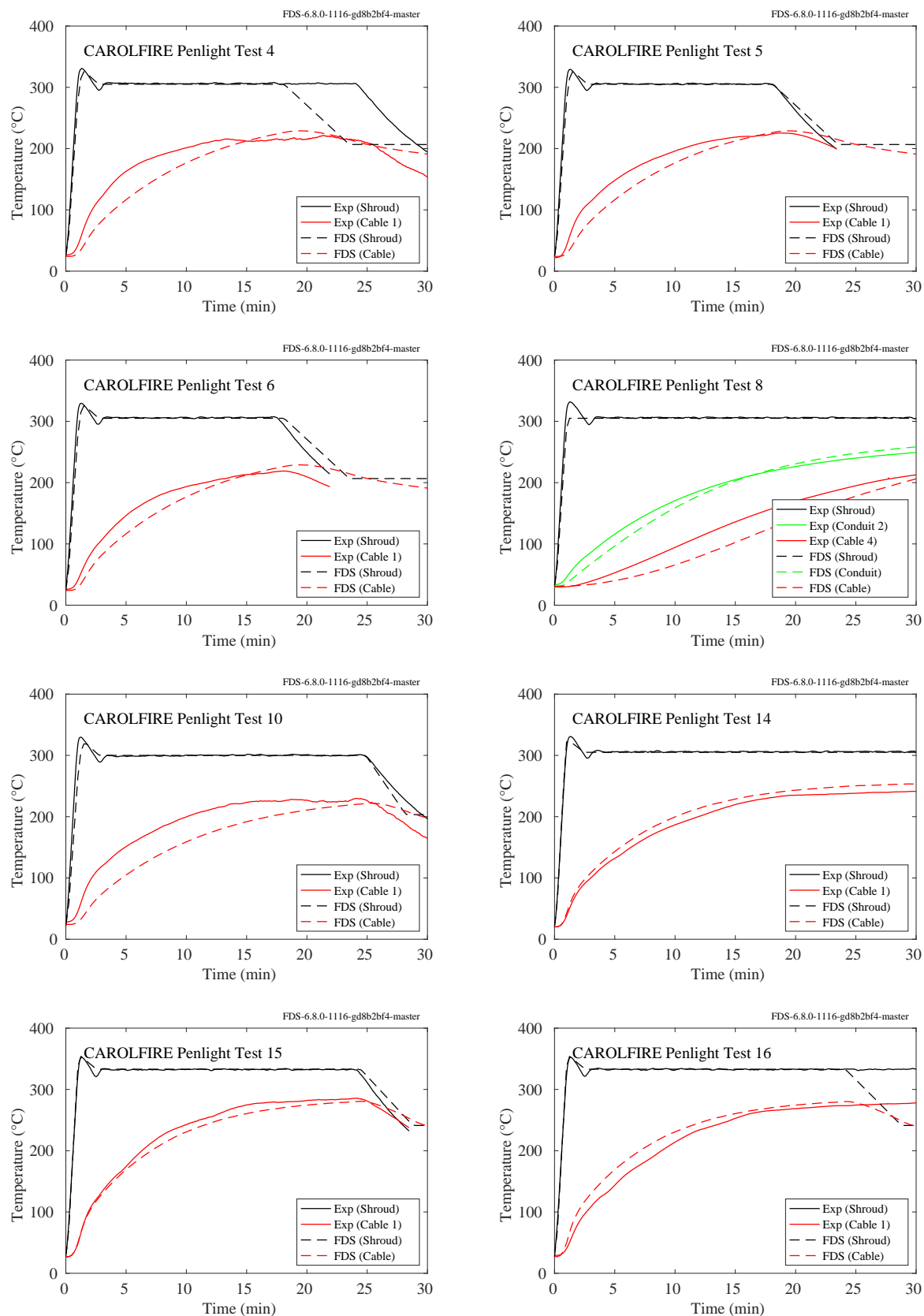


Figure 11.119: CAROLFIRE, electrical cable temperatures, Penlight Tests 4-6, 8, 10, 14-16.

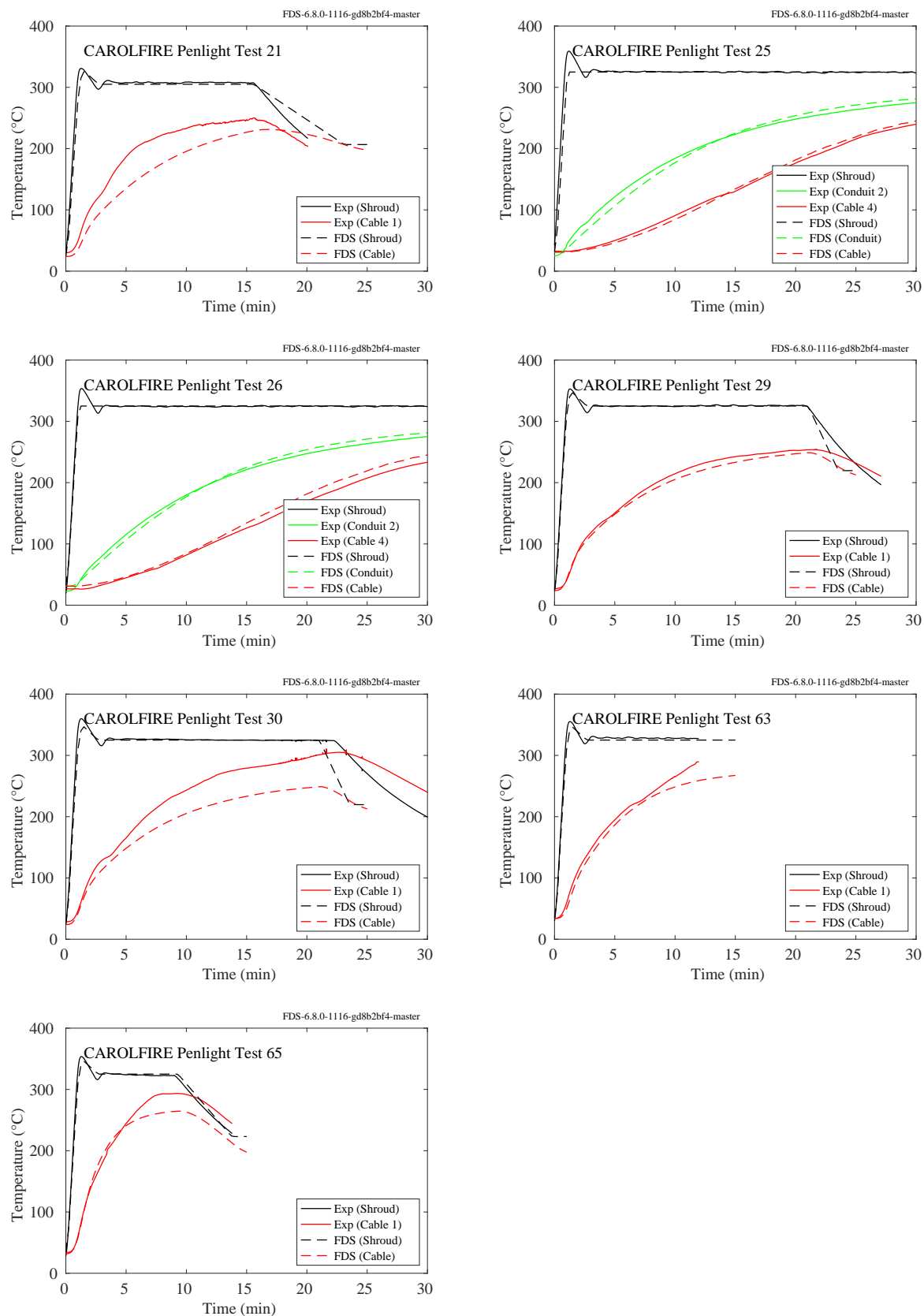


Figure 11.120: CAROLFIRE, electrical cable temperatures, Penlight Tests 21, 25-26, 29-30, 63, 65.

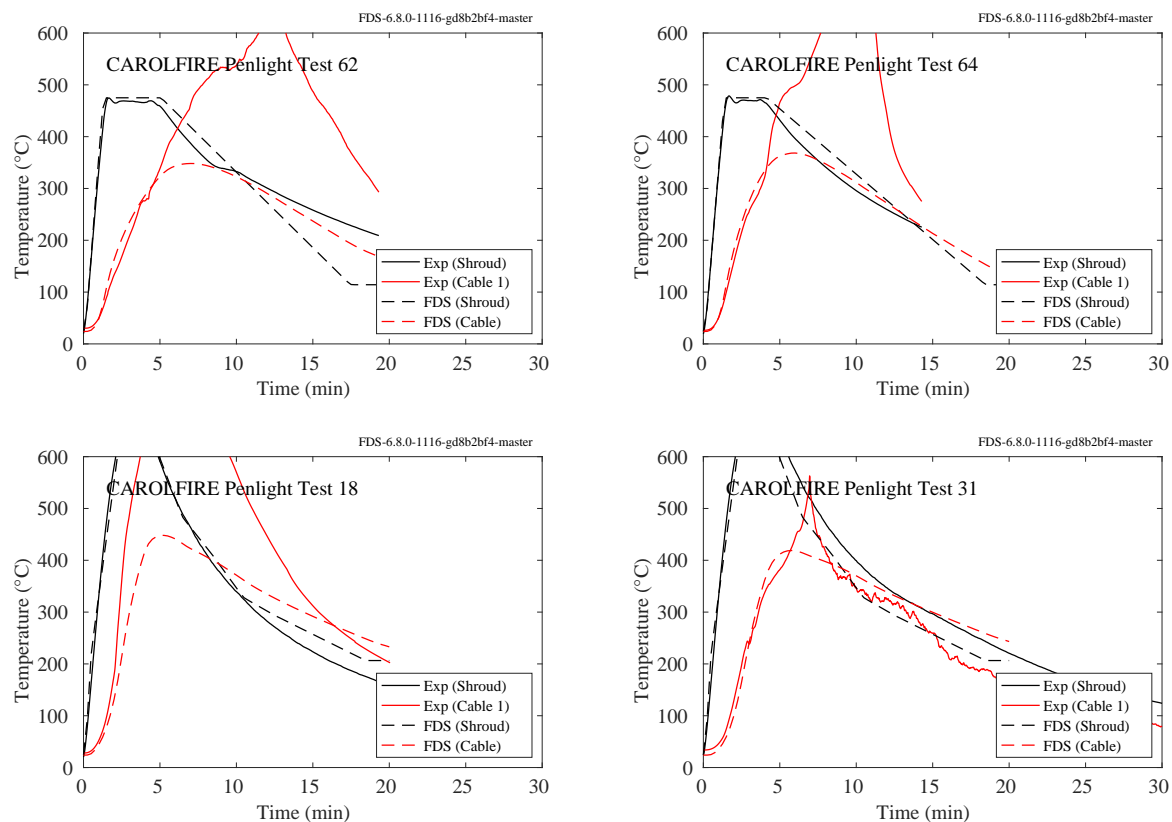


Figure 11.121: CAROLFIRE, electrical cable temperatures, Penlight Tests 18, 31, 62, 64.

11.2.8 Frankman Vegetation Experiments

Results of the Frankman vegetation experiments are shown in Fig. 11.122. Each plot represents a particular fuel sample. “SmEx15”, for example, is the small excelsior at 15 cm from the burner. Details and references can be found in Sec. 3.31.

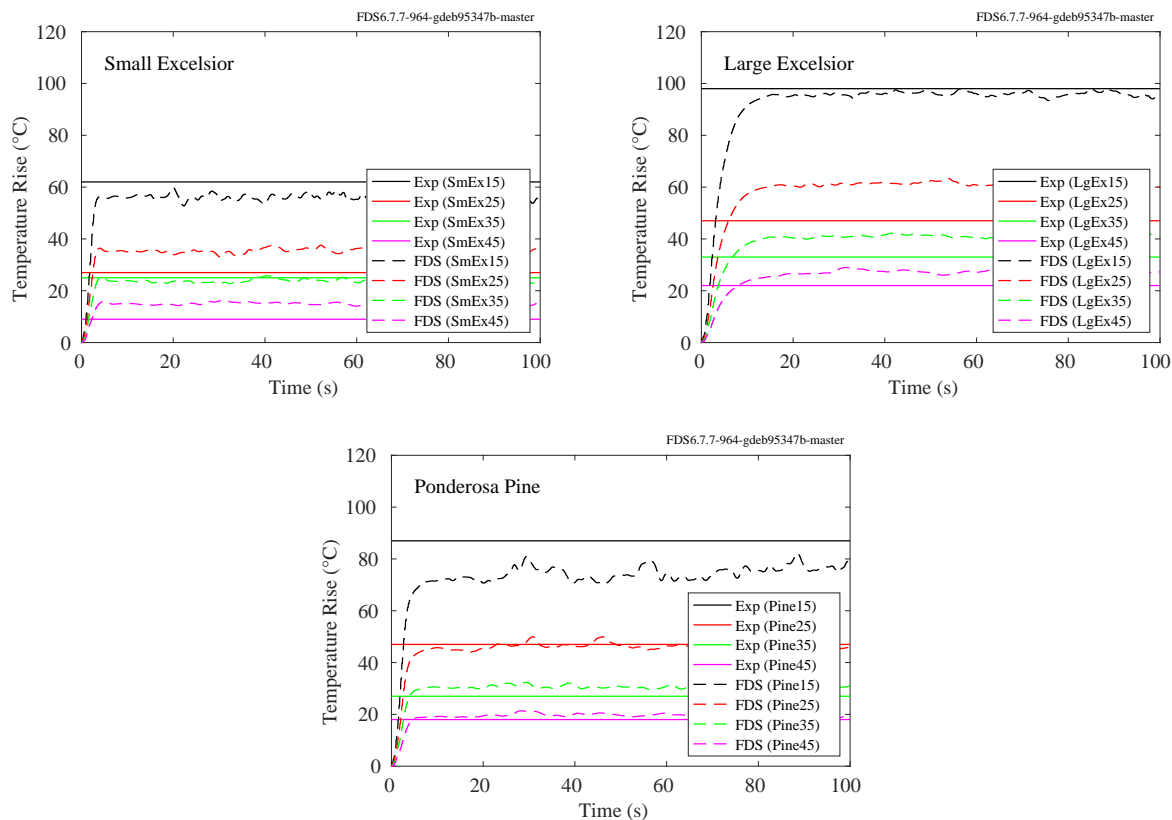


Figure 11.122: Frankman vegetation experiments, fuel temperatures.

11.2.9 PRISME Experiments

In most of the PRISME experiments, instrumented electrical cables were laid within trays at various heights in the test compartment. For the PRISME LEAK series of experiments (Figs. 11.123 and 11.124), the gas temperature in the vicinity of the cables was measured and served as the exposing heat source for calculations using the THIEF (Thermally-Induced Electrical Failure) model [291].

For the PRISME Door experiments, the temperatures of surrogate cables were predicted directly from the predicted thermal environment of the entire compartment. The measurement points in these experiments were labeled, for example, TCA_L2_HE_SURF, meaning thermocouple of the “analytical” cable, compartment 2, *haut* (high), east, surface. BW means *bas* (low) west, for example. Thermocouples were positioned on the cable surface (SURF), halfway towards center (INTER), and center (CENTRE).

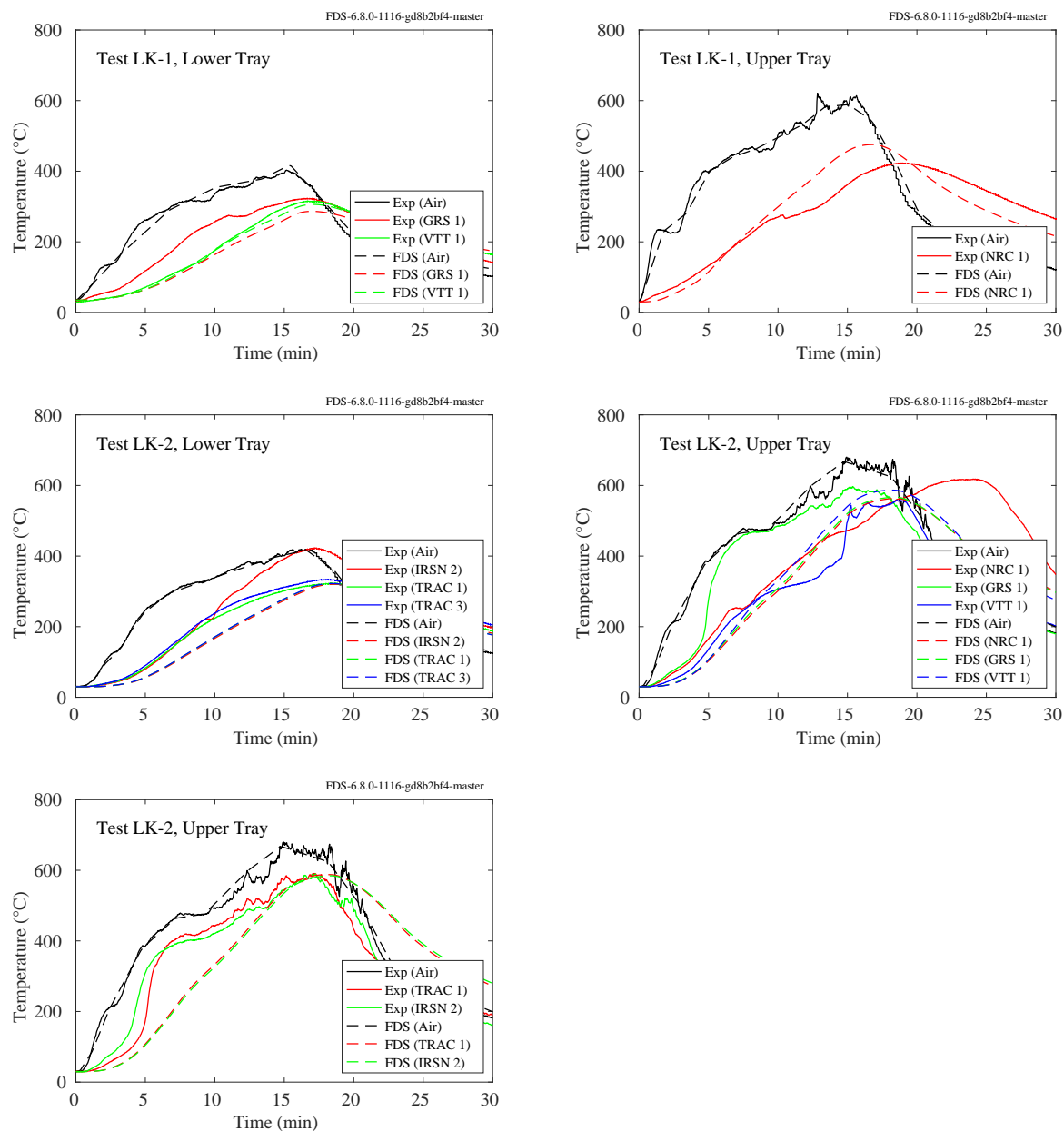


Figure 11.123: PRISME LEAK experiments, cable temperature, Tests 1 and 2.

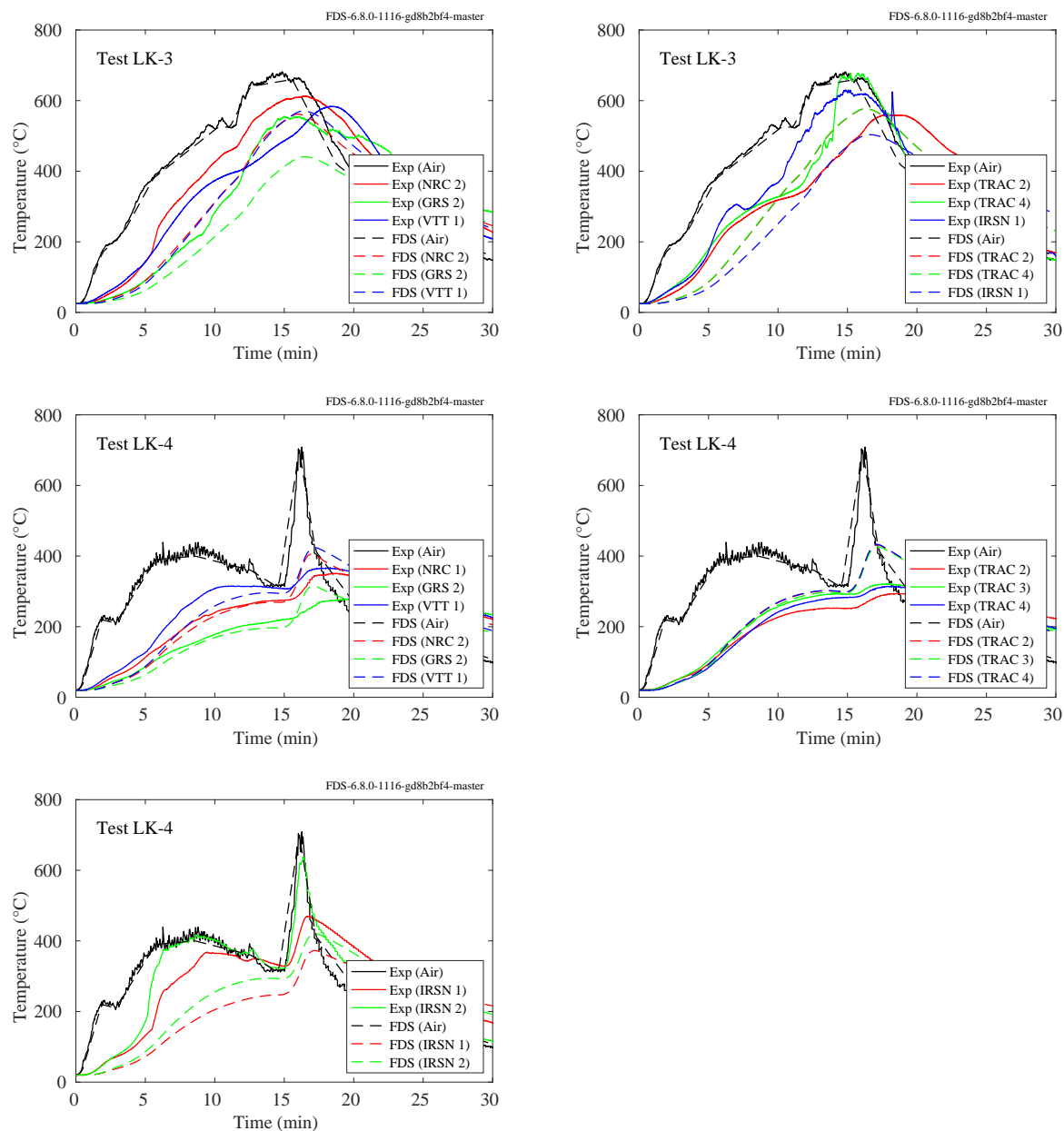


Figure 11.124: PRISME LEAK experiments, cable temperature, Tests 3 and 4.

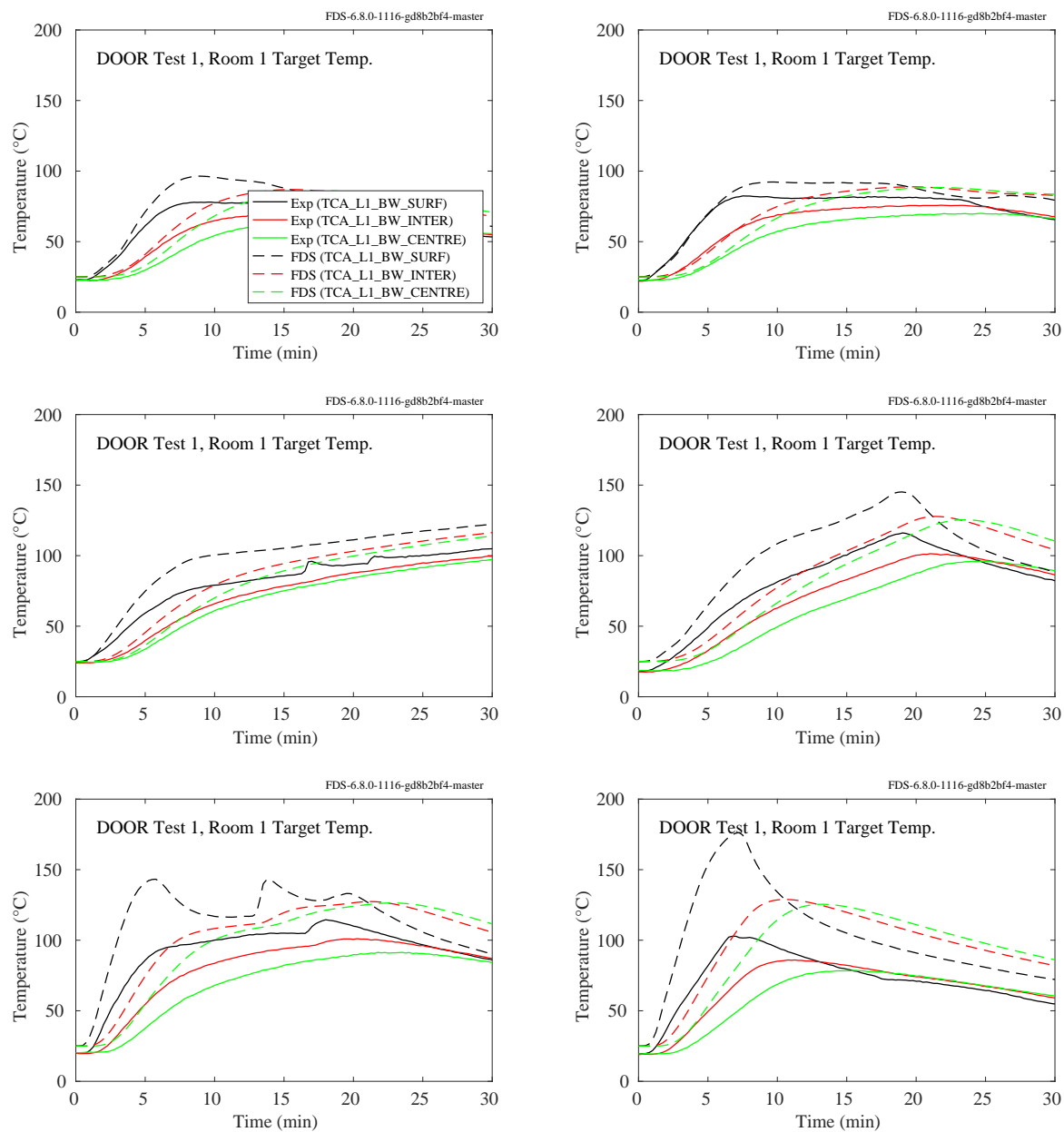


Figure 11.125: PRISME DOOR experiments, cable temperature, Room 1, Cable BW.

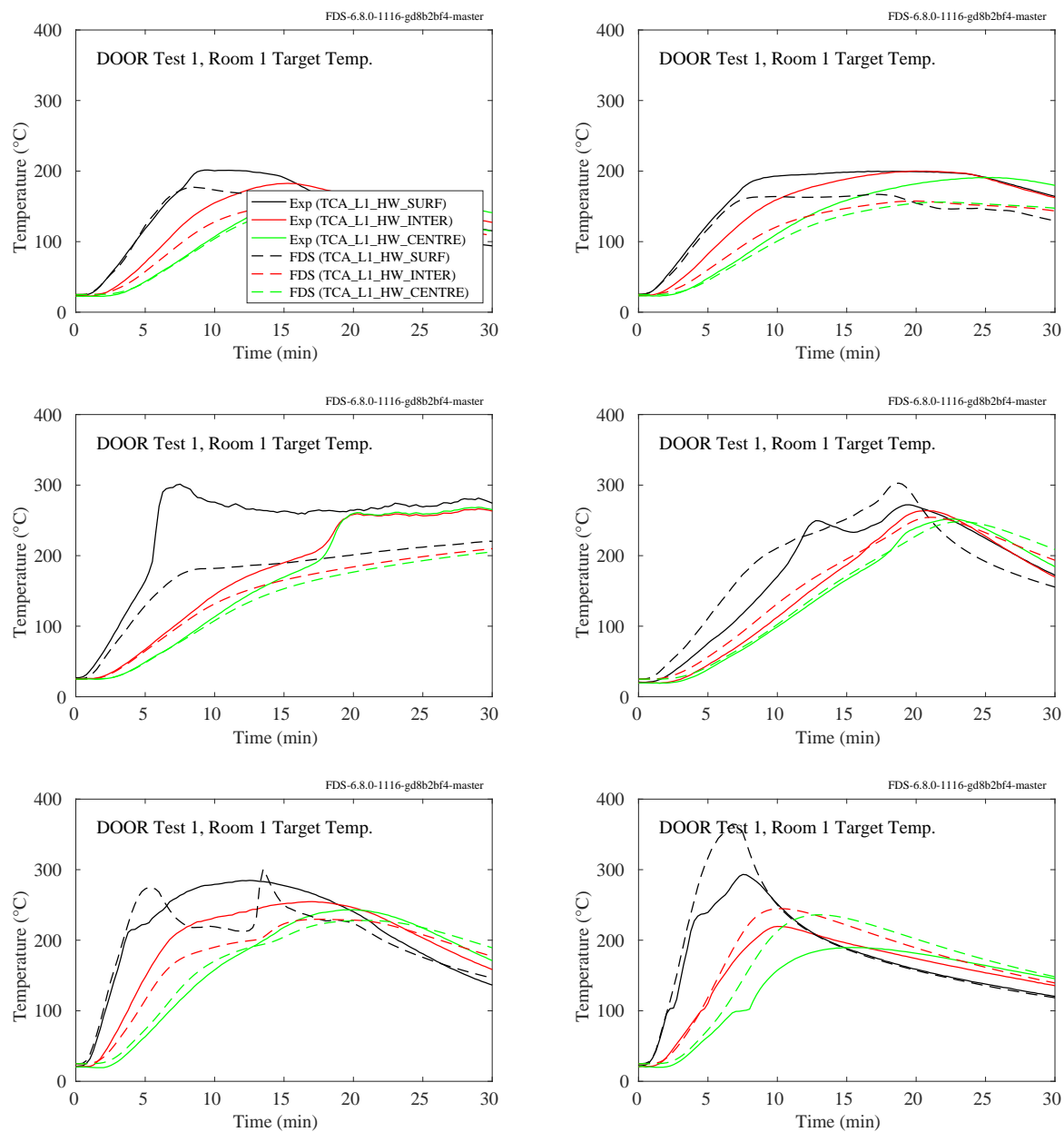


Figure 11.126: PRISME DOOR experiments, cable temperature, Room 1, Cable HW.

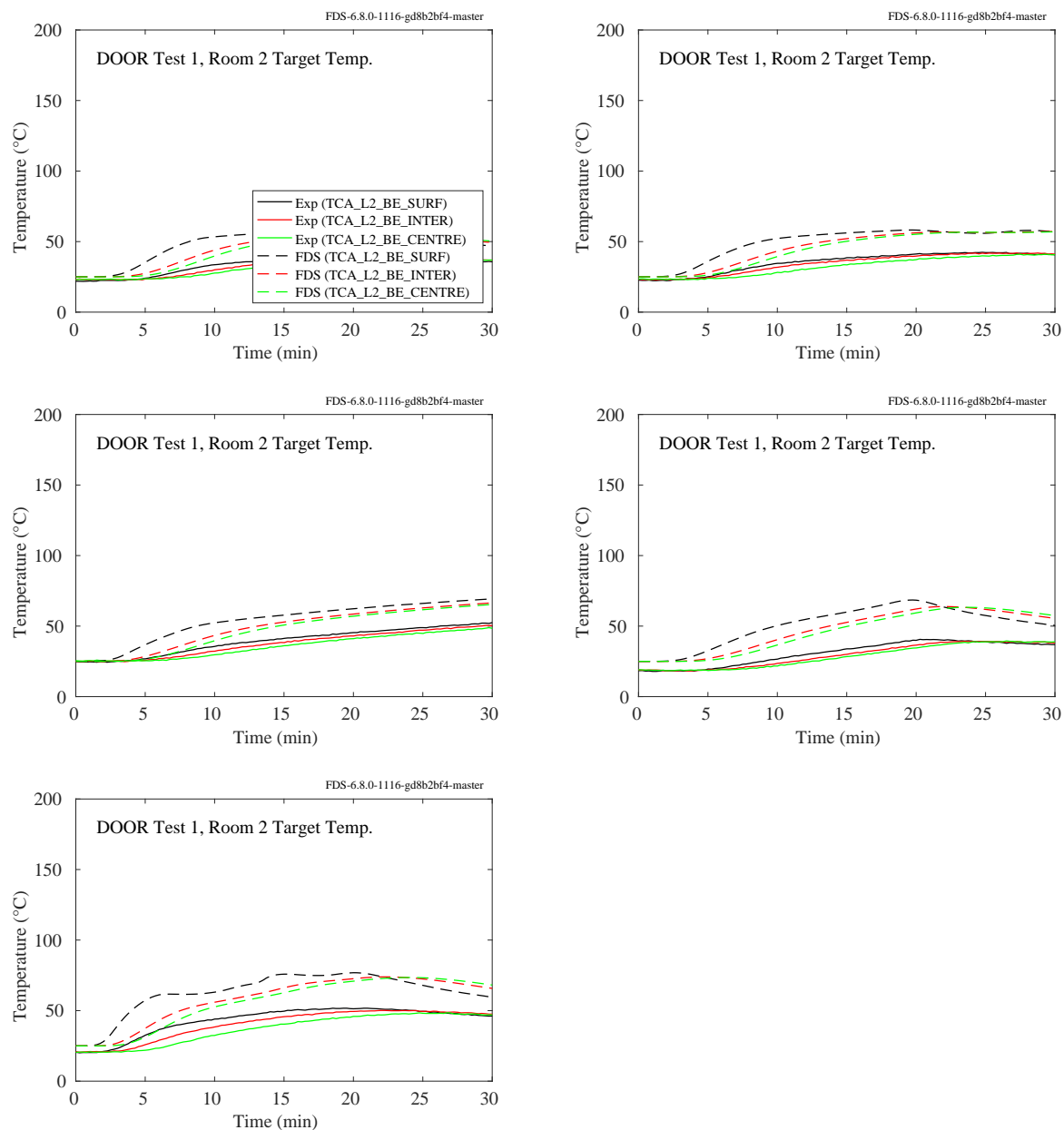


Figure 11.127: PRISME DOOR experiments, cable temperature, Room 2, Cable BE.

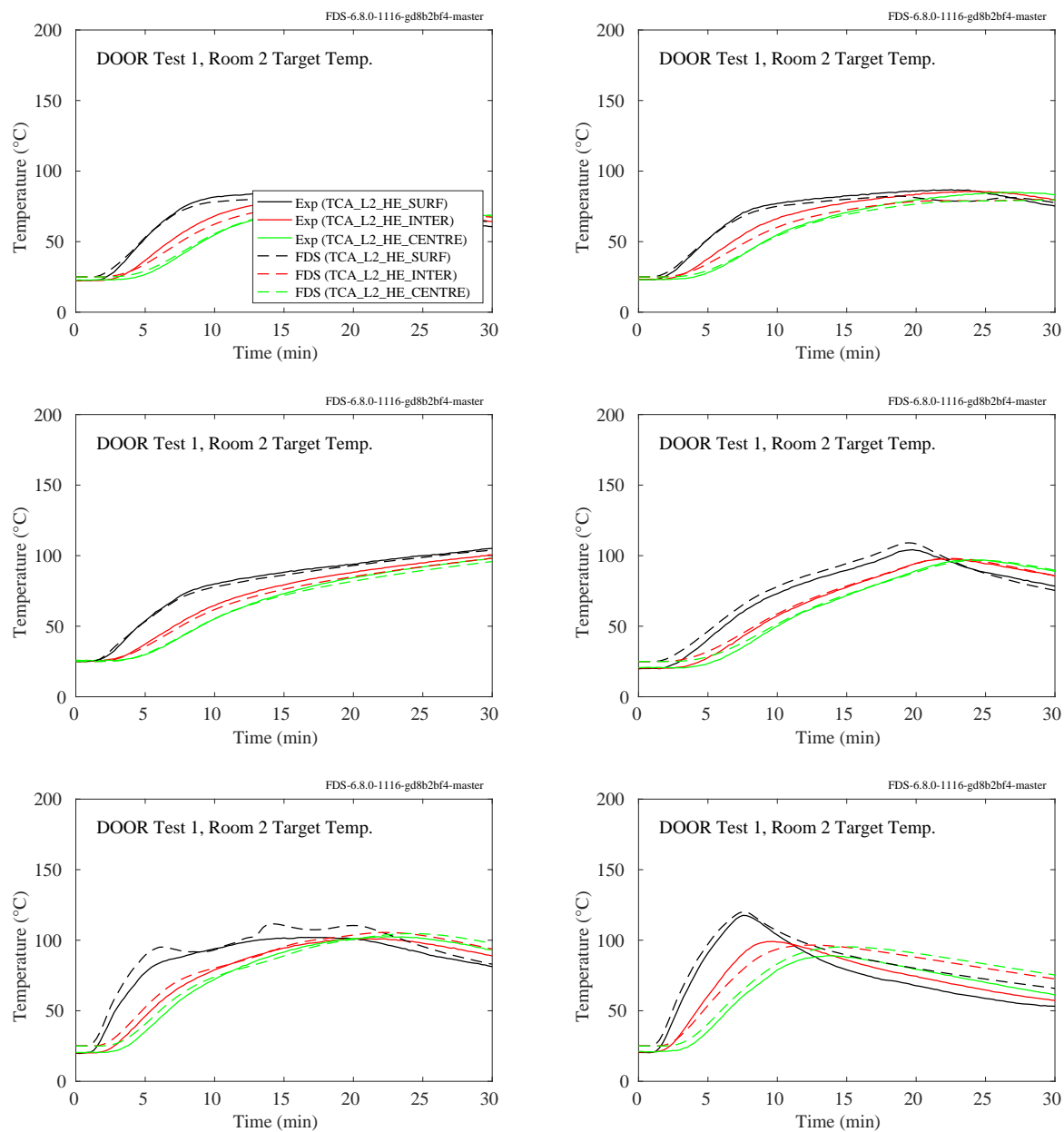


Figure 11.128: PRISME DOOR experiments, cable temperature, Room 2, Cable HE.

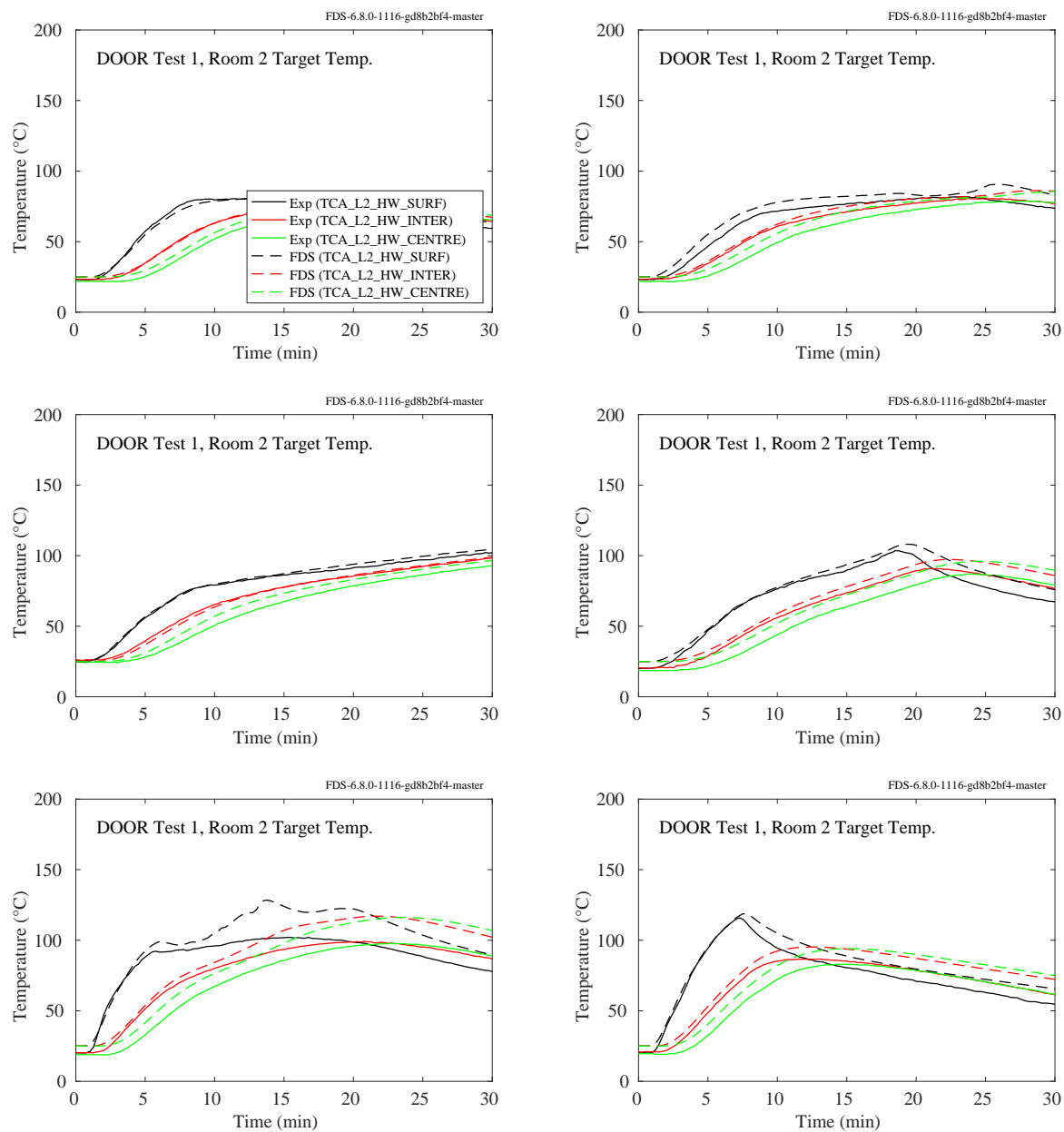


Figure 11.129: PRISME DOOR experiments, cable temperature, Room 2, Cable HW.

11.2.10 Summary of Target Temperature Predictions

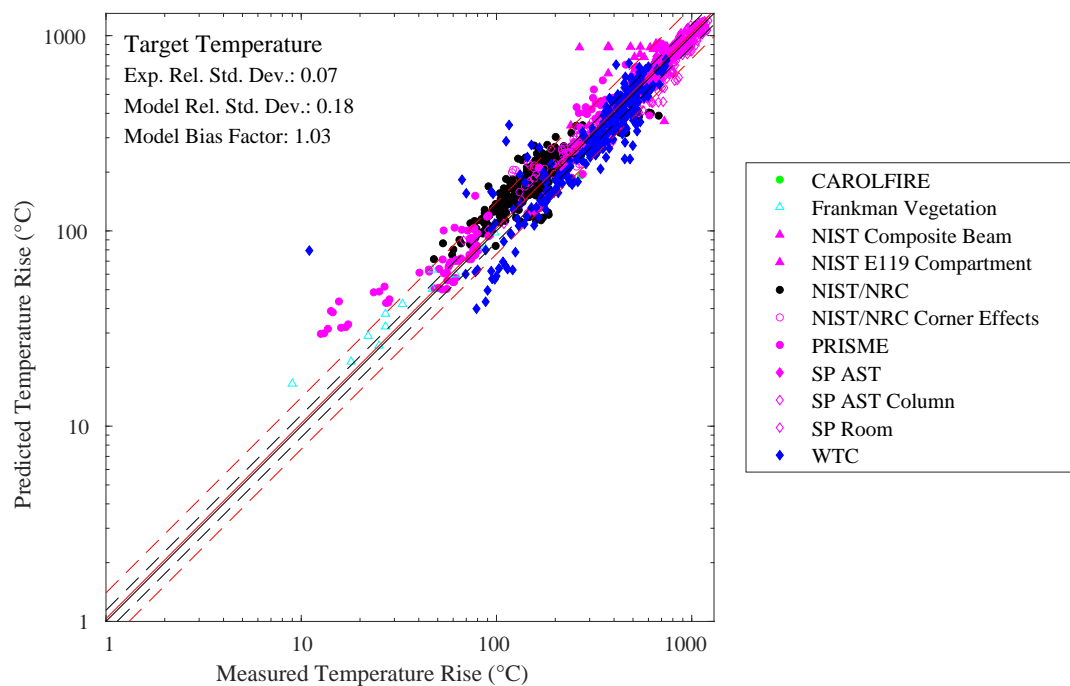


Figure 11.130: Summary of target temperature predictions.

11.2.11 Time to Failure

In addition to comparing the peak temperature predictions and measurements for electrical cables, it is also useful to consider the uncertainty in predicting the time to cable failure. Obviously, the two quantities are related, but from a practical standpoint, it is the time to failure that is of interest in these types of analyses. Figure 11.131 displays results for the CAROLFIRE experiments.

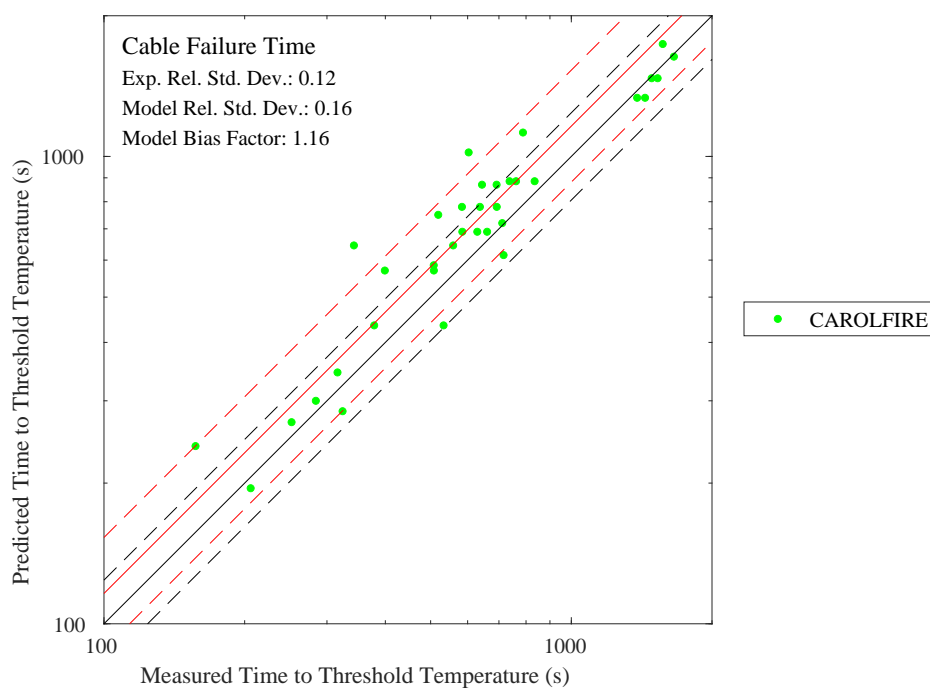


Figure 11.131: Summary of time to failure predictions for electrical cables.

11.3 Liquid Pool Surface Temperature

This section presents predicted liquid pool fire surface temperatures compared with the respective liquid boiling temperatures. Mass loss rate comparisons are shown in Sec. 14.6.

11.3.1 Pool Fires

Figure 11.132 displays the surface temperature of a pan of boiling water. Figure 11.133 displays the surface temperature of 1 m² and 2 m² heptane pool fires. Figure 11.134 displays the surface temperature of various other liquid pool fires.

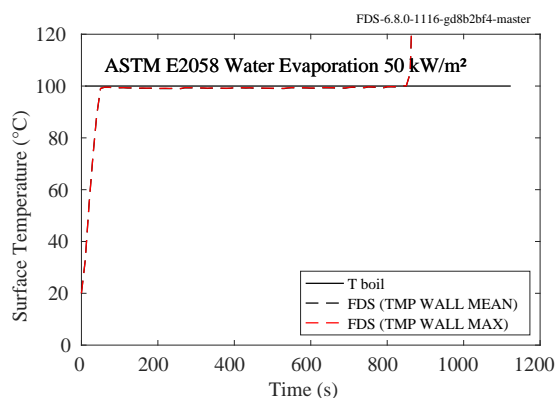


Figure 11.132: ASTM E2058 water evaporation 50 kW/m², surface temperature.

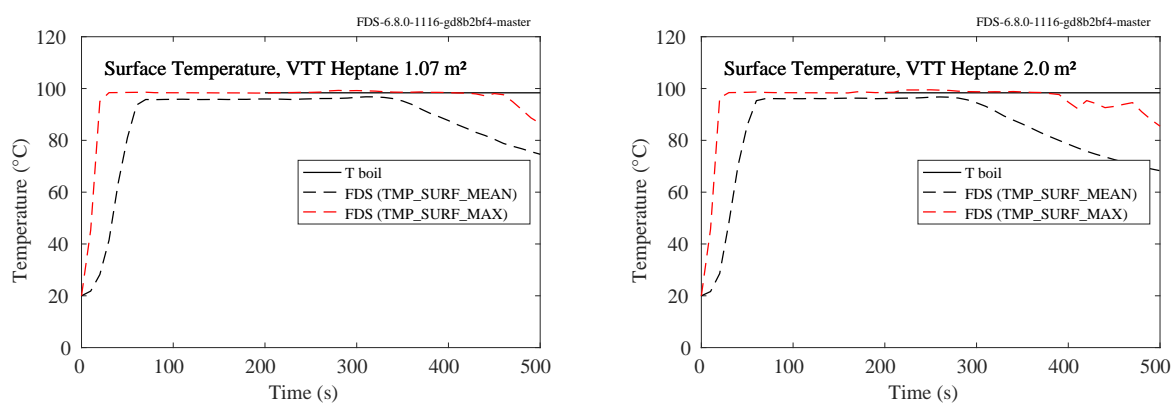


Figure 11.133: VTT heptane pool fire surface temperatures.

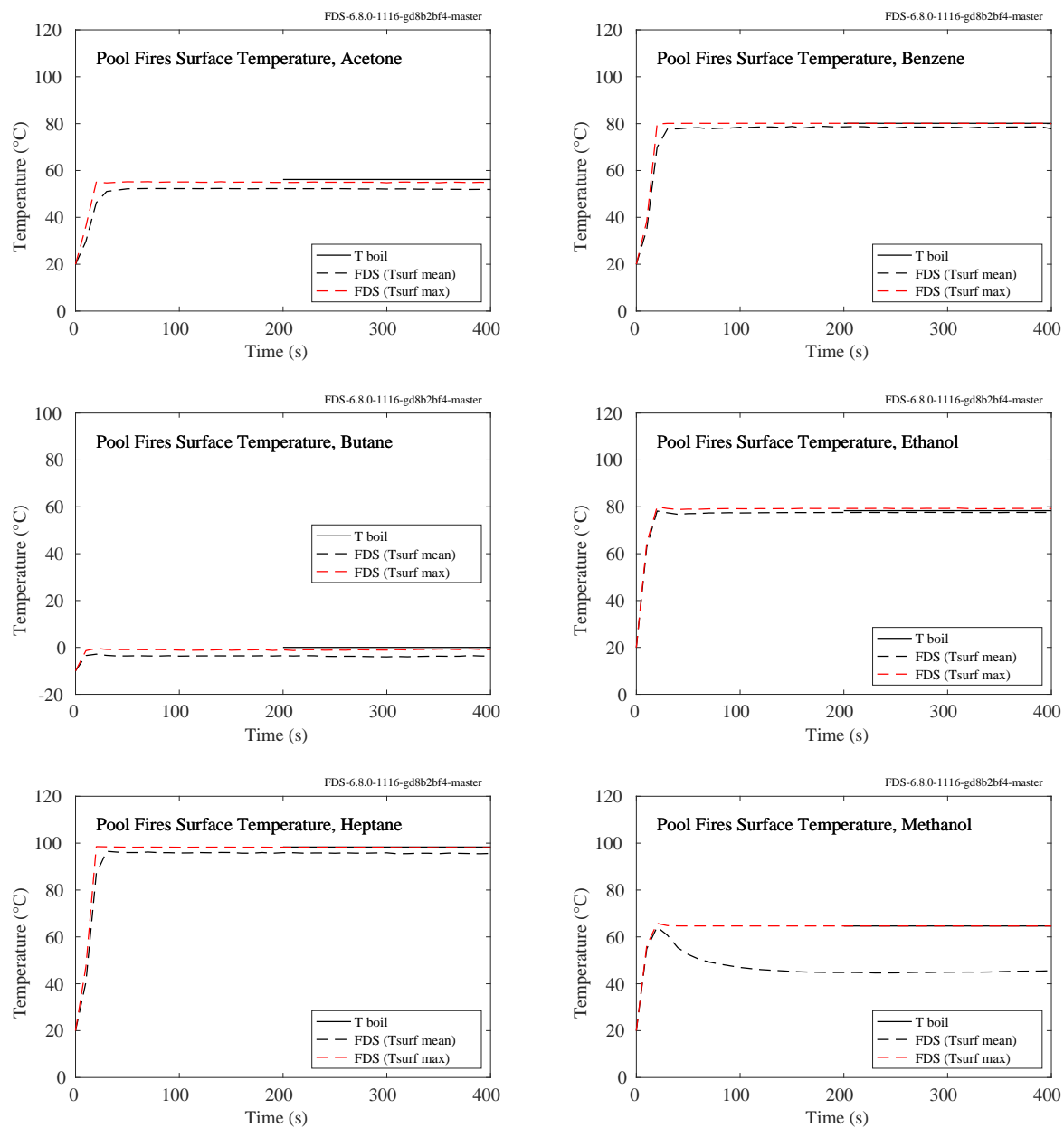


Figure 11.134: Pool fire experiments, surface temperatures.

11.3.2 NIST Pool Fires and Waterloo Methanol

Figure 11.135 displays the mean surface temperature for the 1 m NIST methanol pool fire [364] and the 30 cm Waterloo methanol pool fire [342]. The predicted surface temperatures are compared to the boiling temperature of methanol, 64.7 °C.

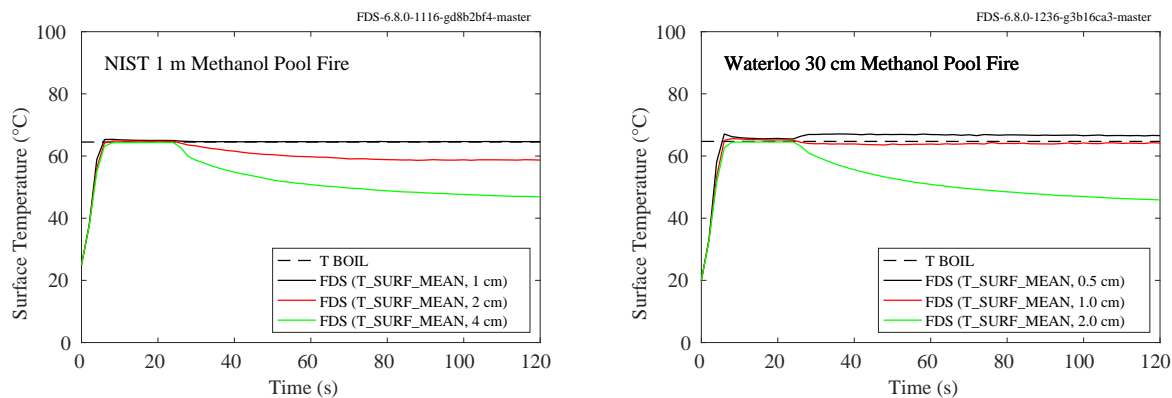


Figure 11.135: NIST 1 m (left) and Waterloo 30 cm (right) methanol pool fires, surface temperature.

11.3.3 Summary of Liquid Pool Surface Temperature Predictions

Figure 11.136 summarizes the temperature predictions for liquid pool surface temperatures under high heat flux conditions such as pool fires.

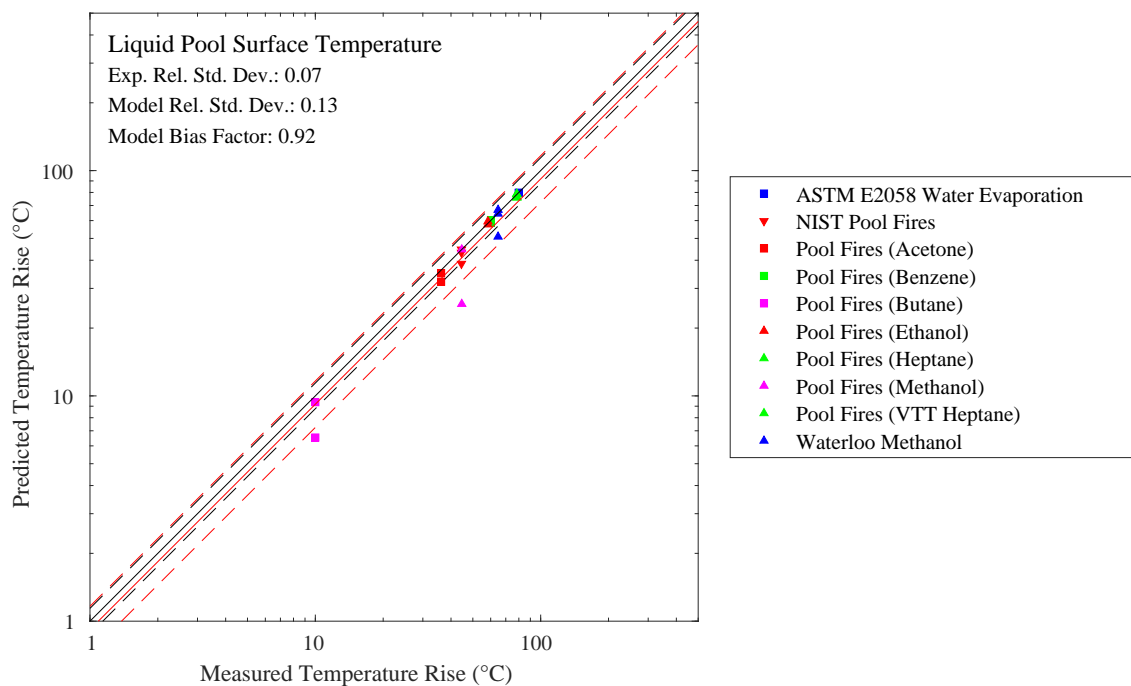


Figure 11.136: Summary of liquid pool surface temperature predictions.

Chapter 12

Heat Flux

This chapter contains a wide variety of heat flux measurements, ranging from less than a kW/m^2 from very small methane gas burners up to about 150 kW/m^2 in full-scale compartment fires. The results are broken up into two broad categories—heat flux to compartment walls, ceiling, and floor, and heat flux to “targets”. A target is any object of interest in a fire simulation, like a steel beam or electrical cable.

There are also sections that look at special cases, like the heat flux measured at a liquid fuel surface, attenuation of thermal radiation by water sprays, and convective heat flux.

12.1 Heat Flux to Walls, Ceiling, and Floor

12.1.1 FAA Cargo Compartments

Measurements of heat flux and surface temperature were made at two ceiling locations (denoted A and B in Fig. 7.10). The heat flux measurements are shown below.

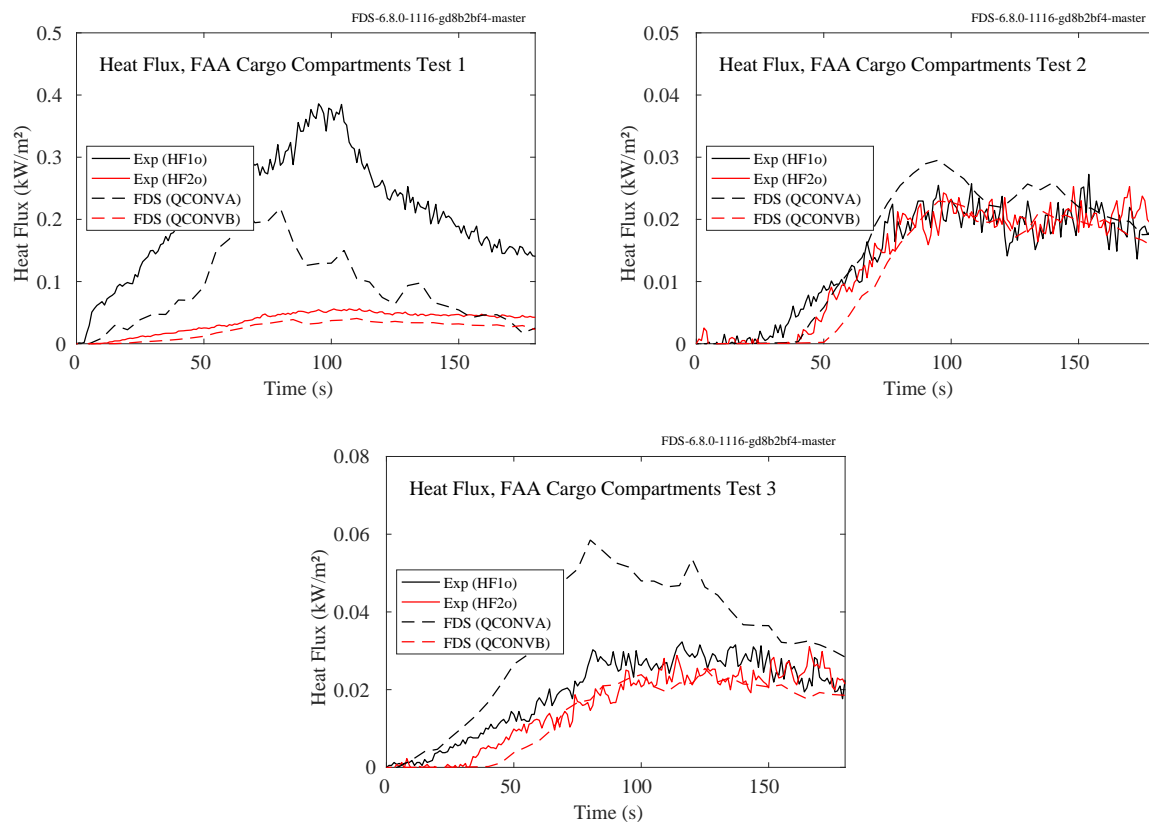


Figure 12.1: FAA Cargo Compartment experiments, heat flux to ceiling.

12.1.2 FM Parallel Panel Experiments

Predicted and measured vertical heat flux profiles for three propane and three propylene fires (30 kW, 60 kW, and 100 kW) sandwiched between two 2.4 m high, 0.6 m wide panels are presented below.

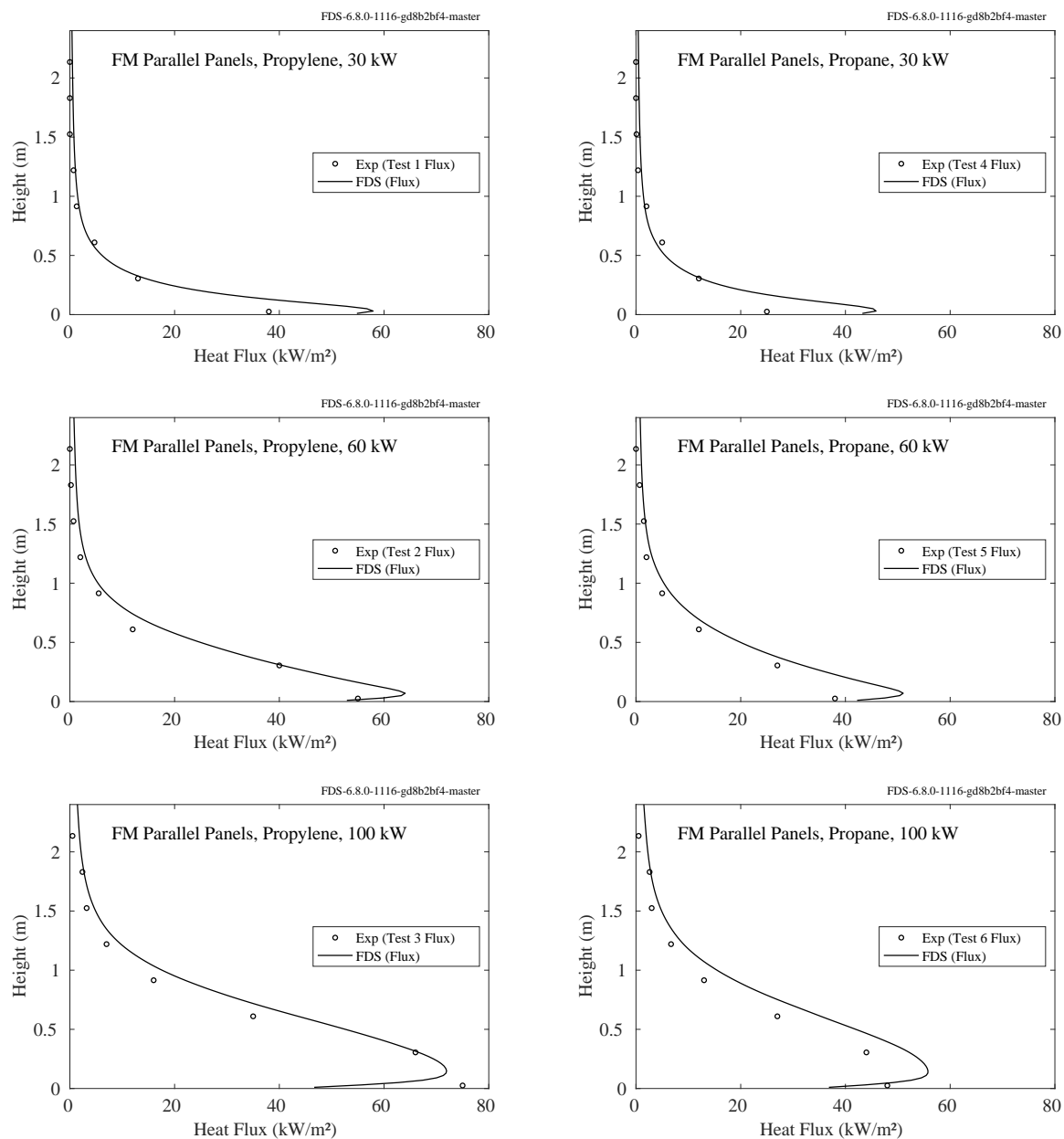


Figure 12.2: FM Parallel Panel experiments, side wall heat flux.

12.1.3 JH/FRA Experiments

Predicted and measured heat fluxes from 6 compartment fires are shown on the following pages. The heat fluxes measured in the quarter and half scale compartments are generally under-predicted by FDS; however, there is better agreement in heat flux predictions in the full-scale. However, the heat fluxes in the continuous flaming region near the burner were underpredicted by FDS at all scales. Note that all the FDS simulations were performed with a grid resolution such that $D^*/\delta x$ was 10-15 at the post-flashover HRR inside the compartment.

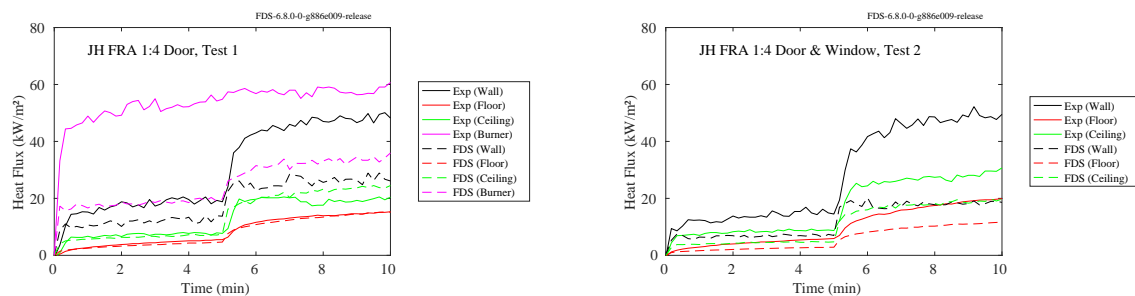


Figure 12.3: JH/FRA room corner experiments, heat flux to the ceiling, wall, and floor 1:4 scale inert lining configurations, Tests 1-2.

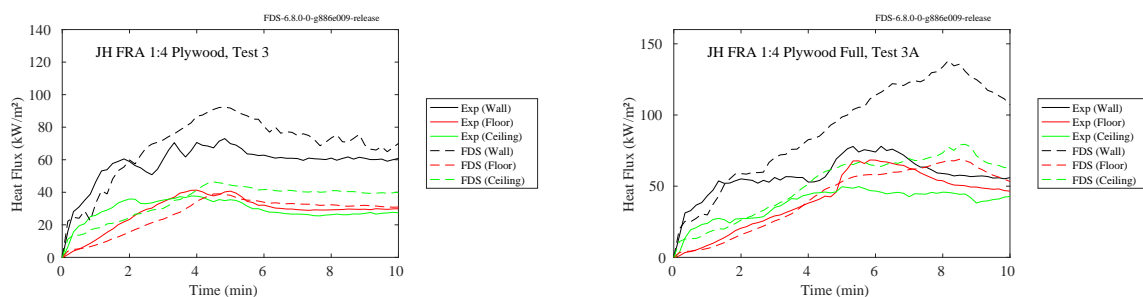


Figure 12.4: JH/FRA room corner experiments, heat flux to the ceiling, wall, and floor, Tests 3 and 3A

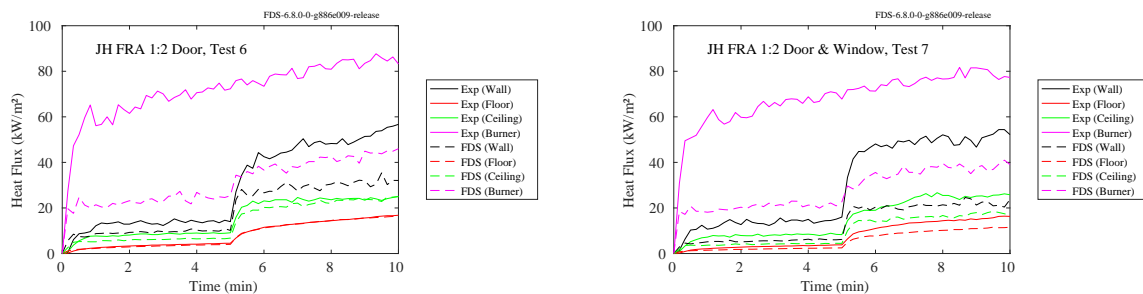


Figure 12.5: JH/FRA room corner experiments, heat flux to the ceiling, wall, and floor, Tests 6-7

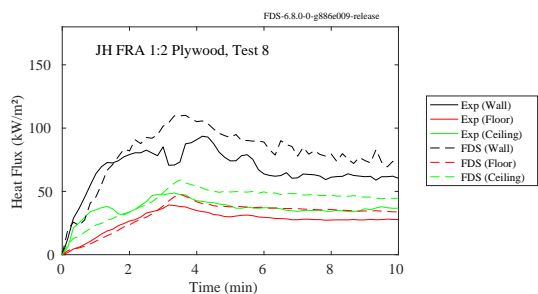


Figure 12.6: JH/FRA room corner experiments, heat flux to the ceiling, wall, and floor Test, 8

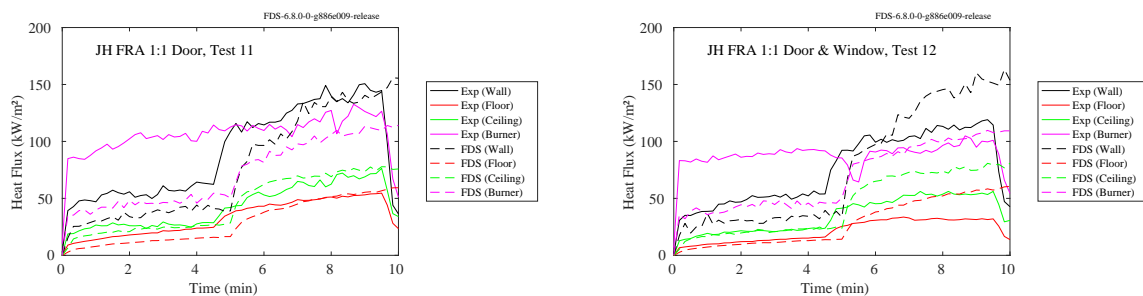


Figure 12.7: JH/FRA room corner experiments, heat flux to the ceiling, wall, and floor, Tests 11-12

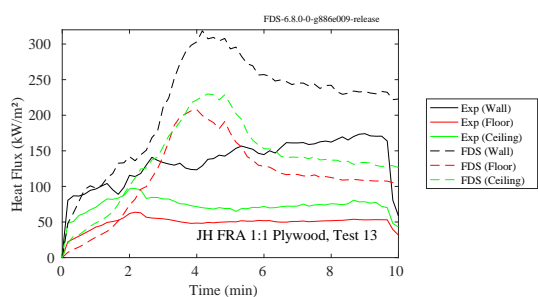


Figure 12.8: JH/FRA room corner experiments, heat flux to the ceiling, wall, and floor, Test 13

12.1.4 FM Vertical Wall Flame Experiments

Figure 12.9 displays the measured and predicted outward flame radiance at heights of 66, 330, 594, and 990 mm above the base of the burner, for a range of burning rates. The radiance is defined as the radiant flux per unit solid angle in the outward normal direction. The radiance of an ideal black body at temperature T is $\sigma T^4/\pi$.

Figure 12.10 displays the measured and predicted heat flux from propylene, ethane, ethylene, and methane wall fires. The fuel flow rates for propylene are 12.68, 17.05, and 22.37 g/m²/s.

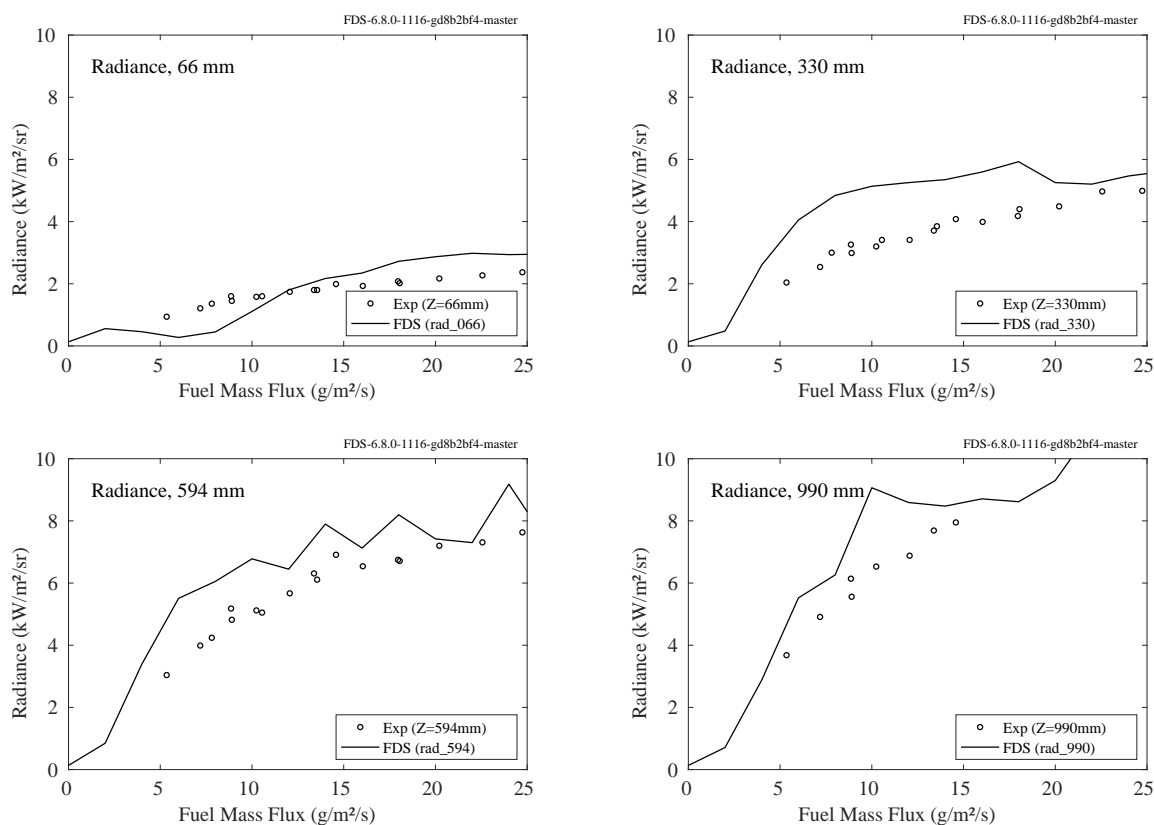


Figure 12.9: Flame radiance as a function of fuel flow rate at heights of 66, 330, 594, and 990 mm.

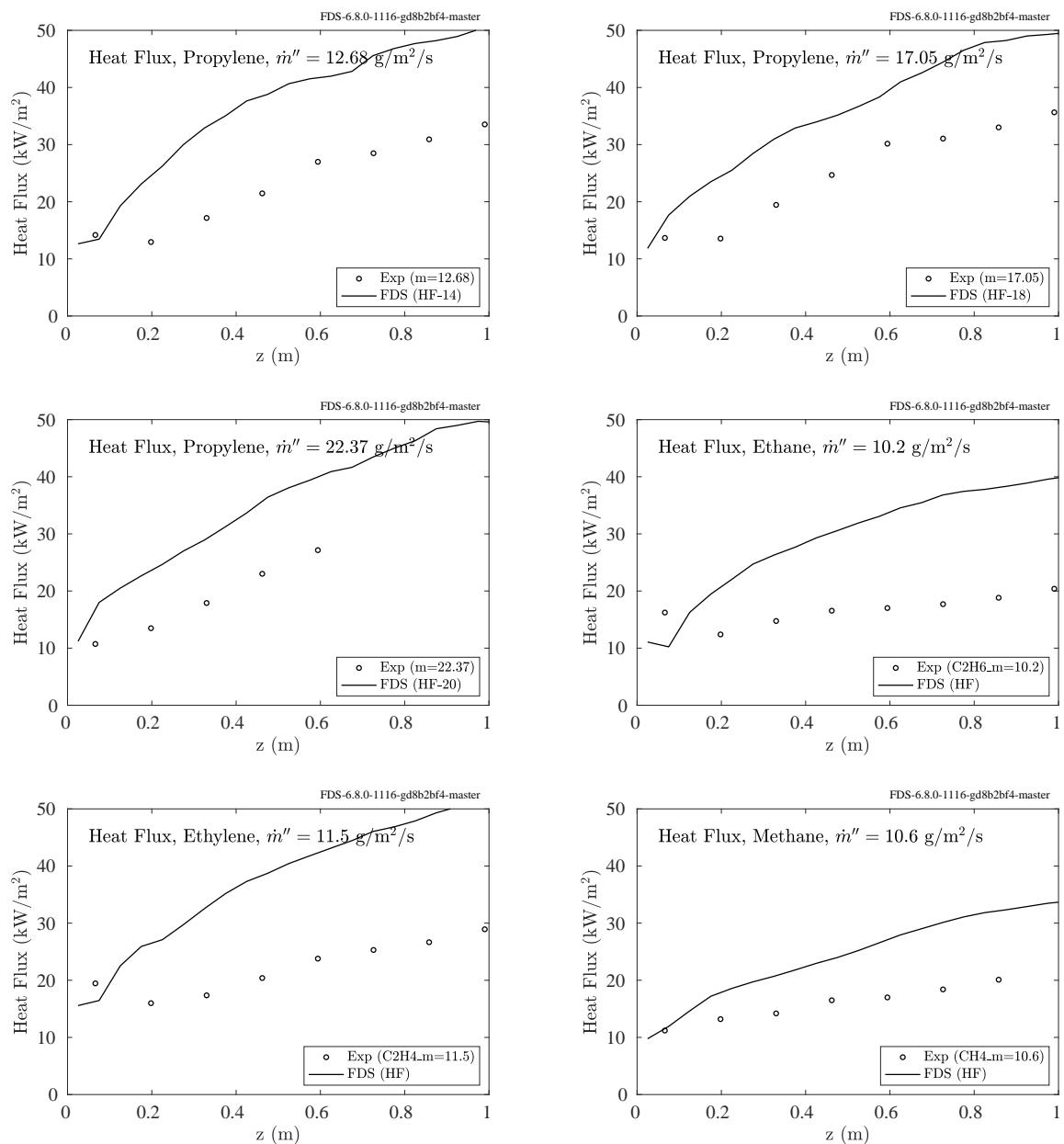


Figure 12.10: Vertical profiles of heat flux to the burner surface for fuel flow rates of 12.68, 17.05, and 22.37 g/m²/s.

12.1.5 NIST E119 Compartment

Heat flux gauges (Gardon, Model 64-20-18) were placed at three locations in the compartment, in water-cooled steel pipes of 25 mm inside diameter. Results are shown in Fig. 12.11. Gauge locations are shown in Fig. 3.27.

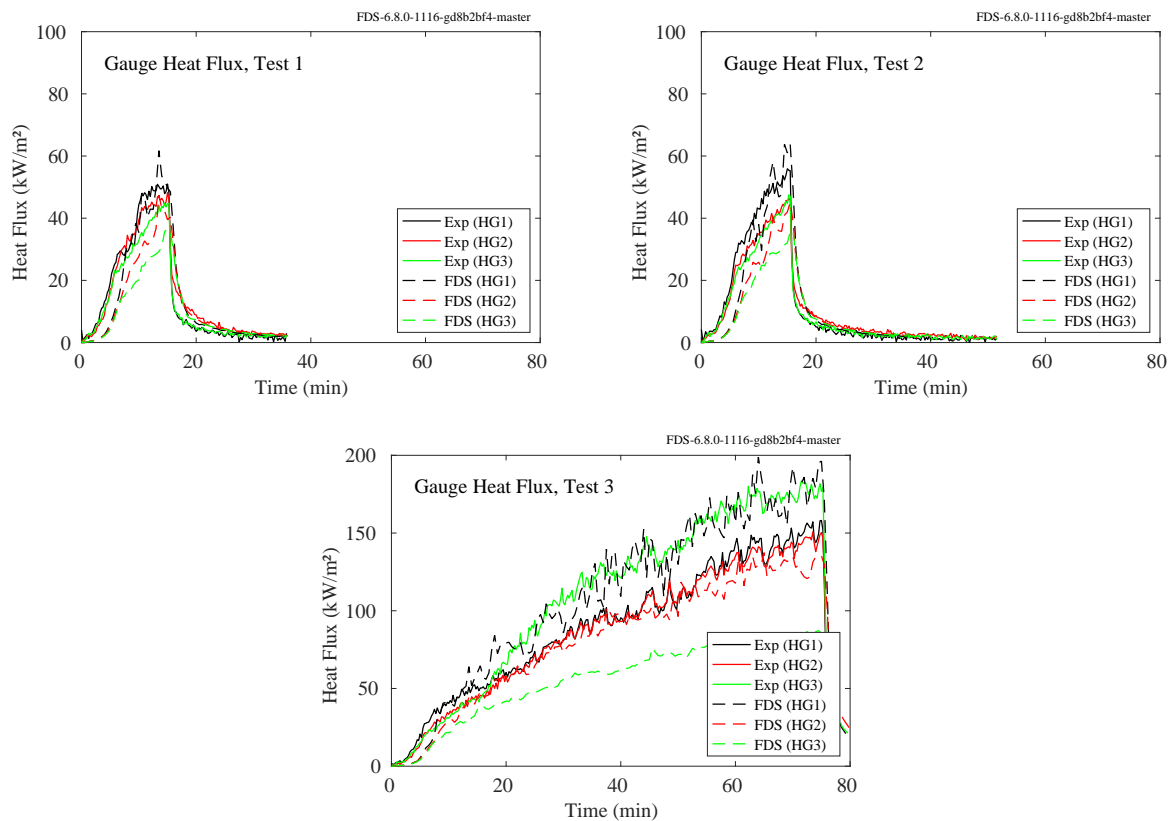


Figure 12.11: NIST E119 Compartment, wall heat fluxes.

12.1.6 NIST/NRC Experiments

Heat flux gauges and thermocouples were positioned at various locations on the walls, floor, and ceiling of the compartment. The locations are given in Table 11.1. The heat flux gauges were not water cooled; thus, they measured the *net* rather than the *gauge* heat flux. However, the net heat flux is a function of the temperature of the heat flux gauge itself, which is not something that is modeled. To better compare model and measurement, the measured net heat flux is converted into a gauge heat flux using the following formula:

$$\dot{q}_{\text{gauge}}'' = \dot{q}_{\text{net}}'' + \sigma \left(T_{\text{gauge}}^4 - T_{\infty}^4 \right) + h \left(T_{\text{gauge}} - T_{\infty} \right) \quad \text{kW/m}^2 \quad (12.1)$$

where $\sigma = 5.67 \times 10^{-11} \text{ kW/m}^2/\text{K}^4$ and $h = 0.005 \text{ kW/m}^2/\text{K}$.

Also, over the course of 15 experiments, numerous heat flux gauges failed, most often due to loss of contact with the wall or faulty thermocouples. All of the measurements from Test 13 and 16 were found to be flawed.

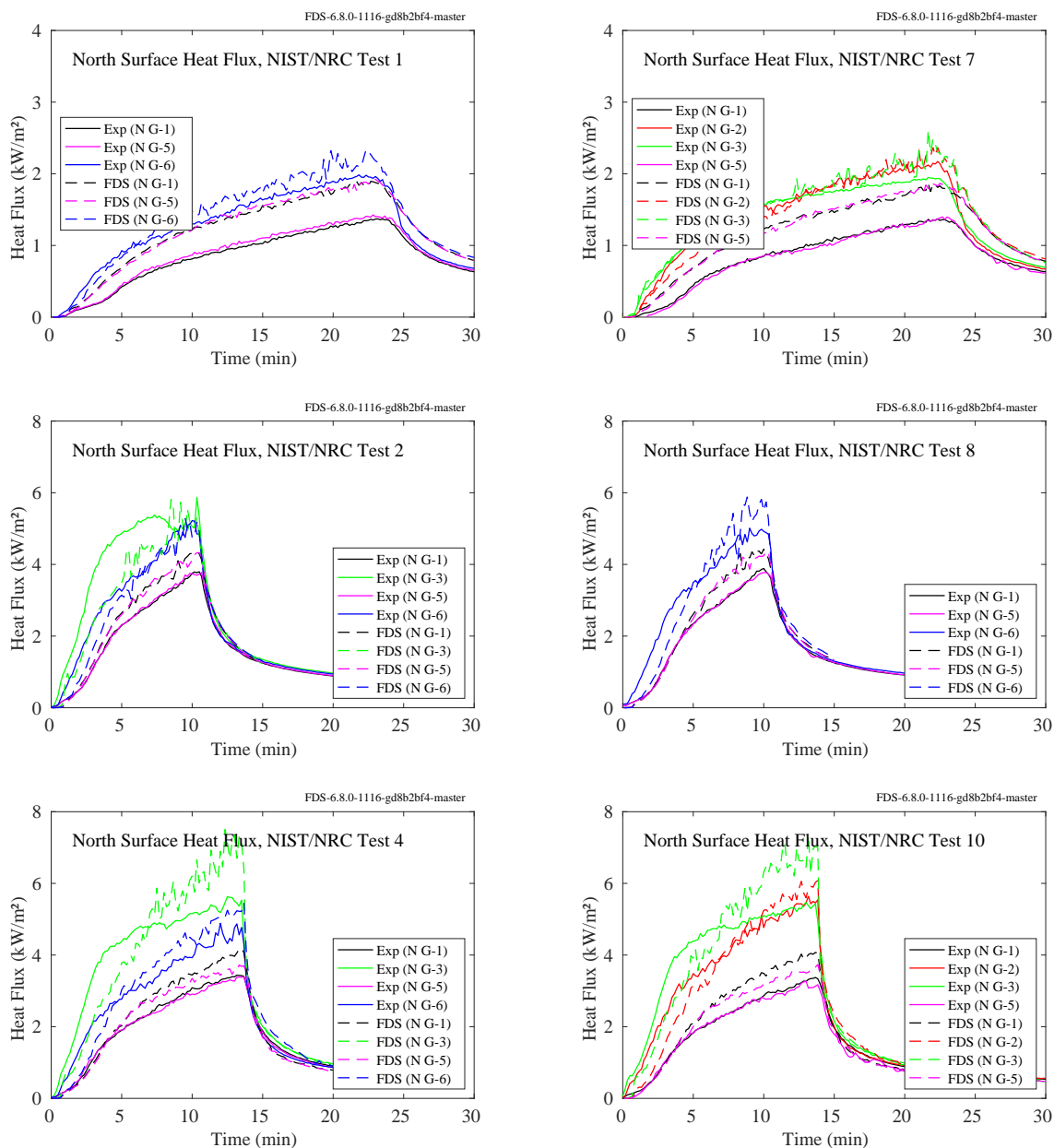


Figure 12.12: NIST/NRC experiments, heat flux to north wall, Tests 1, 2, 4, 7, 8, 10.

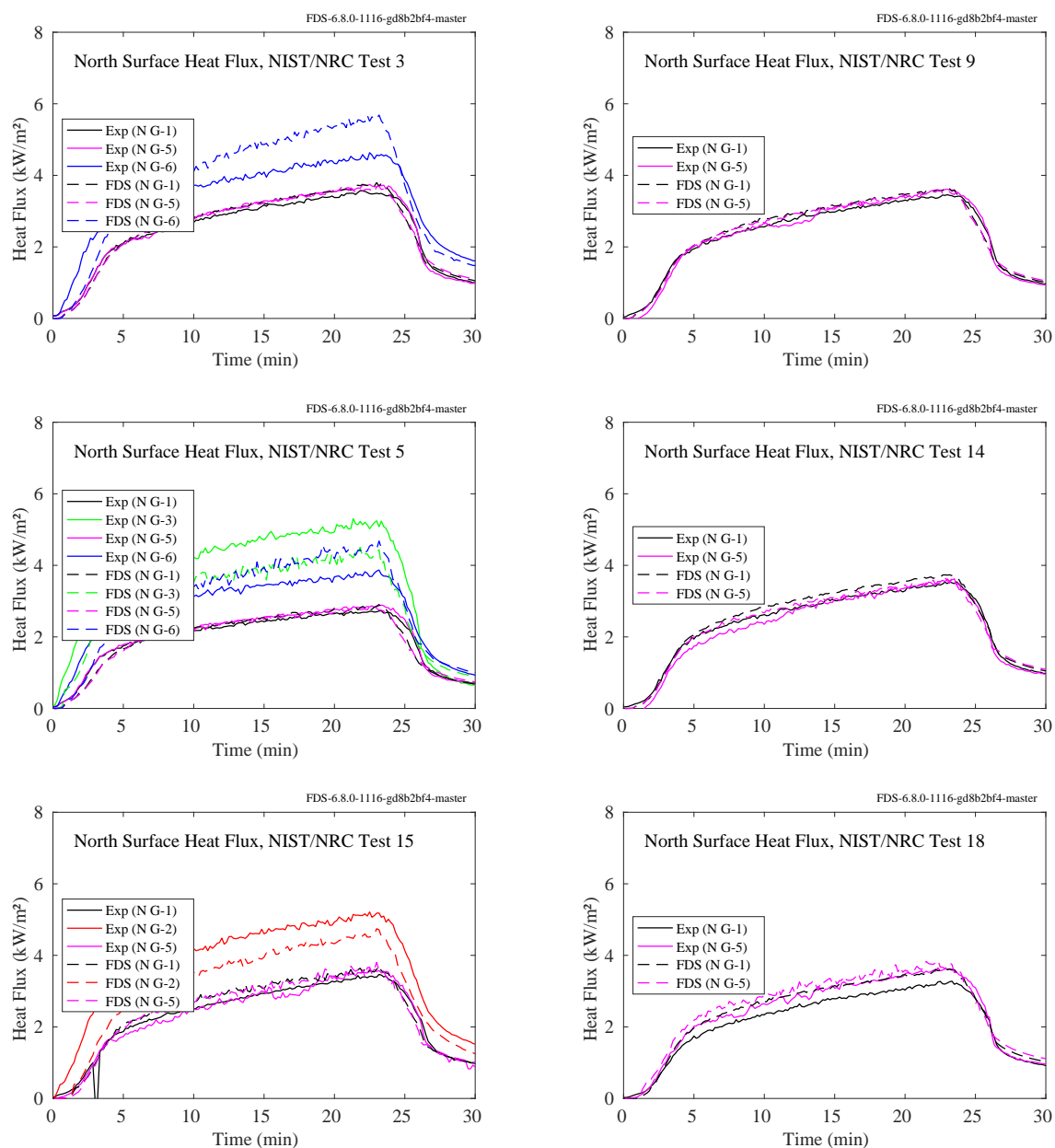


Figure 12.13: NIST/NRC experiments, heat flux to north wall, Tests 3, 5, 9, 14, 15, 18.

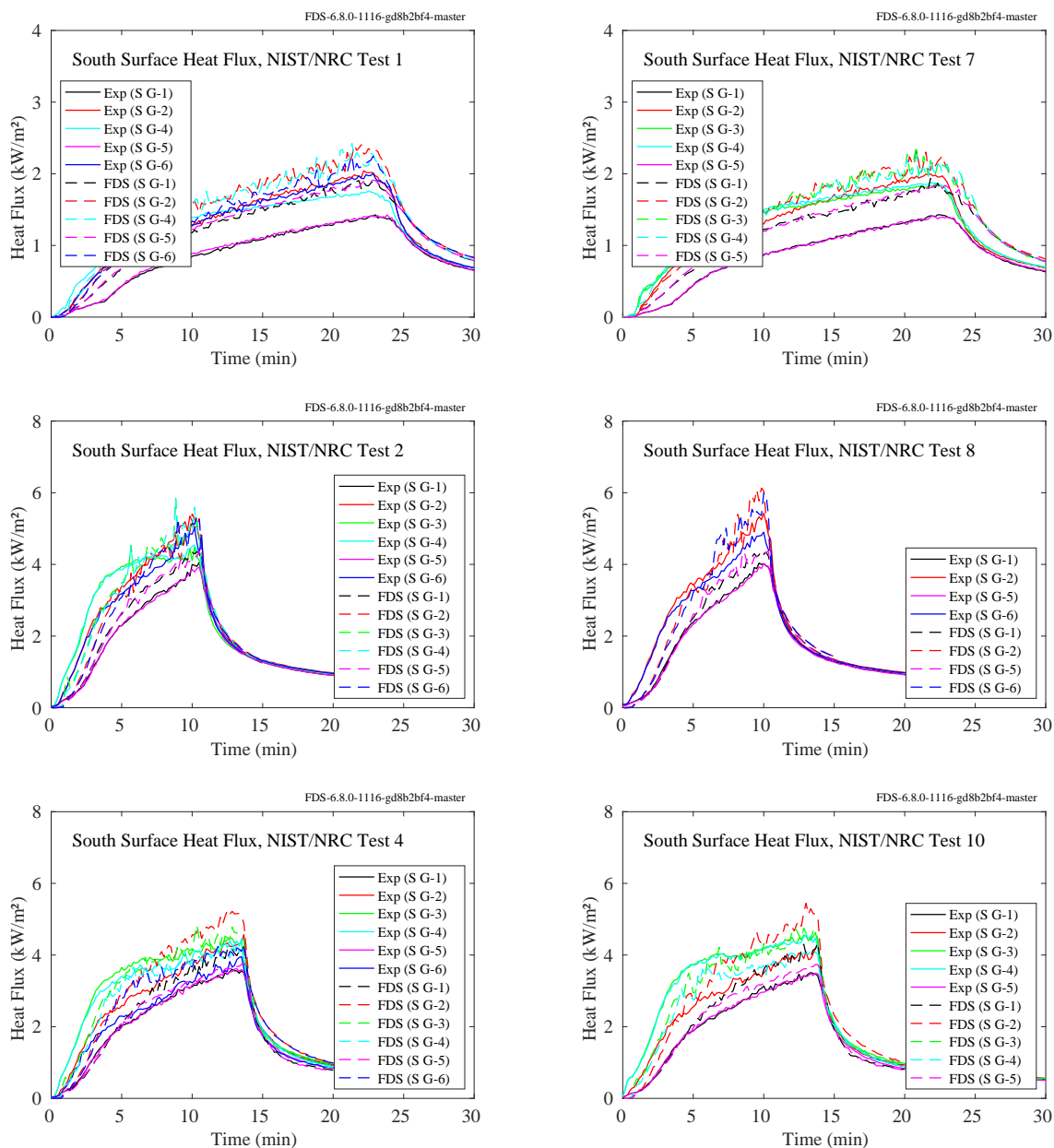


Figure 12.14: NIST/NRC experiments, heat flux to south wall, Tests 1, 2, 4, 7, 8, 10.

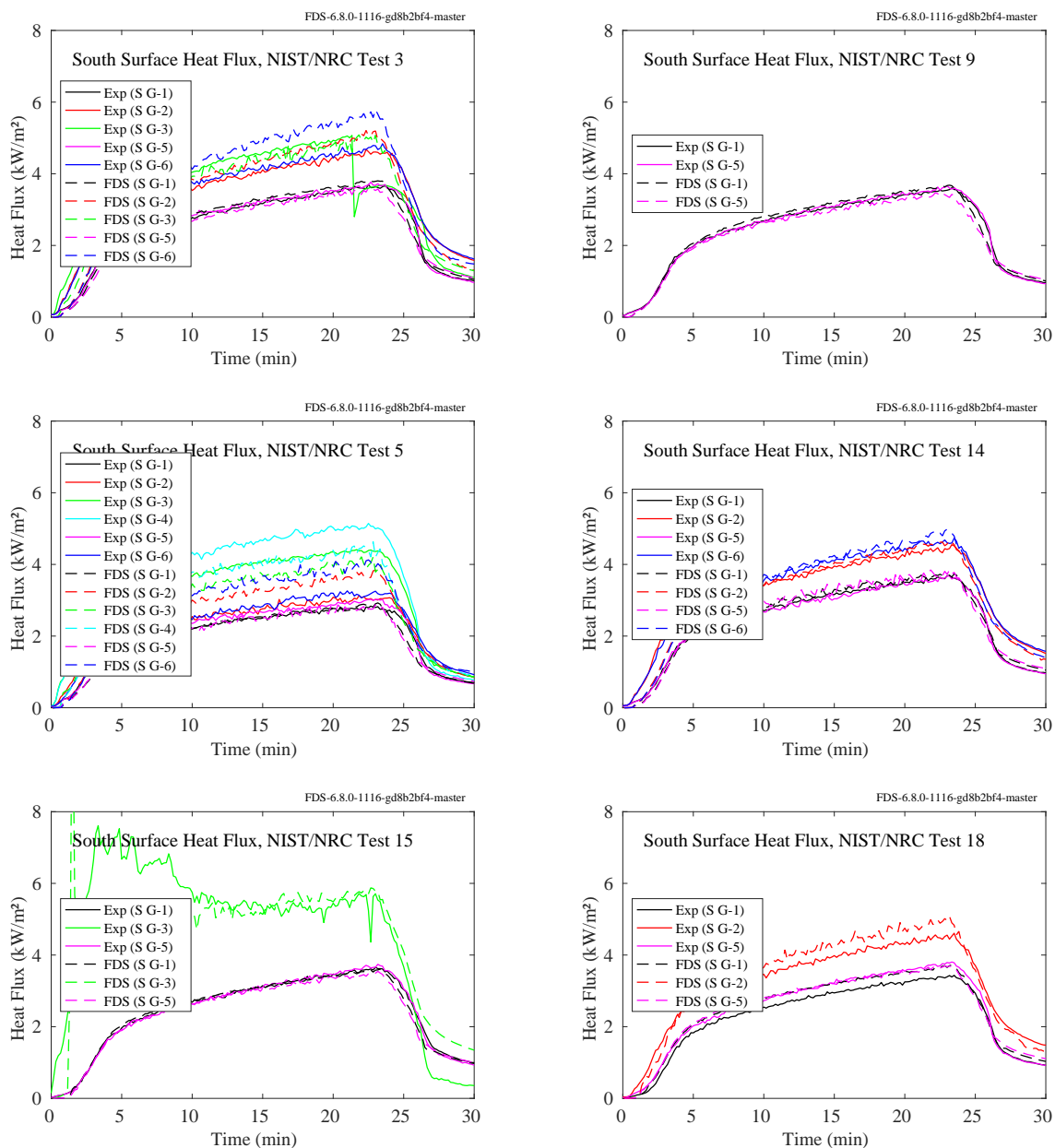


Figure 12.15: NIST/NRC experiments, heat flux to south wall, Tests 3, 5, 9, 14, 15, 18.

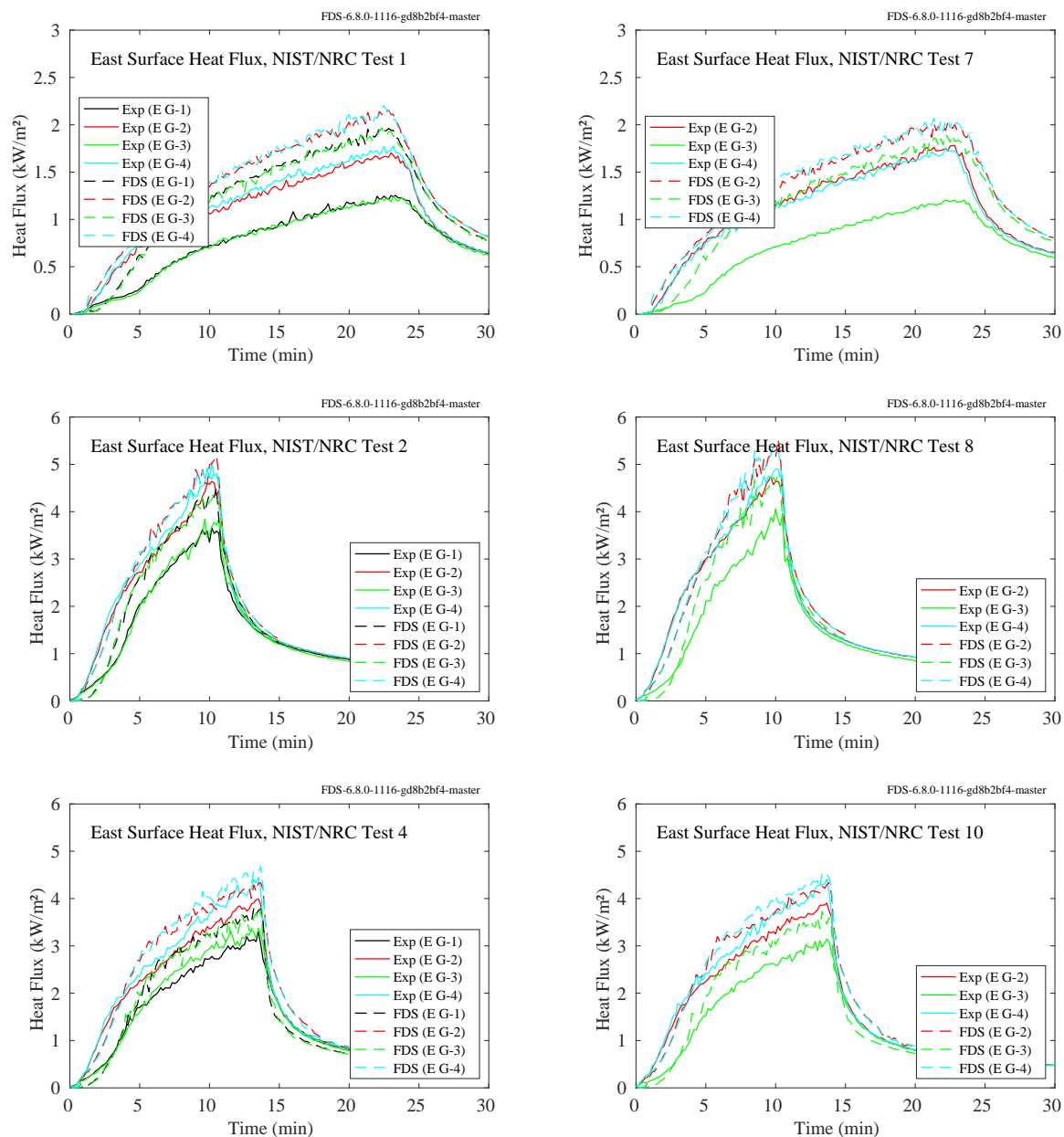


Figure 12.16: NIST/NRC experiments, heat flux to east wall, Tests 1, 2, 4, 7, 8, 10.

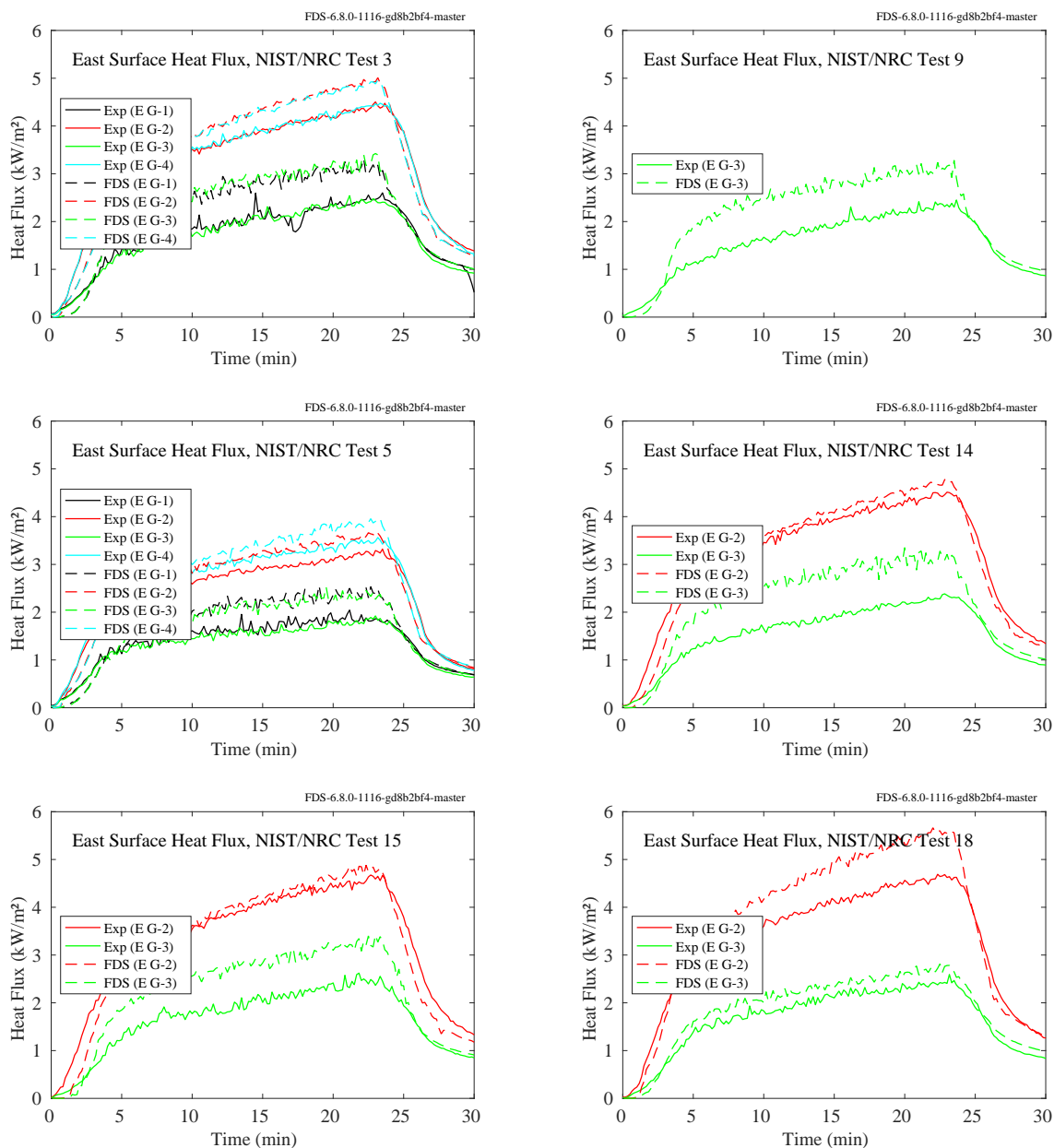


Figure 12.17: NIST/NRC experiments, heat flux to east wall, Tests 3, 5, 9, 14, 15, 18.

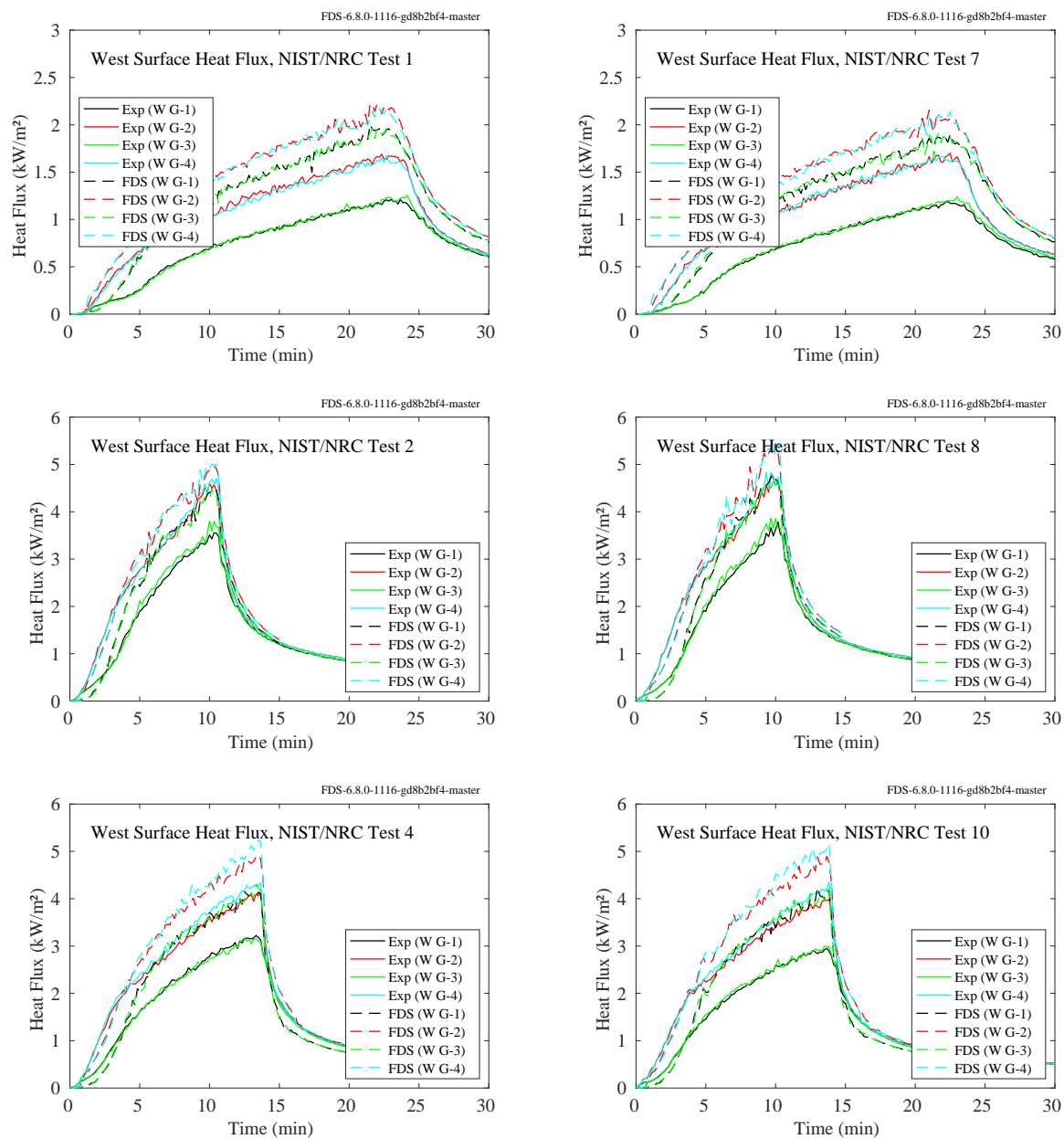


Figure 12.18: NIST/NRC experiments, heat flux to west wall, Tests 1, 2, 4, 7, 8, 10.

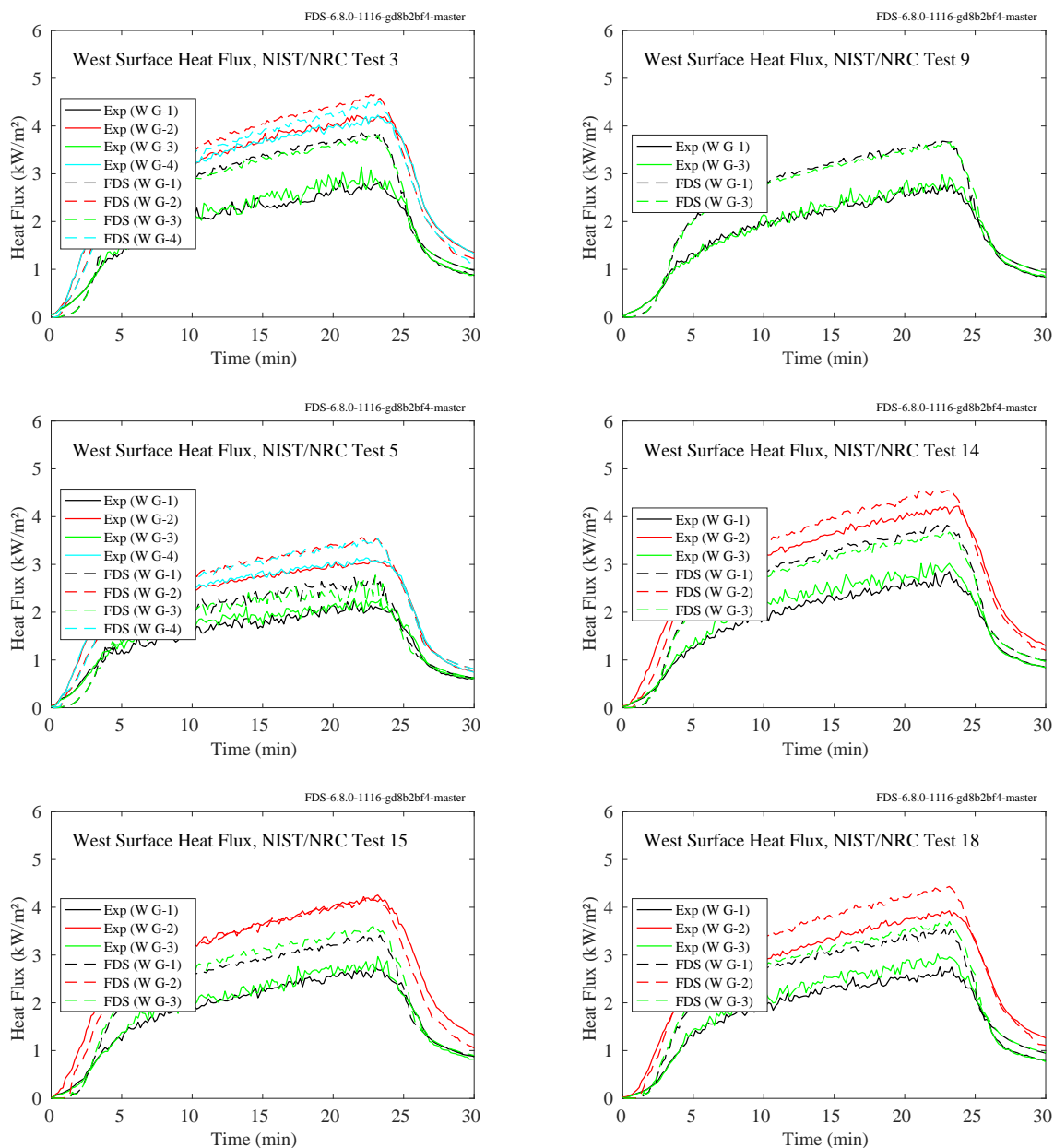


Figure 12.19: NIST/NRC experiments, heat flux to west wall, Tests 3, 5, 9, 14, 15, 18.

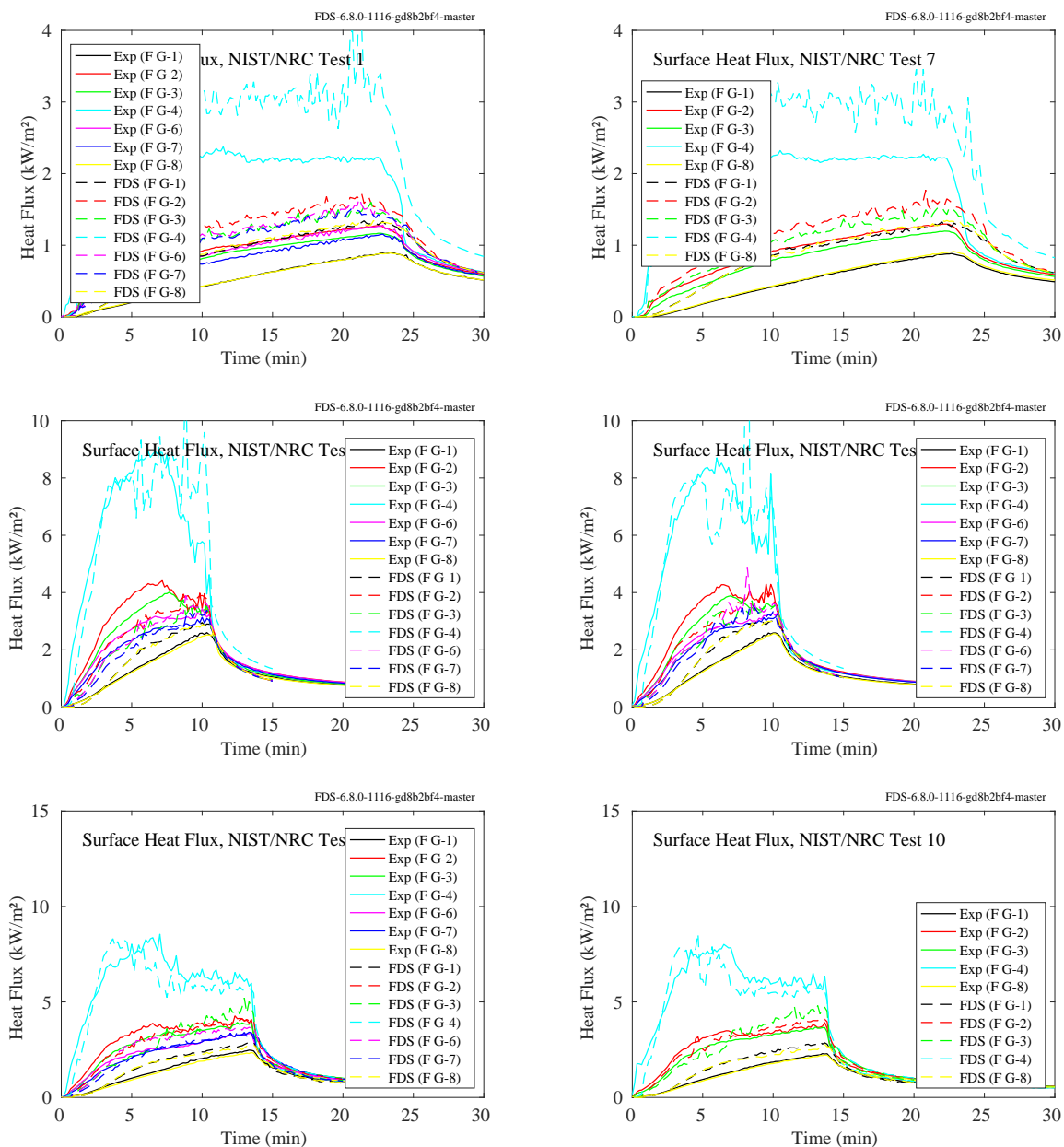


Figure 12.20: NIST/NRC experiments, heat flux to the floor, Tests 1, 2, 4, 7, 8, 10.

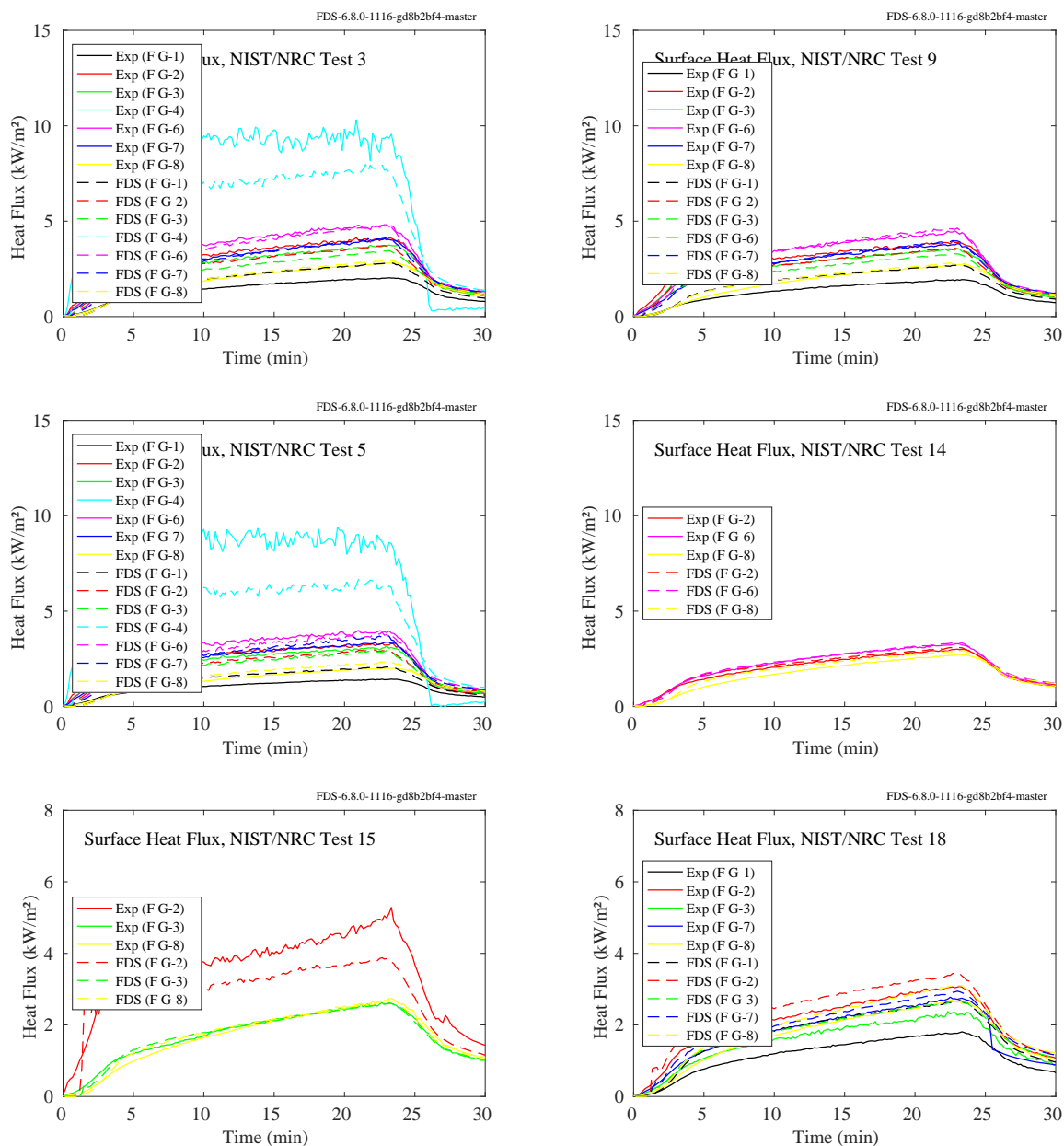


Figure 12.21: NIST/NRC experiments, heat flux to the floor, Tests 3, 5, 9, 14, 15, 18.

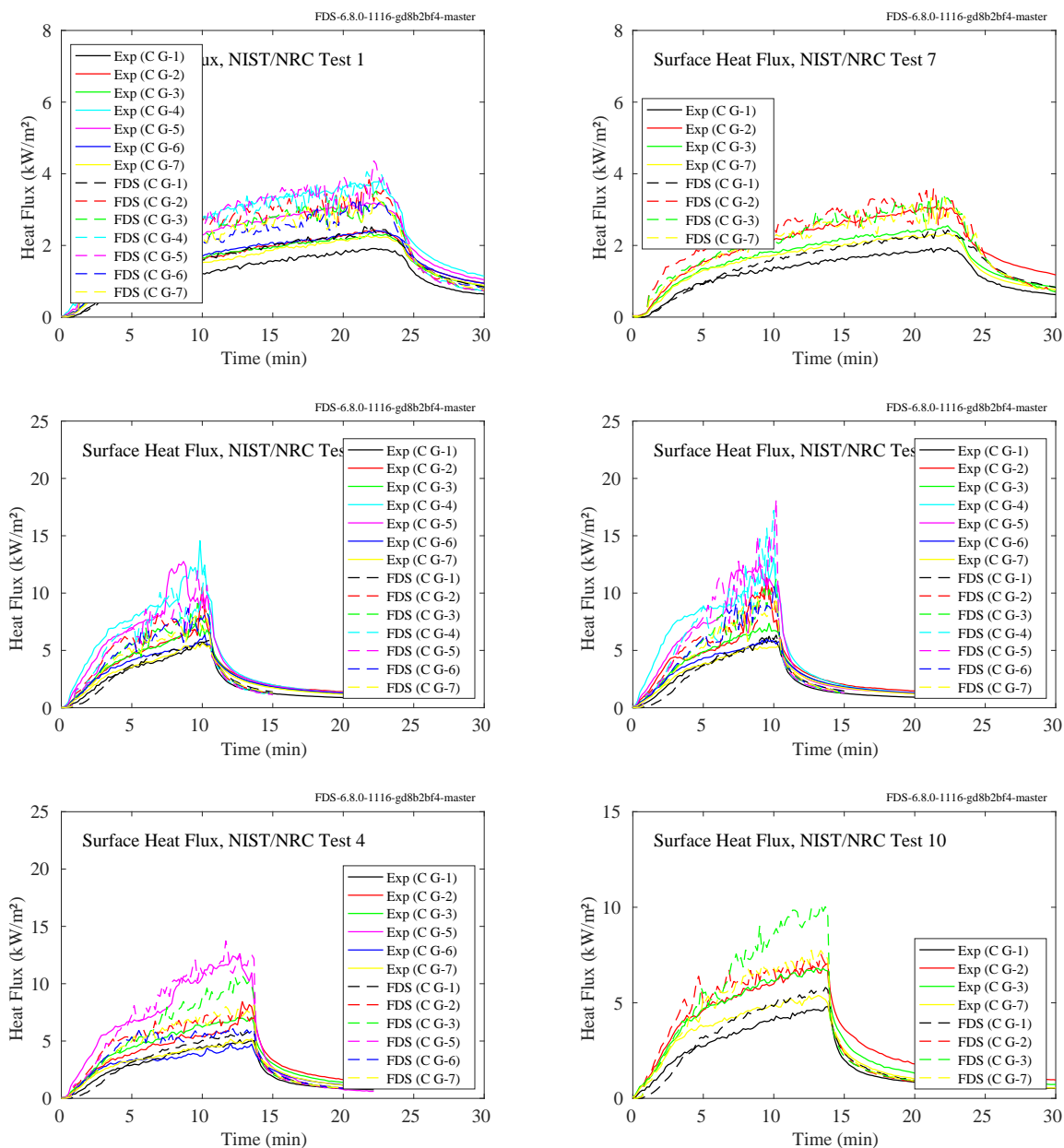


Figure 12.22: NIST/NRC experiments, heat flux to the ceiling, Tests 1, 2, 4, 7, 8, 10.

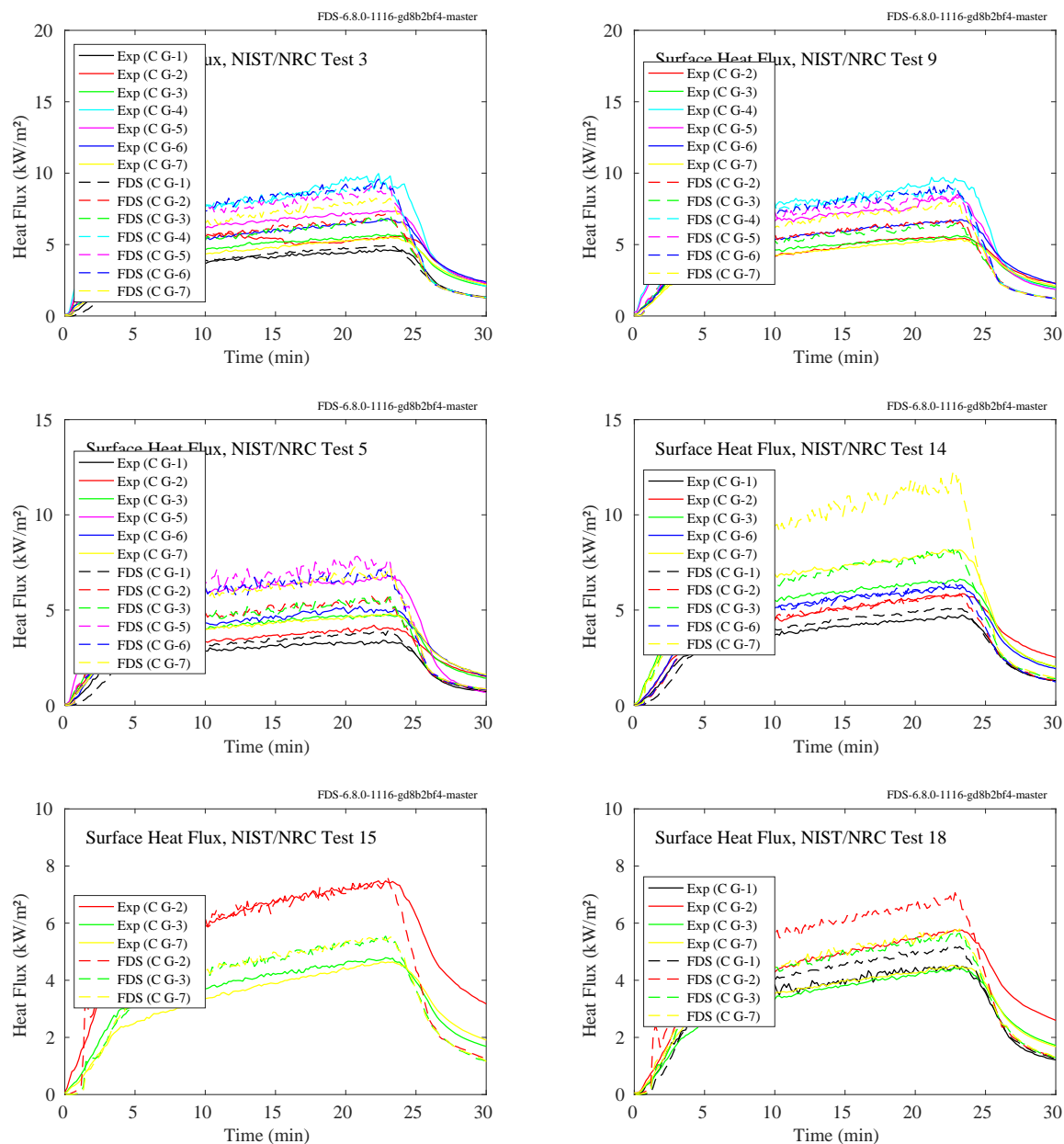


Figure 12.23: NIST/NRC experiments, heat flux to the ceiling, Tests 3, 5, 9, 14, 15, 18.

12.1.7 NIST/NRC Parallel Panel Experiments

The left hand plot of Fig. 12.24 displays predicted and measured vertical heat flux profiles from a 60 kW propane sand burner sandwiched between two 2.4 m high, 0.6 m wide panels separated by 0.3 m. The times of 20 s, 40 s, 60 s, and 80 s correspond to burner heat release rates of 22 kW, 50 kW, 59 kW, and 63 kW. The right hand plot displays contours of heat flux measurements made between -25 cm and 25 cm in the horizontal direction and between 20 cm and 100 cm in the vertical.

The bottom plot displays profiles for an experiment where the panels are lined with PMMA. The profiles are taken at various heat release rates during the growth of the fire, which peaks at approximately 3 MW.

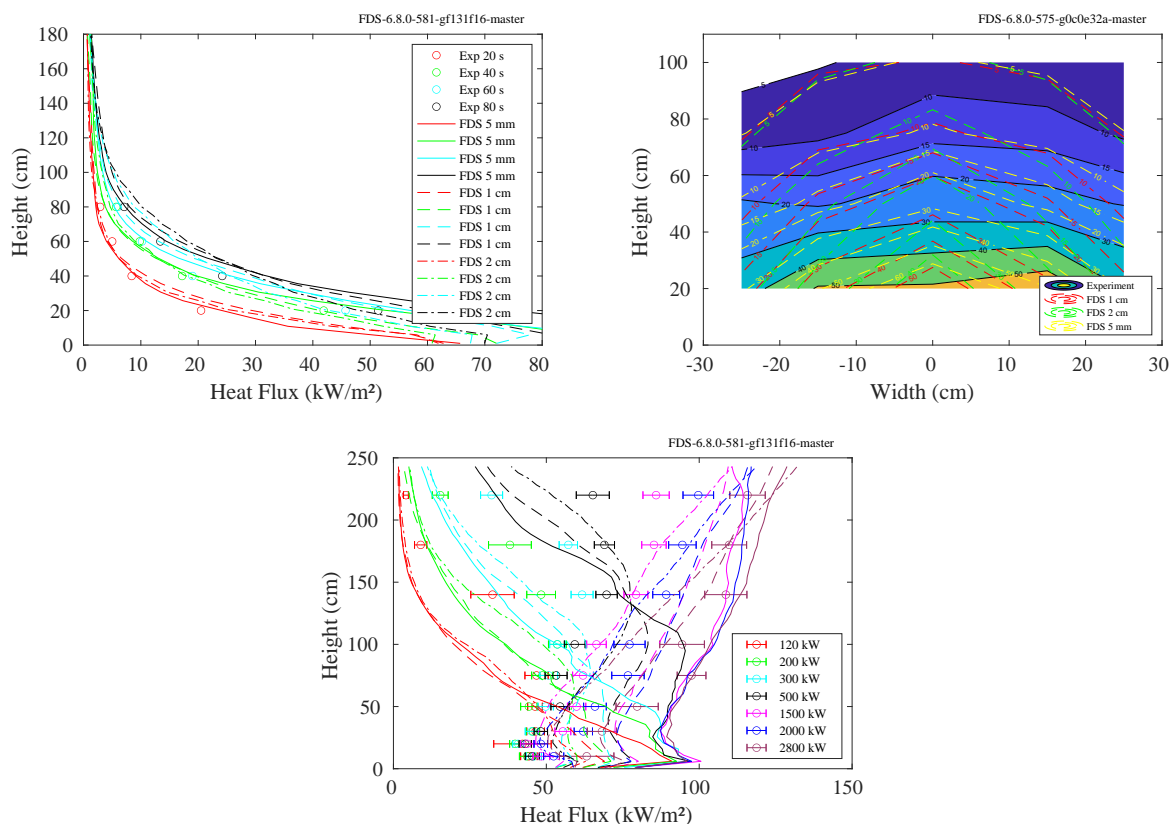


Figure 12.24: NIST/NRC Parallel Panel experiments. Left, heat flux profile from 60 kW propane burner. Right, heat flux profiles at different stages where the panels are lined with PMMA.

12.1.8 NIST Reduced-Scale Enclosure (RSE) Experiments, 2007

Heat flux measurements were made on the floor in the front and rear of the compartment. The compartment was 0.95 m wide by 1.42 m deep by 0.98 m tall with a door 0.48 m wide by 0.81 m tall centered on one of the short walls. Details of the experiments are found in Sec. 3.53.2.

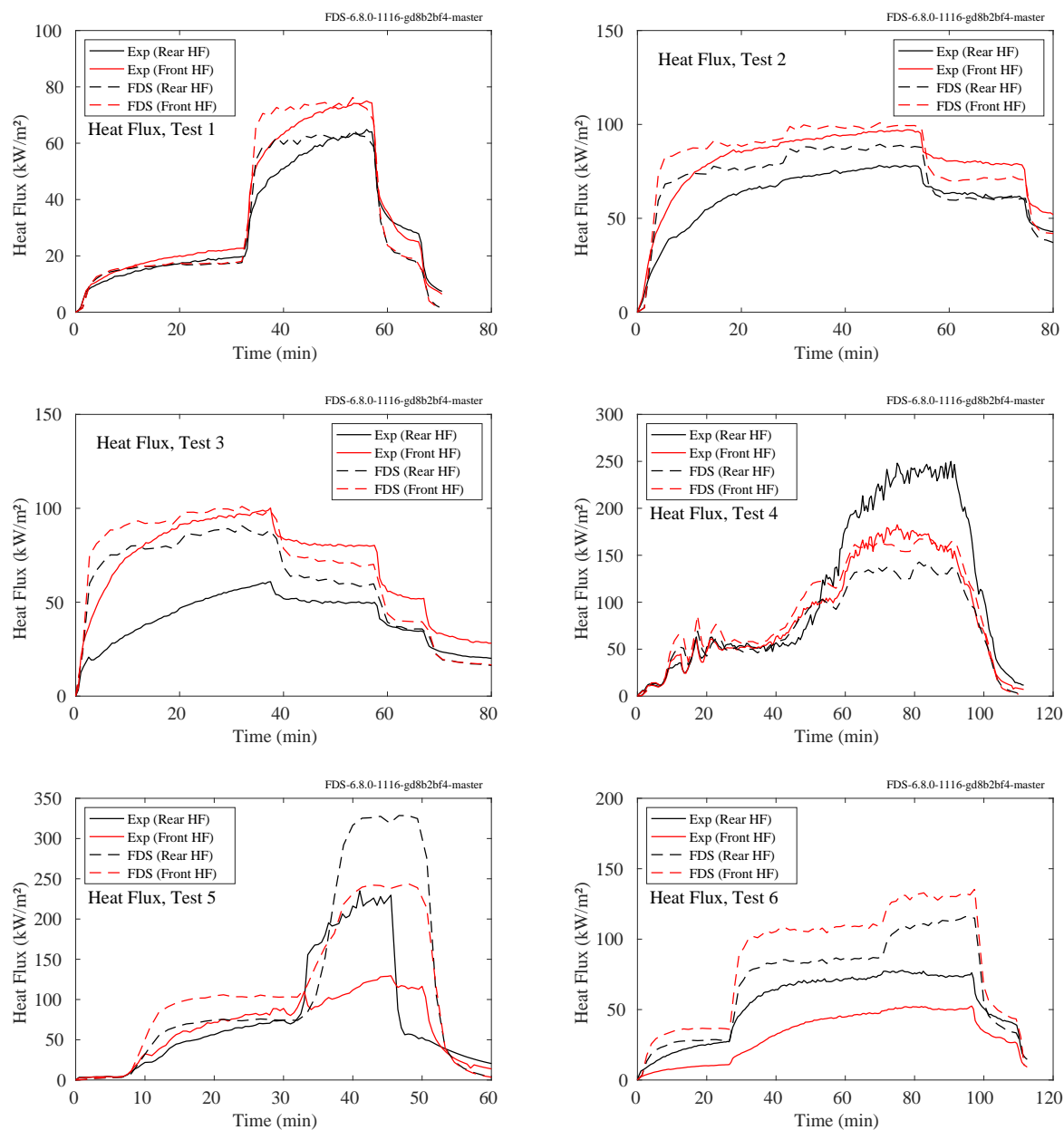


Figure 12.25: Summary of heat flux measurements Test 1-6, NIST RSE 2007.

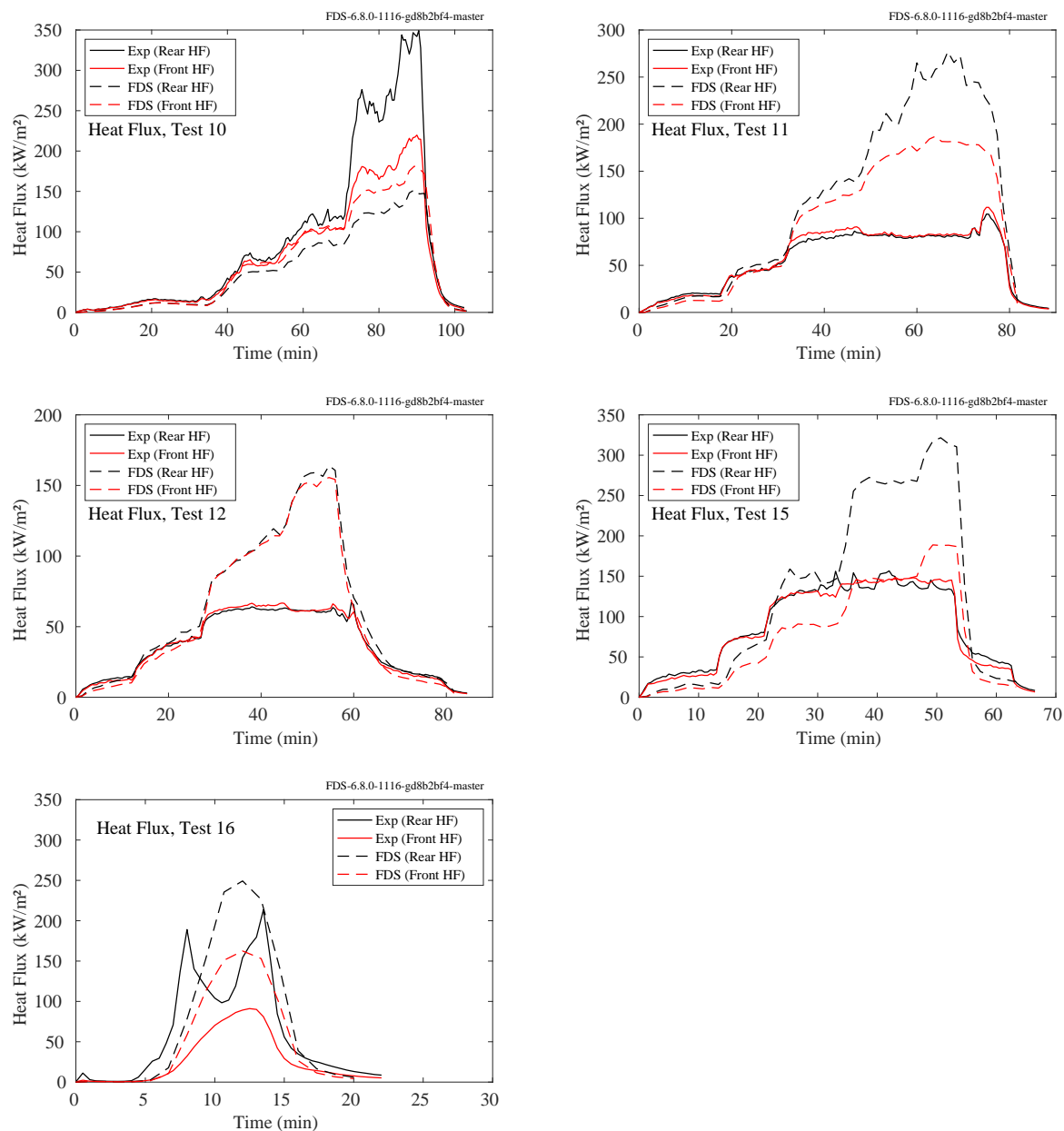


Figure 12.26: Summary of heat flux measurements Tests 10-12, 15-16, NIST RSE 2007.

12.1.9 NRCC Facade Experiments

Figure 12.27 displays the simulation of a 10.3 MW fire inside and outside of a small enclosure. The purpose of the experiment was to measure the heat flux to the exterior facade. The FDS heat flux predictions are made at the location of the green points.

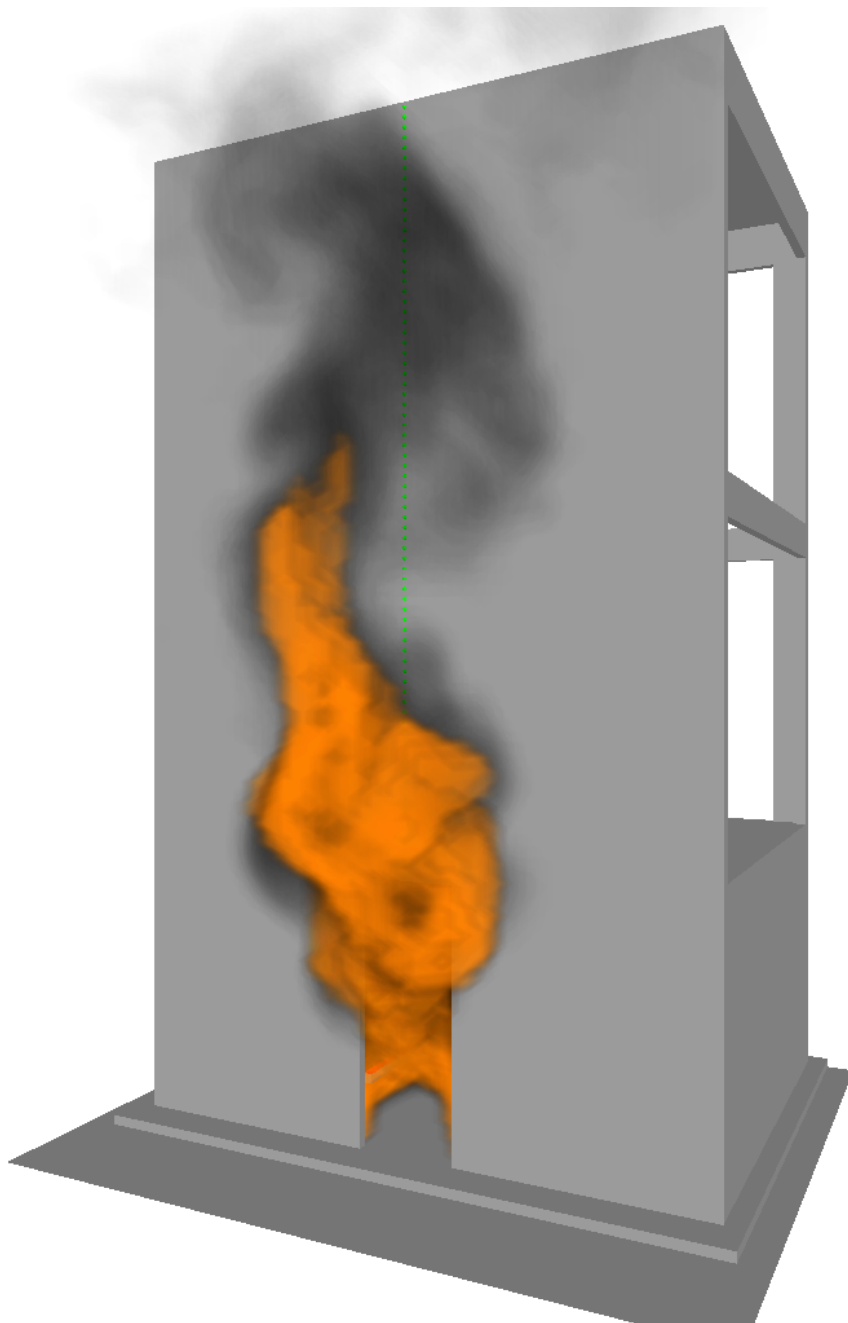


Figure 12.27: Smokeview rendering of one of the NRCC Facade experiments. The door is 0.94 m by 2.70 m tall (referred to as “Window 2” in the comparison plots). The fire is 10.3 MW.

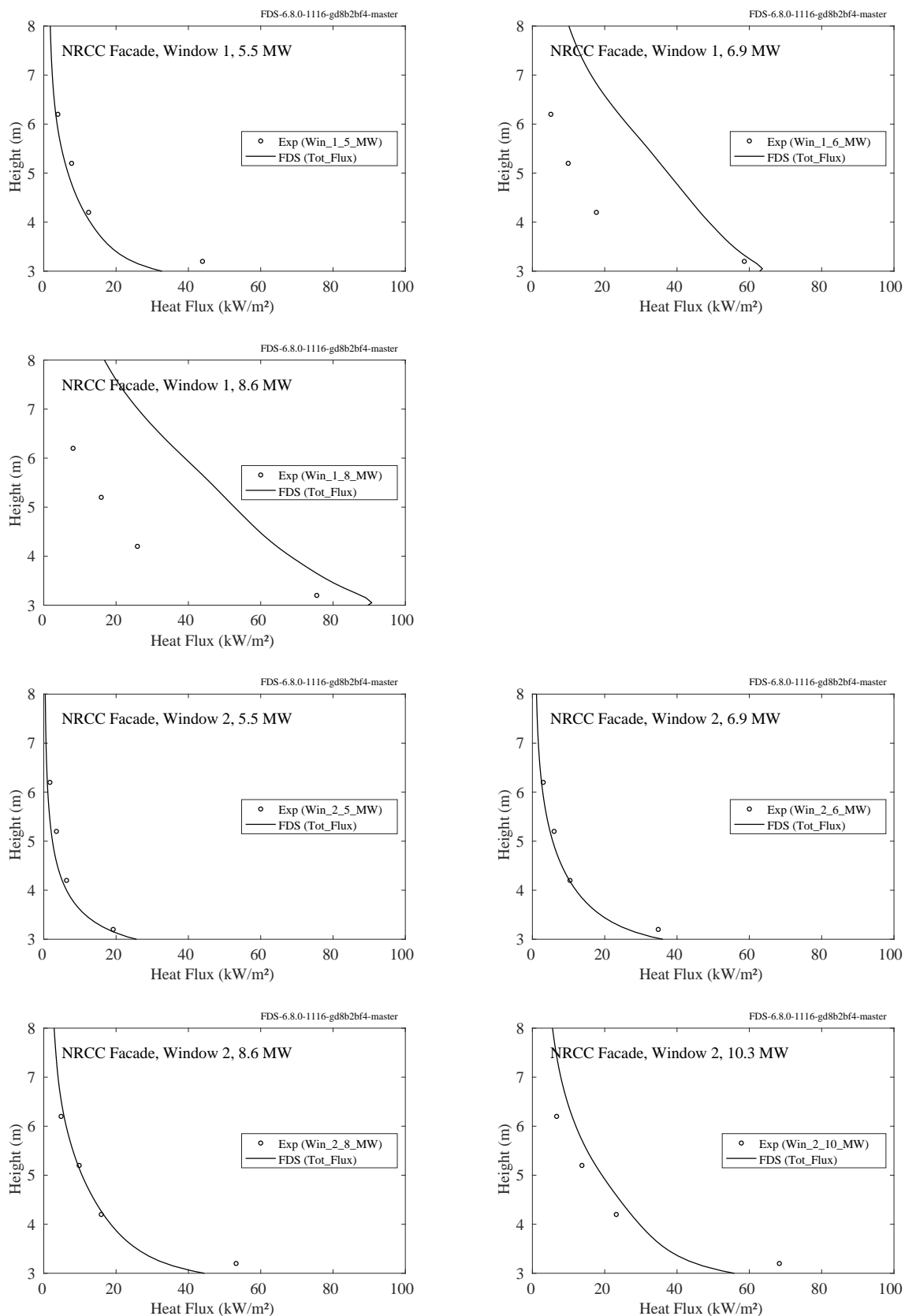


Figure 12.28: NRCC Facade experiments, heat flux, window configuration 1 and 2.

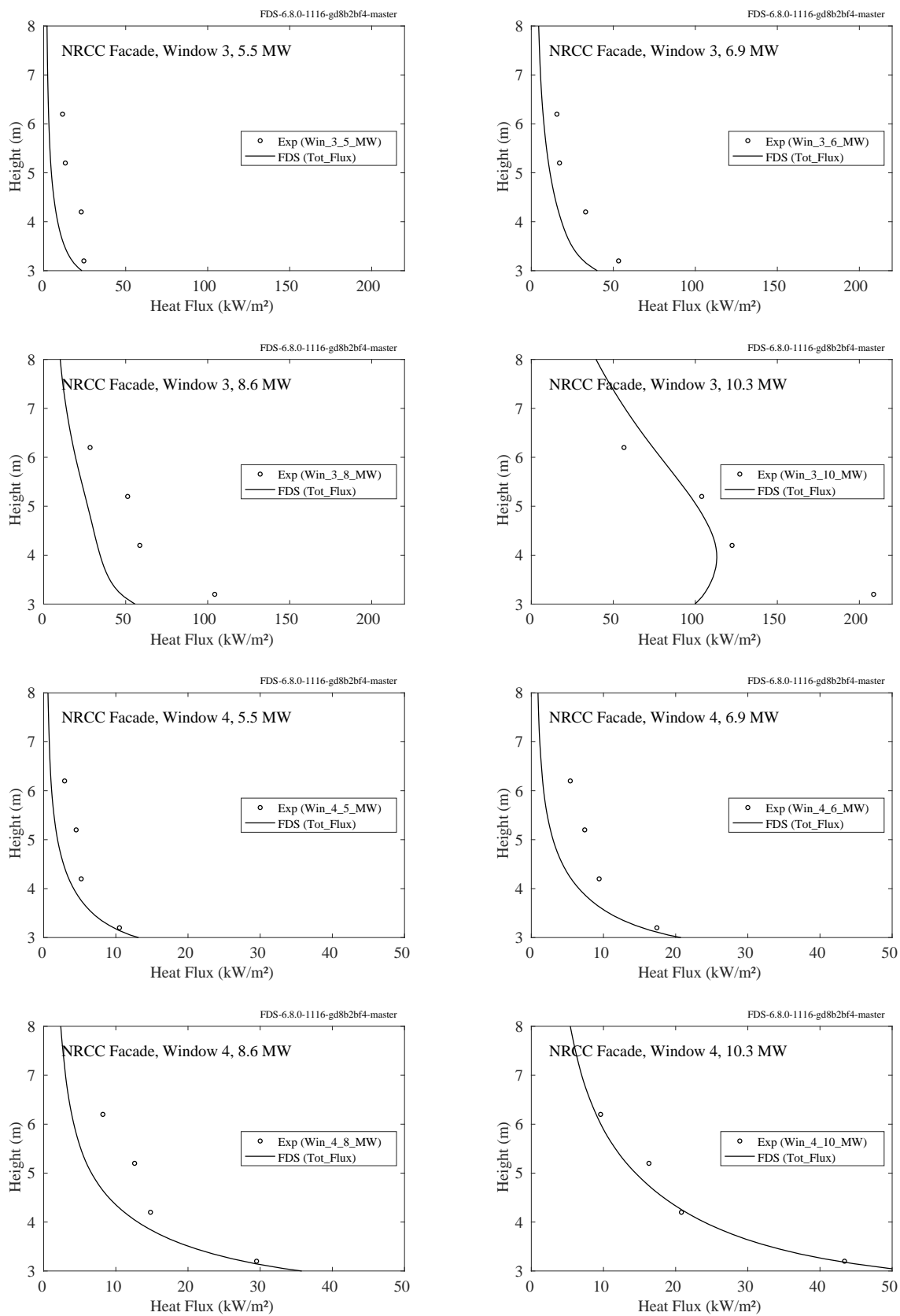


Figure 12.29: NRCC Facade experiments, heat flux, window configuration 3 and 4.

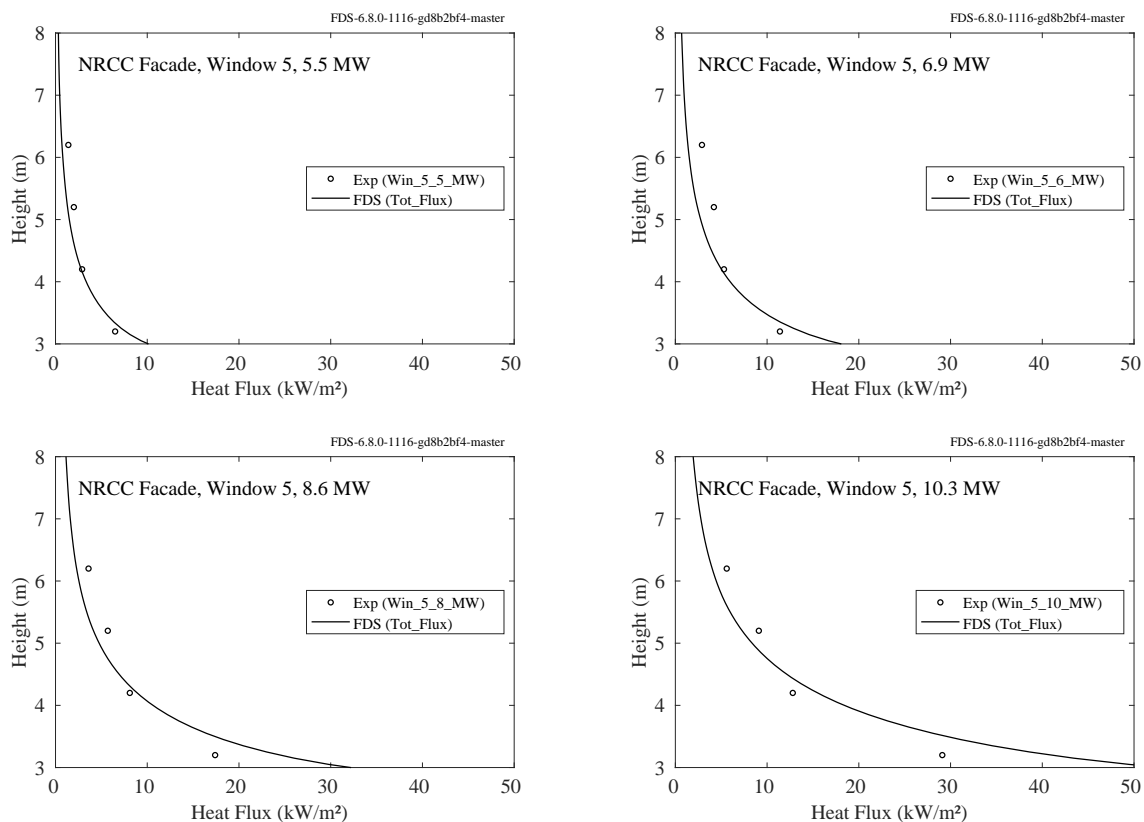


Figure 12.30: NRCC Facade experiments, heat flux, window configuration 5.

12.1.10 NRL/HAI Experiments

Predicted and measured vertical heat flux profiles from 9 propane sand burner fires are shown on the following pages. The parameters for each experiment are listed in Table 12.1 below. Note that all the FDS simulations were performed with a grid resolution such that $D^*/\delta x = 10$.

Table 12.1: Summary of the NRL/HAI Wall Heat Flux Measurements.

Test Number	D (m)	D^* (m)	\dot{Q} (kW)	Q^*	Observed Flame Height (m)
1	0.28	0.30	53	0.85	0.79
2	0.70	0.30	56	0.09	0.36
3	0.48	0.33	68	0.28	0.60
4	0.37	0.39	106	0.84	1.00
5	0.48	0.43	136	0.57	0.87
6	0.48	0.51	204	0.85	1.45
7	0.70	0.52	220	0.36	1.20
8	0.57	0.60	313	0.85	2.20
9	0.70	0.74	523	0.85	2.9 (based on 500 °C)

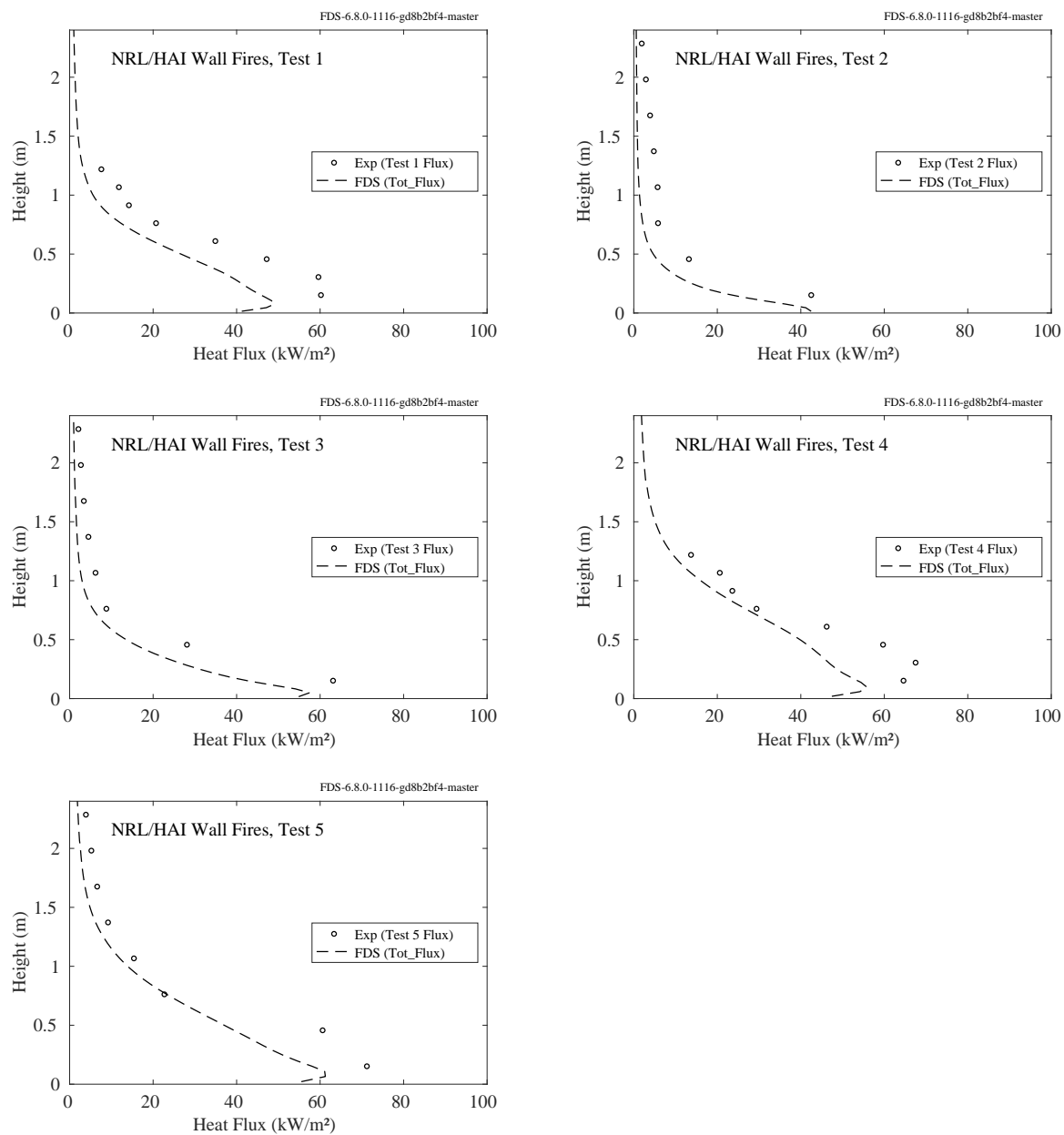


Figure 12.31: NRL/HAI experiments, heat flux to the wall, Tests 1-5.

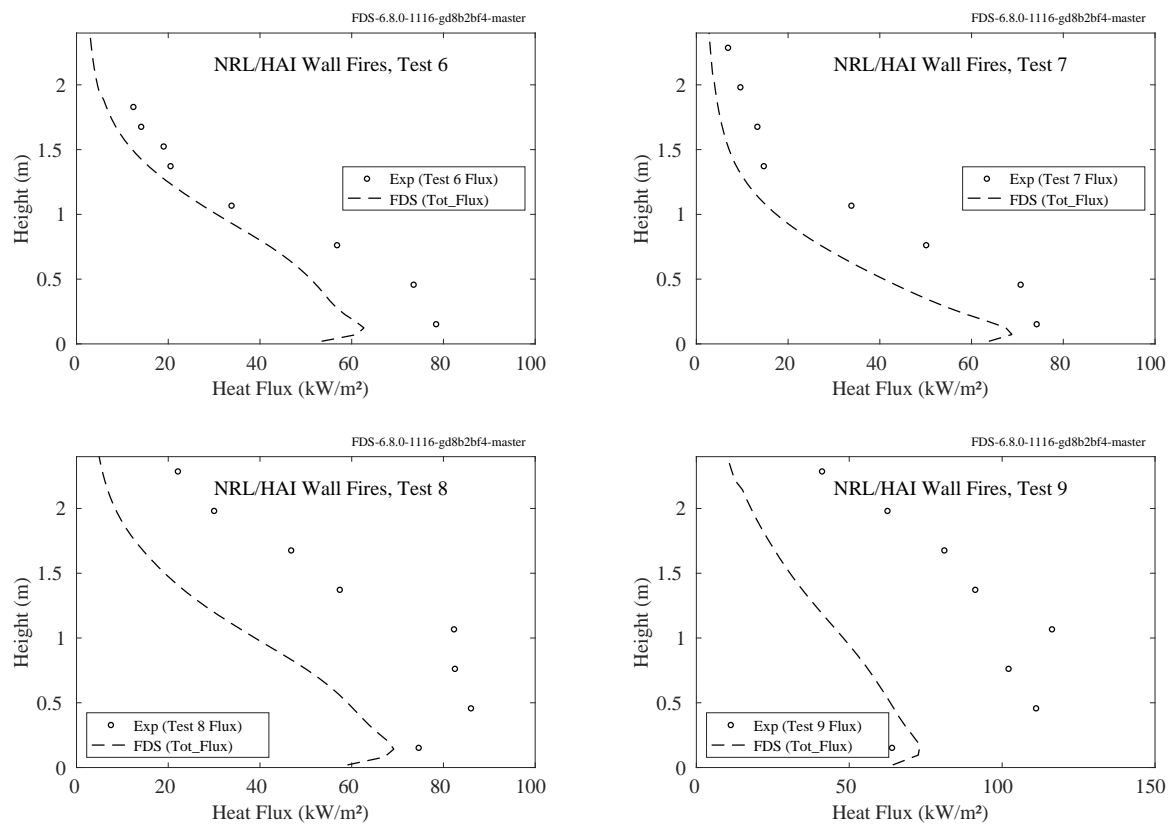


Figure 12.32: NRL/HAI experiments, heat flux to the wall, Tests 6-9.

12.1.11 PRISME DOOR Experiments

Total and radiative heat flux gauges were positioned at various points on the walls. Each room contained a vertical array labeled, for example, FLT_L1_NC265. The FLT indicates a surface total heat flux measurement, L1 indicates compartment 1, which is where the fire was located, NC indicates north wall center, and 265 indicates the number of centimeters above the floor. In addition, each room contained four measurement points centered on each wall at a height of approximately 260 cm. These points are labeled, for example, FLT_L2_SC265, compartment 2, center of south wall, 265 cm high.

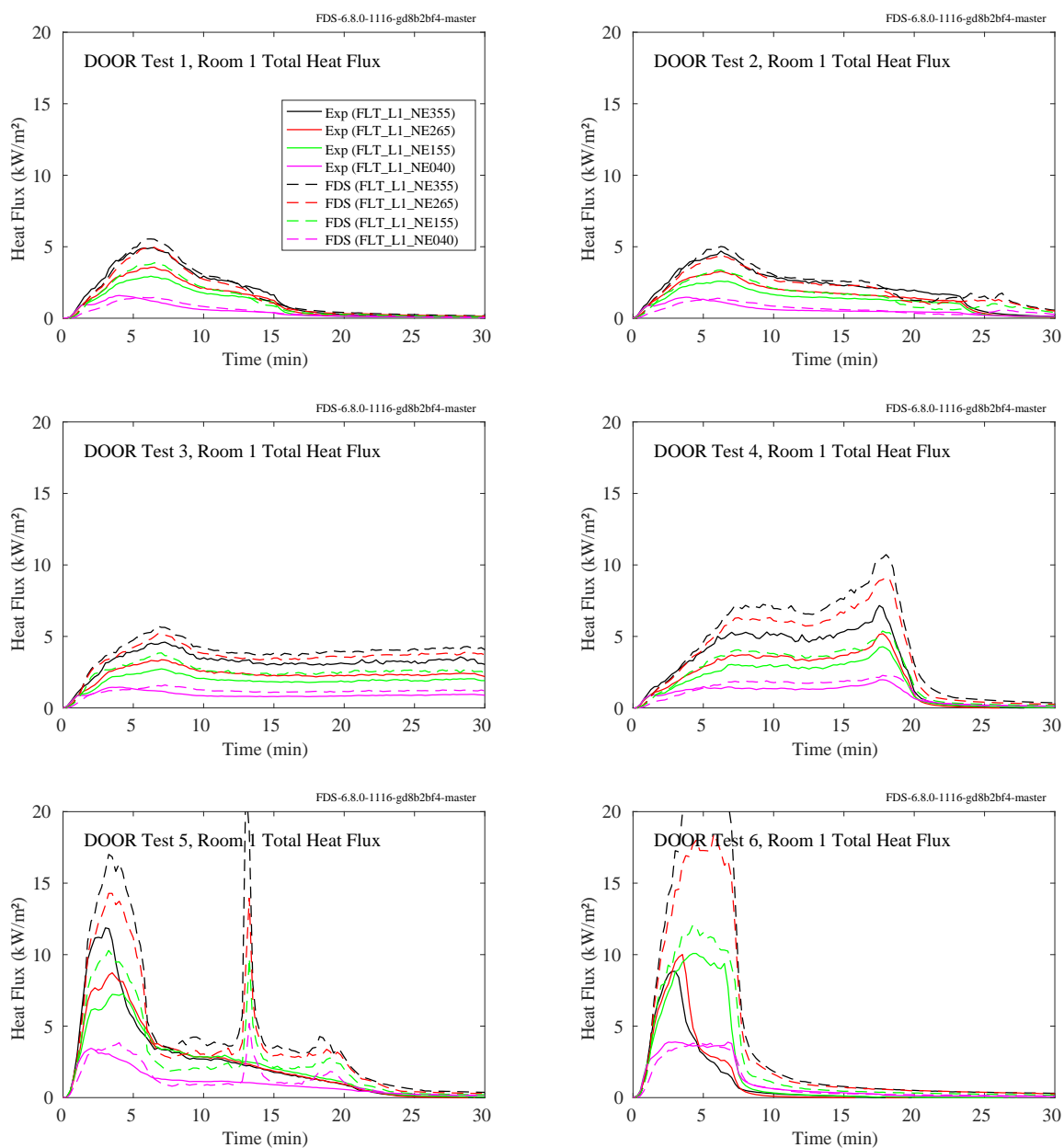


Figure 12.33: PRISME DOOR experiments, total heat flux, vertical array, Room 1.

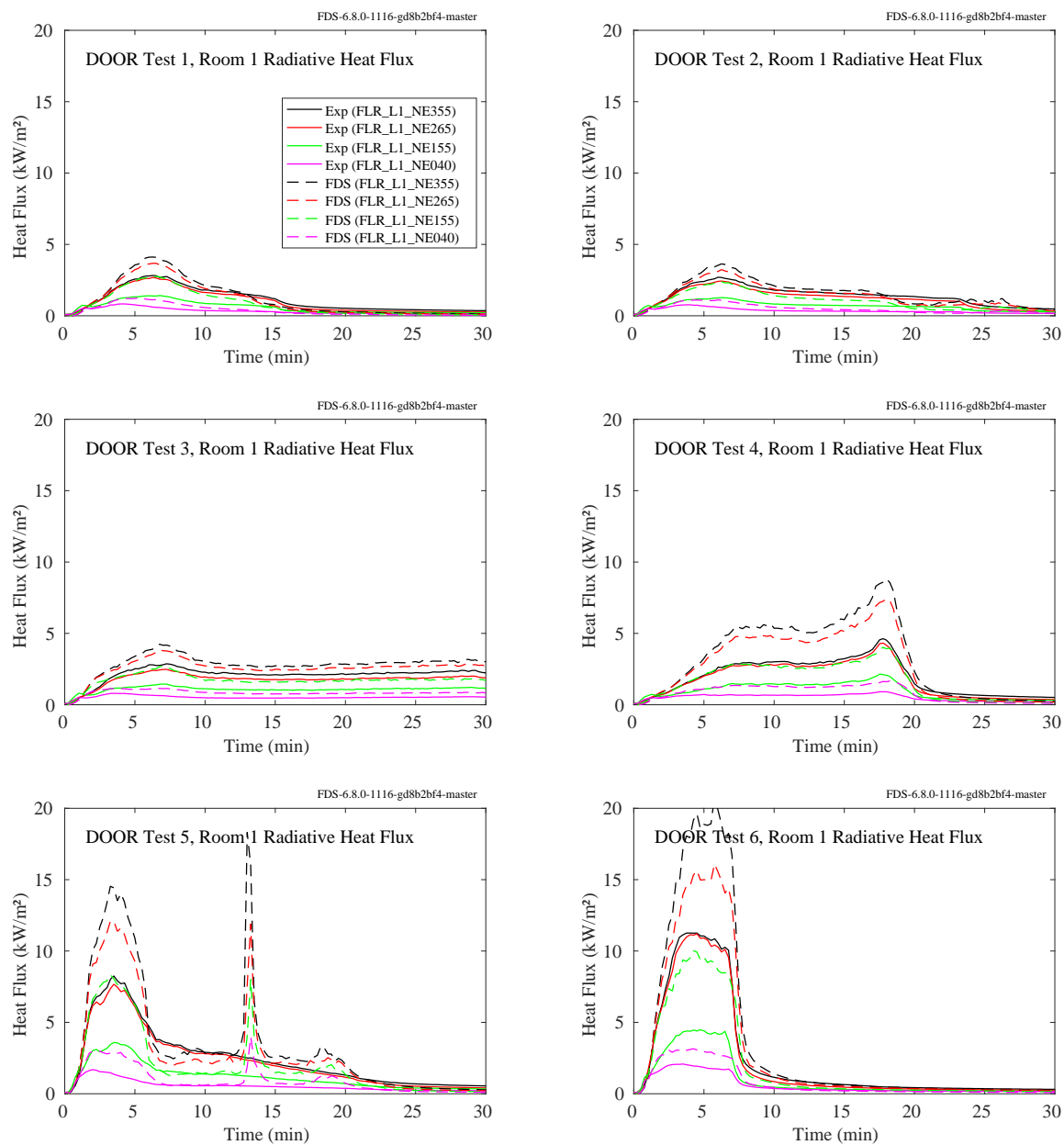


Figure 12.34: PRISME DOOR experiments, radiative heat flux, vertical array, Room 1.

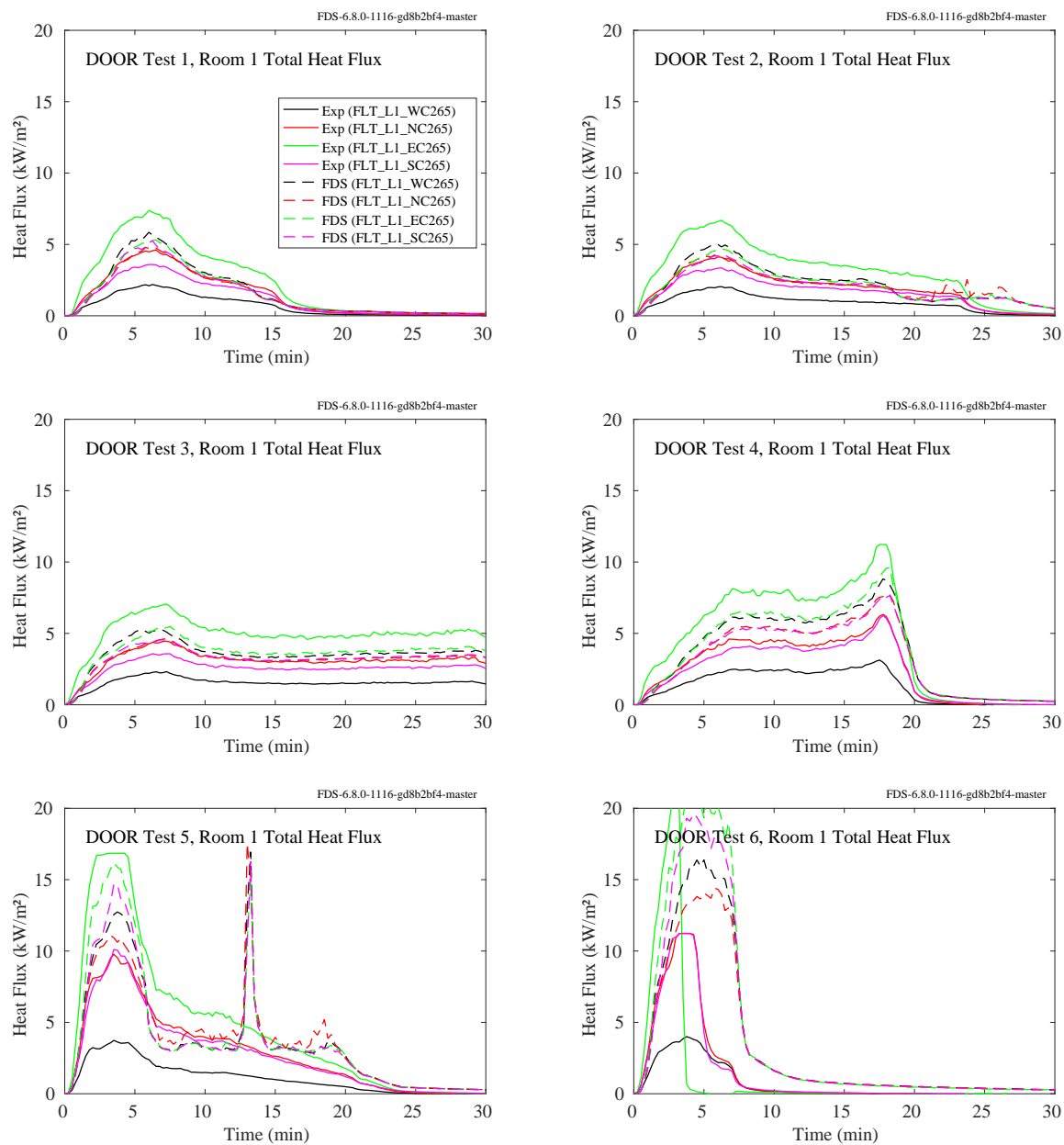


Figure 12.35: PRISME DOOR experiments, total heat flux, four walls, Room 1.

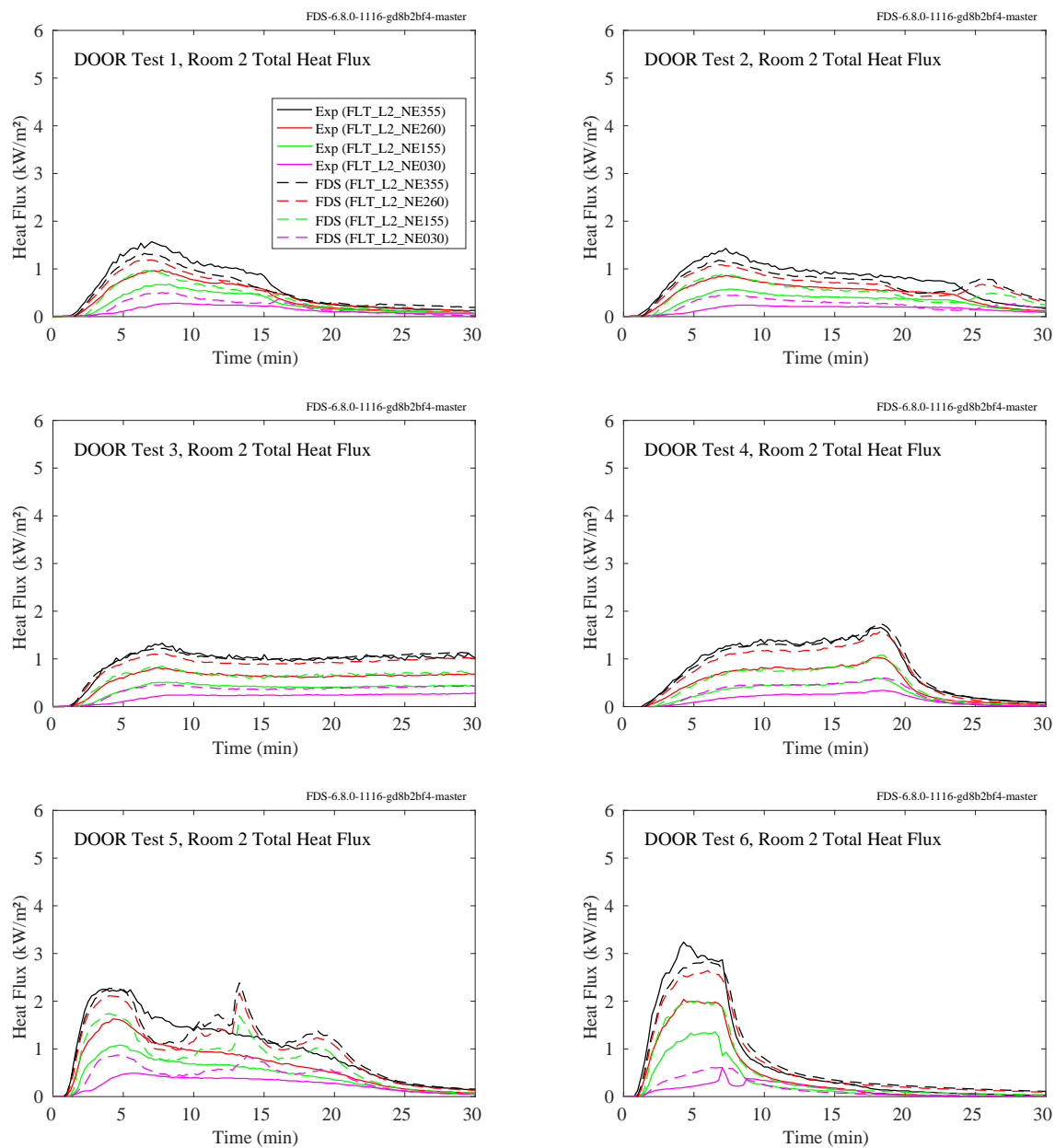


Figure 12.36: PRISME DOOR experiments, total heat flux, vertical array, Room 2.

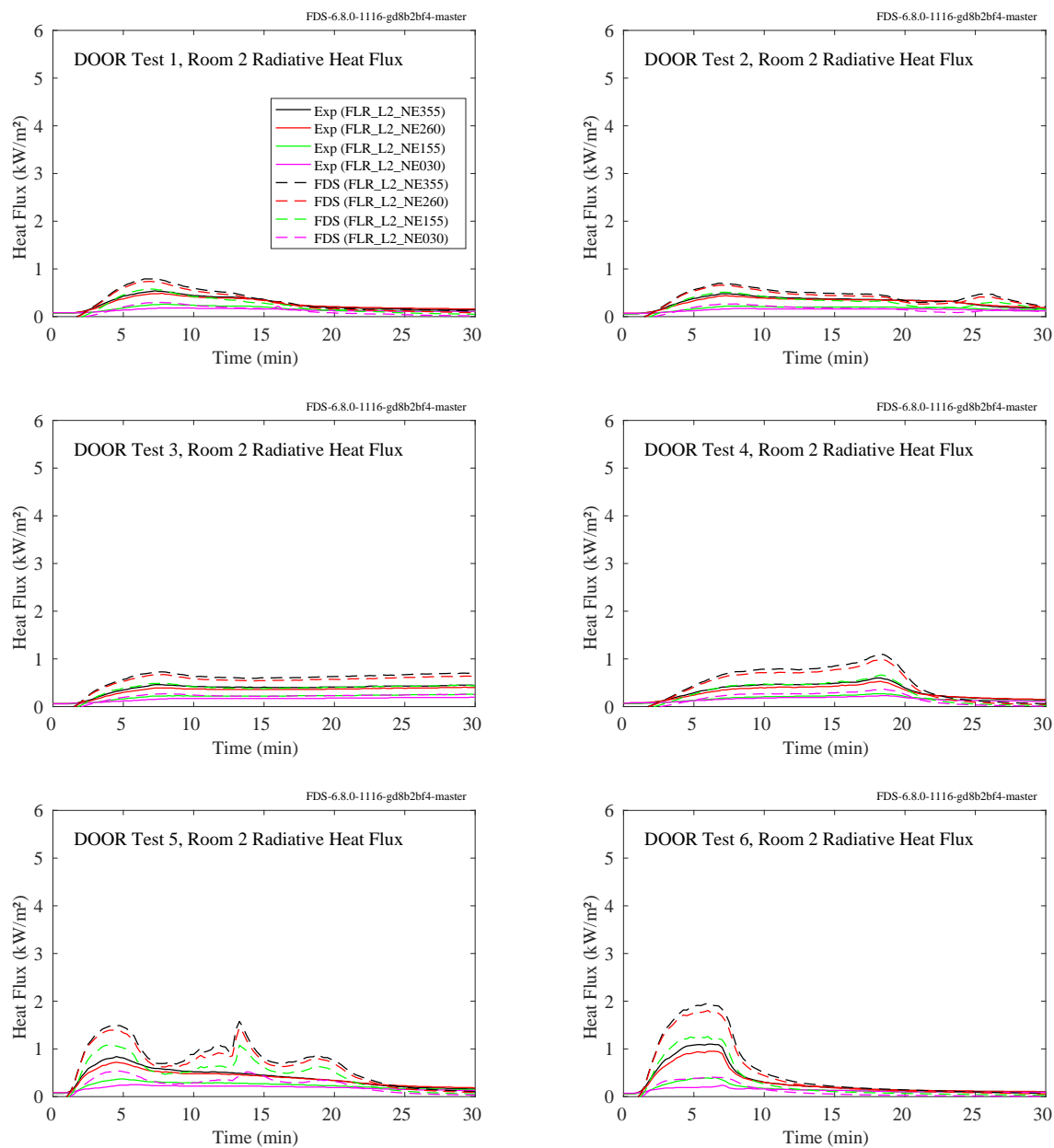


Figure 12.37: PRISME DOOR experiments, radiative heat flux, vertical array, Room 2.

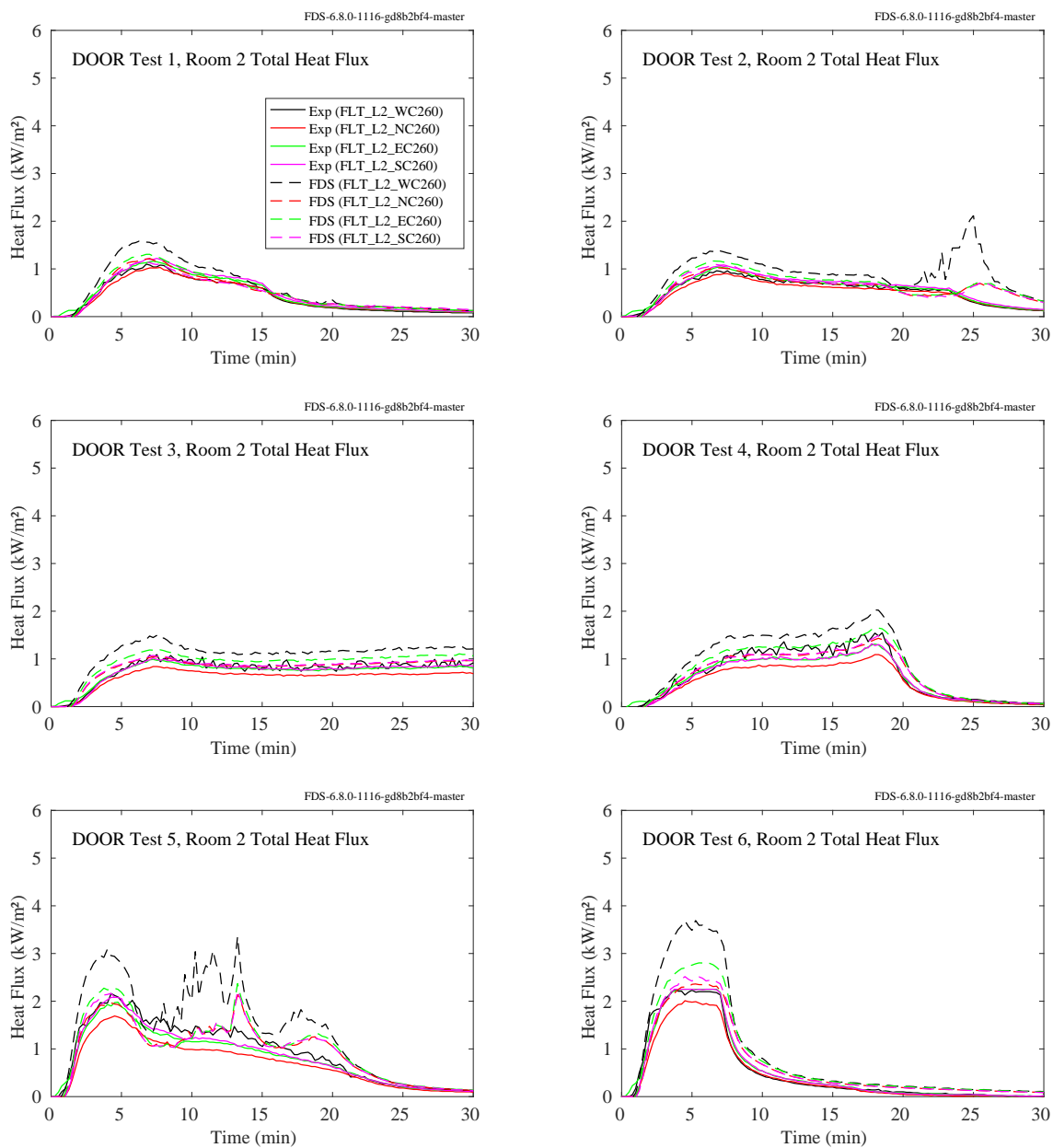


Figure 12.38: PRISME DOOR experiments, total heat flux, four walls, Room 2.

12.1.12 PRISME SOURCE Experiments

Total and radiative heat flux gauges were positioned at various points on the walls. Each room contained a vertical array labeled, for example, FLT_L1_NC265. The FLT indicates a surface total heat flux measurement, L1 indicates compartment 1, which is where the fire was located, NC indicates north wall center, and 265 indicates the number of centimeters above the floor. In addition, each room contained four measurement points centered on each wall at a height of approximately 260 cm. These points are labeled, for example, FLT_L2_SC265, compartment 2, center of south wall, 265 cm high.

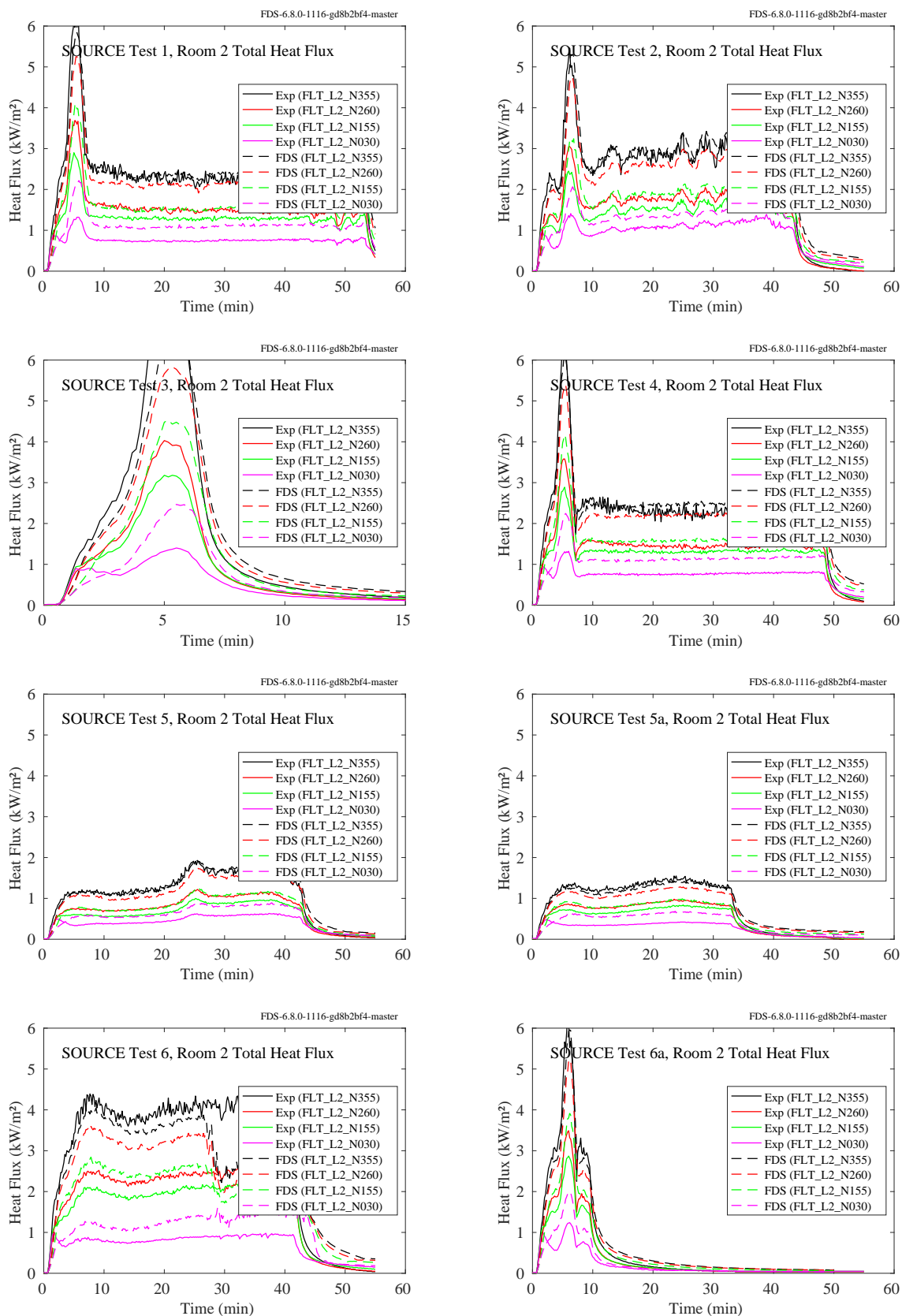


Figure 12.39: PRISME SOURCE experiments, total heat flux, vertical array, Room 2.

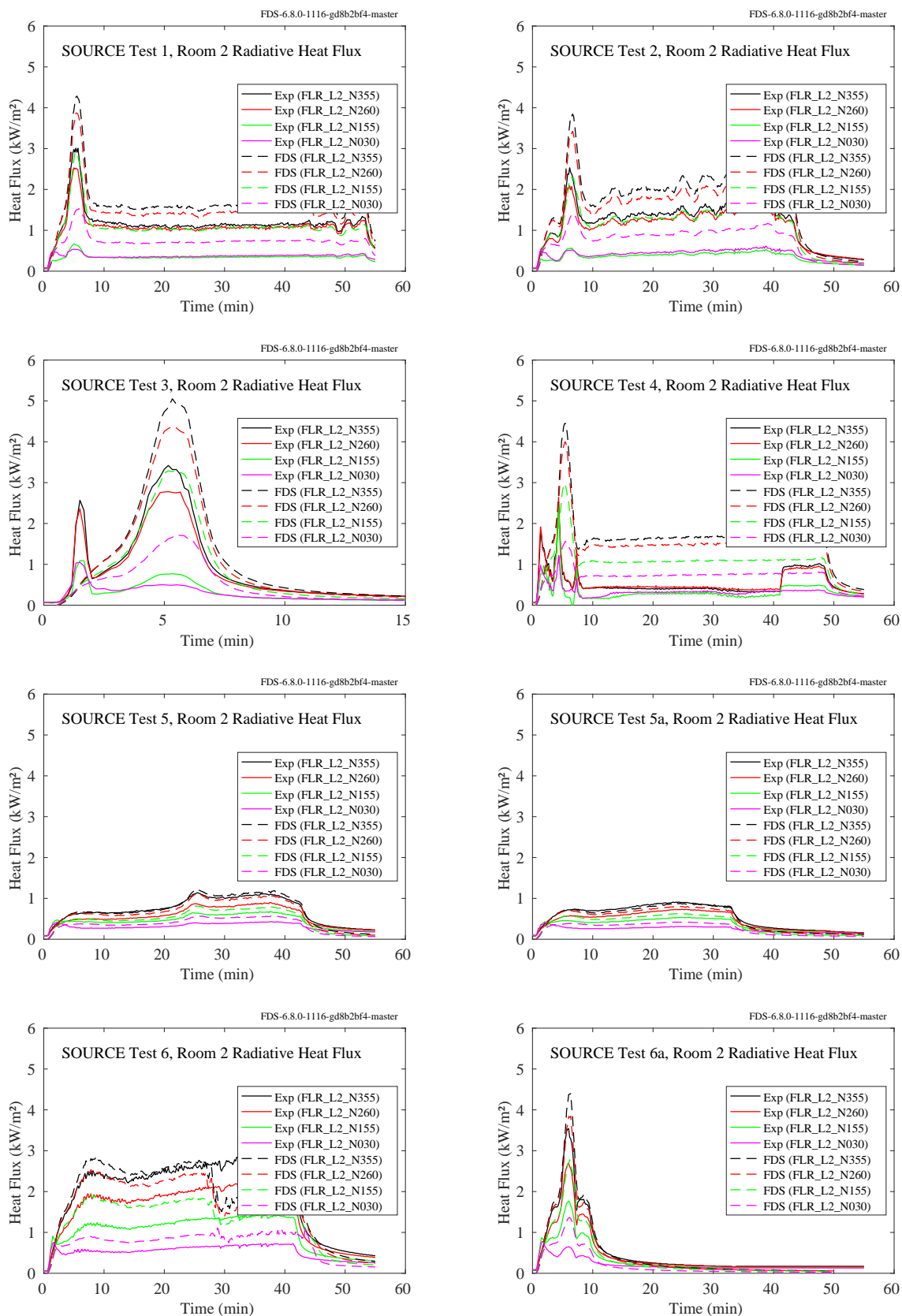


Figure 12.40: PRISME SOURCE experiments, radiative heat flux, vertical array, Room 2.

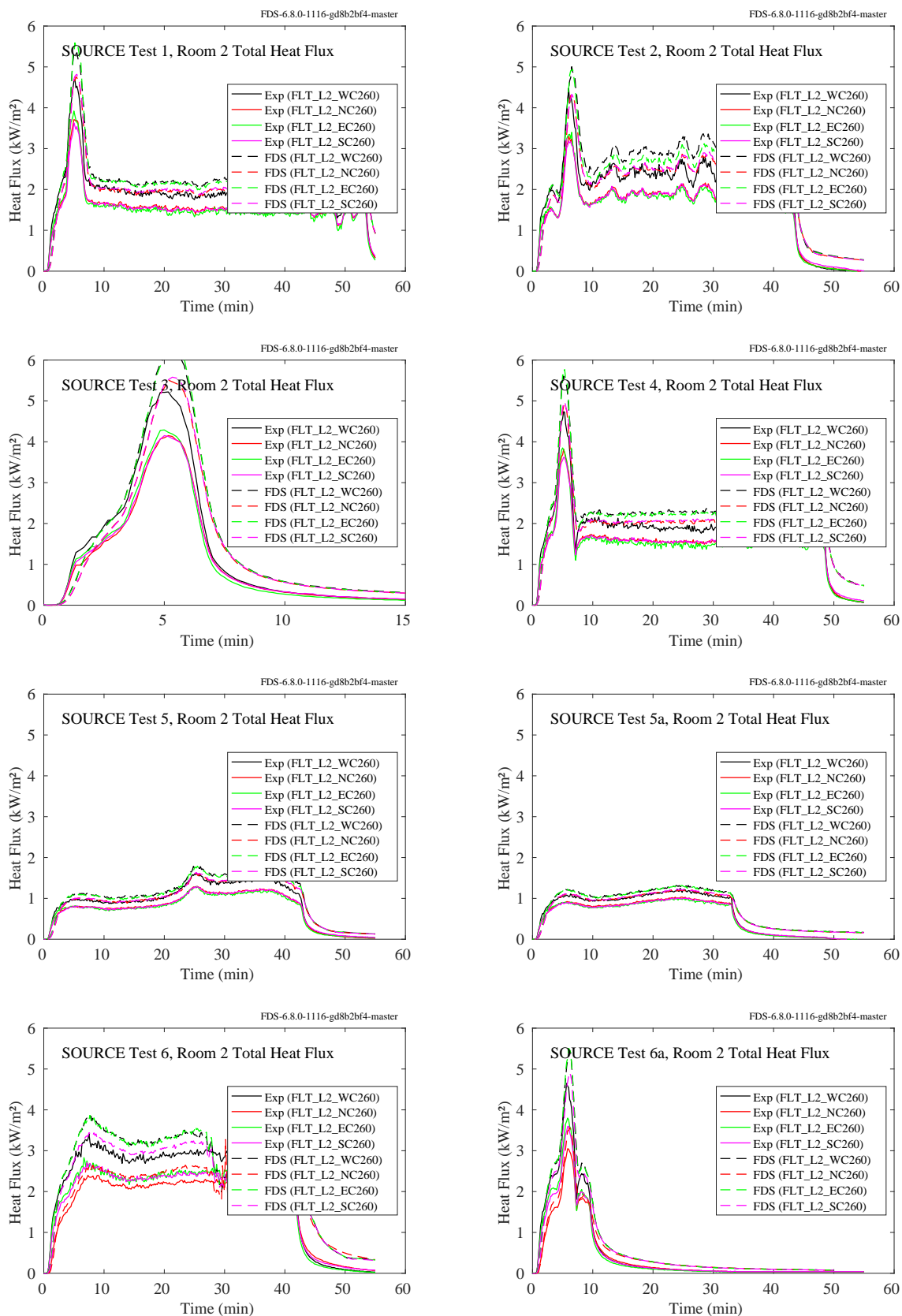


Figure 12.41: PRISME SOURCE experiments, total heat flux, four walls, Room 2.

12.1.13 Ulster SBI Experiments

Predicted and measured vertical heat flux profiles for three propane fire sizes in the single burning item (SBI) enclosure at the University of Ulster are shown on the following page. Measurements were made on two vertical panels that form a corner, at the base of which was a triangular-shaped burner with sides of length 25 cm. Three vertical profiles were measured on each panel at distances of 3.25 cm, 16.5 cm, and 29 cm from the corner.

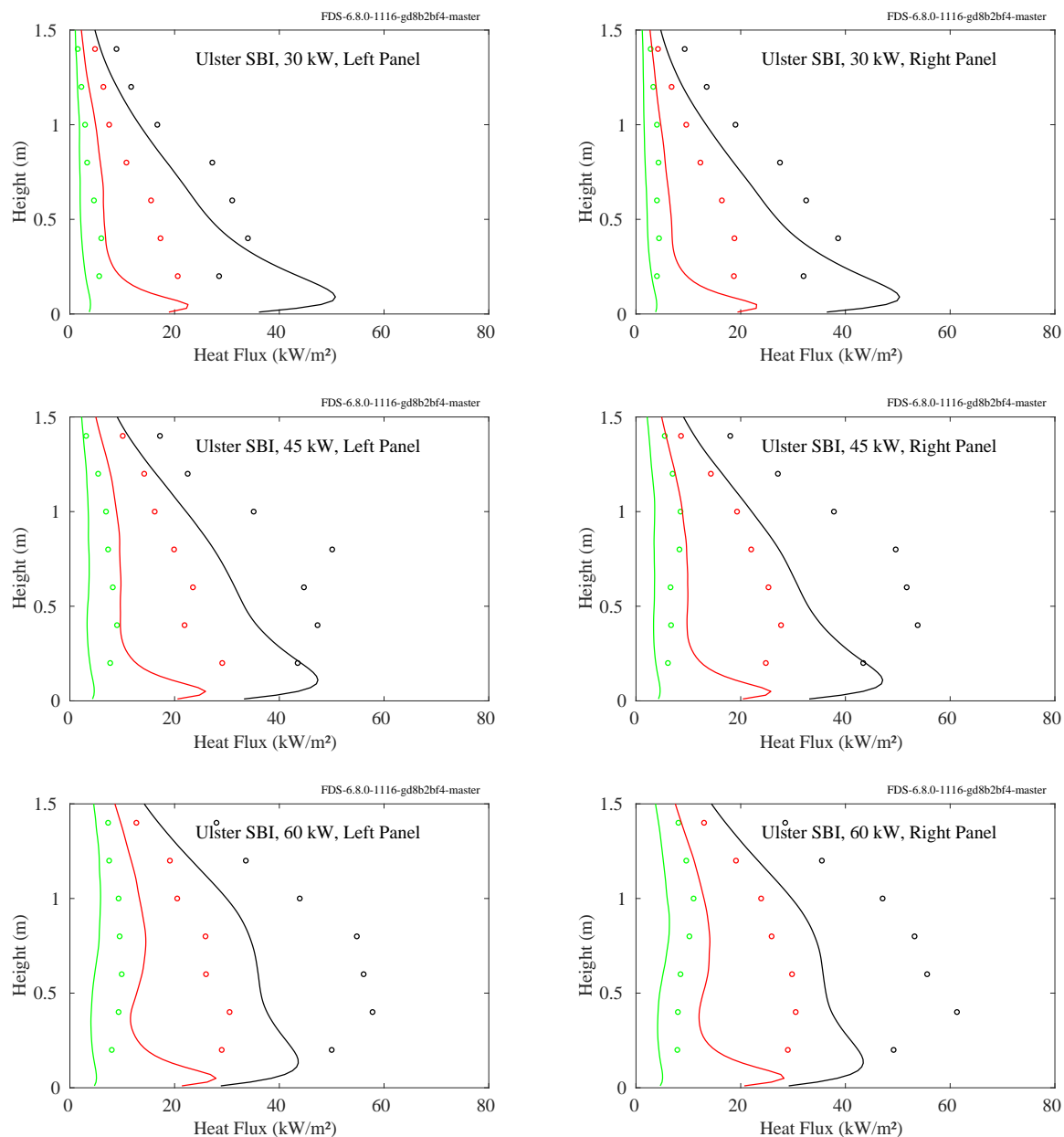


Figure 12.42: Comparison of predicted (lines) and measured (circles) heat fluxes to adjacent panels forming a corner in the single burning item (SBI) apparatus at the University of Ulster.

12.1.14 UMD SBI Experiment

A description of this experiment is given in Sec. 3.94.

Figure 12.43 displays the measured and predicted heat fluxes at 28 locations on a burning vertical panel of PMMA over the course of a 3 min experiment. The measurement points are at heights of 10 cm, 30 cm, 50 cm, 70 cm, 90 cm, 110 cm, and 130 cm above the burner, and horizontal distances of 5 cm, 10 cm, 15 cm, and 22 cm from the corner of the perpendicular panels.

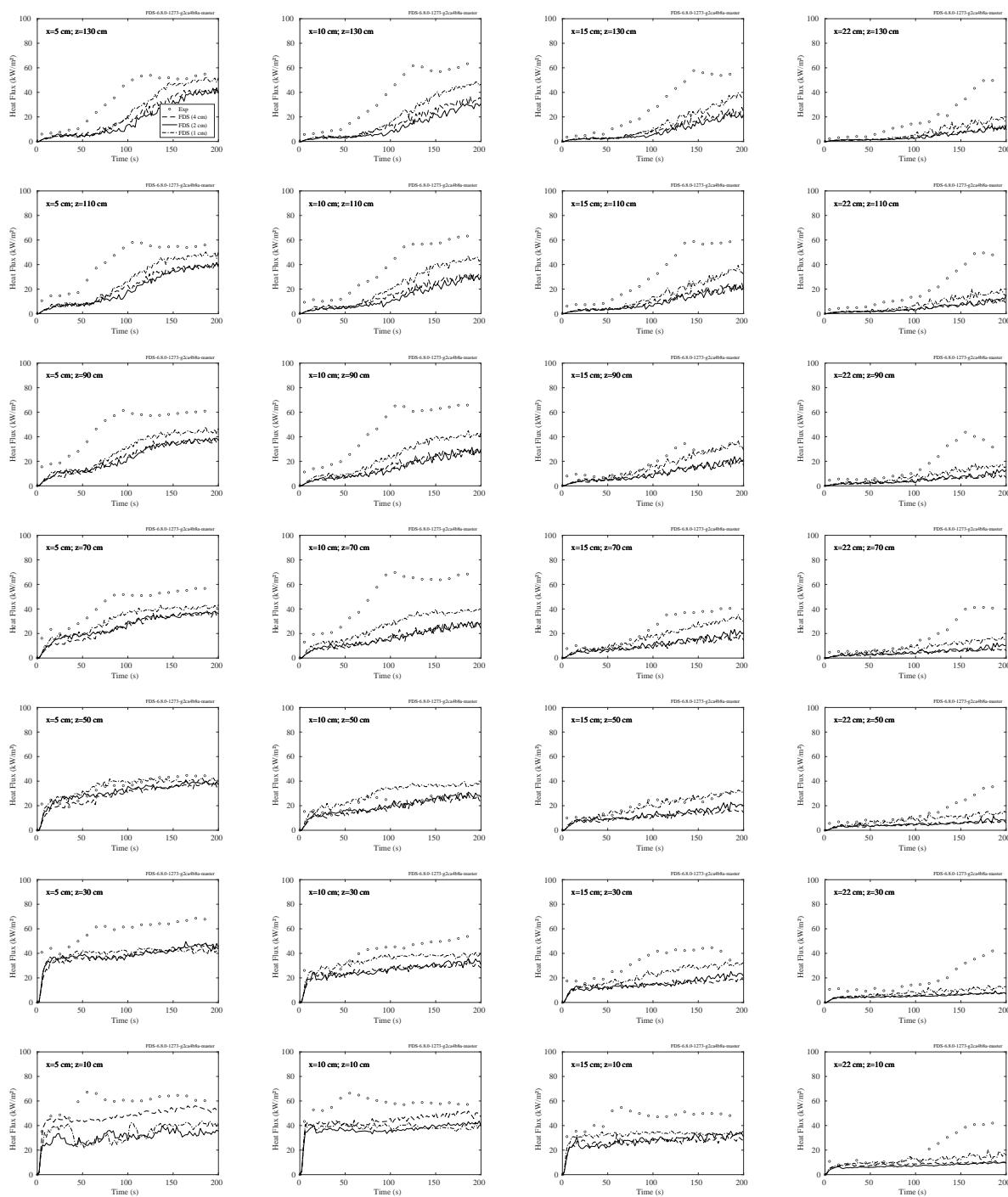


Figure 12.43: UMD SBI, heat flux to PMMA panel at seven vertical locations and four lateral locations.

12.1.15 WTC Experiments

There were a variety of heat flux gauges installed in the test compartment. Most were within 2 m of the fire. Their locations and orientations are listed in Table 12.2. This section contains the measurements at the floor and ceiling.

Table 12.2: Heat flux gauge positions relative to the center of the fire pan in the WTC series.

Name	x (m)	y (m)	z (m)	Orientation	Location
H2FU	0.64	0.63	3.30	$+z$	Truss Support
H2RU	0.64	0.51	3.30	$+z$	Truss Support
H2FD	0.64	0.30	3.15	$-z$	Truss Support
H2RD	0.64	0.42	3.15	$-z$	Truss Support
HCoHF	-0.90	0.84	3.46	$+x$	Column, facing fire
HCoHW	-0.97	0.92	3.27	$+y$	Column, facing north
HCoLF	-0.90	0.84	0.92	$+x$	Column, facing fire
HCoLW	-0.97	0.92	1.02	$+y$	Column, facing north
HF1	1.06	0.13	0.13	$+z$	Floor
HF2	1.56	0.10	0.13	$+z$	Floor
HCe1	-0.45	0.35	3.82	$-z$	Ceiling
HCe2	0.05	0.35	3.82	$-z$	Ceiling
HCe3	0.80	0.35	3.82	$-z$	Ceiling
HCe4	2.56	0.35	3.82	$-z$	Ceiling

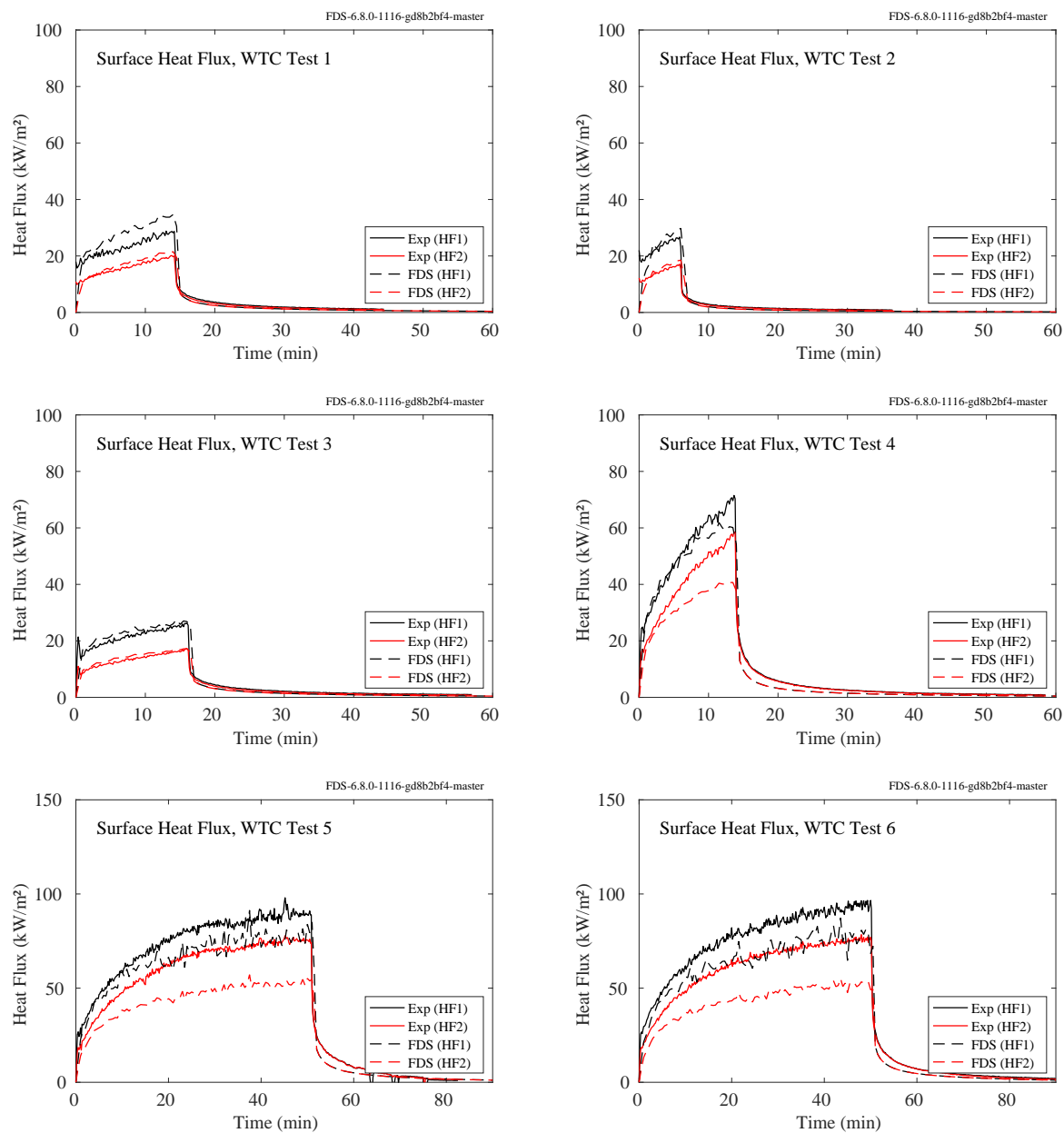


Figure 12.44: WTC experiments, heat flux to the floor.

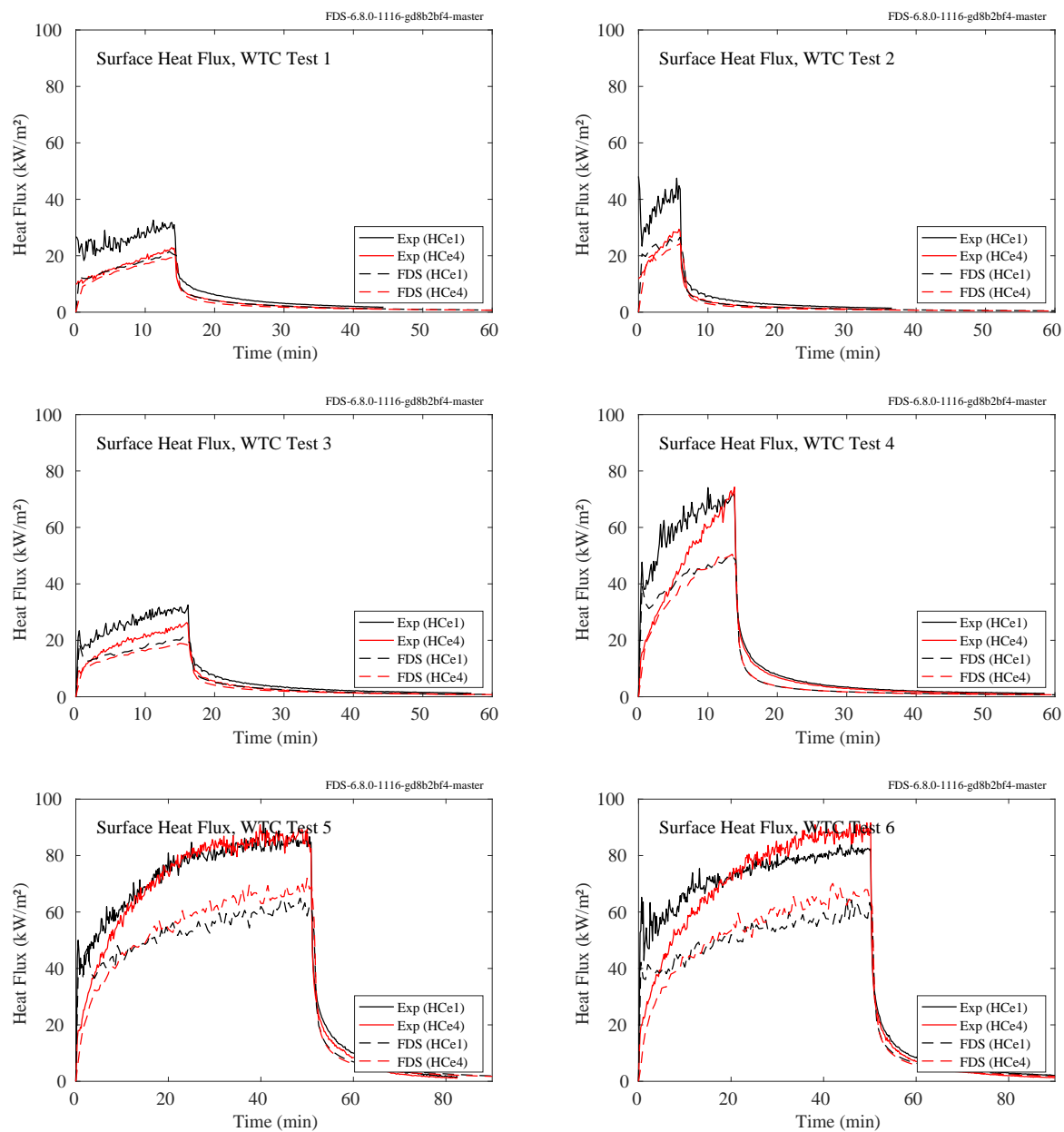


Figure 12.45: WTC experiments, heat flux to the ceiling.

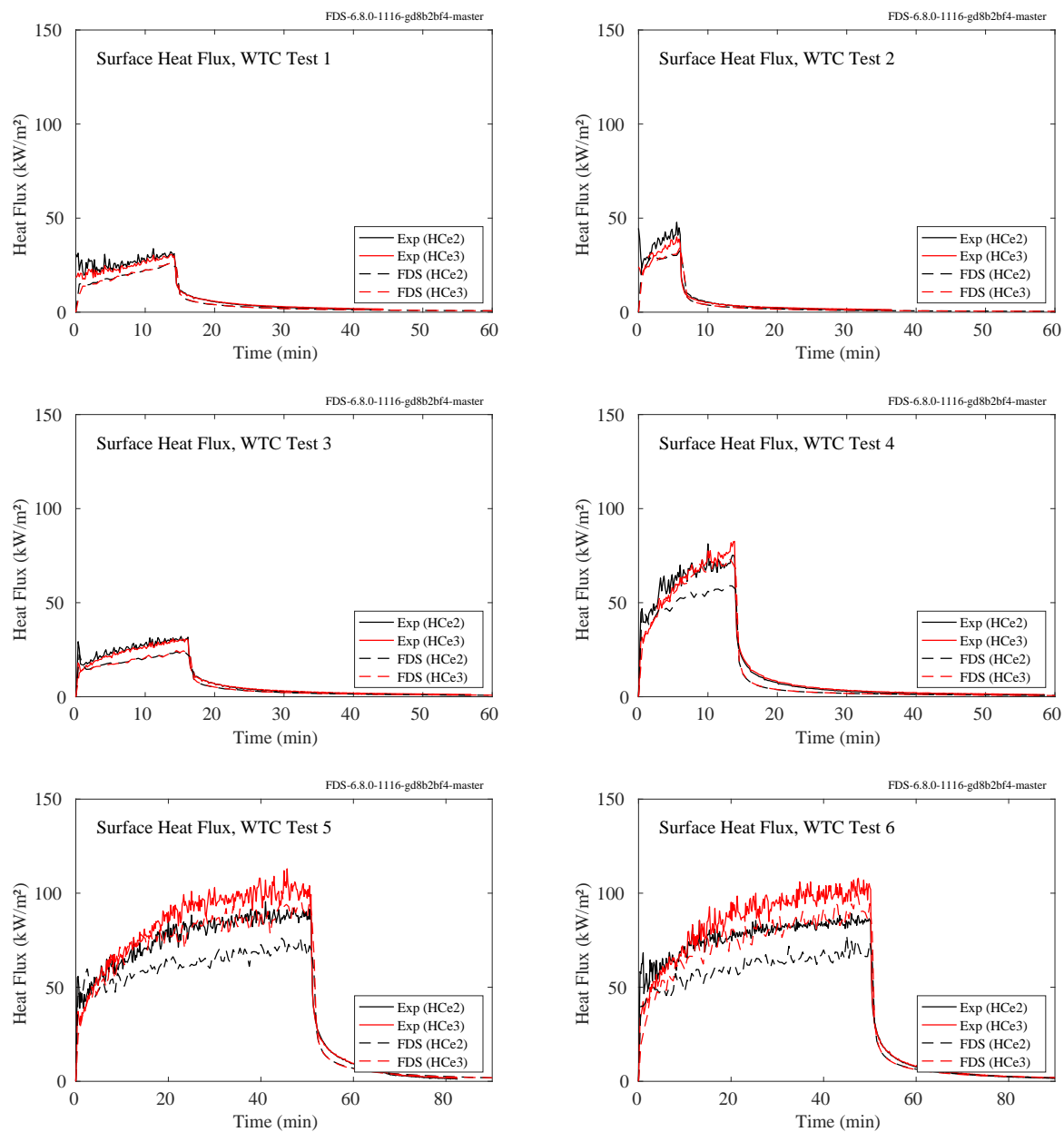


Figure 12.46: WTC experiments, heat flux to the ceiling.

12.1.16 Summary of Wall, Ceiling and Floor Heat Flux Predictions

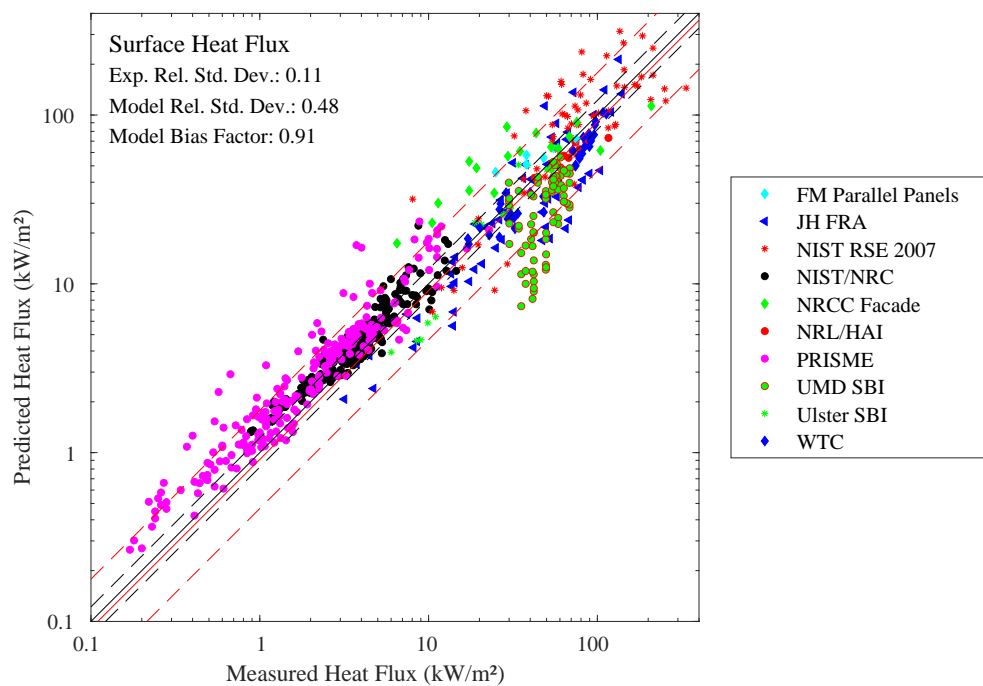


Figure 12.47: Summary of surface heat flux predictions.

12.2 Heat Flux to Targets

The heat flux measurements are broken up into two broad categories—heat flux to walls, floors, and ceiling, and heat flux to “targets”. A target is any object of interest in a fire, like a steel beam or electrical cable. The following subsections consider heat flux to targets.

12.2.1 Fleury Experiments

The plots on the following pages contain comparisons of predicted and measured heat fluxes from a series of propane burner fires. Heat flux gauges were mounted on moveable dollies that were placed in front of, and to the side of, burners with dimensions of 0.3 m by 0.3 m (1:1 burner), 0.6 m by 0.3 m (2:1 burner), and 0.9 m by 0.3 m (3:1 burner). The heat release rates were set to 100 kW, 150 kW, 200 kW, 250 kW, and 300 kW. The gauges were mounted at heights of 0 m, 0.5 m, 1.0 m, and 1.5 m relative to the top edge of the burner. Each page contains the results for a given HRR.

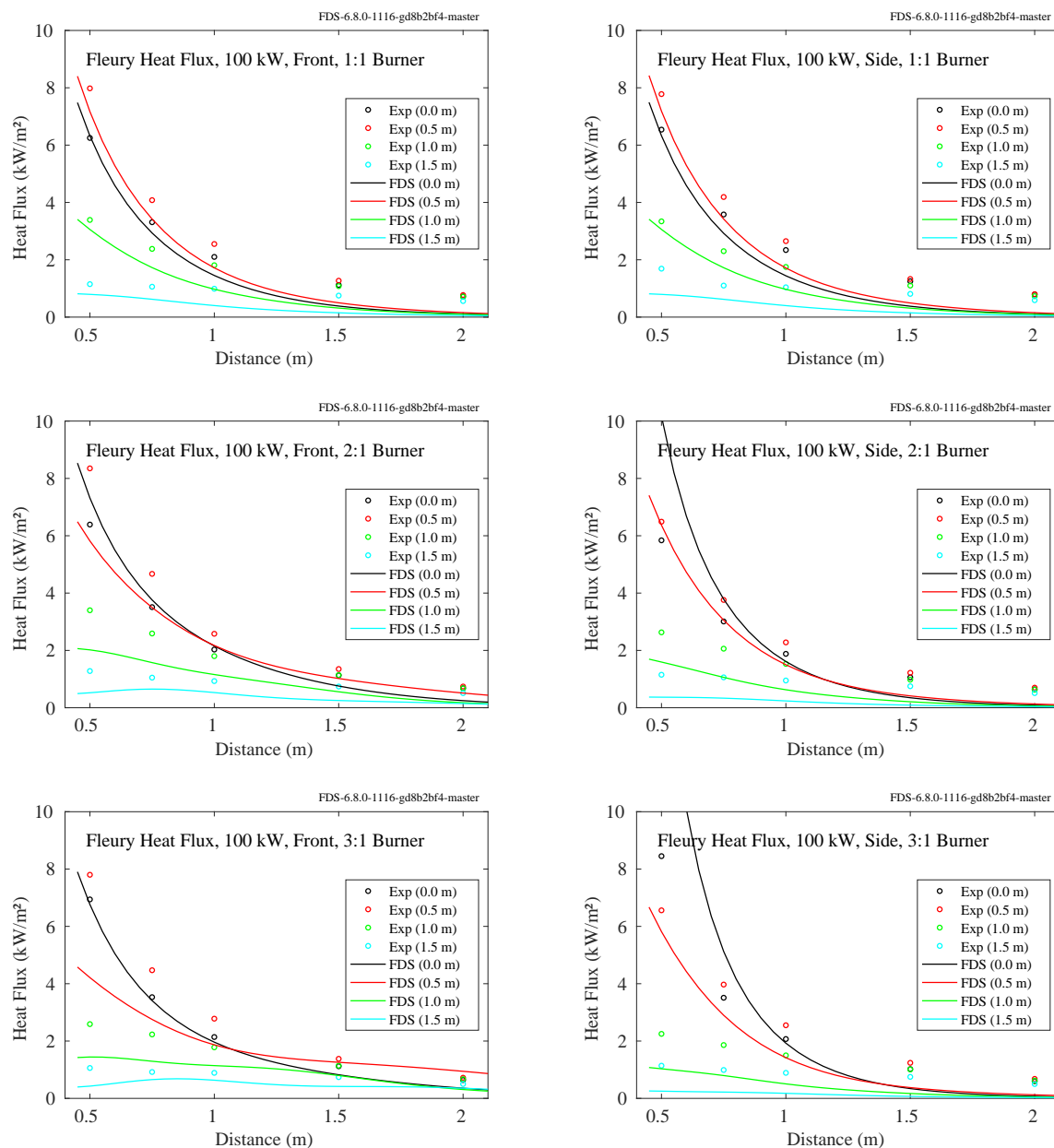


Figure 12.48: Comparison of predicted (lines) and measured (circles) heat flux for the 100 kW Fleury fires.

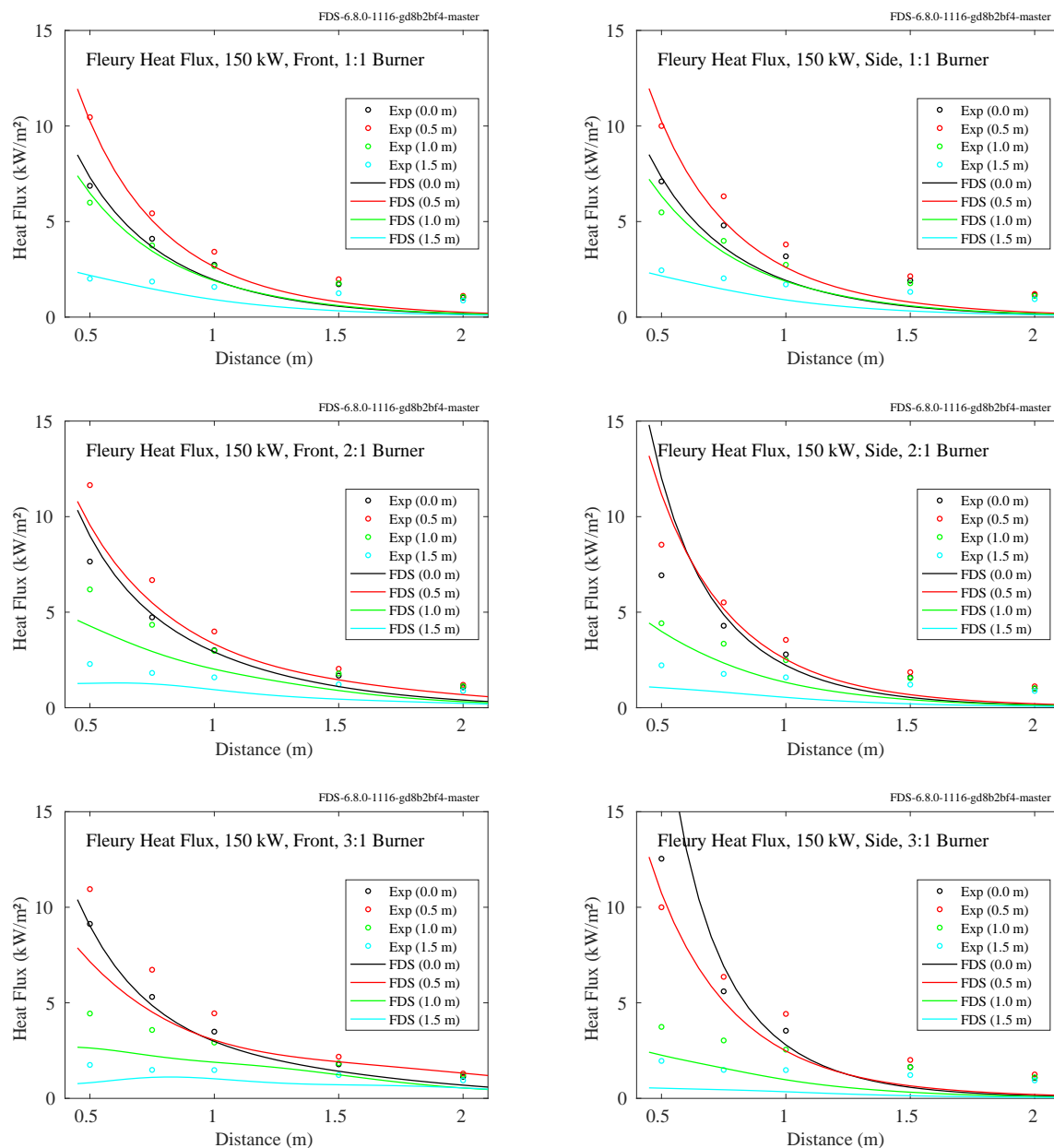


Figure 12.49: Comparison of predicted (lines) and measured (circles) heat flux for the 150 kW Fleury fires.

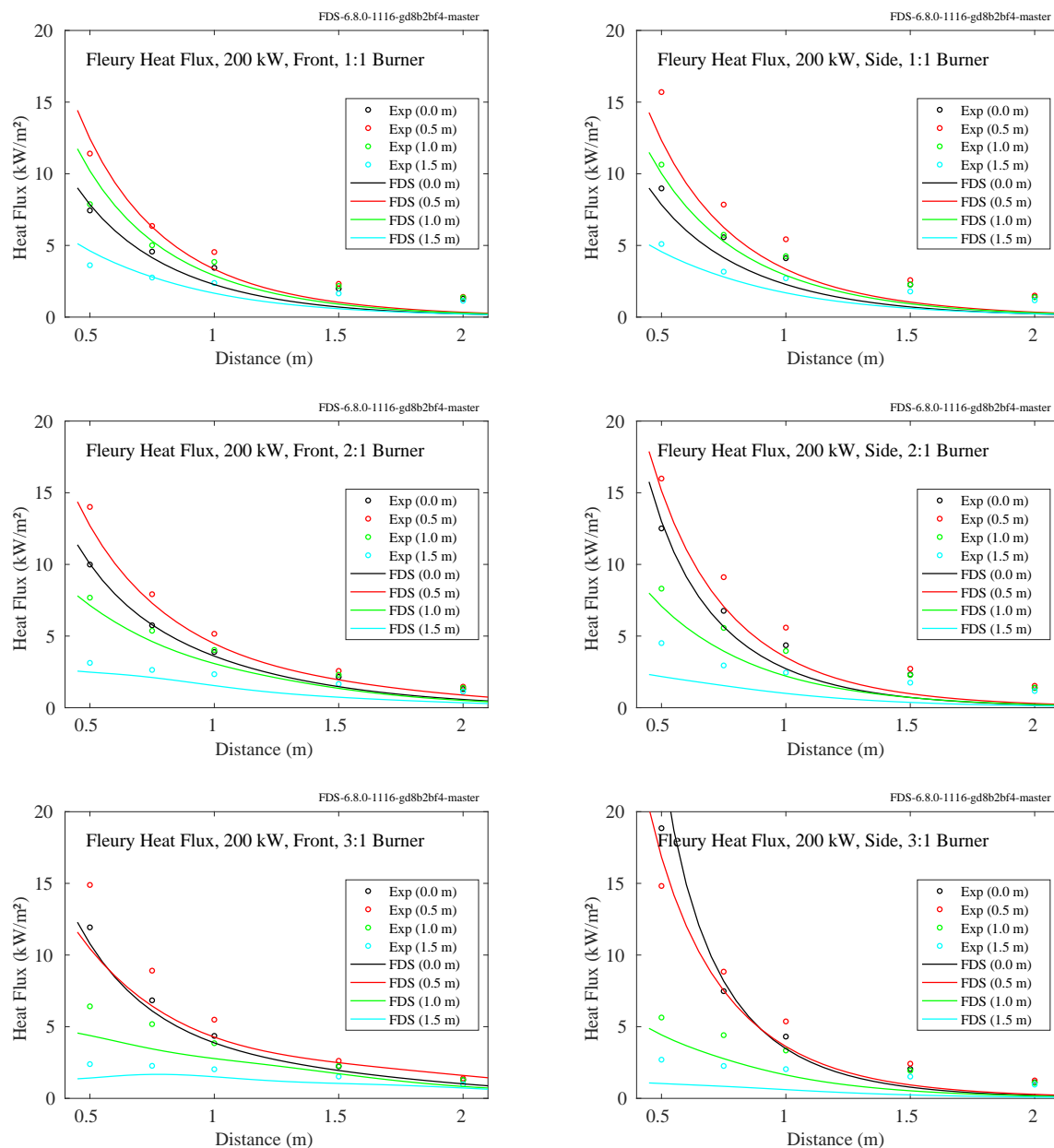


Figure 12.50: Comparison of predicted (lines) and measured (circles) heat flux for the 200 kW Fleury fires.

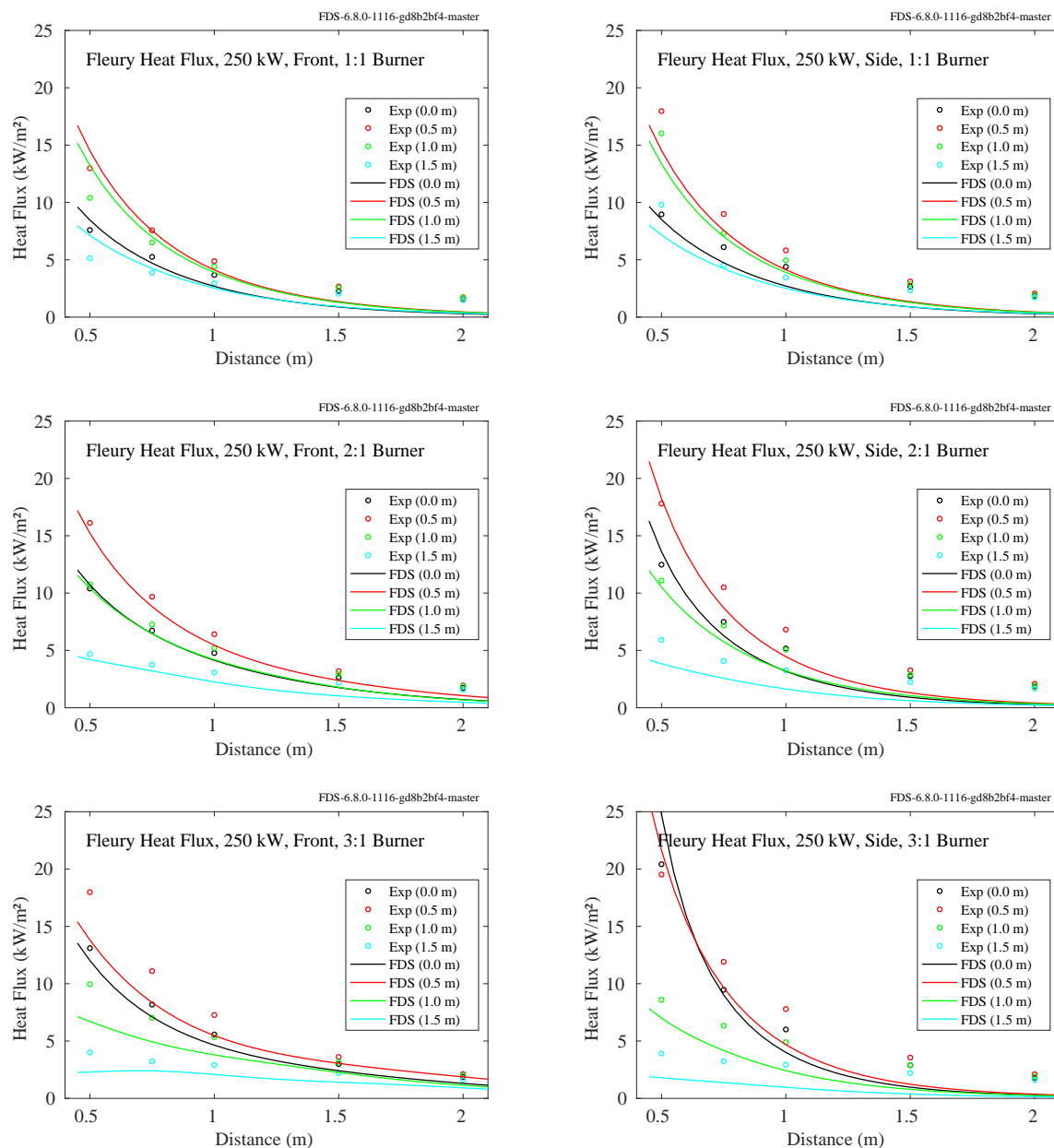


Figure 12.51: Comparison of predicted (lines) and measured (circles) heat flux for the 250 kW Fleury fires.

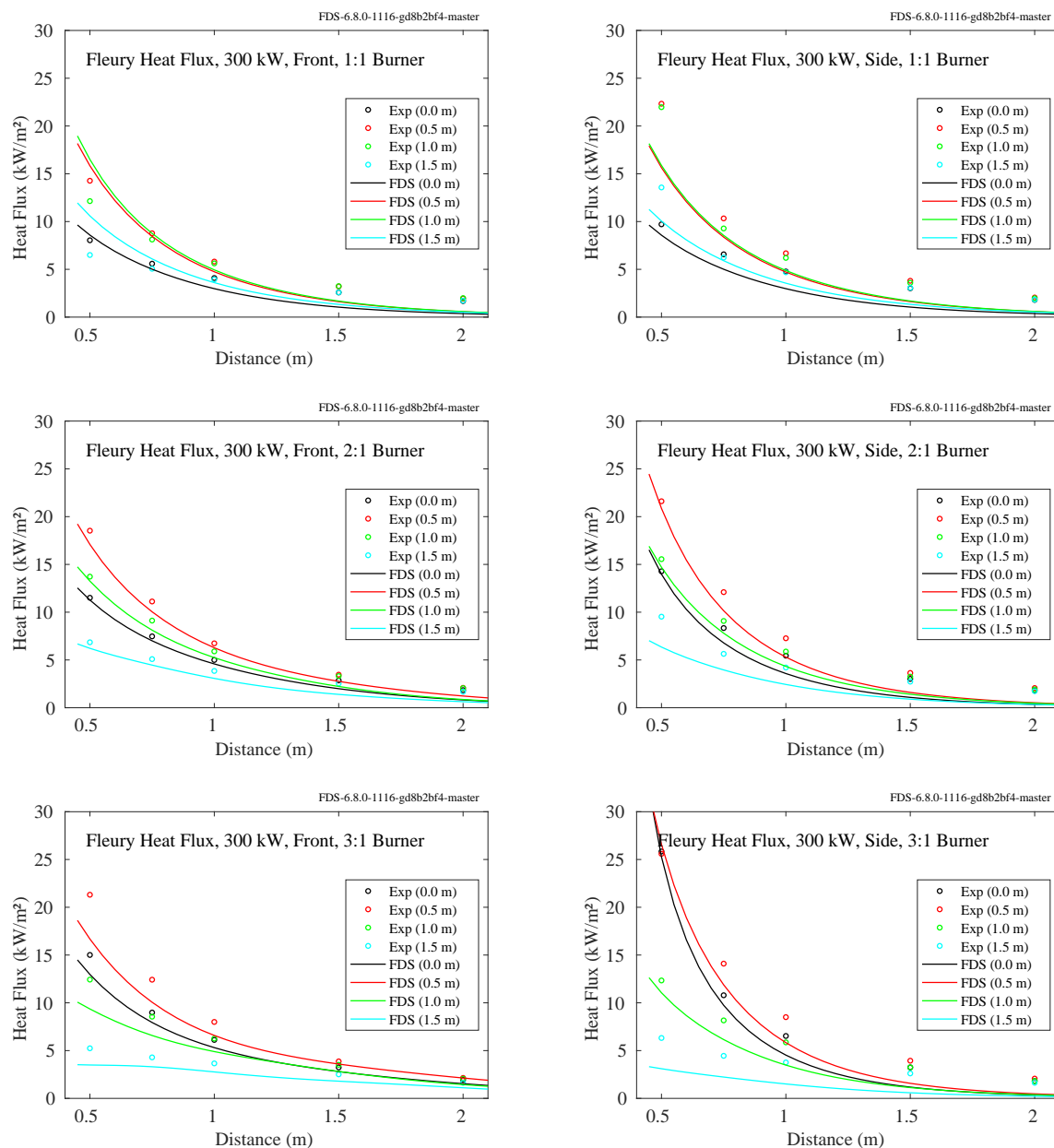


Figure 12.52: Comparison of predicted (lines) and measured (circles) heat flux for the 300 kW Fleury fires.

12.2.2 Hamins Gas Burner Experiments

Predicted and measured radial and vertical heat flux profiles from 30 methane, 34 propane, and 16 acetylene gas burner fire experiments conducted by Anthony Hamins [376] are displayed in this section. The relevant information about the fires is included in Tables 12.3, 12.4, and 12.5. In each table, D is the diameter of the burner and R_0 is the radial distance from the burner centerline to the position of the vertical heat flux measurements. \dot{Q} is the product of the mass loss rate, \dot{m} , and the heat of combustion. The heat of combustion of acetylene is 48.2 kJ/g; and for propane, 46.4 kJ/g. For the methane experiments, either methane (50.03 kJ/g) or natural gas (49.4 kJ/g) was used. \dot{Q}'' is the heat release rate per unit area, and

$$\dot{Q}^* = \frac{\dot{Q}}{\rho_\infty T_\infty c_p \sqrt{g} D D^2} \quad ; \quad D^* = \left(\frac{\dot{Q}}{\rho_\infty T_\infty c_p \sqrt{g}} \right)^{2/5} \quad (12.2)$$

Note that in the test matrices, the values to the right of the double lines indicate parameters used in the simulations. The values for radiative fraction, χ_{rad} , are suggested by Hamins [376]. The quantity $D^*/\delta x$ is an indicator of grid resolution, where D^* is the characteristic burner dimension and δx is the grid cell size.

Methane Experiments

Table 12.3: Parameters of the Hamins methane burner experiments. The asterisk after the Test No. indicates that natural gas was used as fuel. The soot and CO yields were assumed to be zero.

Test No.	D (m)	R_0 (m)	\dot{Q} (kW)	\dot{m} (g/s)	\dot{Q}'' (kW/m ²)	\dot{Q}^*	χ_{rad}	$D^*/\delta x$
1	0.1	0.13	0.42	0.0085	53.5	0.12	0.13	8.6
2	0.1	0.13	0.61	0.0122	77.7	0.18	0.13	10.0
3	0.1	0.13	0.78	0.0155	99.3	0.22	0.13	11.0
4	0.1	0.13	1.11	0.0222	141.3	0.32	0.16	12.7
5	0.1	0.13	1.89	0.0378	240.6	0.54	0.16	15.7
6*	0.35	0.40	11.2	0.226	115.9	0.14	0.08	6.4
7*	0.35	0.40	15.3	0.310	159.0	0.19	0.10	7.2
8*	0.35	0.40	10.5	0.212	109.0	0.13	0.08	6.2
9*	0.35	0.40	6.67	0.135	69.3	0.08	0.07	5.2
10*	0.35	0.64	19.3	0.391	200.7	0.24	0.12	7.9
11*	0.35	0.63	27.0	0.546	280.3	0.34	0.15	9.1
12*	0.35	0.81	40.6	0.822	422.2	0.51	0.18	10.7
13*	0.35	0.92	63.5	1.285	659.9	0.80	0.21	12.8
14*	0.35	0.92	90.3	1.828	938.7	1.13	0.22	14.7
15	0.35	0.92	178	3.567	1854.6	2.24	0.20	19.3
16	0.35	0.92	210	4.194	2180.8	2.63	0.20	20.6
17	0.35	0.92	34.0	0.679	353.2	0.43	0.16	9.9
18	0.35	0.90	145	2.904	1510.0	1.82	0.28	17.8
19	0.35	0.90	125	2.495	1297.7	1.56	0.23	16.7
20*	1.0	1.00	49.0	0.997	62.4	0.04	0.14	5.8
21*	1.0	1.00	81.0	1.648	103.1	0.07	0.15	7.0
22*	1.0	1.00	112	2.282	142.8	0.10	0.17	8.0
23*	1.0	1.00	129	2.635	164.8	0.12	0.18	8.5
24*	1.0	0.79	52.7	1.069	67.1	0.05	0.12	5.9
25*	1.0	0.79	69.7	1.414	88.8	0.06	0.12	6.6
26*	1.0	0.79	87.3	1.771	111.2	0.08	0.13	7.3
27*	1.0	0.79	102	2.081	130.6	0.09	0.13	7.7
28*	1.0	0.79	121	2.462	154.5	0.11	0.14	8.3
29*	1.0	0.79	138	2.793	175.3	0.12	0.16	8.7
30*	1.0	0.79	172	3.482	218.5	0.16	0.18	9.5

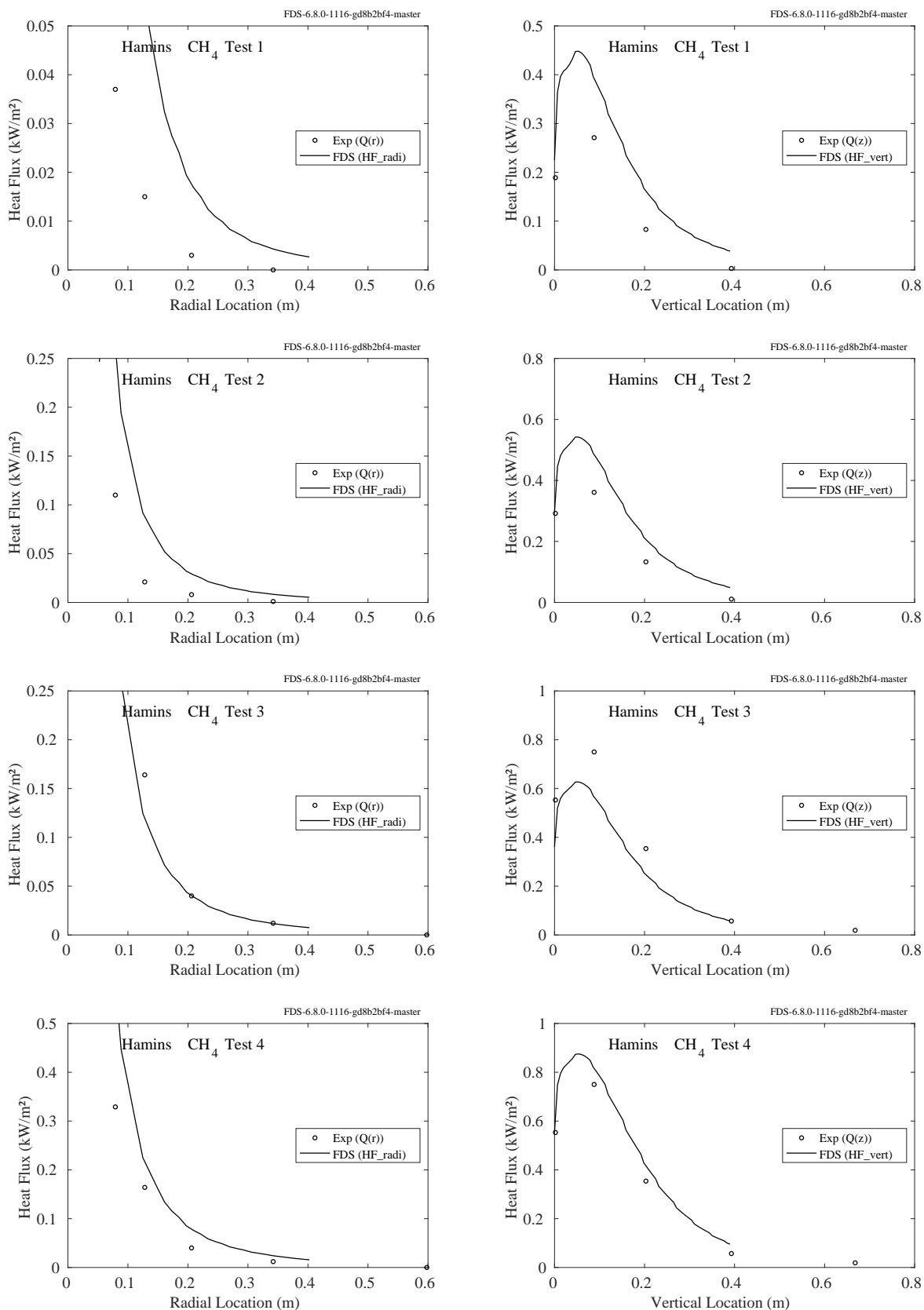


Figure 12.53: Comparison of predicted and measured heat fluxes, Hamins Methane Tests 1-4.

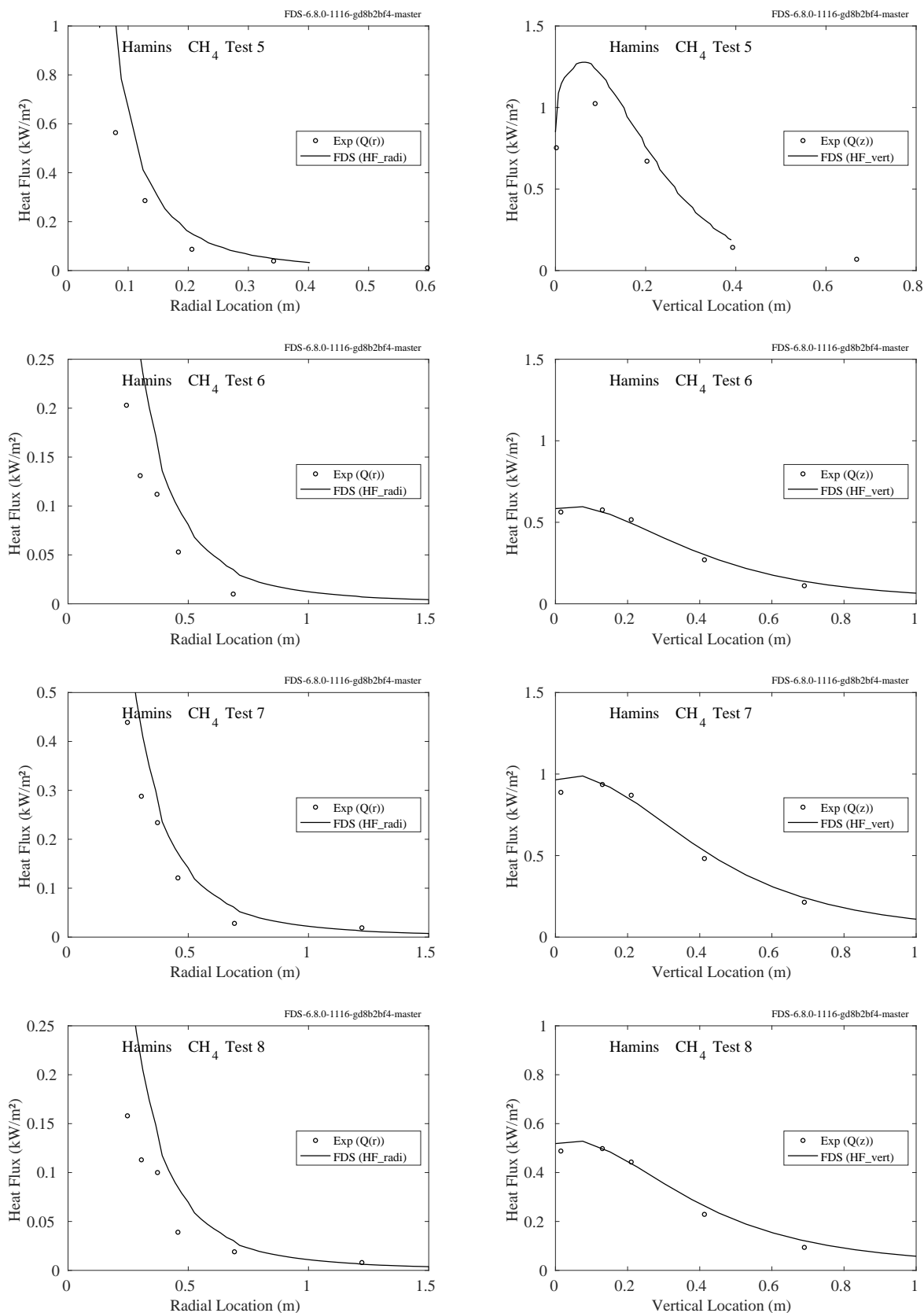


Figure 12.54: Comparison of predicted and measured heat fluxes, Hamins Methane Tests 5-8.

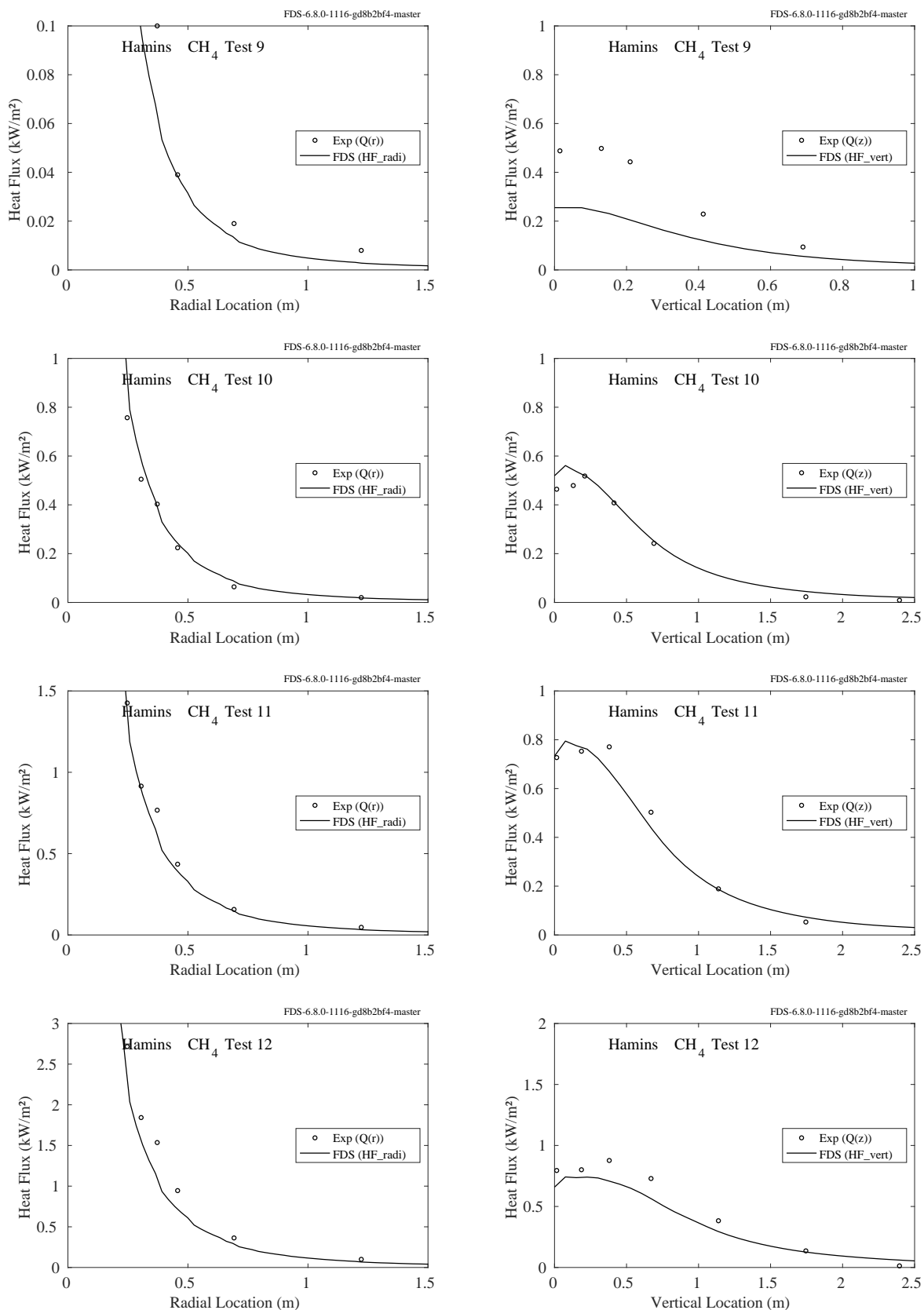


Figure 12.55: Comparison of predicted and measured heat fluxes, Hamins Methane Tests 9-12.

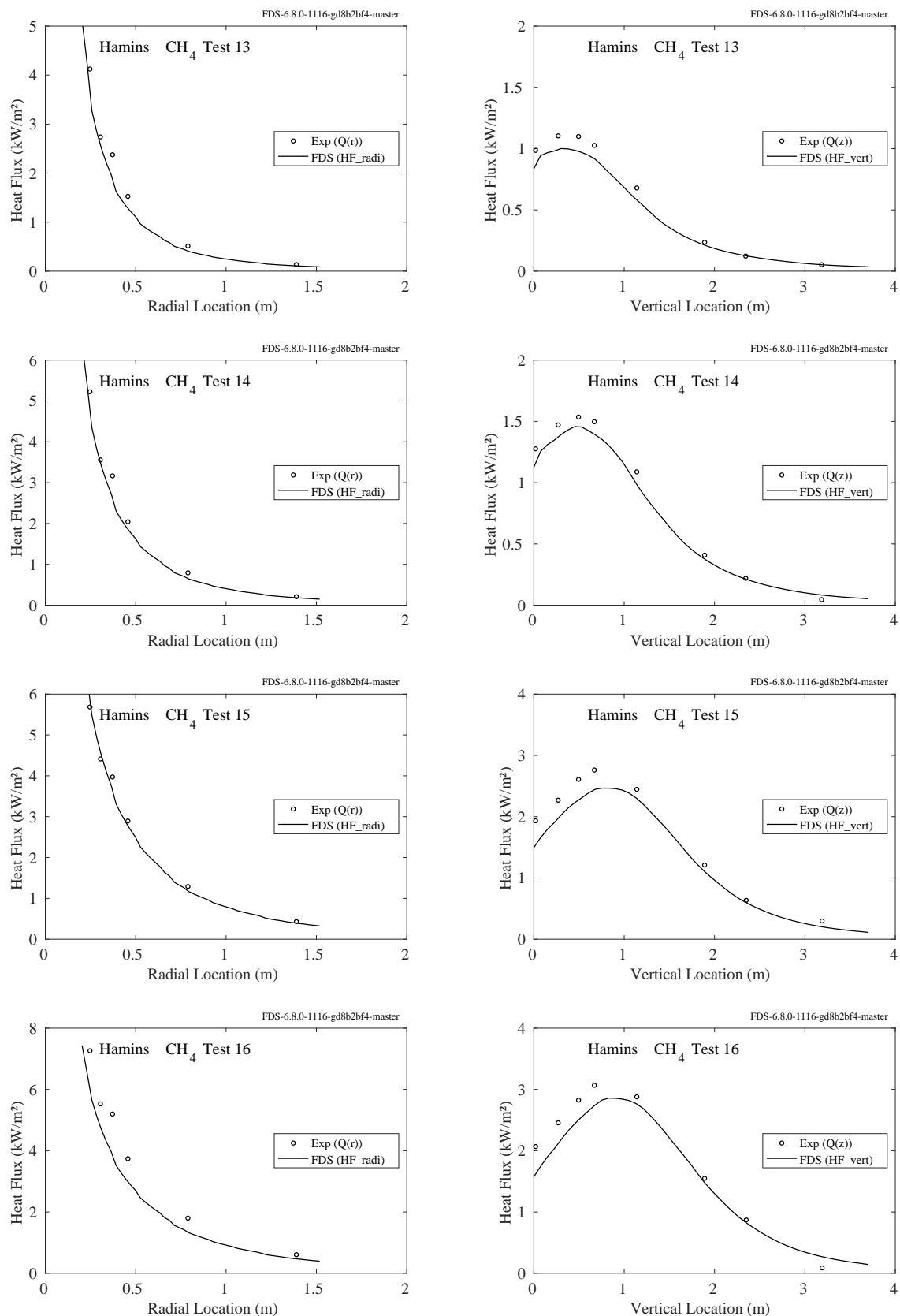


Figure 12.56: Comparison of predicted and measured heat fluxes, Hamins Methane Tests 13-16.

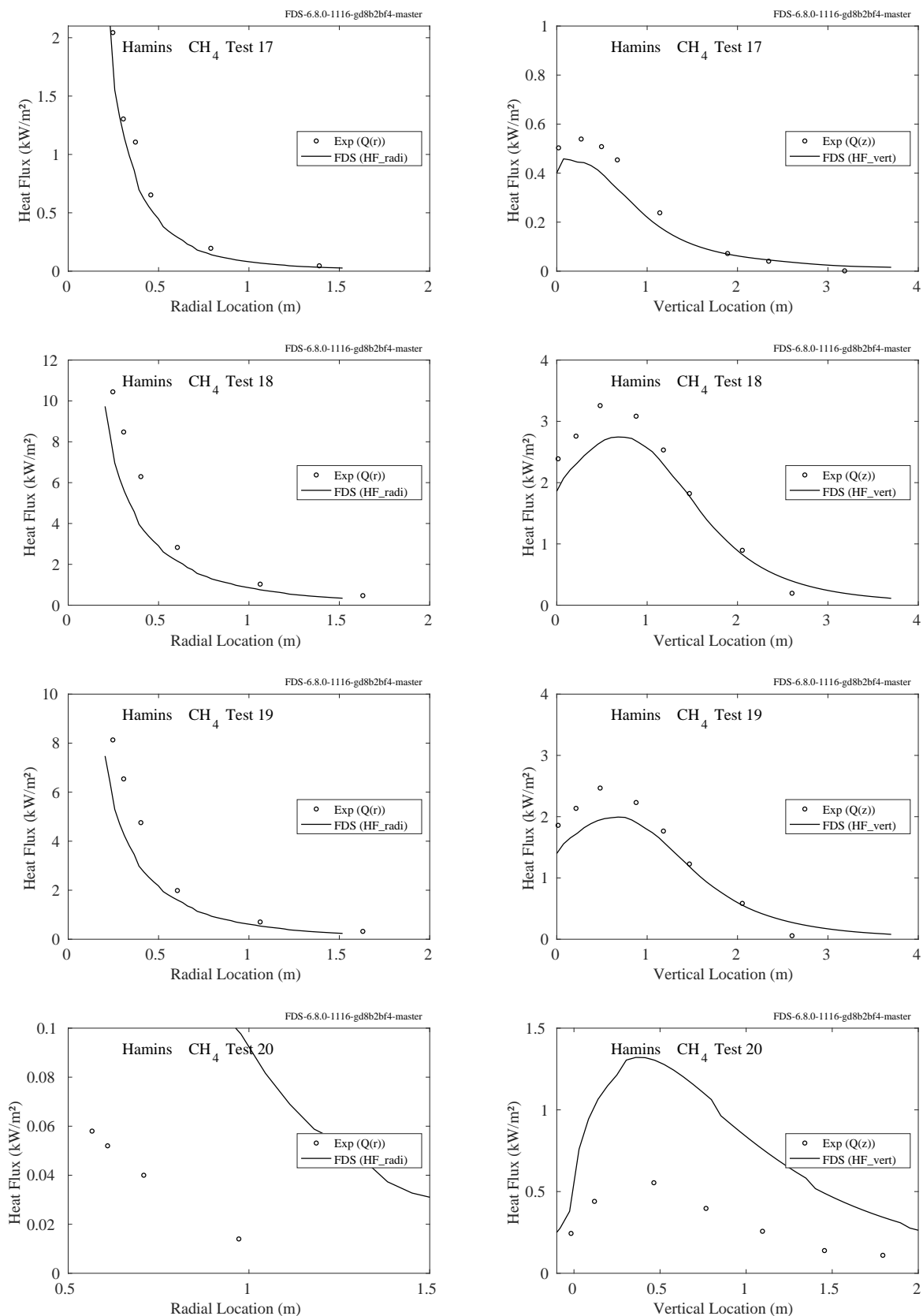


Figure 12.57: Comparison of predicted and measured heat fluxes, Hamins Methane Tests 17-20.

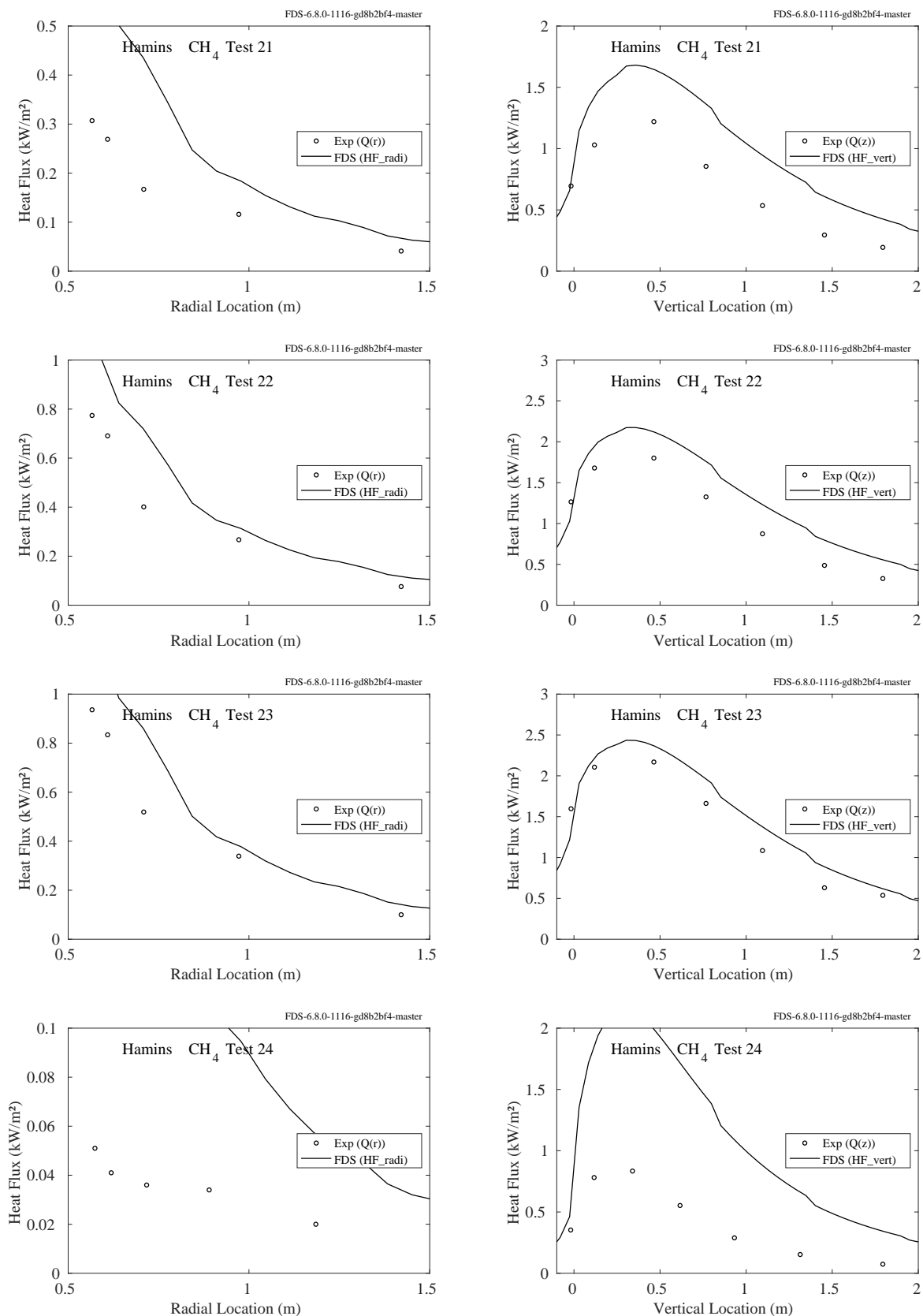


Figure 12.58: Comparison of predicted and measured heat fluxes, Hamins Methane Tests 21-24.

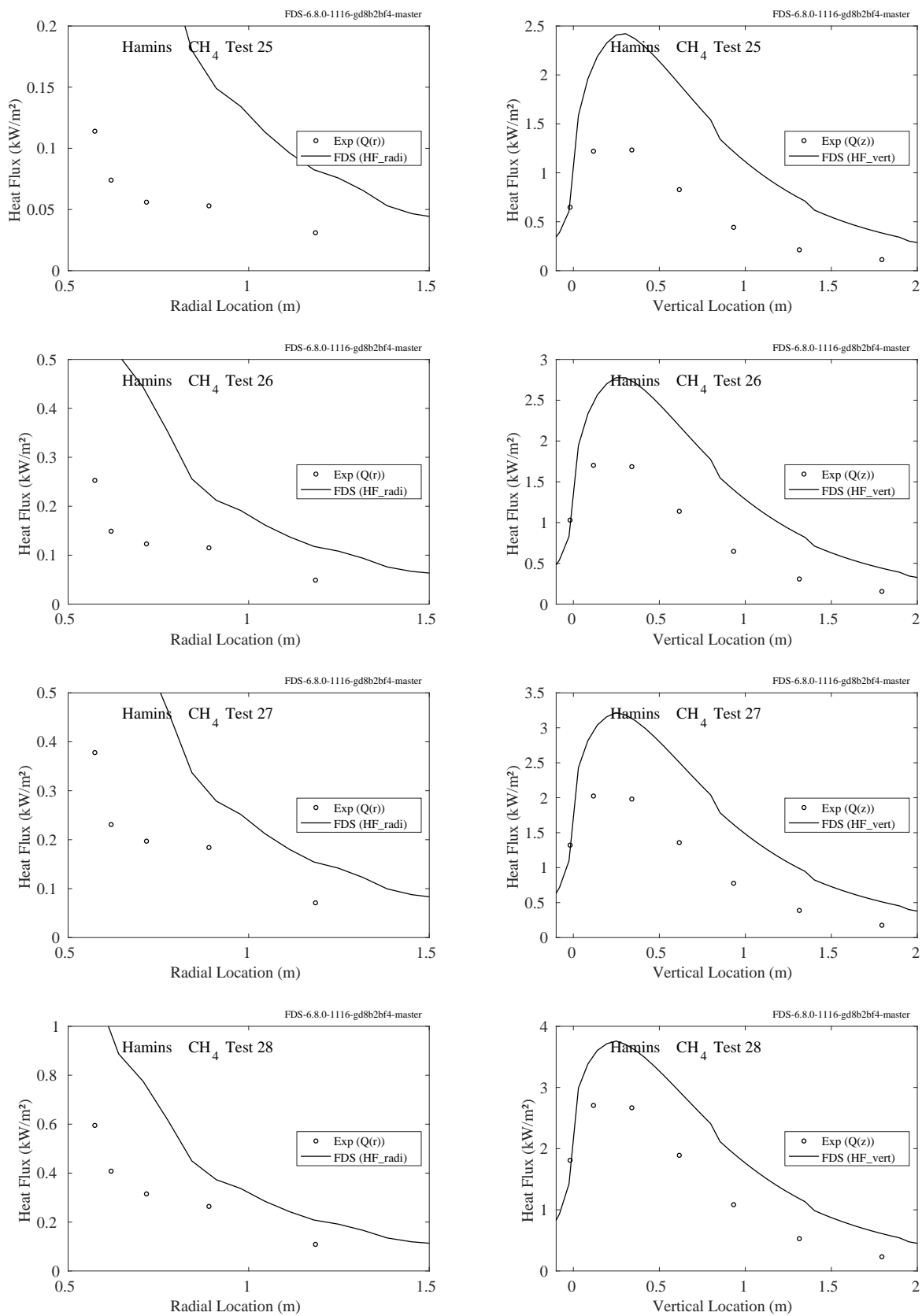


Figure 12.59: Comparison of predicted and measured heat fluxes, Hamins Methane Tests 25-28.

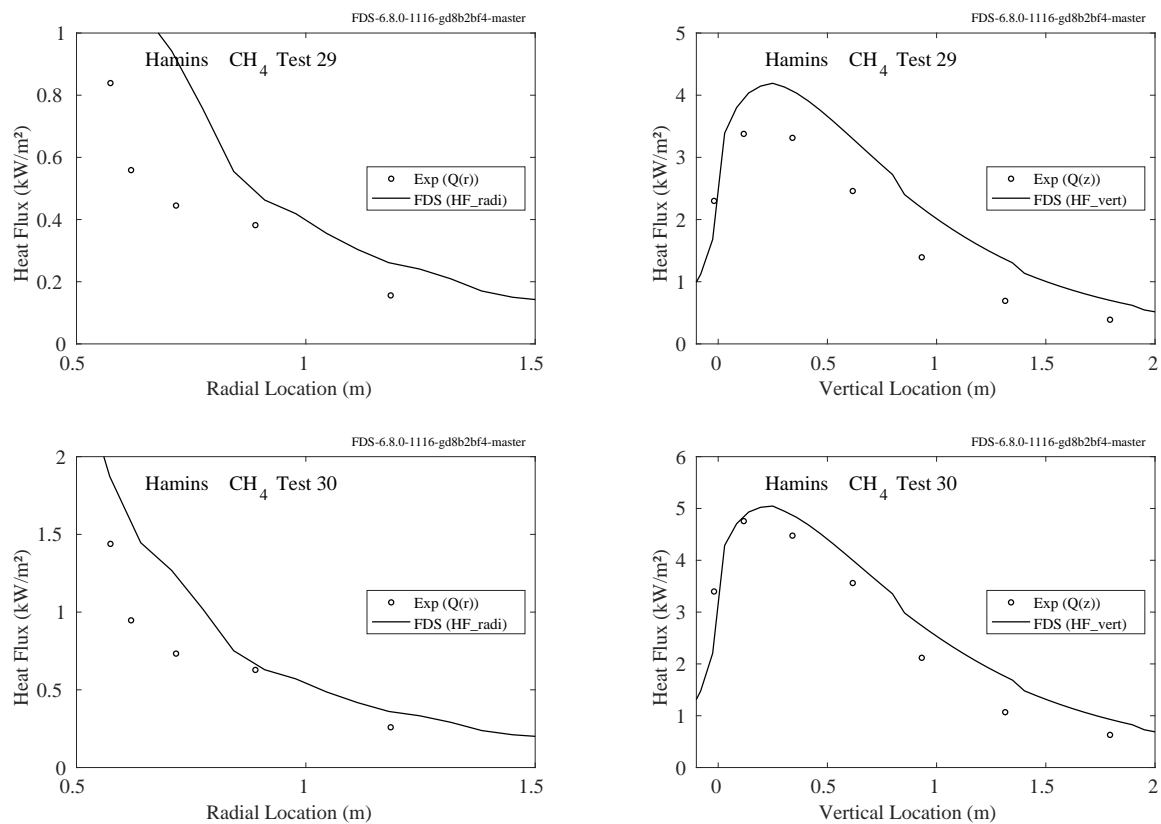


Figure 12.60: Comparison of predicted and measured heat fluxes, Hamins Methane Tests 29-30.

Propane Experiments

Table 12.4: Parameters of the Hamins propane burner experiments. Note that in all cases, the soot and CO yields were taken to be 0.024 and 0.005, respectively, based on the measurements of Tewarson [151].

Test No.	D (m)	R_0 (m)	\dot{Q} (kW)	\dot{m} (kg/s)	\dot{Q}'' (kW/m ²)	\dot{Q}^*	χ_{rad}	$D^*/\delta x$
1	0.1	0.26	2.7	0.058	343.8	0.78	0.22	9.0
2	0.1	0.26	6.8	0.148	870.9	1.96	0.27	13.1
3	0.1	0.26	11.8	0.254	1499.9	3.38	0.29	16.3
4	0.1	0.37	17.9	0.386	2277.8	5.14	0.29	19.2
5	0.1	0.37	25.2	0.543	3203.5	7.22	0.30	22.1
6	0.1	0.49	36.9	0.796	4698.3	10.6	0.30	25.7
7	0.1	0.13	0.4	0.010	56.0	0.13	0.12	4.4
8	0.1	0.13	0.8	0.017	99.3	0.22	0.12	5.5
9	0.1	0.13	0.6	0.013	76.4	0.17	0.12	4.9
10	0.1	0.13	1.0	0.021	123.5	0.28	0.15	6.0
11	0.1	0.13	1.4	0.031	183.3	0.41	0.18	7.0
12	0.1	0.13	2.2	0.046	273.7	0.62	0.23	8.2
13	0.1	0.19	3.4	0.074	434.2	0.98	0.24	9.9
14	0.1	0.19	5.6	0.122	718.1	1.62	0.26	12.1
15	0.1	0.28	11.9	0.257	1513.9	3.41	0.26	16.3
16	0.1	0.28	24.8	0.535	3156.4	7.12	0.29	21.9
17	0.35	0.92	33.9	0.732	352.8	0.43	0.25	9.9
18	0.35	0.92	124.9	2.694	1298.1	1.56	0.30	16.7
19	0.35	0.57	20.0	0.431	207.9	0.25	0.18	8.0
20	0.35	0.57	15.6	0.336	162.0	0.20	0.14	7.3
21	0.35	0.39	19.0	0.409	197.3	0.24	0.13	7.9
22	0.35	0.39	14.6	0.316	152.2	0.18	0.10	7.1
23	0.35	0.68	108.2	2.334	1124.5	1.36	0.29	15.8
24	0.35	0.68	102.3	2.207	1063.7	1.28	0.31	15.5
25	0.35	0.68	79.7	1.719	828.4	1.00	0.28	14.0
26	0.35	0.51	12.0	0.258	124.5	0.15	0.08	6.6
27	1.0	0.81	55.2	1.190	70.2	0.05	0.11	6.0
28	1.0	0.81	81.7	1.761	104.0	0.07	0.15	7.1
29	1.0	0.81	107.3	2.315	136.7	0.10	0.18	7.9
30	1.0	1.00	136.4	2.943	173.7	0.12	0.22	8.7
31	1.0	0.97	55.6	1.199	70.8	0.05	0.12	6.1
32	1.0	0.97	82.5	1.779	105.0	0.07	0.14	7.1
33	1.0	0.97	107.9	2.326	137.3	0.10	0.17	7.9
34	1.0	0.97	137.3	2.963	174.9	0.12	0.23	8.7

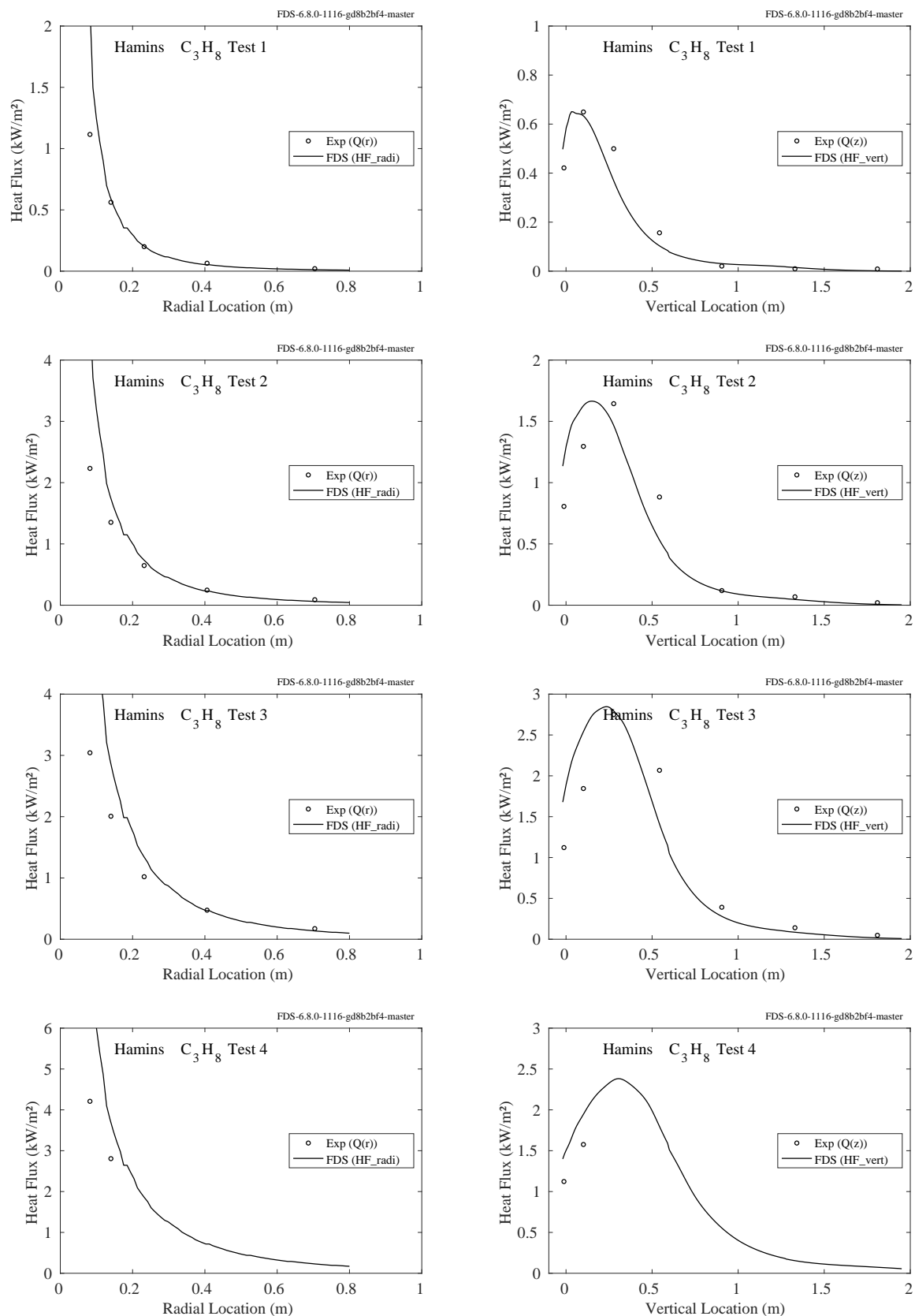


Figure 12.61: Comparison of predicted and measured heat fluxes, Hamins Propane Tests 1-4.

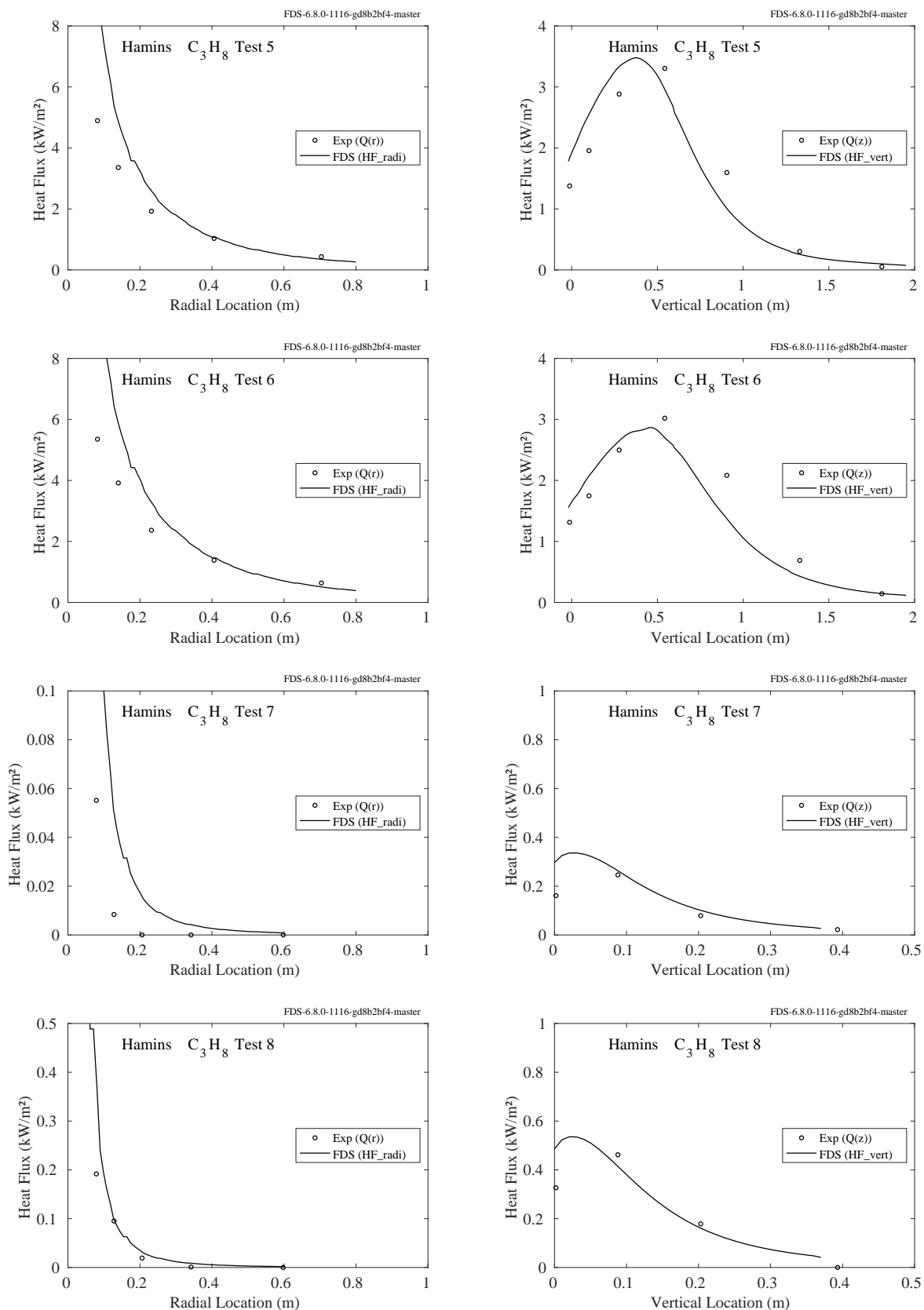


Figure 12.62: Comparison of predicted and measured heat fluxes, Hamins Propane Tests 5-8.

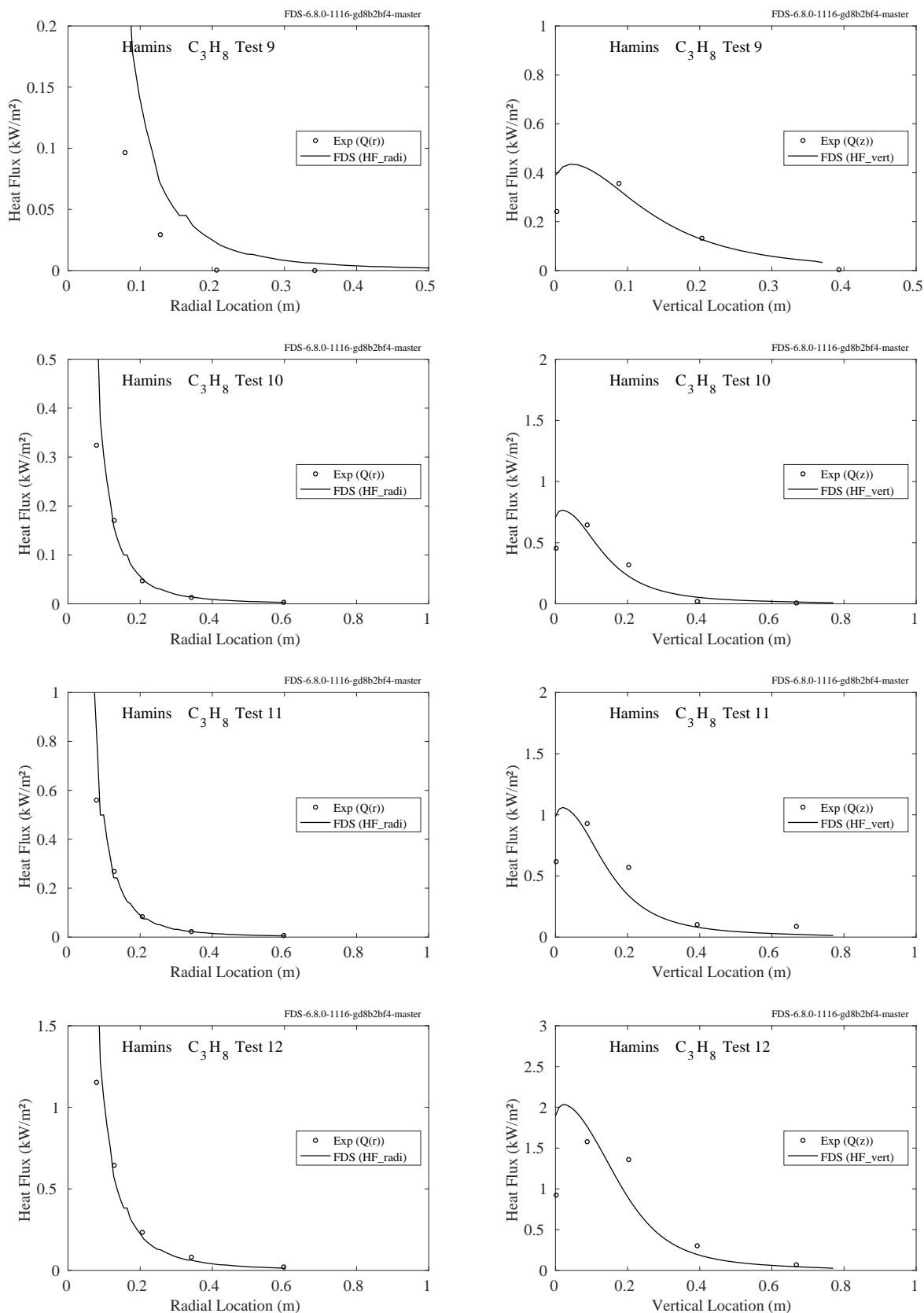


Figure 12.63: Comparison of predicted and measured heat fluxes, Hamins Propane Tests 9-12.

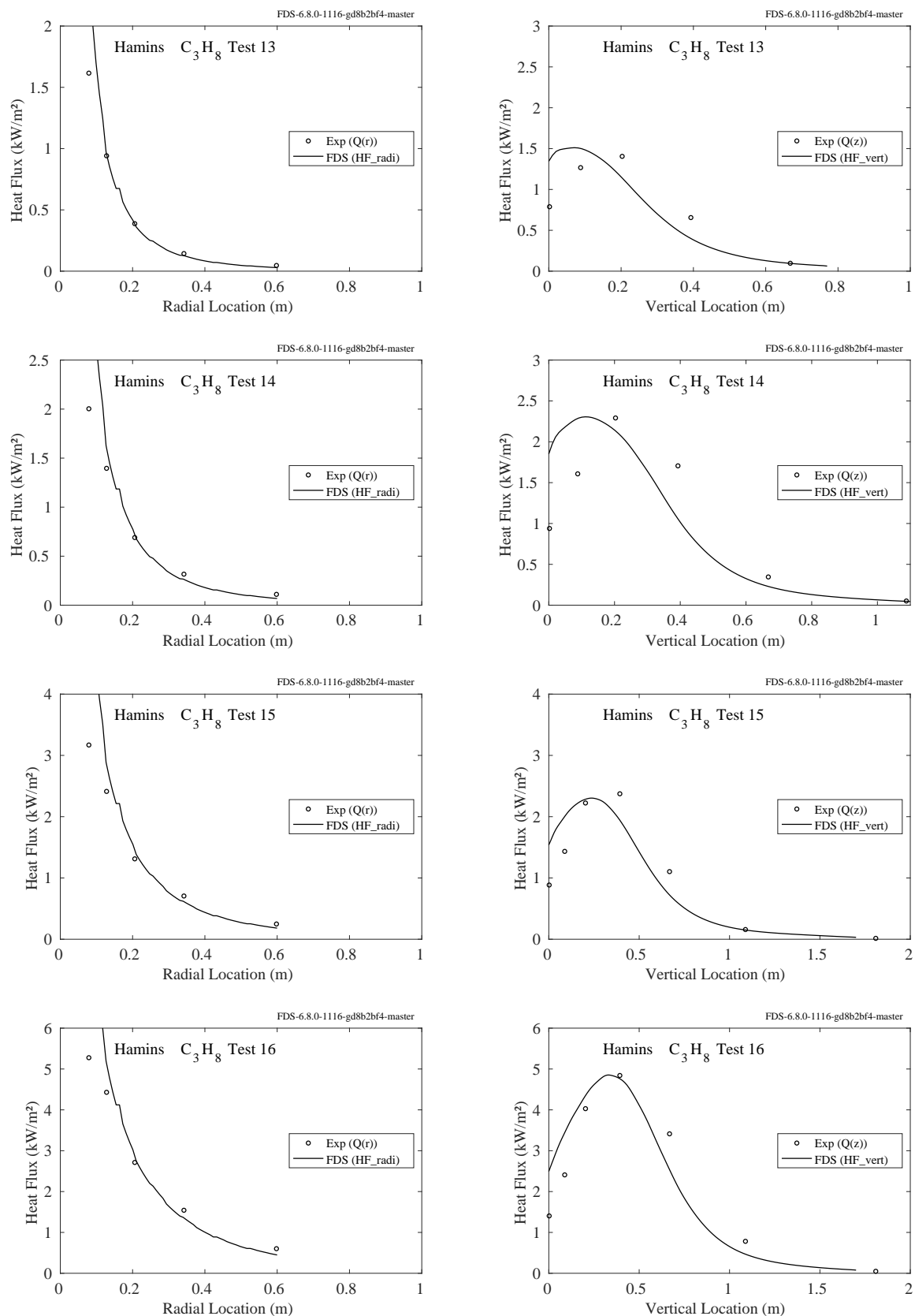


Figure 12.64: Comparison of predicted and measured heat fluxes, Hamins Propane Tests 13-16.

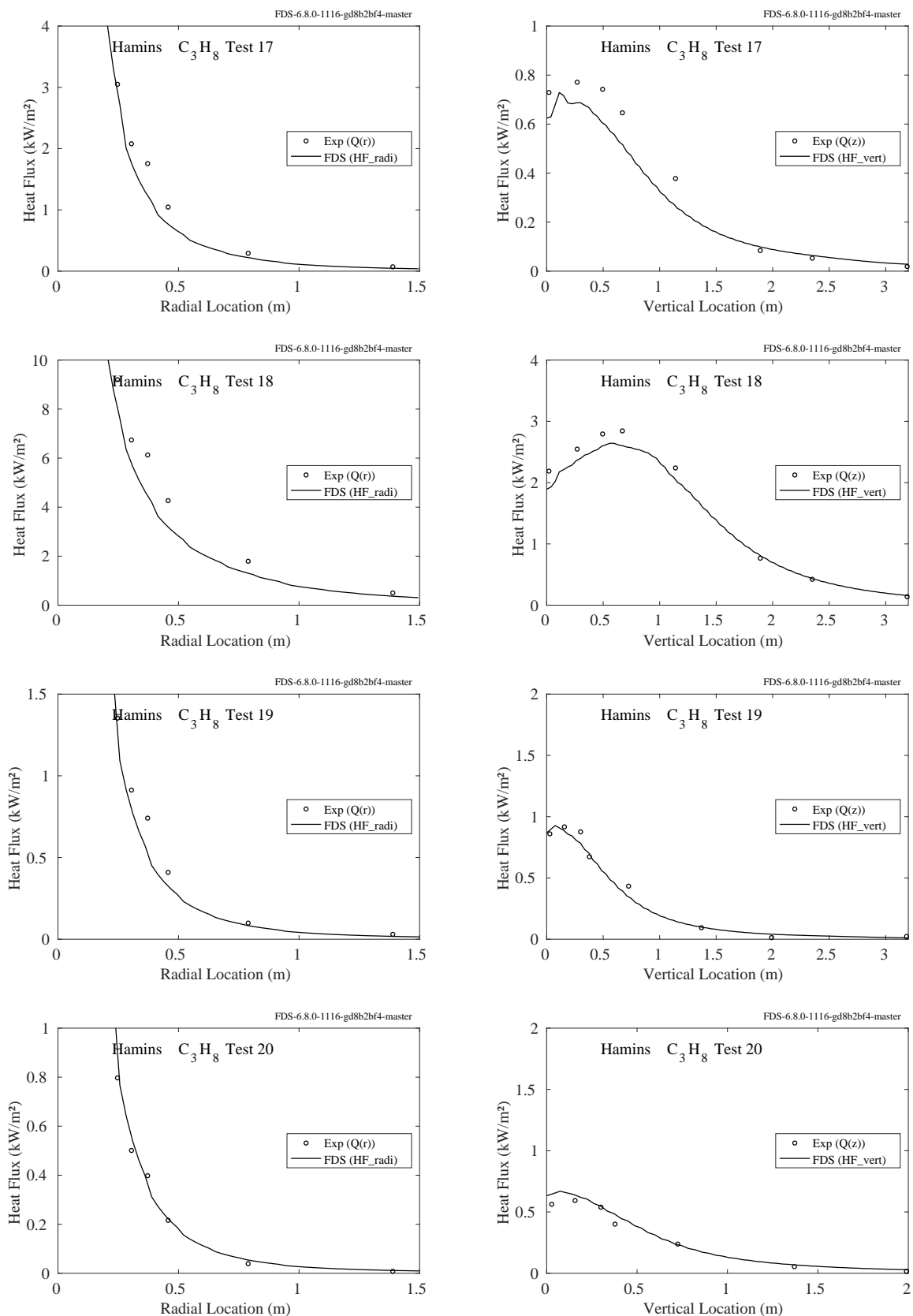


Figure 12.65: Comparison of predicted and measured heat fluxes, Hamins Propane Tests 17-20.

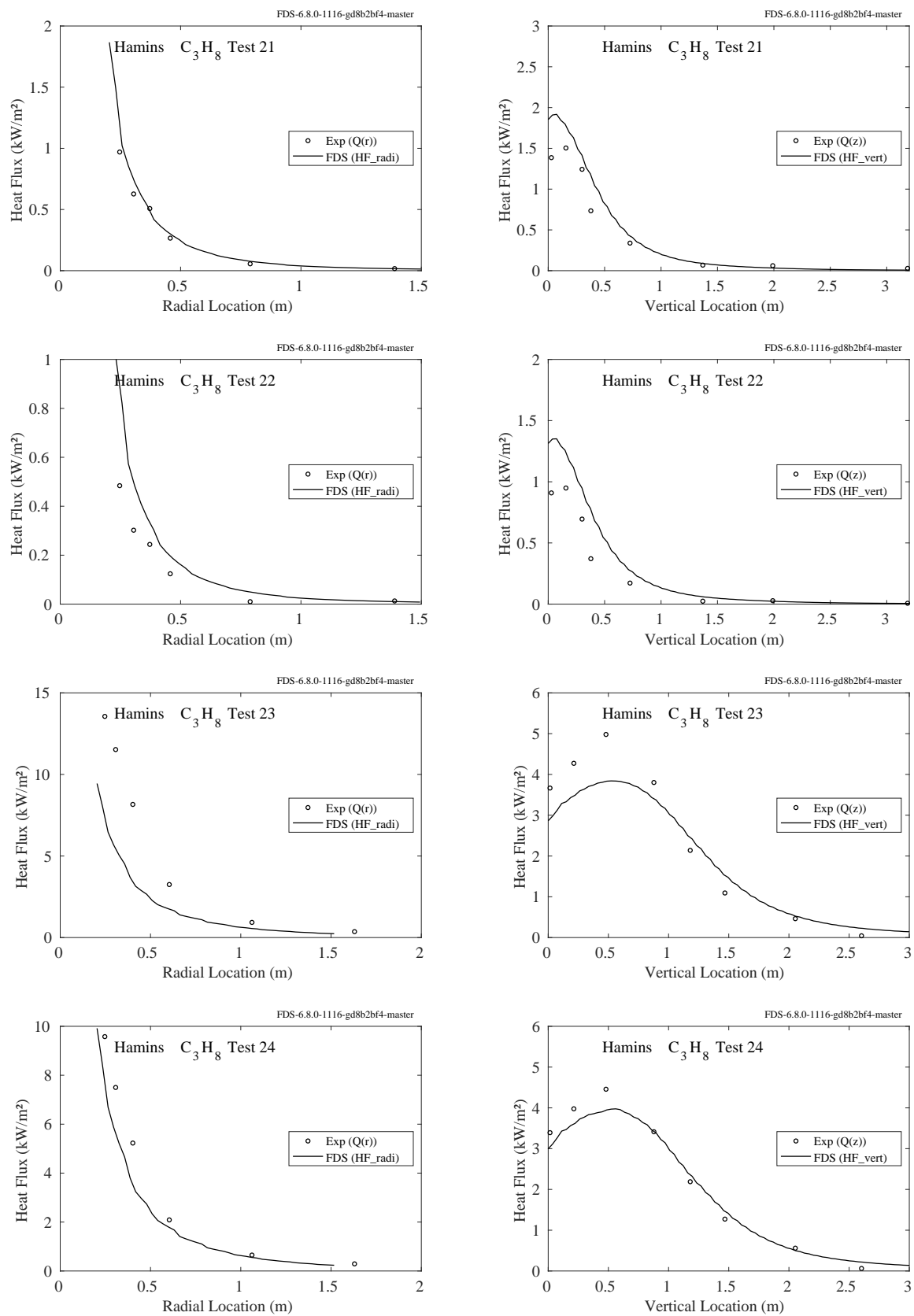


Figure 12.66: Comparison of predicted and measured heat fluxes, Hamins Propane Tests 21-24.

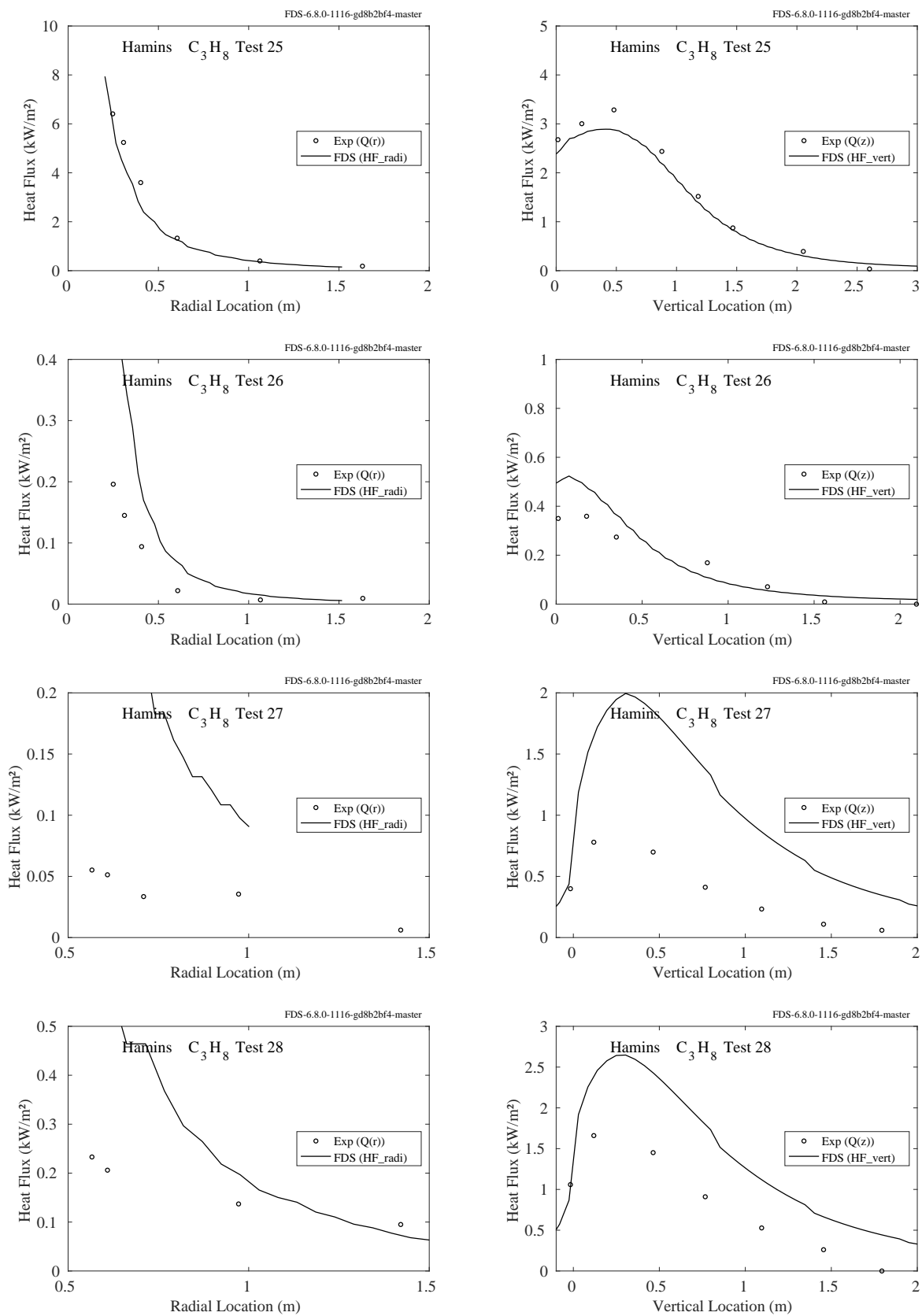


Figure 12.67: Comparison of predicted and measured heat fluxes, Hamins Propane Tests 25-28.

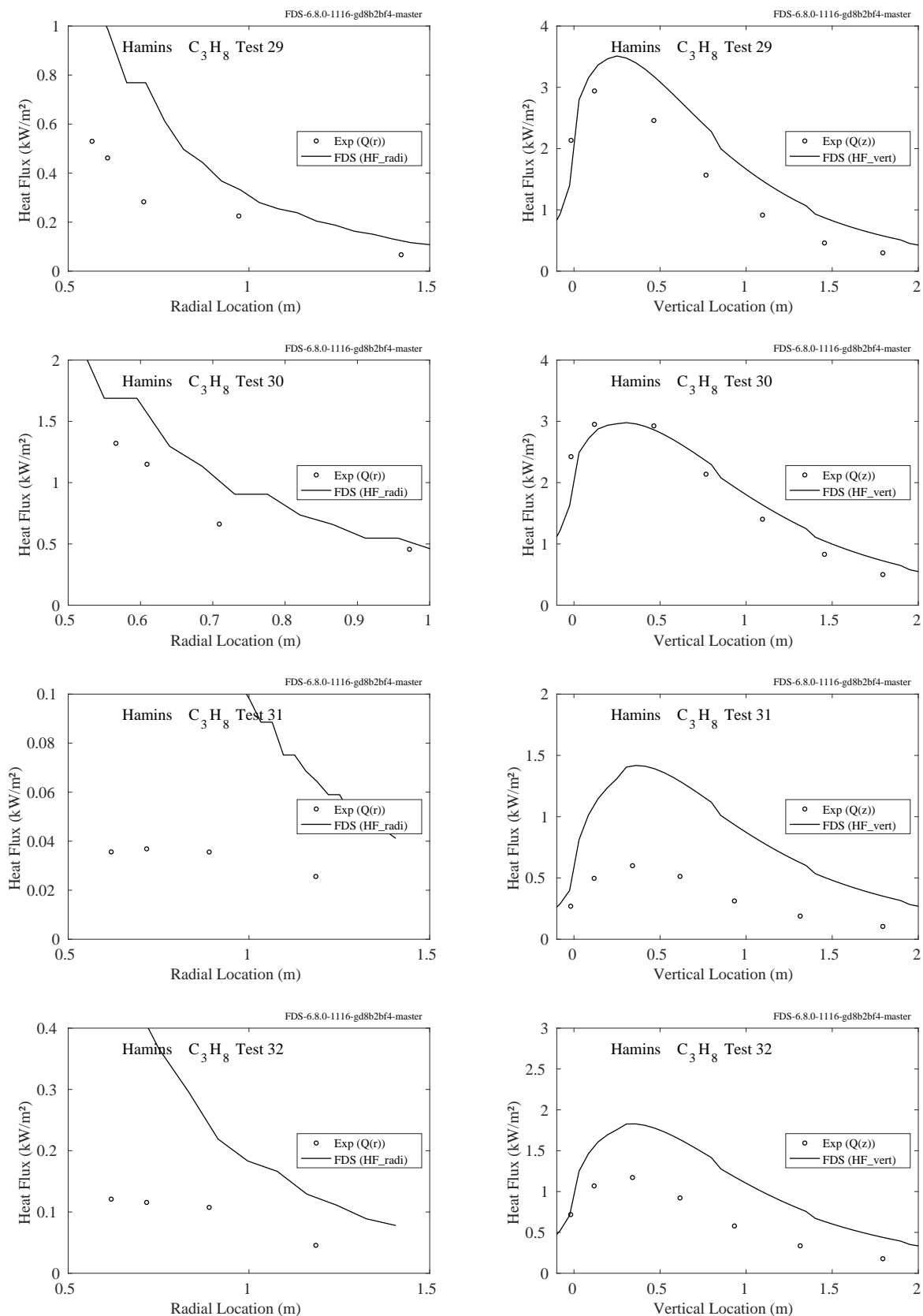


Figure 12.68: Comparison of predicted and measured heat fluxes, Hamins Propane Tests 29-32.

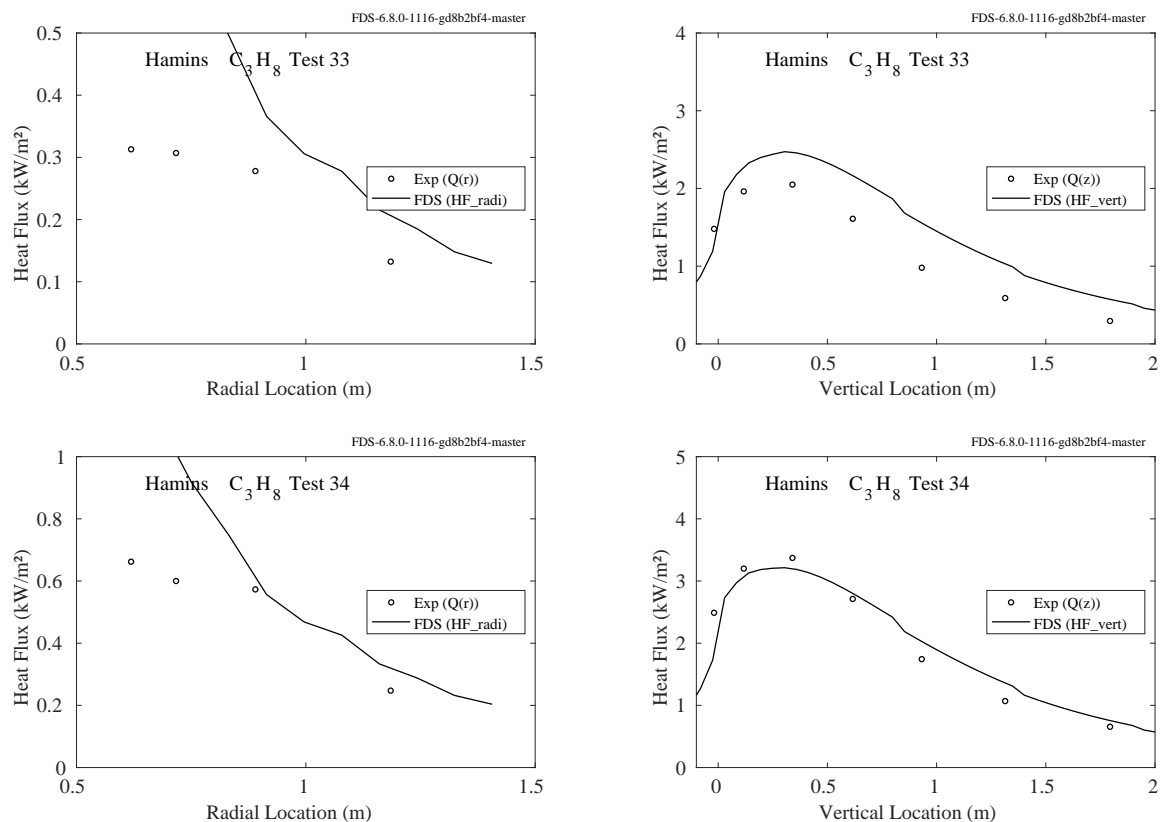


Figure 12.69: Comparison of predicted and measured heat fluxes, Hamins Propane Tests 33-34.

Acetylene Experiments

Table 12.5: Parameters of the Hamins acetylene burner experiments. Note that in all cases, the soot and CO yields were taken to be 0.096 and 0.042, respectively, based on the measurements of Tewarson [151].

Test No.	D (m)	R_0 (m)	\dot{Q} (kW)	\dot{m} (kg/s)	\dot{Q}'' (kW/m ²)	\dot{Q}^*	χ_{rad}	$D^*/\delta x$
1	0.10	0.13	0.45	0.009	57.3	0.13	0.12	4.4
2	0.10	0.13	0.56	0.012	71.3	0.16	0.15	4.8
3	0.10	0.13	0.90	0.019	114.6	0.26	0.18	5.8
4	0.10	0.13	1.29	0.027	164.2	0.37	0.27	6.7
5	0.10	0.13	1.54	0.032	196.1	0.44	0.31	7.2
6	0.35	0.39	12.5	0.259	129.9	0.16	0.13	6.7
7	0.35	0.51	11.0	0.229	114.3	0.14	0.09	6.3
8	0.35	0.51	20.4	0.424	212.0	0.26	0.22	8.1
9	0.35	0.51	31.3	0.648	325.3	0.39	0.33	9.6
10	0.35	0.69	38.2	0.793	397.0	0.48	0.38	10.4
11	0.35	0.69	48.0	1.000	498.9	0.60	0.41	11.4
12	0.35	0.69	62.4	1.290	648.6	0.78	0.42	12.7
13	0.35	0.69	76.3	1.580	793.0	0.96	0.43	13.8
14	0.35	0.69	109.2	2.270	1135.0	1.37	0.44	15.9
15	0.35	0.69	117.2	2.430	1218.2	1.47	0.43	16.3
16	0.35	0.69	134.7	2.790	1400.0	1.69	0.46	17.3

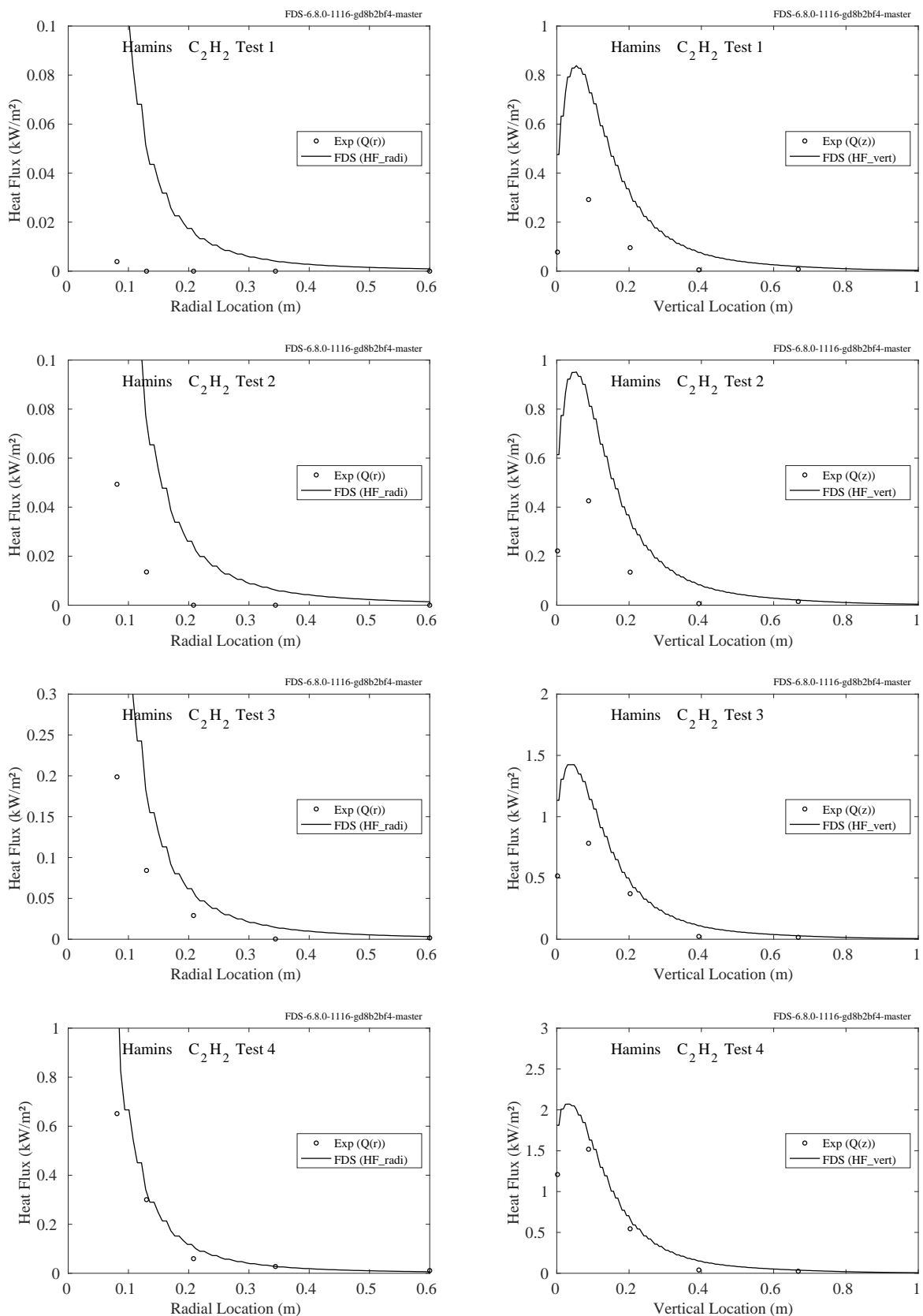


Figure 12.70: Comparison of predicted and measured heat fluxes, Hamins Acetylene Tests 1-4.

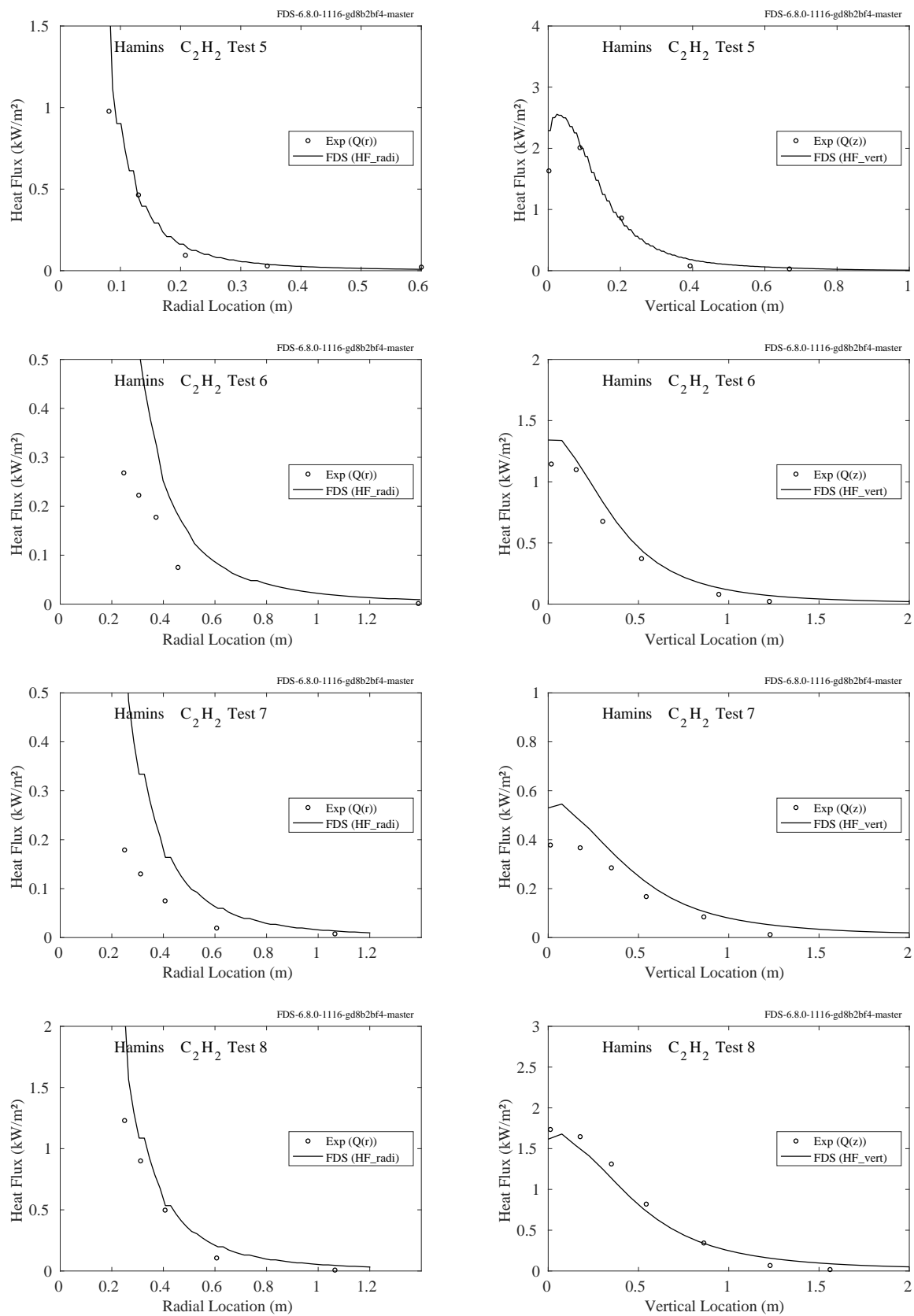


Figure 12.71: Comparison of predicted and measured heat fluxes, Hamins Acetylene Tests 5-8.

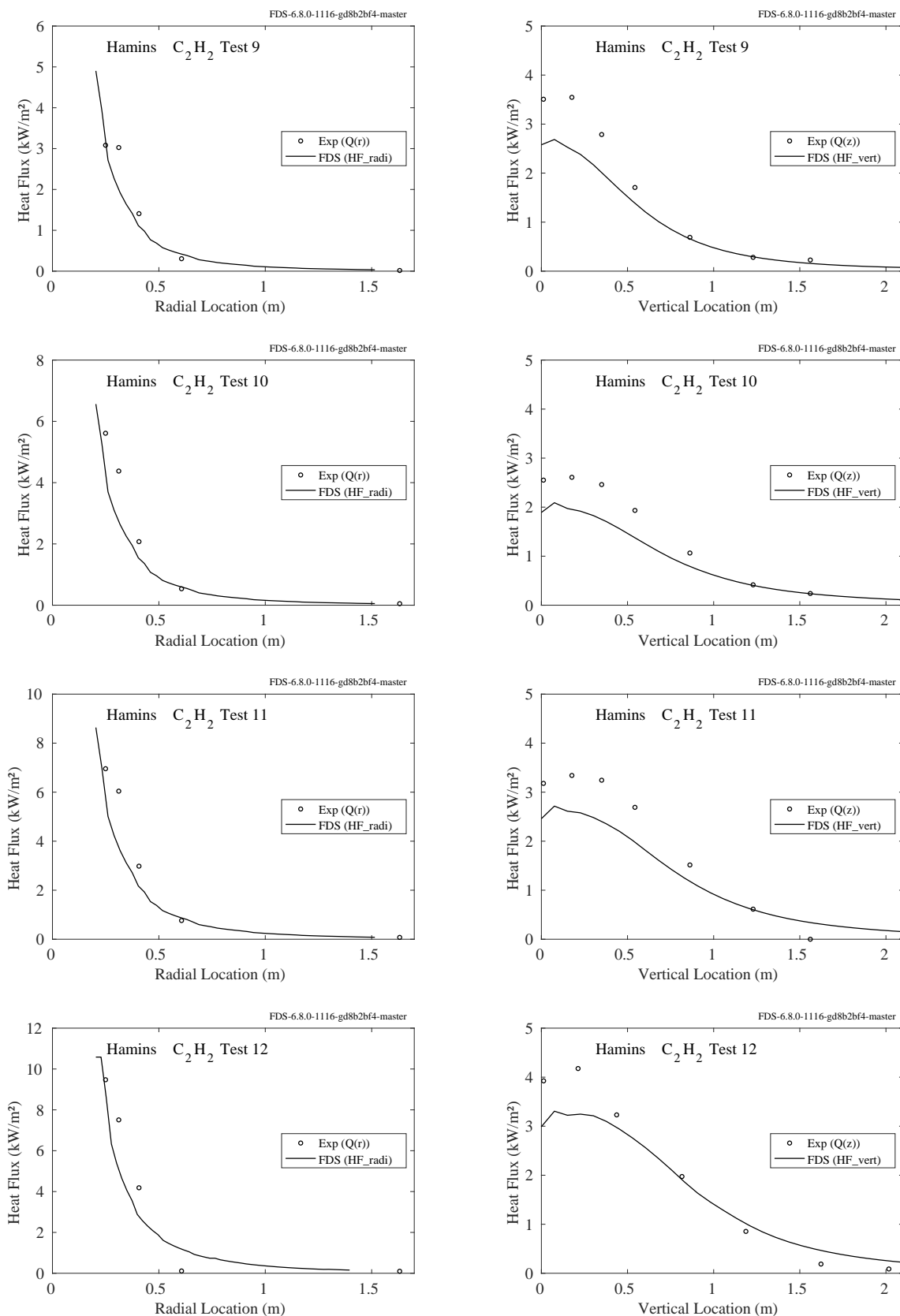


Figure 12.72: Comparison of predicted and measured heat fluxes, Hamins Acetylene Tests 9-12.

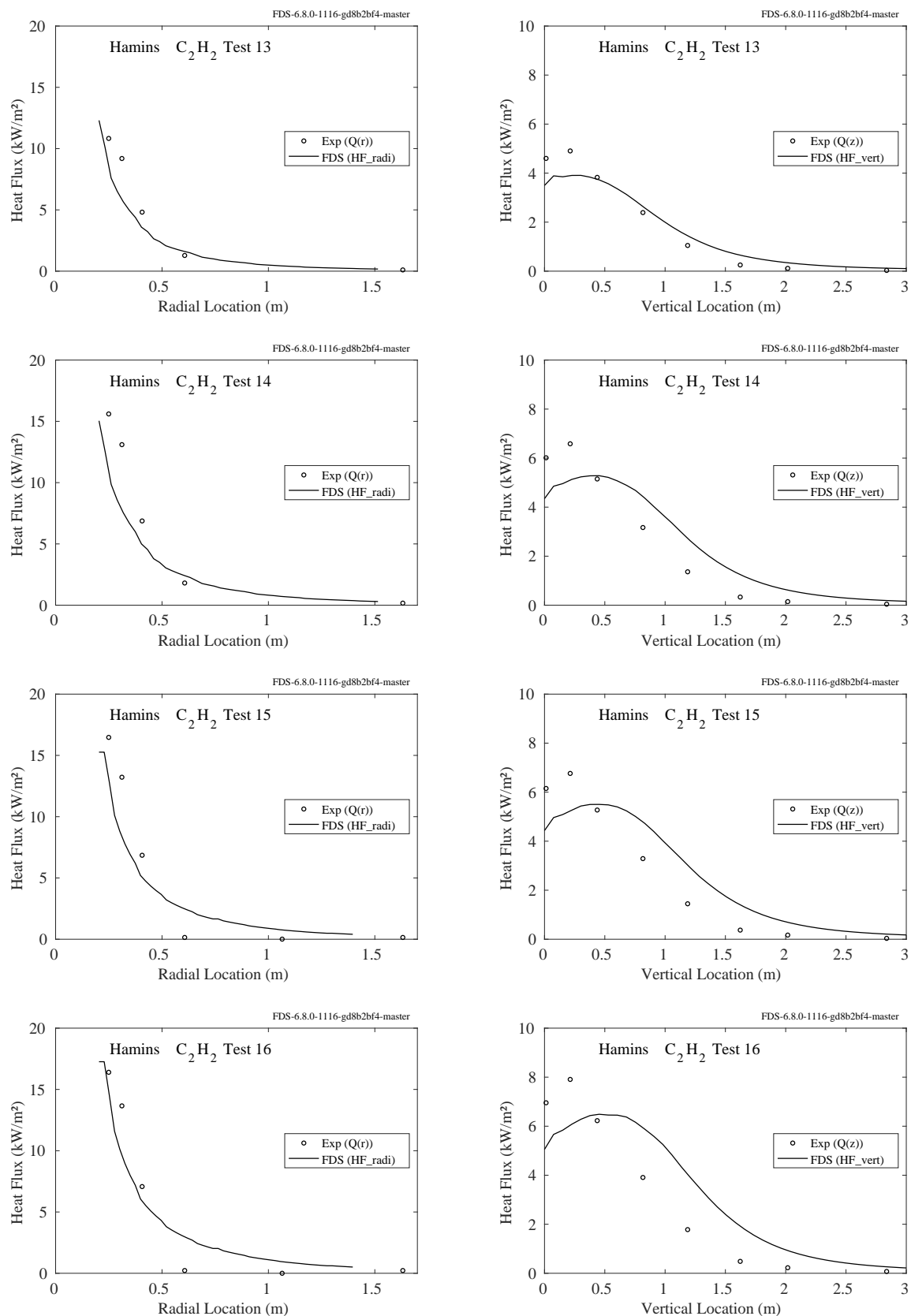


Figure 12.73: Comparison of predicted and measured heat fluxes, Hamins Acetylene Tests 13-16.

12.2.3 BGC/GRI LNG Fires

A description of the 13 LNG trench fire experiments is given in Sec. 3.7.

Figures 12.75 and 12.76 compare predicted and measured heat fluxes to radiometers at various distances from the LNG trench fire. The general layout of the facility is shown in Fig. 12.74. The radiometers were positioned approximately 1.2 m off the ground along the axis lines shown in the figure. The wind direction was typically perpendicular to the longer dimension of the trench.

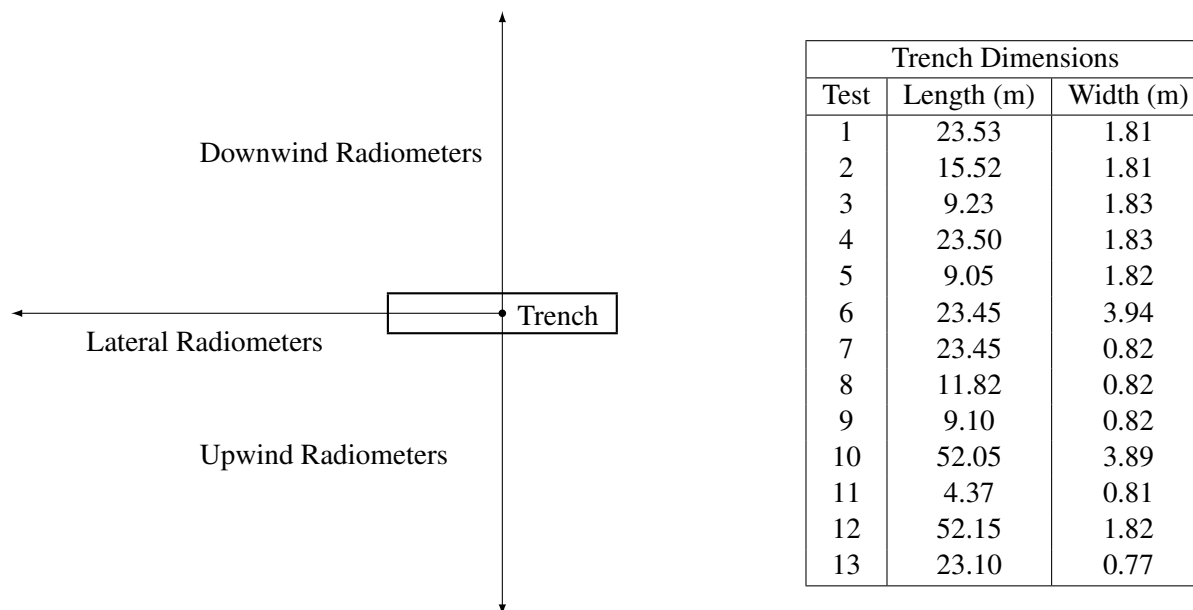


Figure 12.74: Schematic diagram of BGC/GRI test facility.

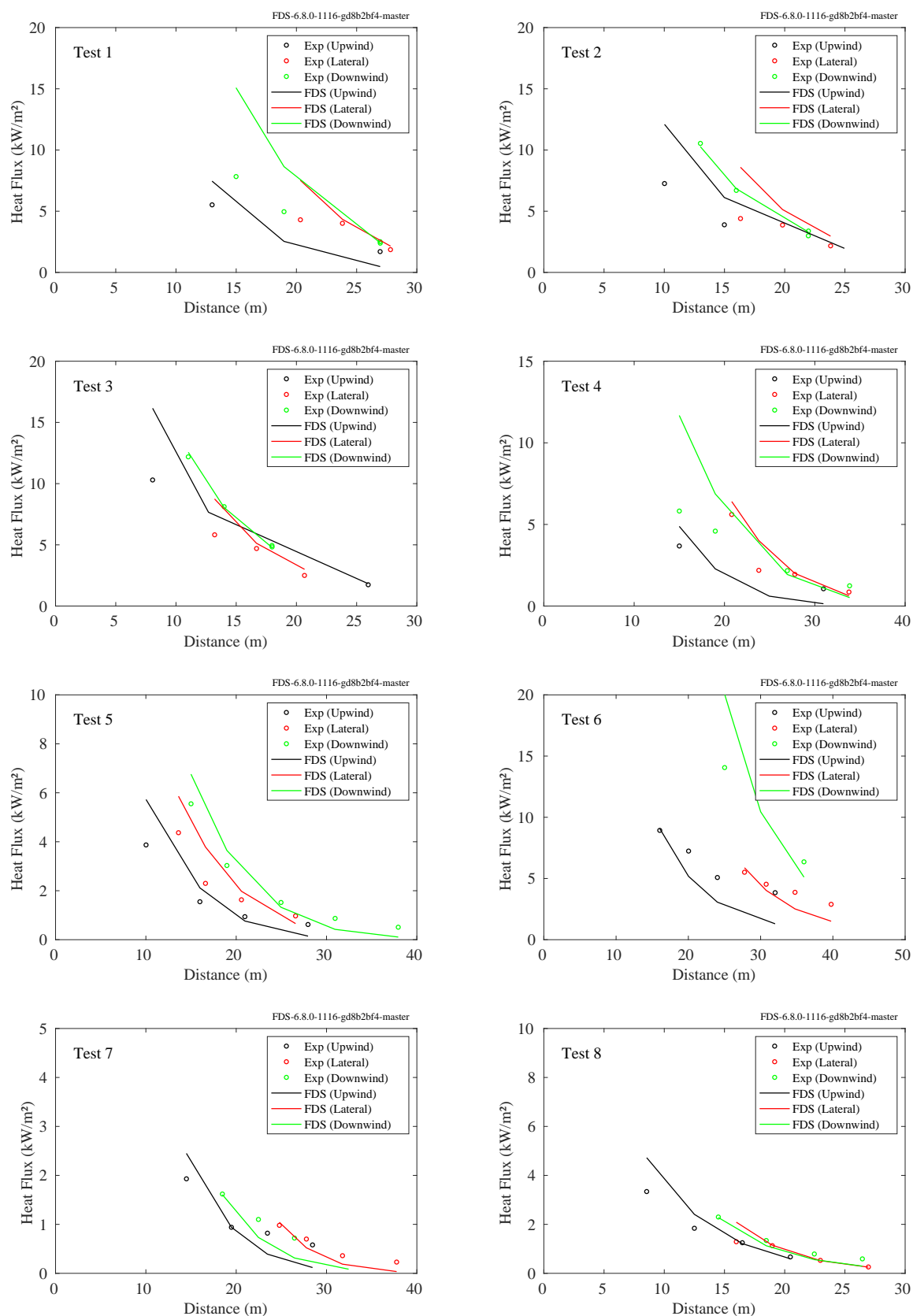


Figure 12.75: BGC/GRI LNG Fires, heat flux profiles for Tests 1-8.

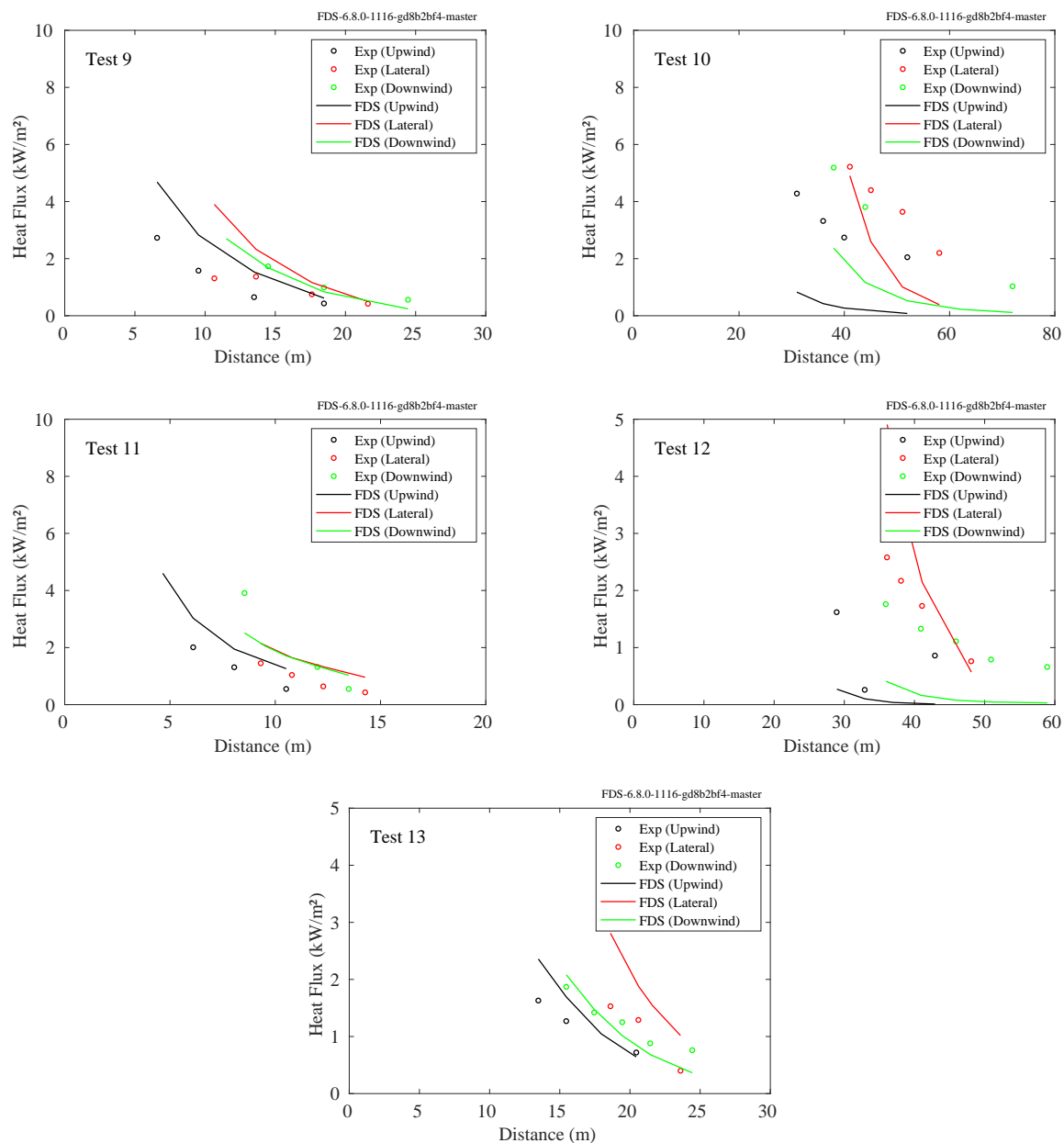


Figure 12.76: BGC/GRI LNG Fires, heat flux profiles for Tests 9-13.

12.2.4 Loughborough Jet Fire Experiments

A brief description of the experiments and modeling is found in Sec. 3.45.

The plots on the following pages present near-field and far-field heat flux measurements of natural gas jet fires. Figures 12.78 through 12.80 compare measured and predicted heat fluxes to a 0.9 m diameter, 16 m long pipe segment engulfed in the fire. The locations of the gauges are shown in Fig. 12.77.

Figure 12.81 presents the far-field radiometer predictions and measurements. Table 12.6 lists the radiometer coordinates relative to the center of the target pipe.

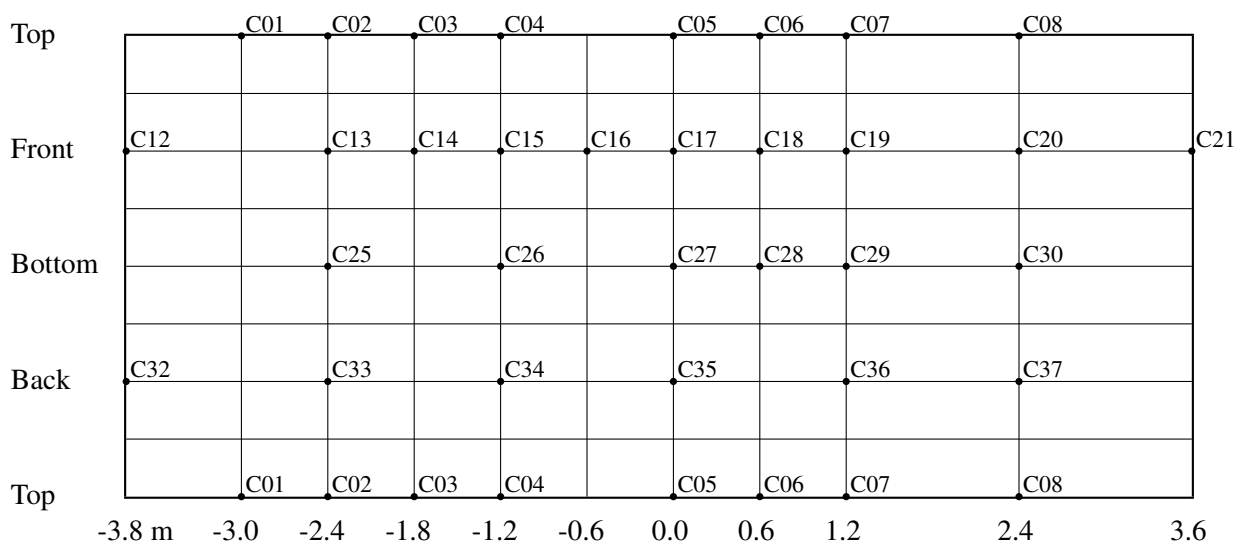


Figure 12.77: Location of the heat flux gauges mounted on the target pipe segment for the Loughborough Jet Fires. The pipe is oriented in the north-south direction, with the negative positions to the north. The “Front” of the pipe faces the jet.

Table 12.6: Radiometer positions (m) relative to the center of the target pipe, Loughborough Jet Fires.

Test No.	Rad 1 (N,W)	Rad 2 (N,W)	Rad 3 (N,W)	Rad 4 (S,W)	Rad 5 (S,W)	Rad 6 (S,W)	Rad 7 (S,W)	Rad 8 (S,W)	Rad 9 (S,W)
1	(20,5)	(15,0)	(15,5)	(15,0)	(15,5)	(20,0)	(20,5)	(25,0)	(30,0)
2	(30,0)	(20,0)	(20,5)	(15,0)	(20,0)	(20,5)	(30,0)	(30,5)	(40,0)
3	(35,0)	(25,0)	(25,5)	(20,0)	(25,0)	(25,5)	(35,0)	(35,5)	(52,0)

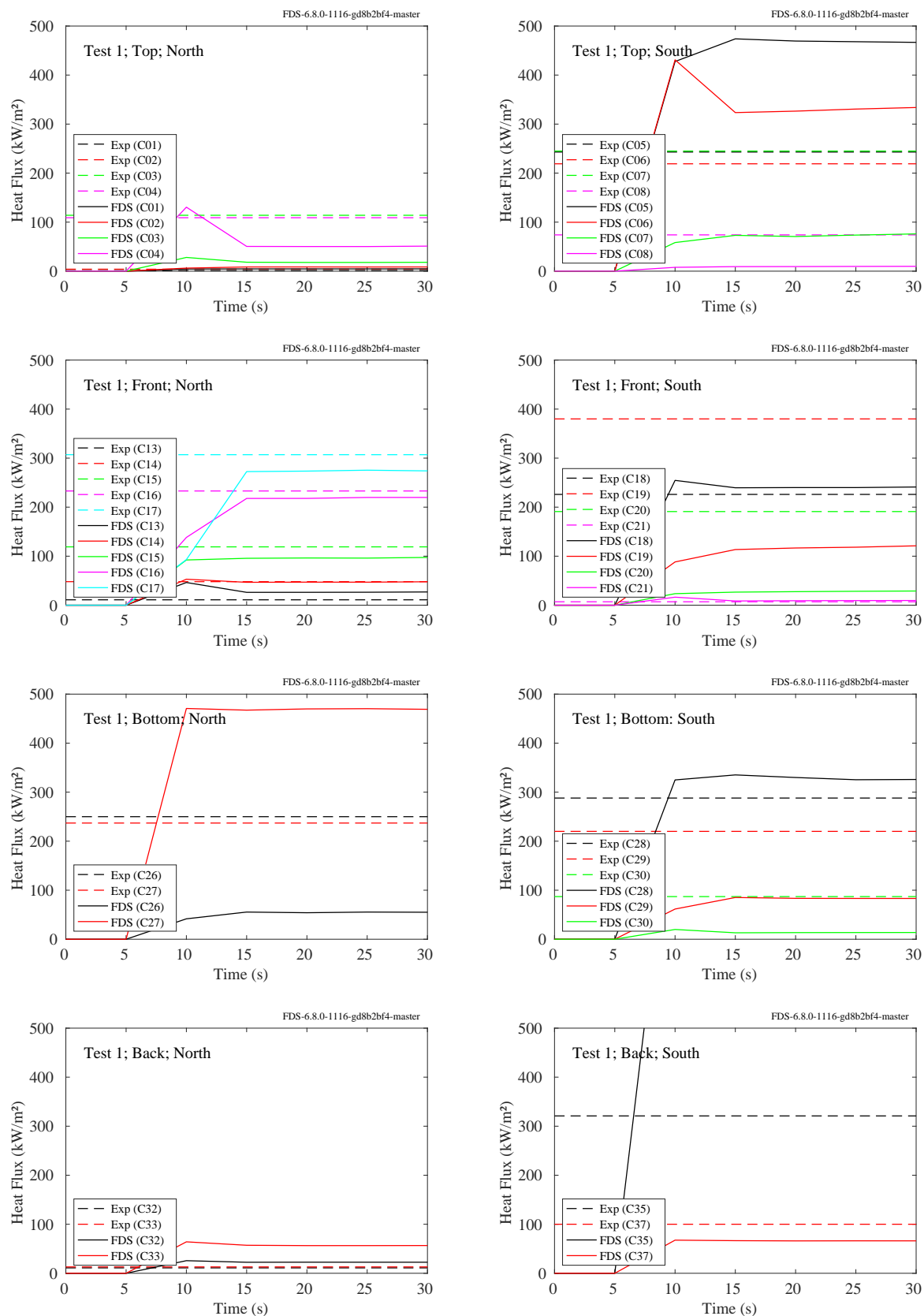


Figure 12.78: Loughborough Jet Fires, heat flux to pipe, Test 1.

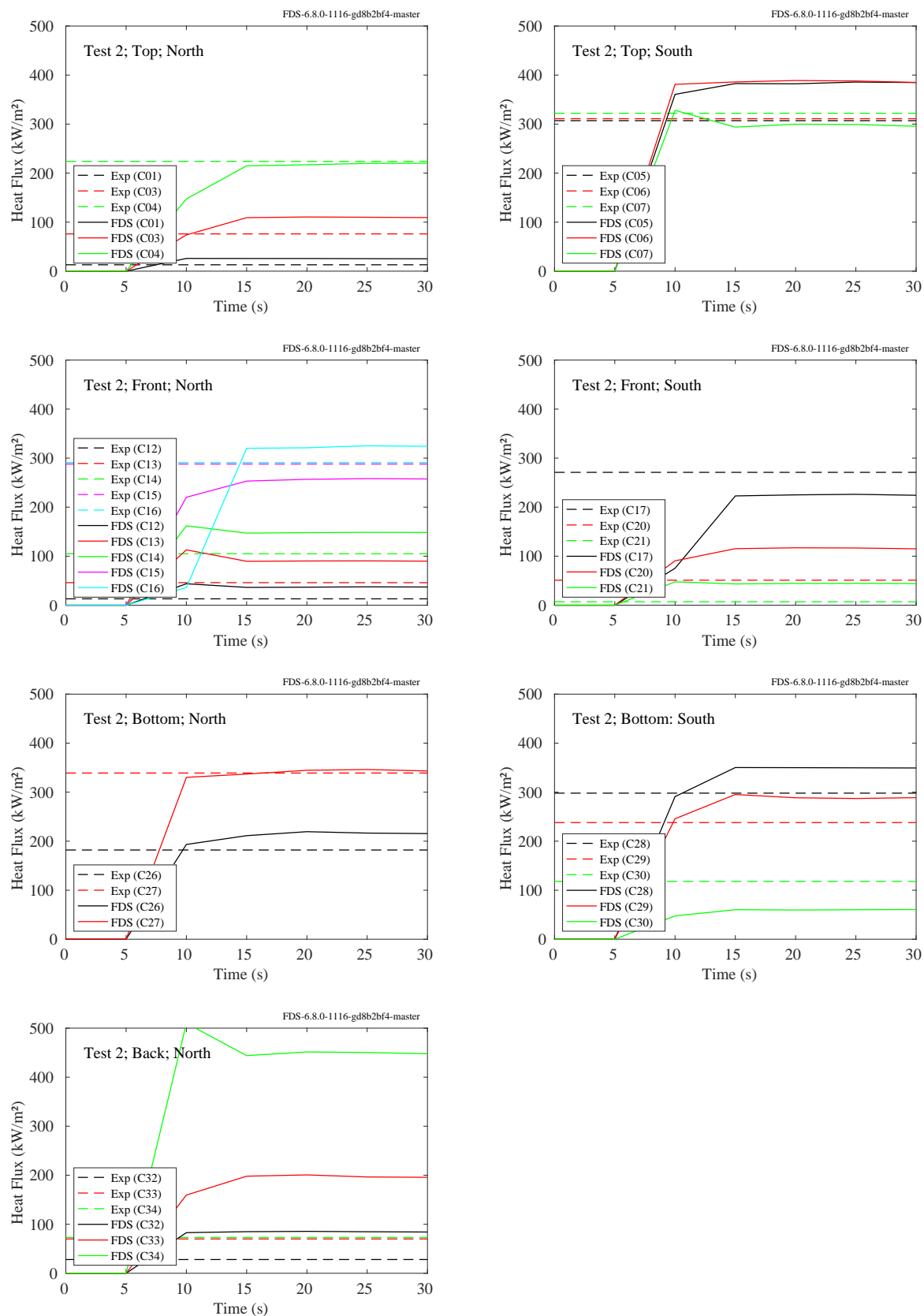


Figure 12.79: Loughborough Jet Fires, heat flux to pipe, Test 2.

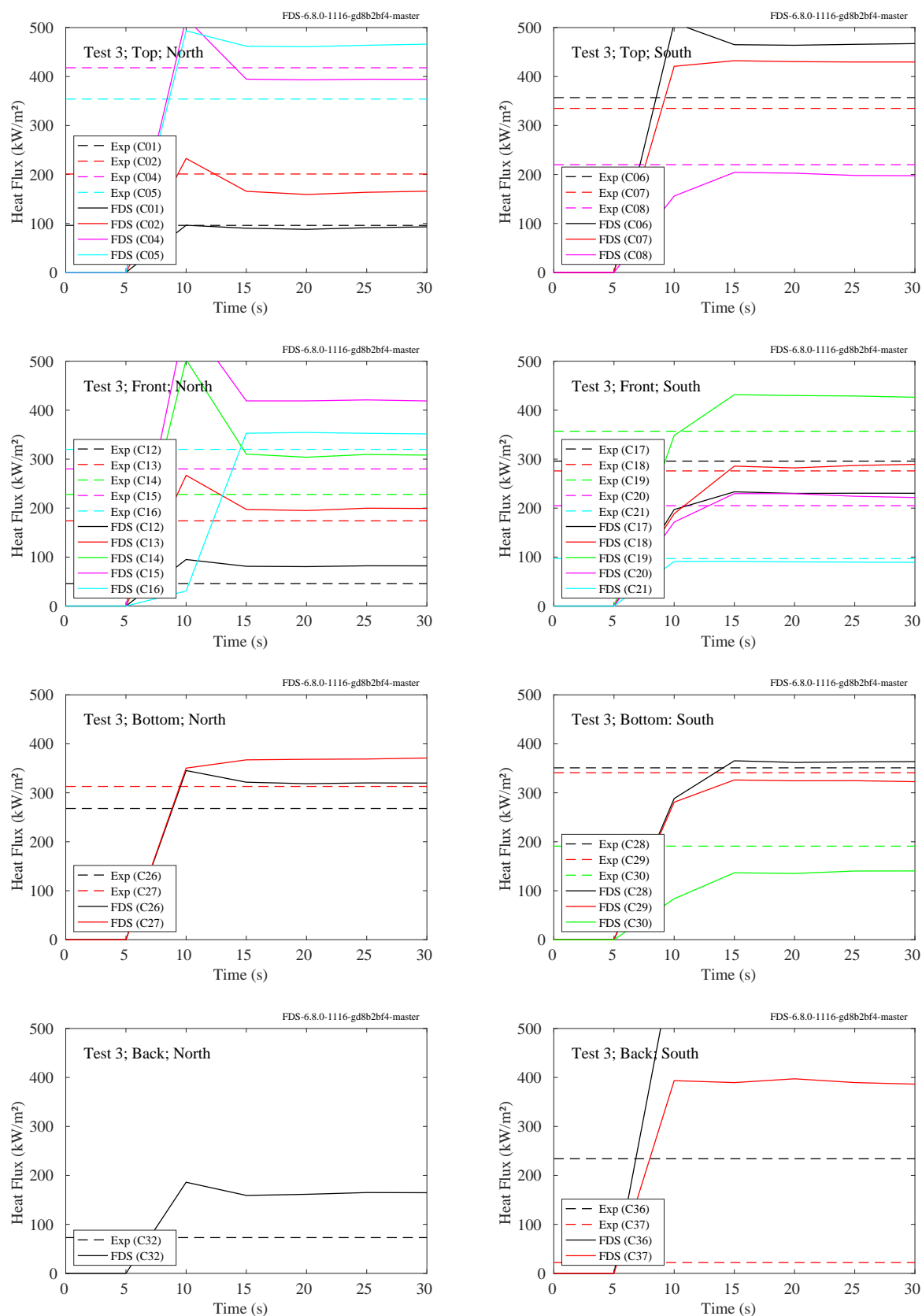


Figure 12.80: Loughborough Jet Fires, heat flux to pipe, Test 3.

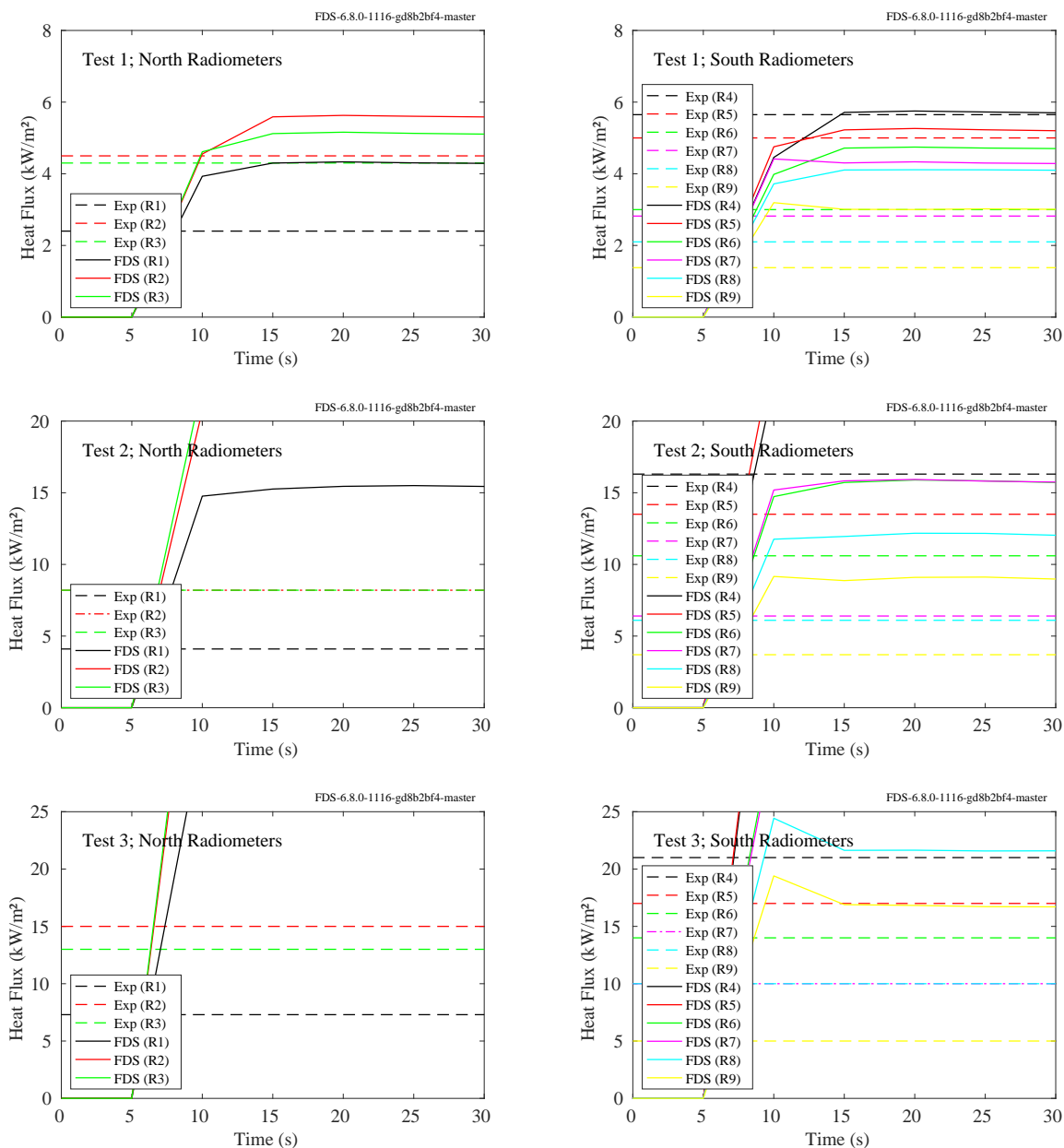


Figure 12.81: Loughborough Jet Fires, far-field radiometers.

12.2.5 Montoir LNG Fires

A brief description of these experiments can be found in Sec. 3.48. Figure 12.82 indicates the radial lines emanating outwards from the 35 m pool along which the radiometers were positioned. Figures 12.83 through 12.85 display the results of measured and predicted heat fluxes along the radial lines.

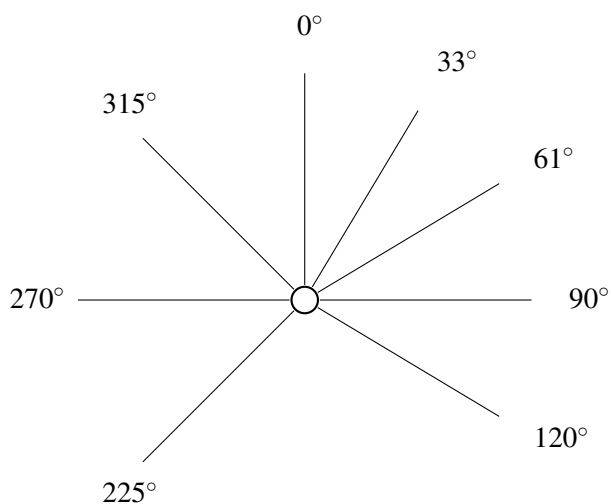


Figure 12.82: Layout of the Montoir LNG Fires.

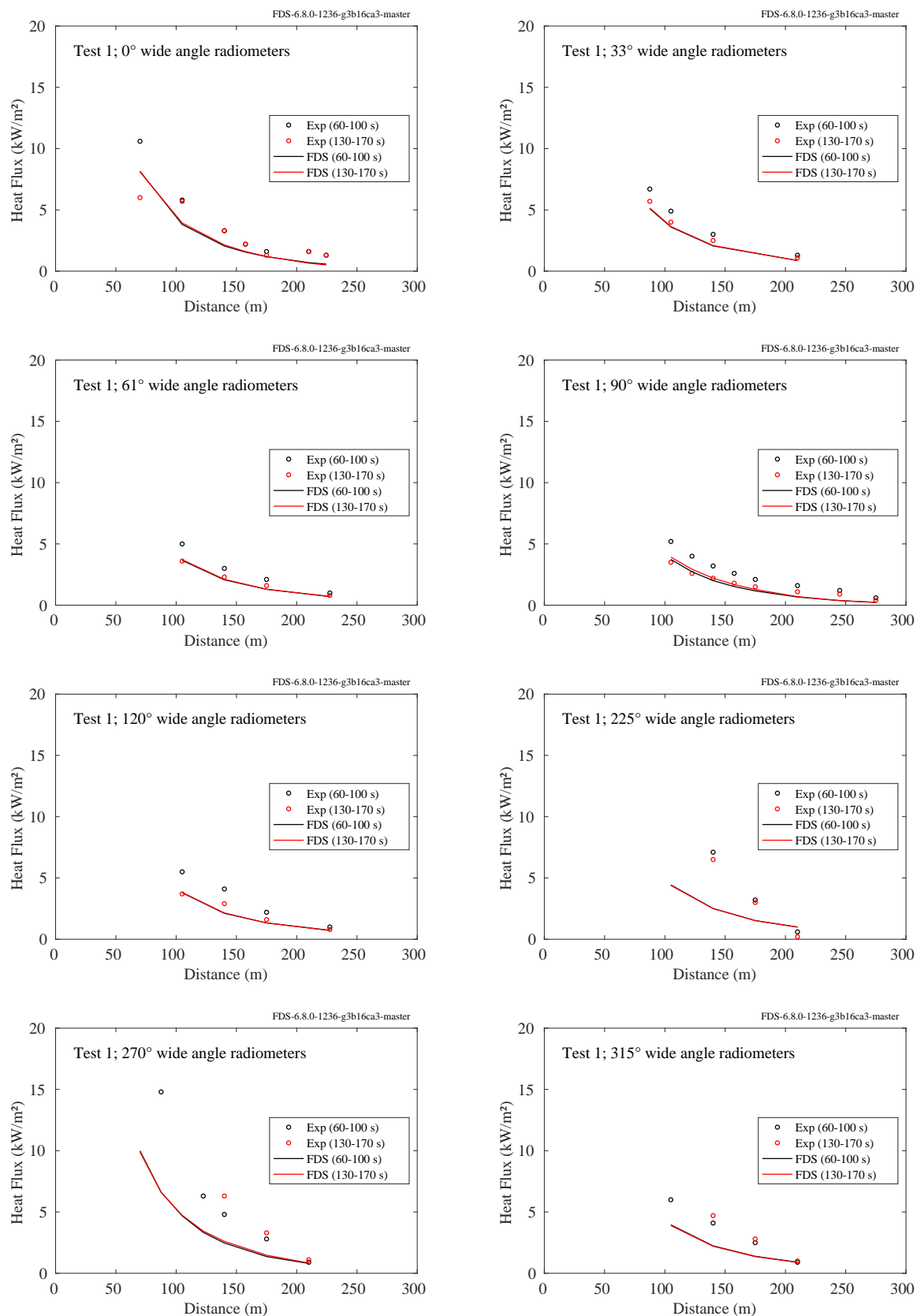


Figure 12.83: Montoir LNG Fires, far-field radiometers, Test 1.

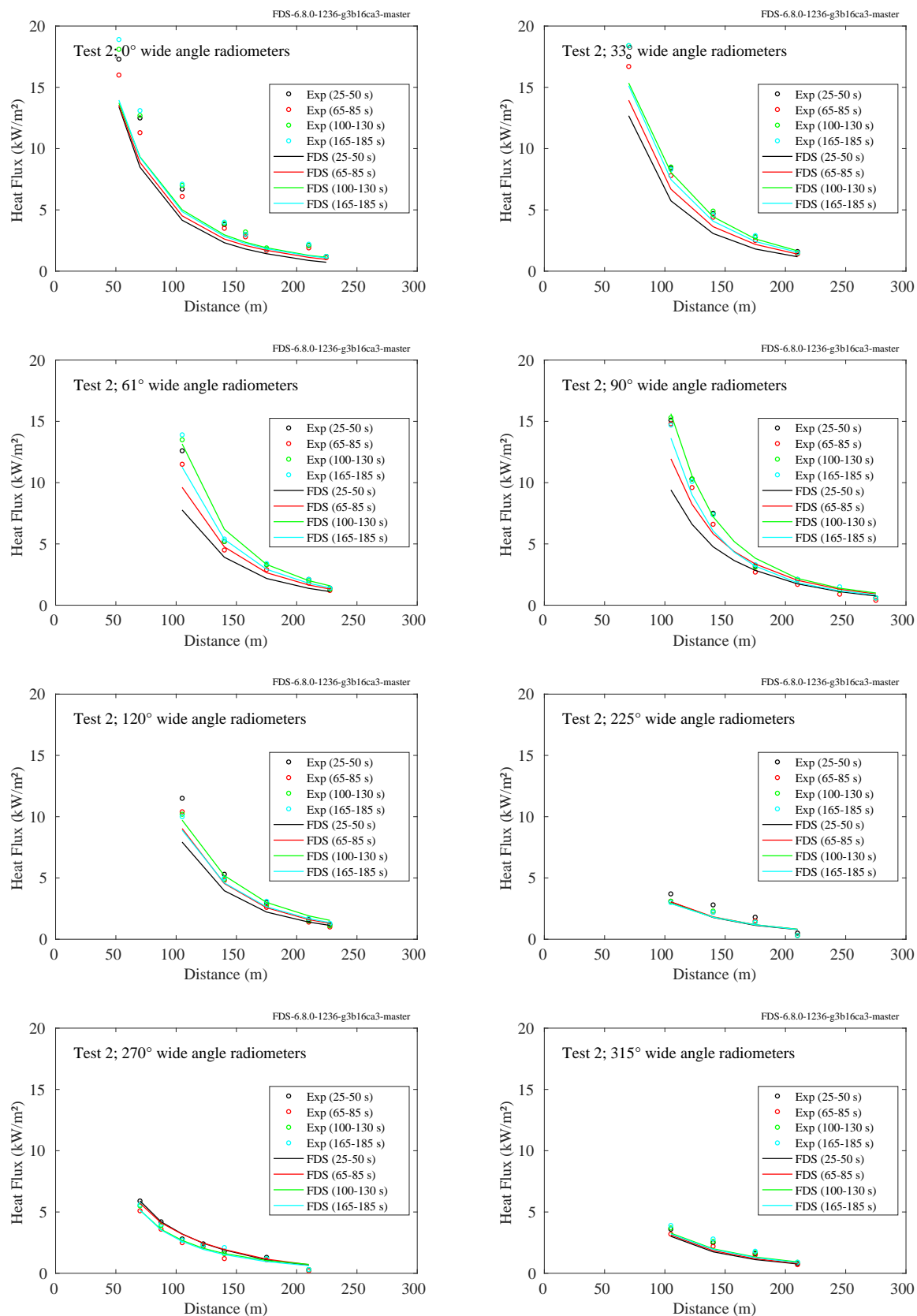


Figure 12.84: Montoir LNG Fires, far-field radiometers, Test 2.

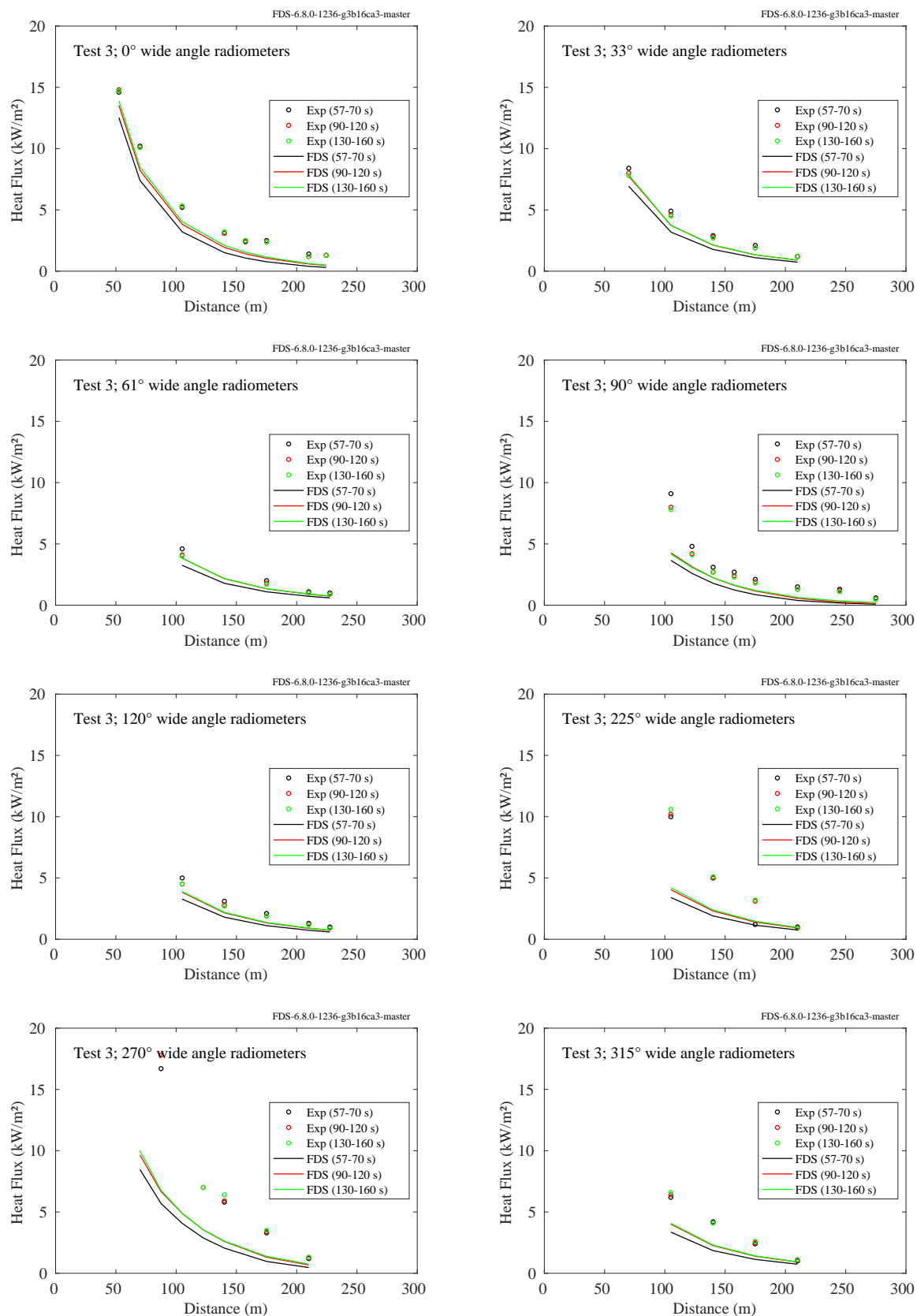


Figure 12.85: Montoir LNG Fires, far-field radiometers, Test 3.

12.2.6 NIST Douglas Firs

A description of the experiments and modeling assumptions are given in Sec. 3.52. Heat flux gauges were positioned on two vertical arrays, a distance of 2 m and 3 m from the burning trees. Average experimental values for test condition are shown below.

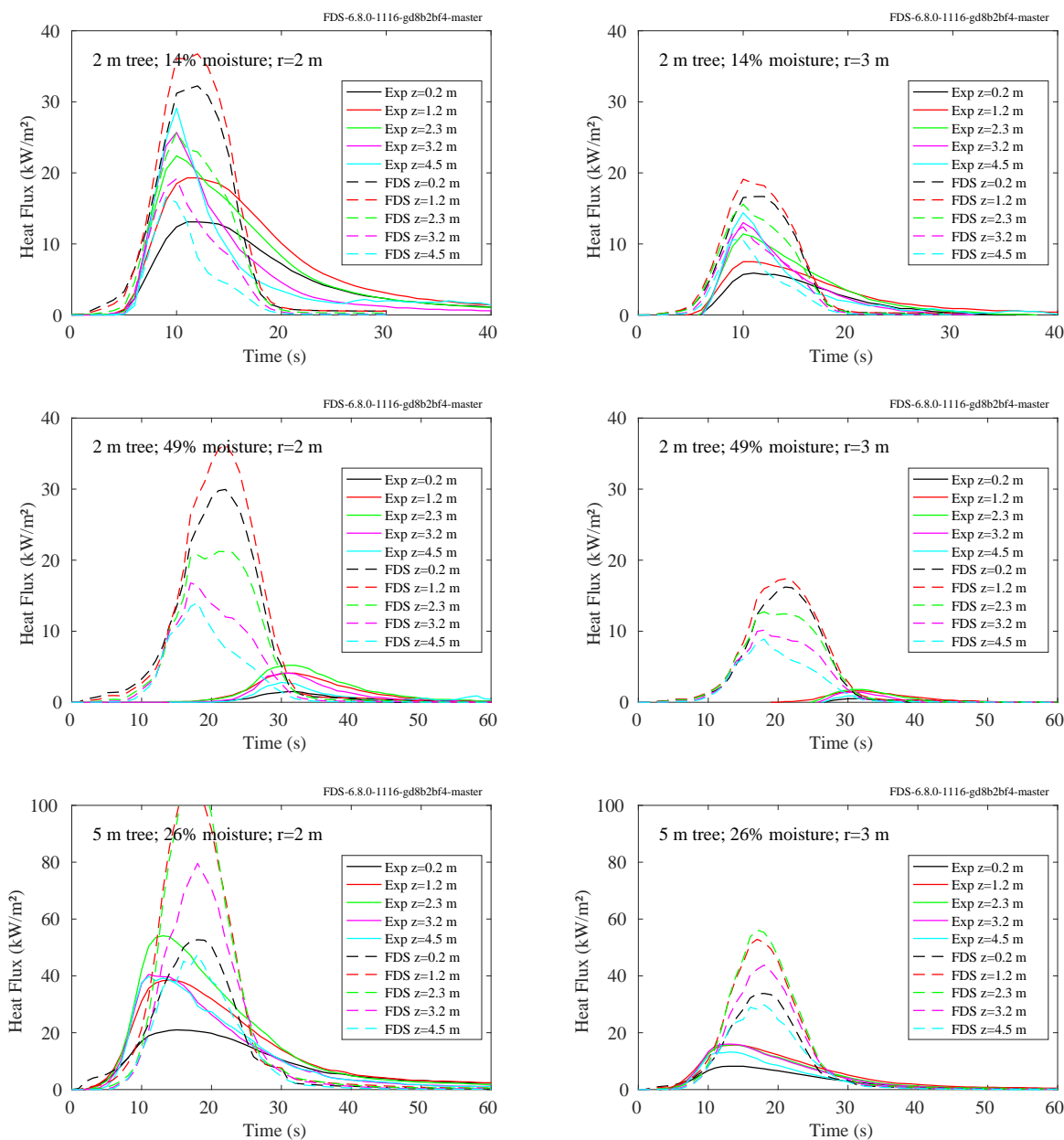


Figure 12.86: NIST Douglas Firs, heat flux at a distance of $x = 2$ m and $x = 3$ m

12.2.7 NIST/NRC Experiments

Cables of various types (power and control), and configurations (horizontal, vertical, in trays or free-hanging), were installed in the test compartment. For each of the four cable targets considered, measurements of the radiative and total heat flux were made with gauges positioned near the cables themselves. The following pages display comparisons of these heat flux predictions and measurements for Control Cable B, Horizontal Cable Tray D, Power Cable F and Vertical Cable Tray G.

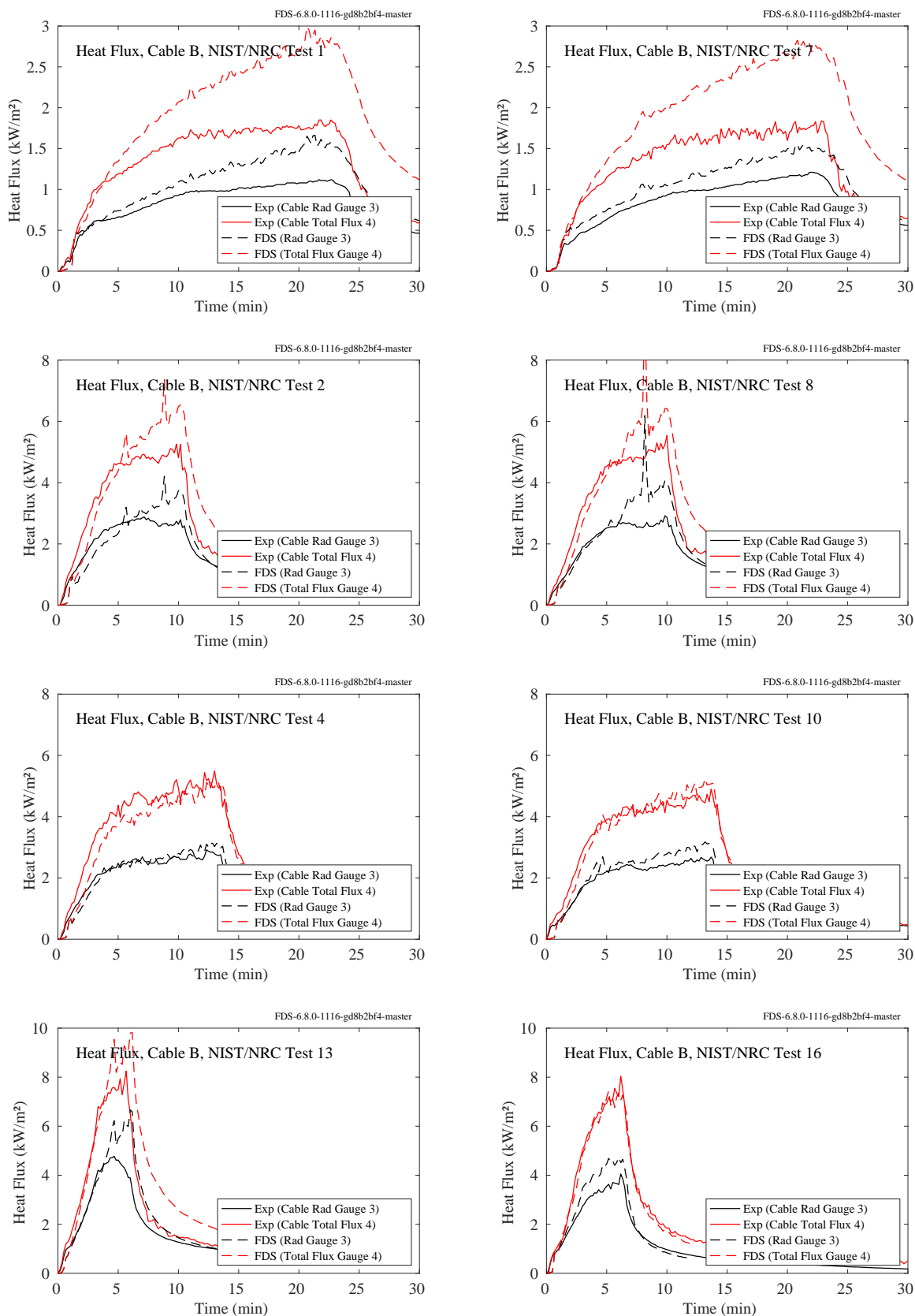


Figure 12.87: NIST/NRC experiments, heat flux to Cable B, Tests 1, 2, 4, 7, 8, 10, 13, 16.

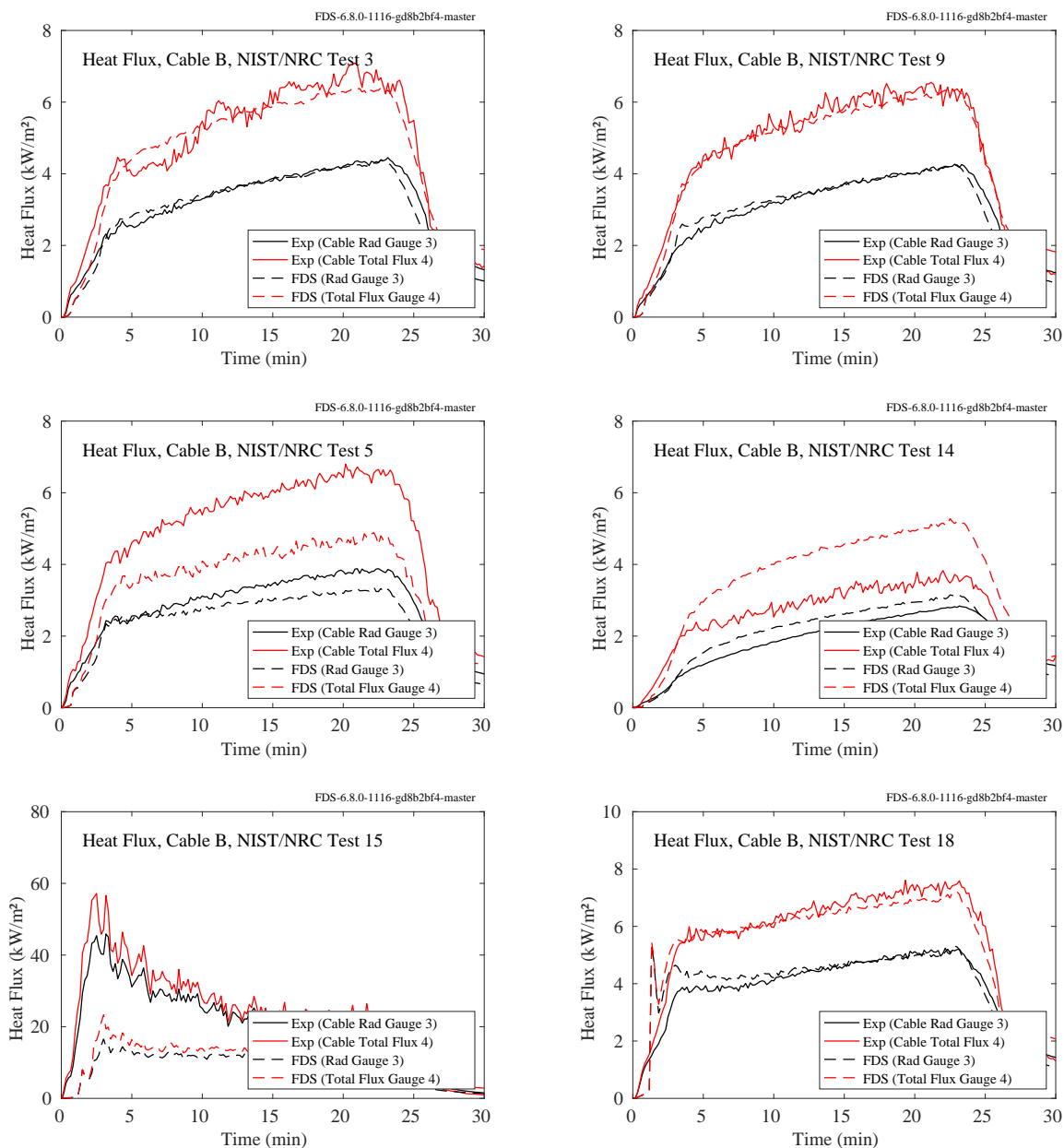


Figure 12.88: NIST/NRC experiments, heat flux to Cable B, Tests 3, 5, 9, 14, 15, 18.

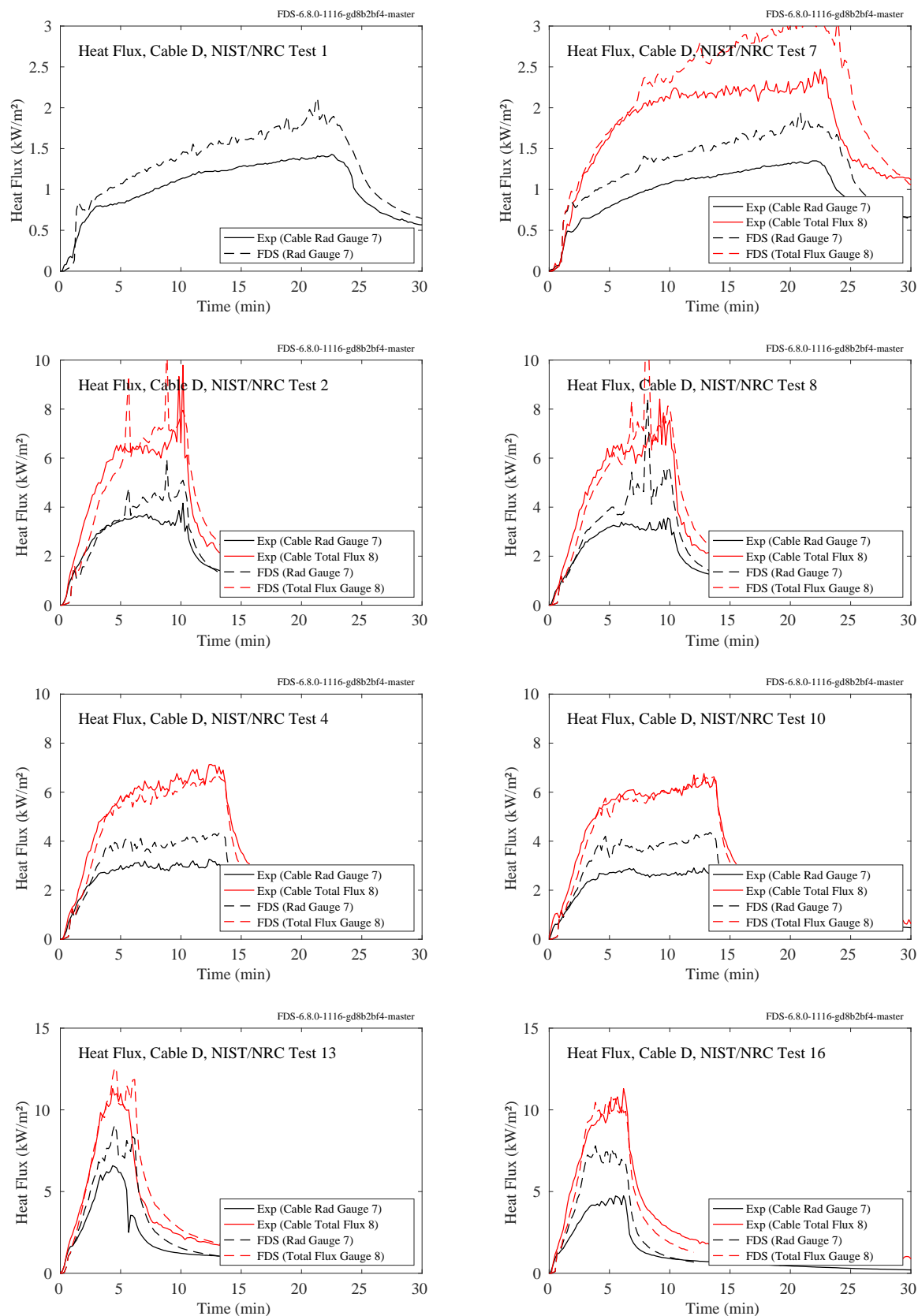


Figure 12.89: NIST/NRC experiments, heat flux to Cable D, Tests 1, 2, 4, 7, 8, 10, 13, 16.

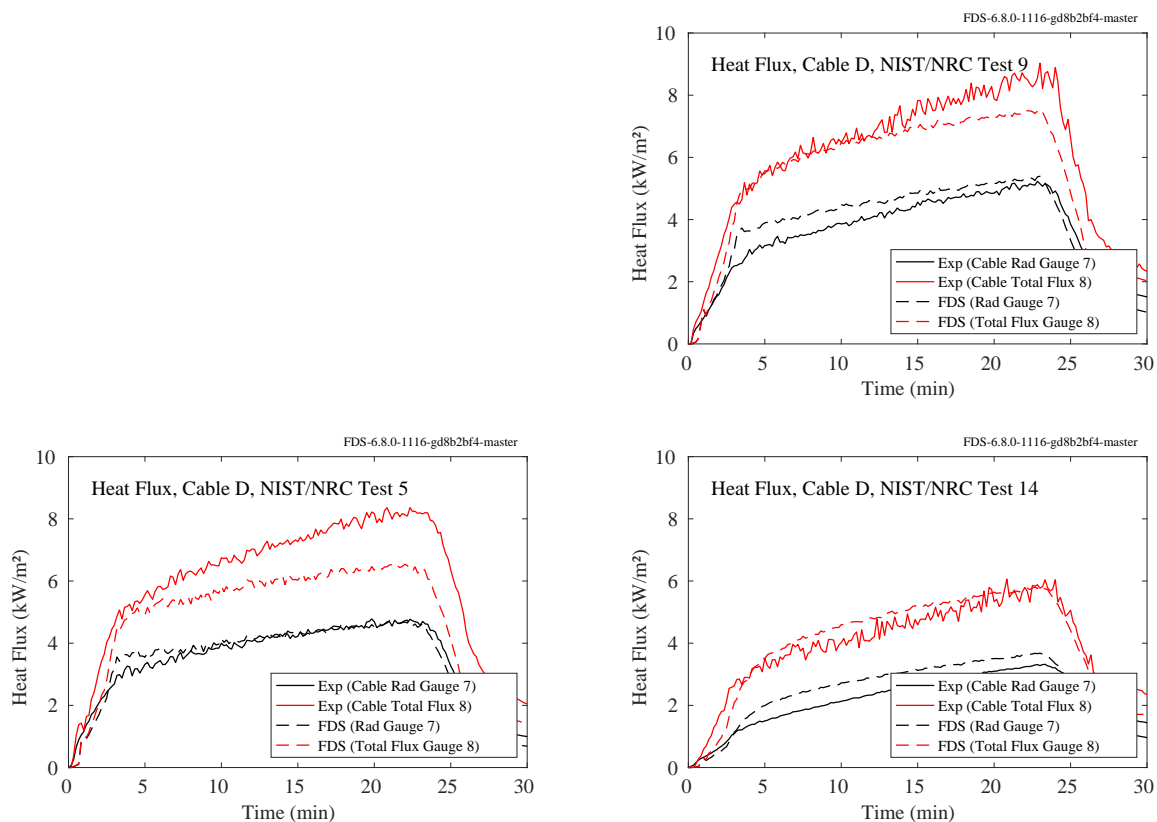


Figure 12.90: NIST/NRC experiments, heat flux to Cable D, Tests 5, 9, 14.

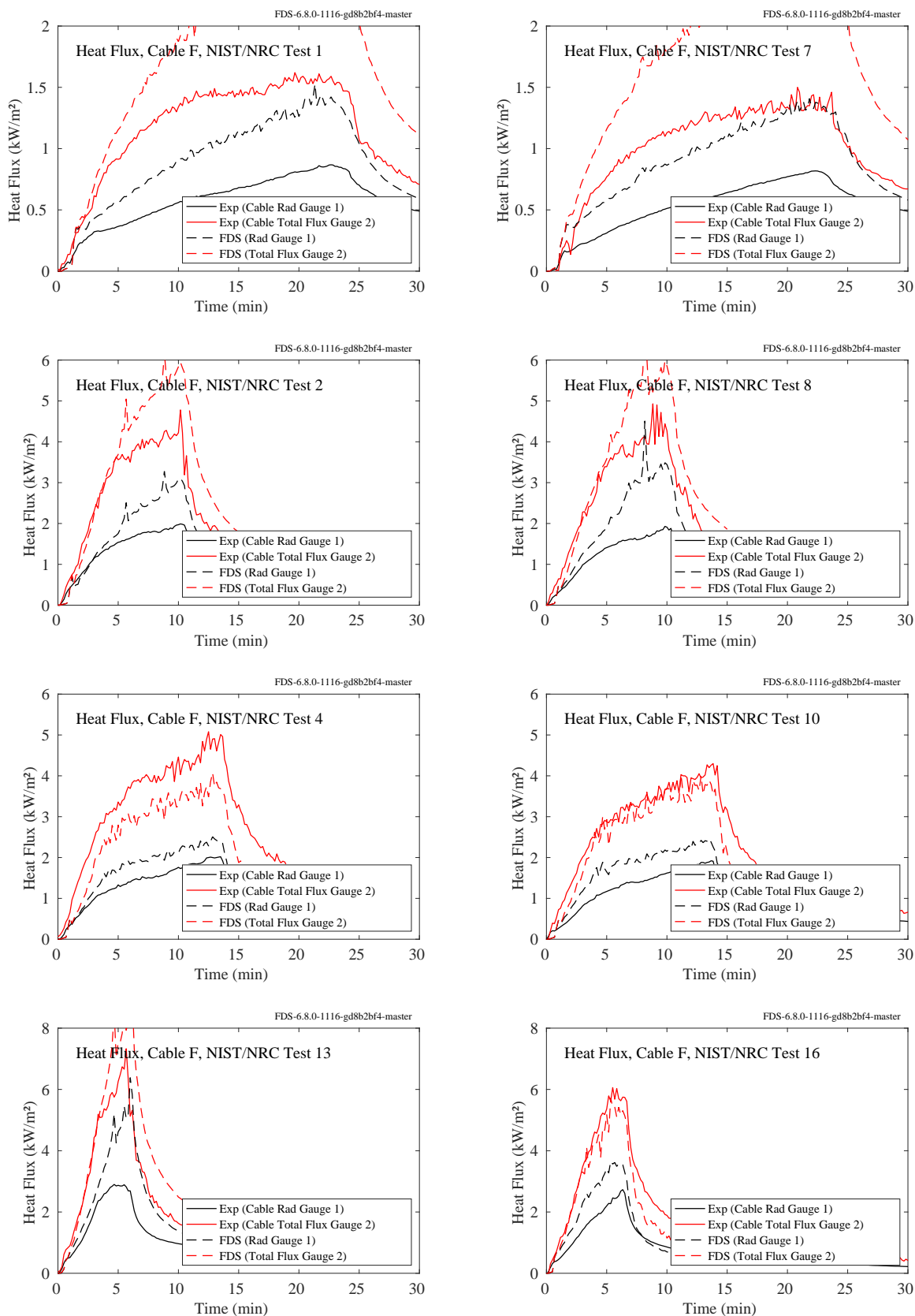


Figure 12.91: NIST/NRC experiments, heat flux to Cable F, Tests 1, 2, 4, 7, 8, 10, 13, 16.

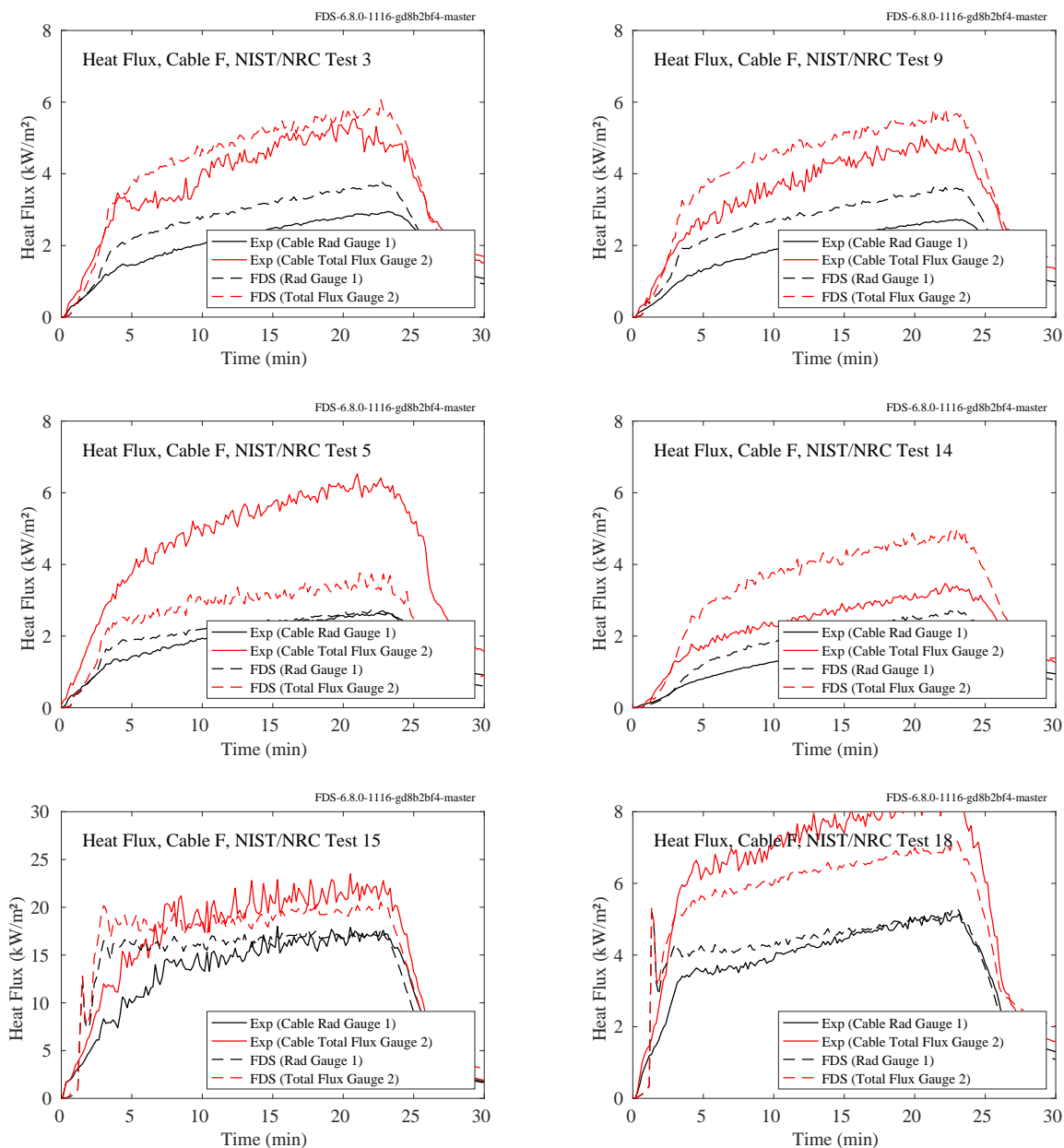


Figure 12.92: NIST/NRC experiments, heat flux to Cable F, Tests 3, 5, 9, 14, 15, 18.

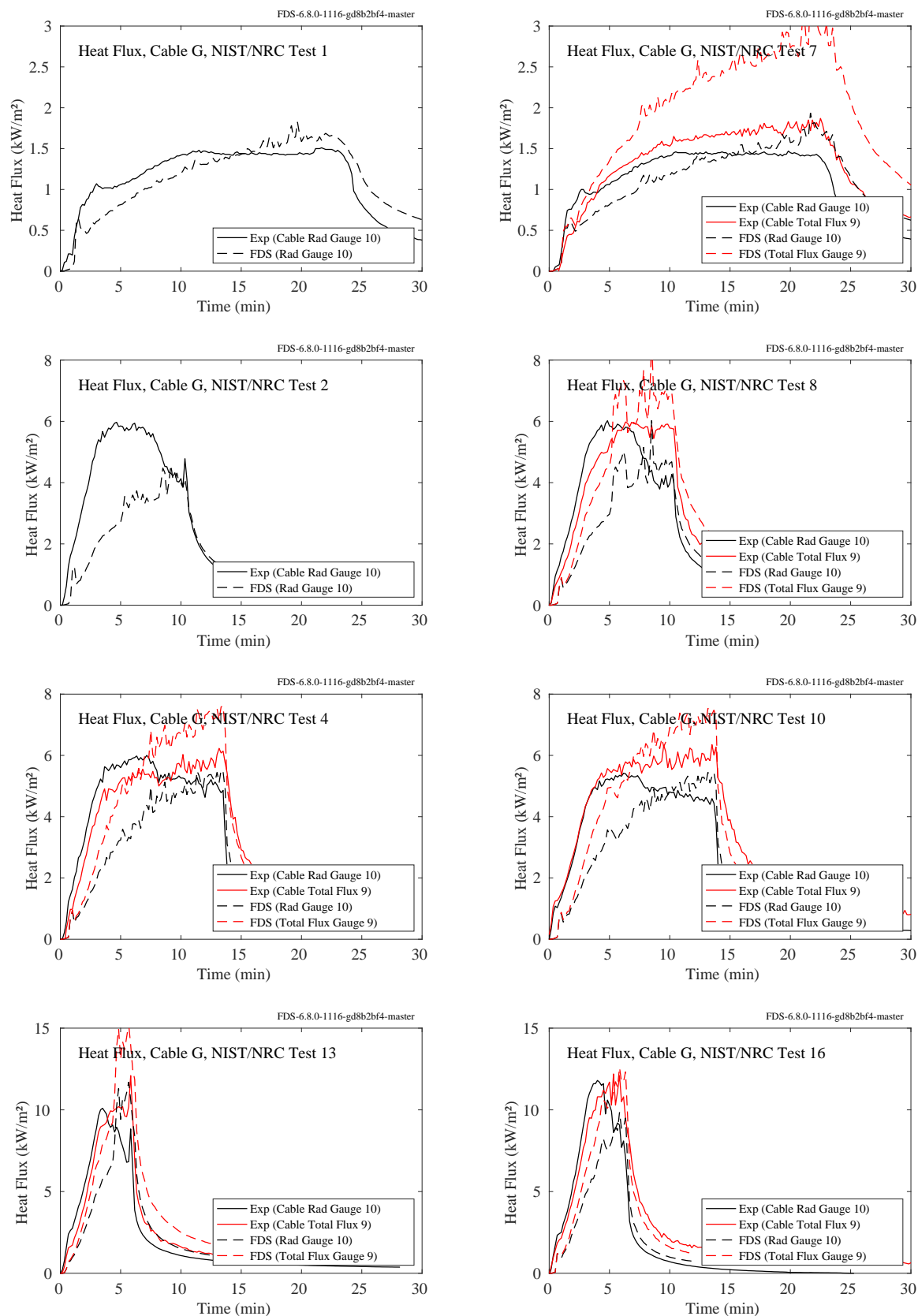


Figure 12.93: NIST/NRC experiments, heat flux to Cable G, Tests 1, 2, 4, 7, 8, 10, 13, 16.

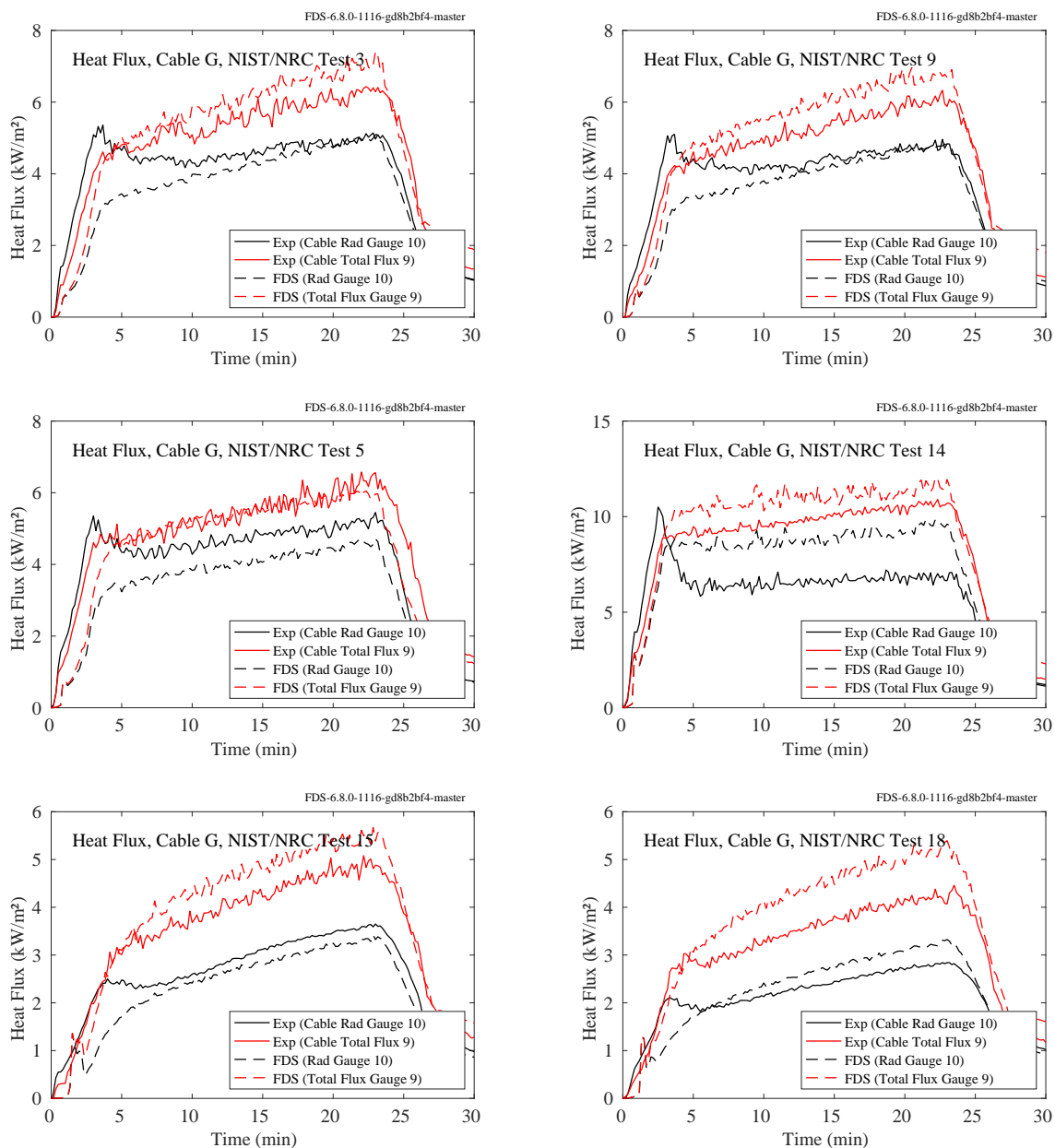


Figure 12.94: NIST/NRC experiments, heat flux to Cable G, Tests 3, 5, 9, 14, 15, 18.

12.2.8 NIST Pool Fires

A description of the NIST Pool Fire experiments and modeling is given in Sec. 3.61. On the following pages are comparisons of heat flux measurements and predictions at various locations and orientations.

- Figure 12.95 displays downward radiative and total heat flux near the liquid pool surface of a 30 cm methanol fire. The radiative heat flux measurements were made by Hamins et al. [343] and the *total* heat flux measurements were made by Kim et al. [377].
- Figure 12.96 displays radial and vertical profiles of *total* heat flux for a 30 cm methanol fire extending beyond the outer rim of the pan [377]. The vertical profile was made at $r = 60$ cm. Additional radial measurements were made by Klassen et al. [378].
- Figure 12.97 displays a radial profile of the total heat flux in the downward direction for a 100 cm pan methanol fire. The radial distance ranges from the burner edge ($r = 50$ cm) to $r = 200$ cm. The positions of the heat flux gauges were located $z = 1$ cm above the fuel surface and oriented in the upward direction [364].
- Figure 12.98 displays radial profiles of the total heat flux emitted radially away from the fire at heights of $z = 41$ cm, $z = 61$ cm, and $z = 81$ cm above the fuel surface. The heat flux gauges were oriented in the horizontal direction towards the fire centerline [364].

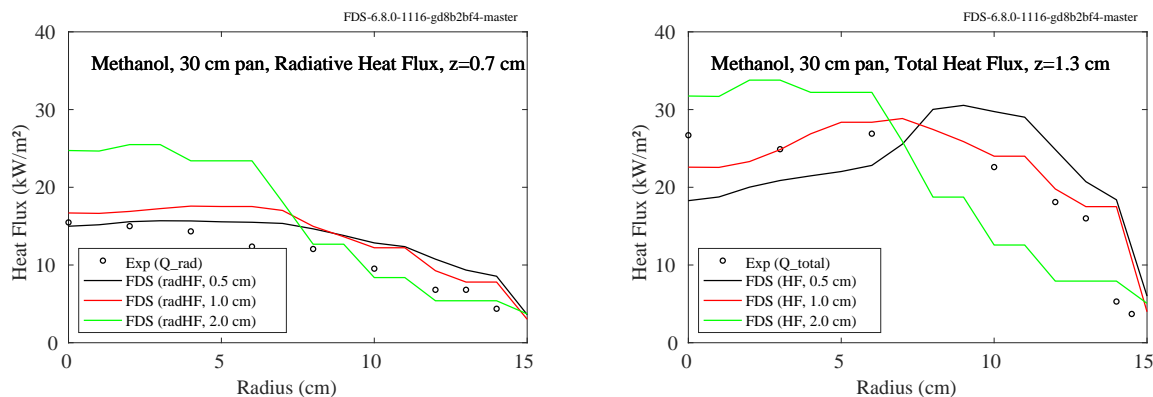


Figure 12.95: NIST Pool Fires, 30 cm methanol fire, radial profiles of downward radiative and total heat flux, respectively, at $z = 0.7$ cm (left) and $z = 1.3$ cm (right).

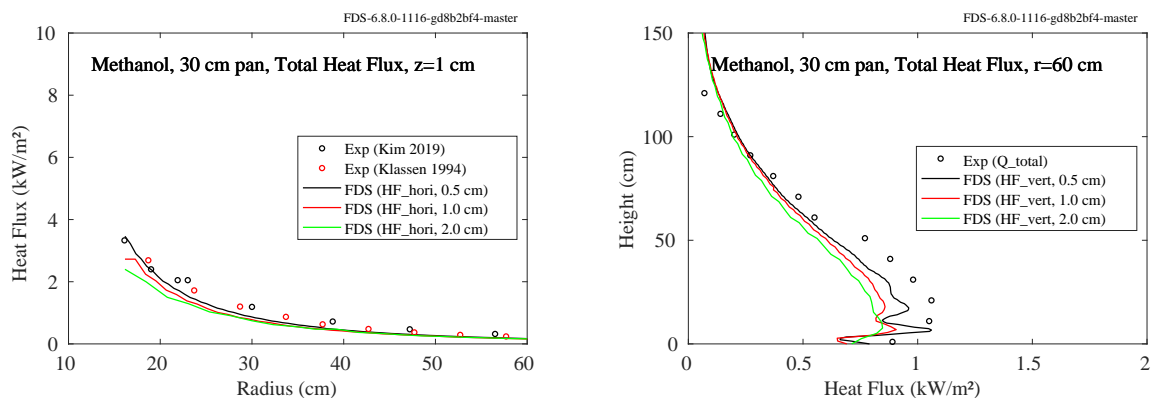


Figure 12.96: NIST Pool Fires, 30 cm methanol fire, radial and vertical profiles of total heat flux from a 30 cm methanol fire.

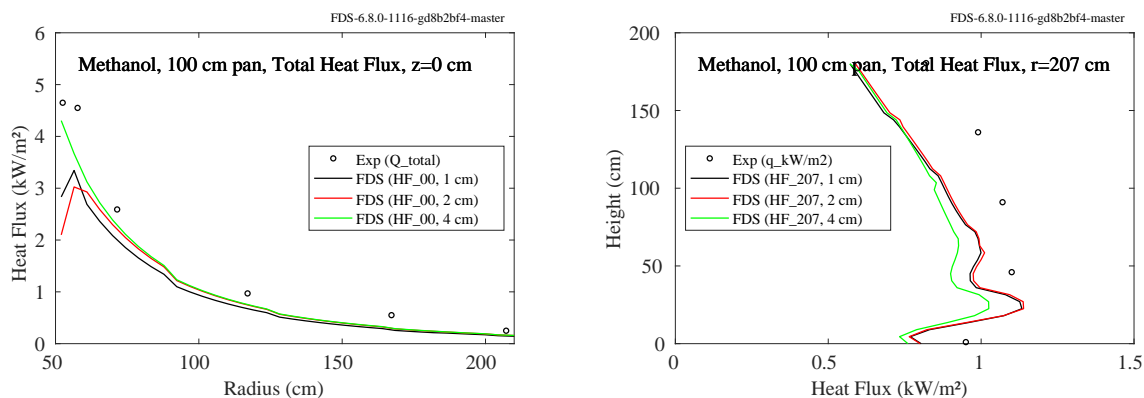


Figure 12.97: NIST Pool Fires, 100 cm methanol fire, total heat flux downward at $z = 0$ cm (left) and outward at $r = 207$ cm (right).

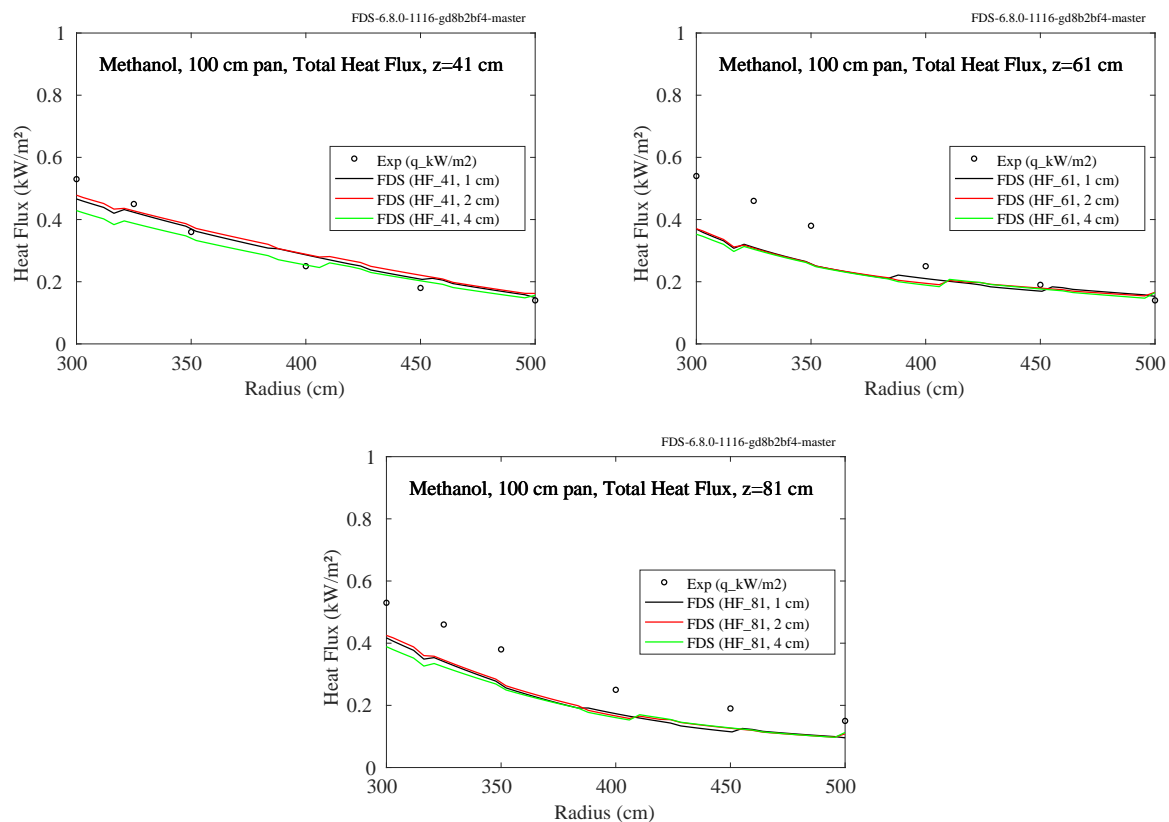


Figure 12.98: NIST Pool Fires, 100 cm methanol fire, total heat flux outward at $z = 41$ cm, $z = 61$ cm, and $z = 81$ cm.

12.2.9 NIST Structure Separation Verification

The NIST Structure Separation Verification experiments are described in Sec. 3.64. Below in Figs. 12.99 and 12.100 we plot FDS results for two grid resolutions against the time series of the gauge heat flux data from the verification tests using the NFRL 8 MW calibration burner with natural gas fuel.

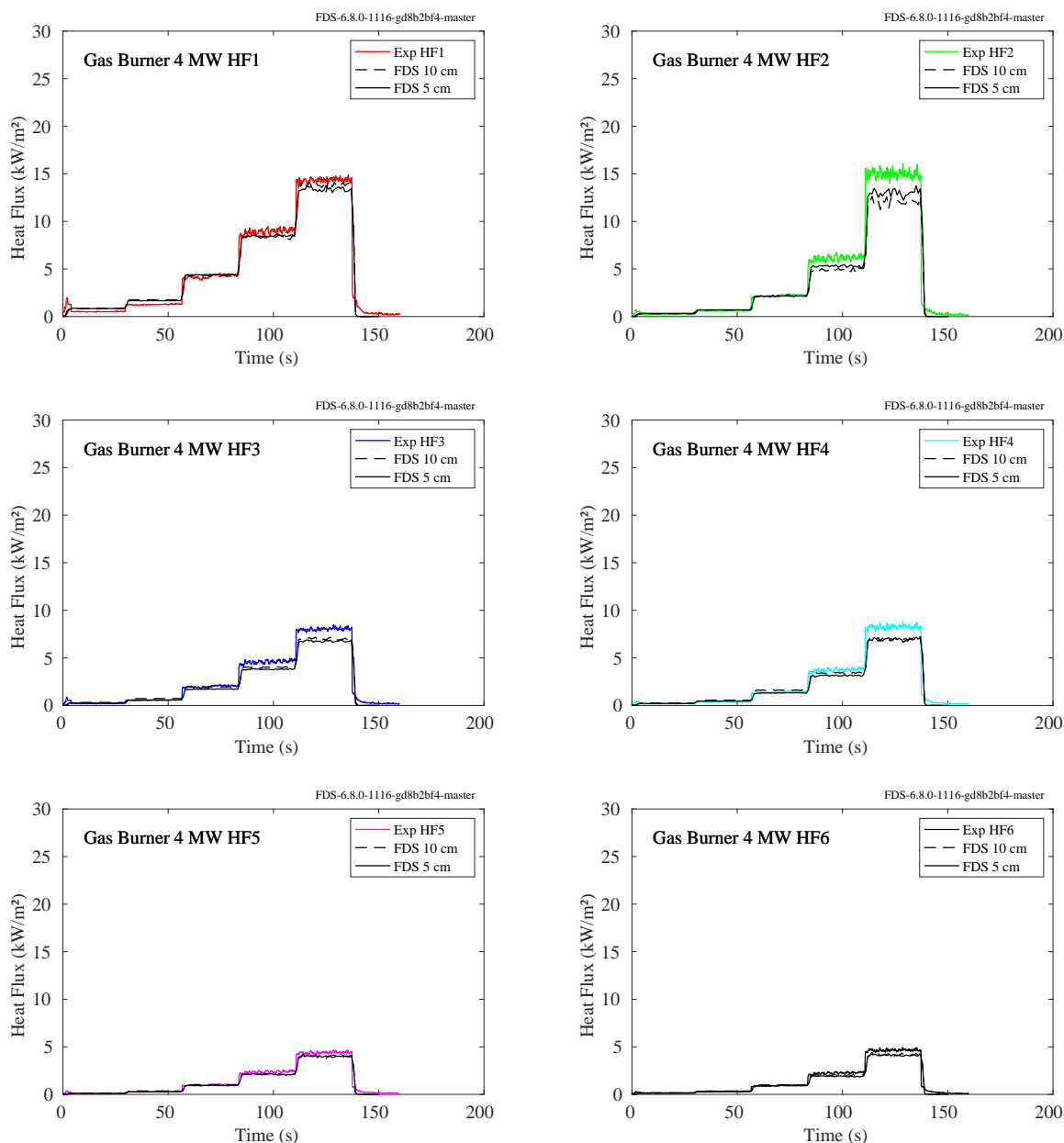


Figure 12.99: NIST Structure Separation Verification heat flux (4 MW max heat release rate). Gauges HF1, HF3, and HF5 are positioned at burner level (1 m off the floor) and, respectively, 2 m, 3 m, and 4 m away from the burner center. Gauges HF2, HF4, and HF6 are positioned 2 m above burner level (3 m off the floor) and likewise 2 m, 3 m, and 4 m away from the burner center.

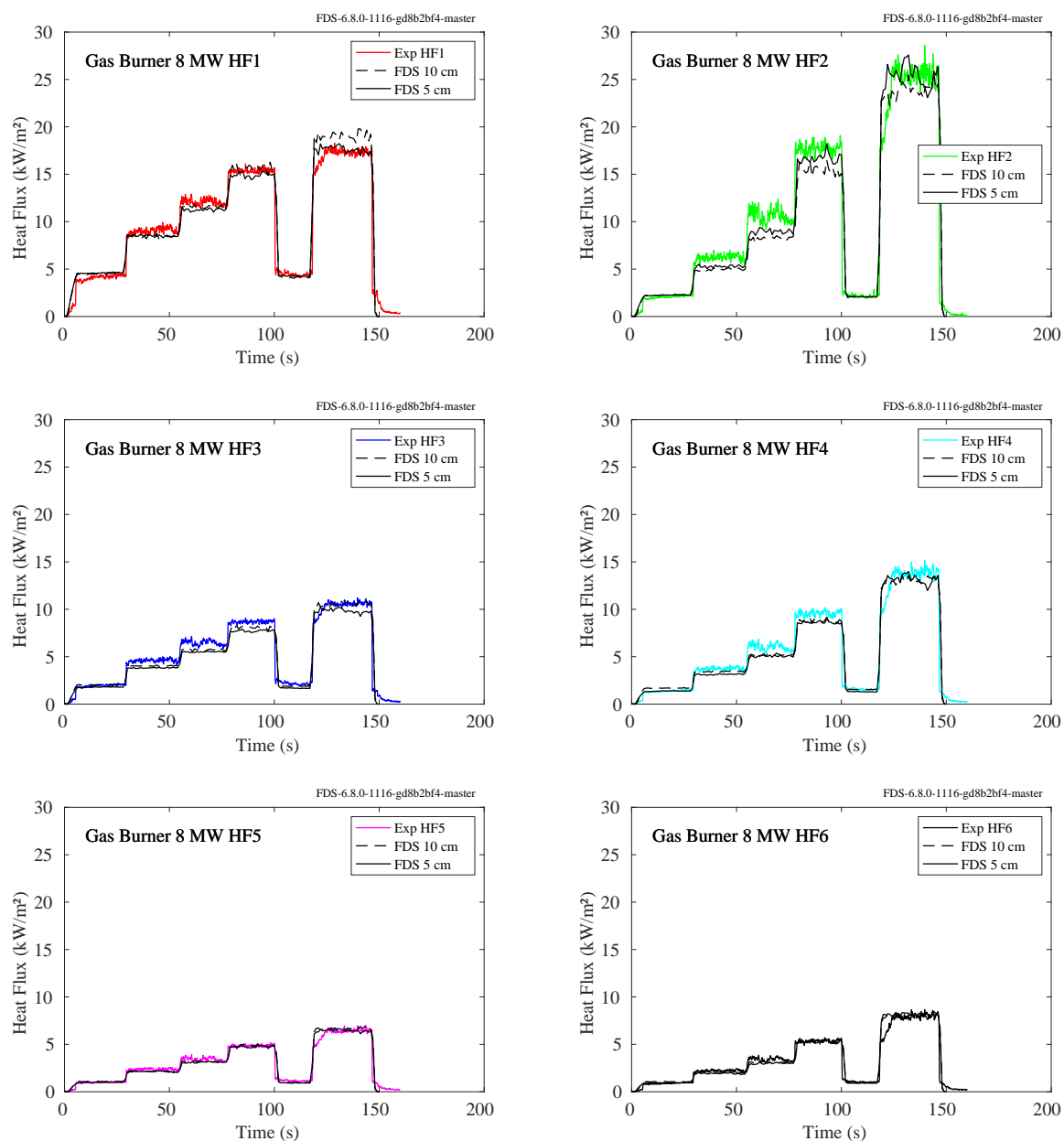


Figure 12.100: NIST Structure Separation Verification heat flux (8 MW max heat release rate). Gauges HF1, HF3, and HF5 are position at burner level (1 m off the floor) and, respectively, 2 m, 3 m, and 4 m away from the burner center. Gauges HF2, HF4, and HF6 are positioned 2 m above burner level (3 m off the floor) and likewise 2 m, 3 m, and 4 m away from the burner center.

12.2.10 Phoenix LNG Fires

A description of the two LNG pool fire experiments is given in Sec. 3.69.

The general layout of the facility is shown in Fig. 12.101. Wide-angle and narrow-angle radiometers were positioned at various heights off the ground and at various inclination angles along the axes shown in the figure.

Figure 12.102 compares predicted and measured heat fluxes for the wide-angle radiometers as a function of distance from the LNG pool fires. These radiometers were positioned along all four directional axes. Figure 12.103 compares predicted and measured heat flux for the narrow-angle radiometers along the north and south axes. There were three measurement towers along each axis. The nearest tower contained five narrow-angle radiometers at various inclination angles. The further two towers contained one narrow-angle radiometer each, along with one wide-angle radiometer. The vertical axes of the plots in Fig. 12.102 represent the “spot height” of the radiometers; that is, the height of the fire plume at which the radiometers were aimed. The “spot diameter” of the various radiometers ranged from 5 m to 15 m.

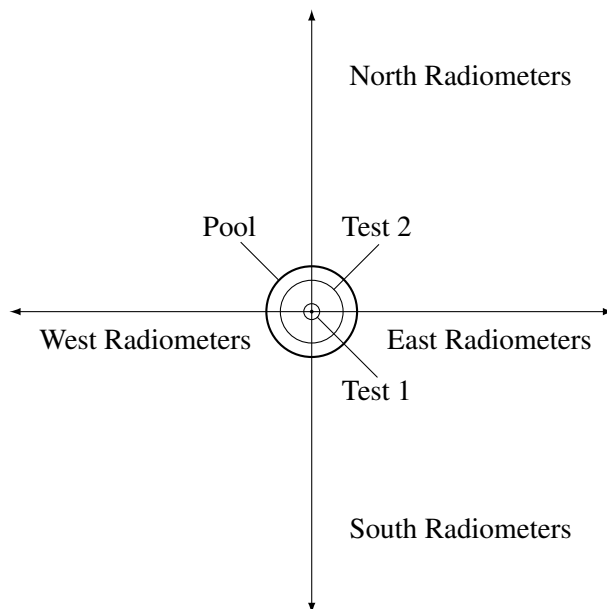


Figure 12.101: Layout of the Phoenix LNG Fires.

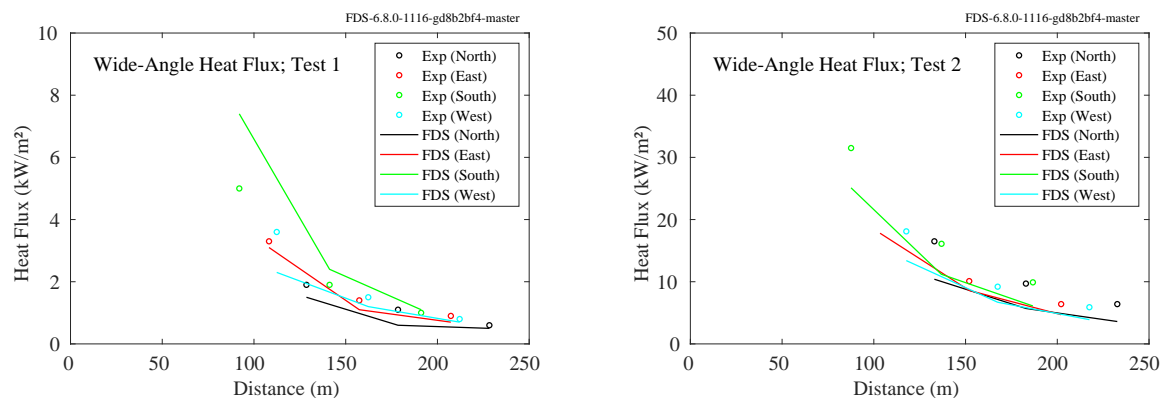


Figure 12.102: Phoenix LNG Fires, radial profiles of wide-angle heat flux.

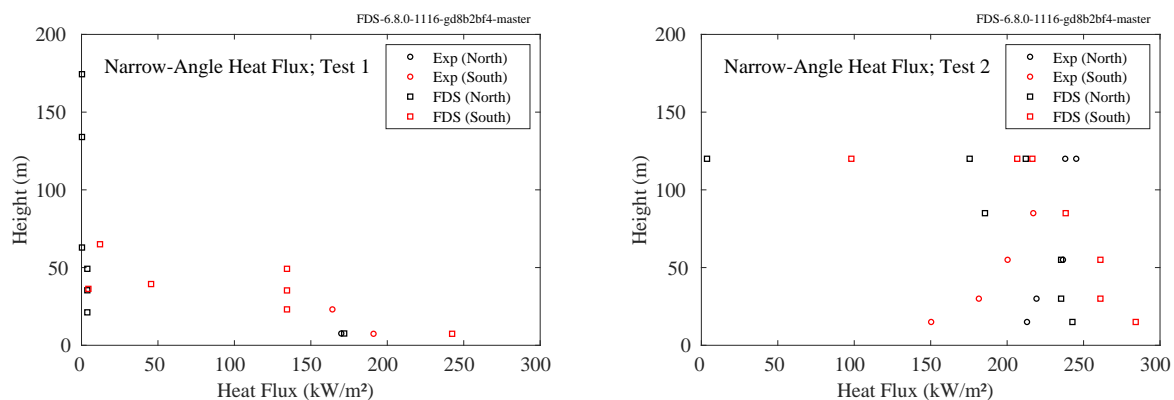


Figure 12.103: Phoenix LNG Fires, vertical profiles of narrow-angle heat flux.

12.2.11 Sandia Methane Burner Experiments

A brief summary of these experiments and the modeling strategy is found in Sec. 3.75.

On the following pages are comparisons of vertical profiles of the measured and predicted heat flux approximately 9 m from the centerline of a 3 m diameter methane burner of various heat release rates. There were two types of gauges used in the experiments—a conventional wide-angle heat flux gauge and a narrow-angle radiometer designed to measure the surface emissive power (SEP) of the fire. The narrow-angle radiometer had a view angle of 5° which was focused on a circular patch of flame of diameter approximately 0.8 m. This narrow-angle heat flux is modeled in FDS as the radiance ($\text{kW}/\text{m}^2/\text{sr}$) of a single ray multiplied by π sr. The unit sphere is discretized into approximately 600 solid angles, and the angle closest to the radiometer direction vector is used.

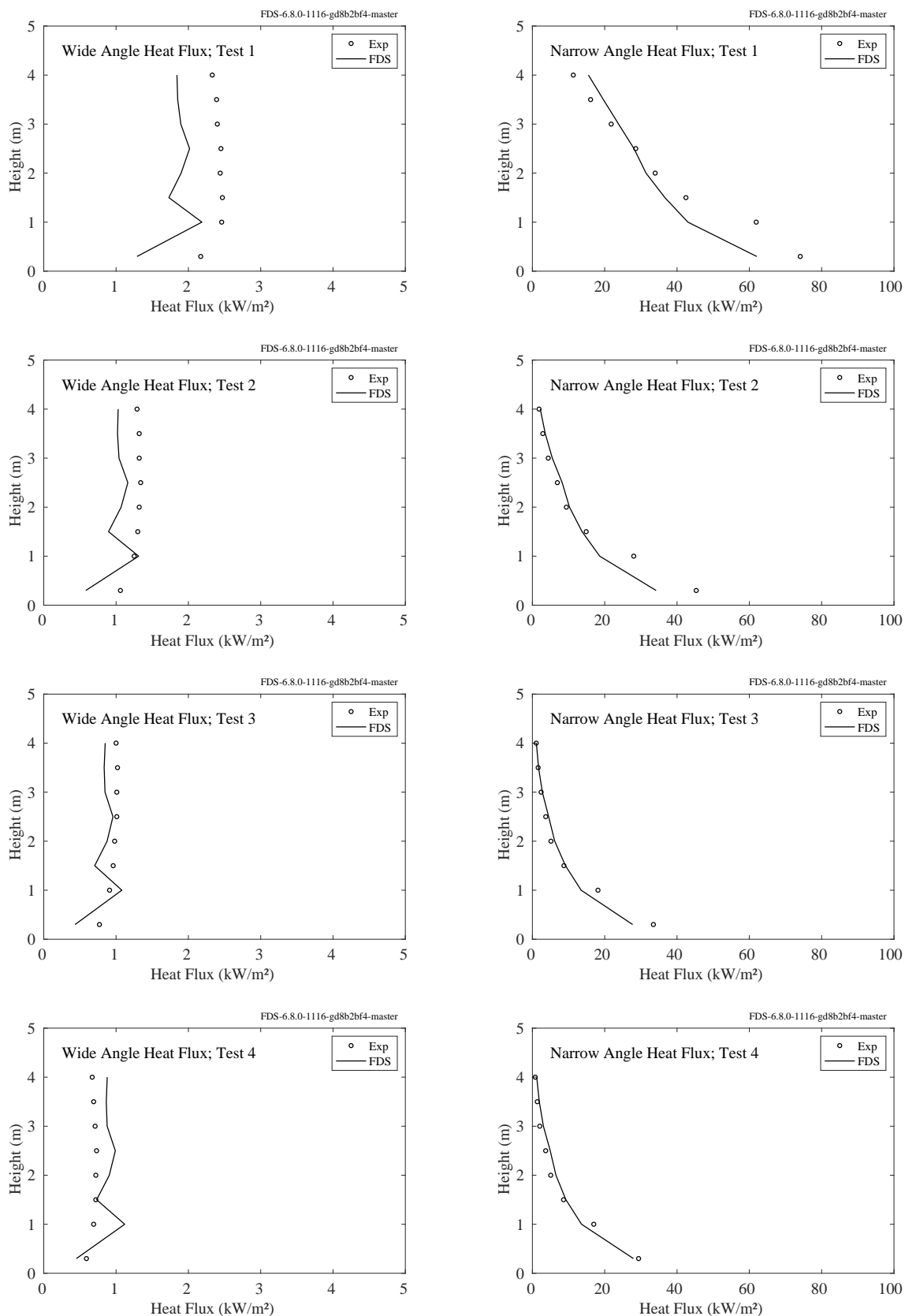


Figure 12.104: Sandia Methane Burner, heat flux, Tests 1-4.

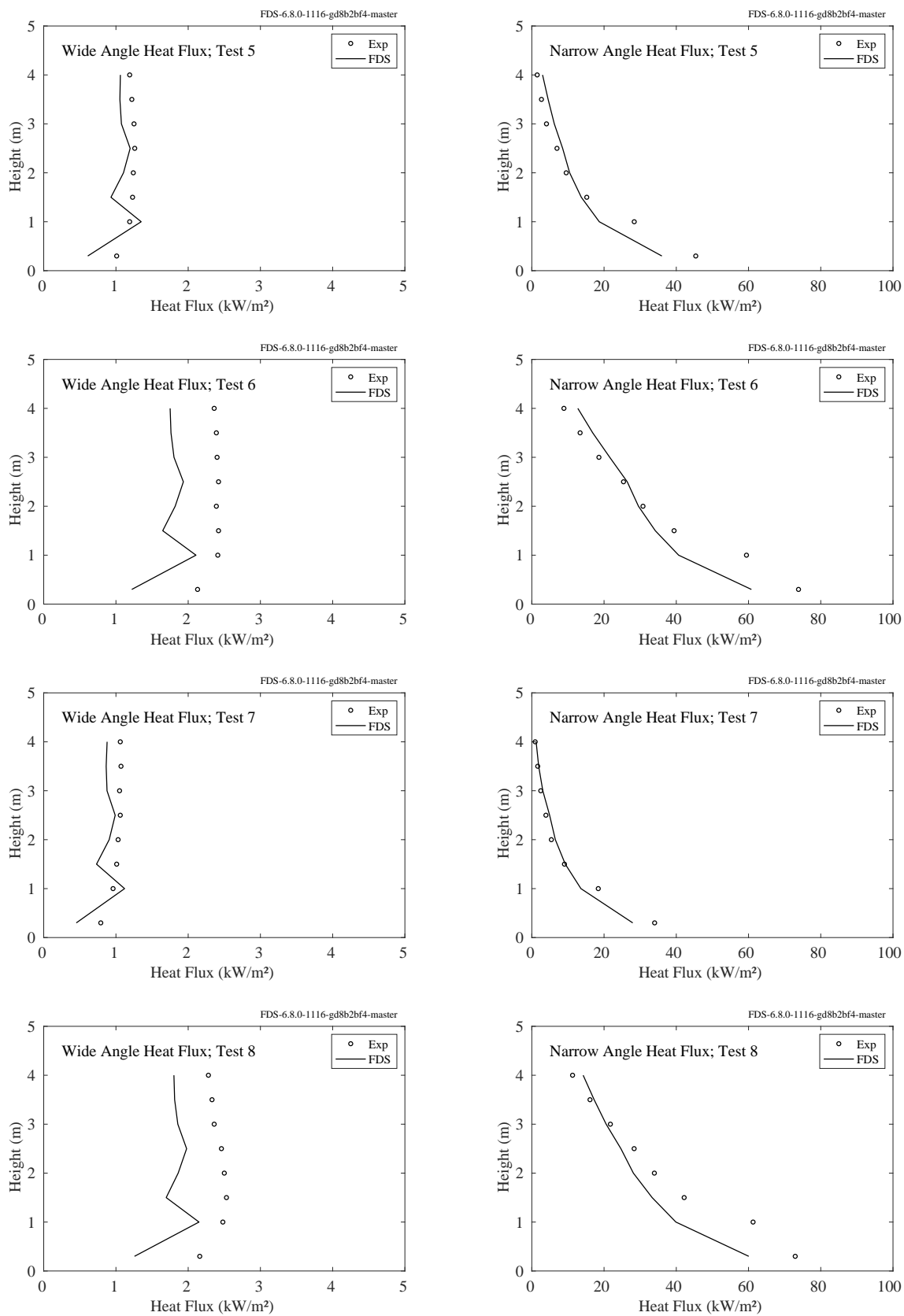


Figure 12.105: Sandia Methane Burner, heat flux, Tests 5-8.

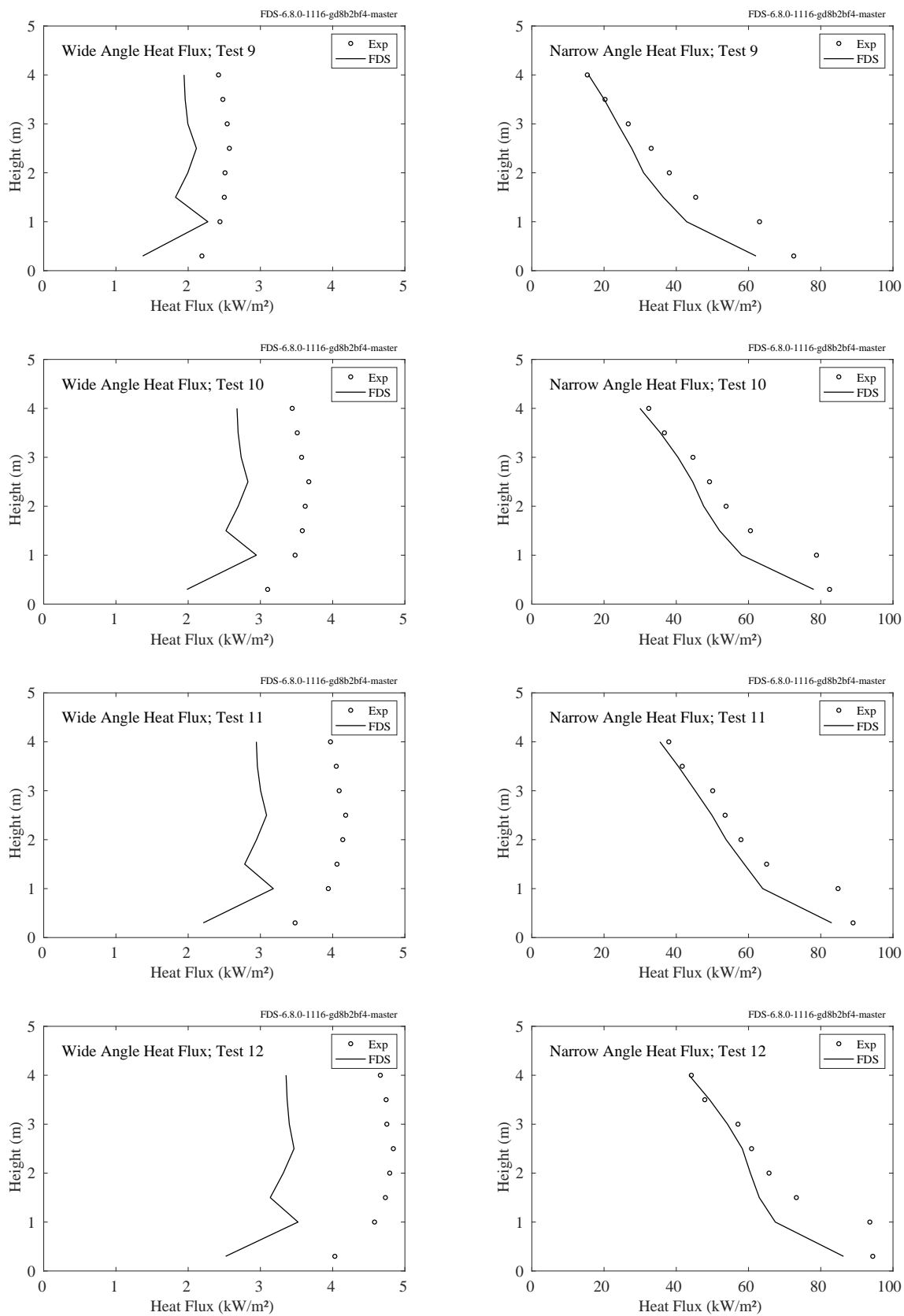


Figure 12.106: Sandia Methane Burner, heat flux, Tests 9-12.

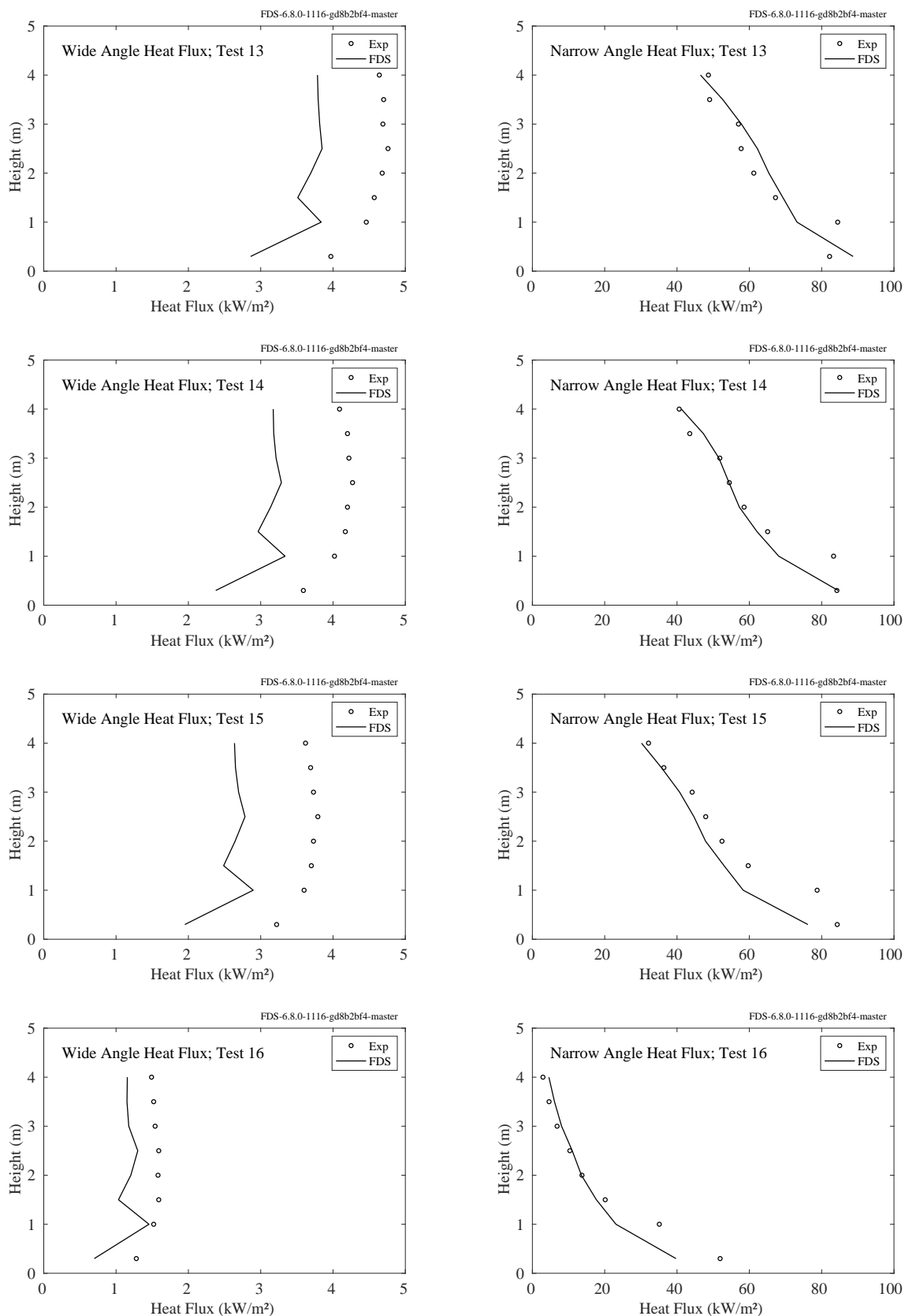


Figure 12.107: Sandia Methane Burner, heat flux, Tests 13-16.

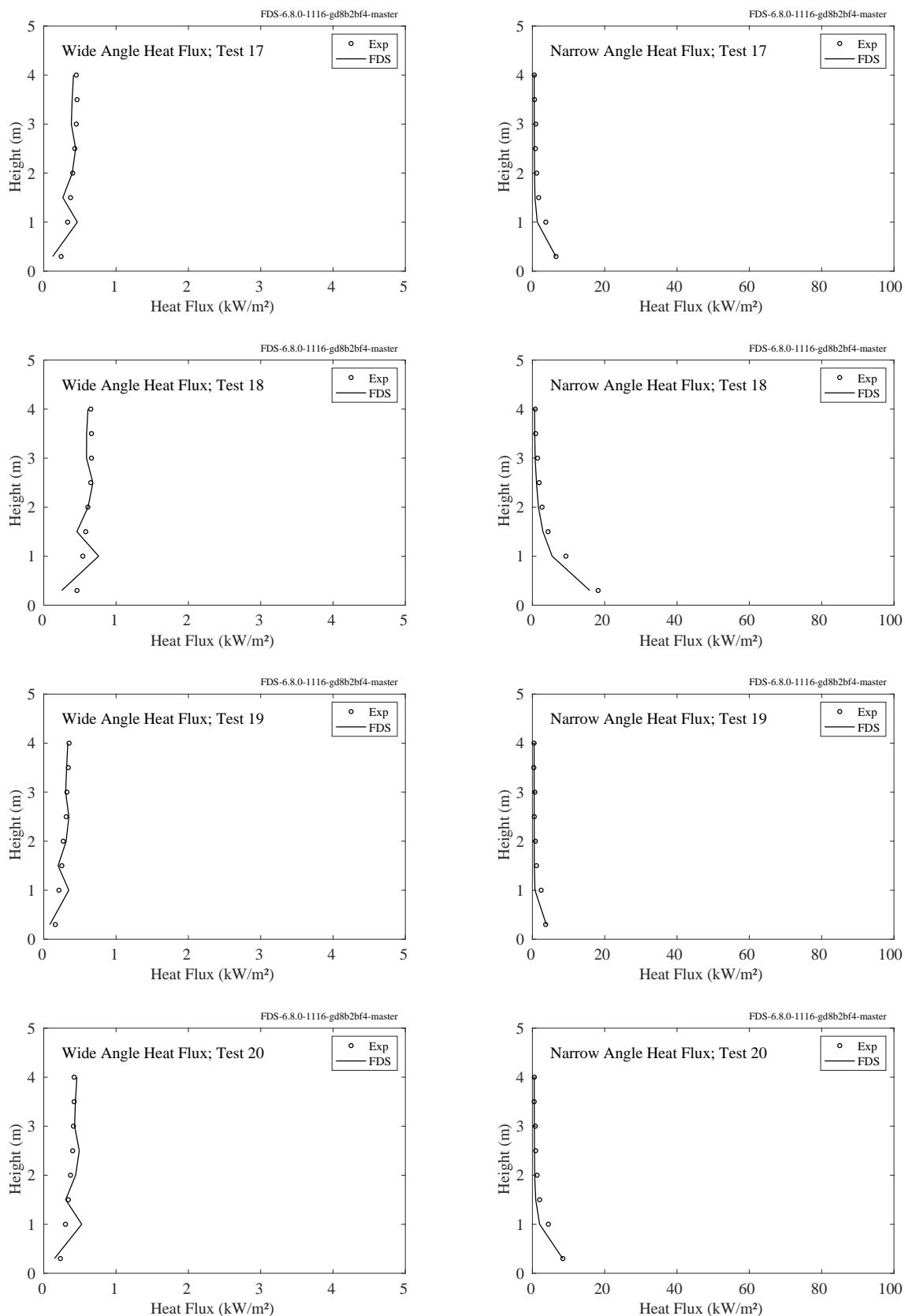


Figure 12.108: Sandia Methane Burner, heat flux, Tests 17-20.

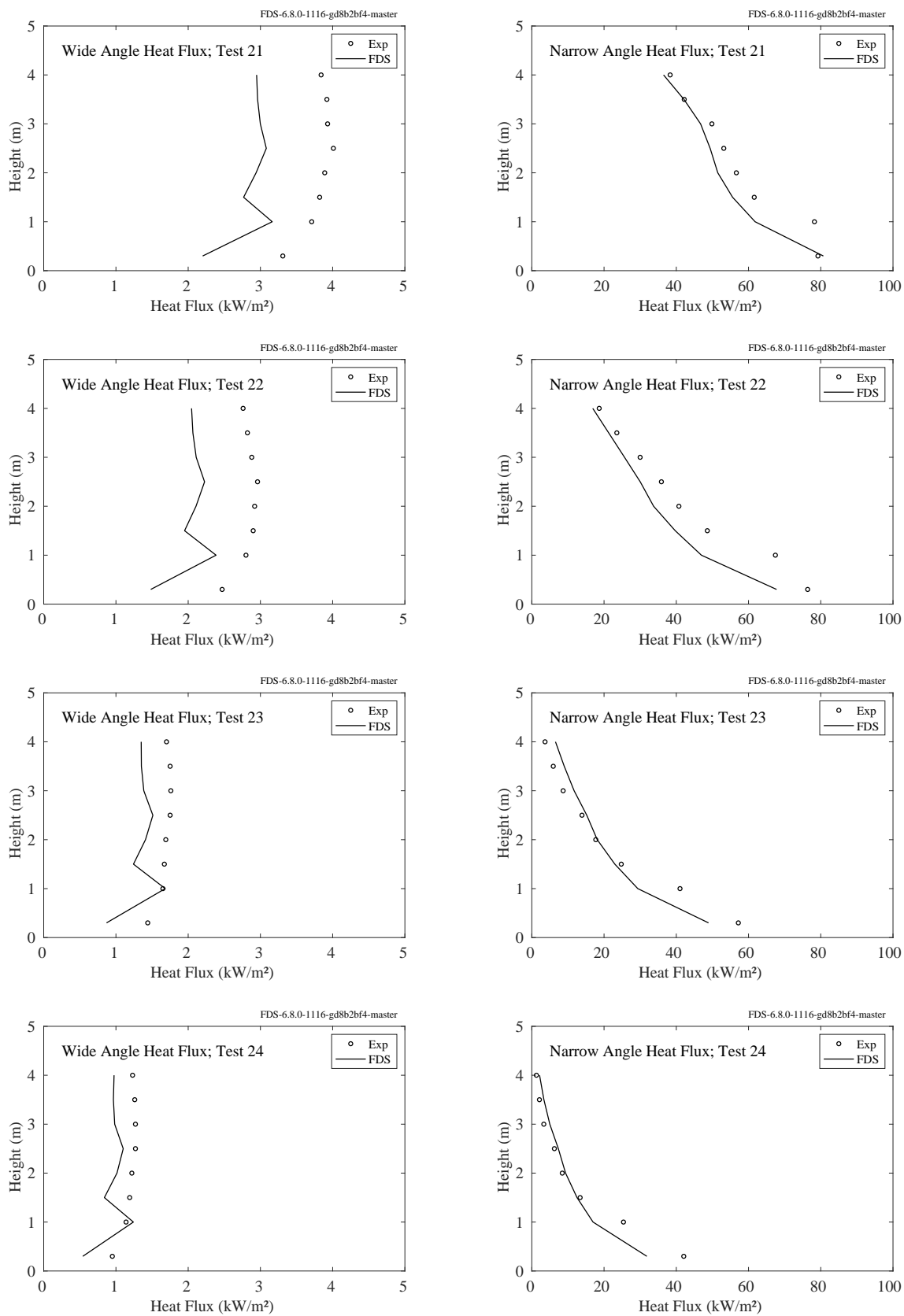


Figure 12.109: Sandia Methane Burner, heat flux, Tests 21-24.

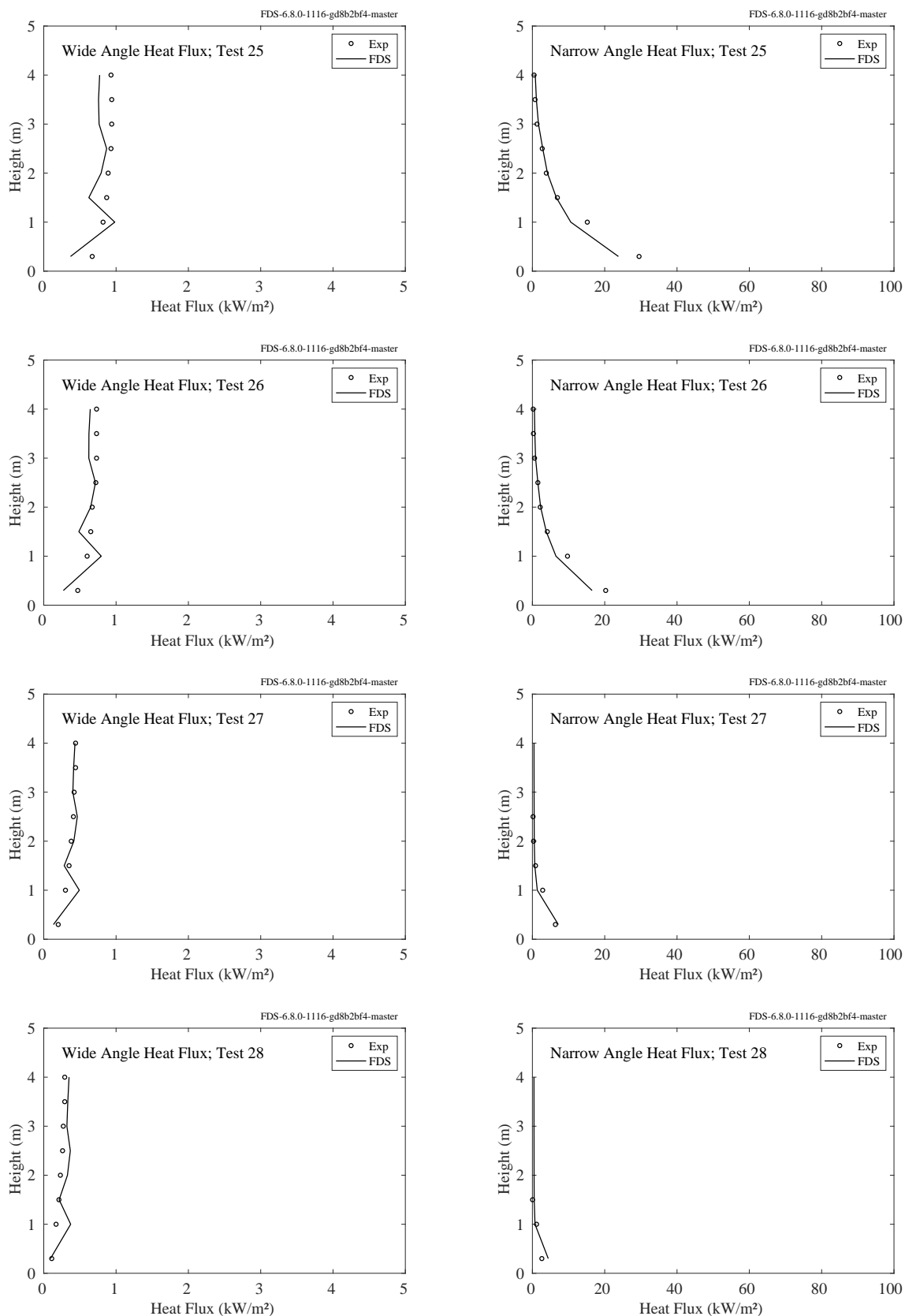


Figure 12.110: Sandia Methane Burner, heat flux, Tests 25-28.

12.2.12 Shell LNG Fireballs

A brief description of the experiments and modeling assumptions is given in Sec. 3.79.

Figure 12.111 compares the measured and predicted heat flux from three large fireballs at a distance of 100 m from the test vessel. Experiment 4 also includes measurements at distances of 40 m and 70 m.

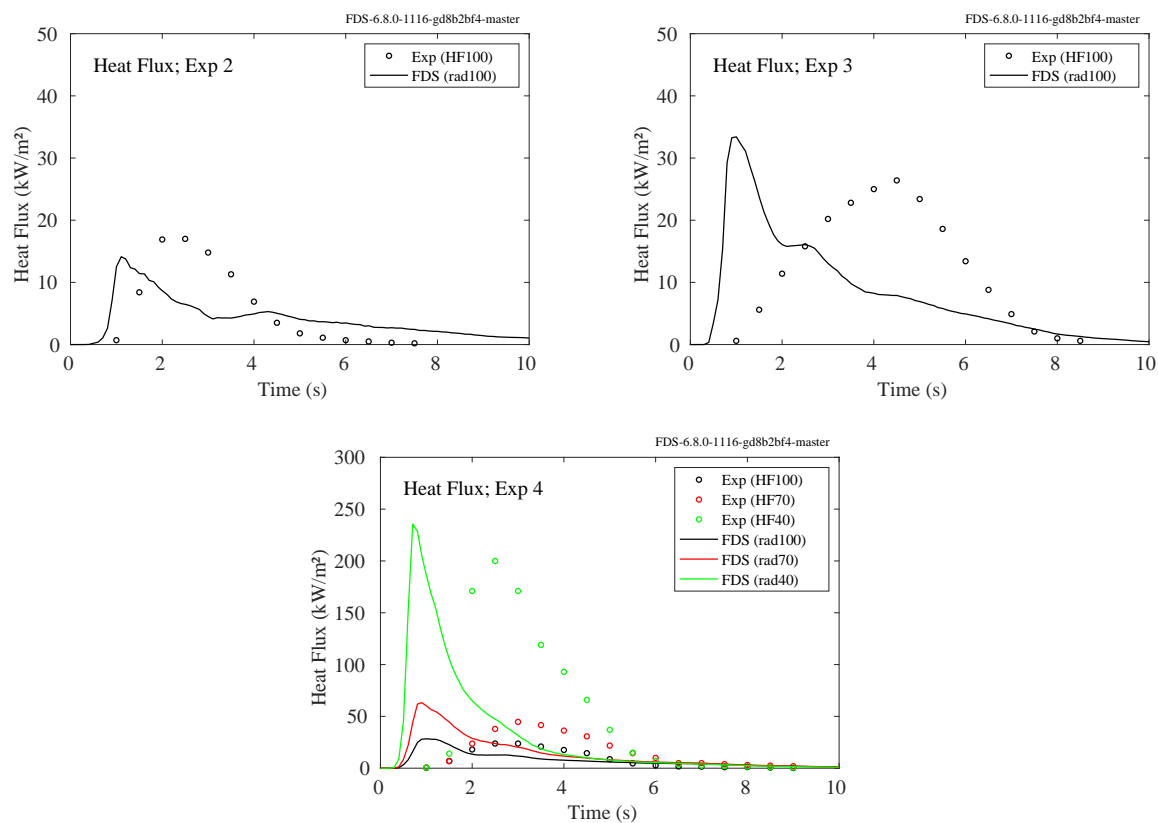


Figure 12.111: Heat flux for the Shell LNG Fireball experiments.

12.2.13 UMD SBI Experiment

A description of this experiment can be found in Sec. 3.94.

Figure 12.112 displays measured and predicted radiative heat flux to a vertical array of gauges (10 cm, 35 cm, 60 cm, 85 cm, 110 cm, 135 cm above the burner). The array is at a distance of 1 m from a PMMA corner fire in the SBI (Single Burning Item) apparatus.

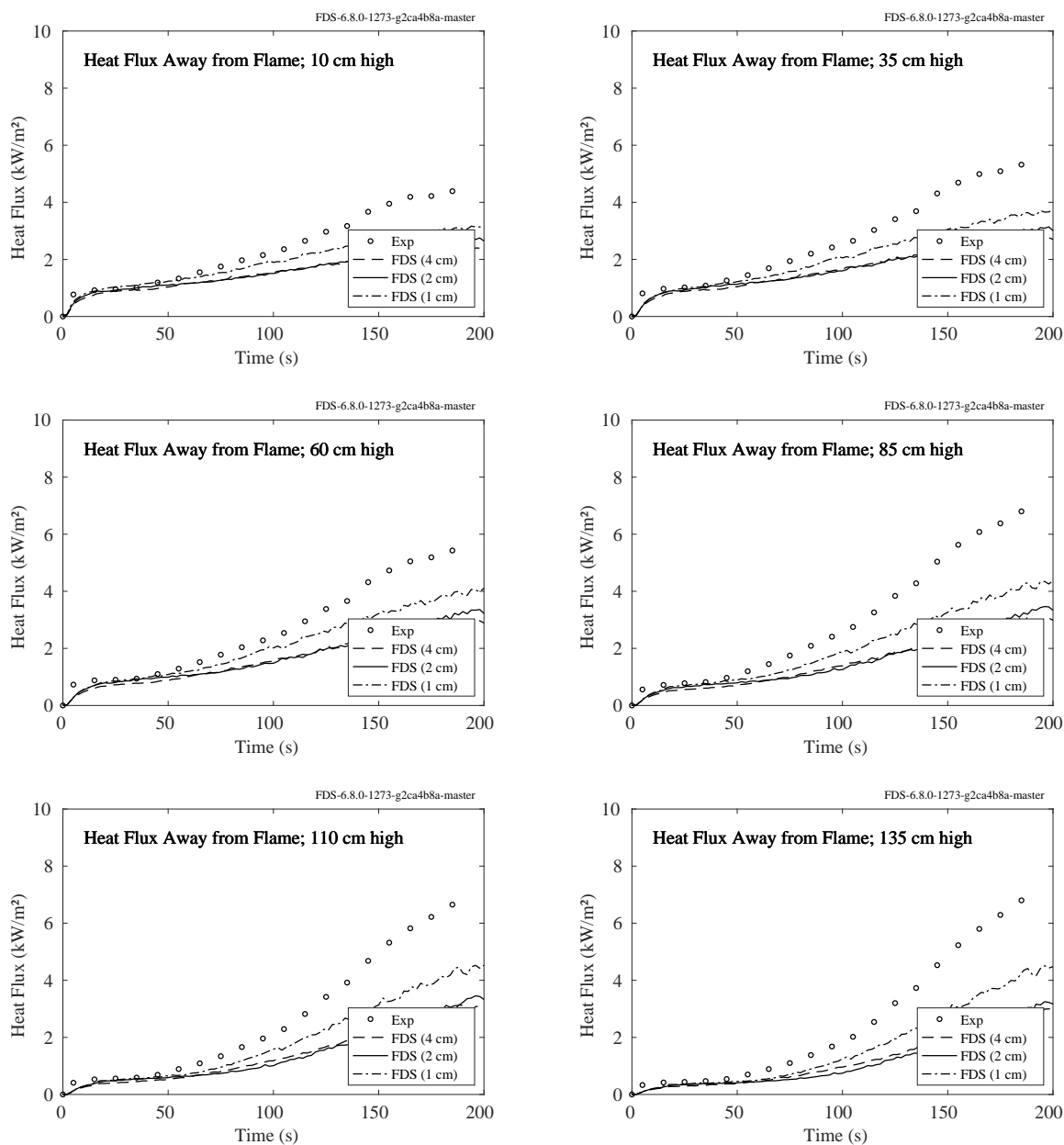


Figure 12.112: UMD SBI, radiative heat flux at six vertical locations.

12.2.14 UMD Line Burner

In the UMD line burner experiments, radiative heat flux was measured at a distance of 1 m normal to the flame sheet. In the FDS calculations the domain is extended to encompass the heat flux measurement location; two devices are placed at the 1 m distance on either side of the flame as shown in Fig. 12.113. This figure also shows a slice contour of integrated radiation intensity to confirm the pattern is smooth.

The radiative fraction and radiative heat flux as functions of oxygen volume fraction in the coflow have been measured by White et al. [332]. FDS does not employ a specified radiative fraction in these simulations. Rather it uses a three step reaction mechanism that produces CO and soot in the first step and the oxidation of these species in the second and third. The source of thermal radiation is the CO, CO₂, water vapor, and soot in the flame, as calculated by RadCal. Figure 12.114 displays the measured and predicted global radiative fraction and heat flux.

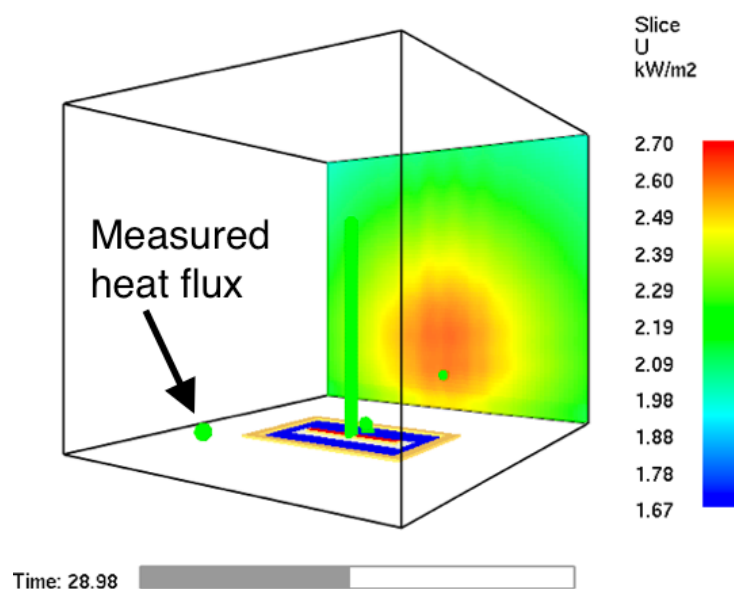


Figure 12.113: UMD Line Burner contour of integrated radiation intensity.

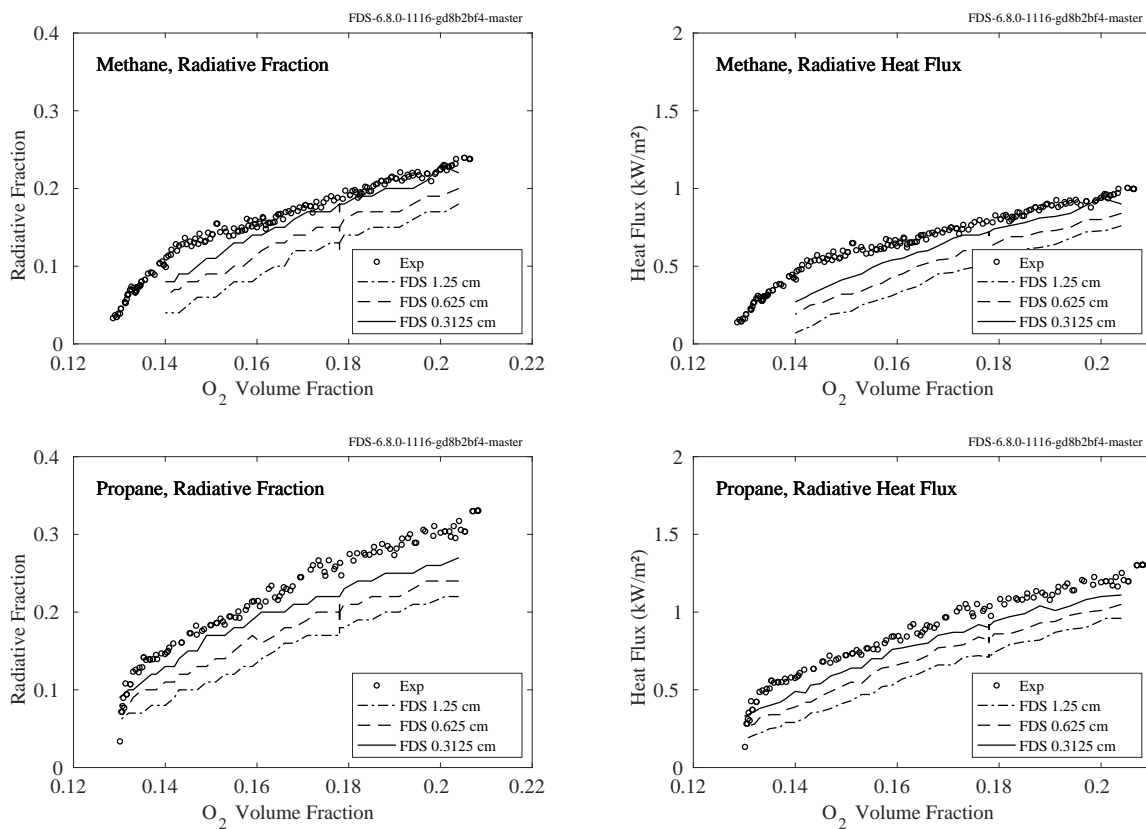


Figure 12.114: The plots on the left compare measured and predicted radiative fraction, and the plots on the right compare measured and predicted heat flux to a target 1 m away from the flame.

12.2.15 WTC Experiments

There were a variety of heat flux gauges installed in the test compartment. Most were within 2 m of the fire. Their locations and orientations are listed in Table 12.2.

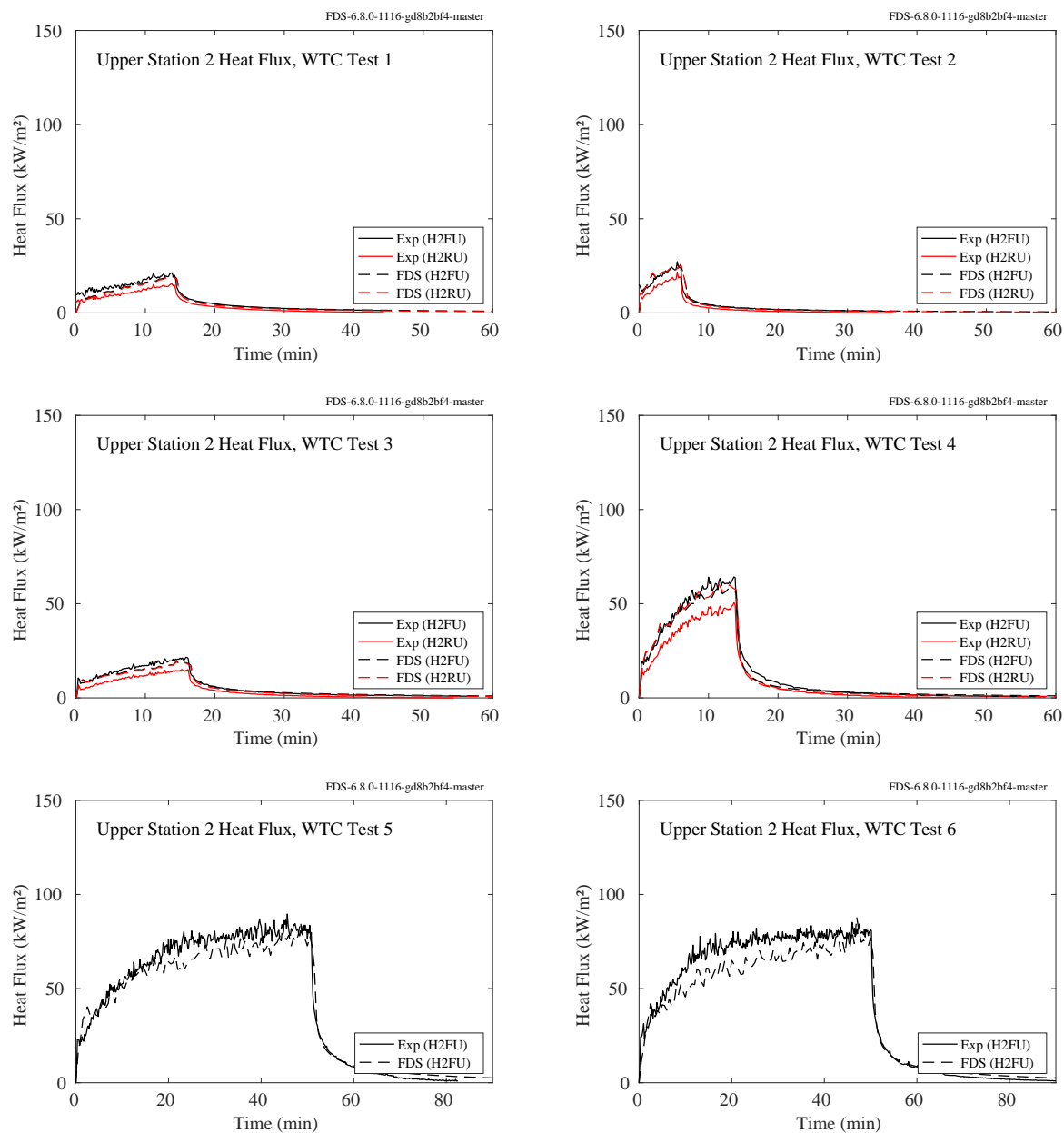


Figure 12.115: WTC experiments, heat flux at Station 2, high position.

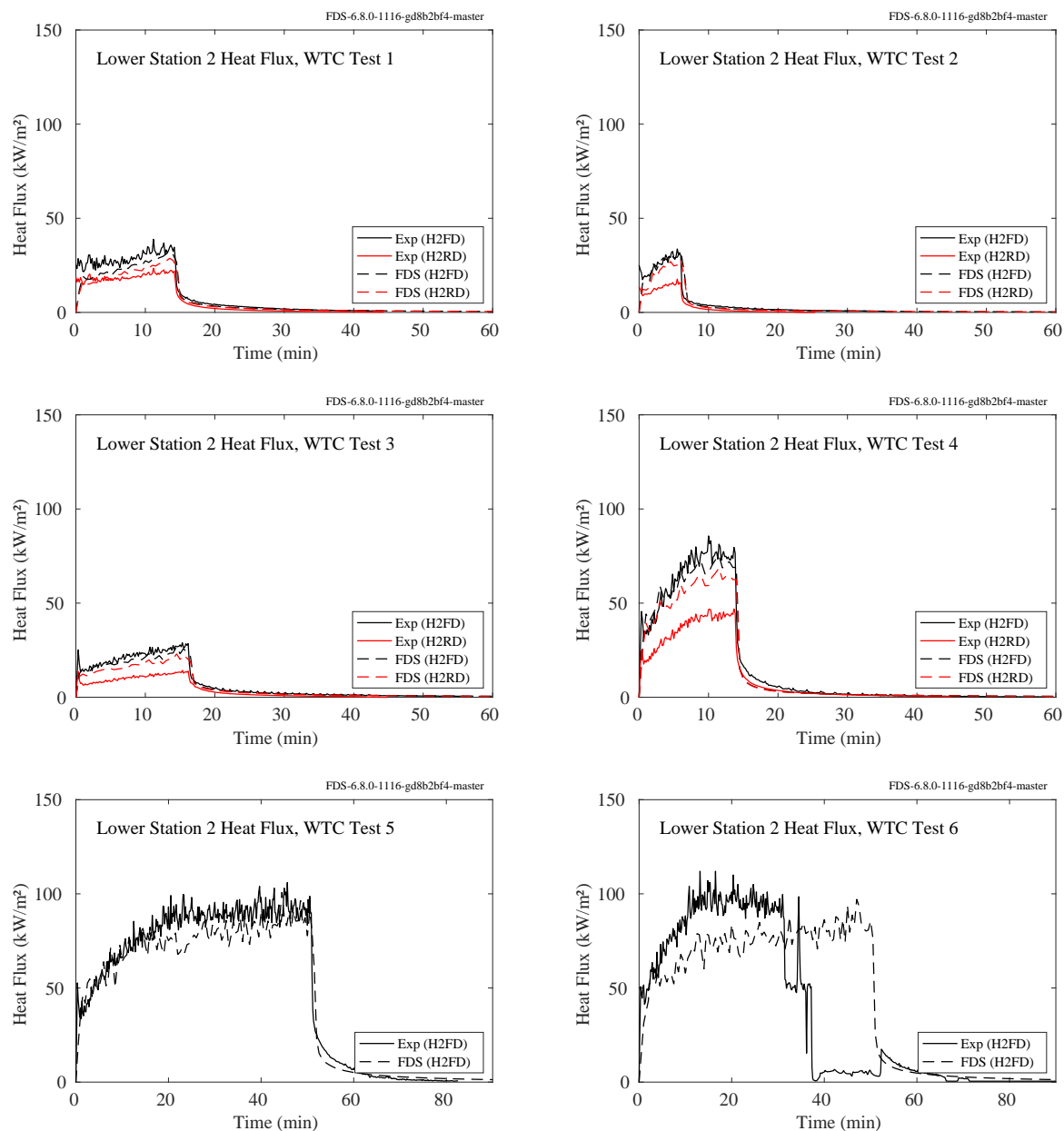


Figure 12.116: WTC experiments, heat flux at Station 2, low position.

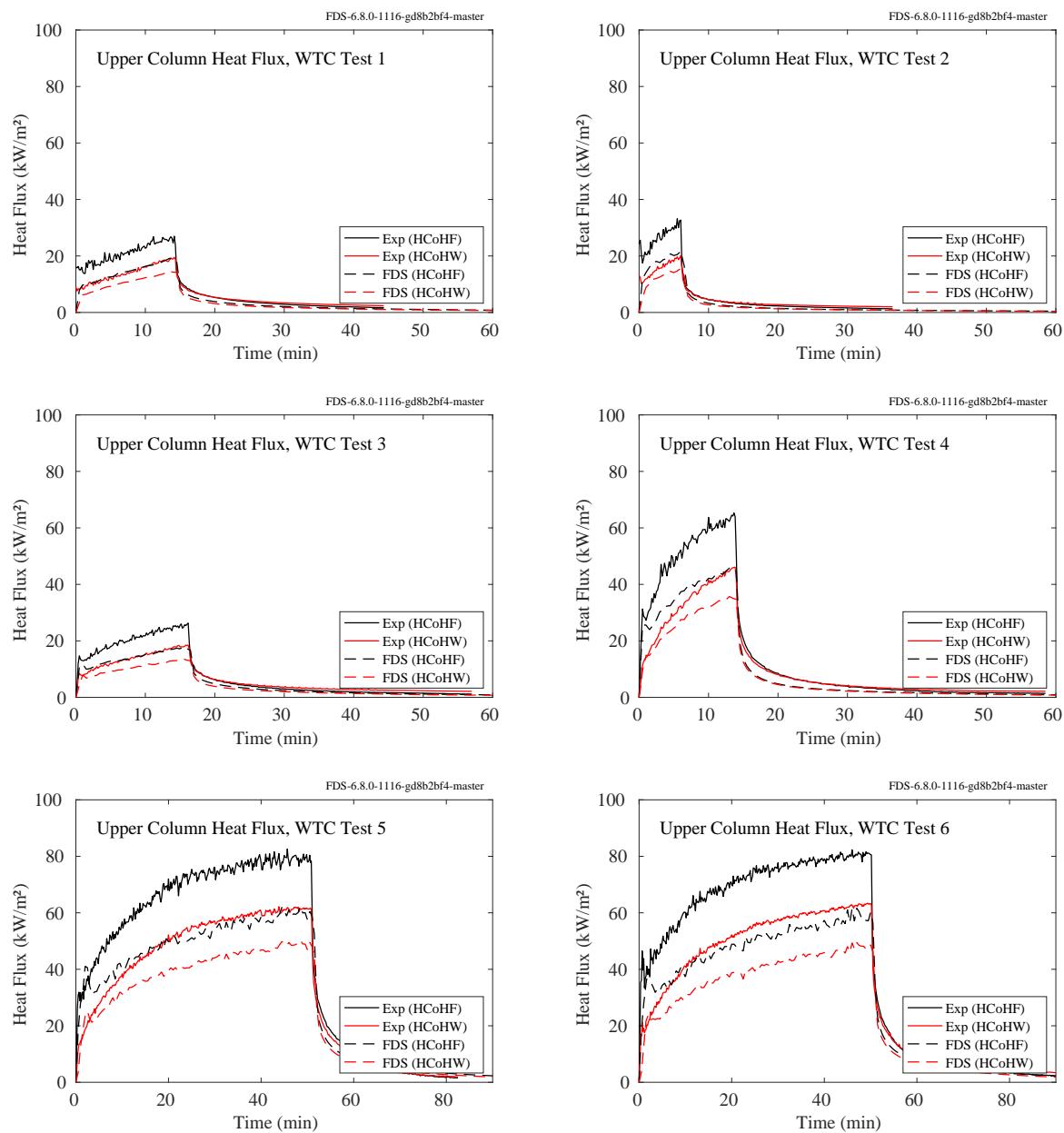


Figure 12.117: WTC experiments, heat flux to upper column.

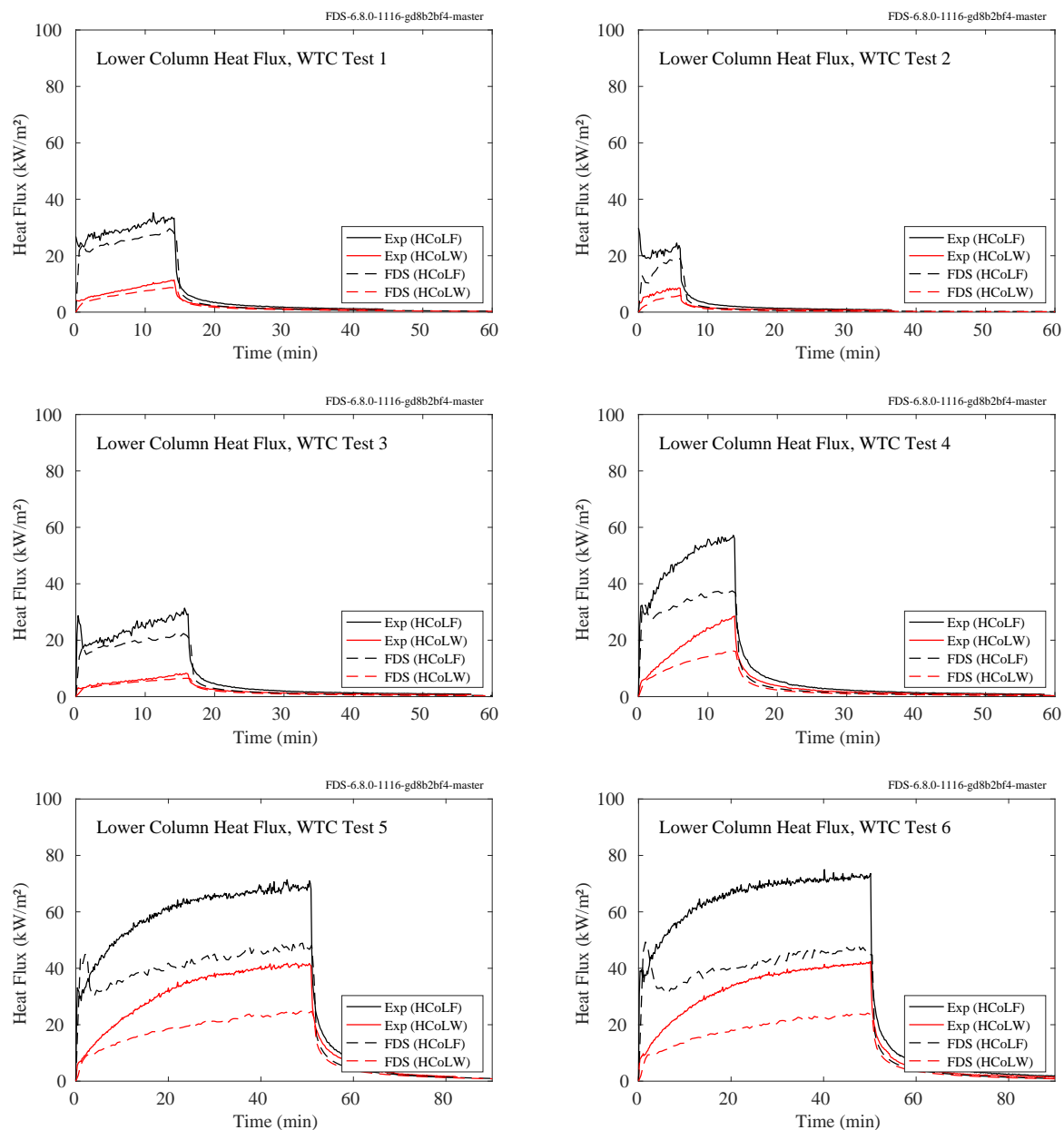


Figure 12.118: WTC experiments, heat flux to lower column.

12.2.16 Summary of Target Heat Flux Predictions

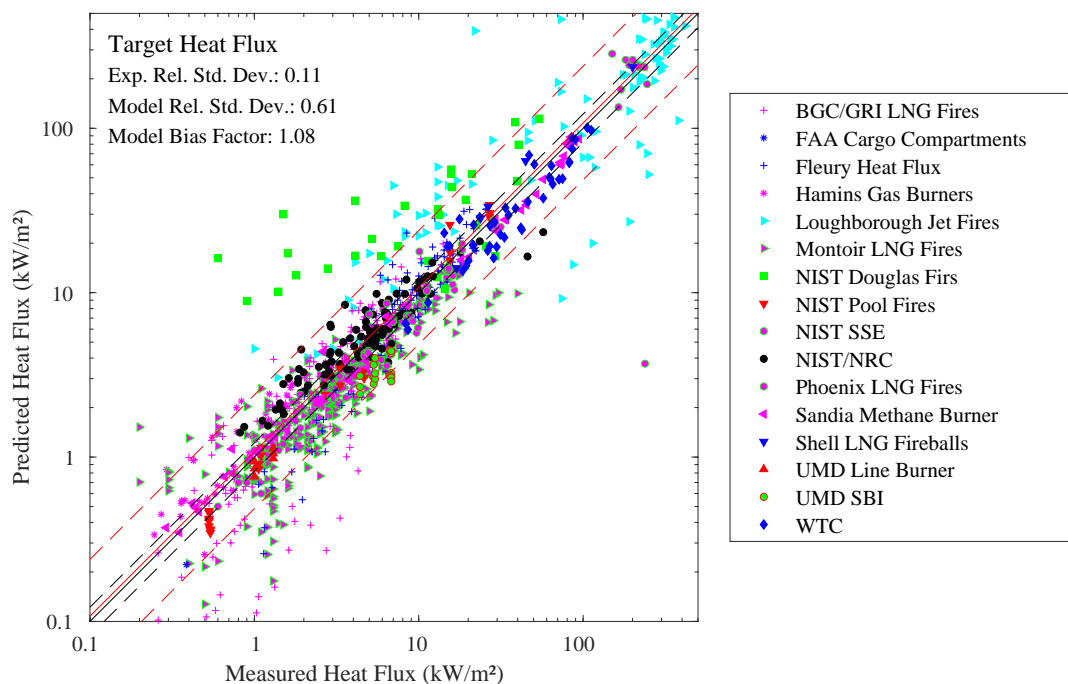


Figure 12.119: Summary of target heat flux predictions.

12.3 Attenuation of Thermal Radiation in Water Spray

This section presents the results of simulations of spray experiments where the reduction of thermal radiation by a fine water spray was measured.

12.3.1 BRE Spray Experiments

Attenuation of thermal radiation by a water spray was measured using three full-cone type hydraulic nozzles at eight different pressures. The initial droplet speeds were determined using a simple hydraulic relation, $v = 0.9\sqrt{2P/\rho}$. The median drop size distributions were determined by assuming $d_m \propto p^{-1/3}$ and finding the constant of proportionality by fitting to the experimental PDPA measurement 1 m below the nozzles. Measured median diameters, $d_{v,50}$, are compared against mean diameters, d_{43} . The arithmetic mean of the droplets is used for vertical velocity. The comparison of predicted and measured attenuation, Fig. 12.121, is made at a distance of 4 m from the heat source.

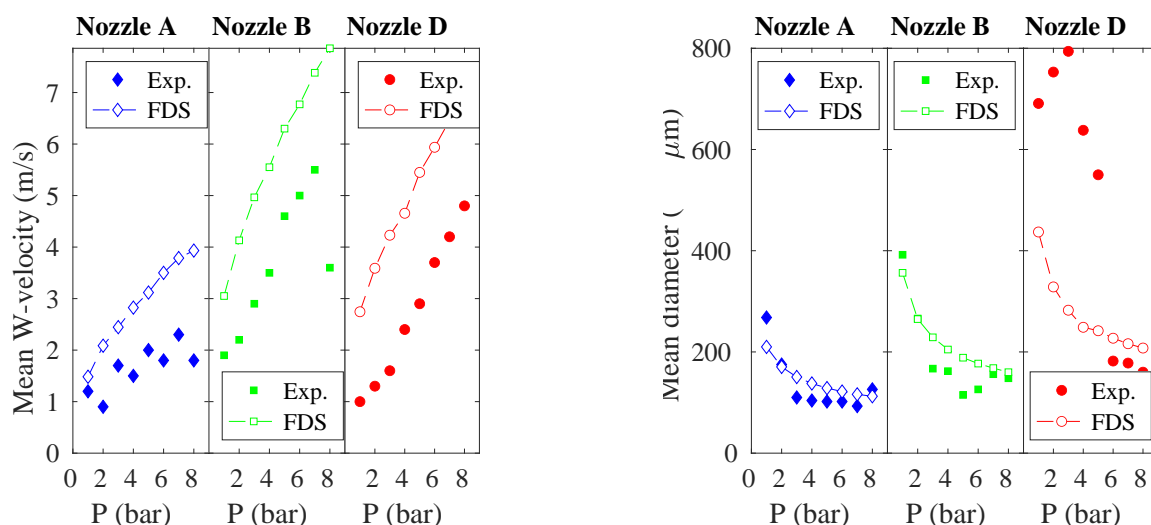


Figure 12.120: Comparison of experimental and predicted droplet speeds and mean diameters for the three nozzles and different pressures.

12.3.2 LEMTA Spray Experiments

The attenuation of thermal radiation was measured at five heights in water sprays produced by seven full-elliptic type hydraulic nozzles. The operating pressure was 4 bar. The initial speed was deduced from the water flow rate and the orifice diameter. The droplet size at the injection point was determined by comparing the predicted and measured results at the PDPA measurement location 0.2 m below the nozzles. The comparison of predicted and measured attenuations, Fig. 12.121, is made at five locations.

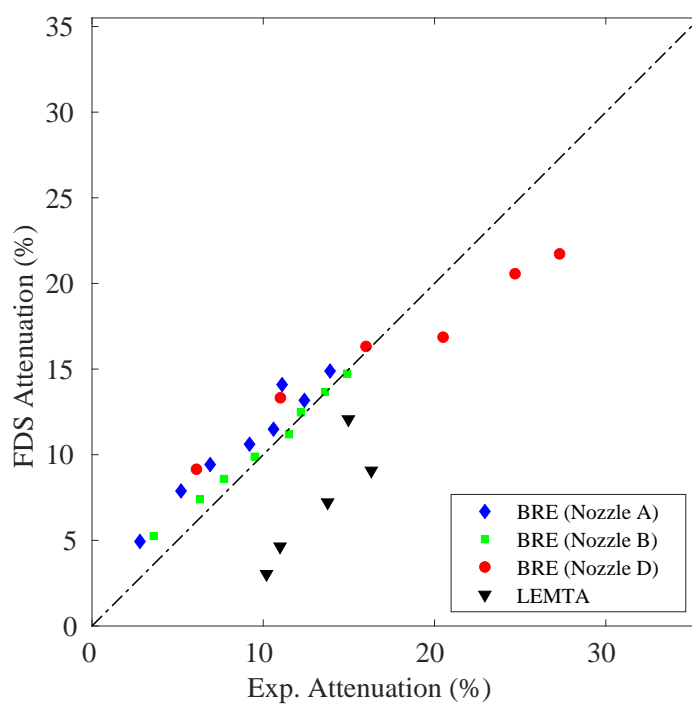


Figure 12.121: Comparison of predicted and measured radiation attenuation in the spray experiments at BRE and at LEMTA.

12.4 Water Spray Cooling

12.4.1 LEMTA Spray Cooling Experiments

The results of the LEMTA Spray Cooling experiment is shown in Fig. 12.122 for three different nozzles and two plate orientations, horizontal and vertical.

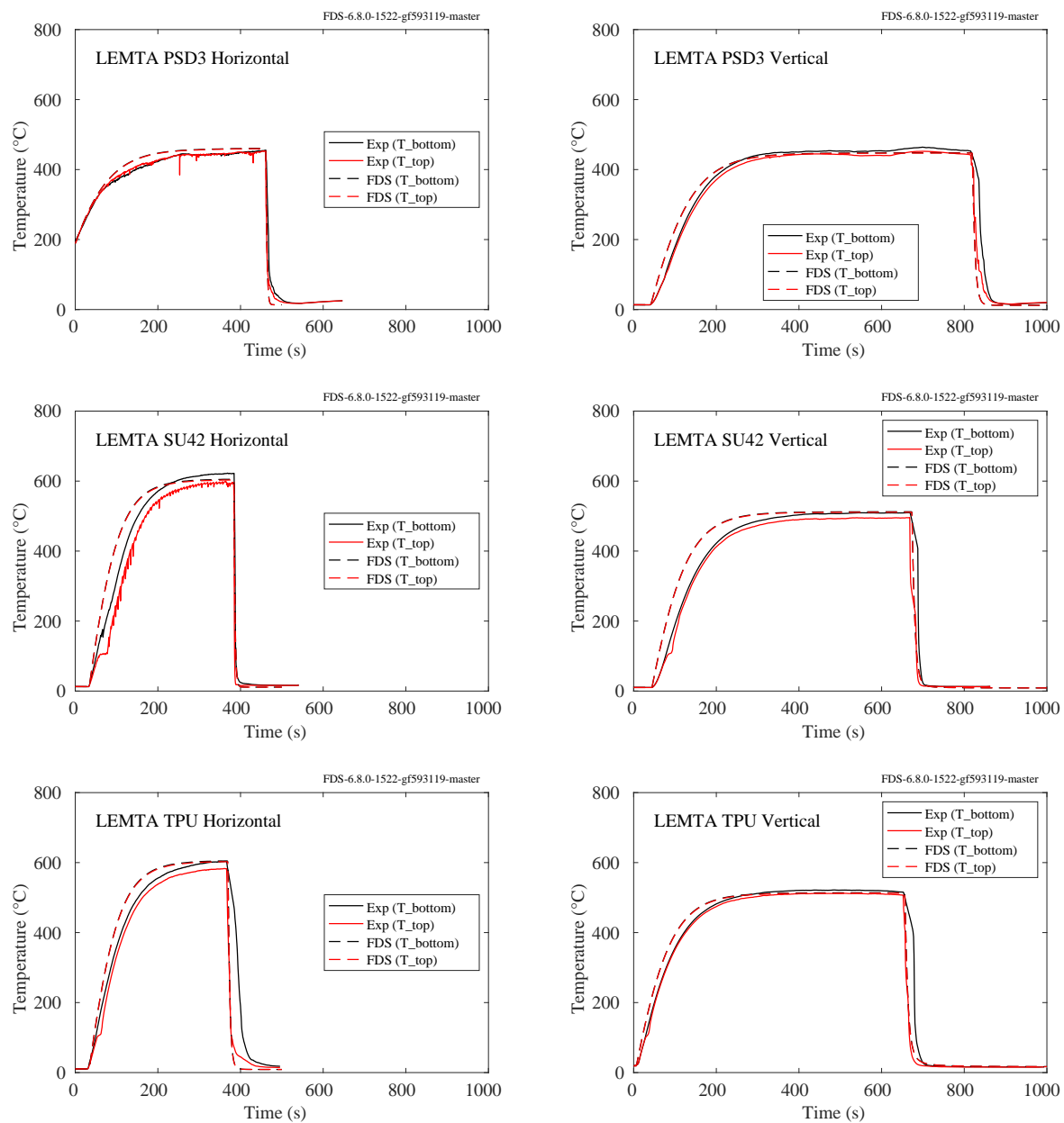


Figure 12.122: Temperature of the top and bottom of a heated steel plate cooled with a water spray.

12.5 Convective Heat Flux

This section focuses specifically on experiments that primarily involved convective heat transfer.

12.5.1 Bouchair Solar Chimney

The plots on the following pages compare the predicted air mass flow rates through the test apparatus shown in Fig. 3.5. The measurements were made at both the inlet and outlet of the thermal cavity. Note that in Bouchair's thesis [156], the measurements were presented as mass flow rates per unit length of the inlet slot, 1.4 m. In the plots on the following pages, the measurements and simulation results are presented simply as a total mass flux, kg/s.

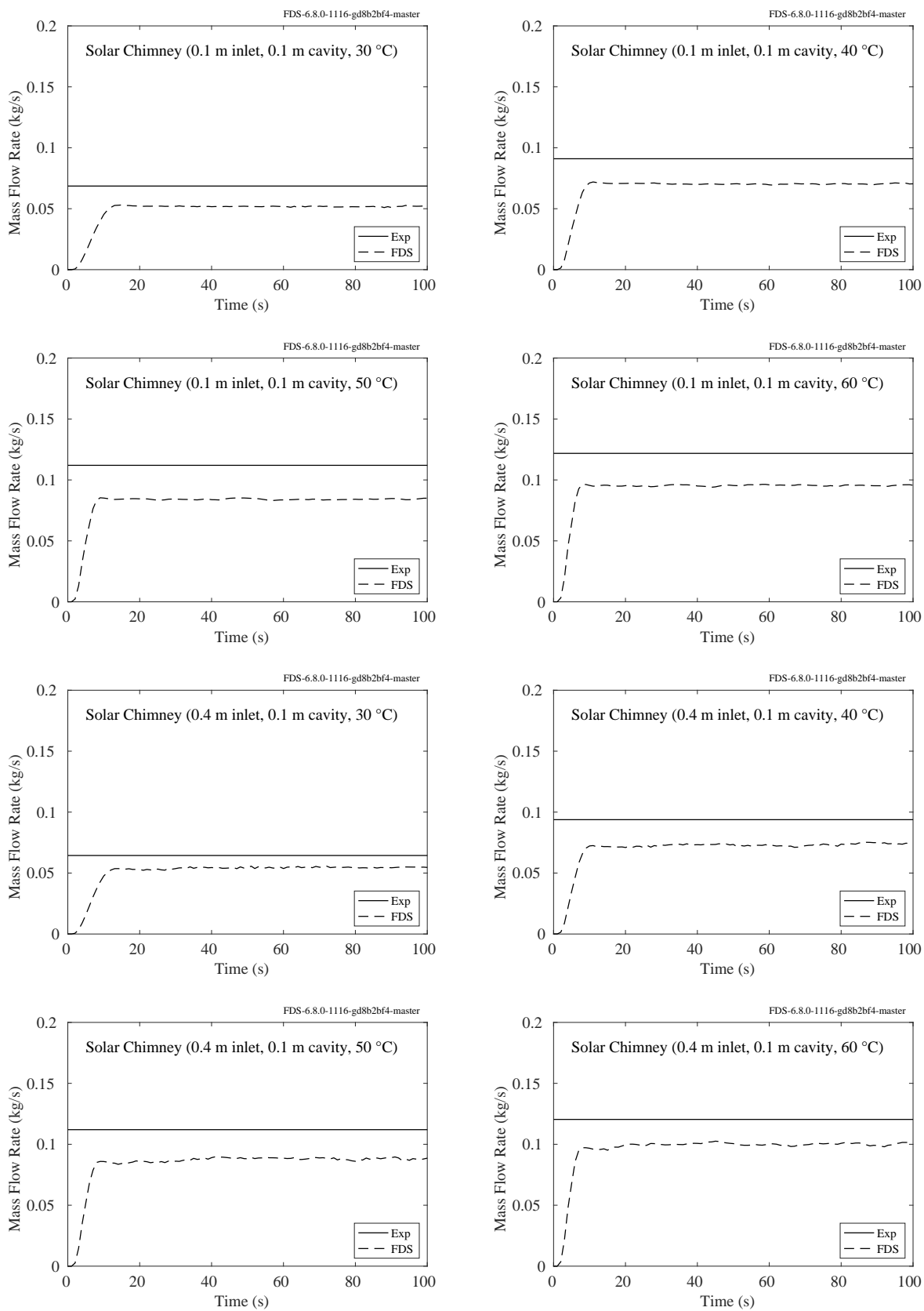


Figure 12.123: Bouchair Solar Chimney, 0.1 m thermal cavity.

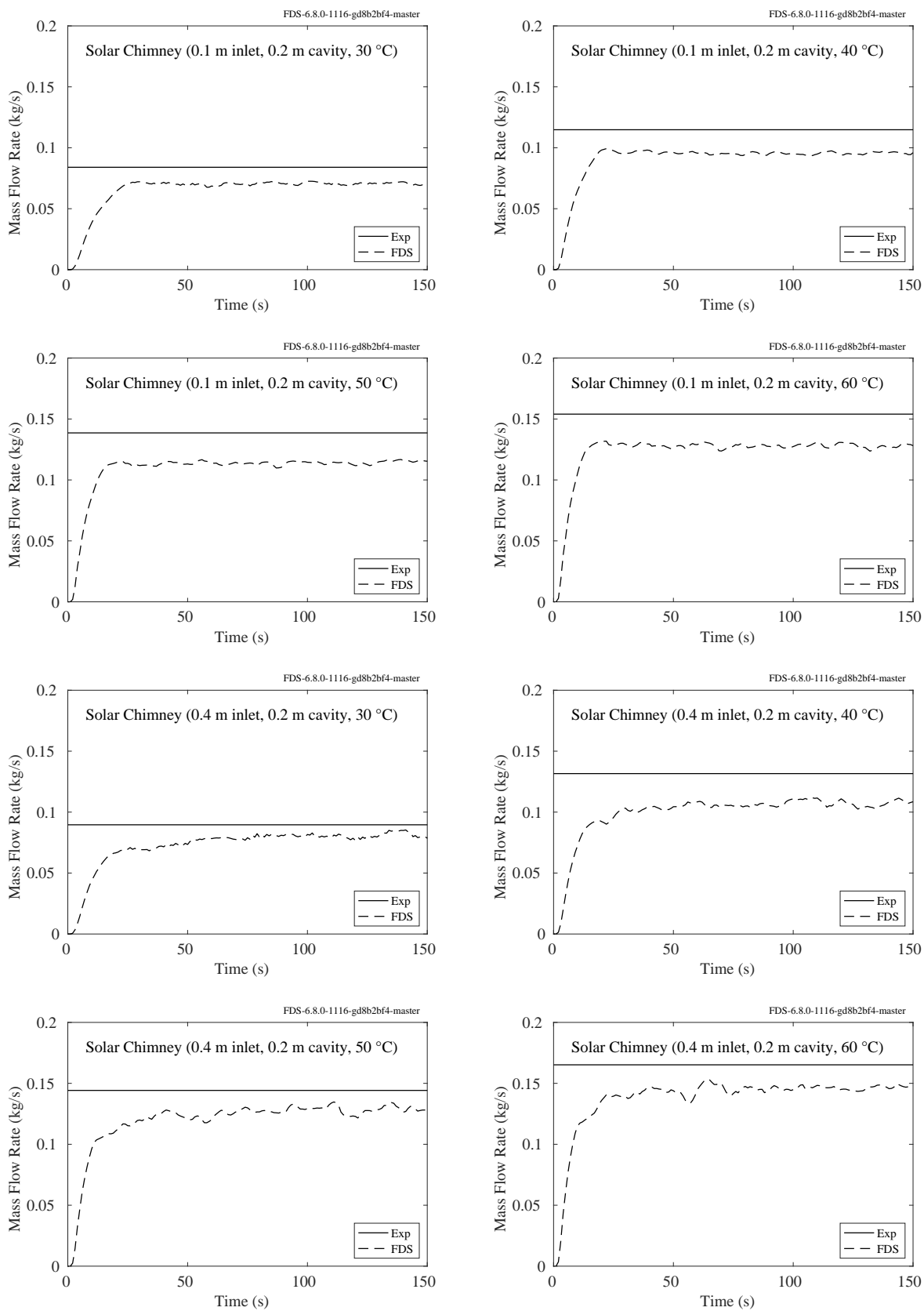


Figure 12.124: Bouchair Solar Chimney, 0.2 m thermal cavity.

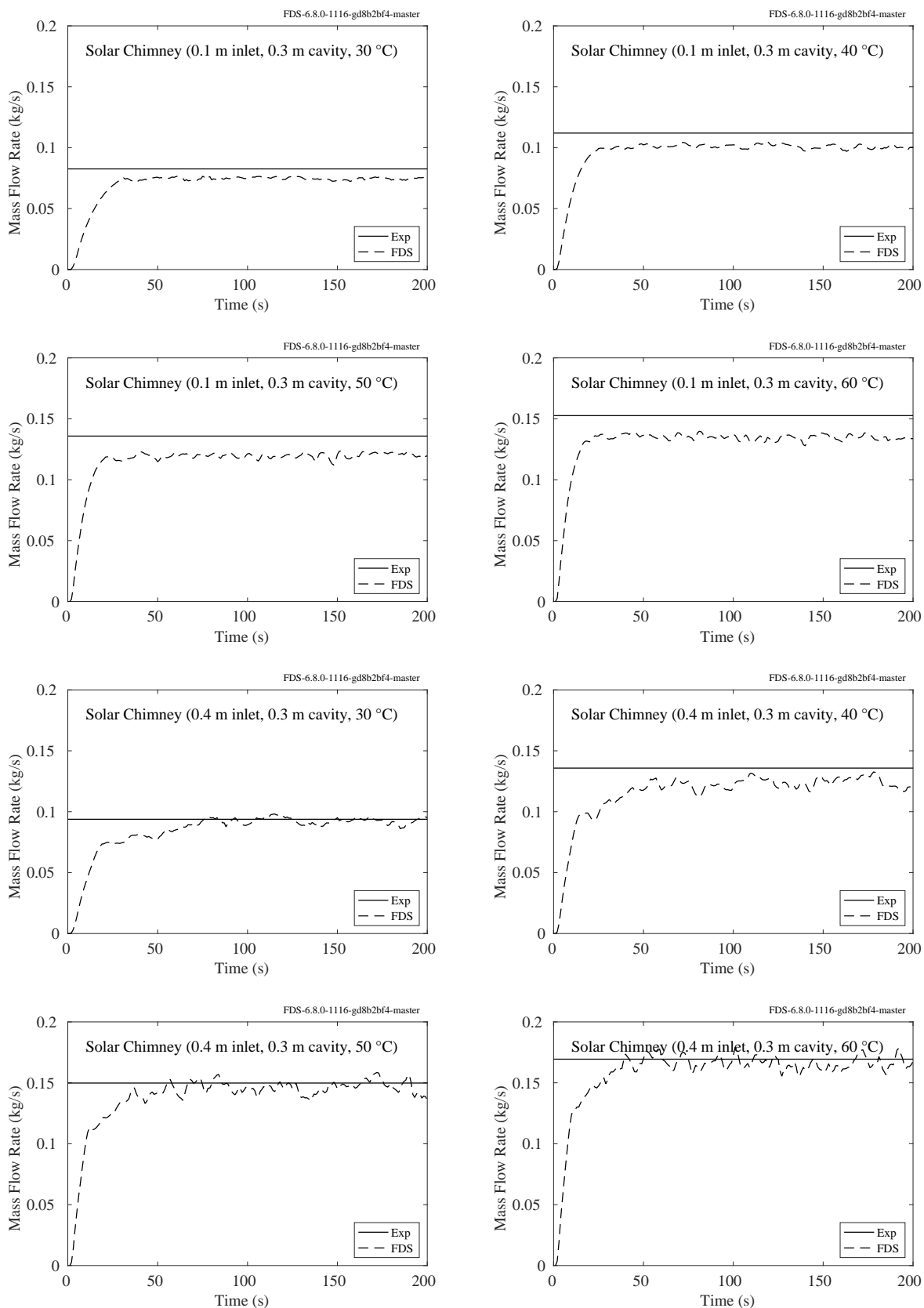


Figure 12.125: Bouchair Solar Chimney, 0.3 m thermal cavity.

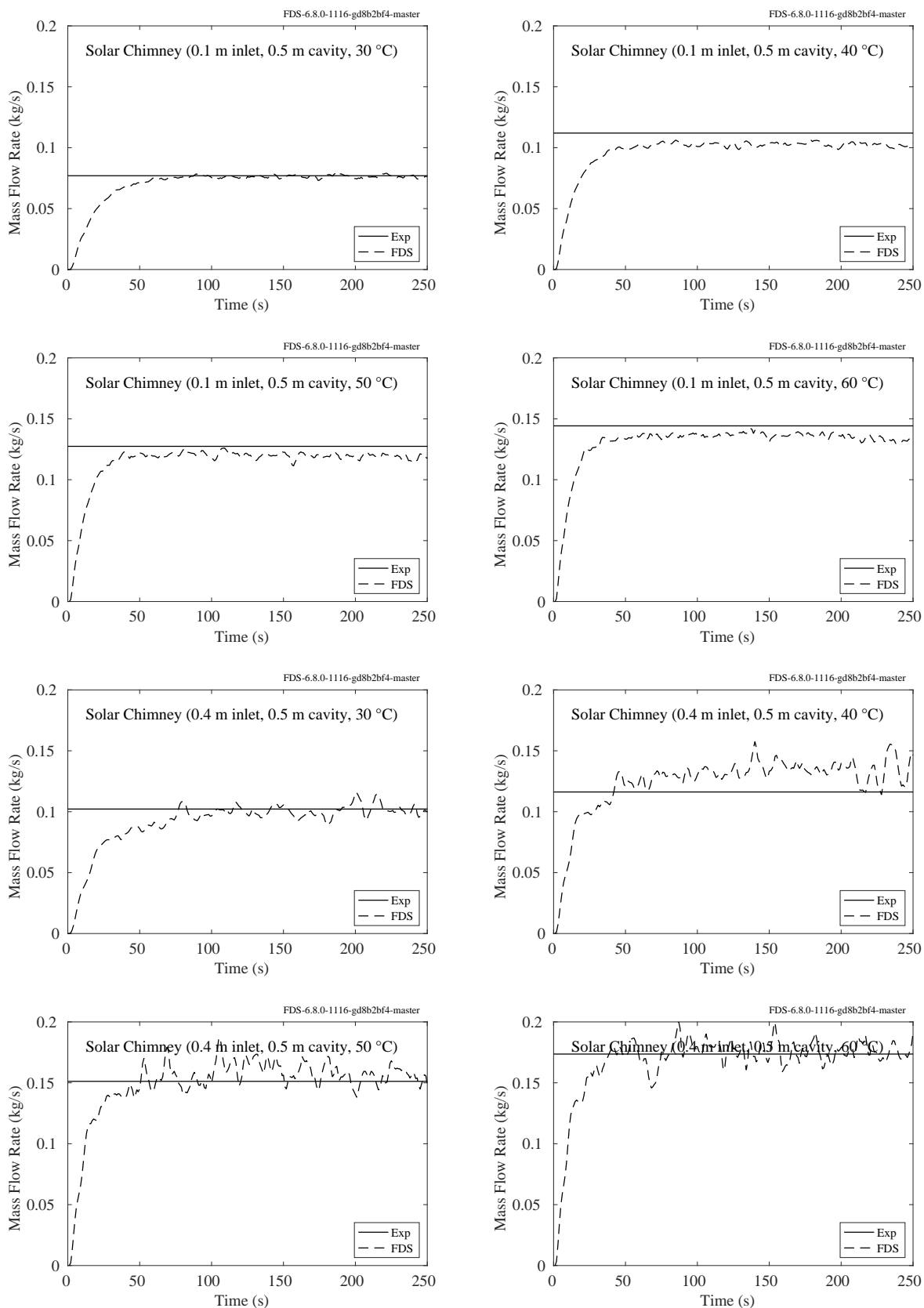


Figure 12.126: Bouchair Solar Chimney, 0.5 m thermal cavity.

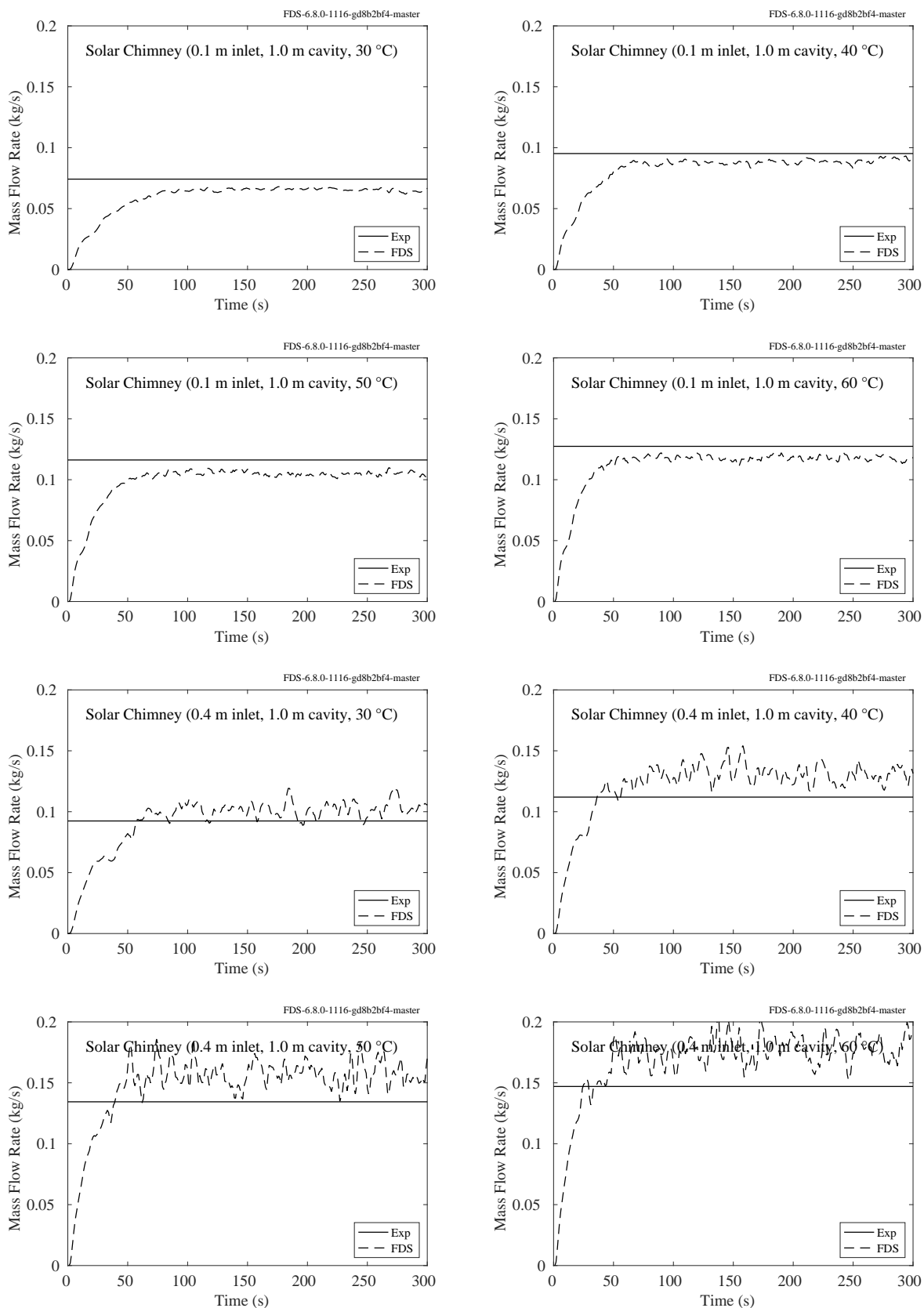


Figure 12.127: Bouchair Solar Chimney, 1.0 m thermal cavity.

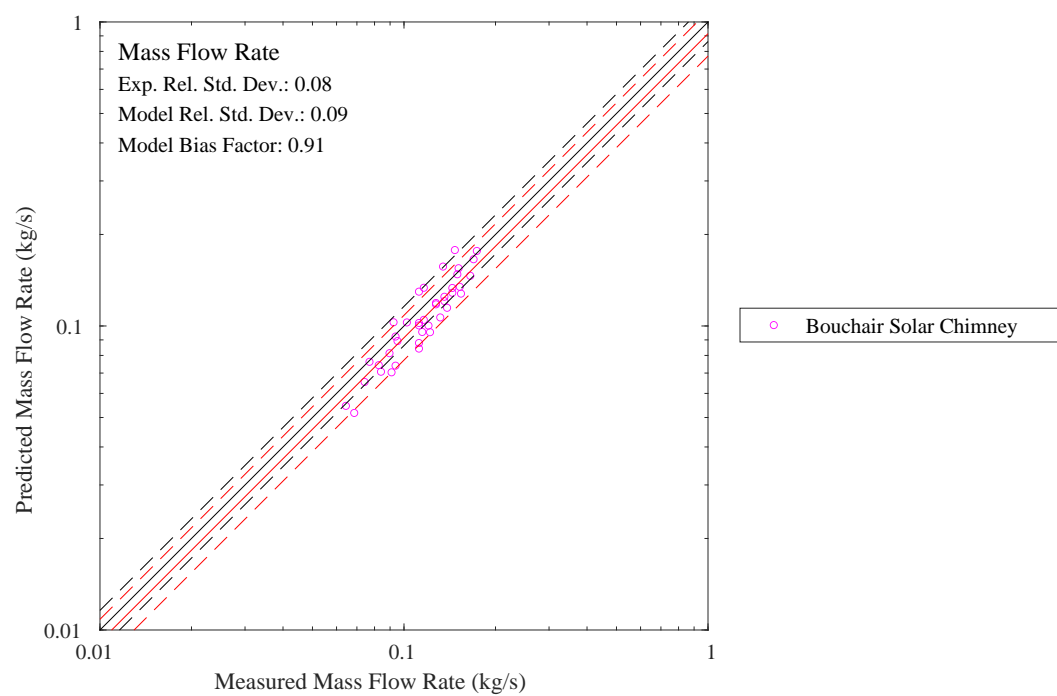


Figure 12.128: Summary of Bouchair Solar Chimney results.

12.6 Radiation Source Term

12.6.1 FM Burner Experiments

Figure 12.129 displays mean and rms vertical profiles of the radiation emission, in units of kW/m, from a 15 kW, 13.7 cm (inner) diameter ethylene burner at ambient oxygen concentrations of 21 %, 19 %, 17 %, and 15 %. Figure 12.130 displays the predicted total radiant fraction for the four ambient oxygen levels.

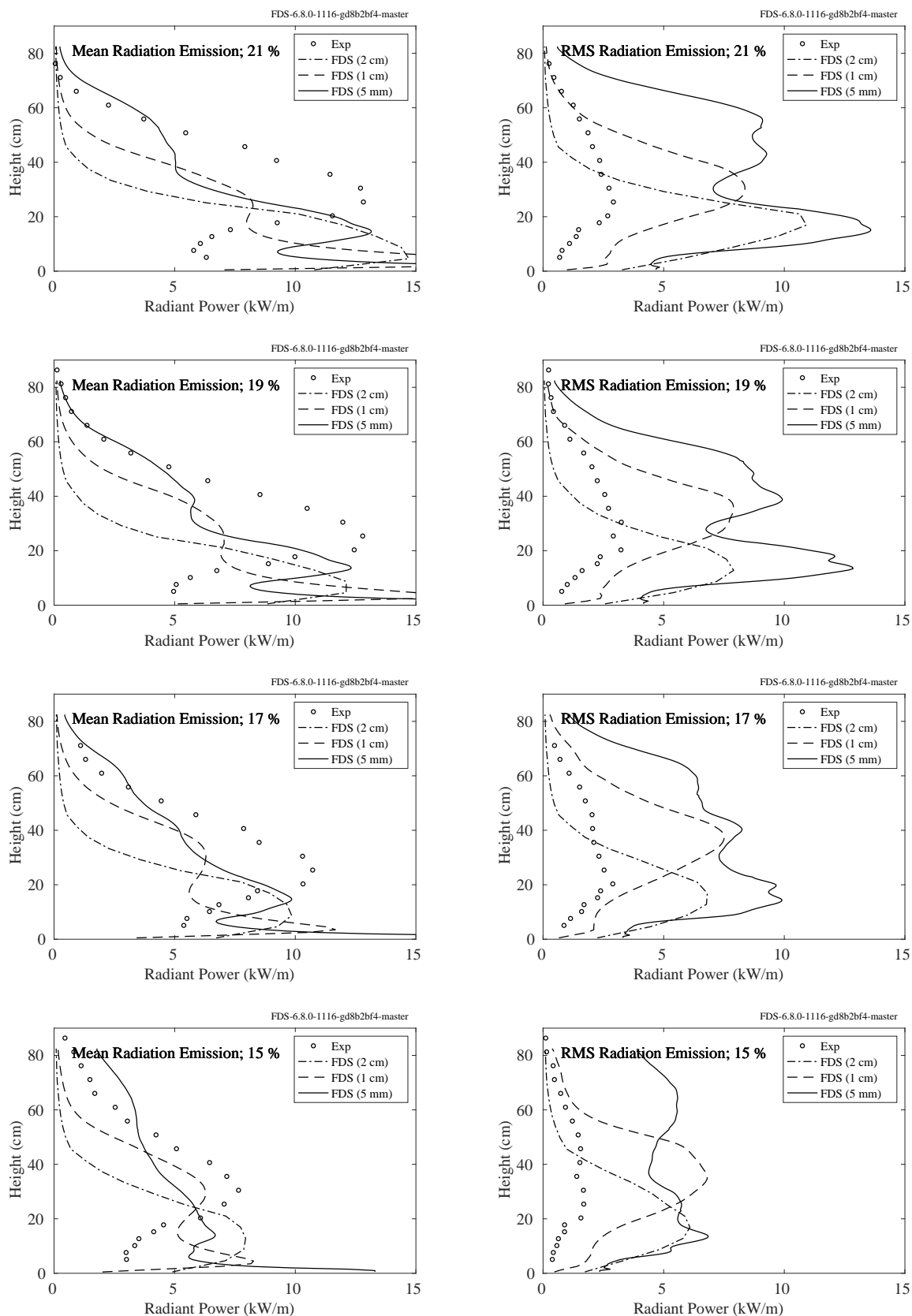


Figure 12.129: FM Burner experiments, mean and rms vertical heat flux profiles.

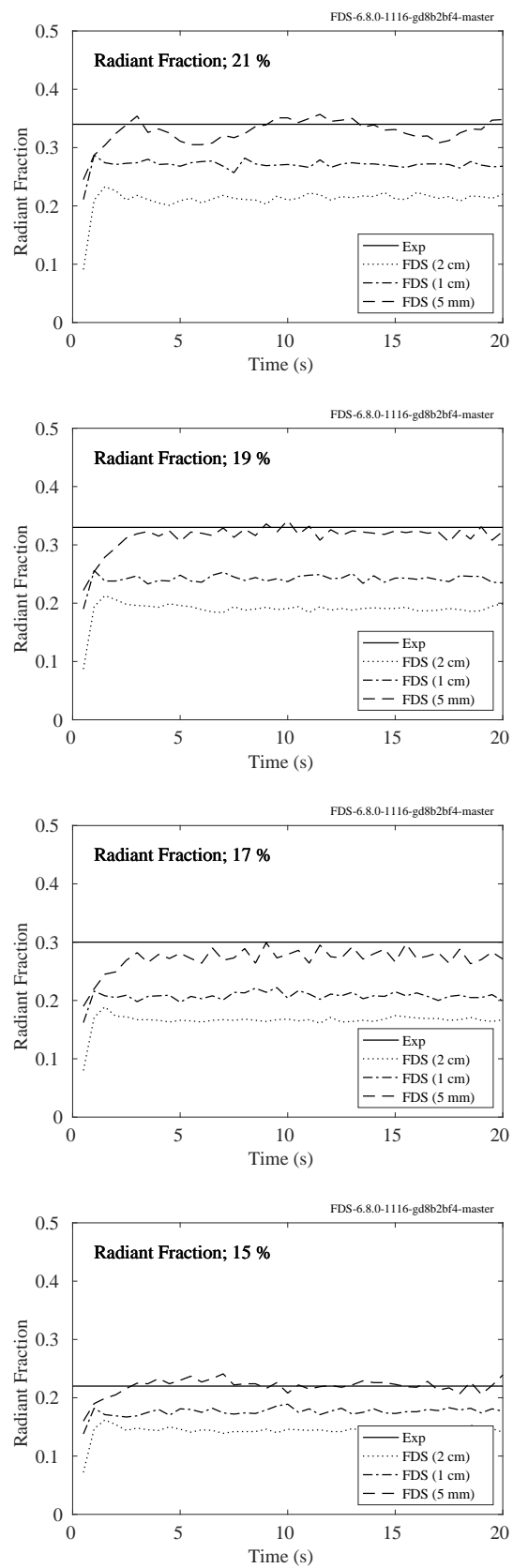


Figure 12.130: FM Burner experiments, radiant fraction for four oxygen levels.

12.7 Condensation Heat Flux

This section focuses on experiments involving condensation onto surfaces.

12.7.1 SETCOM Experiments

The following plot shows the results of modeling the SETCOM experiments.

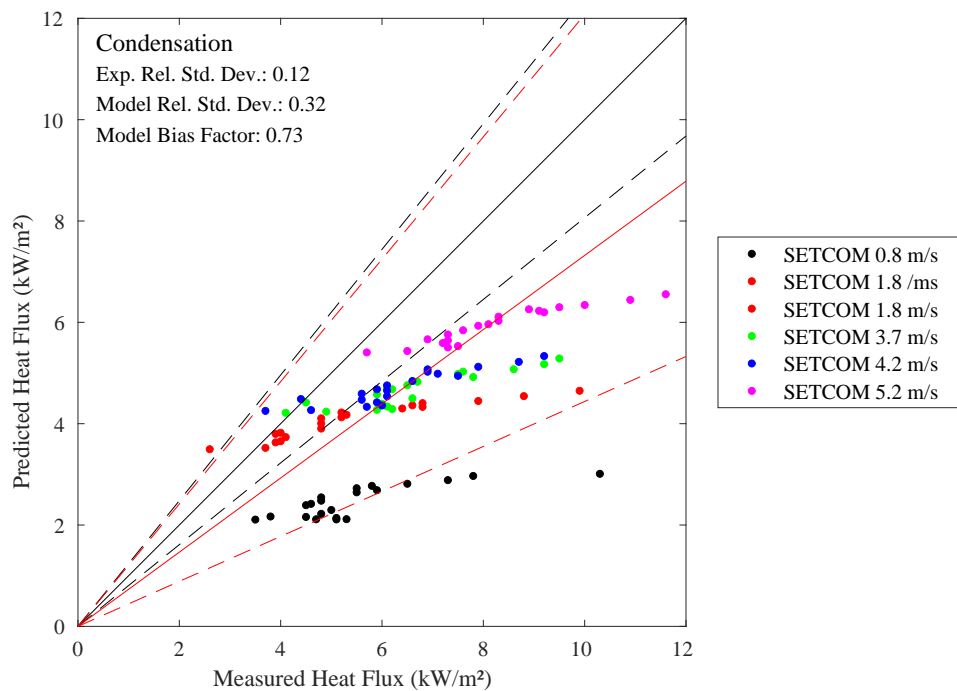


Figure 12.131: Summary of SETCOM results.

Chapter 13

Suppression

This chapter looks at validation exercises where the aim is to predict the extinguishment of a fire.

13.1 Minimum Agent Concentration Experiments

In the following sections, results of experiments are presented in which relatively small flames are extinguished due to the introduction of an inerting agent in the oxidizer stream.

13.1.1 Cup Burner Experiments

A cup burner is an apparatus used to determine the minimum extinguishing concentration (MEC) for combinations of fuels and suppression agents. Sixteen fuels (acetone, acetylene, benzene, butane, dodecane, ethanol, ethylene, heptane, hexane, hydrogen, methane, methanol, octane, propane, propanol, and toluene) and five suppression agents (argon, carbon dioxide, helium, nitrogen, and sulfur hexafluoride) are considered. For the simulations, the MEC is found when the post-ignition HRR remains below 1×10^{-10} kW. The critical flame temperatures specified for the fuel reactions are shown in Table 3.8. The extinguishing agent concentration is measured at the outer edge of the cup burner tube at a level slightly below the cup rim. Results are shown in Fig. 13.1 where color indicates the fuel and shape indicates the extinguishing agent.

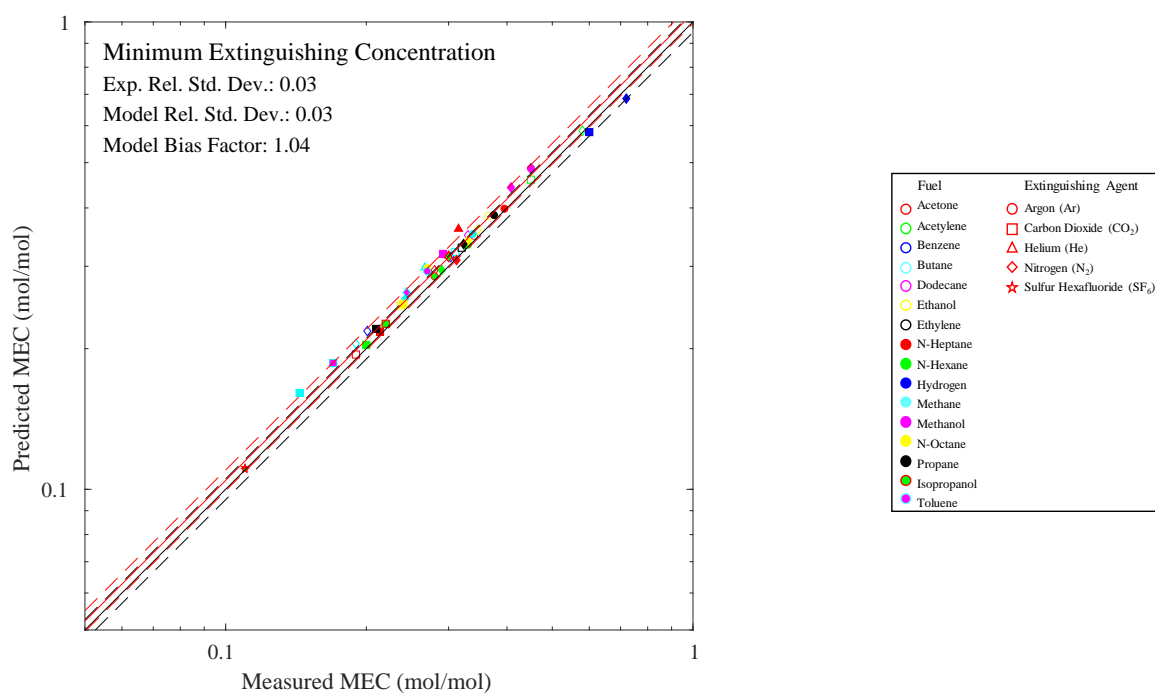


Figure 13.1: Comparison of measured and predicted minimum extinguishing volume fractions for the cup burner tests. Fuel type is indicated by color, and extinguishing agent is indicated by shape.

13.1.2 FM Burner Experiments

A description of the FM Burner experiments can be found in Sec. 3.25. Briefly, a 15.2 cm round steel burner generating a 10 kW fire was supplied with oxygen by an air stream from below that was slowly diluted with nitrogen until the flame extinguished. In the FDS simulations, nitrogen is added to the air stream supplied through the floor of the enclosure, linearly decreasing the oxygen volume fraction over one minute of simulated time. In Fig. 13.2, the combustion efficiency, η , is plotted as a function of oxygen volume fraction for all four fuels tested and compared with the measurements of Zeng and Wang [210]. The auto-ignition temperature (AIT) threshold for each fuel is set according to the Beyler's chapter in the SFPE Handbook [152]. The modeled burner is piloted using a ring of 36 particles ejecting enough fuel to produce 1 kW (to match the experimental pilot).

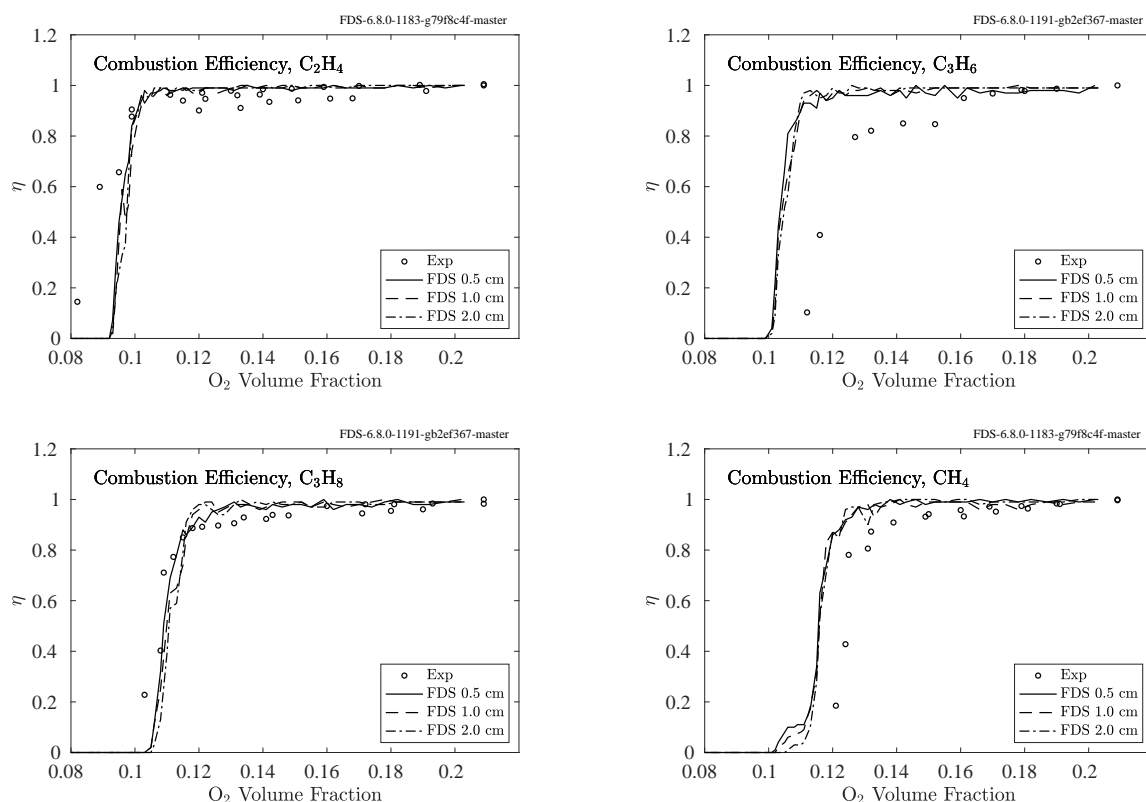


Figure 13.2: FM Burner combustion efficiency.

13.1.3 UMD Line Burner

A description of UMD Line Burner experiments can be found in Sec. 3.93. In the experiments, the oxygen co-flow was slowly diluted with nitrogen until the flame weakened and eventually extinguished. In the FDS simulations, the nitrogen co-flow is setup with a ramp in time to achieve a linear decrease in the co-flow oxygen volume fraction over one minute of real time. In Fig. 13.3, we plot the combustion efficiency as a function of oxygen volume fraction for both methane and propane and compare with the measurements of White et al. [332]. Note that the FDS results are presented for three different grid resolutions corresponding to $W/\delta x = 4, 8$, and 16 ($\delta x = 1.25$ cm, 0.625 cm, and 0.3125 cm, respectively), where $W = 5$ cm is the width of the burner. A simple re-ignition model with an ignition temperature threshold set to the SFPE Handbook [262] value of the Auto-Ignition Temperature (AIT) for methane and propane is used. A piloted ignition region (AIT = 0 K) is set just within the near field of the line burner. Details of the re-ignition model and pilot region as well as parameter sensitivity studies are provided in White et al. [379].

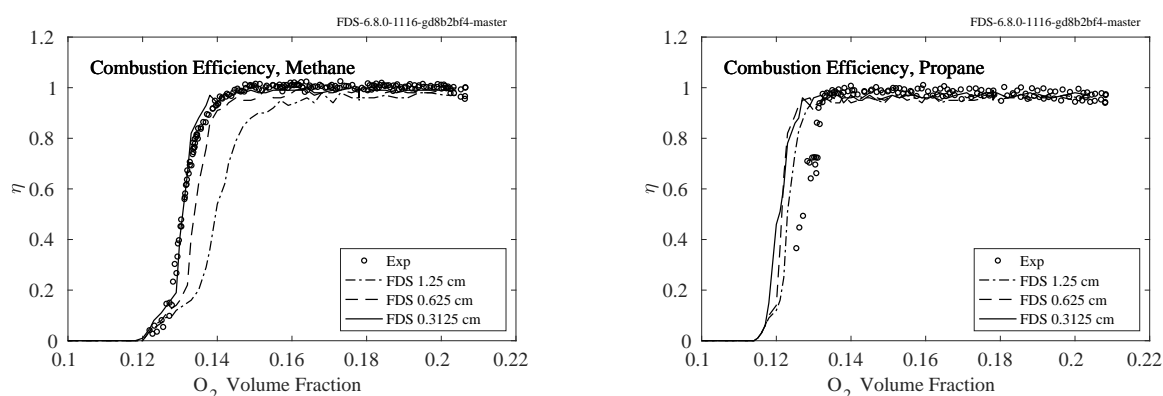


Figure 13.3: UMD Line Burner combustion efficiency.

13.2 Compartment Fire Extinction

The following sections present results for experiments in which fires within forced ventilation compartments either self-extinguish due to lack of oxygen, or extinguish due to a water mist system.

13.2.1 LLNL Enclosure Experiments

The figures on the following pages contain plots of the heat release rate in both the experiments and the simulation. The experimental curve is just the value reported in the test report, which drops to zero instantly at the reported extinguishment time. In cases where the model does not predict extinction, the extinction time data is not used in the summary scatter plot, Fig. [13.19](#).

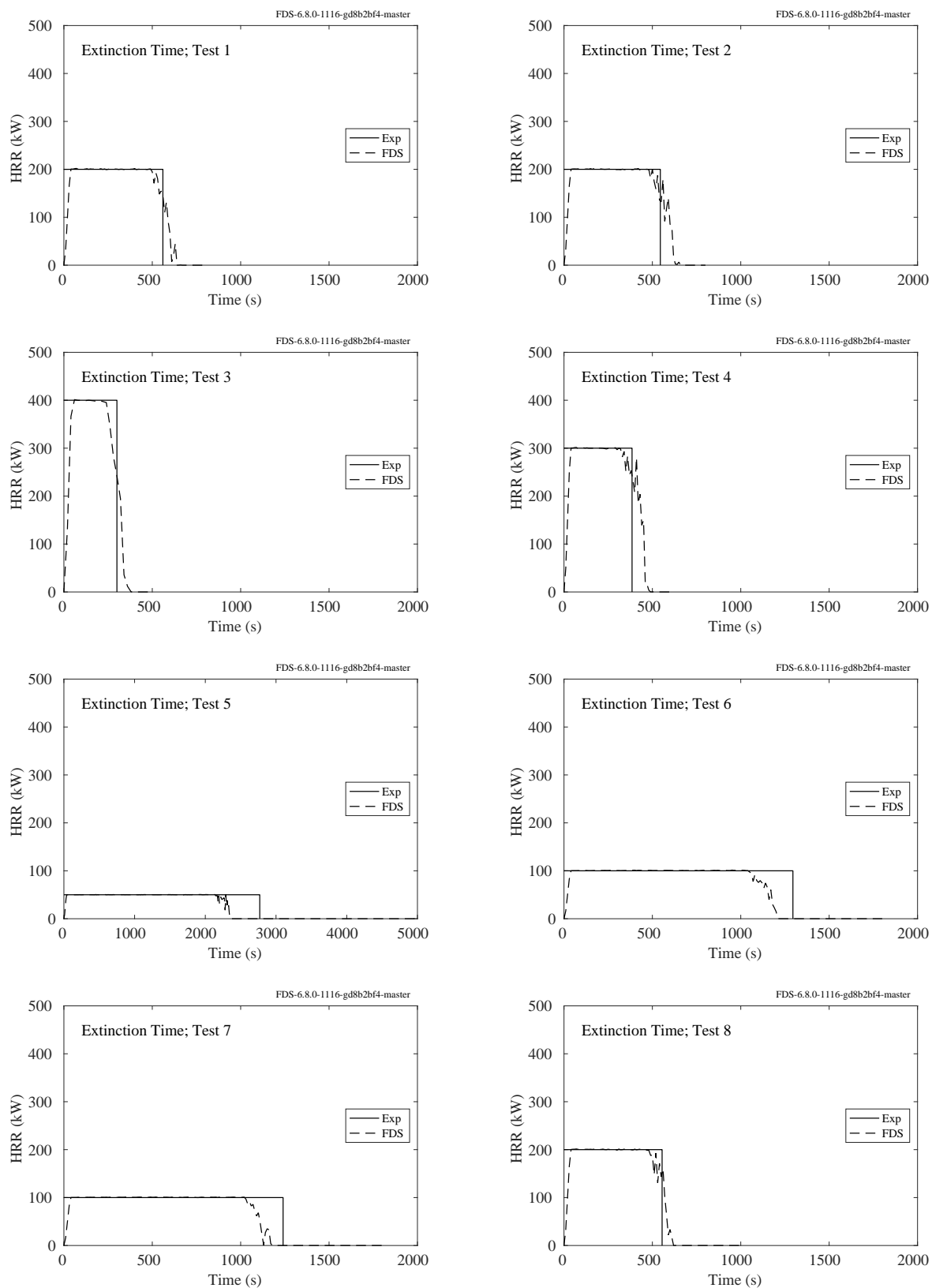


Figure 13.4: LLNL Extinction Time, Tests 1-8.

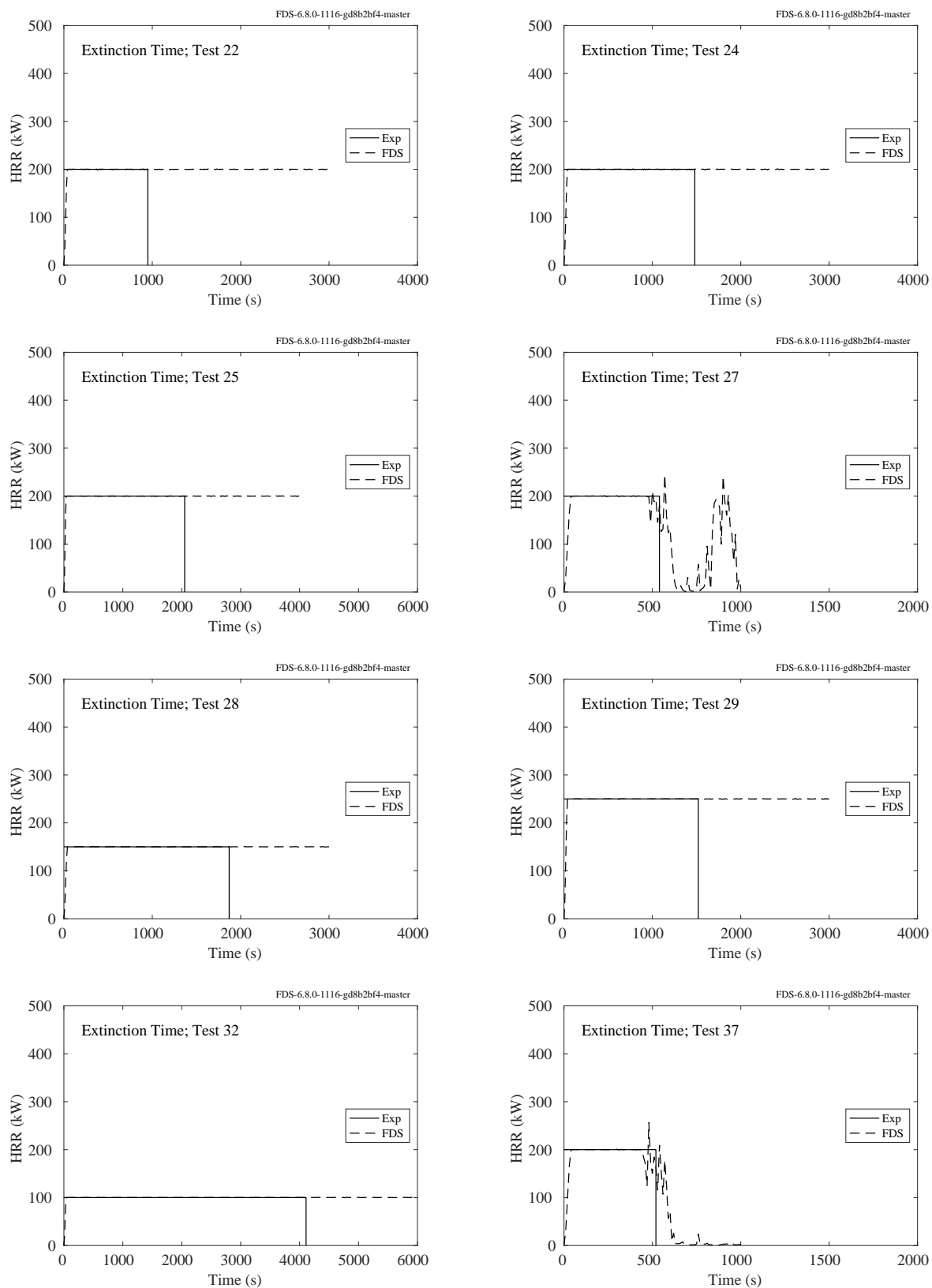


Figure 13.5: LLNL Extinction Time, Tests 22, 24, 25, 27, 28, 29, 32, 37.

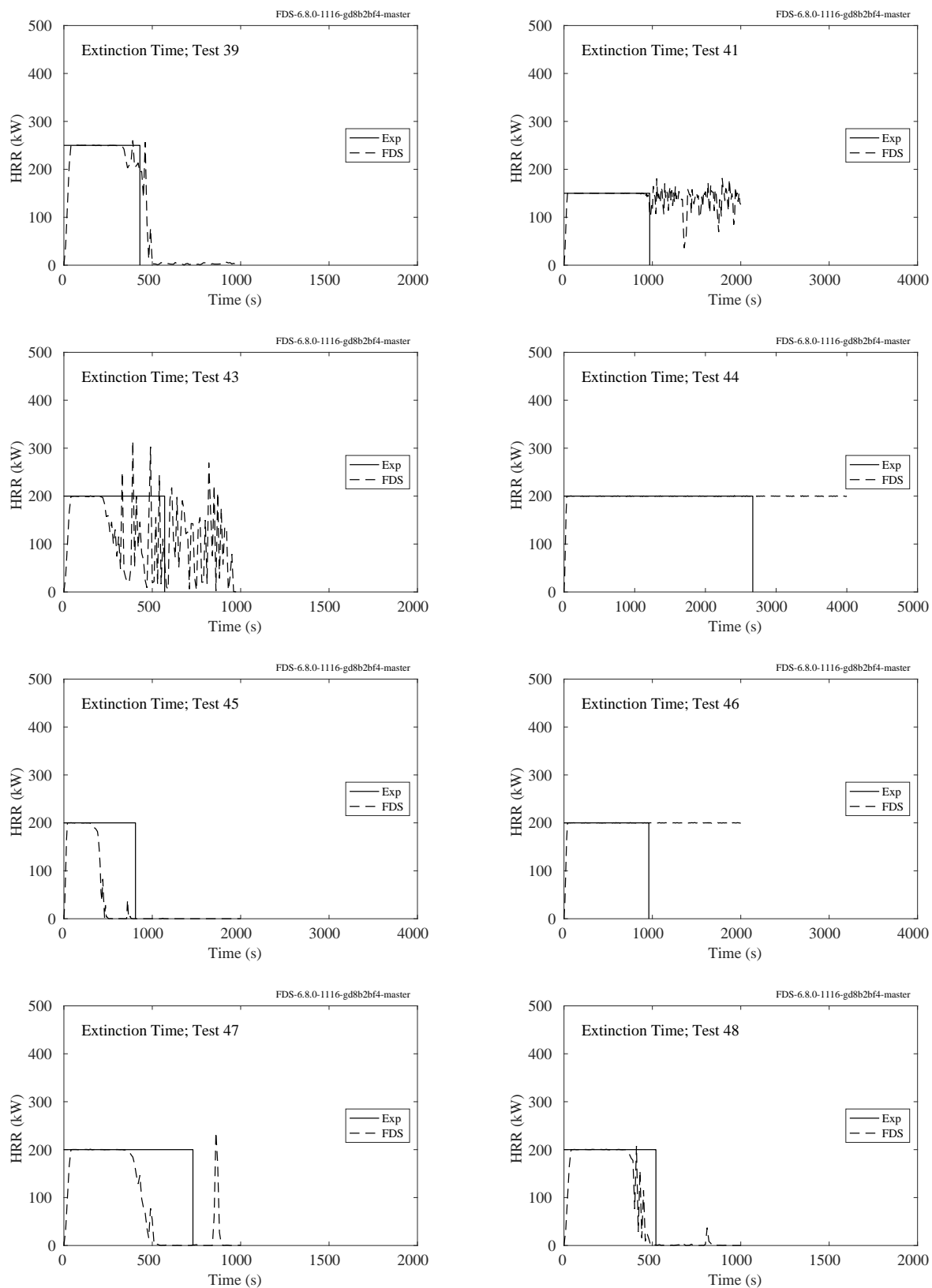


Figure 13.6: LLNL Extinction Time, Tests 39, 41, 43-48.

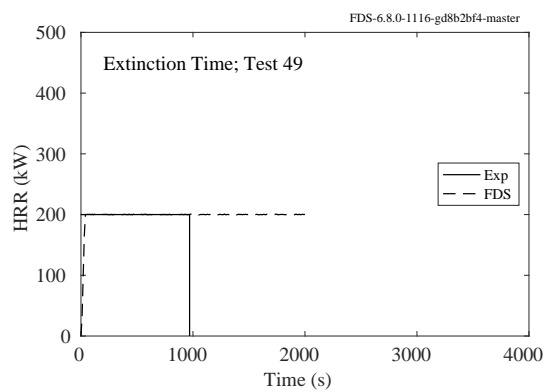


Figure 13.7: LLNL Extinction Time, Test 49.

13.2.2 NIST/NRC OLIVE-Fire Experiments

These experiments involve fires within large, steel electrical enclosures. A brief description of the experiments and photographs of the enclosures are found in Sec. 3.57. Table 13.1 lists the leakage and vent areas of the enclosures, along with the measured maximum heat release rate (HRR).

Figures 13.8 through 13.12 compare predicted versus measured heat release rates and gas species near the ceiling of each enclosure. The HRR plots on the left contain two sets of curves. The black curves represent the nominal HRR based solely on the metered natural gas flow. The gas flow was ramped up in increments of 25 kW, 50 kW, or 100 kW until the HRR determined via oxygen consumption calorimetry (red curves) diverged, at which point the maximum achievable HRR within the enclosure had been reached.

Table 13.1: Summary of NIST/NRC OLIVE-Fire Experiments.

Exp. No.	Encl. No.	Leak Area (m ²)	Vent Area (m ²)	Total Area (m ²)	Max HRR (kW)
3	5	0.060	0.032	0.092	160
4	5	0.060	0	0.060	105
8	5	0.060	0.108	0.168	230
9	6	0.017	0	0.017	45
12	2	0.170	0.164	0.334	580
13	2	0.170	0	0.170	270
15	3	0.039	0	0.039	70
16	3	0.039	0.016	0.055	100
17	3	0.039	0.032	0.071	130
19	8	0.079	0	0.079	165
22	7	0.036	0.008	0.044	65
23	7	0.033	0.008	0.041	60
24	7	0.058	0.008	0.066	180
26	4	0.043	0.030	0.073	120
27	4	0.043	0.030	0.073	125
29	1	0.110	0	0.110	240
30	1	0.110	0.070	0.180	250
31	1	0.110	0.070	0.180	400

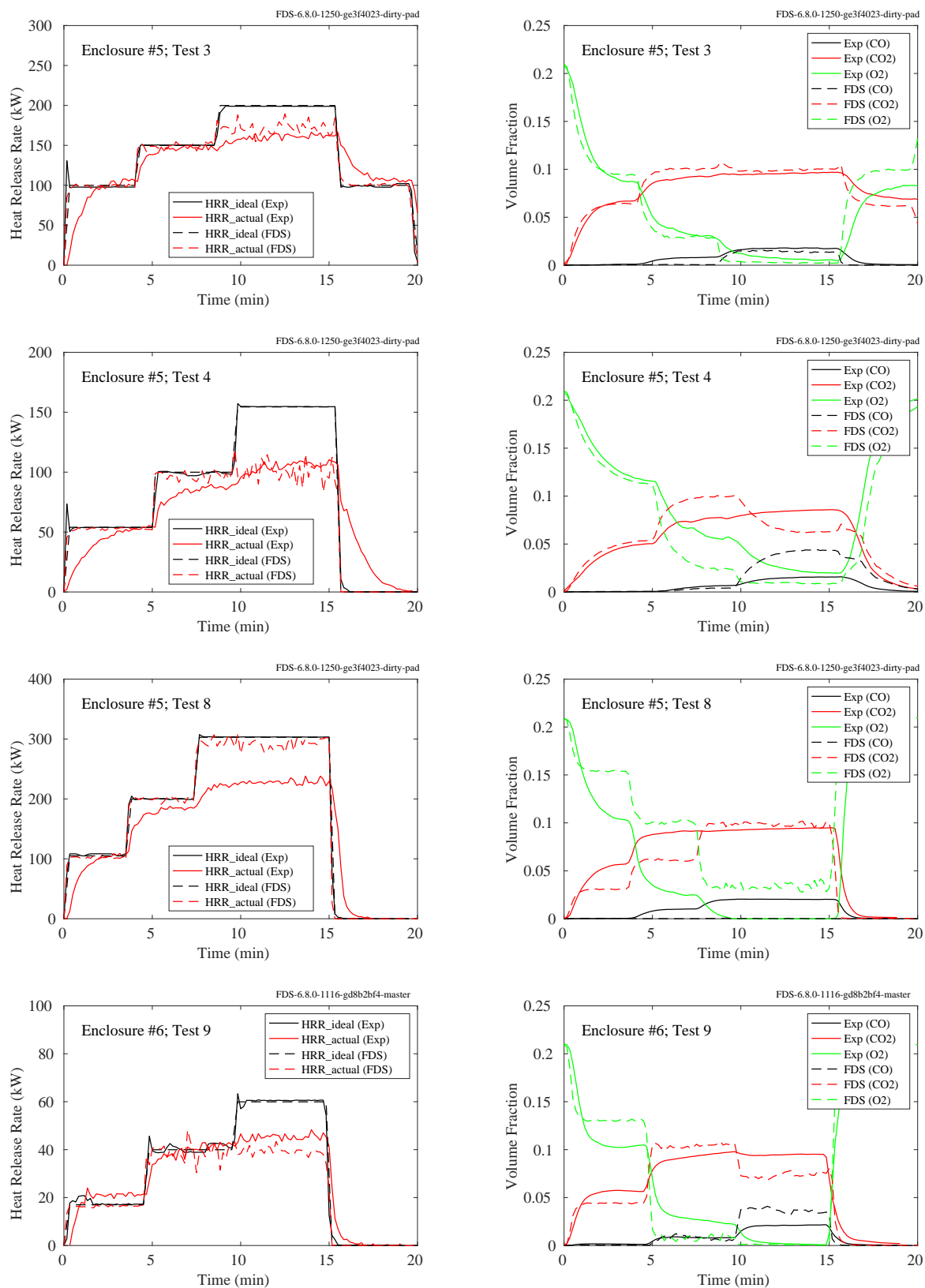


Figure 13.8: NIST/NRC OLIVE-Fire maximum HRR and gas concentrations, Tests 3, 4, 8, 9.

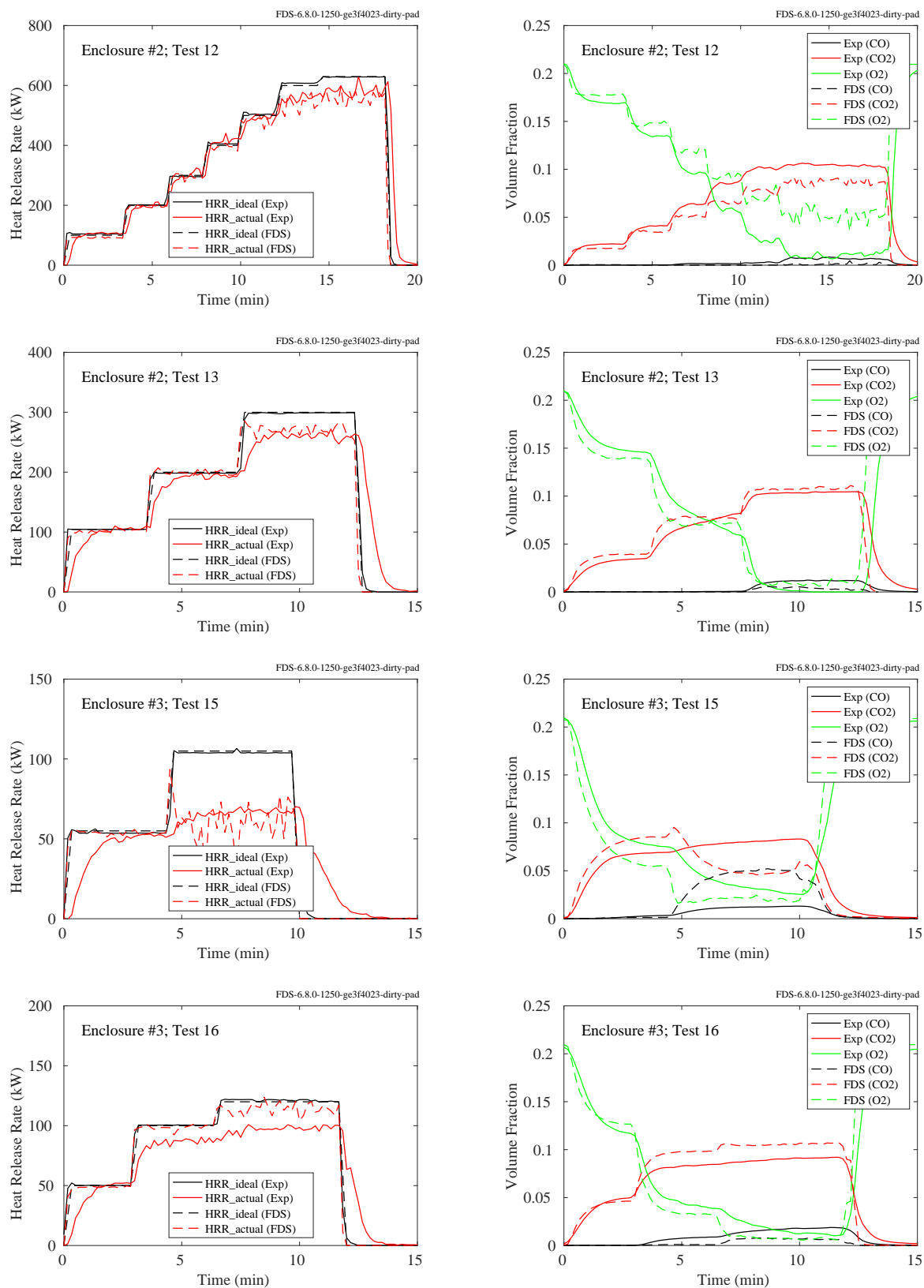


Figure 13.9: NIST/NRC OLIVE-Fire maximum HRR and gas concentrations, Tests 12, 13, 15, 16.

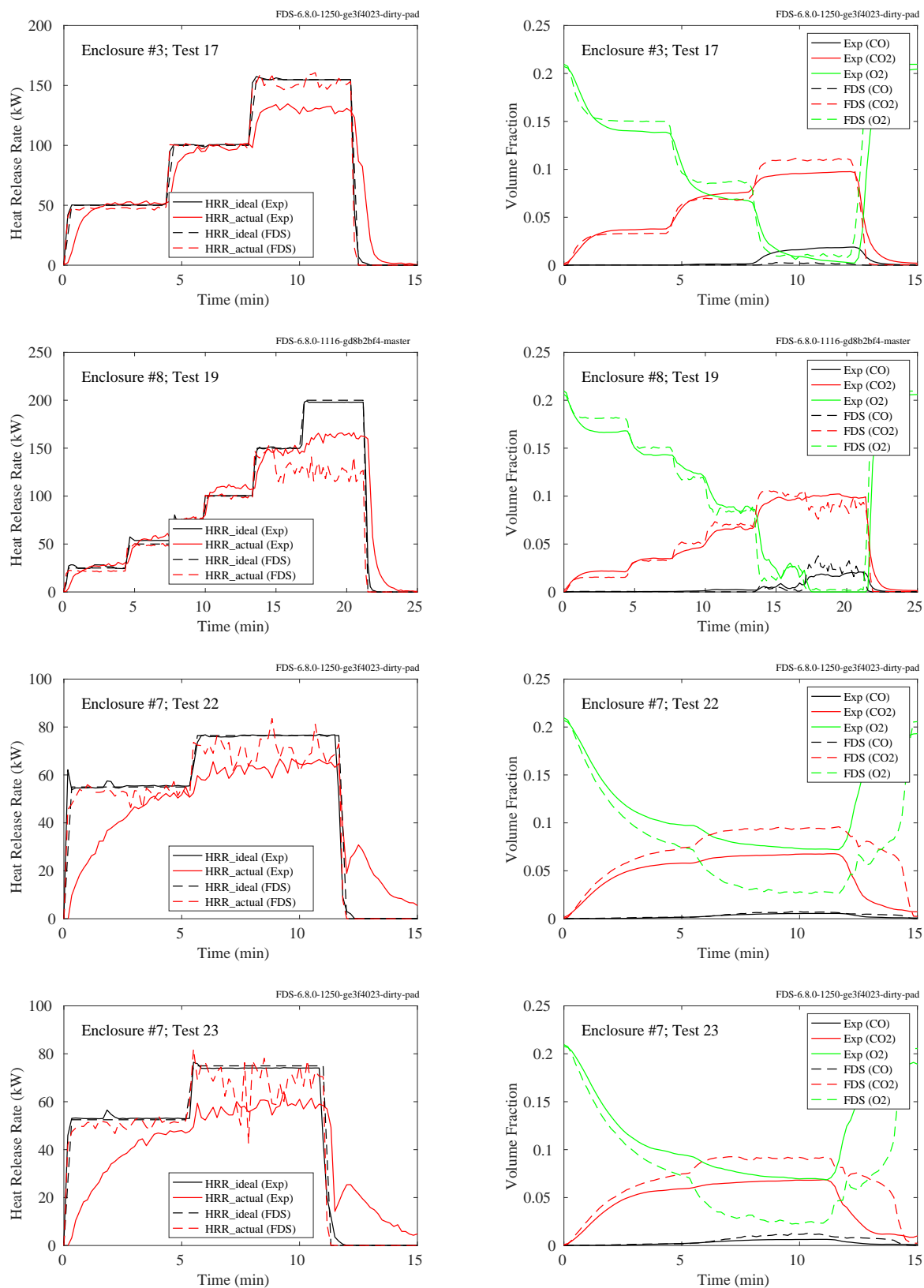


Figure 13.10: NIST/NRC OLIVE-Fire maximum HRR and gas concentrations, Tests 17, 19, 22, 23.

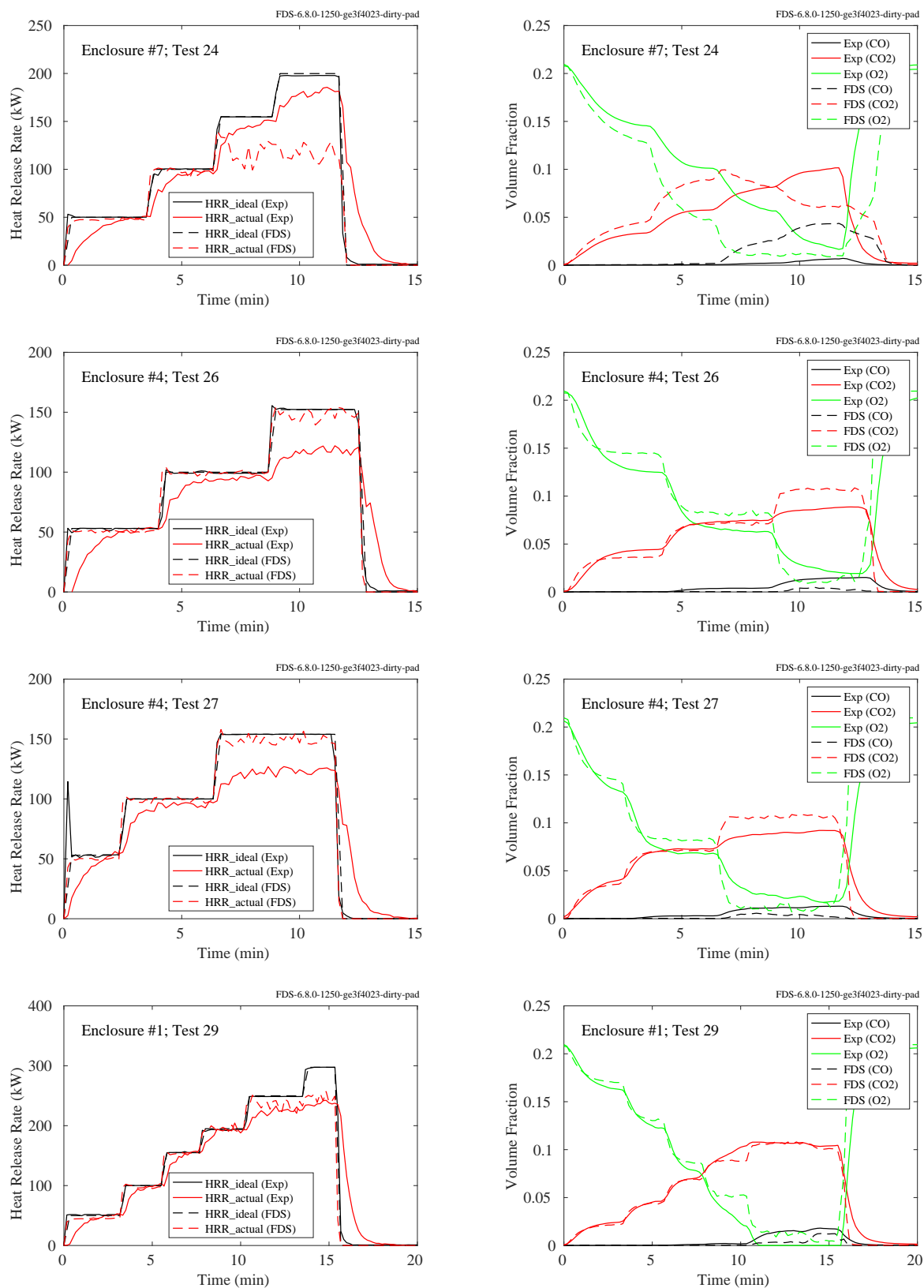


Figure 13.11: NIST/NRC OLIVE-Fire maximum HRR and gas concentrations, Tests 24, 26, 27, 29.

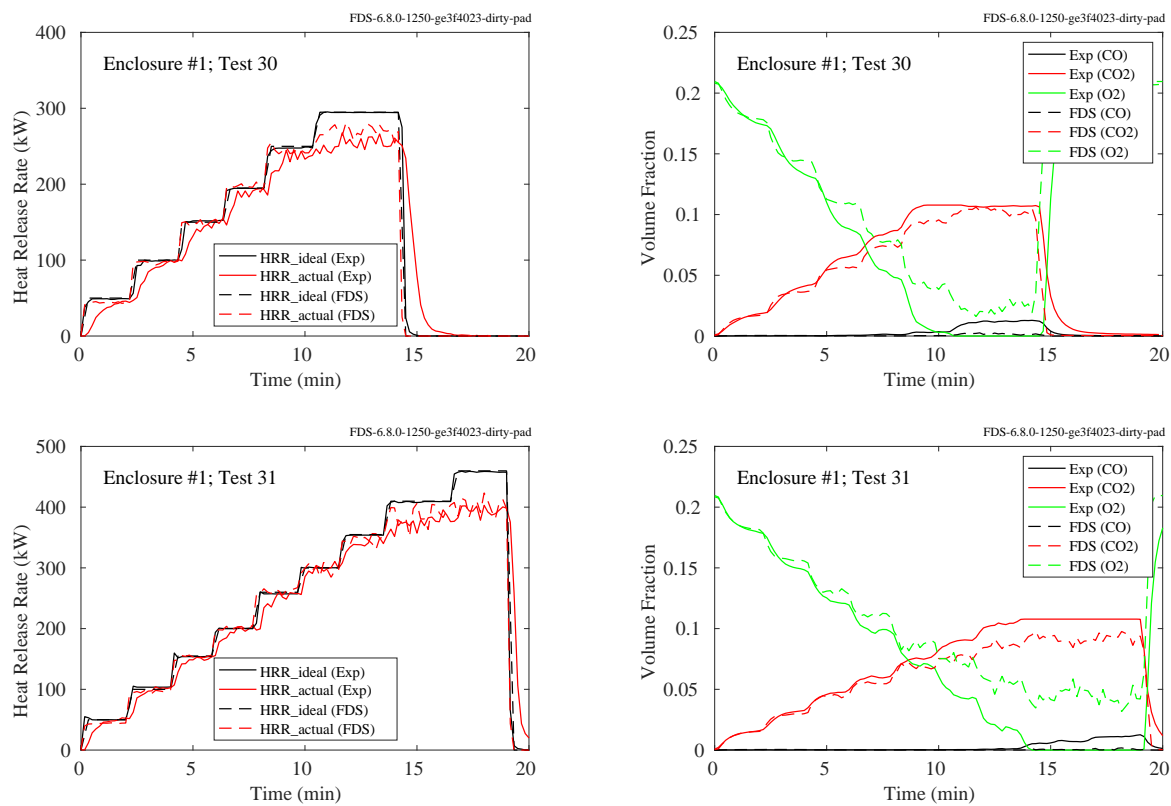


Figure 13.12: NIST/NRC OLIVE-Fire maximum HRR and gas concentrations, Tests 30, 31.

13.2.3 SWJTU Tunnel Experiments

The figures below display the heat release rate as a function of time for the SWJTU Tunnel experiments.

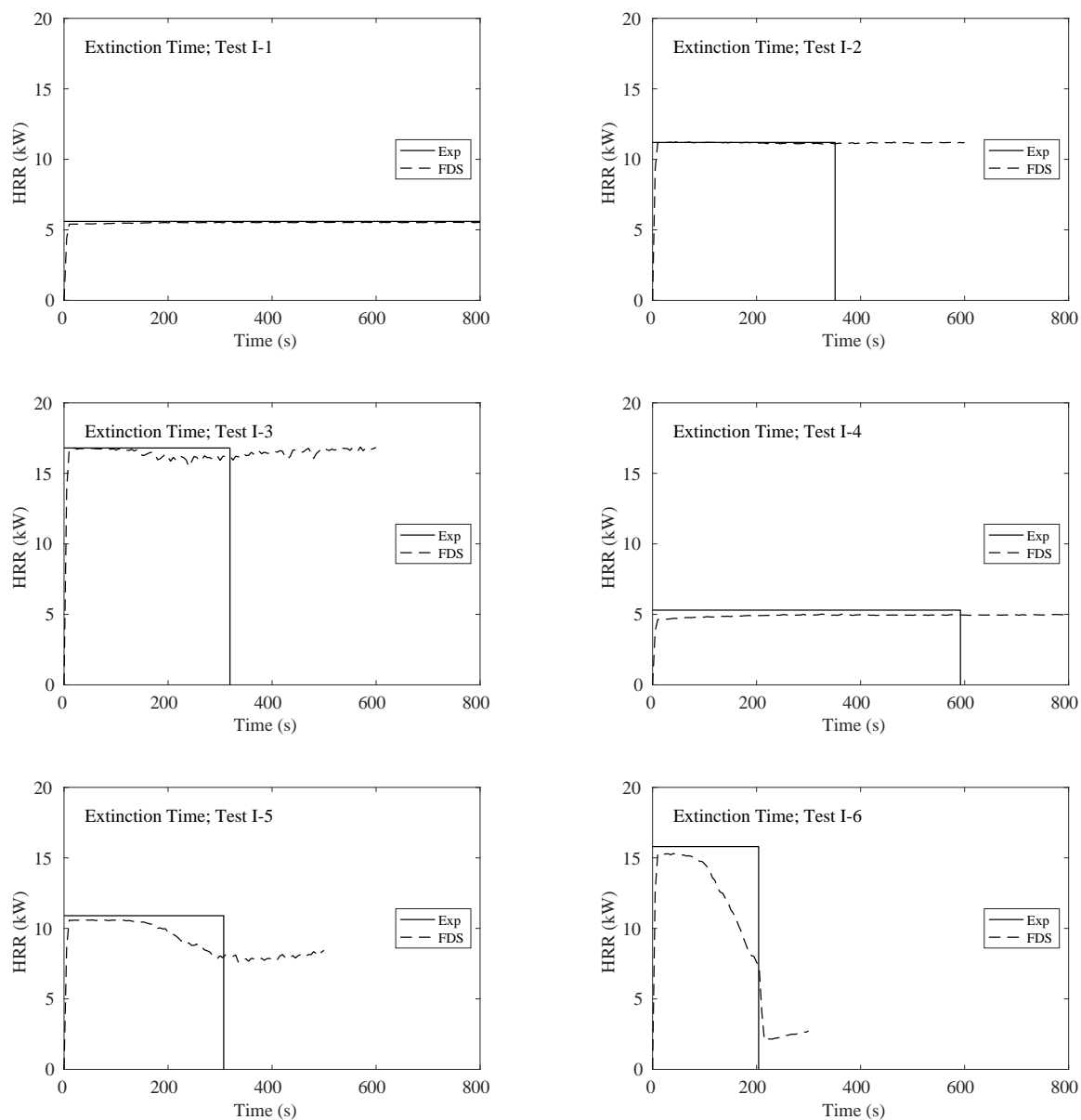


Figure 13.13: SWJTU Tunnel experiments, extinction time.

13.2.4 USCG/HAI Water Mist Suppression Tests

The following pages contain comparisons of the predicted heat release rates for fires that are suppressed with a water mist system. In all cases, the flow rate of liquid fuel is specified in the model, but the decrease in HRR due to the extinguishing system is predicted by the model. Table 13.2 reports the observed extinguishment times. Figure 13.19 compares the measured versus predicted extinguishment times. For the simulations, the extinguishment time is taken to be when the HRR drops to half of its specified value.

In cases where there is no reported fire extinction or the model does not predict extinction, the extinction time data is not used in the summary scatter plot, Fig. 13.19.

Table 13.2: Recorded extinguishment times for the USCG/HAI water mist suppression tests in a small shipboard machinery space. “No” means that the fire was not extinguished within 600 s of nozzle activation.

System		Navy	Grinnell	Fogtec	Chemetron	Fike
Number of Nozzles		6	6	6	15	6
Operating Pressure (bar)		70	13	100	12	21
Flow Rate (L/min)		68	75	22	70	48
Assumed Median Drop Size (μm)		175	225	100		200
Assumed Initial Velocity (m/s)		75	32	90		41
Assumed Spray Angle (deg.)		120	90	120		90
Fire Scenario	Ventilation	Extinguishment Time (s)				
1.0 MW Spray	Closed	15	26	21	27	21
1.0 MW Spray	Natural	15	40	32	43	35
1.0 MW Spray	Forced	17	55	76	357	133
0.5 MW Spray	Closed	34	70	39	53	56
0.5 MW Spray	Natural	41	117	67	158	140
0.5 MW Spray	Forced	124	No	No	No	No
0.25 MW Spray	Closed	157	360	169	314	277
0.25 MW Spray	Natural	206	No	290	525	566
0.25 MW Spray	Forced	No	No	No	No	No

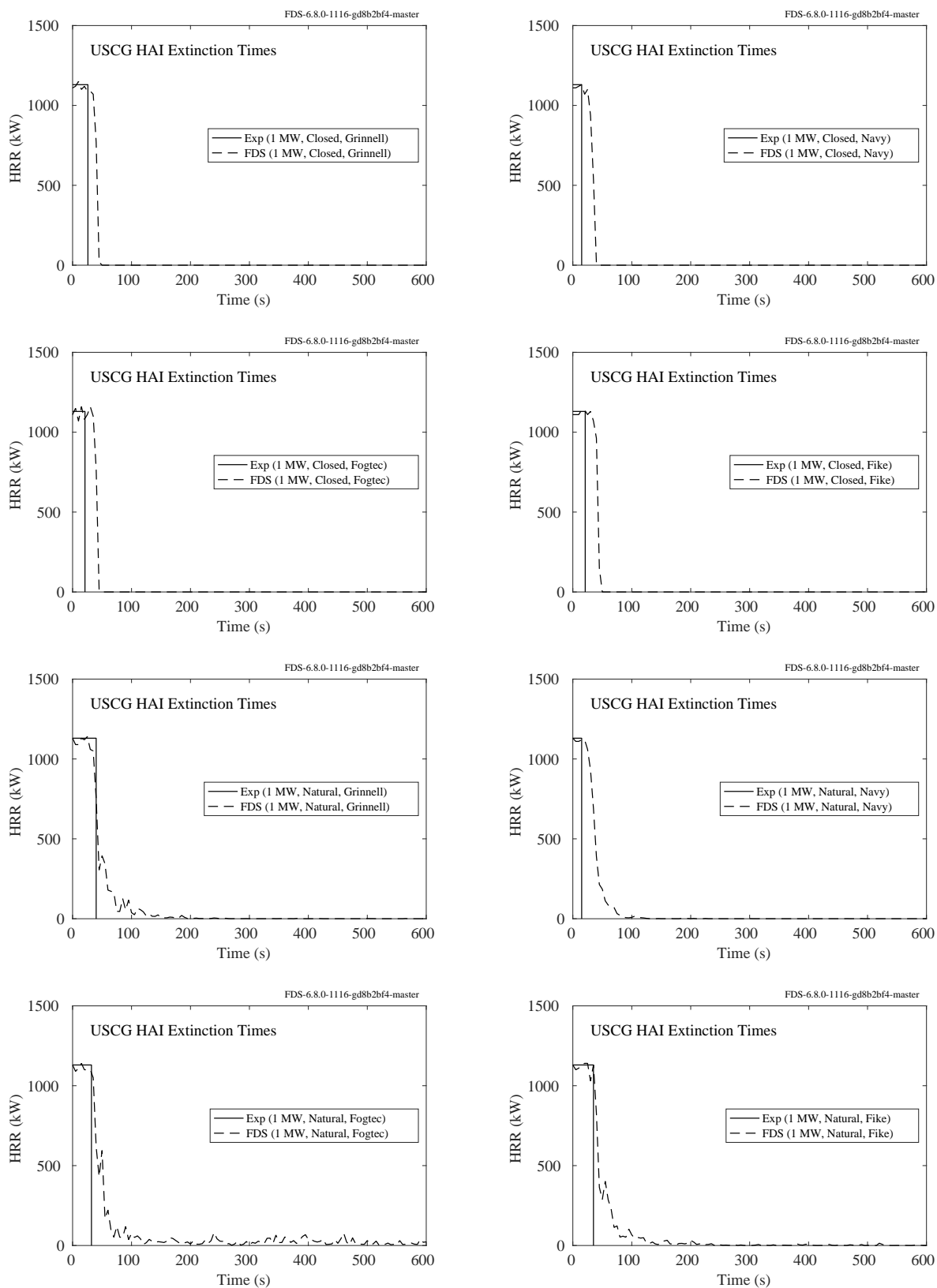


Figure 13.14: USC/HAI experiments, extinction time.

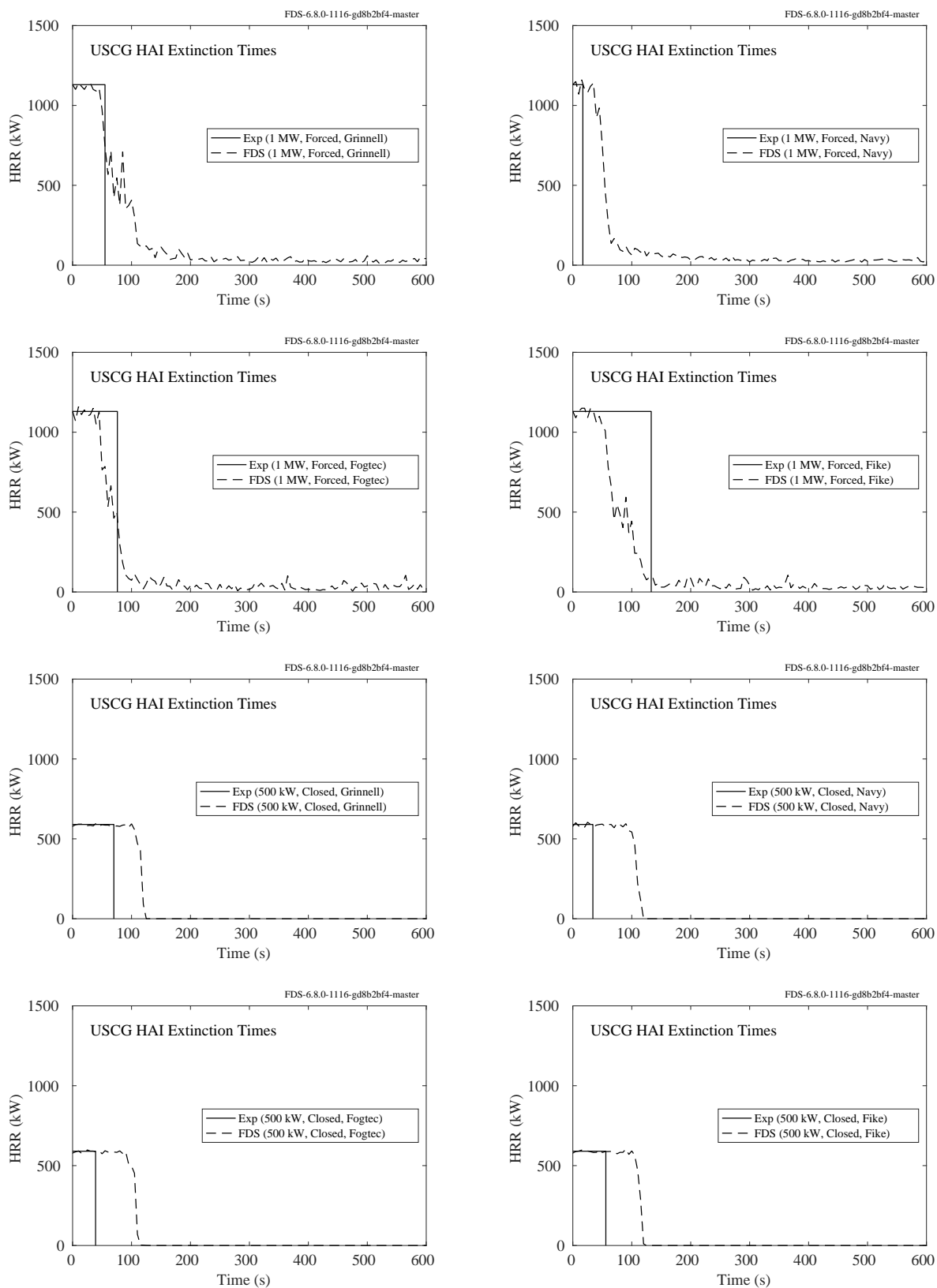


Figure 13.15: USCG/HAI experiments, extinction time.

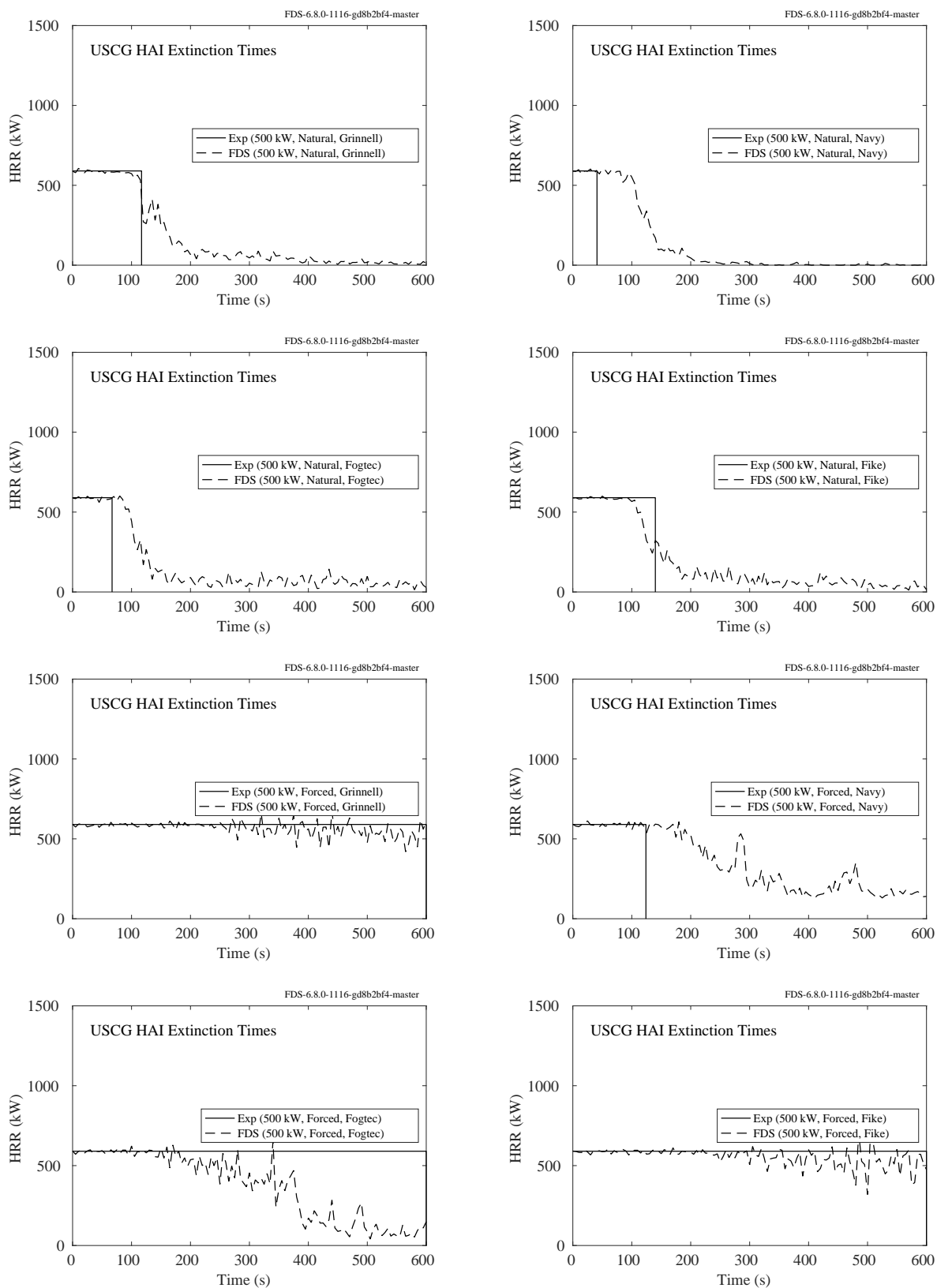


Figure 13.16: USCG/HAI experiments, extinction time.

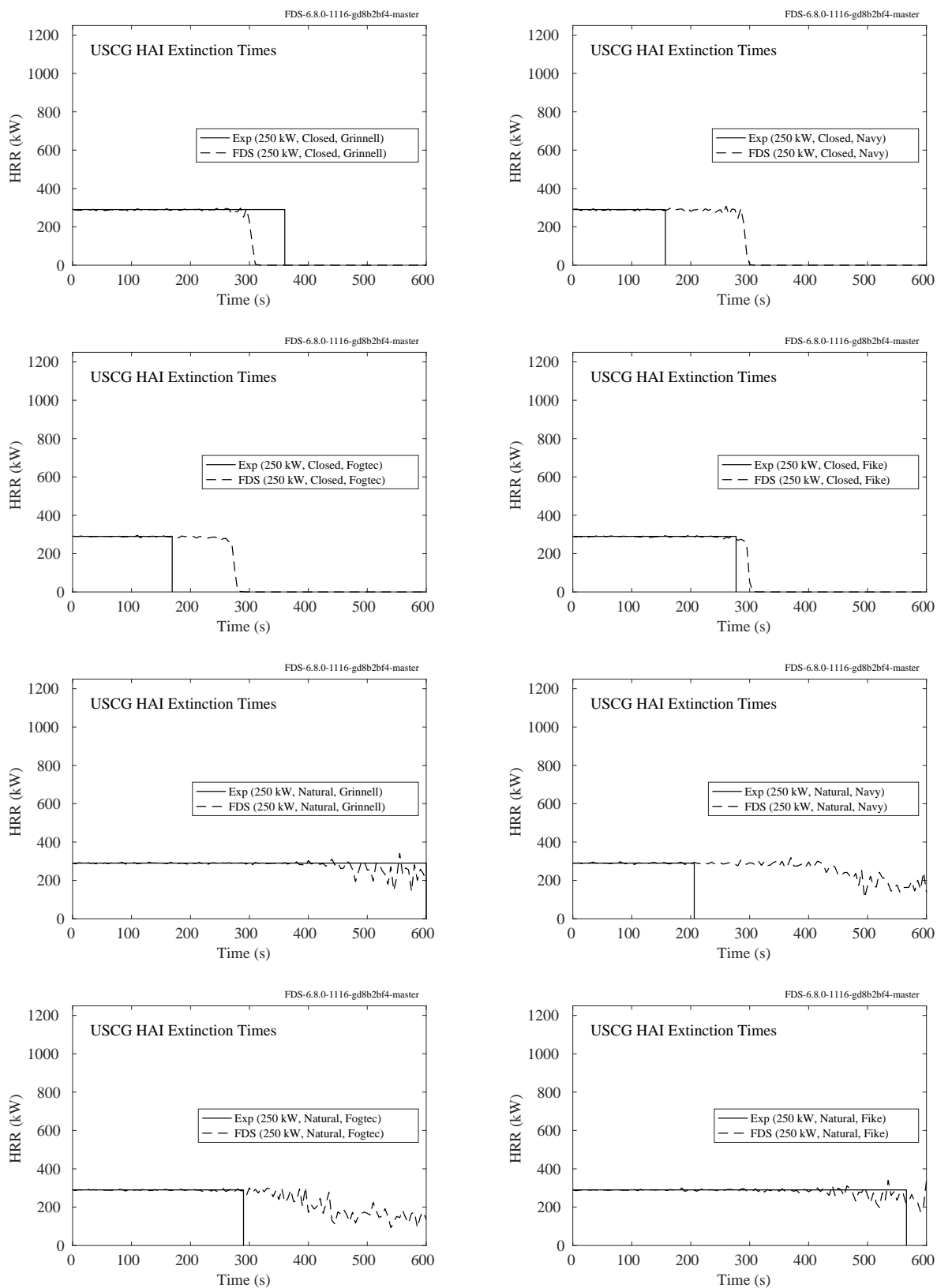


Figure 13.17: USCG/HAI experiments, extinction time.

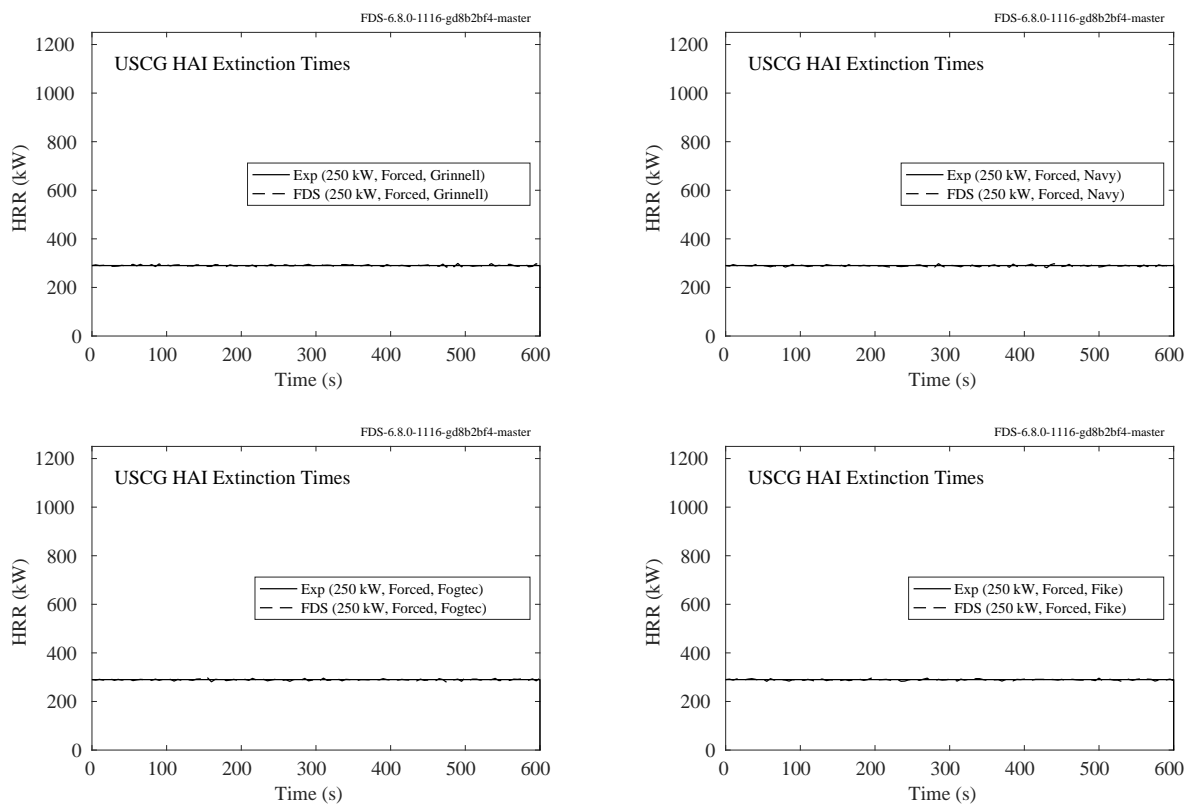


Figure 13.18: USCG/HAI experiments, extinction time.

13.2.5 Summary, Flame Extinction Time

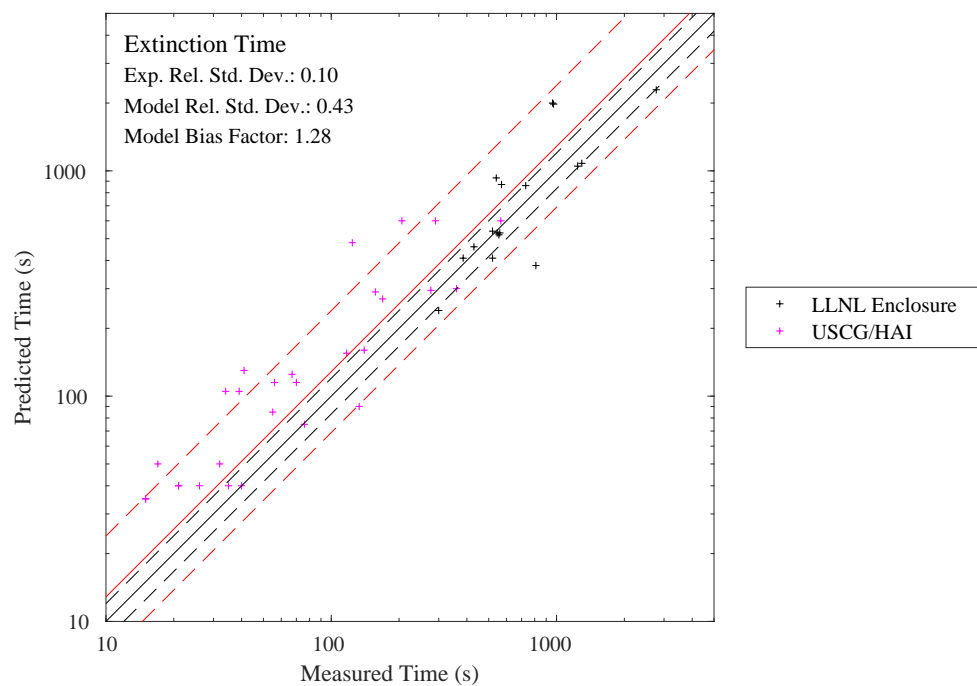


Figure 13.19: Comparison of measured and predicted extinguishment times for the USCG/HAI water mist suppression tests.

13.3 Theobald Hose Stream Experiments

Figures 13.20—13.22 show scatter plots for the maximum range, the maximum height, and the distance to the point of maximum height for the Theobald Hose Stream experiments [321]. There are approximately 90 experiments using four different nozzle types (6, 7, 9 [Rouse], 10) with different nozzle diameters (13 mm, 19 mm, 25.4 mm). Note that the solid circles on the scatter plots below are scaled by the nozzle diameter. The experiments also varied the hose pressure (and hence exit velocity) from 2.1 bar to 6.2 bar and firing angle (relative to horizontal) from 20° to 45°.

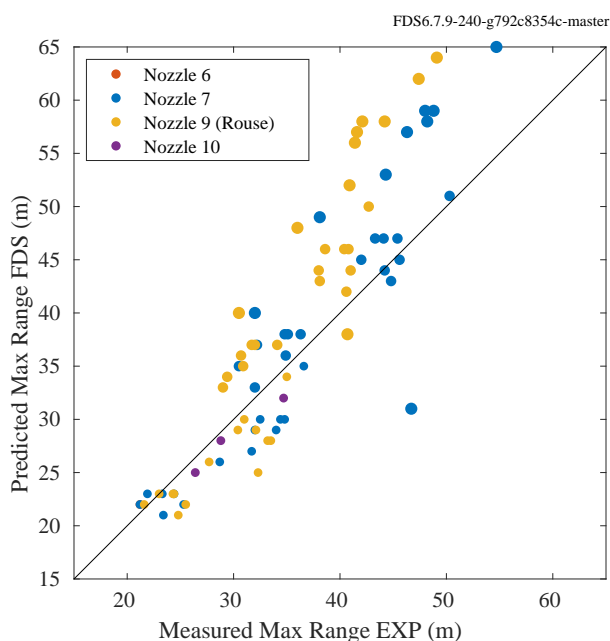


Figure 13.20: Theobald Hose Stream, maximum range.

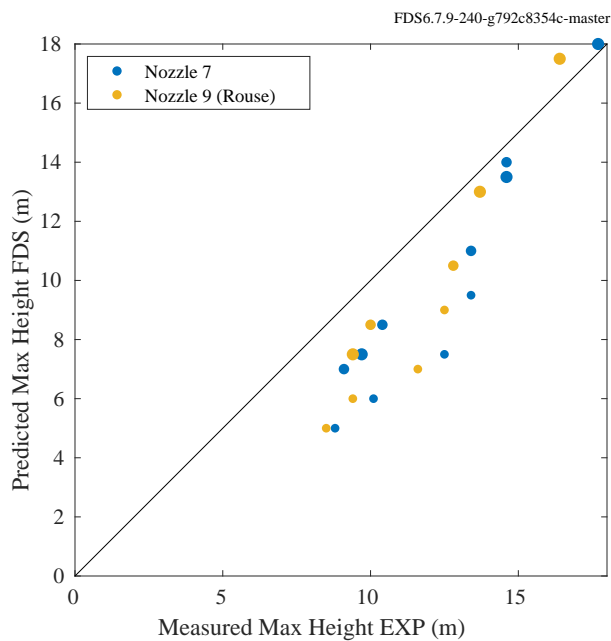


Figure 13.21: Theobald Hose Stream, maximum height.

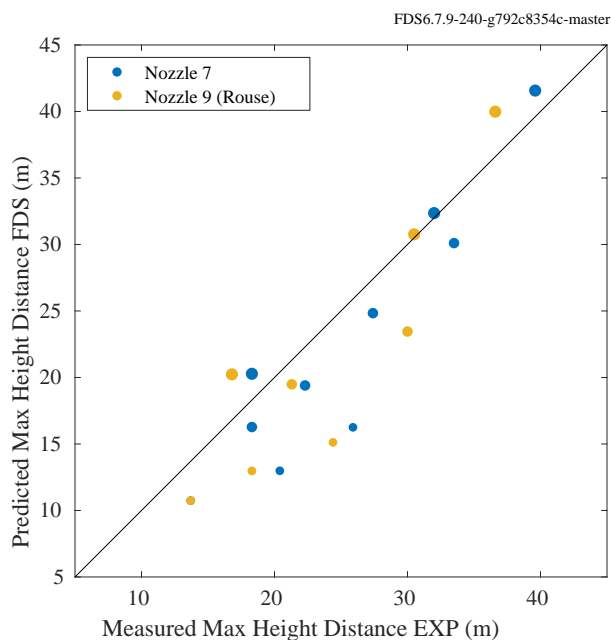


Figure 13.22: Theobald Hose Stream, distance to the point of maximum height.

13.4 VTT Water Spray Experiments

Figure 13.23 presents profiles of mean droplet diameter, mean velocity, and droplet flux below a single 74° hollow-cone water mist nozzle. The pressure behind the nozzle was 2 MPa, and the flow constant was 0.077 L/min/bar^{1/2}. The experimental data represents average values at each distance calculated over the four measuring points at that distance (except for the point at the spray axis). A comparison of droplet speed, mist flux and Sauter mean diameter (D_{32}) profiles are shown in Fig. 13.23. Comparisons are shown at 40 cm and 62 cm vertical distances from the nozzle. Simulation results are reported for three spatial resolutions: 1 cm, 2 cm, and 4 cm.

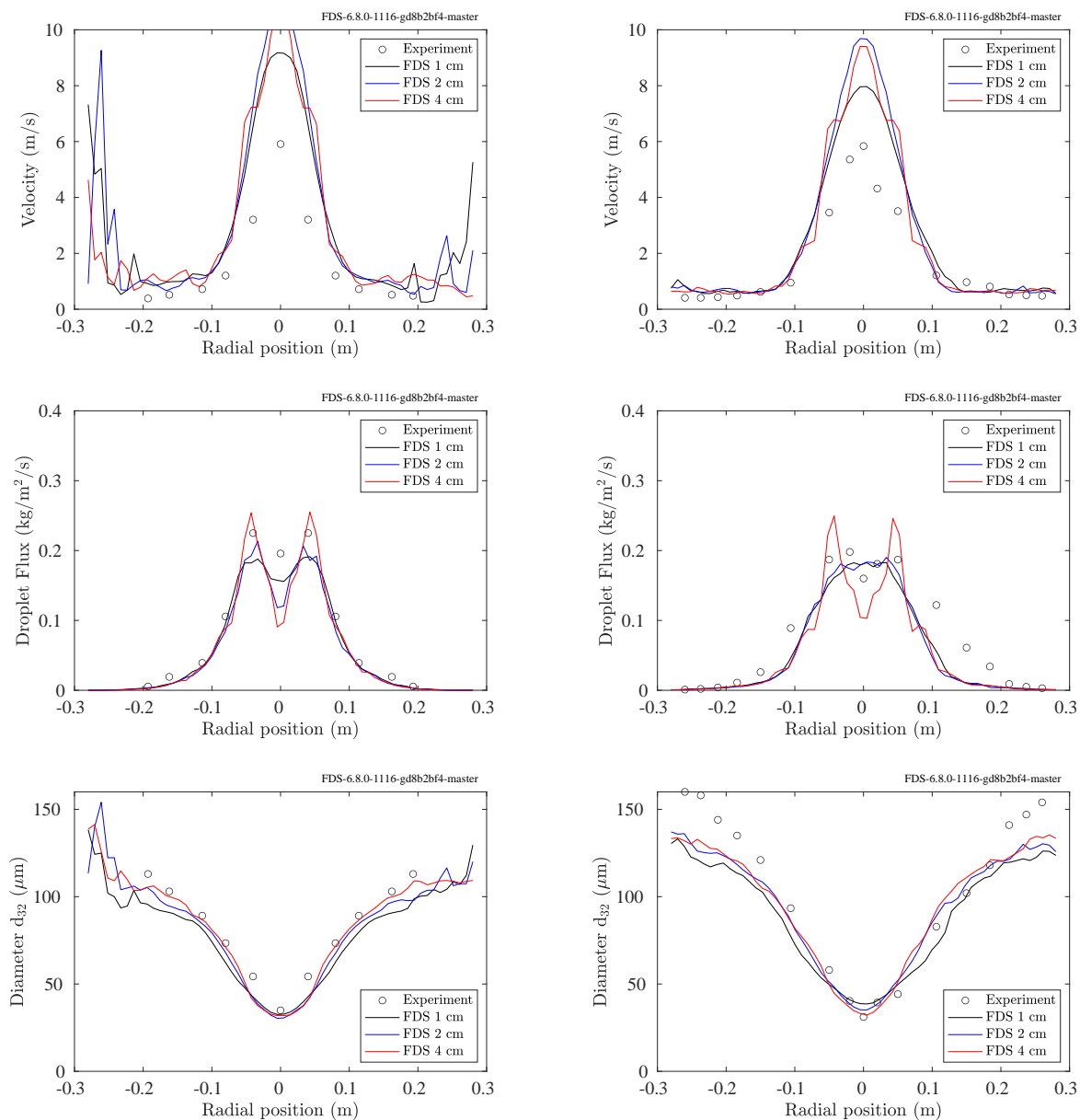


Figure 13.23: Comparison of predicted and experimental droplet speed (top), droplet flux (middle) and mean diameter (bottom) profiles of the LN-2 nozzle. The left column corresponds to measurements made 40 cm from the nozzle, while the right column corresponds to measurements made 62 cm from the nozzle.

Chapter 14

Burning Rate and Fire Spread

This chapter contains a series of validation exercises where the aim is to *predict* the burning and spread rate of the fire. Most of the simulations included in the previous chapters involved a *specified* burning or heat release rate. Here, the objective is to apply measured thermophysical properties of the material and predict its burning rate, either with a specified heat flux or as a free burn.

14.1 FAA Polymers

The U.S. Federal Aviation Administration (FAA) has studied various plastics that are commonly used aboard commercial aircraft.

This section presents measured properties of various polymers and the numerical predictions of their mass loss and/or burning rates under constant heat heating. Two types of experiments are considered. First, the NIST Gasification Apparatus is used to measure the mass loss rate of non-burning samples in a nitrogen atmosphere. Second, the standard Cone Calorimeter [380] is used to measure the heat release rate of materials in a normal atmosphere. When just the mass loss rate of a non-burning sample has been measured, FDS is run in “solid phase only” mode; that is, a 1-D heat conduction calculation is performed in a single grid cell. The result is the predicted mass loss rate as a function of time. To simulate a cone calorimeter experiment, FDS simulates the burning of a 10 cm by 10 cm sample with a specified heat flux to represent the effect of the cone heater. The cone itself is not included in the simulation. As the sample burns, FDS predicts the additional radiative and convective heating of the sample as a result of the fire.

In general, the burning/gasification rate of a charring polymer is more difficult to predict than a non-charring one because there are more parameters that need to be measured and more complicated behavior, like intumescence, need to be considered.

14.1.1 Glossary of Terms

Assumption: Characteristics were assumed from known properties in similar materials.

Cone Calorimeter (ASTM E 1354 [380]) The Cone Calorimeter exposes a small sample to a constant external radiant heat flux simulating exposure of the sample to a large scale fire. The device records mass loss data along with heat release data through oxygen consumption calorimetry. From this a variety of heat release related properties can be found including heat of combustion.

Constant Volume: The material is assumed to maintain a constant volume during the solid phase reactions.

Direct: Direct measurement of densities is performed by measuring the dimensions and mass of the sample.

DSC: (ASTM E 2070 [381]) A Differential Scanning Calorimeter precisely raises the temperature of a small sample of material at a constant rate. This coupled with knowledge of heat absorbed by the sample allows for the calculation of the specific heat function of a material as well as heats of reaction and phase change.

Estimated: Characteristics were approximated based on known properties in similar materials.

FTIR: Fourier Transform Infrared Spectroscopy uses a spectrometer to simultaneously characterize the absorption of all frequencies of infrared light. In testing a sample is exposed to infrared light and a detector records light that has passed through the sample. A Fourier transform of detector measurement is then translated into absorption information.

Gasification Apparatus: Similar to the Cone Calorimeter however flaming is prevented. This is done typically through the introduction of inert purge gases.

Inherited: The properties of the product or component are assumed to be the same as the original material.

Inverse Analysis: Property was established by fitting a model to measured temperatures from the Cone Calorimeter or Gasification Apparatus.

IS: (ASTM E 1175 [382]) An Integrating Sphere, or an Ulbricht Sphere, is a hollow cavity whose interior has a high diffuse reflectivity. A sample placed inside the sphere is exposed to incident radiation and reflectivity measured. Emissivity can be determined from this information. The standard above is for measurement of Solar reflectivity, and was not necessarily precisely followed.

Laser Flash: (ASTM E1461 [383]) In the Laser Flash Method one surface of a sample is rapidly heated using a single pulse from a laser. Heat sensors on the opposite side of the sample record the arrival of the resulting temperature disturbance. From this thermal diffusivity/thermal conductivity can be calculated.

Literature: Results were found within previously published literature.

MCC: (ASTM D 7309 [384]) The Microscale Combustion Calorimeter (MCC) rapidly pyrolyzes a milligram size sample in an inert atmosphere. The pyrolyzate is then exposed to an abundance of oxygen. Heat release history is obtained from oxygen consumption. Similar to TGA with heat release recorded rather than mass loss rate.

Pulsed Current: Can refer to different types of tests. Generally, a sample is positioned between two electrodes in a sealed chamber with an inert atmosphere. The sample is heated through pulses of current. Measurements of the sample and the chamber can give information regarding specific heat, emissivity, or other material properties.

TGA: (ASTM E 1131 [385]) In Thermal Gravimetric Analysis (TGA) a small sample is heated at uniform rate, generally in a Nitrogen (N₂) atmosphere. The percentage weight loss of the sample is recorded relative to the sample's temperature. Rate constants can then be fitted to the data. Similar to MCC with mass loss recorded instead of heat release.

TLS: (ASTM D 5930 [386]) The Transient Line Source method records temperature of a single point at a fixed distance in a sample over time using a probe. Given knowledge of the heat exposure of the sample the thermal conductivity can be found from the slope of the recorded data.

14.1.2 Non-Charring Polymers, HDPE, HIPS, and PMMA

A non-charring polymer is considered one of the easiest solids to model because it typically involves only a single, first order reaction that converts solid plastic to fuel vapor. No residue is formed and the plastic is completely pyrolyzed. Table 14.1 lists nine parameters for each polymer studied. These values have been input directly into FDS, and the predicted mass loss rates are compared with measured values from the NIST Gasification Apparatus, a device that pyrolyzes the solid in a nitrogen environment to prevent combustion of fuel gases. The results are shown in Fig. 14.1. The exposing heat flux was 52 kW/m². A 1 cm layer of insulation was placed under the sample. Its properties are given in Ref. [207].

Table 14.1: Input parameters for FAA Polymers non-charring samples. Courtesy S. Stoliarov, M. McKinnon and J. Li, University of Maryland. See Sec. 14.1.1 for an explanation of terms.

Property	Units	HDPE	HIPS	PMMA	Unc. (%)	Method	Ref.
Density	kg/m ³	860	950	1100	5	Direct	[207]
Conductivity	W/m/K	0.29	0.22	0.20	15	TLC	[207]
Specific Heat	kJ/kg/K	3.5	2.0	2.2	15	DSC	[387]
Emissivity		0.92	0.86	0.85	20	IS	[388]
Absorption Coef.	m ⁻¹	1300	2700	2700	50	FTIR	[389]
Pre-Exp. Factor	s ⁻¹	4.8×10^{22}	1.2×10^{16}	8.5×10^{12}	50	TGA	[207]
Activation Energy	J/mol	3.49×10^5	2.47×10^5	1.88×10^5	3	TGA	[207]
Heat of Reaction	kJ/kg	920	1000	870	15	DSC	[387]

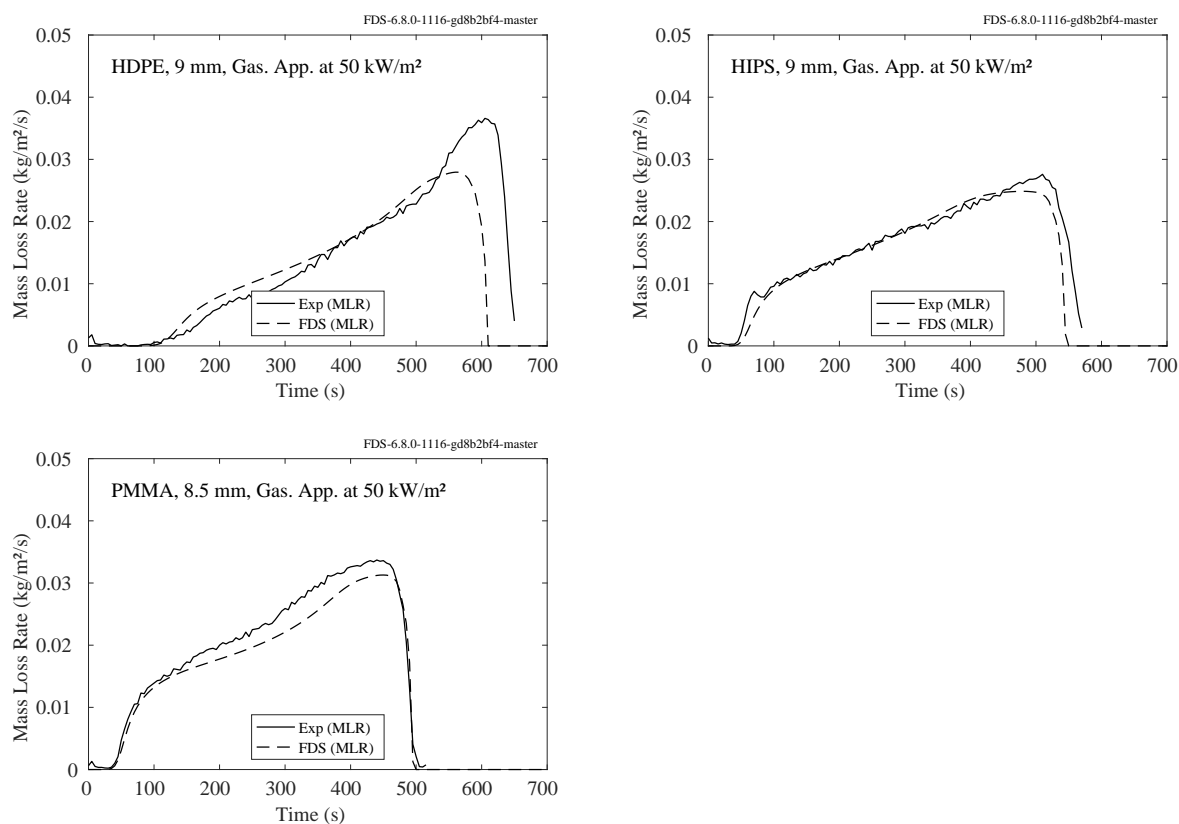


Figure 14.1: Comparison of predicted and measured mass loss rates for three non-charring polymers exposed to a heat flux of 52 kW/m² in a nitrogen environment.

14.1.3 Complex Non-Charring Polymers: PP, PA66, POM, and PET

The polymers described in this section exhibit slightly more complex behavior than those in the previous section because they exhibit foaming and bubbling as they degrade. Table 14.2 lists the properties of each polymer. In the model, the polymers melt to form a liquid with identical properties as the solid. The melting is characterized by a relatively fast reaction that occurs near the melting temperature with a heat of reaction equivalent to a heat of melting. The predicted mass loss rates are compared with measured values from the NIST Gasification Apparatus, a device that pyrolyzes the solid in a nitrogen environment to prevent combustion of fuel gases. The results are shown in Fig. 14.2. The exposing heat flux is 50 kW/m². A thin sheet of aluminum foil and a 2.5 cm layer of Foamglas insulation underlies the sample. Its properties are given in Ref. [303].

Table 14.2: Input parameters for FAA Polymers complex non-charring samples [303]. Courtesy S. Stoliarov, G. Linteris and R.E. Lyon. See Sec. 14.1.1 for an explanation of terms.

Property	Units	PP	PA66	POM	PET	Unc. (%)	Method
Density	kg/m ³	910	1150	1425	1380	5	Direct
Conductivity	W/m/K	0.24	0.34	0.28	0.29	15	TLC
Specific Heat	kJ/kg/K	2.68	2.54	1.88	2.01	15	DSC
Emissivity		0.96	0.95	0.95	0.903	20	IS
Absorption Coef.	m ⁻¹	966	3920	3550	2937	50	FTIR
Pre-Exp. Factor	s ⁻¹	1.6×10^{23}	5.7×10^{17}	3.7×10^{10}	4.50×10^{18}	50	TGA
Activation Energy	J/mol	3.52×10^5	2.74×10^5	1.57×10^5	2.81×10^5	3	TGA
Heat of Reaction	kJ/kg	1310	1390	1570	1800	15	DSC
Heat of Melting	kJ/kg	80	55	141	37	15	DSC
Melting Temperature	K	158	262	165	253	15	DSC

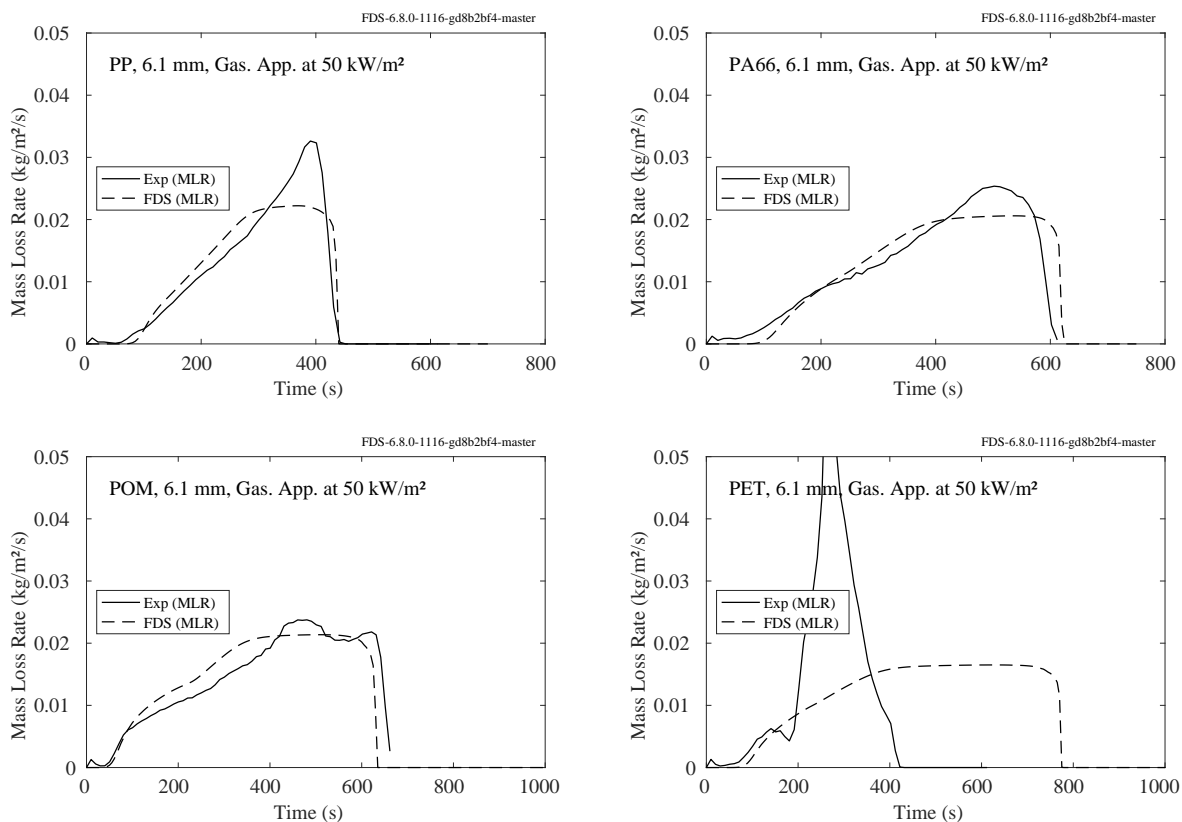


Figure 14.2: Comparison of predicted and measured mass loss rates for four complex non-charring polymers exposed to a heat flux of 50 kW/m² in a nitrogen environment.

14.1.4 Polycarbonate (PC)

Table 14.3 lists the measured properties of polycarbonate. These values have been input directly into FDS, and the predicted heat release rates are compared with measured values from the Cone Calorimeter. The results for samples of various thicknesses and imposed heat fluxes are shown in Fig. 14.3. A 1 cm layer of Kaowool insulation was placed under the sample. Its properties are given in Ref. [208]. It is assumed that the polymer undergoes a single step reaction that forms fuel gas and char.



Table 14.3: Properties of polycarbonate (PC). Courtesy S. Stoliarov, University of Maryland. See Sec. 14.1.1 for an explanation of terms.

Property	Units	Value	Method	Reference
Polymer Density	kg/m ³	1180 ± 60	Direct	[208]
Polymer Conductivity	W/m/K	0.22 ± 0.03	Literature	[208]
Polymer Specific Heat	kJ/kg/K	1.9 ± 0.3	DSC	[387]
Polymer Emissivity		0.90 ± 0.05	IS	[388]
Polymer Absorption Coef.	m ⁻¹	1770 ± 590	FTIR	[389]
Char Density	kg/m ³	248	Cone Calorimeter	[208]
Char Conductivity	W/m/K	0.37	Cone Calorimeter	[208]
Char Specific Heat	kJ/kg/K	1.72 ± 0.17	Pulsed Current	[208, 390]
Char Emissivity		0.85 ± 0.05	Pulsed Current	[208, 390]
Char Absorption Coef.	m ⁻¹	Opaque	Assumption	[208]
Pre-Exp. Factor	s ⁻¹	(1.9 ± 1.1) × 10 ¹⁸	TGA	[208]
Activation Energy	J/mol	(2.95 ± 0.06) × 10 ⁵	TGA	[208]
Heat of Reaction	kJ/kg	830 ± 140	DSC	[387]
Heat of Combustion	kJ/kg	25600 ± 130	MCC	[208]
Combustion Efficiency		0.84 ± 0.03	Cone Calorimeter	[208]

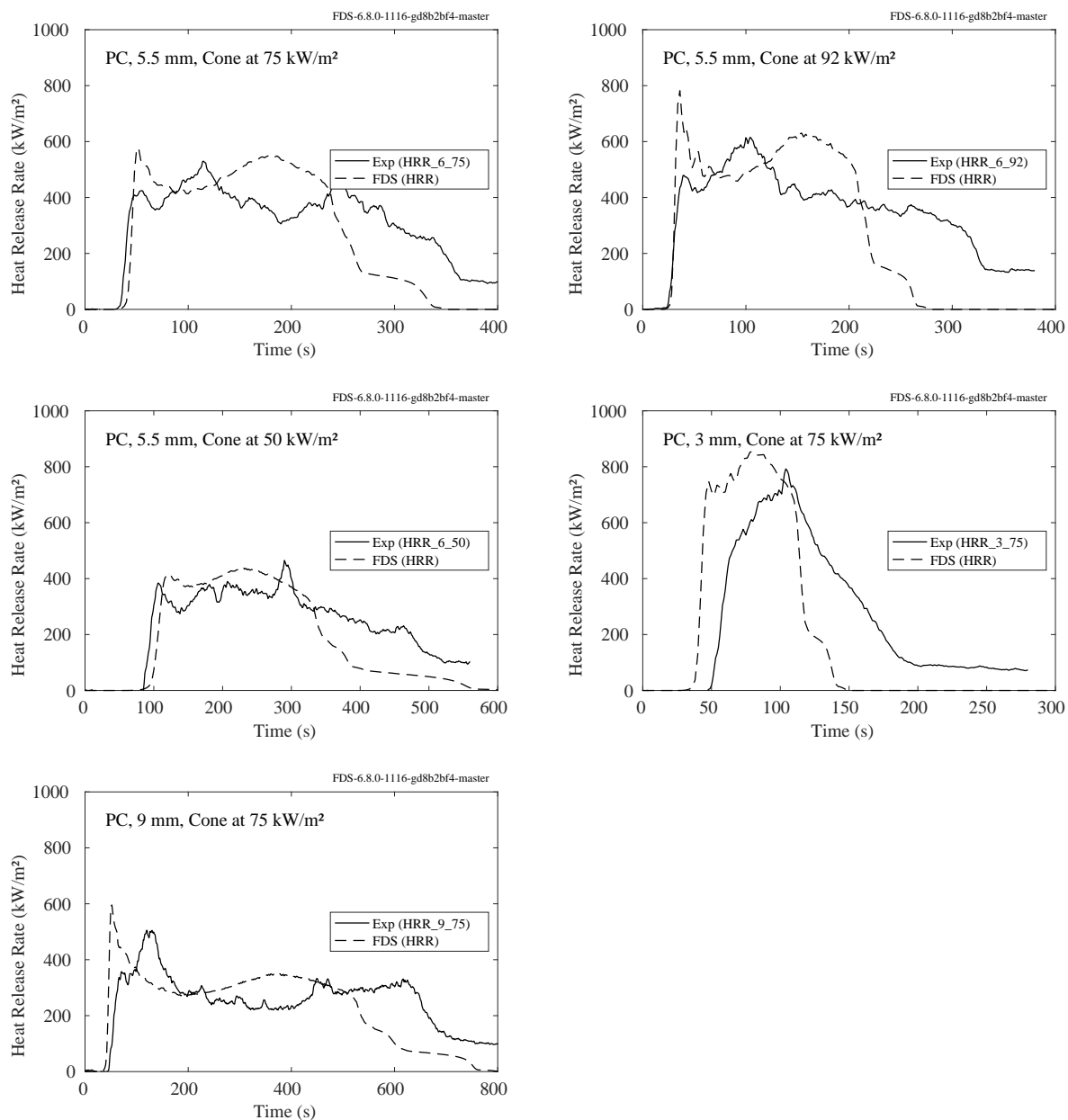


Figure 14.3: Comparison of predicted and measured heat release rates for polycarbonate (PC).

14.1.5 Poly(vinyl chloride) (PVC)

Table 14.4 lists the measured properties of poly(vinyl chloride). These values have been input directly into FDS, and the predicted heat release rates are compared with measured values from the Cone Calorimeter. The results for samples of various thicknesses and imposed heat fluxes are shown in Fig. 14.4. A 1 cm layer of Kaowool insulation was placed under the sample. Its properties are given in Ref. [208].

It is assumed that the polymer decomposes via a two-step reaction:

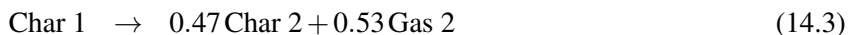


Table 14.4: Properties of poly(vinyl chloride) (PVC). Courtesy S. Stoliarov, University of Maryland. See Sec. 14.1.1 for an explanation of terms.

Property	Units	Value	Method	Reference
Polymer Density	kg/m ³	1430 ± 70	Direct	[208]
Polymer Conductivity	W/m/K	0.17 ± 0.01	Literature	[208]
Polymer Specific Heat	kJ/kg/K	1.55 ± 0.25	DSC	[387]
Polymer Emissivity		0.90 ± 0.05	IS	[388]
Polymer Absorption Coef.	m ⁻¹	2145 ± 715	FTIR	[389]
Char 1 Density	kg/m ³	629	Constant Volume	[208]
Char 1 Conductivity	W/m/K	0.17	Inherited	[208]
Char 1 Specific Heat	kJ/kg/K	1.55 ± 0.25	Inherited	[208]
Char 1 Emissivity		0.90 ± 0.05	Inherited	[208]
Char 1 Absorption Coef.	m ⁻¹	2453	Inverse Analysis	[208]
Char 2 Density	kg/m ³	296	Constant Volume	[208]
Char 2 Conductivity	W/m/K	0.26	Inverse Analysis	[208]
Char 2 Specific Heat	kJ/kg/K	1.72 ± 0.17	Pulsed Current	[208, 390]
Char 2 Emissivity		0.85 ± 0.05	Pulsed Current	[208, 390]
Char 2 Absorption Coef.	m ⁻¹	Opaque	Assumption	[208]
Reac 1 Pre-Exp. Factor	s ⁻¹	$(1.4 \pm 0.8) \times 10^{33}$	TGA	[208]
Reac 1 Activation Energy	J/mol	$(3.67 \pm 0.07) \times 10^5$	TGA	[208]
Reac 1 Char Yield		0.44 ± 0.01	TGA	[208]
Reac 1 Heat of Reaction	kJ/kg	170 ± 17	DSC	[387]
Gas 1 Heat of Combustion	kJ/kg	2700 ± 300	MCC	[208]
Gas 1 Combustion Efficiency		0.75 ± 0.03	Cone Calorimeter	[208]
Reac 2 Pre-Exp. Factor	s ⁻¹	$(3.5 \pm 2.1) \times 10^{12}$	TGA	[208]
Reac 2 Activation Energy	J/mol	$(2.07 \pm 0.04) \times 10^5$	TGA	[208]
Reac 2 Char Yield		0.47 ± 0.01	TGA	[208]
Reac 2 Heat of Reaction	kJ/kg	1200 ± 900	DSC	[387]
Gas 2 Heat of Combustion	kJ/kg	36500 ± 1800	MCC	[208]
Gas 2 Combustion Efficiency		0.75 ± 0.03	Cone Calorimeter	[208]

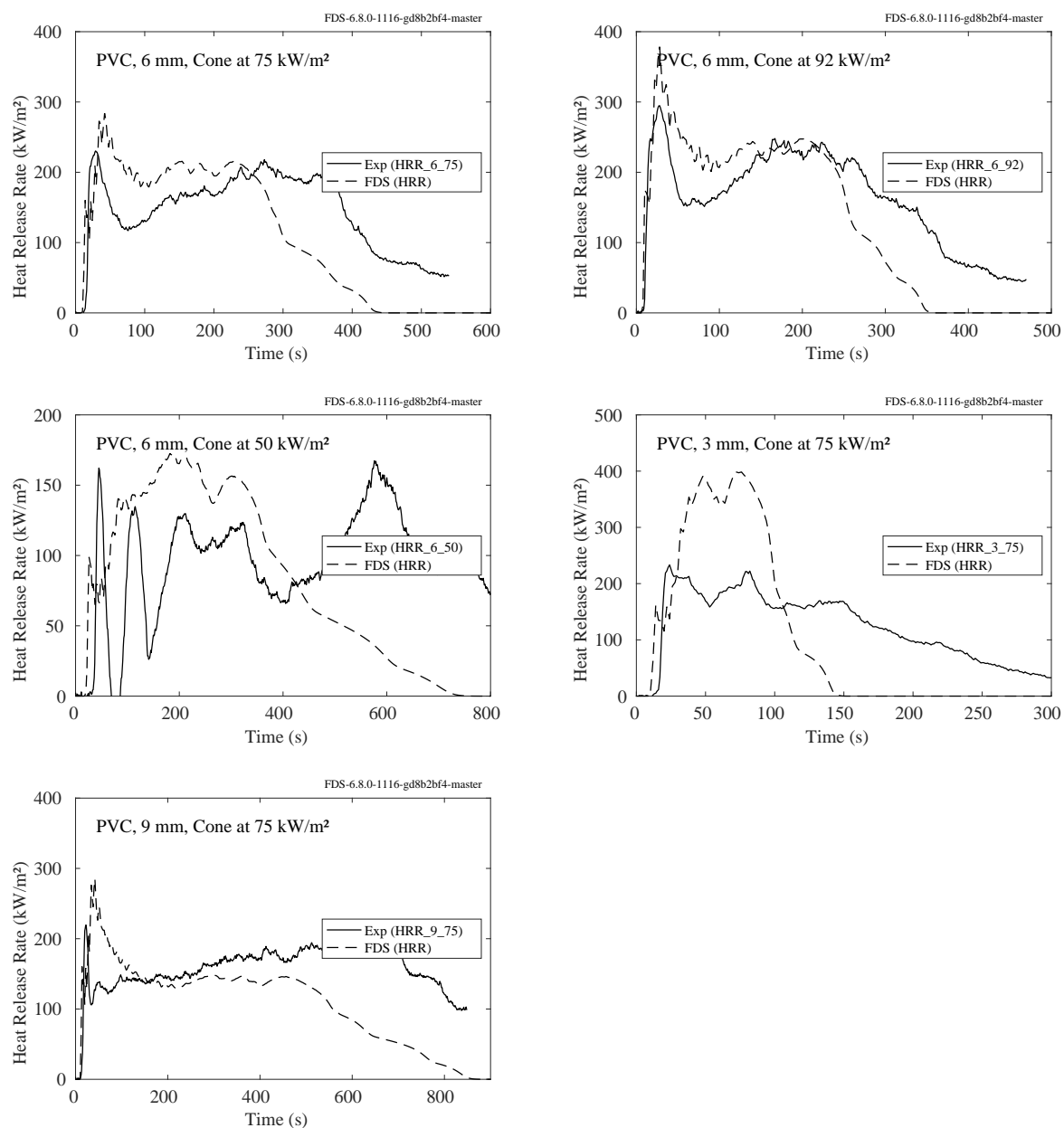
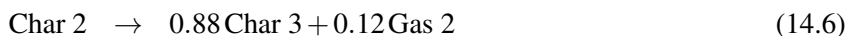
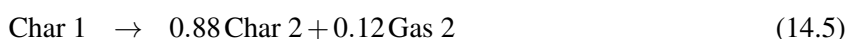


Figure 14.4: Comparison of predicted and measured heat release rates for poly(vinyl chloride) (PVC).

14.1.6 Poly(aryl ether ether ketone)) (PEEK)

Table 14.5 lists the measured properties of poly(aryl ether ether ketone)¹. Its property values have been input directly into FDS, and the predicted heat release rates are compared with measured values from the Cone Calorimeter. It is assumed that the polymer decomposes via a four-step reaction:



It is also assumed that the gaseous fuel molecule is $\text{C}_{19}\text{H}_{12}\text{O}_3$. A 1 cm layer of Kaowool insulation was placed under the sample. Its properties are given in Ref. [208].

The results for 3.9 mm samples at imposed heat fluxes of 50 kW/m^2 , 70 kW/m^2 , and 90 kW/m^2 are shown in Fig. 14.5. Note that the plots on the left are the results of simulations of the solid phase only, where the heat feedback from the fire is assumed to be 15 kW/m^2 and it is applied at the time of ignition. The plots on the right are from 3-D simulations of the solid sample and the fire. In these cases, the radiative feedback is not specified but rather calculated.

¹Trade name VICTREX PEEK 450G. The sample has been thoroughly dried.

Table 14.5: Properties of poly(aryl ether ether ketone) (PEEK). Courtesy E. Oztekin, U.S. FAA and S. Stolarov, University of Maryland. See Sec. 14.1.1 for an explanation of terms.

Property	Units	Value	Method	Reference
Polymer Density	kg/m ³	1300	Direct	[391]
Polymer Conductivity	W/m/K	0.28	Inverse Analysis	[391]
Polymer Specific Heat	kJ/kg/K	2.05	Inverse Analysis	[391]
Polymer Emissivity		0.90	Inverse Analysis	[391]
Polymer Absorption Coef.	m ⁻¹	1690	Inverse Analysis	[391]
Char 1 Density	kg/m ³	810	Constant Volume	[391]
Char 1 Conductivity	W/m/K	0.37	Inverse Analysis	[391]
Char 1 Specific Heat	kJ/kg/K	0.24	Assumed	[391]
Char 1 Emissivity		1	Assumed	[391]
Char 1 Absorption Coef.	m ⁻¹	81000	Assumed opaque	[391]
Char 2 Density	kg/m ³	710	Constant Volume	[391]
Char 2 Conductivity	W/m/K	0.37	Inverse Analysis	[391]
Char 2 Specific Heat	kJ/kg/K	0.27	Assumed	[391]
Char 2 Emissivity		1	Assumed	[391]
Char 2 Absorption Coef.	m ⁻¹	71000	Assumed opaque	[391]
Reac 1 Pre-Exp. Factor	s ⁻¹	1.0×10^{32}	TGA	[391]
Reac 1 Activation Energy	J/mol	5.57×10^5	TGA	[391]
Reac 1 Char Yield		0.62	TGA	[391]
Reac 1 Heat of Reaction	kJ/kg	350	Inverse Analysis	[391]
Gas 1 Heat of Combustion	kJ/kg	16000	Cone calorimetry	[391]
Gas 1 Combustion Efficiency		1	Assumed	[391]
Reac 2 Pre-Exp. Factor	s ⁻¹	1.0×10^3	TGA	[391]
Reac 2 Activation Energy	J/mol	8.9×10^4	TGA	[391]
Reac 2 Char Yield		0.88	TGA	[391]
Reac 2 Heat of Reaction	kJ/kg	0	Assumed	[391]
Gas 2 Heat of Combustion	kJ/kg	27000	Cone Calorimetry	[391]
Gas 2 Combustion Efficiency		1	Assumed	[391]
Reac 3 Pre-Exp. Factor	s ⁻¹	1.0×10^5	TGA	[391]
Reac 3 Activation Energy	J/mol	1.47×10^5	TGA	[391]
Reac 3 Char Yield		0.88	TGA	[391]
Reac 3 Heat of Reaction	kJ/kg	0	Assumed	[391]
Reac 4 Pre-Exp. Factor	s ⁻¹	1.0×10^3	TGA	[391]
Reac 4 Activation Energy	J/mol	1.29×10^5	TGA	[391]
Reac 4 Char Yield		0	TGA	[391]
Reac 4 Heat of Reaction	kJ/kg	0	Assumed	[391]

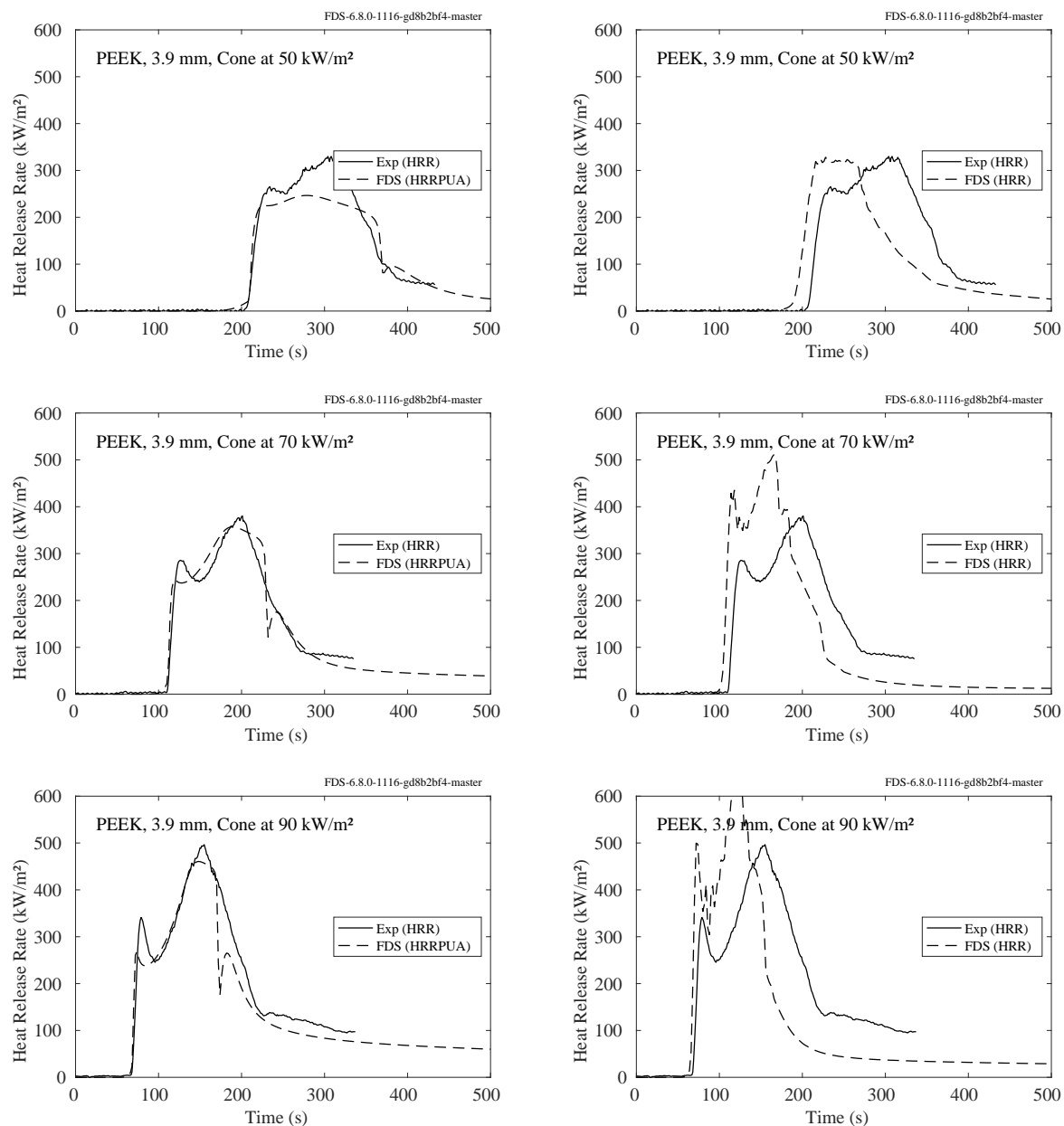


Figure 14.5: Comparison of predicted and measured heat release rates for poly(aryl ether ether ketone) (PEEK). The plots on the left include only a simulation of the solid phase with an added heat flux of 15 kW/m² to account for the radiative feedback from the flame. The plots on the right are 3-D simulations of the solid sample and the fire.

14.1.7 Poly(butylene terephthalate) (PBT)

Samples of poly(butylene terephthalate) (PBT)² have been burned without oxygen in the Gasification Apparatus and with oxygen in the Cone Calorimeter. The properties of PBT are listed in Table 14.6. It is assumed that the polymer undergoes a single step reaction that forms fuel gas and no char.

The results of the simulations are shown in Fig. 14.6. Note that the effect of the flame radiation heat feedback to the sample surface is accounted for by increasing the imposed heat fluxes of 35 kW/m² by 39 %, 50 kW/m² by 22 %, and 70 kW/m² by 6 % [392].

Table 14.6: Properties of poly(butylene terephthalate) (PBT). Courtesy S. Stoliarov, University of Maryland, and Florian Kempel. See Sec. 14.1.1 for an explanation of terms. Note that the Specific Heat and Conductivity result from averaging the reported temperature dependent properties over the room to decomposition temperature range (300 K – 650 K). The heat capacity value is increased by 0.13 kJ/kg/K to account for the heat of melting (-46 kJ/kg), which takes place at 493 K.

Property	Units	Value	Method	Reference
Density	kg/m ³	1300 ± 70	Direct	[392]
Specific Heat	kJ/kg/K	2.23 ± 0.34	DSC	[392]
Conductivity	W/m/K	0.29 ± 0.05	TLS	[392]
Emissivity		0.88 ± 0.05	FTIR	[393]
Absorption Coefficient	m ⁻¹	2561 ± 140	FTIR	[393]
Pre-Exp. Factor	s ⁻¹	$(2.49 \pm 0.62) \times 10^{14}$	TGA	[392]
Activation Energy	J/mol	$(2.12 \pm 0.53) \times 10^5$	TGA	[392]
Heat of Reaction	kJ/kg	507	DSC, Literature	[392, 394]
Heat of Combustion	kJ/kg	19500	Cone Calorimeter	[392]
Combustion Efficiency		1	Assumption	[392]

²Tradename Arnite T06-200, DSM Engineering Plastics

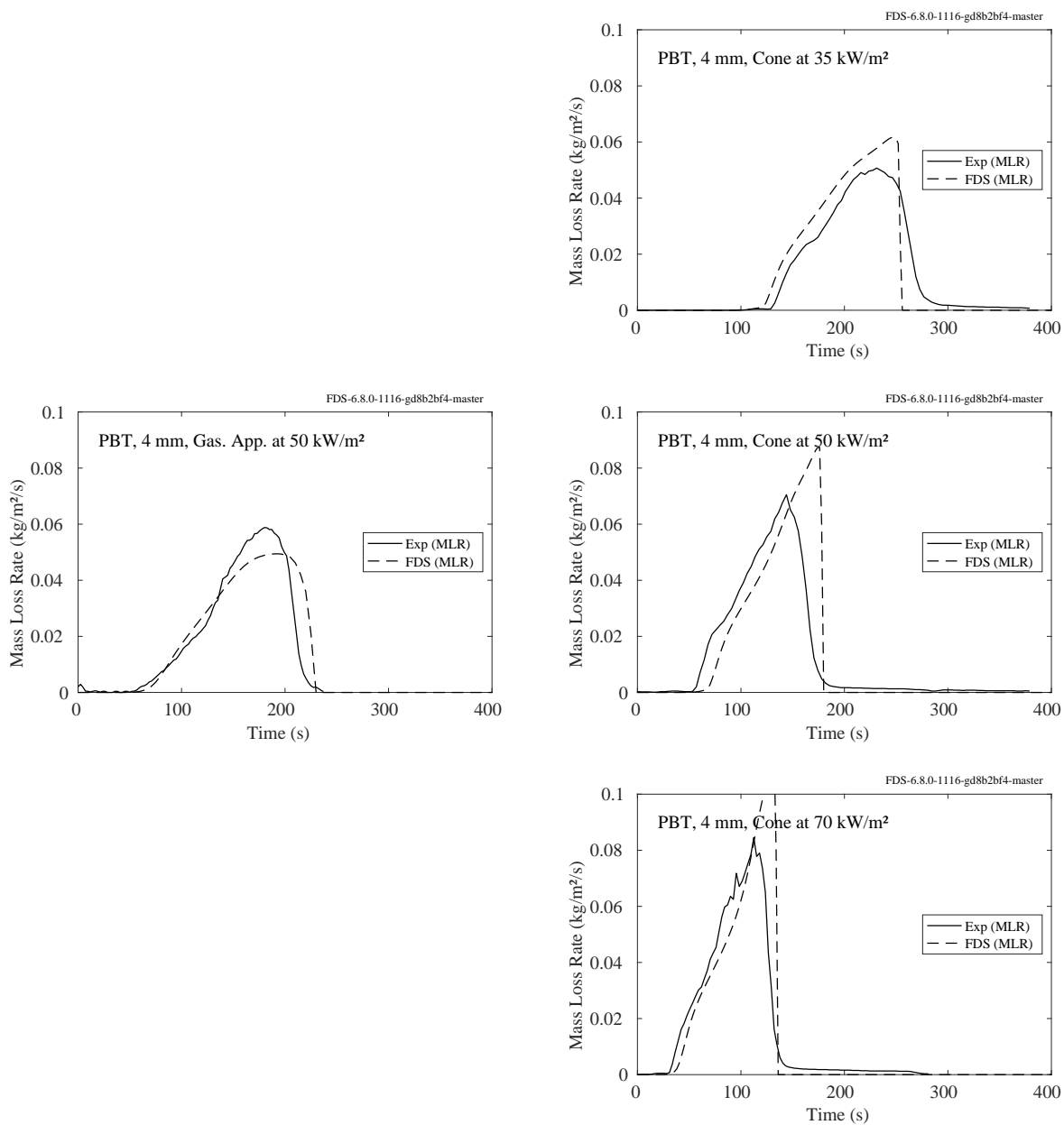


Figure 14.6: Comparison of predicted and measured mass loss rates for poly(butylene terephthalate) (PBT) in both the Gasification Apparatus and Cone Calorimeter.

14.1.8 PBT with Glass Fibers (PBT-GF)

Samples of poly(butylene terephthalate) (PBT), blended with 30 % by mass glass fibers³, have been burned without oxygen in the Gasification Apparatus and with oxygen in the Cone Calorimeter. The properties of PBT-GF are listed in Table 14.7. It is assumed that the polymer undergoes a single step reaction that forms fuel gas and char.



The results of the simulations are shown in Fig. 14.7. Note that the effect of the flame radiation heat feedback to the sample surface is accounted for by increasing the imposed heat fluxes of 35 kW/m² by 33 %, 50 kW/m² by 16 %, and 70 kW/m² by 5 % [392].

Table 14.7: Properties of poly(butylene terephthalate) with glass fibers (PBT-GF). Courtesy S. Stoliarov, University of Maryland. See Sec. 14.1.1 for an explanation of terms. Note that the Polymer Specific Heat and Polymer Conductivity are the result of averaging the reported temperature dependent properties over the room to decomposition temperature range (300 K – 650 K). The heat capacity value is increased by 0.09 kJ/kg/K to account for the heat of melting (-32 kJ/kg), which takes place at 493 K.

Property	Units	Value	Method	Reference
Polymer Density	kg/m ³	1520 ± 80	Direct	[392]
Polymer Specific Heat	kJ/kg/K	1.68 ± 0.26	DSC	[392]
Polymer Conductivity	W/m/K	0.36 ± 0.06	TLS	[392]
Polymer Emissivity		0.87 ± 0.05	FTIR	[393]
Polymer Absorption Coef.	m ⁻¹	2860 ± 150	FTIR	[393]
Char Density	kg/m ³	482	Constant Volume	[392]
Char Specific Heat	kJ/kg/K	0.85	Literature	[395]
Char Conductivity	W/m/K	0.07 ± 0.02	Laser Flash	[392]
Char Emissivity		0.85	Literature	[396]
Char Absorption Coef.	m ⁻¹	10000	Estimated	[392]
Pre-Exp. Factor	s ⁻¹	$(2.49 \pm 0.63) \times 10^{14}$	TGA	[392]
Activation Energy	J/mol	$(2.12 \pm 0.53) \times 10^5$	TGA	[392]
Heat of Reaction	kJ/kg	355	DSC, Literature	[392, 394]
Heat of Combustion	kJ/kg	19500	Cone Calorimeter	[392]
Char Yield		0.32 ± 0.05	Gasification Device	[392]
Combustion Efficiency		1	Assumption	[392]

³Tradename Arnite TV4-261, DSM Engineering Plastics

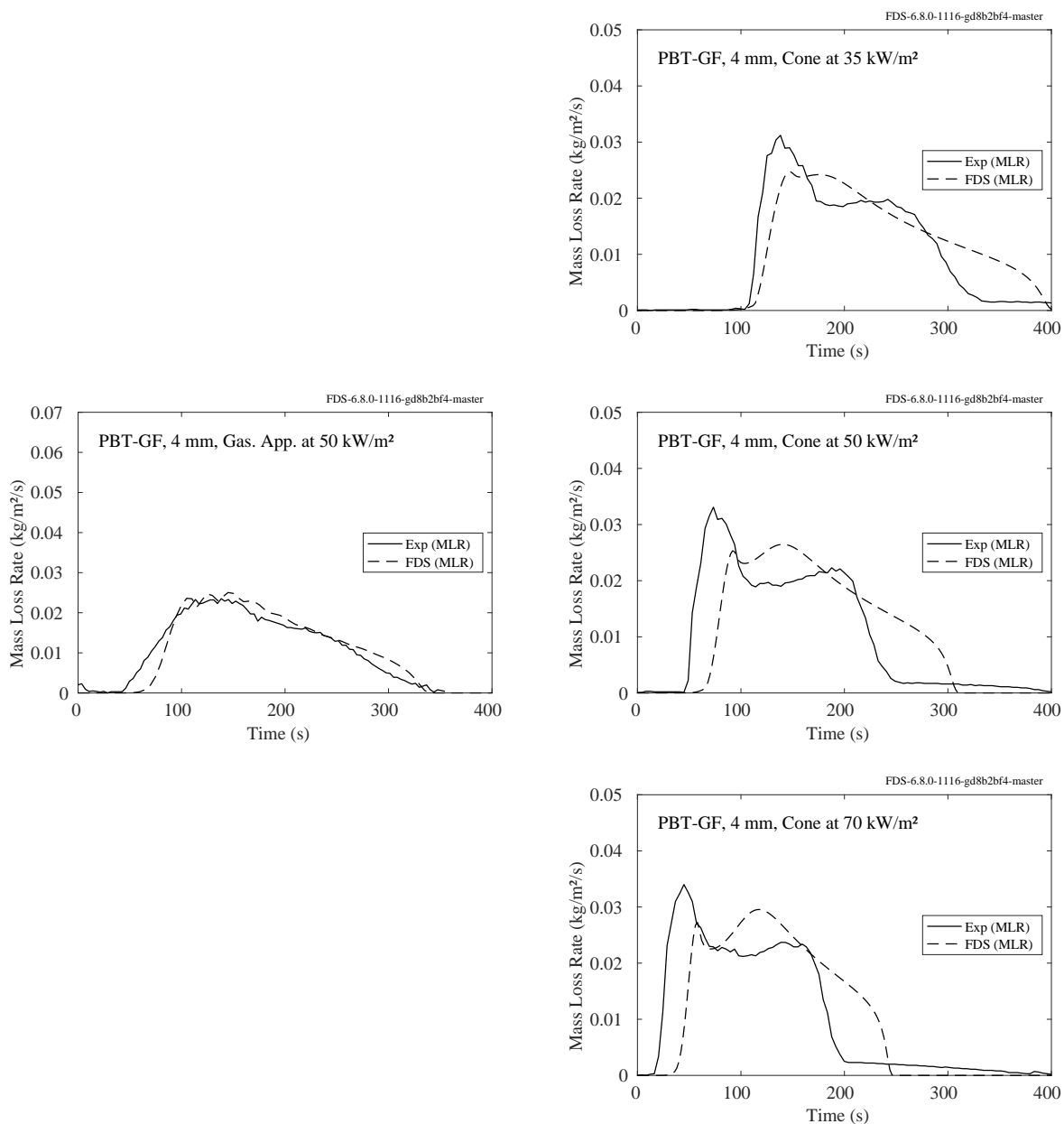


Figure 14.7: Comparison of predicted and measured mass loss rates for poly(butylene terephthalate) with glass fibers (PBT-GF) in both the Gasification Apparatus and Cone Calorimeter.

14.2 NIST Polymers

Black PMMA was chosen as the first material to be studied by the MaCFP Condensed Phase Subgroup. Its properties are listed in Table 14.8. It is assumed that the solid decomposes in two steps [397].

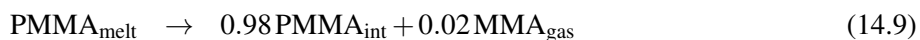


Table 14.8: Input parameters for PMMA [397].

Property	Units	Value	Unc.
Density	kg/m ³	1210	30
Conductivity	W/m/K	0.16 $T < 395 \text{ K}$ $0.34 - 4.2 \times 10^{-4} T$ $T > 395 \text{ K}$	
Specific Heat	kJ/kg/K	$-1.39 + 8.33 \times 10^{-3} T$ $T < 395 \text{ K}$ $0.851 + 3.07 \times 10^{-3} T$ $T > 395 \text{ K}$	
Emissivity		0.96	
Absorption Coef.	m ⁻¹	2870	280
Pre-Exp. Factor	s ⁻¹	4.95×10^{16} Step 1 1.35×10^{11} Step 2	
Activation Energy	J/mol	1.64×10^5 Step 1 1.64×10^5 Step 2	
Heat of Reaction	kJ/kg	5 Step 1 817 Step 2	

Figure 14.8 displays the results of measurements performed at NIST and FDS simulations of pyrolyzing black PMMA in the TGA (10 K/min), MCC (60 K/min) and DSC (10 K/min). Figure 14.9 displays results of the Gasification Apparatus (50 kW/m²) and Cone Calorimeter (25 kW/m²).

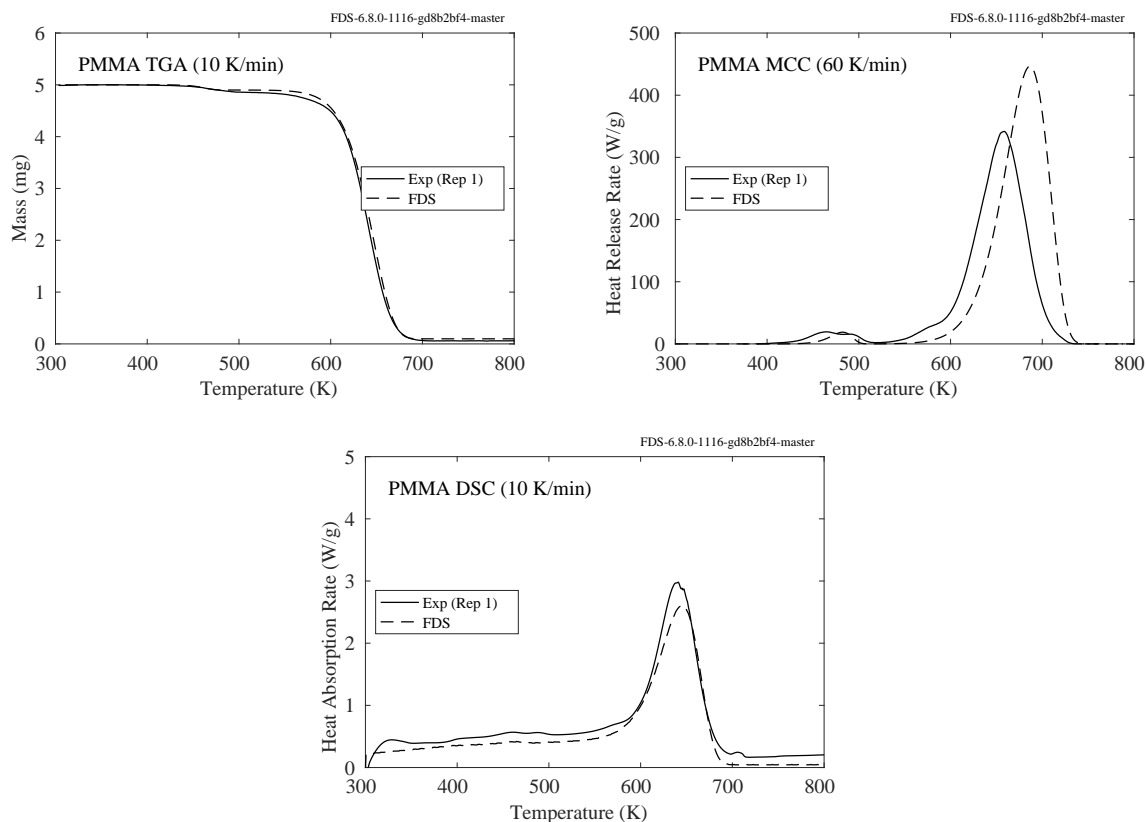


Figure 14.8: (Top left) Mass of a 5 mg sample of black PMMA undergoing Thermo-Gravimetric Analysis in nitrogen with a heating rate of 10 K/min. (Top right) Heat release rate of a small sample of PMMA in the Micro-Combustion Calorimeter with a heating rate of 60 K/min. (Bottom) Heat flow into a small sample of PMMA in the Differential Scanning Calorimeter at 10 K/min.

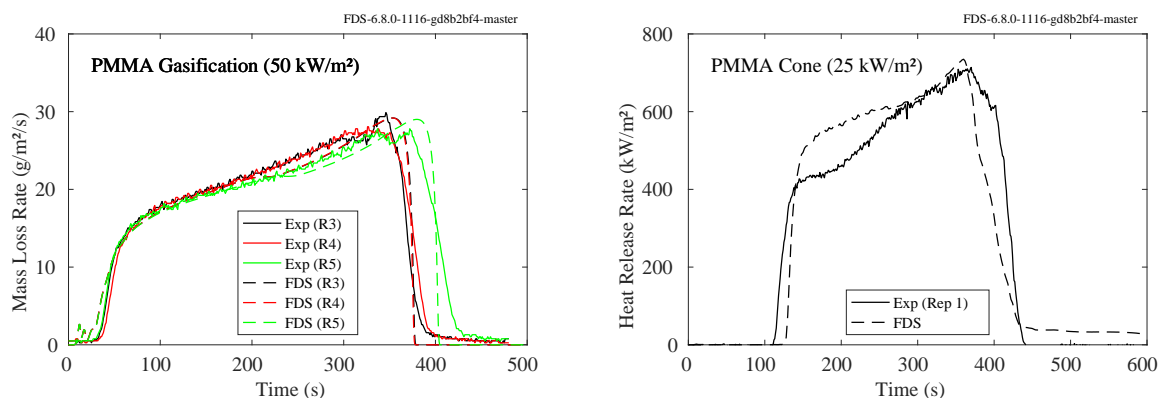


Figure 14.9: (Left) Mass loss rate of a 6 mm thick sample of PMMA exposed to 50 kW/m² in the Gasification Apparatus. (Right) Heat release rate of a 6 mm thick sample of PMMA exposed to 25 kW/m² in the Cone Calorimeter.

14.3 UMD Polymers

This section contains a description of seven polymers analyzed by J. Li for his doctoral thesis at the University of Maryland [398]. In addition to the thesis itself, details of the measurement techniques can be found in Refs. [328, 329, 393, 330, 331].

In the experiments, samples of seven different polymers were exposed to several different heat flux levels in the controlled atmosphere pyrolysis apparatus (CAPA) developed at the University of Maryland. This apparatus is similar to a cone calorimeter, but with a nitrogen environment. Thus, it is similar in function to the Gasification Apparatus. In each experiment, a roughly 6 mm sample was placed upon a wire mesh with no insulated backing. The top side of the sample was exposed to a specified heat flux, while the bottom remained exposed to ambient conditions. The mass loss rate of the sample was measured, and in the sections to follow the measured values are compared to FDS predictions. The seven polymers are organized into groups with one, two, or three degradation steps.

14.3.1 One-Step Degradation: ABS, HIPS, and PMMA

These three polymers are assumed to pyrolyze according to the following single step process:



The properties of the virgin polymer, the char, and the reaction kinetics are listed in Table 14.9.

Table 14.9: Properties of ABS, HIPS, and PMMA. Note that the temperature dependence of the thermal conductivity is assumed to be linear, unlike some of those reported in Ref. [398].

Property	Units	ABS	HIPS	PMMA
Polymer Density	kg/m ³	1050	1060	1160
Polymer Cond.	W/m/K	$0.30 - 0.00028 T$	$0.10 + 0.0001 T$	$0.45 - 0.00038 T, T < 378 \text{ K}$ $0.27 - 0.00024 T, T \geq 378 \text{ K}$
Polymer Spec. Heat	kJ/kg/K	$1.58 + 0.0013 T$	$0.59 + 0.0034 T$	$0.60 + 0.0036 T$
Polymer Emissivity		0.95	0.95	0.95
Polymer Abs. Coef.	m ⁻¹	1800	2250	2240
Char Density	kg/m ³	80	Same as Polymer	Same as Polymer
Char Conductivity	W/m/K	$0.13 - 0.00054 T$	Same as Polymer	Same as Polymer
Char Specific Heat	kJ/kg/K	$0.82 + 0.00011 T$	Same as Polymer	Same as Polymer
Char Emissivity		0.86	Same as Polymer	Same as Polymer
Char Abs. Coef.	m ⁻¹	2500	Opaque	Same as Polymer
Pre-Exp. Factor	s ⁻¹	1.00×10^{14}	1.70×10^{20}	8.60×10^{12}
Activation Energy	J/mol	2.19×10^5	3.01×10^5	1.88×10^5
Heat of Reaction	kJ/kg	460	689	846
Heat of Combustion	kJ/kg	28750	29900	24450
Residue Fraction		0.023	0.043	0.015

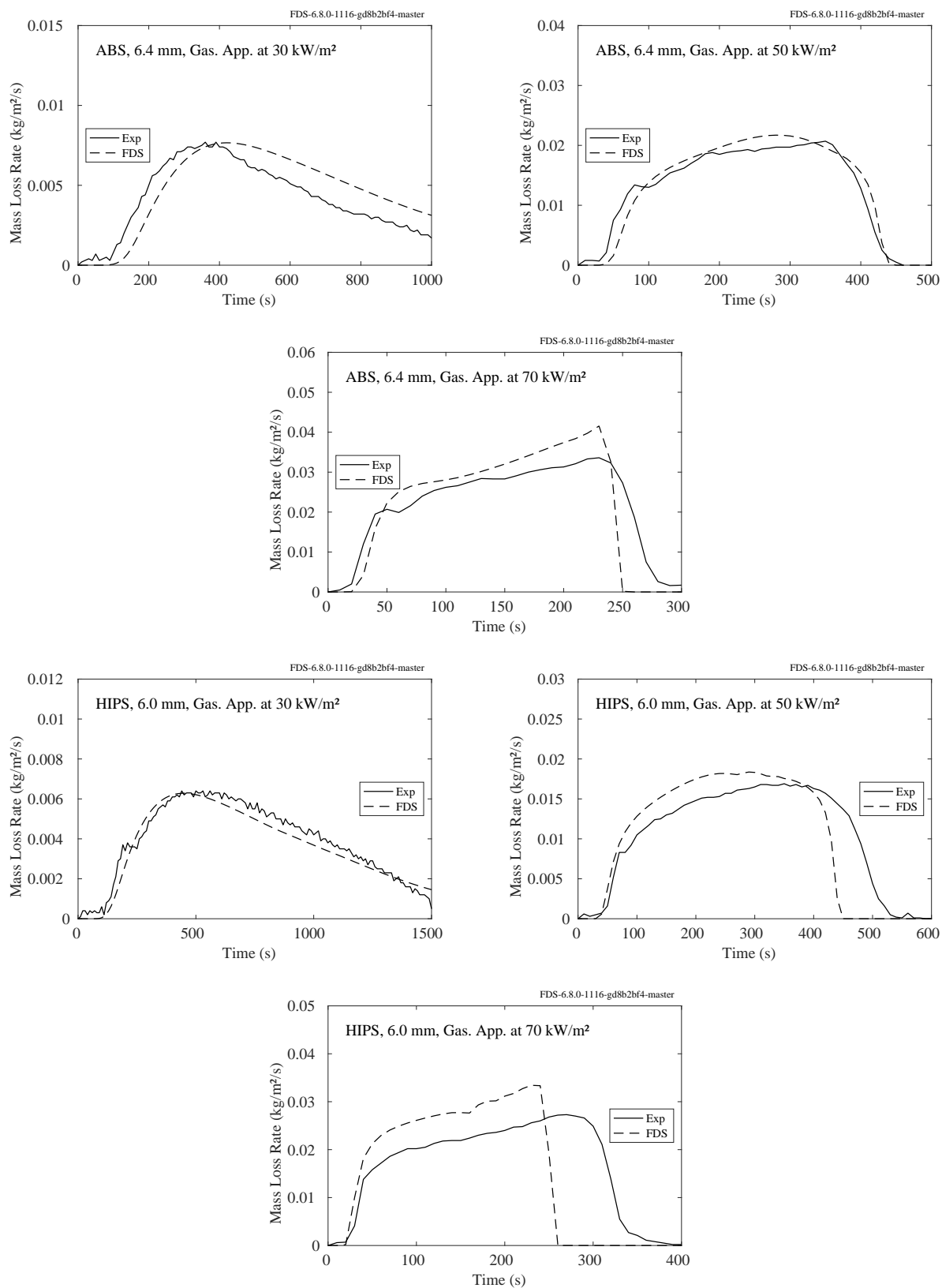


Figure 14.10: Comparison of predicted and measured mass loss rates for ABS and HIPS.

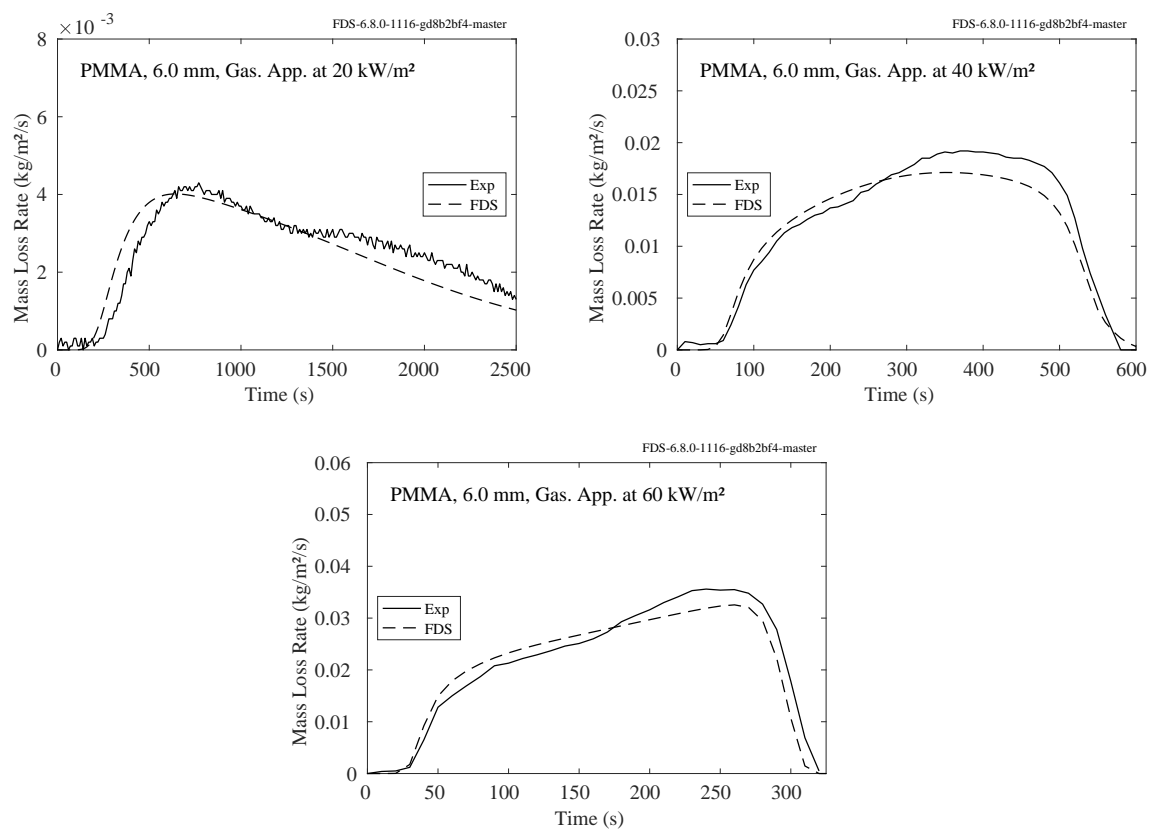
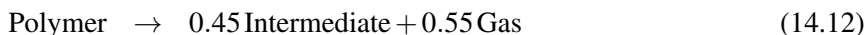


Figure 14.11: Comparison of predicted and measured mass loss rates for PMMA.

14.3.2 Two-Step Degradation: Kydex

This polymer is assumed to pyrolyze according to the following two step process:



The properties of the polymer and the reaction kinetics are listed in Table 14.10 and the mass loss rate comparisons are shown on the following page. Note that nominal exposing heat flux values of 30 kW/m², 50 kW/m², and 70 kW/m² were changed slightly in the simulations to account for the fact that the intumescent material surface moved closer to the heater during the course of the experiment [331].

Table 14.10: Properties of Kydex. Note that the temperature dependence of the thermal conductivity is assumed to be linear, unlike some of those reported in Ref. [398].

Property	Units	Kydex
Polymer Density	kg/m ³	1350
Polymer Cond.	W/m/K	$0.28 - 0.00029 T$
Polymer Spec. Heat	kJ/kg/K	$-0.62 + 0.00593 T$
Polymer, Int. Emissivity		0.95
Polymer Abs. Coef.	m ⁻¹	2135
Int. Density	kg/m ³	Same as Char
Int. Cond.	W/m/K	$0.55 + 0.00003 T$
Int. Spec. Heat	kJ/kg/K	$0.27 + 0.00301 T$
Int. Abs. Coef.	m ⁻¹	3000
Char Density	kg/m ³	100
Char Conductivity	W/m/K	$0.21 + 0.00034 T$
Char Specific Heat	kJ/kg/K	$1.15 + 0.00010 T$
Char Emissivity		0.86
Char Abs. Coef.	m ⁻¹	10000
Reac. 14.12 Pre-Exp. Factor	s ⁻¹	6.03×10^{10}
Reac. 14.12 Act. Energy	J/mol	1.41×10^5
Reac. 14.12 Heat of Reac.	kJ/kg	180
Reac. 14.12 Residue Frac.		0.45
Reac. 14.13 Pre-Exp. Factor	s ⁻¹	1.36×10^{10}
Reac. 14.13 Act. Energy	J/mol	1.74×10^5
Reac. 14.13 Heat of Reac.	kJ/kg	125
Reac. 14.13 Residue Frac.		0.31
Gas Heat of Combustion	kJ/kg	12650

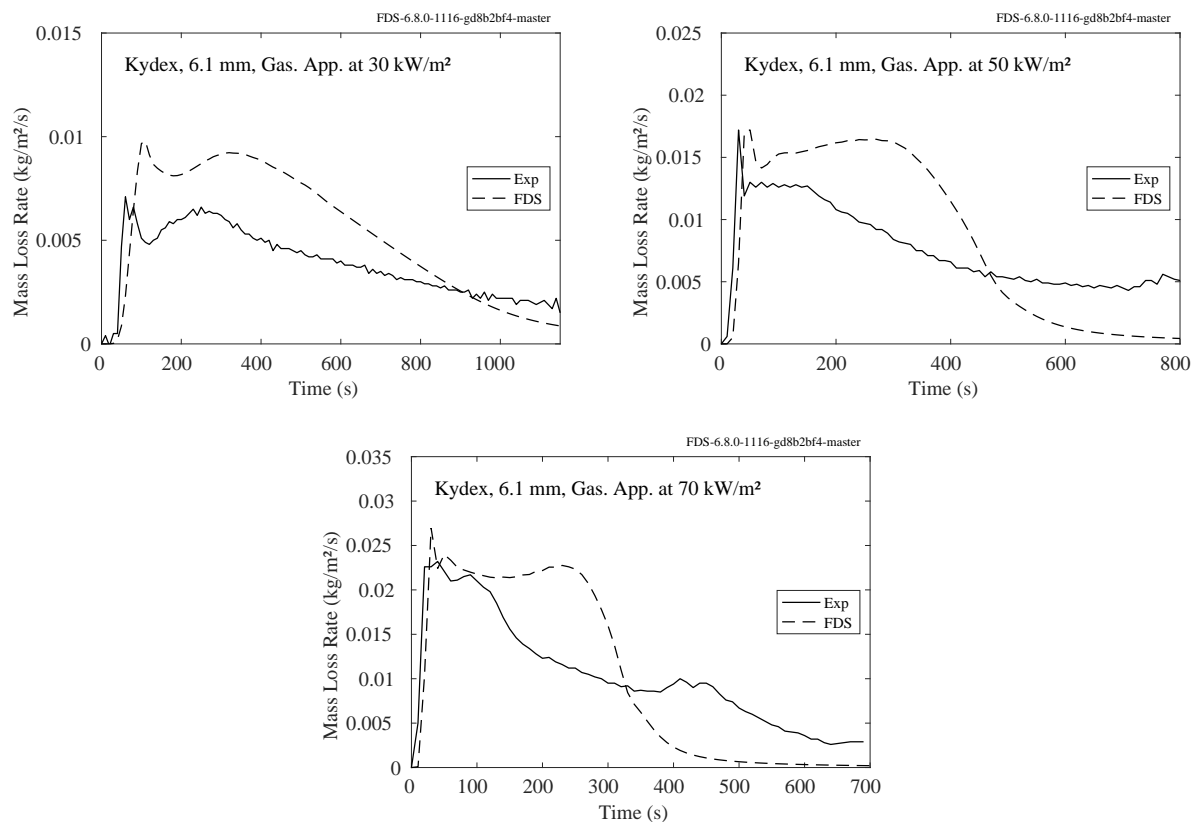
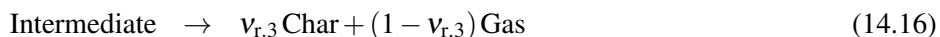
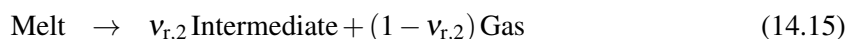


Figure 14.12: Comparison of predicted and measured mass loss rates for Kydex.

14.3.3 Three-Step Degradation: PEI, PET, and POM

These three polymers are assumed to pyrolyze following the three-step process:



The property data is listed in Table 14.11 and the mass loss rate comparisons are shown on the subsequent pages.

Table 14.11: Properties of PEI, PET, and POM. Note that the temperature dependence of the thermal conductivity is assumed to be linear, unlike some of those reported in Ref. [398].

Property	Units	PEI	PET	POM
Polymer, Melt Density	kg/m ³	1285	1385	1424
Polymer Cond.	W/m/K	$0.40 - 0.00040 T$	$0.34 - 0.00046 T$	$0.25 + 0.00002 T$
Polymer Spec. Heat	kJ/kg/K	$-0.04 + 0.00410 T$	$-0.27 + 0.00464 T$	$-1.86 + 0.0099 T$
Polymer, Melt, Int. Emiss.		0.95	0.95	0.95
Polymer Abs. Coef.	m ⁻¹	1745	1940	3050
Melt Cond.	W/m/K	$0.32 - 0.00033 T$	$0.33 - 0.00002 T$	$0.21 + 0.00001 T$
Melt Spec. Heat	kJ/kg/K	$1.88 + 0.00057 T$	$2.05 - 0.00021 T$	$1.65 + 0.00120 T$
Melt Abs. Coef.	m ⁻¹	128500	Same as Polymer	Same as Polymer
Int. Density	kg/m ³	Same as Char	730	Same as Polymer
Int. Cond.	W/m/K	$0.45 + 0.00019 T$	$0.45 + 0.00020 T$	$0.19 - 0.00006 T$
Int. Spec. Heat	kJ/kg/K	$1.59 + 0.00031 T$	$1.44 - 0.00005 T$	Same as Melt
Int. Abs. Coef.	m ⁻¹	8000	1025	Same as Polymer
Char Density	kg/m ³	80	80	Same as Int.
Char Conductivity	W/m/K	$0.45 + 0.00013 T$	$0.34 + 0.00046 T$	Same as Polymer
Char Specific Heat	kJ/kg/K	$1.30 + 0.00004 T$	$0.82 + 0.00011 T$	Same as Int.
Char Emissivity		0.86	0.86	Same as Polymer
Char Abs. Coef.	m ⁻¹	Same as Int.	8000	Same as Polymer
Reac. 14.14 Pre-Exp. Factor	s ⁻¹	1	1.50×10^{36}	2.69×10^{42}
Reac. 14.14 Act. Energy	J/mol	0	3.80×10^5	3.82×10^5
Reac. 14.14 Heat of Reac.	kJ/kg	1	30	192
Reac. 14.14 Residue Frac.		1	1	1
Reac. 14.15 Pre-Exp. Factor	s ⁻¹	7.66×10^{27}	1.60×10^{15}	3.84×10^{14}
Reac. 14.15 Act. Energy	J/mol	4.65×10^5	2.35×10^5	2.00×10^5
Reac. 14.15 Heat of Reac.	kJ/kg	-80	220	1192
Reac. 14.15 Residue Frac.		0.65	0.18	0.4
Reac. 14.16 Pre-Exp. Factor	s ⁻¹	6.50×10^2	3.53×10^4	4.76×10^{44}
Reac. 14.16 Act. Energy	J/mol	0.88×10^5	0.96×10^5	5.90×10^5
Reac. 14.16 Heat of Reac.	kJ/kg	-5	250	1352
Reac. 14.16 Residue Frac.		0.77	0.72	0.018
Gas Heat of Combustion	kJ/kg	18050	15950	14350

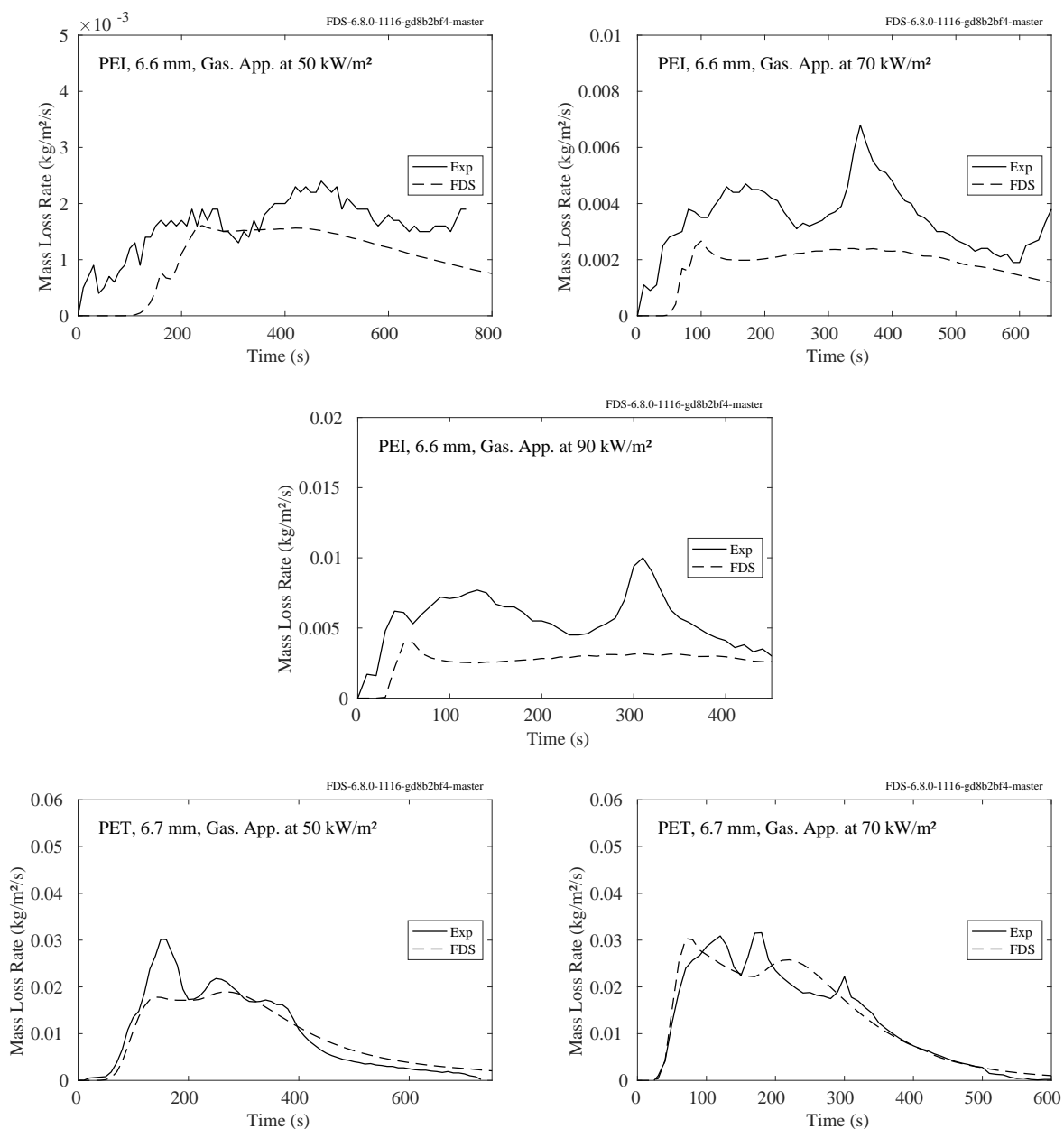


Figure 14.13: Comparison of predicted and measured mass loss rates for PEI and PET.

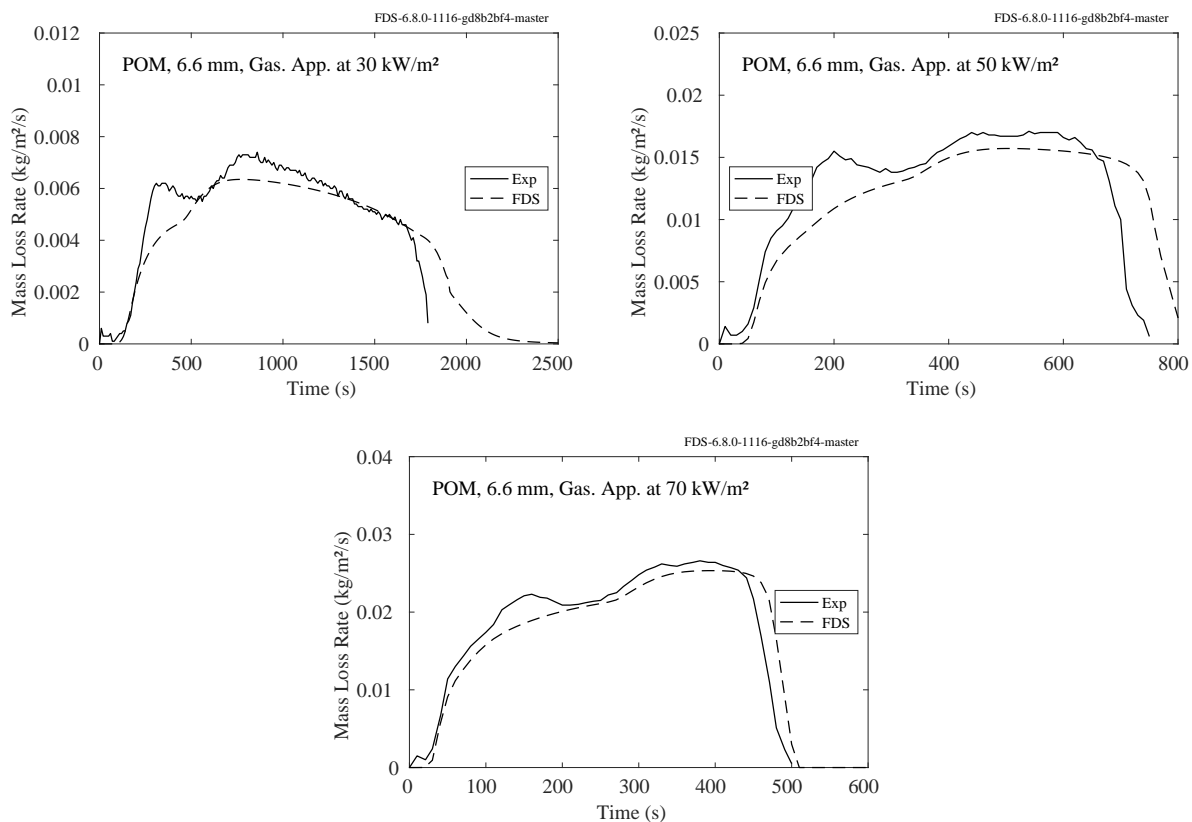


Figure 14.14: Comparison of predicted and measured mass loss rates for POM.

14.4 Corrugated Cardboard

Table 14.12 lists the measured properties of a double-wall corrugated cardboard with the conventional U.S. designation 69-23B-69-23C-69. Corrugated cardboard is characterized by alternating layers of homogeneous, planar liner boards and corrugated sections made up of periodic flutes. The numbers in the specification indicate the areal density in lb/(1000 ft²) and the letters indicate the flute designation (B indicates a range of 45 to 52 flutes per foot and C indicates a range of 39 to 43 flutes per foot). It is assumed that each layer consists of the same lingo-cellulosic, charring material with the density defined as the mass of the solid material divided by the volume of the layer. This representation requires slightly different definitions for the properties of each unique layer – liner board (LB), C-flute layer (CFL), and B-flute layer (BFL).

The reaction mechanism for the cardboard material includes one reaction to describe the release of residual moisture and three sequential reactions to describe the thermal degradation of the virgin material to a final residual char. Each of the initial solid components (LB, CFL, and BFL) undergoes the same four-step mechanism.

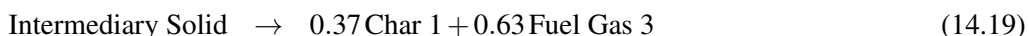


Table 14.12: Properties of corrugated cardboard. Courtesy M. McKinnon, University of Maryland. See Sec. 14.1.1 for an explanation of terms.

Property	Units	Value	Method	Reference
Moisture Density	kg/m ³	1000	Direct	[399]
Moisture Conductivity	W/m/K	0.1	Inherited	[399]
Moisture Specific Heat	kJ/kg/K	4.19	Literature	[400]
Moisture Emissivity		0.7	Inherited	[399]
LB Density	kg/m ³	520	Direct	[399]
LB Conductivity	W/m/K	0.1	Inverse Analysis	[399]
LB Specific Heat	kJ/kg/K	1.8	DSC	[399]
LB Emissivity		0.7	Inverse Analysis	[399]
LB Intermediary Density	kg/m ³	468	Constant Volume	[399]
LB Intermediary Conductivity	W/m/K	$0.05 + 7.5 \times 10^{-11} \times T^3$	Inverse Analysis	[399]
LB Intermediary Specific Heat	kJ/kg/K	1.55	DSC	[399]
LB Intermediary Emissivity		0.775	Inverse Analysis	[399]
LB Char 1 Density	kg/m ³	173	Constant Volume	[399]
LB Char 1 Conductivity	W/m/K	$1.5 \times 10^{-10} \times T^3$	Inverse Analysis	[399]
LB Char 1 Specific Heat	kJ/kg/K	1.3	DSC	[399]
LB Char 1 Emissivity		0.85	Literature	[401]
LB Char 2 Density	kg/m ³	102	Constant Volume	[399]
LB Char 2 Conductivity	W/m/K	$1.5 \times 10^{-10} \times T^3$	Inverse Analysis	[399]
LB Char 2 Specific Heat	kJ/kg/K	1.3	DSC	[399]
LB Char 2 Emissivity		0.85	Literature	[401]
CFL Density	kg/m ³	49	Constant Volume	[399]
CFL Conductivity	W/m/K	0.1	Inverse Analysis	[399]

Table 14.12: Continued

CFL Specific Heat	kJ/kg/K	1.8	DSC	[399]
CFL Emissivity		0.7	Inverse Analysis	[399]
CFL Intermediary Density	kg/m ³	44	Constant Volume	[399]
CFL Intermediary Conductivity	W/m/K	$0.05 + 7.5 \times 10^{-10} \times T^3$	Inverse Analysis	[399]
CFL Intermediary Specific Heat	kJ/kg/K	1.55	DSC	[399]
CFL Intermediary Emissivity		0.775	Inverse Analysis	[399]
CFL Char 1 Density	kg/m ³	16	Constant Volume	[399]
CFL Char 1 Conductivity	W/m/K	$1.5 \times 10^{-9} \times T^3$	Inverse Analysis	[399]
CFL Char 1 Specific Heat	kJ/kg/K	1.3	DSC	[399]
CFL Char 1 Emissivity		0.85	Literature	[401]
CFL Char 2 Density	kg/m ³	9.4	Constant Volume	[399]
CFL Char 2 Conductivity	W/m/K	$1.5 \times 10^{-9} \times T^3$	Inverse Analysis	[399]
CFL Char 2 Specific Heat	kJ/kg/K	1.3	DSC	[399]
CFL Char 2 Emissivity		0.85	Literature	[401]
BFL Density	kg/m ³	74	Constant Volume	[399]
BFL Conductivity	W/m/K	0.1	Inverse Analysis	[399]
BFL Specific Heat	kJ/kg/K	1.8	DSC	[399]
BFL Emissivity		0.7	Inverse Analysis	[399]
BFL Intermediary Density	kg/m ³	67	Constant Volume	[399]
BFL Intermediary Conductivity	W/m/K	$0.05 + 7.5 \times 10^{-10} \times T^3$	Inverse Analysis	[399]
BFL Intermediary Specific Heat	kJ/kg/K	1.55	DSC	[399]
BFL Intermediary Emissivity		0.775	Inverse Analysis	[399]
BFL Char 1 Density	kg/m ³	25	Constant Volume	[399]
BFL Char 1 Conductivity	W/m/K	$1.5 \times 10^{-9} \times T^3$	Inverse Analysis	[399]
BFL Char 1 Specific Heat	kJ/kg/K	1.3	DSC	[399]
BFL Char 1 Emissivity		0.85	Literature	[401]
BFL Char 2 Density	kg/m ³	15	Constant Volume	[399]
BFL Char 2 Conductivity	W/m/K	$1.5 \times 10^{-9} \times T^3$	Inverse Analysis	[399]
BFL Char 2 Specific Heat	kJ/kg/K	1.3	DSC	[399]
BFL Char 2 Emissivity		0.85	Literature	[401]
Reaction 1 Pre-Exp. Factor	s ⁻¹	6.14	TGA	[399]
Reaction 1 Activation Energy	J/mol	23500	TGA	[399]
Reaction 1 Heat of Reaction	kJ/kg	2445	Literature	[400]
Reaction 1 Char Yield		0	TGA	[399]
Reaction 2 Pre-Exp. Factor	s ⁻¹	7.95×10^9	TGA	[399]
Reaction 2 Activation Energy	J/mol	1.30×10^5	TGA	[399]
Reaction 2 Char Yield		0.9	TGA	[399]
Reaction 2 Heat of Reaction	kJ/kg	0	DSC	[399]
Fuel Gas 2 Heat of Combustion	kJ/kg	18500	MCC	[399]
Reaction 3 Pre-Exp. Factor	s ⁻¹	2×10^{11}	TGA	[399]
Reaction 3 Activation Energy	J/mol	1.60×10^5	TGA	[399]
Reaction 3 Char Yield		0.37	TGA	[399]
Reaction 3 Heat of Reaction	kJ/kg	126	DSC	[399]
Fuel Gas 3 Heat of Combustion	kJ/kg	13600	MCC	[399]

Table 14.12: Continued

Reaction 4 Pre-Exp. Factor	s^{-1}	0.0261	TGA	[399]
Reaction 4 Activation Energy	J/mol	17000	TGA	[399]
Reaction 4 Char Yield		0.59	TGA	[399]
Reaction 4 Heat of Reaction	kJ/kg	0	DSC	[399]
Fuel Gas 4 Heat of Combustion	kJ/kg	14000	MCC	[399]

Table 14.13 lists the composition and thickness of each of the layers. The sample is insulated with 28 mm of Kaowool PM board, manufactured by ThermalCeramics (www.thermalceramics.com). The gasification

Table 14.13: Cardboard composition and dimensions.

Layer	Composition	Thickness (mm)
1	Liner Board	0.64
2	C Flute Layer	3.2
3	Liner Board	0.64
4	B Flute Layer	2.1
5	Liner Board	0.64
6	Kaowool	28

experiments were conducted in a modified cone calorimeter referred to as the controlled atmosphere pyrolysis apparatus (CAPA) [402], in which the sample is surrounded by nitrogen to prevent ignition. Measured and predicted mass loss rates at imposed heat fluxes of 20 kW/m², 40 kW/m², and 60 kW/m² are shown in Fig. 14.15.

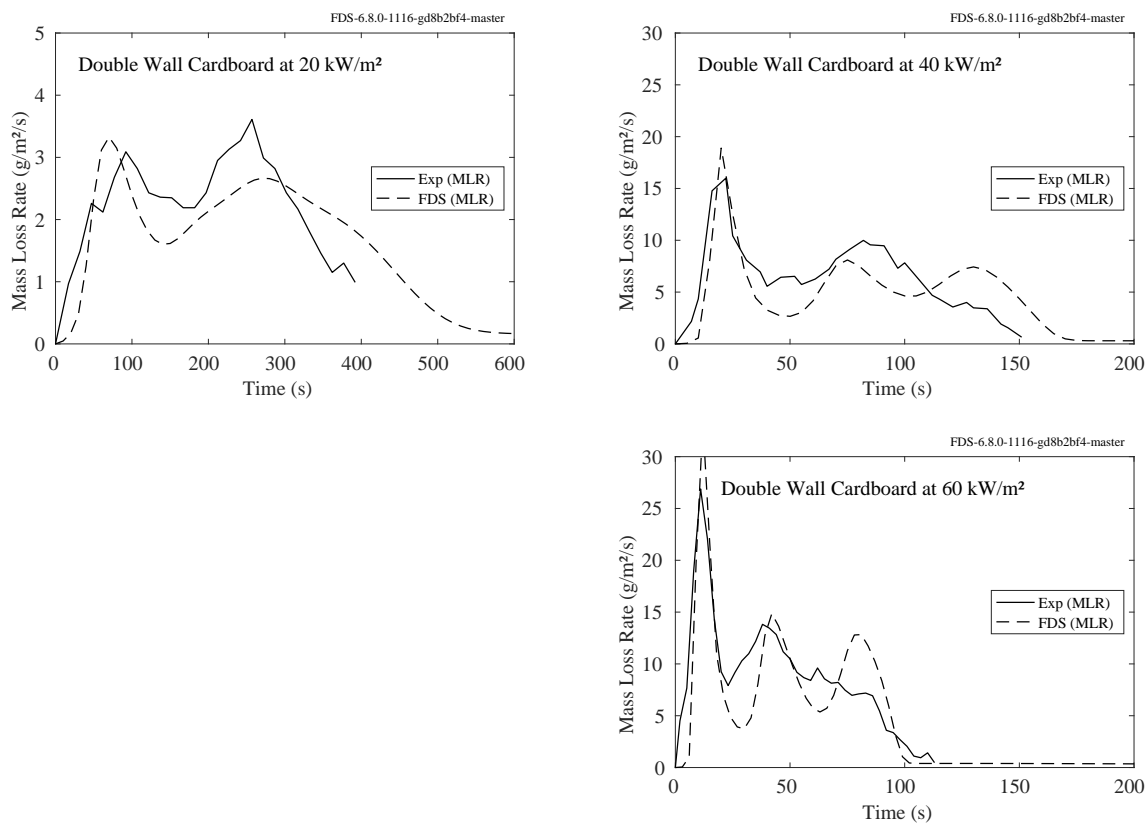


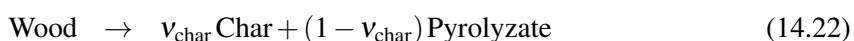
Figure 14.15: Mass loss rate of corrugated cardboard.

14.5 Wood Cribs and Similar Wood/Paper Combustibles

A common combustible used in fire research and testing is a wood crib; that is, a uniform array of wooden dowels of nearly square cross section. However, a stack of wooden pallets can be viewed as a wood crib as well. Whatever its form, these cribs tend to burn at a consistent and predictable rate, making them ideal for fire testing.

14.5.1 Aalto Woods

Cone calorimeter measurements for 2 cm thick samples of spruce and pine under flaming, inert, and smoldering conditions are shown in Figures 14.16 and 14.17. Water evaporates and wood pyrolyzes through their independent reactions, and in presence of oxygen, char residue from wood pyrolysis oxidizes:



The parameters for the reactions are listed in Table 14.14.

Table 14.14: Properties of spruce and pine, as estimated by PROPTI [145].

Property	Units	Spruce	Pine
Moisture			
Density	kg/m ³	1000	
Conductivity	W/m/K	0.6	
Specific Heat	kJ/kg/K	4.2	
Emissivity, ϵ		0.9	
Pre-Exp. Factor, A	s ⁻¹	8.37×10^{12}	
Activation Energy, E	J/mol	1.21×10^5	
Heat of Reaction	kJ/kg	2500	
Wood			
Density	kg/m ³	408	493
Conductivity	W/m/K	$3.16 \times 10^{-4} T - 0.0305$	$3.57 \times 10^{-4} T - 0.00462$
Specific Heat	kJ/kg/K	$0.0044 T - 0.414$	
Emissivity, ϵ		0.9	0.9
Pre-Exp. Factor, A	s ⁻¹	2.12×10^{11}	1.8×10^{11}
Activation Energy, E	J/mol	1.91×10^5	1.85×10^5
Reaction Order, n_s		1.89	1.89
Char Yield, v_{char}		0.15	0.16
Heat of Reaction	kJ/kg	112	140
Heat of Combustion	kJ/kg	13750	13850
Char			
Density	kg/m ³	52.5	104
Conductivity	W/m/K	$8.2 \times 10^{-5} T + 0.091$	
Specific Heat	kJ/kg/K	$1.43 + 0.000355 T - 7.32 \times 10^4 / T^2$	
Emissivity, ϵ		0.84	0.84
Pre-Exp. Factor, A	s ⁻¹	3.75	1.79
Activation Energy, E	J/mol	27685	27685
n_{O_2}		0.68	0.68
Heat of Reaction	kJ/kg	-32000	-32000

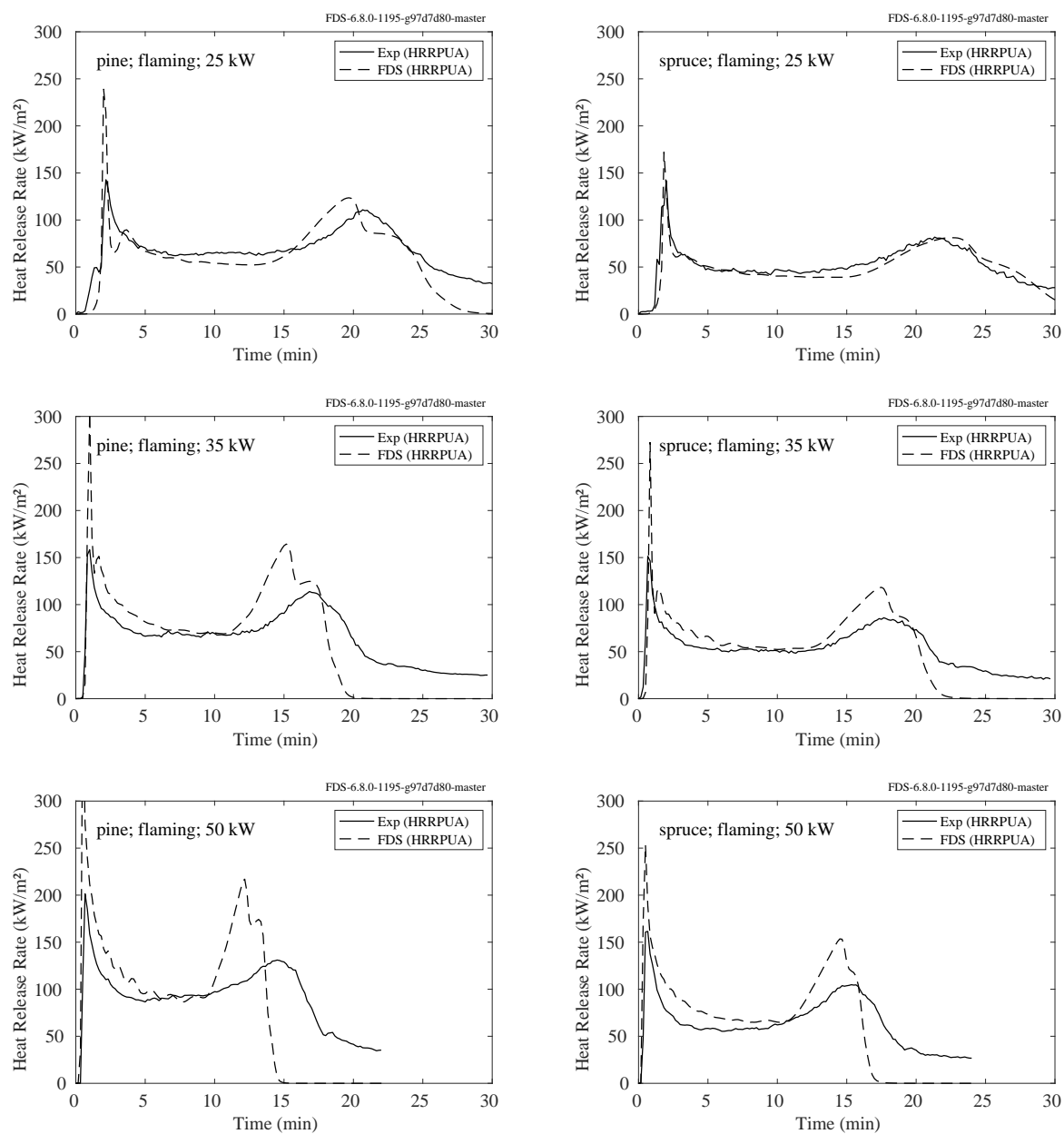


Figure 14.16: Aalto Woods heat release rates.

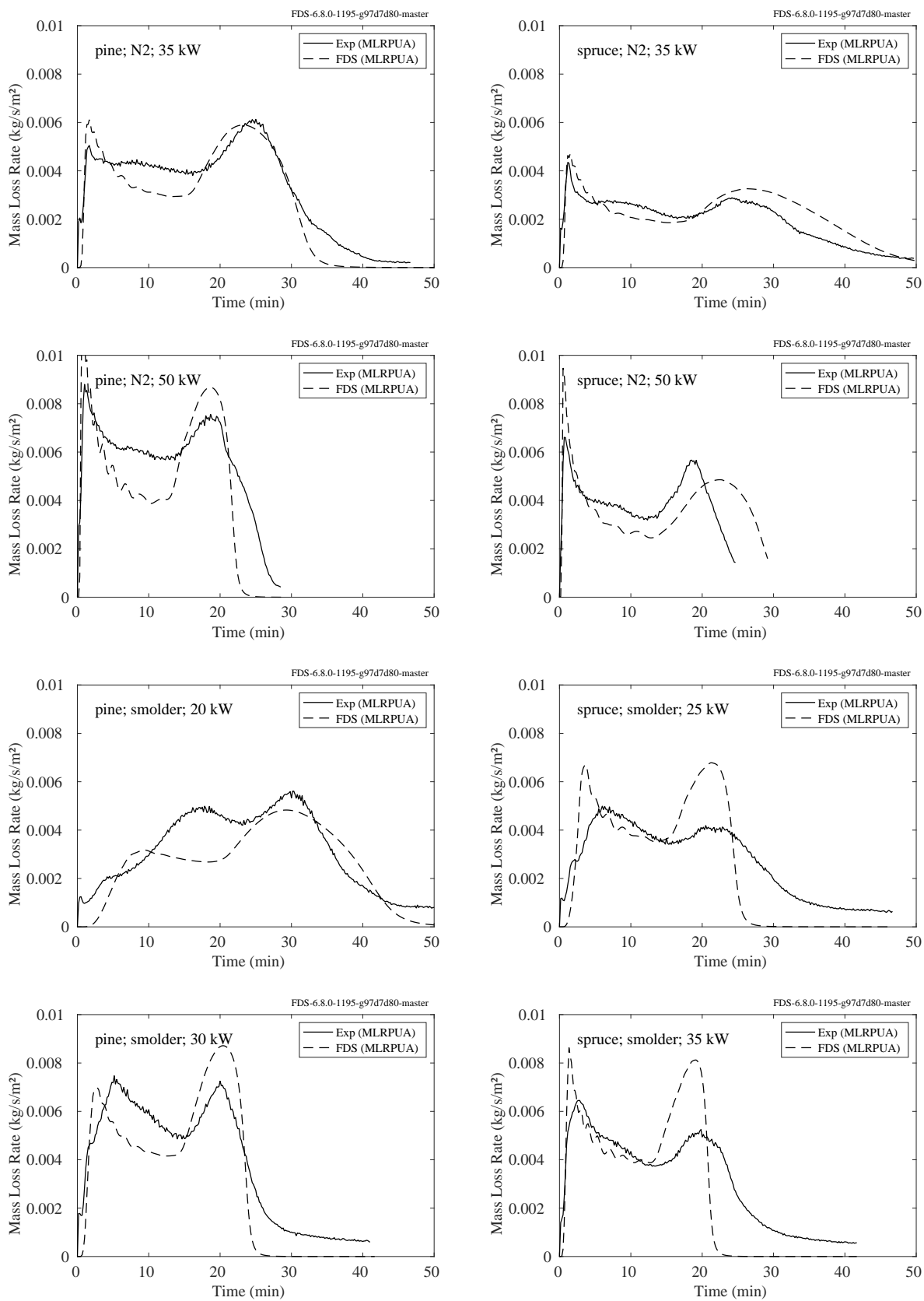


Figure 14.17: Aalto Woods mass loss rates.

The model for spruce estimated using the cone calorimeter measurements is employed in predicting heat release rates in an ISO 9705 room corner test [146], and in a modified room corner test [147] (in Finnish, English description of the test available in [37]). The selected test for simulation from [146] is M12, where the walls and ceiling of the test compartment is lined with 10 mm thick spruce timber. In the modified room corner test [147], the back wall opposite to the door opening, 240 cm length of an adjacent side wall, and a triangle shaped section of the ceiling connecting the two, are lined with 22 mm thick spruce timber. The gas burner is located in the timber-lined corner. All the other surfaces in the modified test, and the floor in M12 [146] test are of concrete, as are the backing surfaces for timber.

For simulations of both room corner tests [146, 147], concrete properties are assumed as given for lightweight concrete in [147]: thickness of 20 cm, thermal conductivity of 0.1 W/(m K) and thermal diffusivity of $2 \times 10^{-7} \text{ m}^2/\text{s}$. Assuming a specific heat of 0.88 kJ/(kg K) for concrete [403], gives a density of 568 kg/m³ from thermal diffusivity.

Figure 14.18 shows heat release rates in room corner test M12 and in the modified room corner test. The burner output of 100 kW is reduced from both the experimental and simulation data, thus the figure shows only the heat release contribution from burning timber.

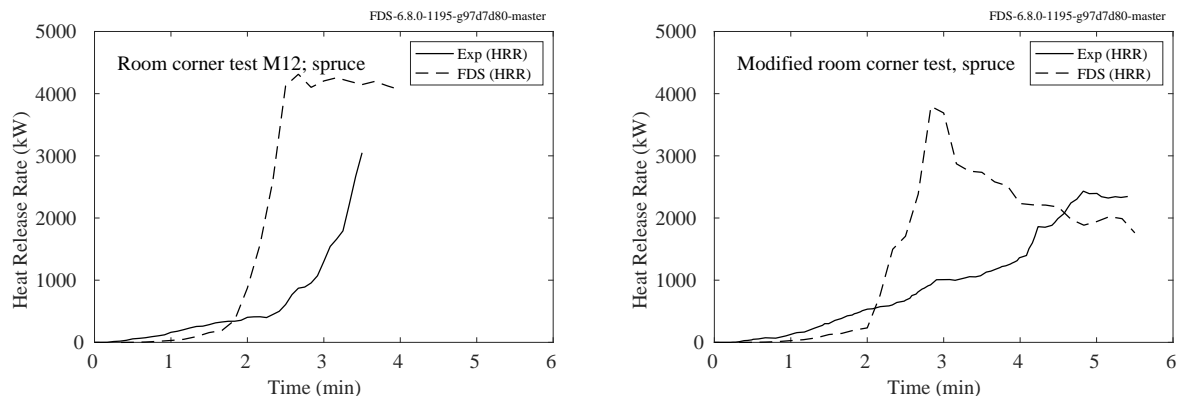


Figure 14.18: Heat release in room corner tests, Aalto Woods model

14.5.2 BST/FRS Wood Crib Experiments

Figures 14.19 through 14.21 display comparisons of the measured and predicted gas temperatures along three “crib lines” within a long compartment filled with 33 wooden cribs. The experiments are described in Sec. 3.12. The crib lines are located at row 2 (back), 6 (middle) and 10 (front). Each measurement is an average of three thermocouples at the same distance.

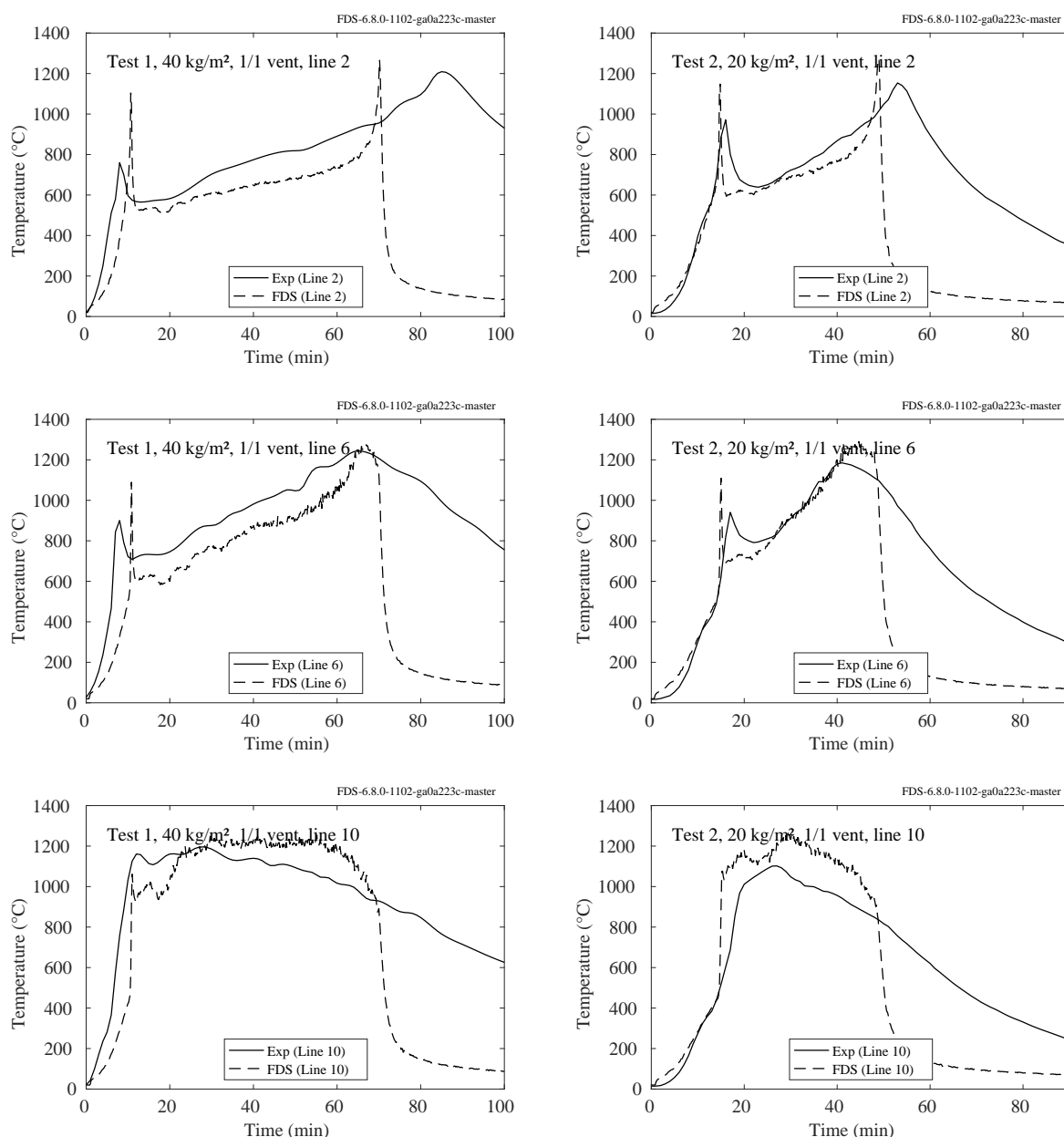


Figure 14.19: BST/FRS Wood Cribs temperatures, Tests 1 (left) and 2 (right).

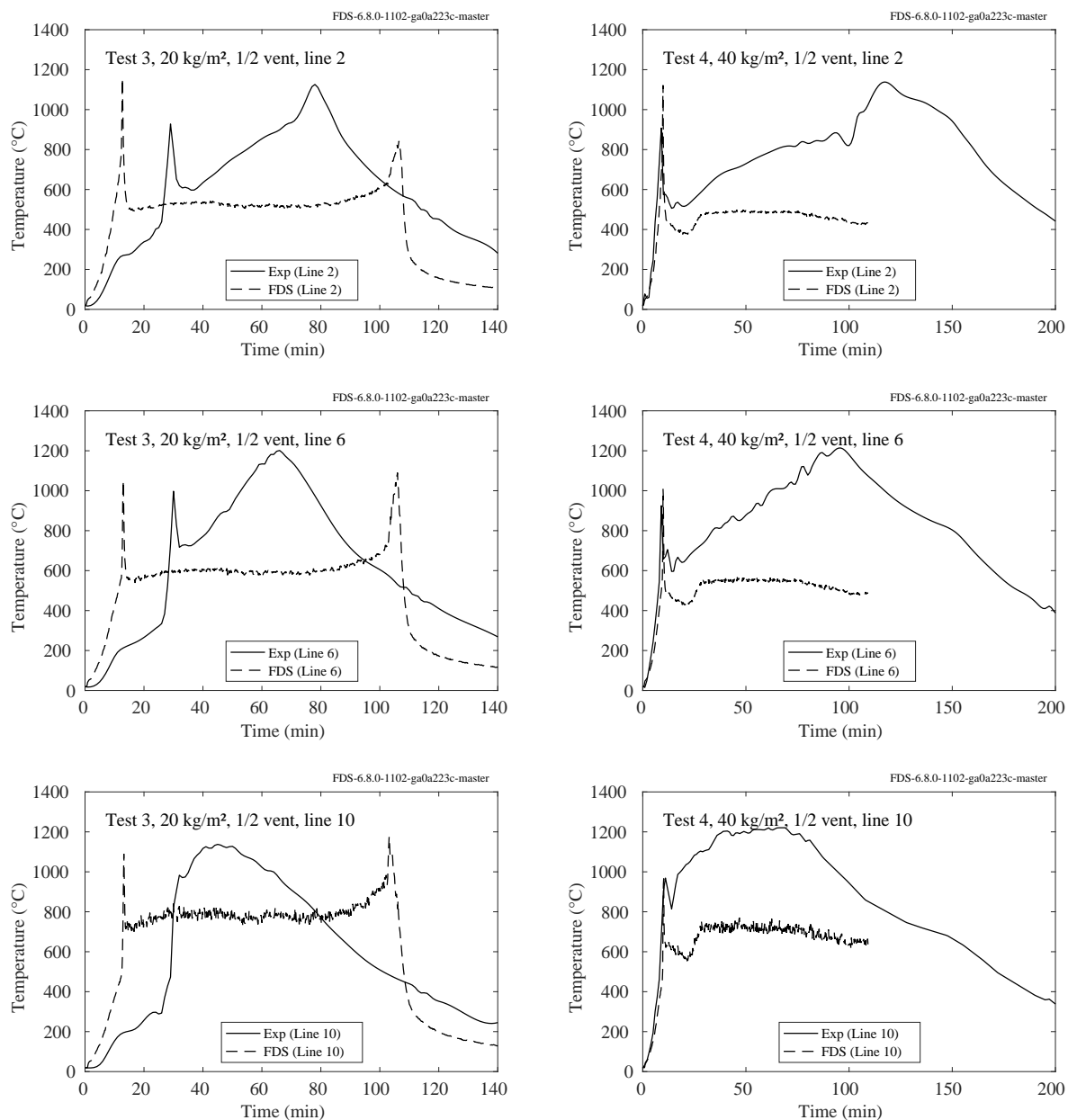


Figure 14.20: BST/FRS Wood Cribs temperatures, Tests 3 (left) and 4 (right).

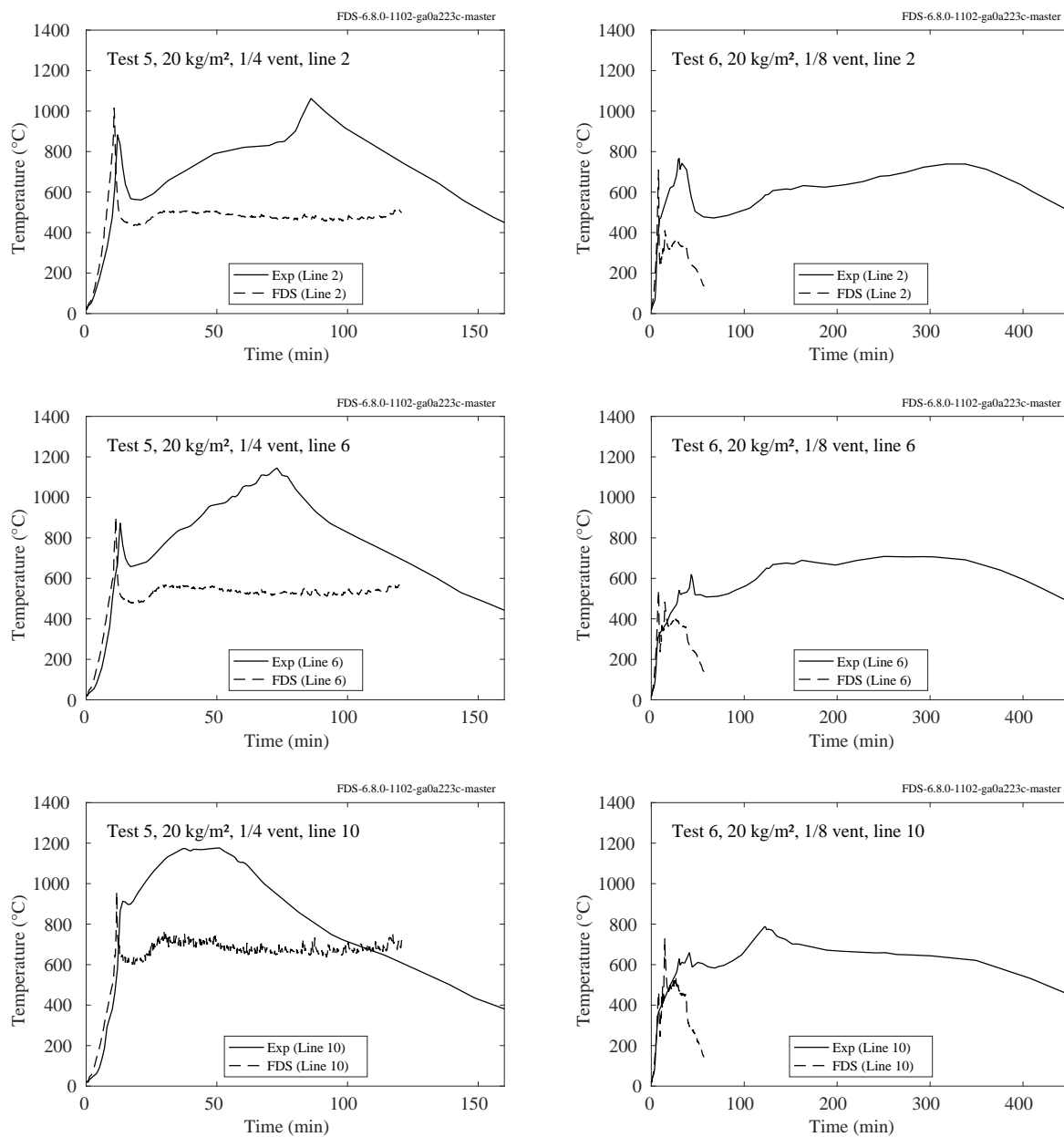


Figure 14.21: BST/FRS Wood Cribs temperatures, Tests 5 (left) and 6 (right).

14.5.3 NIST/NRC Transient Combustibles

Figure 14.22 compares measured and predicted heat release rates for a single wood crib and arrays of multiple cribs. The simulations are all performed using Lagrangian particles as surrogates for the 56 cm long, 3.8 cm square pine sticks. The grid resolution in all cases is 8 cm, with additional simulations performed with 4 cm and 2 cm resolution for the single crib.

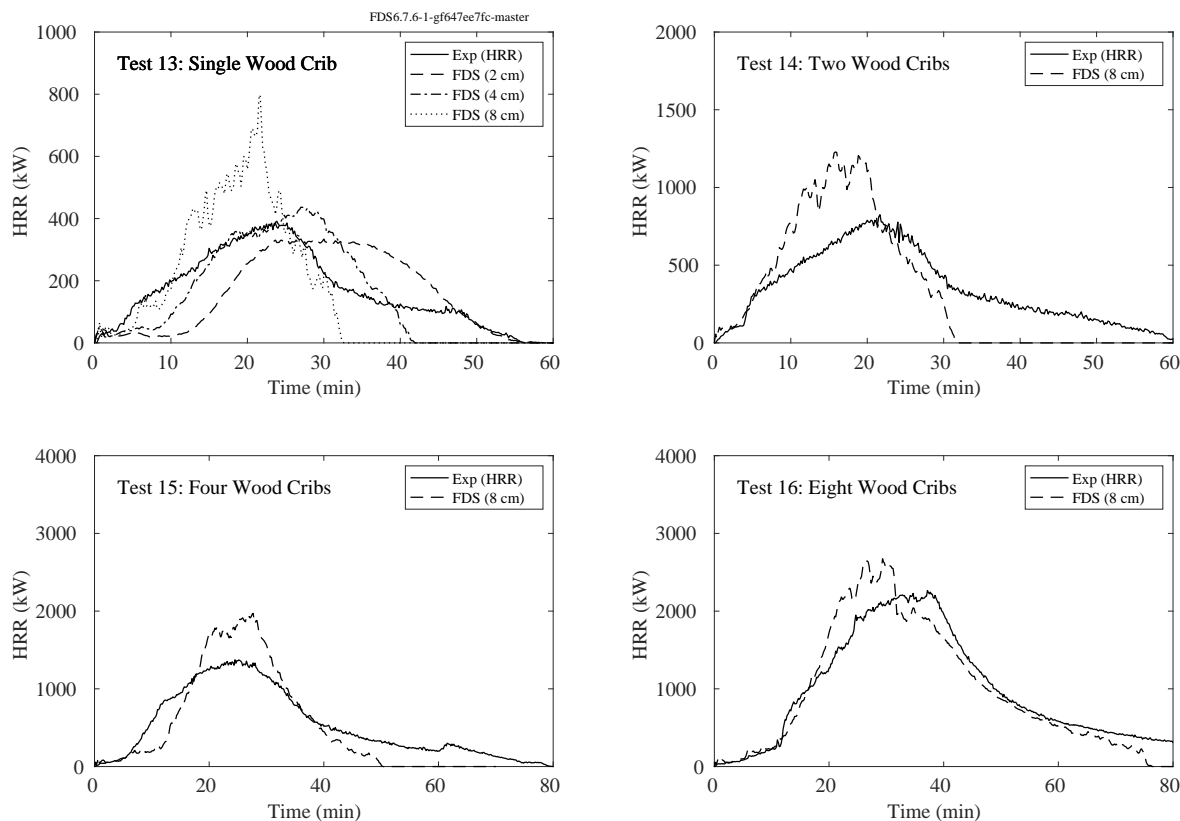


Figure 14.22: NIST/NRC Transient Combustibles: wood cribs.

Figure 14.23 compares measured and predicted heat release rates for a single cardboard box filled with shredded craft paper and arrays of multiple boxes. The simulations are all performed using Lagrangian particles as surrogates for the small paper strips. The grid resolution in all cases is 5 cm.

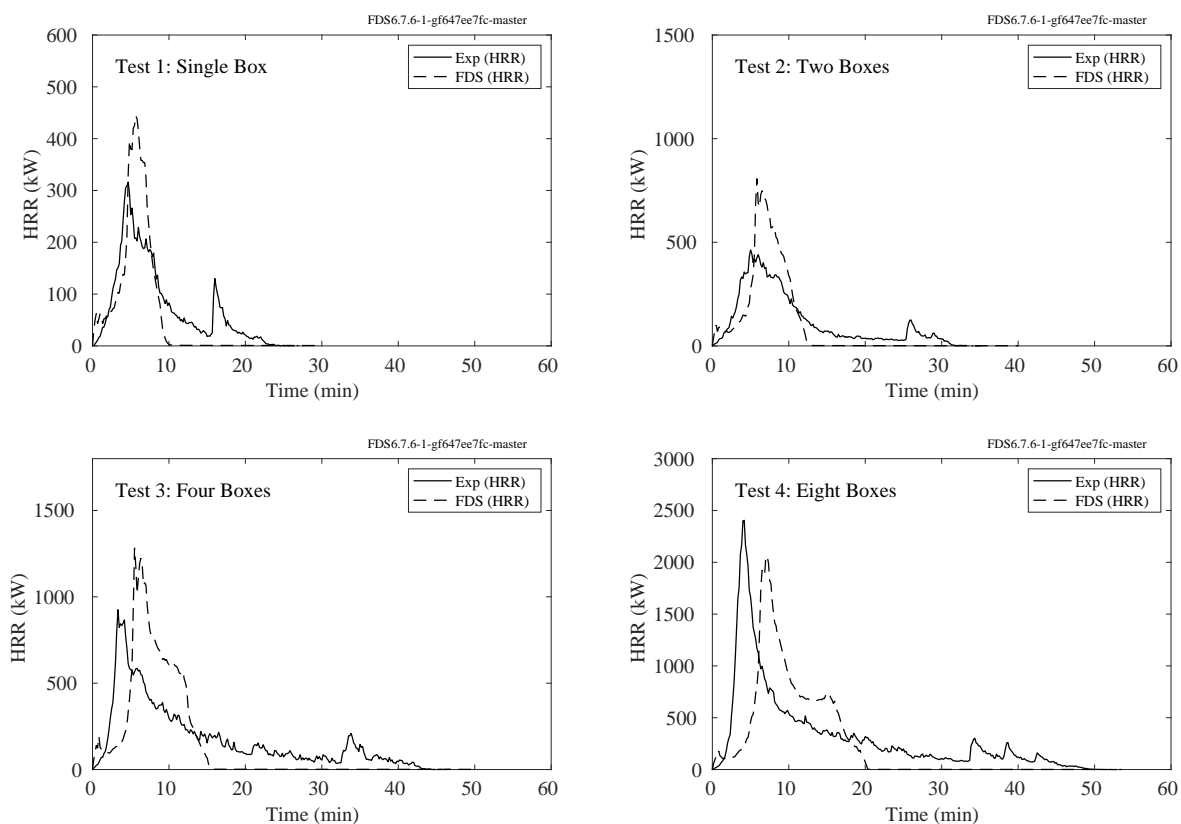


Figure 14.23: NIST/NRC Transient Combustibles: boxes.

Figure 14.24 compares measured and predicted heat release rates for a stack of two, four and eight wood pallets. The simulations are all performed using Lagrangian particles as surrogates for the wooden planks. The grid resolution in all cases is 6 cm.

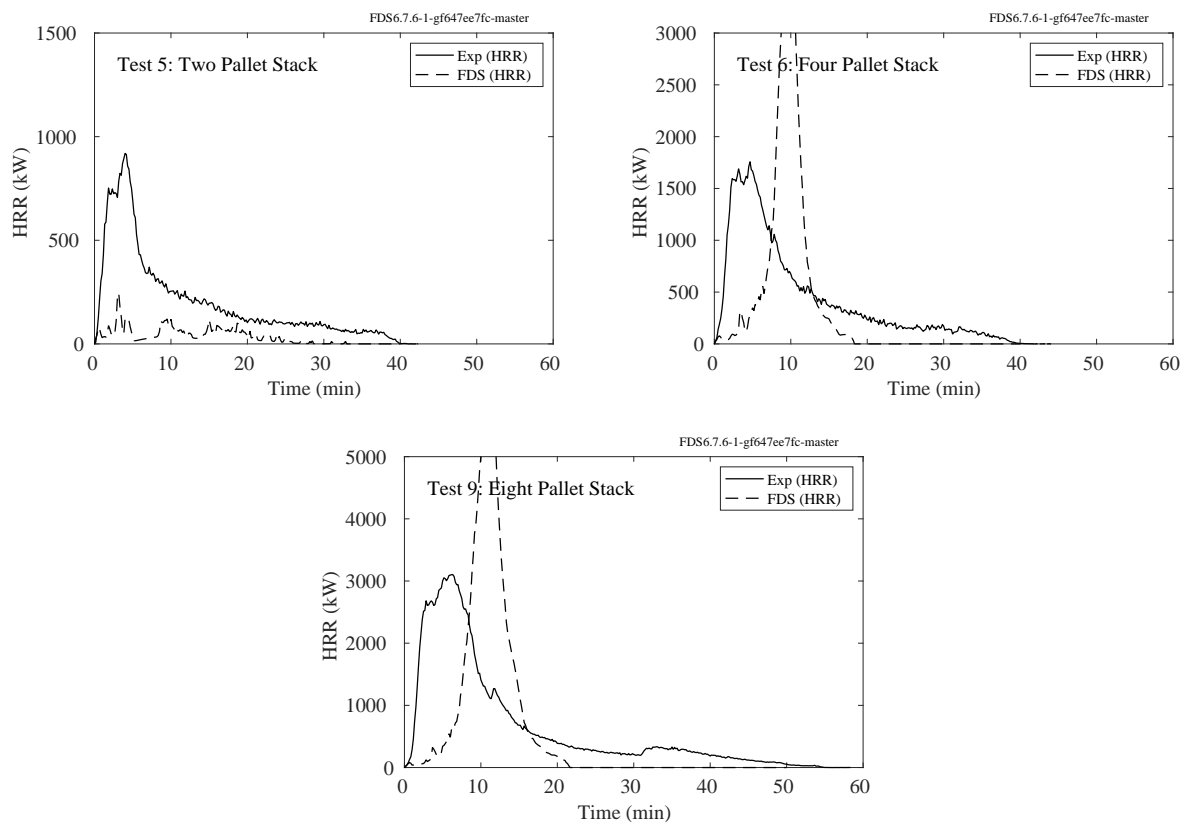


Figure 14.24: NIST/NRC Transient Combustibles: pallets.

14.5.4 SP Wood Crib Experiments

These experiments and the modeling strategy are described in Sec. 3.84. Briefly, four piles of 1:4 scale wood pallets are positioned in a wind tunnel with various separation distances. The upwind pile is ignited and the fire spreads from pile to pile. The wind velocity for Test 1 is 0.3 m/s; and for Test 12 it is 0.9 m/s. For all others, it is 0.6 m/s. Tests 1, 4, and 12 have only a single pile; the rest have four.

Figures 14.25 and 14.26 display the measured and predicted HRR for 11 of the 12 SP Wood Crib experiments. Test 2 was set up differently than the other experiments and was not used in the analysis.

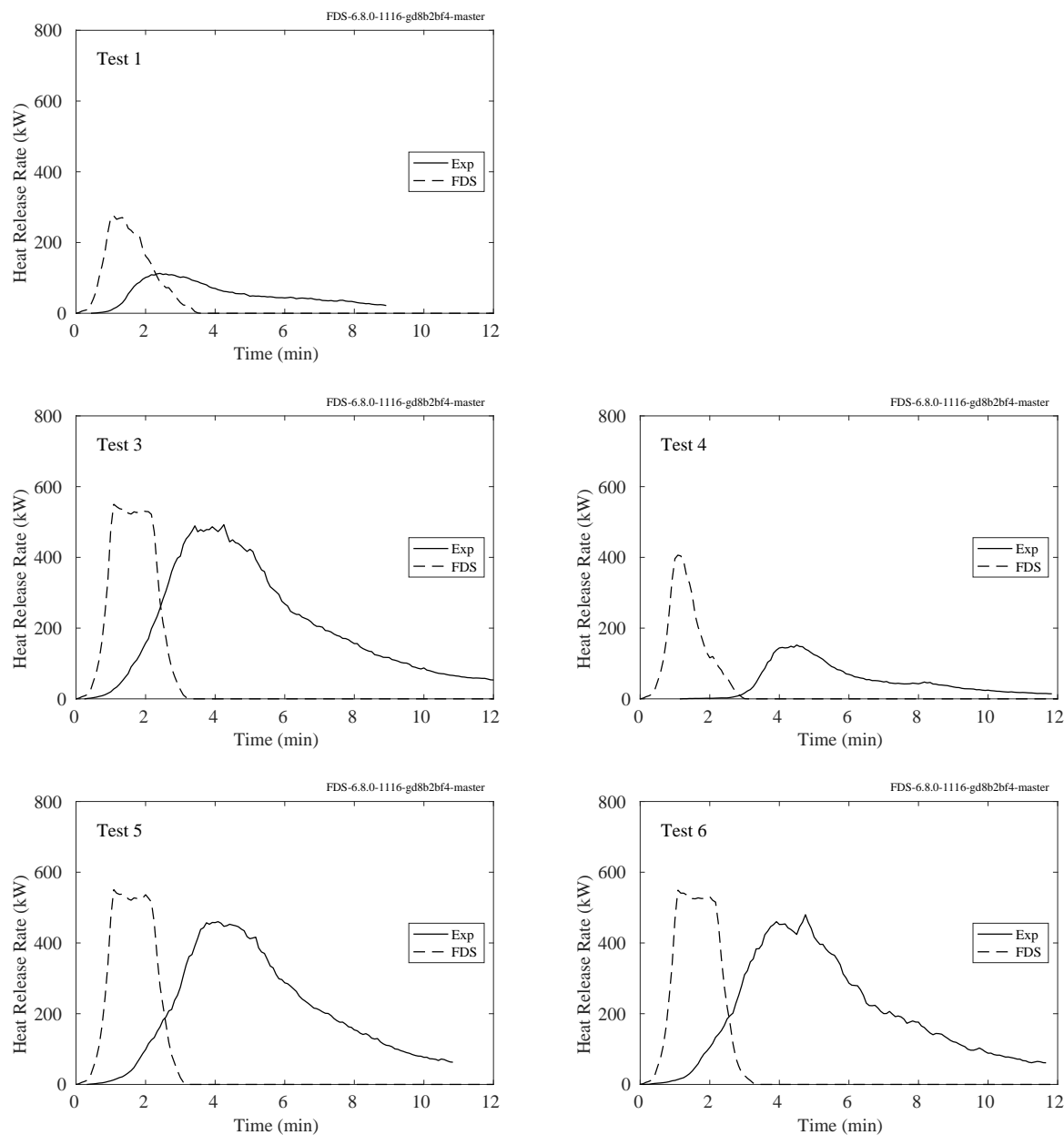


Figure 14.25: SP Wood Crib heat release rates, Tests 1-6.

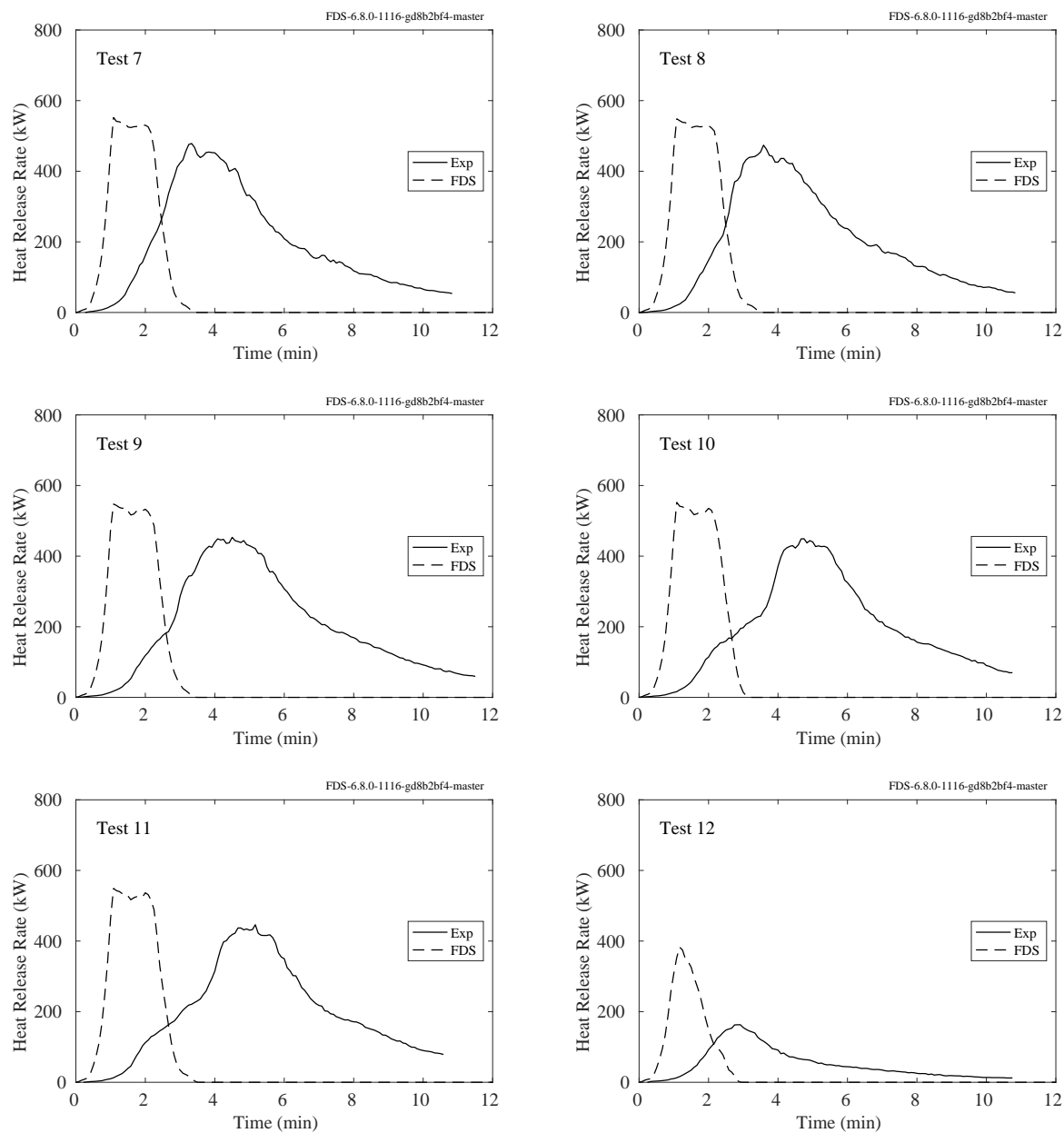


Figure 14.26: SP Wood Cribs heat release rates, Tests 7-12.

14.6 Liquid Pool Fires

14.6.1 DoJ/HAI Pool Fires

Table [14.15](#) lists the relevant parameters for a series of gasoline and kerosene pool fire experiments.

Figures [14.27](#) through [14.32](#) display measured and predicted burning rate of a variety of gasoline and kerosene pool fires in 0.3 m, 0.6 m, and 1.2 m square pans of various depths and two substrates—concrete and vinyl.

Table 14.15: Summary of DoJ/HAI Diked Fire Tests.

Test ID	Pan Side Length (m)	Fuel	Depth (mm)	Substrate
DSF1-C-CC-G-1-0.093	0.31	Gasoline	1	Coated Concrete
DSF2-C-CC-G-5-0.093	0.31	Gasoline	5	Coated Concrete
DSF3-C-CC-G-10-0.093	0.31	Gasoline	10	Coated Concrete
DSF4-C-CC-G-20-0.093	0.31	Gasoline	20	Coated Concrete
DSF5-C-CC-K-1-0.093	0.31	Kerosene	1	Coated Concrete
DSF6-C-CC-K-5-0.093	0.31	Kerosene	5	Coated Concrete
DSF7-C-CC-K-10-0.093	0.31	Kerosene	10	Coated Concrete
DSF8-C-CC-K-20-0.093	0.31	Kerosene	20	Coated Concrete
DSF9-C-CC-G-1-0.372	0.61	Gasoline	1	Coated Concrete
DSF10-C-CC-G-5-0.372	0.61	Gasoline	5	Coated Concrete
DSF11-C-CC-G-10-0.372	0.61	Gasoline	10	Coated Concrete
DSF12-C-CC-G-20-0.372	0.61	Gasoline	20	Coated Concrete
DSF13-C-CC-K-1-0.372	0.61	Kerosene	1	Coated Concrete
DSF14-C-CC-K-5-0.372	0.61	Kerosene	5	Coated Concrete
DSF15-C-CC-K-10-0.372	0.61	Kerosene	10	Coated Concrete
DSF16-C-CC-K-20-0.372	0.61	Kerosene	20	Coated Concrete
DSF17-C-CC-G-1-1.488	1.22	Gasoline	1	Coated Concrete
DSF18-C-CC-G-2-1.488	1.22	Gasoline	2	Coated Concrete
DSF19-C-CC-G-3-1.488	1.22	Gasoline	3	Coated Concrete
DSF20-C-CC-G-4-1.488	1.22	Gasoline	4	Coated Concrete
DSF21-C-CC-G-5-1.488	1.22	Gasoline	5	Coated Concrete
DSF22-C-CC-G-20-1.488	1.22	Gasoline	20	Coated Concrete
DSF25-C-V-G-1-0.093	0.31	Gasoline	1	Vinyl
DSF26-C-V-G-5-0.093	0.31	Gasoline	5	Vinyl
DSF27-C-V-G-10-0.093	0.31	Gasoline	10	Vinyl
DSF28-C-V-G-20-0.093	0.31	Gasoline	20	Vinyl
DSF29-C-V-K-1-0.093	0.31	Kerosene	1	Vinyl
DSF30-C-V-K-5-0.093	0.31	Kerosene	5	Vinyl
DSF31-C-V-K-10-0.093	0.31	Kerosene	10	Vinyl
DSF32-C-V-K-20-0.093	0.31	Kerosene	20	Vinyl
DSF33-C-V-G-1-0.372	0.61	Gasoline	1	Vinyl
DSF34-C-V-G-5-0.372	0.61	Gasoline	5	Vinyl
DSF35-C-V-G-10-0.372	0.61	Gasoline	10	Vinyl
DSF36-C-V-G-20-0.372	0.61	Gasoline	20	Vinyl
DSF37-C-V-K-1-0.372	0.61	Kerosene	1	Vinyl
DSF38-C-V-K-5-0.372	0.61	Kerosene	5	Vinyl
DSF39-C-V-K-10-0.372	0.61	Kerosene	10	Vinyl
DSF40-C-V-K-20-0.372	0.61	Kerosene	20	Vinyl
DSF41-C-V-G-1-1.488	1.22	Gasoline	1	Vinyl
DSF42-C-V-G-2-1.488	1.22	Gasoline	2	Vinyl
DSF43-C-V-G-3-1.488	1.22	Gasoline	3	Vinyl
DSF44-C-V-G-4-1.488	1.22	Gasoline	4	Vinyl
DSF45-C-V-G-5-1.488	1.22	Gasoline	5	Vinyl
DSF46-C-V-G-15-1.488	1.22	Gasoline	15	Vinyl

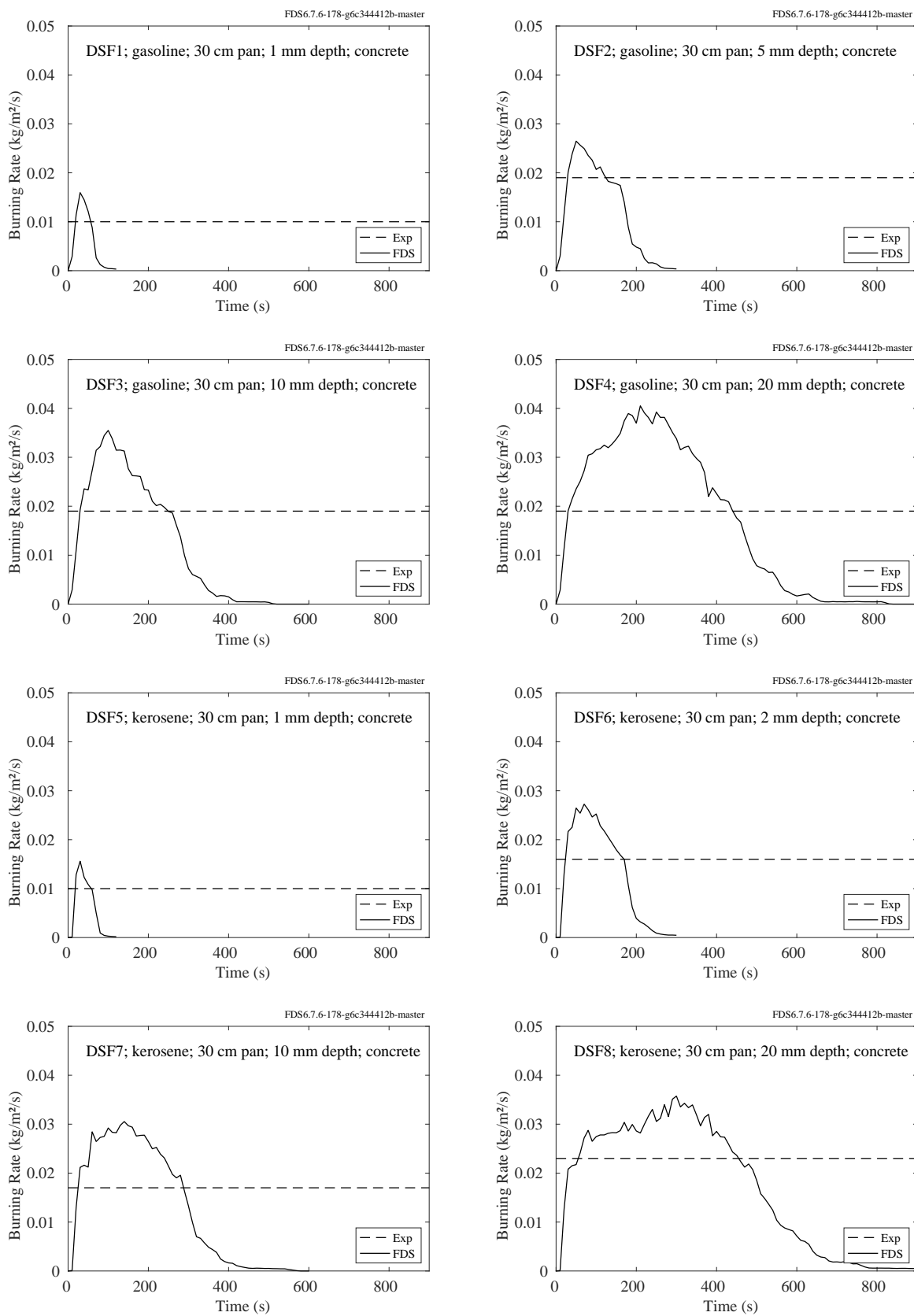


Figure 14.27: DoJ/HAI Pool Fires, Tests 1-8.

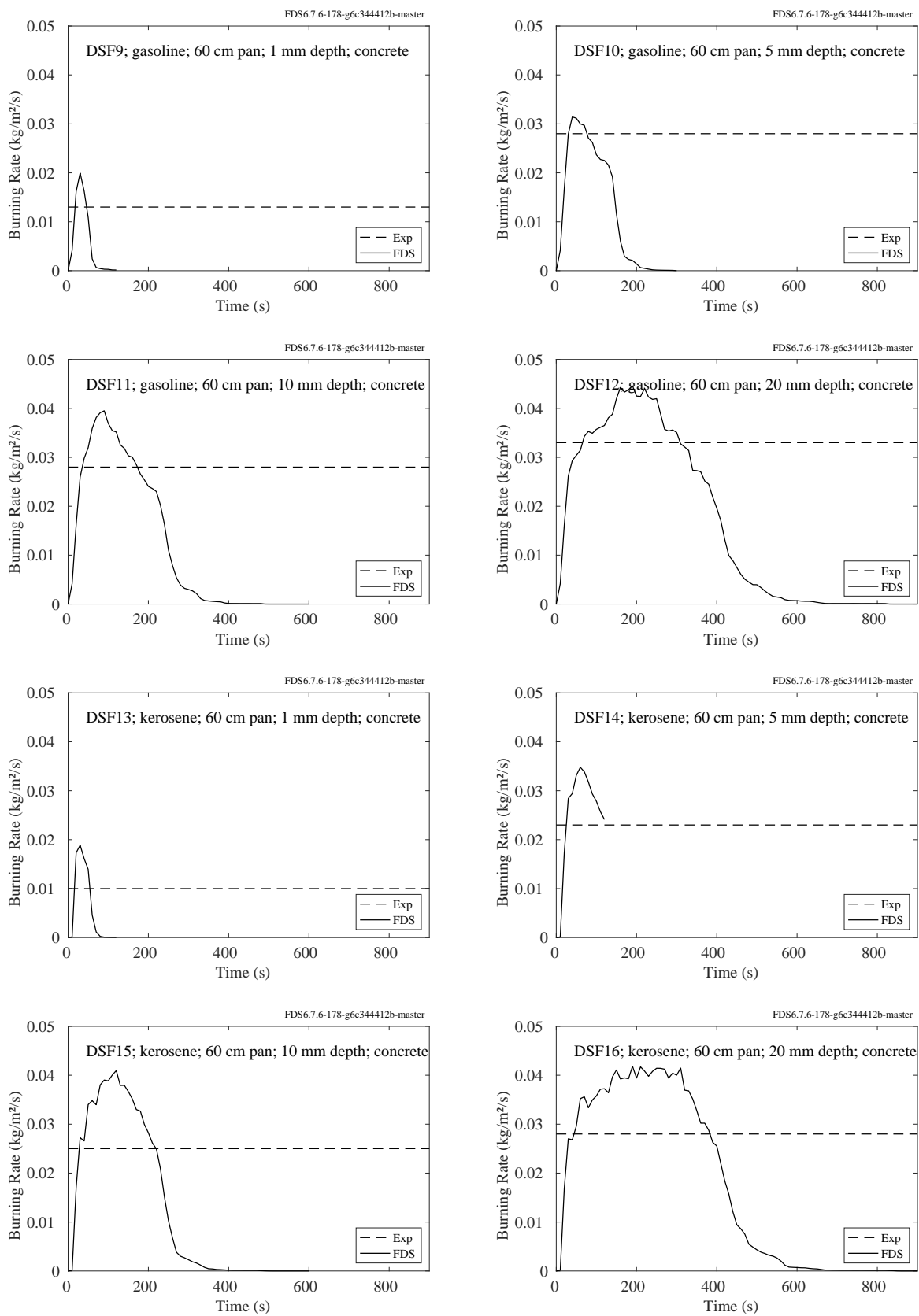


Figure 14.28: DoJ/HAI Pool Fires, Tests 9-16.

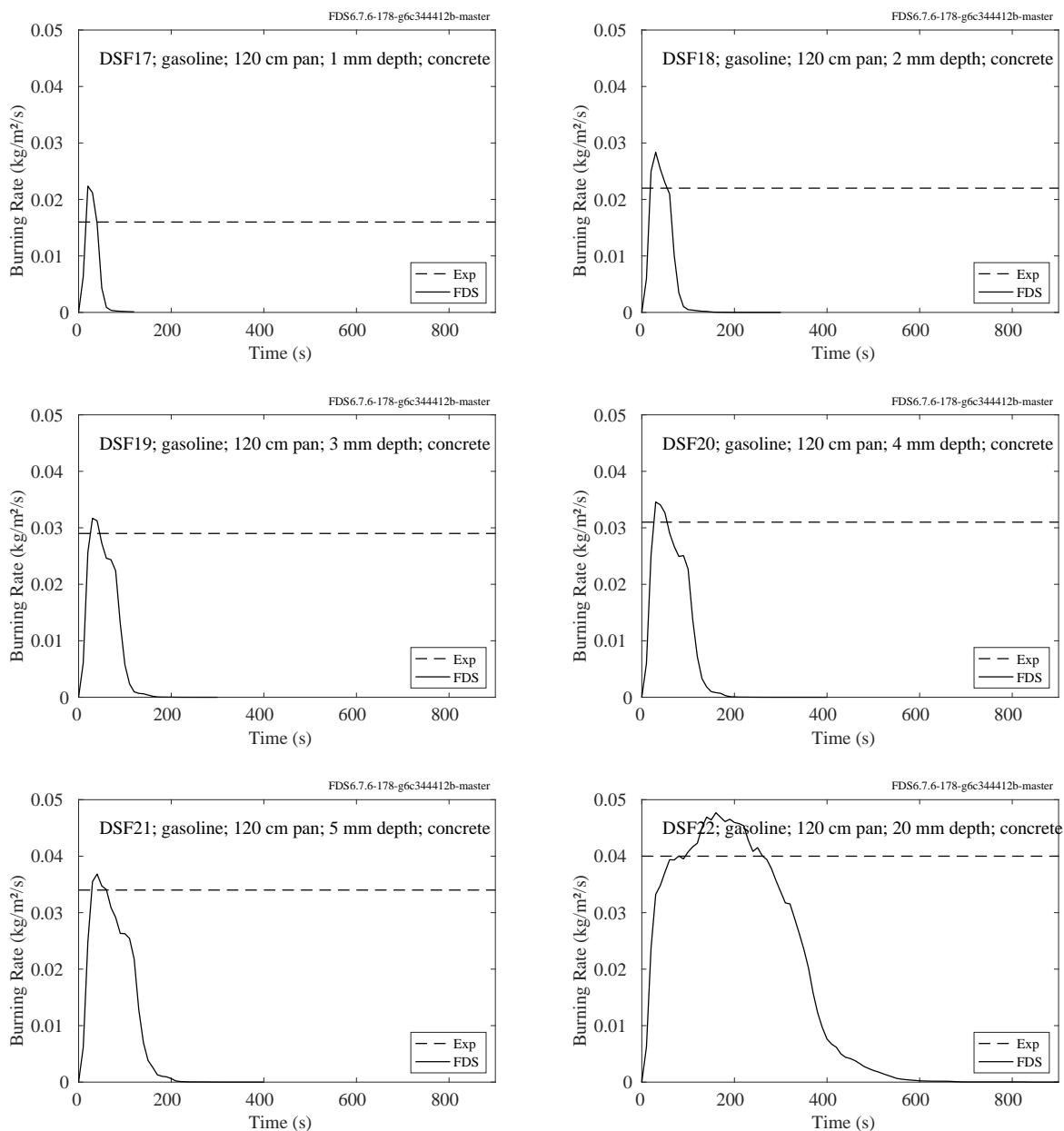


Figure 14.29: DoJ/HAI Pool Fires, Tests 17-22.

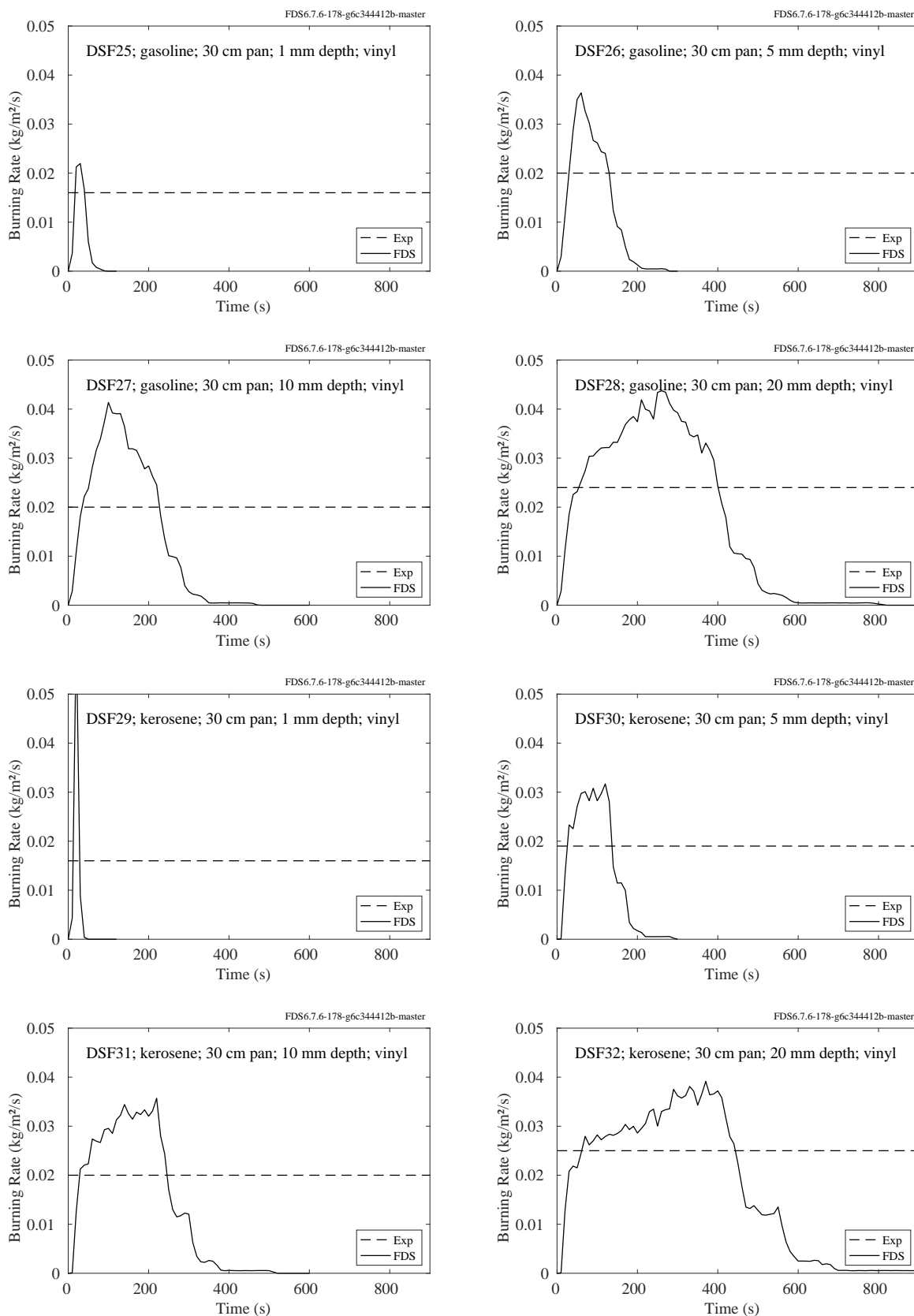


Figure 14.30: DoJ/HAI Pool Fires, Tests 25-32.

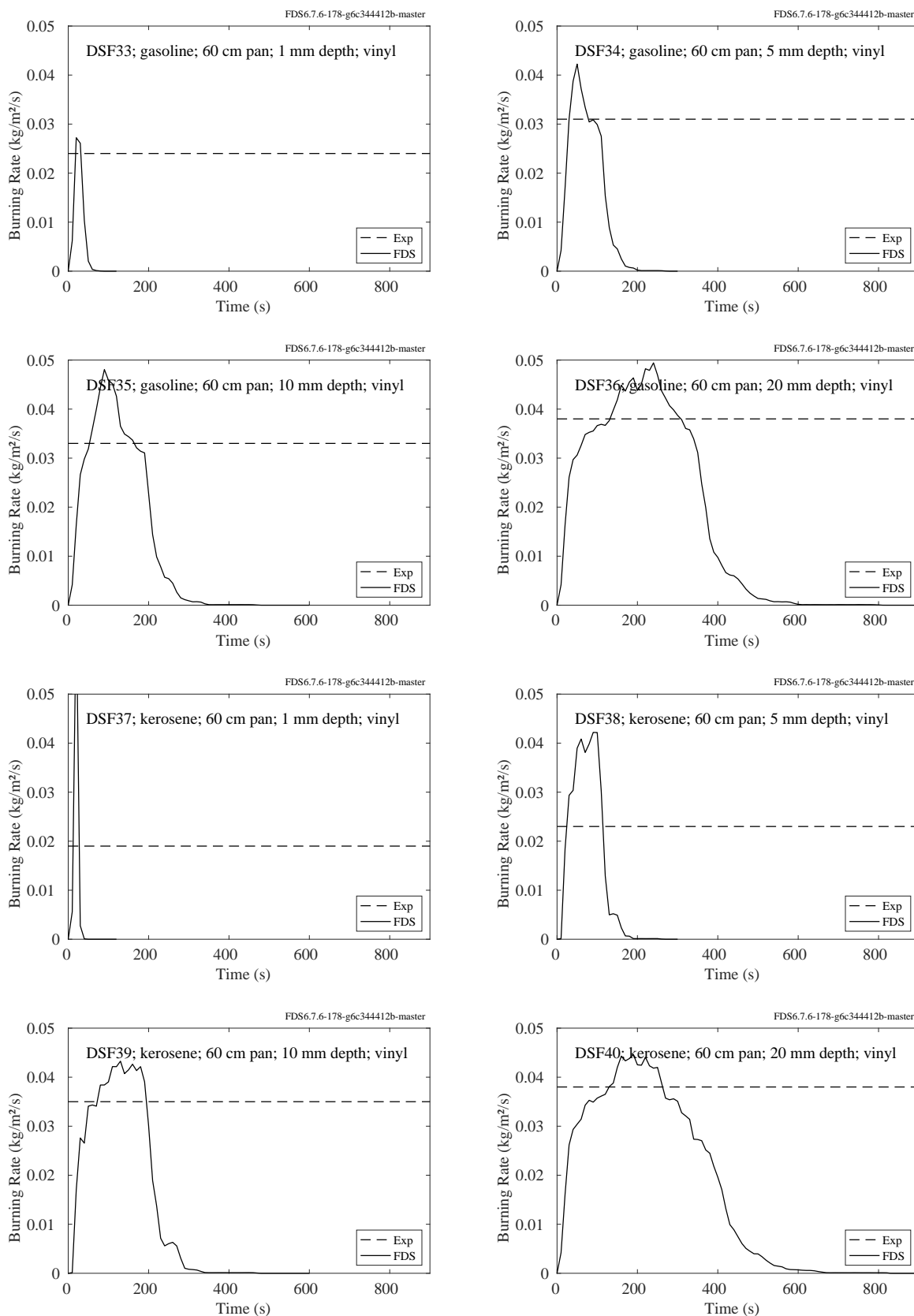


Figure 14.31: DoJ/HAI Pool Fires, Tests 33-40.

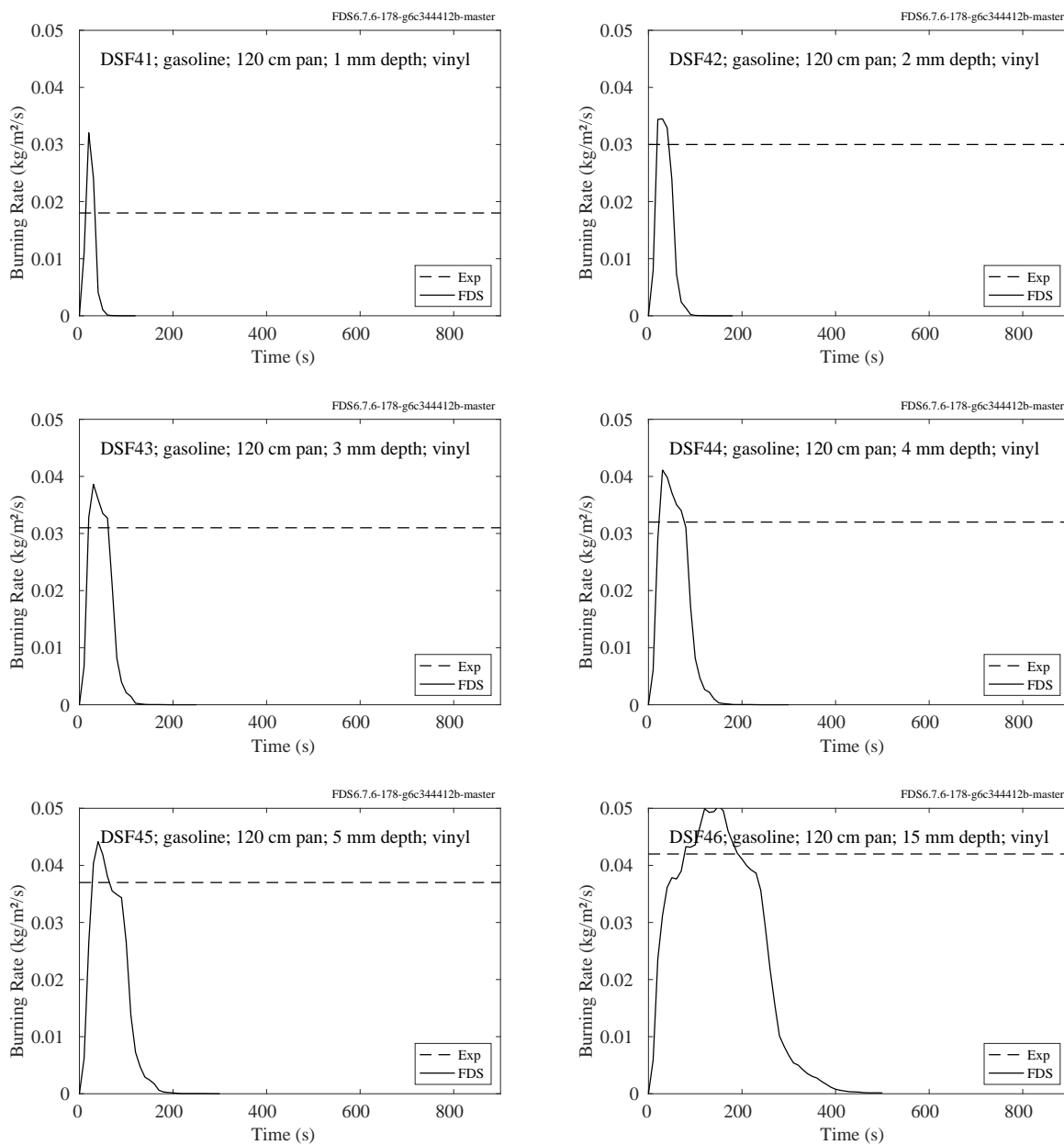


Figure 14.32: DoJ/HAI Pool Fires, Tests 41-46.

14.6.2 LEMTA/UGent Pool Fires

These experiments are described in Section [3.42](#).

Shown on the following pages are comparisons of measured and predicted burning rates of heptane and methanol pools, along with temperatures measured at various heights (5 mm, 20 mm, 35 mm) above the floor of the pan for which the starting depth of the liquid was approximately 46 mm.

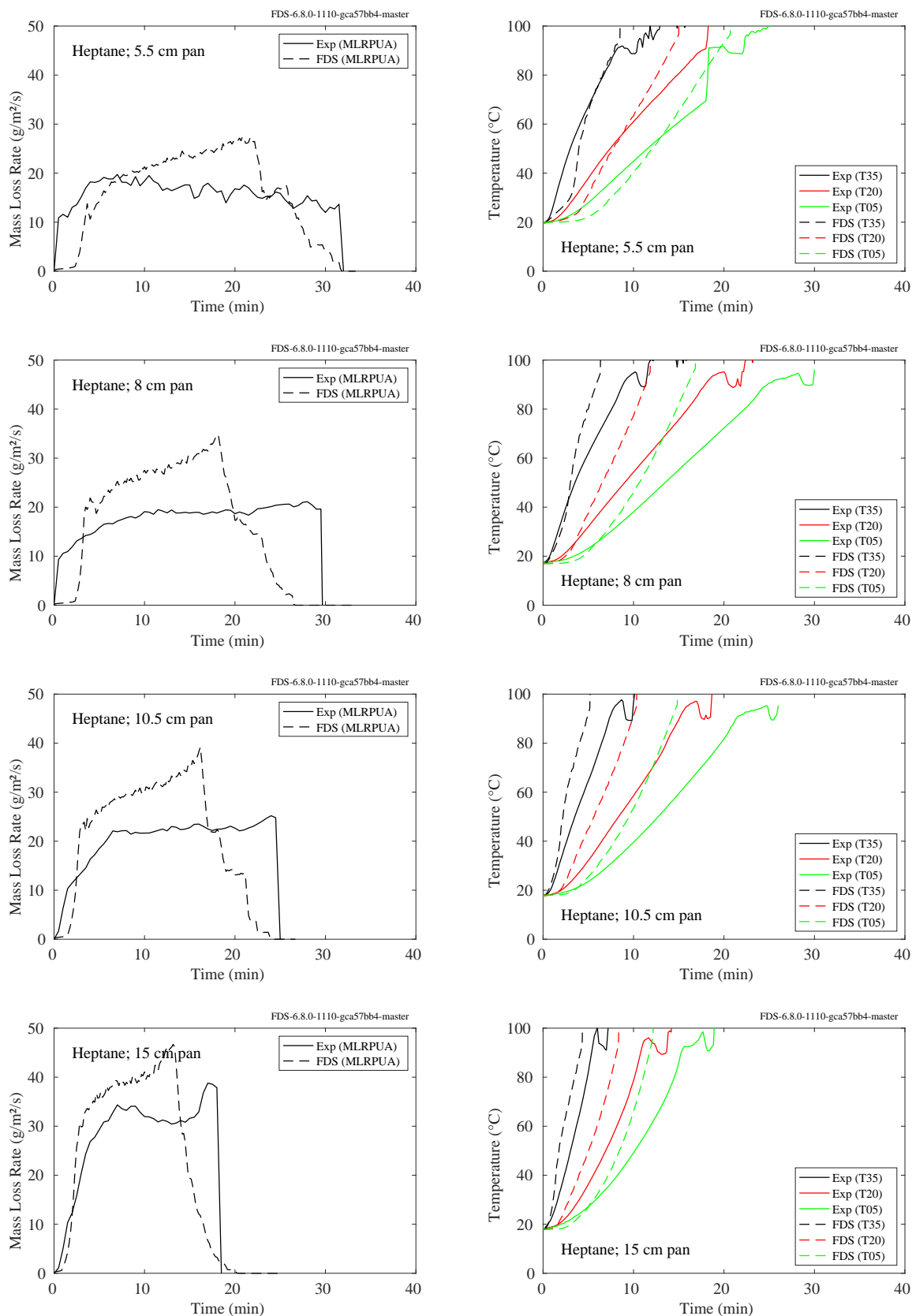


Figure 14.33: LEMTA/UGent Pool Fires burning rate and sub-surface temperature, heptane.

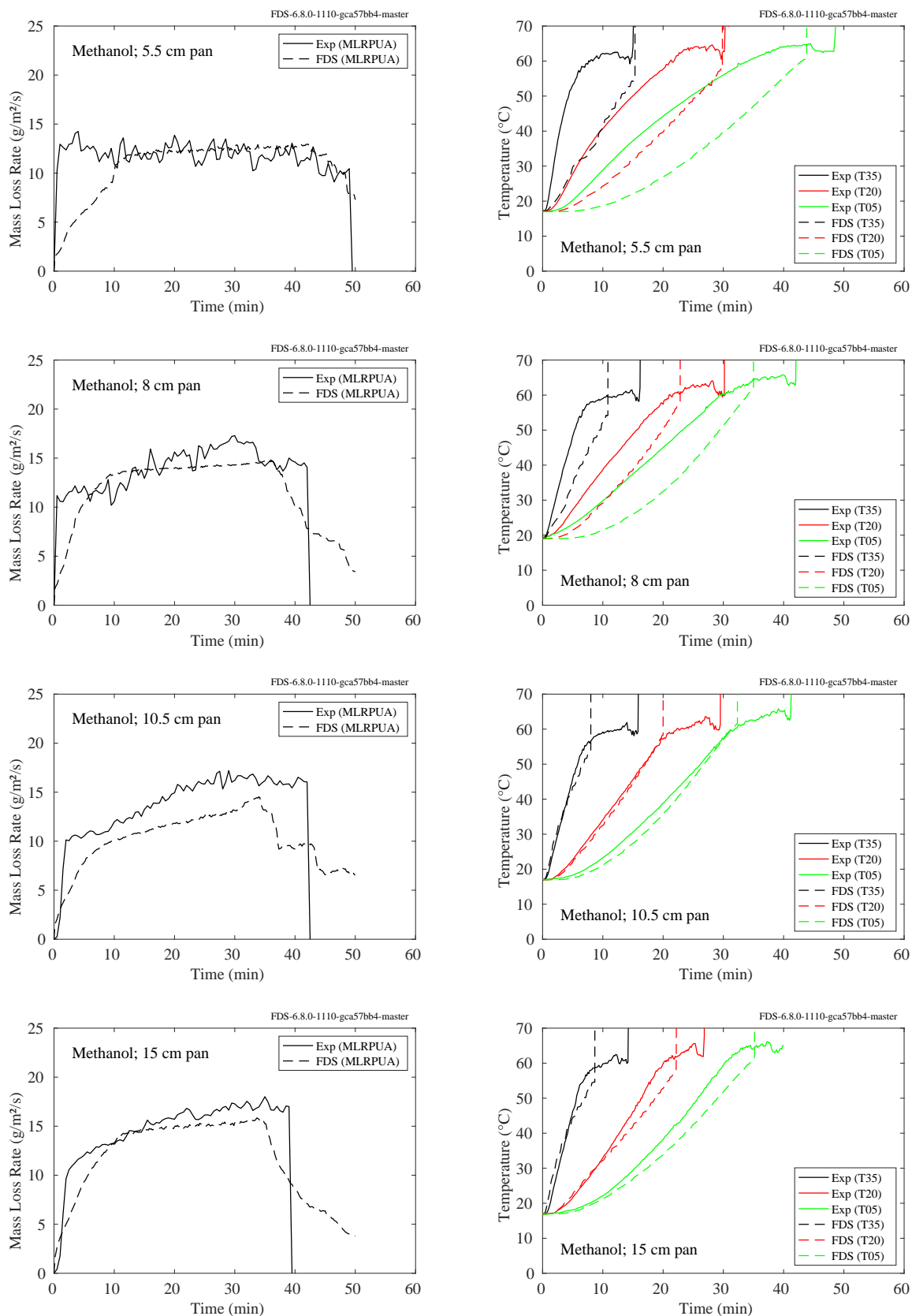


Figure 14.34: LEMTA/UGent Pool Fires burning rate and sub-surface temperature, methanol.

14.6.3 Pool Fire Measurements

Shown below are comparisons of measured and predicted evaporation/burning rates of various liquid pools. Surface temperature comparisons of these same experiments are shown in Sec. 11.3.

Figure 14.35 compares the measured and predicted evaporation rate of water subjected to a 50 kW/m² heat flux.

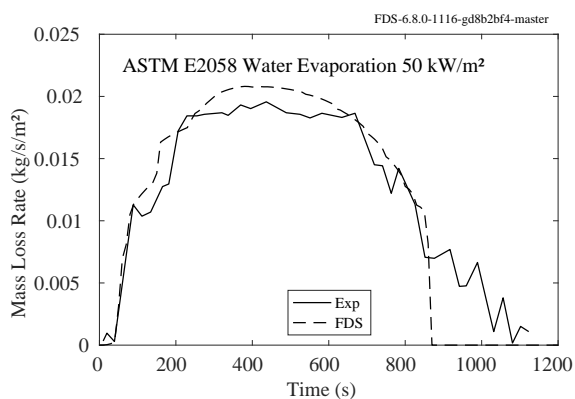


Figure 14.35: ASTM E2058 fire propagation apparatus water evaporation at 50 kW/m² heat flux.

Figure 14.36 shows the measured and predicted mass loss rates of 1.17 m (1.07 m²) and 1.6 m (2.0 m²) diameter heptane pool fires. The measured mass loss rates are averages of two or three individual experiments.

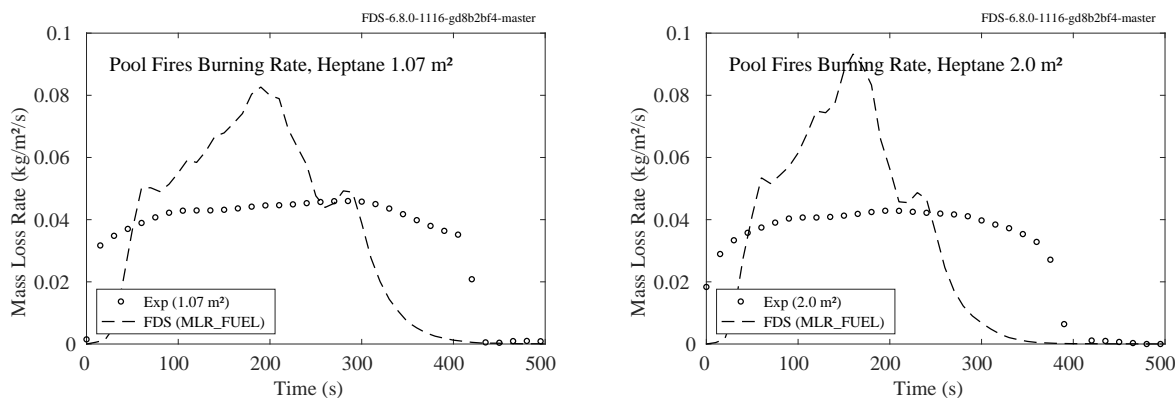


Figure 14.36: VTT Large Hall Test burning rate.

Figure 14.37 compares predicted and measured burning rates of a variety of liquid fuels.

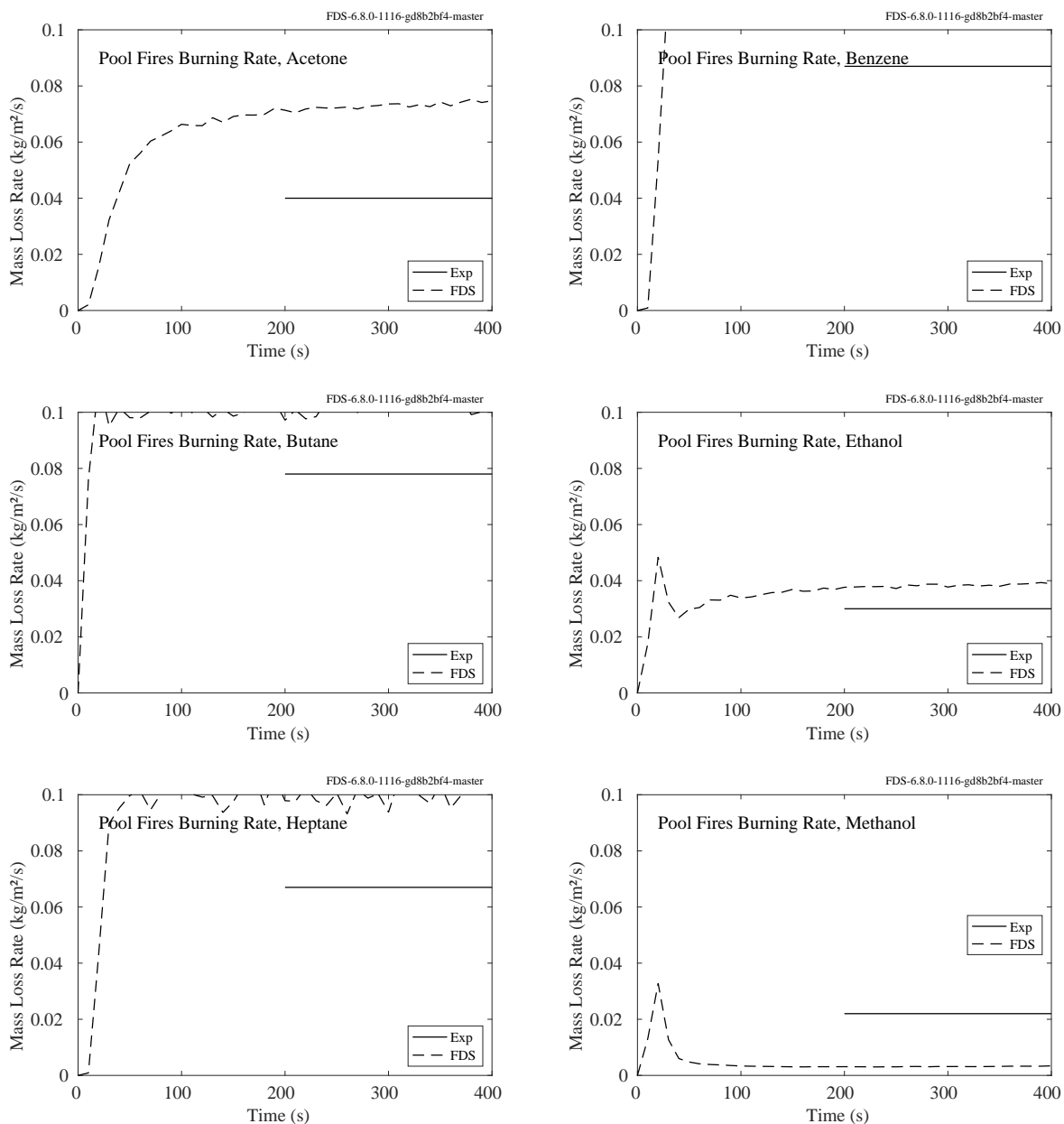


Figure 14.37: Comparison of burning rates for various liquid pool fires.

14.6.4 NIST Pool Fires

Figure 14.38 displays the measured and predicted burning rate of a 100 cm diameter methanol pool fire experiment conducted by Sung et al. at NIST [364].

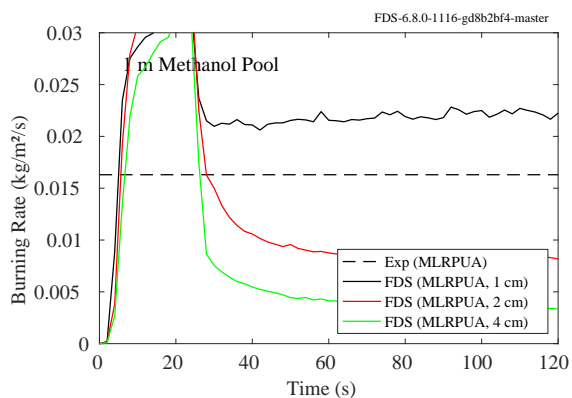


Figure 14.38: Burning rate of a 1 m methanol pool fire.

14.6.5 Waterloo Methanol Pool Fire

Figure 14.39 displays the measured and predicted burning rate for a 30 cm diameter methanol pool fire experiment conducted by Weckman at the University of Waterloo [342]. The experimental result came after at least 10 min of burning, whereas the model is only run for 2 min.

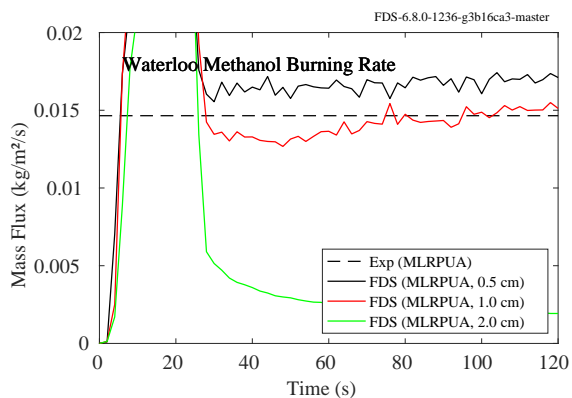


Figure 14.39: Waterloo Methanol mass loss rate.

14.7 Vertical Flame Spread

14.7.1 NIST/NRC Parallel Panel Experiments

The figures below contain predictions of the burning rate of various plastics in a parallel panel apparatus described in Sec. 3.58.

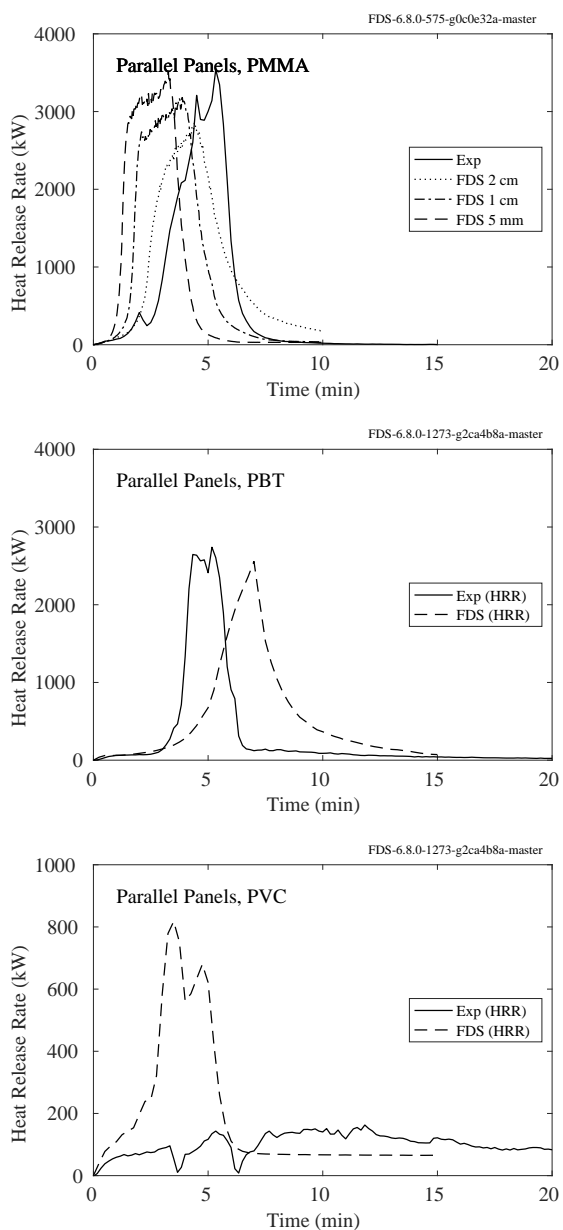


Figure 14.40: NIST/NRC Parallel Panels experiments.

14.7.2 UMD SBI Experiment

A description of this experiment is given in Sec. 3.94.

Figure 14.41 displays the measured and predicted HRR for upward spread over PMMA panels in the SBI (Single Burning Item) apparatus.

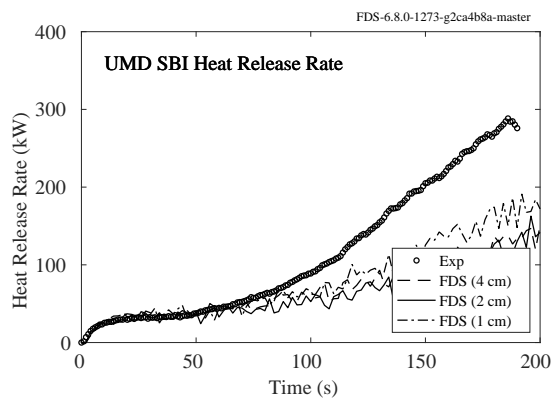


Figure 14.41: UMD SBI experiment, heat release rate.

14.8 Scaling Pyrolysis (SPyro)

FDS has a scaling-based pyrolysis model (SPyro) which dynamically scales a reference heat release rate per unit area curve based on the energy absorbed on the surface. This section evaluates the performance of FDS in scaling the burning rate using this model. Each heat flux shown in the figures in this section is a validation heat transfer level (i.e., the reference heat flux is not shown). Validation statistics are calculated based on the peak HRRPUA.

14.8.1 Aalto Woods Experiments

Table 14.16 lists the relevant parameters for modeling the cone calorimeter experiments for this study. Note that the published properties from the test report are simplified in this analysis. Each multi-phase properties is represented as single bulk value. In addition, the temperature-dependent thermal conductivity and specific capacity are fixed at an average value. The ignition temperatures were calculated based on times to ignition at the lower heat fluxes using the other properties. The results of the simulations are shown below.

Table 14.16: Properties of Aalto Woods [145].

Material	Δ (mm)	ρ $\left(\frac{\text{kg}}{\text{m}^3}\right)$	k $\left(\frac{\text{W}}{\text{m}\cdot\text{K}}\right)$	c_p $\left(\frac{\text{kJ}}{\text{kg}\cdot\text{K}}\right)$	ϵ (—)	T_{ign}^a (°C)	ΔH_c $\left(\frac{\text{MJ}}{\text{kg}}\right)$	Y_s^b $\left(\frac{\text{g}}{\text{g}}\right)$
Pine Flaming	20.0	493	0.10	0.91	0.90	485	13.8	0.015
Spruce Flaming	20.0	408	0.06	0.91	0.90	487	13.8	0.015

^a T_{ign} is calculated based on measured times to ignition.

^b Y_s based on data from the SFPE handbook [151].

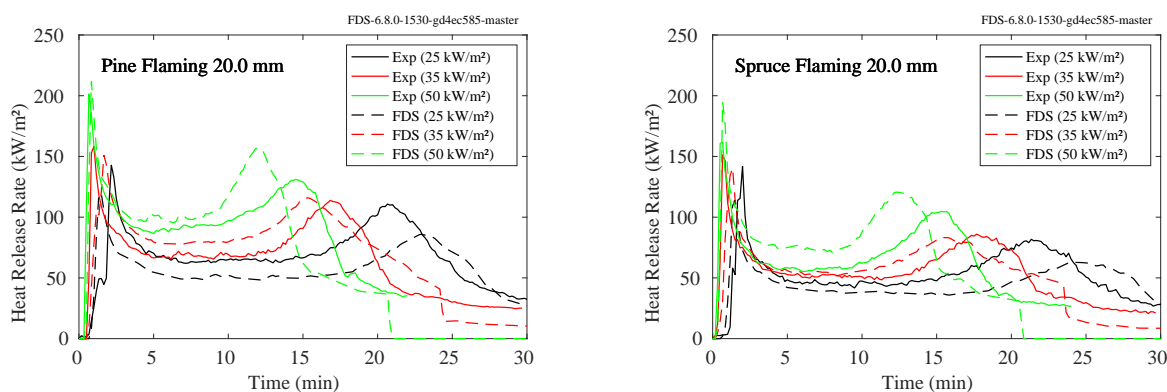


Figure 14.42: Aalto Woods - Comparison of predicted and measured heat release rate per unit area using scaling-based approach for cone calorimeter experiments.

14.8.2 FAA Polymers Experiments

Table 14.17 lists the relevant parameters for modeling the cone calorimeter experiments for this study. Note that the published properties from the test report are simplified in this analysis. Each multi-phase properties is represented as single bulk value. In addition, the temperature-dependent thermal conductivity and specific capacity are fixed at an average value. The ignition temperatures were calculated based on times to ignition at the lower heat fluxes using the other properties. The results of the simulations are shown on the following pages.

Table 14.17: Properties of FAA Polymers [207, 303].

Material	Δ^a (mm)	ρ $\left(\frac{\text{kg}}{\text{m}^3}\right)$	k $\left(\frac{\text{W}}{\text{m}\cdot\text{K}}\right)$	c_p $\left(\frac{\text{kJ}}{\text{kg}\cdot\text{K}}\right)$	ε (—)	T_{ign}^b (°C)	ΔH_c $\left(\frac{\text{MJ}}{\text{kg}}\right)$	Y_s $\left(\frac{\text{g}}{\text{g}}\right)$
HDPE	3.2, 8.1, 27.0	860	0.29	3.50	0.92	410	47.5	0.060
HIPS	3.2, 8.1, 27.0	950	0.22	2.00	0.86	425	39.2	0.164
PBT	4.0	1300	0.29	2.23	0.88	291	19.5	0.020
PBTGF	4.0	1520	0.36	1.68	0.87	235	19.5	0.020
PC	3.0, 5.5, 9.0	1180	0.22	1.90	0.90	530	25.6	0.112
PEEK	3.9	1300	0.28	2.05	0.90	463	22.8	0.020
PMMA	3.2, 8.1, 27.0	1100	0.20	2.20	0.85	373	33.5	0.022
PVC	3.0, 6.0, 9.0	1430	0.17	1.55	0.90	435	36.5	0.172

^a Comma separation indicates tests at multiple thicknesses.

^b T_{ign} is calculated based on measured times to ignition.

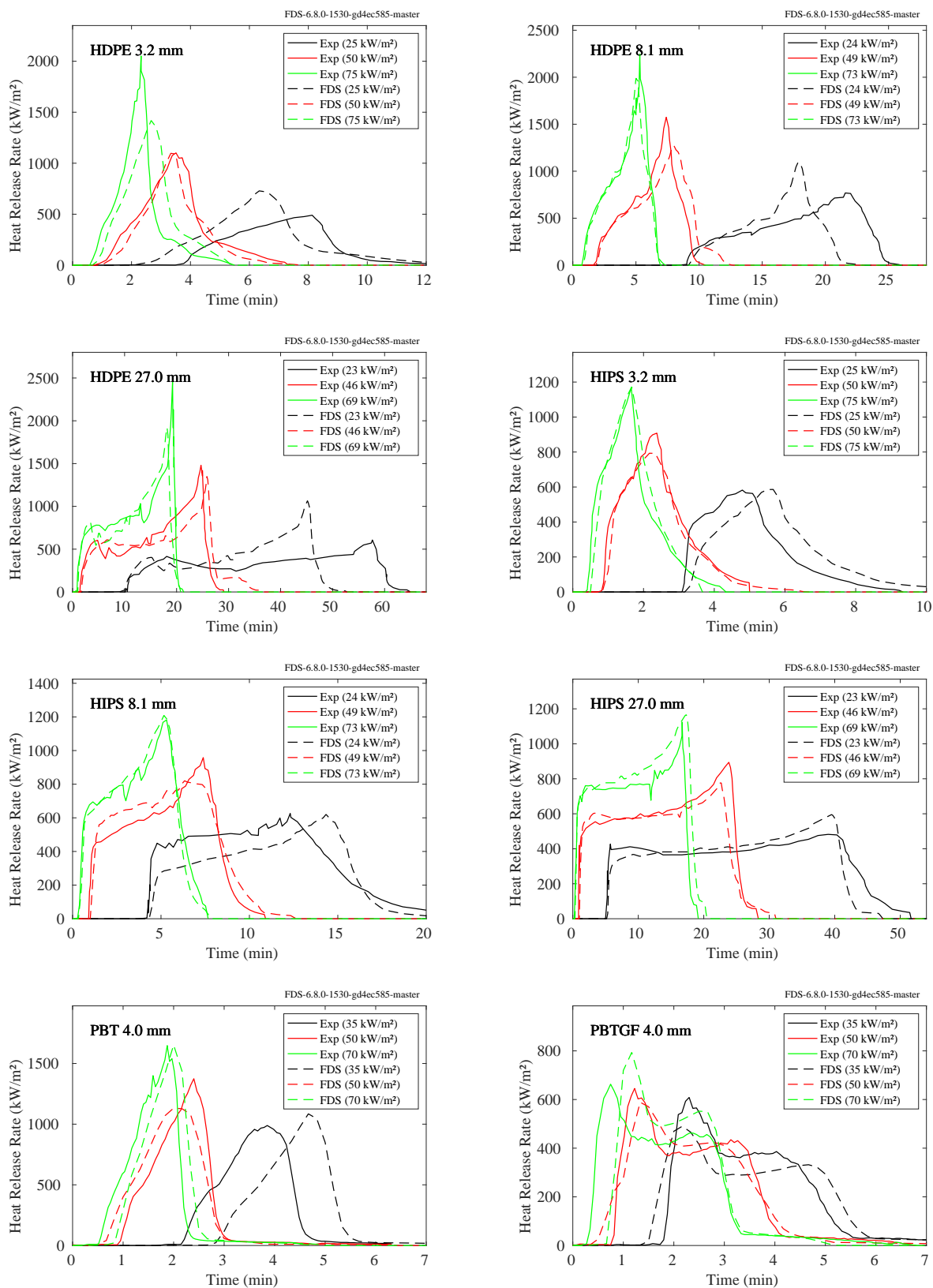


Figure 14.43: FAA Polymers - Comparison of predicted and measured heat release rate per unit area using scaling-based approach for cone calorimeter experiments.

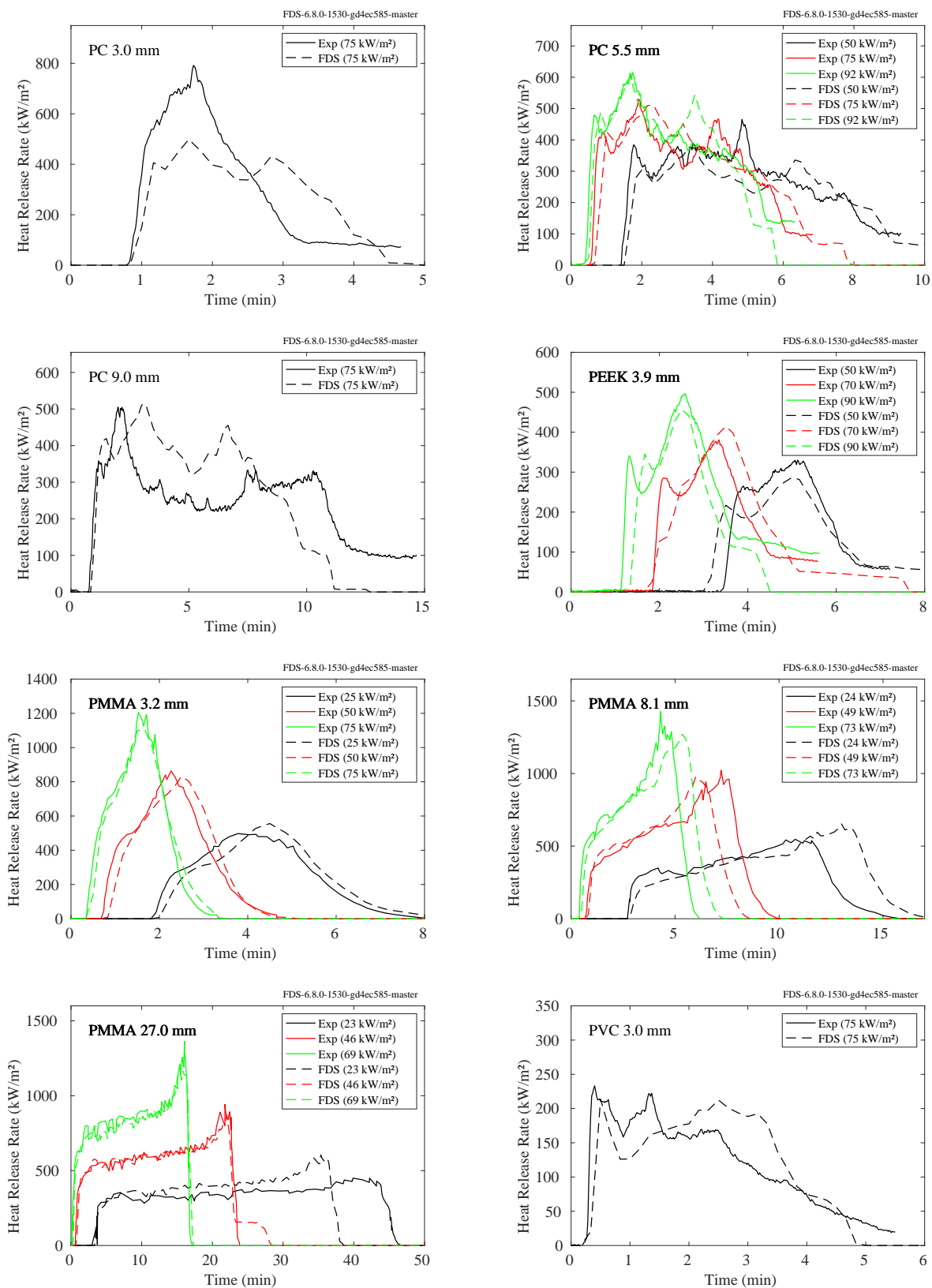


Figure 14.44: FAA Polymers - Comparison of predicted and measured heat release rate per unit area using scaling-based approach for cone calorimeter experiments.

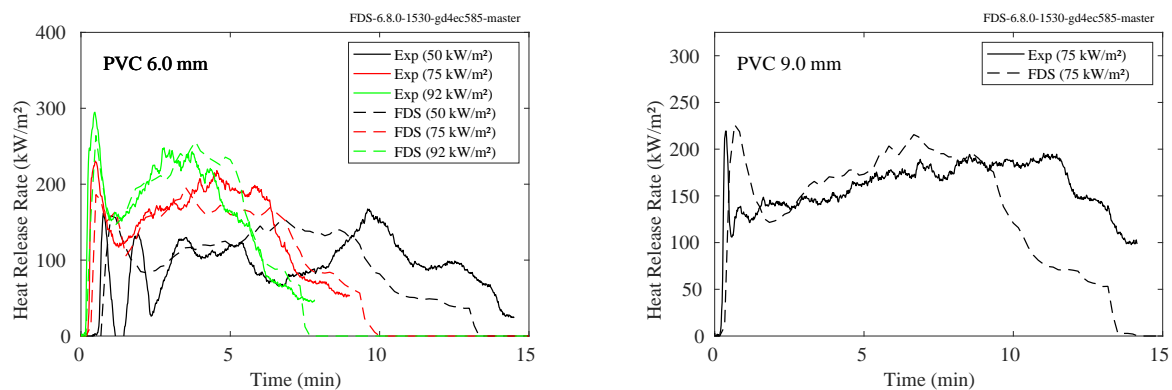


Figure 14.45: FAA Polymers - Comparison of predicted and measured heat release rate per unit area using scaling-based approach for cone calorimeter experiments.

14.8.3 FPL Wood Experiments

Table 14.18 lists the relevant parameters for modeling the cone calorimeter experiments for this study. Note that the test reports in this study did not provide thermal properties. Fixed values of specific heat capacity, 1.0 (kJ/(kg · K)), thermal conductivity, 0.4 (W/m · K), and emissivity, 1.0, are used to calculate an effective ignition temperature. The results of the simulations are shown on the following pages.

Table 14.18: Properties of FPL Materials [219].

Material	Δ (mm)	ρ $\left(\frac{\text{kg}}{\text{m}^3}\right)$	T_{ign}^a (°C)	ΔH_c $\left(\frac{\text{MJ}}{\text{kg}}\right)$	Y_s $\left(\frac{\text{g}}{\text{g}}\right)$	Test # (—)
Hardboard	7.2	972	410	14.5	0.007	670a-b, 682a-b, 697a-b, 710a-b
Lumber Redoak	19.8	775	434	10.9	0.004	675a-b, 687a-b, 702a-b, 753a-b
OSB	11.5	754	406	13.1	0.010	669a-b, 681a-b, 696a-b, 709a-b
Plywood Douglas Fir	11.8	482	398	12.6	0.007	454a-b, 456a-c, 457a-c
Plywood Douglas Fir FRT	12.5	604	361	7.3	0.002	543a, 544a, 545a, 546a
Plywood Oak	12.7	502	446	12.4	0.001	1a-c, 2a-c, 3a-c, 4a-c
Plywood Southern Pine FRT	11.2	741	505	7.4	0.001	665a-b, 677a-b, 690a-b, 705a-b
Waferboard	13.0	712	425	13.3	0.010	674a-b, 686a-b, 701a-b, 752a-b

^a T_{ign} is calculated based on measured times to ignition. Assumed values used for thermal properties when not measured.

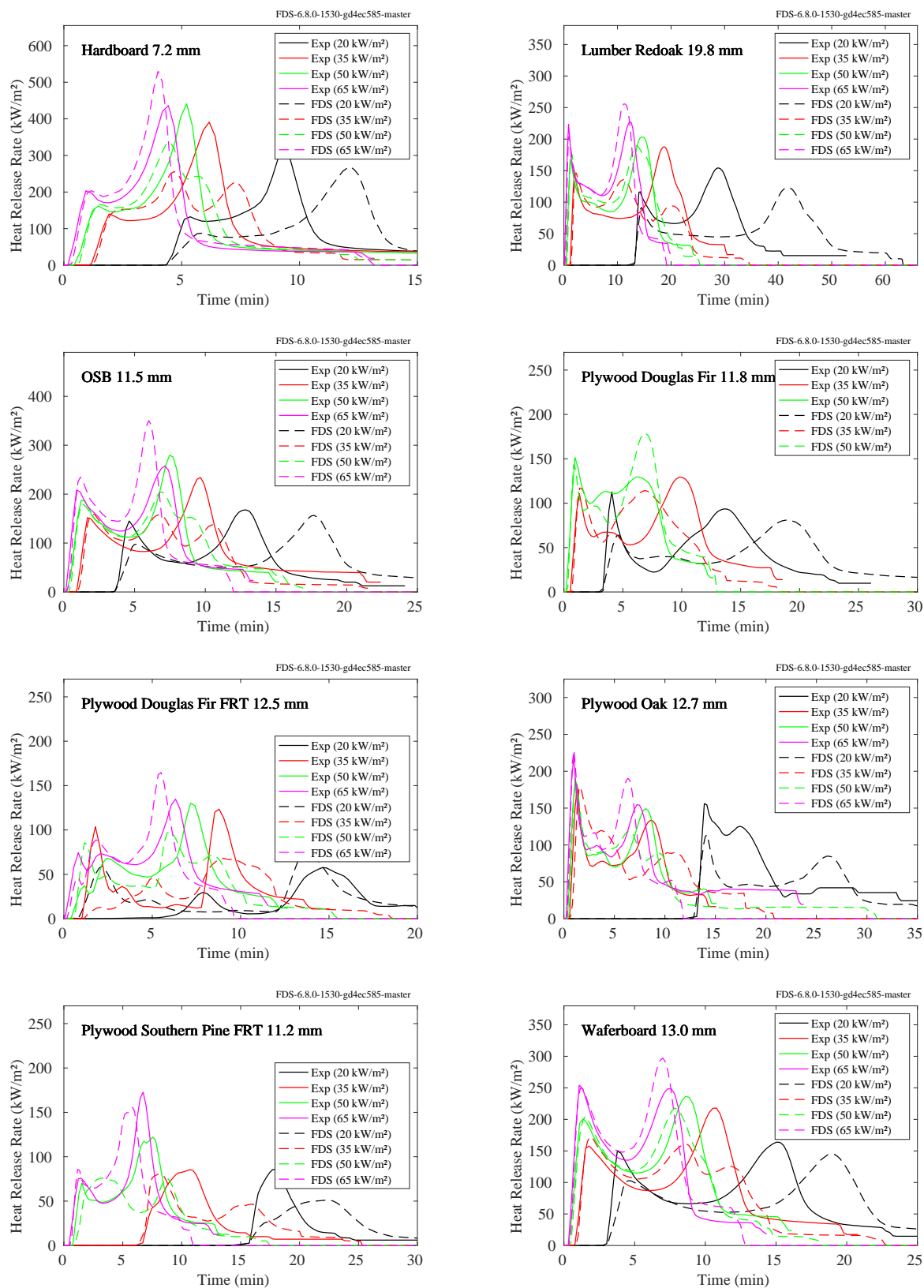


Figure 14.46: FPL materials - Comparison of predicted and measured heat release rate per unit area using scaling-based approach for cone calorimeter experiments.

14.8.4 FSRI/NIJ Experiments

Table 14.19, Table 14.20, and Table 14.21 lists the relevant parameters for modeling the cone calorimeter experiments for this study. Note that the published properties from the test report are simplified in this analysis. Each multi-phase properties is represented as single bulk value. In addition, the temperature-dependent thermal conductivity and specific capacity are fixed at an average value. The ignition temperatures were calculated based on times to ignition at the lower heat fluxes using the other properties.

Table 14.19: Properties of FSRI Materials, other materials [221].

Material	Δ (mm)	ρ $\left(\frac{\text{kg}}{\text{m}^3}\right)$	k $\left(\frac{\text{W}}{\text{m}\cdot\text{K}}\right)$	c_p $\left(\frac{\text{kJ}}{\text{kg}\cdot\text{K}}\right)$	T_{ign}^a (°C)	ΔH_c $\left(\frac{\text{MJ}}{\text{kg}}\right)$	Y_s $\left(\frac{\text{g}}{\text{g}}\right)$
Asphalt Shingle	3.0	1219	0.08	1.01	520	36.6	0.117
Cellulose Insulation	37.7	68	0.05	1.74	592	11.9	0.001
Cotton Rug	6.1	263	0.07	1.56	522	19.4	0.018
Cotton Sheet	0.2	550	0.03	1.45	450	14.7	0.001
EPDM Membrane	7.8	1200	0.14	1.46	459	35.2	0.161
Excelsior	2.0	360	0.03	1.38	470	13.7	0.013
Expanded Polystyrene Board	27.1	28	0.03	1.38	671	33.8	0.104
Face Shield ^b	19.3	664	0.07	1.35	578	14.1	0.002
Feather Pillow Feathers ^b	0.8	671	0.03	1.49	456	8.2	0.007
Fiberglass Reinforced Panel	6.4	524	0.12	1.66	514	27.3	0.069
Gypsum Wallboard	13.0	591	0.15	1.10	448	6.3	0.001
Hemp Sheet	0.4	523	0.04	1.79	410	17.0	0.001
House Wrap	0.1	714	0.15	1.57	484	1.5	0.052
Latex Pillow Foam ^b	3.3	677	0.13	1.58	440	32.8	0.094
Lightweight Gypsum Wallboard	12.9	494	0.13	1.15	547	8.1	0.001
Low Density Fiberboard	12.6	214	0.06	1.35	503	16.6	0.003
Overstuffed Chair Assembly	4.2	379	0.10	1.47	478	24.9	0.026
Paper-faced R30 Fiberglass Insulation	2.0	360	0.03	1.38	470	13.7	0.013
PE Foam Pipe Insulation	14.3	35	0.06	2.58	579	43.9	0.058
Polyisocyanurate Foam Board	13.7	52	0.04	1.47	589	23.5	0.001
Pressure Treated Deck ^b	19.3	664	0.07	1.35	578	14.1	0.002
Roof Felt	1.1	726	0.06	1.74	394	28.3	0.067
Rubber Band ^b	4.7	404	0.10	1.55	549	33.5	0.001
Rubber Foam Pipe Insulation	12.8	52	0.04	1.47	587	19.5	0.061
Rug Pad	4.1	176	0.05	1.10	540	27.9	0.055
Wool Rug	16.6	226	0.06	1.33	502	21.0	0.010

^a T_{ign} is calculated based on measured times to ignition. Assumed value for emissivity of 1 is used.

^b Material not available in web interface. See FSRI database github (https://github.com/ulfsri/fsri_materials_database/tree/main/01_Data)

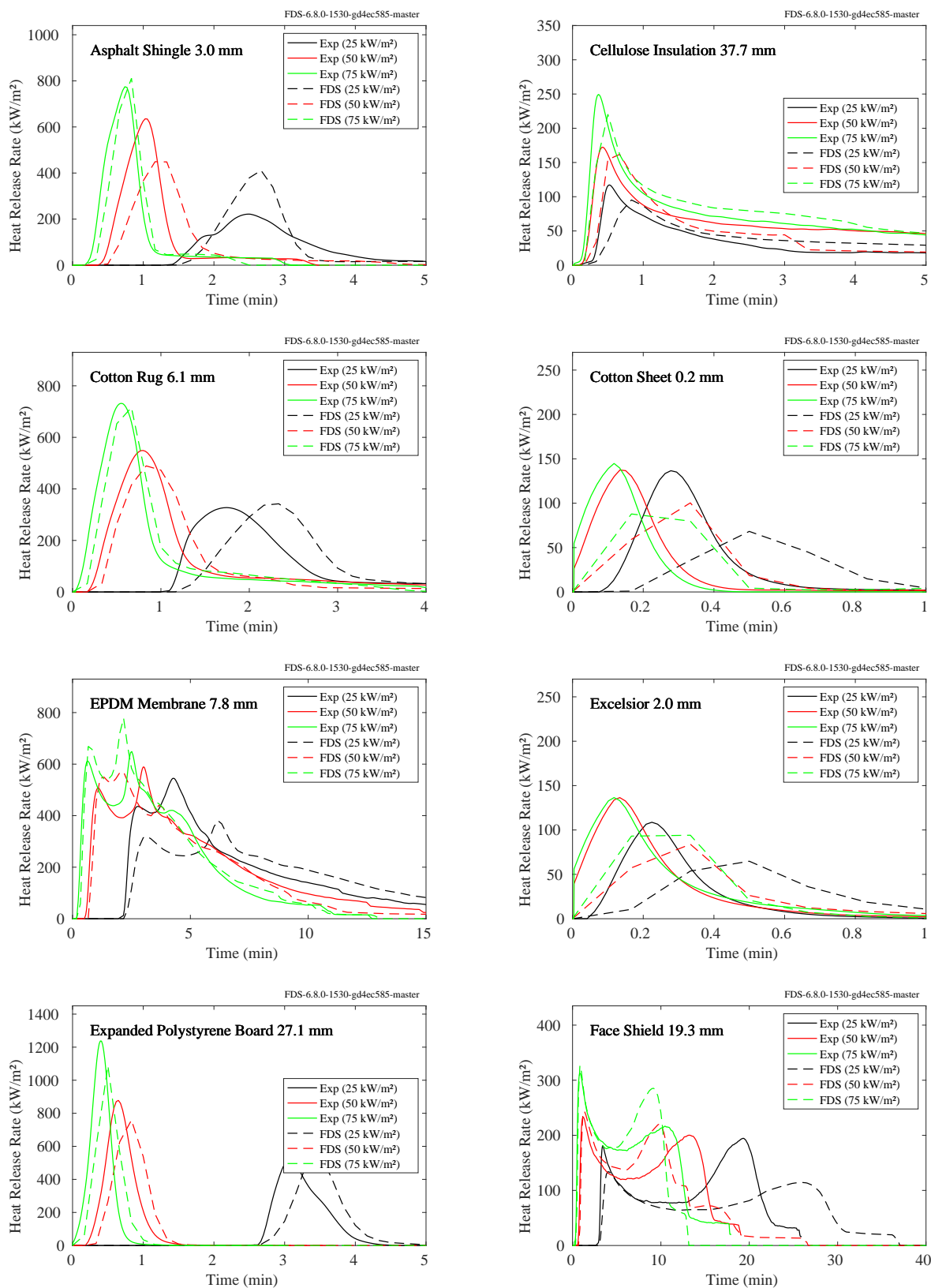


Figure 14.47: FSRI, other materials - Comparison of predicted and measured heat release rate per unit area using scaling-based approach for cone calorimeter experiments.

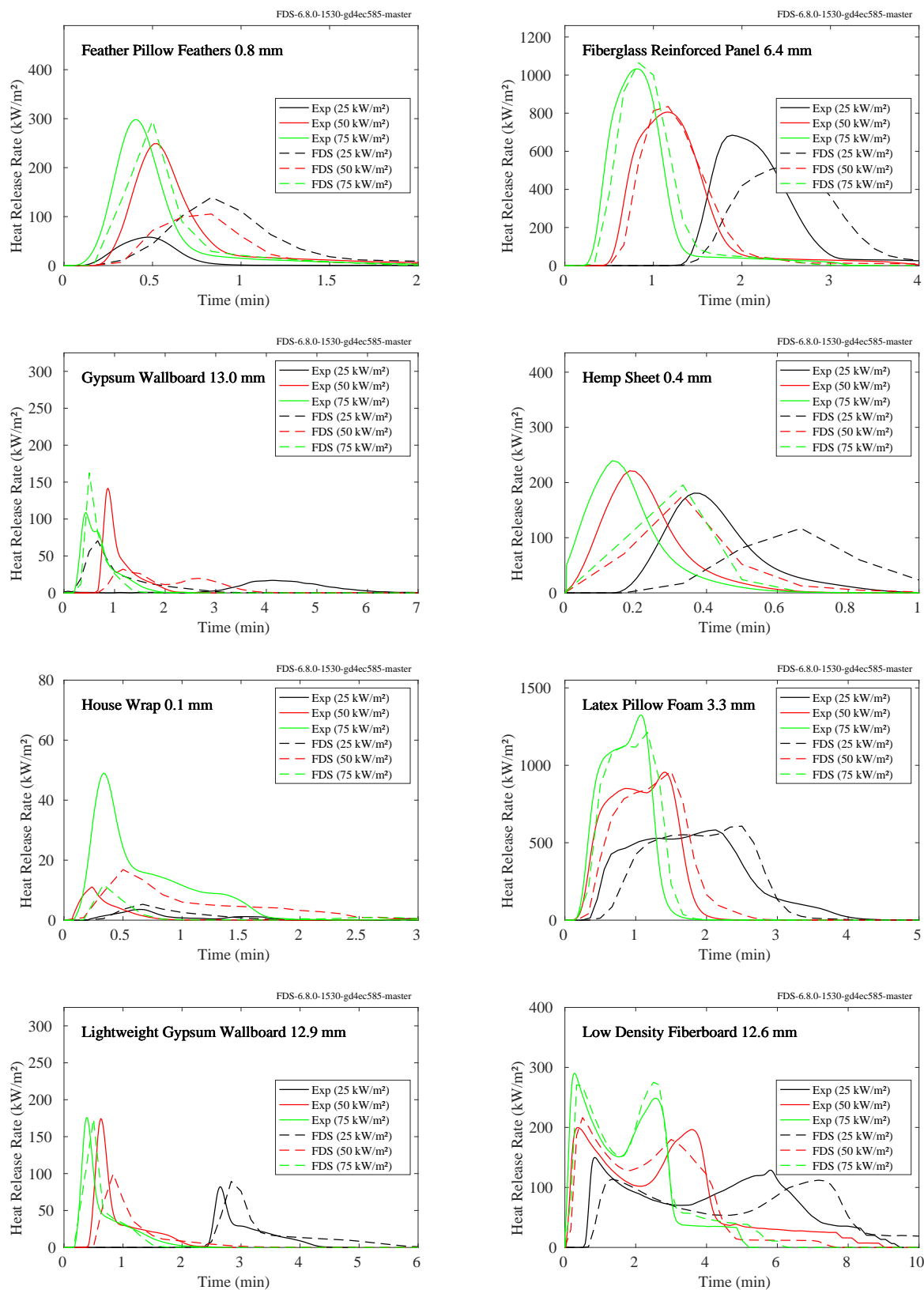


Figure 14.48: FSRI, other materials - Comparison of predicted and measured heat release rate per unit area using scaling-based approach for cone calorimeter experiments.

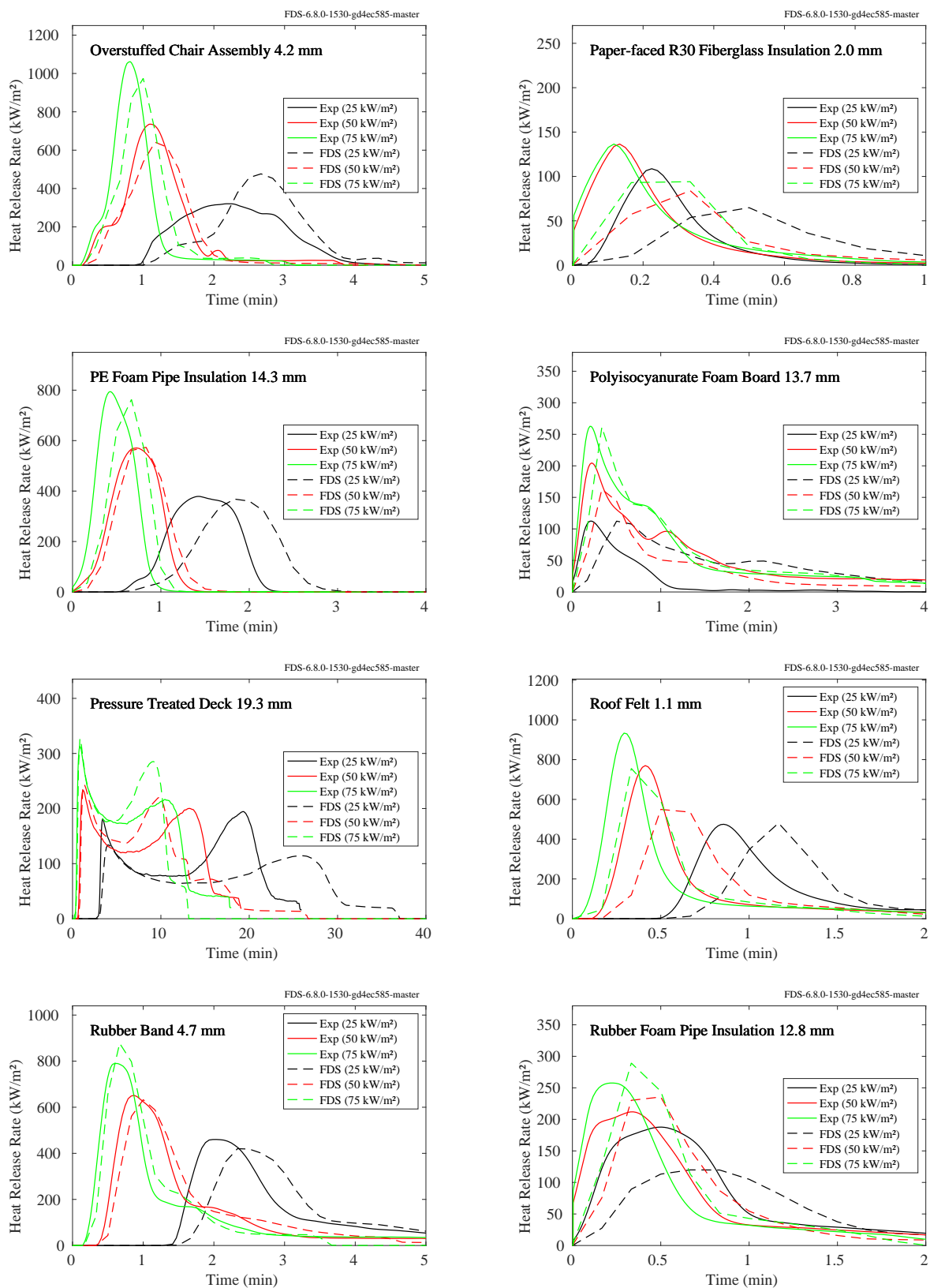


Figure 14.49: FSRI, other materials - Comparison of predicted and measured heat release rate per unit area using scaling-based approach for cone calorimeter experiments.

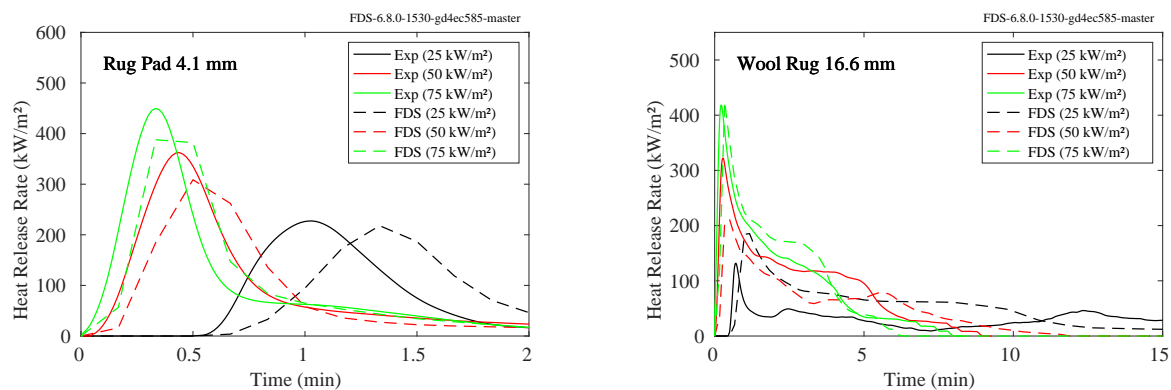


Figure 14.50: FSRI, other materials - Comparison of predicted and measured heat release rate per unit area using scaling-based approach for cone calorimeter experiments.

Table 14.20: Properties of FSRI Materials, polymer materials [221].

Material	Δ (mm)	ρ $\left(\frac{\text{kg}}{\text{m}^3}\right)$	k $\left(\frac{\text{W}}{\text{m}\cdot\text{K}}\right)$	c_p $\left(\frac{\text{kJ}}{\text{kg}\cdot\text{K}}\right)$	T_{ign}^a (°C)	ΔH_c $\left(\frac{\text{MJ}}{\text{kg}}\right)$	Y_s $\left(\frac{\text{g}}{\text{g}}\right)$
ABS	3.0	1100	0.39	1.35	388	35.4	0.102
Black PMMA	8.7	1182	0.15	1.48	436	29.5	0.006
Cotton Raw ^b	2.4	664	0.07	1.35	388	17.3	0.088
HDPE	3.2	971	0.30	1.92	481	49.1	0.026
HIPS	3.0	1067	0.13	1.35	499	35.9	0.111
High Temperature Scba Facepiece ^b	37.2	737	0.12	1.28	527	14.2	0.001
LDPE	3.2	927	0.22	2.60	420	48.9	0.026
Memory Foam Carpet Pad	12.4	134	0.04	1.87	486	30.6	0.024
Nylon	3.4	1070	0.15	1.84	533	36.3	0.020
Nylon Carpet High Pile ^b	13.7	188	0.06	1.53	615	36.0	0.049
Overstuffed Chair Polyester - Batting	1.5	404	0.10	1.55	596	17.6	0.051
Overstuffed Chair - Polyester Fabric	0.5	360	0.03	1.38	571	19.6	0.054
Overstuffed Chair - Polyurethane Foam	0.8	927	0.22	2.60	173	29.2	0.014
PC	5.3	1220	0.18	1.26	451	26.2	0.090
PET	6.5	1401	0.19	1.17	527	19.9	0.049
PETG	2.6	1314	0.16	1.25	529	23.8	0.040
PMMA	2.8	1182	0.15	1.48	440	26.8	0.014
PP	3.2	887	0.15	1.92	460	48.6	0.040
PVC	3.2	1388	0.14	1.08	506	11.8	0.068
PlasticC ^b	3.0	1058	0.12	1.37	499	35.3	0.121
Plastic Laminate Countertop	37.2	737	0.12	1.28	527	14.2	0.001
Polyester Bed Skirt	1.2	432	0.02	1.61	614	19.6	0.040
Polyester Microfiber Sheet	1.0	457	0.02	2.08	609	20.5	0.036
Low Pile Polyolefin Carpet	7.2	214	0.06	1.35	501	40.3	0.074
Rebond Foam Carpet Pad	9.0	86	0.04	1.82	520	33.3	0.025
Vinyl Plank Flooring	2.4	664	0.07	1.35	388	17.3	0.088
Vinyl Siding	1.2	1377	0.10	1.10	534	10.6	0.099
Vinyl Tile	7.9	726	0.06	1.74	551	16.1	0.061

^a T_{ign} is calculated based on measured times to ignition. Assumed value for emissivity of 1 is used.

^b Material not available in web interface. See FSRI database github (https://github.com/ulfsri/fsri_materials_database/tree/main/01_Data)

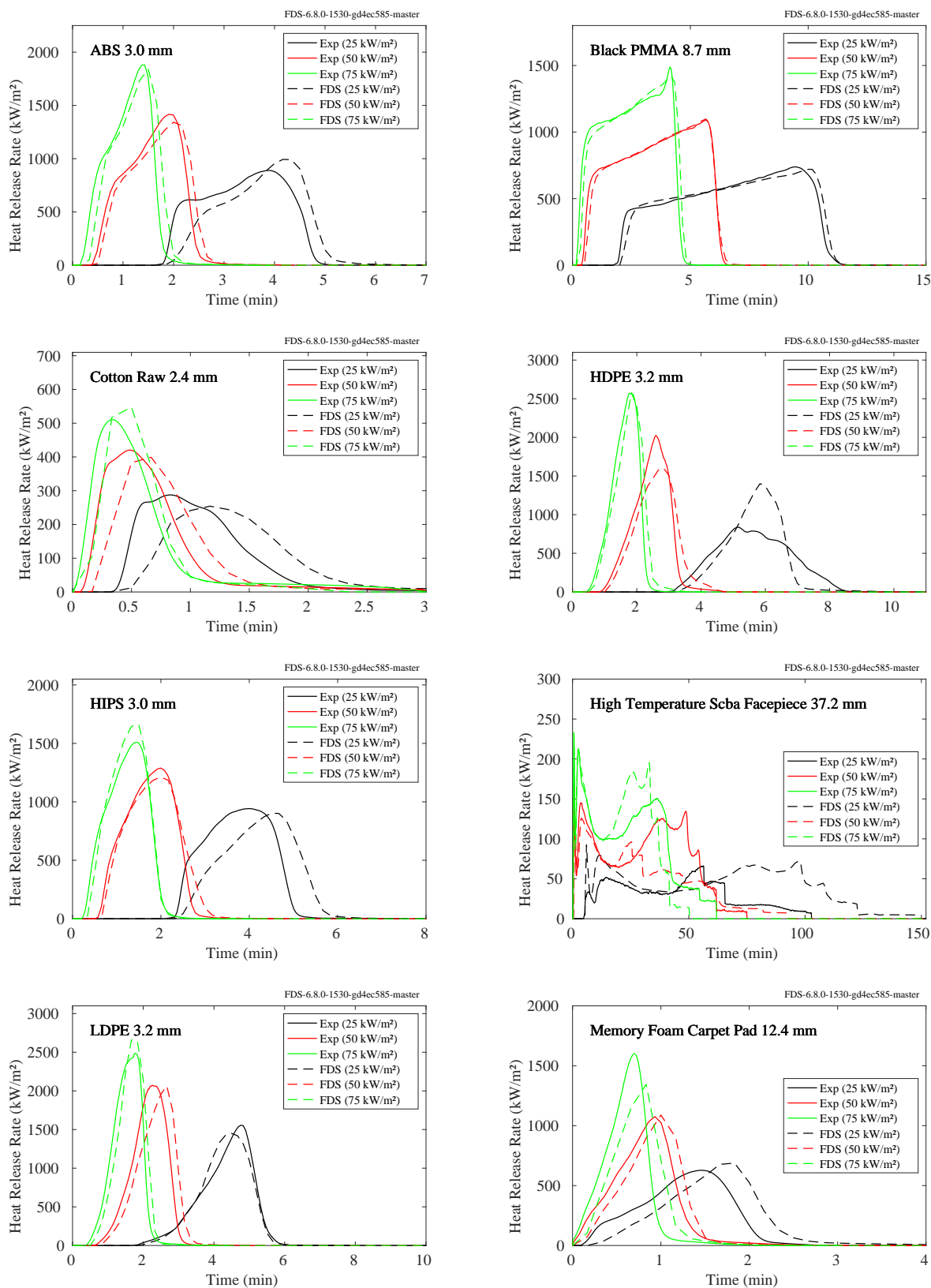


Figure 14.51: FSRI, polymer materials - Comparison of predicted and measured heat release rate per unit area using scaling-based approach for cone calorimeter experiments.

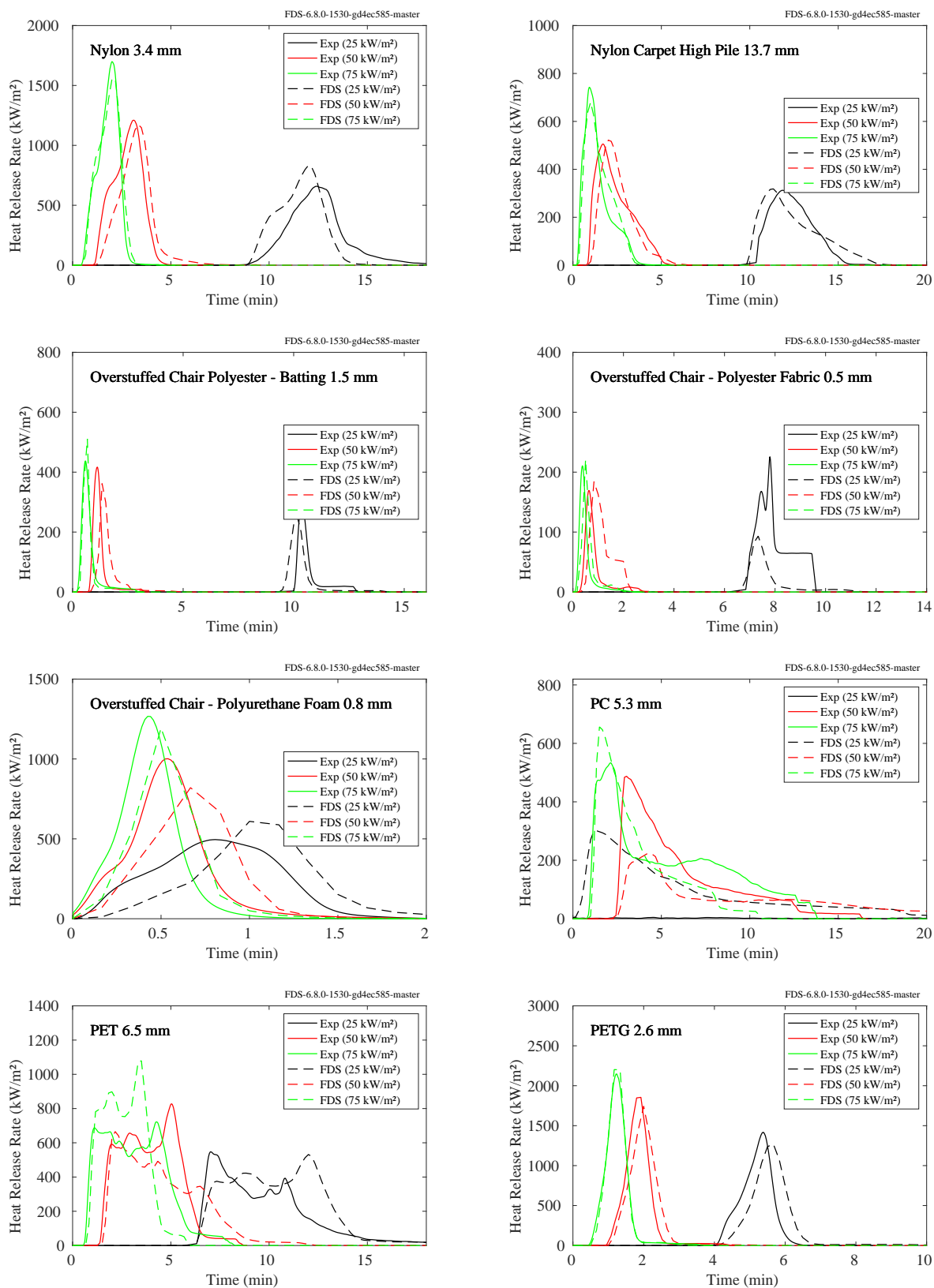


Figure 14.52: FSRI, polymer materials - Comparison of predicted and measured heat release rate per unit area using scaling-based approach for cone calorimeter experiments.

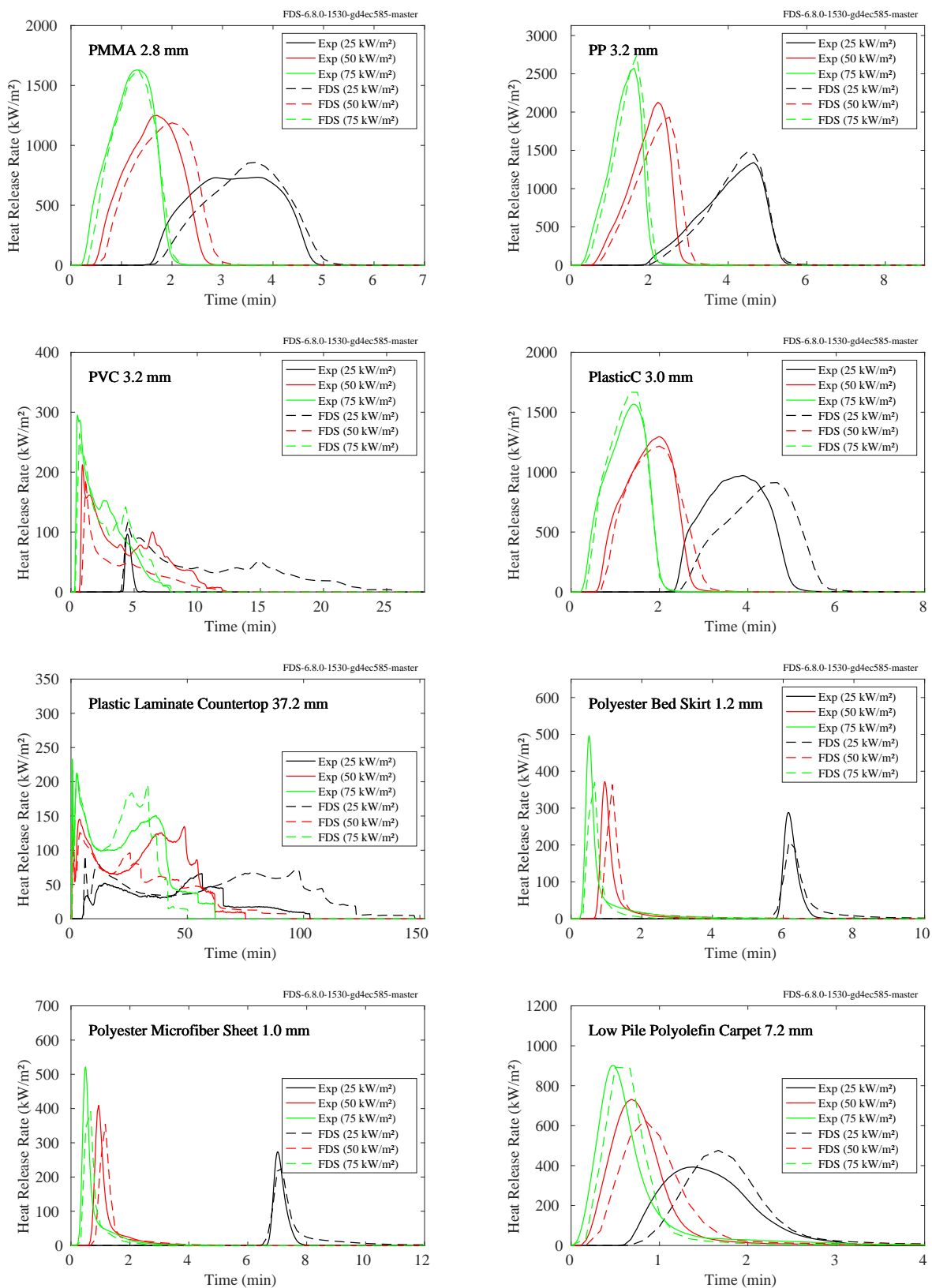


Figure 14.53: FSRI, polymer materials - Comparison of predicted and measured heat release rate per unit area using scaling-based approach for cone calorimeter experiments.

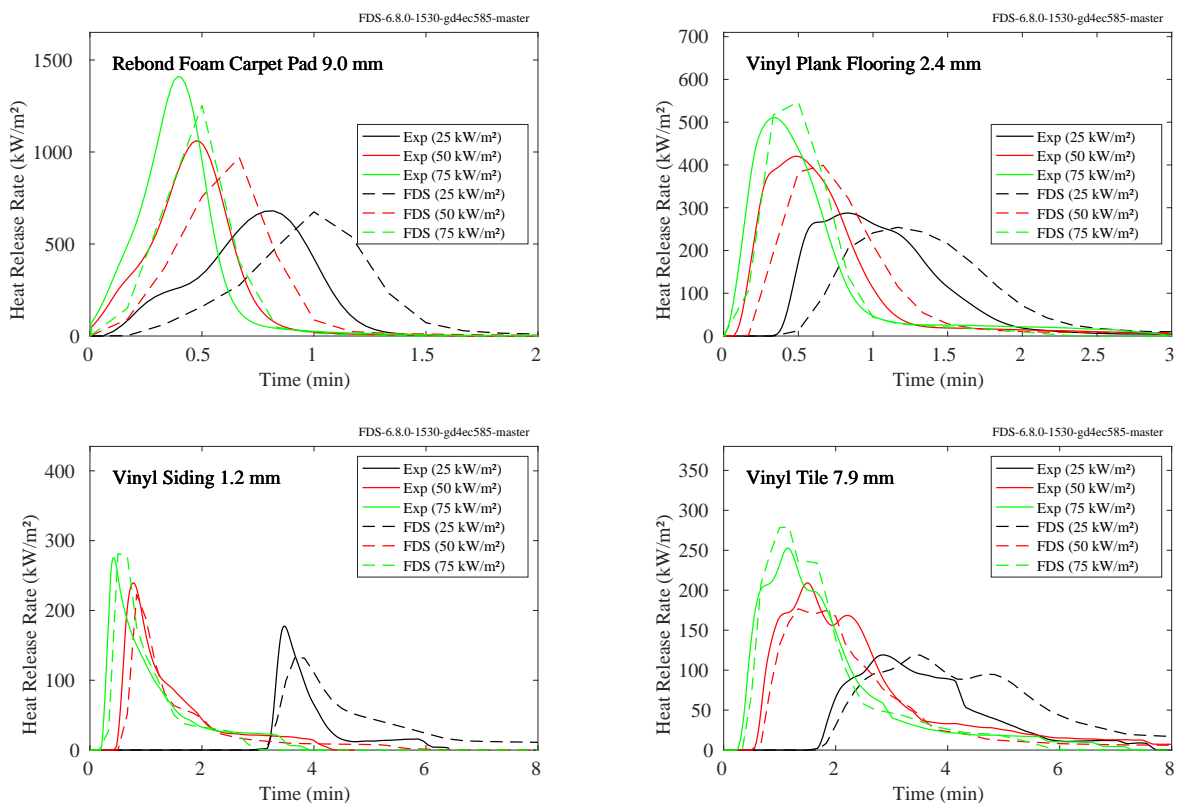


Figure 14.54: FSRI, polymer materials - Comparison of predicted and measured heat release rate per unit area using scaling-based approach for cone calorimeter experiments.

Table 14.21: Properties of FSRI Materials, Wood-Based materials [221].

Material	Δ (mm)	ρ $\left(\frac{\text{kg}}{\text{m}^3}\right)$	k $\left(\frac{\text{W}}{\text{m}\cdot\text{K}}\right)$	c_p $\left(\frac{\text{kJ}}{\text{kg}\cdot\text{K}}\right)$	T_{ign}^a (°C)	ΔH_c $\left(\frac{\text{MJ}}{\text{kg}}\right)$	Y_s $\left(\frac{\text{g}}{\text{g}}\right)$
Basswood Panel	19.8	404	0.10	1.55	551	15.7	0.005
Composite Deck Board	13.3	1103	0.23	1.57	403	28.8	0.001
Engineered Flooring	9.0	815	0.13	1.60	482	16.8	0.001
Engineered Wood Furniture	12.1	927	0.22	2.60	364	17.1	0.003
Engineered Wood Table ^b	89.8	379	0.10	1.47	567	12.6	0.002
Eucalyptus Flooring	15.6	1025	0.18	1.67	444	14.7	0.001
Homasote	13.3	448	0.08	1.55	544	15.6	0.003
Luan Panel	5.9	345	0.07	1.58	504	15.0	0.007
MDF	19.4	737	0.12	1.28	518	14.4	0.003
Masonite Board ^b	3.1	1127	0.12	1.52	515	16.1	0.007
OSB	16.9	598	0.12	1.58	522	15.5	0.006
Oak Flooring	19.9	714	0.15	1.57	493	14.2	0.003
Pallet Wood	3.0	1067	0.13	1.35	499	35.9	0.111
Particleboard	20.3	677	0.13	1.58	536	13.1	0.001
Pine Siding	18.9	328	0.11	1.84	466	16.9	0.001
Plywood	8.7	1182	0.15	1.48	436	29.5	0.006
Wood Stud	46.2	379	0.10	1.47	488	15.0	0.001

^a T_{ign} is calculated based on measured times to ignition. Assumed value for emissivity of 1 is used.

^b Material not available in web interface. See [FSRI database](#).

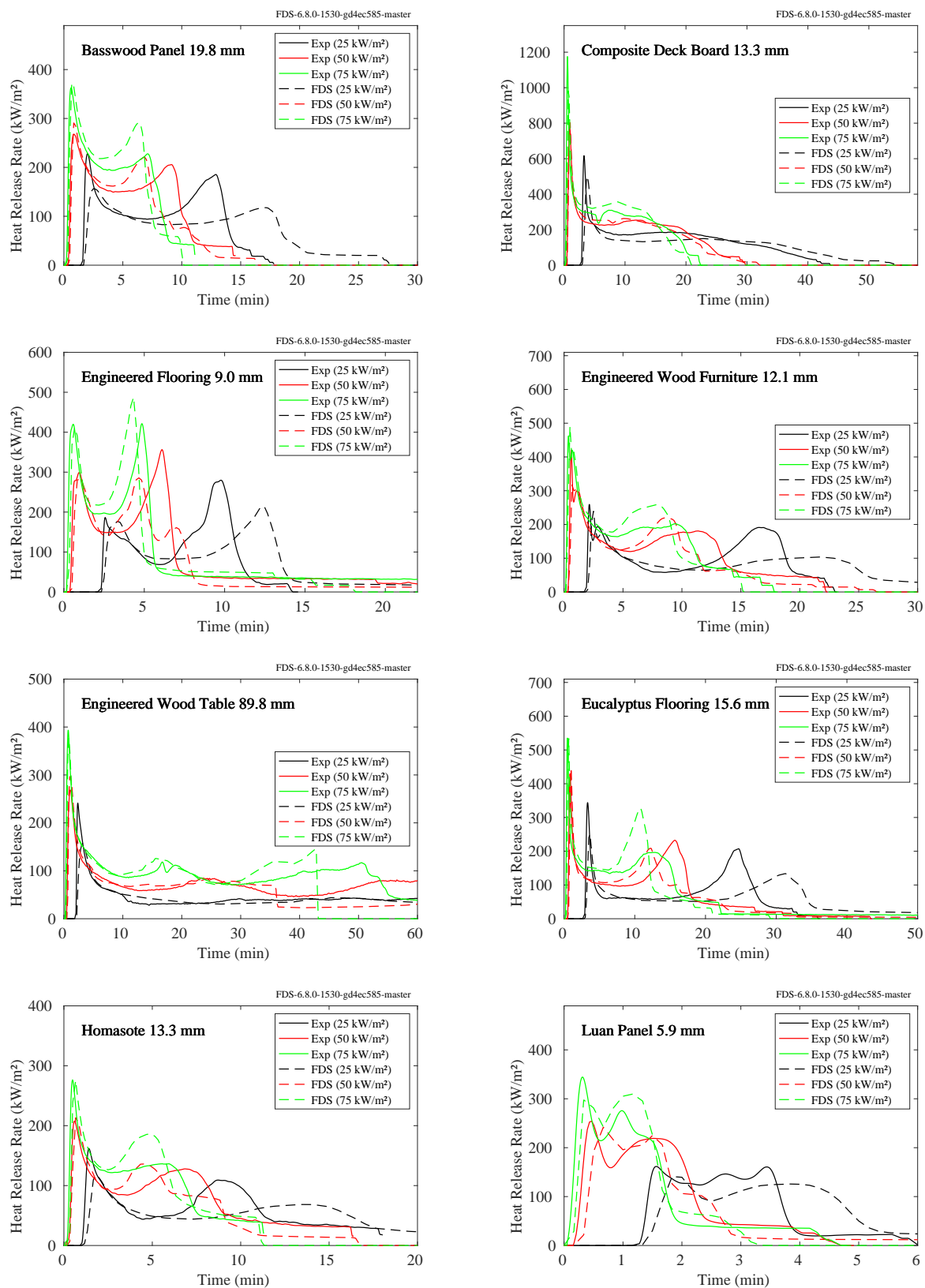


Figure 14.55: FSRI, wood-based materials - Comparison of predicted and measured heat release rate per unit area using scaling-based approach for cone calorimeter experiments.

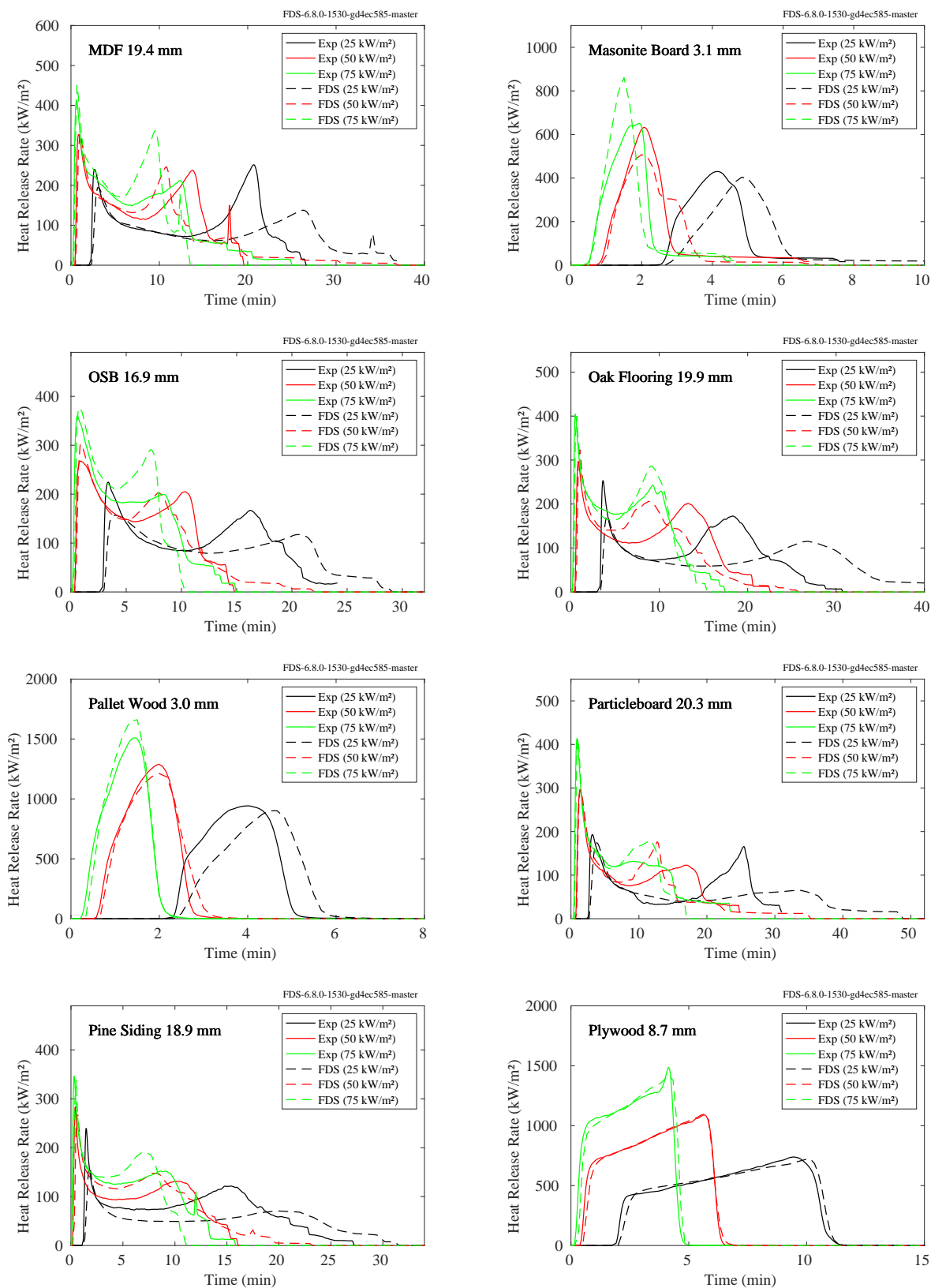


Figure 14.56: FSRI, wood-based materials - Comparison of predicted and measured heat release rate per unit area using scaling-based approach for cone calorimeter experiments.

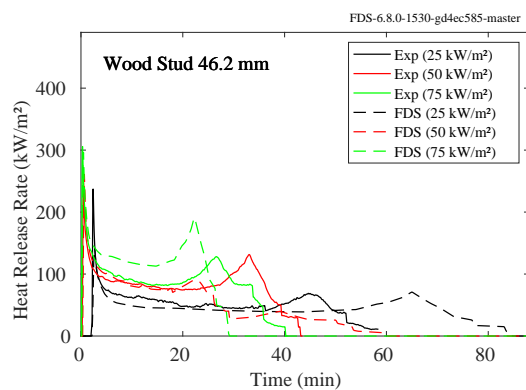


Figure 14.57: FSRI, wood-based materials - Comparison of predicted and measured heat release rate per unit area using scaling-based approach for cone calorimeter experiments.

14.8.5 JH Experiments

Table 14.22 lists the relevant parameters for modeling the cone calorimeter experiments for this study. Note that the published properties from the test report are simplified in this analysis. Each multi-phase properties is represented as single bulk value. In addition, the temperature-dependent thermal conductivity and specific capacity are fixed at an average value. The ignition temperatures were calculated based on times to ignition at the lower heat fluxes using the other properties. The results of the simulations are shown on the following pages.

Table 14.22: Properties of JH Materials [230, 233].

Material	Δ (mm)	ρ $\left(\frac{\text{kg}}{\text{m}^3}\right)$	k $\left(\frac{\text{W}}{\text{m}\cdot\text{K}}\right)$	c_p $\left(\frac{\text{kJ}}{\text{kg}\cdot\text{K}}\right)$	ε (—)	T_{ign}^a (°C)	ΔH_c $\left(\frac{\text{MJ}}{\text{kg}}\right)$	Y_s $\left(\frac{\text{g}}{\text{g}}\right)$
Acrylic	4.5	1178	0.24	0.62	0.88	387	24.9	0.033
Black PMMA	9.2	1154	0.12	1.52	0.95	374	23.3	0.006
CPS Balsa Facesheet	15.9	630	0.39	0.62	0.70	437	11.4	0.041
CPS Plywood Facesheet	12.7	630	0.39	0.51	0.70	544	10.2	0.020
Cardboard	4.1	128	0.23	0.69	0.93	462	12.0	0.001
FRP	12.7	1897	0.39	1.41	0.95	414	20.0	0.050
MDF	19.2	688	0.31	0.40	0.99	524	12.8	0.003
OSB	16.1	573	0.38	0.63	0.93	385	12.8	0.011
PC Blend	4.5	1320	0.89	0.67	0.93	448	24.5	0.233
PVC Blend	3.3	1314	0.29	0.42	0.88	534	21.4	0.151
Phenolic Resin Fiberglass	3.3	1846	0.35	1.29	0.89	511	23.9	0.238
Plywood	6.3	625	0.29	3.13	1.00	266	21.6	0.006
Vinyl Ester Resin FRP	4.5	1600	0.54	4.00	0.80	440	19.4	0.180
White Pine	19.1	499	0.31	0.60	0.90	421	12.0	0.015
White Spruce	37.2	430	0.24	1.10	0.90	399	12.0	0.015

^a T_{ign} is calculated based on measured times to ignition.

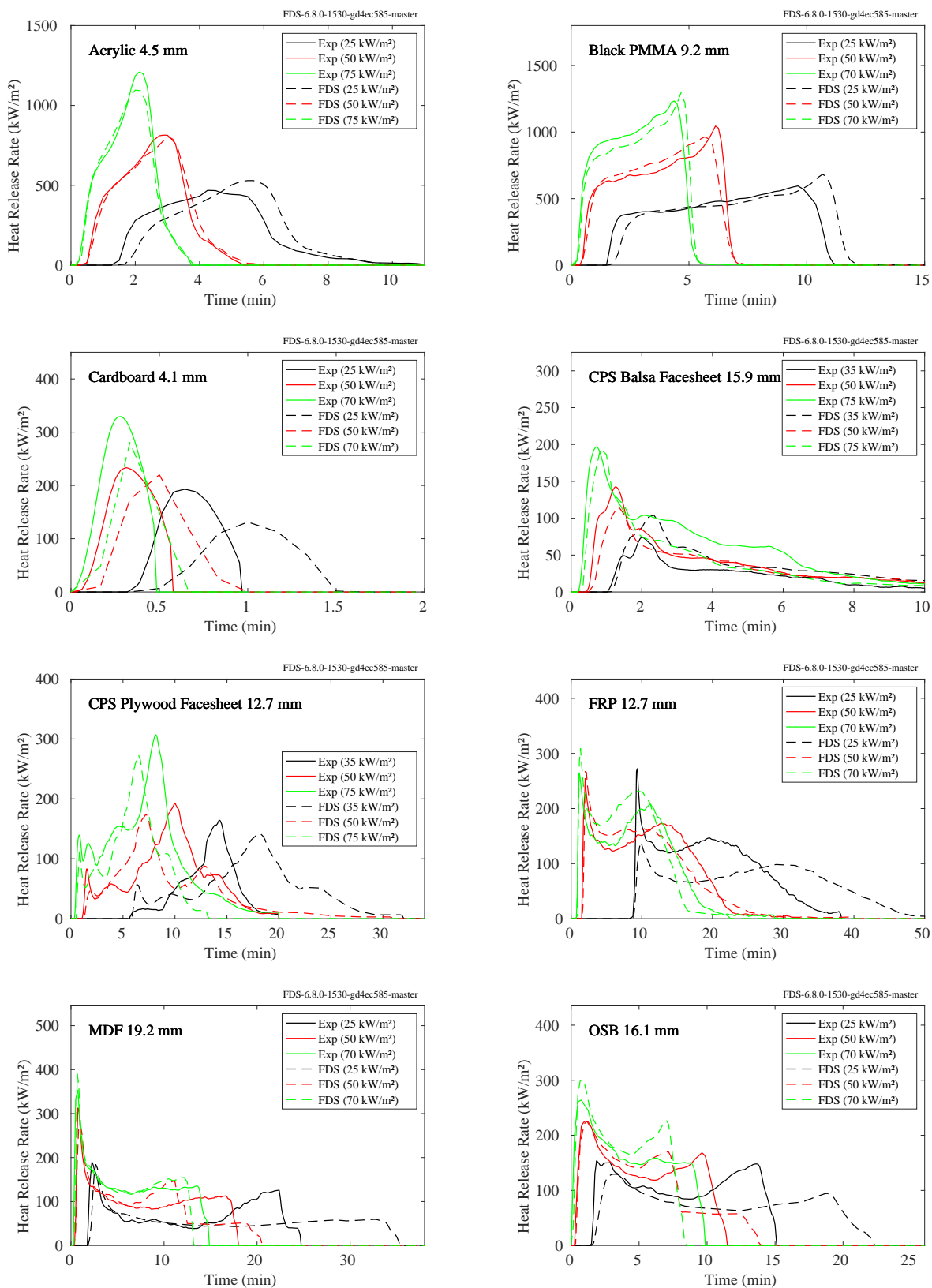


Figure 14.58: JH materials - Comparison of predicted and measured heat release rate per unit area using scaling-based approach for cone calorimeter experiments.

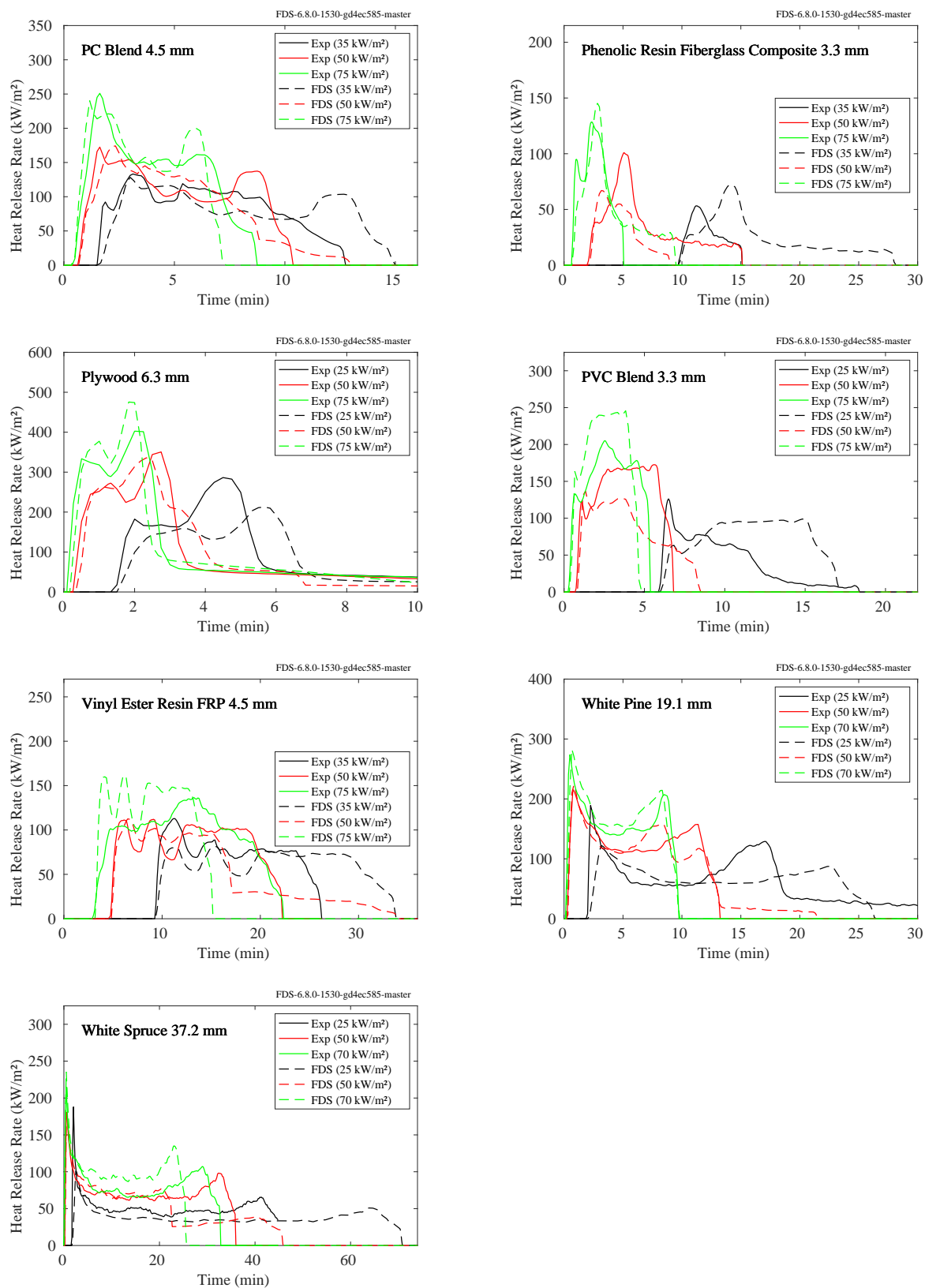


Figure 14.59: JH materials - Comparison of predicted and measured heat release rate per unit area using scaling-based approach for cone calorimeter experiments.

14.8.6 RISE Experiments

Table 14.23, Table 14.24, Table 14.25, Table 14.26, and Table 14.27 lists the relevant parameters for modeling the cone calorimeter experiments for this study. Note that the test reports in this study did not provide thermal properties. Fixed values of specific heat capacity, 1.0 (kJ/(kg · K)), thermal conductivity, 0.4 (W/m · K), and emissivity, 1.0, are used to calculate an effective ignition temperature. The results of the simulations are shown on the following pages.

Table 14.23: Properties of RISE Materials, mixture materials [304].

Material ^c	Δ (mm)	ρ $\left(\frac{\text{kg}}{\text{m}^3}\right)$	T_{ign}^a (°C)	ΔH_c $\left(\frac{\text{MJ}}{\text{kg}}\right)$	Y_s^b $\left(\frac{\text{g}}{\text{g}}\right)$	Test # (—)
80 Wool 20 Nylon, Glue, Plywood	22.0	576	275	14.3	0.050	1821-1829, 2206-2208
Carpet, Glue, Aluminum Plate	5.0	1293	300	17.7	0.050	1673-1678, 2178-2180
Carpet, Glue, Recor Sealing	10.0	222	436	22.2	0.050	1679, 1681, 1682, 1687-1692, 2181-2183, 2353-2355
Fabric Vandalize Protected, Foam	42.0	88	366	13.0	0.050	2385-2390
Fabric, Foam	28.0	164	514	19.2	0.050	1658, 1659, 1661, 1662, 1664-1666, 1668, 1669, 2222-2224, 2409-2411
Fabric, Protection Layer, Foam	32.0	124	348	14.8	0.050	1744-1749, 1751, 1753, 1754, 2216-2218, 2392- 2395, 2401, 2402
FR EPS, Calcium Silicate Board	25.0	37	547	25.4	0.190	137-145
HPL Melamine, Polyester Film	13.4	1638	195	3.2	0.050	1716-1718, 1720-1725, 2343-2345
Melamine, Calcium Silicate	12.5	1055	572	8.5	0.003	133-136
PE, XLPE	40.0	372	590	25.8	0.050	493-495
Polyolefin, EPR	18.1	278	547	19.9	0.050	414-416
Polyolefin, EPR	32.2	278	547	19.9	0.050	407, 409, 410
Polyolefin, PA	2.5	632	549	22.3	0.050	516-518
Polyolefin, PA	6.0	632	476	22.3	0.050	513-515
Polyolefin, PP	8.7	513	493	25.7	0.050	446-448
Polyolefin, XLPE	18.1	392	556	28.4	0.050	473-475
Polyolefin, XLPE	25.0	392	553	28.4	0.050	484-486
Polyolefin, XLPE	38.1	392	552	28.4	0.050	455-457
Polyolefin, XLPE	45.0	392	552	28.4	0.050	464-466
Pur Rigid, Plastic Faced Steel Sheet	79.0	170	497	10.2	0.072	80-85

^a T_{ign} is calculated based on measured times to ignition. Assumed values used for thermal properties when not measured.

^b Y_s fixed at 0.05 when measurements were not available.

^c Comma separation indicates layers of material.

Table 14.24: Properties of RISE Materials, mixture materials [304].

Material ^c	Δ (mm)	ρ $\left(\frac{\text{kg}}{\text{m}^3}\right)$	T_{ign}^a (°C)	ΔH_c $\left(\frac{\text{MJ}}{\text{kg}}\right)$	Y_s^b $\left(\frac{\text{g}}{\text{g}}\right)$	Test # (—)
PVC, EPR	32.5	170	508	13.9	0.050	411-413
PVC, XLPE	17.7	405	341	22.4	0.050	467-469
PVC, XLPE	22.0	405	341	22.4	0.050	477-479
PVC, XLPE	35.0	405	341	22.4	0.050	490-492
PVC, XLPE	38.6	405	342	22.4	0.050	449-451
PVC, XLPE	46.0	405	341	22.4	0.050	458-460
RPPVC, EPR	16.5	618	389	11.5	0.050	417-419
RPPVC, PEF	4.5	531	404	5.1	0.050	487-489
RPPVC, PVC	14.0	478	413	13.8	0.050	528-530
RPPVC, XLPE	17.7	429	463	19.0	0.050	470-472
RPPVC, XLPE	22.5	429	461	19.0	0.050	480-482
RPPVC, XLPE	39.3	429	462	19.0	0.050	452-454
RPPVC, XLPE	45.0	429	462	19.0	0.050	461-463
Synthetic Rubber, Glue, Plywood	15.0	1096	435	15.0	0.050	1806, 1808-1811, 1813-1820, 1830-1838, 2202-2204, 2209-2211, 2380-2382
Zhpolyolefin, PP	8.4	509	561	29.0	0.050	608-610
Zhpolyolefin, XLPE	13.0	412	528	27.3	0.050	499-501
Zhpolyolefin, XLPE	27.0	412	527	27.3	0.050	496-498

^a T_{ign} is calculated based on measured times to ignition. Assumed values used for thermal properties when not measured.

^b Y_s fixed at 0.05 when measurements were not available.

^c Comma separation indicates layers of material.

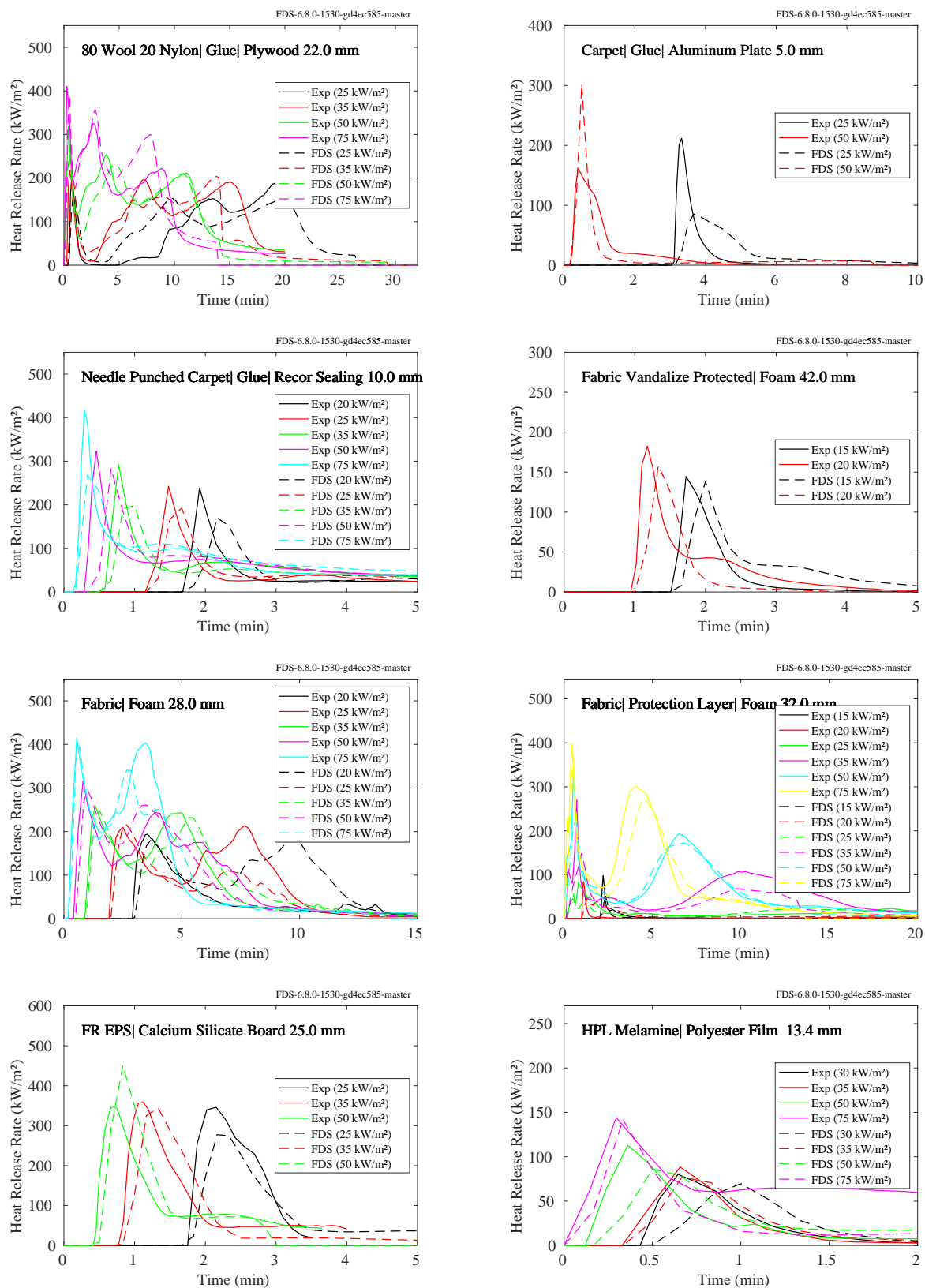


Figure 14.60: RISE, mixture materials - Comparison of predicted and measured heat release rate per unit area using scaling-based approach for cone calorimeter experiments.

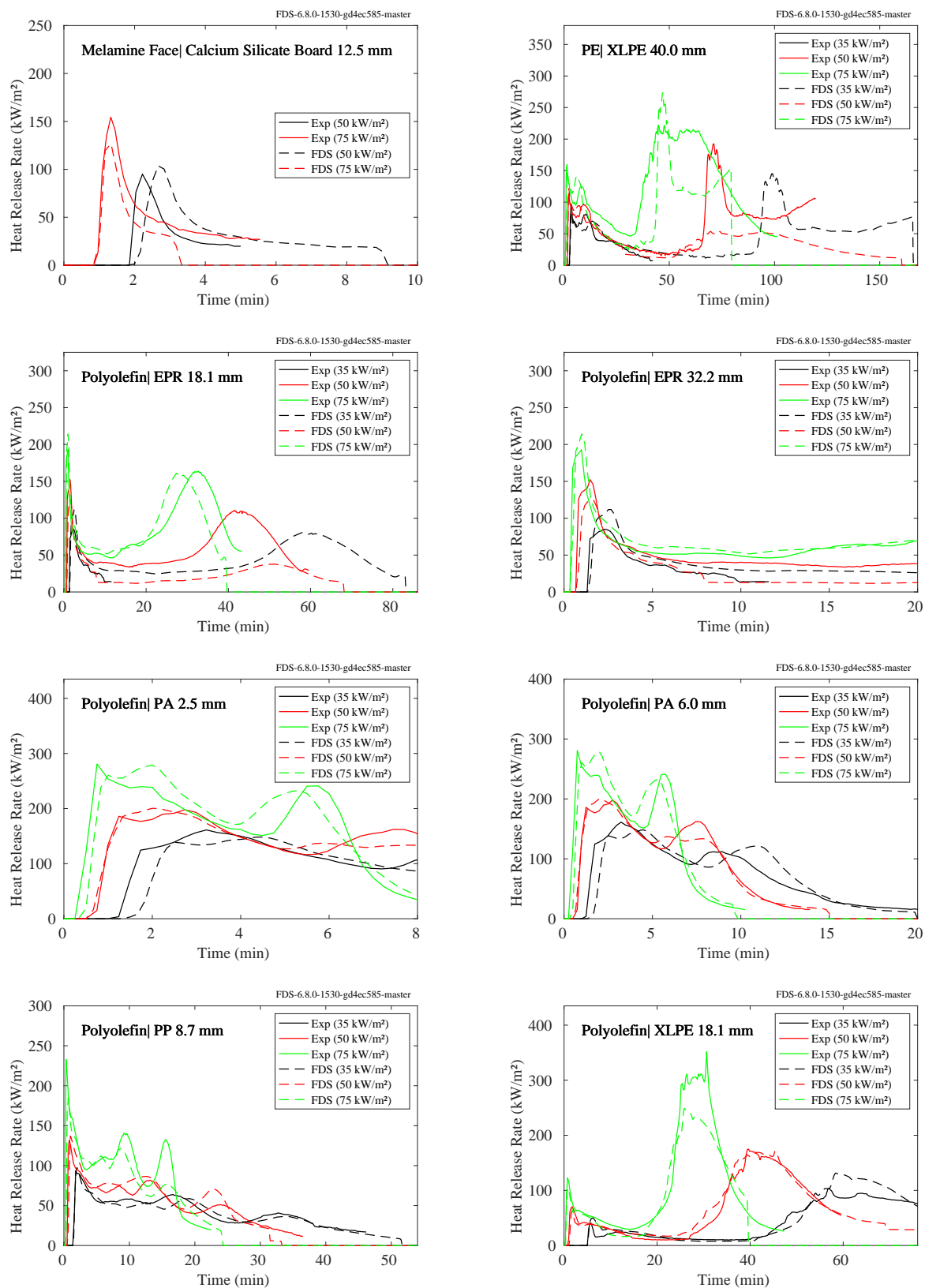


Figure 14.61: RISE, mixture materials - Comparison of predicted and measured heat release rate per unit area using scaling-based approach for cone calorimeter experiments.

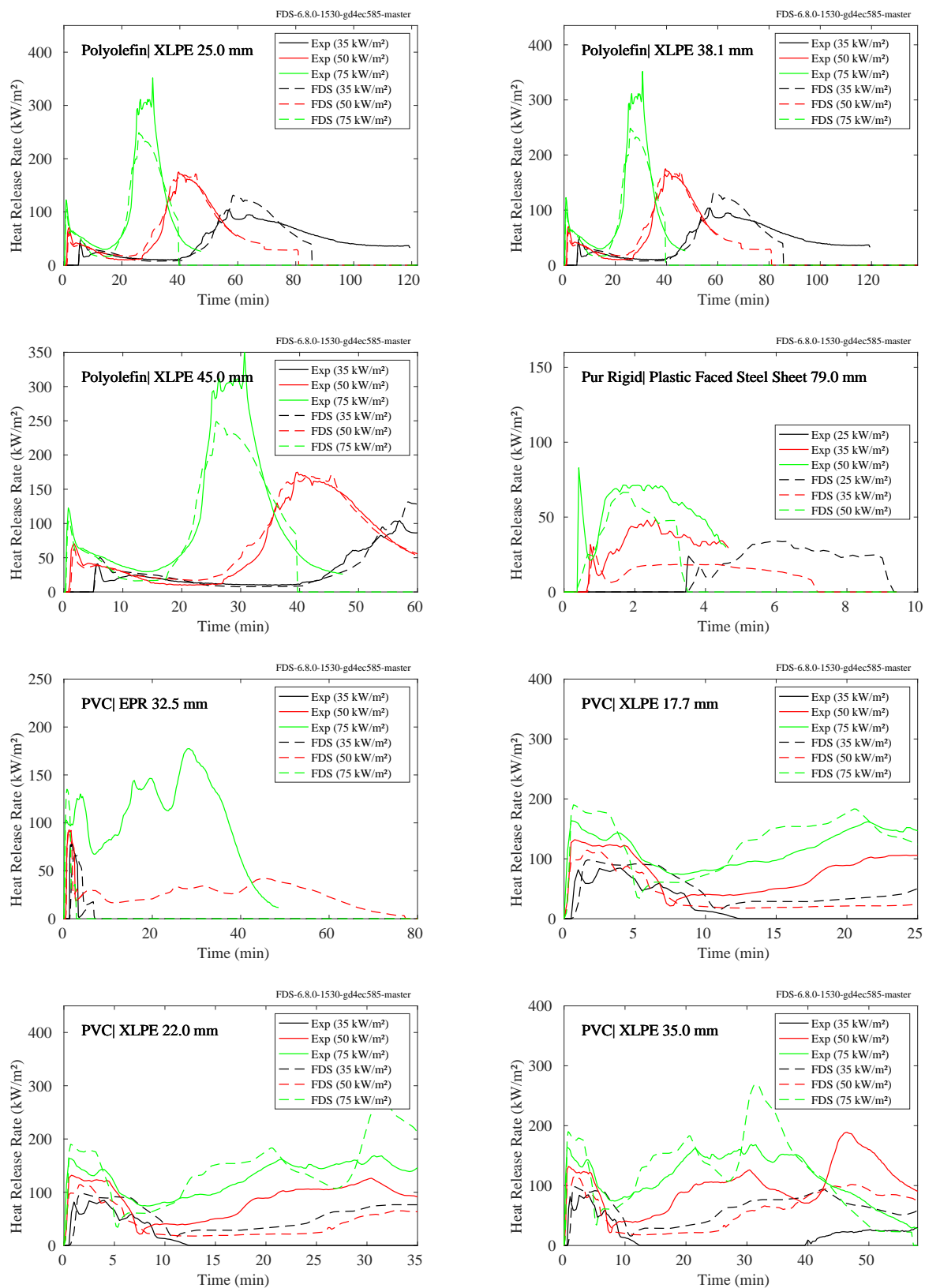


Figure 14.62: RISE, mixture materials - Comparison of predicted and measured heat release rate per unit area using scaling-based approach for cone calorimeter experiments.

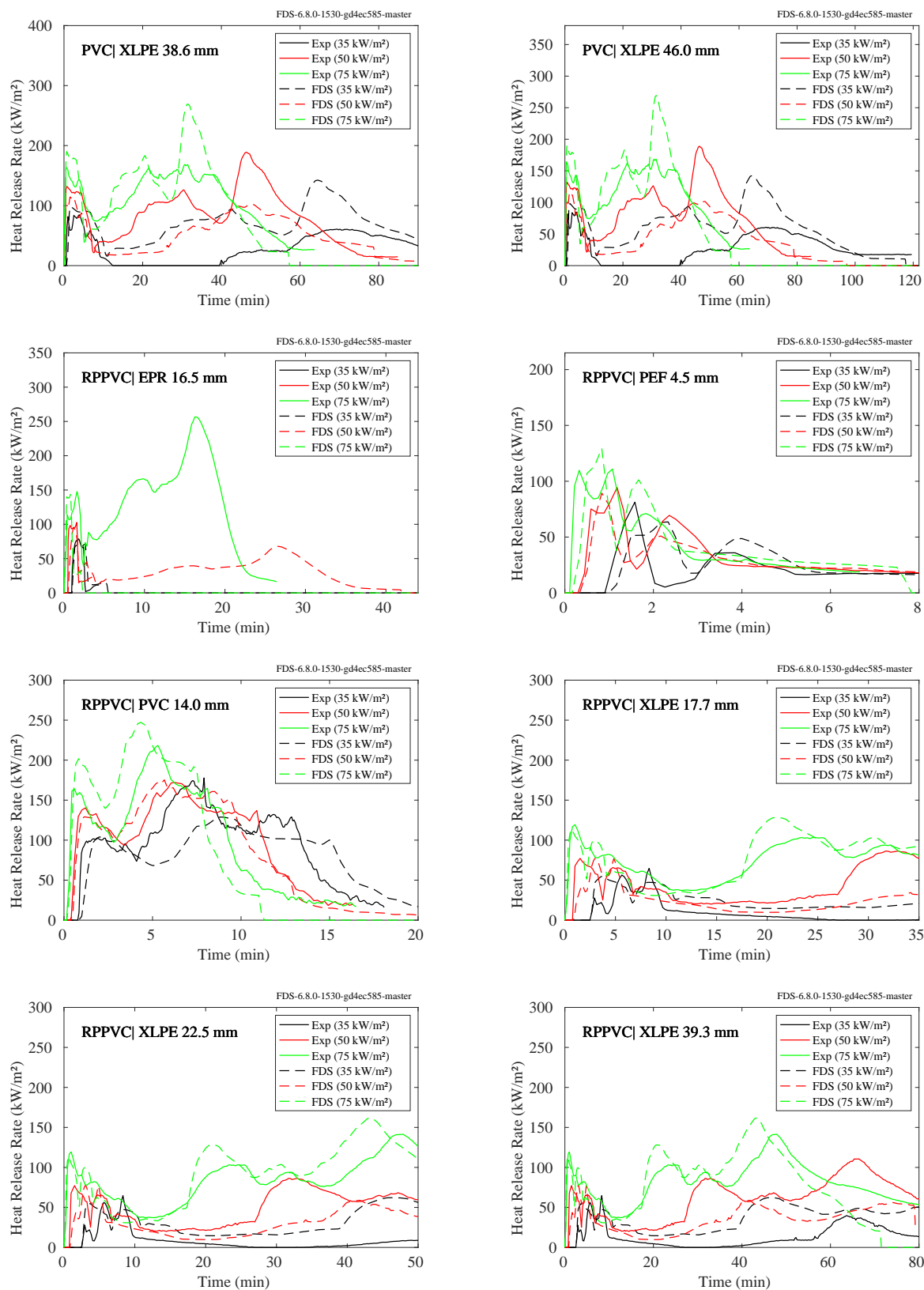


Figure 14.63: RISE, mixture materials - Comparison of predicted and measured heat release rate per unit area using scaling-based approach for cone calorimeter experiments.

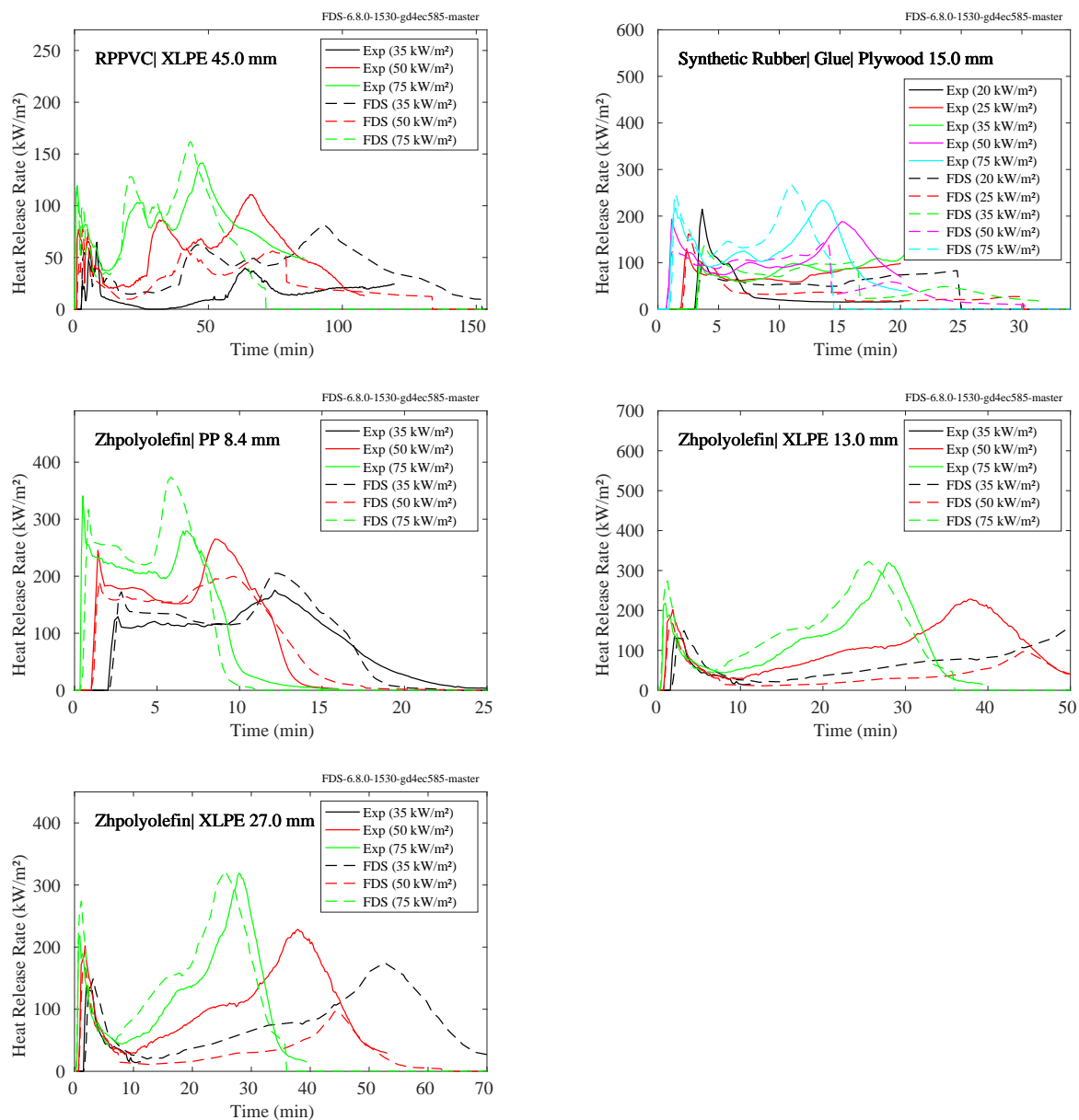


Figure 14.64: RISE, mixture materials - Comparison of predicted and measured heat release rate per unit area using scaling-based approach for cone calorimeter experiments.

Table 14.25: Properties of RISE Materials, other materials [304].

Material	Δ (mm)	ρ $\left(\frac{\text{kg}}{\text{m}^3}\right)$	T_{ign}^a (°C)	ΔH_c $\left(\frac{\text{MJ}}{\text{kg}}\right)$	Y_s^b $\left(\frac{\text{g}}{\text{g}}\right)$	Test # (—)
Aluminium Honey Comb Coated With HPL	22.7	514	537	17.3	0.050	1785-1793, 2362-2364
HPL Compact	4.0	1610	500	13.8	0.050	1695-1699, 1701-1705, 2184-2186
Wool Fabric Mixed Fabric	0.5	910	409	19.3	0.050	1776-1784, 2193-2195, 2356-2361

^a T_{ign} is calculated based on measured times to ignition. Assumed values used for thermal properties when not measured.

^b Y_s fixed at 0.05 when measurements were not available.

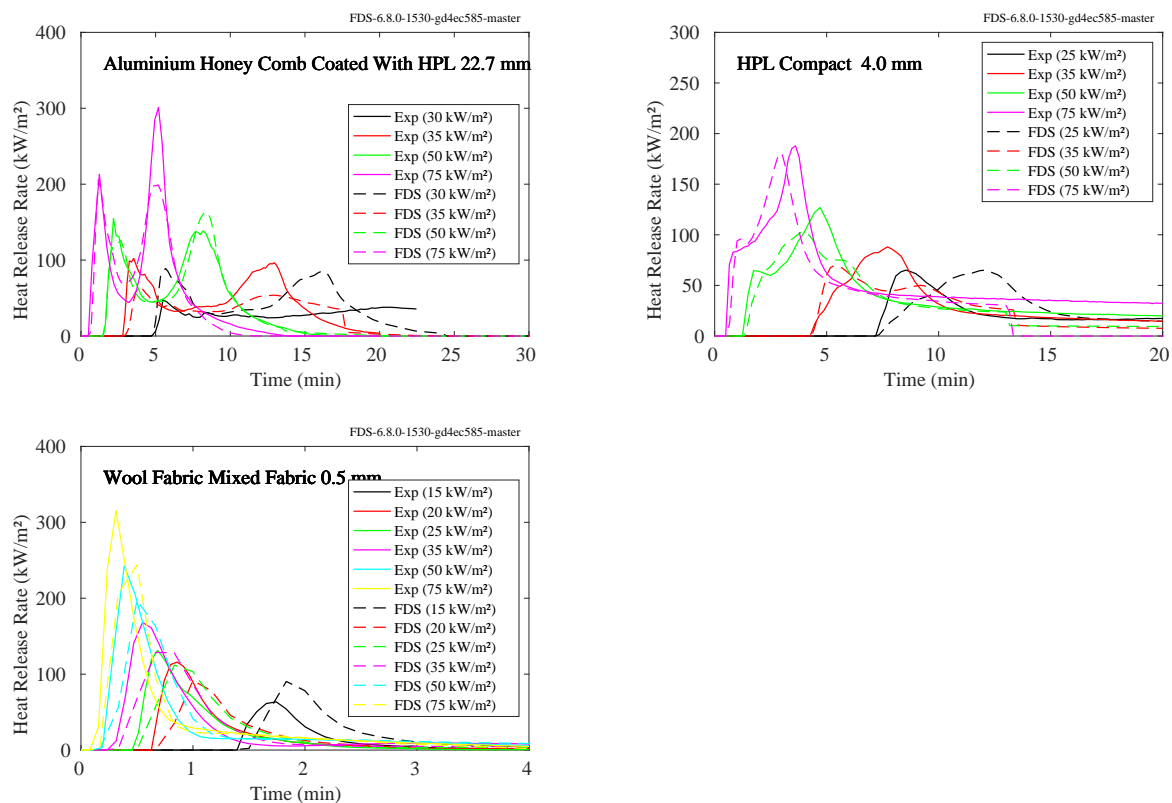


Figure 14.65: RISE, other materials - Comparison of predicted and measured heat release rate per unit area using scaling-based approach for cone calorimeter experiments.

Table 14.26: Properties of RISE Materials, polymer materials [304].

Material ^c	Δ (mm)	ρ $\left(\frac{\text{kg}}{\text{m}^3}\right)$	T_{ign}^a (°C)	ΔH_c $\left(\frac{\text{MJ}}{\text{kg}}\right)$	Y_s^b $\left(\frac{\text{g}}{\text{g}}\right)$	Test # (—)
FR Polycarbonate	16.0	175	584	21.5	0.080	240, 244, 248, 251
Paint GFK Polyester With Gel-coat Laminated	4.8	2022	355	10.5	0.050	1726-1734, 2336-2338
Paint GRP Polyester With Gel-coat Laminated	4.8	2019	334	5.5	0.050	2173-2175, 2340-2342
Polyester	2.1	408	604	23.6	0.050	543-545
Polyolefin	2.9	472	649	23.8	0.050	510-512
PVC	2.9	560	388	13.1	0.050	537-539
PVC, PVC	10.0	500	290	13.3	0.050	503-505
PVC, PVC	14.5	500	291	13.3	0.050	525-527
PVC, PVC	18.0	500	292	13.3	0.050	506, 507, 509
PVC, PVC	21.4	500	291	13.3	0.050	420-422
PVC, PVC	8.2	500	292	13.3	0.050	436-438
PVC, PVC	9.4	500	290	13.3	0.050	423-425
PVDF	1.9	410	645	19.8	0.050	540-542
RPPVC	2.9	542	411	13.0	0.050	433-435
Solid Acrylic	12.3	1903	456	15.1	0.050	1794-1798, 1800, 1801, 1804, 1805, 2199-2201
Transparent Polycarbonate	2.3	1579	528	13.2	0.050	1707, 1708, 1710-1715, 2187-2189

^a T_{ign} is calculated based on measured times to ignition. Assumed values used for thermal properties when not measured.

^b Y_s fixed at 0.05 when measurements were not available.

^c Comma separation indicates layers of material.

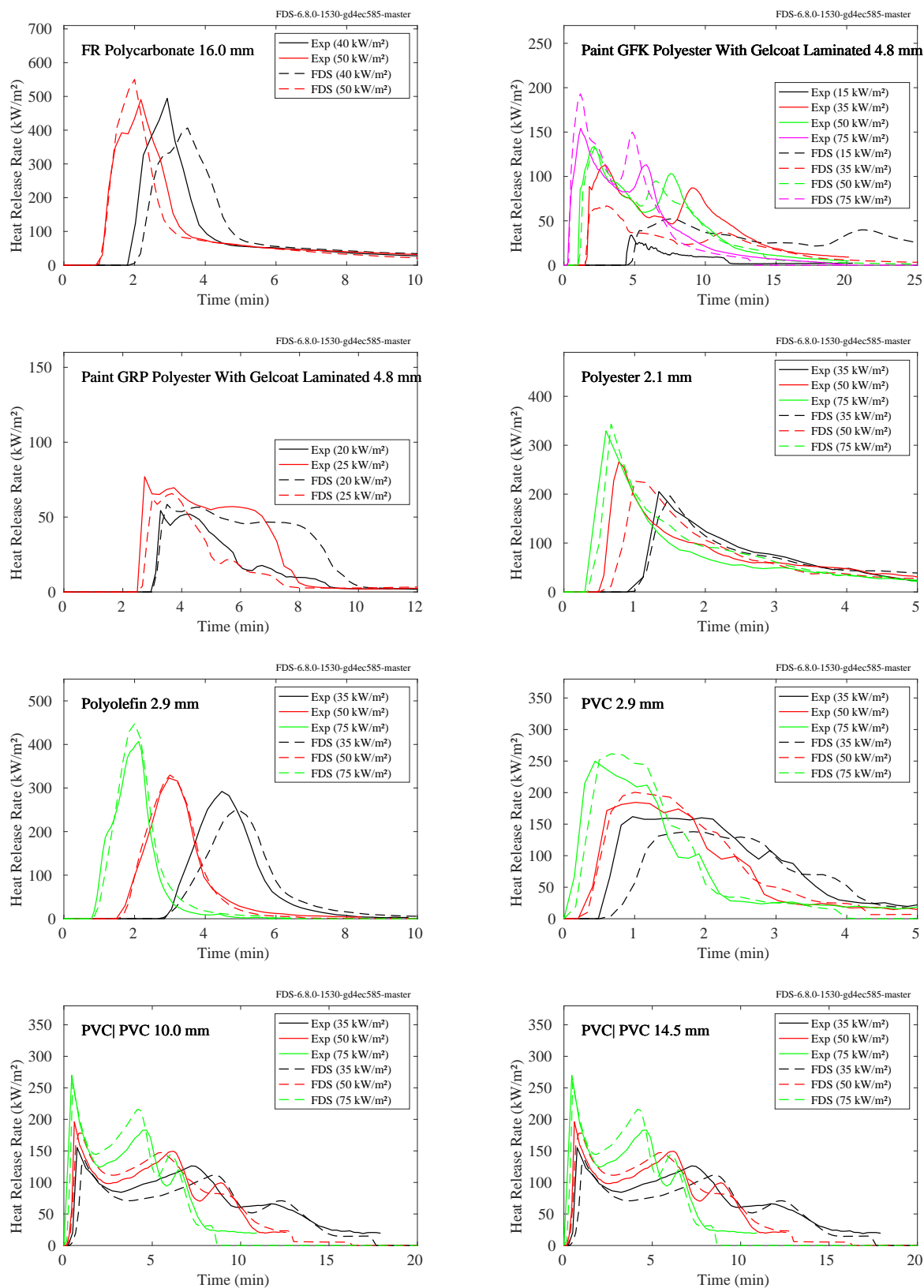


Figure 14.66: RISE, polymer materials - Comparison of predicted and measured heat release rate per unit area using scaling-based approach for cone calorimeter experiments.

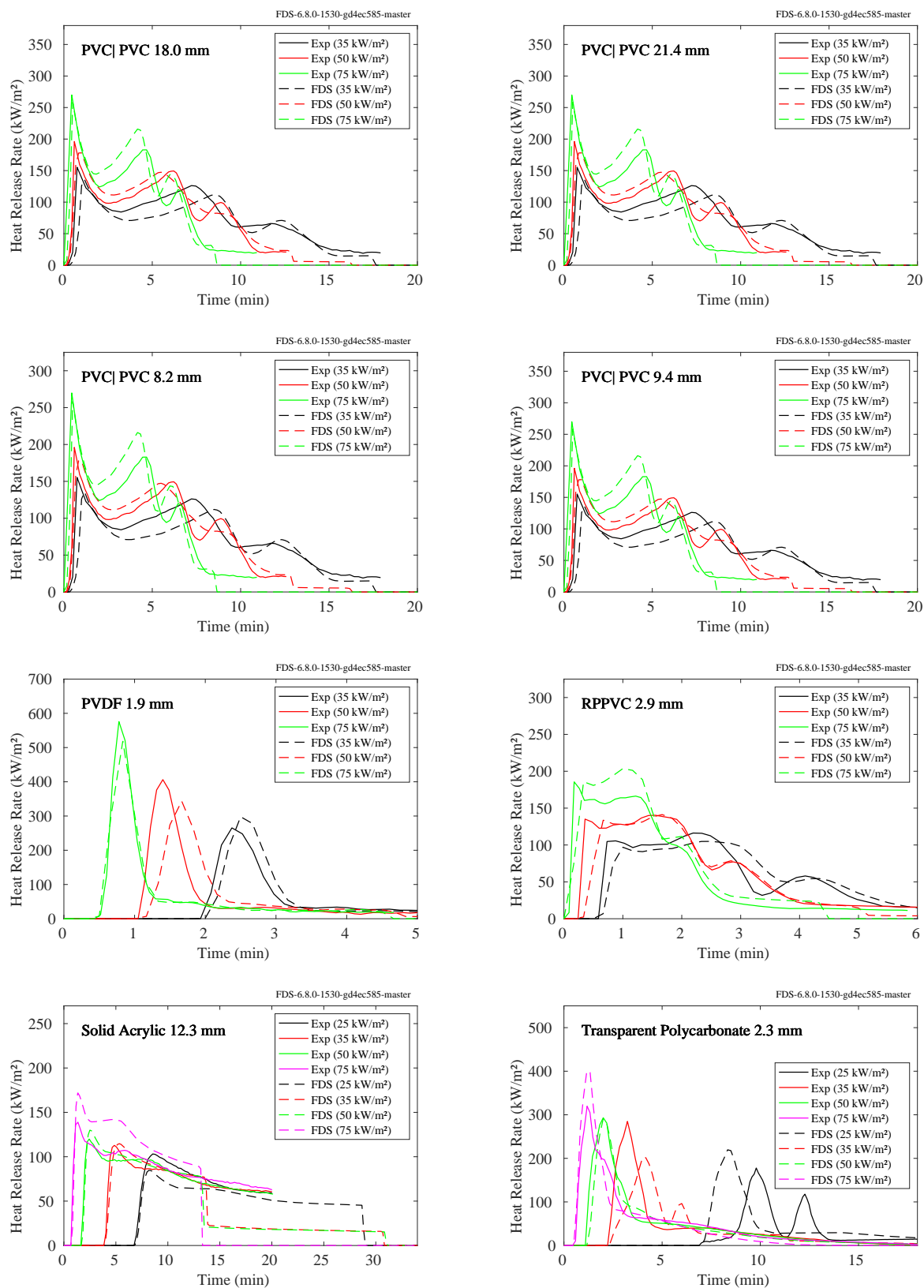


Figure 14.67: RISE, polymer materials - Comparison of predicted and measured heat release rate per unit area using scaling-based approach for cone calorimeter experiments.

Table 14.27: Properties of RISE Materials, Wood-Based materials [304].

Material	Δ (mm)	ρ $\left(\frac{\text{kg}}{\text{m}^3}\right)$	T_{ign}^a (°C)	ΔH_c $\left(\frac{\text{MJ}}{\text{kg}}\right)$	Y_s^b $\left(\frac{\text{g}}{\text{g}}\right)$	Test # (—)
FR Particle Board	12.0	517	364	7.4	0.049	158-161
FR Particle Board	16.0	517	368	7.4	0.049	146-151, 72, 73
FR Particle Board	79.0	517	381	7.4	0.049	162-167
MDF Board	12.0	700	424	12.2	0.007	241, 243, 246, 249
Spruce	10.0	450	297	12.5	0.007	245, 247, 250

^a T_{ign} is calculated based on measured times to ignition. Assumed values used for thermal properties when not measured.

^b Y_s fixed at 0.05 when measurements were not available.

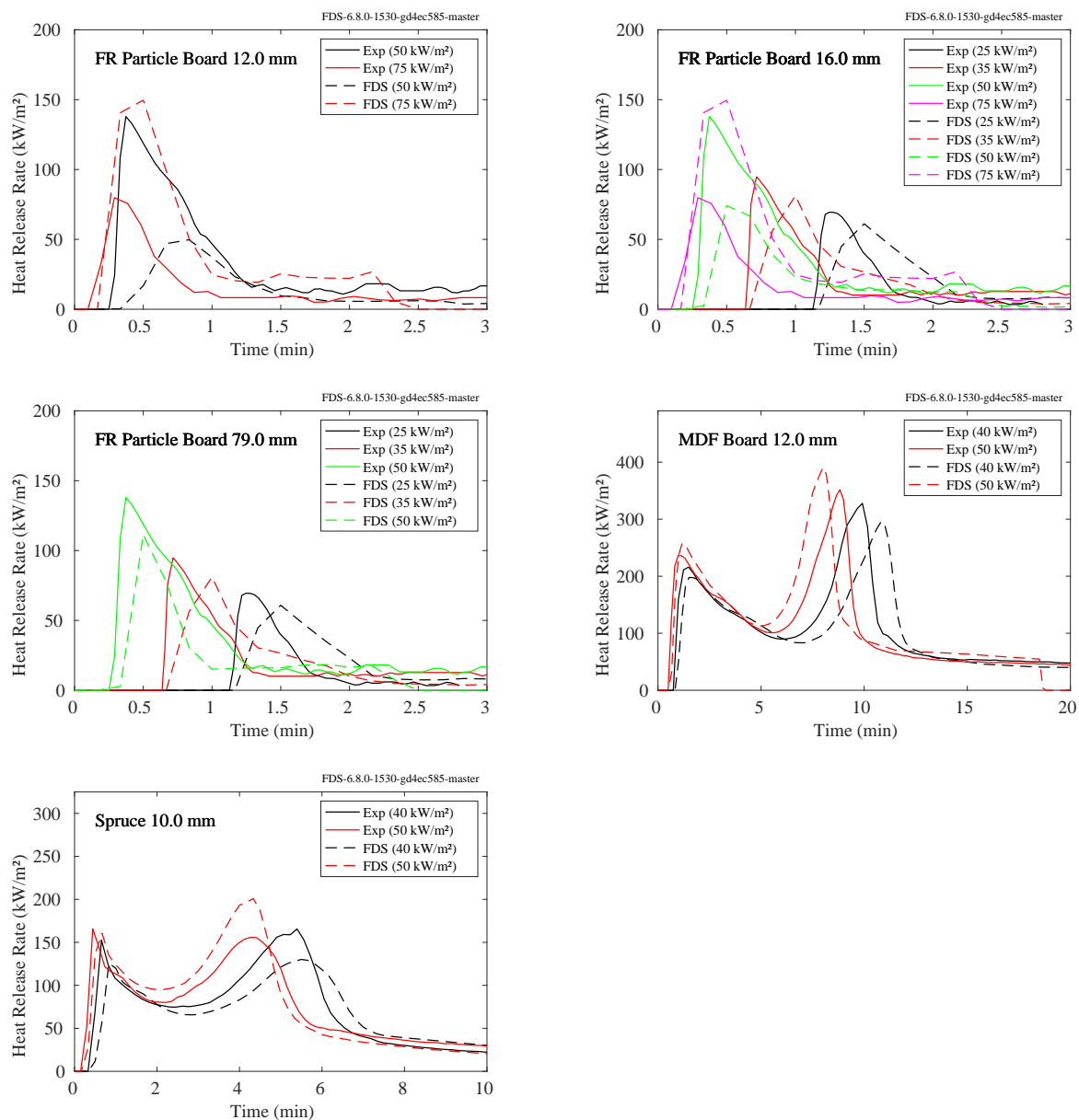


Figure 14.68: RISE, wood-based materials - Comparison of predicted and measured heat release rate per unit area using scaling-based approach for cone calorimeter experiments.

14.9 Compartment Fires

This section evaluates the performance of FDS in predicting the growth of a fire in an enclosure for well characterized materials. Measurements and predictions of HRR in each test configuration are compared.

In the U.S., the NFPA 286 room-corner test is the common standard large scale test used to measure the contribution of interior finish materials on fire growth and regulate the use of interior finish in certain building occupancies. The room is 2.4 m wide by 3.6 m long by 2.4 m high, and has a doorway 2 m (79.5 in) in height and 0.78 m (37.5 in) in width. The lining materials are installed on ceiling and walls. A propane gas burner measuring 0.3 m x 0.3 m is placed in one of the back corners, in contact with the walls. The HRR for the burner is 40 kW for 5 minutes, and then 160 kW for 10 minutes.

Many of these cases are in the NFPA 286/ISO 9705 room-corner configuration (or a modification thereof).

14.9.1 JH/FRA Reduced Scale Compartment Experiments

The Federal Railroad Administration (FRA) in the U.S. sponsored a series of small to intermediate-scale enclosure experiments to evaluate the impact of modern materials on HRRs in fully-developed railcar fires. The following pages compare FDS predictions of room-corner testing of scaled compartments.

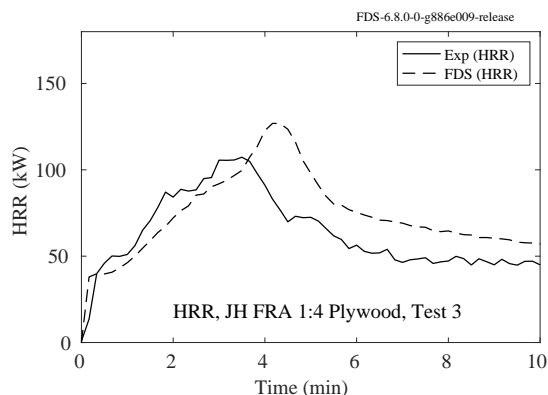


Figure 14.69: JH/FRA experiments, HRR, 1:4 scale plywood half lining configuration, Test 3.

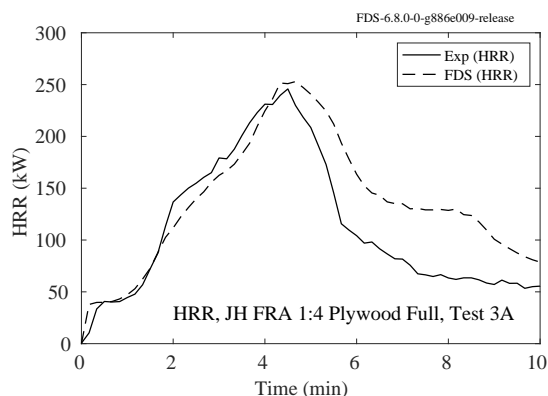


Figure 14.70: JH/FRA experiments, HRR, 1:4 scale plywood full lining configuration, Test 3A.

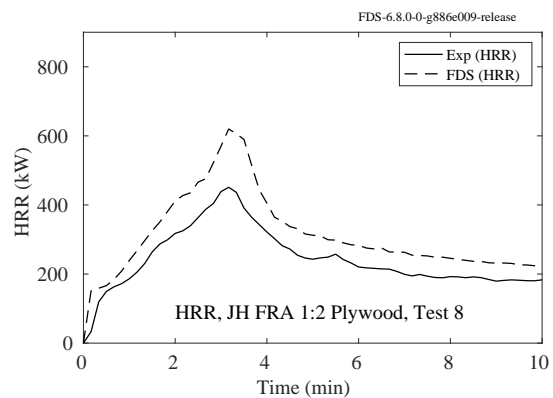


Figure 14.71: JH/FRA experiments, HRR, 1:2 scale plywood half lining configuration, Test 8.

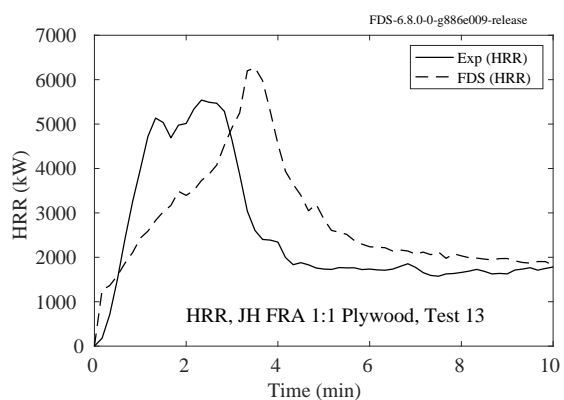


Figure 14.72: JH/FRA experiments, HRR, 1:2 scale plywood half lining configuration, Test 13.

14.10 Wildland Fire Burning and Spread Rates

The following sections present examples of fire spread through vegetation, both small and full-scale. Summary plots of burning and spread rates are presented in Figs. 14.125 and 14.128.

14.10.1 Crown Fires

This section presents the rate of spread for simulations of crown fires. For a description of the experiments and simulations, see Sec. 3.14. The experimental data consists of 57 observed crown fires. The simulations are performed with comparable conditions, but not all input parameters can be gleaned from the experimental reports. Thus, the comparison is largely qualitative, and has not been quantified in any way other than the comparison plot in Fig. 14.73.

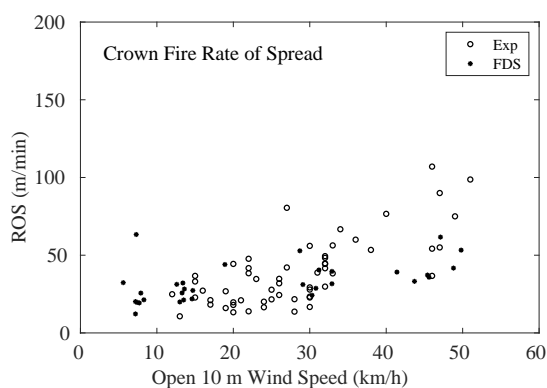


Figure 14.73: Comparison observed and predicted rates of spread for a variety of crown fires.

14.10.2 CSIRO Grassland Fires

This section presents the rate of spread for simulations of two of the CSIRO Grassland Fire experiments. For details of the experiments and simulations, see Sec. 3.15. The first experiment, C064, was conducted on a 100 m by 100 m plot; the second, F19, was conducted on a 200 m by 200 m plot. The results of the simulations are shown in Fig. 14.74. The fire front in the FDS simulations is defined as the location of the maximum gas temperature in a 1 m wide, 1 m tall strip along the centerline of the grass field. The experimental points were determined from aerial photography.

For each case, we perform simulations with three different fuel models—one using Lagrangian particles to represent the vegetation, one using the Boundary Fuel Model (BFM), and the other using Rothermel-Albini fuel models in a level set fire spread simulation. For each fuel model, we also run at three different grid resolutions, as indicated in the plots in Fig. 14.74. The Lagrangian particle and Boundary Fuel Model require higher grid resolution $\delta x = [1, 0.5, 0.25]$ m. The level set simulations are designed for relatively coarse grids, in this case we run at $\delta x = [20, 10, 5]$ m.

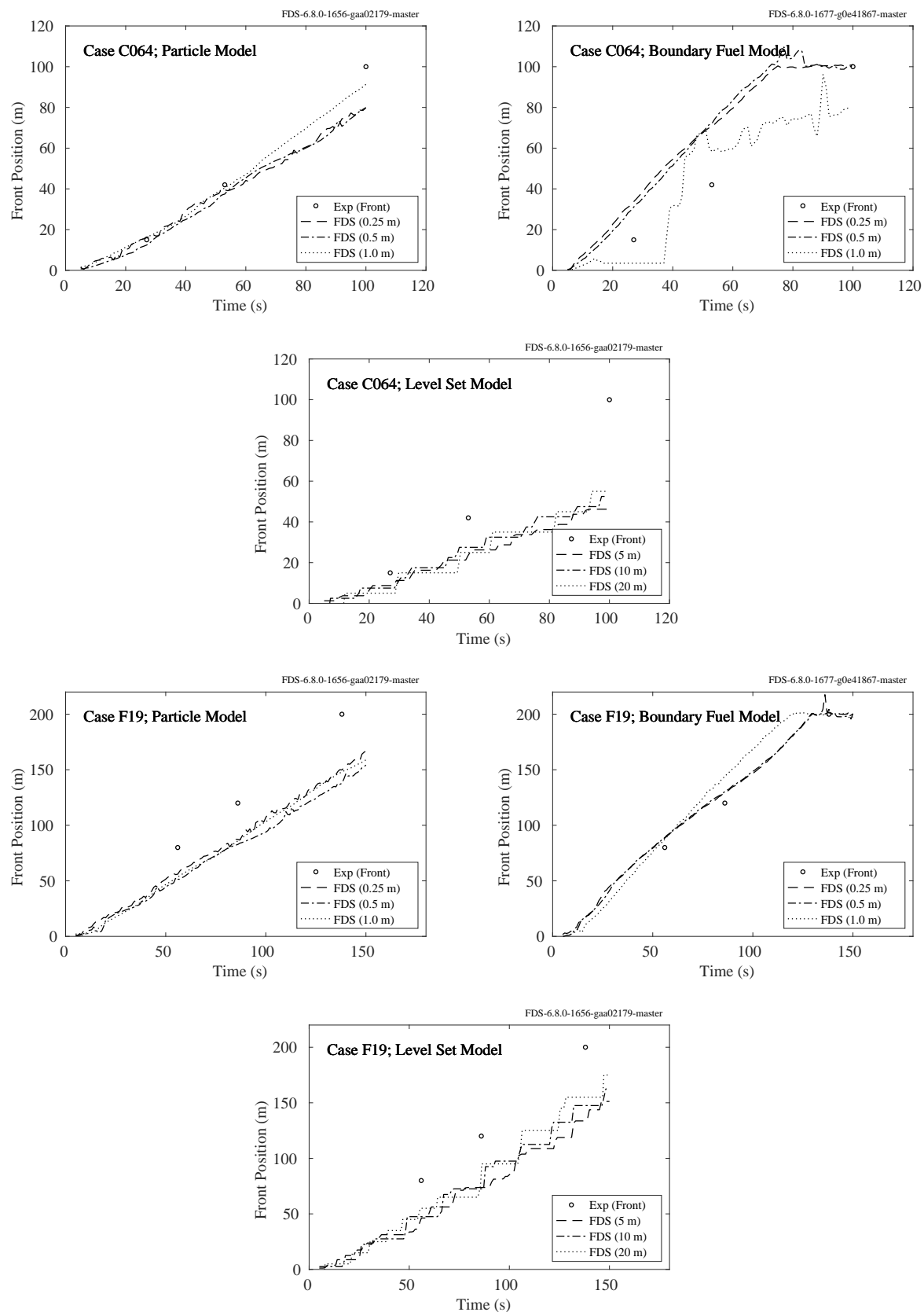


Figure 14.74: Comparison of the measured and predicted fire front position for the CSIRO Grassland Fires using three different methods of fire spread.

14.10.3 USFS/Catchpole Experiments

Figures 14.75 through 14.119 present the results of 354 simulations of the USFS/Catchpole experiments. A brief description is given in Sec. 3.96. The paper by Catchpole et al. [336] reports a single rate of spread for each experiment, which is depicted in the figures as a straight black line. The rate of spread of the simulations was calculated by fitting the best line through the data points over a time interval between 10 % and 90 % of the observed transit time of the real fire over the 8 m fuel bed. The red dashed line is the best fit line from which the rate of spread is taken.

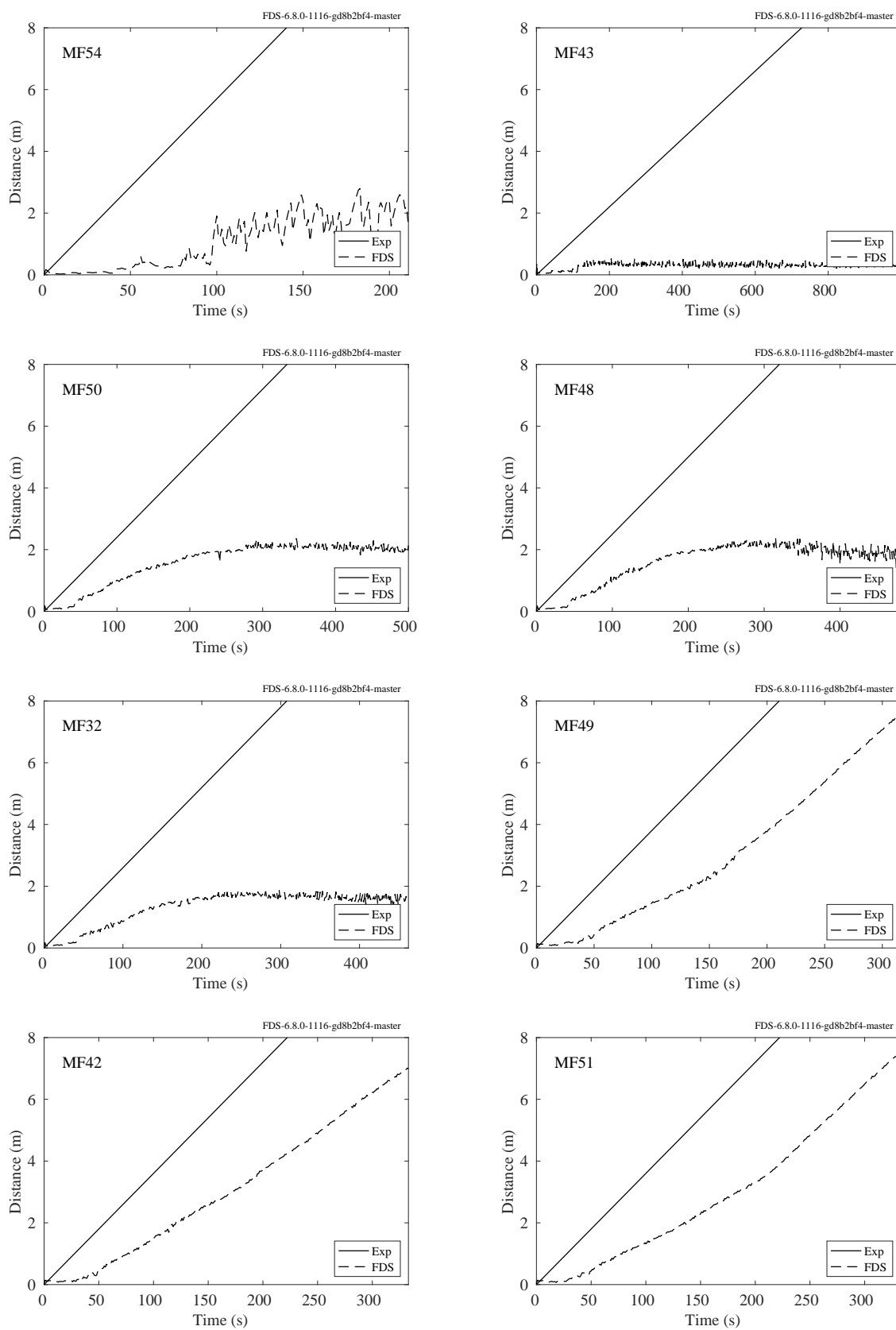


Figure 14.75: Flame front, USFS/Catchpole experiments

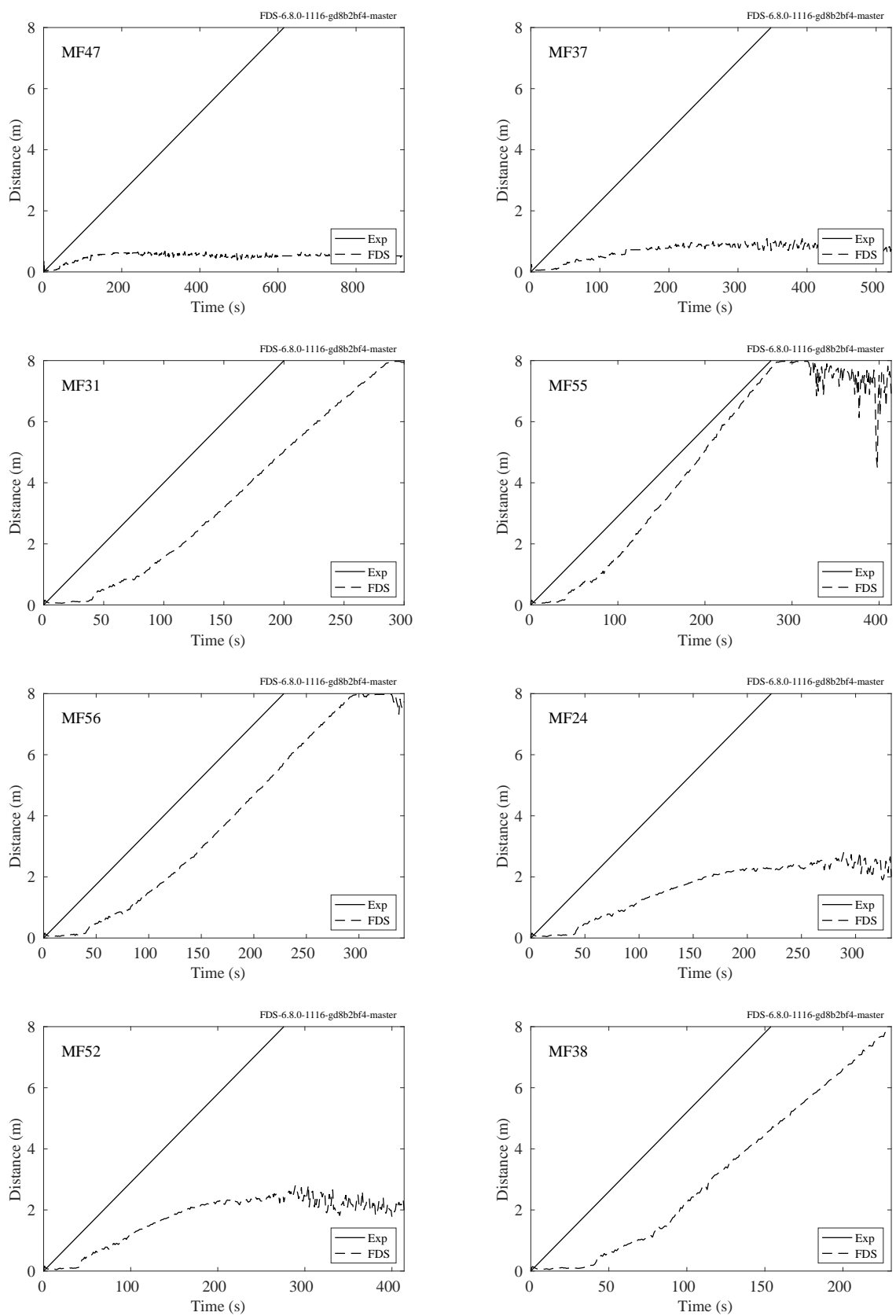


Figure 14.76: Flame front, USFS/Catchpole experiments

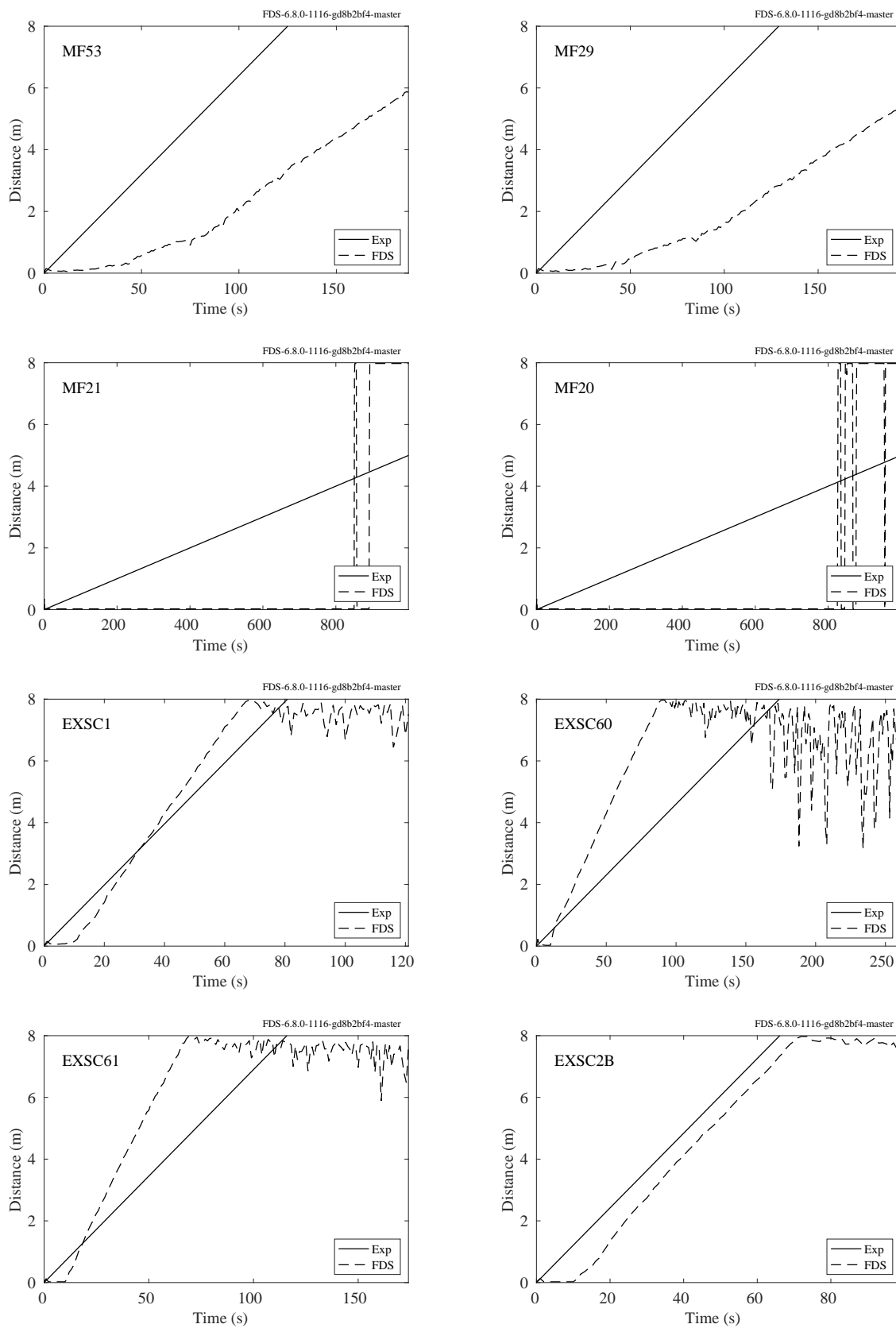


Figure 14.77: Flame front, USFS/Catchpole experiments

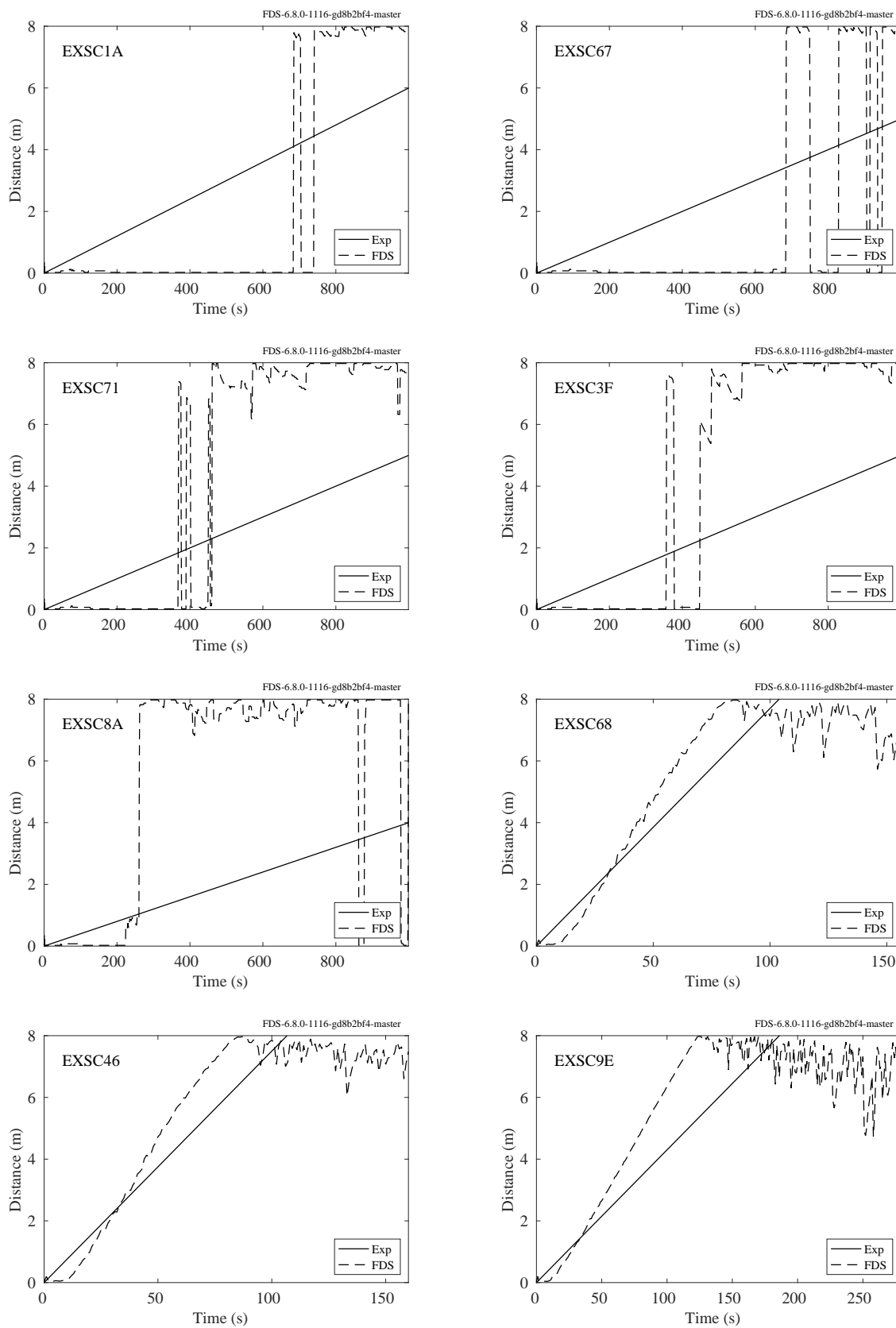


Figure 14.78: Flame front, USFS/Catchpole experiments

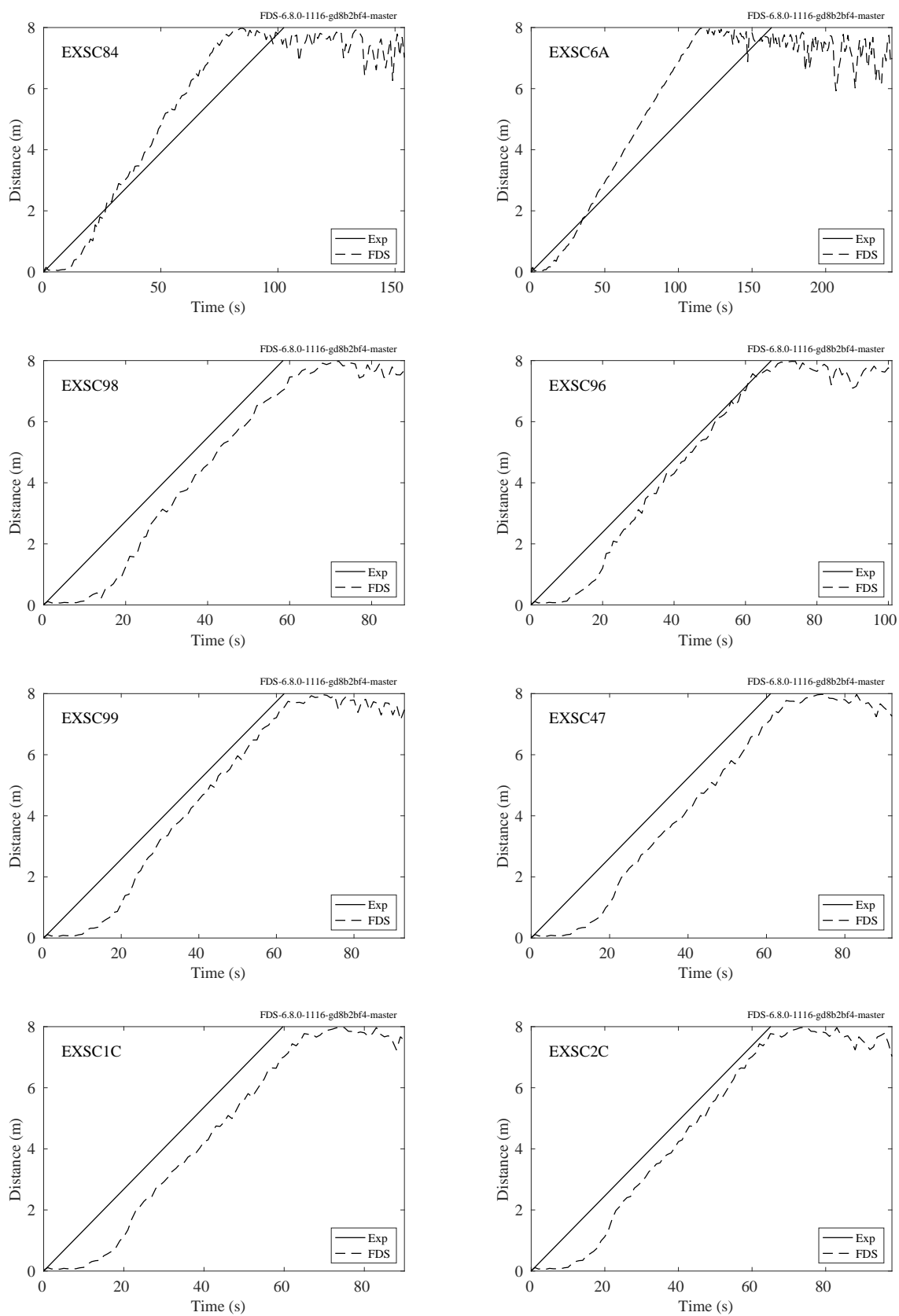


Figure 14.79: Flame front, USFS/Catchpole experiments

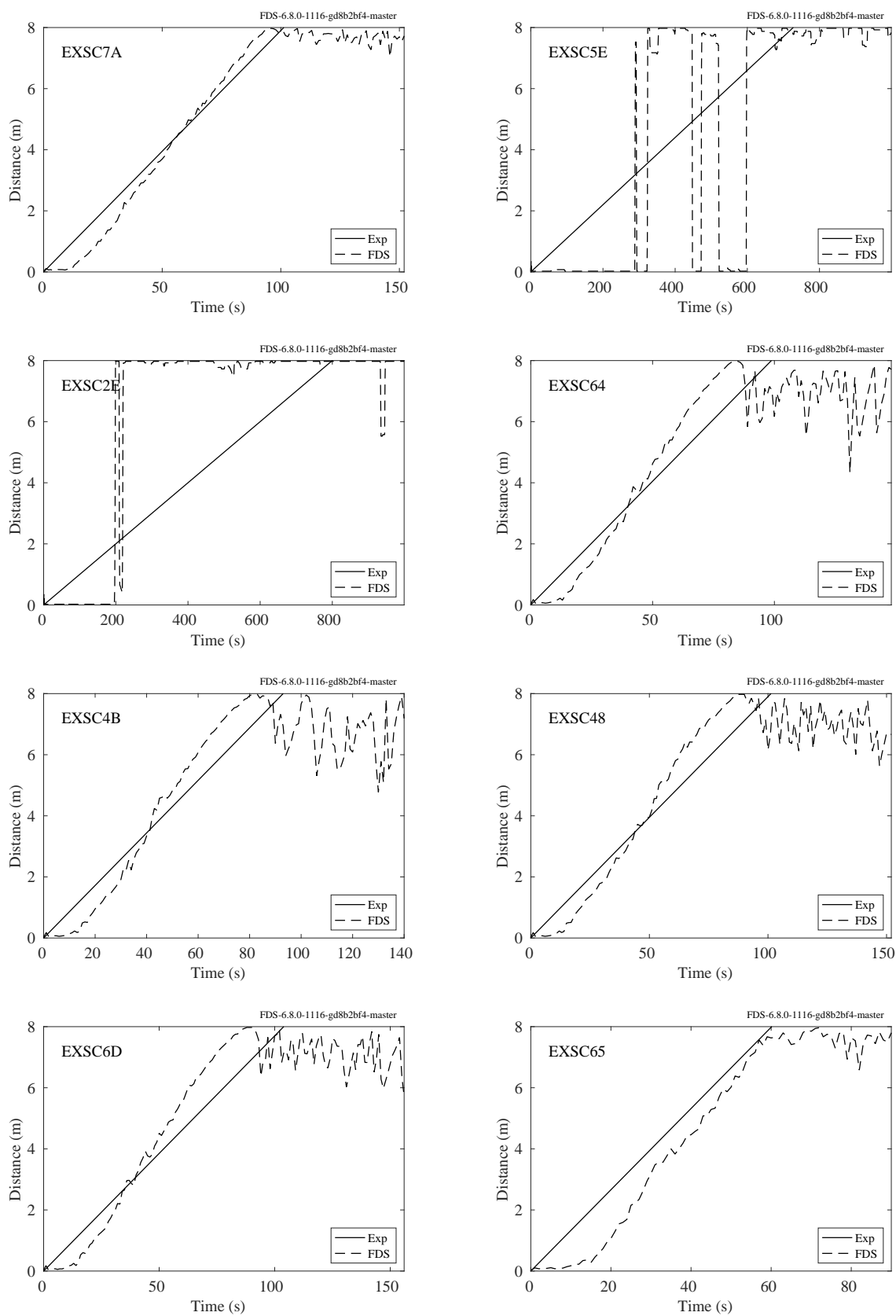


Figure 14.80: Flame front, USFS/Catchpole experiments

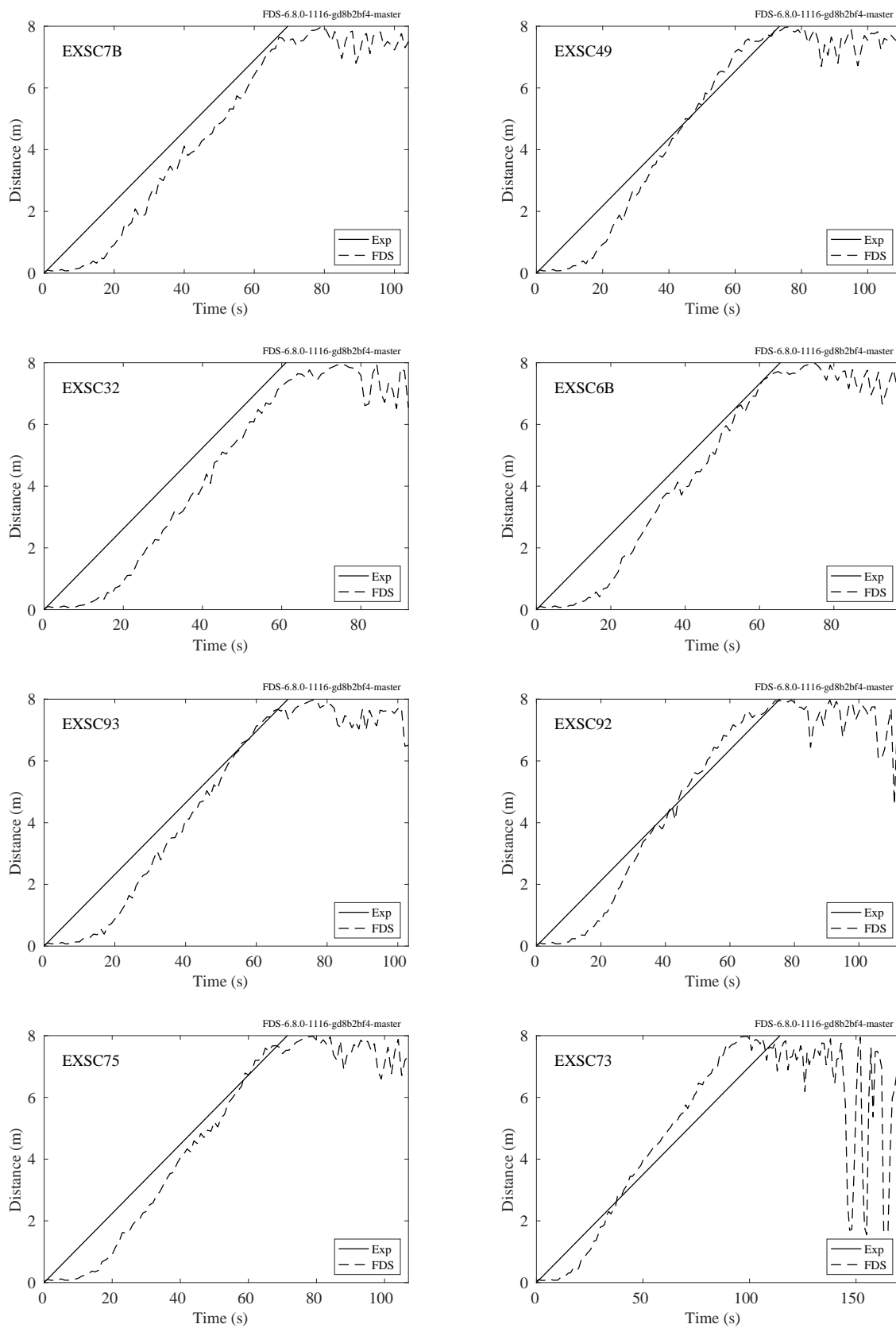


Figure 14.81: Flame front, USFS/Catchpole experiments

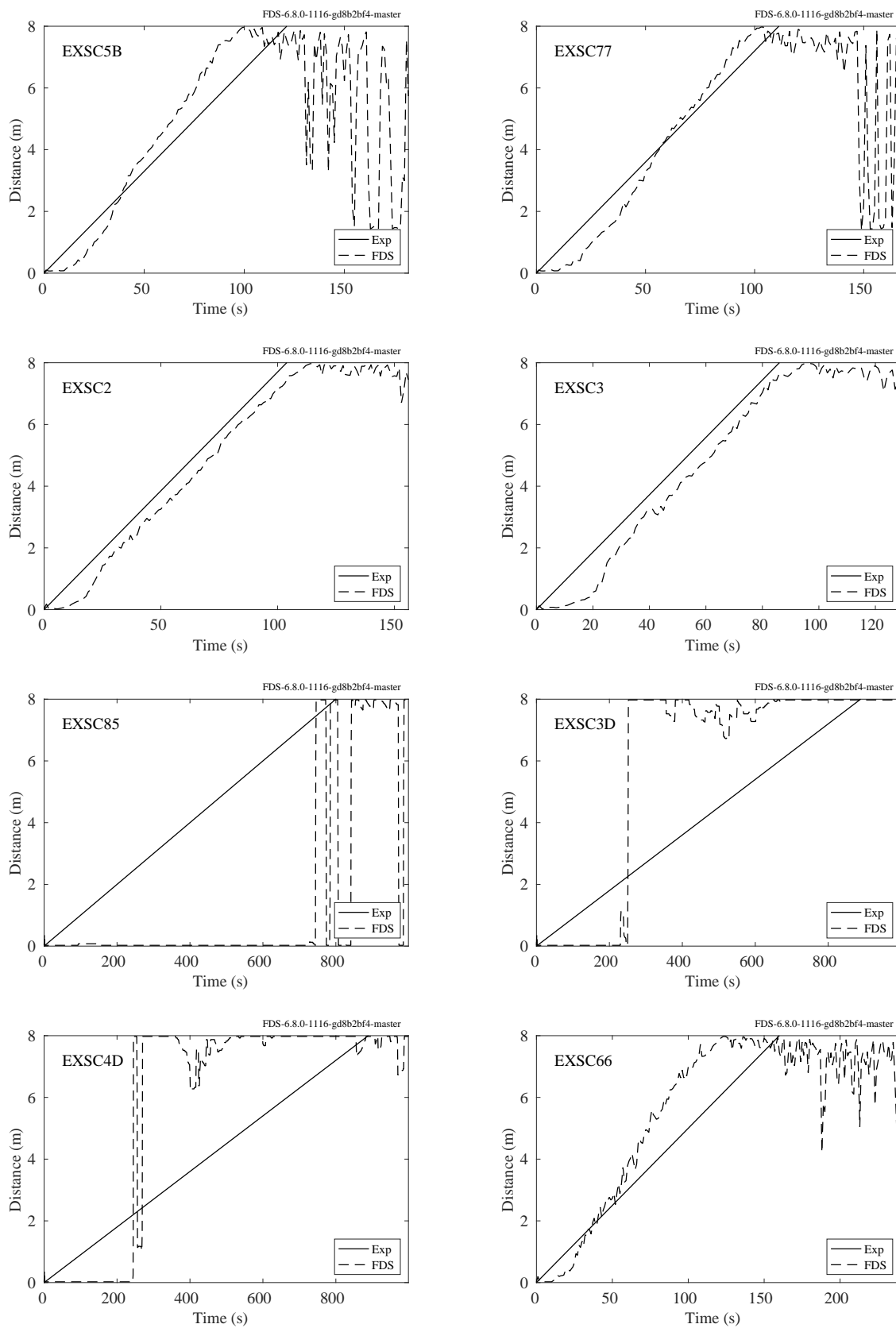


Figure 14.82: Flame front, USFS/Catchpole experiments

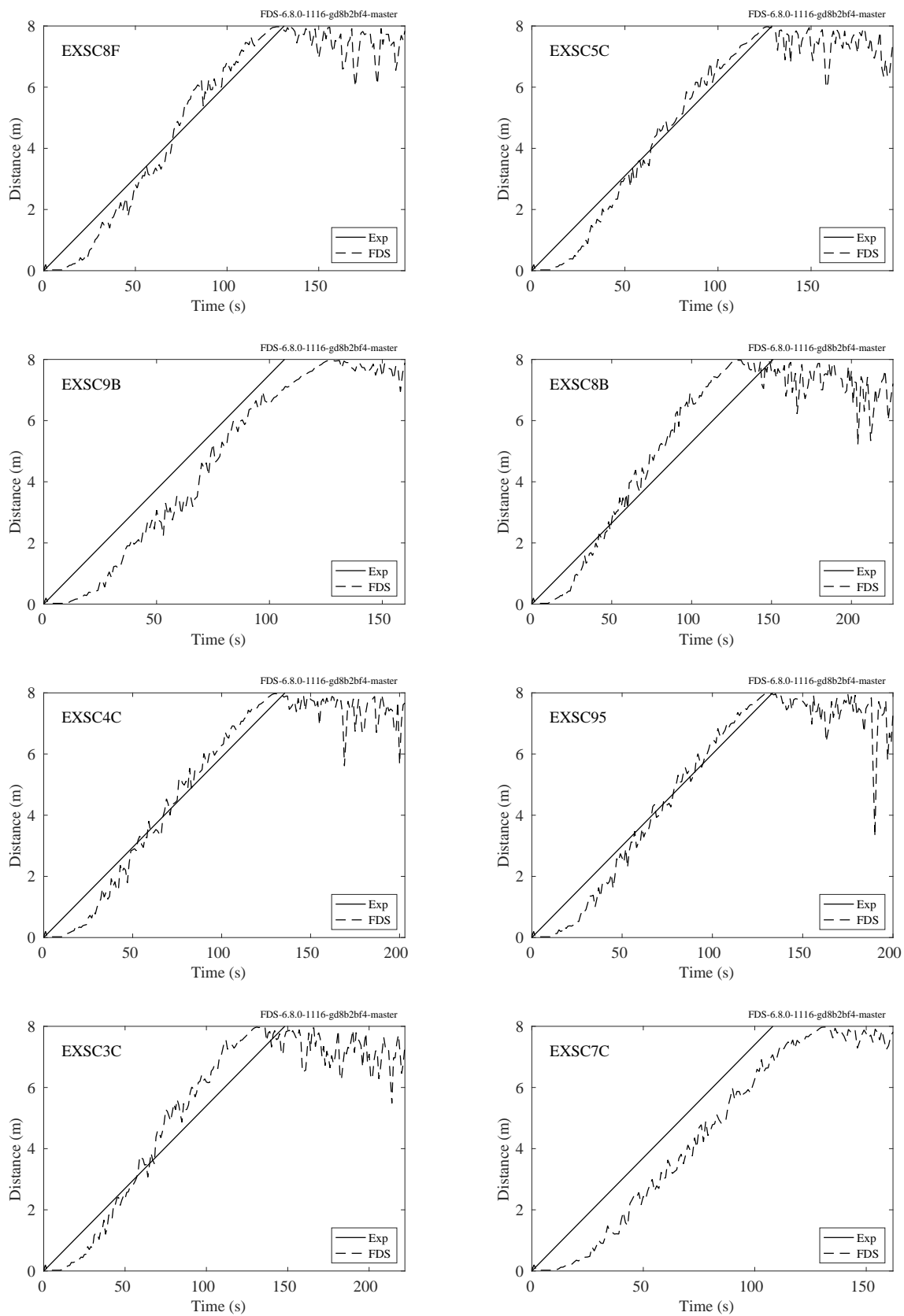


Figure 14.83: Flame front, USFS/Catchpole experiments